

Lecture Notes in Electrical Engineering 632

Ahmad Nor Kasruddin Nasir · Mohd Ashraf Ahmad ·  
Muhammad Sharfi Najib · Yasmin Abdul Wahab ·  
Nur Aqilah Othman · Nor Maniha Abd Ghani ·  
Addie Irawan · Sabira Khatun ·  
Raja Mohd Taufika Raja Ismail · Mohd Mawardi Saari ·  
Mohd Razali Daud · Ahmad Afif Mohd Faudzi *Editors*

# InECCE2019

Proceedings of the 5th International  
Conference on Electrical, Control &  
Computer Engineering, Kuantan,  
Pahang, Malaysia, 29th July 2019

# Lecture Notes in Electrical Engineering

## Volume 632

### Series Editors

Leopoldo Angrisani, Department of Electrical and Information Technologies Engineering, University of Napoli Federico II, Naples, Italy

Marco Arteaga, Departament de Control y Robótica, Universidad Nacional Autónoma de México, Coyoacán, Mexico

Bijaya Ketan Panigrahi, Electrical Engineering, Indian Institute of Technology Delhi, New Delhi, Delhi, India  
Samarjit Chakraborty, Fakultät für Elektrotechnik und Informationstechnik, TU München, Munich, Germany

Jiming Chen, Zhejiang University, Hangzhou, Zhejiang, China

Shanben Chen, Materials Science and Engineering, Shanghai Jiao Tong University, Shanghai, China

Tan Kay Chen, Department of Electrical and Computer Engineering, National University of Singapore, Singapore, Singapore

Rüdiger Dillmann, Humanoids and Intelligent Systems Laboratory, Karlsruhe Institute for Technology, Karlsruhe, Germany

Haibin Duan, Beijing University of Aeronautics and Astronautics, Beijing, China

Gianluigi Ferrari, Università di Parma, Parma, Italy

Manuel Ferre, Centre for Automation and Robotics CAR (UPM-CSIC), Universidad Politécnica de Madrid, Madrid, Spain

Sandra Hirche, Department of Electrical Engineering and Information Science, Technische Universität München, Munich, Germany

Faryar Jabbari, Department of Mechanical and Aerospace Engineering, University of California, Irvine, CA, USA

Limin Jia, State Key Laboratory of Rail Traffic Control and Safety, Beijing Jiaotong University, Beijing, China

Janusz Kacprzyk, Systems Research Institute, Polish Academy of Sciences, Warsaw, Poland

Alaa Khamis, German University in Egypt El Tagamoa El Khames, New Cairo City, Egypt

Torsten Kroeger, Stanford University, Stanford, CA, USA

Qilian Liang, Department of Electrical Engineering, University of Texas at Arlington, Arlington, TX, USA

Ferran Martín, Departament d'Enginyeria Electrònica, Universitat Autònoma de Barcelona, Bellaterra, Barcelona, Spain

Tan Cher Ming, College of Engineering, Nanyang Technological University, Singapore, Singapore

Wolfgang Minker, Institute of Information Technology, University of Ulm, Ulm, Germany

Pradeep Misra, Department of Electrical Engineering, Wright State University, Dayton, OH, USA

Sebastian Möller, Quality and Usability Laboratory, TU Berlin, Berlin, Germany

Subhas Mukhopadhyay, School of Engineering & Advanced Technology, Massey University, Palmerston North, Manawatu-Wanganui, New Zealand

Cun-Zheng Ning, Electrical Engineering, Arizona State University, Tempe, AZ, USA

Toyoaki Nishida, Graduate School of Informatics, Kyoto University, Kyoto, Japan

Federica Pascucci, Dipartimento di Ingegneria, Università degli Studi "Roma Tre", Rome, Italy

Yong Qin, State Key Laboratory of Rail Traffic Control and Safety, Beijing Jiaotong University, Beijing, China

Gan Woon Seng, School of Electrical & Electronic Engineering, Nanyang Technological University, Singapore, Singapore

Joachim Speidel, Institute of Telecommunications, Universität Stuttgart, Stuttgart, Germany

Germano Veiga, Campus da FEUP, INESC Porto, Porto, Portugal

Haitao Wu, Academy of Opto-electronics, Chinese Academy of Sciences, Beijing, China

Junjie James Zhang, Charlotte, NC, USA

The book series *Lecture Notes in Electrical Engineering* (LNEE) publishes the latest developments in Electrical Engineering—quickly, informally and in high quality. While original research reported in proceedings and monographs has traditionally formed the core of LNEE, we also encourage authors to submit books devoted to supporting student education and professional training in the various fields and applications areas of electrical engineering. The series cover classical and emerging topics concerning:

- Communication Engineering, Information Theory and Networks
- Electronics Engineering and Microelectronics
- Signal, Image and Speech Processing
- Wireless and Mobile Communication
- Circuits and Systems
- Energy Systems, Power Electronics and Electrical Machines
- Electro-optical Engineering
- Instrumentation Engineering
- Avionics Engineering
- Control Systems
- Internet-of-Things and Cybersecurity
- Biomedical Devices, MEMS and NEMS

For general information about this book series, comments or suggestions, please contact [leontina.dicecco@springer.com](mailto:leontina.dicecco@springer.com).

To submit a proposal or request further information, please contact the Publishing Editor in your country:

#### **China**

Jasmine Dou, Associate Editor ([jasmine.dou@springer.com](mailto:jasmine.dou@springer.com))

#### **India, Japan, Rest of Asia**

Swati Meherishi, Executive Editor ([Swati.Meherishi@springer.com](mailto:Swati.Meherishi@springer.com))

#### **Southeast Asia, Australia, New Zealand**

Ramesh Nath Premnath, Editor ([ramesh.premnath@springernature.com](mailto:ramesh.premnath@springernature.com))

#### **USA, Canada:**

Michael Luby, Senior Editor ([michael.luby@springer.com](mailto:michael.luby@springer.com))

#### **All other Countries:**

Leontina Di Cecco, Senior Editor ([leontina.dicecco@springer.com](mailto:leontina.dicecco@springer.com))

**\*\* Indexing: The books of this series are submitted to ISI Proceedings, EI-Compendex, SCOPUS, MetaPress, Web of Science and Springerlink \*\***

More information about this series at <http://www.springer.com/series/7818>

Ahmad Nor Kasruddin Nasir ·  
Mohd Ashraf Ahmad · Muhammad Sharfi Najib ·  
Yasmin Abdul Wahab ·  
Nur Aqilah Othman · Nor Maniha Abd Ghani ·  
Addie Irawan · Sabira Khatun ·  
Raja Mohd Taufika Raja Ismail ·  
Mohd Mawardi Saari · Mohd Razali Daud ·  
Ahmad Afif Mohd Faudzi  
Editors

# InECCE2019

Proceedings of the 5th International  
Conference on Electrical, Control &  
Computer Engineering, Kuantan, Pahang,  
Malaysia, 29th July 2019

*Editors*

See next page

ISSN 1876-1100                      ISSN 1876-1119 (electronic)  
Lecture Notes in Electrical Engineering  
ISBN 978-981-15-2316-8              ISBN 978-981-15-2317-5 (eBook)  
<https://doi.org/10.1007/978-981-15-2317-5>

© Springer Nature Singapore Pte Ltd. 2020

This work is subject to copyright. All rights are reserved by the Publisher, whether the whole or part of the material is concerned, specifically the rights of translation, reprinting, reuse of illustrations, recitation, broadcasting, reproduction on microfilms or in any other physical way, and transmission or information storage and retrieval, electronic adaptation, computer software, or by similar or dissimilar methodology now known or hereafter developed.

The use of general descriptive names, registered names, trademarks, service marks, etc. in this publication does not imply, even in the absence of a specific statement, that such names are exempt from the relevant protective laws and regulations and therefore free for general use.

The publisher, the authors and the editors are safe to assume that the advice and information in this book are believed to be true and accurate at the date of publication. Neither the publisher nor the authors or the editors give a warranty, expressed or implied, with respect to the material contained herein or for any errors or omissions that may have been made. The publisher remains neutral with regard to jurisdictional claims in published maps and institutional affiliations.

This Springer imprint is published by the registered company Springer Nature Singapore Pte Ltd. The registered company address is: 152 Beach Road, #21-01/04 Gateway East, Singapore 189721, Singapore

*Editors*

Ahmad Nor Kasruddin Nasir  
Faculty of Electrical and Electronics  
Engineering  
Universiti Malaysia Pahang  
Pekan, Pahang  
Malaysia

Muhammad Sharfi Najib  
Faculty of Electrical and Electronics  
Engineering  
Universiti Malaysia Pahang  
Pekan, Pahang  
Malaysia

Nur Aqilah Othman  
Faculty of Electrical and Electronics  
Engineering  
Universiti Malaysia Pahang  
Pekan, Pahang  
Malaysia

Addie Irawan  
Faculty of Electrical and Electronics  
Engineering  
Universiti Malaysia Pahang  
Pekan, Pahang  
Malaysia

Raja Mohd Taufika Raja Ismail  
Faculty of Electrical and Electronics  
Engineering  
Universiti Malaysia Pahang  
Pekan, Pahang  
Malaysia

Mohd Razali Daud  
Faculty of Electrical and Electronics  
Engineering  
Universiti Malaysia Pahang  
Pekan, Pahang  
Malaysia

Mohd Ashraf Ahmad  
Faculty of Electrical and Electronics  
Engineering  
Universiti Malaysia Pahang  
Pekan, Pahang  
Malaysia

Yasmin Abdul Wahab  
Faculty of Electrical and Electronics  
Engineering  
Universiti Malaysia Pahang  
Pekan, Pahang  
Malaysia

Nor Maniha Abd Ghani  
Faculty of Electrical and Electronics  
Engineering  
Universiti Malaysia Pahang  
Pekan, Pahang  
Malaysia

Sabira Khatun  
Faculty of Electrical and Electronics  
Engineering  
Universiti Malaysia Pahang  
Pekan, Pahang  
Malaysia

Mohd Mawardi Saari  
Faculty of Electrical and Electronics  
Engineering  
Universiti Malaysia Pahang  
Pekan, Pahang  
Malaysia

Ahmad Afif Mohd Faudzi  
Faculty of Electrical and Electronics  
Engineering  
Universiti Malaysia Pahang  
Pekan, Pahang  
Malaysia

# Preface

The 5th International Conference on the Electrical, Control and Computer Engineering 2019 (*InECCE2019*) is a bi-annual conference, organized by the Faculty of Electrical and Electronics Engineering, Universiti Malaysia Pahang (UMP). The fifth installation of *InECCE2019*, this year, was held on 29 July 2019 at Swiss-Garden Beach Resort Hotel, Kuantan, Pahang Malaysia. As the 5th in the series, the flagship conference was able to gather experts, research scholars, academicians and engineers from the field of electrical, electronic, control and computer engineering. It attracted participation of esteemed researchers from both the local and international arenas by providing a forum for exchanging novel ideas, knowledge and research outputs confronting the issues related to the advancement of new technologies for shaping the future engineering in our civilized society. This agrees with the conference theme “Sustainable Engineering and Technologies” as both engineering and technologies are two important arenas that need further attention in the modern world.

*InECCE2019* proceeding comprises 74 technical papers contributed by authors from 5 different countries. It provides an opportunity for readers to enjoy with a selection of refereed papers that were presented during the conference. The papers had been classified into the three engineering tracks as: Control and Instrumentation, Applied Electronic and Computer, and Electrical Power and Energy.

Part I of the proceeding presents recent research and development outputs related to control, optimization and instrumentation engineering. The main contributions to this part are various applications of optimization algorithms in the area of control. These include symbiotic organism search algorithm, fish swarm algorithm, simulated Kalman filter, salp swarm algorithm, grey wolf optimizer and sine cosine algorithm. Several related applications are presented in this part including optimization of neural network, Fuzzy-PID controller, PID-P<sub>ω</sub> controller and fictitious reference iterative tuning for autonomous underwater vehicle, DC motor system,

actuated mobile robot and twin rotor system. Sensing devices very important to ensure smooth running of control related applications and instrumentation. Hence, various types of developed sensing devices are also presented here, which include electrical capacitance tomography, thermal sensor and electronic nose.

Part II presents state-of-the-art research findings related to applied electronic and computer engineering. It comprises various techniques and applications of image processing and electroencephalogram, EEG for recognition, detection and classification in health monitoring such as rubeosis iridis, breast cancer, diabetes and salivary ferning pattern. Other related applications are recognition of human activity, gender, face, fingerprint as well as autism pattern are depicted in this part too. Some industry problems solving strategies are also included here, which are tree recognition used in oil palm plantation, skateboard manoeuvring system, intrusion detection, road death forecasting based on machine learning and camera orientation determination for a robotic system. The essential techniques and devices that are need to be used in electronic communication, such as the radio communication network, antenna pattern and RFID, are also presented.

Part III presents the current global challenge related to electrical power and energy. The focus of this part is mainly on developing technologies that can produce sustainable energy without relying on the limited natural fossil fuel and coal. Instead, alternative energy harvesting technologies that can produce energy from natural resources like wind, water and solar are more sustainable. It has significant contribution on reducing pollution and avoid global warming problem. Hence, methods on optimizing energy and power management are great importance in the current trend. Therefore, in part III, various strategies and methods for developing technologies based on wind turbine system, photovoltaic solar module, hydrokinetic river and battery-powered system are presented. Other applications include optimization of energy and power management for various power generation systems.

This conference is the result of the hard work of the organizing committee members as well as all the reviewers who took time off from their busy schedule to help ensure the conference only accepted chapters of the highest quality. The reviewers are the backbone of a conference. Their commitment, diligence and expertise helped maintain the high quality of the technical chapters. On behalf of the committee members, we would like to express our sincere appreciation to the reviewers for their dedication, time and patience.

We would like to take this opportunity to thank all authors for their valuable research contributions and for selecting *InECCE2019* to showcase their state-of-the-art research works. Thanks are also due to the members of our international advisory panel; their presence gave us a sense of assurance and confidence. The keynote speaker, having reached the top of his chosen track, with a great view of the entire territory, would like to express our gratitude. Sincere gratitude to our



supporters and sponsors, especially Faculty of Electrical and Electronics Engineering and UMP who provided the much needed resources and assistance; and Board of Engineers Malaysia for approved continuous professional development hours. Finally, it is a blessing to be associated with the members of *InECCE2019* organizing committee. Their hard work and tireless efforts have made this conference a reality and success.

Pekan, Malaysia

Ahmad Nor Kasruddin Nasir  
Mohd Ashraf Ahmad  
Muhammad Sharfi Najib  
Yasmin Abdul Wahab  
Nur Aqilah Othman  
Nor Maniha Abd Ghani  
Addie Irawan  
Sabira Khatun  
Raja Mohd Taufika Raja Ismail  
Mohd Mawardi Saari  
Mohd Razali Daud  
Ahmad Afif Mohd Faudzi

# Contents

## **Instrumentation, Control and Artificial Systems**

<b>Position Control of Pneumatic Actuator Using Cascade Fuzzy Self-adaptive PID</b> . . . . .	3
Mohd Iskandar Putra Azahar, Addie Irawan, Raja Mohd Taufika and Mohd Helmi Suid	
<b>Effect of Excitation Frequency on Magnetic Response Induced by Front- and Back-Side Slits Measured by a Differential AMR Sensor Probe</b> . . . . .	15
M. A. H. P. Zaini, M. M. Saari, N. A. Nadzri, A. M. Halil, A. J. S. Hanifah and M. Ishak	
<b>Model-Free PID Controller Based on Grey Wolf Optimizer for Hovering Autonomous Underwater Vehicle Depth Control</b> . . . . .	25
Mohd Zaidi Mohd Tumari, Amar Faiz Zainal Abidin, Ahmad Anas Yusof, Mohd Shahrieel Mohd Aras, Nik Mohd Zaitul Akmal Mustapha and Mohd Ashraf Ahmad	
<b>Experimental Study of Optimization of Electrode Dimension for Non-invasive Electrical Resistance Tomography Application</b> . . . . .	37
Yasmin Abdul Wahab, Mahanum Muhammad Sakri, Mohd Anwar Zawawi, Muhammad Sharfi Najib and Normaniha Abd Ghani	
<b>A Fictitious Reference Iterative Tuning Method for Buck Converter-Powered DC Motor Control System</b> . . . . .	47
Mohd Syakirin Ramli, Seet Meng Sian, Mohd Naharudin Salim and Hamzah Ahmad	
<b>Depth Evaluation of Slits on Galvanized Steel Plate Using a Low Frequency Eddy Current Probe</b> . . . . .	59
N. A. Nadzri, M. M. Saari, M. A. H. P. Zaini, A. M. Halil, A. J. S. Hanifah and M. Ishak	

<b>Sensitivity Maps Preparation for Electrical Capacitance Tomography Using Finite Element Approach</b> .....	67
Wan A. N. Ropandi, N. A. Zulkifli, J. Pusppanathan, F. A. Phang, N. D. Nawi, M. E. Johana and N. H. A. Ngadiman	
<b>Infrared Thermal Sensor for a Low Cost and Non-invasive Detection of Skin Cancer</b> .....	77
A. Noora Safrin, B. Pooja, K. Hema, P. Padmapriya, Vigneswaran Narayanamurthy and Fahmi Samsuri	
<b>T-Way Strategy for Sequence Input Interaction Test Case Generation Adopting Fish Swarm Algorithm</b> .....	87
Mostafijur Rahman, Dalia Sultana, Sabira Khatun, Mohd Falfazli Mat Jusof, Syamimi Mardiah Shaharum, Nurhafizah Abu Talip Yusof, Khandker M. Qaiduzzaman, Md Hasibul Hasan, Md Mushfiqur Rahman, Md Anwar Hossen and Afsana Begum	
<b>Development of AC and DC Drive Coils for a Small Volume Magnetic Particle Imaging System</b> .....	101
Mohd Mawardi Saari, Ahmad Zahir Irsyad Razak, Mohd Aufa Hadi Putera Zain, Nurul A'in Nadzri, Mohd Razali Daud and Hamzah Ahmad	
<b>A Diversity-Based Adaptive Synchronous-Asynchronous Switching Simulated Kalman Filter Optimizer</b> .....	113
Nor Azlina Ab. Aziz, Nor Hidayati Abdul Aziz, Badaruddin Muhammad, Zuwairie Ibrahim, Marizan Mubin, Norrima Mokhtar and Mohd Saberi Mohamad	
<b>Combinatorial Test Suite Generation Strategy Using Enhanced Sine Cosine Algorithm</b> .....	127
Kamal Z. Zamli, Fakhrud Din, Abdullah B. Nasser and AbdulRahman Alsewari	
<b>Classification of Lubricant Oil Geometrical Odor-Profile Using Cased-Based Reasoning</b> .....	139
Suhaimi Mohd Daud, Muhammad Sharfi Najib, Nurdiyana Zahed, Muhammad Faruqi Zahari, Nur Farina Hamidon Majid, Suziyanti Zaib, Mujahid Mohamad, Addie Irawan and Hadi Manap	
<b>Optimization of Quaternion Based on Hybrid PID and <math>P_\omega</math> Control</b> . . . .	153
Balya Darohini, M. F. Abas, N. Md. Saad, Dwi Pebrianti, H. Ahmad, M. H. Ariff and M. R. Arshad	

**Elimination-Dispersal Sine Cosine Algorithm for a Dynamic Modelling of a Twin Rotor System** . . . . . 167  
 Shuhairie Mohammad, Mohd Falfazli Mat Jusof, Nurul Amira Mhd Rizal, Ahmad Azwan Abd Razak, Ahmad Nor Kasruddin Nasir, Raja Mohd Taufika Raja Ismail and Mohd Ashraf Ahmad

**The Investigation of Meat Classification Based on Significant Authentication Features Using Odor-Profile Intelligent Signal Processing Approach** . . . . . 179  
 Nur Farina Hamidon Majid, Muhammad Sharfi Najib, Suhaimi Mohd Daud, Nurdiyana Zahed, Muhamad Faruqi Zahari, Suziyanti Zaib, Mujahid Mohamad, Tuan Sidek Tuan Muda and Hadi Manap

**The Study of Raw Water Based on Quality Parameter Using Smell-Print Sensing Device** . . . . . 193  
 Suziyanti Zaib, Muhammad Sharfi Najib, Suhaimi Mohd Daud, Nurdiyana Zahed, Muhamad Faruqi Zahari, Nur Farina Hamidon Majid, Mujahid Mohamad and Hadi Manap

**Camera Orientation Determination Based on Copper Wire Spool Shape** . . . . . 205  
 Farah Adiba Azman, Mohd Razali Daud, Amir Izzani Mohamed, Addie Irawan, R. M. Taufika R. Ismail and Mohd Mawardi Saari

**A Modified Symbiotic Organism Search Algorithm with Lévy Flight for Software Module Clustering Problem** . . . . . 219  
 Nurul Asyikin Zainal, Kamal Z. Zamli and Fakhruddin Din

**Classification of Agarwood Types (Malaccensis and Crassna) Between Oil and Smoke Using E-Nose with CBR Classifier** . . . . . 231  
 Mujahid Mohamad, Muhammad Sharfi Najib, Suhaimi Mohd Daud, Nurdiyana Zahed, Muhamad Faruqi Zahari, Nur Farina Hamidon Majid, Suziyanti Zaib and Hadi Manap

**Applied Electronics and Computer Engineering**

**SCAR-CNN: Secondary-Classification-After-Refinement Convolutional Neural Network for Fine-Grained Categorization** . . . . . 247  
 Bernard Jun Kai Cheah, Abduljalil Radman and Shahrel Azmin Suandi

**Forecasting Road Deaths in Malaysia Using Support Vector Machine** . . . . . 261  
 Nurul Qastalani Radzuan, Mohd Hasnun Arif Hassan, Anwar P. P. Abdul Majeed, Khairil Anwar Abu Kassim, Rabi'u Muazu Musa, Mohd Azraai Mohd Razman and Nur Aqilah Othman

**Investigation of Dimensionality Reduction on Numerical Attribute Features in a Finger Vein Identification System** . . . . . 269  
 Ei Wei Ting, M. Z. Ibrahim, D. J. Mulvaney, W. N. A. W. Samsudin and S. Khatun

**Intelligent Gender Recognition System for Classification of Gender in Malaysian Demographic** . . . . . 283  
 Yap Su Chi and Syafiq Fauzi Kamarulzaman

**A Novel Approach Towards Tamper Detection of Digital Holy Quran Generation** . . . . . 297  
 Md. Milon Islam, Muhammad Nomani Kabir, Muhammad Sheikh Sadi, Md. Istiak Morsalin, Ahsanul Haque and Jing Wang

**A Comparative Study of AFM-Assisted Direct and Least-Square Attitude Determination Algorithm** . . . . . 309  
 Suqing Yan, Yue Wu, Yuanfa Ji, Kamarul Hawari Ghazali and Xiyan Sun

**Design and Development of Wearable Human Activity Recognition for Healthcare Monitoring** . . . . . 323  
 Hamzah Ahmad, Nurul Syafiqah Mohd, Nur Aqilah Othman, Mohd Mawardi Saari and Mohd Syakirin Ramli

**Region of Interest Extraction of Finger-Vein Image Using Watershed Segmentation with Distance Transform** . . . . . 333  
 Lim Yuan Zhang and Bakhtiar Affendi Rosdi

**The Classification of Skateboarding Trick Manoeuvres Through the Integration of Image Processing Techniques and Machine Learning** . . . . . 347  
 Muhammad Nur Aiman Shapiee, Muhammad Ar Rahim Ibrahim, Mohd Azraai Mohd Razman, Muhammad Amirul Abdullah, Rabiū Muazu Musa, Mohd Hasnun Arif Hassan and Anwar P. P. Abdul Majeed

**Review and Analysis of Risk Factor of Maternal Health in Remote Area Using the Internet of Things (IoT)** . . . . . 357  
 Marzia Ahmed, Mohammad Abul Kashem, Mostafijur Rahman and Sabira Khatun

**Recent Trends and Open Challenges in EEG Based Brain-Computer Interface Systems** . . . . . 367  
 Mamunur Rashid, Norizam Sulaiman, Mahfuzah Mustafa, Sabira Khatun, Bifta Sama Bari and Md Jahid Hasan

**Early Rubeosis Iridis Detection Using Feature Extraction Process** . . . . . 379  
 Rohana Abdul Karim, Nur Amira Adila Abd Mobin, Nurul Wahidah Arshad, Nor Farizan Zakaria and M. Zabri Abu Bakar

**Multi-hop File Transfer in WiFi Direct Based Cognitive Radio Network for Cloud Back-Up** ..... 389  
 N. J. Shoumy, D. M. Rahaman, S. Khatun, W. N. Azhani, M. H. Ariff, M. N. Morshed, M. Islam, S. N. A. Manap and M. F. M. Jusof

**The Multifocus Images Fusion Based on a Generative Gradient Map** ..... 401  
 Ismail and Kamarul Hawari Bin Ghazali

**A Comparative Analysis of Four Classification Algorithms for University Students Performance Detection** ..... 415  
 Dipta Das, Asif Khan Shakir, Md. Shah Golam Rabbani, Mostafijur Rahman, Syamimi Mardiah Shaharum, Sabira Khatun, Norasyikin Binti Fadilah, Khandker M. Qaiduzzaman, Md. Shariful Islam and Md. Shohel Arman

**Open-Set Face Recognition in Video Surveillance: A Survey** ..... 425  
 Wasseem N. Ibrahim Al-Obaydy and Shahrel Azmin Suandi

**Hardware Development of Auto Focus Microscope** ..... 437  
 Dwi Pebrianti, Rosyati Hamid, Faradila Naim, Mohd Falfazli Mat Jusof, Nurul Wahidah Arshad and Luhur Bayuaji

**Overview on Fingerprinting Authentication Technology** ..... 451  
 N. Sulaiman and Q. A. Tajul Ariffin

**Bandwidth and Gain Enhancement of a Modified Ultra-wideband (UWB) Micro-strip Patch Antenna Using a Reflecting Layer** ..... 463  
 Bifta Sama Bari, Sabira Khatun, Kamarul Hawari Ghazali, Md. Moslemuddin Fakir, Mohd Hisyam Mohd Ariff, Mohd Faizal Jamlos, Mamunur Rashid, Minarul Islam, Mohd Zamri Ibrahim and Mohd Falfazli Mat Jusof

**Oil Palm Tree Detection and Counting in Aerial Images Based on Faster R-CNN** ..... 475  
 Xinni Liu, Kamarul Hawari Ghazali, Fengrong Han, Izzeldin Ibrahim Mohamed, Yue Zhao and Yuanfa Ji

**EEG Pattern of Cognitive Activities for Non Dyslexia (Engineering Student) due to Different Gender** ..... 483  
 E. M. N. E. M. Nasir, N. A. Bahali, N. Fuad, M. E. Marwan, J. A. Bakar and Danial Md Nor

**Intelligent Autism Screening Using Fuzzy Agent** ..... 495  
 Nurul Najihah Che Razali, Ngahzaifa Ab. Ghani and Syifak Izhar Hisham

<b>Ultra Wide Band (UWB) Based Early Breast Cancer Detection Using Artificial Intelligence</b> .....	505
Bifta Sama Bari, Sabira Khatun, Kamarul Hawari Ghazali, Md. Moslemuddin Fakir, Wan Nur Azhani W. Samsudin, Mohd Falfazli Mat Jusof, Mamunur Rashid, Minarul Islam and Mohd Zamri Ibrahim	
<b>Design and Analysis of Circular Shaped Patch Antenna with Slot for UHF RFID Reader</b> .....	517
Mohd Hisyam Mohd Ariff, Muhammad Solihin Zakaria, Rahimah Jusoh, Sabira Khatun, Mohammad Fadhil Abas and Mohd Zamri Ibrahim	
<b>Analysis of EEG Features for Brain Computer Interface Application</b> .....	529
Mamunur Rashid, Norizam Sulaiman, Mahfuzah Mustafa, Mohd Shawal Jadin, Muhd Sharfi Najib, Bifta Sama Bari and Sabira Khatun	
<b>Hybrid Sampling and Random Forest Based Machine Learning Approach for Software Defect Prediction</b> .....	541
Md Anwar Hossen, Md. Shariful Islam, Nurhafizah Abu Talip Yusof, Md. Sakib Rahman, Fatema Siddika, Mostafijur Rahman, Sabira Khatun, Mohamad Shaiful Abdul Karim and S. M. Hasan Mahmud	
<b>kNN and SVM Classification for EEG: A Review</b> .....	555
M. N. A. H. Sha'abani, N. Fuad, Norezmi Jamal and M. F. Ismail	
<b>Flexible Graphene-Silver Nanowires Polydimethylsiloxane (PDMS) Directional Coupler</b> .....	567
Nor Nadiah Aliff, Noorlindawaty Md Jizat, Nazihah Ahmad and Mukter Uz-Zaman	
<b>Investigating the Possibility of Brain Actuated Mobile Robot Through Single-Channel EEG Headset</b> .....	579
Mamunur Rashid, Norizam Sulaiman, Mahfuzah Mustafa, Sabira Khatun, Bifta Sama Bari, Md Jahid Hasan and Nawfan M. M. A. Al-Fakih	
<b>Campus Hybrid Intrusion Detection System Using SNORT and C4.5 Algorithm</b> .....	591
Slamet, Izzeldin I. Mohamed and Fahmi Samsuri	
<b>Image Segmentation of Women's Salivary Ferning Patterns Using Harmony Frangi Filter</b> .....	605
Heri Pratikno and Mohd Zamri Ibrahim	
<b>Autonomous Self-exam Monitoring for Early Diabetes Detection</b> .....	623
Rohana Abdul Karim, Nur Alia Fatiha Azhar, Nurul Wahidah Arshad, Nor Farizan Zakaria and M. Zabri Abu Bakar	

**Quantitative Assessment of Remote Code Execution Vulnerability in Web Apps** ..... 633  
 Md Maruf Hassan, Umam Mustain, Sabira Khatun,  
 Mohamad Shaiful Abdul Karim, Nazia Nishat and Mostafijur Rahman

**Sustainable Energy and Power Engineering**

**A Salp Swarm Algorithm to Improve Power Production of Wind Plant** ..... 645  
 Ahmad Zairi Mohd-Zain and Mohd Ashraf Ahmad

**Improvement of Performance and Response Time of Cascaded Five-Level VSC STATCOM Using ANN Controller and SVPWM During Period of Voltage Sag** ..... 655  
 Mohamad M. Almelian, Izzeldin I. Mohd, Abu Zaharin Ahmad,  
 Mohamed A. Omran, Muhamad Z. Sujod, N. M. Elasager  
 and Mohamed Salem

**Development of Maximum Power Point Tracking for Doubly-Fed Induction Generators in Wind Energy Conversion Systems** ..... 669  
 Duy C. Huynh, Khai H. Nguyen and Matthew W. Dunnigan

**Development of PV Module Power Degradation Analyzer** ..... 681  
 Mohd Shawal Jadin, Muhammad Aiman Ibrahim and Norizam Sulaiman

**Direct Power Control Method of Maximum Power Point Tracking (MPPT) Algorithm for Pico-Hydrokinetic River Energy Conversion System** ..... 691  
 W. I. Ibrahim, M. R. Mohamed and R. M. T. R. Ismail

**Load Estimation of Single-Phase Diode Bridge Rectifier Using Kalman Filter** ..... 705  
 Nor Syuhaida Othman and Hamzah Ahmad

**A Study on Residual Current Device Nuisance Tripping Due to Grounding Resistance Value** ..... 717  
 Izzatul Liyana, Farhan Bin Hanaffi and Mohd Hendra Bin Hairi

**DC-Link Protection for Grid-Connected Photovoltaic System: A Review** ..... 725  
 Wan Nur Huda Aqilah Alias, Muhamad Zahim Sujod  
 and Nor Azwan Mohamed Kamari

**An Improved Efficiency of Solar Photo Voltaic System Applications by Using DC-DC Zeta Converter** ..... 737  
 A. S. Veerendra, M. R. Mohamed, M. H. Sulaiman and K. Peddakapu



**Hydrophobic Sol-Gel Based Self-cleaning Coating for Photovoltaic Panels** . . . . . 753  
Siti Nur Nashya Azlika Hamidon, Amirjan Nawabjan,  
Ahmad Sharmi Abdullah and Siti Maherah Hussin

**Effect of Graphene Oxide Nanoparticles on Thermal Properties of Paraffin Wax** . . . . . 767  
Nurul Humaira Muhd Zaimi, Amirjan Nawabjan,  
Shaharin Fadzli Abdul Rahman and Siti Maherah Hussin

**Reliability Performance of Low Voltage (LV) Network Configuration** . . . . . 783  
Mohd Ikhwan Muhammad Ridzuan, Muhammad Adib Zufar Rusli  
and Norhafidzah Mohd Saad

**Detailed Non-Linear Constrained Multi-Objective Optimal Operation of Power Systems Including Renewable Energy Sources** . . . . . 795  
Duy C. Huynh, Hong V. Nguyen and Matthew W. Dunnigan

**Voltage Sag Immunity Testing for AC Contactors in Industrial Environment** . . . . . 809  
Hazri Dahalan Razip and Abu Zaharin Ahmad

**Vertical Axis Wind Turbines: An Overview** . . . . . 821  
A. Yusof and M. R. Mohamed

**Hyperheuristics Trajectory Based Optimization for Energy Management Strategy (EMS) of Split Plug-In Hybrid Electric Vehicle** . . . . . 837  
Muhammad Ikram Mohd Rashid, Ahmad Amir Solihin Mohd Apandi,  
Hamdan Daniyal and Mohd Ashraf Ahmad

**Utilization of Filter Harmonic Current Based on Shunt HPF Within the Acceptable IEEE-519 Standard** . . . . . 849  
Mohamed A. Omran, Izzeldin I. Mohd, Abu Zaharin Ahmad,  
Mohamad M. Almelian, Fahmi Samsuri, Muhamad Z. Sujod,  
Walid K. A. Hasan and Mohamed Salem

**Vehicle-to-Grid as Frequency Regulator in a Micro Grid System** . . . . . 859  
Mohd Redzuan Ahmad and Laylatun Qadrina Amrizal

**Development of PV Module Hotspot Detector** . . . . . 875  
Mohd Shawal Jadin, Kamil Ashman Bin Zamridin  
and Ahmad Syahiman Mohd Shah

**Comparative Analysis for LED Driver with Analog and Digital  
Controllers** ..... 885  
Shaheer Shaida Durrani, Abu Zaharin, Bakri Hassan  
and Ruhaizad Bin Ishak

**Characterization of Positive Porous Electrode Felt for Organic Redox  
Flow Battery Application** ..... 899  
A. C. Khor, K. F. Chong and M. R. Mohamed

# **Instrumentation, Control and Artificial Systems**

# Position Control of Pneumatic Actuator Using Cascade Fuzzy Self-adaptive PID



Mohd Iskandar Putra Azahar, Addie Irawan, Raja Mohd Taufika and Mohd Helmi Suid

**Abstract** Pneumatic systems are widely used in the industrial automation with its advantages in high power ratio, low cost and cleanliness fluid medium. However, the complex nonlinearities of pneumatics system make this system having difficulty to perform precise motion control especially in providing precise steady state tracking error on rod piston and stable pressure control. To overcome this issue, a cascade control technique named Fuzzy Self-Adaptive PID (CFSAPID) control is proposed. The adaptive tuning by Fuzzy Logic Controller (FLC) is designed as tuner for PID controller. The proposed CFSAPID is simulated and verified on single-piston double acting valve pneumatic system model plant, and compared with single FSAPID controller. Five parameters are focused for analysis including piston rise time, piston settling time, piston velocity, pressure on piston chambers and force friction. The capability of proposed CFSAPID has been successfully verified by simulation studies.

**Keywords** Pneumatic actuator · Fuzzy logic · PID control · Motion control

## 1 Introduction

A pneumatic system is one of the common tools in industrial automation applications with its advantage in providing high power/force to weight ratio, cost-effective, less maintenance, simple structure, and cleanliness fluid medium. However, due to its complex nonlinearities such as compressibility of air, nonlinear valve and friction make position control of the pneumatic actuation system remains a difficult task. Proportional, Integral and Derivative (PID) control is the earliest closed-loop control system technique. Due to its simplistic algorithm, it is extensively used in the industrial application. However, the PID controller is a linear control system which is irrelevant for application with highly nonlinear such as pneumatic system. Pneumatic system control requires significantly high accuracy in positioning and actuator

---

M. I. P. Azahar · A. Irawan (✉) · R. M. Taufika · M. H. Suid  
Robotics and Unmanned Systems Research Group, Faculty of Electrical and Electronics Engineering, Universiti Malaysia Pahang, 26600 Pekan, Pahang, Malaysia  
e-mail: [addieirawan@ump.edu.my](mailto:addieirawan@ump.edu.my)

© Springer Nature Singapore Pte Ltd. 2020

A. N. Kasruddin Nasir et al. (eds.), *InECCE2019*, Lecture Notes in Electrical Engineering 632, [https://doi.org/10.1007/978-981-15-2317-5\\_1](https://doi.org/10.1007/978-981-15-2317-5_1)

rigidity under different external loads [1]. Therefore, some modification on the PID control structure is required. This can be seen in some efforts by researchers such as PID-based cascaded controller [2–4], Nonlinear PID control [5–7], Fractional order PID control [8] and Fuzzy Adaptive PID control [9, 10]. These proposed methods had proven the effectiveness of adaptive PID control in various applications. Moreover, other control strategies also have been designed for pneumatic position control such as Fuzzy Logic Controller (FLC) [11, 12], Neural Network-based controller (NN) [13, 14] and Sliding Mode Controller (SMC) [15–17]. Both of these Model-Free and Model-based types were applied to cater the precision on the pneumatic piston rod motion, as well as the stability of the system in facing friction forces. Saleem et.al had applied a cascade PID control with Particle Swarm Optimization (PSO) algorithm for pneumatic position control for fast and optimal tuning on giving better transient and steady state responses [2]. On the other hand, fractional order PID control also is done by [8, 18] in providing optimal steady state tracking performance as well as energy consumption on pneumatic servo system associated with multivariable multi-objective genetic algorithm (MMGA). Mu et al. had approach predictive fuzzy control on servo pneumatic with neural network combination [19]. The imaginary plant was proposed in predictive method in improving the teaching signals makes steady state tracking error improved if compared to the conventional PID control. Same goes to the other approaches such as reported in [4, 13, 17, 20] in which are mainly emphasized on steady state error tracking by considering some nonlinearities in pneumatics' valve and actuator system.

## 2 Mathematical Model of Pneumatic System

The accurate models are significant in the design of pneumatic systems as well as for their control purposes. Assumptions of steady state are often used in industrial practice for component sizing problem [21]. Unfortunately, this procedure is ineffective at all even though the system has significant nonlinearity rates. Thus, a better process design based on the dynamic system should be considered. The development of the mathematical model for the pneumatic system involves four main points to consider; cylinder dynamics, frictional dynamics, pressure dynamics, and valve dynamics. Cylinder dynamics can be expressed in Eq. 1 as follow:

$$\ddot{x}_{rp} = \frac{A_1 P_1 - A_2 P_2 - (F_f - F_L)}{M} \quad (1)$$

$\ddot{x}_{rp}$  is the acceleration of the rod-piston.  $A_1$  and  $A_2$  is the annulus area each of the chambers of the rod-piston.  $P_1$  and  $P_2$  represent the absolute pressures in chamber 1 and chamber 2 of the pneumatic cylinder.  $F_f$  and  $F_L$  represent the internal frictional force inside the pneumatic cylinder chamber and external frictional force of payloads, respectively.  $M$  represent the combined mass of the rod-piston and payloads. Frictional force dynamics can be determined in Eq. 2 as follow:

$$F_f = \beta_0 z + \beta_1 \dot{z} + \beta_2 \dot{x}_{rp} \quad (2)$$

$\beta_0$ ,  $\beta_1$  and  $\beta_2$  are bristles spring coefficient, bristles damping coefficient, and viscous friction coefficient, respectively.  $\dot{x}_{rp}$  is the velocity of the rod-piston.  $z$  and  $\dot{z}$  represented the bristles internal state and bristles average deflection, respectively. Pressure dynamics can be defined in Eq. 3 as follow:

$$\dot{P}_{i(i=1,2)} = \frac{kRT\dot{m}_{i(i=1,2)}}{V_{0i(i=1,2)} + A_{i(i=1,2)}(L/2 \pm x_{rp})} - \frac{kP_{i(i=1,2)}A_{i(i=1,2)}\dot{x}_{rp}}{V_{0i(i=1,2)} + A_{i(i=1,2)}(L/2 \pm x_{rp})} \quad (3)$$

$\dot{m}_{i(i=1,2)}$  is the mass flow rate while  $V_{0i(i=1,2)}$  is the dead volumes of air.  $L$  denoted for the length of rod-piston stroke.  $k$ ,  $R$  and  $T$  are represented the ratio of specific heats of air, ideal constant of gas and absolute temperature of the air, respectively. According to Karpenko and Sepehri, have stated that the valve spool position,  $x_{pv}$  is directly proportional to the input signal,  $u$  with a valve spool position gain,  $k_{pv}$  [22].

$$\dot{x}_{pv} = -\frac{x_{pv} + uk_{pv}}{\tau} \quad (4)$$

$$u = \frac{A_{pv}}{wk_{pv}} \quad (5)$$

where  $\tau$ ,  $w$  and  $A_{pv}$  are the valve spool time constant, area gradient of valve orifice and effective area of valve orifice, respectively.

$$\dot{m}_{i(i=1,2)} = \pm A_{pv}\phi_{i(i=1,2)} \quad (6)$$

$$\Phi_{i(i=1,2)}(P_u, P_d) = \begin{cases} \Phi_{i(i=1,2)}(P_s, P_{i(i=1,2)}) & A_{pv} \geq 0 \\ \Phi_{i(i=1,2)}(P_{i(i=1,2)}, P_{atm}) & A_{pv} < 0 \end{cases} \quad (7)$$

$$\Phi_{i(i=1,2)}(P_u, P_d) = \begin{cases} \frac{C_d P_u}{\sqrt{T}} \sqrt{\frac{k}{R}} \left(\frac{2}{k+1}\right)^{\frac{k+1}{k-1}} & \text{if } \frac{P_d}{P_u} < \left(\frac{2}{k+1}\right)^{\frac{k}{k+1}} \\ \frac{C_d P_u}{\sqrt{T}} \sqrt{\frac{k}{R}} \left(\frac{2}{k-1}\right)^{\frac{1}{k}} \left(\frac{P_u}{P_d}\right)^{\frac{1}{k}} \sqrt{1 - \left(\frac{P_u}{P_d}\right)^{\frac{k-1}{k}}} & \text{if } \frac{P_d}{P_u} \geq \left(\frac{2}{k+1}\right)^{\frac{k}{k+1}} \end{cases} \quad (8)$$

$\Phi_{i(i=1,2)}$  is the normalized mass flow rate of the fixed area of the valve orifice,  $P_s$  and  $P_{atm}$  both are the supply pressure and atmosphere pressure, respectively.  $C_d$ ,  $P_u$  and  $P_d$  are the discharge coefficient of valve orifice, upstream pressure and downstream pressure, respectively.

### 3 Cascade Fuzzy Self-adaptive PID Controller Design

In most studies, two control strategies that are often used for position control of pneumatic systems are PID and Fuzzy Logic control (FLC) [2–12]. There is a various way in integrating between these two control systems such as reported in [23, 24]. For this study, a cascading method has been selected in PID and FLC integration named as Cascade Fuzzy Self-Adaptive PID (CFSAPID) control. The proposed control method is to cater both linear and nonlinear states of pneumatic actuation system where the FLC algorithm is used as parameter tuner for PID controller to perform two layers control system structure as shown in Fig. 1. The layers consist of the outer loop with position feedback and inner loop with velocity feedback, whereby both loops used a Fuzzy Self-Adaptive PID (FSAPID) control system with the structure as shown in Fig. 2.

$x_d(t)$ ,  $e(t)$  and  $u(t)$  refers to the pneumatic cylinder rod-piston desired position, pneumatic cylinder rod-piston position error and input signal, respectively.  $x_{rp}$  and  $\dot{x}_{rp}$  are the pneumatic cylinder rod-piston position and velocity, respectively. For the FLC system structure, the Mamdani-type is used [25] where the input and output of the fuzzy system are linguistic variables. Moreover, a single FLC controller has two antecedence and three consequences where two input variables linguistic are from the rod piston position error,  $e(t)$  and rate change of error,  $\Delta e(t)$ , while  $\Delta K_p$ ,  $\Delta K_i$  and  $\Delta K_d$  are the outputs gains for PID controller in which are obtained by fuzzy inference calculation.

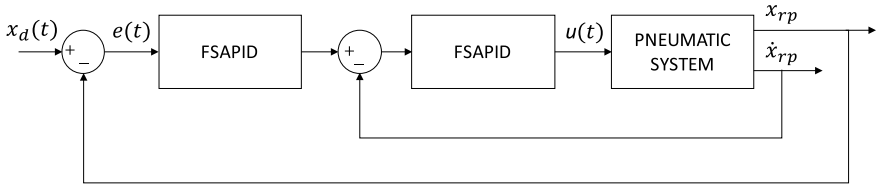


Fig. 1 Overview on proposed CFSAPID control structure of pneumatic system

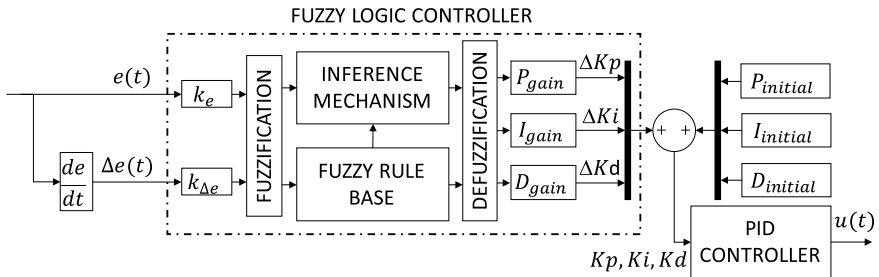


Fig. 2 Overview on FSAPID control structure

**Table 1** PID initial and gain parameter values

Controller	Loop	$P_{initial}$	$P_{gain}$	$I_{initial}$	$I_{gain}$	$D_{initial}$	$D_{gain}$
FSAPID	Single loop	30	50	0.1	0.15	0.01	0.01
CFSAPID	Outer loop	30	50	0.1	0.15	0.01	0.01
	Inner loop	10	3	0.01	0.01	0.1	0.1

On the other hand, the parameter values of  $P_{initial}$ ,  $I_{initial}$  and  $D_{initial}$  are the pre-defined fixed parameter and randomly selected values as for the initial PID gains.  $P_{gain}$ ,  $I_{gain}$  and  $D_{gain}$  are the gains value for the  $\Delta k_p$ ,  $\Delta k_i$  and  $\Delta k_d$ , respectively, as shown in self-adaptive tuning Eq. (9) as follows (Table 1):

$$\begin{bmatrix} K_p \\ K_i \\ K_d \end{bmatrix} = \begin{bmatrix} \Delta K_p(P_{gain}) + P_{initial} \\ \Delta K_i(I_{gain}) + I_{initial} \\ \Delta K_d(D_{gain}) + D_{initial} \end{bmatrix} \tag{9}$$

FSAPID and CFSAPID outer-loop have same parameters of  $P_{initial}$ ,  $I_{initial}$ ,  $D_{initial}$ ,  $P_{gain}$ ,  $I_{gain}$  and  $D_{gain}$  while the CFSAPID inner-loop has different and have been set with the appropriate parameters where inner-loops are faster than outer-loops. The linguistic variables of input and output parameters of FLC are divided into seven sections by the membership function set as listed in Table 2. By this selection, the FSAPID has 49 rules as shown in Table 3. The FLC works on the knowledge base containing IF-THEN sets linguistic rules for undetermined predicates and fuzzy control mechanism.

When  $|e|(t)$  is relatively large, the  $K_p$  value should use a relatively large value to provide fast system response and reduce the time constant.  $K_d$  should use a relatively small value to avoid occurring beyond the control range at the start while  $K_i$  should not be used to prevent large overshoot. When  $|e|(t)$  is within a modest range,  $K_p$  needs to use a relatively small value to minimize the overshoot response.  $K_d$  value should use a medium value while  $K_i$  value needs to be increased with the appropriate rate. When  $|e|(t)$  is relatively small,  $K_p$  and  $K_i$  should use a relatively large value to have a better steady state and to avoid the occurrence of oscillations at the equilibrium

**Table 2** Linguistic variables

Symbol	Definition
NL	Negative Large
NM	Negative Medium
NT	Negative Tiny
ZE	Zero
PT	Positive Tiny
PM	Positive Medium
PL	Positive Large



**Table 3** Fuzzy rules set of  $\Delta K_p$ ,  $\Delta K_i$  and  $\Delta K_d$ 

$\Delta K_p$ $\Delta K_i$ $\Delta K_d$		$e(t)$						
		NL	NM	NT	ZE	PT	PM	PL
$\Delta e(t)$	NL	PL NL NT	PL NL PT	PM NM PL	PM NM PL	PT NT PL	ZE ZE PM	ZE ZE NT
	NM	PL NL NT	PL NL PT	PM NM PL	PT NT PM	PT NT PM	ZE ZE PT	NT ZE ZE
	NT	PM NL ZE	PM NM PT	PM NT PM	PT NT PM	ZE ZE PT	NT PT PT	NT PT ZE
	ZE	PM NM ZE	PM NM PT	PT NT PT	ZE ZE PT	NT PT PT	NM PM PT	NM PM ZE
	PT	PT NM ZE	PT NT ZE	ZE ZE ZE	NT PT ZE	NT PT ZE	NM PM ZE	NM PL ZE
	PM	PT ZE NL	ZE ZE PT	NT PT NT	NM PT NT	NM PM NT	NM PL NT	NL PL NL
	PL	ZE ZE NL	ZE ZE NM	NM PT NM	NM NM NM	NM PM NT	NL PL NT	NL PL NL

point while  $K_d$  value should be appropriate. In this design, the base rule with two antecedences and three consequence are as follows:

“If  $e(t)$  is NL and  $\Delta e(t)$  is NL, then  $\Delta K_p$ ,  $\Delta K_i$  and  $\Delta K_d$  is PL, NL and NT, respectively”.

The domain of fuzzy subset is defined in Eq. (10) as follows:

$$[e(t), \Delta e(t)] = \{-1, -0.8, -0.6, -0.4, -0.2, 0, 0.2, 0.4, 0.6, 0.8, 1\} \quad (10)$$

The triangular shape function is selected for membership function input and output as shown in Fig. 3.

## 4 Results and Discussion

For the verification purposes, a proposed CFSAPID was simulated on the double-acting cylinder with proportional valve pneumatic model plant, and analysis on its performances was conducted by comparing this controller with the same plant with single FSAPID controller. As shown in Fig. 4, a rod piston position with the CFSAPID

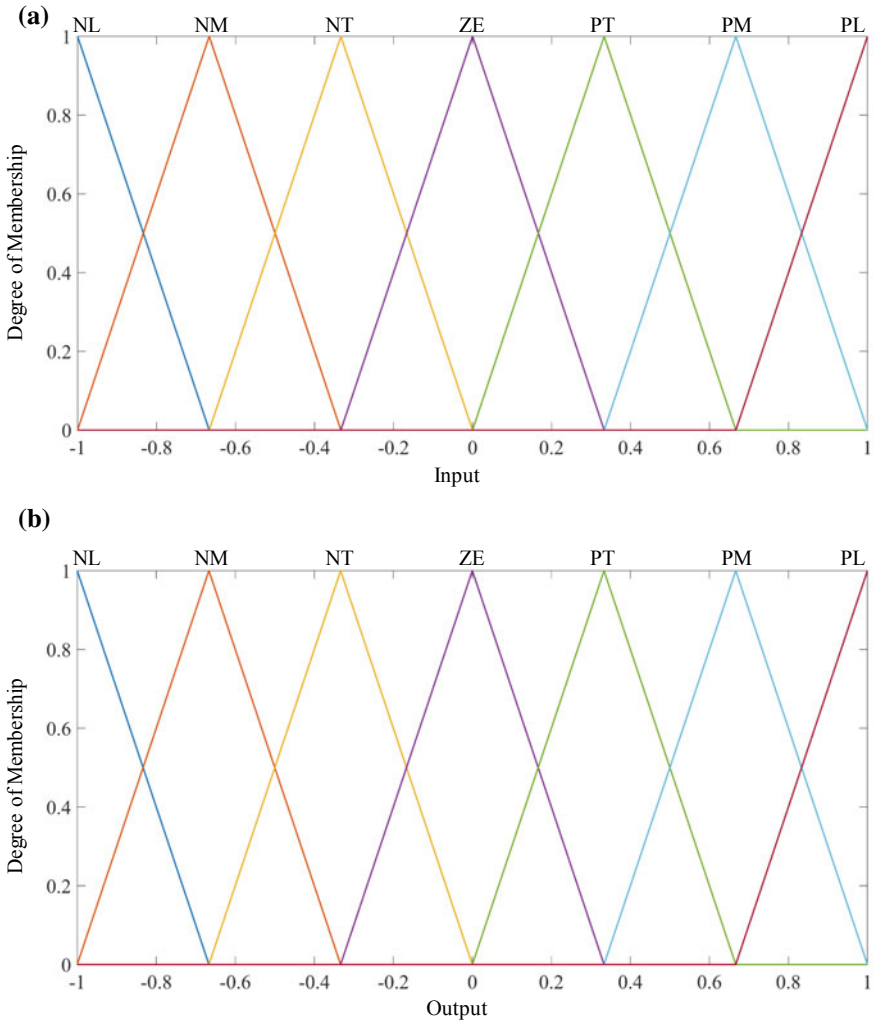


**Fig. 3** FLC membership functions. **a** Inputs variable of  $e(t)$  and  $\Delta e(t)$ , **b** Outputs variable of  $\Delta K_p$ ,  $\Delta K_i$  and  $\Delta K_d$

controller is faster in terms of step response in achieving the desired position has a better steady-state error, in comparison to the same plant with FSAPID controller. The settling time for rod piston control with CFSAPID system is about 0.8 s faster than the single FSAPID with almost no vibration. On the other hand, in terms of vibration in velocity performances, as shown in Fig. 5, FSAPID performing about 0.3 m/s slower than the piston rod control with CFSAPID.

The performance of each controller in terms of rod piston position is summarized in Table 4. In cylinder chambers performance as shown in Fig. 5, rod piston control

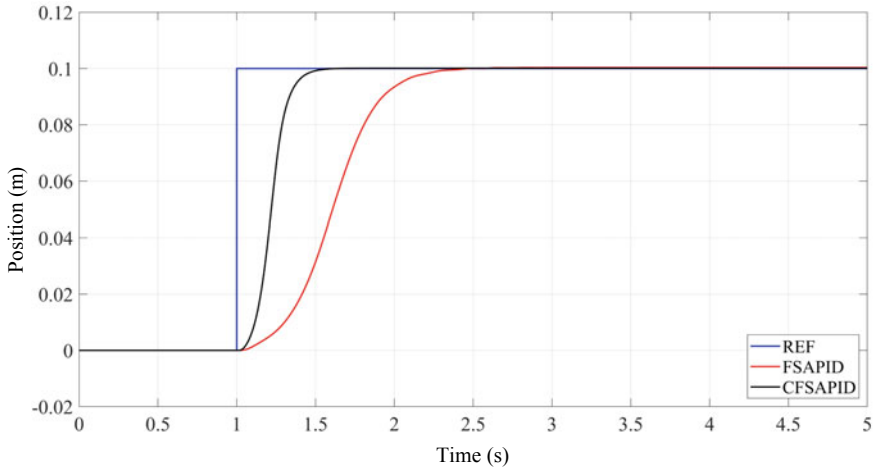


**Fig. 4** Pneumatic cylinder rod piston position performances; FSAPID versus CFSAPID

with proposed CFSAPID performing faster response if compare with the system with only FSAPID controller. Exponentially increment of pressure dynamic in pneumatic cylinder chamber 1 can be seen in Fig. 5a in which pneumatic rod piston with CFSAPID having a very short rising time at about 0.2 s and faster settling time at about 0.5 s if compare to the system with single FSAPID that take about 0.6 s for rise time and take about 1.2 s for the settling time. It is different from the chamber 2 as shown in Fig. 5b where pressure dynamic in pneumatic cylinder chamber 2 with CFSAPID control shows less oscillation if compare to the system with single FSAPID with a small overshoot before achieving constant pressure at about 1.5 s. On the other hand, CFSAPID has a lower overshoot rate than FSAPID.

According to Figs. 6 and 7, viscous friction occurs with the relationship between velocity and frictional force of cylinder rod piston. Frictional force in the pneumatic cylinder will increase when the velocity of the rod piston increases. When the rod piston force has reached the breakaway force, static friction will change to dynamic friction. On the other hand, when the piston rod has reached to the setpoint, velocity and frictional force are in rest condition where the friction is within a static friction range as shown in Fig. 7. Almost no oscillation in friction force for the pneumatic with CFSAPID but a bit high force overshoot at about 0.25 s before reaching the controllable state at about 0.5 s as shown in Fig. 7. It is different from the pneumatic system with FSAPID where oscillating force frictions occurred at a very long period after small overshoot force from 2 to 3 s.

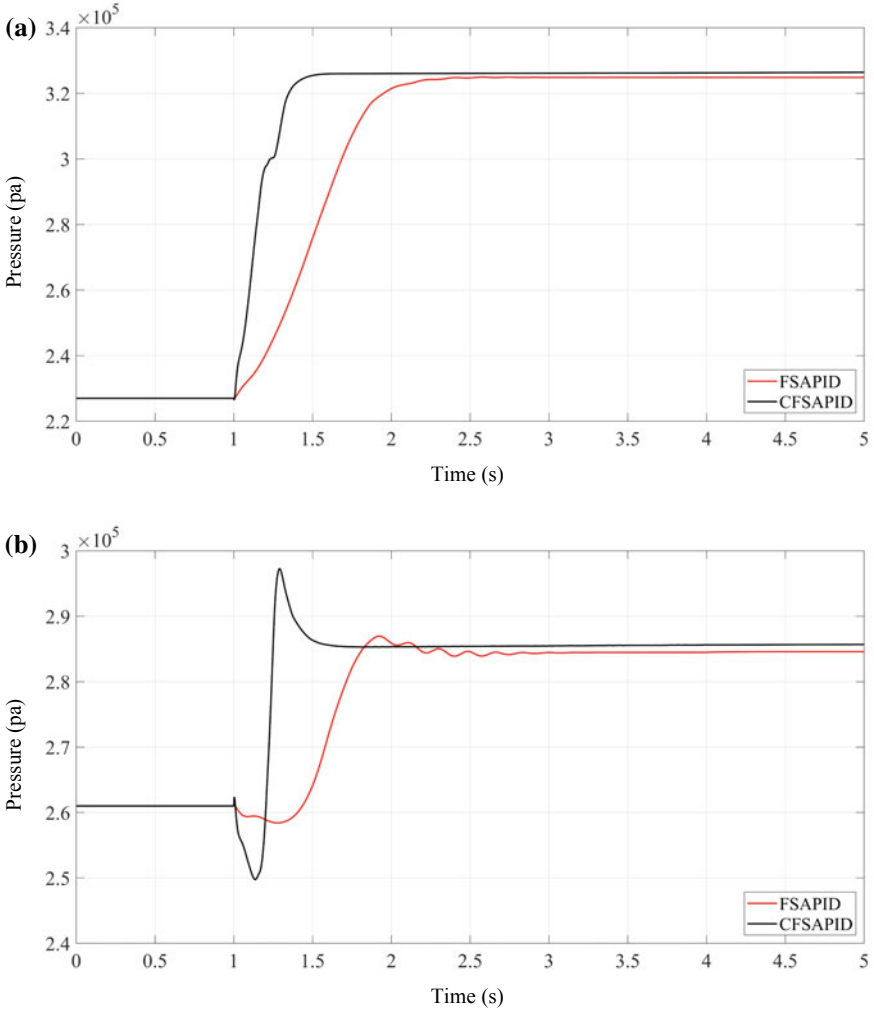


**Fig. 5** Pressure in cylinder chamber performances. **a** Pressure in pneumatic cylinder chamber 1, **b** Pressure in pneumatic cylinder chamber 2

**Table 4** Step response of the system

Performance	Controller	
	FSAPID	CFSAPID
Rise time	1.6231 s	1.2192 s
Settling time	2.1863 s	1.4416 s
Overshoot	0.3599 mm	0.1115 mm
Undershoot	$6.5327e-04$ mm	0.0079 mm
Steady state error	0.3357 mm	0.0109 mm

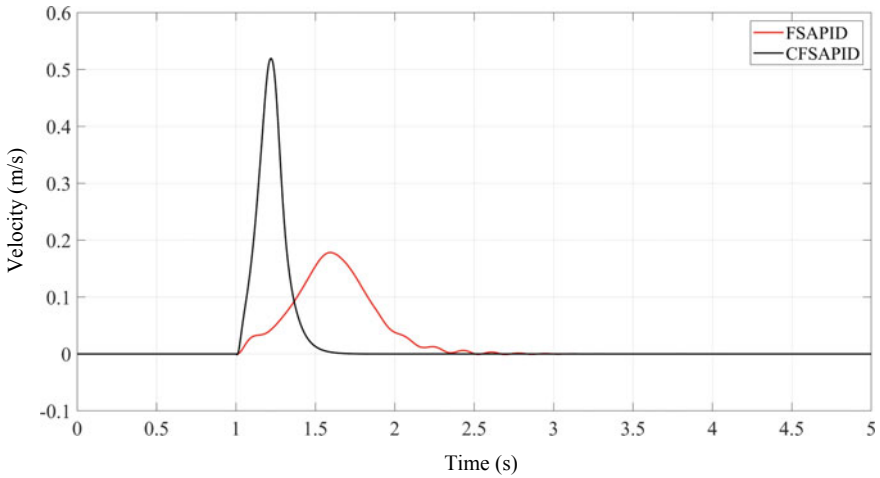


**Fig. 6** Pneumatic cylinder rod piston velocity performances; FSAPID versus CFSAPID

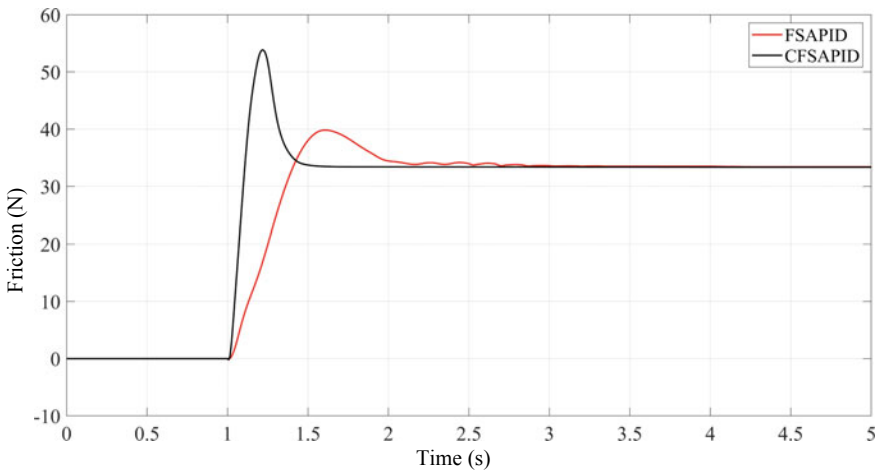


**Fig. 7** Pneumatic friction performances; FSAPID versus CFSAPID

## 5 Conclusion

In this paper, the cascade method of FSAPID control, named as CFSAPID control for pneumatic rod piston position control is presented. The simulation of CFSAPID was run on a single piston double acting pneumatic system plant to control pneumatic rod piston position. The simulation was run and analysis is done by comparing with the same system plant with single FSAPID controller. The overall results show CFSAPID performs better in short rise time and settling time of the rod piston if compare

to the single FSAPID. The pressure on the piston chambers were also stable for the pneumatic system with CFSAPID with fast responses and stable pressure state. Moreover, the velocity rod piston also higher for the system with CFSAPID makes stable friction control is achieved earlier than the system with single FSAPID. The high overshoot scenario by the proposed CFSAPID in some states need to be reduced or eliminated and this task is projected as future progress and improvement for this research.

**Acknowledgements** This work is supported by Universiti Malaysia Pahang (UMP) Research Grant (RDU180398).

## References

1. Lai WK, Rahmat M, Wahab APIDN (2012) Modeling and controller design of pneumatic actuator system with control valve. *Int J Smart Sens Intell Syst* 5(3):624–644
2. Saleem A, Taha B, Tutunji T, Al-Qaisia A (2015) Identification and cascade control of servo-pneumatic system using Particle Swarm Optimization. *Simul Model Pract Theory* 52:164–179
3. Haraguchi D, Kanno T, Tadano K, Kawashima K (2015) A Pneumatically driven surgical manipulator with a flexible distal joint capable of force sensing. *IEEE Trans Mechatronics* 20(6):1–12
4. Xie S, Mei J, Liu H, Wang Y (2018) Hysteresis modeling and trajectory tracking control of the pneumatic muscle actuator using modified Prandtl-Ishlinskii model. *Mech Mach Theory* 120:213–224
5. Rahmat MF, Najib S, Salim S, Sunar NH, Ahmad 'Athif MF, Zool Hilmi I, Huda K (2012) Identification and non-linear control strategy for industrial pneumatic actuator. *Int J Phys Sci* 7(17):2565–2579
6. Syed Salim SN et al (2014) Position control of pneumatic actuator using self-regulation nonlinear PID. *Math Probl Eng* 2014:1–12
7. Salim SNS, Ismail ZH, Rahmat MF, Faudzi AAM, Sunar NH, Samsudin SI (2013) Tracking performance and disturbance rejection of pneumatic actuator system. In: 9th Asian control conference, pp 1–6
8. Ren H, Fan J, Kaynak O (2019) Optimal design of a fractional-order proportional-integral-differential controller for a pneumatic position servo system. *IEEE Trans Ind Electron* 66(8):6220–6229
9. Li L, Xie J, Huang J (2013) Fuzzy adaptive PID control of large erecting system. *J Theor Appl Inf Technol* 47(1):412–418
10. Jiangtao F, Qinhe G, Wenliang G (2017) Mathematical modeling and fuzzy adaptive PID control of erection mechanism. *Telecommun, Comput, Electron Control* 15(1):254–263
11. Najjari B, Barakati M, Mohammadi A, Fotuhi MJ, Bostanian M (2014) Position control of an electro-pneumatic system based on PWM technique and FLC. *ISA Trans* 53(2):647–657
12. Soares dos Santos MP, Ferreira JAF (2014) Novel intelligent real-time position tracking system using FPGA and fuzzy logic. *ISA Trans* 53(2):402–414
13. Abu mallouh M (2008) Force velocity control with neural network compensation for contour tracking with pneumatic actuation. Ph.D. Thesis, Queen's University
14. Dehghan B, Surgenor BW (2013) Comparison of fuzzy and neural network adaptive methods for the position control of a pneumatic system. In: 26th IEEE Canadian conference on electrical and computer engineering, pp 1–4
15. Soon CC, Ghazali R, Jaafar HI, Hussien SYS (2017) Sliding mode controller design with optimized PID sliding surface using particle swarm algorithm. *Procedia Comput Sci* 105:235–239

16. Yang H, Sun J, Xia Y, Zhao L (2018) Position control for magnetic rodless cylinders with strong static friction. *IEEE Trans Ind Electron* 65(7):5806–5815
17. Fan C, Hong GS, Zhao J, Zhang L, Zhao J, Sun L (2019) The integral sliding mode control of a pneumatic force servo for the polishing process. *Precis Eng* 55:154–170
18. Junyi C, Binggang C (2011) Fractional-order control of pneumatic position servosystems. *Math Probl Eng* 2011:1–14
19. Mu S, Goto S, Shibata S, Yamamoto T (2019) Intelligent position control for pneumatic servo system based on predictive fuzzy control. *Comput Electr Eng* 75:112–122
20. Ramezani S, Baghestan K (2018) Observer-based nonlinear precise control of pneumatic servo systems. *Proc Inst Mech Eng, Part E: J Process Mech Eng*, 0954408918756906
21. Hildebrandt A, Neumann R, Sawodny O (2010) Optimal system design of SISO-servopneumatic positioning drives. *IEEE Trans Control Syst Technol* 18(1):35–44
22. Karpenko M, Sepehri N (2004) Design and experimental evaluation of a nonlinear position controller for a pneumatic actuator with friction. In: *Proceedings of the 2004 American control conference*, pp 5078–5083
23. Zhao L, Xia Y, Yang Y, Liu Z (2017) Multicontroller positioning strategy for a pneumatic servo system via pressure feedback. *IEEE Trans Ind Electron* 64(6):4800–4809
24. Faris Hikmat O, Mohd Faudzi AA, Omer Elnimair M, Osman K (2014) PI adaptive neuro-fuzzy and receding horizon position control for intelligent pneumatic actuator. *J Teknologi* 67(3):17–24
25. Mamdani EH, Assilian S (1975) An experiment in linguistic synthesis with a fuzzy logic controller. *Int J Man-Mach Stud* 7(1):1–13

# Effect of Excitation Frequency on Magnetic Response Induced by Front- and Back-Side Slits Measured by a Differential AMR Sensor Probe



M. A. H. P. Zaini, M. M. Saari, N. A. Nadzri, A. M. Halil, A. J. S. Hanifah and M. Ishak

**Abstract** Defects in steel structures are one of the major problems that may affect the functionality of the structure. Thus, the detection of the defects is fairly crucial to prevent any unwanted accident from occurring. Nondestructive Testing (NDT) is a group of methods that is widely used to detect those defects, especially cracks. This paper will be focusing on the detection of cracks (artificial slits) by using the Magnetic Flux Leakage (MFL) technique in the magnetic method of NDT. A non-saturated differential MFL probe consists of two AMR sensors has been fabricated for the detection of front as well as backside slits. A measurement system which incorporates the developed probe attached on an XY-stage, a set/reset circuit, an amplifier circuit, a DAQ card, and PC is constructed where an XY-stage controller and a digital lock-in amplifier are developed with the implementation of LabVIEW. Then, the developed MFL probe's performance is evaluated by running several line scan measurements on a 2-mm galvanized steel plate sample engraved with artificial slits with depths that varies from 1.0 to 1.6 mm with variable excitation frequencies. The results show promising output where the slits could be successfully detected and its position could be further estimated. Furthermore, the correlation between the slit depth and difference (delta value) between the signal peaks and troughs could also be founded. Consequently, the optimum excitation frequency can be determined by plotting a graph of the slope of trend line of the delta values versus the frequency.

**Keywords** Non-destructive testing · NDT · Magnetic flux leakage · MFL · Anisotropic magnetoresistance · AMR

---

M. A. H. P. Zaini (✉) · M. M. Saari · N. A. Nadzri  
Faculty of Electrical and Electronics Engineering, Universiti Malaysia Pahang,  
26600 Pekan, Pahang, Malaysia  
e-mail: [mek18006@stdmail.ump.edu.my](mailto:mek18006@stdmail.ump.edu.my)

A. M. Halil · A. J. S. Hanifah · M. Ishak  
Faculty of Mechanical and Manufacturing Engineering, University Malaysia Pahang,  
Pekan Campus, 26600 Pekan, Pahang, Malaysia

© Springer Nature Singapore Pte Ltd. 2020  
A. N. Kasruddin Nasir et al. (eds.), *InECCE2019*, Lecture Notes in Electrical  
Engineering 632, [https://doi.org/10.1007/978-981-15-2317-5\\_2](https://doi.org/10.1007/978-981-15-2317-5_2)



## 1 Introduction

Nowadays, non-destructive testing (NDT) is considered as a commonly used method in evaluating defects in steel structures, like cracks. The NDT itself consists of a few methods, including visual inspection, radiography, ultrasonic and magnetic method. Visual inspection is considered as the simplest method as it only requires a trained inspector to check defects or irregularities visually [1]. However, the result of the inspection based on this method is subjective based on factors that affect his/her decisions such as experience. Meanwhile, the radiography method is focusing on the usage of X-rays for defect evaluation [2]. As the result shows the exact geometry of the defect in steel structure, the X-rays, however, do pose a threat towards human as it is quite harmful and lethal. The ultrasonic measurement, however, uses high frequency sound wave as its base component for the defect detection in steel structures [3, 4]. On the other hand, the magnetic method relies on the theory of the electromagnetism for it to be operable in non-destructive testing applications [5, 6]. By comparing all the methods, the magnetic method is rather favorable and considered as the most popular method mainly due to its traits which is fast, safe and non-contact. Also, this is because the steel structures themselves possess strong magnetic properties and also conductive in nature. In the magnetic method, there are two main principles of measurement that exist. The two principles of measurements are the eddy current and flux leakage measurements [7].

One of the principles of measurements that exists in the magnetic method is the eddy current measurement. There are several techniques that are based on the eddy current measurement such as the Pulse Eddy Current (PEC), Eddy Current Testing (ECT) and Remote Field Testing (RFT) [8–10]. The main principle of these measurements is the study of the eddy current properties which are induced after applying magnetic field to a conductive material. Conventionally, the ECT technique utilizes an excitation coil and a detection coil, where the excitation coil will emit a primary magnetic field after it is supplied with an AC current signal and the detection coil will detect the emergence of secondary magnetic field from the sample [11]. Then, the eddy current circulation in the material will be disturbed in the presence of cracks. An improved version of ECT probe which uses a small magnetic sensor replacing the bulky induction coil is then introduced. By depending on the frequency response characteristic and localized detection performance, the magnetic sensor can further provide a more apparent signal of crack detection [12]. Furthermore, the position of the excitation coil and the magnetic sensor is quite crucial to get a more stable signal, where the stability of the sensor can be compromised when the coil is aligned with the sensor [13].

Besides that, the flux leakage measurement is another principle of the measurements in the magnetic method. The setup is almost identical as the eddy current measurement, where it utilizes an excitation coil and a detection coil, but it also requires a yoke to boost the magnetization signal in order to saturate the sample. In addition, the detection principle is different from the eddy current measurement, where this technique depends on the magnetic flux's disruption in the ferromagnetic

material whenever there is a crack present. This technique can be divided into two methods which are the Magnetic Particle Inspection (MPI) and the Magnetic Flux Leakage (MFL). The MPI uses substances like iron fillings as a tool to detect the flux leakages. MFL, however, utilizes a detection coil or magnetic sensor for the flux leakage detection [6]. The requirement of achieving magnetic saturation in the metallic material can be further discarded, where an upgrade is introduced by utilizing a sensitive magnetic sensor is introduced [7]. However, an understanding between the excitation field, flux leakage and the flaws in the compound are quite complex and crucial in the design of the MFL systems as well as its analysis [14].

In this research, an MFL probe which is non-saturated as well as compact and small in size is developed. To apply the differential technique, the probe is created by using 2 AMR sensors (HMC1001, Honeywell), where one sensor is referenced to others. The probe's main purpose is to assess the front and back side slits. A galvanized steel plate with a thickness of 2 mm is used as the sample, where it is engraved with artificial slits of different depths that vary from 1 to 1.6 mm. Then, the artificial slits are assessed using the developed system. Consequently, by analyzing the magnetic response of the sample, the developed MFL probe's performance in characterizing the slits is evaluated.

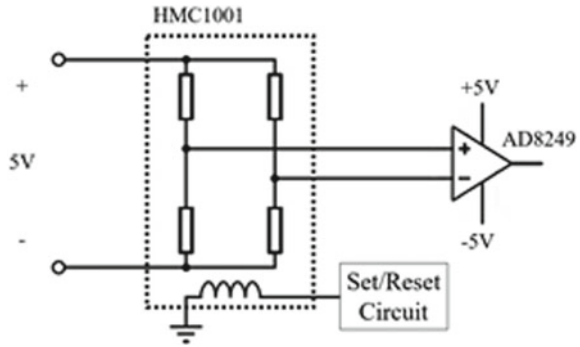
## 2 Experimental Setup

### 2.1 MFL Probe

For the MFL probe, it is constructed from a few components including two AMR sensors, a set/reset circuit, a home-made amplifier circuit, and two yoke ends. The non-saturation technique of MFL is applied within this research by utilizing a sensitive magnetic sensor. It is worth to note that SQUID is deemed as the most sensitive sensor among the other magnetic sensors [15] as it has the lowest noise. However, the SQUID sensor may not be easily compacted because it requires a complicated heat insulation structure which requires liquid helium or liquid helium for cooling [16, 17].

AMR sensors, however, is small in size while they do offer sensitive detection. In this research, the Honeywell HMC1001 AMR sensor is chosen, where it consists of 4 resistive magnetoresistive (MR) elements in a Wheatstone bridge connection. Each MR element is wounded with a set/reset strap as shown in Fig. 1. Whenever the AMR sensor is exposed with a strong magnetic field, its sensitivity, however, could decrease and becomes saturated. This problem can be encountered by applying a high-pulse current to the set/reset strap [18] to regain its sensitivity. Hence, a set/reset circuit is developed in this study. This circuit can be controlled either manually or automatically, where its main purpose is to provide the high-pulse current into the set/reset strap.

**Fig. 1** Schematic diagram of one HMC1001 AMR sensor connected to an AD8249 instrumentation amplifier and a set/reset circuit



Then, to apply the differential detection technique, two AMR sensors are used and fabricated in the MFL probe. In general, one AMR sensor will output an absolute value. This could mean that the magnetic response acquired by the AMR sensor contains not only flux leakages' signal, but it could also be embedded with noises, especially the environmental noises. Thus, to eliminate the noises of the background and increase the probe's sensitivity, a differential probe is fabricated by using two AMR sensors, where the response from sensor 2 is referenced with sensor 1 or vice versa. The baseline is set to be 4 mm between the two sensors. A Data Acquisition (DAQ) card (NI-USB 6212) is used to acquire the output signal of the sensor. Also, an amplifier circuit incorporating two instrumentation amplifiers (INA) for the AMR sensors is developed. The gain of each INA is 40 dB.

To improve the stability of the sensors, two excitation coils are placed on both sides of the AMR sensors and are wound at both yoke's ends with magnet wires with a diameter of 0.65 mm for 100 turns. Then, two ferrite rods are used as the cores for both yoke ends. This is to further improve the magnetization signal, consequently, increasing the strength of the signal of the flux leakages.

## 2.2 Measurement System

As shown in Fig. 2, the measurement system incorporates the developed MFL probe, power supply, DAQ card, and PC. The excitation coils are wound both yokes ends, where each end is connected with a power supply where it will supply signal with variable frequencies to the excitation coils. Then, the DAQ card will capture the amplified signal and fed it to the PC. Furthermore, an XY-stage with a dimension of 55 cm  $\times$  45 cm is used, where the MFL probe is attached. Then, through a virtual instrument (LabVIEW, National Instruments), a VI to control the XY-stage is developed.

In this research, a lock-in amplifier (LIA) is vital as it assists in extracting signal amplitudes and phases from a tremendously noisy environment. Instead of using the analog LIA, a digital LIA is constructed as shown in Fig. 3. This is due to the bulky

**Fig. 2** Schematic diagram of the MFL system

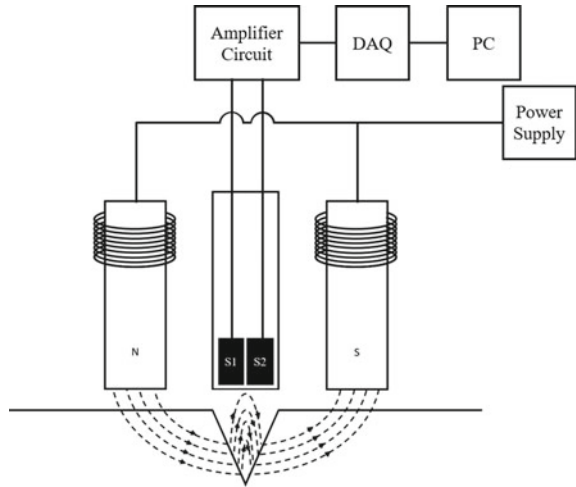
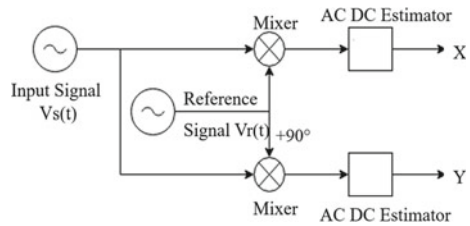


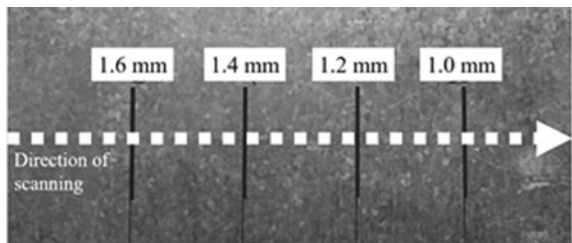
**Fig. 3** The block diagram of the digital lock-in amplifier



size of the analog LIA which may limit the flexibility of the usage of the MFL system. While, for the digital LIA, only a DAQ card is needed, as the data from the DAQ card are streamed to the PC. Via LabVIEW, the digital LIA is constructed. Finally, the measurement system is developed by integrating the DAQ system and the XY-stage controller by using LabVIEW.

As for the sample, the 2-mm thick galvanized steel plate is engraved with a laser engraver to create artificial slits with different depths that vary from 1 to 1.6 mm on the sample. Then, to evaluate the depth of the slits, line scan measurements are conducted as illustrated in Fig. 4, while the line scanning resolution is established at 1 mm.

**Fig. 4** Line scanning procedure on the galvanized steel sample



The measurement is done for  $90^\circ$  magnetization angle from the sample's surface. Then, the amplitude is fixed at 0.3 A, while the excitation frequency is varied to be 10 Hz, 30 Hz, 70 Hz, 110 Hz and 310 Hz.

### 3 Results and Discussions

#### 3.1 Front Side and Back Side Measurement

Figure 5 shows the result of the line scan of the front side measurement at an amplitude of 0.3 A and a frequency of 70 Hz. Meanwhile, Fig. 6 shows the result of back side measurement with the same settings as the front side measurement. The results were separated following their real and imaginary parts as output by the lock-in amplifier.

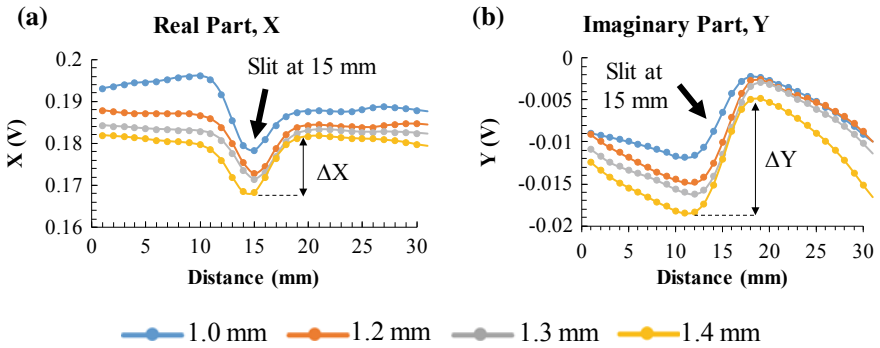


Fig. 5 Raw waveforms for a real and b imaginary parts of front side slits measurements at a frequency of 70 Hz and an amplitude of 0.3 A

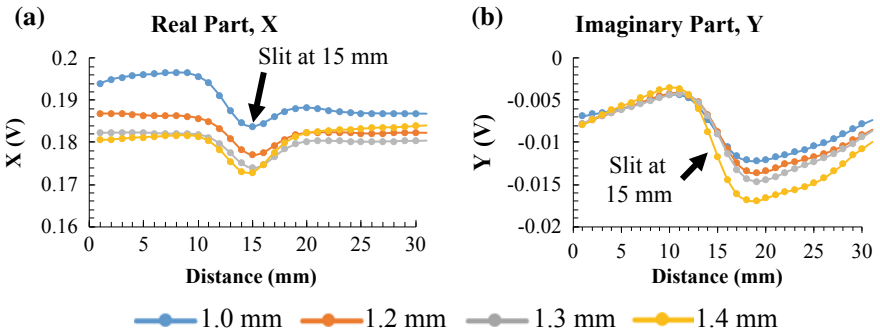


Fig. 6 Raw waveforms for a real and b imaginary parts of back side slits measurements at a frequency of 70 Hz and an amplitude of 0.3 A

The real part showed the detected signal which was in-phase with the magnetization signal, while the imaginary part showed the detected signal that was out-of-phase compared to the magnetization signal. Roughly, it was suspected that the real part represented the flux leakage signal, while, the imaginary part represented the eddy current signal. For the real part, it could be observed that at the location of slit, the signal was minimum. Meanwhile, for the imaginary part, the location of the slit was shown where the intensity of the signal was changing either from maximum to minimum or from minimum to maximum.

For the real part of both front side measurements as in Fig. 5a and back side measurement as in Fig. 6a, the signal patterns were almost identical. Both graphs showed minimum values at the location of the slit. However, the overall minimum values of the back-side measurement could be seen to be higher compared to the overall minimum values of the front side measurement. Meanwhile, the imaginary part of the measurement could be seen in Fig. 5b for front side measurement and Fig. 6b for back side measurement. For the imaginary part of the front side measurement and back-side measurement, their signal patterns contradicted to each other, where the imaginary part of the front side measurement was inverted compared to the signal patterns of the imaginary part of the back-side measurement. This could be explained due to the eddy current dependency that governed the front surface.

For each raw waveform, delta values for both the front side and back side measurement were calculated for both real and imaginary parts. For front side measurement, the delta values  $\Delta X$  were obtained from the signal by calculating the difference between the signal's peaks and troughs. The case for the imaginary part was also the same where the delta values  $\Delta Y$  is calculated from the difference of the signal's peaks and troughs.

From Figs. 7a and 8a, which represent the delta values of the real part for front and back side measurements respectively, the overall delta values of the front side measurement were higher compared to the delta values of the back side measurement. For both measurements, the delta values for the real parts did show an increase

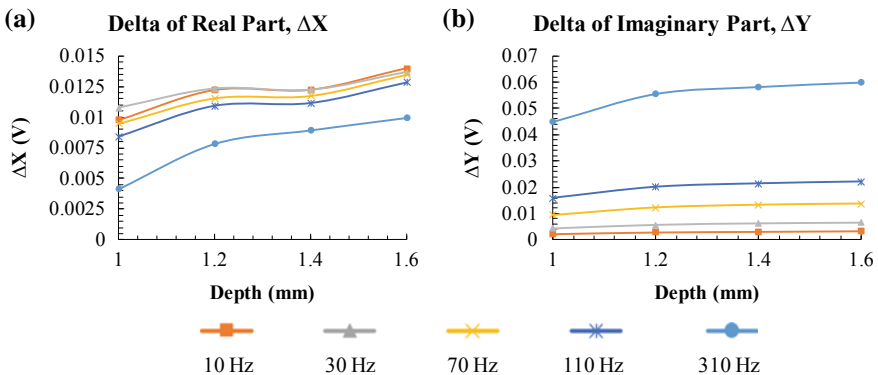


**Fig. 7** Signal differences for **a** real and **b** imaginary parts of the front side measurements

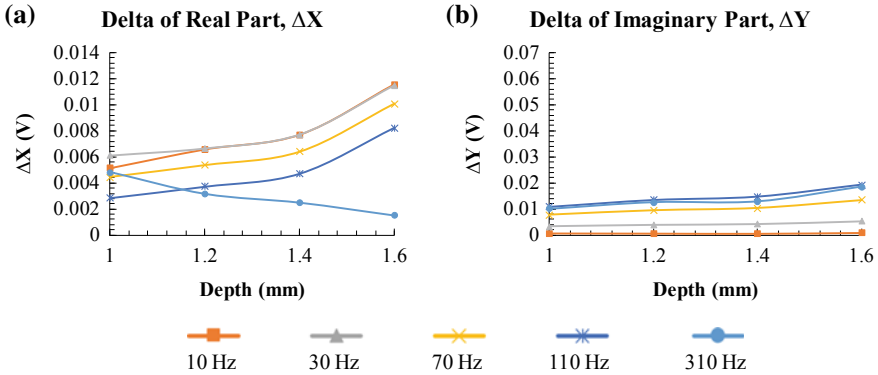


**Fig. 8** Signal differences for **a** real and **b** imaginary parts of the back side measurements

whenever the depth of slit was increased. However, for the 310-Hz data of the delta values of the real part for backside measurement did not agree with the said relationship as in Fig. 8a. Also, the frequency did affect the delta values where, as the frequency increases, the delta values decrease. This relationship was agreed by both the delta values of real parts for both front and back side measurements except for the 310 Hz data of the delta values of the real part for back side measurement.

For the delta values of imaginary parts for the front and back side measurements as in Figs. 7b and 8b, the delta values showed an increase when the slit depth increased. The delta values of the imaginary part for front side measurement were higher in overall compared to its back-side counterpart. Effect of frequency of the delta values of the imaginary part could be seen for front side measurement as the delta values increased with regards of frequency, same with the back-side measurement. However, the increase of delta values of the imaginary part for back side measurement was smaller compared to the front-side measurement.

From these delta value graphs, the front side measurement tended to have higher delta values, while the delta values of the back-side measurement were lower.

### 3.2 Graph of Slope of Trendline of the Delta Values of Real and Imaginary Parts of the Front Side and Back Side Measurement

Then, trendlines from each delta values graphs were generated and the slope of the delta values was calculated and plotted as shown in Fig. 9. The slope of trendlines of the front side measurement for both real and imaginary part could be seen to be increasing as the frequency increased. However, the case is not the same for back-side measurement. For real part of back side measurement, the slope of trendlines decreased as frequency was increased, meanwhile, for back side measurement, its

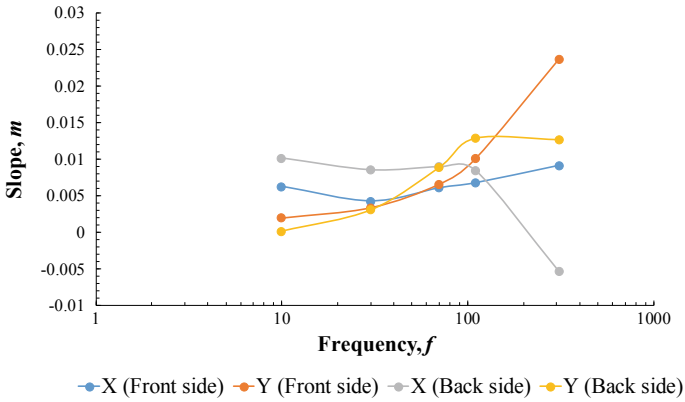


**Fig. 9** Graph of slope of trendline of the delta values of real and imaginary part for the front and back side measurements with respect to frequency

slope of trendlines of the imaginary part increased as the frequency was increased, but the slope would reach saturation at 110 Hz and started to decrease afterward. From the graph, the maximum overall of the slope of trendlines was at the frequency of 110 Hz. Thus, this showed that the front side and back side measurement at 110 Hz frequency was the optimum frequency value since the changes of delta values based on slit depth was higher compared to other frequencies for both real and imaginary parts for the front and back side measurements.

### 4 Conclusions

As a conclusion, a non-saturated differential MFL probe has been fabricated, where it consisted of two AMR sensors. The developed probe was used to evaluate the magnetic responses of the artificial front and back side slits on a galvanized steel plate with variable depths varied from 1.0 to 1.6 mm. From the raw signal of both real and imaginary part, the position of the slit could be estimated. Also, the correlation between the slit’s depth and the difference between the raw signal’s peaks and troughs could be found for real and imaginary parts during the front and back side measurements. Roughly, the overall signal produced from the front-side measurement was higher compared to the back-side measurement. Furthermore, from the slope of the trendline of the delta values, it could be seen that the optimum frequency for the real and imaginary parts for both front and back side measurement was at 110 Hz where the overall slope was at maximum. The results showed that the optimum excited frequency could be at 110 Hz to produce better output for front and back side measurements.



**Acknowledgements** The authors would like to thank to the Ministry of Higher Education of Malaysia (grant no. RDU160115) and Universiti Malaysia Pahang (grant no. RDU170377) for laboratory facilities and financial assistance.

## References

1. Mccrea A, Chamberlain D, Navon R (2002) Automated inspection and restoration of steel bridges—a critical review of methods and enabling technologies. *Autom Constr* 11:351–373
2. Tillack GR, Nockemann C, Bellon C (2000) X-ray modeling for industrial applications. *NDT&E Int* 33:481–488
3. Goglio L, Rossetto M (1999) Ultrasonic testing of adhesive bonds of thin metal sheets. *NDT&E Int* 32:323–331
4. Jiao J, Sun J, Li N, Song G, Wu B, He C (2014) Micro-crack detection using a collinear wave mixing technique. *NDT&E Int* 62:122–129
5. Jiles DC (1988) Review of magnetic methods for nondestructive evaluation. *NDT&E Int* 21:311–319
6. Jiles DC (1990) Review of magnetic methods for nondestructive evaluation (Part 2). *NDT Int* 23:83–92
7. Tsukada K, Yoshioka M, Kawasaki Y, Kiwa T (2010) Detection of back-side pit on a ferrous plate by magnetic flux leakage method with analyzing magnetic field vector. *NDT&E Int* 43:323–328
8. Auld BA, Moulder JC (1999) Review of advances in quantitative eddy current nondestructive evaluation. *J Nondestr Eval* 18:3–36
9. Kasai N, Fujiwara Y, Sekine K, Sakamoto T (2008) Evaluation of back-side flaws of the bottom plates of an oil-storage tank by the RFECT. *NDT&E Int* 41:525–529
10. Lebrun B, Jayet Y, Baboux JC (1997) Pulsed eddy current signal analysis: application to the experimental detection and characterization of deep flaws in highly conductive materials. *NDT&E Int* 30:163–170
11. Pohl R, Erhard A, Montag H, Thomas H, Wu H (2004) NDT techniques for railroad wheel and gauge corner inspection. *NDT&E Int* 37:89–94
12. Tsukada K, Hayashi M, Nakamura Y, Sakai K, Kiwa T (2018) Small eddy current testing sensor probe using a tunneling magnetoresistance sensor to detect cracks in steel structures. *IEEE Trans Magn* 54:1–5
13. Nadzri NA, Saari MM, Halil AM, Ishak M (2018) Development of eddy current testing system for welding inspection. In: 2018 9th IEEE control and system graduate research colloquium, pp 94–98
14. Wang ZD, Gu Y, Wang YS (2012) A review of three magnetic NDT technologies. *J Magn Magn Mater* 324(4):382–388
15. Tumanski S (2007) Induction coil sensors—a review. *Meas Sci Technol* 18(3)
16. Saari MM, Sakai K, Kiwa T, Sasayama T, Yoshida T, Tsukada K (2015) Characterization of the magnetic moment distribution in low-concentration solutions of iron oxide nanoparticles by a high- $T_c$  superconducting quantum interference device magnetometer. *J Appl Phys* 117(17):17B321
17. Saari MM, Ishihara Y, Tsukamoto Y, Kusaka T, Morita K, Sakai K (2015) Optimization of an AC/DC high- $T_c$  SQUID magnetometer detection unit for evaluation of magnetic nanoparticles in solution. *IEEE Trans Appl Supercond* 25:3–6
18. He, D. (2017). AMR sensor and its application on nondestructive evaluation. In *Magnetic sensors - development trends and applications*, pp 133–154

# Model-Free PID Controller Based on Grey Wolf Optimizer for Hovering Autonomous Underwater Vehicle Depth Control



**Mohd Zaidi Mohd Tumari, Amar Faiz Zainal Abidin, Ahmad Anas Yusof, Mohd Shahrieel Mohd Aras, Nik Mohd Zaitul Akmal Mustapha and Mohd Ashraf Ahmad**

**Abstract** Traditionally, the wearisome effort is required to tune the PID parameters and always resulting in erroneous system behavior. The objective of the present work paper is to develop a tuning method for model-free PID controller parameters by using Grey Wolf Optimizer (GWO) to control the depth of Hovering Autonomous Underwater Vehicle (HAUV). The speed of HAUV thrusters is controlled by a PID controller where the tuning for three PID parameters is done by using GWO algorithms. Sum Square Error (SSE), percentage overshoot and settling time of the depth response are chosen as the fitness functions. The differential equation of the HAUV system in heave direction is considered with the aim to confirm the design of PID controller. The proposed approach is compared with Sine Cosine Algorithm (SCA). The time response specifications of input tracking of HAUV with the presences of external disturbances, model nonlinearities, buoyancy force, hydrodynamic drag force and added mass on the HAUV system are considered as a control scheme performance while the convergence curve of the fitness function indicates the performance of optimization algorithm. Finally, the suggested tuning method promises a fast depth tracking capability as shown in simulation results.

**Keywords** Grey wolf optimization · Hovering autonomous underwater vehicle (HAUV) · PID controller

---

M. Z. M. Tumari (✉) · A. F. Zainal Abidin  
Centre for Robotics and Industrial Automation, Fakulti Teknologi Kejuruteraan Elektrik & Elektronik, Universiti Teknikal Malaysia Melaka, Hang Tuah Jaya, 76100 Durian Tunggal, Melaka, Malaysia  
e-mail: [mohdzaidi.tumari@utem.edu.my](mailto:mohdzaidi.tumari@utem.edu.my)

A. A. Yusof  
Fakulti Kejuruteraan Mekanikal, Universiti Teknikal Malaysia Melaka, Hang Tuah Jaya, 76100 Durian Tunggal, Melaka, Malaysia

M. S. Mohd Aras  
Fakulti Kejuruteraan Elektrik, Universiti Teknikal Malaysia Melaka, Hang Tuah Jaya, 76100 Durian Tunggal, Melaka, Malaysia

N. M. Z. A. Mustapha · M. A. Ahmad  
Faculty of Electrical and Electronics, Universiti Malaysia Pahang, 26600 Pekan, Pahang, Malaysia

## 1 Introduction

Generally, in the oil and gas industries, the Hovering Autonomous Underwater Vehicle (HAUV) is used to do an inspection of the underwater pipeline. This task requires HAUV to maintain at prescribed depth accurately. However, it is difficult to control the HAUV in heave movement underwater because of the perturbation from ocean currents and waves generated from the wind [1]. Therefore, the performance of the HAUV system during hovering at prescribed depth will be disturbed. Moreover, a HAUV model is difficult to derive precisely because of the presence of hydrodynamic damping force and added mass that disrupt the HAUV system [2].

In this work, we propose a controller for the HAUV system in order to achieve a preferred depth perfectly. The objective of the HAUV system is to stabilize and maintain the desired depth or can be called as “station keeping”. Therefore, a considerable amount of literature reporting on HAUV depth control has been referred. For example, fuzzy-PID controller [3], LQR based on Genetic Algorithm (GA) [4], Active Disturbance Rejection Controller (ADRC) [5], fuzzy logic controller [6], PSO-PID controller [7], optional internal model control (OIMC) [8], nonlinear PID controller with adaptive compensation [9], extended state observer-based back-stepping control [10] and single input fuzzy logic controller [11].

Furthermore, a model-free PID controller would offer us a reassuring method for the HAUV depth control system. Model-free PID means the design of the controller without knowing an exact model of the system. Thus, it is easier to control the HAUV system just by tuning the parameters of model-free PID. PID is well known for its reliability and robustness and it has been widely used on the numbers of applications such as in [12–14]. Despite PID controller is able to solve those system control problems, the tuning of PID parameters is a very tedious task. So, it is important to decrease the tuning time for the PID controller to take full benefits of it. Hence, for optimal tuning of PID gains, soft computing optimization techniques have been implemented during the last few decades.

The aim of this study is to find the optimal value of PID controller parameters for nonlinear HAUV system. Thus, with the purpose to tune 3 parameters of PID controller, a grey wolf optimizer (GWO) [15], which is in the class of nature-inspired based optimization, is selected to tune control parameters;  $K_p$ ,  $K_i$ , and  $K_d$  to the optimal values for the desired response of the system. A large and growing body of literature has investigated GWO in various applications such as improved protection of wind power generation systems [16], vehicle engine connecting rod [17] and unmanned aerial vehicles [18]. So far, however, there has been no literature reporting the GWO tuned PID for HAUV system. Thus, this work is to implement the GWO to tune the PID controller for the HAUV system and share the results for other researchers. To verify the effectiveness of the suggested control technique, a nonlinear differential equation of the HAUV system in [19] in heave direction is considered. The time response specifications of depth tracking capability with the presences of external disturbances, model nonlinearities, buoyancy force, hydrodynamic drag force and added mass on the HAUV system are considered as a control

scheme performance while the convergence curve of the fitness function indicates the performance of optimization algorithm. Efficacy of the GWO tuning is compared with Sine Cosine Algorithm (SCA).

## 2 HAUV Model

Figure 1 shows a HAUV model in [19] that maneuver in the vertical axis. The dynamic differential equation of the HAUV model in heave-axis is derived in (1) where  $M_A$ ,  $M_{RB}$ ,  $D_Q$ ,  $z$ ,  $D_L$ ,  $\tau$ ,  $w$  and  $g$  represents added mass, rigid-body mass, quadratic hydrodynamic damping coefficient, depth of the HAUV, linear hydrodynamic damping coefficient, thruster force, external disturbances and net buoyancy force, respectively.

$$(M_{RB} + M_A)\ddot{z} + (D_L + D_Q|\dot{z}|)\dot{z} + g = \tau + w \quad (1)$$

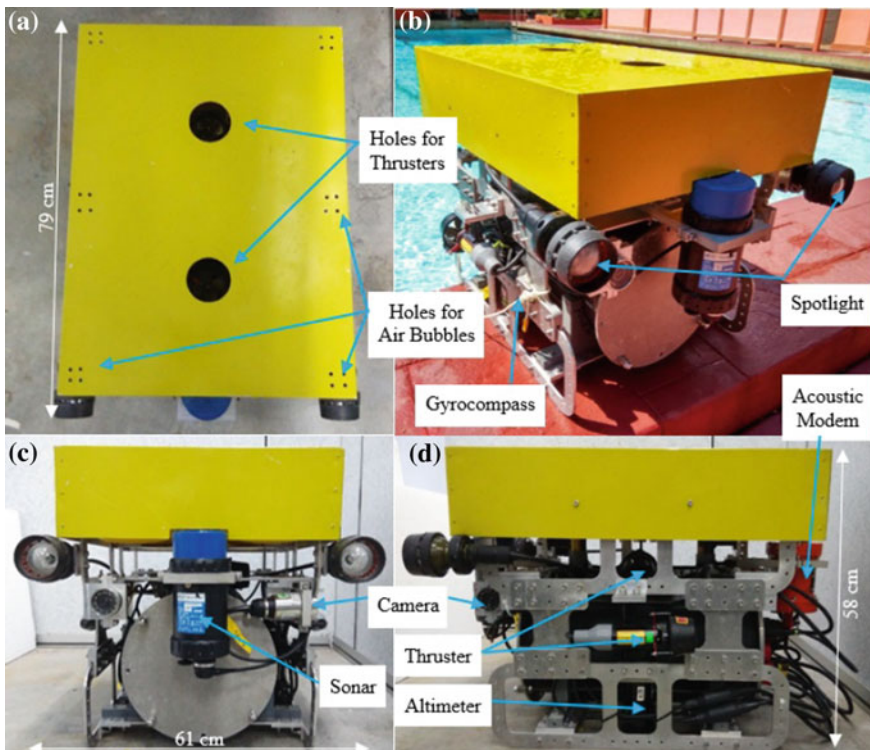


**Fig. 1** HAUV established by UCRG. **a** Top perspective. **b** Isometric perspective. **c** Front perspective. **d** Left perspective [2]

**Table 1** HAUV parameters developed by UCRG [2]

Parameters	Values
$M_{RB}$	63.50 kg
$M_A$	44.59 kg
$D_L$	0 kg/s
$D_Q$	185.47 g/m
g	1.96 N

External disruption used in this simulation is wave current. The model of the wave current is obtained in (2) [20]. The wave current is simulated as a sinusoidal force performing on the HAUV system in downward movement with 0.1 Hz frequency and 2 N amplitude.

$$w = 2 \sin(0.2\pi t)N \quad (2)$$

Figure 1 shows the photo of the HAUV system established by Underwater, Control, and Robotics Group (UCRG) Universiti Sains Malaysia (USM). The HAUV has a dimension of 58 cm high, 61-centimeter-wide, and 79-centimeter-long. The buoyant of this HAUV is set to be slightly positive by equipped it with passive buoyancy element. Two vertical thrusters are used to control the HAUV in heave movement. The parameters of the HAUV system is shown in Table 1. For simulation works, only parameters in the heave direction are considered.

### 3 Controller Design

#### 3.1 PID Controller

Figure 2 shows the PID control scheme for the HAUV system, where  $e(t)$ ,  $w(t)$ ,  $z_d(t)$ ,  $z(t)$ , and  $u(t)$  are error, wave current, reference, measurement of depth and control input, respectively. G is the plant is the HAUV model. Transfer function of PID controller is given by (3).

$$TF_{PID} = K_p + \frac{K_i}{s} + K_d s \quad (3)$$

where  $K_d$  is a derivative gain,  $K_i$  is an integral gain and  $K_p$  is a proportional gain.

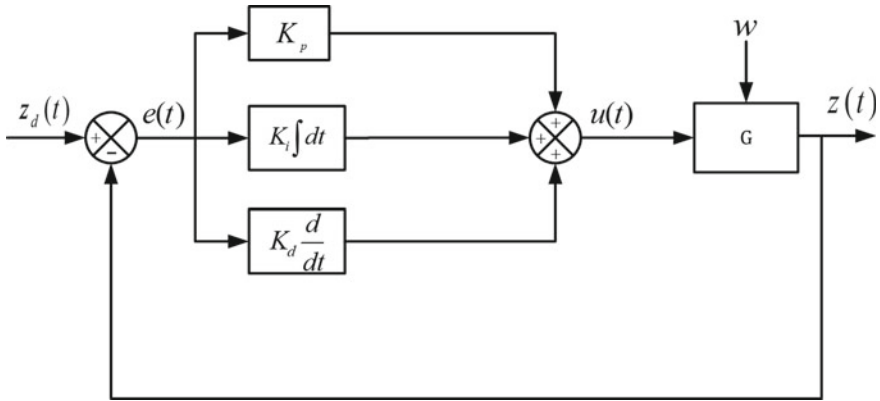


Fig. 2 PID control scheme for HAUV system

### 3.2 Grey Wolf Optimization (GWO)

GWO is a Swarm Intelligence (SI) algorithm motivated by the grey wolves hunting for prey in nature [15]. These wolves hunt the prey by following the social hierarchy that divided as alphas, beta, delta, and omega. The alphas are the uppermost level in the hierarchy, followed by beta, delta, and omega. The alphas are the sturdiest in the group, therefore other wolves need to follow the alpha orders. The methods of hunting are; (1) Finding, chasing and reaching prey, (2) Surrounding and harassing prey till it becomes standstill and (3) Attacking the prey [15]. The mathematical model of the GWO algorithm is developed as follows.

The position update equation of the pack is as in [14]

$$\vec{D} = \left| \vec{C} \cdot \vec{X}_p(t) - \vec{X}(t) \right| \quad (4)$$

$$\vec{X}(t+1) = \vec{X}_p(t) - \vec{A} \cdot \vec{D} \quad (5)$$

where  $t$  is the current iteration.  $\vec{A}$  and  $\vec{C}$  are coefficients vectors,  $\vec{X}_p$  is the location of the prey, and  $\vec{X}$  indicates the position vector of a grey wolf. The vectors  $\vec{A}$  and  $\vec{C}$  are calculated as the following equations:

$$\vec{A} = 2\vec{a} \cdot \vec{r}_1 - \vec{a} \quad (6)$$

$$\vec{C} = 2\vec{r}_2 \quad (7)$$

where components of  $\vec{a}$  is linearly decreased from 2 to 0 with iterations and  $r_1, r_2$  are pseudorandom numbers in range [0, 1].

The entire pack reaches the target and attack by updating the position based on the best solutions of the alpha, beta, and delta as in (8)–(10).

$$\vec{D}_\alpha = \left| \vec{C}_1 \cdot \vec{X}_\alpha - \vec{X} \right|, \quad \vec{D}_\beta = \left| \vec{C}_2 \cdot \vec{X}_\beta - \vec{X} \right|, \quad \vec{D}_\delta = \left| \vec{C}_3 \cdot \vec{X}_\delta - \vec{X} \right| \quad (8)$$

$$\vec{X}_1 = \vec{X}_\alpha - \vec{A}_1 \cdot \vec{D}_\alpha, \quad \vec{X}_2 = \vec{X}_\beta - \vec{A}_2 \cdot \vec{D}_\beta, \quad \vec{X}_3 = \vec{X}_\delta - \vec{A}_3 \cdot \vec{D}_\delta \quad (9)$$

$$\vec{X}(t+1) = \frac{\vec{X}_1 + \vec{X}_2 + \vec{X}_3}{3} \quad (10)$$

Let  $X_i$  is the position vector for particle  $i$ . There are 3 PID parameters to be adjusted, so the design parameter is defined in (11):

$$X_i = \left[ K_p \quad K_i \quad K_d \right] \quad (11)$$

The swarm particles,  $X_i$  are initially set randomly using (12) where  $u_b$  is an upper boundary and  $l_b$  is a lower boundary is constraint space fixed for the particles, while  $r_3$  is random real-number between [0, 1].

$$X_i = l_b + (u_b - l_b) \times r_3 \quad (12)$$

For this simulation, an improved GWO algorithm using a priority-based fitness technique is recommended for PID tuning [21]. Sum squared error (SSE) of depth,  $z$  is set as uppermost primacy, followed by percentage overshoot and settling time of depth response. The main concern is to get the smallest number of those fitness functions which are as shown in (13)–(15).

$$f_1(X) = \text{Fitness}_1 = \text{SSE} = \sum e^2(t)dt \quad (13)$$

$$f_2(X) = \text{Fitness}_2 = \text{PO} = \frac{y_{\max} - y_{\text{final}}}{y_{\text{final}}} \times 100\% \quad (14)$$

$$f_3(X) = \text{Fitness}_3 = \text{Settling Time} = T_s \quad (15)$$

The best solution is updated by using Eq. (16)

$$X_{t+1}^* = \begin{cases} X_t^i, & f_1(X_t^i) < f_1(X_t^*) \text{ AND } f_2(X_t^i) < f_2(X_t^*) \text{ AND } f_3(X_t^i) < f_3(X_t^*) \\ X_t^*, & \text{otherwise} \end{cases} \quad (16)$$

The simulation stopped after iteration reached the maximum value and the best PID parameters obtained by GWO algorithm is presented.

### 4 Results and Discussion

The simulation works are done with MATLAB 2017b, Microsoft Window 10, 8 GB RAM and Intel Core i7-6700 Processor (3.41 GHz). The HAUV model in (1) is designed via Simulink.

The simulation is run for 0.25 s and the sampling time is 0.01 s. The number of agents is set to 10 and the maximum iterations are set to 1000. This combination contributes to 10,000 number of evaluations. The lower boundary and upper boundary for each design parameters in (5) are fixed as follow:

$$\begin{aligned}
 \text{lower boundary} &= l_b = [0 \quad 0 \quad 0] \\
 \text{upper boundary} &= u_b = [100,000 \quad 100,000 \quad 100,000]
 \end{aligned}$$

Efficacy of the GWO tuning is compared with the SCA algorithm [22] with the same number of agents and maximum iterations for a fair comparison. Table 2 shows the best PID parameters tuned by using the GWO and SCA algorithm.

Figure 3 shows the HAUV depth response tuned by GWO and SCA algorithm. Based on the results, both tuning approaches fulfilled the station keeping performance although there is an external disturbance applied to the system. The results also show

**Table 2** PID parameters based on GWO and SCA algorithm

PID gain	GWO	SCA
$K_p$	100,000	100,000
$K_i$	99,848.001	17,531.813
$K_d$	1967.579	2407.703

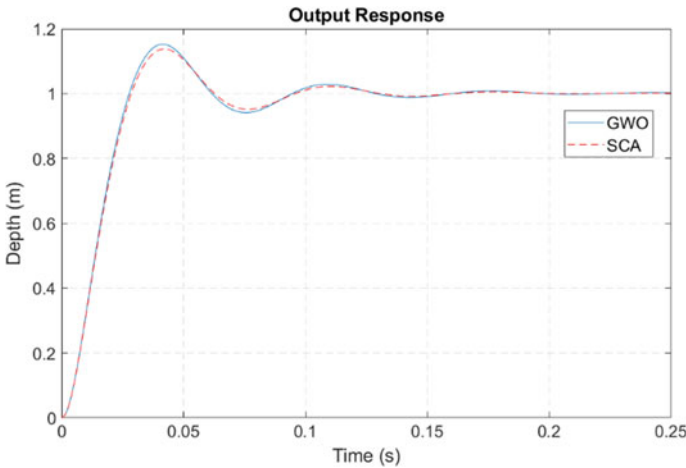


**Fig. 3** Depth response of HAUV system



that with GWO algorithm, the HAUV is able to settle at the desired depth (1 m) in about 0.1177 s with no steady state error occurred. Nonetheless, there is a small overshoot happened at about 15.14%. Whereas, by using SCA, the settling time is 0.1143 s and also no steady-state error and smaller overshoot about 13.67%. It was found that the rise time for GWO tuning and SCA tuning are 0.0196 s and 0.0194 s, respectively.

Figures 4a, 5a and 6a show the convergence curve for fitness function; sum squared error, percentage overshoot and settling time, respectively for 1000 iterations. To zoom those convergence curve better, Figs. 4b, 5b and 6b show the close-up view for 50 iterations. From the results, although SCA produces better in time response

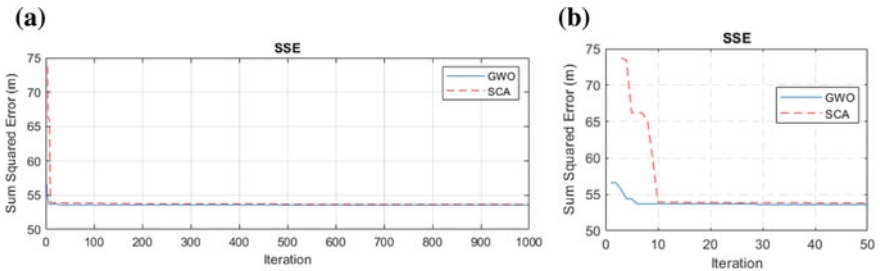


Fig. 4 Sum squared error convergence curve a 1000 iteration b 50 iteration

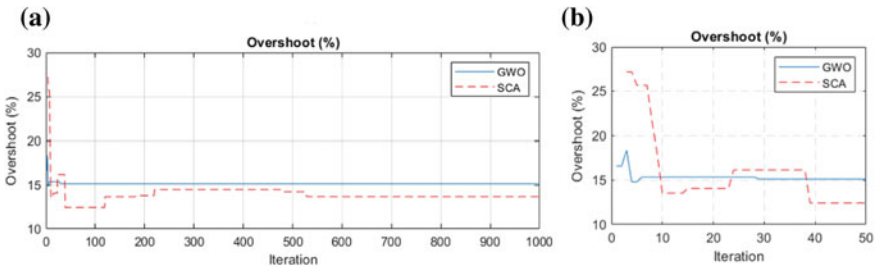


Fig. 5 Percentage overshoot convergence curve a 1000 iteration b 50 iteration

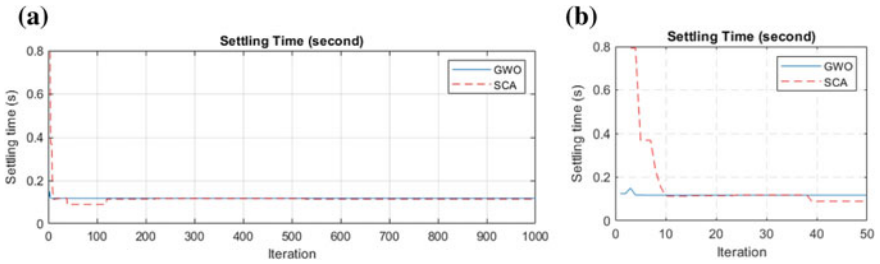


Fig. 6 Settling time convergence curve a 1000 iteration b 50 iteration

specifications, GWO algorithm converges faster to exploit the optimum compared to SCA algorithm. In Fig. 5, the sum squared error for GWO algorithm is smaller (53.59) compared to SCA (53.68). In an optimization problem, the faster agents to exploit the optimum and less fitness function is better. But, in the control field, the performance is better if the system has a faster rise and settling time, less overshoot and less steady state error.

Figure 7 illustrates the HAUV response for various depth; 3, 1, and 4 m. The simulation runs for 10 s for each depth. From the results, both algorithms have a good response with fast rise and settling time, steady state error equal to zero and minor overshoot. Therefore, it is valid to mention that the GWO tuning for PID is able to control the HAUV in the heave direction successfully. Table 3 shows the time response specification for the HAUV system.

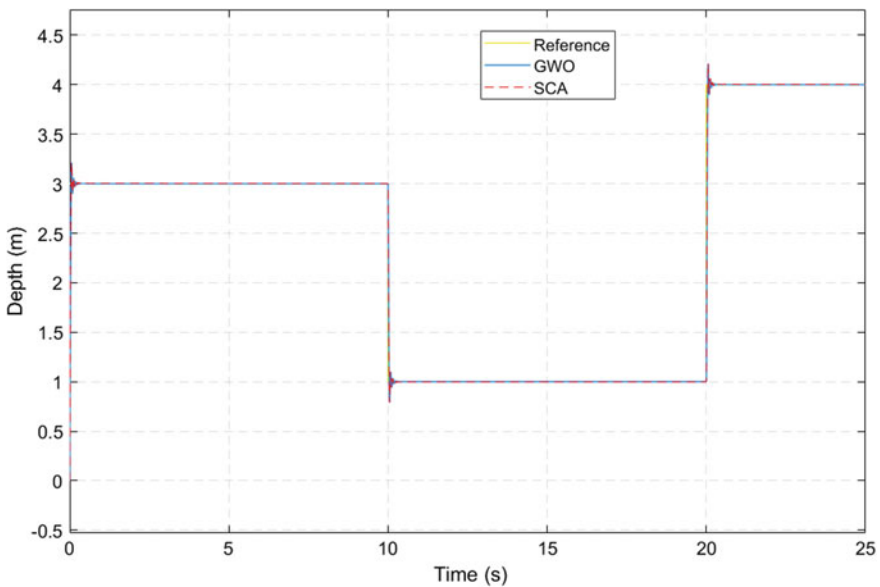


Fig. 7 HAUV response for different depth

Table 3 The specifications of HAUV time response

PID tuning technique	Settling time, Ts (s)	Rise time, Tr (s)	Percentage overshoot, %OS (%)	Sum squared error (SSE)	Steady state error
GWO	0.1177	0.0196	15.14	53.59	0.0
SCA	0.1143	0.0194	13.67	53.68	0.0

## 5 Conclusion

The priority-based fitness approach is implemented on GWO algorithm to tune the parameters of the PID controller for the HAUV system has been presented. It is shown that GWO tuning is more efficient compared to SCA in terms of exploitation to the optimum. From simulation results, it is confirmed that the suggested tuning method can solve the control problem of HAUV in heave direction underwater in aforesaid sectors. A future study investigating experimental works on the HAUV system by implementing a model-free controller would be very interesting.

**Acknowledgements** This work was funded by Universiti Teknikal Malaysia Melaka under research grant PJP/2018/FTK(10B)/S01610.

## References

1. Aras MSM, Abdullah SS, Shah HNM, Rashid MZA, Aziz MAA (2013) Robust control of adaptive single input fuzzy logic controller for unmanned underwater vehicle. *J Theor Appl Inf Technol* 57(3):372–379
2. Song YS, Arshad MR (2017) Robust optimal depth control of hovering autonomous underwater vehicle. In: 2017 IEEE 2nd international conference on automatic control and intelligent systems (I2CACIS 2017). Kota Kinabalu, Sabah, Malaysia, pp 191–195
3. Hu B, Tian H, Qian J, Xie G, Mo L, Zhang S (2013) A fuzzy-PID method to improve the depth control of AUV. In: *Proceeding of 2013 IEEE international conference on mechatronics and automation*. Takamatu, Japan, pp 1528–1533
4. Syahroni N, Seo YB, Choi JW (2008) Depth control of autonomous underwater vehicle based on open control platform. In: *Proceedings of the 17th world congress, international Federation of automatic control*. Seoul, Korea, pp 3707–3712
5. Tao C, Wei Z, Jiajia Z, Haomiao Y, Xiaofu L, Yue H (2014) Depth control of AUV using active disturbance rejection controller. In: *Proceedings of the 33rd Chinese control conference*. Nanjing, China, pp 7948–7952
6. Aras MSM, Abdullah SS, Othman SY, Sulaiman M, Basar MF, Zambri MKM, Kamarudin MN (2016) Fuzzy logic controller for depth control of underwater remotely operated vehicle. *J Theor Appl Inf Technol* 91(2):275–288
7. Mohd Tumari MZ, Zainal Abidin AF, Hussin MSF, Abd Kadir AM, Mohd Aras MS, Ahmad MA (2019) PSO fine-tuned model-free PID controller with derivative filter for depth control of hovering autonomous underwater vehicle. In: *Lecture notes in electrical engineering*, vol 538. Springer, pp 3–13
8. Gao D, Cheng J, Yang Q (2016) Depth control for underactuated AUV in vertical plane using optimal internal model controller. In: 2016 28th Chinese control and decision conference (CCDC). Yinchuan, China, pp 5292–5296
9. Zhang G, Du C, Huang H, Wu H (2016) Nonlinear depth control in under-actuated AUV. In: *Proceeding of 2016 IEEE international conference on mechatronics and automation*. Harbin, China, pp 2482–2486
10. Gharesi N, Ebrahimi Z, Forouzandeh A, Arefi MM (2017) Extended state observer-based backstepping control for depth tracking of the underactuated AUV. In: 2017 5th international conference on control, instrumentation, and automation (ICCIA). Shiraz, Iran, pp 354–358
11. Mohd Aras MS, Abdullah SS, Jaafar HI, Yusof AA, Mohd Tumari MZ, Yan HG (2019) Optimization of single input fuzzy logic controller using PSO for unmanned underwater vehicle. In: *Lecture notes in electrical engineering*, vol 538. Springer, pp 15–26

12. Mohd Tumari MZ, Shabudin L, Zawawi MA, Ahmad Shah LH (2013) Active sway control of a gantry crane using hybrid input shaping and PID control schemes. In: IOP conference series: materials science and engineering, vol 50(1), p 012029
13. Mohd Tumari MZ, Saealal MS, Rashid WNA, Saat S, Nasir MA (2017) The vehicle steer by wire control system by implementing PID controller. *J Telecommun, Electron Comput Eng (JTEC)* 9(3–2):43–47
14. Abdul Shukor NS, Ahmad MA, Mohd Tumari MZ (2017) Data-driven PID tuning based on safe experimentation dynamics for control of Liquid Slosh. In: IEEE 8th control and system graduate research colloquium (ICSGRC), Aug 4–5. Shah Alam, Malaysia, pp 62–66
15. Mirjalili S, Mirjalili SM, Lewis A (2014) Grey wolf optimizer. *Adv Eng Softw* 69:46–61
16. Rezaei N, Uddin MN, Amin IK, Othman ML, Abidin IZ (2018) Grey wolf optimization based improved protection of wind power generation systems. In: IEEE industry applications society annual meeting (IAS), pp 1–8
17. Yıldız BS, Yıldız AR (2018) Comparison of grey wolf, whale, water cycle, ant lion and sine-cosine algorithms for the optimization of a vehicle engine connecting rod. *Mater Test* 60(3):311–315
18. Radmanesh M, Kumar M, Sarim M (2018) Grey Wolf optimization based sense and avoid algorithm in a Bayesian framework for multiple UAV path planning in an uncertain environment. *Aerosp Sci Technol* 77:168–179
19. Fossen TI (1991) Nonlinear modeling and control of underwater vehicles. Ph.D. thesis, Department of Engineering Cybernetics, Norwegian University of Science and Technology, Trondheim
20. Kim J, Joe H, Yu SC, Lee JS, Kim M (2016) Time-delay controller design for position control of autonomous underwater vehicle under disturbances. *IEEE Trans Industr Electron* 63(2):1052–1061
21. Jaafar HI, Mohamed Z, Zainal Abidin AF, Ab Ghani Z (2012) PSO-tuned PID controller for a nonlinear gantry crane system. In: 2012 IEEE international conference on control system, computing and engineering, Nov 23–25. Penang, Malaysia, pp 515–519
22. Mirjalili S (2016) SCA: a sine cosine algorithm for solving optimization problems. *Knowl-Based Syst* 96:120–133

# Experimental Study of Optimization of Electrode Dimension for Non-invasive Electrical Resistance Tomography Application



Yasmin Abdul Wahab, Mahanum Muhamad Sakri, Mohd Anwar Zawawi, Muhammad Sharfi Najib and Normaniha Abd Ghani

**Abstract** Electrical resistance tomography is used to reconstruct the image of the objects within the medium of interest based on electrical conductivity distribution. Besides, the ordinary technique of ERT applied the invasive technique and causing corrosion to the electrodes because of the contact between the electrode and the conductive liquid. Therefore, the ERT system proposed in this work is to investigate the optimize dimension of the electrode in ERT using an experimental approach for non-invasive measurement. In this project, four electrodes are used as transmitter and receiver. All the electrodes are arranged side by side around the pipe. In this process, only one electrode is used as a transmitter and the rest as a receiving sensor. When water is inserted in the pipe, the output of the voltage will be compressed and recorded. Nine different dimensions are investigated and it produces a different voltage output. Therefore, the appropriate electrode dimension must be determined as it also affects the conductivity of the conducting medium. In addition, the appropriate electrode dimension which is 35.34 mm (width)  $\times$  250 mm (height) was chosen as the optimize dimension from the experiment to improve the performance of the existing system.

**Keywords** ERT · Electrode · Non-invasive

## 1 Introduction

Tomography is introduced in a medical field started in the 1950s. Later, its applications have essentially to industrial usage called industrial process tomography (IPT) in the 1970s [1]. Industrial process tomography is generally a cross sectional imaging of parameters of industrial processes and usually a function of time [2].

Nowadays, process tomography (PT) systems play an imperative role in the industrial environment as they provide means to monitor process flows without altering or stalling the industrial processes [3]. Together with providing the cross-sectional

---

Y. Abdul Wahab (✉) · M. Muhamad Sakri · M. A. Zawawi · M. S. Najib · N. Abd Ghani  
Faculty of Electrical and Electronic Engineering Technology, Universiti Malaysia Pahang, 26600  
Pekan, Pahang, Malaysia  
e-mail: [yasmin@ump.edu.my](mailto:yasmin@ump.edu.my)

images of closed pipes or vessels, these systems offer important flow information such as concentration profile, velocity profile, flow rate and compositions. In addition, this PT consists of many advantages such as low cost, non-intrusive, non-invasive and no radiation [4]. Thus, process tomography is one of the important techniques in industrial process tomography. There are several types of process tomography such as electrical resistance tomography (ERT), electrical capacitance tomography (ECT), ultrasonic tomography (UT), and optical tomography (OT).

Although ERT method has proven its usefulness and the great number of researchers and institutions of the interest, there is still have an opportunity to innovate and improve this method by designing and use of new sensing techniques and hardware development. The ERT system proposed in this work is expected to identify an optimized size of the electrode dimension (width  $\times$  height). Therefore, the non-invasive ERT system using an experimental technique is proposed for this project.

## 2 The Basic Principle of ERT

Electrical resistance tomography (ERT) is used to reconstruct an image of resistance or conductivity distribution of the region of interest [5]. Resistance is the opposition that a substance offers to the flow of electric current. It is represented by the uppercase letter  $R$  with the standard unit of ohm, ( $\Omega$ ). Ohm's law states that the voltage,  $V$  directly proportional to current,  $I$  and resistor,  $R$ . When rearrange back the equation, the expression can be like in (1).

$$R = \frac{V}{I} \Omega \quad (1)$$

Based on the electrode mounted on the pipe boundary, the resistance can be measured by an exciting current/voltage signal and measured the voltage/current signal [6].

Most of the researchers implement an insulating pipe as a vessel, with the non-invasive ERT sensor around the boundary of the non-conducting pipe wall [7]. Thus, it causes the current signal cannot be supplied at a source because it blocks the electricity from penetrating the non-conductivity. Another alternative method is by supply a voltage as a source and then measure a current as a received signal.

Besides, conductivity is a measurement of electron flow in a medium (conductor or insulator) under the influence of an external electric field. In other words, conductivity is defined as the ability of a material to conduct electricity. Electric current can flow easily through a material with high conductivity. Conductivity is measured in siemens per meter and is often represented using the Greek letter  $\sigma$ . The electrical conductivity can be presented based on the (2).

$$\sigma = \frac{L}{RA} (\Omega m) \tag{2}$$

As for non-invasive ERT system,  $L$  is the inner diameter of the pipe.  $R$  is the resistance of the medium of interest while  $A$  is the area of the electrode. In addition, the conductance,  $G$  can be defined based on the (3) [8]. Subsequently, a conductive medium is needed as a main medium in the ERT system to ensure that the electrical signal can be propagated significantly inside the vessel. Here, the voltage signal was excited at the transmitter and the current signal that proportional to the conductance was measured at each of the receivers.

$$G = \frac{\sigma A}{L} = \frac{I}{V} = \frac{I}{R} \tag{3}$$

### 3 Methodology

Figure 1 illustrates the basic diagram of the ERT system during the experiment. The main focus is on electrode optimization. In this project, only 4 channels electrodes were attached non-invasively at acrylic pipe with 60 mm outer diameter, 3 mm thickness and 500 mm in length. The signal generator circuit is applied to the excitation source, Tx with 20 V<sub>pp</sub>, 5 MHz. Then, the current signal received by each of the receivers, Rx were processed and converted into voltage measurement using signal

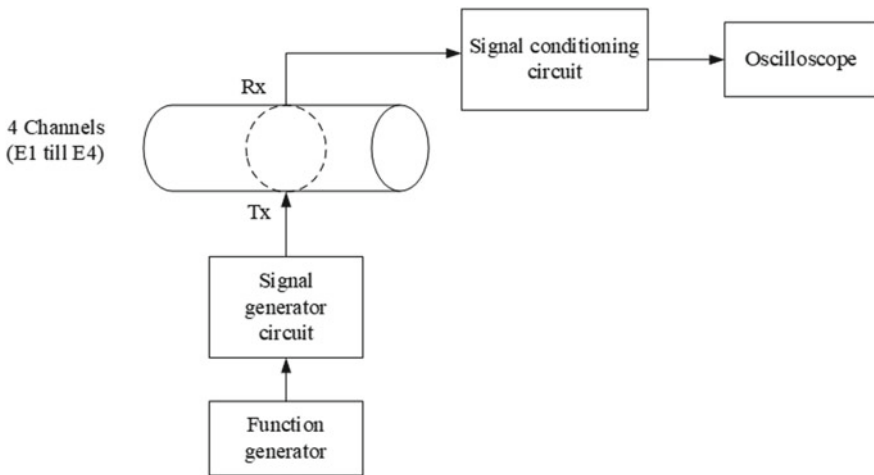


**Fig. 1** Basic diagram of ERT system

conditioning circuit and it was obtained using an oscilloscope. The example of the experimental set-up is shown in Fig. 2. The measurement process started with channel 1, E1 as an excitation source and the received signals were measured at each of the receiver, E2 till E4. Then, the process was repeated with channel 2 as the excitation source and other channels as a receiver. The measurement was completed when all the channels became a excitation source.

In the same way, the material of the electrodes must be determined. Basically, the material of the electrodes must have high electrical conductivity such as copper, aluminum, brass and zinc. Table 1 shows a comparison between the conductive materials. It can be observed that the copper showed the highest value of electrical

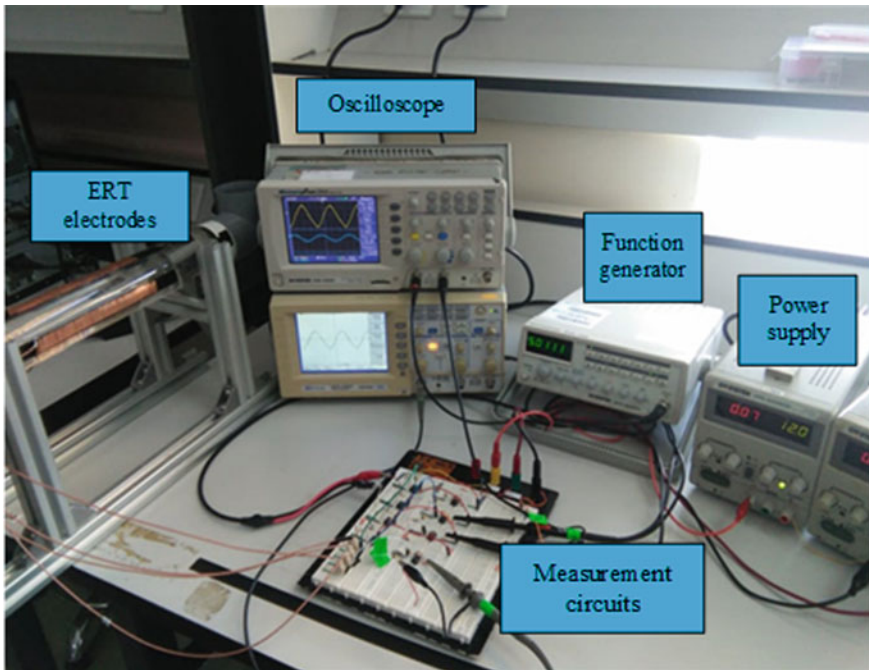


Fig. 2 Experimental set-up of ERT

Table 1 Electrical conductivity for different types of conductor [9]

Conductor	Electrical conductivity (S/m)
Copper	$5.8 \times 10^7$
Aluminum	$4.1 \times 10^7$
Zinc	$1.7 \times 10^7$
Brass	$1.5 \times 10^7$



**Table 2** Width of each of the electrode

Percentages, $X$ (%)	Width, $W$ (mm)
25	11.78
50	23.56
75	35.34

conductivity compared to other materials. Therefore, a copper had been chosen as the material for the electrodes in this research.

The placement of the electrodes on the outer surface of the acrylic pipe is done carefully. It was to make sure that the detecting electrodes receive the same amount of electric field distribution during the excitation [10]. In addition, a few dimensions of electrodes had been chosen during the experiment. The selection of the width of the electrodes is according to the formula circumference of the pipe. Thus, the cross-section area of the pipeline (circle) is divided equally into 4 sectors. Then, it was multiplied with a percentage of the coverage area of the electrode,  $X\%$ . The percentage of coverage area was chosen with an interval of 25% each. It means that there were three different sizes to be tested to get the optimized width. Hence, the width,  $W$  of each of the electrode is calculated by using Eq. (4) and the value of width is shown in Table 2.

$$W = \frac{2\pi r}{4} \times X\% \tag{4}$$

Next, all the three values of the selection widths were multiplied with the length,  $L$  of 150 mm, 200 mm, and 250 mm, respectively to get the area of the electrode,  $A$ . The calculation is based on Eq. (5). The selection of this three dimension of the electrode length was in the range of 30–50% out of the length of the pipe used. Table 3 shows the detail value of the dimension of electrodes after the calculations had been made. In addition, Fig. 3 exemplifies an electrode dimension [35 mm (width) × 250 mm (height)] with their bottom and upper details. The area other than a sensing area of the electrode was shielded by connecting it to the ground to avoid surrounding

**Table 3** The dimension of each of the electrode

Width (mm)	Length, $L$ (mm)		
	$L = 150$ mm	$L = 200$ mm	$L = 250$ mm
11.78	1.767	2.356	2.945
23.56	3.534	4.712	5.890
35.34	5.301	7.068	8.835

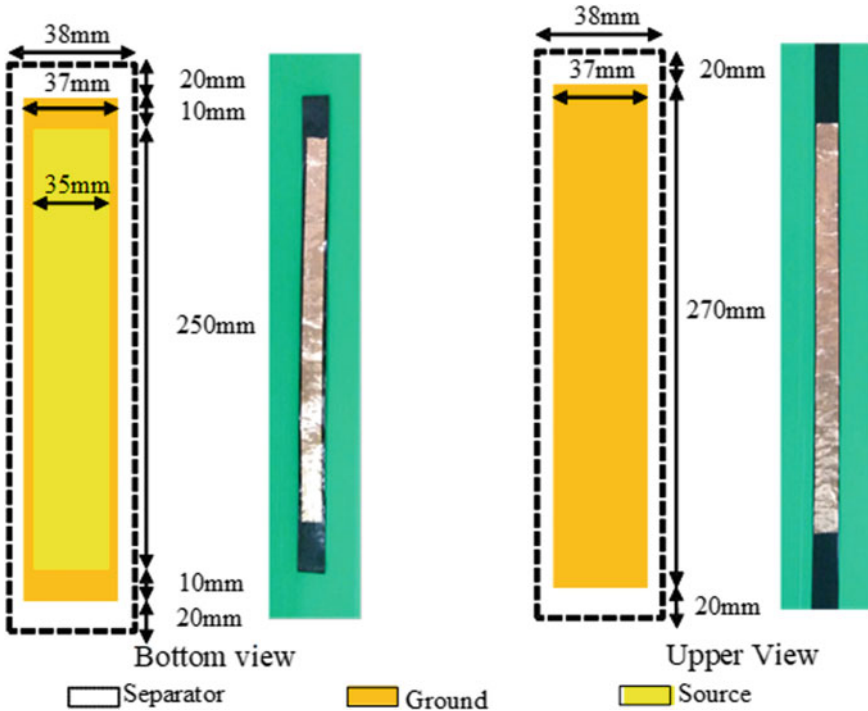


Fig. 3 Example of electrode dimension

noise. It means that nine experiments were conducted in other to get the optimize dimension of the ERT electrode.

$$A = W \times L \tag{5}$$

### 4 Results and Discussion

The outputs from the signal conditioning circuit at each electrode were measured using the digital oscilloscope. Voltage readings were taken at three different conditions of water level in the horizontal pipe; full, half and quarter of the pipe (see Fig. 4). The half and quarter experiments were also done to observe the limitation of the signal received by each of the receivers with the tested dimension. Moreover, each of the receiver readings was measured five times for each of the conditions and the average value for each of the receiver was obtained and analyzed. Table 4 shows the results for all widths and lengths of electrodes chosen at three different conditions of water level in the pipe.

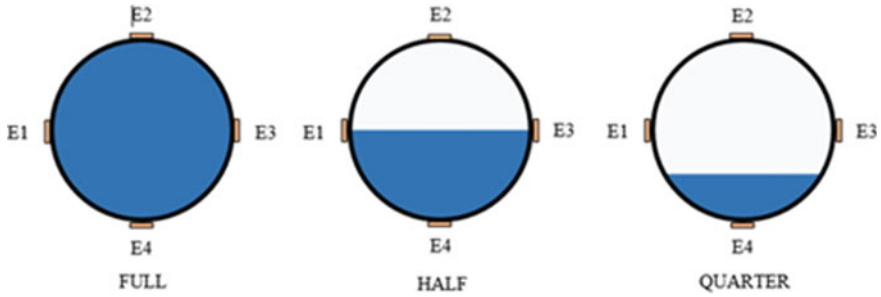


Fig. 4 The water level in the pipe

Based on Table 4, regardless of any dimensions, it can be observed that the decrement of water level in the pipe also decrease the sensor readings. For instance, for 75% covering an area of the electrode with 250 mm length, the sensor reading at receiver 1 was 2.8 V (full water), 1.7 V (half water) and 1.1 V (quarter water), respectively. Meanwhile, for the smaller dimension of electrodes which is 25% with 150 mm length, the receiver 1 read 0.7 V (full water), 0.5 V (half water) and 0.4 V (quarter water), respectively. This is due to position electrodes were not fully covered the conductive liquid and distance of transmitter sensor and receiver sensor was far away from each other. Therefore, it was difficult to detect electrical potential and hence it influences a small reading of signal at the receivers.

Besides, the longer length of electrodes gave the highest value of sensor readings compared to the shortest length of the electrodes. For instance, at width with 75% coverage, the average sensor reading for receiver 4 are around 1.5 V, 2.0 V and 2.5 V for the length of 150 mm, 200 mm and 250 mm, respectively. This is because the length of electrodes affects the dimensions of the electrodes. The smaller dimension of electrodes would detect a low electrical potential if compared to the bigger dimension. The lowest percentages of coverage the area of electrodes gave the small value of sensor readings because the current spread from the transmitter to the receiver with low intensity as the electrode size is small. It shows that the bigger dimension of electrodes gave the highest electrical potential and it is expected easily to be used by the DAS in the image reconstruction in order to get and analyse the image or region of interest.

**Table 4** Measurement of experiment obtained

Width (%)		Length (mm)		
		150	200	250
25				
50				
75				

## 5 Conclusion

In short, the sensor readings performance of non-invasive ERT system for all nine dimensions of electrodes had been analysed. It is proved that the bigger size of the electrode will give the highest value of sensor reading which is hoped that it is suitable enough to be used for the next stage of electrical resistance tomography process. 75% coverage area of electrode width and around 50% electrode length out of pipe length are believed to be the optimize dimension for ERT electrode. For this project, the optimum dimension of the electrode was around 35 mm (width)  $\times$  250 mm (height).

However, since this is a preliminary result, a future investigation with different medium, shape, and sizes of the obstacle inside the pipe is believed can be done as well as an image reconstruction so that it can get more accurate results.

**Acknowledgements** The authors thank the Universiti Malaysia Pahang (RDU170368) for the support of this project.

## References

1. Johana E, Liyana H, Ameran M, Abdul R, Faizan O (2015) Electrical capacitance tomography (ECT): an improved sensitivity distribution using two-differential excitation technique. *J Teknologi* 74:43–50
2. Abdul Wahab Y, Abdul Rahim R, Fazalul Rahiman MH, Abdul Rahim H, Aw SR, Mohd Fadzil NS, Jamaludin J (2014) A review of process tomography application in inspection system. *J Teknologi* 70:35–39
3. Atagi Y, Zhao T, Iso Y, Takei M (2019) Real-time imaging of particles distribution in centrifugal particles-liquid two-phase fields by wireless electrical resistance tomography (WERT) system. *IEEE Access* 7:12705–12713
4. Ridzuan S, Abdul R, Hafiz M, Rahiman F, Rahman F, Yunus M, Shima N (2014) Application study on bubble detection in a metallic bubble column using electrical resistance tomography. *J Teknologi* 69:19–25
5. Rodriguez-frias MA, Yang W (2019) Sensor design for four-electrode electrical resistance tomography with voltage excitation. *IEEE Sens J* 19:4612–4622
6. Yang C, Wang H, Cui Z (2012) Application of electrical resistance tomography in bubble columns for volume fraction measurement. In: 2012 IEEE international instrumentation and measurement technology conference proceedings, pp 1199–1203
7. Wang Y, Wang B, Huang Z, Ji H, Li H (2018) New capacitively coupled electrical resistance tomography (CCERT) system. *Meas Sci Technol* 29:104007
8. Abdul Wahab Y, Abdul Rahim R, Pei Ling L, Fazalul Rahiman MH, Aw SR, Mohd Yunus FR, Abdul Rahim H (2017) Optimisation of electrode dimensions of ERT for non-invasive measurement applied for static liquid–gas regime identification. *Sens Actuators A* 270:1–15
9. Ulaby FT, Michielssen E, Ravaioli U (2010) *Fundamentals of applied electromagnetics*. Pearson, USA
10. Seong CK, Pusppanathan J, Abdul Rahim R, Loon GC, Susiapan YSL, Phang FA, Fazalul Rahiman MH (2015) Hardware development of electrical capacitance tomography (ECT) system with capacitance sensor for liquid measurements. *J Teknologi* 73:13–22

# A Fictitious Reference Iterative Tuning Method for Buck Converter-Powered DC Motor Control System



Mohd Syakirin Ramli, Seet Meng Sian, Mohd Naharudin Salim and Hamzah Ahmad

**Abstract** This paper presents a model-free optimization algorithm for a PID controller based on Fictitious Reference Iterative Tuning and Simulated Kalman Filter. The modeling of a buck converted-powered DC motor system is first provided to form the basis of data collection and fictitious reference signal derivation. The supplied model is however not a necessity in the scope of this work but is provided for the purpose of performance comparison. A cost function is formulated based on the minimization of error between the output response of the desired model with the output response of the closed-loop system. Simulation analyses using Matlab Software have been conducted for results validation and verification. Furthermore, a performance comparison between the proposed method and a model-based controller design has been carried out. From the numerical example, it shows that the system with the tuned PID controller exhibited a better angular velocity trajectory tracking compared to the system with the state feedback controller with integral gain.

**Keywords** Fictitious reference · Model-free · Simulated Kalman filter · Controller tuning · PID control

## 1 Introduction

The usage of a DC motor system can be found in many applications such as home appliances [1], robotics [2], industrial machinery and equipment [3, 4]. There were many studies have been conducted by researchers to design an effective and efficient mechanism to control this system. In general, the commonly used methods for controlling the speed of the motor shaft of a DC motor can be divided into two approaches. For the first approach, the studies focus on the investigation of the topologies of the buck-converter design. For instances, Silva-Ortigoza et al. [5] and Beevi and Noufal [6] proposed the hierarchical control of the buck converter. Meanwhile, a bidirectional DC/DC buck converter system that will allow the motor shaft to rotate

---

M. S. Ramli (✉) · S. M. Sian · M. N. Salim · H. Ahmad  
Faculty of Electrical & Electronics Engineering, Universiti Malaysia Pahang, 26600 Pekan,  
Pahang, Malaysia  
e-mail: [syakirin@ump.edu.my](mailto:syakirin@ump.edu.my)

in both directions was considered in [7]. For the second approach, the studies are intensified on identifying the control algorithms to efficaciously control the switching signals of the buck converter circuit. One way of achieving this is by controlling the Pulse Width Modulation (PWM) signals, where PWM works in reducing the average power delivered by the electrical signal, by effectively chopping it up into discrete parts.

Having said that, the second method of controlling the DC motor by controlling the PWM signal is more prominent. This is due to the simplicity of the buck-converter structure, and the ease implementation of the control algorithm where only the duty ratio of PWM is to be manipulated. Some related studies that focus on designing the control algorithm to control the duty cycle of PWM switching can be found in [8] where the authors proposed PI-type Fuzzy Logic Control structure; in [9] where the sliding mode controller was investigated; and in [10] where the neural network control structure has been considered. However, these model-based methods require accurate modeling of the plant for controller design.

A model-free or data-driven approach in controller design, on the other hand, has recently attracted the interest of the researchers in the field of control theory. Since the model-based controller design may not work well if the plant model does not fall into the assumed model, there is an added advantage if the modeling requirement can be eradicated in the design procedure. Some of the model-free design techniques found in the literatures are the simultaneous-perturbation-stochastic-approximation (SPSA) methods [11], model-free adaptive control (MFAC) [12], unfalsified control(UC) [13], iterative-feedback tuning (IFT) [14], and virtual-reference-feedback tuning (VRFT) [15]. To add further to the list, the fictitious-reference-iterative-tuning (FRIT) also falls into the category of the model-free design approach. First introduced by Kaneko et al. [16], FRIT only requires the set of recorded input-output data in designing the fictitious reference signals, which availed in formulating the cost function for optimization. Comparing FRIT to VRFT, the key difference between them is that the cost function to be minimized in FRIT focuses on the output while that in VRFT focuses on the input. Therefore, FRIT is more intuitively understandable than VRFT from a practical point of view. Some examples of the FRIT applications are the controller design for a non-minimum phase system [17], and impedance matching in multilateral teleoperation system [18]. In these works, they had considered the utilization of FRIT in tuning the Laguerre expansion network which forms part of the controller. In [19], the authors provided detail surveys on the comparison between the model-based control and data-driven control.

In this work, we employed the Simulated Kalman Filter (SKF) algorithm [20] in minimizing the formulated cost function to obtain the optimal PID controller's parameters. The SKF is an estimation-based metaheuristic optimization algorithm which relies on the collection of agents to look for the near optimum solution within a reasonable computational effort [21]. By parameterizing the controller and assigning the agents' position as the controller's gain, the algorithm seeks for the best solutions which correspond to the global minimum of the fitness function.

The rest of the paper is organized as follows. In Sect. 2, we discuss our problem formulation and the modeling of the buck converter-powered DC motor system.

Meanwhile, in Sect. 3 we elucidate our proposed methods. A numerical example is presented in Sect. 4. Finally, our main conclusion is drawn in Sect. 5.

*Mathematical Notation:* Let  $\mathbb{R}$  and  $\mathbb{R}^n$  denote the set of a real number and real vector with dimension  $n$  respectively. We denote the vector norm as  $\|v\| = \sqrt{v^T v}$ , and  $\|v(k)\|_K^2$  implies  $\|v(k)\|_K^2 := \sum_{k=1}^K \|v(k)\|^2$ .

## 2 Problem Statements

Consider the block diagram of the closed system of a buck converter-powered DC motor control system shown in Fig. 1. The design objective is to obtain the optimal PID controller  $G_c(s)$  such that for any set point reference input  $r(t)$ , the angular velocity of  $\omega(t)$  is able to track the trajectory of  $r(t)$  in minimizing the error  $e(t)$ , to satisfy the condition  $\lim_{t \rightarrow \infty} e(t) = 0, \forall t$ . Practically, this can be achieved by having the dynamic of the closed system  $T(s)$  to be identical to the desired model  $T_d(s)$ . Let  $\omega_{rated} \in \mathbb{R}$  is the maximum attainable speed when the control input  $u(t) = 1$  is applied. This is considered as the saturation point of the angular velocity and is needed to ensure that the error signal fed into the controller will be bounded between 0 to 1.

The saturation block takes the input  $u(t)$  to satisfy

$$D_R = \begin{cases} 1 & u(t) \geq 1 \\ u(t) & 0 < u(t) < 1 \\ 0 & u(t) \leq 0, \end{cases} \quad (1)$$

where  $D_R \in \mathbb{R}$  is the duty ratio to control switching of the PWM output signal  $\delta(t) \in \mathbb{R}$ . The chosen PID controller structure is defined by  $G_c(s) = K \left( 1 + \frac{1}{T_i} + T_d \frac{1}{1 + \frac{1}{N_f} s} \right)$  where  $K \in \mathbb{R}$ ,  $T_i \in \mathbb{R}$ ,  $T_d \in \mathbb{R}$  and  $N_f \in \mathbb{R}$  are the proportional gain, the integral time constant, the derivative time constant and filter coefficient, respectively.

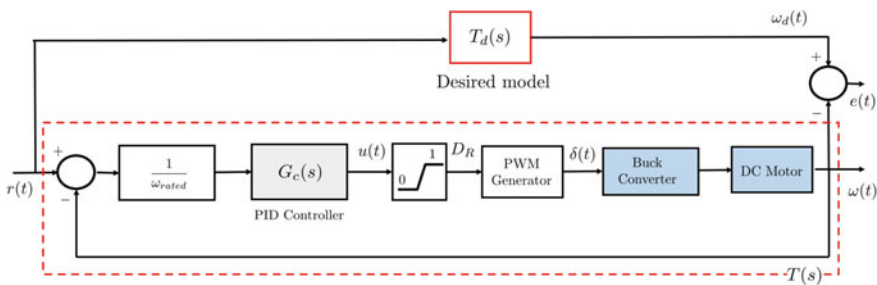


Fig. 1 Block diagram of the closed system



To achieve  $T(s) \equiv T_d(s)$ , the controller  $G_c(s)$  must be properly tuned. This implies that there exist optimal values of  $K$ ,  $T_i$ ,  $T_d$  and  $N_f$  such that the cost function defined in Eq. (2) is minimized.

$$J_1 = \frac{1}{t_f - t_0} \int_{t_0}^{t_f} e^2(t) dt = \frac{1}{t_f - t_0} \int_{t_0}^{t_f} (T_d(s)r(t) - \omega(t)) dt \quad (2)$$

## 2.1 Buck-Converter Powered Dc Motor Model

This section provides a brief description of the modeling of the buck-converter-driven DC motor system which forms the basis for the simulation analysis presented in this paper. Figure 2 delineates the schematic diagram of the DC motor system fed by a buck converter (as indicated in the blue box model in Fig. 1). The dynamic of the overall system can be described as follows [5, 6]

$$L \frac{di}{dt} = -v + E\delta(t) \quad (3)$$

$$C \frac{dv}{dt} = i - i_a \quad (4)$$

$$L_a \frac{di_a}{dt} = v - R_a i_a - K_e \omega \quad (5)$$

$$J \frac{d\omega}{dt} = K_m i_a - B\omega - T_L \quad (6)$$

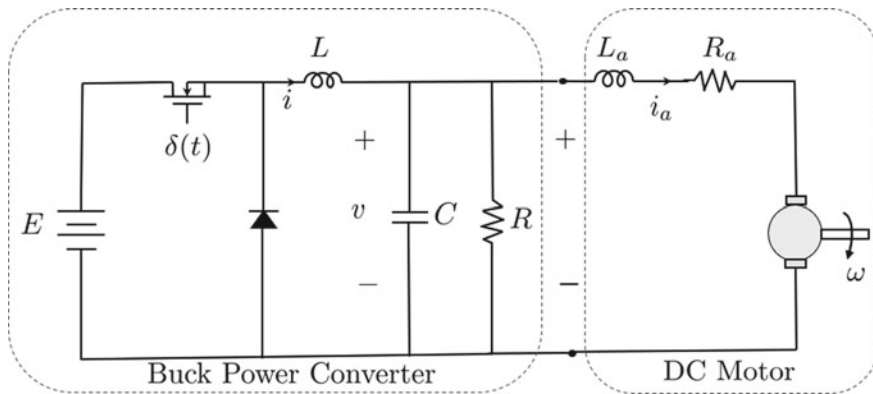


Fig. 2 Schematic of the buck converter powered DC motor system

where  $i$  is the converter input current,  $i_a$  is the DC motor armature current,  $v$  is the converter output voltage,  $\omega$  is the motor angular velocity,  $T_L$  is the load torque,  $K_m$  is the torque constant,  $K_E$  is the back-emf constant,  $J$  is the moment of inertia, and  $B$  is the coefficient of friction. Meanwhile  $L_a$ ,  $R_a$ , and  $L$ ,  $R$  are the armature inductance & resistance, and the converter inductance & resistance, respectively. The signal  $\delta(t)$  is the control input which takes the form of the PWM signals based on the duty ratio of Eq. (1).

**Remark 1** It should be noted that even though the mathematical modeling of the system is provided in this paper, it is not a necessity as our proposed method requires only the input-output data of the plant for controller tuning. The modeling is supplied to provide insights and for results comparison between the model-based technique and our proposed solutions in controller design.

### 3 Algorithm for Controller Tuning

#### 3.1 A Brief Review of SKF Algorithm

In this section, we provide a brief review of the Simulated Kalman Filter (SKF) algorithm which was used in obtaining the optimal controller parameters. First introduced by R.E Kalman in 1960 [22], the Kalman Filter is a well-established state estimation method of a dynamic system that is excited by a stochastic process and measurement noise. Improvised by Ibrahim et al. [20, 21], the SKF algorithm consists for three main stages namely, Stage 1: Initialization, Stage 2: Fitness Evaluation, and Stage 3: Predict, measure and Estimate.

In the initialization stage, the algorithm starts with random initialization of agents' estimated state,  $x(0) \in \mathbb{R}^N$ , within the search space. At the same instant, the initial value of error covariance estimate,  $P(0) \in \mathbb{R}$ , the process noise,  $Q \in \mathbb{R}$ , measurement noise,  $R \in \mathbb{R}$  and the maximum number of iterations,  $t_{\text{Max}}$  are all to be initialized. As reported in [21], the best values of  $P(0)$ ,  $Q$  and  $R$  are 1000, 0.5 and 0.5, respectively.

Next, in the second stage, the iteration begins with the fitness calculation of  $i$ th agent,  $fit_i(x(t))$ . The  $x_{\text{best}}(t) \in \mathbb{R}$  is updated to satisfy the following minimization problem of

$$x_{\text{best}}(t) = \min_{i \in 1, 2, \dots, N} fit_i(x(t)). \quad (7)$$

Then, the true value,  $x_{\text{true}} \in \mathbb{R}$  which represents the best solutions-so-far will be updated. This value is updated if there exists a better solution, i.e.  $x_{\text{best}}(t) < x_{\text{true}}$ .

Finally, in the third stage, the SKF search strategy implements three simple steps; predict-measure-estimate. In the prediction step, the time update equations are used to obtain a priori estimates for the next time step. After the measurement process,

measurement-update equations are used to obtain improved posterior estimates. The prediction of the state and error covariance estimates given the prior estimated are updated based on the following time-update equations:

$$x_i(t|t+1) = x_i(t) \quad (8)$$

$$P(t|t+1) = P(t) + Q. \quad (9)$$

The next step is the measurement, which acts as a feedback to the estimation process. The measurement of each individual agent is simulated based on the following equation:

$$z_i(t) = x_i(t|t+1) + \sin(\text{rand} \times 2\pi) \times |x_i(t|t+1) - x_{true}|. \quad (10)$$

The final step is the estimation. Here, the Kalman gain  $K(t)$  is computed based on the following equation:

$$K(t) = \frac{P(t|t+1)}{P(t|t+1) + R}. \quad (11)$$

Then, the following measurement-update equation are used to improve a posteriori estimates from a priori estimates:

$$x_i(t+1) = x_i(t|t+1) + K(t) \times (z_i(t) - x_i(t|t+1)) \quad (12)$$

$$P(t+1) = (1 - K(t)) \times P(t|t+1). \quad (13)$$

Each agent updates the optimal estimate for that corresponding iteration based on the measured position which was used as feedback and influenced by the gain value,  $K(t)$ . The iteration continues until the maximum number of iterations  $t_{\text{Max}}$  is reached. Further details on the algorithm can be found in [21].

### 3.2 Fictitious Reference Iterative Tuning

The FRIT technique only utilizes the recorded input and output data of the plant to obtain the optimal parameters of the controller. Hence, this approach eliminates the needs of the mathematical model of the plant, as commonly practiced by the model-based control designer. Thus, the FRIT is totally a model-free approach.

Reconsider the closed loop block diagram shown in Fig. 1. Suppose the PID controller can be parameterized in  $\rho$  such that  $G_c(\rho)$ . Redefine the controller gains as  $G_c(s) = K_p + \frac{K_i}{s} + K_d \frac{1}{1+\frac{1}{N_f}s}$  where  $K_p = K$ ,  $K_i = K/T_i$  and  $K_d = KT_d$ ,

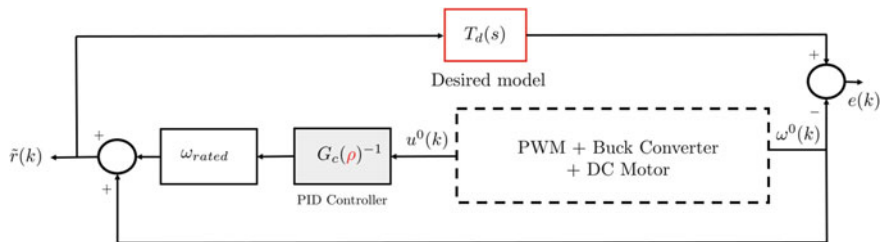


Fig. 3 Fictitious signal  $\tilde{r}(k)$  derivation

respectively. The initial arbitrary controller values are first to be selected, i.e.  $\rho^0 := [K_p^0, K_i^0, K_d^0, N_f^0] \in \mathbb{R}^4$ . Then, the one-shot of experiments has to be performed, in which the input data  $u^0$  and  $\omega^0$  are measured and recorded. These recorded data can then be used to design and formulate the fictitious reference input signal. In Fig. 3, we illustrate the general concept of defining the fictitious signal  $\tilde{r}(k)$  where the signal is formulated as follows:

$$\tilde{r}(k) = \omega_{rated} G_c(\rho)^{-1} u^0(k) + \omega_0(k). \tag{14}$$

Here,  $u^0(k)$  and  $\omega^0(k)$  are the recorded input-output data at the time-instant  $k$ , and  $G_c(\rho)^{-1} = 1/G_c(\rho)$ . Note that in formulating the fictitious signal of Eq. (14), the subsystems consist of the PWM, buck converter and DC motor (as indicated in the dashed box of Fig. 3), are no longer required for signal generation.

By the selection of the fictitious signal in Eq. (14), the optimization problem can be re-formulated. Instead of minimizing the cost function of Eq. (2), we can now define a new cost function of

$$\begin{aligned} J_2 &= \frac{1}{M} \|e(k)\|_M^2 = \frac{1}{M} \|T_d(s)\tilde{r}(k) - \omega^0(k)\|_M^2 \\ &= \frac{1}{M} \|T_d(s)(\omega_{rated} G_c(\rho)^{-1} u^0(k) + \omega_0(k)) - \omega^0(k)\|_M^2, \end{aligned} \tag{15}$$

where  $M$  is the total number of sampled-data taken from the time interval  $t \in [t_0, t_f]$ . Thus, the new control objective is to find a set of optimal parameters  $\rho^* \in \mathbb{R}^4$  such that

$$\rho^* = \arg \min_{\rho} J_2. \tag{16}$$

The following algorithm has been implemented in our work to attain the optimal parameter  $\rho^*$ .

- Step 1. By arbitrary selection of  $\rho^0$ , run one-shot experiment to generate the input-output data of  $u^0$  and  $\omega^0$ .

- Step 2. Initialize the SKF agents' position,  $x(0)$  within the search space. Then, assigning  $\rho := [K_p, K_i, K_d, N_f] = x$ .
- Step 3. Assigning the cost function  $J_2$  of Eq. (15) as the SKF fitness function in Eq. (7).
- Step 4. Iterate the SKF algorithm till  $t_{\text{Max}}$  to attain  $x_{\text{true}}$ .
- Step 5. Assigning the final value of  $x_{\text{true}}$  at  $t_{\text{Max}}$  as the optimal parameters. This implies  $\rho^* := x_{\text{true}} = \arg \min_{\rho} J_2$ .
- Step 6. Validate the performance of the closed-loop system. If the results are unsatisfying, repeat the procedure from **Step 2**.

## 4 Numerical Example

To demonstrate the effectiveness of our proposed method, we present a numerical example and the related results. The Matlab Simulation package has been utilized to perform the simulation analysis. We use the same parameters reported in [11] as follows:  $L_a = 8.9 \times 10^{-3} \text{H}$ ,  $R_a = 6 \Omega$ ,  $K_E = 0.0517 \text{Vs/rad}$ ,  $K_M = 0.0517 \text{Vs/rad}$ ,  $J = 7.95 \times 10^{-6} \text{kgm}^2$ ,  $R = 0.2 \Omega$ ,  $L = 1.33 \times 10^{-6} \text{H}$ ,  $C = 470 \times 10^{-6} \text{F}$ , and  $E = 24 \text{V}$ . Meanwhile, the rated speed is obtained as  $w_{\text{rated}} = 464.22$ . As reported in [11] and [8], we use a similar desired trajectory reference signal given by

$$r(t) = 75(\tanh(30(t - 0.1) + 1)). \quad (17)$$

The dynamic model of the desired transfer function was chosen as a first order system of  $T_d(s) = \frac{1}{0.01s+1}$ . The PWM frequency was set to 1 kHz, with the selected sample-time  $t_s = 0.1 \text{ms}$ . The initial controller gains  $\rho^0 = [0.5, 1.0, 0.25, 0.5]$  were used in generating the initial input-output data  $u^0$  and  $\omega^0$ . Figure 4 depicts the angular

**Fig. 4** Angular velocity and duty responses for  $\rho^0 = [0.5, 1, 0.25, 0.5]$  captured in a time interval  $t_0 = 0 \text{s}$  and  $t_f = 0.3 \text{s}$

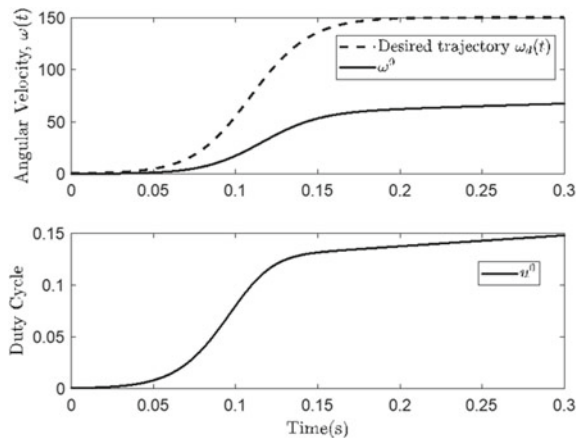
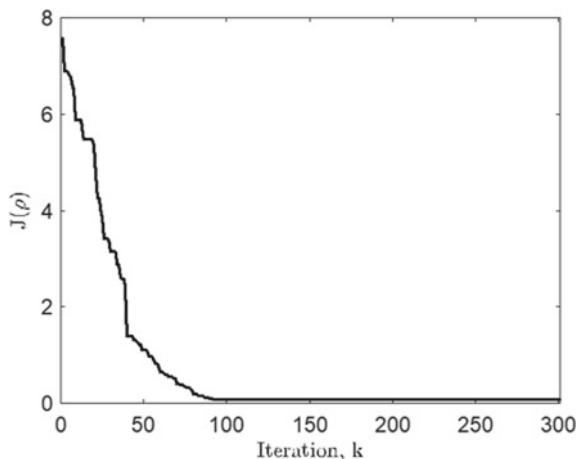


**Fig. 5** The convergence of the cost function  $J_2$



velocity and duty cycle of the untuned system when we use the gain  $\rho^0$ . These data were then adopted to form the fictitious reference signal  $\tilde{r}(k)$  of Eq. (14).

Apart from the parameter setting of the buck-converter power DC motor system, the parameters of the SKF algorithm used in this work are as follows. The best values of  $P$ ,  $Q$  and  $R$  as suggested in [21] are 1000, 0.5, and 0.5 respectively. Whereas, the number of agents is selected as  $N = 1000$ , which are bounded in the region of  $x \in [1, 100]$ . Figure 5 illustrates the convergence of the cost function (15) when we run the SKF algorithm with a maximum number of iterations  $t_{\text{Max}} = 300$ . It can be seen that the cost function already converged to 0.0751 when  $k = 100$  and remained on this value for the rest of iterations. The optimal parameters that minimized  $J_2$  were obtained  $\rho^* = [1.3983, 96.0201, 1.0158, 1.0578]$ . This implies the optimal PID parameters were  $K^* = 1.3983$ ,  $T_i^* = 0.0146$  s,  $T_d^* = 0.7265$  s and  $N_f^* = 1.5078$ , respectively.

For performance comparison with a model-based controller, let the plant of the buck converter powered DC motor system be denoted as

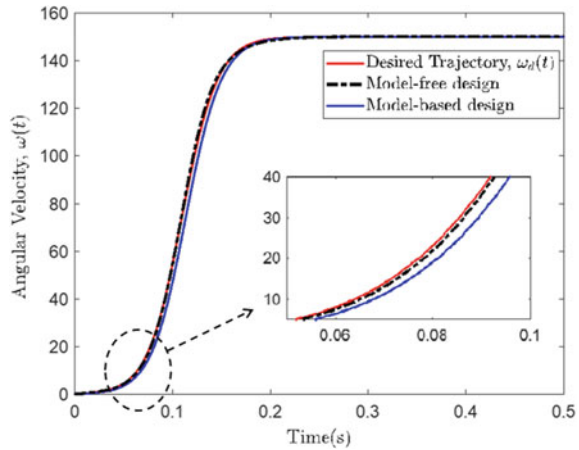
$$G_p(s) = \frac{\omega(s)}{u(s)} := \begin{bmatrix} A & B \\ C & D \end{bmatrix} \quad (18)$$

where

$$A = \begin{bmatrix} 0 & -\frac{1}{L} & 0 & 0 \\ \frac{1}{C} & 0 & -\frac{1}{C} & 0 \\ 0 & \frac{1}{L_a} & -\frac{K_a}{L_a} & -\frac{K_e}{L_a} \\ 0 & 0 & \frac{K_m}{J} & -\frac{B}{J} \end{bmatrix}, B = \begin{bmatrix} \frac{1}{L} & 0 & 0 & 0 \end{bmatrix}^T,$$

$$C = [0 \ 0 \ 0 \ 1], \text{ and } D = 0.$$

**Fig. 6** Performance comparison between the model-free design (PID controller tuned with FRIT and SKF) and model-based design (SFCI controller designed by pole-placement method)



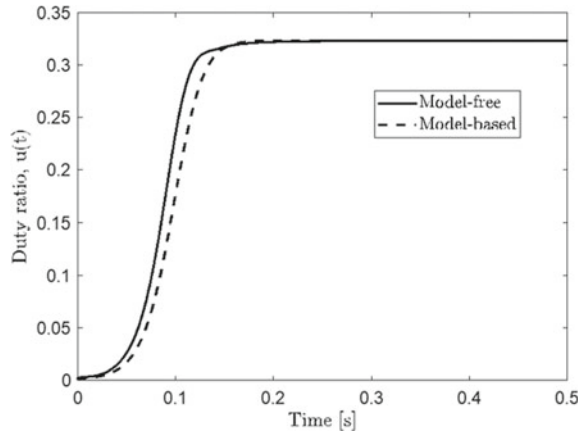
By choosing a State Feedback Controller with Integral Control (SFCI) in the form of  $u(t) = -KX(t) + K_n \int e(t)$ , where  $X(t) := [i(t), v(t), i_a(t), \omega(t)]^T$  are the state variables,  $K^T \in \mathbb{R}^4$  is the state feedback gain,  $K_n \in \mathbb{R}$  is the integral gain, and  $e(t) = r(t) - CX(t)$  is the error. We employed the pole-placement method based on Bass and Gura's approach as discussed in [23] to obtain the controller gains  $K$  and  $K_n$ . It is worth mentioning that since the desired transfer function  $T_d(s)$  was chosen as a first-order dynamic, slight modification has been performed to ensure the suitability of the selected model in obtaining the state feedback gains. By doing so, the desired pole locations were chosen as the roots of the denominator polynomial of the transfer function  $\tilde{T}_d(s) = T_d(s) \frac{(s+1000)^4}{(s+1000.01)^4}$ . It can be clarified that the order of the desired model is raised from first order to the fifth order, but the dynamic of the output response is retained. With this approach, we obtained the values of the gains of the SFCI controller as  $[K, K_n] = [4.5564, 1.3839, 6.0122, 1.0745, 85.5526]$ .

Figure 6 exhibits the output responses of the closed system, utilizing the PID controller tuned by SKF and the SFCI controller designed by the pole placement method. Meanwhile, Fig. 7 depicts the comparison of the duty ratio output between the two controllers. Evidently, it can be observed that the output response of the PID controller tuned by FRIT and SKF exhibited better and faster performance as compared to the SFCI controller. This yields to the cost values  $J_1$  of 0.1703 and 3.3659 for PID and SFCI controllers, respectively.

## 5 Conclusion

In this paper, we present the PID controller tuning method employing FRIT and SKF algorithm. Our presented model-free technique only utilized the set of input-output data to design the fictitious reference signal for the cost function minimization procedure. The performance of the controller has been investigated and validated through

**Fig. 7** Performance comparison in terms of duty ratio between the two controllers



numerical simulation on a buck converter-powered DC motor system. A simple comparison with a state feedback controller designed using a model-based approach was also presented. It can be concluded that the PID controller tuned using the FRIT and SKF exhibits a better angular velocity trajectory tracking response as compared to the SFCI controller designed using the pole placement method. Furthermore, this approach is superior since it eliminates the needs for the mathematical modeling of the system-to-be-controlled in contrast to the model-based controller design.

**Acknowledgements** Special thanks and appreciation belong to Universiti Malaysia Pahang for providing financial assistance towards completing this research work. This paper has been supported under the short-term grant of RDU1703139.

## References

1. Parasiliti F, Villani M, Castello M (2014) PM brushless DC motor with exterior rotor for high-efficiency household appliances. In: 2014 international conference on electrical machines, ICEM 2014, pp 623–628
2. Hwang CC, Liu PL, Li CT, Chen C (2012) Design and analysis of a brushless DC motor for applications in robotics. *IET Electr Power Appl* 6(7):385–389
3. Rajesh D, Ravikumar D, Bharadwaj SK, Vastav BKS (2016) Design and control of digital DC drives in steel rolling mills. *Int Conf Inven Comput Technol, ICICT 2016*:1–5
4. Hall RD, Konstanty WJ (2010) Commutation of DC motors. *IEEE Ind Appl Mag* (16):56–62
5. Silva-Ortigoza R, Hernández-Guzmán VM, Antonio-Cruz M, Muñoz-Carrillo D (2015) DC/DC buck power converter as a smooth starter for a DC motor based on a hierarchical control. *IEEE Trans Power Electron* 30(2):1076–1084
6. Beevi A, Noufal M (2016) Hierarchical control For a buck converter driven DC motor. *Int J Adv Res Electr, Electron Instrum Eng* 5(9):7218–7224
7. Hernandez-Marquez E, Silva-Ortigoza R, Dong SH, Garcia-Rodriguez VH, Saldana-Gonzalez G, Marcelino-Aranda M (2016) A new DC/DC buck-boost converter-DC motor system: modeling and simulation. *Int Conf MechatronS, Electron, Automot Eng, ICMEAE 2016*:101–106



8. Ahmad MA, Raja Ismail RMT, Ramli MS (2010) Control strategy of buck converter driven DC motor: a comparative assessment. *Aust J Basic Appl Sci* (10):4893–4903
9. Linares-Flores J, Sira-Ramírez H (2017) Sliding mode-delta modulation GPI control of a DC motor through a buck converter. *IFAC Proc Vol* 37(21):405–410
10. Kamarposhti MA, Tayebbifar T, Shaker M, Nouri P (2013) The control of buck-boost DC-DC converters for DC motor drives on variable DC voltage by using neural network. *Life Sci J* 10(5):236–240
11. Ahmad MA, Raja Ismail, RMT (2017) A data-driven sigmoid-based PI controller for buck-converter powered DC motor. In: *IEEE symposium on computer applications and industrial electronics*, pp 81–86
12. Li G, Liu L (2012) Robust adaptive coordinated attitude control problem with unknown communication delays and uncertainties. *Procedia Eng* 29:1447–1455
13. Battistelli G, Selvi D, Mari D, Tesi P (2014) Unfalsified approach to data-driven control design. In: *IEEE conference on decision and control*, pp 6003–6008
14. Saleem O, Rizwan M (2019) Performance optimization of LQR-based PID controller for DC-DC buck converter via iterative-learning-tuning of state-weighting matrix. *Int J Numer Model: Electron Netw, Devices Fields*, 1–17
15. Rallo G, Formentin S, Rojas CR, Savaresi SM (2018) Experiment design for virtual reference feedback tuning. In: *IEEE conference on decision and control*, pp 2271–2276
16. Kaneko O, Soma S, Fujii T (2005) A fictitious reference iterative tuning (FRIT) in the two degrees of freedom control scheme and its application to closed-loop system identification. *IFAC Proc Vol* 626–631
17. Nguyen HT, Kaneko O, Yamamoto S (2011) Data-driven IMC for non-minimum phase systems—Laguerre expansion approach. In: *50th IEEE conference on decision and control and european control conference*, pp 476–481
18. Ramli MS, Ahmad H (2018) Data-driven impedance matching in multilateral teleoperation systems. *Indones J Electr Eng Comput Sci* 10(2):713–724
19. Hou ZS, Wang Z (2013) From model-based control to data-driven control: survey, classification and perspective. *Inf Sci* 235:3–35
20. Ibrahim Z et al (2015) A Kalman filter approach for solving unimodal optimization problems. *ICIC Express Lett* 9(12):3415–3422
21. Ibrahim Z, Abdul Aziz NH, Nor NA, Razali S, Mohamad MS (2016) Simulated Kalman filter: a novel estimation-based metaheuristic optimization algorithm. *Adv Sci Lett* 22(10):2941–2946
22. Kalman RE (1960) A new approach to linear filtering and prediction problems. *J Basic Eng* 82:35–45
23. Ramli MS, Rahmat MF (2008) Servomotor control using direct digital control and state space technique. *J Teknologi* 49(D):45–60

# Depth Evaluation of Slits on Galvanized Steel Plate Using a Low Frequency Eddy Current Probe



N. A. Nadzri, M. M. Saari, M. A. H. P. Zaini, A. M. Halil, A. J. S. Hanifah and M. Ishak

**Abstract** This study performs an analysis of a small eddy current probe configuration based on differential anisotropic magnetoresistance (AMR) sensors for characterization of small surface defects in galvanized steel plates. Owing to the advantage of the AMR sensor, the system of eddy current testing (ECT) with the AMR sensor has a huge benefit to detect sub-millimeter defects in steel structures. In this study, an ECT probe is developed by using AMR sensors to perform crack detection in 2-mm galvanized steel plates with regards to the depth of artificial slits where the ECT probe is scanned above the slits' area. The signal that is detected by a lock-in amplifier is investigated with different frequencies of an excitation field. The line-scanned of signal intensity shows a clear intensity change at the crack area. This signal depends on the depth and frequencies. Finally, a correlation between depth and detected signals is clarified with respect to different frequencies.

**Keywords** Slit detection · Steel · Defect · Eddy current testing (ECT) · Anisotropic magnetoresistance (AMR)

## 1 Introduction

To detect and evaluate defects in metallic materials, the magnetic technique is one of the promising techniques in Non-Destructive Test (NDT) where this process is generally used in industries because of its low price and straight forward procedure [1]. This is owing to its ability to inspect metallic compound as the compound is conductive and possesses strong magnetic properties. Eddy current method for NDT is an effective approach to detect irregularity in metal structures. Among of the advantages of eddy current methods are non-contact with the sample material and a

---

N. A. Nadzri (✉) · M. M. Saari · M. A. H. P. Zaini  
Faculty of Electrical and Electronics Engineering, Universiti Malaysia Pahang, 26600  
Pekan, Pahang, Malaysia  
e-mail: [mel17005@stdmail.ump.edu.my](mailto:mel17005@stdmail.ump.edu.my)

A. M. Halil · A. J. S. Hanifah · M. Ishak  
Faculty of Mechanical and Manufacturing Engineering, University Malaysia Pahang, Pekan  
Campus, 26600 Pekan, Pahang, Malaysia

fast test method over other NDT techniques [2]. Defects in metallic components are one of the defects that is a major concern in many industries [3] where it is a critical task in monitoring the safety of the steel structures. Usually, surface cracks are the significant signal of structural damage for all types of structures, materials or systems [4]. Crack can start to develop from sub-millimeter size. Hence, if early detection can be done, it can be used to prevent any sudden fatal accident in the future. NDT is a process that can inspect, test or evaluate materials, component assemblies for discontinuities, or differences in characteristics, without destroying the serviceability of the parts or systems.

Eddy current measurement technique is promising than other technique because the inspection can be done without any contact [5] with the inspected piece. There are few types of non-destructive testing methods that use the principle of electromagnetic as the basis for conducting examinations and one of the methods is known as the eddy current testing (ECT) where it is extensively used for the NDT interpretation of conductive materials. For example, aluminum plates [6, 7]. The benefits of ECT are its non-contact nature, ease, versatility, and speed. It is accessible that lift-off between the coil and the plates strongly influenced the changes of the measured eddy current's signals [8], therefore this effect should be mitigated or compensated by using software and/or hardware-based methods.

In this study, a low-frequency ECT method is applied to enable deeper penetration of electromagnetic waves so that deeper eddy current can be induced [9]. This is because the induced eddy currents are affected by the skin depth effects which means the eddy currents highly distribute on the surface area and decrease as the depth increases. To reach a highly sensitive measurement, a magnetometry system with highly responsive magnetic sensors is developed for this NDT system. Therefore, an AMR sensor (Honeywell HMC1001) is used [10].

To distinguish an outer defect, an ECT with a small size is more beneficial because the small size of ECT probe can be used to measure a tiny or a difficult pattern of crack [11]. Since the AMR sensor is relatively small compared to the induction coil, it will give the advantage to develop an ECT probe to resolve the higher spatial distribution of eddy currents in conductive materials [12–14]. Based on the benefits of the magnetic method, the developed ECT probe is utilized to investigate the frequency response characteristic and localization performance of artificial slits.

## 2 Measurements

### 2.1 *Magnetic Sensor Probe*

There are many types and designs can be found when it comes to ECT probes. The main aim of the ECT probe in this study is to detect surface flaws. Therefore, an ECT probe with small size is more advantageous because the small size of ECT probe can

be used to measure a small or a difficult pattern of crack. Furthermore, by minimizing the size of the probe, it can improve the detection performance of crack.

An AMR sensor has 4 AMR elements to form a Wheatstone bridge and patterned as a resistive strip. When the AMR sensor is introduced by a magnetic field, this causes a resistance change in each AMR element and produce a differential output voltage between the center nodes of the bridge. The magnetic sensor is biased with a 5-V voltage, where the sensitivity of the AMR sensor is comparable to the bias voltage. The sensitivity is calculated to be 0.16 mV/ $\mu$ T in the operational zone of the magnetic response.

To reduce background noise, by using two AMR sensors, a differential technique is used to form a dual-channel sensor probe. The sensor probe consists of two AMR sensor where the size of each the sensor is  $11 \times 4 \text{ mm}^2$  in size and they are placed at the middle of an excitation coil with an  $11.5 \times 11.5 \text{ mm}^2$  area and 60 turns. To produce the excitation magnetic field, the excitation coil is assembled by a 0.1 mm diameter Cu wire. The two AMR sensor are attached together with a distance of 4 mm to perform the differential technique.

### 2.2 Measurement System and Test Sample

The ECT operation is developed with numbers of components such as an ECT probe, the current source for the excitation coil, measuring circuit, lock-in amplifier, XY stage and a personal laptop for data acquisition and analysis. Figure 1 shows the structure of the schematic diagram of the ECT system. In the study, sinusoidal currents with an amplitude  $I = 4 \text{ mA}$  and few values of frequencies are supplied to the excitation coil.

The output voltage of the sensors is amplified with an instrumental amplifier and then connected to the lock-in amplifier. From the lock-in amplifier, there will be two outputs of the signals that are detected and analyzed as a magnetic vector with the

**Fig. 1** **a** Position of AMR sensors. **b** Photograph of the fabricated ECT probe (bottom view)

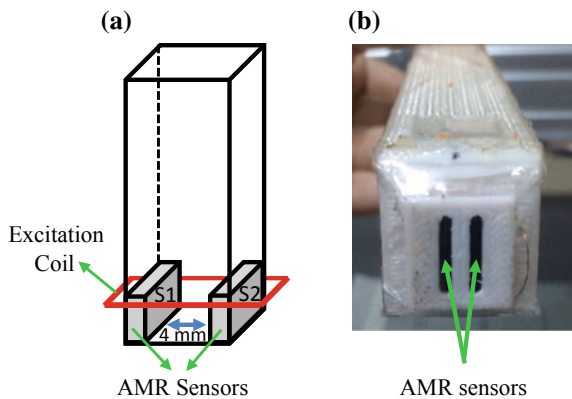
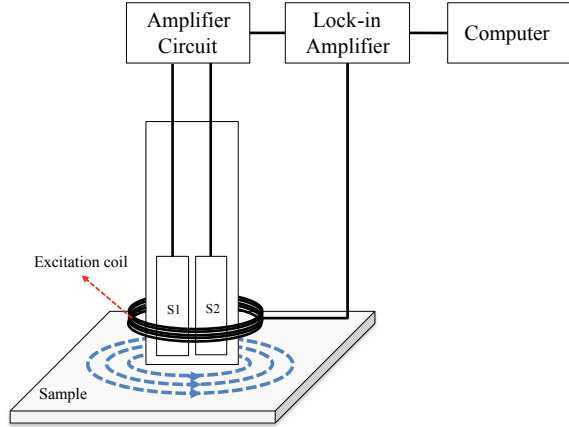


**Fig. 2** Schematic diagram for ECT system



real and imaginary components. The excitation coil is operated with a variable value of frequencies between 90 Hz and 1 kHz.

The test sample is a galvanized steel plate with 2-mm thickness. Five artificial slits with different depths are laser-engraved on the surface of the plate (Fig. 2). The slits have a same length and width of 30 mm and 0.2 mm, respectively, and different depths ranging between 200 and 500  $\mu\text{m}$ . The distance each of the slits is set to be 50 mm and the position of the ECT probe (lift-off) is fixed at 1 mm above the steel plate.

### 3 Results and Discussion

#### 3.1 Signal Analysis

The lock in amplifier was used to detect the outcome and interpret as a magnetic vector with two different output which are the real and imaginary components (real part,  $dB_{z,real}/dx$ ; imaginary,  $dB_{z,ima}/dx$ ). Each detected magnetic field vector was calculated using the following formula:

$$\frac{dB_z}{dx} = \frac{dB_{z,real}}{dx} + j \frac{dB_{z,ima}}{dx} \quad (1)$$

where the first term shows the real component of the magnetic field induced while the second term shows the imaginary component where the information regarding eddy current is contained. The output signal for both components of the steel sample with a 30-mm long slit and 500- $\mu\text{m}$  deep was measured at different frequencies using the dual-channel sensor probe was shown in Fig. 3.

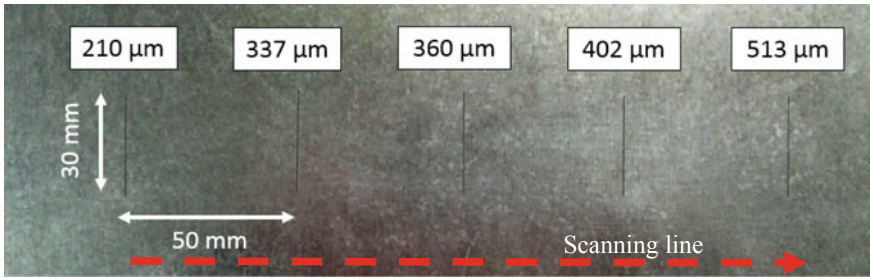


**Fig. 3** Artificial slits (defects) of depth from 500 to 200  $\mu\text{m}$  of a carbon steel plate

Although there were two output signals but only one output that would be taken into consideration throughout the experiment to detect the crack which was  $dB_{z,ima}/dx$ . The real component was neglected because the output detected by the AMR sensor was a mixture of large magnetization and small eddy current signal where the output signal did not show any changes and it was difficult to identify the slit. Moreover, the imaginary output signal showed a clear change of the magnetic response at the slit area compared to the real component.

### 3.2 Frequency Response Characteristic

To verify the characteristic change due to a crack, the experiment began with measuring the magnetic response from each slit, where, a line scanning measurement was conducted by moving the probe horizontally across the slit. Each of the waveforms depicts the line scanned which shows intensity change for the different depth crack at different frequencies.

The frequency of the excitation magnetic field was set to 90 Hz, 300 Hz, 500 Hz, 700 Hz, and 1 kHz to investigate the changes of the magnetic response in each frequency. The slit direction was perpendicular to the scanning direction.

The correlation between the signal intensity change and the depth of the slits were investigated. A delta value ( $\Delta Y$ ) was used to represent the difference between the highest and lowest values of the peaks and trough in the magnetic response waveforms (Fig. 4). When the excitation coil was operated at a 90-Hz frequency, it produced the lowest signal of magnetic response, however, it still showed a slight change of magnetic reaction around the slit area.

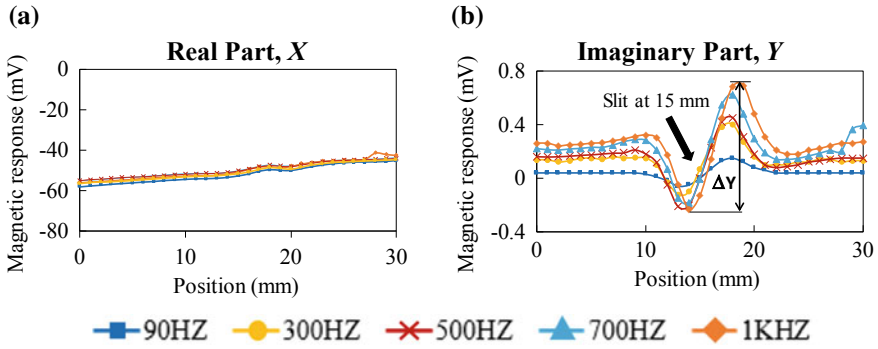


**Fig. 4** **a** The real and **b** imaginary of line-scanned magnetic field intensity of steel plate surface crack with depth 513  $\mu\text{m}$  of surface crack using ECT probe with different frequency

This output signal was related to the skin depth effect where the depth of the eddy current penetration was vice versa with the square-root of the frequency applied. The skin depth,  $\delta$  in the case of a material, can be expressed in the following equation:

$$\delta = \frac{1}{\sqrt{\pi f \mu \sigma}}, \tag{2}$$

where  $f$  is the frequency,  $\sigma$  is the conductivity, and  $\mu$  is the permeability. Therefore, when the 90-Hz magnetic field was applied, the eddy current penetrated deeper compared to other frequencies. Since the slits were on the surface, this caused the magnetic response signal to occur slightly. But the changes in the magnetic response around the slit area increased significantly as the frequency was increased. This was due to all eddy currents that had been generated were accumulated to the surface and this made the magnetic response due to the eddy current became higher. Although different frequencies were applied to the slits, the patterns and the characteristics of each slit showed the same characteristic where there was a change at the slit area.

The delta value showed a small value and slowly increased as the crack went deeper. Since the experiment was conducted with the slits on top of the surface of the metallic sample therefore high selection frequency was better where all the eddy current would linger around on the surface material. However, a low frequency could also be used since the crack still could be detected, but to facilitate the sensors to detect surface cracks, using a high frequency is recommended. The slope of the delta values ( $\Delta Y$ ) against frequency was shown in Fig. 5. From the graph, it shows that the higher the frequency the greater the slope of delta values. This showed that higher frequency was a good selection for surface crack detection (Fig. 6).

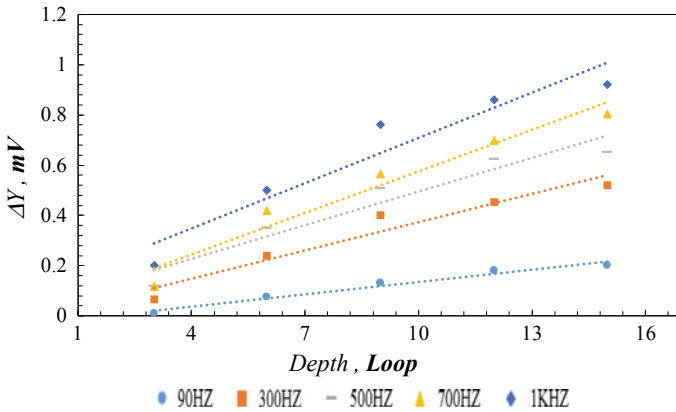
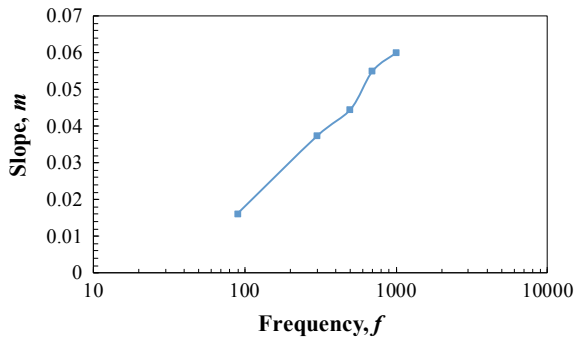


Fig. 5 Signal difference of the different depth of slits with different frequency

Fig. 6 Graph of slope of trendline of the delta values of imaginary part for the front side measurement with respect to frequency



### 4 Conclusion

This paper covers the development of an ECT probe for the nondestructive test by using a dual-channel AMR probe sensor to detect artificial slits in a surface of a ferromagnetic material using the eddy current method. A differential probe, which was used in the ECT system, has been fabricated for sub-millimeter detection of surface slits. This study was further validated by experimental tests on the artificial slits on the surface of the galvanized steel and promising results were obtained. Moreover, a reliable output signal change due to the slits was obtained by the developed system. Even though by applying a low-frequency magnetic field, the detection on the surface crack was possible. The probe was shown to be capable to classify the dependence on the crack depth. Overall, the work demonstrated that the eddy current penetration into the material was affected by the frequency of the excitation current.

**Acknowledgements** The authors would like to thank the Universiti Malaysia Pahang (grant no. RDU170377 and PGRS190321) for laboratory facilities and financial assistance.



## References

1. Tsukada K, Kiwa T, Kawata T, Ishihara Y (2006) Low-frequency eddy current imaging using MR sensor detecting tangential magnetic field components for nondestructive evaluation. *IEEE Trans Magn* 42:3315–3317
2. Postolache O, Ribeiro A, Ramos HG (2009) Weld testing using eddy current probes and image processing. In: XIX IMEKO world congress fundamental and applied metrology, 1–6
3. Saari MM, Nadzri NA, Halil AM, Ishak M, Sakai K, Kiwa T, Tsukada K (2019) Design of eddy current testing probe for surface defect evaluation. *Int J Autom Mech Eng* 16:1–11
4. Hoang N (2018) Detection of surface crack in building structures using image processing technique with an improved Otsu method for image thresholding. *Adv Civil Eng* 2018:10 p. Article ID 3924120
5. García-Martín J, Gómez-Gil J, Vázquez-Sánchez E (2011) Non-destructive techniques based on eddy current testing. *Sensors* 11:2525–2565
6. Sophian A, Tian G, Fan M (2017) Pulsed eddy current non-destructive testing and evaluation: a review. *Chin J Mech Eng* 30:500–514
7. Ghanei S, Kashefi M, Mazinani M (2013) Eddy current nondestructive evaluation of dual phase steel. *Mater Des* 50:491–496
8. Nadzri NA (2018) Development of eddy current testing system for welding inspection. In: 9th IEEE control and system graduate research colloquium, pp 94–98
9. He D, Shiwa M (2014) A magnetic sensor with amorphous wire. *Sensors (Switzerland)* 14:10644–10649
10. He D, (2017) AMR Sensor and its Application on Nondestructive Evaluation. In *Magnetic Sensors - Development Trends and Applications*, pp 133–154
11. Tsukada K, Hayashi M, Nakamura Y, Sakai K, Kiwa T (2018) Small eddy current testing sensor probe using a tunneling magnetoresistance sensor to detect cracks in steel structures. *IEEE Trans Magn* 54(11):1–5
12. Jander A, Smith C, Schneider R (2005) Magnetoresistive sensors for nondestructive evaluation. In: *Proceedings of SPIE*, pp 1–13
13. Tsukada K, Haga Y, Morita K, Song N, Sakai K, Kiwa T, Cheng W (2016) Detection of inner corrosion of steel construction using magnetic resistance sensor and magnetic spectroscopy analysis. *IEEE Trans Magn* 52:1–4
14. Mook G, Magdeburg O (2006) Deep penetrating eddy currents and probes. *Materialprüfung (MATER TEST)*, 1–14

# Sensitivity Maps Preparation for Electrical Capacitance Tomography Using Finite Element Approach



Wan A. N. Ropandi, N. A. Zulkifli, J. Pusppanathan, F. A. Phang, N. D. Nawi, M. E. Johana and N. H. A. Ngadiman

**Abstract** Electrical Capacitance Tomography is part of Electrical Tomography which uses the concept of electric field distribution and it is widely used due to its advantages such as non-invasive, low-cost, high acquisition speed and relatively easy computation. The ECT system involves two computational problems in its mechanism which Forward Problem and Inverse Problem. The forward problem involves the computation of the potentials done at the voltage pick-up electrodes for a given set of current-carrying electrodes. This allows calculation for the distribution of the electrical voltage when the given with condition of known sensor structure and given permittivity distribution. The Forward Problem in this study refers to the sensitivity map which is later used for image reconstruction in the Inverse Problem image. This study explores sensitivity map generation and preparation which can be accomplished using the numerical method, for example, the Finite Element Method. Based on the simulated result, the sensitivity map for each projection shows different strength depending on the position and distance between the electrode pair.

---

W. A. N. Ropandi · N. A. Zulkifli

School of Biomedical Engineering and Health Sciences, Faculty of Engineering, Universiti Teknologi Malaysia, UTM, 81310 Skudai, Johor, Malaysia

J. Pusppanathan (✉)

Sports Innovation Technology Centre (SITC), Institute of Human Centered Engineering (iHumEn), Universiti Teknologi Malaysia, 81310 Skudai, Johor, Malaysia  
e-mail: [jaysuman@utm.my](mailto:jaysuman@utm.my)

F. A. Phang

Centre of Engineering Education (CEE), Universiti Teknologi Malaysia, 81310 Skudai, Johor, Malaysia

N. D. Nawi

Faculty of Social Sciences and Humanities, School of Education, Universiti Teknologi Malaysia, 81310 Skudai, Johor, Malaysia

M. E. Johana

Department of Mechatronic and Robotic Engineering (JER), Faculty of Electrical and Electronic Engineering, Universiti Tun Hussein Onn Malaysia, 86400 Parit Raja, Johor, Malaysia

N. H. A. Ngadiman

School of Mechanical Engineering, Faculty of Engineering, Universiti Teknologi Malaysia, 81310 Skudai, Johor, Malaysia

© Springer Nature Singapore Pte Ltd. 2020

A. N. Kasruddin Nasir et al. (eds.), *InECCE2019*, Lecture Notes in Electrical Engineering 632, [https://doi.org/10.1007/978-981-15-2317-5\\_7](https://doi.org/10.1007/978-981-15-2317-5_7)

**Keywords** Tomography · Sensitivity maps · Finite element method · Electrical capacitance tomography

## 1 Introduction

Electrical Capacitance Tomography (ECT) is a soft-field tomography technique which used an electrical property distribution as their fundamental [1] to reconstruct a tomogram. ECT can be achieved by measuring the changes of capacitance that happen in a homogenous electrical field distribution in order to reconstruct the matter's spatial distribution. The reconstruction method for ECT image can be done through several methods such as back projection [2], iterative [3] method and also hybrid reconstruction algorithm [4]. For every reconstruction method of an ECT system, a sensitivity map is a must [5] where it serves as the basis for image reconstruction by combining different pixels captured at each different location [6].

Sensitivity map, or Jacobian matrix, is a matrix that represents the dynamic changes of capacitance [7] between the sensing electrode when voltage is supplied. Sensitivity maps were created by solving the Poisson equation of the electric field [8]. Normally, the ECT reconstructions are conducted with an assumption of linear relationship [9] between capacitances and the changes in permittivity. The linear model of ECT [10] can be portrayed through the equation,

$$C = SG \quad (1)$$

where,

C capacitance vector

S sensitivity matrix of normalized capacitance with respect to the normalized permittivity

G normalized permittivity vector.

However, Fan and Wang had noted a setback where the path of electrical field projection cannot be predicted accurately, therefore causes non-uniform sensitivity distribution [9]. Zhou et al. also noted that permittivity distribution inside the ECT system is irregular, thus a Finite Element Analysis (FEA) can be used to solve the numeric solution for sensitivity maps [10]. In FEA, the permittivity distribution is assumed to be made up of several elements of pixel [11], where the sensitivity coefficient of each pixel can be represented as

$$S_{ij}(k) = \left( \frac{C_{ij(k)} - C_{ij}^l}{C_{ij}^h - C_{ij}^l} \right) \left( \frac{1}{\varepsilon_h - \varepsilon_l} \right) \mu(k) \quad (2)$$

$$i = 1, 2, 3, \dots, L - 1 \quad j = i + 1, \dots, L \quad k = 1, 2, 3, \dots, N$$

where,

$C_{ij(k)}$	capacitance of electrode pair i-j
$C_{ij}^h$ and $C_{ij}^l$	capacitance of electrode pair at different permittivity, l and h
$\varepsilon_h$	high relative permittivity
$\varepsilon_l$	low relative permittivity
$\mu(k)$	ratio of maximum area to kth area.

Hence, the sensitivity matrix that represents the changes in the distribution of capacitance can be expressed as follows.

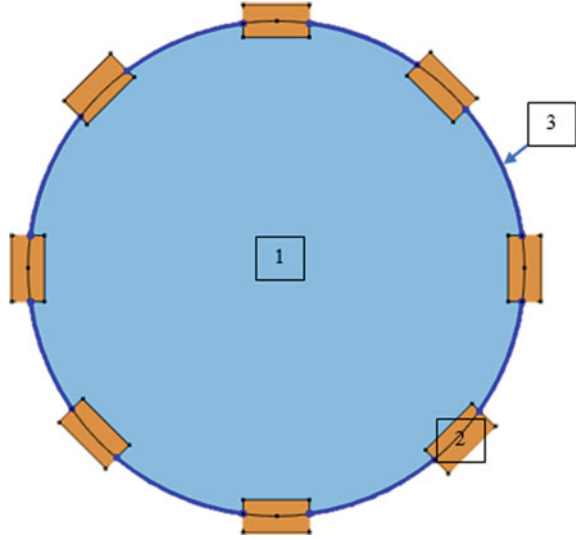
$$\mathbf{S} = \begin{bmatrix} s_{12}(1) & s_{12}(2) & \dots & s_{12}(N) \\ s_{13}(1) & s_{13}(1) & \dots & s_{13}(N) \\ \vdots & \vdots & \ddots & \vdots \\ s_{(L-1)L}(1) & s_{(L-1)L}(2) & \dots & s_{(L-1)L}(N) \end{bmatrix}$$

M. Soleimani et al. stated that the sensitivity map is dependent on the composition inside the ECT system [12]. Sensitivity map remains the same if the changes in the permittivity distribution are low. On the contrary, the pattern of electrical field distribution between a pair of electrode undergoes changes if the electrical field distribution is high. When this condition is met, the sensitivity map needs to be updated for the iteration of image reconstruction because an error in the Jacobian matrix affects the image reconstructed and causes data error [13]. Additionally, during the generation of sensitivity maps the soft field nature might follow which in turn created the ‘soft field effect’ [14] in the image reconstruction. As the sensitivity of the sensitivity map affected (i.e. reduced sensitivity) by ‘soft field effect’ [15], hence the location of the electrode needs to be considered because the sensitivity of electric field strength decrease as the distance is further from the excitation and detection electrode pair, especially on the center region.

## 2 Sensitivity Map Generation

The sensitivity map is obtained through Finite Element Method (FEM) by using software COMSOL Multiphysics. FEM is a numerical approximation method, which is used for the calculation and optimization of differential and integral equations. By applying Finite Element Analysis (FEA), the complex problem was later divided into several nodes of the element which can be solved with relation to one another. FEM is useful for problems with complicated geometries, loadings, and material properties where analytical solutions cannot be obtained. In the engineering field, FEM is a computational technique used to obtain approximate solutions of boundary value problems also known as field problems. The field represents the physical structure while boundary conditions are the constraint that exists in order to solve the boundary value problem (i.e. differential equation of the system).

**Fig. 1** Arrangement of ECT system where (1) sensing region filled with water as medium, (2) copper electrode with measurement  $1.0 \text{ mm} \times 2.0 \text{ mm}$ , (3) electrical shielding using Pyrex glass with thickness of  $2.0 \text{ mm}$



## 2.1 Experimental Set-Up

The sensitivity map is obtained through several steps as follows:

### 2.1.1 Model Configuration

The geometric set up for the miniaturized ECT system simulation is done with three parameters taken into consideration. Those three parameters involved the electrode sensor configuration, the sensing region as well as the electrical shielding. The arrangement of the electrode needs to be symmetrical in order to make sure that the projection path, not overlap, hence causes stray capacitance to occur, with one another and it must fall within the sensing region. The geometric and materials arrangement is chosen based on its application which is for cell monitoring in bioassay application, as depicted in Fig. 1.

### 2.1.2 Physics Interface

As the ECT system involves changes in the dielectric property of a material as well as the electrical field distribution, hence the suitable physics for this simulation is Electrostatic (es). The electrostatic interface in COMSOL Multiphysics involves the concept of electrostatic energy, where it can be arranged in conditions such as boundary and domain that is useful when computing electrostatic forces and capacitance values.

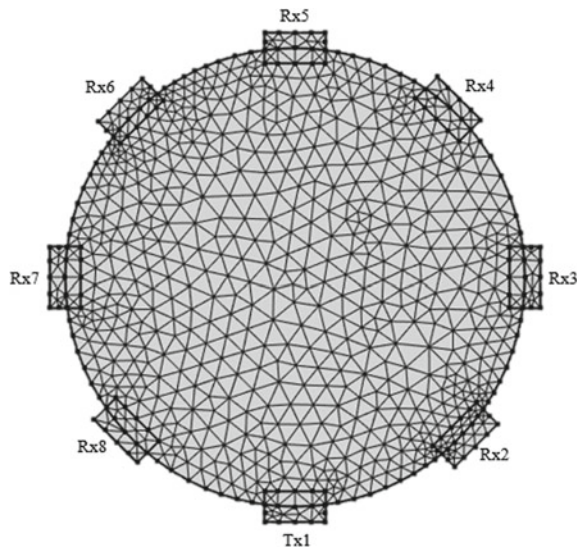
**Table 1** Relative permittivity of material

Material	Relative permittivity ( $\epsilon_r$ )
Air	1.0006
Water	80.1
Pyrex glass	4.3

The simulation is done by means of the electrode pair, where an electrode is excited, acts as the transmitter (Tx) while the grounded electrode, serves as the receiver (Rx). Hence, boundary setting is used in setting up the terminal for both the transmitter (Tx) and receiver (Rx). The voltage injected to each Tx boundary is fixed to 20 V where the process is repeated sequentially for every electrode pair. Domain setting, on the other hand, is used in order to assign the material relative permittivity as shown in Table 1.

### 2.1.3 Meshing and Run Simulation

The meshing process followed after the physics interface is set-up. Meshing is important in every Finite Element Analysis (FEA) as it helps to divide the computational problem into several nodes, representing partial differential equation (PDE) in order to solve them (refer Fig. 2). The size of the mesh element is set to fine meshing as when the mesh is denser, the computation becomes more detailed and decisive [16]. The electrostatic interface chosen is used to numerically solve the PDE governing the sensing region by calculating the electrical potential distribution with the condition of known relative permittivity distribution.

**Fig. 2** Fine meshing in COMSOL Multiphysic

The simulation is repeated by changing the arrangement of Tx and Rx of each electrode pair, to obtain individual projection path until it can produce one scan. For example, electrode 1 is chosen as the voltage sources hence the arrangement is in pair such as 1–2, 1–3 and 1–4 until it reaches the 1–8 to complete 1 one scan. Next, electrode 2 is chosen where the process is repeated the same as stated earlier.

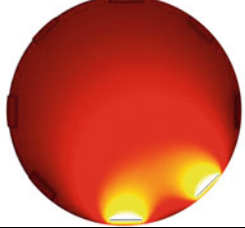
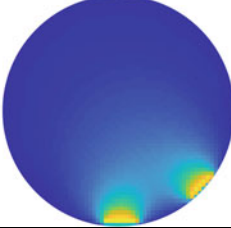
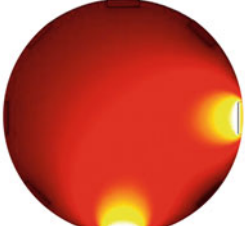
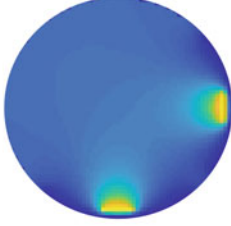
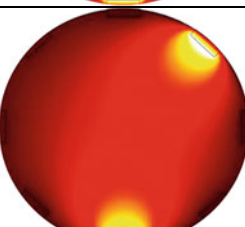
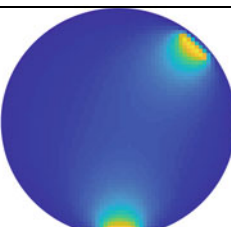
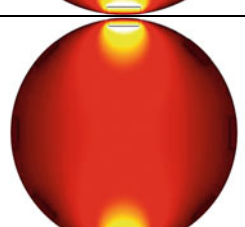
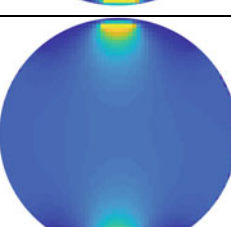
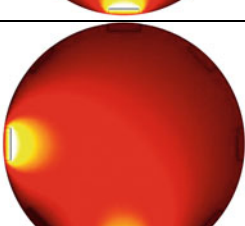
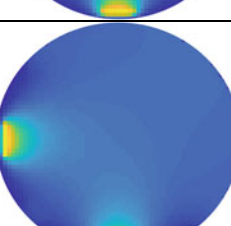
## 2.2 *Post-processing Data*

Based on the simulation result, the electrical potential data for each projection is exported in grid form in sizes of  $64 \times 64$ . Following the concept of a pixel in image processing, the data is imported in Matlab and rearrange in order to form an image of the sensitivity map as shown in the result section.

## 3 Results and Discussion

The sensitivity map generation is done through simulation by using software COM-SOL Multiphysics. Image reconstruction for the sensitivity map is prepared by exporting the data of electrical potential using  $64 \times 64$  resolution where the exported data is arranged in coordinate form. The data is normalized and imported inside Matlab where the normalized electrical potential data is plotted based on their coordinate as shown in Fig. 3.

Based on the result obtained, the projection path in the sensitivity map simulation is clearly defined compared to the one in the reconstructed image. By comparing all the result, the projection path for electrode pair 1–2 is clearly defined for both the simulation and reconstructed image. This is because the grounded electrode 2 is located nearest to the excitation electrode 1, thus capturing stronger electrical potential data. Compared to electrode pair 1–2, the simulation path for projection 1–3 and 1–7 mirrors one another and can still be seen in the reconstructed image, albeit not too distinct because of the increase of distance between the electrode pair. Lastly, the reconstructed sensitivity map for projection 1–4 and 1–5 are not clearly defined with electrode pair 1–5 showing weaker projection path in reconstructed image compare to the pairing 1–4. This is due to the distance between the electrode pair, which is the furthest, that causes the soft field effect. The soft field effect refers to the behavior in an ECT system where the further the region, the lesser the sensitivity. Additionally, during the generation of sensitivity maps the soft field nature might follow which in turn created the ‘soft field effect’ in the image reconstruction. As the sensitivity of the sensitivity map is affected (i.e. reduced sensitivity) by ‘soft field effect’, hence the location of the electrode needs to be considered because the electric field strength decreases as the distance is further from the electrode.

Projection	Simulated projection beam	Reconstructed Map
1-2		
1-3		
1-4		
1-5		
1-7		

**Fig. 3** Sensitivity map obtain from COMSOL simulation and Matlab reconstruction



## 4 Conclusion

Based on the simulation and the image reconstructed, it clearly shows that the electrode configuration plays a major part in determining the sensitivity map generation. Sensitivity map can be generated by reconstructing the electrical potential data taken from the simulation. It is proven that different position and distance between the electrode pair will affect the projection path of the electrode pair. This is because of the soft field effect where the farther the distance between the electrode pair, the weaker the electrical potential distribution. Thus, the distance and size of electrode need to be taken into consideration so that it will fall within the sensing region and at the same time, reduce the soft field effect. Besides, even though the projection is clearly shown in the simulation, further improvement still needs to be done in terms of the chosen resolution in order to make the projection path of sensitivity map more defined as the higher the resolution, the more detailed the image.


## References

1. Ren Z, Kowalski A, Rodgers TL (2017) Measuring inline velocity profile of shampoo by electrical resistance tomography (ERT). *Flow Meas Instrum* 58(September):31–37
2. Rafiei-Naeini M, Wright P, McCann H (2007) Low-noise measurement for electrical impedance tomography. In: International conference on electrical bioimpedance and the 8th conference on electrical impedance tomography, 2007, pp 324–327
3. Ren Z, Member S, Yang W (2015) A miniature two-plate electrical capacitance tomography sensor. *IEEE Sens J* 15(5):3037–3049
4. Mohd Razali NA et al (2015) Miniaturized planar tomography for multiphase stagnant sample detection. *J Teknol* 73(6):99–102
5. Yan H, Liu LJ, Qiang DZ (2009) An iterative electrical capacitance tomography image reconstruction algorithm. 12(2):9–12
6. Marashdeh Q, Teixeira FL (2004) Sensitivity matrix calculation for fast 3-D electrical capacitance tomography (ECT) of flow systems. 40(2):1204–1207
7. Xingxing Z, Jinchuang Z, Wenli F (2016) Computation of sensitivity map in adaptive electrical capacitance volume tomography based on voltage distribution. In: *ICSPCC 2016—IEEE international conference on signal processing, communications and computing, conference proceedings, 2016*, pp 1–4
8. Kang Y, Liu S, Liu J (2018) Image reconstruction algorithm for electrical capacitance tomography based on data correlation analysis. *Flow Meas Instrum* 62(July):113–122
9. Liu QF, Han Y (2013) Analysis of the effect of stray capacitance on a charge/discharge-based electrical capacitance tomography system. *Optik (Stuttg)* 124(23):6009–6012
10. Zhang L, Zhai Y, Wang X, Tian P (2018) Reconstruction method of electrical capacitance tomography based on wavelet fusion. *Meas J Int Meas Confed* 126(May):223–230
11. Fan WR, Wang HX (2010) Maximum entropy regularization method for electrical impedance tomography combined with a normalized sensitivity map. *Flow Meas Instrum* 21(3):277–283
12. Soleimani M (2005) Numerical modelling and analysis of the forward and inverse problems in electrical capacitance tomography. *Int J Inf Syst Sci* 1(1):193–207
13. Oldenborger GA, Routh PS, Knoll MD, Routh S, Knoll MD (2005) Sensitivity of electrical resistivity tomography data to electrode position errors. *Geophys J Int* 163:1–9
14. Ridzuan S et al (2015) Jurnal Teknologi full paper simulation study on electrical resistance tomography using metal wall for bubble detection. 6:31–35

15. Liyana H et al (2018) Sensitivity mapping for electrical tomography using finite element method. *Int J Integr Eng* 10(4):64–67
16. Yunus M, Hafiz M, Rahiman F, Abdul Y (2015) Sensitivity map generation for conducting strategy in electrical resistance tomography. *J Teknol* 17:91–97

# Infrared Thermal Sensor for a Low Cost and Non-invasive Detection of Skin Cancer



A. Noora Safrin, B. Pooja, K. Hema, P. Padmapriya, Vigneswaran Narayanamurthy  and Fahmi Samsuri

**Abstract** Skin cancer is in a rising trend over the years. Though there are of many conventional approaches for skin cancer diagnosis, there is still a massive demand for the device with features of low cost, compact, portable, less diagnosis time, comfortable (no biopsy), high sensitivity and accuracy. The proposed system is the implementation of infrared (IR) thermal sensor in a non-contact manner which detects the temperature of the epidermal layer of skin, where the temperature of the skin varies for the subjects if they have cancer. The device receives the signal from the sensor unit, and it is further processed to detect the various level of skin cancer. The system process optimization was performed, and optimization factors were reported based on the sensor operating distance to detect the values efficiently. From the analysis, it was observed that there's a 2.4 °C temperature difference for the thermometer and infrared thermal sensor reading. Also, the thermometer reading was greater by 2.4 °C comparing to the sensor values. This is attributed to the emissivity nature of the heated objects to the ambiance. This system can also be used as a wearable device by alerting the subject of their condition. This system provides better monitoring with high accuracy through non-invasive technique and early detection can be made to prevent cancer deaths.

**Keywords** Infrared thermal sensor · Skin cancer · Diagnosis · Non-invasive · Temperature variation analysis (TVA)

---

A. Noora Safrin · B. Pooja · K. Hema · P. Padmapriya  
Department of Biomedical Engineering, Veltech Multitech Dr. RR and Dr. SR Engineering College, Chennai 600062, India

V. Narayanamurthy (✉)  
Faculty of Electrical and Electronic Engineering Technology, Universiti Teknikal Malaysia Melaka, 76100 Melaka, Malaysia  
e-mail: [vigjes@gmail.com](mailto:vigjes@gmail.com)

V. Narayanamurthy · F. Samsuri  
Faculty of Electrical and Electronics Engineering, University Malaysia Pahang, 26600 Pekan, Malaysia

© Springer Nature Singapore Pte Ltd. 2020

A. N. Kasruddin Nasir et al. (eds.), *InECCE2019*, Lecture Notes in Electrical Engineering 632, [https://doi.org/10.1007/978-981-15-2317-5\\_8](https://doi.org/10.1007/978-981-15-2317-5_8)

## 1 Introduction

Skin cancer is a disease in which the abnormal growth of cell arises from the skin surface. The malignant cells have the strength to invade and spread over the surrounding tissues of the body. Skin cancer is mainly caused due to UV exposure in a large amount on the human skin surface [1]. UV is a section of the electromagnetic spectrum. It has the wavelength of 320–400 nm which is shorter than that of visible light made it invisible to the naked eyes. UV radiation enters the atmosphere and plays the vital role in situations like eye damage, premature skin aging, skin cancer, etc. UV radiation damages the DNA indirectly by producing a genetic mutation which leads to the development of skin cancer [2]. Both the U.S. development of health and human services and the World Health Organization have identified UV as a proven human carcinogen [3]. The UV radiation which contains a shorter wave is the primary cause of skin reddening, which in turn damages the superficial layer of the skin commonly known as the epidermis [4]. Around 40% of people in the world are affected by skin cancer and is rising [5]. Skin cancer also occurs due to some genetic disorder such as congenital melanocyte nerve syndrome and usage of immune-suppressive drugs increases the risk rate for skin cancer.

Screening and early detection of skin cancer can avoid death. It is important to take a step to develop new technology [6] that is superior in both accuracy and patient comfort. Visual differentiation remains a debatable one in the world [7]. Wearable technologies were also developed for cancer detections [8]. Several techniques [9] like spectroscopy, image processing, and optical method screening take more time, involves complex systems and also the sensitivity of such a method proven some negative result on the test reports [10–12]. Concerning all these into account, the system of low cost, compact, portable, less diagnosis time, comfortable (no biopsy), high sensitivity and accuracy are still of interest [10]. The evidence shows that disease or deviation from normal functioning is accompanied by changes in the temperature of the body, which again affect the temperature of the skin [13]. Thus, accurate data on the human body temperature and skin can help in various disease diagnoses. The proposed system is of simple and low cost which can detect the skin cancer in a non-invasive manner using temperature variation analysis (TVA).

## 2 Device Design and Instrumentation

Generally, the temperature of skin cancer people is greater than that of normal human body temperature due to the disintegration of normal healthy cells. In melanoma, cancer cells arise from the moles of the skin which causes the inflammation and provide an irregular shape to mole around the epidermal layer. The used method is a non-contact localized detection and is considered to be advantageous mainly because of blackbody radiation has almost 40% of its emitted IR-radiation power within this particular spectral region corresponding to the temperature of the skin [14]. This

makes it simpler for the detection of abnormalities in IR radiation from the skin in the presence of skin cancer. Furthermore, at the employed detection wavelengths, IR radiation suffers nearly no absorption from air gas molecules [15], which adds to the merits.

The proposed system is shown in Fig. 1 consists of a sensor unit (Mlx90614 IR thermal sensor), a processing unit (Atmega 328) and display unit consists of 16 × 2 LCD. The IR Thermal Sensor consists of in-built thermopile detector chip and the signal conditioning ASSP unit. Mlx90614 thermal sensor has a high medical accuracy of 0.5 °C and resolution of 0.02 °C. It is small in size and easy to integrate

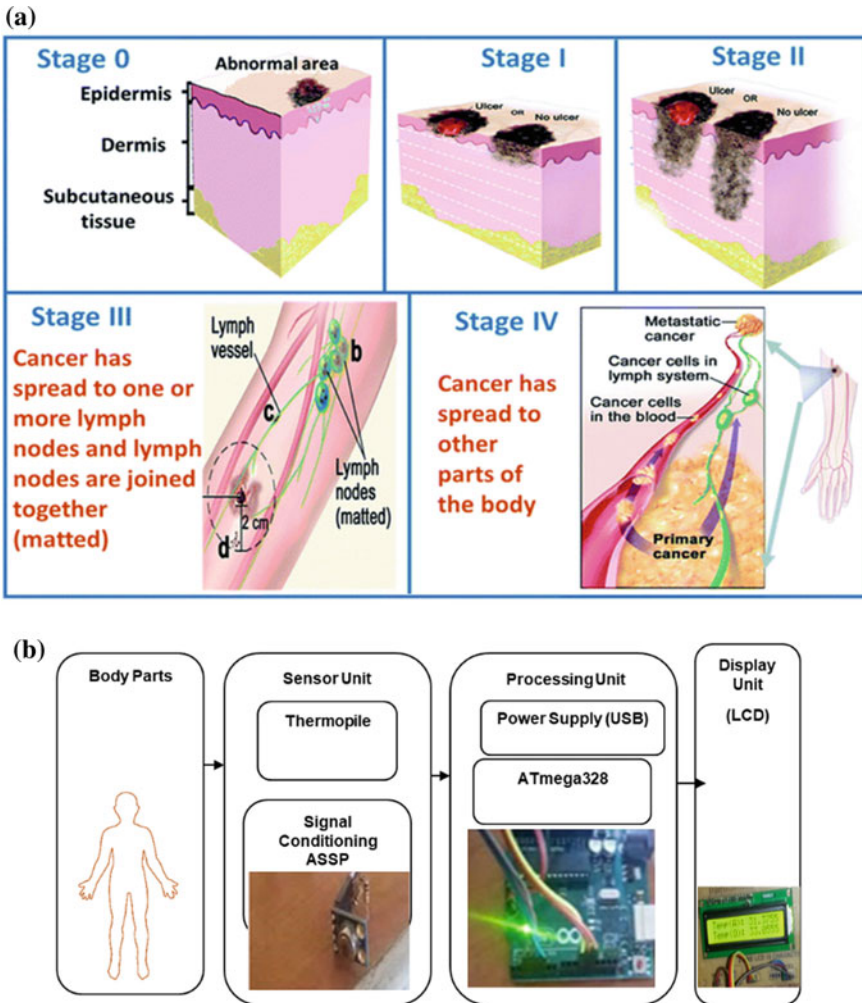
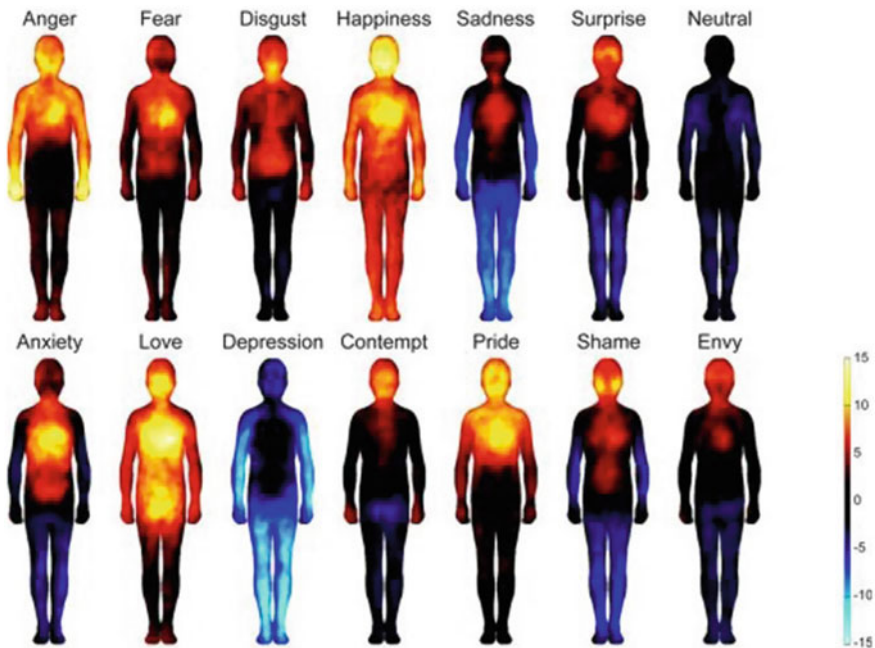


Fig. 1 a Stages of skin cancer. Reproduced from Ref. [10] published by The Royal Society of Chemistry; b block diagram of the proposed system

with the microcontroller. The processor unit consists of an Arduino board. It is an 8-bit AVR RISC based microcontroller combines with 32 KB ISP flash memory with read-while-write capabilities, 1 KB EEPROM. The device operates between 5 volts. The sensor unit picks up the temperature from the subject and converts it to the electrical signal by the combination of the integrated circuit (thermopile and signal conditioning ASSP). These electrical signals are fed into the system for processing and it compares the obtained temperature range with the threshold value which has been programmed in Arduino IDE. The difference in temperature rise between normal spot to cancer spot is used as a factor for skin cancer diagnosis. The processed data will be displayed in the Liquid crystal displaying unit. From Fig. 2, it can be seen that the temperature distribution of the body is almost symmetrical in most cases. If the diagnosing spot is in the symmetrical regions of the body, then the localized measurement is performed at both the symmetrical regions along with the surrounding regions. For instance, if the diagnosis spot is on the left bicep, then the measurement was also performed at the same right bicep, to measure the temperature difference effectively. If the diagnosing spot is in the non-symmetrical regions of the body, then only the surrounding neighbor regions are measured for the difference. In order not to get misinterpreted with the surface inflammation or other injuries, the



**Fig. 2** The body maps show regions whose activation increased (warm colors) or decreased (cool colors) when feeling each emotion. The color bar indicates the t-statistic range. Reproduced from Ref. [16] under CC license

temperature needs to be monitored over a prolonged period of 2 weeks, this helps in arriving at an efficient diagnosis protocol.

### 3 Device Characterization and Feasibility Study

In the experiment analysis, the skin temperature of various body parts was considered. We mainly focused on the body parts which are exposed to UV radiations. UV rays exposed areas in the human body are hand, head, torso, and feet. The various disease conditions which visually appear like malignant melanoma were also considered. In order to show the temperature variation for different diseases and their persistence of temperature for a period of two weeks these considerations were made. Different body parts possess different skin temperature based on the morphological behavior of the melanocytic characteristic of the skin regions. Also, the emissivity factor of different creatures in nature varies. The overall average of skin emissivity is  $0.971 \pm 0.005$  (SD) [17]. Chickenpox is the condition in which the blisters appear like melanoma which lies in the temperature range of  $39^\circ\text{C}$  [18] and for benign melanoma, the temperature is around  $40^\circ\text{C}$  [19]. But in-case of malignant melanoma, the skin temperature at the particular site of the tumor is found to be greater than around  $45^\circ\text{C}$  [20].

To check the ability of non-contact IR thermal sensor, comparison of contact sensor (thermometer) and non-contact Infrared thermal sensor experiments were made, in which ten objects and subjects are involved in the measurement of both surface temperature and skin temperature. Thermometer reading has been measured in contact with the surface of both heated various stainless steel (SS) objects and subject, whereas infrared thermal sensor has been performed in a non-contact manner keeping the sensor at a constant phase, in which the subject and object measurement was done by varying the distance between sensor.

#### 3.1 Comparative Measurement of Object Temperature

We conducted experimental analysis on the 10 objects by varying the distance in case of the infrared thermal sensor while keeping contact with the object in case of the thermometer. Objects were kept at the distance of 5, 10, 15 and 20 cm with respect to the sensor and measurements were performed. Reason for making the distance up to 20 cm is that above 20 cm the temperature reading reaches the ambient temperature. So, the distance of 20 cm is the cut-off distance for the IR thermal sensor. Later the procedure was followed for each and every object by varying the distance at a constant time period. While keeping the sensor in a non-contact manner, only the stable values are considered. Finally, mean of the temperature obtained from IR thermal sensor were calculated at the ambient temperature of  $30^\circ\text{C}$  at the constant time period and the graph was plotted between mean temperature obtained from IR

thermal sensor and thermometer. These measurements were made with the help of heated SS objects.

### ***3.2 Non-invasive Measurement of Skin Temperature***

We made the measurement on the skin temperature of the subject using the IR thermal sensor by varying the distance of the subjects from the sensor unit and the mean value of the temperature of the subject was recorded. Taking hand as a reference, for ten subjects the temperature measurement was performed by varying the distance from 5 to 20 cm at a constant ambient temperature and time period respectively.

## **4 Results**

The results of the comparative measurement of object temperature and measurement of skin temperature are reported in the following sections.

### ***4.1 Comparative Measurement of Object Temperature***

The graphical representation of the conducted experiment is shown in Fig. 3a, b. As the sensor distance increases, the reading drops. It can also be seen that there is a 2.4 °C temperature difference for the thermometer and infrared thermal sensor reading. Also, the thermometer reading is greater by 2.4 °C comparing to the sensor values. Notably, there was a drastic temperature difference between the objects while varying the distance between the IR thermal sensor and the objects; this is due to the emissivity nature of the heated objects to the ambiance.

### ***4.2 Non-invasive Measurement of Skin Temperature***

The graphical representation of the conducted experiment is shown in Fig. 3c. It was observed that the skin temperature of the subjects is found to be less than 45 °C, in case if the skin temperature exceeds above 45 °C, implies a change in the metabolic activity that causes the irregular chemical reaction or poor acid-base balance. Taking temperature as a parameter, from the obtained result we can determine the skin cancer and its related disorder. It was noted that there is a temperature difference between the objects and humans; it was due to the emissivity factor. From the experiment conducted, it can be suggested that the sensor can be placed closer in order to get



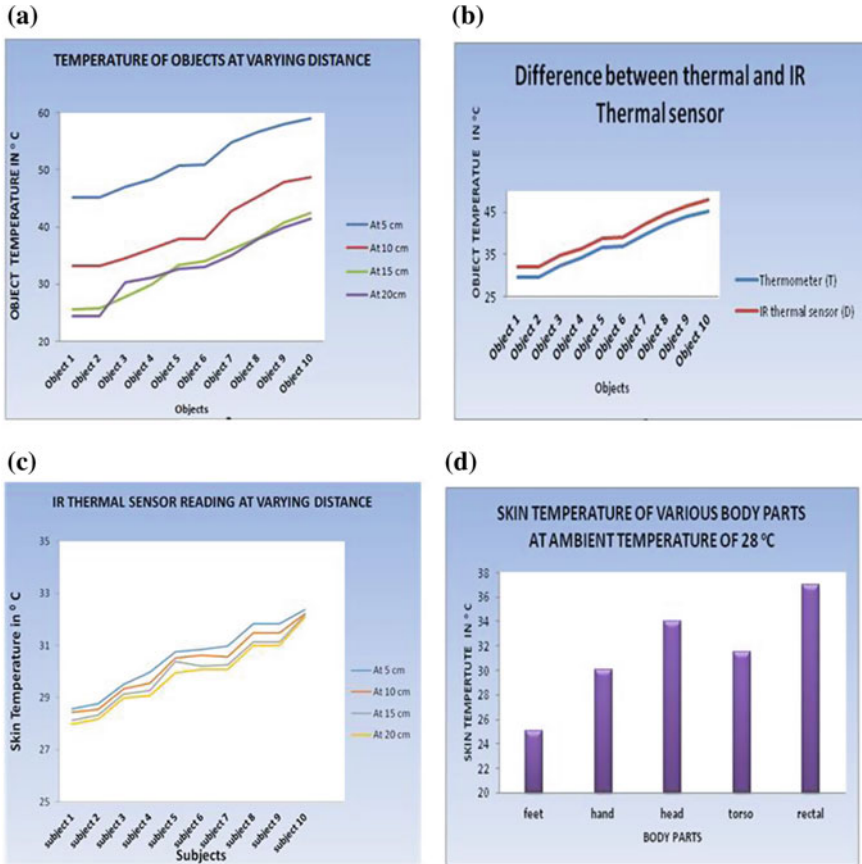


**Fig. 3** **a** Represents the temperature of objects at various distances; **b** represents the accuracy level of infrared thermal sensor over thermometer; **c** represents the measurement of temperature on human hand (10 subjects); **d** represents the skin temperature of various body parts of subjects which are exposed to sun majorly

a precise reading. As the distance between the sensor and the subject increases, the reading decreases.

### 5 Discussion

Various body parts have different skin temperature which ranges from 25 to 34 °C for the fixed ambient temperature. The graphical representation of the skin temperature of body parts is shown in Fig. 3d. The temperature distribution on the body regions varies due to the irregular metabolic activity results in variation in the standard temperature. Body regions which are engaged in damaging of DNA results in increases

in temperature. In order not to mistake with chickenpox or other similar kinds of blisters, the experiment of skin temperature analysis should be followed-up for over two week. The condition of the skin temperature gradually decreases with respect to the recovery time, except for benign and malignant melanoma the skin temperature remains constant throughout the period. It clearly indicates the skin temperature of malignant melanoma is equal to or greater than 45 °C because of continuous metastatic changes whereas for other conditions the temperature will not be constant for an extended period. From the second opinion of a dermatologist and from the various studies the temperature of the benign and malignant tumor was found to be between 40 and 45 °C. Overall the diagnosing setup cost is very low and is an entirely non-contact process. Further, the experiments can be made on skin cancer subjects to detect skin cancer and its related disorder by considering skin temperature variation as a parameter.

## 6 Conclusion

The automation screening device for skin cancer diagnosis has been proposed in a portable design with high accuracy using the IR thermal sensor. IR thermal sensor enjoys its feature of non-contact, harmless and medical resolution of 0.5 °C. Due to the promising features of IR thermal sensor, the distribution of skin temperature can be determined in a short period of time less than 2 s. The IR thermal sensor evidently proved the detection of skin temperature more accurately in a harmless manner. Skin temperature is one of the parameters to detect the skin cancer that occurs due to the changes in the morphological behavior of the skin region. Early detection of skin cancer can reduce the mortality rate and thus the life of many people can be saved. However, diagnosis with unaided eye results in the misinterpretation of data. The proposed system can be used in the urban areas where the routine pathologist is unavailable and the subject themselves can diagnosis their health status with an autonomous system. Screening of early diagnosis of skin cancer can prevent from unnecessary biopsy, thus it also helps the pathologist to provide the proper treatment for the cancerous person. The proposed system is robust and user-friendly due to its simplicity. By this system, the subject can have preliminary knowledge about the level of cancer on their own. It also acts as the wearable alert system for the subject to undergo treatment at the appropriate time.

**Acknowledgements** With gratitude, we thank Dr. P. Thirumaran, Professor, dermatology department in Kilpauk Medical College, Chennai India for providing us clinical guidance in the hospital. We owe our deep gratitude to Dr. Rathy, a dermatologist in St. Isabel's Hospital, Mylapore, Chennai, India who provided great support for this project. Support provided by the faculty and staffs of BME Dept. Veltechmultitech is thankfully acknowledged. PDF scholarship conferred to VN by University Malaysia Pahang is gratefully acknowledged. Fundamental Research Grant Scheme (FRGS—RDU190108) from Ministry of Education, Malaysia is thankfully acknowledged.

## References

1. Kanavy HE, Gerstenblith MR (2011) Ultraviolet radiation and melanoma. In: Seminars in cutaneous medicine and surgery, pp 222–228
2. Saraiya M, Glanz K, Briss PA, Nichols P, White C, Das D, Smith SJ, Tannor B, Hutchinson AB, Wilson KM (2004) Interventions to prevent skin cancer by reducing exposure to ultraviolet radiation: a systematic review. *Am J Prev Med* 27:422–466
3. Bichakjian CK, Halpern AC, Johnson TM, Hood AF, Grichnik JM, Swetter SM, Tsao H, Barbosa VH, Chuang T-Y, Duvic M (2011) Guidelines of care for the management of primary cutaneous melanoma. *J Am Acad Dermatol* 65:1032–1047
4. Gallagher RP, Lee TK, Bajdik CD, Borugian M (2010) Ultraviolet radiation. *Chronic Dis Inj Can* 29
5. Lomas A, Leonardi-Bee J, Bath-Hextall F (2012) A systematic review of worldwide incidence of nonmelanoma skin cancer. *Br J Dermatol* 166:1069–1080
6. Simões M, Sousa J, Pais A (2015) Skin cancer and new treatment perspectives: a review. *Cancer Lett* 357:8–42
7. Parsons SK, Chan JA, Winifred WY, Obadan N, Ratichek SJ, Lee J, Sen S, Ip S (2011) Noninvasive diagnostic techniques for the detection of skin cancers
8. Ray PP, Dash D, De D (2017) A systematic review of wearable systems for cancer detection: current state and challenges. *J Med Syst* 41:180
9. Esteva A, Kuprel B, Novoa RA, Ko J, Swetter SM, Blau HM, Thrun S (2017) Dermatologist-level classification of skin cancer with deep neural networks. *Nature* 542:115
10. Narayanamurthy V, Padmapriya P, Noorasafrin A, Pooja B, Hema K, Nithyakalyani K, Samsuri F (2018) Skin cancer detection using non-invasive techniques. *RSC Adv* 8:28095–28130
11. Rajab M, Woolfson M, Morgan S (2004) Application of region-based segmentation and neural network edge detection to skin lesions. *Comput Med Imaging Graph* 28:61–68
12. Masood A, Al-Jumaily AA (2013) Computer aided diagnostic support system for skin cancer: a review of techniques and algorithms. *Int J Biomed Imaging* 2013
13. Herman C, Cetingul MP (2011) Quantitative visualization and detection of skin cancer using dynamic thermal imaging. *J Vis Exp: JoVE*
14. Diakides M, Bronzino JD, Peterson DR (2012) Medical infrared imaging: principles and practices. CRC Press
15. Vollmer M, Klaus-Peter M (2017) Infrared thermal imaging: fundamentals, research and applications. Wiley
16. Nummenmaa L, Glerean E, Hari R, Hietanen JK (2014) Bodily maps of emotions. *Proc Natl Acad Sci* 111:646–651
17. Togawa T (1989) Non-contact skin emissivity: measurement from reflectance using step change in ambient radiation temperature. *Clin Phys Physiol Meas* 10:39
18. Macleod J (1951) Effect of chickenpox and of pneumonia on semen quality. *Fertil Steril* 2:523–533
19. Moustafa AMN, Muhammed HH, Hassan M (2013) Skin cancer detection using temperature variation analysis. *Engineering* 5:18
20. Vrocher D (2004) Emergency medicine: a comprehensive study guide. *Ann Emerg Med* 44:675–676

# T-Way Strategy for Sequence Input Interaction Test Case Generation Adopting Fish Swarm Algorithm



**Mostafijur Rahman, Dalia Sultana, Sabira Khatun, Mohd Falfazli Mat Jusof, Syamimi Mardiah Shaharum, Nurhafizah Abu Talip Yusof, Khandker M. Qaiduzzaman, Md Hasibul Hasan, Md Mushfiqur Rahman, Md Anwar Hossen and Afsana Begum**

**Abstract** In Combinatorial Input Interaction (CII) based system, the increasing number of input event causes the increasing number of test cases. Since twenty years many useful T-way strategies have been developed to reduce test case size. In order to reduce test cases several T-way sequence input interaction strategies are explored, such as, Bee Algorithm(BA), Kuhn encoding (K), ASP with Clasp, CP with Sugar, Erdem (ER) exact encoding, Tarui (TA) Method, U, UR, D and DR, Brain (BR). However, none of them claim that for all test configuration the produced test cases are best. The reason is that the T-way sequence input interaction is NP-Hard problem. In this research, Fish Swarm algorithm is proposed to adapt with T-way sequence input interaction test strategy. The proposed system is compared with the other renowned search-based T-way strategies. The result shows that the proposed system is able to generate feasible and optimal results.

**Keywords** Software testing · Combinatorial input interaction testing · Sequence input interaction · T-way testing · Fish swarm

## 1 Introduction

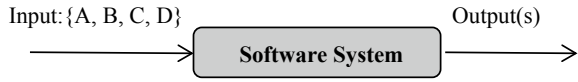
Inadequate software testing may cause blunders. A number of software failures had found in the past histories which led to embarrassment, massive financial losses, injuries and even death. One of them was in 1962, the mission control destroyed the rocket after 293 s of lift off which costs around \$18.5 million. The reason was just missing a single superscript bar in the program code [1], which was not properly tested. Another was in 1978, the Hartford coliseum collapsed, which costs around \$70 million and added \$20 million damage to the local economy. The reason was

---

M. Rahman (✉) · D. Sultana · K. M. Qaiduzzaman · M. H. Hasan · M. M. Rahman · M. A. Hossen · A. Begum  
Department of Software Engineering, Daffodil International University, Dhaka, Bangladesh

S. Khatun · M. F. M. Jusof · S. M. Shaharum · N. A. T. Yusof  
Faculty of Electrical Engineering and Electronics, Universiti Malaysia Pahang, Pahang, Malaysia

**Fig. 1** Framework of sequence input interaction [2]



the coliseum was designed incorrectly using CAD software (i.e., the software design was not properly performed). Therefore, it is very crucial to have adequate software testing.

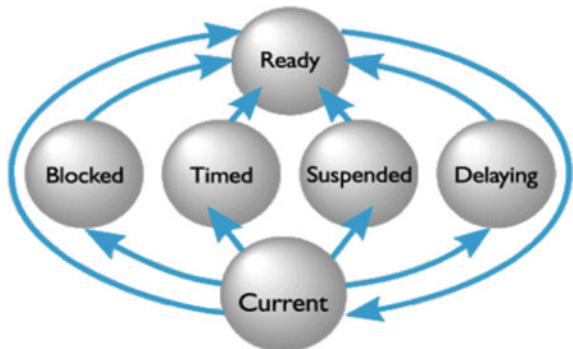
In combinatorial input interaction testing (CIIT), test cases are selected based on some combinatorial fashion. The way is that sample of input parameters are combined in a systematic way. It is a class of test case selection where combination and permutation on sets of parameters are emphasized. The combinatorial input interaction can be segregated into sequence-less input interaction and sequence input interaction. This research focuses on sequence input interaction testing. Figure 1 shows framework of sequence input interaction system where input actions are in permuted form [2].

Mathematically the Sequence Input Interaction (SII) is shown as  $SCA(N; t, E)$ , where SCA indicates Sequence Covering Array (SCA),  $N$  is the number of final test cases,  $t$  indicates strength, and  $E$  is the number of Input Events [2]. The sequence input interaction problem is illustrated from the following example.

Figure 2 shows six tasks activities of Real-Time operating system kernel (RTK) [3]. The tasks are as follows: *Current*, *Ready*, *Blocked*, *Suspended*, *Timed* and *Delaying states*. In the *task running state* or *current state*, after kernel initialization at least one task need to execute. Internal idle task run automatically if there is no application task is ready to execute. In *ready state*, all task are ready to run in priority basis. Task interruption is allow to execute the prioritized task(s). In *suspend state*, tasks are in pause mode for the execution of higher priority task. Kernel can make the suspended task(s) in ready/current state. In *blocked state*, tasks are blocked by interrupt signal and waiting for an event.

In delaying state, suspended tasks are executed automatically by the timer interrupt handler of RTK. In timed state, the task are kept into the ready state either the

**Fig. 2** Real time kernel task states transition diagram [3]



occurrence of event found or time-out constraint expires. In this paper the six task states indicate as  $\{e_0, e_1, e_2, e_3, e_4, e_5\}$  and considered as six events.

To satisfy the whole system in Fig. 2, 6! or 720 test cases need to test. Which is called exhaustive input test sequence. The number of test cases from exhaustive test case can be reduced using T-way sequence strategy to satisfy whole system configuration.

For demonstration of T-way SII problem, SCA (N; 3, 6) configuration is taken as a sample test configuration. In SCA (N; 3, 6), the 3 and 6 indicate the strength and number of test sequence input events respectively. In this demonstration, the six inputs are considered as  $\{e_0, e_1, e_2, e_3, e_4, e_5\}$  and the exhaustive test cases is. 6! or 720 for testing sequence events, which is not practically feasible where the number of input event is higher. Table 1 shows the generated 3-way 120 sequence tuple. Using T-way strategy the 120 3-way tuples are covered by 10 test cases shown in Table 2.

Several researches are published on test case generation for sequence input interaction using T-way strategy. BA [4], adopted the Bee search algorithm for T-way input sequence testing to generate test cases. Kuhn encoding (K) [5] detect the fault earlier and developed SCA to address testing problems using combinatorial methods to provide efficient testing. In ASP with Clasp [6] and CP with Sugar [6], research, the consideration of problem is to find optimal sequence covering arrays by ASP and Control Programming (CP). Two ASP SAT (satisfiable) solvers (Sugar and Clasp) are used both are complicated method to generate test suite. Erdem (ER) exact encoding [7], authors design a new SCA, use two Answer Set Programming (ASP) methods, such as, exact encoding and greedy encoding. Both encoding are sophisticated method to generate test suite. TA [8], author construct a new SCA and shows a simple and explicit construction of covering array associated with the upper bound and lower bound. U [9], UR [9], D [9], DR [9] uses a probability function to test all the t-subsequences coverage by the generated test cases. Here Upper and Down bound is considered for the probability functions. For BR [10], authors use Answer Set Programming (ASP) embed with new way generated Sequence Covering Array (SCA). Authors in [11] presents a unified strategy based on a meta-heuristic algorithm called elitist flower pollination algorithm (eFPA), which is updated version of FPA [11].

Researchers are adopting different types of searching algorithms on sequence input interaction (using T-way strategy) to get minimum number of test cases. However, no one can claim that their strategy for sequence input interaction able to produce optimum number of test cases for all test configurations. Therefore, it is found that the T-way strategy for sequence input interaction is a NP-hard problem [12–15, 17, 18]. So, there is a wide scope for the researcher to embed any search method and produce feasible and competitive number of test case. This paper adopt fish swarm searching algorithm with T-way test strategy for sequence input interaction and produce test cases for different test configurations. The generated test cases sizes for different test configurations are compared with the existing T-way sequence input interacted strategies.

**Table 1** 3-way tuples generated from Fig. 2

No	Tuples	No	Tuples	No	Tuples	No	Tuples
1	[e0, e1, e2]	31	[e2, e5, e3]	61	[e0, e4, e1]	91	[e3, e0, e4]
2	[e0, e1, e3]	32	[e4, e5, e3]	62	[e2, e4, e1]	92	[e3, e0, e5]
3	[e0, e1, e4]	33	[e5, e3, e4]	63	[e3, e4, e1]	93	[e1, e4, e0]
4	[e0, e1, e5]	34	[e5, e4, e3]	64	[e4, e1, e5]	94	[e2, e4, e0]
5	[e0, e2, e3]	35	[e0, e3, e2]	65	[e0, e5, e1]	95	[e3, e4, e0]
6	[e0, e2, e4]	36	[e1, e3, e2]	66	[e2, e5, e1]	96	[e4, e0, e5]
7	[e0, e2, e5]	37	[e3, e2, e4]	67	[e3, e5, e1]	97	[e1, e5, e0]
8	[e0, e3, e4]	38	[e3, e2, e5]	68	[e4, e5, e1]	98	[e2, e5, e0]
9	[e0, e3, e5]	39	[e0, e4, e2]	69	[e5, e1, e4]	99	[e3, e5, e0]
10	[e0, e4, e5]	40	[e1, e4, e2]	70	[e5, e4, e1]	100	[e4, e5, e0]
11	[e1, e2, e3]	41	[e3, e4, e2]	71	[e4, e1, e3]	101	[e5, e0, e4]
12	[e1, e2, e4]	42	[e4, e2, e5]	72	[e4, e3, e1]	102	[e5, e4, e0]
13	[e1, e2, e5]	43	[e0, e5, e2]	73	[e5, e1, e3]	103	[e4, e0, e3]
14	[e1, e3, e4]	44	[e1, e5, e2]	74	[e5, e3, e1]	104	[e4, e3, e0]
15	[e1, e3, e5]	45	[e3, e5, e2]	75	[e3, e1, e2]	105	[e5, e0, e3]
16	[e1, e4, e5]	46	[e4, e5, e2]	76	[e3, e2, e1]	106	[e5, e3, e0]
17	[e2, e3, e4]	47	[e5, e2, e4]	77	[e4, e1, e2]	107	[e3, e0, e2]
18	[e2, e3, e5]	48	[e5, e4, e2]	78	[e4, e2, e1]	108	[e3, e2, e0]
19	[e2, e4, e5]	49	[e4, e2, e3]	79	[e5, e1, e2]	109	[e4, e0, e2]
20	[e3, e4, e5]	50	[e4, e3, e2]	80	[e5, e2, e1]	110	[e4, e2, e0]
21	[e0, e5, e4]	51	[e5, e2, e3]	81	[e1, e0, e2]	111	[e5, e0, e2]
22	[e1, e5, e4]	52	[e5, e3, e2]	82	[e1, e0, e3]	112	[e5, e2, e0]
23	[e2, e5, e4]	53	[e0, e2, e1]	83	[e1, e0, e4]	113	[e2, e0, e1]
24	[e3, e5, e4]	54	[e2, e1, e3]	84	[e1, e0, e5]	114	[e2, e1, e0]
25	[e0, e4, e3]	55	[e2, e1, e4]	85	[e1, e2, e0]	115	[e3, e0, e1]
26	[e1, e4, e3]	56	[e2, e1, e5]	86	[e2, e0, e3]	116	[e3, e1, e0]
27	[e2, e4, e3]	57	[e0, e3, e1]	87	[e2, e0, e4]	117	[e4, e0, e1]
28	[e4, e3, e5]	58	[e2, e3, e1]	88	[e2, e0, e5]	118	[e4, e1, e0]
29	[e0, e5, e3]	59	[e3, e1, e4]	89	[e1, e3, e0]	119	[e5, e0, e1]
30	[e1, e5, e3]	60	[e3, e1, e5]	90	[e2, e3, e0]	120	[e5, e1, e0]

## 2 Proposed T-Way Strategy Adopting Fish Swarm Algorithm

Fish swarm searching algorithm (FSSA) [16] is based on finding more food and keeping the swarm according to its rules. In FSSA, the fishes move toward better positions based on the hypothesis of better positions in the problem space contain

**Table 2** Test cases which covered 120 T-way tuples in the Table 1

No	Test cases	Covered T-way tuple
1	[e0, e1, e2, e3, e4, e5]	20
2	[e0, e5, e4, e3, e2, e1]	20
3	[e2, e1, e5, e4, e0, e3]	19
4	[e3, e4, e5, e1, e0, e2]	19
5	[e4, e1, e3, e2, e0, e5]	15
6	[e5, e2, e3, e0, e1, e4]	15
7	[e1, e0, e4, e5, e2, e3]	5
8	[e3, e2, e5, e4, e0, e1]	5
9	[e0, e2, e3, e1, e4, e5]	1
10	[e0, e2, e4, e5, e1, e3]	1

more food. The fish move toward these better positions without losing their integrity. At first, the fish population is randomly distributed in the problem space with a uniform distribution. Then these fishes follow some other fishes that find more food. As a result, the follower fishes find food and also help each other in finding more food. In FSSA, this behavior is simulated as, each fish  $i$  ( $F_i$ ) choose one fish in a better position randomly. Fish  $F_i$ , which resides at  $X_i$ , chooses fish  $F_j$  ( $f(X_j) < f(X_i)$ ) in order to help it to find food. Using the Eq. (1) given below, these fishes try to approach its position.

$$Y_{i,d} = X_{i,d} + ((X_{i,d} - X_{i,d}) \times \text{rand}(0, 2)) \quad (1)$$

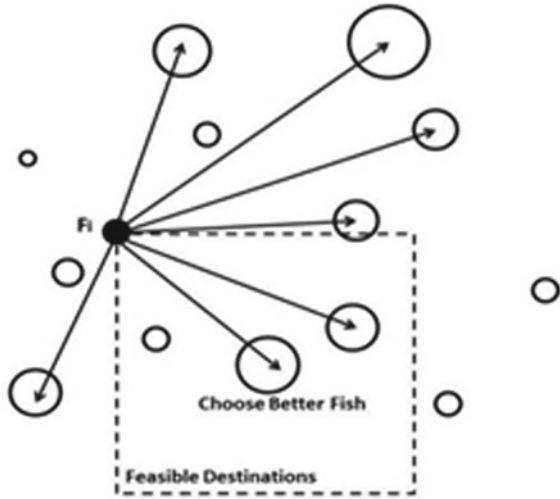
In Eq. (1),  $X_{i,d}$  is equal to the  $d$ th component of the position vector of fish  $F_i$ , and  $\text{rand}(L, R)$  generates a random number with a uniform distribution in the range  $[L, R]$ .  $Y$  vector is a buffer vector. The schematic of the movement of one fish toward a better one is illustrated in Fig. 3.

Every fish is shown by a circle in Fig. 3. The bigger the circle, the fitter the fish will be. In this figure, the fish  $F_i$  considers fitter fish in its swarm and chooses one of them randomly with a uniform distribution. The next position of this fish, if better, will be a point on the 2D cubic feasible destination space. The center of this destination space is the chosen fish (better) by choosing a random number in the range  $[0, 2]$ .

In this research paper the fish swarm algorithm is adopted for test case generation on sequence interacted input based T-way strategy called TSFSSA. Concerning the generation of sequenced interaction elements, every T-way combination of events is covered at least once with respect to the particular order. For the given  $n$  events (i.e.  $1, 2 \dots n$ ), the generate sequence interaction elements list based on the  $t$ -combinations set. For each combination, all possible permutations of corresponding events are added into  $L$ . For instance, for SCA ( $N; 3, 4$ ), the all 3-way combinations set is (i.e.  $\{P1, P2, P3\}, \{P1, P2, P4\}, \{P1, P3, P4\}, \{P2, P3, P4\}$ ). Here, the combination  $\{P1, P2, \text{and } P3\}$  has  $3!$  or 6 permutations (such as,  $\{P1, P2, P3\}, \{P1, P3, P2\}, \{P2, P1, P3\}, \{P2, P3, P1\}, \{P3, P1, P2\}, \text{and } \{P3, P2, P1\}$ ). Like this



**Fig. 3** The movement of fishes toward better food place



the permutation of other three combinations produce  $3!$  or 6 permutations in each. Therefore, the total interaction elements are  $3! + 3! + 3! + 3! = 24$ .

For the proposed strategy (shown in Fig. 4), if the total number of generated T-way tuples is known as well as the condition values, then (theoretically) optimal test configuration can be found. The optimum number of test cases in a test suite is found by taking the first test case (pivot). Then a search is performed by jumping on the left and right side of this test case within a range. The optimum number of test cases will always be an integer value.

All of the elements (test case) are checked and according to some conditions, the jump size is decremented or incremented by 1. This algorithm also checks that all the nodes in the T-way tuples are covered or not. If the condition value ( $d$ ) is equal to 0, it indicates that all of the nodes in T-way tuples are not covered. It indicates that the generated test cases are not correct. On the other hand, all of the nodes in T-way tuples are considered covered, when the condition value is greater than zero. It indicates that the generated test cases are correct. The first test case always can cover the maximum number of tuples (as the  $d$  value is highest). The algorithm search on left and right from the initial test case (pivot) decided by a condition. The condition is, if two different test cases can cover the same maximum number of tuples ( $d$ ), the algorithm will take the closest one from the initial test case. The search process is repeated until the maximum number of improvements has been satisfied. Then, the proposed algorithm adds the best test case in the final test suite. The covered interaction elements are also removed from the interaction list. After that, the interaction elements list is checked, once all interaction elements are covered (i.e., the interaction list is empty), the iteration stops. Otherwise, the iteration continued.

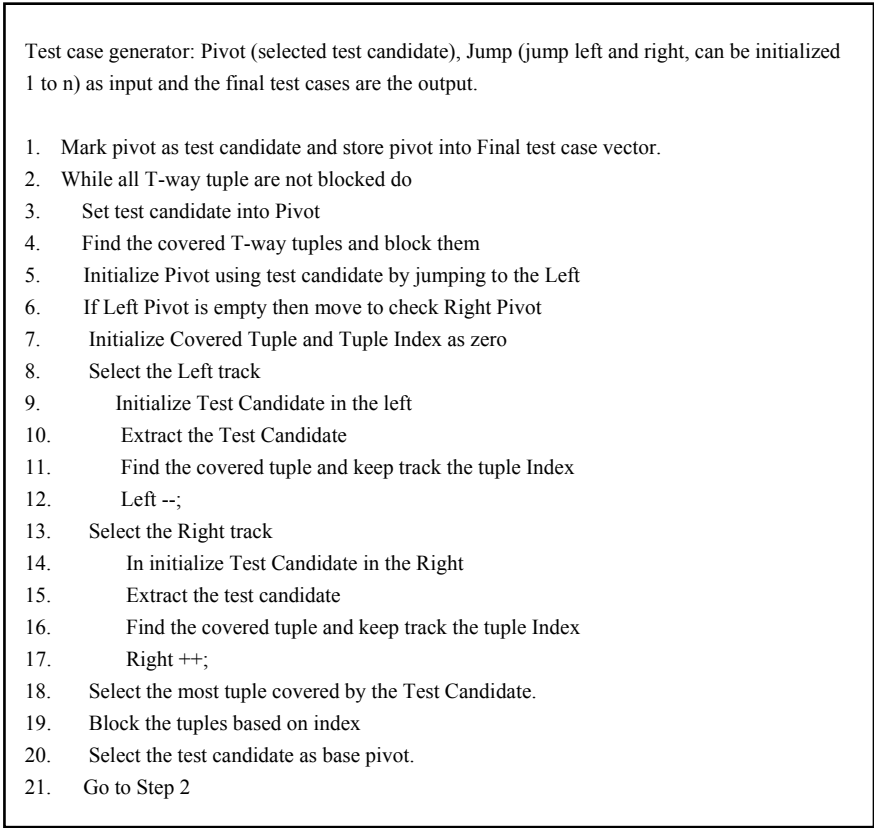


**Fig. 4** Pseudo code for T-way sequence input interaction using fish swarm searching algorithm

### 3 Results and Discussion

In this research, to generate experimental results the Intel (R) Core (TM) i7-3770 CPU@ 3.40 GHz—3.40 GHz, 4 GB of RAM, Windows 10 professional, and 64-bit operating system based platform is used. The c++. Compiler (version 17.12) language is used to implement the algorithm.

Tables 3, 4 and 5 show the generated test case size from the TSFSSA strategy and comparison with existing T-way sequence input test strategies. All experiment results are segregated into three phases.

- Experiment 1 Comparison with existing strategies for SCA (N; t, e); where,  $t = 3$  and  $e$  varied from 4 to 9.
- Experiment 2 Comparison with existing strategies for SCA (N; t, e); where,  $t = 4$  and  $e$  varied from 5 to 9.
- Experiment 3 Comparison with existing strategies for SCA (N; t, e); where,  $t = 5$  and  $t = 6$ , with  $e$  varied from 6 to 8.

**Table 3** Comparison of TSFSSA strategy for sequence input interaction (experiment 1)

Test No.	System config.	BA [4]	K [5]	U [6]	UR [6]	D [6]	DR [6]	ER [7]	TA [8]	ASP [9]	BR [10]	FPA [11]	eFPA [11]	TSFSSA
1	SCA (N; 3, 4)	<b>6<sup>a</sup></b>	<b>6<sup>a</sup></b>	12	12	<b>6<sup>a</sup></b>	8	-	8	-	-	<b>6<sup>a</sup></b>	<b>6<sup>a</sup></b>	<b>6<sup>a</sup></b>
2	SCA (N; 3, 5)	8	8	17	16	8	10	7	8	7	7	7	7	8
3	SCA (N; 3, 6)	9	10	20	18	<b>8</b>	10	<b>8</b>	<b>8</b>	<b>8</b>	<b>8</b>	9	<b>8</b>	10
4	SCA (N; 3, 7)	10	12	23	22	9	12	<b>8</b>	10	<b>8</b>	<b>8</b>	10	10	10
5	SCA (N; 3, 8)	11	12	26	24	10	12	<b>8</b>	10	<b>8</b>	<b>8</b>	11	10	12
6	SCA (N; 3, 9)	13	14	28	26	11	12	<b>9</b>	10	<b>9</b>	<b>9</b>	12	11	12

Noted that

<sup>a</sup>Indicates the optimal number of test cases

**Bold data** indicates the best result among all other strategies, but not the optimal

- Indicates unavailability of the results in the literature for that particular system configuration

**Table 4** Comparison of TSFSSA strategy for sequence input interaction (experiment 2)

Test No.	System config.	BA [4]	K [5]	U [6]	UR [6]	D [6]	DR [6]	FPA [11]	eFPA [11]	TSFSSA
1	SCA (N; <b>4, 5</b> )	28	29	54	54	26	<b>24<sup>a</sup></b>	29	28	<b>24<sup>a</sup></b>
2	SCA (N; <b>4, 6</b> )	36	38	79	78	34	<b>32</b>	36	36	36
3	SCA (N; <b>4, 7</b> )	45	50	98	96	41	<b>40</b>	43	42	41
4	SCA (N; <b>4, 8</b> )	55	56	114	112	47	<b>44</b>	50	48	46
5	SCA (N; <b>4, 9</b> )	62	68	128	126	52	<b>50</b>	57	54	54

Noted that

<sup>a</sup>Indicates the optimal number of test cases

**Bold data** indicates the best result among all other strategies, but not the optimal

– Indicates unavailability of the results in the literature for that particular system configuration

**Table 5** Comparison of TSFSSA strategy for sequence input interaction (experiment 3)

Test No.	System config.	BA [4]	U [6]	UR [6]	D [6]	DR [6]	FPA [11]	eFPA [11]	TSFSSA
1	SCA (N; 5, 6)	159	294	294	149	148	148	152	<b>138</b>
2	SCA (N; 5, 7)	212	437	436	200	198	199	194	<b>191</b>
3	SCA (N; 5, 8)	271	552	550	243	242	247	240	<b>231</b>
4	SCA (N; 5, 9)	329	648	646	284	<b>262</b>	295	283	276
5	SCA (N; 6, 7)	-	-	-	-	-	980	960	<b>851</b>
6	SCA (N; 6, 8)	-	-	-	-	-	1301	1274	<b>1256</b>

Noted that

\* Indicates the optimal number of test cases

**Bold data** indicates the best result among all other strategies, but not the optimal.

- Indicates unavailability of the results in the literature for that particular system configuration

### ***3.1 Comparison Results of TSFSSA Based on Experiment 1***

Table 3 shows the benchmark of TSFSSA strategy with existing strategies for the 3-way test configuration with the number of events 4, 5, 6, 7, 8, and 9. Table 3 shows that, for test configuration 1, TSFSSA able to generate optimal number of test cases compared to U [6], UR [6], DR [6] and TA [8]. For test configuration 2, TSFSSA generates lower number of test cases compared with U [6], UR [6] and DR [6]. Compared with BA [4], K [5], U [6], UR [6], DR [6], and FPA [11] for the test configuration 3, TSFSSA generating lower number of test cases. For the test configuration 4, TSFSSA generates better result than BA [4], K [5], U [6], UR [6], D [6], DR [6], TA [10], FPA [11] and eFPA [11]. For the test configuration 5 TSFSSA generates better result than U [6], UR [6]. For the test configuration 6, TSFSSA generates better result than BA [4], K [5], U [6], and UR [6].

### ***3.2 Comparison Results of TSFSSA Based on Experiment 2***

Table 4, shows comparison of TSFSSA with the existing strategies for the strength 4 and the number of events 5, 6, 7, 8 and 9. For the test configuration 1, TSFSSA generates optimal number of test case. For the test configuration 2, TSFSSA generates better result from K [5], U [6], and UR [6]. For the test configuration 3, TSFSSA generates better result than BA [4], K [5], U [6], UR [6], FPA [11] and eFPA [11]. Besides that, for the test configuration 4, TSFSSA generates better result than BA [4], K [5], U [6], UR [6], D [6], FPA [11] and eFPA [11]. For the test configuration 5, TSFSSA generates better result than BA [4], K [5], U [6], UR [6], and FPA [11].

### ***3.3 Comparison Results of TSFSSA Based on Experiment 3***

Table 5, shows comparison of TSFSSA with the existing strategies for the strength of 5 and 6 events. For the strength 5, three test configurations (for 6, 7, 8 and 9 events) are taken as sample and for the strength 6, two test configurations (for 7, 8 events) are taken as sample. Results show that for the test configurations 1, 2, 3, 5, and 6 TSFSSA generates lowest number of test cases. For the test configuration 4, TSFSSA generates better result from BA [4], U [6], UR [6], D [6], FPA [11] and eFPA [11].

From the above results and discussion, it can be noted that, TSFSSA is compatible to generate feasible number of test cases.

## 4 Conclusion and Future Work

In this research the design and development of a T-way strategy using fish swarm algorithm is successfully completed. The developed strategy is compared with the other renowned strategies for sequence input interaction. It is found that the developed strategy TSFSSA is compatible and efficient (for some test configuration) compare with other strategies. Besides that the results show that the TSFSSA able to produce feasible results. In this research the time to get the output is not taken as a crucial part; however, the lower number of test case is main concern. The higher the number of sequence input interaction, slower the test case generation algorithm because of the adopted searching algorithms. From the literature it is found that the heuristic searches are producing better result than the non-heuristic algorithms. This research can be extended for sequence less input interaction. Besides that different types of searching algorithms can be adopted to check the efficiency on the test case generation.

**Acknowledgements** This research work is supported by research grant RDU1703149 and RDU1703125 funded by Universiti Malaysia Pahang, <http://www.ump.edu.my/>. The authors would also like to thank the Faculty of Electrical and Electronics Engineering, Universiti Malaysia Pahang for financial support.

## References

1. Xiong J (2011) New software engineering paradigm based on complexity. Springer, New York
2. Rahman M (2017) Design of a new T-way strategy for test case generation supporting sequence-less and sequence input interaction. Ph.D. thesis, Universiti Malaysia Perlis (UNIMAP)
3. Testech, "RTKernel", retrieve on 25th April, 2019 from <http://www.testech-elect.com/ontime/rtk45.htm>
4. Zabil MHM, Zamli KZ, Othman RR (2012) Sequence-based interaction testing implementation using Bees algorithm. In: Proceedings of the IEEE symposium on computers and informatics (ISCI), pp 81–85. <https://doi.org/10.1109/isci.2012.6222671>
5. Kuhn DR, Higdon JM, Lawrence JF, Kacker RN, Lei Y (2012) Combinatorial methods for event sequence testing. In: Proceedings of the IEEE 5th international conference on software testing, verification and validation, pp 601–609. <https://doi.org/10.1109/icst.2012.147>
6. Banbara M, Tamura N, Inoue K (2012) Generating event-sequence test cases by answer set programming with the incidence matrix. In: Proceedings of the 28th international conference on logic programming (ICLP'12), pp 86–97. <https://doi.org/10.4230/lipics.iclp.2012.86>
7. Erdem E, Inoue K, Oetsch J, Puhner J, Tompits H, Yilmaz C (2011) Answer set programming as a new approach to event-sequence testing. In: Proceedings of the 2nd international conference on advances in system testing and validation lifecycle, pp 25–34
8. Tarui J (2008) On the minimum number of completely 3-scrambling permutations. *Discret Math* 308(8):1350–1354
9. Chee YM, Colbourn CJ, Horsley D, Zhou J (2013) Sequence covering arrays. *J Discret Math* 27(4):1844–1861
10. Brain M, Erdem E, Inoue K, Oetsch J, Puhner J, Tompits H, Yilmaz C (2012) Event sequence testing using answer-set programming. *Int J Adv Softw* 5:237–251

11. Nasser A, Zamli K, Rahman A, Ahmed B (2018) An elitist-flower pollination based strategy for constructing sequence and sequence-less T-way test suite. *Int J Bio-Inspired Comput* 12(2):115–127
12. Shiba T, Tsuchiya T, Kikuno T (2004) Using artificial life techniques to generate test cases for combinatorial testing. In: *Proceedings of the 28th annual international computer software and applications conference*, pp 72–77
13. Younis MI, Zamli KZ (2009) Assessing combinatorial interaction strategy for reverse engineering of combinatorial circuits. In: *Proceedings of the IEEE symposium on industrial electronics and applications*, pp 473–478. <https://doi.org/10.1109/isiea.2009.5356419>
14. Othman RR, Zamli KZ (2011) T-way strategies and its applications for combinatorial testing. *Int J New Comput Arch Their Appl (IJNCAA)* 1(2):459–473
15. Nie C, Xu B, Shi L, Dong G (2005) Automatic test generation for N-way combinatorial testing. In: *Lecture notes in computer science quality of software architectures and software quality*, pp 203–211. <https://doi.org/10.1007/11558569>
16. Yazdani D, Sadeghi-Ivrih S, Yazdani D, Sepas-Moghaddam A, Meybodi MR (2015) Fish Swarm Search Algorithm: A New Algorithm for Global Optimization. *Int J Artif Intell* 13(2):17–45
17. Rahman M, Othman RR, Ahmad RB, Rahman MM (2014) Event driven input sequence T-way test strategy using simulated annealing. In: *Fifth international conference on intelligent systems, modelling and simulation (ISMS' 14)*, pp 663–667
18. Rahman M, Othman RR, Ahmad RB, Rahman MM (2014) A meta heuristic search based t-way event driven input sequence test case generator. *Int J Simul Syst, Sci Technol (IJSSST)* 15(3):65–71



# Development of AC and DC Drive Coils for a Small Volume Magnetic Particle Imaging System



Mohd Mawardi Saari, Ahmad Zahir Irsyad Razak,  
Mohd Aufa Hadi Putera Zain, Nurul A'in Nadzri, Mohd Razali Daud  
and Hamzah Ahmad

**Abstract** Recent development in a new imaging modality called Magnetic Particle Imaging (MPI) technique has attracted much interests from researchers where it is expected to provide a higher spatial and temporal resolutions of images. The MPI technique works by utilizing an AC field to modulate the magnetic response from magnetic nanoparticles and a gradient DC field to localize the magnetic nanoparticles, where the characteristics of AC and DC fields affect the performance of MPI technique. The purpose of this study is to develop compact DC and AC drive coils as a preliminary step towards implementation in a small volume MPI system. The AC drive coil is designed based on a Helmholtz-coil configuration and resonated at a frequency to lower its circuit impedance. The gradient DC field is realized by combination of permanent magnets and a DC coil to shift a Flux Free Line (FFL) vertically. A 3rd-order Butterworth low-pass filter is implemented in the DC drive coil circuit to protect its DC current source from high-frequency field induction. The AC drive coil is able to be resonated at the designed frequency of 8 kHz and fairly good horizontal and vertical gradient DC fields are obtained. The DC drive coil is able to shift the FFL vertically at 0.33 mm/A and further improvement can be expected in the coil design for future implementation in the small volume MPI system.

**Keywords** Coil · Resonance · Low pass filter · Magnetic particle imaging

## 1 Introduction

*In vivo* imaging system is an important tool in the medical field because it assists in providing accurate diagnosis and treatment process of diseases. It works as a tool to reveal the internal structure of a body by creating visual representation so that abnormalities occurred in the body tissues can be identified. There are several imaging methods used in the medical field such as X-ray radiography, MRI (Magnetic

---

M. M. Saari (✉) · A. Z. I. Razak · M. A. H. P. Zain · N. A. Nadzri · M. R. Daud · H. Ahmad  
Faculty of Electrical and Electronics Engineering Technology, Universiti Malaysia Pahang, Pekan  
Campus, 26600 Pekan, Pahang, Malaysia  
e-mail: [mmawardi@ump.edu.my](mailto:mmawardi@ump.edu.my)

© Springer Nature Singapore Pte Ltd. 2020  
A. N. Kasruddin Nasir et al. (eds.), *InECCE2019*, Lecture Notes in Electrical  
Engineering 632, [https://doi.org/10.1007/978-981-15-2317-5\\_10](https://doi.org/10.1007/978-981-15-2317-5_10)

Resonance Imaging), PET and CT scan systems. Magnetic particle imaging (MPI) is a newly developed *in vivo* tomographic imaging modality that can provide a high sensitivity of spatial and temporal resolutions of imaging. It was first proposed by Gleich and Weizenecker in 2005 [1] and since then, development of MPI systems has shown a rapid progress through various theoretical studies, experiments and hardware implementations [2–13]. MPI technique takes advantage of the non-linear magnetization behaviour of superparamagnetic iron oxide (SPIO) nanoparticles used as tracer to detect the spatial and temporal distribution within a biological body. SPIO nanoparticle has been used as a contrast agent in magnetic resonance imaging (MRI) technique and is proven as the best tracer material for imaging purposes since they are non-toxic material and have a relatively high saturation magnetization in which can improve the signal-to-noise ratio of an image [14].

In brief, MPI technique works by applying gradient DC and AC magnetic fields to SPIO nanoparticle which is located inside a body [1, 4, 5, 11, 15–22]. The magnetization of the SPIO nanoparticle due to the applied magnetic fields will produce a secondary magnetic field consists of harmonics which will be detected by detection coils or sensors. At the location where the gradient DC magnetic field becomes zero, i.e., location of Field Free Point (FFP) or Field Free Line (FFL), the amplitude of the harmonics in the oscillating secondary magnetic field will become maximum. When the gradient magnetic field is non-zero, this will saturate the magnetization of SPIO nanoparticle, hence, suppressing the generated harmonics. By moving the FFL or FFP through the volume of the body, spatial distribution of SPIO nanoparticles can be mapped and localized. The surface of SPIO nanoparticle can be functionalized so that it can bind to detect biological entities such as cancerous tissues, antigens etc. [23] The accumulation of SPIO nanoparticle such as around cancerous tissues can be mapped by an MPI scanner.

This study focuses on developing gradient DC and AC drive coils based on the MPI concept where the AC field is used to modulate the magnetic responses of SPIO nanoparticles at harmonic frequencies, and the gradient DC field is applied to localize the SPIO nanoparticles at FFP or FFL. In order to achieve a high sensitivity MPI scanner using inductive coils, a high intensity of AC magnetic field should be applied at high frequency. The use of a high intensity of AC magnetic field will improve the harmonics generation owing to the nonlinear magnetization response of SPIO nanoparticle. Furthermore, a high homogeneity of the AC magnetic field is also required in order to avoid fading effect in the spatial resolution and. Besides that, a high gradient DC selection field is also needed to saturate the magnetic particle and suppress the generation of harmonics in order to generate Field Free Line (FFL). For these purposes, compact DC and AC drive coils are developed and placed to apply excitation fields to a volume of  $3 \times 3 \times 3$  cm. The AC drive coil is developed based a Helmholtz coil con to achieve a high homogeneity of 3-mT magnetic field. A resonant circuit is implemented in the design of the AC drive coil to reduce its impedance at a high excitation frequency. A 100-Watt audio amplifier is used as an AC current supply for the AC drive coil. For the gradient DC field, a DC drive coil is fabricated around three 100-mT magnets. The polarity of the magnets is arranged so that they can produce a high gradient DC selection field around 3 T/m. The DC

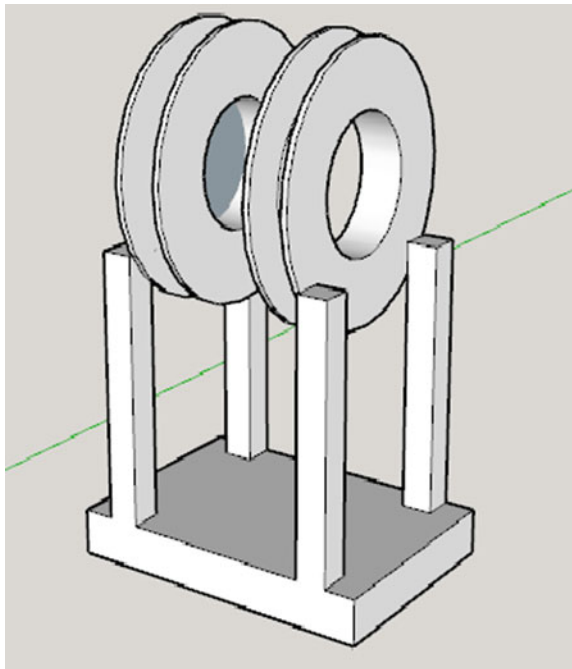
drive coil is powered by a bi-polar DC current supply from  $-6$  to  $6$  A. It should be noted that the induction effect of high frequency AC magnetic field will develop AC voltage at DC coil and may damage DC current supply. To provide a protection for the DC current supply, a passive 3rd-order Butterworth filter is designed to shunt the AC voltage induction at the DC coil.

## 2 Methodology

### 2.1 Development of AC Drive Coil

The AC drive coil is configured to be a Helmholtz coil where it consists of two identical circular coils that are aligned symmetrically on a same axis. The AC drive coil is modelled using a 3-D software and is shown in Fig. (1). In order to achieve a sufficiently high magnetic field strength, the radius of those two circular coils is set to be  $30$  mm. The homogeneity of the magnetic field around the center region of the Helmholtz coil can be maintained at a high value more than  $90\%$  by separating those two coils by distance of  $30$  mm which is same as their radius [24]. The two circular coils are connected in series which means each coil carries an equal electric current with the same direction. The coils are fabricated from a Litz wire with  $60$  strands

**Fig. 1** AC drive coil based on the Helmholtz coil configuration. The radius and spacing between the two identical coils are set to be  $30$  mm



of 0.1 mm copper wires. The resistance and inductance value for the fabricated AC drive coil are measured to be 1.14  $\Omega$  and 0.5176 mH, respectively, using an LCR meter (GW INSTRON LCR-816) at 1 V and 1 kHz. The number of turns  $n$  that is required to produce 3-mT AC excitation field  $\mathbf{B}$  at a distance of  $h$  from the coil is estimated as follows:

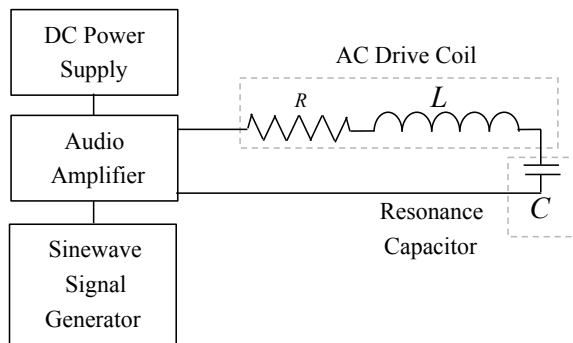
$$\mathbf{B} = \frac{n\mu_0 I \rho^2 \mathbf{a}_n}{2(\rho^2 + h^2)^{3/2}}, \quad (1)$$

where  $\mu_0$ ,  $I$ ,  $\rho$ ,  $h$  and  $\mathbf{a}_n$  are vacuum magnetic permeability, current, radius of the coil, distance from the center of the coil to the measuring point, and the unit vector of the coil axis. From the Eq. (1), the required number of turns for each coil can be calculated to be 60 turns to produce a magnetic flux density of 3 mT at the center of the Helmholtz coil, i.e.,  $h = 1.5$  cm.

## 2.2 Resonant Circuit for AC Drive Coil

The narrowband resonance technique based on series LC circuit is implemented in the AC drive coil circuitry as shown in Fig. (2). The resonant circuit works by lowering the impedance of the AC drive coil circuit by cancelling the reactance of the circuit using a series-connected capacitor at a specific frequency. At the resonance frequency, the inductive reactance and capacitive reactance are equal in magnitude but opposite in direction, causing electrical energy to oscillate between the magnetic field of the inductor and the electrical field of the capacitor. By minimizing the impedance at the resonance frequency, a higher amount of electrical current can be driven through the AC drive coil to produce a higher magnetic field intensity. The impedance characteristic will act like a narrowband filter of the AC drive coil, in which a ‘pure’ single frequency excitation can be produced [24–26]. This will benefit the MPI scanner where the detected harmonics will less be interfered by the excitation field. The ac drive coil is designed to resonate at  $f_r = 8$  kHz where the

**Fig. 2** AC drive coil circuit using resonance technique



required capacitance value  $C$  can be determined using Eq. (2),

$$f_r = \frac{1}{2\pi\sqrt{LC}}, \quad (2)$$

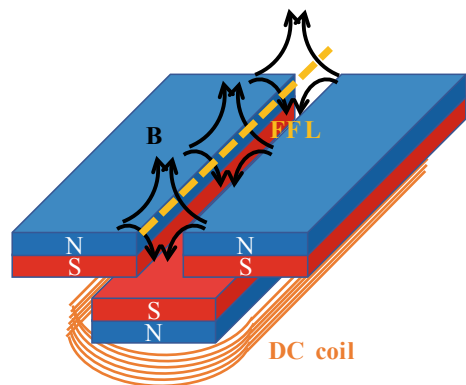
where  $L$  is the inductance of the AC drive coil. The required capacitance value is determined to be  $0.7647 \mu\text{F}$ .

### 2.3 DC Excitation Unit and Passive Butterworth Filter

The gradient DC field with an FFL is formed by using a polarity combination of three 100-mT Neodymium magnets. The magnets are arranged in 2 layers where the FFL is generated along at the gap of the surface magnets. This can be shown in Fig. (3) where the polarity of the magnets is arranged to be same at the interlayer of the magnets. To shift the FFL vertically, the DC drive coil is wound around the lower layer magnet. By manipulating the intensity and direction of the current supplied to the DC drive coil, the FFL can be shifted vertically. However, compared to the AC drive coil, the number of turns for the designed DC coil should be higher to achieve high gradient DC selection field. Due to the constraint of space, the DC drive coil is set to be 50 turns and the DC current is increased in order to achieve a higher DC field.

Passive Butterworth low pass filter is a type of low-pass filter designed to have a frequency response as flat as possible in the passband. In this study, the filter is designed to protect the DC current supply from being damaged by the AC induction of the high frequency AC magnetic field. The Butterworth filter is connected in series between the DC current supply and the DC drive coil. The cut-off frequency of the designed filter should be as low as possible in order to shunt the AC induction. The designing process of the filter is simulated based on 3rd-order Butterworth filter using LC circuit shown in Fig. (4).

**Fig. 3** Arrangement of magnets and DC drive coil



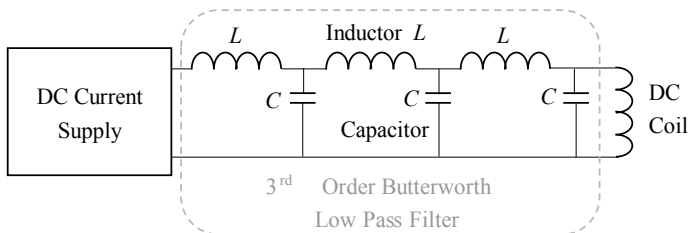


Fig. 4 3rd-order Butterworth low pass filter and DC drive coil

Since the purpose of the filter is to shunt the AC induction of the high frequency AC magnetic field, a pure DC filter is required. The cut-off frequency for the filter is designed to be 1 Hz. Since the cut-off frequency is low, a larger value of capacitors and inductors is needed. For this purpose, three 20  $\mu\text{F}$  capacitors are connected in parallel. From that, the value of inductor is simulated to get the desired cut-off frequency and its frequency response. From the simulated result, the inductance value for each of the inductor is set to be 500 mH.

### 2.4 Experimental Setup

Figure (5) shows the circuit connection to determine the actual resonant frequency of the AC drive coil. A lock-in amplifier used to measure the intensity and phase of the voltage and current flowing through the AC drive coil. The current amplifier is used for generating current from the signal from a function generator. In order to measure the current flowing through the AC drive coil, a 1-k $\Omega$  resistor is connected in series and the voltage across it is measured. The voltage across the AC drive coil and

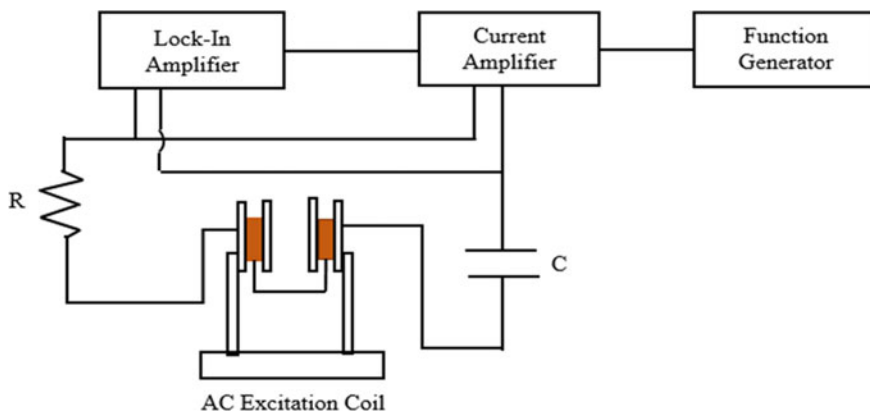
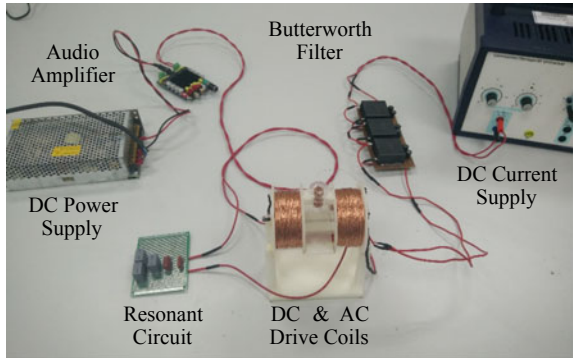


Fig. 5 Diagram of the AC drive coil to determine resonant frequency

**Fig. 6** Image of the connection of AC and DC drive coils



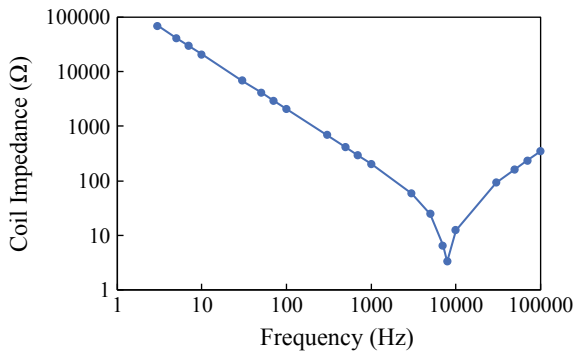
1-k $\Omega$  resistor is measured from 3 to 100 kHz. From Ohm's law, the current flowing through the AC drive coil can be calculated from the measured voltage across the 1-k $\Omega$  resistor. Consequently, the value of the impedance for the AC drive coil can be calculated from the current and the voltage across it. The image of the experimental setup can be shown in Fig. (6).

### 3 Result and Discussions

#### 3.1 Resonance Frequency of AC Excitation Coil

Figure (7) shows the impedance characteristic of the AC drive coil circuit. The coil impedance decreased as the frequency was continuously increased from 3 Hz and after 8 kHz, the impedance started to increase. The resonance frequency could be determined when the impedance reached a minimum point. During this resonant frequency, the flowing current through the AC coil would be maximum, hence reflecting the minimum impedance value of the circuit [24, 25]. The resonance frequency was

**Fig. 7** Impedance of the AC drive coil from 3 to 100 kHz



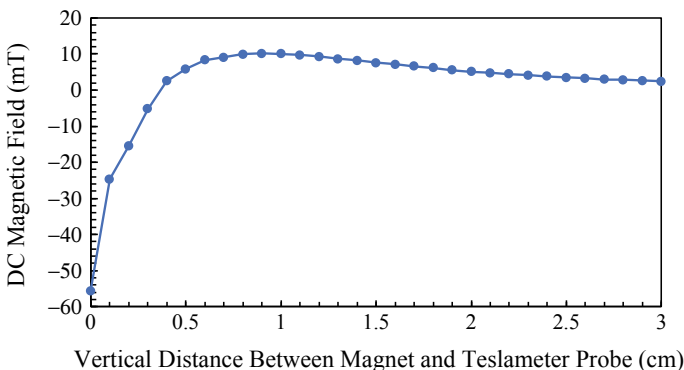
found to be 7.9 kHz which was close to the designed value of 8 kHz. At this resonant frequency, the impedance of the AC drive coil circuit was calculated to be  $3.3328 \Omega$ , which was 2 times bigger compared to the value measured at 1 kHz. This was thought due to the increase of AC resistance of the Litz wire [25].

### 3.2 Field Free Line and DC Excitation Field

Figure (8) shows the DC magnetic field measured using a Teslameter probe when the vertical distance from the surface layer of magnets to the Teslameter probe was varied. From the vertical gradient characteristic, the FFL where the gradient became zero can be estimated around the distance of 0.3 cm. At 0 mm, the measured magnetic field was  $-57$  mT while at 30 mm the magnetic field was 2.4 mT. The polarity change showed the gradient DC characteristic illustrated in Fig. (3). The obtained vertical distance of FFL was within the designed range, which is from 3 to 4 mm from the surface layer of magnets.

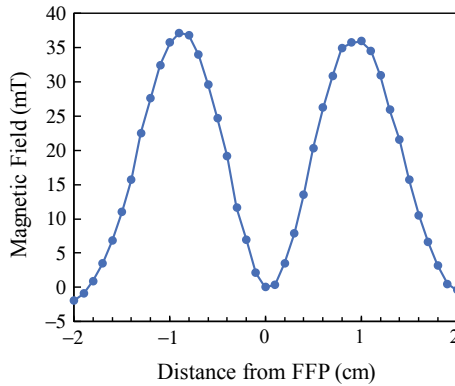
Figure (9) shows the distribution of DC magnetic field with respect to horizontal distance from the FFL measured using the Teslameter probe. As the horizontal distance from the gap of the magnets was increased, the DC magnetic field increased and forming peaks. After peaking of the DC magnetic field, the DC magnetic field started to decrease as the probe was moved further away from the region that contained magnets. This proved that the generated FFL existed only at the gap of the surface layer of the magnets. The obtained gradient magnetic field produced by the magnets between  $-1$  and  $0$  cm was calculated to be  $4$  T/m.

Figure (10) shows the DC magnetic field generated by the DC drive coil when it was supplied by different intensity of DC current. The generated DC field increased linearly when the intensity of the DC current was increased. By inducing the DC current from  $-6$  to  $6$  A to the DC drive coil, the FFL could be shifted within a



**Fig. 8** Gradient DC field at the gap of the magnets with respect to its vertical distance





**Fig. 9** Gradient DC field across the surface layer of the magnets with respect to its horizontal distance from the gap

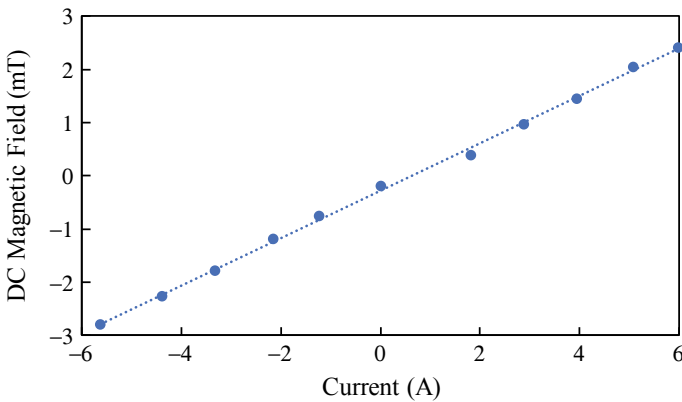
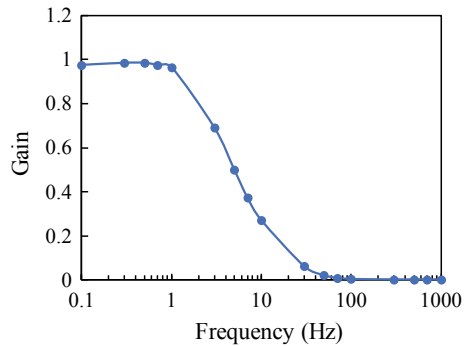


**Fig. 10** DC field produced by the DC drive coil with respect to DC current

range from  $-2$  to  $2$  mm. This proved that the FFL can be shifted vertically without utilizing mechanical movement. Although the shift range was small due to the small number of turns, the magnitude of shifting range was possible to be improved by using a superior design of the DC coil with a higher number of turns and DC current intensity.

Figure (11) shows the gain characteristic of the fabricated Butterworth low pass filter with respect to frequency. The cut-off frequency could be estimated to be around  $2$  Hz, which was close to the designed value of  $1$  Hz. The AC induction of high frequency AC magnetic field could be shunted since the frequency of the AC magnetic field was  $7.9$  kHz. The gain of the produced filter was able to be maintained at close value of  $1$  within the pass band region.

**Fig. 11** Gain characteristic of the Butterworth low pass filter



## 4 Conclusion

DC and AC drive coils were developed for a small volume MPI application purpose. The resonant technique was implemented in order to achieve a high excitation of AC field using the Helmholtz coil configuration. The AC drive coil with its resonance circuit was able to resonate at 7.9 kHz. The FFL was configured by using a combinations of magnet layers and DC drive coil. By using the DC coil with the present of magnets, a high gradient DC field could be achieved. The Butterworth low pass filter with a cut-off frequency of 2 Hz was designed and implemented in the DC drive coil circuit. From the experimental results, the FFL could be shifted vertically using the DC drive coil with using any mechanical movement. The preliminary work of designing drive coils in this study could be expected to provide a basis for the development of compact MPI scanner and there are rooms for further improvements.

**Acknowledgements** This work was supported by Research Management Center of Universiti Malaysia Pahang under grant number of RDU170377.

## References

1. Gleich B, Weizenecker J (2005) Tomographic imaging using the nonlinear response of magnetic particles. *Nature* 435:1214–1217. <https://doi.org/10.1038/nature03808>
2. Graeser M, Knopp T, Szwargulski P et al (2017) Towards picogram detection of superparamagnetic iron-oxide particles using a gradiometric receive coil. *Sci Rep* 7:6872. <https://doi.org/10.1038/s41598-017-06992-5>
3. Bakenecker AC, Ahlborg M, Debbeler C et al (2018) Magnetic particle imaging in vascular medicine. *Innov Surg Sci* 3:179–192
4. Yu EY, Bishop M, Zheng B et al (2017) Magnetic particle imaging: a novel in vivo imaging platform for cancer detection. *Nano Lett* 17. <https://doi.org/10.1021/acs.nanolett.6b04865>
5. Konkle JJ, Goodwill PW, Carrasco-Zevallos OM, Conolly SM (2013) Projection reconstruction magnetic particle imaging. *IEEE Trans Med Imaging* 32:338–347. <https://doi.org/10.1109/TMI.2012.2227121>

6. Sasayama T, Tsujita Y, Morishita M et al (2016) Three-dimensional magnetic nanoparticle imaging using small field gradient and multiple pickup coils. *J Magn Magn Mater* 427:144–150. <https://doi.org/10.1016/j.jmmm.2016.10.107>
7. Weizenecker J, Gleich B, Rahmer J et al (2009) Three-dimensional real-time in vivo magnetic particle imaging. *Phys Med Biol* 54:L1–L10. <https://doi.org/10.1088/0031-9155/54/5/L01>
8. Vogel P, Ruckert M, Klauer P et al (2013) Traveling wave magnetic particle imaging. *IEEE Trans Med Imaging* 33:400–407. <https://doi.org/10.1109/TMI.2013.2285472>
9. Croft LR, Goodwill PW, Konkle JJ et al (2016) Low drive field amplitude for improved image resolution in magnetic particle imaging. *Med Phys* 43. <https://doi.org/10.1118/1.4938097>
10. Lu K, Goodwill PW, Saritas EU et al (2013) Linearity and shift invariance for quantitative magnetic particle imaging. *IEEE Trans Med Imaging* 32:1565–1575. <https://doi.org/10.1109/TMI.2013.2257177>
11. Konkle JJ, Goodwill PW, Hensley DW, et al (2015) A convex formulation for magnetic particle imaging X-space reconstruction. *PLoS One* 10. <https://doi.org/10.1371/journal.pone.0140137>
12. Shah SA, Ferguson RM, Krishnan KM (2014) Slew-rate dependence of tracer magnetization response in magnetic particle imaging. *J Appl Phys* 116. <https://doi.org/10.1063/1.4900605>
13. Bauer LM, Situ SF, Griswold MA, Samia ACS (2015) Magnetic particle imaging tracers: state-of-the-art and future directions. *J Phys Chem Lett* 6
14. Saari MM, Suhaimi NS, Sulaiman MH et al (2019) Influence of viscosity on dynamic magnetization of thermally blocked iron oxide nanoparticles characterized by a sensitive AC magnetometer. *J Supercond Nov Magn*. <https://doi.org/10.1007/s10948-019-5031-6>
15. Buzug TM, Bringout G, Erbe M et al (2012) Magnetic particle imaging: introduction to imaging and hardware realization. *Z Med Phys* 22:323–334. <https://doi.org/10.1016/j.zemedi.2012.07.004>
16. Goodwill PW, Conolly SM (2010) The x-space formulation of the magnetic particle imaging process: 1-D signal, resolution, bandwidth, SNR, SAR, and magnetostimulation. *IEEE Trans Med Imaging* 29:1851–1859. <https://doi.org/10.1109/TMI.2010.2052284>
17. Weizenecker J, Gleich B, Borgert J (2008) Magnetic particle imaging using a field free line. *J Phys D Appl Phys* 41:105009. <https://doi.org/10.1088/0022-3727/41/10/105009>
18. Colombo S, Lebedev V, Tonyushkin A et al (2016) Towards a mechanical MPI scanner based on atomic magnetometry. 1–6
19. Weber A, Werner F, Weizenecker J et al (2016) Artifact free reconstruction with the system matrix approach by overscanning the field-free-point trajectory in magnetic particle imaging. *Phys Med Biol* 61:475–487. <https://doi.org/10.1088/0031-9155/61/2/475>
20. Tay ZW, Goodwill PW, Hensley DW et al (2016) A high-throughput, arbitrary-waveform, MPI spectrometer and relaxometer for comprehensive magnetic particle optimization and characterization. *Sci Rep* 6:34180. <https://doi.org/10.1038/srep34180>
21. Zheng B, Goodwill PW, Dixit N et al (2017) Optimal broadband noise matching to inductive sensors: application to magnetic particle imaging. *IEEE Trans Biomed Circuits Syst* 11:1041–1052. <https://doi.org/10.1109/TBCAS.2017.2712566>
22. Bauer LM, Hensley DW, Zheng B et al (2016) Eddy current-shielded x-space relaxometer for sensitive magnetic nanoparticle characterization. *Rev Sci Instrum* 87. <https://doi.org/10.1063/1.4950779>
23. Tsukada K, Tsunashima K, Jinno K et al (2019) Using magnetic field gradients to shorten the antigen-antibody reaction time for a magnetic immunoassay. *IEEE Trans Magn* 1–5. <https://doi.org/10.1109/tmag.2019.2894904>
24. Saari MM, Suhaimi NS, Razali S et al (2018) Development of a resonant excitation coil of AC magnetometer for evaluation of magnetic fluid. *J Telecommun Electron Comput Eng* 10
25. Saari MM, Suhaimi NS, Lah NAC et al (2018) A sensitive AC magnetometer using a resonant excitation coil for magnetic fluid characterization in nonlinear magnetization region. In: 2018 IEEE international magnetics conference (INTERMAG). IEEE, pp 1–4
26. Saari MM, Che Lah NA, Sakai K et al (2018) Harmonics distribution of iron oxide nanoparticles solutions under diamagnetic background. *J Magn Magn Mater* 452:145–152. <https://doi.org/10.1016/j.jmmm.2017.12.054>

# A Diversity-Based Adaptive Synchronous-Asynchronous Switching Simulated Kalman Filter Optimizer



Nor Azlina Ab. Aziz, Nor Hidayati Abdul Aziz, Badaruddin Muhammad, Zuwairie Ibrahim, Marizan Mubin, Norrima Mokhtar and Mohd Saberi Mohamad

**Abstract** The original Simulated Kalman Filter (SKF) is an optimizer that employs synchronous update mechanism. The agents in SKF update their solutions after all fitness calculations, prediction process, and measurement process are completed. An alternative to synchronous update is asynchronous update. In asynchronous update, only one agent does fitness calculation, prediction, measurement, and estimation processes at one time. Recent study found that the original SKF is subjected to premature convergence. Thus, synchronous and asynchronous mechanisms are combined in SKF to address the premature convergence problem in SKF. At first, the SKF starts with synchronous update. If no improved solution is found, the SKF changes its update mechanism. The decision to switch from synchronous to asynchronous or vice versa is made based on the information of the population. In this paper, population's diversity is used as switching indicator. Using the CEC2014 benchmark test suite, experimental results indicate that the proposed diversity-based adaptive switching synchronous-asynchronous SKF outperforms the original SKF significantly.

**Keywords** Simulated kalman filter · Synchronous · Asynchronous

## 1 Introduction

Kalman filtering has been used as a population-based optimizer [1]. In 2015, another metaheuristic algorithm called simulated Kalman filter (SKF) has been proposed for numerical optimization problems [2–5]. It was introduced as population-based

---

N. A. Ab. Aziz · N. H. A. Aziz  
Multimedia University, Melaka, Malaysia

B. Muhammad (✉) · Z. Ibrahim  
Universiti Malaysia Pahang, Pahang, Malaysia  
e-mail: [badaruddin@ump.edu.my](mailto:badaruddin@ump.edu.my)

M. Mubin · N. Mokhtar  
University of Malaya, Kuala Lumpur, Malaysia

M. S. Mohamad  
Universiti Malaysia Kelantan, Kelantan, Malaysia

metaheuristics, where the search for optimal solution is conducted by a group of agents. The agents of SKF work like Kalman filters, where they go through prediction, measurement, and estimation process in every iteration. The measurement in SKF is a simulated measurement which is obtained using mathematical equation.

Many studies on SKF can be found in literature. For example, the SKF has been studied fundamentally [6, 7]. The SKF also has been extended for binary optimization problems [8] and combinatorial optimization problems [9–11]. Hybridization of SKF with particle swarm optimization (PSO), gravitational search algorithm (GSA), and opposition-based learning [12–17] have also been proposed for better performance. Other variants called parameter-less SKF and randomized SKF algorithms were proposed in [18, 19]. The SKF has also been applied for real world problems like the adaptive beamforming in wireless cellular communication [20–23], airport gate allocation problem [24, 25], feature selection of EEG signal [26, 27], system identification [28, 29], image processing [30, 31], assembly sequence planning [32], controller tuning [33], and PCB drill path optimization [34, 35].

In optimization, adaptive optimization algorithms change their optimization mechanism [36] or parameters [37] or both the parameters and the search mechanism [38] according to the condition of the search. Parameter setting greatly affects the performance of an optimizer and this setting can change with time. The usage of adaptive parameters ensures the best parameter setting is used in each situation. The adaptive mechanism on the other hand allows the agents' search behavior to change according to their current state, for example from exploration to exploitation. These metrics could be used in adaptive works: fitness of the search agents, the agent's distribution or diversity, and the period of the search.

As a population-based metaheuristic algorithm, the SKF's agents conduct the search for optimal solution through information sharing. The evaluation of the candidate solutions found by SKF agents and the Kalman filter's procedure of predict, measure and estimate are done iteratively. How the agents move from evaluation to the Kalman procedure, either as a group or individually is determined by the iteration strategy. The group-oriented iteration strategy is known as synchronous update while the individual-oriented iteration strategy is known as asynchronous update. However, a recent study found that the original SKF suffers from premature convergence and the performance of the SKF could be improved if the premature convergence problem in SKF is properly addressed [39]. Hence, a switching between synchronous and asynchronous updates is introduced in SKF. Diversity is used as the switching indicator. Thus, the switching can be done adaptively. The performance of diversity-based adaptive switching synchronous-asynchronous SKF (DASSA-SKF) is compared with the original SKF using CEC2014 benchmark function, where it is found that statistically DASSA-SKF is better than the original SKF.

## 2 The Simulated Kalman Filter

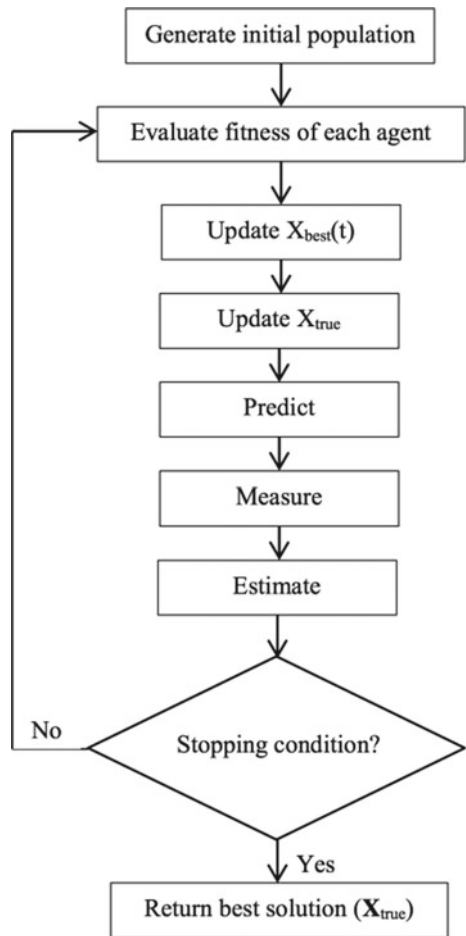
The SKF algorithm follows the algorithm shown in Fig. 1. One iteration consists of fitness evaluation, *update* the best solution, *predict*, *measure*, and *estimate*.

Using  $n$  agents, a set of solution can be denoted as  $\mathbf{X}(t) = \{\mathbf{X}_1(t), \mathbf{X}_2(t), \dots, \mathbf{X}_n(t)\}$ , where  $t$  is the iteration number. The SKF starts with random initialization of solutions. In each iteration, the fitness of the agents' are evaluated. Then, the agent with the best fitness value is identified as the best solution of the current population,  $\mathbf{X}_{best}(t)$ . Next, the best  $\mathbf{X}_{best}(t)$  from the first iteration is selected as  $\mathbf{X}_{true}$ .

During the prediction phase, the current predicted state,  $\mathbf{X}_i(t|t + 1)$ , is assumed to be the estimated value;

$$\mathbf{X}_i(t|t + 1) = \mathbf{X}_i(t) \tag{1}$$

**Fig. 1** The flowchart of the simulated Kalman filter optimizer



The error covariant is also updated as follows;

$$\mathbf{P}(t|t+1) = \mathbf{P}(t) + \mathbf{Q} \quad (2)$$

where  $\mathbf{P}(t)$  and  $\mathbf{P}(t|t+1)$  denote the current error covariant estimate and current transition error covariant estimate, respectively. Note that the error covariant estimate is influenced by the process noise,  $\mathbf{Q}$ .

In SKF, measurements are simulated using an agent's prediction and  $\mathbf{X}_{true}$ . The dimensional wise calculation of measured value for each dimension of agent  $i$ th is calculated as follows;

$$\mathbf{Z}_i(t) = \mathbf{X}_i(t|t+1) + \sin(2\pi r_i(t) \times \delta_1) \quad (3)$$

$$\delta_1 = |\mathbf{X}_i(t|t+1) - \mathbf{X}_{true}| \quad (4)$$

where  $r_i(t)$  is a random value within the range of [0,1]. The estimation phase follows the measurement phase and the estimated next value is updated using (5);

$$\mathbf{X}_i(t+1) = \mathbf{X}_i(t|t+1) + K(t) \times \delta_2 \quad (5)$$

$$\delta_2 = (\mathbf{Z}_i(t) - \mathbf{X}_i(t|t+1)) \quad (6)$$

where  $K(t)$  is the Kalman gain, which is calculated as follows;

$$K(t) = \mathbf{P}(t|t+1) / (\mathbf{P}(t|t+1) + \mathbf{R}) \quad (7)$$

where  $\mathbf{R}$  is the measurement noise. Then, the current error covariant estimate is updated in estimation phase using (8);

$$\mathbf{P}(t+1) = (1 - K(t)) \times \mathbf{P}(t|t+1) \quad (8)$$

These steps continue until at the end of the number of fitness evaluation.

### 3 The Proposed Diversity-Based Adaptive Synchronous-Asynchronous Switching SKF (DASAS-SKF)

The flowchart of the DASAS-SKF is shown in Fig. 2. The synchronous and asynchronous SKF are indicated at the left and right sides, respectively. A switching strategy is proposed in this paper that alternates between the synchronous update and asynchronous update. The decision to switch is made adaptively based on the

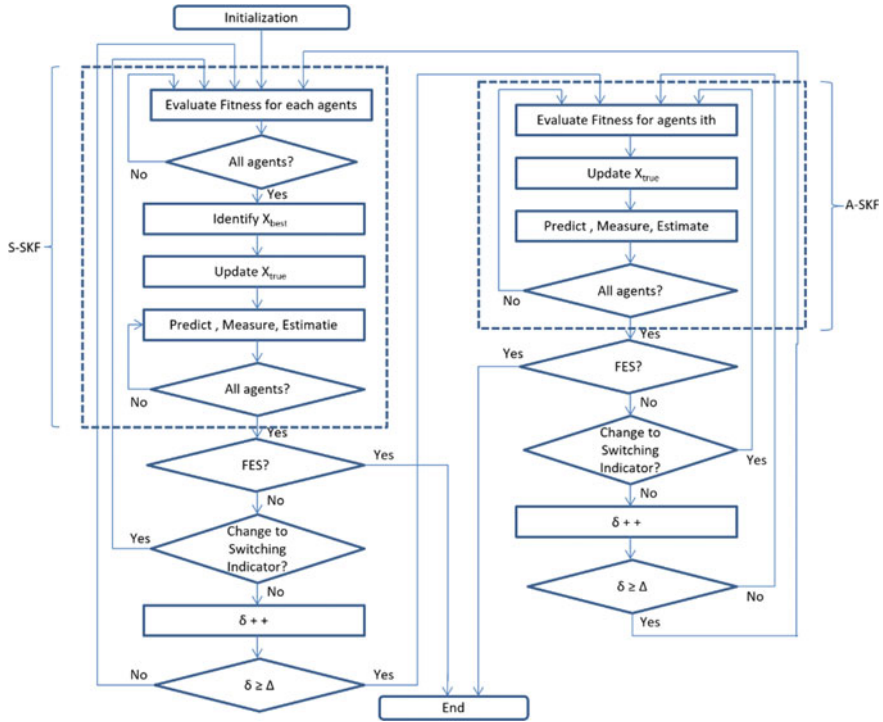


Fig. 2 The flowchart of the DASAS-SKF

population’s diversity. The calculation of diversity starts with the computation of the mean position using (9) for each dimension.

$$\bar{x}^d = \frac{1}{N} \sum_{i=1}^N x_i^d \tag{9}$$

where  $x_i^d$  is the agent  $i$ th position in dimension  $d$ th and  $N$  is the number of agents. Next, the diversity of agents’ position with respect to the mean position for every dimension is calculated as follows.

$$\bar{D} = \frac{1}{N} \sum_{i=1}^N |x_i^d - \bar{x}_i^d| \tag{10}$$

Finally, the population’s position diversity is calculated as follows.

$$D = \frac{1}{D} \sum_{d=1}^D \bar{D} \tag{11}$$



where  $D$  represents the dimension size of the problem.

Also, a counter,  $\delta$ , is important in DASAS-SKF. Initially,  $\delta = 0$ . If the population's diversity is found to be static,  $D(t + 1)/D(t) = 1$ , then the  $\delta$  is incremented. A population's iteration strategy is switched if the indicator is found to be static for  $\Delta$  number of fitness evaluation, or  $\delta \geq \Delta$ . The  $\Delta$  is a threshold value in DASAS-SKF or a stagnant indicator to indicate that the population might trapped within local optima and the agents had prematurely converged. Note that  $\Delta$  is written in percentage of the total number of iterations. As the iteration strategy switches from synchronous to asynchronous and vice versa, the  $\delta$  is reset or  $\delta = 0$ . The DASAS-SKF stops after maximum number of fitness evaluation (FES).

## 4 Experiment Result and Discussion

Performance evaluation was implemented based on the CEC2014 benchmark test suite for single-objective optimization [40]. This test suite consists of 30 functions which can be grouped into unimodal functions, simple multimodal functions, hybrid functions, and composition functions.

In this study, the parameter setting used for the experiments are as the following. The population size,  $N = 100$ , the dimension size,  $D = 30$ , the maximum function evaluation,  $FES = 10,000 \times D$ , and the number of independent run,  $T = 30$ . Following the original SKF setting parameter [2],  $P(0) = 1000$ ,  $Q = 0.5$ , and  $R = 0.5$ . Also, the SKF starts with synchronous update. Different  $\Delta$  values,  $\Delta = \{5\%, 10\%, 15\%, 20\%, 25\%, 30\%, 35\%, 40\%, 45\%, 50\%, 55\%, 60\%, 65\%, 70\%, 75\%, 80\%, 85\%, 90\%, 95\%\}$  were also considered in experiments.

The average fitness error values are tabulated in Tables 1, 2, 3, 4 and 5. This error values indicate how close the fitness values obtained with reference to the fitness values of the solutions. The error value is written in bold if it is smaller than the SKF.

The Wilcoxon signed rank test is a pairwise non-parametric statistical analysis procedure. According to [41], for comparison of metaheuristics algorithms, non-parametric tests are more appropriate compare to parametric tests. Often, the data from experiments involving metaheuristics algorithms do not meet the conditions for validity of parametric test. Therefore, non-parametric tests are more suitable. The Wilcoxon signed ranks test identifies if significant difference exists between two algorithms being compared. A small value of significant level shows bigger difference between the two algorithms being analysed.

The statistical values of Wilcoxon signed rank test are shown in Table 5. Only  $R^+$  and  $R^-$  are shown in this table. With the level of significance at least 10%, if the  $R^+ < 152$  and  $R^- < R^-$ , the improvement is significant. Hence, the test shows that, absolutely, the proposed DASAS-SKF is significantly better than the original SKF.

**Table 1** The mean error values of SKF versus DASAS-SKF ( $\Delta = 5 - 20\%$ )

Function	SKF	DASAS-SKF $\Delta = 5\%$	DASAS-SKF $\Delta = 10\%$	DASAS-SKF $\Delta = 15\%$	DASAS-SKF $\Delta = 20\%$
1	4.860E+05	<b>2.290E+05</b>	<b>2.320E+05</b>	<b>2.880E+05</b>	<b>3.660E+05</b>
2	2.450E+08	<b>1.050E+04</b>	<b>5.130E+04</b>	<b>9.180E+05</b>	<b>2.890E+06</b>
3	1.841E+04	<b>4.840E+03</b>	<b>6.184E+03</b>	<b>8.074E+03</b>	<b>8.952E+03</b>
4	3.646E+01	<b>1.659E+01</b>	<b>1.476E+01</b>	<b>1.729E+01</b>	<b>3.535E+01</b>
5	2.002E+01	<b>2.000E+01</b>	<b>2.000E+01</b>	<b>2.000E+01</b>	<b>2.000E+01</b>
6	2.195E+01	<b>1.667E+01</b>	<b>1.574E+01</b>	<b>1.583E+01</b>	<b>1.532E+01</b>
7	1.635E-01	1.986E-01	2.558E-01	9.148E-02	<b>1.163E-01</b>
8	5.878E+00	3.768E-01	<b>1.891E+00</b>	<b>2.004E+00</b>	<b>2.694E+00</b>
9	9.087E+01	<b>6.978E+01</b>	<b>7.190E+01</b>	<b>7.798E+01</b>	<b>6.598E+01</b>
10	2.263E+02	<b>2.648E+01</b>	<b>6.735E+01</b>	<b>1.085E+02</b>	<b>1.397E+02</b>
11	2.640E+03	<b>2.439E+03</b>	<b>2.481E+03</b>	<b>2.596E+03</b>	2.677E+03
12	3.592E-01	<b>2.043E-01</b>	<b>1.851E-01</b>	<b>1.899E-01</b>	<b>1.811E-01</b>
13	4.443E-01	<b>3.580E-01</b>	<b>3.426E-01</b>	<b>3.375E-01</b>	<b>3.506E-01</b>
14	2.593E-01	<b>2.372E-01</b>	<b>2.311E-01</b>	<b>2.271E-01</b>	<b>2.343E-01</b>
15	2.192E+01	<b>1.730E+01</b>	<b>1.768E+01</b>	<b>1.586E+01</b>	<b>1.538E+01</b>
16	1.060E+01	<b>1.022E+01</b>	<b>1.041E+01</b>	<b>1.017E+01</b>	<b>1.046E+01</b>
17	1.050E+05	<b>1.030E+05</b>	1.300E+05	1.380E+05	1.130E+05
18	1.150E+07	<b>1.682E+03</b>	<b>1.619E+03</b>	<b>2.129E+03</b>	<b>5.347E+03</b>
19	2.050E+01	<b>1.578E+01</b>	<b>1.203E+01</b>	<b>1.467E+01</b>	<b>1.261E+01</b>
20	2.984E+04	<b>6.680E+03</b>	<b>9.934E+03</b>	<b>1.095E+04</b>	<b>1.443E+04</b>
21	2.610E+05	<b>1.320E+05</b>	<b>1.870E+05</b>	<b>1.540E+05</b>	<b>2.310E+05</b>
22	6.217E+02	<b>4.797E+02</b>	<b>5.259E+02</b>	<b>4.914E+02</b>	<b>5.236E+02</b>
23	3.181E+02	<b>3.158E+02</b>	<b>3.160E+02</b>	<b>3.163E+02</b>	<b>3.162E+02</b>
24	2.310E+02	<b>2.268E+02</b>	<b>2.277E+02</b>	<b>2.283E+02</b>	<b>2.290E+02</b>
25	2.151E+02	<b>2.141E+02</b>	<b>2.144E+02</b>	<b>2.144E+02</b>	<b>2.143E+02</b>
26	1.204E+02	<b>1.004E+02</b>	<b>1.071E+02</b>	<b>1.071E+02</b>	<b>1.137E+02</b>
27	5.985E+02	<b>5.559E+02</b>	<b>5.795E+02</b>	<b>5.083E+02</b>	<b>5.715E+02</b>
28	1.574E+03	1.767E+03	1.631E+03	1.587E+03	<b>1.389E+03</b>
29	2.477E+03	<b>1.061E+03</b>	<b>9.765E+02</b>	<b>9.054E+02</b>	<b>1.084E+03</b>
30	5.438E+03	<b>2.531E+03</b>	<b>2.897E+03</b>	<b>2.847E+03</b>	<b>3.005E+03</b>

**Table 2** The mean error values of SKF versus DASAS-SKF ( $\Delta = 25\% - 45\%$ )

Function	DASAS-SKF $\Delta = 25\%$	DASAS-SKF $\Delta = 30\%$	DASAS-SKF $\Delta = 35\%$	DASAS-SKF $\Delta = 40\%$	DASAS-SKF $\Delta = 45\%$
1	2.630E+05	2.950E+05	4.250E+05	2.940E+05	2.870E+05
2	2.330E+06	7.110E+06	2.100E+06	2.290E+06	3.580E+06
3	1.077E+04	1.125E+04	1.205E+04	7.602E+03	8.323E+03
4	1.974E+01	1.570E+01	1.643E+01	2.838E+01	3.413E+01
5	2.000E+01	2.000E+01	2.000E+01	2.000E+01	2.001E+01
6	1.612E+01	1.621E+01	1.541E+01	1.572E+01	1.631E+01
7	1.240E-01	1.395E-01	1.135E-01	1.108E-01	1.821E-01
8	4.437E+00	4.129E+00	3.913E+00	4.732E+00	4.760E+00
9	7.529E+01	6.970E+01	7.038E+01	6.622E+01	6.736E+01
10	1.518E+02	1.426E+02	1.513E+02	1.725E+02	1.709E+02
11	2.622E+03	2.514E+03	2.540E+03	2.477E+03	2.595E+03
12	2.086E-01	2.214E-01	1.994E-01	2.023E-01	2.183E-01
13	3.869E-01	3.303E-01	3.680E-01	3.420E-01	3.502E-01
14	2.128E-01	2.333E-01	2.280E-01	2.221E-01	2.279E-01
15	1.365E+01	1.485E+01	1.472E+01	1.514E+01	1.764E+01
16	1.038E+01	1.062E+01	1.043E+01	1.051E+01	1.056E+01
17	1.440E+05	1.570E+05	1.470E+05	1.230E+05	1.370E+05
18	1.385E+04	2.530E+05	1.291E+04	1.035E+03	3.400E+05
19	1.392E+01	1.654E+01	1.433E+01	1.641E+01	1.110E+01
20	1.775E+04	1.723E+04	1.789E+04	1.751E+04	1.612E+04
21	1.710E+05	1.810E+05	2.110E+05	2.340E+05	1.790E+05
22	5.459E+02	5.152E+02	5.554E+02	5.043E+02	5.478E+02
23	3.160E+02	3.162E+02	3.162E+02	3.163E+02	3.162E+02
24	2.281E+02	2.299E+02	2.284E+02	2.286E+02	2.295E+02
25	2.142E+02	2.140E+02	2.146E+02	2.137E+02	2.143E+02
26	1.137E+02	1.104E+02	1.071E+02	1.137E+02	1.137E+02
27	5.870E+02	6.066E+02	5.851E+02	5.735E+02	6.043E+02
28	1.662E+03	1.651E+03	1.571E+03	1.670E+03	1.599E+03
29	1.012E+03	8.810E+02	1.055E+03	1.046E+03	9.940E+02
30	2.864E+03	2.974E+03	3.273E+03	3.079E+03	3.796E+03

**Table 3** The mean error values of DASAS-SKF ( $\Delta = 50\% - 70\%$ )

Function	DASAS-SKF $\Delta = 50\%$	DASAS-SKF $\Delta = 55\%$	DASAS-SKF $\Delta = 60\%$	DASAS-SKF $\Delta = 65\%$	DASAS-SKF $\Delta = 70\%$
1	<b>3.090E+05</b>	<b>2.090E+05</b>	5.380E+05	<b>2.960E+05</b>	<b>4.120E+05</b>
2	<b>1.530E+07</b>	<b>6.070E+06</b>	<b>2.720E+07</b>	<b>6.100E+06</b>	<b>4.060E+06</b>
3	<b>1.119E+04</b>	<b>9.143E+03</b>	<b>1.121E+04</b>	<b>1.092E+04</b>	<b>9.508E+03</b>
4	<b>2.383E+01</b>	<b>2.064E+01</b>	<b>3.315E+01</b>	<b>2.823E+01</b>	<b>3.763E+01</b>
5	<b>2.001E+01</b>	<b>2.001E+01</b>	<b>2.000E+01</b>	<b>2.001E+01</b>	<b>2.001E+01</b>
6	<b>1.536E+01</b>	<b>1.577E+01</b>	<b>1.559E+01</b>	<b>1.590E+01</b>	<b>1.547E+01</b>
7	3.513E-01	1.918E-01	<b>1.460E-01</b>	1.884E-01	1.272E-01
8	7.125E+00	6.286E+00	5.899E+00	5.096E+00	6.348E+00
9	<b>7.831E+01</b>	<b>7.247E+01</b>	<b>7.422E+01</b>	<b>6.868E+01</b>	<b>7.150E+01</b>
10	<b>1.768E+02</b>	<b>1.486E+02</b>	<b>1.707E+02</b>	<b>1.586E+02</b>	2.528E+02
11	2.703E+03	<b>2.553E+03</b>	<b>2.621E+03</b>	<b>2.601E+03</b>	<b>2.479E+03</b>
12	<b>2.021E-01</b>	<b>2.301E-01</b>	<b>2.573E-01</b>	<b>2.359E-01</b>	<b>2.089E-01</b>
13	<b>3.467E-01</b>	<b>3.518E-01</b>	<b>3.708E-01</b>	<b>3.747E-01</b>	<b>3.477E-01</b>
14	<b>2.220E-01</b>	<b>2.309E-01</b>	<b>2.176E-01</b>	<b>2.278E-01</b>	<b>2.421E-01</b>
15	<b>1.430E+01</b>	<b>1.396E+01</b>	<b>1.262E+01</b>	<b>1.657E+01</b>	<b>1.654E+01</b>
16	<b>1.058E+01</b>	<b>1.059E+01</b>	<b>1.040E+01</b>	<b>1.047E+01</b>	<b>1.056E+01</b>
17	1.160E+05	1.280E+05	1.660E+05	1.710E+05	1.640E+05
18	<b>1.470E+05</b>	<b>2.850E+05</b>	<b>3.460E+05</b>	<b>4.300E+05</b>	<b>8.740E+05</b>
19	<b>1.416E+01</b>	<b>9.915E+00</b>	<b>1.140E+01</b>	<b>1.614E+01</b>	<b>1.479E+01</b>
20	<b>2.200E+04</b>	<b>2.373E+04</b>	<b>2.304E+04</b>	<b>2.109E+04</b>	<b>2.548E+04</b>
21	<b>2.480E+05</b>	<b>1.710E+05</b>	<b>2.280E+05</b>	<b>2.140E+05</b>	<b>2.560E+05</b>
22	<b>5.228E+02</b>	<b>5.433E+02</b>	<b>4.798E+02</b>	<b>5.553E+02</b>	<b>6.023E+02</b>
23	<b>3.163E+02</b>	<b>3.165E+02</b>	<b>3.166E+02</b>	<b>3.169E+02</b>	<b>3.162E+02</b>
24	<b>2.280E+02</b>	<b>2.285E+02</b>	<b>2.295E+02</b>	<b>2.286E+02</b>	<b>2.289E+02</b>
25	<b>2.143E+02</b>	<b>2.139E+02</b>	<b>2.144E+02</b>	<b>2.142E+02</b>	2.150E+02
26	<b>1.104E+02</b>	<b>1.104E+02</b>	<b>1.137E+02</b>	<b>1.171E+02</b>	<b>1.104E+02</b>
27	<b>5.871E+02</b>	<b>5.974E+02</b>	<b>5.902E+02</b>	<b>5.641E+02</b>	<b>5.253E+02</b>
28	1.774E+03	1.639E+03	1.677E+03	1.808E+03	1.612E+03
29	<b>1.221E+03</b>	<b>1.162E+03</b>	<b>1.144E+03</b>	<b>9.595E+02</b>	<b>1.437E+03</b>
30	<b>3.419E+03</b>	<b>3.219E+03</b>	<b>3.389E+03</b>	<b>2.969E+03</b>	<b>3.114E+03</b>

**Table 4** The mean error values of DASAS-SKF ( $\Delta = 75\% - 95\%$ )

Function	DASAS-SKF $\Delta = 75\%$	DASAS-SKF $\Delta = 80\%$	DASAS-SKF $\Delta = 85\%$	DASAS-SKF $\Delta = 90\%$	DASAS-SKF $\Delta = 95\%$
1	<b>4.900E+05</b>	5.550E+05	5.370E+05	1.070E+06	1.820E+06
2	<b>2.340E+07</b>	<b>1.810E+07</b>	<b>3.290E+06</b>	<b>5.220E+06</b>	<b>2.670E+07</b>
3	<b>7.976E+03</b>	<b>1.065E+04</b>	<b>1.386E+04</b>	<b>8.319E+03</b>	<b>1.271E+04</b>
4	<b>3.422E+01</b>	<b>3.459E+01</b>	<b>3.555E+01</b>	4.257E+01	7.854E+01
5	<b>2.001E+01</b>	<b>2.001E+01</b>	<b>2.001E+01</b>	<b>2.001E+01</b>	<b>2.001E+01</b>
6	<b>1.559E+01</b>	<b>1.495E+01</b>	<b>1.615E+01</b>	<b>1.607E+01</b>	<b>1.580E+01</b>
7	<b>1.229E-01</b>	1.638E-01	1.779E-01	<b>1.288E-01</b>	<b>1.565E-01</b>
8	6.158E+00	5.942E+00	<b>5.654E+00</b>	6.393E+00	5.564E+00
9	<b>7.373E+01</b>	<b>7.423E+01</b>	<b>7.299E+01</b>	<b>7.446E+01</b>	<b>7.291E+01</b>
10	<b>1.896E+02</b>	<b>1.805E+02</b>	<b>2.180E+02</b>	<b>2.253E+02</b>	<b>1.708E+02</b>
11	2.652E+03	<b>2.408E+03</b>	2.650E+03	<b>2.377E+03</b>	2.671E+03
12	<b>2.501E-01</b>	<b>2.317E-01</b>	<b>2.147E-01</b>	<b>2.578E-01</b>	<b>2.346E-01</b>
13	<b>3.603E-01</b>	<b>3.421E-01</b>	<b>3.688E-01</b>	<b>3.284E-01</b>	<b>3.324E-01</b>
14	<b>2.261E-01</b>	<b>2.300E-01</b>	<b>2.331E-01</b>	<b>2.373E-01</b>	<b>2.207E-01</b>
15	<b>1.357E+01</b>	<b>1.282E+01</b>	<b>1.465E+01</b>	<b>1.641E+01</b>	<b>1.556E+01</b>
16	<b>1.053E+01</b>	<b>1.050E+01</b>	1.064E+01	<b>1.056E+01</b>	1.065E+01
17	1.850E+05	2.510E+05	3.160E+05	4.250E+05	5.520E+05
18	<b>1.950E+06</b>	<b>4.440E+06</b>	<b>1.660E+05</b>	<b>1.420E+06</b>	<b>2.340E+06</b>
19	<b>9.038E+00</b>	<b>1.576E+01</b>	<b>1.528E+01</b>	<b>1.502E+01</b>	2.081E+01
20	<b>2.271E+04</b>	<b>2.363E+04</b>	<b>2.458E+04</b>	<b>2.698E+04</b>	<b>2.219E+04</b>
21	<b>1.990E+05</b>	<b>2.500E+05</b>	3.390E+05	4.510E+05	3.930E+05
22	<b>5.996E+02</b>	<b>5.273E+02</b>	<b>5.209E+02</b>	<b>5.245E+02</b>	<b>5.354E+02</b>
23	<b>3.161E+02</b>	<b>3.163E+02</b>	<b>3.164E+02</b>	<b>3.160E+02</b>	<b>3.166E+02</b>
24	<b>2.297E+02</b>	<b>2.293E+02</b>	<b>2.294E+02</b>	<b>2.291E+02</b>	<b>2.290E+02</b>
25	<b>2.149E+02</b>	<b>2.140E+02</b>	<b>2.150E+02</b>	<b>2.142E+02</b>	<b>2.148E+02</b>
26	<b>1.170E+02</b>	<b>1.038E+02</b>	<b>1.170E+02</b>	1.237E+02	<b>1.171E+02</b>
27	<b>5.316E+02</b>	<b>5.447E+02</b>	<b>5.793E+02</b>	<b>5.805E+02</b>	<b>5.893E+02</b>
28	1.682E+03	<b>1.537E+03</b>	1.804E+03	<b>1.573E+03</b>	1.615E+03
29	<b>1.328E+03</b>	9.383E+02	<b>1.051E+03</b>	<b>1.026E+03</b>	<b>1.070E+03</b>
30	<b>3.141E+03</b>	<b>3.153E+03</b>	<b>3.144E+03</b>	<b>3.137E+03</b>	<b>3.892E+03</b>

**Table 5** Statistical values of Wilcoxon signed rank test

$\Delta$ (%)	R+	R-
5	<b>22</b>	443
10	<b>47</b>	418
15	<b>41</b>	424
20	<b>42</b>	423
25	<b>47</b>	418
30	<b>60</b>	405
35	<b>26</b>	439
40	<b>45</b>	420
45	<b>60</b>	405
50	<b>80</b>	385
55	<b>54</b>	411
60	<b>78</b>	387
65	<b>50</b>	415
70	<b>81</b>	384
75	<b>97</b>	368
80	<b>60</b>	405
85	<b>125</b>	340
90	<b>118</b>	347
95	<b>147</b>	318

## 5 Conclusion

It is observed that more better solutions were found with  $\Delta = \{5\%$ . This indicates that the DASAS-SKF benefited from higher number of switching. Anyway, this paper proves that the SKF algorithm with adaptive switching between synchronous and asynchronous updates is superior (by observing how close the fitness values obtained with reference to the fitness values of the solutions) than the original SKF for all values of stagnant indicator,  $\Delta$ . Indirectly, the performance improvement shows that the premature convergence in SKF can be addressed by the switching between the synchronous and asynchronous updates.

**Acknowledgements** This research is supported by the Fundamental Research Grant Scheme awarded by the Ministry of Higher Education Malaysia to Universiti Malaysia Pahang (RDU170106).

## References

1. Toscano R, Lyonnet P (2009) Heuristic Kalman algorithm for solving optimization problems. *IEEE Trans Syst Man Cybern Part B (Cybern)* 39(5):1231–1244
2. Ibrahim Z, Abdul Aziz NH, Ab Aziz NA, Razali S, Shapiai MI, Nawawi SW, Mohamad MS (2015) A Kalman filter approach for solving unimodal optimization problems. *ICIC Express Lett* 9:3415–3422
3. Ibrahim Z, Abdul Aziz NH, Ab Aziz NA, Razali R, Mohamad MS (2016) Simulated Kalman filter: a novel estimation-based metaheuristic optimization algorithm. *Adv Sci Lett* 22:2941–2946
4. Abd Aziz NH, Ibrahim Z, Razali S, Ab Aziz NA (2016) Estimation-based metaheuristics: a new branch of computational intelligence. In: *The national conference for postgraduate research 2016, NCON-PGR*, vol 1, pp 469–476
5. Kalman RE (1960) A new approach to linear filtering and prediction problems. *ASME J Basic Eng* 82:35–45
6. Abd Aziz NH, Ibrahim Z, Razali, Bakare TA, Ab Aziz NA (2016) How important the error covariance in simulated Kalman filter?. In: *The national conference for postgraduate research 2016, NCON-PGR*, vol 1, pp 315–320
7. Abd Aziz NH, Ab Aziz NA, Mat Jusof MF, Razali S, Ibrahim Z, Adam A, Shapiai MI (2018) An analysis on the number of agents towards the performance of the simulated Kalman filter optimizer. In: *8th international conference on intelligent systems, modelling and simulation*, vol 1, pp 16–21
8. Md Yusof Z, Ibrahim I, Satiman SN, Ibrahim Z, Abd Aziz NH, Ab. Aziz NA (2015) BSKF: binary simulated Kalman filter. In: *Third international conference on artificial intelligence, modelling and simulation*, pp 77–81
9. Md Yusof Z, Ibrahim I, Ibrahim Z, Abas KH, Ab Aziz NA, Abd Aziz NH, Mohamad MS (2016) Local optimum distance evaluated simulated Kalman filter for combinatorial optimization problems. In: *The national conference for postgraduate research 2016, NCON-PGR*, vol 1, pp 892–901
10. Md Yusof Z, Ibrahim Z, Ibrahim I, Mohd Azmi KZ, Ab Aziz NA, Abd Aziz NH, Mohamad MS (2016) Distance evaluated simulated Kalman filter for combinatorial optimization problems. *ARPN J Eng Appl Sci* 11:4904–4910
11. Md Yusof Z, Ibrahim Z, Ibrahim I, Mohd Azmi KZ, Ab Aziz NA, Abd Aziz NH, Mohamad MS (2016) Angle modulated simulated Kalman filter algorithm for combinatorial optimization problems. *ARPN J Eng Appl Sci* 11:4854–4859
12. Muhammad B, Ibrahim Z, Mat Jusof MF, Ab Aziz NA, Abd Aziz NH, Mokhtar N (2017) A hybrid simulated Kalman filter—gravitational search algorithm (SKF-GSA). In: *International conference on artificial life and robotics*, pp 707–710
13. Muhammad B, Ibrahim I, Mohd Azmi KZ, Abas KH, Ab Aziz NA, Abd Aziz NH, Mohamad MS (2016) Performance evaluation of hybrid SKF algorithms: hybrid SKF-PSO and hybrid SKF-GSA. In: *The national conference for postgraduate research 2016, NCON-PGR*, vol 1, pp 865–874
14. Muhammad B, Ibrahim I, Mohd Azmi KZ, Abas KH, Ab Aziz NA, Abd Aziz NH, Mohamad MS (2016) Four different methods to hybrid simulated Kalman filter (SKF) with particle swarm optimization (PSO). In: *The national conference for postgraduate research 2016, NCON-PGR*, vol 1, pp 843–853
15. Muhammad B, Ibrahim I, Mohd Azmi KZ, Abas KH, Ab Aziz NA, Abd Aziz NH, Mohamad MS (2016) Four different methods to hybrid simulated Kalman filter (SKF) with gravitational search algorithm (GSA). In: *The national conference for postgraduate research 2016, NCON-PGR*, vol 1, pp 854–864
16. Muhammad B, Ibrahim Z, Ghazali KH, Mohd Azmi KZ, Ab Aziz NA, Abd Aziz NH, Mohamad MS (2015) A new hybrid simulated Kalman filter and particle swarm optimization for continuous numerical optimization problems. *ARPN J Eng Appl Sci* 10:17171–17176

17. Ibrahim Z, Mohd Azmi KZ, Ab Aziz NA, Abd Aziz NH, Muhammad B, Mat Jusof MF, Shapiai MI (2018) An oppositional learning prediction operator for simulated Kalman filter. In: The 3rd international conference on computational intelligence and applications, vol 1, pp 139–143
18. Abd Aziz NH, Ibrahim Z, Ab Aziz NA, Razali S (2017) Parameter-less simulated Kalman filter. *Int J Softw Eng Comput Syst* 3:129–137
19. Abd Aziz NH, Ab Aziz NA, Ibrahim Z, Razali S, Mat Jusof MF, Abas KH, Mohamad MS, Mokhtar N (2017) Simulated Kalman filter with randomized Q and R parameters. In: International conference on artificial life and robotics, pp 711–714
20. Lazarus K, Noordin NH, Mat Jusof MF, Ibrahim Z, Abas KH (2017) Adaptive beamforming algorithm based on a simulated Kalman filter. *Int J Simul Syst Sci Technol* (18):10.1–10.5
21. Lazarus K, Noordin NH, Mohd Azmi KZ, Abd Aziz NH, Ibrahim Z (2016) Adaptive beamforming algorithm based on generalized opposition-based simulated Kalman filter. In: The national conference for postgraduate research 2016, Ncon-Pgr, pp 1–9
22. Lazarus K, Noordin NH, Ibrahim Z, Mat Jusof MF, Mohd Faudzi MA, Subari N (2017) An opposition-based simulated Kalman filter algorithm for adaptive beamforming. In: IEEE international conference on applied system innovation, pp 91–94
23. Lazarus, K., Noordin, N.H., Ibrahim, Z., Abas, K.H.: Adaptive beamforming algorithm based on simulated Kalman filter. *ASIA Multi Conference On Modelling And Simulation*, pp. 19–23 (2016)
24. Md Yusof Z, Satiman SN, Mohd Azmi KZ, Muhammad B, Razali S, Ibrahim Z, Aspar Z, Ismail S (2015) Solving airport gate allocation problem using simulated Kalman filter. In: International conference on knowledge transfer, pp 121–127
25. Mohd Azmi KZ, Md Yusof Z, Satiman SN, Muhammad B, Razali S, Ibrahim Z, Ab Aziz NA, Abd Aziz NH (2016) Solving airport gate allocation problem using angle modulated simulated Kalman filter. In: The national conference for postgraduate research 2016, NCON-PGR, pp 875–885
26. Muhammad B, Mat Jusof MF, Shapiai MI, Adam A, Md Yusof Z, Mohd Azmi KZ, Abd Aziz NH, Ibrahim Z, Mokhtar N (2018) Feature selection using binary simulated Kalman filter for peak classification of EEG signals. In: 8th international conference on intelligent systems, modelling and simulation, pp 1–6
27. Adam A, Ibrahim Z, Mokhtar N, Shapiai MI, Mubin M, Saad I (2016) Feature selection using angle modulated simulated Kalman filter for peak classification of EEG signals. *SpringerPlus* (5):1520
28. Muhammad B, Mohd Azmi KZ, Ibrahim Z, Mohd Faudzi AA, Pebrianti D (2018) Simultaneous computation of model order and parameter estimation for system identification based on opposition-based simulated Kalman filter. In: SICE international symposium on control systems, pp 105–112
29. Mohd Azmi KZ, Ibrahim Z, Pebrianti D (2017) Simultaneous computation of model order and parameter estimation for ARX model based on single and multi swarm simulated Kalman filter. *J Telecommun, Electron, Comput Eng* 9:151–155
30. Ann NQ, Pebrianti D, Bayuaji L, Daud MR, Samad R, Ibrahim Z, Hamid R, Syafrullah M (2018) SKF-based image template matching for distance measurement by using stereo vision. In: Intelligent manufacturing and mechatronics, pp 439–447
31. Ann NQ, Pebrianti D, Ibrahim Z, Mat Jusof MF, Bayuaji L, Abdullah NRH (2018) Illumination-invariant image matching based on simulated Kalman filter (SKF). *J Telecommun Electron Comput Eng* (10):31–36
32. Mustapa A, Md Yusof Z, Adam A, Muhammad B, Ibrahim Z (2018) Solving assembly sequence planning using angle modulated simulated Kalman filter. In: IOP conference series: materials, science, and engineering, vol 319, p 012044
33. Muhammad B, Pebrianti D, Abdul Ghani N, Abd Aziz NH, Ab Aziz NA, Mohamad MS, Shapiai MI, Ibrahim Z (2018) An application of simulated Kalman filter optimization algorithm for parameter tuning in proportional-integral-derivative controllers for automatic voltage regulator system. In: SICE international symposium on control systems, pp 113–120



34. Abd Aziz NH, Ab Aziz NA, Ibrahim Z, Razali S, Abas KH, Mohamad MS (2016) A Kalman filter approach to PCB drill path optimization problem. In: IEEE conference on systems, process and control, pp 33–36
35. Abd Aziz NH, Ibrahim Z, Ab Aziz NA, Md Yusof Z, Mohamad MS (2018) Single-solution simulated Kalman filter algorithm for routing in printed circuit board drilling process. In: Intelligent manufacturing and mechatronics, pp 649–655
36. Kaucic M (2013) A multi-start opposition-based particle swarm optimization algorithm with adaptive velocity for bound constrained global optimization. *J Global Optim* 55:165–188
37. Zhan Z-H, Zhang J, Li Y, Chung HS-H (2009) Adaptive particle swarm optimization. *IEEE Trans Syst Man Cybern-Part B Cybern* 39:1362–1381
38. Liu C, Ouyang C (2010) An adaptive fuzzy weight PSO algorithm. In: Fourth international conference on genetic and evolutionary computing, pp 8–10
39. Mohd Azmi KZ, Ibrahim Z, Pebrianti D, Mat Jusof MF, Abdul Aziz NH, Ab. Aziz NA (2019) Enhancing simulated Kalman filter algorithm using current optimum opposition-based learning. *Mekatronika* 1(1):1–13
40. Liang JJ, Qu BY, Suganthan PN (2013) Problem definitions and evaluation criteria for the CEC 2014 special session and competition on single objective real-parameter numerical optimization. In: Journal of global optimization. Tech. Rep. 201311. Computational intelligence laboratory, Zhengzhou University, Zhengzhou, China and Nanyang Technological University, Singapore
41. García S, Molina D, Lozano M, Herrera F (2008) A study on the use of non-parametric tests for analyzing the evolutionary algorithms' behaviour: a case study on the CEC'2015 special session on real parameter optimization. *J Heuristics* 15:617–644

# Combinatorial Test Suite Generation Strategy Using Enhanced Sine Cosine Algorithm



Kamal Z. Zamli, Fakhrud Din, Abdullah B. Nasser  
and AbdulRahman Alsewari

**Abstract** Owing to its simplicity and having no control parameters, the Sine Cosine Algorithm (SCA) has attracted much attention among researchers. Although useful, the SCA algorithm adopts a linear magnitude update to determine its sine or cosine position updates. In the actual searching process, the magnitude update is rarely linear. In fact, the magnitude update is also non-exponential and is highly dependent on the problem domain and its search topology. For this reason, our work proposes a combination of linear and exponential magnitude update for the search displacement. In doing so, we adopt the combinatorial testing problem as our case study. Combinatorial testing strategies generate test data which cover all required interactions among parameter values of a system-under-test in order to explore interaction faults. Our evaluation gives promising results on the improved performance over the original SCA algorithm. As far as test data generation time is concerned, the enhanced SCA outperformed all its counterparts, whereas its results in terms of test suite sizes are comparable to other parameter free meta-heuristic algorithms.

**Keywords** Meta-heuristics · Sine cosine algorithm · T-way testing

## 1 Introduction

Optimization relates to the process of finding the most optimal solution (be it maximization or minimization of one or more variables) from a set of feasible solutions [1]. Owing to combinatorial explosion problem, exhaustive search from all the feasible solutions is infeasible given limitation in terms of resources and time. For this

---

K. Z. Zamli (✉) · F. Din · A. B. Nasser · A. Alsewari  
Faculty of Computer Systems and Software Engineering, Universiti Malaysia Pahang, 26300  
Kuantan, Pahang, Malaysia  
e-mail: [kamalz@ump.edu.my](mailto:kamalz@ump.edu.my)

F. Din  
e-mail: [fakhruddin@uom.edu.pk](mailto:fakhruddin@uom.edu.pk)

F. Din  
Department of Computer Science & IT, University of Malakand, Dir Lower, Chakdara, KPK,  
Pakistan

reason, many researchers have opted to get an approximate solution based on the use of meta-heuristic algorithms. Much useful progress can be seen in the literature in terms of the new development of meta-heuristic algorithms (i.e. parameterized meta-heuristic versus parameter free meta-heuristic). In the case of parameterized meta-heuristic algorithms (e.g. Particle Swarm Optimization (PSO) [2] requires the setting for inertia weight  $w$ , and social parameters  $c1$  and  $c2$ ), there are predefined set of control parameters that enable the balance control for exploration (i.e. roaming the unexplored territory) and exploitation (i.e. exploiting the neighborhood knowledge on the best and profitable region). Setting the right values for these parameters can be a daunting task as improper setting can cause entrapment in local optima as well unnecessarily long convergence. For parameter-less meta-heuristic algorithms (such as Teaching Learning based Optimization (TLBO) [3], Jaya [4], etc.), there are no real parameters to control exploration and exploitation (except only the population size and maximum iteration). The downside of this approach is that exploration and exploitation are performed in a predefined manner (e.g. one after the other in the case of TLBO). As the nature of exploration and exploitation are inherently dynamic, their preset division may guide the algorithm to reach to poor solutions.

In this paper, our work deals with a new parameter free meta-heuristic algorithm called the Sine Cosine Algorithm (SCA) [5]. In the current form, the SCA algorithm exploits the linear magnitude update of either its sine or cosine search operators. In the actual searching process, the magnitude update is rarely linear. In fact, the magnitude update is also non-exponential and is highly dependent on the problem domain and its search topology. For this reason, our work proposes a combination of linear and exponential magnitude update for the search displacement. In doing so, we adopt the combinatorial testing problem as our case study.

The rest of the paper is organized as follows. Section 2 gives an overview of t-way testing. Section 3 illustrates the related work. Section 4 highlights our enhanced SCA algorithm. Finally, Sect. 5 elaborates on experimental results and conclusion.

## 2 Overview of T-Way Testing

Combinatorial testing relates to the process of generating a t-way test suite (where  $t$  indicates the required interaction strength). In combinatorial testing, the combination of every t-way interaction must be covered at least once in the final test suite [6]. To illustrate the basic of t-way testing, consider the following hypothetical ACME Pizza Ordering System adopted from [7] (Fig. 1).

There are three parameters as follows:

- Pizza size parameter (P1) has two values {Large Pizza, Medium Pizza}
- Spicy parameter (P2) has two values {Spicy checked, Spicy unchecked}
- Extra cheese parameter (P3) has two values {Extra Cheese checked, Extra Cheese unchecked}.

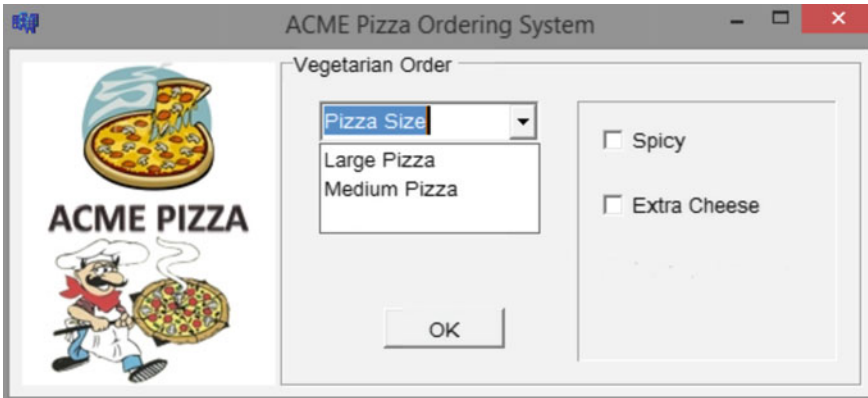


Fig. 1 ACME pizza ordering system

For simplicity, let the corresponding values for each parameter be represented as 0 and 1 respectively. Figure 2 demonstrates the exhaustive set (a), the pairs of interaction (b) and the complete 2-way test suite (c). Remapping from each value as 0 and 1, one can reproduce the actual test suite. It should be noted that there are 50 percent reduction as far as the number of test cases is concerned. At  $t=3$ , the number of test cases will slightly increase. In reality, the selection of interaction strength ( $t$ ) is based on the experience of the testers themselves.

Mathematically, covering array (CA) provides a convenient way for representing  $t$ -way test suites. To be Specific, the covering array notation  $CA(N; t, k, v)$  represents a combinatorial construct which is generated as  $N \times K$  dimensional array based on parameter values, and where each  $N \times t$  sub-array combines ordered set of

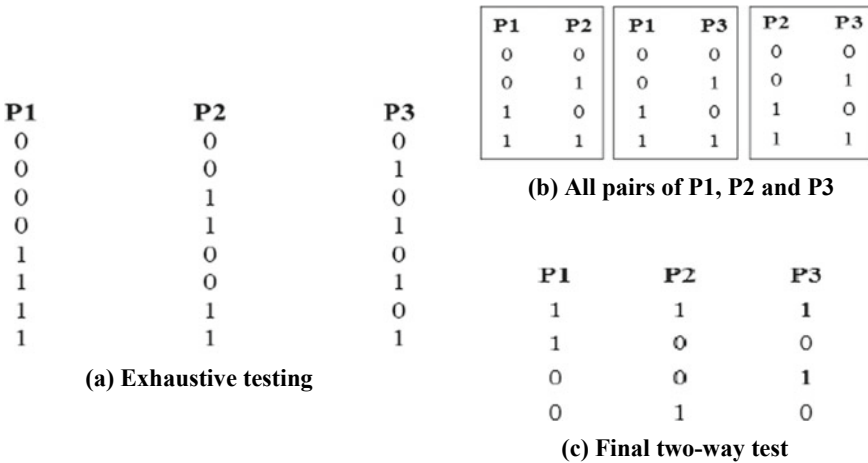


Fig. 2 ACME test suite at  $t = 2$

parameter values of size  $t$  at least once. CA ( $N; t, v^k$ ) is an alternate representation of a covering array. For system-under-test with varying number of parameter values, Mixed Covering Array (MCA) is introduced. The notation for MCA is MCA ( $N; t, k, (v_1, v_2, \dots, v_k)$ ) which can also be expressed as MCA ( $N; t, k, v^k$ ). Considering our example in Fig. 2, we can represent our solution as CA ( $4; 2, 2^3$ ).

### 3 Related Works

Generally, t-way test suite generation strategies are classified into two main approaches: the algebraic and computational approaches [8].

Concerning the algebraic approach, the t-way test suite is constructed by adopting lightweight computations [9]. Here, test cases are constructed without enumerating interactions between parameter values. An algebraic approach can be based on two different methods for test suite construction. The first method is based on mathematical functions [10–12], whereas the second one employs a recursive process to construct smaller test suites from larger test suites. On the negative note, the aforementioned methods based on the algebraic approach can only construct test data for small configurations.

Computational approaches employ greedy algorithms for test suite construction [13]. Each iteration of construction process tries to cover maximum number of t-way combinations. The construction process can either be one parameter at time (OPAT) or one test at time (OTAT) [14]. OPAT strategies begin test suit construction for the first two parameters or smallest t-combinations. Then it extends the test suite horizontally by adding one parameter per iteration and continues this process until the fulfillment of t-way criteria. Examples of such approach are IPO [15], IPOG [16], IPOG-D [17], IPOF and IPAD2 [15].

OTAT strategies start generating one test case per iteration involved all the parameters that cover the maximum number of combinations. The iteration continues until all the t-combinations are covered. Due to its efficiency, there are many strategies that adopts OTAT techniques such as AETG [18], Jenny [19], TConfig [20], and WHITCH [21]. Recently, many OTAT based strategies adopt meta-heuristic algorithms for generating t-way test suite.

In the literature, many meta-heuristic algorithms have been used successfully for generating t-way test suite such as Simulated Annealing (SA) [22], Genetic Algorithm (GA) [18], Ant Colony Algorithm (ACA) [23], Particle Swarm Optimization (PSO) [24], Harmony Search (HS) [25], Flower Pollination Algorithm (FPA) [26], Cuckoo Search (CS) [27] and Bat Algorithm [28].

Recently, new strategies based on more than single meta-heuristic algorithms have been proposed [7, 14, 29–31]. These new strategies attempt to improve the search process for generating test suite by adopting hybridization methods such as Hybrid-FPA [30], Tabu search Hyper-heuristic [29], Q-Learning Sine-Cosine [7], and Fuzzy-TLBO [14].

As far as modifications related to the  $r_1$  parameter of SCA, two exponential factors  $\alpha$  and  $\beta$  have been introduced for addressing continuous optimization problems [32]. Both these factors have assigned different constant values in order to nonlinearly decrease  $r_1$ . In [33], the value of  $r_1$  is decreased only exponentially as it was found more effective than other decreasing methods such as linear and parabola. In this study, the value of  $r_1$  is decreased both exponentially and linearly which is found more effective for addressing the test suite generation problem.

### 4 Original Sine Cosine Algorithm and Its Enhancement

The Sine Cosine Algorithm (SCA) is a new population-based meta-heuristic algorithm [5] that exploits the sine and cosine function for its individual population’s position vector updates. The position updates are based on:

$$X_i^{t+1} = X_i^t + r_1 \times \sin(r_2) + |r_3 P_i^t - X_i^t|, \quad r_4 < 0.5 \tag{1}$$

$$X_i^{t+1} = X_i^t + r_1 \times \cos(r_2) \times |r_3 P_i^t - X_i^t|, \quad r_4 \geq 0.5 \tag{2}$$

where  $X_i^t$  is the position of the current solution in the  $i$ -th dimension at the  $t$ -th iteration,  $r_1/r_2/r_3/r_4$  are random numbers between  $[0,1]$ ,  $P_i^t$  is position of the best destination point in the  $i$ -th dimension, and  $||$  indicates the absolute value. There are four values that control the actual search of SCA namely  $r_1, r_2, r_3,$  and  $r_4$ . Referring to Fig. 3,  $r_1$  dictates the radius of the search circle (i.e. displacement size). In the original SCA,  $r_1$  is linearly updated based on the iteration using the following equation:

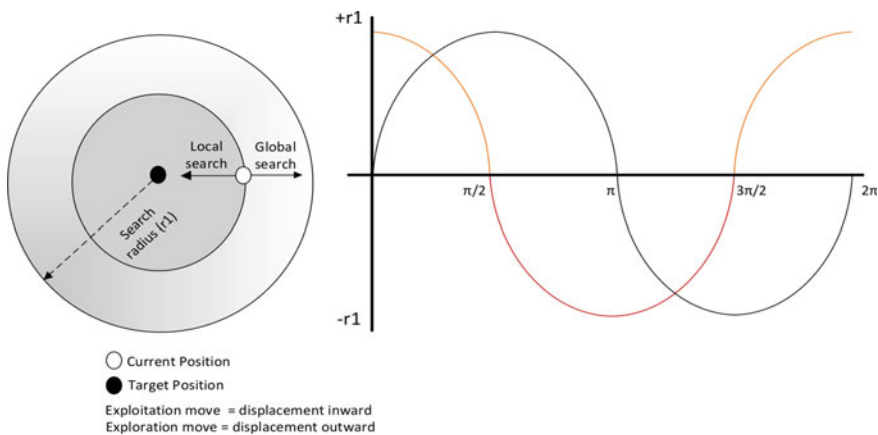


Fig. 3 Sine cosine search representation [7]

$$r_i = M \times \left(1 - \frac{t}{T}\right) \quad (3)$$

where  $t$  is the current iteration,  $T$  is the maximum number of iterations and  $M$  is a constant.  $r_2$  defines how the movement should be either inward for exploitation move (i.e. when sine and cosine are negative) or outward for exploration move (i.e. when sine and cosine are positive) as can be seen in Fig. 3. Next,  $r_3$  is the random weightage from the best position to affect the displacement from the current best. Finally,  $r_4$  serves as the probability switch between the sine and cosine search selection.

Going back to Eq. 3, the current updates of  $r_1$  is linear. In the actual searching process, the magnitude changes of  $r_1$  cannot be necessarily fixed as linear owing to the potential difference in the search topology. For this reason, we proposed to do away with Eq. 3, and introduce it as a combination of exponential (Eq. 4) and linear update (Eq. 5) as follows:

$$r_1 = M \times e^{(\log(\frac{\min M}{M}) \times \frac{t}{T})}, \quad r_4 < 0.5 \quad (4)$$

$$r_i = M \times \left(1 - \frac{t}{T}\right), \quad r_4 \geq 0.5 \quad (5)$$

Thus, the pseudo code for the enhanced SCA algorithm can be seen in Fig. 4.

We maintain the use of  $r_4$  as probability switch between exponential or linear update of  $r_1$ . However, we introduce a constant value minimum  $M$  which indicates

<p>Input: The population of solutions <math>X = \{X_1, X_2... X_D\}</math> and the constant magnitude <math>M</math>  Output: The best solution <math>X_{best}</math></p> <p>[1]. <b>Begin</b></p> <p>[2]. Random initialization of population <math>X = \{X_1, X_2... X_D\}</math></p> <p>[3]. <b>While</b> (Not stopping criteria)</p> <p>[4].     Initialize <math>r_i</math> using Eq. 4 or Eq. 5</p> <p>[5].     <b>For</b> iter = 1 until iter <math>\leq</math> M (max iteration)</p> <p>[6].     <b>For</b> population count = 1 until the count <math>\leq</math> population size</p> <p>[7].         Evaluate each solution within <math>X</math> according to fitness function</p> <p>[8].     Update the best solution obtain so far, <math>P_i^t = X_{best}</math></p> <p>[9].     Generate values for <math>r_2, r_3, r_4</math> within the interval [0,1] randomly</p> <p>[10].         Evaluate Eq. 1 or Eq. 2 for updating position of each solution within <math>X</math></p> <p>[11].         Evaluate Eq. 4 or Eq. 5 for updating <math>r_i</math> adaptively</p> <p>[12].     <b>End For</b></p> <p>[13].     <b>End For</b></p> <p>[14].     <b>End While</b></p> <p>[15].     Obtain and display the best solution (<math>X_{best}</math>)</p> <p>[16]. <b>End</b></p>
---

**Fig. 4** Enhanced sine cosine algorithm pseudo code

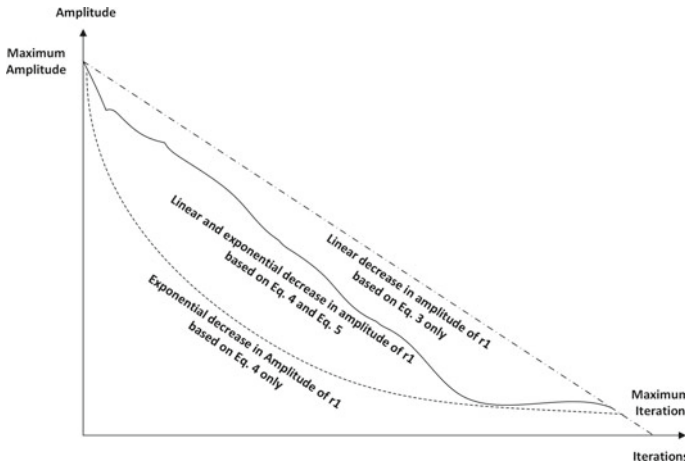


Fig. 5 The effect on  $r_1$  magnitude update

the most minimum possible displacement ( $\Delta$ ) required in the search process. We analyze the effect of the modification on the value of  $r_1$  during the search process in Fig. 5. We can see that using only Eq. 3 yields a linear update (sparse dotted line) while using only Eq. 4 yields an exponential update (close dotted line). A combination of Eqs. 3 and 4 yield a more realistic update of  $r_1$ .

## 5 Experimental Results and Conclusion

In order to evaluate its performance, we compare the performance of enhanced SCA against other t-way strategies based on parameter free meta-heuristic algorithms including original SCA [5], TLBO [3] and Jaya [4]. Performance evaluation criteria encompass size (i.e., optimal test suite size) and time (i.e., test suite generation time). Five CAs:  $CA_1 = CA(N; 2, 3^{13})$ ;  $CA_2 = CA(N; 2, 10^5)$ ;  $CA_3 = CA(N; 2, 10^{10})$ ;  $CA_4 = CA(N; 3, 3^6)$ ;  $CA_5 = CA(N; 3, 6^6)$ ;  $CA_6 = CA(N; 3, 10^6)$  and one MCA:  $MCA_7 = MCA(N; 3, 5^2 4^2 3^2)$  are selected to gauge the performance of the proposed strategy against its counterparts. Experimental results are presented in Table 1; each cell displays the minimum (i.e., best) test suite size and the average suite size for each competing strategy. Best results obtained by each strategy are marked with bold text. For each result reported here, all strategies are executed 20 times. This ensures that the results meet statistical significance. Finally, population size and number iterations are two common parameters of meta-heuristic algorithms. In this study, population size and number of iterations are set to 40 and 100, respectively for all the implemented meta-heuristic algorithms as well as the proposed algorithm. The maximum value for constant  $M$  of SCA is set as the largest parameter for each covering array. All the experiments are conducted on a Windows 10 desktop



**Table 1** Comparison with other parameter free meta-heuristic algorithms

CA	TLBO			Jaya			Original sine cosine algorithm			Enhanced sine cosine algorithm		
	Size		Ave time (s)	Size		Ave time (s)	Size		Ave time (s)	Size		Ave time (s)
	Best	Ave		Best	Ave		Best	Ave		Best	Ave	
CA <sub>1</sub>	<b>18</b>	<b>18.8</b>	70.48	19	19.2	31.39	20	21.80	16.25	21	21.80	<b>16.45</b>
CA <sub>2</sub>	<b>117</b>	119.5	78.24	<b>117</b>	120.7	90.19	118	119.30	22.39	<b>117</b>	<b>119.0</b>	<b>21.16</b>
CA <sub>3</sub>	155	157.20	116.49	157	172.05	86.71	156	157.35	77.18	<b>153</b>	<b>157.10</b>	<b>71.21</b>
CA <sub>4</sub>	<b>33</b>	38.85	43.32	<b>33</b>	38.90	<b>12.17</b>	<b>33</b>	<b>37.75</b>	13.71	<b>33</b>	38.20	13.64
CA <sub>5</sub>	323	326.70	165.28	323	327.40	95.70	<b>322</b>	326.20	88.22	323	<b>326.15</b>	<b>84.10</b>
CA <sub>6</sub>	<b>1481</b>	1496.50	999.65	1483	1499.25	<b>777.10</b>	1482	1486.80	780.11	<b>1481</b>	<b>1486.20</b>	779.89
MCA <sub>7</sub>	<b>100</b>	<b>108.8</b>	86.19	<b>100</b>	116.3	105.05	101	122.40	27.30	<b>100</b>	115.30	<b>24.21</b>

computer with 2.81 GHz Core i7 CPU, 8 GB DDR3 RAM, and 512 MB Flash HDD. Moreover, Java is the implementation language for the all the strategies and their related algorithms. The complete results can be seen in Table 1.

The complete results can be seen in Table 1. Three main observation can be highlighted here. Firstly, the performance of enhanced SCA outperforms its predecessor in term of getting the most minimum test suite size. In fact, the performance of enhanced SCA also outperforms Jaya and matches with that of TLBO (in terms of getting the most number of cases with minimum test suite size). Secondly, in terms of average test suite size, the enhanced SCA produces competitive results with other algorithms as the delta difference between best test suite sizes is well within not more than 15%. As far as average execution time is concerned, SCA and its enhancement outperform TLBO and Jaya. This finding indicates that the computation of SCA is lightweight (as all the implementation uses the same language implementation and adopts the same data structure).

Summing up, our work has elaborated on the enhancement of the SCA. Then, we have adopted the SCA into an optimization problem related to the t-way test generation problem. Our results have been promising as we have demonstrated an improved performance of the SCA against its predecessor. In fact, the enhanced SCA also can match the performance of other parameter free algorithms like TLBO and Jaya. As part of future work, we are also looking to adopt our enhanced SCA for software module clustering problems as well as constraints software product line test generation problem.

**Acknowledgements** The work reported in this paper is funded by Fundamental Research Grant from Ministry of Higher Education Malaysia titled: A Reinforcement Learning Sine Cosine based Strategy for Combinatorial Test Suite Generation. We thank MOHE for the contribution and support, Grant Number: RDU170103.

## References

1. Ahmed BS, Sahib MA, Gambardella LM, Afzal W, Zamli KZ (2016) Optimum design of PI $\lambda$ D $\mu$  controller for an automatic voltage regulator system using combinatorial test design. *PLoS ONE* 11(11):e0166150
2. Kennedy J, Eberhart R (1995) Particle swarm optimization. In: *Proceedings of the IEEE international conference on neural networks*. IEEE, Perth, Australia, pp 1942–1948
3. Rao RV, Sivasani VJ, Vakharia DP (2011) Teaching learning-based optimization: a novel method for constrained mechanical design optimization problems. *Comput Aided Des* 43(3):303–315
4. Rao RV (2016) Jaya: a simple and new optimization algorithm for solving constrained and unconstrained optimization problems. *Int J Ind Eng Comput* 7(1):19–24
5. Mirjalili S (2016) SCA: a sine cosine algorithm for solving optimization problems. *Journal* 96:120–133
6. Ahmed BS, Zamli KZ, Afzal W, Bures M (2017) Constrained interaction testing: a systematic literature study. *IEEE Access* 5
7. Zamli KZ, Din F, Ahmed BS, Bures M (2018) A hybrid Q-learning sine-cosine-based strategy for addressing the combinatorial test suite minimization problem. *PLoS ONE* 13(5):e0195675

8. Alsewari AA, Zamli KZ (2011) Interaction test data generation using Harmony Search Algorithm. In: Proceedings of the IEEE symposium on industrial electronics and applications, IEEE, Langkawi, Malaysia, pp 559–564
9. Younis MI, Zamli KZ, Isa NAM (2008) Algebraic strategy to generate pairwise test set for prime number parameters and variables. In: Proceedings of the international symposium on information technology. IEEE, Kuala Lumpur, Malaysia, pp 1–4
10. Hartman A, Raskin L (2004) Problems and algorithms for covering arrays. *Discret Math* 284(1):149–156
11. Mandl R (1985) Orthogonal latin squares: an application of experiment design to compiler testing. *Commun ACM* 28(10):1054–1058
12. Bush KA (1952) Orthogonal arrays of index unity. *Ann Math Stat* 23(3):426–434
13. Younis MI, Zamli KZ, Isa NAM (2008) A strategy for grid based t-way test data generation. In: Proceedings of the distributed framework and applications. IEEE, Penang, Malaysia, pp 73–78
14. Zamli KZ, Din F, Baharom S, Ahmed (2017) Fuzzy adaptive teaching learning-based optimization strategy for the problem of generating mixed strength t-way test suites. *Eng Appl Artif Intell* 59:35–50
15. Forbes M, Lawrence J, Lei Y, Kacker RN, Kuhn DR (2008) Refining the in-parameter-order strategy for constructing covering arrays. *J Res Nat Inst Stand Technol* 113(5):287
16. Lei Y, Kacker R, Kuhn DR, Okun V, Lawrence J (2007) IPOG: a general strategy for t-way software testing. In: 14th annual IEEE international conference and workshops on the engineering of computer-based systems, 2007. ECBS'07. IEEE, pp 549–556
17. Lei Y, Kacker R, Kuhn DR, Okun V, Lawrence J (2008) IPOG/IPOG-D: efficient test generation for multi-way combinatorial testing. *Softw Test Verif Reliability* 18(3):125–148
18. Cohen DM, Dalal SR, Fredman ML, Patton GC (1997) The AETG system: an approach to testing based on combinatorial design. *IEEE Trans Softw Eng* 23(7):437–444
19. Jenkins B (2003) Jenny. Available [Online]: <http://www.burtleburtle.net/bob/math/>. Accessed 16 Dec 2018
20. Williams A (2008) TConfig. Available [Online]: <http://www.site.uottawa.ca/~awilliam/>. Accessed 16 Dec 2018
21. Hartman A, Klinger T, Raskin L (2010) IBM intelligent test case handler. *Discret Mathematics* 284(1):149–156
22. Cohen MB, Colbourn CJ, Ling ACH (2008) Constructing strength three covering arrays with augmented annealing. *Discret Mathematics* 308(13):2709–2722
23. Shiba T, Tsuchiya T, Kikuno T (2004) Using artificial life techniques to generate test cases for combinatorial testing. In: Proceedings of the 28th annual international conference on computer software and applications. IEEE, Hong Kong, China, pp 72–77
24. Ahmed BS, Zamli KZ (2011) A review of covering arrays and their application to software testing. *J Comput Sci* 7(9):1375–1385
25. Alsewari ARA, Zamli KZ (2012) Design and implementation of a harmony-search-based variable-strength t-way testing strategy with constraints support. *Inf Softw Technol* 54(6):553–568
26. Nasser AB, Zamli KZ, Alsewari AA, Ahmed BS (2018) An elitist-flower pollination-based strategy for constructing sequence and sequence-less t-way test suite. *Int J Bio-Inspired Computation* 12(2):115–127
27. Nasser AB, Sariara YA, Alsewari ARA, Zamli KZ (2015) A cuckoo search based pairwise strategy for combinatorial testing problem. *J Theor Appl Inf Technol* 82(1)
28. Alsariara YA, Zamli KZ (2015) A bat-inspired strategy for t-way interaction testing. *Adv Sci Lett* 21(7):2281–2284
29. Zamli KZ, Alkazemi BY, Kendall G (2016) A tabu search hyper-heuristic strategy for t-way test suite generation. *Appl Soft Comput* 44:57–74
30. Nasser AB, Zamli KZ, Alsewari AA, Ahmed BS (2018) Hybrid flower pollination algorithm strategies for t-way test suite generation. *PLoS ONE* 13(5):e0195187

31. Zamli KZ, Din F, Kendall G, Ahmed BS (2017) An experimental study of hyper-heuristic selection and acceptance mechanism for combinatorial t-way test suite generation. *Inf Sci* 399:121–153
32. Suid MH, Ahmad MA, Ismail MRTR, Ghazali MR, Irawan A, Tumari MZ (2018) An improved sine cosine algorithm for solving optimization problems. In: *IEEE conference on systems, process and control*. IEEE, Melaka, Malaysia, pp 209–213
33. Qu C, Zeng Z, Dai J, Yi Z, He W (2018) A modified sine-cosine algorithm based on neighborhood search and greedy levy mutation. *Comput Intell Neurosci*

# Classification of Lubricant Oil Geometrical Odor-Profile Using Cased-Based Reasoning



**Suhaimi Mohd Daud, Muhammad Sharfi Najib, Nurdiyana Zahed, Muhammad Faruqi Zahari, Nur Farina Hamidon Majid, Suziyanti Zaib, Mujahid Mohamad, Addie Irawan and Hadi Manap**

**Abstract** The lubricant oil is one of the petroleum refinery product. The lubricant oil usage is very important in order to make sure the operation of vehicle engine at the highest performance. In determining the lubricant oil adulteration level, there were so many methods of classification using various instruments such as ICP-MS, AAS and Dielectric Spectroscopy. E-nose is one of the significant instrument using odor approach to classify the odor of the sample. The purpose of this study is to classify the lubricant oil degradation level based on odor-pattern that extracted from the odor data that collected using electronic nose. The lubricant oil sample consists of 4 levels of lubricant oil adulteration level which are virgin lube oil, 3000, 7000 and 10,000 km lubricant oil sample. Pre-processing technique was applied by implementing normalization formulation in order to standardize the odor raw data. Normalized data very beneficial in features extraction process, so that the significant odor-patterns can be established. In this study, geometry average calculation method was applied in order to establish the odor-profile for lubricant oil sample. The odor-pattern then were

---

S. M. Daud (✉) · M. S. Najib · N. Zahed · M. F. Zahari · N. F. H. Majid · S. Zaib · M. Mohamad · A. Irawan · H. Manap  
Universiti Malaysia Pahang, 26600 Pekan, Pahang, Malaysia  
e-mail: [suhaimimohddaud@gmail.com](mailto:suhaimimohddaud@gmail.com)

M. S. Najib  
e-mail: [sharfi@ump.edu.my](mailto:sharfi@ump.edu.my)

N. Zahed  
e-mail: [nurdiyanazahed92@gmail.com](mailto:nurdiyanazahed92@gmail.com)

N. F. H. Majid  
e-mail: [nurfarinahamidonmajid@gmail.com](mailto:nurfarinahamidonmajid@gmail.com)

S. Zaib  
e-mail: [suziyantizaib@gmail.com](mailto:suziyantizaib@gmail.com)

M. Mohamad  
e-mail: [mujahidmohamadtaha@yahoo.com.my](mailto:mujahidmohamadtaha@yahoo.com.my)

A. Irawan  
e-mail: [addieirawan@ump.edu.my](mailto:addieirawan@ump.edu.my)

H. Manap  
e-mail: [hadi@ump.edu.my](mailto:hadi@ump.edu.my)

classified using case-based reasoning classifier. Based on the classification results, it shows that the accuracy of the classification is 100% correct classification.

**Keywords** E-nose · Lubricant oil · Geometric mean · Odor-features · Case-based reasoning

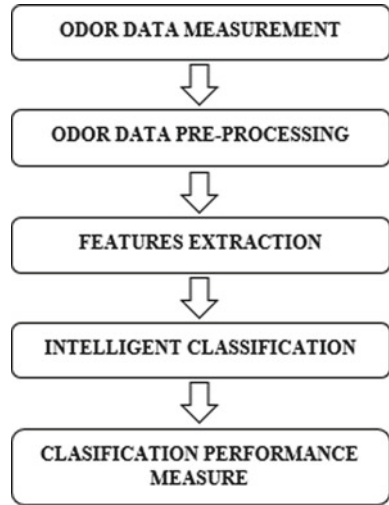
## 1 Introduction

Lubricant oil is one of the largest production of petroleum refinery and it is one of the largest areas of research and innovation [1–4]. The analysis on lubricant oil is very important to ensure the engine at the best performance level by protecting it from the effects of heat, reducing friction between two moving parts and avoiding the entry of contaminants [3]. There are many techniques used for lubricant oil analysis in order to monitor the quality of lubricant oil such as Dielectric Spectroscopy, ICP-OES, AAS and ICP-MS [5–9]. However, user faced complexity on the experimental procedure, high cost of installation and only authorized chemist can operate these instruments [10]. Because of that, electronic nose was chosen as the alternative way to determine and analyze the degradation level of lubricant oil samples based on the geometrical odor-profile in order to overcome the limitations that occurred in the existing method. The usage of e-nose in the automotive industry is a significant approach in order to control its quality and performance based on the degree of aroma intensity and the level of lubricant oil adulteration identification [11, 12]. Thus, the classification of lubricant oil based on odor-profile using electronic nose is very useful with the combination of geometric mean features extraction technique and Case-based Reasoning classification algorithm in the e-nose system [13]. Case-based Reasoning (CBR) is an approach to solve the problem by using the past cases and experiences by obtaining the similarity percentages by comparing the current case or unknown sample with the database of lubricant oil [14, 15]. CBR has its own specialty by providing good classification solutions and suitable for a weak domain field. Compared to other classification techniques, CBR does not have data splitting ratio (training data and testing data) and reuses the previous solution or past experience in order to solve current problems by implementing 4 beneficial CBR cycle which are retrieve, reuse, revise and retain [16–19]. This paper presents a significant classification technique of lubricant oil adulteration level based on geometrical odor-profile using e-nose instrument and Case-based Reasoning classifier.

## 2 Methodology

Figure 1 shows the overall flowchart for lubricant oil geometrical odor-profile classification study using CBR.

**Fig. 1** Overall flowchart for lubricant oil odor-profile classification



The first stage of the study was done by collecting the raw data of lubricant oil odor using e-nose hardware. Next, data pre-processing and features extraction step was performed by using normalization and geometric mean calculation technique respectively in order to establish the lubricant oil odor-profile. Afterward, the odor-profile were then classified using CBR classification technique. Lastly, the performance of the classification result was evaluated.

### 2.1 Data Measurement

Figure 2 shows the experimental setup for odor raw data measurement using e-nose. This instrument consists of a set of the chemical sensor array, odor chamber, e-nose suction pump and microcontroller. 5 W/40 grade from semi-synthetic oil type was used in this study as the sample. The samples consist of 4 different levels of oil degradation based on vehicle journey mileage which are virgin oil (0 km) and 3 used oil samples (3000, 7000 and 10,000 km).

The experiment started by placing a volume of 3 mL of lubricant oil sample into the sample dish for odor data recording process. 3 mL of lubricant oil sample is

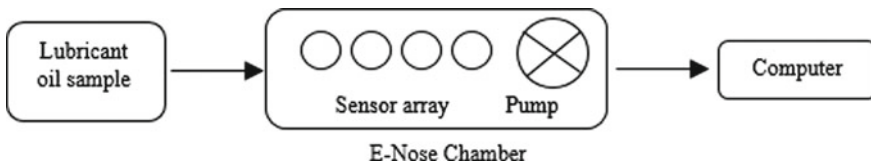


**Fig. 2** Electronic nose experimental setup

**Table 1** Template table of lubricant oil odor raw data

Data measurement	S1	S2	S3	S4
1	DM <sub>11</sub>	DM <sub>12</sub>	DM <sub>13</sub>	DM <sub>14</sub>
2	DM <sub>21</sub>	DM <sub>22</sub>	DM <sub>23</sub>	DM <sub>24</sub>
.	.	.	.	.
.	.	.	.	.
1000	DM <sub>10001</sub>	DM <sub>10002</sub>	DM <sub>10003</sub>	DM <sub>10004</sub>

sufficient and volatile for enough for odor data collection since the sample dish size suitable for 3 mL volume sample. The suction pump that located inside the upper part of e-nose sucks the odor into the e-nose chamber and the sensor array played its role by taking the data reading of lubricant oil odor. The data were sent to computer via USB cable for data monitoring and data storage purpose. 2 min were spent for each experiment, so that 200 data measurements (DMs) were able to be collected within this period of time. 5 repeated experiments were done for every sample so that the data can be calculated by using geometric mean formulation. The raw data collected will then be tabulated in Table 1.

## 2.2 Data Pre-Processing

The raw data then were normalized by using Eq. (1). The normalized value can be obtained by dividing every row of the raw data with the highest value from its own row. Thus, the value will be standardized in the range between zeros to one (0–1). The normalized value is very useful for odor-profile extraction.

$$R' = \frac{R}{R_{\max}} \quad (1)$$

## 2.3 Feature Extraction

From the normalized value, the features of each sample were extracted. The normalized value then was calculated using the geometrical mean as shown in Eq. (2). Then, the geo-mean normalized value was clustered into 40 cases. 10 cases represent for each sample (0 km, 3000 km, 7000 km and 10,000 km) respectively. The cases of each group were tabulated and stored into CBR memory as “stored cases” or the “previous experiences” for the classification process.



$$GM = \left( \prod_{i=1}^n a_i \right)^{\frac{1}{n}} \tag{2}$$

### 2.4 Intelligent Classification

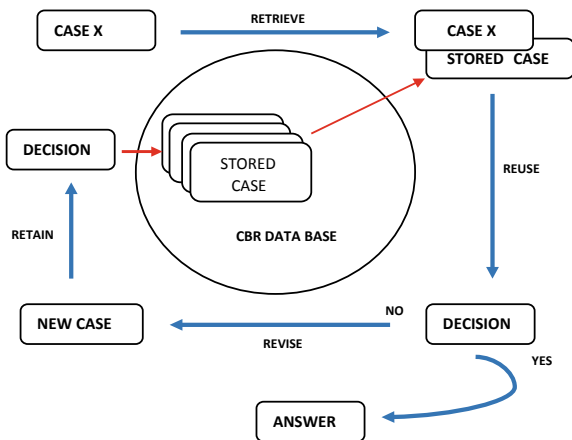
Case-based Reasoning (CBR) is one of the well-known classifier technique was used in this study as classifier. 4 cycles of CBR which are retrieve, reuse, revise and retain were used in order to perform the classification.

The cycle shown in Fig. 3 starts with the unknown lubricant oil that represents the current case. The odor-profile from the unknown oil sample went through the retrieval phase to retrieve the stored cases inside the stored case database. Since CBR is learning from previous cases, the system compared the unknown odor-profile oil sample with the stored odor-profile of previous cases. If the unknown sample has high similarity percentage with stored oil sample, the system will reuse the information from stored case to give a decision or answer. This classification technique very different than other classification technique (ANN, K-NN) because this technique requires no data training.

In Eq. (3), T and S represent the target case and source case respectively, n is the number of attribution for lubricant oil sample, i is the single attribution for each case, f is the similarity function formulation for lubricant oil sample and w represents the weight of each attribution.

$$Similarity(T, S) = \frac{\sum_{i=1}^n f(T_i, S_i) \times w_i}{\sum_{i=1}^n w_i} \tag{3}$$

Fig. 3 CBR cycle for lubricant oil classification



## 2.5 Performance Measure

Confusion matrix is one of the promising method used by various researcher in order to measure the performance of classification for any intelligent classifier. Equation (4)–(7) was used in order to determine the overall accuracy (ACC), true positive rate (TPR), true negative rate (TNR), and positive predictive value (PPV) for overall lubricant oil sample classification process.

$$TPR = \frac{TP}{TP + FN} \quad (4)$$

$$TNR = \frac{TN}{TN + FP} \quad (5)$$

$$PPV = \frac{TP}{TP + FP} \quad (6)$$

$$ACC = \frac{TP + TN}{P + N} \quad (7)$$

True Positive Rate (TPR) also known as sensitivity of the classification was calculated by dividing the true positive value of classification result with the summation of true positive (TP) and false negative (FN) of the classification. The formulation of sensitivity follows the Eq. (4) above. True Negative Rate (TNR) formulation can be referred to Eq. (5) above. This is also known as specificity of the CBR classification. It was calculated by dividing true negative (TN) with the summation of false positive (FP) and true negative (TN). While, for Positive Predictive Value (PPV) or precision of the classification, it was determined by dividing true positive (TP) with the summation of true positive (FP) and false positive (FP). Last but not least, for the accuracy (ACC) of the classification was calculated by dividing the summation of true positive and true negative with total case (P+N).

P, N, TP, TN, FP and FN in this study focus on the result of CBR voting process. For TP, let say that these cases were predicted 'A', then the actual result is also 'A'. Same concept also applied in TN which were that the cases were predicted 'B', then the actual result is also 'B'. For FP, the predicted result is 'A'. However, the actual result is 'B' and same goes to FN. The predicted results were 'B', but the actual result is 'A'. The accuracy measurement in this study is performed to measure the performance of the CBR accuracy based on lubricant oil samples and how often the correct classification occurs. By other hand, the measurement for sensitivity is calculated the number of "yes" prediction when the case is truly "yes". Next is specificity is evaluated by calculating the total of "No" prediction when the case is actually "No".

### 3 Result and Discussion

Figure 4 below shows the raw data measurement against sensor array for 4 lubricant oil sample. 4 different lubricant oil samples consist of 0 km (virgin oil), 3000, 7000 and 10,000 km lubricant oil sample. Y-axis indicates the raw data measurement value which is in resistance value while the X-axis indicates the sensor array. S1, S2, S3 and S4 represents sensor 1, sensor 2, sensor 3 and sensor 4 respectively that installed in the e-nose.

The maximum sensor reading that recorded by e-nose for all samples is at sensor S1 while S3 shows the minimum sensor reading for all oil samples. Raw odor data containing  $1000 \times 4$  data measurement for each sample. The total of data measurement for all samples are  $4000 \times 4$  data measurement.

#### 3.1 Data Normalization and Odor-Pattern Establishment Process

Previously,  $4000 \times 4$  data measurements were collected during the experiment based on 4 lubricant oil samples. In order to perform pre-processing technique on the data, normalization formulation was performed in order to standardize the data.

Figure 5 shows the normalized data for 0, 3000, 7000 and 10,000 km lubricant oil sample. Y-axis indicates the normalized value while the X-axis indicates the sensor array. S1, S2, S3 and S4 represents sensor 1, sensor 2, sensor 3 and sensor 4 respectively that installed in the e-nose. Normalization formulation technique was

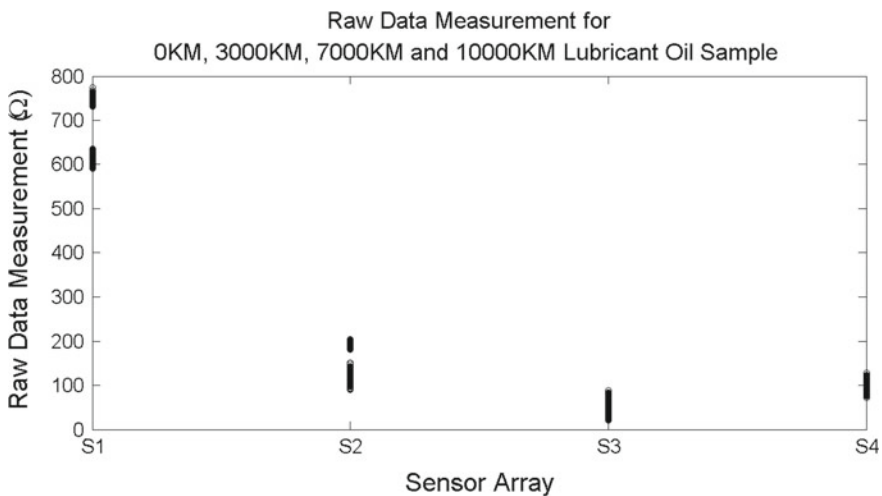


Fig. 4 Raw data measurement for 0, 3000, 7000 and 10,000 km lubricant oil sample

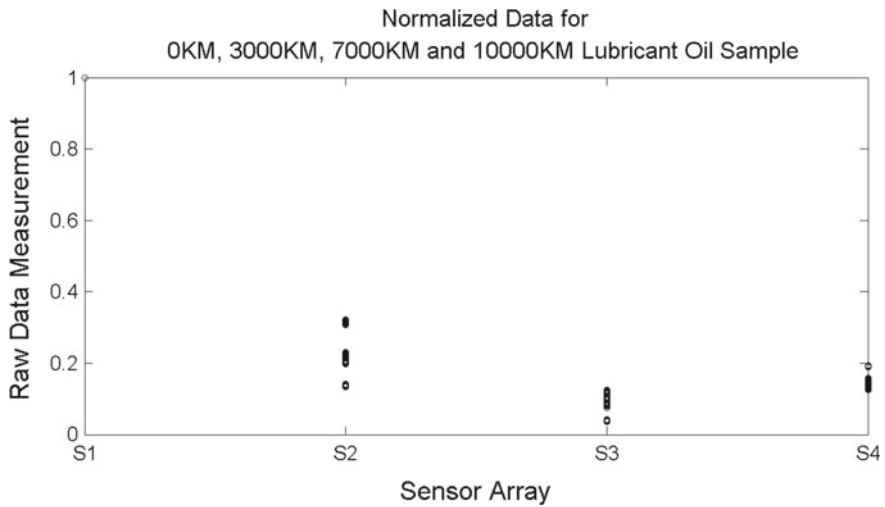


Fig. 5 Normalized data for 0, 3000, 7000 and 10,000 km lubricant oil sample

performed by dividing every value in every row of data measurements with the maximum value from its own row. 4000 normalized data then were regrouped into 4 sample groups that represent 0, 3000, 7000 and 10,000 km lube oil. Next, 1000 normalized data per group were clustered into 10 cases.

Figure 6 shows the graph of normalized value against sensor array for 0, 3000, 7000 and 10,000 km lubricant oil sample using geometric mean. The X-axis indicates the sensor array and Y-axis portray the normalized value of the sensor resistance

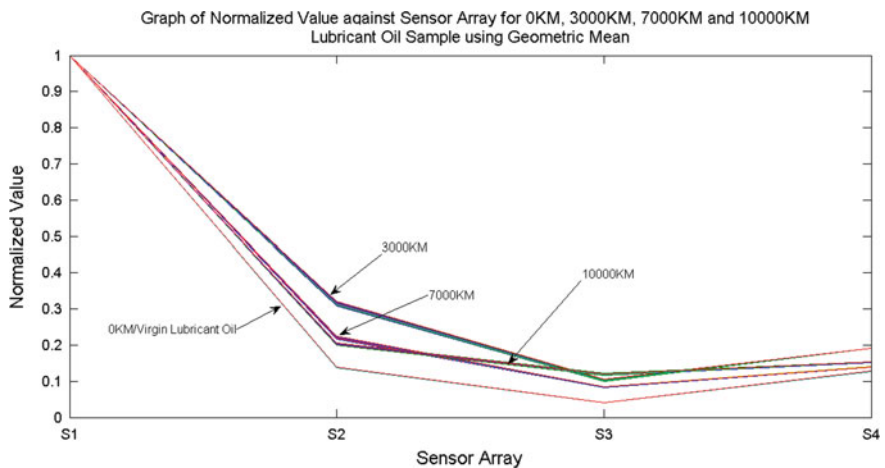


Fig. 6 Graph of normalized value against sensor array for 0, 3000, 7000 and 10,000 km lubricant oil sample

response. In this graph, 4 lines were plotted that indicated as 4 sensors used in the e-nose. In S2, S3 and S4, it shows the changes in the normalized value respectively when the oil used is in different mileage. Thus, the lubricant oil odor volatility is different when the mileage change. It shows that the degree of lubricant oil aroma changes when the lubricant oil changes due to the movement of the engine. So that, the mileage of the lubricant oil influenced the changes of the degree of lubricant oil odor. Table 3 shows the CBR case library for lubricant oil samples. The table consists of 40 cases that represent 10 cases for every sample. First 10 cases (case\_01 until case\_10) represents 0 km oil sample. For the next 10 cases (case\_11 until case\_20), (case\_21 until case\_30) and (case\_31 until case\_40) represents 3000 km, 7000 km and 10,000 km lubricant oil sample respectively. S1, S2, S3 and S4 are the sensors installed in the e-nose. These cases will act as “stored cases” and will be included in the CBR memory in order to perform the classification process.

Refer to the table above, the maximum normalized value entire column S1 that shows the value of ‘1.0000’, while the lowest normalized value is in the whole S3 column for all cases which is showing the value in the range of 0.039904 to 0.121460. Column S1 consists of the same value ‘1.0000’ because of the previous raw data were divided with the highest value in each row. Since the highest value for each row in every sample fell on S1, every row of the data measurement need to be divided with the S1 value. Thus, when then the data measurement was normalized, it was resulting value ‘1.0000’ in column S1 in Table 2 for every row of normalized data. The sensors that set up in the e-nose have different sensitivity.

Table 3 shows the CBR similarity formulation. Attributes S1—S4 indicates as the sensors used in the e-nose. The ‘source’ is the stored case or the database of lubricant oil sample in CBR classification system. ‘Target’ is the current case or case that need to be tested. The ‘similarity’ of two cases below is calculated using Eq. (3) which is similarity formulation between 2 cases. Normalized weight was calculated by dividing each weight with the total weight. The similarity calculation for every sensor was added in order to obtain the similarity percentage between 2 cases. In order conduct the odor-profile classification, the expert of lubricant oil need to determine the local weight for each attribution and the value of the weight can be heuristically changed in order to get a better classification result.

### 3.2 CBR Performance Measure

Table 4 shows the confusion matrix for CBR voting results. For every sample,  $k = 1$ ,  $k = 2$  and  $k = 3$  were voted to be in their own group. The total case for this study after 3 times of voting process for every case is 120 cases.

Each oil sample group consists of 30 cases. In confusion matrix table, there is actual case and predicted case. Actual case is the real case of the sample. While for predicted case, it comes from the CBR formulation and voting part, it shows that 30 cases for each sample were predicted to be in their group. Thus, total true positive for each group is 30 and the total true positive for all samples is 120 (Table 5).

**Table 2** Odor-profile for 0, 3000, 7000 and 10,000 km lubricant oil sample

Sample	Case ID	S1	S2	S3	S4
0 km	Case 1	1.000	0.136153	0.039918	0.127198
	Case 2	1.0000	0.136639	0.040225	0.127476
	Case 3	1.0000	0.136125	0.040152	0.127134
	Case 4	1.0000	0.137055	0.040381	0.127570
	Case 5	1.0000	0.138128	0.039904	0.127858
	Case 6	1.0000	0.138689	0.040212	0.128040
	Case 7	1.0000	0.138751	0.040573	0.128081
	Case 8	1.0000	0.139510	0.040432	0.127867
	Case 9	1.0000	0.13980	0.040273	0.128229
	Case 10	1.0000	0.139314	0.040267	0.127872
3000 km	Case 11	1.0000	0.308969	0.099891	0.191804
	Case 12	1.0000	0.311059	0.100362	0.191749
	Case 13	1.0000	0.312344	0.101219	0.191772
	Case 14	1.0000	0.313369	0.101685	0.191374
	Case 15	1.0000	0.315138	0.102972	0.191086
	Case 16	1.0000	0.316236	0.103533	0.191024
	Case 17	1.0000	0.317810	0.103660	0.191444
	Case 18	1.0000	0.319078	0.104383	0.191589
	Case 19	1.0000	0.320085	0.104591	0.191469
	Case 20	1.0000	0.321243	0.105341	0.191562
7000 km	Case 21	1.0000	0.217427	0.082348	0.142026
	Case 22	1.0000	0.218267	0.082946	0.140250
	Case 23	1.0000	0.219537	0.082699	0.141567
	Case 24	1.0000	0.220219	0.083191	0.141115
	Case 25	1.0000	0.221629	0.084593	0.141507
	Case 26	1.0000	0.222053	0.084265	0.141140
	Case 27	1.0000	0.223360	0.084793	0.139598
	Case 28	1.0000	0.223760	0.083570	0.140133
	Case 29	1.0000	0.224374	0.085460	0.139617
	Case 30	1.0000	0.225029	0.085570	0.139677
10,000 km	Case 31	1.0000	0.199333	0.115911	0.152485
	Case 32	1.0000	0.200636	0.116869	0.152815
	Case 33	1.0000	0.201255	0.117587	0.152978
	Case 34	1.0000	0.202981	0.118163	0.152871
	Case 35	1.0000	0.202818	0.119314	0.153016
	Case 36	1.0000	0.203917	0.120748	0.153454

(continued)

**Table 2** (continued)

Sample	Case ID	S1	S2	S3	S4
	Case 37	1.0000	0.204478	0.120179	0.153727
	Case 38	1.0000	0.204872	0.120521	0.153771
	Case 39	1.0000	0.205460	0.121460	0.154202
	Case 40	1.0000	0.205569	0.120684	0.153416

**Table 3** CBR formulation table

Sensor	Source	Target	Similarity	Weight	Norm weight	Norm_w*sim
S1	1.0000	1.0000	1.0000	1	0.25	0.24999975
S2	0.13615	0.136639	0.999514	1	0.25	0.24987825
S3	0.03991	0.040222	0.999691	1	0.25	0.24992225
S4	0.12719	0.127476	0.999722	1	0.25	0.24993025
Percentage similarity between 2 cases (%)						<b>99.97</b>

**Table 4** Confusion matrix table

Total case = 120		Predicted case			
		0 km	3000 km	7000 km	10,000 km
Actual case	<b>0 km</b>	30	0	0	0
	<b>3000 km</b>	0	30	0	0
	<b>7000 km</b>	0	0	30	0
	<b>10,000 km</b>	0	0	0	30

**Table 5** CBR performance evaluation

Performance evaluation	0 km	3000 km	7000 km	10,000 km
Total case	30	30	30	30
True positive	30	30	30	30
False positive	0	0	0	0
True negative	90	90	90	90
False negative	0	0	0	0
TPR = $TP/(TP+FN)*100\%$	100	100	100	100
TNR = $[TN/(TN+FP)]*100\%$	100	100	100	100
PPV = $[TP/(TP+FP)]*100\%$	100	100	100	100
ACC = $[(TP+TN)/(P+N)]*100\%$	100	100	100	100
Overall sensitivity (%)	<b>100</b>			
Overall specificity (%)	<b>100</b>			
Overall precision (%)	<b>100</b>			
Overall accuracy (%)	<b>100</b>			

The total positive rate, total negative rate, positive predictive value and the accuracy of every sample showed 100% respectively for each of the oil sample. The overall sensitivity, specificity, precision and accuracy show 100% for lubricant oil sample classification using the CBR classification technique.

## 4 Conclusion

This study demonstrates that 4 lubricant oil samples which are 0, 3000, 7000 and 3000 km have a different smell-print between each sample. The differences of degradation level between samples were caused by the changes of lubricant oil contents and properties that influenced the changes of aroma and odor-profile of the samples. Even though the lubricant odor-pattern plotted look similar between each other, The lubricant oil sample can be 100% correctly classified. CBR showed an excellent classification result by classifying the sample even the source cases that stored in the memory consist of small number of data. The classification of lubricant oil sample based on geometrical mean odor-profile using case-based reasoning classification technique has successfully achieved 100% correct classification.

**Acknowledgements** This research and development are supported by Universiti Malaysia Pahang (UMP) Research Grant (RDU180332)

## References

1. Comesaña-garcía Y, Cavado-osorio A, Linchenat-dennes E, Dago-morales Á (2013) Classification of kerosene using physicochemical data and multivariate techniques. *CENIC J Chem Sci* 44(1):13–22
2. Samsudin AR, Tin SL, Alif A, Robert KM, Tan CF (2012) Promising techniques of automotive engine lubrication oil monitoring system—a critical review towards enhancement. *Int J Eng Sci* 1(2):228–233
3. Kamal RS, Ahmed NS, Nasser AM (2013) Study the efficiency of some compounds as lubricating oil additives. *Appl Petrochemical Res* 3(1):1–8
4. Niculescu R, Iorga-Simăn V, Trică A, Clenci A (2016) Study on the engine oil's wear based on the flash point. In: *IOP conference series: materials science and engineering* 147(1)
5. Wolak A, Zajac G, Gołębiowski W (2019) Determination of the content of metals in used lubricating oils using AAS. *Pet Sci Technol* 37(1):93–102
6. Gong Y, Guan L, Feng X, Wang L, Yu X (2016) In-situ lubricating oil condition sensing method based on two-channel and differential dielectric spectroscopy combined with supervised hierarchical clustering analysis. *Chemom Intell Lab Syst* 158:155–164
7. Zali MA, Ahmad WKW, Retnam A, Catrina N (2015) Concentration of heavy metals in virgin, used, recovered and waste oil: a spectroscopic study. *Procedia Environ Scis* 201–204
8. Søndergaard J, Asmund G, Larsen MM (2015) Trace elements determination in seawater by ICP-MS with on-line pre-concentration on a Chelex-100 column using a 'standard' instrument setup. *MethodsX* 2(June):323–330
9. Usman AI, Seydou H, Abubakar A (2017) Validation of atomic absorption spectroscopy (AAS) for trace elements analysis of environmental samples. *Res Rev J Phys* 6(2):8–13



10. Carter JA, Barros AI, Nóbrega JA, Donati GL (2018) Traditional calibration methods in atomic spectrometry and new calibration strategies for inductively coupled plasma mass spectrometry. *Front Chem* 6:1–25
11. Mawardzi MFRM, Japper-Jaafar A, Najib MS, Daud SM, Ya TMYST (2019) Intelligent classification of waxy crude oil odor-profile at different temperature. *IOP Conf Ser Mater Sci Eng* 469(1):1–10
12. Daud SM, Najib MS, Zahed N (2016) Classification of lubricant oil odor-profile using case-based reasoning. In: *IEEE conference on systems, process and control (ICSPC2016)*, pp 16–18
13. Daud SM, Najib MS, Zahed N, Jusof MFM, Jusoh MFC, Hassim MIIN Special Issue. *J Fundam Appl Sci* 256–275
14. Mawardzi MFRM, Japper-Jaafar A, Najib MS, Daud SM, Ya TMYST (2019) Classification of waxy crude oil odor-profile using gas sensor array. *IOP Conf Ser Mater Sci Eng* 469(1):1–9
15. Zahed N, Najib MS, Fatin N, Nik N, Azhani M (2016) Classification of honey odor-profile using case-based reasoning technique (Cbr). *ARNP J Eng Appl Sci* 11(10):6675–6679
16. Zahed N, Najib MS (2016) Odour-Profile classification of gelam, acacia and tualang honey based on K-nearest neighbors technique. In: *The national conference for postgraduate research 2016, Universiti Malaysia Pahang*, pp 404–412
17. Zahari MF, Julius TA, Halim FA, Najib MS, Ghazali KH, Azoddein AAM (2015) Intelligent classification hazardous gas using sensors array. *J Adv Inf Technol* 6(4):233–237
18. Mohammed MA, Ibrahim DA (2016) Case based reasoning shell framework as decision support tool. *Indian J Sci Technol* 9:1–8
19. Choudhury N, Ara S (2016) A survey on case-based reasoning in medicine. *Int J Adv Comput Sci Appl* 7(8):136–144

# Optimization of Quaternion Based on Hybrid PID and $P_\omega$ Control



Balya Darohini, M. F. Abas, N. Md. Saad, Dwi Pebrianti, H. Ahmad, M. H. Ariff and M. R. Arshad

**Abstract** The aim of this article is to present an optimization of full non-linear quaternion based on hybrid control scheme using Genetic Algorithm (GA). A comprehensive objective is used to find novel solutions to design hybrid controller based on PID and  $P_\omega$  control so that the performance and functionality system and may be compromised. The proposed hybrid control algorithm and quadrotor attitude model have been implemented in the fully quaternion space without any conversion and calculations in the Euler's angles. In this paper, the optimized quaternion with fitness function composed of  $K_P$ ,  $K_I$ ,  $K_D$ , and  $P_\omega$  are proposed, and the output effective waveform is shown by simulations using MATLAB.

**Keywords** Genetic algorithm · Quaternion · UAV · PID controller · Crossover · Mutation

## 1 Introduction

Quadrotor has become very popular and it required complicated tasks that enable fast respond, efficient and reliable control algorithms under uncertain conditions. It is becoming very popular nowadays to use quaternion instead of Euler angles. It is possible to use quaternion feedback signal form to design linear and non-linear controllers of attitude and position. In the last decade, numerous new small flying unmanned vehicles have appeared. Among them are the mini UAVs of fix-wing type [1]. This type of UAVs is light enough to be handled with a single hand. VTOL based UAVs have also appeared which includes conventional helicopter [2], duct type [3], tilt-rotor [4], tri-rotor [5], six-rotor [5] and eight-rotor [6]. The increase of the amount of rotor in a single VTOL aircraft enables more weight to be carried.

---

B. Darohini · M. F. Abas (✉) · N. Md. Saad · D. Pebrianti · H. Ahmad · M. H. Ariff  
Faculty of Electrical and Electronics Engineering, Universiti Malaysia Pahang, 26600 Pekan,  
Pahang, Malaysia  
e-mail: [mfadhil@ump.edu.my](mailto:mfadhil@ump.edu.my)

M. R. Arshad  
School of Electrical & Electronic Engineering, Engineering Campus, Universiti Sains Malaysia,  
14300 Nibong Tebal, Penang, Malaysia

For an under-actuated system, the control algorithm should be highly robust and fast response. Many Euler angle-based control has been research on which varies from simple Proportional Integral Derivative (PID) to hybrid nonlinear control system such as sliding mode control with back-stepping control [7–12]. Control algorithm based on Euler angle is prone to gimbal lock. In order to overcome this problem, many researches on Quaternion angle-based control algorithm which specifically deal to increase robustness, adaptability, stability/detectability and accuracy [13–17].

In this paper, a new approach is proposed for the full nonlinear quaternion based on hybrid PID and  $P_\omega$  by optimization using GA, where  $K_P$ ,  $K_I$ ,  $K_D$ , and  $P_\omega$  are considered. First, the evaluation value  $K_P$ ,  $K_I$ ,  $K_D$ , and  $P_\omega$  to the fitness function in order to get an optimized model were introduced. Then GA can autonomously synthesize a model with simpler and enhance performance than a previous design.

In the next section, the fundamental properties and the corresponding algebra of the quaternion mathematics are being presented, while in Sect. 3 the quaternion-based quadrotor modeling is analyzed. In Sect. 4 the full quaternion-based control scheme is established and in Sect. 5 an overview of GA using MATLAB is described. Therefore, in Sect. 6 shows the simulation result of a new approach for the full nonlinear quaternion of an optimized model. Finally, Sect. 7 concludes.

## 2 Quaternion Math

The basic algebraic concept of quaternion going to be presented in this section for building the mathematical background for following the previous modeling as stated in [18] and the proposed control scheme. The reader is referred to the publications [18] for a more depth description and comprehensive analysis of this mathematical tool.

Equations (1) and (2) represent the most of two significance approaches. The  $q_1$  to  $q_3$  quaternion units are called the quaternion vector part, whereas  $q_0$  is the scalar part.

$$\mathbf{q} = q_0 + q_1\mathbf{i} + q_2\mathbf{j} + q_3\mathbf{k} \quad (1)$$

$$\mathbf{q} = [q_0q_1q_2q_3]^T \quad (2)$$

The result of Kronecker product, denoted as  $\otimes$  are the multiplication of two quaternions  $\mathbf{p}$  and  $\mathbf{q}$  are presented in the following equations. Whereas,  $\mathbf{p}$  represents one rotation and  $\mathbf{q}$  represents another rotation, while  $\mathbf{p} \otimes \mathbf{q}$  represents the combined rotation. Multiplication of quaternion is non-commutative.

$$\begin{aligned}
 \mathbf{p} \otimes \mathbf{q} &= \begin{bmatrix} p_0q_0 - p_1q_1 - p_2q_2 - p_3q_3 \\ p_0q_1 + p_1q_0 + p_2q_3 - p_3q_2 \\ p_0q_2 - p_1q_3 + p_2q_0 + p_3q_1 \\ p_0q_3 + p_1q_2 - p_2q_1 + p_3q_0 \end{bmatrix} \\
 \mathbf{p} \otimes \mathbf{q} &= \mathbf{Q}(\mathbf{p})\mathbf{q} = \begin{bmatrix} p_0 - p_1 - p_2 - p_3 \\ p_1p_0 - p_3p_2 \\ p_2p_3p_0 - p_1 \\ p_3 - p_2p_1p_0 \end{bmatrix} \begin{bmatrix} q_0 \\ q_1 \\ q_2 \\ q_3 \end{bmatrix} \\
 &= \bar{\mathbf{Q}}(\mathbf{p})\mathbf{q} = \begin{bmatrix} q_0 - q_1 - q_2 - q_3 \\ q_1q_0q_3 - q_2 \\ q_2 - q_3q_0q_1 \\ q_3q_2 - q_1q_0 \end{bmatrix} \begin{bmatrix} p_0 \\ p_1 \\ p_2 \\ p_3 \end{bmatrix}
 \end{aligned}$$

The norm/length of a quaternion is defined as shown in Eq. (3), for any complex number. Plus, the unit quaternion is unitary length of all presented quaternion approached.

$$\text{Norm}(\mathbf{q}) = \mathbf{q} = \sqrt{q_0^2 + q_1^2 + q_2^2 + q_3^2} \tag{3}$$

Meanwhile, quaternion complex conjugates are the same as normal complex numbers. The sign of the complex part is switched as in Eq. (4).

$$\text{Conj}(\mathbf{q}) = \mathbf{q}^* = [q_0 - q_1 - q_2 - q_3]^T \tag{4}$$

The inverse of a quaternion is defined as in Eq. (5), as the normal inverse of a complex number. Moreover, the inverse is the same as its conjugate if quaternion is unitary.

$$\text{Inv}(\mathbf{q}) = \mathbf{q}^{-1} = \frac{\mathbf{q}^*}{q^2} \tag{5}$$

The derivative of a quaternion requires some algebraic manipulation: (a) as in Eq. (6) in case that the angular velocity vector is in the fixed frame of reference, and (b) as in Eq. (7) if the angular velocity vector is in the body frame of reference.

$$\dot{\mathbf{q}}_\omega(\mathbf{q}, \omega) = \frac{1}{2}\mathbf{q} \otimes \begin{bmatrix} 0 \\ \omega \end{bmatrix} = \frac{1}{2}(\mathbf{Q})\mathbf{q} \begin{bmatrix} 0 \\ \omega \end{bmatrix} \tag{6}$$

$$\dot{\mathbf{q}}_{\omega'}(\mathbf{q}, \omega') = \frac{1}{2}\mathbf{q} \otimes \begin{bmatrix} 0 \\ \omega' \end{bmatrix} = \frac{1}{2}(\bar{\mathbf{Q}})\mathbf{q} \begin{bmatrix} 0 \\ \omega' \end{bmatrix} \tag{7}$$

where  $\omega = [\omega_x \omega_y \omega_z]^T$ . Quaternion can be used as a rotation operator if it's a unit quaternion. However, the transformation is built up by multiplication of normal

quaternion and conjugated quaternion as depicted in Eq. (8). Thus,  $\mathbf{q}$  is the rotated vector  $\mathbf{v}$  from the fixed frame to the body frame.

$$\omega = \mathbf{q} \otimes \begin{bmatrix} 0 \\ \mathbf{v} \end{bmatrix} \otimes \mathbf{q}^* \quad (8)$$

The Eqs. (9), (10) and (11) below are the rewritten of  $v$  in Eq. (8) with the x, y and z axis.

$$R_x(\mathbf{q}) = \mathbf{q} \otimes \begin{bmatrix} 0 \\ 1 \\ 0 \\ 0 \end{bmatrix} \otimes \mathbf{q}^* = \begin{bmatrix} q_0^2 + q_1^2 - q_2^2 - q_3^2 \\ 2(q_1q_2 + q_0q_3) \\ 2(q_1q_3 - q_0q_2) \end{bmatrix} \quad (9)$$

$$R_y(\mathbf{q}) = \mathbf{q} \otimes \begin{bmatrix} 0 \\ 0 \\ 1 \\ 0 \end{bmatrix} \otimes \mathbf{q}^* = \begin{bmatrix} 2(q_1q_2 - q_0q_3) \\ q_0^2 - q_1^2 + q_2^2 - q_3^2 \\ 2(q_2q_3 + q_0q_1) \end{bmatrix} \quad (10)$$

$$R_z(\mathbf{q}) = \mathbf{q} \otimes \begin{bmatrix} 0 \\ 0 \\ 0 \\ 1 \end{bmatrix} \otimes \mathbf{q}^* = \begin{bmatrix} 2(q_1q_3 + q_0q_2) \\ 2(q_2q_3 - q_0q_1) \\ q_0^2 - q_1^2 - q_2^2 + q_3^2 \end{bmatrix} \quad (11)$$

It should be noted that Eq. (12) are the extracted of quaternion vector in rotation matrix that rotates a point in a fixed coordinate system. Note that, the angle sign will be change whenever a coordinate system is rotating as in Eq. (13), so that the same outcomes for the conjugating of quaternion in Eq. (8).

$$R(\mathbf{q}) = [ R_x(\mathbf{q}) \ R_y(\mathbf{q}) \ R_z(\mathbf{q}) ] \quad (12)$$

$$R(\mathbf{q}) = \begin{bmatrix} R_x(\mathbf{q})^T \\ R_y(\mathbf{q})^T \\ R_z(\mathbf{q})^T \end{bmatrix} \quad (13)$$

Specify a reference or creates error can be done by using the notation denotes in Eq. (14) that represent the rotation of rotation vector as it has a direct physical connection, where  $\mathbf{u}$  is the rotation axis (unit vector) and  $\alpha$  is the angle of rotation.

$$\mathbf{q} = \cos\left(\frac{\alpha}{2}\right) + \mathbf{u} \sin\left(\frac{\alpha}{2}\right) \quad (14)$$

Finally, utilizing Eqs. (15) and (16) respectively can be performed for the conversion from Euler angles to quaternion and from quaternion to Euler angle. If the aim is to represent an orientation in angles, this property is very useful, while retaining

the overall dynamics of the system in a quaternion form.

$$q = \begin{bmatrix} \cos\left(\frac{\phi}{2}\right) \cos\left(\frac{\theta}{2}\right) \cos\left(\frac{\psi}{2}\right) + \sin\left(\frac{\phi}{2}\right) \sin\left(\frac{\theta}{2}\right) \sin\left(\frac{\psi}{2}\right) \\ \sin\left(\frac{\phi}{2}\right) \cos\left(\frac{\theta}{2}\right) \cos\left(\frac{\psi}{2}\right) - \cos\left(\frac{\phi}{2}\right) \sin\left(\frac{\theta}{2}\right) \sin\left(\frac{\psi}{2}\right) \\ \cos\left(\frac{\phi}{2}\right) \sin\left(\frac{\theta}{2}\right) \cos\left(\frac{\psi}{2}\right) + \sin\left(\frac{\phi}{2}\right) \cos\left(\frac{\theta}{2}\right) \sin\left(\frac{\psi}{2}\right) \\ \cos\left(\frac{\phi}{2}\right) \cos\left(\frac{\theta}{2}\right) \sin\left(\frac{\psi}{2}\right) - \sin\left(\frac{\phi}{2}\right) \sin\left(\frac{\theta}{2}\right) \cos\left(\frac{\psi}{2}\right) \end{bmatrix} \quad (15)$$

$$\begin{bmatrix} \phi \\ \theta \\ \psi \end{bmatrix} = \begin{bmatrix} \text{atan2}(2(q_0q_1 + q_2q_3), q_0^2 - q_1^2 - q_2^2 + q_3^2) \\ \text{asin}(2(q_0q_2 - q_3q_1)) \\ \text{atan2}(2(q_0q_3 + q_1q_2), q_0^2 + q_1^2 - q_2^2 - q_3^2) \end{bmatrix} \quad (16)$$

### 3 Quaternion Based Quadrotor Modelling

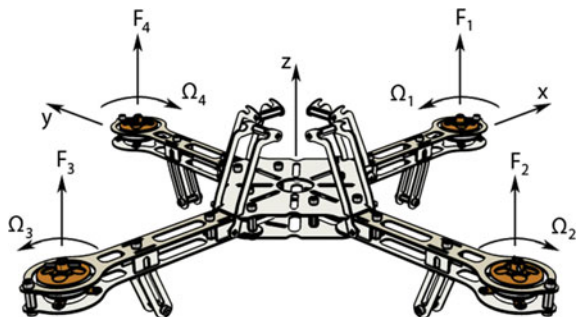
Figure 1 depicted the modelling of quadrotor’s attitude dynamics which been assumed as rigid and symmetrical. The effects of gravity are neglected while the differential forces will affect the rotation created by the propeller.

The Eq. (17) are the Euler-Newton equations for translational and rotational dynamics of a rigid body and the derivation of physical model by the utilization of Newton’s laws of motion as well as producing a frame dependent model for modelling the physics of quadrotor.

$$\begin{bmatrix} F \\ \tau \end{bmatrix} = \begin{bmatrix} m & 0 \\ 0 & I_{cm} \end{bmatrix} \begin{bmatrix} a_{cm} \\ \dot{\omega} \end{bmatrix} + \begin{bmatrix} 0 \\ \omega \times (I_{cm} \cdot \omega) \end{bmatrix} \quad (17)$$

where  $\omega$  is defined as:

**Fig. 1** A sketch of quadrotor without propeller attached [18]



$$\omega = \begin{bmatrix} \omega_x \\ \omega_y \\ \omega_z \end{bmatrix}$$

Thus, the full dynamics of the quadrotor's rigid body rotations describing the entire rotation dynamics of the Quadrotor on a quaternion form in Eq. (18) as below; produced by the combination of the right-hand quaternion derivation of Eq. (7) with the dynamics rotation from Eq. (17).

$$\begin{cases} \dot{\mathbf{q}} = -\frac{1}{2} \begin{bmatrix} 0 \\ \omega \end{bmatrix} \otimes \mathbf{q} \\ \dot{\omega} = I_{cm}^{-1} \cdot \tau - I_{cm}^{-1} [\omega \times (I_{cm} \cdot \omega)] \end{cases} \quad (18)$$

The obtained results in this Section can be directly generalized for modeling the attitude dynamics of other types of UAV frames than the Quadrotor, as long as the control signal to torque relationship can be found.

## 4 Controller Synthesis

This section presents the feedback control scheme for the quadrotor's attitude stabilization. In order to calculate the necessary driving torque and measure the system's state, the quaternion measurements and angular rates are needed as suggested in Eq. (18).

The proposed hybrids of control scheme for the attitude problem of a quadrotor are the novelty of this article. The utilization of quaternions has been made for all calculations and measurements with no Euler angles transformations. While retaining simplicity with no singularities issues, the controller result can be implemented straightforward.

Error quaternion,  $\mathbf{q}_{err}$  must be calculated by multiplying the reference,  $\mathbf{q}_{ref}$ , with the conjugate of the estimated quaternion,  $\mathbf{q}_m$ , as shown in Eq. (19) in order to utilize the error calculation of quaternion between the desired  $\mathbf{q}_{ref}$  and the measured quaternion-based response of the quadrotor  $\mathbf{q}_m$ . Error around each axis of rotation can be utilized by calculating the difference quaternion using Kronecker product:

$$\mathbf{q}_{err} = \mathbf{q}_{ref} \otimes \mathbf{q}_m^* \quad (19)$$

Axis error in Eq. (20) are resulted from the direct connects of quaternion to the error sine in Eq. (14) by the vector.

$$Axis_{err} = \begin{bmatrix} q_1^{err} \\ q_2^{err} \\ q_3^{err} \end{bmatrix} \quad (20)$$

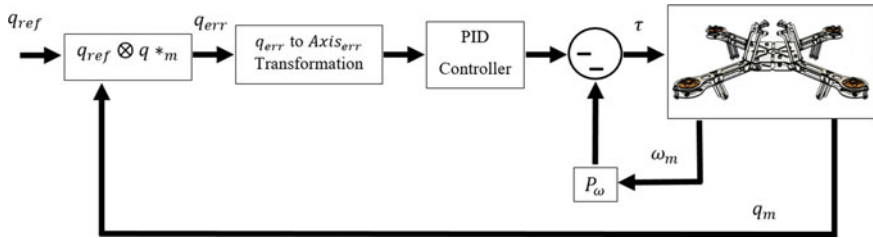


Fig. 2 Full block diagram of hybrid PID and  $P_\omega$  controller in nonlinear quaternion [18]

When designing the controller, the improvisation has been done, which is a hybrid of PID controller and proportional controller,  $P_\omega$  had been implemented as shown in Fig. 2. The proposed hybrid approach indicates  $P_\omega$  for the inner angular velocity and PID controller for the reference tracking of angular velocity. The hybrid controllers have been combined effectively to cater the attitude regulation problem as the full mathematical formulation of the hybrid control scheme depicted follows:

$$\tau = - \left[ P + I \frac{1}{s} + D \frac{N}{1 + N \frac{1}{s}} \right] \begin{bmatrix} q_1^{err} \\ q_2^{err} \\ q_3^{err} \end{bmatrix} - P_\omega \begin{bmatrix} \omega_x \\ \omega_y \\ \omega_z \end{bmatrix} \tag{21}$$

It should be noted that Eq. (21) is straight forward to be implemented. Therefore, the value of  $K_P$ ,  $K_I$ ,  $K_D$  and  $P_\omega$  are generated by the optimization of quaternion using GA.

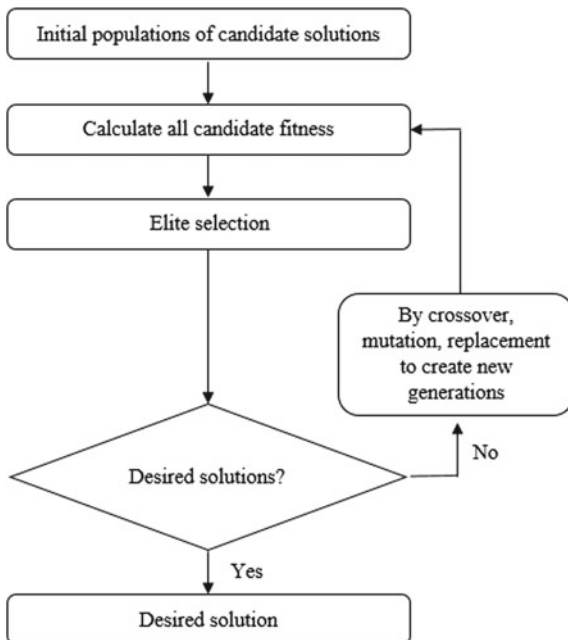
### 5 Genetic Algorithm

Genetic Algorithm (GA) is a computer-based search technique for accurate or approximate solutions to optimization and search problems. It is a specific class of Evolutionary Algorithm (EA) that uses evolutionary biology-inspired techniques such as inheritance, mutation, selection and crossover where it involves a search by an individual population. A graphical representation of the GA mechanisms is shown in Fig. 3.

In these case, the optimization will be focusing on four variables data which is  $K_P$ ,  $K_I$ ,  $K_D$  and  $P_\omega$  using MATLAB. Each  $K_P$ ,  $K_I$ ,  $K_D$  and  $P_\omega$  value will be generated randomly in the initialization of GA population. The fitness function of all candidates ( $K_P$ ,  $K_I$ ,  $K_D$  and  $P_\omega$ ) will be evaluated by GA in order to indicates how well a candidate satisfied the design specification (simulation). Furthermore, the individuals that not related are replaced by crossover and mutation while the elite individuals are preserved in each generation. The lower band for the candidates are set to 1 while the upper band is 100 in the evaluation for the fitness of variables. The GA evolution will continue until the best individuals are determined.



**Fig. 3** The evolutionary process of GA



The fittest paradigm survival will increase the elite population by generation with involving a competitive selection that discards poor solutions. The desired value for roll = 0, pitch = 1 and yaw = 0 are set for the simulation model to indicates the output. Thus, the extraction of desired solution from pool at some point can be executed. This process makes GA suitable for continuous and combinatorial problems. The range of representational approaches will be used by GA to ensure that the set of possible candidates is a close match for the set of possible solutions of the problem. The steady state error is calculated for all 100 data by the summation of average roll, pitch and yaw with the simulation output respectively.

## 6 Result and Discussion

Every part of simulation was carried out on the full nonlinear quadrotor model using MATLAB as presented in [17], which the quadrotor’s parameters were set as  $I_{xx} = I_{yy} = 6.5 \times 10^{-4} \text{ kg m}^2$  and  $I_{zz} = 1.2 \times 10^{-3} \text{ kg m}^2$ . The quaternion-based controllers have been optimized by GA and the experimental data have been acquired and inputted into MATLAB.

The GA optimization of quaternion have been run repeatedly to see the best result and optimum value of  $K_P$ ,  $K_I$ ,  $K_D$  and  $P_\omega$  and generate the Penalty Value by Generation graph respectively. Thus, the optimized value of  $K_P$ ,  $K_I$ ,  $K_D$  and  $P_\omega$  produced by each optimization using GA can be concluded as in Table 1:

**Table 1** Optimized value for PID and  $P_\omega$

No.	$K_P$	$K_I$	$K_D$	$P_\omega$
1	92.0371	2.1353	10.9572	1.0000
2	<b>98.8350</b>	<b>3.0368</b>	<b>2.8706</b>	<b>1.0000</b>
3	43.6589	16.6915	1.0152	1.0000
4	84.7665	57.9781	19.7096	1.0000
5	20.1102	2.7230	79.3913	1.0000
6	11.7354	1.2797	19.6057	1.0000
7	82.3073	50.2179	19.7988	1.0000
8	17.1120	1.4655	94.5454	36.0000
9	46.0015	14.6602	98.6523	1.0000
10	91.1668	90.3591	14.3838	1.0000

The most optimum global value is  $K_P = 98.8350$ ,  $K_I = 3.0368$ ,  $K_D = 2.8706$  and  $P_\omega = 1.0000$  as been highlighted in Table 1 while the other global value produce overshoot and some sinusoidal waveform as an output. A step response at different time instances has been considered where step has been requested around each axis. The obtained results are depicted in Figs. 4, 5 and 6 from each axis respectively. The reference signal and the system’s responses have been differentiating by color accordingly. Based on Figs. 4, 5 and 6 the roll, pitch and yaw waveforms achieved 99.82% similar to the reference signal with better response with no overshoot. They also have good rise time and settling time for the time respond with no strange effects can be witnessed from it.

While, shown in Figs. 7, 8 and 9, are the roll, pitch and yaw step responses using the proportional  $P^2$  controller as in [17]. Clearly, it’s indicates the system’s responses

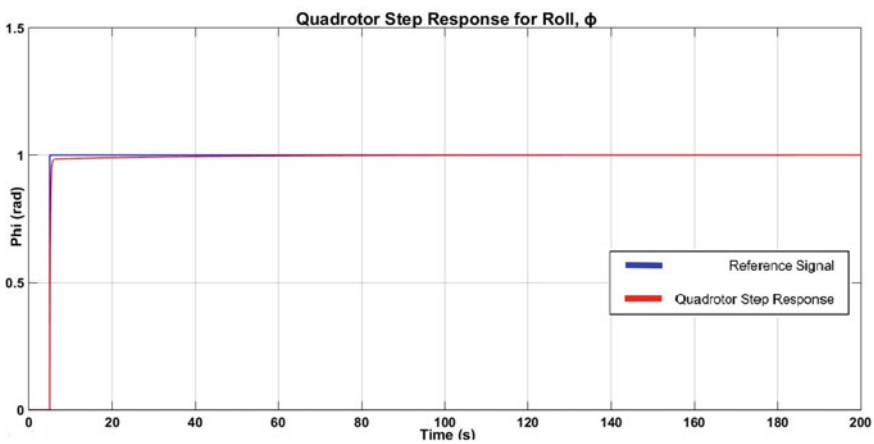


**Fig. 4** Quadrotor step response for roll

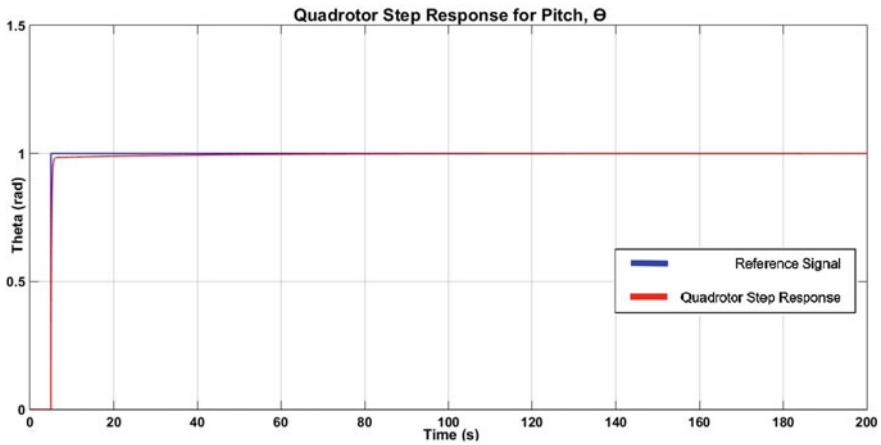


Fig. 5 Quadrotor step response for pitch

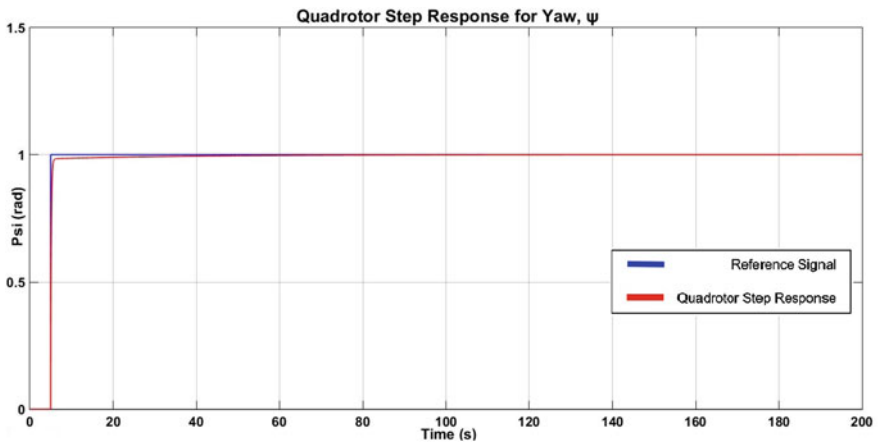


Fig. 6 Quadrotor step response for yaw

waveforms produced are slower and achieved the reference signal around 88.48%. Then, comparably it's proven that the optimized quaternion-based control scheme proposed performs well than the previous controller with differences 11.34%. Therefore, it can be concluded that the proposed hybrid of PID controller and proportional controller,  $P_{\omega}$  performs very well and robust with very good reference tracking.

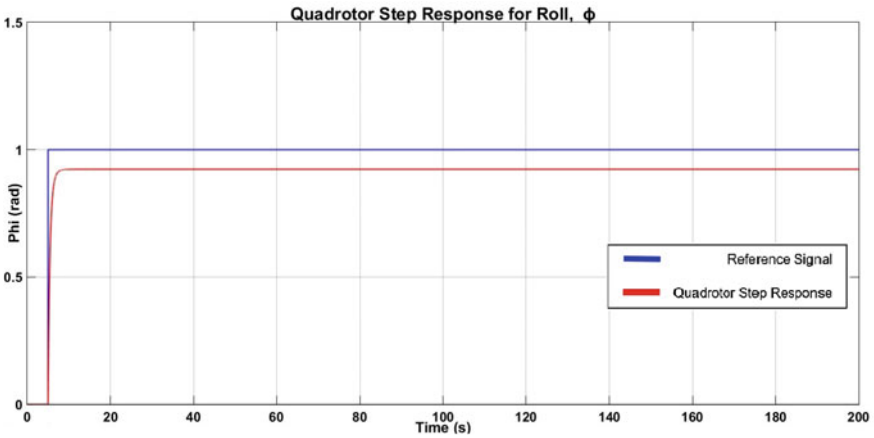


Fig. 7 Quadrotor step response for roll

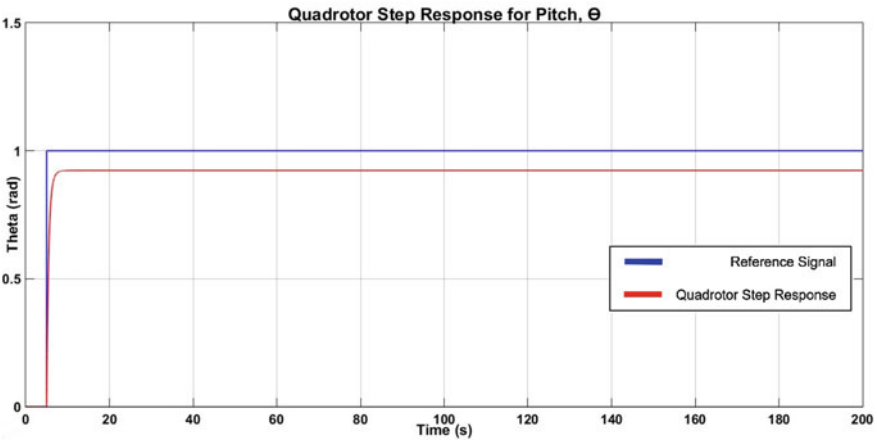
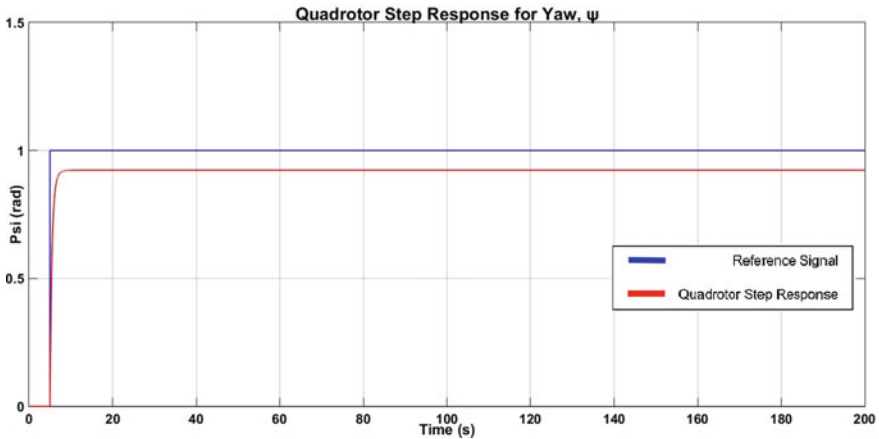


Fig. 8 Quadrotor step response for pitch

## 7 Conclusion

The full non-linear quaternion based on proposed hybrid PID and  $P_\omega$  control has been presented in this article. The purpose and the novelty of the article is to present the optimization of non-linear quaternion based on the hybrid control scheme development that utilize in fully quaternion with no conversion of Euler angles that has been



**Fig. 9** Quadrotor step response for yaw

applied directly to the quaternion error for solving the quadrotor attitude problem. The proven efficiency of proposed scheme is simulated using MATLAB and have been presented thoroughly.

**Acknowledgements** The authors would like to thank UMP for financing the research project under UMP research Scheme RDU1703315.

## References

1. Castillo P, Lozano R, Dzul A (2016) Modelling and control of mini flying machines, Automatica, Springer, 2005; Conference 2016, LNCS, vol 9999. Springer, Heidelberg, pp 1–13
2. Barczyk M, Lynch AF (2012) Integration of a triaxial magnetometer into a helicopter UAV GPS aided inertial navigation system. IEEE Trans Aerosp Electron Syst
3. Armutcuoglu O, Tekinalp O (2004) Tilt duck vertical takeoff and landing uninhabited aerial vehicle concept design study. J Aircraft 41(2):215–223
4. Kendoul F, Fantoni I, Lozano R (2006) Modelling and control of a small autonomous aircraft having two tilting rotors. IEEE Trans Rob 22(6):1297–1302
5. Prior SD, Karamanoglu M, Odedra S, Foran T, Erbil MA (2009) Development of co-axial tri-rotor UAV. Bristol Int Unmanned Aerial Veh Syst Conf
6. Romero H, Salazar S, Lozano R (2009) Real time stabilization of an eight rotor UAV using optical flow. IEEE Trans Rob 25(4):809–817
7. Abas MFB, Pebrianti D, Ali SAM, Iwakura D, Song Y, Nonami K, Fujiwara D (2013) Circular leader-follower formation control of quad-rotor aerial vehicles. J Robot Mechatron 25(1)
8. Zhao B, Xian B, Zhang Y, Zhang X (2015) Nonlinear robust adaptive tracking control of a quadrotor UAV via immersion and invariance methodology. IEEE Trans Ind Electron 62(5):2891–2902
9. Xue K, Wang C, Li Z, Chen H (2016) Online adaptive error compensation SVM-based sliding mode control of an unmanned aerial vehicle. Int J Aerosp Eng

10. Modirrousta A, Khodabandeh M (2014) Adaptive robust sliding mode controller design for disturbances. In: Proceeding 2nd RSI/ISM International Conference on Robotics and Mechatronics, pp 870–877
11. Ghaffar AA, Richardson T (2015) Model reference adaptive control and LQR control for quadrotor with parametric uncertainties, vol 9, no 2, pp 244–250
12. Chen F, Jiang R, Zhang K, Jiang B, Tao G (2016) Robust backstepping sliding-mode control and observer-based fault estimation for a quadrotor UAV. *IEEE Trans Ind Electron* 63(8):5044–5056
13. Zulu A, John S (2014) A review of control algorithms for autonomous quadrotors. *Open J Appl Sci* 4:547–556
14. Ghiglino P, Forshaw JL, Lappas VJ (2015) OQTAL: optimal quaternion tracking using attitude error linearization. *IEEE Trans Aerosp Electron Syst* 51(4):2715–2731
15. Djamel K, Abdellah M, Benallegue A (2016) Attitude optimal backstepping controller based quaternion for a UAV. *Math Probl Eng*
16. Di Lucia S, Tipaldi GD, Burgard W (2015) Attitude stabilization control of an aerial manipulator using a quaternion-based backstepping approach. In: 2015 European conference on mobile robots ECMR 2015—proceedings
17. Chovancova A, Fico T, Hubinsky P, Duchon F (2015) Comparison of various quaternion-based control methods applied to quadrotor with disturbance observer and position estimator. *Robot Auton Syst* 79:87–98
18. Fresk E, Nikolakopoulos G (2013) Full quaternion based attitude control for a quadrotor. In: 2013 European control conference (ECC), pp 3864–3869

# Elimination-Dispersal Sine Cosine Algorithm for a Dynamic Modelling of a Twin Rotor System



**Shuhairie Mohammad, Mohd Falfazli Mat Jusof, Nurul Amira Mhd Rizal, Ahmad Azwan Abd Razak, Ahmad Nor Kasruddin Nasir, Raja Mohd Taufika Raja Ismail and Mohd Ashraf Ahmad**

**Abstract** This paper presents an improved version of Sine Cosine Algorithm (SCA). The original SCA is a simple algorithm and it offers a good accuracy. However, for some problems and fitness landscapes, the accuracy achievement of the algorithm is not at optimal. Search agents of the algorithm stuck at the local optima. The proposed new algorithm which is called an Elimination-Dispersal Sine-Cosine Algorithm adopts Elimination-Dispersal (ED) strategy from Bacterial Foraging Algorithm. The ED helps search agents to solve the local optima problem. At the same time, an elitism approach is applied in the proposed algorithm. The elitism ensures some agents continue the next search operation from the currently best found solution. The proposed algorithm is tested on CEC2014 benchmark functions that have various fitness landscapes and properties. The accuracy performance is compared with the original SCA and analyzed. It also is applied to acquire and optimize a dynamic model for a Twin Rotor System (TRS). Result of the modelling shows that the proposed algorithm achieves a better accuracy and thus present less modelling error and better dynamic response for the TRS.

**Keywords** Elimination-dispersal · Sine cosine algorithm · Twin rotor system · Dynamic modelling · System identification

## 1 Introduction

Twin Rotor System (TRS) is a multi-input multi-output (MIMO) system used as a laboratory prototype that mimics a real helicopter system during a hovering mode. It consists of a dynamic behaviour of a real helicopter system. A helicopter system is a common air transportation used to carry humans or goods from an area that is hardly accessible using ground transportations. The travel time using the helicopter system is also faster. Operating a helicopter system in the air is always challenging.

---

S. Mohammad · M. F. M. Jusof · N. A. M. Rizal · A. A. A. Razak · A. N. K. Nasir (✉) · R. M. T. R. Ismail · M. A. Ahmad  
Faculty of Electrical & Electronics Engineering, Universiti Malaysia Pahang, 26600 Pekan, Pahang, Malaysia  
e-mail: [kasruddin@ump.edu.my](mailto:kasruddin@ump.edu.my)

There is a high possibility that the system is exposed to various disturbances such as wind speed, earth surface, hills and mountains. These elements of disturbances cause the helicopter system become unstable and unreliable transport. An accident can easily happen without a proper control of the system during the hovering mode operation. Therefore, the study of dynamic modelling and controlling a twin rotor system during hovering mode is highly important. This is to ensure the comfort and safety of the passengers are always at the optimum level.

In literature a lot of studies on the dynamic modelling and control design of the TRS are found. A study about sensor-fault tolerant control for the TRS was presented in [1]. An estimator was designed to estimate all states and sensors faults. A state feedback controller was then designed based on the fault free state estimator. Result of the work showed that the proposed control strategy was effective for controlling the TRS. A lead-lag controller for stabilizing both pitch and yaw angles for the TRS was proposed in [2]. The study proved that the lead lag controller able to reduce steady state error significantly and able to overcome some drawbacks of PID controller.

Dynamic modelling for a TRS can be categorized into analytical and intelligent approaches. A dynamic model using the analytical approach was presented [3, 4]. A Lagrange formula was adopted and several assumptions were considered in the formula development. The developed nonlinear equation was linearized prior to its representation in state space model. Due to the assumptions and linearized strategy in the formula development, the developed model might not represent the dynamic of the system accurately. An intelligent approach is considered as an alternative to the conventional analytical approach.

Using an intelligent approach, dynamic modelling of the TRS can be done via hybrid system identification and optimization algorithm approach. An optimization algorithm is used as a tool to optimize parameters of a candidate structure for the dynamic model of the TRS. A study on dynamic modelling based on fuzzy logic structure was presented in [5, 6]. Spiral dynamic optimization algorithm was adopted to acquire and optimize fuzzy rules and universe of discourse of the fuzzy membership function. An application of a nonparametric modelling approach and a neural network model structure to represent the TRS was presented in [7]. An improved adaptive BFA was adopted to train the neural network model. A study of a feedforward neural network as the structure to model the TRS was presented in [8]. All weights and bias of the neural network structure were optimized by chaos enhanced stochastic fractal search algorithm. Another work on developing a dynamic model of the TRS was presented in [9]. The authors applied gradient descent search method to optimize friction coefficients of the developed model. All the works presented that the dynamic model of the TRS can be acquired optimally with the application of an optimization algorithm.

This paper presents an Elimination-Dispersal Sine Cosine Algorithm (EDSCA). It is an improved version of Sine Cosine Algorithm (SCA) [10]. The original SCA is a simple algorithm and it offers a good accuracy. However, for some problems and fitness landscapes, the accuracy achievement of the algorithm is not at optimal. Search agents of the algorithm stuck at the local optima. Elimination and Dispersal (ED) phase of BFA is incorporated into the original SCA. The proposed algorithm



is applied to optimize a dynamic model of a Twin Rotor System (TRS). Structure of this paper is organized as follows. Section 2 explains the proposed EDSCA. Performance test of the proposed EDSCA on CEC2014 benchmark functions is explained in Sect. 3. Section 4 presents detail description of the TRS. Section 5 presents the parametric dynamic modelling of the TRS. Result and discussion of the benchmark functions performance test and modelling work are elaborated in Sect. 6. Finally, conclusion of the paper is presented in Sect. 7.

## 2 Elimination-Dispersal Sine Cosine Algorithm

The Elimination-Dispersal Sine Cosine Algorithm (EDSCA) is a synergy between Elimination-Dispersal (ED) and Sine Cosine Algorithm (SCA). The ED adopted from Bacterial Foraging Algorithm (BFA) [11]. The advantage of utilizing the ED is to relocate all search agents to various new locations. This may give chances to the relocated agents to find a better solution. It also set free all the agents that are trapped inside the local optima space and restart the search operation from various new fresh locations. For the ED implementation, the agents are sorted based on their fitness cost  $f_{\min}$  and divided into two groups. The first group consists of agents with better or lower cost. The rest of the agents are assigned into the second group before being eliminated and dispersed. The ED equation adopted in this work is shown as (1).

$$X_i^{t+1} = X_{\min} + (X_{\max} - X_{\min}) \times rand \quad (1)$$

where  $X_i^{t+1}$  is an updated position of  $i$ th agent in  $t + 1$  iteration. The  $X_{\min}$  and  $X_{\max}$  represent the lower and upper boundaries of the feasible search space respectively. The  $rand$  is a generated random number.

The sine and cosine terms are the essential elements of the Sine-Cosine Algorithm (SCA). Both terms depict an oscillation behaviour if plotted in terms of a time-domain response. The crucial part is to utilize the two terms to generate a circular shape or a circle. This strategy allows all search agents to possibly move  $360^\circ$  around its current position. Mathematical formulations of the sine and cosine terms for generating the optimization algorithm are presented as (2) and (3). Both equations drive all search agents to move from their current location to a new location within the feasible search space.

$$X_i^{t+1} = X_i^t + r_1 \times \sin(r_2) \times r_3 |P^t - X_i^t| \quad (2)$$

$$X_i^{t+1} = X_i^t + r_1 \times \cos(r_2) \times r_3 |P^t - X_i^t| \quad (3)$$

where  $r_1$  is an adaptive formula of the search agents step size,  $r_2$  is an equation for the sine and cosine terms serves to generate a random direction for the agents motion.

It represents a stochastic feature of the algorithm. The  $r_3$  is a random parameter of the relative position of  $i$ th agent to the best agent in the population. The term  $r_1$  is defined as (4).

$$r_1(t) = a - t \frac{a}{T} \quad (4)$$

where  $a$  is a pre-defined constant and is considered as a maximum step size of the agents to move within the search space. The  $t$  and  $T$  are the current iteration and the maximum iteration of the algorithm respectively. The equation  $r_1$  is generated such that the value is getting smaller as the current iteration,  $t$  is increased towards  $T$ . The formula of  $r_2$  is presented as (5).

$$r_2 = 2 \times \pi \times rand \quad (5)$$

where  $rand$  is a generated random number. The parameter  $r_3$  is simply a generated random value.

The proposed EDSCA consists of 9 main steps. Description of the EDSCA is presented as follows.

**Step 1:** Initialize  $i$ th agents position,  $X_i$  and the maximum iteration,  $T$ .

**Step 2:** Update cost function,  $f(X_i)$  value of every single agent,  $i$ .

**Step 3:** Determine the best agent  $X_{f_{\min}}$ . Agent with the lowest cost function value,  $f_{\min}$  is considered as the best agent and is assigned as destination position,  $P^f$ .

**Step 4:** Update every single individual  $i$ th agent position using (2) and (3).

**Step 5:** Update cost function,  $f(X_i)$  value of every single agent,  $i$ .

**Step 6:** Determine the best agent  $X_{f_{\min}}$ . Agent with the lowest cost function value,  $f_{\min}$  is considered as the best agent and is assigned as destination position,  $P^f$ .

**Step 7:** Check if all agents have updated their position using (2) and (3). If it is true, apply the ED strategy using (1) and repeat Step 4 until Step 7.

**Step 8:** Check if the ED has reached the maximum value,  $ED_{\max}$ . If it is true, proceed to Step 9. If it is not true, repeat Step 4 until Step 8.

**Step 9:** Check if the iteration has reached the maximum value,  $T$ . If it is true, stop the algorithm. If it is not true, repeat Step 4 until Step 9.

### 3 Benchmark Functions Test

Benchmark functions are used to test the performance of the developed algorithm. In this work, the developed algorithm was tested on four different benchmark functions. Their corresponding mathematical representations are shown in Table 1. All the four benchmark functions have the test range between  $[-100, 100]$ , 10 dimensions and a unimodal fitness landscape. Functions 1–3 have a rotated feature while function 4 has a shifted and a rotated features. Details description of the functions can be found

**Table 1** Benchmark functions

Function no	Equation of the benchmarks functions
1	$f_1(x) = \sum_{i=1}^D (10^6)^{\frac{i-1}{D-1}} x_i^2$
2	$f_2(x) = x_1^2 + 10^6 \sum_{i=2}^D x_i^2$
3	$f_3(x) = 10^6 x_1^2 + \sum_{i=2}^D x_i^2$
4	$f_4(x) = \sum_{i=1}^{D-1} (100(x_i^2 - x_{i+1})^2 + (x_i - 1)^2)$

in [12]. In this work, 51 independent runs were conducted for each function. The constant,  $a$  for the SCA was set as 2. For the EDSCA, the  $r_1$  was set as a constant 0.5. A total of 100,000 function evaluations and 50 agents were defined for both algorithms. The ED for EDSCA was set to 4 repeated runs.

### 4 Twin Rotor System

Twin Rotor System (TRS) used in this work is a laboratory prototype system. It exhibits a highly nonlinear, cross coupling effect and a complex behaviour of a helicopter system. The system consists of a main rotor used to rotate the system about pitch axis and a tail rotor used to rotate the system about yaw axis. Consider the elevation angle is the angle about the pitch axis and it represents angular position of the system to move the system in a vertical direction. Angle about the yaw axis represents a rotational motion of the system to move in a horizontal direction. The main and tail rotors are linked together by a solid rod which is pivoted to the main body of the system. The TRS is connected to a signal conditioning circuit where it allows an analogue signal to be converted into a digital signal and vice versa. For data manipulation, analysis and control purposes, the signal is applied into a desktop. Detail descriptions of the TRS can be found in [6].

### 5 Parametric Modelling of a Twin Rotor System

A dynamic model for vertical channel of the TRS is considered in this work. Autoregressive—Moving—Average (ARMA) model was chosen as the candidate structure for the vertical channel. The general mathematical representation of the ARMA model is shown as (6).

$$\frac{Y(z)}{U(z)} = \frac{\sum_{j=0}^7 b_j z^{-1}}{1 + \sum_{i=1}^8 a_i z^{-1}} \tag{6}$$

For the vertical channel of the TRS, an eight order transfer function was used. Expanding (6), the complete discrete transfer function is shown as (7). It shows that the highest order of the denominator part of the discrete transfer function is an 8th order. It is noted that the transfer function has 16 unknown coefficients where the values must be acquired and optimized. This can be completed via a parametric modelling approach using system identification and application of the proposed optimization algorithm.

$$\frac{Y(z)}{U(z)} = \frac{b_0 z^8 + b_1 z^7 + b_2 z^6 + b_3 z^5 + b_4 z^4 + b_5 z^3 + b_6 z^2 + b_7 z}{z^8 + a_1 z^7 + a_2 z^6 + a_3 z^5 + a_4 z^4 + a_5 z^3 + a_6 z^2 + a_7 z^1 + a_8} \tag{7}$$

A parametric modelling is developed based on a pair of recorded input-output data. The recorded data was taken from the real TRS. For this experiment a total of 6000 data were captured. 4000 of the data was used in the modelling phase while the remaining unused data was used for the validation phase. The block diagram representation of the parametric modelling for the modelling phase is shown in Fig. 1. The twin rotor system and the parametric model represent the actual TRS and the model to be estimated and optimized respectively. Mathematical equation of the parametric model is shown as (7). The optimization algorithms are the algorithms of interest in this work i.e. EDSCA and SCA. The  $u(t)$  represents an input signal that is supplied into the system while the  $y(t)$  is an output signal that coming out from the system. The  $\hat{y}(t)$  is the estimated response from the parametric model. Notice that the output responses from the real system and parametric model are compared. The difference between the 2 output responses is considered as the error  $e(t)$  in the modelling phase. The optimization algorithms will then train and optimize the coefficients of the parametric model as it receives an error signal in the modelling phase. The process will be repeated until the algorithm has reached a stopping condition.

**Fig. 1** Block diagram of the modelling phase

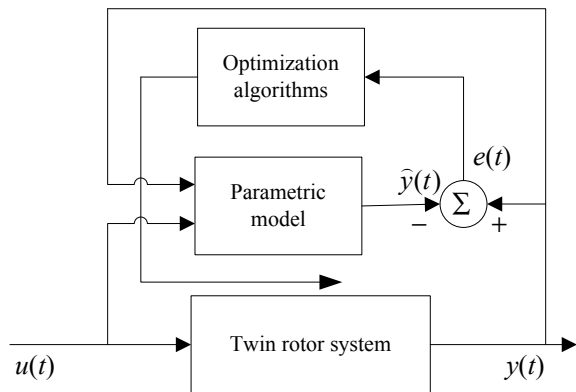
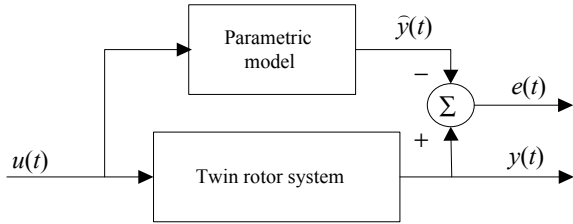


**Fig. 2** Block diagram of the validation phase



The error function or cost function for the work is shown as (8).  $K$  is the total number of sampled input-output data.  $e(t)$  is the error in the modelling phase or the difference between the output response from the parametric model and actual TRS.  $w$  is a tuneable constant used to amplify the error,  $e(t)$ .

$$f(t) = \left( \frac{1}{K} \sqrt{\sum_{t=1}^K e^2(t)} \right) w \tag{8}$$

The parametric model that has been acquired and optimized in the modelling phase should be validated by the remaining and unused input-output data. Validation phase block diagram representation of the parametric model is shown in Fig. 2. The unused input data that was supplied into the actual TRS is injected into the estimated model of the vertical channel of the TRS. The output response from the estimated model is then compared with the remaining unused output data recorded from the actual TRS. The difference between the two output responses is considered as the error  $e(t)$  in the validation phase.

## 6 Result and Discussion

### 6.1 Result of the Benchmark Functions Test

Performance test with the benchmark functions is discussed based on the achievement of the SCA and EDSCA algorithms to reach the theoretical optima solution of each function. The algorithm is considered as more accurate if the solution attained is closer to the theoretical optima solution. The theoretical optima solution for functions 1, 2, 3, and 4 were set at 100, 200, 300 and 400 respectively. Table 2 presents the error value between the actual reached solution and the theoretical optima solution. An algorithm is considered as more accurate if the error is smaller. It is noted from the table that the EDSCA achieved a smaller error for all functions compared to SCA and thus achieved better accuracy.

Graphical representation of the performance test is shown in Fig. 3. All graphs in the figures represent the convergence plot of the two algorithms in finding the theoretical optima solution. The vertical axis represents the error between the achieved

**Table 2** Error represents accuracy achievement

Function no	Algorithm	
	EDSCA	SCA
1	$2.24 \times 10^7$	$4.24 \times 10^7$
2	$2.26 \times 10^8$	$8.19 \times 10^8$
3	$1.01 \times 10^4$	$1.11 \times 10^4$
4	<b>510.80</b>	560.10

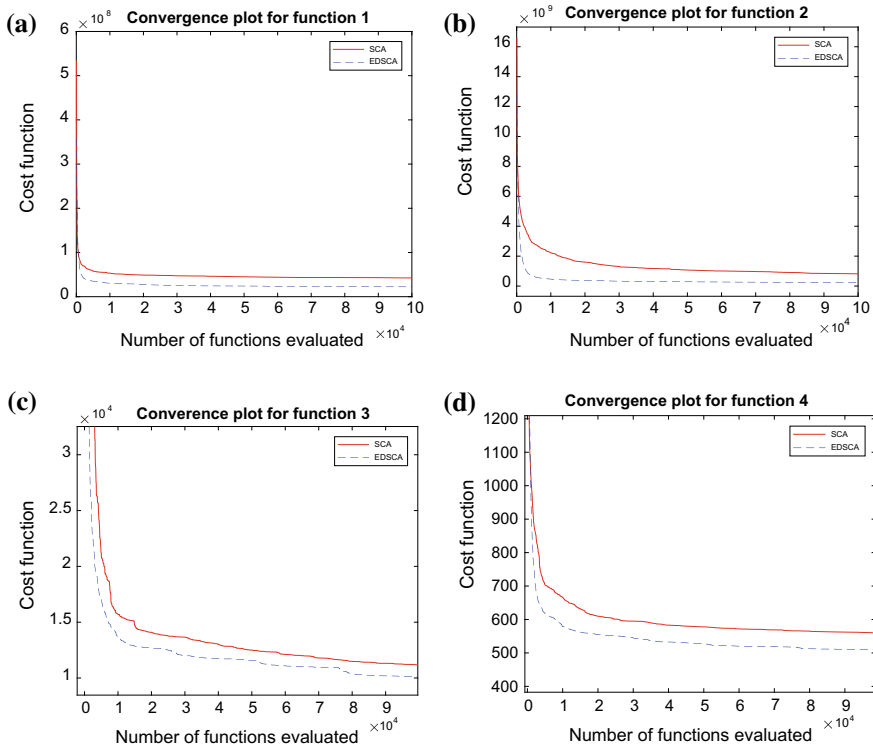


**Fig. 3** Convergence plot, **a** function 1 and **b** function 2, **c** function 3 and **d** function 4

solution and the theoretical value while the horizontal axis represents the number of functions evaluated. As shown in all figures, the convergence graphs of the EDSCA have achieved lower error value for all functions. The result is in-line with the result presented in Table 2 where the EDSCA achieved smaller error value. All the plotted graphs also have shown that both SCA and EDSCA have almost similar convergence speed. Noted from function 3, there is an obvious effect of the ED strategy at  $2.5 \times 10^4$ ,  $5 \times 10^4$  and  $7.6 \times 10^4$ .

### 6.2 Result of the Parametric Modelling

In the parametric modelling, both SCA and EDSCA algorithms were set up with 50 agents, 16,000 number of function evaluation and 16 dimensions. The search range was defined between  $[-100, 100]$  and the constant  $a$  for the SCA was set as 2 while for the EDSCA the  $r_1$  was set as a constant 0.5. Comparison of the convergence plot for the two algorithms is shown in Fig. 4. It is noted from the figure that the SCA has faster convergence speed while the EDSCA has presented a slight delay to converge. However, SCA has trapped at a local optima solution and not able to converge further after 13,000 function evaluation. On the other hand, the convergence graph of the EDSCA has intercepted the SCA graph at 3000 function evaluation and it slowly converged further until 6500 function evaluation before trapped at a local optima. The final accuracy achievement for both algorithms is presented in Table 3. The accuracy achievement of SCA and EDSCA were at 37.31 and 22.57 respectively. It shows that the proposed EDSCA has reached a better accuracy.

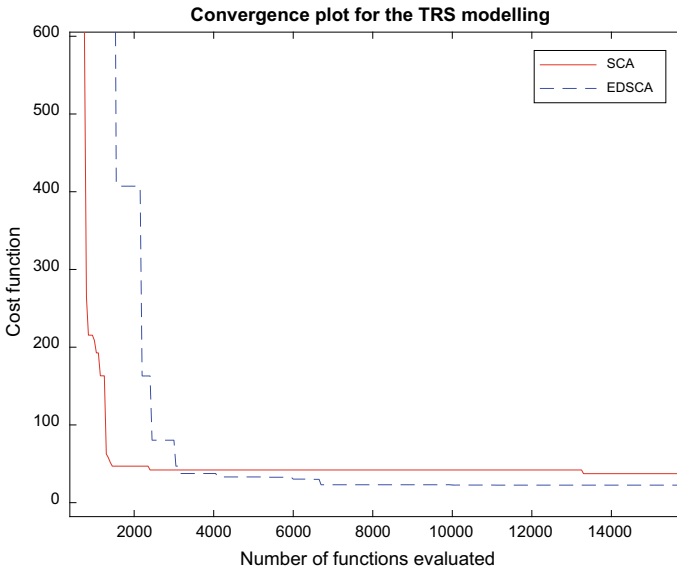


Fig. 4 Convergence plot for TRS modelling

Table 3 Parametric modelling

Algorithm	Modelling phase		
	Convergence graph	VC TRS range	Error range
EDSCA	<b>22.57</b>	$[-0.90, 1.03]$	<b><math>[-0.12, 0.11]</math></b>
SCA	37.31	$[-0.91, 0.96]$	$[-0.22, 0.20]$

The output response of the estimated model or the parametric model and the error in the modelling phase were recorded. The input response injected into and output responses coming out from the vertical channel of the TRS has a range between  $[-1, 1]$ . Figure 5a shows the output responses of the estimated models that were trained and optimized by both SCA and EDSCA algorithms. The figure shows that both responses have almost similar patterns. The best response is the one that can follow exactly the output response that was recorded from the actual TRS. Figure 5b shows graph of error in the modelling phase. The figure shows that EDSCA has achieved a smaller range of error in the modelling phase. The numerical result of the error range and the range of output response of the estimated model are presented in Table 3.

Output response of the estimated model in the validation phase is shown in Fig. 6a. The plotted graphs show that both SCA and EDSCA can model the vertical channel of the TRS satisfactorily. Output response from both algorithms also almost identical. Figure 6b shows graph of the error in the validation phase. It shows that the proposed EDSCA has achieved a smaller range of the error compared to SCA. The numerical result of the error range and the range of the estimated model response are presented

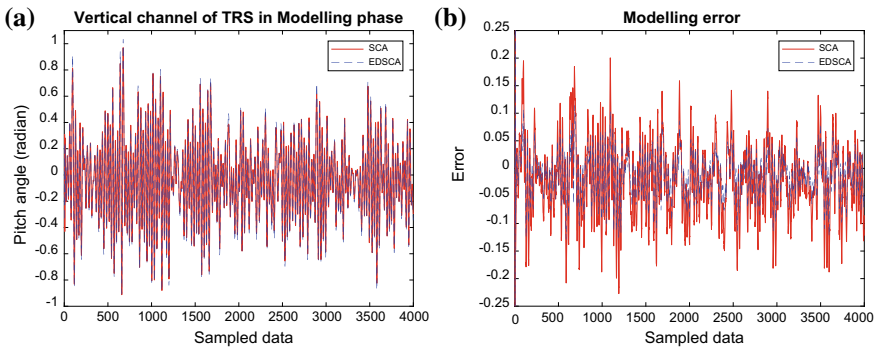


Fig. 5 Vertical channel of the TRS, a modelling phase and b error in modelling phase

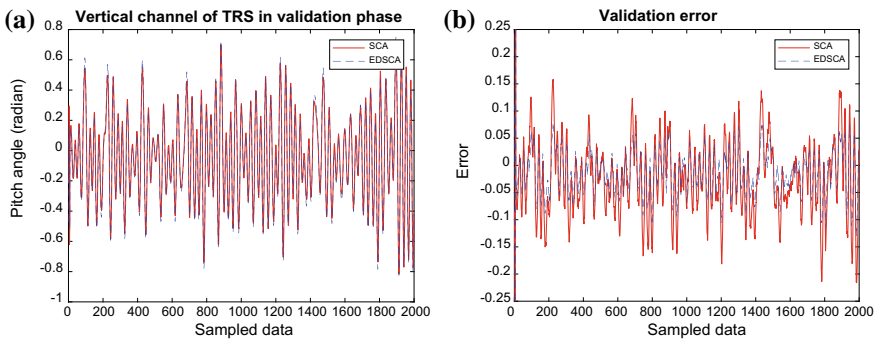


Fig. 6 Vertical channel of the TRS, a validation phase and b error in validation phase



**Table 4** Parametric modelling—Validation phase

Algorithm	Validation phase	
	VC TRS	Error range
EDSCA	[−0.82, 0.75]	[−0.12, 0.07]
SCA	[−0.81, 0.69]	[−0.21, 0.15]

in Table 4. Both graphical plot and the numerical result show that the error range in the validation phase is significantly smaller. This confirms and in-line with the modelling result that showing the EDSCA has higher accuracy.

## 7 Conclusion

An Elimination-Dispersal Sine Cosine Algorithm (EDSCA) has been presented in this paper. An Elimination-Dispersal (ED) adopted from foraging strategy of *Escherichia Coli* bacteria in human intestine has been synergized with the Sine Cosine Algorithm (SCA). Using the strategy, some agents have been relocated to a better position and set free the algorithm from a local optima solution. The proposed EDSCA algorithm has been tested on various CEC2014 benchmark functions with different fitness landscapes and features. It also has been applied to acquire and optimize a dynamic model of a vertical channel of a Twin Rotor System (TRS) through a system identification approach. Result of the benchmark functions test has shown that the proposed EDSCA algorithm outperformed the original SCA significantly. Result of the dynamic modelling shows both EDSCA and SCA algorithms have successfully modelled the vertical channel satisfactorily. The proposed EDSCA has achieved a smaller error and produced a better response. In the future the algorithm will be used to optimize a nonlinear fuzzy logic controller for the TRS.

**Acknowledgements** This research is financially supported by the Fundamental Research Grant Scheme (FRGS/1/2016/ICT02/UMP/02/1) with the RDU number RDU160103. It is awarded by the Ministry of Higher Education Malaysia (MOHE) through Research and Innovation Department, Universiti Malaysia Pahang (UMP) Malaysia.

## References

1. Pazera M, Buciakowski M, Witczak M (2018) Robust multiple sensor fault-tolerant control for dynamic non-linear systems. Application to the aerodynamical twin-rotor system. *Int J Appl Math Comput Sci* 28(2):297–308
2. Deniz M, Tatlicioglu E, Bayrak A (2018) Experimental verification of lead-lag compensators on a twin rotor system. *Electrical, control and communication engineering. J Riga Tech Univ* 14(2):164–171
3. Quanser Inc. (2010) Quanser 2-DOF Helicopter Manual, Technical report, Quanser
4. Twin Rotor MIMO 33-007-PCI—Feedback Instruments Ltd. [www.feedback-instruments.com](http://www.feedback-instruments.com)

5. Nasir ANK, Tokhi MO (2015) An improved spiral dynamic optimization algorithm with engineering application. *IEEE Trans Syst Man Cybern Syst* 45(6):943–954
6. Nasir ANK, Tokhi MO, Omar ME, Ghani NMA (2014) An improved spiral dynamic algorithm and its application to fuzzy modelling of a twin rotor system. In: 2014 world symposium on computer applications & research (WSCAR), Sousse, 2014, pp 1–6
7. Nasir ANK, Tokhi MO, Ghani NMA (2015) Novel adaptive bacterial foraging algorithms for global optimisation with application to modelling of a TRS. *Exp Syst Appl* 42(3):1513–1530
8. Tuan AZ, Rahman NA, Abdul Jalil A, Kamil R (2018) Non-parametric dynamic modeling of twin rotor system using chaos-enhanced stochastic fractal search algorithm. In: Proceedings of the 62nd annual conference of the institute of systems, control and information engineers (ISCIE), 16–18 May 2018. Kyoto, pp 1–4
9. Fotuhi MJ, Hazem ZB, Bingtil Z (2018) Comparison of joint friction estimation models for laboratory 2 DOF double dual twin rotor aero-dynamical system. In: IECON 2018—44th annual conference of the IEEE industrial electronics society. Washington, DC, pp 2231–2236
10. Mirjalili S (2016) SCA: a sine cosine algorithm for solving optimization problems. *Knowl Syst* 1–14
11. Passino KM (2002) Biomimicry of bacterial foraging for distributed optimization and control. *IEEE Control Syst Mag* 22(3):52–67
12. Liang JJ, Qu BY, Suganthan PN (2014) Problem definitions and evaluation criteria for the CEC 2014 special session and competition on single objective real-parameter numerical optimization. Technical report, 201311, Computational Intelligence Laboratory, Zhengzhou University, Zhengzhou

# The Investigation of Meat Classification Based on Significant Authentication Features Using Odor-Profile Intelligent Signal Processing Approach



Nur Farina Hamidon Majid, Muhammad Sharfi Najib, Suhaimi Mohd Daud, Nurdiyana Zahed, Muhamad Faruqi Zahari, Suziyanti Zaib, Mujahid Mohamad, Tuan Sidek Tuan Muda and Hadi Manap

**Abstract** Meat is the flesh or another edible part of an animal and includes uncooked meat prepared or otherwise but does not include meat products. Meat is the most valuable livestock product and for many people serves as their first-choice source of animal protein. Fraud meat products are causing annoyance to consumer's, especially Muslim users. There are many cases that have been brought to the public attention regarding fraud on meat products such as incidences of meat that is labeled, certified or sold as halal may not be so. This project sets out to identify two types of different meat which is beef meat and pork meat. Therefore, the significant authentication features using odor-profile intelligent signal processing approach which is Electronic Nose (E-nose) was used to measure odor-profile from meat. E-nose is one of the chemical-based sensor arrays instruments which have a capability to measure odor-profile based sample data. The data measurement of odor-profile for different meat samples was collected based on the designated experimental procedure. Then, the normalized and their unique features were extracted using statistical tools for feature extraction. The input of features will be inserting into Case-Based Reasoning (CBR) library and intelligently classified using CBR method and will be validated based specific performance measure. From the CBR performance measures result, it is observed that the classification of CBR is 100%.

**Keywords** Meat · Electronic nose (E-nose) · Case-based reasoning (CBR) · Odor-profile

---

N. F. H. Majid · M. S. Najib (✉) · S. M. Daud · N. Zahed · M. F. Zahari · S. Zaib · M. Mohamad · T. S. T. Muda · H. Manap  
Universiti Malaysia Pahang, 26600 Pekan, Pahang, Malaysia  
e-mail: [sharfi@ump.edu.my](mailto:sharfi@ump.edu.my)

T. S. T. Muda  
e-mail: [sidek@ump.edu.my](mailto:sidek@ump.edu.my)

H. Manap  
e-mail: [hadi@ump.edu.my](mailto:hadi@ump.edu.my)

## 1 Introduction

Food is made up of nutrients that have influenced all aspects of life, especially mental health. In order to survive and be healthy, humans need to obtain nutrients from foods. The requirements of energy and nutrients are different due to differences in race, age, sex, and physical activity level and people living in different places take nutrients from different kinds of food [1]. At the world level, there are the organizations that care about food for people such as the World Health Organization (WHO) [2]. In Malaysia, the Department of Islamic Development Malaysia (JAKIM) is the agency responsible for Islamic affairs including halal certification in Malaysia [3]. JAKIM has developed the Halal Meat and Poultry Production for Malaysian Protocol to guide in the production of halal meat and poultry.

Meat can be defined as animal flesh used for human consumption [4]. Meat is good for boost immunity, improves digestion, improves blood circulation and protects heart health. In this project, the focus is more on imported meat which is beef and pork meat. Science and technology have always played an important role in the food industry, in ensuring that society's need for safe and good quality food is met in a sustainable way [5]. There is a Maqasid Shariah parameter in technology development in halal authentication.

Maqasid Shariah is defined as objectives or purposes behind the Islamic law that also solutions to contemporary problems faced by Muslims. Maqasid Shariah is divided into three according to the levels of necessity which is Daruriyyah, Hajiyyah and Tahsiniyyah. Daruriyyah is essential elements for a human being. The absence of these elements may cause harm and damage to human life. The necessities are further classified by the scholars into five elements of preservations to protect from any harms. These preservations are known as Protection of religion (din), life (nafs), lineage (nasl), intellect (aql) and property (mal). Hajiyyah is less essential for human life compares to Daruriyyah. These are requirements for the human being to live without facing difficulties and the lack of any of these needs is not a matter of life and death, especially on an individual basis. Tahsiniyyah is complementary and desirable factors that give perfection and additional values to human life. Islam encourages us to achieve these purposes and to have a better life [6, 7]. For researchers, this technology development is at the current level of Hajiyyah due to fraudulent activity, and the forgery of meat products especially meat is still under control by the government [8].

In order to detect the meat, there are several authentication techniques that have been reported which is Fourier Transform Infrared (FTIR), Electronic Nose (E-nose) and Polymerase Chain Reaction (PCR) assays [8]. In this research, the E-nose is the focusing device used to detect odor profile from different meat which is beef and pork meat. During recent years, E-noses have been widely used in food analysis and proved to provide a fast, simple, non-expensive and non-destructive method of food assessment and quality control [9].

E-nose is an instrument which combines an array of chemical sensors that can respond to a variety of complex odors [10, 11]. Odor data collected by the E-nose need to be processed and analyzed to identify rules and patterns in the data. Thus,

the classification of meat based on odor-profile using E-nose is very useful with the combination of Case-Based Reasoning (CBR) classification algorithm in the E-nose system [12].

CBR required no training and suitable for a weak domain field and the classification process faster as compared to other techniques [13]. CBR is creating as a four-step process of human or computer reasoning which called CBR cycle which are retrieve, reuse, revise and retain [14]. Retrieve phase is the solution of the most similar case from the case base to solve a new problem [15]. Reuse phase is the solution and information in that case to solve the new case problem [15]. Revise phase is the solution that gets from the retrieval case and mapping with the target problem to fit the new situation [16]. The result is retained as a new case in the case base if the solution works well with the new situation [15]. CBR reuse the previous solution or past experience in order to solve the current problem [16]. The performance measure is to determine the percentage of sensitivity, specificity, and accuracy from the result of CBR [16]. The confusion matrix is formed from the four outcomes produced as a result of binary classification which are False positives (FP), False negatives (FN), True positives (TP), True negatives (TN).

This paper presents the classification technique of meat based on odor-profile using E-nose and CBR classifier. E-nose was used to collect the odor data in order to establish the odor-profile of the meat samples. Then, the classification process takes place by using CBR classifier.

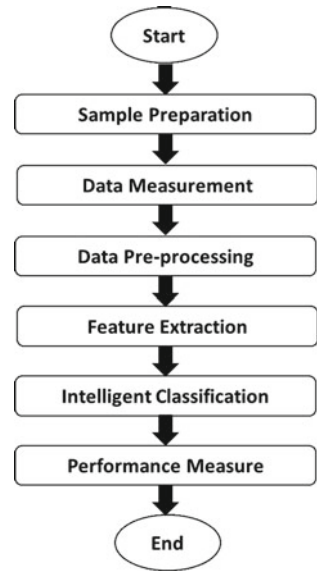
## 2 Methodology

Figure 1 shows the flowchart for the whole experiment. The experiment is started with the sample preparation of meat which is beef and pork meat. Next, the experimental setup process which is E-nose in order to get data for each sample is explained then continue to collect data measurement. Then, the data pre-processing method that used normalization and mean calculation technique. Next, feature extraction that used clustering, mean technique. The classification of odor-profile is applied by using Case-Based Reasoning (CBR). Lastly, a performance measure of sensitivity, specificity, and accuracy is observed and calculated by using the confusion matrix.

### 2.1 Sample Preparation

There are six different samples of meat for this experiment which are three from beef meat and three from pork meat. The sample consists of beef meat at 9.40 AM, at 10.40 AM and at 11.40 AM and pork meat at 9.40 PM, at 10.40 PM and at 11.40 PM. The meat sample was measured their weight with 200 g for each sample. Meat sample was obtained from the slaughterhouse in Malaysia. The sample was leaves at room temperature between the experiments.

**Fig. 1** Flowchart for the whole experiment



## 2.2 Experimental Setup

For this experiment, E-nose is the main instrument for the classification of the meat sample. Figure 2 shows the E-nose setup. Based on that figure, the components that are used in order to complete the experiment are a computer, a microcontroller, pump, sensor array and E-nose chamber. Each component has their own function. Computer is to display the data that from E-nose, microcontroller is to detect response sensor, pump is to make the odor from sample is spread, sensor array is to detect the odor from sample and pipe as the flow the odor from sample to the sensor array. The meat sample was placed into a container with the cover. E-nose pump was acted to inhale the odor from meat and trapping it in the E-nose chamber. The odor sensed by the sensor array and was produced resistance value readings by connecting the sensor

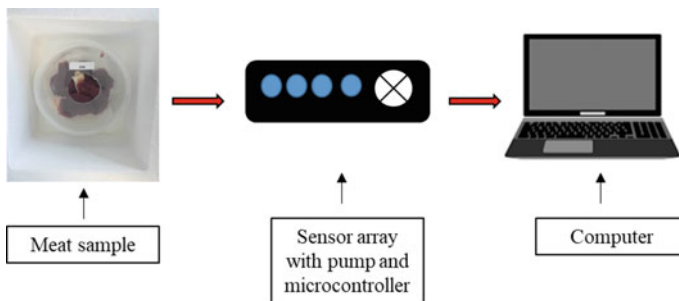


**Fig. 2** E-nose setup

arrays with the microcontroller by using USB cable with computer, and was sent to the computer for data collection.

### **2.3 Data Measurement**

The data measurement resistance response from E-nose for two different meat samples was collected and stored in the computer for analysis. Each sample was measured until 200 measurements with five repeated experiments. Total data measurement that collected is 1000 data measurement for each sample. The data in the serial monitor from Arduino was transfer into Microsoft Excel. The output from E-nose which 1000 cross 4 was called raw data.

### **2.4 Data Pre-processing**

In this section, it will show the raw data measurement that has to undergo the pre-processing process in order to get normalized value (0–1) and as the fixed range for all sample by using MATLAB software. In this process, the data measurement was used two techniques which is normalization technique and mean calculation technique. The data measurement has been normalized by using normalization technique in order to avoid error during classification and the less exactness of results. The equation that used for normalization technique is shown below:

$$R' = \frac{R}{R_{\max}} \quad (1)$$

From Eq. (1), R has represented the sensor reading in resistance, ohm ( $\Omega$ ) and  $R_{\max}$  is the maximum value of sensor reading in each data measurement. After the data measurement has been normalized, the mean normalized data was calculated. in order to minimize the data set from 5 normalized data set (1000 cross 4 of normalized data) into 1 normalized data set (200 crosses 4 of normalized data) for each sample.

### **2.5 Feature Extraction**

This section will show mean normalized data for beef and pork meat were clustered into several cases and was plotted in order to get the odor-profile pattern by using the mean feature in MATLAB software. Mean feature or cluster of data is a technique that is used for statistical analysis. The data have been mean normalized which 200 mean normalized cross 4 for each sample beef and pork will cluster into 10 cases. Each case consists of 20 mean normalized data. Then the mean normalized data for

each case was compressed by from 20 mean normalized data into 1 mean normalized data by using mean calculation for all experiment for each case. The final data is 10 crosses 4 data measurement for each sample.

## 2.6 CBR Classification

Step for CBR are CBR similarity calculation and CBR voting. The step for intelligent classification will complete with performed the performance measure. There are 4 steps in CBR cycle of meat. There are retrieve, reuse, revise and retain phase. In this experiment, only retrieve and reuse step was used. Retrieval phase solution of the most similar case from the case base to solve a new problem. Reuse phase is the solution and information in that case to solve the new case problem. The CBR case library was the datasets from a mean feature in feature extraction process. The case library acted as a stored case in CBR memory. In order to perform CBR computation, CBR similarity must be measured first. The CBR similarity calculation was repeated for each case. The formula represents in Eq. (2).

$$\text{Similarity } (T, S) = \frac{\sum_{i=1}^n f(T_i, S_i) \times w_i}{\sum_{i=1}^n w_i} \quad (2)$$

where,

$T$  is the target case for meat sample

$S$  is the source case for meat sample

$n$  is the number of attributions of the sensor

$w$  is the weight factor for CBR calculation.

## 2.7 Performance Measure

The CBR classification for beef and pork meat was completed by calculating the percentage of specificity, sensitivity, and accuracy measured by using confusion matrix. The formula was shown in the equation below.

$$\text{Specificity} = \frac{\text{TN}}{\text{TN} + \text{FP}} \quad (3)$$

$$\text{Sensitivity} = \frac{\text{TP}}{\text{TP} + \text{FN}} \quad (4)$$

$$\text{Accuracy} = \frac{\text{TP} + \text{TN}}{\text{P} + \text{N}} \quad (5)$$



where,

TP represents true positive

TN represents true negative

FP represents false positive

FN represents false negative.

Confusion matrix was represented the actual case and predicted case for the sample which beef and pork meat. The number of true positive, false positive, true negative and false negative was determined from CBR voting table result.

### 3 Results and Discussion

#### 3.1 Feature Extraction

Results from mean normalized data for beef and pork meat were clustered into several cases and was plotted in order to get the odor-profile pattern by using the mean feature. The result from mean normalized data that tabulated which is 200 cross 4 normalized data for each sample was clustered into 10 cases for each sample. Resulting in 180 cases for all sample (beef and pork meat). Each case consists of 20 normalized data. Then 20 cross 4 normalized data were reduced into 1 cross 4 normalized data by using average or mean technique. The mean technique was done in order to make the data fewer. Resulting, the data was plotted on a graph as odor pattern as shown below.

Figure 3 shows the graph of a combination of odor pattern for beef and pork meat sample at different time. The x-axis has represented the sensors array that is used in E-nose which is S1, S2, S3, and S4. The y-axis has represented by the value of mean normalized data in resistance, ohm ( $\Omega$ ). The green line (case 1–case 10) is indicated beef meat at 9.40 AM, the yellow line (case 11–20) is indicated beef meat at 10.40 AM, the cyan line (case 21–30) is indicated beef meat at 11.40 AM, the red line (case 31–40) is indicated pork meat at 9.40 PM, the magenta line (case 41–50) is indicated pork meat at 10.40 PM and the blue line (case 51–60) is indicated pork meat at 11.40 PM.

The pattern for all the meat samples shows significant differences and variance especially the green line that indicated beef meat at 9.40 AM and the cyan line that indicated beef meat at 11.40 AM. It shows the slightly different between sensor S2 and sensor S4 for beef meat. The reading of sensors is depending on the sensitivity of chemical sensors towards the odor from meat sample and environment. The higher the reading sensor shows the higher the sensitivity and significant towards odor from the sample. Resulting, this data was set as an input feature for CBR performance which CBR case library.

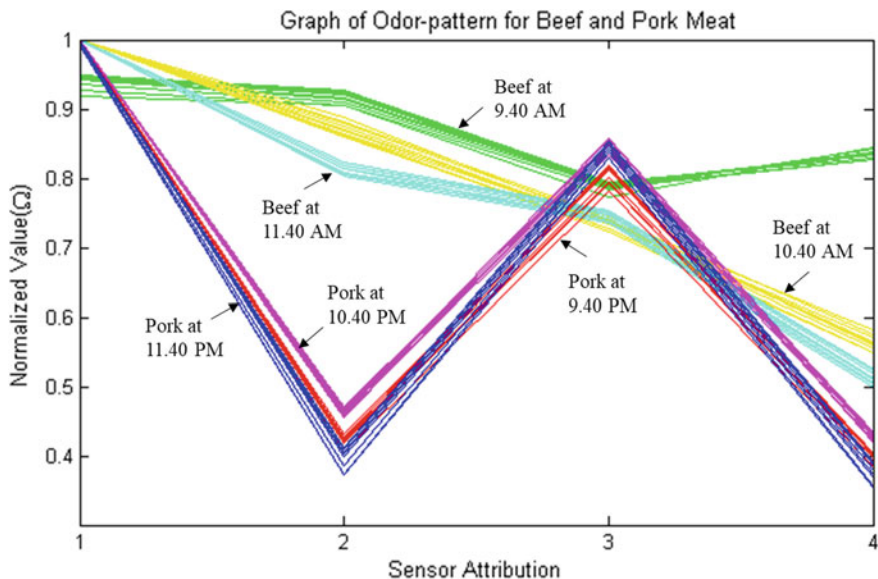


Fig. 3 Graph of a combination of odor pattern for beef and pork meat sample

### 3.2 CBR Classification

Refer to Table 1 it shows the CBR case library for beef and pork meat sample. The CBR case library is taken from a mean feature. The case library acted as a stored case in CBR memory.

Table 2 shows the CBR similarity calculation in order to find similarity percentage among the case. For this table, the similarity was calculated between case 1 and case 2 among 60 cases from CBR case library. The first column shows the sensor attribution in E-nose which is S1, S2, S3, and S4. The second column shows the source or stored case. For this table, case 1 is assigned as a source. For the third column shows the target or current case. Case 2 is assigned as a target for this calculation. Next, in column four shows the calculation of similarity between 2 cases which are between source and target by using the formula in Eq. (2). Then, the similarity was multiplied with normalized weight as shown in column seven. Resulting, the total or similarity between two cases got from the summation of each data in column seven.

Then the data was tabulated in CBR performance. The three highest value among case in each row was determined and selected. The result of three highest value was tabulated in CBR voting table. CBR voting is one of the techniques that important in order to measure the performance measure. This technique was used to make sure the case for each sample is in their own sample group. Based on the voting result, the highest value for each sample was located on their own sample class. The result from CBR voting was transferred into Confusion table in Table 3.

**Table 1** CBR case library for beef and pork meat

Case	S1 ( $\Omega$ )	S2 ( $\Omega$ )	S3 ( $\Omega$ )	S4 ( $\Omega$ )
Case 1	0.92	0.90	0.77	0.84
Case 2	0.93	0.91	0.78	0.84
Case 3	0.94	0.91	0.79	0.84
Case 4	0.94	0.91	0.79	0.83
Case 5	0.95	0.92	0.79	0.83
Case 6	0.95	0.92	0.79	0.84
Case 7	0.95	0.92	0.79	0.83
Case 8	0.95	0.93	0.79	0.83
Case 9	0.95	0.92	0.79	0.83
Case 10	0.94	0.92	0.79	0.83
Case 11	1.00	0.89	0.74	0.58
Case 12	1.00	0.88	0.73	0.57
Case 13	1.00	0.86	0.72	0.55
Case 14	1.00	0.86	0.73	0.55
Case 15	1.00	0.86	0.73	0.55
Case 16	1.00	0.87	0.74	0.56
Case 17	1.00	0.87	0.74	0.56
Case 18	1.00	0.87	0.73	0.56
Case 19	1.00	0.88	0.75	0.58
Case 20	1.00	0.88	0.74	0.56
Case 21	1.00	0.81	0.74	0.51
Case 22	1.00	0.81	0.74	0.50
Case 23	1.00	0.80	0.74	0.50
Case 24	1.00	0.80	0.74	0.51
Case 25	1.00	0.81	0.75	0.51
Case 26	1.00	0.81	0.75	0.51
Case 27	1.00	0.82	0.75	0.52
Case 28	1.00	0.82	0.75	0.52
Case 29	1.00	0.82	0.75	0.52
Case 30	1.00	0.82	0.75	0.53
Case 31	1.00	0.41	0.78	0.38
Case 32	1.00	0.42	0.79	0.40
Case 33	1.00	0.42	0.80	0.39
Case 34	1.00	0.42	0.80	0.39
Case 35	1.00	0.42	0.81	0.40
Case 36	1.00	0.43	0.82	0.40

(continued)

**Table 1** (continued)

Case	S1 ( $\Omega$ )	S2 ( $\Omega$ )	S3 ( $\Omega$ )	S4 ( $\Omega$ )
Case 37	1.00	0.43	0.82	0.40
Case 38	1.00	0.42	0.82	0.40
Case 39	1.00	0.43	0.82	0.40
Case 40	1.00	0.43	0.82	0.40
Case 41	1.00	0.47	0.84	0.43
Case 42	1.00	0.46	0.83	0.42
Case 43	1.00	0.47	0.84	0.43
Case 44	1.00	0.47	0.85	0.43
Case 45	1.00	0.47	0.85	0.43
Case 46	1.00	0.46	0.85	0.43
Case 47	1.00	0.46	0.85	0.42
Case 48	1.00	0.46	0.85	0.42
Case 49	1.00	0.46	0.86	0.42
Case 50	1.00	0.46	0.86	0.43
Case 51	0.99	0.37	0.84	0.36
Case 52	0.99	0.37	0.83	0.35
Case 53	0.99	0.39	0.84	0.37
Case 54	1.00	0.40	0.85	0.39
Case 55	1.00	0.41	0.85	0.39
Case 56	1.00	0.41	0.85	0.39
Case 57	1.00	0.41	0.85	0.39
Case 58	1.00	0.41	0.85	0.39
Case 59	1.00	0.40	0.85	0.38
Case 60	1.00	0.40	0.84	0.37

**Table 2** CBR similarity calculation between case 1 and case 2

Attribution	Source	Target	Similarity	Weight	Normalized weight	Similarity * normalized weight
S1	0.92	0.93	0.99	1.00	0.25	0.25
S2	0.90	0.91	1.00	1.00	0.25	0.25
S3	0.77	0.78	0.99	1.00	0.25	0.25
S4	0.84	0.84	1.00	1.00	0.25	0.25
The similarity between 2 cases						1.00

**Table 3** Performance classification for beef and pork meat classification using CBR

	Beef at 9.40 AM	Beef at 10.40 AM	Beef at 11.40 AM	Pork at 9.40 PM	Pork at 10.40 PM	Pork at 11.40 PM
Total cases	180					
Condition positive (P)	30	30	30	30	30	30
Condition negative (N)	150	150	150	150	150	150
True positive (TP)	30	30	30	30	30	30
True negative (TN)	150	150	150	150	150	150
False positive (FP)	0	0	0	0	0	0
False negative (FN)	0	0	0	0	0	0
Sensitivity (%)	100	100	100	100	100	100
Specificity (%)	100	100	100	100	100	100
Accuracy (%)	100	100	100	100	100	100
Overall sensitivity	100					
Overall specificity	100					
Overall accuracy	100					

### 3.3 Performance Measure

The result from calculation performance measure of data after obtained CBR voting. The percentage of sensitivity, specificity, and accuracy was measured by using confusion matrix. Table 3 shows the performance classification for beef and pork meat classification using CBR. Based on the table CBR voting, each sample consists of 30 number of real positive case and 150 number of the real negative case in data.

The sensitivity, specificity, and accuracy were calculated by using the Eqs. (3)–(4). The sensitivity is a division of the number of true positive result with the summation of true positive and false negative result while the specificity is a division of the

number of true negative result with the summation of true negative and false positive result. Lastly, accuracy is a division of summation true positive and true negative result with the positive and negative result. Resulting, the performance measures using sensitivity and specificity are 100%. The classification of beef and pork meat sample by using CBR is 100% accuracy.

## 4 Conclusion

In conclusion, the odor-profile for beef and pork meat was successfully developed. The result shows the difference between beef and pork meat in term of graph odor pattern. By applying CBR as intelligent classification, the different type of meat can be classified with 100% specificity, sensitivity and accuracy.

**Acknowledgements** This research and development are supported by Universiti Malaysia Pahang (UMP) Research Grant (UIC16031) and (UIC160904). Thank you to the Department of Veterinary Services Malaysia (DVS) for the provided the equipment for this research.

## References

1. Ma G (2015) Food, eating behavior, and culture in Chinese society. *J Ethn Foods* 2(4):195–199
2. World Health Organization (WHO), Constitution of The World Health Organization (Supplement) (2006)
3. Halal Hub Division (2016) The recognised foreign halal certification bodies and authorities
4. Hasan N et al (2012) Meat and fish freshness inspection system based on odor sensing. *Sensors (Switzerland)* 12(11):15542–15557
5. Nurrulhidayah AF, Che Man YB, Jamaludin MA, Rahman SA (2012) The contribution of science and technology in determining the permissibility (Halalness) of food products. *Revel Sci* 02(01):1–8
6. Muda TST, Ahmad R, dan Usul JF, Islam AP Halal Haram Makanan Menurut Imam Syafi'i: Analisis Dari Perspektif Maqasid Al-Shari'ah
7. Ramli A, Mokhtar M, Malaysia UK, Muda TST, Aziz BA (2016) Pembangunan Industri Halal: Konsep Halalan-Toyyiban dan Pengurusan Keselamatan Industri dalam Kerangka Maqasid al-Shariah Halal Industry Development: The Concept of Halalan-Toyyiban and Industrial Safety Management within the Framework of Maqasid al-Shari. *Ulum Islam J* 18:91–114
8. Ramli MA, Salahudin A (2016) Pembangunan Teknologi Autentikasi Halal dari Perspektif Maqasid al-Shari'ah. *J Nanomater* 171–186
9. Górska-Horczyzak E, Guzek D, Mołęda Z, Wojtasik-Kalinowska I, Brodowska M, Wierzbicka A (2016) Applications of electronic noses in meat analysis. *Food Sci Technol* 36(3):389–395
10. Marco S et al (2014) A biomimetic approach to machine olfaction, featuring a very large-scale chemical sensor array and embedded neuro-bio-inspired computation. In: *Microsystem Technologies*, pp 729–742
11. Lorwongtragool P, Sowade E, Watthanawisuth N, Baumann RR, Kerdcharoen T (2014) A novel wearable electronic nose for healthcare based on flexible printed chemical sensor array. *Sensors (Switzerland)* 14(10):19700–19712

12. Najib MS, Azih SH, Zahed N, Zahari MF, Mamat WMA, Manap H (2016) Intelligent odor-profile classification of kelulut honey using case-based reasoning technique (CBR). *ARPN J Eng Appl Sci* 11(10):6680–6684
13. Zamberan NH, Zahed N, Halim FA, Zahari MF, Mamat WMA, Manap H (2018) Fish quality study using odor-profile case-based reasoning (CBR) classification technique. *ARPN J Eng Appl Sci* 11(10):6691–6696
14. Zahari MF, Julius TA, Halim FA, Najib MS, Ghazali KH, Azoddein AAM (2015) Intelligent classification hazardous gas using sensors array. In: 8th international conference advanced computing theory engineering, vol 6, no 4, pp 233–237
15. Abdul Halim F, Sharfi Najib M, Ghazali K, Aziz Mohdazoddein A, Faruqi Zahari M (2015) Classification of odor profile ammonia in fertilizer. *Int J Adv Sci Eng Technol* 1(3):2321–9009
16. Daud SM, Najib MS, Zahed N (2017) Classification of lubricant oil odor-profile using case-based reasoning. In: *Proceedings—2016 IEEE conference on systems, process and control, ICSPC 2016*

# The Study of Raw Water Based on Quality Parameter Using Smell-Print Sensing Device



Suziyanti Zaib, Muhammad Sharfi Najib, Suhaimi Mohd Daud, Nurdiyana Zahed, Muhamad Faruqi Zahari, Nur Farina Hamidon Majid, Mujahid Mohamad and Hadi Manap

**Abstract** Water is a renewable natural resource and comprises about 70% of earth whilst the balance is land. Cleanliness and purity of drinking water is important for human health worldwide, thus it is important to know the water body source content so that consumption of it does not give any risk to human body's health. This study focuses on establishing a case library profile and classification of water based on recommended by Ministry of Health (MOH). This study water quality parameters such as iron (Fe) and pH is obtained using Electronic nose (E-nose). E-nose is an instrument that mimics human nose that has the ability to sniff in advance for volatile odor. However, colourless and odourless chemical usually undetectable by normal eyes or noses. Case Based Reasoning (CBR) is used in performing the intelligent classification that involved CBR computation, voting and performance measure. The similarity result shows that the technique accomplished to classify with 97.5% accuracy, 88.0% specificity and 92.2% accuracy.

**Keywords** Water quality · E-nose · CBR

## 1 Introduction

Water sources are an essential role in supporting the lives of individuals, communities, the social and economic development of a region or state, and the ecosystem of the environment [1]. Approximately 99% of the water supply in Malaysia comes from rivers and streams in the country [2]. Water can be drunk only if the concentration of components is within the limits set by special regulations [3]. In general, pollutant in water body sources are known as point and non-point source and monitoring its quality has become a major concern to certify current condition and long term pattern for future management [4].

---

S. Zaib · M. S. Najib (✉) · S. M. Daud · N. Zahed · M. F. Zahari · N. F. H. Majid · M. Mohamad · H. Manap  
Universiti Malaysia Pahang, 26600 Pekan, Pahang, Malaysia  
e-mail: [sharfi@ump.edu.my](mailto:sharfi@ump.edu.my)

H. Manap  
e-mail: [hadi@ump.edu.my](mailto:hadi@ump.edu.my)

© Springer Nature Singapore Pte Ltd. 2020  
A. N. Kasruddin Nasir et al. (eds.), *InECCE2019*, Lecture Notes in Electrical Engineering 632, [https://doi.org/10.1007/978-981-15-2317-5\\_17](https://doi.org/10.1007/978-981-15-2317-5_17)



A set of guidelines for safe and portable water supply in Malaysia has been provided by the Drinking Water Quality Surveillance Unit of the Ministry of Health Malaysia and was legislated under the guidance of experts from the World Health Organization (WHO) with a panel from the Public Works Department (PWD), Department of Chemistry (DOC) and Department of Environment (DOE) [5]. Thus, monitoring of drinking water quality is very important because the possibility of drinking water resources (from rivers and groundwater) becomes polluted is very high [6]. An agency of water supply carries out routine testing and monitoring of the quality of the water that is produced, while the public health protection agency conducts independent surveillance audits of water quality to determine whether the water-supply agency is fulfilling its responsibility [7].

Normally physical parameters are recommended in monitoring water quality for small communities [6]. The organic and inorganic forms of metals and nutrients and measurement of ammonia nitrogen (NH<sub>3</sub>-N) and iron (Fe) are used for chemical parameters [6]. Iron is essential for human health but it is also a toxic metal and WHO has fixed a sanitary security limit, 2 mg/L and it was originated from aesthetic reasons for iron (coloration of water) [8]. In aquatic system, heavy metals are a risk and hazard to human health due to their impacts on the quality of the water, foods and ecosystems [9]. Even though heavy metals are a common term defined in the literature, it is widely documented and regularly applied to the widespread pollutants of soils and water bodies with it entered into human body through air, water and food [10]. For the pH of water, generally it scale varies from 0 to 14, 7 is considered that water is neutral while lower of it referred acidic and a pH greater than 7 known as basic and normally, water pH ranges from 6 to 8.5 [11, 12].

E-nose is a device engineered to crudely mimic the human olfactory system for smells and taste sensors (gas and liquid sensors) and their communication with the human brain [13–16]. The odorant defined as a gaseous chemical component which encourage or stimulate the human olfactory system, while an odor is the sensorial response of the olfactory organ due to sniffing certain volatile substances [17]. First of all, data from sensor are collected and recorded using an E-nose system and then, statistics software is utilized to extract qualitative and quantitative information [18]. In an E-nose system there are three components; (a) the sample conditioning unit, which delivers odor from the headspace of the sample; (b) a test chamber in which a sensor array is placed (c) the processing unit that analyses sensor response for pattern recognition [19]. E-nose has various features that make it compatible for on-site water analysis [20]. Next, the recent availability of commercial sensor array to detect and characterize the headspace odor offering faster and an easier techniques for monitoring changes in water and waste water quality [19].

In pre-processing, normalization is one of the important steps to increase the accuracy of classification [21, 22]. There are several equation which were applied for normalization and the choices of equation in this research is using Eq. (1) [21, 23, 24].

$$R' = \frac{R}{R_{\max}} \quad (1)$$

Every row in raw data measurement was divided by the highest value from its own row in order to get the normalization value [23, 24]. It can be said, a normalization method is used to reduce the data fluctuation and restructure the measurement data according to the concentration levels to make the features invariant with the concentration levels [25].

There were various artificial techniques that can be used to classify odour data like Artificial Neural Network (ANN), Discriminant Factor Analysis (DFA), k-Nearest Neighbour (k-NN), Principal Component Analysis (PCA) and Case Based Reasoning (CBR) [26, 27]. CBR is an approach to solve new problems by using the past cases and experiences by comparing the similarity percentage with the current cases [23, 28]. CBR cycle cover four process which is retrieval, reuse, revise and retain [24, 26, 29, 30]. Its begins with the emergence of a new case/problem followed by case retrieval which involves measuring similarities between the new case and historical cases [29]. This is the core stage of the CBR cycle, and its accuracy is heavily impacted by predetermined similarity assessment criteria [29].

Similarity's result from CBR computation is chosen as current case to CBR performance template followed with a voting technique using three highest similarity value from each case is selected and applied for all the cases to observe weather the value selected is from the same sample type with the case [31]. Equation (2) used to calculated the similarity [23]:

$$\text{Similarity } (T, S) = \frac{\sum_{i=1}^n f(T_j, S_i) \times w_i}{\sum_i^n w_i} \tag{2}$$

## 2 Methodology

### 2.1 Raw Water Sampling and Preparation

The samples used in this project were divided into two main category, raw water and drinking water (treated water) with different solutions to represent two quality parameter, pH and iron which followed the recommendation by Ministry of Health Malaysia showed in Table 1. The sample preparation is done in laboratory with the

**Table 1** Recommended raw water quality and drinking water quality standard

Parameter	Acceptable value (mg/l)		Sample preparation (mg/l)
	Raw water	Drinking water	
pH	5.5–9.0	6.5–9.0	4.0 and 7.0
Iron	1.0	0.3	0.3, 0.4, 1.0 and 1.1

help of chemist and lab technician to prepare the solution of iron 0.3, iron 0.4, iron 1.0, iron 1.1 mg/l, and pH solution of 7.0 and 4.0.

The water sample's solution used were measured and set to 50 ml per sample using beaker and pipette to measure the volume for specific concentration for each sample by dilution process using Eq. (3)

$$M1V1 = M2V2 \quad (3)$$

where  $M$  is the molarity of the solution and  $V$  is the volume of the solution.

## ***2.2 Data Pre-processing***

In data pre-processing, two technique were involved; normalization technique and mean calculation technique. In detail, normalization technique used to reduce the value by dividing each raw data with the highest value of its own row in order to get the range value between 0 and 1 that is also known as feature scaling.

## ***2.3 Features Extraction***

In feature extraction, the 200 normalized data (ND) for each sample is clustered into 10 cases which lead to each case having 20 ND. Next, mean calculation is used again to get only 10 data case with each case containing 1 ND. The cluster value is plotted for both samples that is known as odour pattern. The mean data of ND was declared as input in CBR.

## ***2.4 CBR Classification***

The data from feature extraction in then stored as input to the CBR with 10 cases for each sample and it's known as CBR computation. The similarity was obtained by comparing the stored case with the current case which is continuously repeated to compare 60 cases of stored case with current case, this process is repeated from case 1 until case 60 to get the rank of similarity. The results from CBR computation that acts as retrieval phase was then fed through the confusion matrix and voting technique. The voting in CBR functions in order to get the result to be able to know the sample was correct by choosing the three highest similarities for each case in proximity matrix.

## 2.5 Performance Measure

The last step sample classification is to find the performance measure. Performance measured was calculated to know the percentage of sensitivity, specificity and accuracy of sample classification by applying CBR technique.

## 3 Result and Discussion

### 3.1 Data Measurement

The resulting data was taken 5 times for each sample to get 5 different reading results for one sample reading by connected the hardware part with PC. In one reading sample contain 200 data measurement that resulted to 1000 data for one sample is read by one sensor. In conclusion, there 6000 raw data for 6 sample named by sample A1 for iron 1.0 mg/l, A2 for iron 0.3 mg/l, A3 for pH 7.0, B1 for iron 1.1 mg/l, B2 for iron 0.4 mg/l, and B3 for pH 4.0. The graph pattern of raw data was not consistent, so it needs to proceed to pre-processing process to clearly observe odour profile pattern for each sample.

### 3.2 Data Pre-processing

In data pre-processing, the result from normalization technique and mean calculation technique was obtained to get the odour profile for six samples A1, A2, A3, B1, B2 and B3 were used in the next process. The result from normalized data for 6000 raw data is shown in the graph below with the horizontal axis showing sensor attribution or sensor array while vertical axis showing the reading of signals; normalize reading in the range between 0 until 1. The x-mark represents 3000 ND for sample A1, A2, A3 while circle plot represent another 3000 ND for sample B1, B2 and B3. Based on the two types of pattern (circle and x-mark) it shows some slight difference especially on the sensor 2 (S2), sensor 3 (S3) and sensor 4 (S4) while for sensor 1 (S1) shows no significant difference at all.

Next, mean calculation is applied to get the only one data set for each sample by dividing the total of ND with the total of data set in each row. Hence, 200 ND for each data set of sample is used mean calculation technique to get only one. So from 6000 ND, the overall now becomes 1200 ND for 6 sample which is 200 ND (Fig. 1).

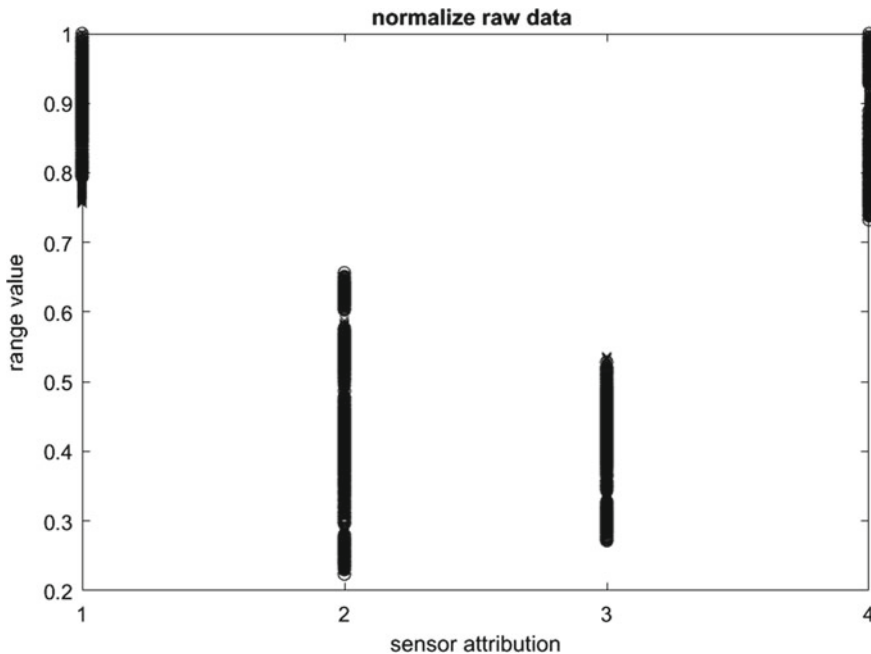


Fig. 1 Normalize raw data for six sample

### 3.3 Features Extraction

The 200 ND is then clustered into 10 cases to form only 20 ND for each case. Next 20 ND for each of case is then fed through the mean calculation again to get only one value for one case in order to get the odour profile for the each sample. In the end there only 60 ND with 10 ND illustrated for each sample and the odour pattern is clearly classified in the Fig. 2.

The reaction of sample odour with the gas sensor is represented above as vertical axis showing the quantitative value of the resistance reading in ohm whilst horizontal axis shows the sensor attribution or sensor array. From the odour pattern above x-mark represents sample A1, A2 and A3 while circle represent for sample B1, B2 and B3. It clearly shows significant difference in S4 between sample A and B through magenta and green colour respectively that shows same difference between the two groups. Moreover S2 and S3 also have the same condition for A2 and A3 as for the other samples the difference is so small. As for S1 almost dominant by red and black which is B1 and B3 from the same group and it can conclude all the data for S1 is almost close to each other for six samples in the range of 0.9–1.0.

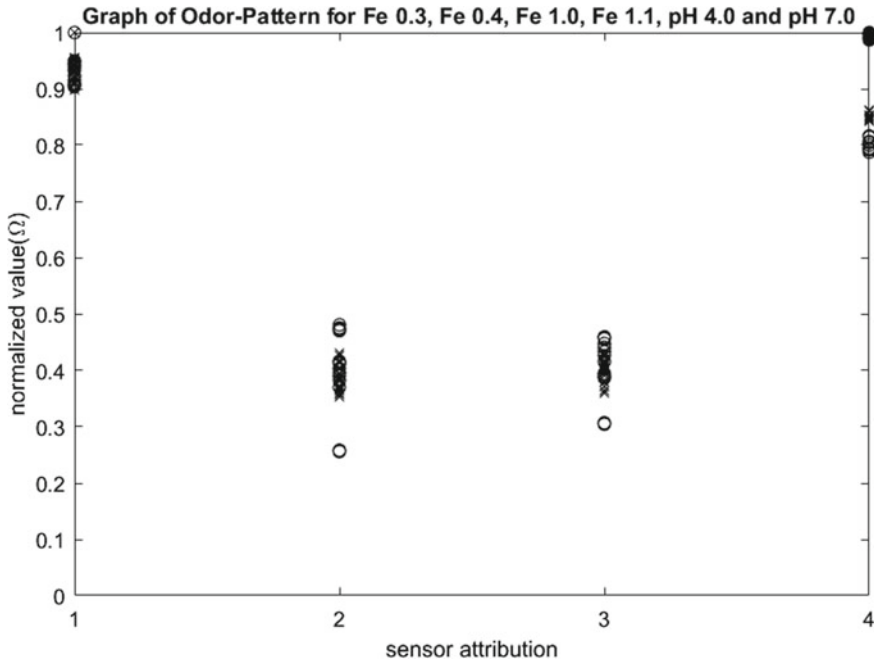


Fig. 2 Odor pattern for sample A and sample B

### 3.4 Performance Measure

Next, the data from feature extraction was stored as input to the CBR for the next step which is performance measures. The similarity is obtained by comparing the stored case with the current case and was summarized into proximity matrix shown in Fig. 3.

In the simplest way to conclude, when case 1 as current case and compared with the stored case and if the stored case belongs to case 1, the similarity is 100% same this is illustrated in black colour. While if stored case is case 2 then the compared result shows 99.9048% similarity. This process is repeated until all 60 cases is compared by filled in the stored case and current case. The summarized results are shown in Tables 2 and 3.

The next process is voting with the highest similarity represented in pink, second highest in yellow and the third highest green. The purpose of this is to make sure the top three of similarity is in correct group. The result of voting shows that the top three rank of sample A and sample B are overall in the correct group for A2, A3, B2 and B3. From the voting results the performance measurement is then calculated using confusion matrix based on CBR.

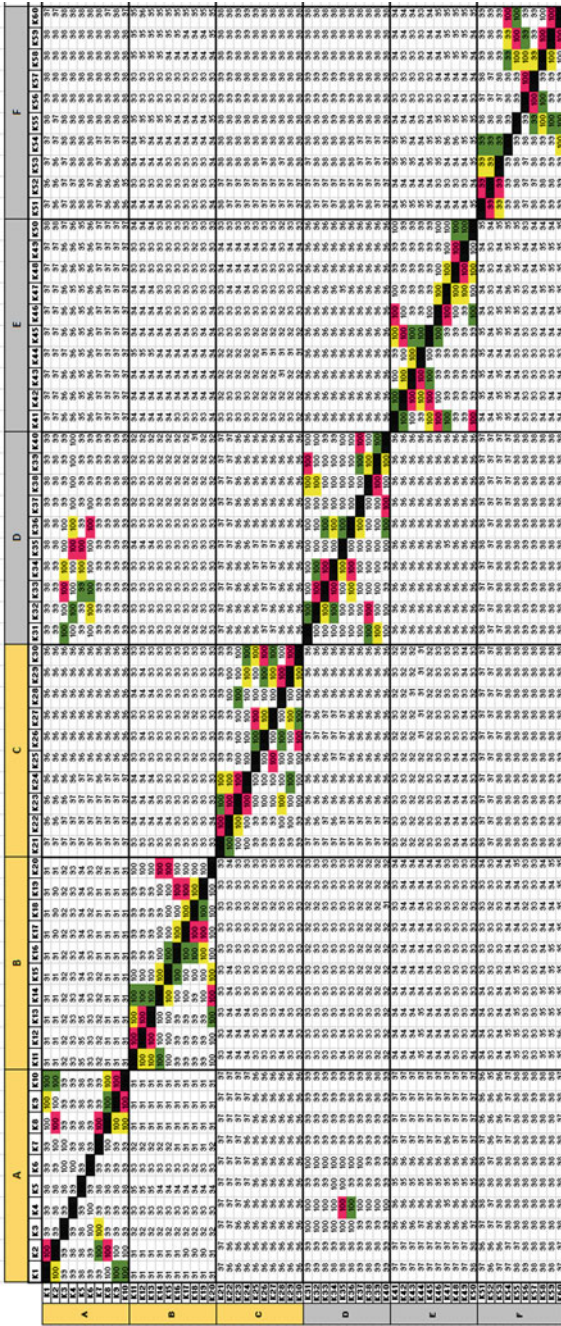


Fig. 3 Proximity matrix for sample A and sample B

**Table 2** Result of confusion matrix for sample A and sample B

		Predicted	
		Sample A	Sample B
Actual	Sample A	78	12
	Sample B	2	88
Total		180	

**Table 3** Results of performance measure

Total cases	180
Condition positive (P)	90
Condition negative (N)	90
True positive (TP)	78
True negative (TN)	88
False positive (FP)	12
False negative (FN)	2
Sensitivity (%)	97.5
Specificity (%)	88
Accuracy (%)	92.2

The performance measured is then calculated using confusion matrix to get the accuracy, sensitivity and accuracy of the sample. The confusion matrix is a  $2 \times 2$  table, two rows and two columns that represents the number of false positive, false negative, true positive and true negative is illustrated in Table 2. The sample A is for recommended quality parameter of water by MOH while sample B does not meet with regulation that is suggested by MOH. It is shown that the accuracy of E-nose toward the samples are 92.2% that indicated the E-nose device had highest sensitivity closely to 100% in detecting and differentiating odour molecules for sample A and sample B. The specificity is 88% and the sensitivity of the sample is 97%.

One sample contains 30 cases from 3 highest of similarity where six cases are applied in this project to become the total cases of 180. For TP there are 78 cases which were predicted sample; A which is follows the water parameter quality for iron and pH and the results is same. While 88 cases is TN showing that the predicted and results is shows sample B which is the water not following the parameter quality for raw water and treated water based on iron and pH value. The accuracy for intelligence classification is 92.2% which is the frequent of the classifier is correctly detect the sample is followed the recommended parameter. Meanwhile the sensitivity and specificity are the one method to quantifying the diagnostic ability of the test.



## 4 Conclusion

In conclusion, the case library profile for samples A and Sample B were established. The case library was drawn from the data measurement from smell print device that undergoes pre-processing technique. The case library than is used for CBR technique.

As the odor profile and case library had been done from smell print device, the classification of samples done using CBR technique. The classification of raw water quality parameter for iron and pH from odor profile is successful with the accuracy, sensitivity and specificity approximately approach to 100%.

**Acknowledgements** We would like to thanks and appreciate all staff and students of Faculty Electrical and Electronic Engineering, Universiti Malaysia Pahang (UMP) that involved in this project and also the staff at water's laboratory at AKSB for giving contribution in providing the sample. This research and development are supported by UMP Research Grant (UIC160301 and UIC160904).

## References

1. Fitriati U, Eriyanie E (2015) A study on water quality of raw water sources of Pdam (Municipal Water Company) Bandarmasih 1(1)
2. Azlan A, Khoo HE, Idris MA, Ismail A, Razman MR (2012) *Sci World J Eval Miner Content Drink Water Malay*
3. Petracchia L, Liberati G, Giuseppe Masciullo S, Grassi M, Fraioli A (2006) Water, mineral waters and health. *Clin Nutr* 25(3):377–385
4. Mohd-Asharuddin S, Zayadi N, Rasit W, Othman N (2016) Water quality characteristics of Sembrong dam reservoir, Johor, Malaysia. *IOP Conf Ser Mater Sci Eng* 136(1)
5. Rwoo MA et al (2017) Assessment of drinking water quality using principal component analysis and partial least square discriminant analysis: a case study at water treatment plants, Selangor, pp 157–173
6. Ngadiman N, Bahari NI, Kaamin M, Hamid NB, Mokhtar M, Sahat S (2016) Water quality of hills water, supply water and RO water machine at Ulu Yam Selangor. *IOP Conf Ser Mater Sci Eng* 136(1)
7. S. Edition, Guidelines for drinking-water quality, vol 3 (1997)
8. W. Treatment, F. Group, R. I. Forum (2010) Of conservation science effect of water treatment residuals (aluminum and iron ions) on human health and drinking water distribution systems, vol 1, no 3, pp 175–182
9. Souza AM, Salviano AM, Melo JFB, Felix WP, Belém CS, Ramos PN (2016) Seasonal study of concentration of heavy metals in waters from lower São Francisco river basin, Brazil. *Braz J Biol* 76(4):967–974
10. Gautam RK, Sharma SK, Mahiya S, Chattopadhyaya MC (2014) Chapter 1. Contamination of Heavy metals in aquatic media: transport, toxicity and technologies for remediation. *Heavy Met Water*, 1–24
11. Mohsin M, Sahib DN (2013) Assessment of drinking water quality and its impact on residents health in Bahawalpur city, vol 3, no 15, pp 114–128
12. Mohanty B, Beran MG, Keval KP, Dhruvit KT, Vimal GS (2017) Design and construction of a modified rapid sand filter for treatment of raw water. *J Res* 3(May):8–13
13. Baldwin E, Bai J, Plotto A, Dea S (2011) Electronic noses and tongues: applications for the food and pharmaceutical industries. *Sensors* 11(5):4744–4766

14. Röck F, Barsan N, Weimar U (2008) Electronic nose: current status and future trends. *Chem Rev* 108(2):705–725
15. Wilson A, Baietto M (2009) Applications and advances in electronic-nose technologies. *Sensors* 9(7):5099–5148
16. Rapid detection of aromas using integrated gas chromatography with multiarray sensors, 26 June 2001
17. Blanco-Rodríguez A et al (2018) Development of an electronic nose to characterize odours emitted from different stages in a wastewater treatment plant. *Water Res* 134:92–100
18. I. Transactions and O.N. Instrumentation (2009) Design of a portable e-nose instrument for gas classifications, vol 58, no 10, pp 3609–3618
19. Canhoto OF, Magan N (2003) Potential for detection of microorganisms and heavy metals in potable water using electronic nose technology. *Biosens Bioelectron* 18(5–6):751–754
20. Goschnick J, Koronczí I, Frietsch M, Kiselev I (2005) Water pollution recognition with the electronic nose Kamina. *Sens Actuators B Chem* 106(1):182–186
21. Zahed N, Najib MS (2016) Odour-profile classification of Gelam, Acacia and Tualang honey based on k-nearest neighbors technique. National conference for postgraduate research 2016. University of Malaysia Pahang, pp 404–412
22. Abdul Halim F, Sharfi Najib M, Ghazali K, Aziz Mohdazoddein A, Faruqi Zahari M (2015) Classification of odor profile ammonia in fertilizer. *Int J Adv Sci Eng Technol* 1(3):2321–9009
23. Daud SM, Najib MS, Zahed N, Jusof MH, Jusoh MF, Hassim MI (2017) Classification of lubricant oil adulteration level using case-based reasoning. *J Fundam Appl Sci* 9(4S):256–275
24. Daud SM, Najib MS, Zahed N (2016) Classification of lubricant oil odor-profile using case-based reasoning. In: *IEEE conference on system, process and control (ICSPC2016)*, pp 16–18
25. Omatu S, Yano M (2016) E-nose system by using neural networks. *Neurocomputing* 172:394–398
26. Zahari MF, Julius TA, Halim FA, Najib MS, Ghazali KH, Azoddein AAM (2015) Intelligent classification hazardous gas using sensors array. *J Adv Inf Technol* 233–237
27. Zahari MF et al (2016) Gaharu sensor: classification using case based reasoning (CBR), vol 1, no 8, p 4
28. Perikos I, Hatzilygeroudis I (2017) A case-based reasoning approach to convert natural language into first order logic. In: *Proceedings—19th IEEE international conference on computational science and engineering, 14th IEEE international conference on embedded and ubiquitous computing and 15th international symposium on distributed computing and applications to business, engineering*, pp 1–4
29. Candidate XH, Xia B, Skitmore M, Chen Q (2016) The application of case-based reasoning in construction management research: an overview. *Autom Constr* 72:65–74
30. Aamodt A (1994) Case-based reasoning : foundational issues, methodological variations, and system approaches, vol 7, pp 39–59
31. Zahed N, Najib MS, Fatin N, Nik N, Azhani M (2016) Classification of honey odor-profile using case-based reasoning technique (Cbr). *ARPN J Eng Appl Sci* 11(10):6675–6679

# Camera Orientation Determination Based on Copper Wire Spool Shape



Farah Adiba Azman, Mohd Razali Daud, Amir Izzani Mohamed, Addie Irawan, R. M. Taufika R. Ismail and Mohd Mawardi Saari

**Abstract** A simple and inexpensive system but effective in performing required tasks is the most preferable in industry. In this study, a vision system is developed to solve the peg-in-hole problem of a robot-like forklift to pick up copper wire spool arranged side by side on a rack, without using any sensors, except a low-cost camera. Inspired by how human perceive an object orientation based on its shape, an algorithm is developed to determine robot orientation based on the shape of a copper wire spool relative to camera position and yaw angle. The center point of the spool (CPS) should be on the center line of camera FOV (CFOV) if the camera is perpendicular or  $0^\circ$  parallel to the spool. Thus, the coordinate of the CPS and the CFOV is same. Instead, when the camera is seeing the spool from the angle less or bigger than  $0^\circ$ , the CPS and CFOV will be different, and the difference shows the position and the yaw angle of the camera relative to the spool. A copper wire spool has three circles; the outer circle, the taper part around its center hole and the center hole itself. The proposed system uses Circular Hough Transform (CHT), filtering, binary, morphology and Sobel edge detection of the sampled images from real-time video recording to determine the orientation of the camera related to the copper wire spool shape, in which the center coordinate of the three circles was determined. Results from the experiments that had been done show that the system is able to determine the orientation of the camera related to the spool.

---

F. A. Azman · M. R. Daud (✉) · A. I. Mohamed · A. Irawan · R. M. T. R. Ismail · M. M. Saari  
Faculty of Electrical & Electronics Engineering, Instrumentation and Control Engineering  
Research Centre, Universiti Malaysia Pahang, 26600 Pekan, Pahang, Malaysia  
e-mail: [mrzali@ump.edu.my](mailto:mrzali@ump.edu.my)

A. I. Mohamed  
e-mail: [amirizzani@ump.edu.my](mailto:amirizzani@ump.edu.my)

A. Irawan  
e-mail: [addieirawan@ump.edu.my](mailto:addieirawan@ump.edu.my)

R. M. T. R. Ismail  
e-mail: [rajamohd@ump.edu.my](mailto:rajamohd@ump.edu.my)

M. M. Saari  
e-mail: [mmawardi@ump.edu.my](mailto:mmawardi@ump.edu.my)

**Keywords** Circle detection · Copper wire spool · Camera orientation · Vision-based system

## 1 Introduction

Robotic manipulator is widely used in the manufacturing process for grasping and insertion (peg-in-hole) tasks because it is a reliable system to maintain productivity and quality [1]. The peg-in-hole problems are also widely discussed in robotic research due to complexity in applying control algorithm that requires position and force feedback. This lead to encourage some researchers have tried to solve the problem without sensor, as presented by [2, 3]. However, some researchers utilized a camera to navigate the robot hand nearer to the hole, or to determine the pose of the peg and hole, before the force or torque sensor was used. Lin et al. employed three kinds of cameras; Kinect, Bumblebee stereo and a high-resolution camera to support the peg-in-hole insertion process by two 6 D.O.F robotic arms equipped with a force sensor [4]. Chang employs binocular vision to observe a manipulator and a target for insertion of USB flash drive to a USB square hole automatically. The vision system was also used to control the movement of the robotic arm through a visual servo controller [5].

In order to detect circular shape, many researches improved Circular Hough Transform (CHT) to avoid false circle detections because CHT involves high computation [6–8]. Yao et al. proposed Curvature Aided Hough Transform for Circle Detection (CACD) to detect circles in a complex scene. However, it needs a proper edge detection method to avoid false circle detections [9]. Canny edge detection method is one of the methods commonly used to obtain the correct results and reduce the noise of the image despite the fact that the method has a flaw which it may not traverse all weak edge pixels [10–13]. Hussin et al. use color detection method to detect an object in a complex scene image and it involves only one color. Due to lighting intensity, the object cannot be detected accurately [14]. In addition, the vision system also has some flaws such as the existence of dust, the need for extra lighting, occlusions and distortions which can occur noise of an image [15]. The development of circles detection is still needed especially for circles shape with many noises. Therefore, addition of filters in image processing can minimize the noise of an image. Filters that usually be used by researches are Gaussian Filter [16, 17], Mexican Hat Filter [18] and Median Filter [19].

In this study, a cheap camera which is Logitech Webcam C270 is put on a forklift-like robot, which will autonomously pick up a copper wire spool (a cylindrical object on which the copper wire is wound and having a rim at each end). For simulation process, the proposed algorithm uses Circular Hough Transform combined with another image processing techniques; filtering, binary, morphology and edge detection to track the spool and determine a stop position that enables the robot moving closer to the spool and insert the center cylindrical shaft through the center hole of the spool.

However, the scope of this study is limited to the development of the vision system and focus on camera orientation verified through simulations using real-time video recording.

## 2 Theoretical Background

The process of tracking and checking the alignment of the spool and camera only will be guided by a web camera. Based on the images taken from a real-time video recording, the vision system guides the camera to stop at the correct position. Referring to the isometric projection perspective, as shown in Fig. 1, the correct position is where the front and back circles (rims) of the spool are sharing the same center. From the side view of isometric projection, they overlapped each other and seen as only one circle.

While the camera moves to the location where the spools are located, it is scanning its side and search for the spool. The spool will be detected starting from the point when it enters the field of view (FOV) of the camera. The robot orientation is depending on the camera orientation. As the spool reaching the center of the FOV, the centers of the big and small circle will become overlapping and finally sharing the same center point, as illustrated by Fig. 2. In the implementation of the system, a center with coordinate (320, 240) is plotted at the center of the image frame of

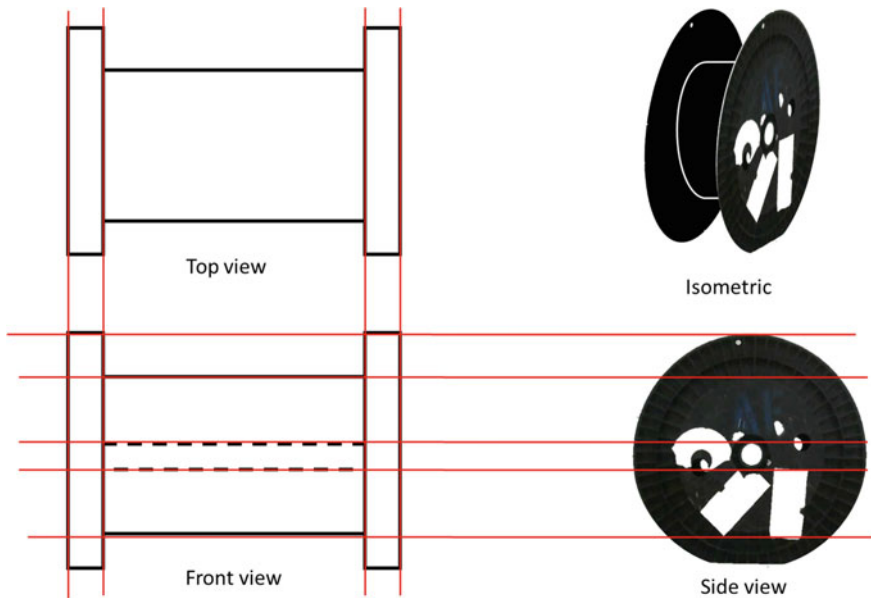


**Fig. 1** Isometric projection of a spool

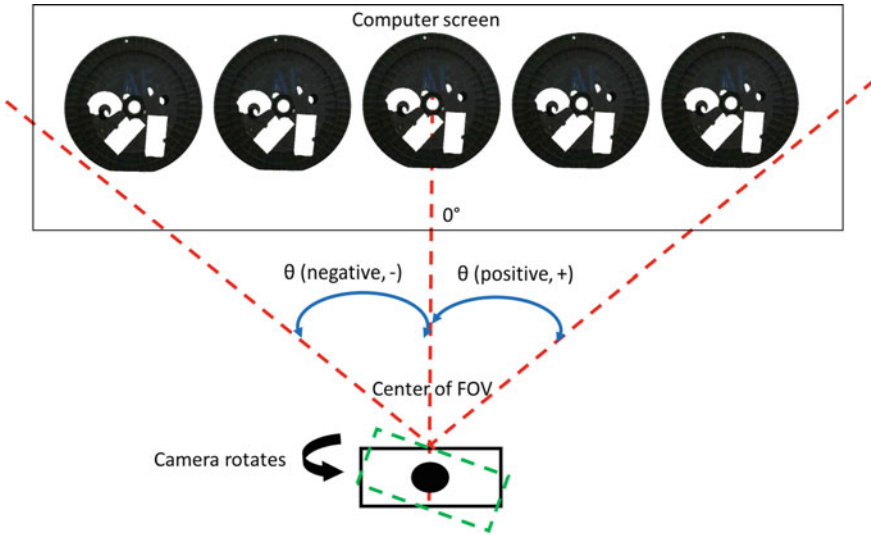


Fig. 2 Camera and spool orientation during image capturing

the camera. When the big and small circle center of the spool is overlapped by the virtual center, it means the robot is at the correct position and the camera can move forward. While moving forward, the camera orientation (yaw angle) is confirmed by determining the position of the spool on the frame image as shown in Fig. 2. The camera orientation (yaw angle) is considered  $0^\circ$  (parallel to spool) if the spool is at the center of the frame image. The spool image will shift to the right-hand side of the image frame if the yaw angle is positive and likewise for the negative yaw angle.

### 3 Proposed Algorithm

The proposed algorithm follows several steps to detect the copper wire spool circle and confirm the alignment of the camera and copper wire spool. The general idea is described as follows. Images are preprocessed to obtain a circle by using unsharp filtering. In most filtering methods, unsharp filtering is the most effective method to prevent false circle detection by using Circular Hough Transform (CHT). CHT is applied after the preprocessing method. The alignment of the camera and copper wire spool is determined by using several formulas as follows.

### 3.1 Copper Wire Spool Detection

Images are acquired using Logitech HD Webcam C270 and processed using MATLAB programming platform. The real-time video is applied and previewed in grayscale color. The resolution of the video used in this system is  $640 \times 480$  pixels. The steps are listed as follows:

- Step 1. Filtering. Unsharp filter is applied to overcome false detection. Unsharp filter is a simple sharpening operator to unsharp contrast enhancement of the grayscale image. There are 3 types of filter are used which are Median, Prewitt and Unsharp filtering to compare the effectiveness of circle detection by using the CHT method.
- Step 2. Binary operation. The image is converted to binary with 0.3 threshold value. All connected components that have fewer than 100 pixels from the binary image are removed by using 'bwareaopen' function.
- Step 3. Morphological operation. Morphological apply a structuring element to an input image, creating an output image of the same size. The erosion and dilation methods are applied in this system.
- Step 4. Edge detection. It is applied to obtain accurate edges of an input image. Edge detection method is compared between Canny and Sobel method and Canny method is applied due to the effectiveness of circle detection.
- Step 5. Circular Hough Transform (CHT) is applied after image processing. CHT is applied to identify the characteristics of copper wire spool. CHT is one of the methods to detect the circular image in a vision system. A reference center with coordinates (320, 240) is displayed on the screen in green color, serves as a reference center
- Step 6. The camera will detect the copper wire spool whenever the system detects big circle within the radius range shown in Rule 1. The big circle is previewed in red color and the screen will display "Spool detected".
- Step 7. The camera will detect small circle whenever the system detects small circle radius range shown in Rule 1. The small circle is previewed in blue color

$$\text{Rule 1} = \begin{cases} 1, & 100 \leq \text{radii1} \leq 250(\text{Big circle}) \\ 1, & 10 \leq \text{radii2} \leq 25(\text{Small circle}) \\ 0, & \text{otherwise} \end{cases}$$

### 3.2 Camera and Spool Alignment

The copper wire spool and camera are considering at the center of the frame when the center of big and small circle overlap the reference center (320, 240) calculated

**Table 1** Coordinate of spool circles

X1, Y1	Big circle coordinate
X2, Y2	Small circle coordinate
320, 240	Reference center

by using (X, Y) coordinate. Due to slight errors, the distance between the center can be accepted within error range  $\pm 3$  pixels as shown in Rule 2. The steps are listed as follows:

$$\text{Rule2} = \begin{cases} 1, & -3 \leq \text{distance center 1} \leq 3(\text{Big circle}) \\ 1, & -3 \leq \text{distance center 2} \leq 3(\text{Small circle}) \\ 0, & \text{otherwise} \end{cases}$$

- Step 1. The screen displayed “Centers overlapped” when both small and big circle center overlapped the reference center.
- Step 2. The camera will focus on the small circle to make sure the orientation of the camera (yaw angle) and copper wire spool at  $0^\circ$ .
- Step 3. The small circle center must overlap the reference center if the camera is moving forward, backward and the screen will display “Center aligned”.
- Step 4. The copper wire spool is considered not aligned when there are more than one circles displayed at the center of the spool. The mathematical equation to determine small and big circle centers overlapped the reference center is shown in Eqs. (1) and (2). For aligning position, the coordinate for both circles must be (0, 0) by using both Eqs. (1) and (2) and the camera orientation must be in  $0^\circ$  position (Table 1).

$$\text{Distance center 1} = ((320 - X1), (240 - Y1)) \tag{1}$$

$$\text{Distance center 2} = ((320 - X2), (240 - Y2)) \tag{2}$$

From the steps mentioned above, the alignment of the spool and camera must satisfy two conditions which are the big and small circle center must overlap the reference center when the yaw angle of the camera is at  $0^\circ$ . Secondly, the number of small circle detection is one.

Referring to Fig. 3, it shows the condition of camera orientation when it is in align position. In align position, at  $20^\circ$  angle, the spool is viewed as half spool image. Camera orientation only affects the spool position image on the frame. It does not affect the spool orientation. The camera orientation theory is proved by using Eq. (3) below.

$$a = \tan \theta(b) \tag{3}$$



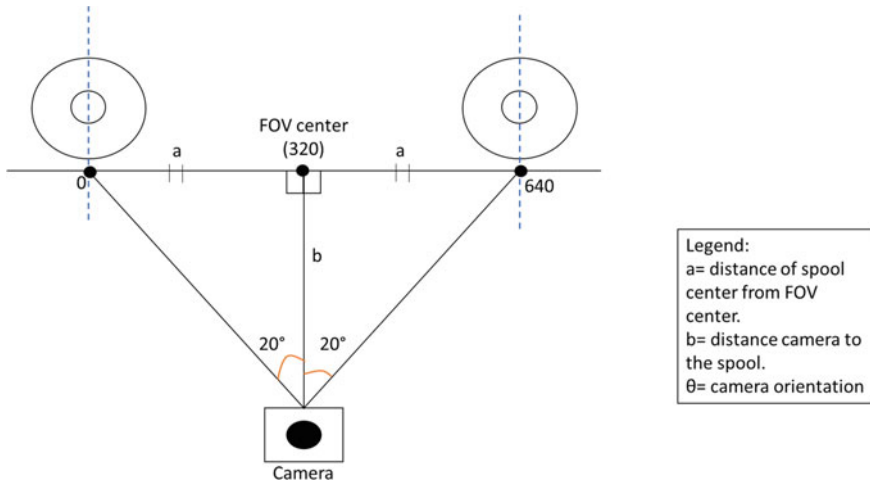


**Fig. 3** Camera orientation parameters relative to spool position and orientation

As it can be seen,  $a$  refers to distance of circle center from FOV center, where  $b$  is the distance of the camera to the copper wire spool and  $\theta$  is refers to the camera orientation. In this paper, the distance of the camera to the spool is taken from 40 to 100 cm due to its effectiveness of circle detection. The overflow of the proposed algorithm is shown in Fig. 4.

### 4 Experimental Results and Discussion

The experiments performed in an indoor environment which is in the lab of Faculty of Electrical and Electronic Engineering (FKEE) UMP. This experiment is performed by using MATLAB software with Logitech C270. Figure 5 shows that the copper wire spool (circle) is detected by using Unsharp filter and CHT method. By using the proposed method, the system can detect the copper wire spool by detecting the big and small circle which is in red and blue color. The copper wire spool can be detected within the range 40–110 cm from the camera due to the range that has been set in this system. It is because if the distance of the camera to the spool is less than 40 cm, it will affect the accuracy of the circle detection due to lighting and noise that hard to be eliminated and cause false circle detections. Based on the results, Unsharp filter can prevent false circle detection. It fits the expected results of this paper.

From the results shown in Fig. 5, the screen displayed “Spool detected” whenever the spool is detected. The red and blue circle stands for big and small circle whereas the green center is for reference center. All figures above show that the copper wire spool is not aligned. Next, Fig. 6 shows that when the copper wire spool is considered align when it satisfies all align conditions. The copper wire spool is at the center of

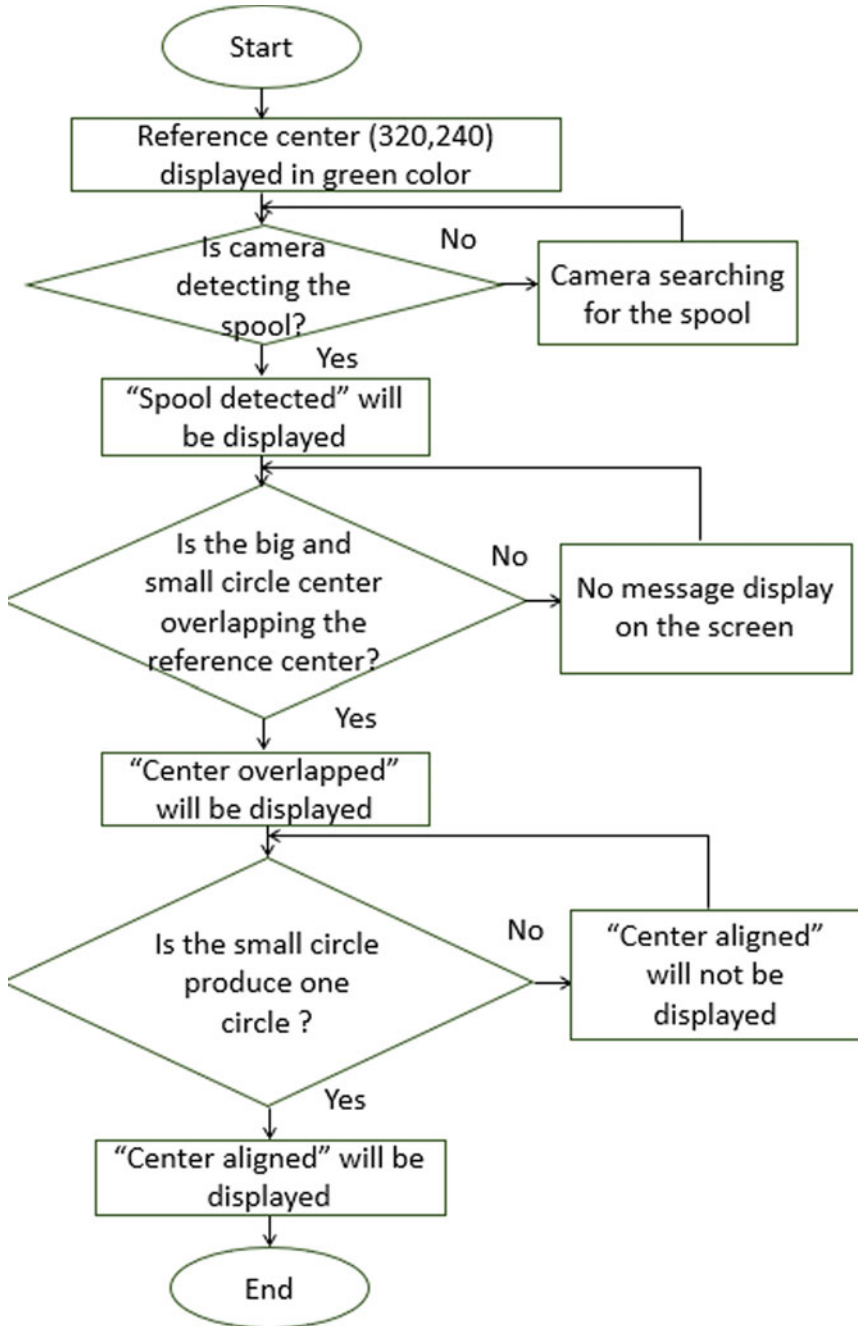


Fig. 4 Flowchart of the proposed algorithm

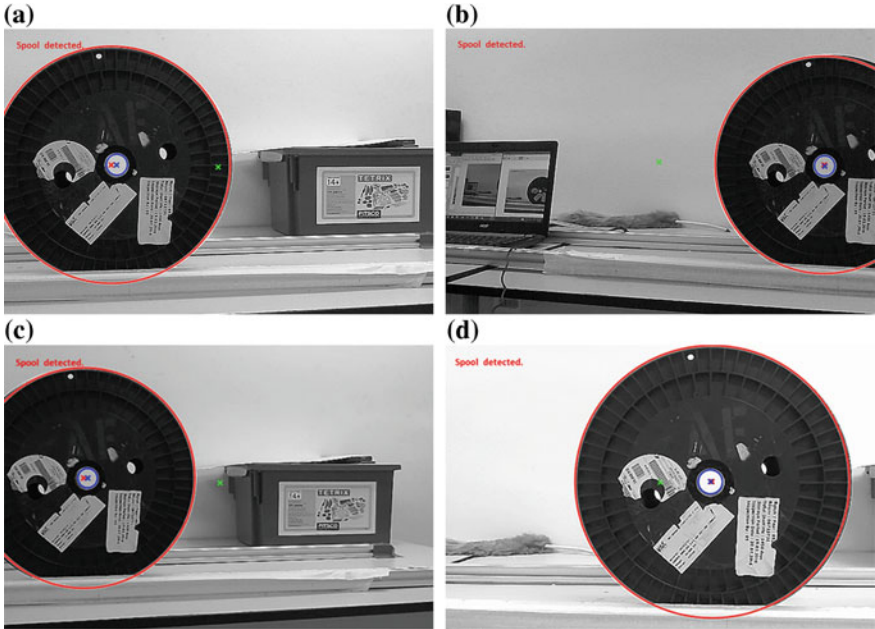


Fig. 5 Spool detected in random distances and camera's angles

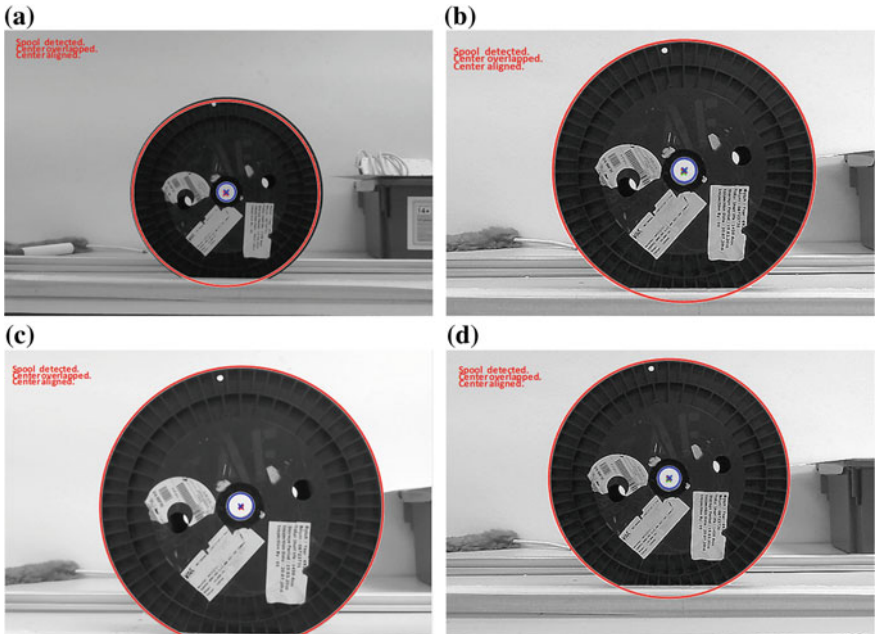


Fig. 6 Spool detected in align position

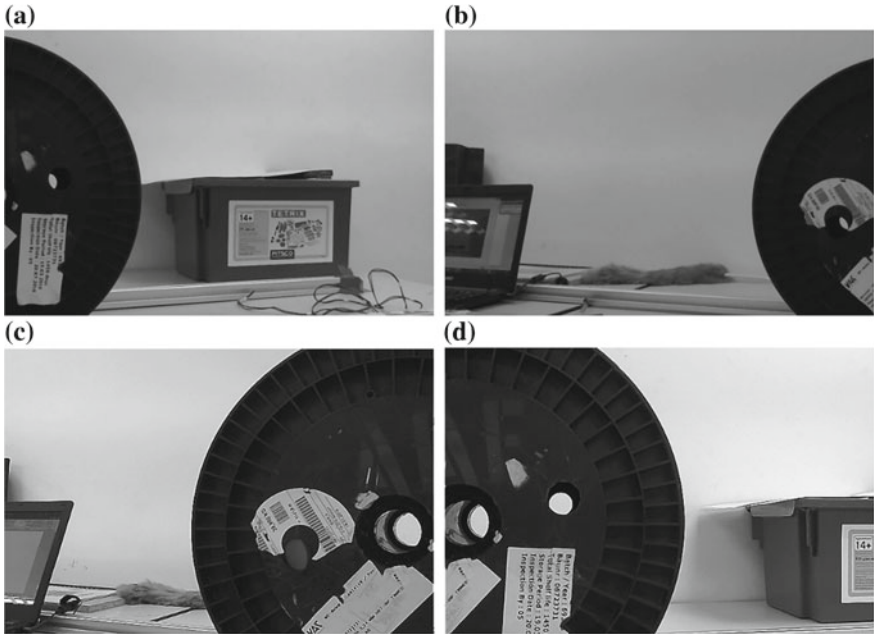


Fig. 7 Spool not detected in many situations

the frame which is both small and big circle center overlapped the reference center and the screen displayed “Center overlapped”. It also shows that there is only one small circle displayed on the screen at 0°.

When copper wire spool cannot be detected, the screen will not display anything until the camera detects the copper wire spool. Figure 7 shows the condition of copper wire spool that cannot be detected. The reasons the copper wire spool cannot be detected are the distance between camera to the spool is less than 40 cm and the shape of the spool (circle) is not like a circle such as a semi-circle.

Next, Fig. 8 shows that the camera and the copper wire spool are not aligned. Thus, the small circle detected as two circles. The analysis on camera and copper wire spool orientation are shown in Table 2 and Fig. 8. From the analysis, it shows that when the camera is aligned with the spool at 0°, the orientation of the spool is not changed although the orientation camera is changed to other angles. The position of the spool is changed due to the orientation of the camera.

The relationship of camera orientation and distance of the FOV center to circle center is shown in Table 2. All the analysis is taken whenever the distance of the camera to the copper wire spool is from 70 to 100 cm. FOV center is considered as 0 cm and the experimental value is compared to the theoretical value. The theoretical value is calculated by using Eq. (3).

From Table 2, it shows that the differences between the experimental and theoretical value are lesser. For 20° or -20° angle, it is when the camera shows capture the

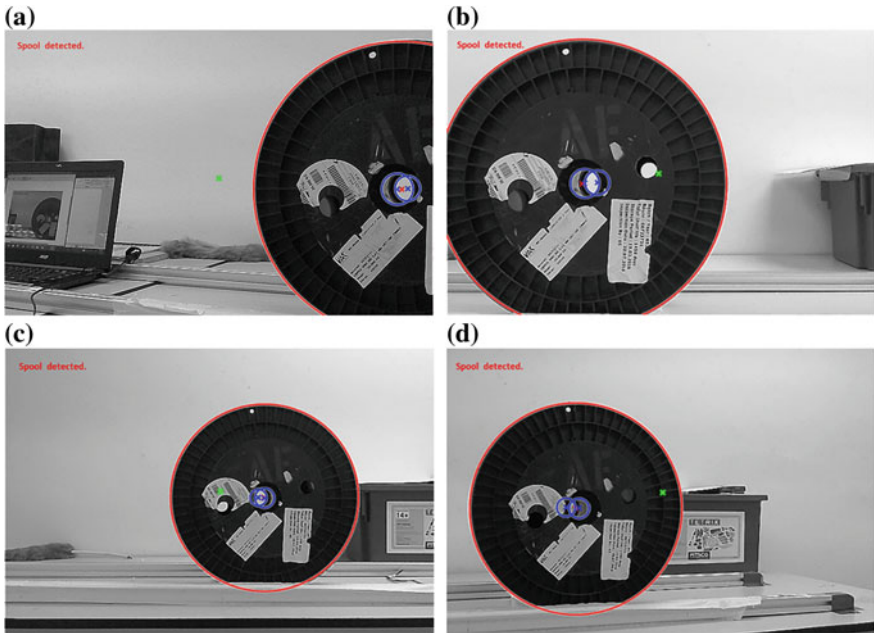


**Fig. 8** Spool is not aligned in random distances and camera’s angles

spool in semi-circle. Although the distance from the camera to the spool is change, it does not affect the camera’s view and copper wire spool orientation. It only affects the size of the spool in the frame and the distance of the FOV center to the circle center at once. All the analysis is taken when the copper wire spool is in align position and only the camera’s orientation is changed. Since it is proved that the orientation of the camera can be calculated, the correct position of the copper wire spool can be determined. However, there are some values produce high error rate. It is due to errors in camera orientation value in real-time experiment.

## 5 Conclusion

This paper proposed an alternative solution to the peg-in-hole problem without using sensors such as force and torque sensor. The results showed that the proposed system could track and determine the correct position for the camera to stop moving forward when the copper wire spool and camera is confirming aligned. Based on the experimental results, the Unsharp filter with Circular Hough Transform (CHT) can detect true circles and prevent false detections. However, these proposed works can be improved in order to reduce the error rate and determine the relationship between camera orientation and camera movement with high accuracy.

**Table 2** Relationship of camera orientation and distance of FOV center to circle center

No./distance camera to spool (cm)		Camera orientation (°)	Distance of FOV center to circle center	
			Experimental value (cm)	Theoretical value (cm)
1	100	-5	10.69	8.75
2		-10	18.37	17.63
3		-15	27.18	26.79
4		-20	35.16	36.4
5		5	6.11	8.75
6		10	18.11	17.63
7		15	22.46	26.79
8		20	35.66	36.4
9	90	-5	5.19	7.87
10		-10	16.65	15.87
11		-15	20.43	24.12
12		-20	31.71	32.76
13		5	9.24	7.87
14		10	16.31	15.87
15		15	24.89	24.12
16		20	32.13	32.76
17	80	-5	8.21	7.00
18		-10	14.35	14.11
19		-15	22.08	21.44
20		-20	28.20	29.12
21		5	4.61	7.00
22		10	14.65	14.11
23		15	17.75	21.44
24		20	28.52	29.12
25	70	-5	5.52	6.12
26		-10	12.21	12.34
27		-15	23.21	18.76
28		-20	25.00	25.48
29		5	6.09	6.12
30		10	12.86	12.34
31		15	18.77	18.76
32		20	24.92	25.48

**Acknowledgements** This research is supported by Universiti Malaysia Pahang Internal Grant of RDU1703143. The authors would also like to thank the Faculty of Electrical and Electronics Engineering Universiti Malaysia Pahang for providing the facilities to conduct this research and financial support throughout the process.

## References

1. Suzuki Y, Koyama K, Ming A, Shimojo M (2015) Grasping strategy for moving object using net-structure proximity sensor and vision sensor. In: 2015 IEEE international conference on robotics and automation (ICRA), pp 1403–1409
2. Park H, Park J, Lee DH, Park JH, Baeg MH, Bae JH (2017) Compliance-based robotic peg-in-hole assembly strategy without force feedback. *IEEE Trans Ind Electron* 64:6299–6309
3. Polverini MP, Zanchettin AM, Castello S, Rocco P (2016) Sensorless and constraint based peg-in-hole task execution with a dual-arm robot. In: Proceedings—IEEE international conference on robotics and automation, pp 415–420
4. Lin LL, Yang Y, Song YT, Nemeč B, Ude A, Rytz JA, Buch AG, Kruger N, Savarimuthu TR (2015) Peg-in-hole assembly under uncertain pose estimation. In: Proceedings world congress on intelligent control and automation, pp 2842–2847
5. Chang WC, Wu CH (2017) Automated USB peg-in-hole assembly employing visual serving. In: 2017 3rd international conference on automation, control and robots, ICCAR 2017, pp 352–355
6. Yadav VK, Batham S, Acharya AK, Paul R (2014) Approach to accurate circle detection: circular hough transform and local maxima concept. In: 2014 international conference on electronics and communication systems, ICECS 2014, pp 3–7
7. Lo R-C, Hsu H-C (2016) A circular band extraction method based on extended hough transform. *Int J Pattern Recognit Artif Intell* 30:1655021
8. Djekoune AO, Messaoudi K, Amara K (2017) Incremental circle hough transform: an improved method for circle detection. *Opt Int J Light Electron Opt* 133: 17–31
9. Yao Z, Yi W (2016) Curvature aided Hough transform for circle detection. *Expert Syst Appl* 51:26–33
10. Ogawa K, Ito Y, Nakano K (2010) Efficient Canny edge detection using a GPU. In: 2010 first international conference on communication, networks and computings, pp 279–280
11. Shrivakshan GT, Chandrasekar C (2012) A comparison of various edge detection techniques used in image processing. *Int J Comput Sci Issues* 9:269–276
12. De Natale FGB, Boato G (2017) Detecting morphological filtering of binary images. *IEEE Trans Inf Forensics Secur* 12:1207–1217
13. Othman Z, Rafiq M, Kadir A (2009) Comparison of Canny and Sobel edge detection in MRI images. *Comput Sci Biomech Tissue Eng Group Inf Syst* 133–136
14. Hussin R, Juhari MR, Kang NW, Ismail RC, Kamarudin A (2012) Digital image processing techniques for object detection from complex background image. *Proc Eng* 41:340–344
15. Tsarouchi P, Matthaiakis SA, Michalos G, Makris S, Chrysosolouris G (2016) A method for detection of randomly placed objects for robotic handling. *CIRP J Manuf Sci Technol* 14:20–27
16. Meng Y, Zhang Z, Yin H, Ma T (2018) Automatic detection of particle size distribution by image analysis based on local adaptive canny edge detection and modified circular Hough transform. *Micron* 106:34–41
17. Tooei MHDH, Mianroodi JR, Norouzi N, Khajooeizadeh A (2011) An innovative implementation of circular Hough transform using eigenvalues of covariance matrix for detecting circles. In: Proceedings ELMAR-2011, pp 397–400

18. Lestriandoko NH, Sadikin R (2017) Circle detection based on hough transform and Mexican Hat filter. In: Proceeding—2016 international conference on computer, control, informatics and its application. Recent Prog. Comput. Control. Informatics Data Sci. IC3INA 2016, pp 153–157
19. Li D, Nan F, Xue T, Yu X (2017) Circle detection of short arc based on randomized Hough transform. In: 2017 IEEE international conference on mechatronics and automation (ICMA), pp 258–263



# A Modified Symbiotic Organism Search Algorithm with Lévy Flight for Software Module Clustering Problem



Nurul Asyikin Zainal, Kamal Z. Zamli and Fakhrud Din

**Abstract** To date, there are much increasing trends on adopting parameter free meta-heuristic algorithms for solving general optimization problems. With parameter free algorithms, there are no parameter controls for tuning. As such, the adoption of parameter free meta-heuristic algorithms is often straightforward. On the negative note, exploration (i.e. roaming the search space thoroughly) and exploitation (i.e. manipulating the current known best neighbor) are pre-set. As the search spaces are problem dependent, any pre-set exploration and exploitation can lead to entrapment in local optima. In this paper, we investigate the use of Lévy flight to enhance the exploration of a parameter free meta-heuristic algorithm, called Modified Symbiotic Organism Search Algorithm (MSOS), via its population initialization. Our experimentations involving the software module clustering problems have been encouraging, as MSOS gives competitive results against existing selected parameter free meta-heuristic algorithms. For all the given module clustering problems, MSOS generates overall best mean results.

**Keywords** Search based software engineering · Software module clustering · Symbiotic organism search

## 1 Introduction

In line with rapid advancement of computing technologies, software line of codes (LOCs) is getting larger to accommodate ever increasing demands for functionalities

---

N. A. Zainal (✉) · K. Z. Zamli · F. Din

Faculty of Computer Systems & Software Engineering, Universiti Malaysia Pahang, 26300 Gambang, Kuantan, Pahang, Malaysia

K. Z. Zamli

e-mail: [kamalz@ump.edu.my](mailto:kamalz@ump.edu.my)

F. Din

e-mail: [fakhruddin@uom.edu.pk](mailto:fakhruddin@uom.edu.pk)

F. Din

Department of Computer Science & IT, University of Malakand, Khyber Pakhtunkhwa, Pakistan

© Springer Nature Singapore Pte Ltd. 2020

A. N. Kasruddin Nasir et al. (eds.), *InECCE2019*, Lecture Notes in Electrical Engineering 632, [https://doi.org/10.1007/978-981-15-2317-5\\_19](https://doi.org/10.1007/978-981-15-2317-5_19)

219

from the users. Furthermore, there is an increasing trend that indicates the popularity of outsourcing LOCs to geographically distributed software engineering teams in order to accommodate development costs to third world countries (i.e. where the costs of programmers and software engineers are relatively cheap). Often, the main challenge of these development models is on dealing with software comprehension, evolution, and maintenance [1, 2]. Clustering of LOCs into small modules and packages can help to alleviate such challenges. Related literature, in fact, suggests that modularized software eases both development and maintenance of software systems [3]. Recently, the area of Search based Software Engineering treats the problem of software module clustering as an optimization problem.

Hill Climbing (HC) has been exploited by Mancoridis and Mitchell in a tool known as Bunch [4]. Similarly, Mahdavi et al. [5] employ combinations of hill climbs for modularization problem. Kumari and Sirvinas [6] attempt to address the software module clustering problem with Genetic algorithm (GA). Concerning multi-objective approach, Praditwong et al. [7] and Huang et al. [8] have adopted Pareto optimality concept based on HC.

To date, much of the existing work on software module clustering deals with parameterized algorithms. With parameter free algorithms, there are no parameter controls for tuning [9, 10]. As such, the adoption of parameter free meta-heuristic algorithms is often straightforward. On the negative note, exploration (i.e. roaming the search space thoroughly) and exploitation (i.e. manipulating the current known best neighbor) are pre-set. As the search spaces are problem dependent, any pre-set exploration and exploitation can lead to entrapment in local optima. Addressing these issues, we investigate the use of Lévy flight to enhance the exploration of a parameter free meta-heuristic algorithm, called Modified Symbiotic Organism Search Algorithm (MSOS), via its population initialization. The prospect of adopting MSOS is in line with the *No Free Lunch theorem* [11] which suggests that no single meta-heuristic can outperform all others even over different instances of the same problem (e.g. [12–27]). Our experimentation involving the software module clustering problems have been encouraging, as MSOS is able to give competitive results against existing selected parameter free meta-heuristic algorithms in the given case studies. The proposed algorithm can be helpful for software engineers in efficient software module clustering process as the findings of this study are encouraging. Moreover, other possible application venues for the algorithm can be t-way testing, software product line (SPL) testing and test redundancy reduction.

The rest of the paper is organized as follows. Section 2 describes the software module clustering problem. Section 3 gives an overview of SOS and its successor MSOS. Section 4 presents our benchmark comparison with other parameter free meta-heuristic algorithms. Section 5 presents our discussion. Finally, Sect. 6 presents the conclusion of the work.

## 2 The Problem of Software Module Clustering

The problem of software module clustering involves partitioning a set of modules into clusters by considering coupling and cohesion. Coupling measures dependency within clusters. The higher the coupling, the less readable the piece of code will be and thus the harder the code for bugs fixing. Cohesion, on the other hand, measures software module cluster internal strength. Therefore, better cluster distribution helps in enhancing source code comprehension and improve functionality-cluster-module traceability.

To allow its quantification, Mitchell and Mancoridis [4] (and later refined by Praditwong et al. [7]) define Modularization Quality (MQ) measure as the sum of the ratio of intra-edges and inter-edges in each cluster, called Modularization Factor ( $MF_k$ ) for cluster  $k$  based on the use of Module Dependency Graph (MDG) [4]. Mathematically,  $MF_k$  can be formally expressed as follows:

$$MF_k = \begin{cases} 0 & \text{if } i = 0 \\ \frac{i}{i+\frac{1}{2}j} & \text{if } i > 0 \end{cases} \quad (1)$$

where  $i$  = weight of intra-edges and  $j$  = weight of inter-edges. The term  $\frac{1}{2}j$  is for splitting the penalty of inter-edges across the two clusters that are connected by that edge. The summation of  $MF_k$  results in MQ as follows:

$$MQ = \sum_{k=1}^n MF_k \quad (2)$$

where  $n$  = number of clusters.

Figure 1 highlights a snapshot of two cluster modularization of a class diagram (i.e. referred to as  $MF_1$  and  $MF_2$ ). Here, the class relationship is often one way when the navigation arrow is specified. If there are no specified navigation, the relationship is considered two way (and counts as two edges for MQ calculation). Considering the example in Fig. 1, the most minimum possible cluster is 1 whilst the maximum possible clusters are 6. The goal is to find the clusters from 2 to 5 that maximizes the MQ. In this case, the total MQ is 1.5. It should be noted that considering different clustering possibilities yields different MQ. The goal here is to maximize MQ.

## 3 Symbiotic Organism Search and Its Modification

Symbiotic Organism Search (SOS) [28] is one of the recently proposed population based meta-heuristic algorithms that mimics real life symbiosis interactions. Here, every organism is assumed to interact with other organism in all three symbiosis categories which are mutualism, commensalism, and parasitism.

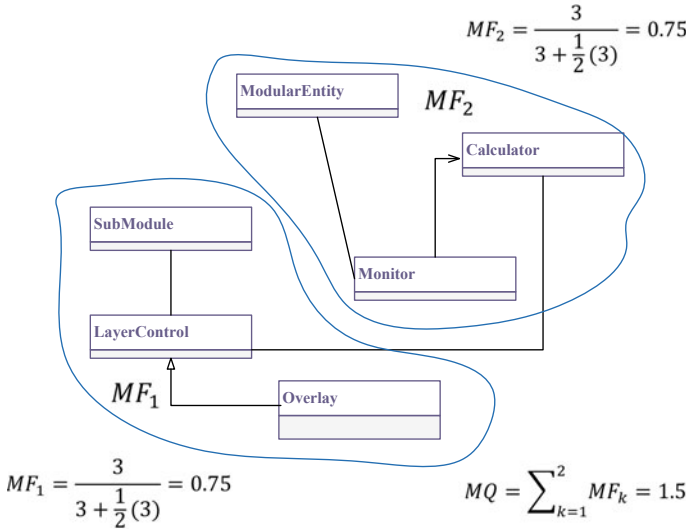


Fig. 1 Sample MQ calculation

Within SOS, mutualism phase mimics the interactions between two organisms that get the benefits of living and co-exist together. To increase the chances of survival in the ecosystem, organism  $X_i^t$  is matched with a random organism  $X_j^t$  and the candidate solutions are calculated by measuring the differences between the best solutions and the average of these two organisms (Mutual Vector). Therefore, when interactions between two organisms which are far away, the movement represents the exploration of the search space. Equations 3 and 4 summarize the mutualism interaction.

$$Mutual\_vector = \frac{X_i^t + X_j^t}{2} \tag{3}$$

$$X_i^{t+1} = X_i^t + rand(0, 1) \cdot (X_{best} - Mutual\_vector \cdot BF_1) \tag{4}$$

where  $X_i^{t+1}$  is new solution obtained using current solution of  $X_i^t$ ;  $rand(0, 1)$  = random value from population;  $X_{best}$  is the current best solution;  $BF_1$  = a random number either 1 or 2.

Concerning commensalism phase, only one organism gets the benefits from the interactions while the other organism is unaffected by the collaborations. Based on these interactions, commensalism phase in SOS is calculated based on Eq. 5.  $X_j^t$  will be picked randomly and assumed to be a passive receiver in a commensalism interaction with organism  $X_i^t$ .

$$X_i^{t+1} = X_i^t + rand(-1, 1) \cdot (X_{best} - X_j^t) \tag{5}$$

where  $X_i^{t+1}$  is a new solution obtained using current solution of  $X_i^t$ ;  $X_j^t$  is a random solution from population;  $X_{best}$  is the current best solution.

Here,  $(X_{best} - X_j^t)$  is reflecting the benefits of  $X_j^t$  towards the improvement of  $X_i^t$  in search for better candidate solution. Best solutions are used as reference points so that the new candidate solution will be exploited around that region only to facilitate convergence.

Following the concept of the survival of the fittest, parasitism phase in SOS involves duplicating organism  $X_i^t$ , that is, by modifying its characteristics using some random number. This duplicated organism will be compared with randomly selected organism  $X_j^t$ . If  $X_j^t$  has better fitness, then  $X_j^t$  is immune from the parasite (and the parasite is discarded). Meanwhile, if the parasite wins, the current  $X_j^t$  will be killed and the parasite assumes the position of  $X_j^t$  as highlighted in Eq. 6.

$$X_{parasite\_vector} = rand(lb, ub) \tag{6}$$

where  $X_{parasite\_vector}$  is a new modified parasite;  $lb$  is for lower bound;  $ub$  is for upper bound.

For all the phases, each organism interacts with other organism randomly. Every organism will go through each phase in sequence for every iteration until termination criteria are met.

As exploration of SOS may be limited as the displacement for global search is based on the average mutual vectors from two populations (as in the commensalism phase), our work explores the adoption of Lévy flight to initialize the initial population candidates. With Lévy flight, the exploration of the search space can be enhanced to ensure that the initial populations are diverse and far from each other. Essentially, the Lévy flight is a random walk interspersed by small and/or long jumps with various distance steps. Eq. 7 defines the Lévy flight.

$$Lévy(\lambda) = \frac{\lambda \Gamma(\lambda) \sin\left(\frac{\pi\lambda}{2}\right)}{\pi} \cdot \frac{1}{s^{1+\lambda}}, \quad (s \gg s_0 > 0) \tag{7}$$

where  $\lambda$  is the step size to control the Lévy flight, if  $\lambda > 0$ ,  $Lévy(\lambda)$  represents the flight behavior of the population based on the Lévy distribution. The recommended value of distribution factor  $\lambda$  is selected from 0.3 to 1.99 [29].  $\Gamma(\lambda)$  is standard gamma function. This distribution is valid for large steps  $s > 0$ . The actual initialization can be defined by Eq. 8 as follows:

$$X_i^t = (lb + rand(0,1) \cdot (ub - lb)) \oplus Lévy(\lambda) \tag{8}$$

where  $X_i^t$  is a newly initialized solution;  $lb$  represents lower bound;  $ub$  represents upper bound;  $\oplus$  represents exclusive OR operation.

```

Input: The population  $X = \{X_1, X_2, \dots, X_n\}$ 
Output: Final  $X_{best}$ 
1 Set maximum partition = no. of modules/2
2 For(i = 1 to population size) do // Lévy Flight Initialization
3 Initialize  $X_i^t$  using Eq. 8 within lower and upper bound limits
4 End // For
5 Obtain initial  $X_{best}$ 
6 While(Not maximum fitness function evaluations) do
7 For(i = 1 to population size) do // Commensalism Phase
8 Calculate mutual vector using Eq. 3
9 Update  $X_i^{t+1}$  using Eq. 4
10 If ( $f(X_i^{t+1})$  is better than  $f(X_i^t)$ ) then
11  $X_i^t = X_i^{t+1}$ 
12 End //For
13 For( $i = 1$  to population size) do // Mutualism Phase
14 Randomly select one learner  $X_j^t$  from the population  $X$  such that  $i \neq j$ 
15 Update  $X_i^{t+1}$  using Eq. 5
16 If( $f(X_i^t)$  is better than  $f(X_j^t)$ ) then
17  $X_i^t = X_j^t$ 
18 End //For
19 For( $i = 1$  to population size) do // Parasitism Phase
20 Update  $X_i^{t+1}$  using Eq. 6
21 If( $f(X_i^t)$  is better than  $f(X_j^t)$ ) then
22  $X_i^t = X_j^t$ 
23 End //For
24 Update  $X_{best}$ 
25 End //While
26 Return  $X_{best}$ 

```

**Fig. 2** Modified SOS algorithm with Lévy flight

Apart from using Lévy flight to initialize the populations, we have also changed the flow of SOS. At any particular loop in the original SOS structure, a selected potential candidate solution from the current undergo all the phases (i.e. mutualism, commensalism, and parasitism) in sequence. In this paper, we propose to loop through all populations in sequence instead of interleaving them one after the other as suggested by the original algorithm. With the changes, we hope to increase the effectiveness of exploration and sharing of the information about the search space. Based on this aforementioned modification, the complete pseudo code of the modified SOS algorithm can be summarized in Fig. 2.

## 4 Benchmarking Case Studies

Our benchmarking experiments focus on characterizing the performances of MSOS and its predecessor SOS and other parameter free meta-heuristic algorithm (i.e. TLBO and Jaya). We opt to select three case studies (refer to Figs. 3, 4 and 5). Case study 1 with eight modules relates to the robot controller class diagram (see Fig. 3). Meanwhile, case study 2 with nine modules relates to printer controller class

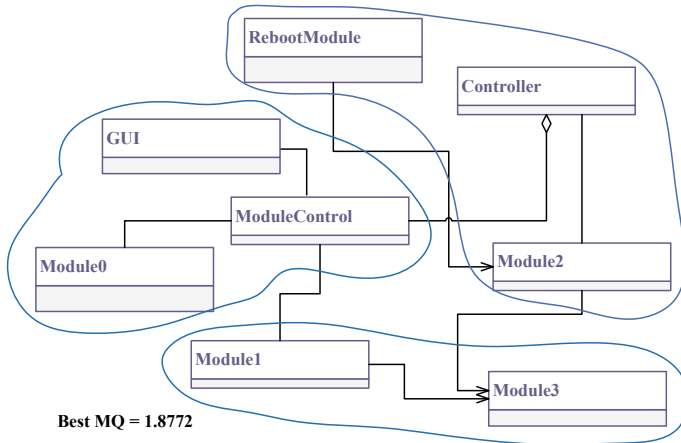


Fig. 3 Robot controller class diagram

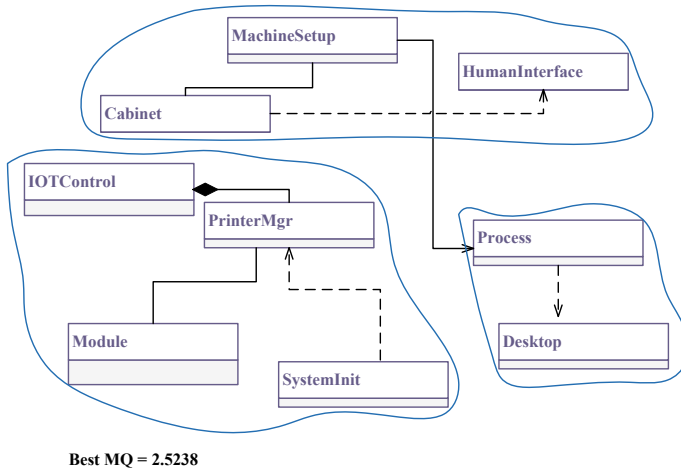
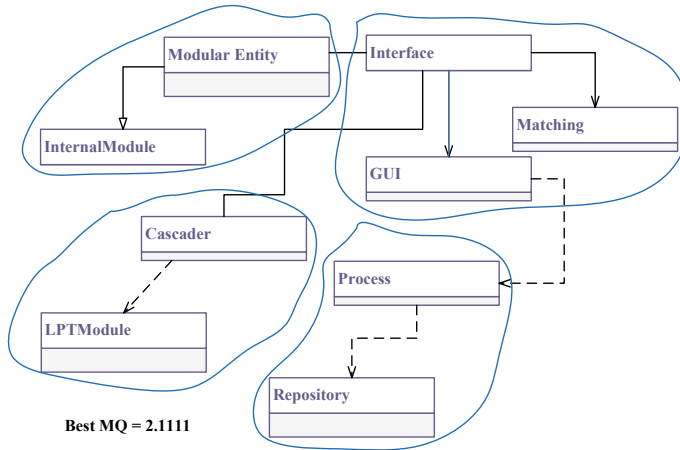


Fig. 4 Printer interface class diagram

diagram (see Fig. 4). Case study 3 having nine modules deals with matching interface class diagram (see Fig. 5). These case studies are actually students' class projects for an undergraduate course. Although the chosen case studies are rather small, it is enough to demonstrate the usefulness of our approach.

Here, we don't use the number of iterations as the stopping criteria owing to fairness issues. For instance, SOS and MSOS has three fitness function evaluation per iteration as compared to two in the case of TLBO. For the case of Jaya, only one fitness function evaluation per iteration. As such, the number of iterations cannot be used as the stopping criteria. Thus, in all our experiments, we set the same number of



**Fig. 5** Matching interface class diagram

population size of 40, and the same number of maximum fitness function evaluations of 2500.

Our experimental platform comprises of a PC running Windows 10, CPU 2.9 GHz Intel Core i5, 16 GB 1867 MHz DDR3 RAM and a 512 MB of flash HDD. In all the experiments, we have executed all the algorithms 20 times to ensure statistical significance. The best MQ and the mean MQ for each experiment is reported side-by-side. The best mean cell entries are marked in bold font. Here, we do not consider the execution time as the implementation of TLBO, Jaya, SOS, and MSOS use different data structures and different implementation languages. As such, unlike comparison of MQs which is independent of the implementation details and its computing environment, the comparison of time is unfair.

## 5 Discussion

Table 1 summarizes the results. Referring to Table 1, we note that all algorithms can achieve the best MQ owing to small enumeration of all possible combinations. Figures 3 till 5 summarize the clusters that yield the best MQ. Summing up, MSOS gives the best overall mean in two-out-of-three cases (i.e. case study 1 and 2). TLBO comes in second scoring the best mean in case study 3. Putting MSOS and TLBO aside, SOS comes in third. Jaya performs last having the worsts mean for all case studies.

Significant improvement can be seen in the performance of MSOS against its predecessor. The fact that the initial populations are scattered across the search space (owing to the adoption of Lévy flight) ensures consistent converge to the best MQ. As a result, the mean of MQ is larger as compared to SOS.



**Table 1** Comparative MQ performance of TLBO, Jaya, SOS and MSOS

Case studies	TLBO [30]		Jaya [31]		SOS [28]		MSOS	
	Best	Mean	Best	Mean	Best	Mean	Best	Mean
Robot controller	1.8772	1.8330	1.8772	1.7890	1.8772	1.8330	1.8772	<b>1.8772</b>
Printer interface	2.5238	2.3630	2.5238	2.2480	2.5238	2.2920	2.5238	<b>2.3810</b>
Matching interface	2.1111	<b>2.0940</b>	2.1111	2.043	2.1111	2.059	2.1111	2.0890

## 6 Conclusion

Summing up, this paper has demonstrated the effectiveness of Modified Symbiotic Organism Search Algorithm (MSOS) for software module clustering applications. MSOS has outperformed its predecessor SOS as well as TLBO in terms of generating the optimal MQ measure. As the scope of future work, we are exploring the potential of adopting chaotic maps in place of using Lévy flight motion to ensure diversity of the initial populations. Finally, we will also be looking into the adoption of MSOS for other optimization problems particularly on test redundancy problems as well as combinatorial test suite generation.

**Acknowledgements** The work reported in this paper is funded by “Fundamental Research Grant from Ministry of Higher Education Malaysia titled: A Reinforcement Learning Sine Cosine based Strategy for Combinatorial Test Suite Generation (grant no: RDU170103)”. We thank MOHE for the support.

## References

1. Lucca GAD, Fasolino AR, Pace F, Tramontana P, Carlini UD (2002) Comprehending web applications by a clustering-based approach. In: 10th international workshop on program comprehension. IEEE, Paris, pp 261–270
2. Jahnke JH (2004) Reverse engineering software architecture using rough clusters. In: IEEE annual meeting of the fuzzy information processing. Alberta, pp 4–9
3. Sommerville I (2015) Software engineering, 10th edn. Pearson, Harlow
4. Mitchell BS, Mancoridis S (2006) On the automatic modularization of software systems using the bunch tool. IEEE Trans Soft Eng 32(3):193–208
5. Mahdavi K, Harman M, Hierons RM (2003) A multiple hill climbing approach to software module clustering. In: International conference on software maintenance. Amsterdam, pp 315–324
6. Kumari AC, Srinivas K (2016) Hyper-heuristic approach for multi-objective software module clustering. J Syst Softw 117:384–401
7. Praditwong K, Harman M, Yao X (2011) Software module clustering as a multi-objective search problem. IEEE Trans Soft Eng 37(2):264–282

8. Huang J, Liu J, Yao X (2017) A multi-agent evolutionary algorithm for software module clustering problems. *Soft Comput* 21(12):3415–3428
9. Zamli KZ (2018) Enhancing generality of meta-heuristic algorithms through adaptive selection and hybridization. In: *International conference on information and communications technology*. IEEE, Yogyakarta, pp 67–71
10. Zamli KZ, Din F, Ramli N, Ahmed BS (2019) Software module clustering based on the fuzzy adaptive teaching learning based optimization algorithm. [arXiv:1902.11159](https://arxiv.org/abs/1902.11159)
11. Wolpert DH, Macready WG (1997) No free lunch theorems for optimization. *IEEE Trans Evol Comput* 1(1):67–82
12. Alsewari ARA, Zamli KZ (2012) A harmony search based pairwise sampling strategy for combinatorial testing. *Int J Phys Sci* 7(7):1062–1072
13. Din F, Alsewari ARA, Zamli KZ (2017) A parameter free choice function based hyper-heuristic strategy for pairwise test generation. In: *IEEE international conference on software quality, reliability and security companion*. IEEE, Prague, pp 85–91
14. Din F, Zamli KZ (2018) Fuzzy adaptive teaching learning-based optimization strategy for gui functional test cases generation. In: *7th international conference on software and computer applications*. ACM, Kuantan, pp 92–96
15. Nasser AB, Zamli KZ, Alsewari ARA, Ahmed BS (2018) Hybrid flower pollination algorithm strategies for t-way test suite generation. *PLoS ONE* 13(5):e0195187
16. Younis MI, Zamli KZ, Isa NAM (2008) MIPOG-modification of the IPOG strategy for t-way software testing. In: *Distributed frameworks and applications*. IEEE, Penang, pp 1–6
17. Younis MI, Zamli KZ, Isa NAM (2008) Algebraic strategy to generate pairwise test set for prime number parameters and variables. In: *International symposium on information technology*. IEEE, Kuala Lumpur, pp 1–4
18. Zamli KZ, Alkazemi BY, Kendall G (2016) A tabu search hyper-heuristic strategy for t-way test suite generation. *Appl Soft Comput* 44:57–74
19. Zamli KZ, Din F, Ahmed BS, Bures M (2018) A hybrid q-learning sine-cosine-based strategy for addressing the combinatorial test suite minimization problem. *PLoS ONE* 13(5):e0195675
20. Zamli KZ, Din F, Kendall G, Ahmed BS (2017) An experimental study of hyper-heuristic selection and acceptance mechanism for combinatorial t-way test suite generation. *Inf Sci* 399:121–153
21. Ahmed BS, Gambardella LM, Afzal W, Zamli KZ (2017) Handling constraints in combinatorial interaction testing in the presence of multi objective particle swarm and multithreading. *Inf Softw Technol* 86:20–36
22. Ahmed BS, Sahib MA, Gambardella LM, Afzal W, Zamli KZ (2016) Optimum design of PI $\lambda$ DM controller for an automatic voltage regulator system using combinatorial test design. *PLoS ONE* 11(11):e0166150
23. Alsewari ARA, Zamli KZ (2011) Interaction test data generation using harmony search algorithm. In: *IEEE symposium on industrial electronics and applications*. IEEE, Langkawi, pp 559–564
24. Din F, Zamli KZ (2018) Hyper-heuristic-based strategy for pairwise test case generation. *Adv Sci Lett* 24(10):7333–7338
25. Nasser AB, Alsewari ARA, Tairan NM, Zamli KZ (2017) Pairwise test data generation based on flower pollination algorithm. *Malay J Comput Sci* 30(3):242–257
26. Nasser AB, Zamli KZ, Alsewari ARA, Ahmed BS (2018) An elitist-flower pollination-based strategy for constructing sequence and sequence-less t-way test suite. *Int J Bio-Inspired Comput* 12(2):115–127
27. Ahmed BS, Zamli KZ, Afzal W, Bures M (2017) Constrained interaction testing: a systematic literature study. *IEEE Access* 5
28. Cheng M-Y, Prayogo D (2014) Symbiotic organisms search: a new metaheuristic optimization algorithm. *Comput Struct* 139:98–112
29. Pavlyukevich I (2007) Lévy flights, non-local search and simulated annealing. *J Comput Phys* 226(2):1830–1844

30. Rao RV, Savsani VJ, Vakharia DP (2011) Teaching-Learning-based optimization: a novel method for constrained mechanical design optimization problems. *Comput Aided Des* 43(3):303–313
31. Rao RV (2016) Jaya: a simple and new optimization algorithm for solving constrained and unconstrained optimization problems. *Int J Ind Eng Comput* 7(1):19–24

# Classification of Agarwood Types (Malaccensis and Crassna) Between Oil and Smoke Using E-Nose with CBR Classifier



Mujahid Mohamad, Muhammad Sharfi Najib, Suhaimi Mohd Daud, Nurdiyana Zahed, Muhamad Faruqi Zahari, Nur Farina Hamidon Majid, Suziyanti Zaib and Hadi Manap

**Abstract** The issue of quality of agarwood quality among sellers and buyers is still ongoing due to manual olfactory methods. This study purpose classification of Malaccensis and Crassna agarwood in oil and smoke by electronic nose using Case-based Reasoning classifier. The CBR performance measurement shows that classification of agarwood Malaccensis and Crassna for both oil and smoke using CBR technique can achieve 100% classification success.

**Keywords** E-nose · CBR · Agarwood · Malaccensis · Crassna · Intelligent classification

## 1 Introduction

Diseased wood of the genus *Aquilaria* (Thymelaeaceae) is a type of fragrant wood which known as Gaharu in South East Asia or Agarwood [1, 2]. Agarwood can be found mainly in Southeast Asian countries such as Vietnam, Indonesia, and Malaysia [3]. Agarwood is used in a large domain [1]. Nowadays more than 18 countries throughout Southeast Asia and the Middle East have participated in agarwood trade [1]. The price is depending on agarwood quality which can be divided into different grades. Finding the grade of agarwood is a major problem in this area, An review on 2017 was suggested one of principle on the classification of agarwood is depend on origin or species because the qualities are varied through the species [1]. In Malaysia and Indonesia forest, *Aquilaria* is one of the main agarwood species and has a huge population [4, 5]. Beside Malaccensis there are 18 more accepted species of *Aquilaria* [1]. Malaccensis and Crassna are the best known species which produced high quality and multipurpose used [6].

---

M. Mohamad · M. S. Najib (✉) · S. M. Daud · N. Zahed · M. F. Zahari · N. F. H. Majid · S. Zaib · H. Manap  
Faculty of Electrical and Electronics Engineering, Universiti Malaysia Pahang, 26600 Pahang, Malaysia  
e-mail: [sharfi@ump.edu.my](mailto:sharfi@ump.edu.my)

Agarwood oil quality assessment is typically carried out manually via the human olfactory system which produces different results and inconsistency from traders and buyers [6]. Traditionally, there are 7 physical properties have been used on grading agarwood namely resin content, sinkage, color, scene/aroma, agarwood-inducing method, formation time and place of origin [1]. Through all of these properties, scene/aroma was claimed to be the most important property for quality assessment [1–8]. However, the traditional technique is not quantitative measurement which is questionable and can be manipulated on many aspects which mean there is a need for the qualitative measurement method [1].

The modern technique identified 3 properties on classifying the agarwood grade into qualitative indicator which is color, scene/aroma and chemical [1]. In chemical analysis, several studies were conducted through high-resolution melting (HRM) [7], Support Vector Machine (SVM) [8, 9], headspace solid phase microextraction (HS-SPME), Gas Chromatography-Mass Spectrometry (GC/GCMS), Gas Chromatography-olfactometry (GC-O), headspace preheating system combined with gas chromatography-mass spectrometry (HS GC-MS), and Partial least squares-discriminant analysis (PLS-DA) [1–6, 10–12]. Study on color or image was utilized with Fuzzy C-Means (FCM) [13] and Image Processing Technique [14].

Focusing on classification by scene/aroma, utilized non-targeted headspace solid-phase microextraction (HS-SPME) combined with gas chromatography/mass spectrometry (GC/MS) and multivariate analysis to analyze aromatic characteristics which successfully classified agarwood. Besides that, feed forward artificial neural network defined by “32-8-1 architecture” and trained via Levenberg-Marquardt back propagation (LMBP) algorithm, can successfully grade agarwood with a 100% classification rate [1]. However, the drawback of these techniques is a large amount of procedure, data and facilities (32 number of sensors) led to a large amount of time and money spend.

An electronic nose (E-nose) contains an array of sensors which detect the presence of gases molecule on the surrounding environment, molecule detected by the sensors produces an electric signal which passes to the computer system for further analysis. E-nose has large advantages including detection on small changes in volatile and also exhibit good identification on some compounds compared to GC-MS [15]. The complexity of most food aromas makes it difficult to characterize the quality of the final product with conventional flavor analysis techniques such as gas chromatography, spectroscopy, and chemical analysis. This gives the advantages over the e-nose which can solve the complexity of the aroma into the unique pattern.

E-nose is structured with 3 important elements which are sensor array, microelectronic devices, and data processing algorithms [15]. Sensor array as the indicator for detection agarwood sample [16] which all sensors generate response signals during odor's collection. Therefore, the odor sample is composed of two dimensions: “number of sensors” and “response time series” [17].

E-nose system can be divided into 3 part which are sampling system technique, detection system, and data processing systems and pattern recognition methods [15]. There are several methods that can imply to classify the quality of Gaharu such as k-Nearest Neighbor (k-NN), Relevance Vector Machine (RVM), Self-Organizing

Map (SOM), Radial Basis Function (RBF), Support Vector Machine (SVM), Artificial Neural Network (ANN) and Case-Based Reasoning (CBR). Literature has been shown that data recognition methods used in classifying agarwood quality were successfully employed, however, there are some drawback should overcome such as a large number of resources used which led to time-consuming and high cost.

CBR is much better compared to RBR, Artificial Neural Network (ANN) and other statistical and machine learning techniques [18]. CBR is suitable for the domain with uncertain knowledge and theory [18–21]. Case-based reasoning means using old experiences to understand and solve new problems [20]. CBR gives the solution when there is no algorithm for particular problems, give warning to the potential problems from previous remembered problems, focus on the important part of problems by pointing on the features of the problems [20]. There are several steps for classifying using CBR which is retrieved, reuse, revise and retain. Retrieve is the most crucial step in CBR which is to recall a previous case that stored in CBR. Then, it will retrieve the best similar cases to compare with the new case. The best similarity cases will reuse in order to revise the case and retained it when it was solved [22]. The latest study on agarwood classification using CBR was employed on 2016 where the result of accuracy was 86.7% which is considered to be a gap that can be improved and refined as suggested by that paper [22].

This study purposes a method of classification of agarwood species (Malaccensis and Crassna) between two different mediums; oil and smoke, using e-nose with case-based reasoning classifier. The benefit toward society is in economic development due to the high demand for grading technique of agarwood.

## 2 Methodology

Figure 1 shows the overall flowchart for the research of classification of agarwood types using case-based reasoning. E-nose was used to collect the data measurement, the data was then being pre-processed, the features or odor profile pattern for each sample was extracted. The pattern was classified using CBR classifier. Lastly, the classification results were evaluated using confusion matrix and performance measurement in order to get the percentages of accuracy, specificity, and sensitivity of the classification.

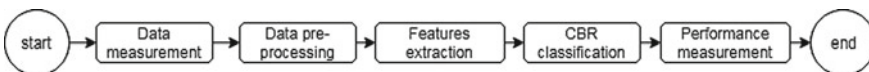


**Fig. 1** Overall flowchart

### 2.1 Data Measurement

Data from two samples of agarwood: Malaccensis and Crassna, for both oil and smoke has been collected by E-nose. Figure 2 shows the experimental setup for agarwood data measurement employ by e-nose.

The 200 data measurement was collected after every 5 min and were repeated for 5 times (experiment) resulting in total 1000 data every sample. E-nose was acted as an inhaler to the odor released from agarwood samples. Sensor array was controlled by a microcontroller that used to read the resistance value and send it to the computer for data collection. The data collection was recorded in Table 1 as raw data with a total of 1000 measurements. Table 1 indicated a sample of a set of overall measured data.

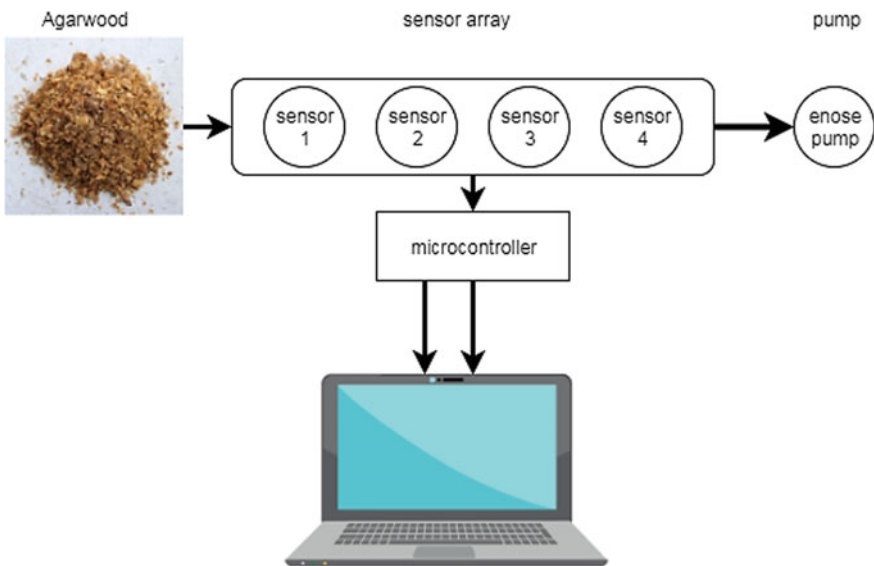


Fig. 2 Experimental setup

Table 1 Table of agarwood data measurement

Data measurements	Sensor 1	Sensor 2	Sensor 3	Sensor 4
DATA <sub>1</sub>	DATA1 <sub>1</sub>	DATA1 <sub>2</sub>	DATA1 <sub>3</sub>	DATA1 <sub>4</sub>
DATA <sub>2</sub>	DATA2 <sub>1</sub>	DATA2 <sub>2</sub>	DATA2 <sub>3</sub>	DATA2 <sub>4</sub>
DATA <sub>3</sub>	DATA3 <sub>1</sub>	DATA3 <sub>2</sub>	DATA3 <sub>3</sub>	DATA3 <sub>4</sub>
.	.	.	.	.
DATA1000	DATA1000 <sub>1</sub>	DATA1000 <sub>2</sub>	DATA1000 <sub>3</sub>	DATA1000 <sub>4</sub>

**Table 2** Table of normalized agarwood data

Data measurements	S1	S2	S3	S4
NDATA <sub>1</sub>	NDATA1 <sub>1</sub>	NDATA1 <sub>2</sub>	NDATA1 <sub>3</sub>	NDATA1 <sub>4</sub>
NDATA <sub>2</sub>	NDATA2 <sub>1</sub>	NDATA2 <sub>2</sub>	NDATA2 <sub>3</sub>	NDATA2 <sub>4</sub>
NDATA <sub>3</sub>	NDATA3 <sub>1</sub>	NDATA3 <sub>2</sub>	NDATA3 <sub>3</sub>	NDATA3 <sub>4</sub>
.	.	.	.	.
NDATA1000	NDATA1000 <sub>1</sub>	NDATA1000 <sub>2</sub>	NDATA1000 <sub>3</sub>	NDATA1000 <sub>4</sub>

## 2.2 Data Pre-Processing

Collected data were normalized to get a standard measurement value. Data were normalized using Eq. 1:

$$R' = \frac{R}{R_{\max}} \tag{1}$$

The normalized data was tabulated in Table 2.

## 2.3 Features Extraction

Each agarwood sample (normalized data are shown in Table 2) was merged using mean calculation for 200 data through all 5 experiments and was divided into 10 cases which gives 40 cases for all 4 samples. The data cases were visually presented in the graph (odor-profile pattern) in Fig. 3. The mean of normalized odor-profile forms features. The classification of CBR stored cases (odor-profile pattern) was recorded.

## 2.4 CBR Classification

CBR was used to differentiate the pattern of agarwood odor profile. CBR uses past experience or stored cases to differentiate the sample in the expected cases. In CBR library of agarwood odor-profile, 10 cases of 4 groups agarwood samples were established. In retrieval phase of CBR, 1 out of 40 cases was set to be current case and the remaining are set to be stored case. Then the similarities distance was calculated in percentage for the remaining 39 cases using this equation:

$$similarity(T, S) = \frac{\sum_{i=0}^n f(T_i, S_i) \times w_i}{\sum_{i=0}^n w_i} \tag{2}$$



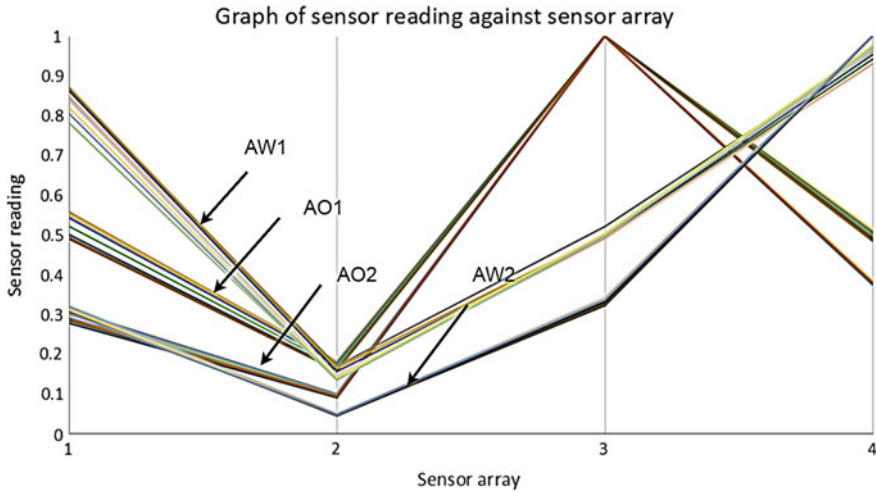


**Fig. 3** Raw data of agarwood using E-nose

## 2.5 Performance Measurement

Classifications of agarwood using CBR was evaluated to determine the accuracy, percentage of sensitivity, and specificity of the classification system based on agarwood samples for performance measurement.

## 3 Results and Discussion

Figure 3 shows the sensor reading values on the relation between 4 samples agarwood which are Malaccensis smoke (AW1), Malaccensis oil (AO1), Crassna smoke (AW2), Crassna oil (AO2), all gives total 40 patterns comes from 4000 data.

The x-axis specify the number of sensors S1, S2, S3 and S4 while Y-axis shows normalized sensor reading the value of agarwood sample. The 10 values were plotted for every sample in the graph showed which indicates the number of cases. S3 shows the highest value for sample AO1 compared to other samples. S2 shows the lowest reading value for sample AW2. Reading values on S1, S2 and S3 show interception between two samples AO2 and AW2, AO1 and AW1, and AW1 and AW2.

S3 and S4 are good for differentiating between medium because the reading values are almost identical on the same medium and differ on the different medium. S1 and S2 are good for differentiate between agarwood types because Malaccensis reading value is far larger than crassna for S1 and small different for S2.

Table 3 shows the CBR library for agarwood *Malaccensis* and *Crassna* in two medium oil and smokes. Row indicates cases values corresponding to sensors number which totals up to 40 cases. Case01 to Case10 indicates *Malaccensis* agarwood oil denoted as AO1, Case11 to Case20 indicates sample *Crassna* agarwood oil, AO2, Case21 to Case30 indicates sample *Malaccensis* agarwood smoke, AW1 and Case31 to Case40 indicates sample *Crassna* agarwood smoke, AW2.

Table 4 shows a similarity computation for every case. Similarity calculation was per-formed between two cases through all 40 cases. Features are set to be e-nose sensors S1, S2, S3, and S4. Source and target are the two compared cases also

**Table 3** CBR library for agarwood malaccensis and crassna for oil and smoke

Case ID	S1	S2	S3	S4
Case01	0.545160684	0.177827188	1.000000000	0.500243076
Case02	0.558294680	0.182664156	1.000000000	0.502841776
Case03	0.556567318	0.181594899	1.000000000	0.510834960
Case04	0.552740310	0.180445409	1.000000000	0.512688064
Case05	0.543179915	0.178051768	1.000000000	0.507039960
Case06	0.522381530	0.170389147	1.000000000	0.501787128
Case07	0.501477077	0.162848638	1.000000000	0.492674593
Case08	0.490601175	0.160165004	1.000000000	0.493259621
Case09	0.493790566	0.161648598	1.000000000	0.489744398
Case10	0.493893471	0.161161842	1.000000000	0.485743718
Case11	0.278808521	0.091997308	1.000000000	0.378766986
Case12	0.285694717	0.093978638	1.000000000	0.379923044
Case13	0.291444610	0.095962393	1.000000000	0.382186717
Case14	0.303891578	0.100686298	1.000000000	0.385435039
Case15	0.308639559	0.100464542	1.000000000	0.384036535
Case16	0.312801338	0.101389604	1.000000000	0.385647711
Case17	0.311290978	0.100498936	1.000000000	0.381201107
Case18	0.299957963	0.096929839	1.000000000	0.375098064
Case19	0.291177036	0.094638370	1.000000000	0.376697631
Case20	0.289218125	0.094379180	1.000000000	0.379847247
Case21	0.867071826	0.171109101	0.521429457	0.962769842
Case22	0.871014286	0.165857428	0.499091373	0.964223998
Case23	0.862990568	0.157621090	0.494367638	0.953544270
Case24	0.843317346	0.145704680	0.492099523	0.942160129
Case25	0.840928226	0.144893755	0.493022099	0.930116749
Case26	0.849018071	0.144493493	0.491877750	0.930941777
Case27	0.839976542	0.148496489	0.502402476	0.965789020

(continued)

**Table 3** (continued)

Case ID	S1	S2	S3	S4
Case28	0.820809519	0.142196889	0.504498969	0.976267532
Case29	0.805577990	0.136687259	0.497149884	0.970431635
Case30	0.782283209	0.136012381	0.499016908	0.971437930
Case31	0.313384823	0.047004038	0.323211973	1.000000000
Case32	0.311565164	0.046498885	0.323509033	1.000000000
Case33	0.306229491	0.047261669	0.327693353	1.000000000
Case34	0.312943506	0.049336398	0.332362043	1.000000000
Case35	0.319895545	0.050261127	0.336659938	1.000000000
Case36	0.321586597	0.050271463	0.340624923	1.000000000
Case37	0.315795769	0.049427845	0.342636807	1.000000000
Case38	0.314514645	0.049375335	0.341881792	1.000000000
Case39	0.312224631	0.049547272	0.339998477	1.000000000
Case40	0.303782167	0.048807171	0.338143931	1.000000000

**Table 4** Similarity computation

Features	Source	Target	Sim	Weight	norm_w	sim*norm_W
S1	0.54516	0.55829	0.98687	1	0.25	0.98687
S2	0.17783	0.18266	0.99516	1	0.25	0.99516
S3	1.00000	1.00000	1.00000	1	0.25	1.00000
S4	0.50024	0.50284	0.99740	1	0.25	0.99740
Total or global similarity between two cases (%)						99.4858

known as stored case and current case. Sim or similarity between the stored case and current case was calculated using Eq. (2). The normal similarity was got from the multiplication of similarity and normalized weight or norm\_w. All features in each row were under-goes the same calculation procedure was then added together resulting similarity percentage between two cases.

Table 5 shows the weight vector assigned to each e-nose sensor array. By defaults weight vector was set to 1. As this far, this value gives positive classification performance.

**Table 5** Weight vector

Weight vector	Attributes (E-nose sensors)
W1 = 1	S1
W2 = 1	S2
W3 = 1	S3
W4 = 1	S4

Table 6 showing the outcome of CBR voting. CBR library of 4 samples (40 cases) of Malaccensis and Crassna agarwood oil and smoke. Case01 to Case10 indicate Malaccensis oil agarwood sample. While Case11 to Case20 indicate Crassna oil agarwood sample. For Case21 to Case30 indicate Malaccensis smoke agarwood sample. Lastly, Case31 to Case40 indicate Crassna smoke agarwood sample. The value of K indicate the similarity distance between each CaseID and its voting value.  $K = 1$  indicates the nearest value to CaseID while  $K = 3$  indicates the third highest value to CaseID. The CBR voting resulting in all CaseID have 100% voting. It means that all K values for all CaseID are located in the same voting group.

**Table 6** CBR voting

Voting				Percentage accuracy (%)
Case ID	K = 1	K = 2	K = 3	
Case01	AO1	AO1	AO1	100
Case02	AO1	AO1	AO1	100
Case03	AO1	AO1	AO1	100
Case04	AO1	AO1	AO1	100
Case05	AO1	AO1	AO1	100
Case06	AO1	AO1	AO1	100
Case07	AO1	AO1	AO1	100
Case08	AO1	AO1	AO1	100
Case09	AO1	AO1	AO1	100
Case10	AO1	AO1	AO1	100
Case11	AO2	AO2	AO2	100
Case12	AO2	AO2	AO2	100
Case13	AO2	AO2	AO2	100
Case14	AO2	AO2	AO2	100
Case15	AO2	AO2	AO2	100
Case16	AO2	AO2	AO2	100
Case17	AO2	AO2	AO2	100
Case18	AO2	AO2	AO2	100
Case19	AO2	AO2	AO2	100
Case20	AO2	AO2	AO2	100
Case21	AW1	AW1	AW1	100
Case22	AW1	AW1	AW1	100
Case23	AW1	AW1	AW1	100
Case24	AW1	AW1	AW1	100
Case25	AW1	AW1	AW1	100
Case26	AW1	AW1	AW1	100

(continued)

**Table 6** (continued)

Voting				Percentage accuracy (%)
Case ID	K = 1	K = 2	K = 3	
Case27	AW1	AW1	AW1	100
Case28	AW1	AW1	AW1	100
Case29	AW1	AW1	AW1	100
Case30	AW1	AW1	AW1	100
Case31	AW2	AW2	AW2	100
Case32	AW2	AW2	AW2	100
Case33	AW2	AW2	AW2	100
Case34	AW2	AW2	AW2	100
Case35	AW2	AW2	AW2	100
Case36	AW2	AW2	AW2	100
Case37	AW2	AW2	AW2	100
Case38	AW2	AW2	AW2	100
Case39	AW2	AW2	AW2	100
Case40	AW2	AW2	AW2	100

Performance evaluation for agarwood *Malacensis* and *Crassna* in two different medium oil and smoke using CBR classifier has been shown in Table 7. Sensitivity, specificity, and accuracy are the elements required in performing analysis.

*Malacensis* oil, *Crassna* oil, *Malacensis* smoke, and *Crassna* smoke sample shows the value 1.00 indicate the 100% sensitive. The specificity and accuracy for

**Table 7** Performance evaluation for malaccensis and crassna agarwood in oil and smoke classification using CBR

Performance evaluation	K = 1	K = 2	K = 3
Criteria/Indices	Value	Value	Value
Total cases	40	40	40
AO1 cases	10	10	10
AO2 cases	10	10	10
AW1 cases	10	10	10
AW2 cases	10	10	10
True AO1	10	10	10
False AO1	0	0	0
True AO2	10	10	10
False AO2	0	0	0
True AW1	10	10	10
False AW1	0	0	0
True AW2	10	10	10

(continued)

**Table 7** (continued)

Performance evaluation	K = 1	K = 2	K = 3
False AW2	0	0	0
Sensitivity AO1	1	1	1
Sensitivity AO2	1	1	1
Sensitivity AW1	1	1	1
Sensitivity AW2	1	1	1
Specificity AO1	1	1	1
Specificity AO2	1	1	1
Specificity AW1	1	1	1
Specificity AW2	1	1	1
Accuracy AO1	1	1	1
Accuracy AO2	1	1	1
Accuracy AW1	1	1	1
Accuracy AW2	1	1	1
Overall sensitivity	1	1	1
Overall specificity	1	1	1
Overall accuracy	1	1	1

every sample achieving 100% in percentage indicated by the value 1.00. This performance table has shown that the classification of agarwood Malaccensis and Crassna in a different medium of oil and smoke using CBR technique can achieve 100%.

## 4 Conclusion

Results on this paper showed that the agarwood samples; Malaccensis oil, Crassna oil, Malaccensis smoke, and Crassna smoke, have their own odor profile. Different agarwood properties have different odor profile. Case-based reasoning, CBR technique employed on the classification of agarwood in two medium; oil and smoke, across different species; Malaccensis and Crassna showed the positive result with 100% classification rate.

**Acknowledgements** This research and development are supported by Bio-Aromatic Research Centre of Excellent (BARCE) University Malaysia Pahang (UMP) and Malaysia Technical University (MTUN) RDU192803 grant.

## References

1. Liu Y, Wei J, Gao Z, Zhang Z, Lyu J (2017) A review of quality assessment and grading for agarwood. *Chin Herb Med* 9(1):22–30
2. Najib MS, Taib MN, Ali NAM, Arip MNM, Jalil AM (2011) Classification of agarwood grades using ANN. In: International conference on electrical, control and computer engineering (InECCE), pp 367–372
3. Hung CH, Lee CY, Yang CL, Lee MR (2014) Classification and differentiation of agarwoods by using non-targeted HS-SPME-GC/MS and multivariate analysis. *Anal Methods*
4. Ali NAM, Ismail N, Taib NM (2012) Analysis of agarwood oil (*aquilaria malaccensis*) based on GC-MS data. In: Proceedings—2012 IEEE 8th international colloquium on signal processing and its applications, CSPA 2012
5. Ismail N, Rahiman MHF, Taib MN, Ibrahim M, Zareen S, Tajuddin SN (2016) A review on agarwood and its quality determination. In: Proceedings—2015 6th IEEE control and system graduate research colloquium, (ICSGRC, 2015), pp 103–108
6. Lias S, Mohamad Ali NA, Jamil M, Tolmanan MSY, Misman MA (2018) A study on the application of electronic nose coupled with DFA and statistical analysis for evaluating the relationship between sample volumes versus sensor intensity of agarwood essential oils blending ratio. In: MATEC web of conferences, vol 201, p 02008
7. Lee SY, Lamasudin DU, Mohamed R (2018) Rapid detection of several endangered agarwood-producing *aquilaria* species and their potential adulterants using plant DNA barcodes coupled with high-resolution melting (Bar-HRM) analysis. *Holzforschung*
8. Ismail NS, Ismail NS, Rahiman MHF, Taib MN, Ali NAM, Tajuddin SN (2019) Polynomial tuned kernel parameter in SVM for agarwood oil for quality classification. In: Proceedings—2018 IEEE International conference on automatic control and intelligent systems (I2CACIS, 2018), pp 77–82
9. Kamarulzaini KAA, Ismail N, Rahiman MHF, Taib MN, Ali NAM, Tajuddin SN (2018) Evaluation of RBF and MLP in SVM kernel tuned parameters for agarwood oil quality classification. In: Proceedings—2018 IEEE 14th International Colloquium on Signal Processing & Its Applications (CSPA, 2018), pp 250–254
10. Haron MH, Taib MN, Ismail N, Mohd Ali NA, Tajuddin SN (2019) Statistical analysis of agarwood oil compounds based on GC-MS data. In: 2018 9th IEEE control and system graduate research colloquium, pp 27–30
11. Kao W-Y, Hsiang C-Y, Ho S-C, Ho T-Y, Lee K-T (2018) Chemical profiles of incense smoke ingredients from agarwood by headspace gas chromatography-tandem mass spectrometry. *Molecules* 23(11):2969
12. Ismail SN et al (2017) Discriminative analysis of different grades of gaharu (*aquilaria malaccensis* lamk.) via <sup>1</sup>H-NMR-based metabolomics using PLS-DA and random forests classification models *Molecules*, vol 22, no. 10
13. Amin MRM, Bejo SK, Ismail WIW, Mashohor S (2012) Colour extraction of agarwood images for fuzzy C-means classification. *Walailak J Sci Technol* 9(4):445–459
14. Abdullah A, Nik Ismail NK, Abdul Kadir TA, Md Zain J, Jusoh NA, Mohd Ali N (2007) Agar wood grade determination system using image processing technique. In: Proceedings International conference on electrical engineering and informatics, 2016, pp 427–429
15. Kiani S, Minaei S, Ghasemi-Varnamkhasti M (2016) Application of electronic nose systems for assessing quality of medicinal and aromatic plant products: A review. *J Appl Res Med Aromat Plants* 3(1):1–9
16. Zahed N, Najib MS, Tajuddin SN (2018) Categorization of gelam, acacia and tualang honey odor-profile using k-nearest neighbors. *Int J Softw Eng Comput Syst* 4(1):15–28
17. Wu D, Cheng Y, Luo D, Wong KY, Hung K, Yang Z (2019) POP-CNN: predicting odor's pleasantness with convolutional neural network
18. Elmogy SHM (2015) Case based reasoning: case representation methodologies *Int J Adv Comput Sci Appl* 6(11)

19. Chen D, Burrell P (2001) Case-based reasoning system and artificial neural networks: a review. *Neural Comput Appl*
20. Kolodner JL (1992) An introduction to case-based reasoning. *Artif Intell Rev*
21. Craw S, Aamodt A (2018) Case based reasoning as a model for cognitive artificial intelligence. In: *Lecture notes in computer science (including subseries lecture notes in artificial intelligence and lecture notes in bioinformatics)*, vol 11156 LNAI, pp 62–77
22. Zahari MF et al (2016) Gaharu Sensor: Classification Using Case Based Reasoning (CBR). *Jeecie* 1(8):38–41



# **Applied Electronics and Computer Engineering**

# SCAR-CNN: Secondary-Classification-After-Refinement Convolutional Neural Network for Fine-Grained Categorization



Bernard Jun Kai Cheah, Abduljalil Radman and Shahrel Azmin Suandi

**Abstract** The majority of existing approaches for fine-grained image recognition that work on attention-based learning, have their respective Top-K prediction accuracy better than Top-1 prediction. It is to say, there is a significant number of correct class falls in the range of Top-K predictions where  $K = 2, 3, 4, 5$ . This is the indirect indication for researchers not to neglect the need to explore the possibility of getting better prediction based on the discriminative feature of Top-K classes. This paper presents Secondary-Classification-After-Refinement Convolutional Neural Network (SCAR-CNN) which have an adaptive secondary classification model built on top of primary classification Top-K classes. Our focus is also on how to maximize the effect of removing unwanted classes in secondary classification, by performing image-enhancement on the input image of primary classification. Experiments show that these approaches achieve 86.9% of total accuracy as compared to the current state-of-the-art 86.5%.

**Keywords** Fine-grained categorization · Image up-scaling · Secondary classification

## 1 Introduction

Recent published work shows that deep convolutional neural network (CNN) represents the common approach to achieve excellent results in fine-grained categorization without extensive feature engineering [1]. CNN is capable of extracting insignificant object features based on the object appearance representation in pixel. CNN-based classification gives great performance, however, the state-of-the-art part-based representation for fine-grained categorization shows significant increase in Top-K (where  $K = 2, 3, 4, 5$  and so on) accuracy compared to its respective Top-1 accuracy [2].

---

B. J. K. Cheah (✉) · A. Radman · S. A. Suandi  
Intelligent Biometric Group, School of Electrical and Electronic Engineering,  
Universiti Sains Malaysia, Engineering Campus, Nibong Tebal 14300,  
Pulau Pinang, Malaysia  
e-mail: [bernard.ueee93@student.usm.my](mailto:bernard.ueee93@student.usm.my)

© Springer Nature Singapore Pte Ltd. 2020  
A. N. Kasruddin Nasir et al. (eds.), *InECCE2019*, Lecture Notes in Electrical Engineering 632, [https://doi.org/10.1007/978-981-15-2317-5\\_21](https://doi.org/10.1007/978-981-15-2317-5_21)

247

Accordingly, Top-K prediction might significantly improve the final classification results, due to the Top-K prediction usually carries the top K similar classes. Consequently, the classification results can be improved by appending specialized CNN with relatively less number of classes in a classification system. There is absolutely no issue to perform classification in a single CNN with more number of classes which have been already proven in the literature [2]. Indeed, specialized network is in fact theoretically better in learning discriminative features between “close classes”. In this paper, the term “close classes” refers to the top similar classes obtained by CNN. Thus, a Secondary-Classification-After-Refinement Convolutional Neural Network (SCAR-CNN) for fine-grained categorization is introduced in this paper.

Apart from this, part-based fine-grained feature learning approaches in the literature seldom mentioned the way to handle pixel information passed from localization module to classification module. The regions of localized part with low resolution have constant change of size on case-by-case basis. Localized parts of image with dynamic resolution are usually the source of classification module, while the input image resolution of CNN in classification module is always fixed. Therefore, a suitable image up-scaling method that can indeed recover fine details for low resolution images is required. Image up-scaling method plays essential role to avoid massive loss of useful information which is essential to attain high classification performance by CNN [3]. Moreover, the quality of processed image will be worse off if the image up-scaling method is not carefully chosen. This problem is critical when the localized part image resolution deviates a lot from the input image resolution of CNN. High intra-class variance and low inter-class variance will exist in the image space of the specific part location, in turn, seriously affect the performance of classification. In this research, the most suitable image up-scaling method is determined and evaluated.

SCAR-CNN is designed to deal with the problems stated above. Figure 1 illustrates the overall pipeline of SCAR-CNN. SCAR-CNN is a part-based convolutional neural network (CNN) segregates object of interest into few part locations and specializes classification function of CNN into a specific part location. In this research, CNN-based image up-scaling method in SCAR-CNN so as to minimize the loss of pixel information is introduced. Furthermore, we exploit Top-K classes information in order to enhance current performance of fine-grained categorization in terms of accuracy.

## 2 Related Work

Fine-grained categorization problem has been addressed as a result of the success of large scale image categorization breakthrough in recent years. Over the years, there are a number of successful solutions in the literature [4–6] to solve this problem. In contrast to the general object category, fine-grained categorization proceeds along two dimensions, which are discriminative feature learning and part based representation.

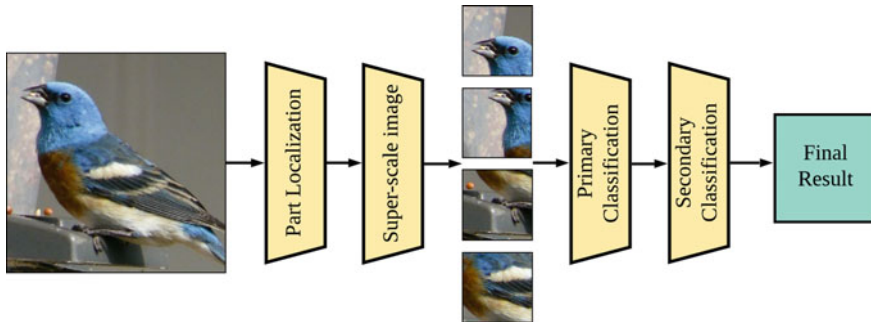


**Fig. 1** The Secondary-Classification-After-Refinement Convolutional Neural Network (SCAR-CNN) hybrid architecture was proposed in this paper. SCAR-CNN is a part-based approach for fine-grained categorization image up-scale with CNN super-resolution technique and exploitation of Top-K classes information after primary classification. SCAR-CNN was designed specifically to enhance current performance of fine-grained categorization in term of accuracy

The majority of existing approaches attempted to extract image features with a deep convolutional neural network (CNN) [7–9], due to the success of CNN in giving significant improvement for fine-grained categorization. He et al. [10] optimized residual functions and in turn scaled up the deep residual network (ResNet) that could learn stronger feature representation. Bilinear Convolutional Neural Network (B-CNN) was introduced by Lin and Maji [1, 11] which comprises of two CNN feature extractors running in parallel and its output result is derived by bilinear pooling. B-CNN is suitable for fine-grained categorization with its special translation-invariant manner. In a different approach, B-CNN with a low-rank classification model that leverages bilinear feature pooling for fine-grained classification was proposed by Kong and Fowlke [12]. Deep attention-based spatially recurrent B-CNN was also introduced by Wu and Wang [13]. Hierarchical bilinear pooling implementation by Yu et al. [14] was proposed in order to have powerful discriminative feature learning in CNN. Besides that, there are also some suggestions to improve CNN categorization such as the spatially weighted representation by Fisher Vector [15]. In a different manner, Cai et al. [3] proposed Resolution-Aware Convolutional Neural Network (RACNN) for fine-grained categorization of the low-resolution image on the Caltech-UCSD Birds 200-2011 dataset by having convolutional super-resolution layers being integrated in front of CNN [16–18].

On the contrary, the difference of object appearance between close categories was exploited as unique feature properties that stay in the object pixel values. Part-based representation is having two processes which are part localization and fine-grained categorization. Zhang et al. [19] and Lin et al. [5] trained a part localization model by using both bounding boxes and part annotations, the detected part locations were cropped and fine-tuned separate CNN for categorization. However, Wei et al. [20] did not use bounding boxes in the testing phase while some other researchers did it to ensure precise localization result. Unlike Huang et al. [4] and Krause et al. [21] who were only using the result from segmentation to localize entire object or parts,

respectively, Wei suggested Mask-CNN to localize parts and selecting useful deep convolutional descriptors using masks from segmentation to proceed fine-grained categorization. Multi-Attention Convolutional Neural Network (MA-CNN) [22] and Recurrent Attention Convolutional Neural Network (RA-CNN) were proposed by Zheng et al. [23] taking the advantages of CNN to promote learning mutually for both localization and categorization, where part localization performance is optimized by classification loss.

In order to localize objects of interest effectively in fine-grained categorization, the authors of [4, 5, 19, 24] proposed to leverage extra annotations of bounding boxes and parts which are not practical as compared to unsupervised approach for large-scale real problems [22, 23]. Xiao et al. [25] proposed to have two level domain net on both object and parts in weakly supervised CNN model, where object-level attention feeds relevant patches in a variety of scales and part-level attention focuses on local patterns. It was conducted under weak supervision by providing the only label of relevant category. Similar approaches were adopted by Zheng et al. [22], Fu et al. [23] and Wei et al. [20]. Some other part-based representation methods like picking deep filter responses [26] and multi-grained descriptors [27] were proposed, an unsupervised way for CNN to respond to specific patterns consistently was adopted as well. Bao et al. [28] presented a different approach to have variational generative adversarial networks that are capable of generating realistic and diverse samples with fine-grained category labels to enlarge dataset size for fine-grained categorization.

### 3 Methodology

In this section, we present Secondary-Classification-After-Refinement Convolutional Neural Network (SCAR-CNN) for fine-grained categorization. SCAR-CNN consists three main modules for different tasks which are part localization, primary classification and secondary classification. Part localization and primary classification are designed according to multi-attention concept in MA-CNN architecture [22]. In SCAR-CNN, default image up-scaling (also known as image super-scaling) used in MA-CNN is replaced by CNN-based method after part localization. Secondary classification is added in SCAR-CNN for the improvement of prediction result.

#### 3.1 Datasets

Caltech-UCSD Birds 200 fine-grained dataset [29] has been primarily used to carry out evaluation in this research (Fig. 2). The dataset contains a total of 200 bird categories with 5994 images for training and 5794 images for testing. Referring to MA-CNN approach, part localization module and primary classification module in SCAR-CNN are optimized with iterative training by classification loss and channel grouping loss as well. Thus, object bounding box and parts annotation of training

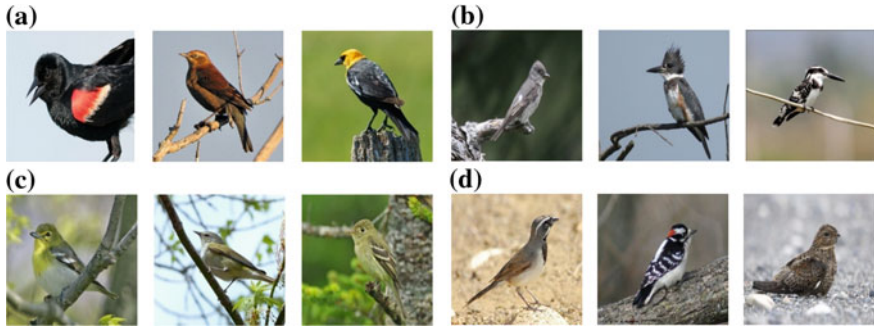


**Fig. 2** Four sets of images from Caltech-UCSD Birds 200 fine-grained dataset. Each set has three images from different bird species. Set (a) illustrates three subspecies from same species category with significant differences in appearance. They are labelled as “Red Winged Blackbird” (left), “Rusty Blackbird” (middle) and “Yellow Headed Blackbird” (right) in dataset. Sets (b), (c) and (d) are three sets of bird species with subtle feature differences that primary classification gets confused in the experiment

dataset are not required. Regardless of training process or testing process, the following image pre-processing steps are adopted. Firstly, full-sized image is cropped equally from center and resized by keeping aspect ratio to 448 by 448 pixels. The image is then translated to the format that fits the network input of part localization model. Secondly, it is after the process of localization. The respective region of parts are cropped out from original image and resized to 224 by 224 pixels. Part images are used for the subsequent primary classification and secondary classification. In secondary classification, training dataset is used to generate an optimized pre-trained weights for transfer learning later. To the best knowledge of authors, the latest excellent performance using Caltech-UCSD Birds 200 is reported in [30].

### 3.2 Part Localization

Part-based localization and feature learning is the future direction to solve fine-grained categorization problem (e.g., bird species). Zheng et al. [22] mentioned not to ignore the fact that there is mutual correlation between part localization (e.g., beak of bird) and fine-grained feature learning (e.g., shape of beak). In this research, MA-CNN architecture as the backbone of SCAR-CNN is adopted. The official released weights of part localization model is used to generate multiple part attention maps and proceed to channel grouping. Eventually, there are four resultant part representations (also known as part images in this paper) generated for each testing image which represent feet, tails, beaks and wings of bird. Based on our analysis, the resultant part images resolution from Caltech-UCSD Birds 200 fine-grained dataset is in the range of 85 by 85 pixels to 100 by 100 pixels. It is to say part images have to be

up-scaled to 224 by 224 pixels for primary classification. This is due to the fact that the input resolution of CNN model is fixed to 224 by 224 pixels.

In MA-CNN, Bilinear Interpolation method (BI) has been used as the default image up-scaling method. In our work, we propose other image-upscaling method like Bicubic Interpolation over  $4 \times 4$  pixel neighborhood, Lanczos Interpolation over  $8 \times 8$  pixel neighborhood and image super-resolution technique by Residual Dense Network (RDN) [3, 31]. Blind/Referenceless Image Spatial Quality Evaluator (BRISQUE) [32] has been used to perform image quality assessment on the output images from each image up-scaling method. BRISQUE checks image quality by comparing input image to the default evaluation model that has been computed from images of natural scenes with similar distortions. Since there are five images (one object and four parts) generated from one testing image, 28,970 images in total are evaluated. The image quality assessment provides the evidence to decide which image up-scaling method is the most suitable to be used in SCAR-CNN. For the case of RDN, the network architecture configuration is shown as follows:

- Number of Residual Dense Blocks (RDB) = 20
- Number of convolutional layers stacked inside a RDB = 6
- Number of feature maps of each convolutional layers inside the RDBs = 64
- Number of feature maps for convolutions outside of RDBs and of each RDB output = 64
- Super-scale factor = 2.

### 3.3 Primary Classification

The primary classification model in SCAR-CNN is designed using VGG-19 CNN model. Differed from MA-CNN authors' approach, we propose to have the primary classification process running in multiple instances. The source of each instance consists of a pair of images which are the object-level image (whole bird object) and part representation. Same object-level image is used while its respective part representation is not repeated between instances. The purpose of giving each instance a pair of image is to leverage the part feature ensemble for each case. There are two types of instances in the design of SCAR-CNN. First type instance has one object-level image paired with four part representation. Second type instance has one object-level image paired with only one part representations. In both types of instance, the respective pair of image is fed into their part-CNN for feature extraction. All feature representation map of each instance is then concatenated into fully-connected fusion layer with softmax function. The joint part-based feature representations  $J_a$  of first type instance is presented by Eq. 1 and the joint part-based feature representations  $J_b$  of second type instance is presented by Eq. 2. There are five instances running simultaneously on each testing image in SCAR-CNN. The prediction result of five instances are passed down to secondary classification module for further analysis.

$$J_a = \{P_1, P_2, P_3, P_4, P_O\} \quad (1)$$

$$J_b = \{P_i, P_O\} \quad (2)$$

where  $P_i$  denotes the extracted part description by part-CNN;  $P_O$  denotes the feature extracted from object-level images;  $i$  denotes the number of part.

### 3.4 Secondary Classification

In this section, we proposed the secondary classification as a solution to let CNN learn better from discriminative features between “close classes”. A secondary classification module is appended to SCAR-CNN after primary classification. Convolutional neural network (CNN) with smaller number of classes is used for secondary classification where the candidate classes is refined from primary classification result. The purpose is to improve final classification performance by utilizing new CNN trained with a “more relevant” reference pool. This is inspired by [2] which having evidence CNN to do decision refinement (secondary classification in our context). In contrast to [2] system architecture design, we select single ResNet-50 CNN model as the backbone of fully-connected fusion layer classifier. During inference, Top-K classes in the prediction of primary classification are recorded for secondary classification. Let’s take an example saying that the Top-3 prediction result from primary classification has “Class A”, “Class B” and “Class C” out of 200 species. Secondary classification model will adaptively make final prediction out of “Class A”, “Class B” and “Class C”. The highest score of these three classes from secondary classification softmax function will be the predicted class of SCAR-CNN.

ResNet-50 is trained by Caltech-UCSD Birds 200 training dataset and later, the pre-trained model has been reused on a new testing image prediction. Transfer learning is carried out by using the pre-trained model based on the Top-K classes obtained from primary classification. The respective reference pool (training images) of each testing image is used for transfer learning. Reference pool is collected from Caltech-UCSD Birds 200 training dataset based on the jurisdiction from Top-K class conditional probabilities (joint part-based feature representations with 4 parts) upon which predictions are made in primary classification. Besides that, we append training set of top class from joint part-based feature representations with 1 part in reference pool as well. The reference pool is relatively a lot smaller in secondary classification than primary classification. Therefore, training process to best fit ResNet-50 and feature learning of “close classes” with subtle difference in appearance can be achieved effectively. In SCAR-CNN, object-level image is used to proceed secondary classification for the final result.



## 4 Experiments

In this section, we present the experiment results of image quality with different image up-scaling method as well as the classification results using SCAR-CNN in different experimental scenario. SCAR-CNN was examined by using 5794 images from Caltech-UCSD Birds 200 fine-grained dataset. It should be noted that there are two sub-sections of SCAR-CNN analysis with two experimental scenario. In the first scenario, the classes of secondary classification model takes only the Top-K classes from one instance result in primary classification (classification result from joint part-based feature representations with 4 parts in Eq. 1). In the second scenario, the classes of secondary classification is similar as first scenario but considering also the top class from the remaining 4 instances (classification result from joint part-based feature representations with 1 part in Eq. 2).

### 4.1 Image Up-Scaling Method

Bilinear Interpolation (BI), Bicubic Interpolation (BC), Lanczos Interpolation (LI) and Residual Dense Network (RDN) are evaluated by BRISQUE. BRISQUE has score between 0 (best) and 100 (worst). Table 1 presents the average image quality score of each method. RDN score (13.62) which is the lowest among the four image up-scaling method. It is to say the up-scaled image quality using RDN is better-off against BI, BC and LI. BI is the default image up-scaling method in MA-CNN, therefore, we also select testing samples to compare the image quality with BI and RDN. Figure 3 shows one of the testing sample by putting part images of different image up-scaling method side-by-side in visual. The result of BI is on the left and the result of RDN is on the right. The part images from both sides have actual image resolution of 224 by 224 pixels. Human vision is subjective to observe blurry set of images on the left. To being coherent, we also perform image quality assessment for this testing sample. Image quality assessment result follows the sequence of image frame colour: starting from red, yellow, green and then blue colour. Part images that covered by same image frame colour represent the identical part location from same testing image. In this case, Bilinear Interpolation image up-scaling method recorded BRISQUE score of 43.20, 34.70, 39.05 and 54.65. Image up-scaling method with Residual Dense Network recorded BRISQUE score of 38.99, 26.86, 30.03 and 39.62. Once again, our experimental results show that the image up-scaled by using BI provide comparatively low image quality.

Besides that, we perform image quality assessment by taking all testing images into account. We merely compare BI and RDN in this assessment case by case. Experimental results show that 26,085 (90.04%) of images have better quality up-scaled by RDN, on the other hand, 2885 (9.96%) of images have better quality up-scaled by BI. Thus, image super-resolution technique by RDN is selected to upscale the output image from part localization before primary classification.

**Table 1** The evaluation results of image up-scaling method by BRISQUE

Image up-scaling method	Score
Bilinear Interpolation (BI)	44.17
Bicubic Interpolation (BC)	37.14
Lanczos Interpolation (LI)	36.16
Residual Dense Network (RDN)	<b>13.62</b>



**Fig. 3** Results of two sets of part images being up-scaled respectively by Bilinear Interpolation Method (left) and Residual Dense Network (right). The image frame colour in each set of part images represent same part location of same testing image. This figure is best viewed in colour and the part images do not comply with the actual image size

### 4.2 First Classification Scenario

First classification scenario denotes the secondary classification result is solely based on the Top-K classes of first type instance from primary classification. In this scenario, classification task with Top-1 denotes the absence of secondary classification. This is because only top one class from primary classification is used for secondary classification. Table 2 shows how different image up-scaling method after part localization stage and Top-K classes from primary classification affect the overall inference result in term of accuracy. Overall result shows that the combination of RDN image up-scaling method and Top-2 classes from primary classification give the best accuracy of 86.91%. Without considering the case of Top-1 classes prediction, the trend of accuracy is decreasing when Top-K classes is developing. The trend indicates that secondary classification model with more classes tend to give more false prediction. This is due to the fact that secondary classification model has to describe more object-level image with subtle features differences.

**Table 2** Secondary classification accuracy on condition that it is in first classification scenario. Secondary classification is performed on Top-K classes from primary classification where K has maximum value of 5. “Top-1” denotes the absence of secondary classification

Image up-scaling methods	Accuracy (%)				
	Top-1	Top-2	Top-3	Top-4	Top-5
Bilinear Interpolation method (BI)	86.58	83.36	82.67	82.29	81.77
RDN image up-scaling method (RDN)	86.10	<b>86.91</b>	86.27	85.93	85.76

The results in Table 2 show consistent improvement of prediction result when RDN image up-scaling method is applied before primary classification. This is the evidence to prove that better testing image quality can improve the overall classification result. In the absence of secondary classification, however, overall accuracy with RDN image up-scaling method drops slightly to 86.10% as compared to 86.58% with Bilinear Interpolation Method. In other words, RDN image up-scaling method is better than Bilinear Interpolation Method as if it was proven in previous sub-section if and only if secondary classification was present.

### 4.3 Second Classification Scenario

Second classification scenario denotes the secondary classification result is based on both Top-K classes of first type instance and Top-1 class of second type instances from primary classification. Therefore, Top-1 in secondary classification scenario denotes the number of classes in secondary classification CNN model can be either one or more than one. Table 3 shows how different image up-scaling method after part localization stage, Top-K classes from first type instance in primary classification and the four Top-1 classes from second type instances in primary classification, affect the inference result of secondary classification in term of accuracy. The prediction results that are made bold exceed the current state-of-the-art accuracy. Once again, SCAR-CNN prediction result is better by applying RDN image up-scaling method after part localization. The combination of RDN and Top-1 prediction class achieves the highest 89.96% accuracy. Top-1 accuracy is better than Top-2, Top-3 and so on, which is different from what has been presented on the first classification scenario. This is because the correct class tends to be in either Top-K classes in the first type instance or Top-1 class in the second type instance. In this scenario, Top-1 provides sufficient classes for secondary classification in most testing cases, which consequently, increase the chances of obtaining correct inference result.

**Table 3** Secondary classification accuracy on condition that it is in second classification scenario. Secondary classification is performed on Top-K classes from primary classification where K has maximum value of 5

Image up-scaling methods	Accuracy (%)				
	Top-1	Top-2	Top-3	Top-4	Top-5
Bilinear Interpolation method (BI)	84.15	83.62	83.25	82.29	82.13
RDN image up-scaling method (RDN)	<b>86.96</b>	<b>86.65</b>	86.08	85.81	85.60

#### 4.4 Overall Result

The best result of Second Classification Scenario slightly higher than the best result of First Classification Scenario, scoring 86.96% and 86.91%, respectively. According to the results, we can also conclude that RDN super-scaling method is necessary to improve the quality of low-resolution part images before proceeding to primary classification. In addition, setting top class of all five instances (first type instance and second type instances) in primary classification (First Classification Scenario) as classes in secondary classification CNN model produces slightly better result than solely having Top-K classes from first type instance in primary classification that resulted from joint part-based feature representations with four parts. Rounding off to the nearest one decimal places, our solution SCAR-CNN achieved 86.9% of overall accuracy in both cases stated in First Classification Scenario and Second Classification Scenario. The comparison results of our solution with the previous works in Table 4 illustrate that the proposed solution is slightly surpass the state-of-the-art accuracy on Caltech-UCSD Birds 200 fine-grained dataset by 0.46% ( $\frac{86.9-86.5}{86.5} \times 100\%$ ).

## 5 Conclusion

In this paper, we presented Secondary-Classification-After-Refinement Convolutional Neural Network for Fine-Grained Categorization (SCAR-CNN) for fine-grained categorization model that performs multiple part localization, primary classification on general classes and secondary classification on Top-K classes according to the result of previous stage. Experimental result demonstrated that SCAR-CNN outperforms the previous state-of-the-art methods in term of accuracy. SCAR-CNN achieved 86.9% of overall accuracy in both cases stated in First Classification Scenario and Second Classification Scenario. Theoretically, higher image resolution contains more useful information for inference. In the future, we will conduct the research on how higher input image resolution affects the performance of primary classification and secondary classification in SCAR-CNN.

**Table 4** Comparison results on CUB-200-2011 dataset. Train Anno. denotes using bounding box or part annotation in training. The result of SCAR-CNN is taking the best combination with highest accuracy in the respective First Classification Scenario and Second Classification Scenario

Approach	Train Anno.	Accuracy (%)
MG-CNN [27]	✓	83.0
FCAN [33]	✓	84.3
SPDA-CNN [24]	✓	85.1
B-CNN (250k-dims) [1]	✓	85.1
PN-CNN [34]	✓	85.4
Mask-CNN [20]	✓	85.4
PDFR [26]		84.5
RACNN [23]		85.3
RAM [35]		86.0
MACNN [22]		86.5
MAMC [30]		86.5
Our SCAR-CNN (first classification scenario)		<b>86.9</b>
Our SCAR-CNN (second classification scenario)		<b>86.9</b>

**Acknowledgements** This research is partly supported by Universiti Sains Malaysia Research University Individual (RUI) Research Grant No.: 1001/PELECT/8014056.

## References

1. Lin T-Y, Roy Chowdhury A, Maji S (2018) Bilinear convolutional neural networks for fine-grained visual recognition. *IEEE Trans Pattern Anal Mach Intell* 40(6):1309–1322
2. Bargal SA, Zunino A, Petsiuk V, Zhang J, Saenko K, Murino V, Sclaroff S (2018) Guided zoom: questioning network evidence for fine-grained classification. *Computer Research Repository (CoRR)* 1812:02626
3. Cai D, Chen K, Qian Y, Kämäräinen J-K (2019) Convolutional low-resolution fine-grained classification. *Pattern Recogn Lett* 119:166–171
4. Huang S, Xu Z, Tao D, Zhang Y (2016) Part-stacked CNN for fine-grained visual categorization. In: 2016 IEEE conference on computer vision and pattern recognition (CVPR), pp 1173–1182
5. Lin D, Shen X, Lu C, Jia J (2015) Deep LAC: deep localization, alignment and classification for fine-grained recognition. In: 2015 IEEE conference on computer vision and pattern recognition (CVPR), pp 1666–1674
6. Zhang Y, Wei X-S, Wu J, Cai J, Lu J, Nguyen V-A, Do MN (2016) Weakly supervised fine-grained categorization with part-based image representation. *IEEE Trans Image Process* 25(4):1713–1725
7. Wang J, Fu J, Xu Y, Mei T (2016) Beyond object recognition: visual sentiment analysis with deep coupled adjective and noun neural networks. In: International joint conference on artificial intelligence (IJCAI-16), p 7
8. Krizhevsky A, Sutskever I, Hinton GE (2017) ImageNet classification with deep convolutional neural networks. *Commun ACM* 60(6):84–90

9. Fu J, Mei T, Yang K, Lu H, Rui Y (2015) Tagging personal photos with transfer deep learning. In: Proceedings of the 24th international conference on world wide web—WWW '15, pp 344–354. ACM Press, New York, NY, USA
10. He K, Zhang X, Ren S, Sun J (2016) Deep residual learning for image recognition. In: 2016 IEEE conference on computer vision and pattern recognition (CVPR), pp 770–778
11. Lin T-Y, Maji S (2017) Improved bilinear pooling with CNNs. In: British machine vision conference (BMVC), vol 2017
12. Kong S, Fowlkes C (2017) Low-rank bilinear pooling for fine-grained classification. In: 2017 IEEE conference on computer vision and pattern recognition (CVPR), pp 7025–7034
13. Wu L, Wang Y (2017) Where to focus: deep attention-based spatially recurrent bilinear networks for fine-grained visual recognition. Computer Research Repository (CoRR), vol abs/1709.0
14. Yu C, Zhao X, Zheng Q, Zhang P, You X (2018) Hierarchical bilinear pooling for fine-grained visual recognition. In: European conference on computer vision (ECCV), pp 595–610
15. Perronnin F, Larlus D (June 2015) Fisher vectors meet neural networks: a hybrid classification architecture. In: 2015 IEEE conference on computer vision and pattern recognition (CVPR), pp 3743–3752
16. Zhao B, Wu X, Feng J, Peng Q, Yan S (2017) Diversified visual attention networks for fine-grained object classification. IEEE Trans Multimedia 19(6):1245–1256
17. Anderson A, Shaffer K, Yankov A, Corley C, Hodas NO (2017) Beyond fine tuning: a modular approach to learning on small data. Computer Research Repository (CoRR), vol. abs/1611.0, no. Nathan Hodas
18. Hu Q, Wang H, Li T, Shen C (2017) Deep CNNs with spatially weighted pooling for fine-grained car recognition. IEEE Trans Intell Transp Syst 18(11):3147–3156
19. Zhang N, Donahue J, Girshick R, Darrell T (2014) Part-based R-CNNs for fine-grained category detection. In: European conference on computer vision (ECCV), pp 834–849
20. Wei X-S, Xie C-W, Wu J, Shen C (2018) Mask-CNN: localizing parts and selecting descriptors for fine-grained bird species categorization. Pattern Recogn 76:704–714
21. Krause J, Jin H, Yang J, Fei-Fei L (June 2015) Fine-grained recognition without part annotations. In: 2015 IEEE conference on computer vision and pattern recognition (CVPR), pp 5546–5555
22. Zheng H, Fu J, Mei T, Luo J (2017) Learning multi-attention convolutional neural network for fine-grained image recognition. In: 2017 IEEE international conference on computer vision (ICCV), pp 5219–5227
23. Fu J, Zheng H, Mei T (2017) Look closer to see better: recurrent attention convolutional neural network for fine-grained image recognition. In: 2017 IEEE conference on computer vision and pattern recognition (CVPR), pp 4476–4484
24. Zhang H, Xu T, Elhoseiny M, Huang X, Zhang S, Elgammal A, Metaxas D (2016) SPDA-CNN: unifying semantic part detection and abstraction for fine-grained recognition. In: 2016 IEEE conference on computer vision and pattern recognition (CVPR), pp 1143–1152
25. Xiao T, Xu Y, Yang K, Zhang J, Peng Y, Zhang Z (June 2015) The application of two-level attention models in deep convolutional neural network for fine-grained image classification. In: 2015 IEEE conference on computer vision and pattern recognition (CVPR), pp 842–850
26. Zhang X, Xiong H, Zhou W, Lin W, Tian Q (2016) Picking deep filter responses for fine-grained image recognition. In: 2016 IEEE conference on computer vision and pattern recognition (CVPR), pp 1134–1142
27. Wang D, Shen Z, Shao J, Zhang W, Xue X, Zhang Z (December 2015) Multiple granularity descriptors for fine-grained categorization. In: 2015 IEEE international conference on computer vision (ICCV), pp 2399–2406
28. Bao J, Chen D, Wen F, Li H, Hua G (2017) CVAE-GAN: fine-grained image generation through asymmetric training. In: International conference on computer vision (ICCV)
29. Welinder P, Branson S, Mita T, Wah C, Schroff F (2010) Caltech-UCSD Birds 200, tech. rep, California Institute of Technology

30. Sun M (2018) Multi-attention multi-class constraint for fine-grained image recognition. In: European conference on computer vision (ECCV), vol. abs/1806.0
31. Zhang Y, Tian Y, Kong Y, Zhong B, Fu Y (2018) Residual dense network for image super-resolution. In: 2018 IEEE/CVF conference on computer vision and pattern recognition, pp 2472–2481
32. Mittal A, Moorthy AK, Bovik AC (2012) No-reference image quality assessment in the spatial domain. *IEEE Trans Image Process* 21(12):4695–4708
33. Liu X, Xia T, Wang J, Yang Y, Zhou F, Lin Y (2016) Fully convolutional attention networks for fine-grained recognition. *Computer Research Repository (CoRR)*, vol. abs/1603.0
34. Branson S, Horn GV, Belongie SJ, Perona P (2014) Bird species categorization using pose normalized deep convolutional nets. *British Machine Vision Conference (BMVC)*, vol. abs/1406.2
35. Li Z, Yang Y, Liu X, Zhou F, Wen S, Xu W (2017) Dynamic computational time for visual attention. In: 2017 IEEE international conference on computer vision workshops (ICCVW), pp 1199–1209

# Forecasting Road Deaths in Malaysia Using Support Vector Machine



Nurul Qastalani Radzuan, Mohd Hasnun Arif Hassan ,  
Anwar P. P. Abdul Majeed, Khairil Anwar Abu Kassim,  
Rabiu Muazu Musa, Mohd Azraai Mohd Razman and Nur Aqilah Othman

**Abstract** An average of 6,350 people died every year in Malaysia due to road traffic accidents. A published data of Malaysian road deaths in 20 years since 1997 reveals that the number of fatalities has not really declined with a difference of less than 10% from one year to the next. Forecasting the number of fatalities is beneficial in planning a countermeasure to bring down the death toll. A predictive model of Malaysian road death has been developed using a time-series model known as autoregressive integrated moving average (ARIMA). The model was used in the previous Road Safety Plan of Malaysia to set a target death toll to be reduced in 2020, albeit being inaccurate. This study proposes a new approach in forecasting the road deaths, by means of a machine learning algorithm known as Support Vector Machine. The length of various types of road, number of registered vehicles and population were among the eight features used to develop the model. Comparison between the actual road deaths and the prediction demonstrates a good agreement, with a mean absolute percentage error of 2% and an R-squared value of 85%. The Linear kernel-based Support Vector Machine was found to be able to predict the road deaths in Malaysia with reasonable accuracy. The developed model could be used by relevant stakeholders in devising appropriate policies and regulations to reduce road fatalities in Malaysia.

---

N. Q. Radzuan · M. H. A. Hassan (✉)

Faculty of Mechanical and Automotive Engineering Technology, Universiti Malaysia Pahang,  
26600 Pekan, Pahang, Malaysia  
e-mail: [mhasnun@ump.edu.my](mailto:mhasnun@ump.edu.my)

A. P. P. A. Majeed · M. A. M. Razman

Faculty of Manufacturing and Mechatronics Engineering Technology, Universiti Malaysia  
Pahang, 26600 Pekan, Pahang, Malaysia

N. A. Othman

Faculty of Electrical and Electronics Engineering Technology, 26600 Pekan, Pahang, Malaysia

K. A. A. Kassim

Malaysian Institute of Road Safety Research (MIROS), Lot 125-135, Jalan TKS 1, Taman Kajang  
Sentral, 43000 Kajang, Selangor, Malaysia

R. M. Musa

Centre for Fundamental and Liberal Education, Universiti Malaysia Terengganu, 21030 Kuala  
Nerus, Terengganu, Malaysia

© Springer Nature Singapore Pte Ltd. 2020

A. N. Kasruddin Nasir et al. (eds.), *InECCE2019*, Lecture Notes in Electrical  
Engineering 632, [https://doi.org/10.1007/978-981-15-2317-5\\_22](https://doi.org/10.1007/978-981-15-2317-5_22)

261



**Keywords** Road traffic accident · Road death · Prediction · Machine learning · Support vector machine

## 1 Introduction

Road traffic accidents account for 4.6% of death cases in Malaysia in 2017 [1]. This is the main cause of deaths among youth in Malaysia at 22.5%. Although the percentage has reduced from the previous year (5.4% in 2016), annual death cases in Malaysia has not actually decreased since 1997. Figure 1 shows the percentage difference of road deaths in Malaysia compared to the previous year, starting from 1997 until 2017. It is seen that the differences are less than 10%, either increasing or decreasing. But the number has not really changed for almost 2 decades now, with an annual average of road deaths of 6,350 cases.

It is essential to be able to project how the number of deaths due to road traffic accidents in Malaysia will change, either growing or reducing before any action plan can be proposed. An autoregressive integrated moving average (ARIMA) model was proposed in 1998 to predict road fatalities in Malaysia [2]. This model has been further updated and used by Sarani et al. [3] to predict the number of road deaths in Malaysia in 2020.

Using the model, Sarani et al. predicted that there will be 8,760 road deaths in 2015, and this number will keep on increasing in 2020 with 10,716 fatalities. These figures have been used in the Road Safety Plan of Malaysia 2014–2020 [4]. Nonetheless, it is observed that the prediction made was inaccurate. In 2015, there were 6,706 road deaths recorded. The model has overpredicted fatalities by 31%. Owing to this flawed prediction, the government of Malaysia has set a wrong fatalities reduction

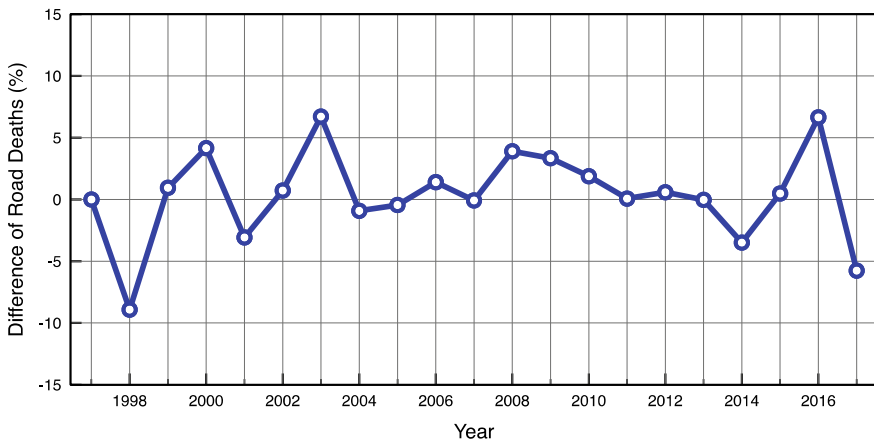


**Fig. 1** The difference in road death from the previous year in Malaysia from 1997 until 2017

target, that is to bring the fatality down to 25% from the predicted value of 8,760–6,570. Considering the actual road deaths in 2015, the target should have been 5,030 instead.

In order to support the Decade of Action for Road Safety 2011–2020, the national policymaker together with the state government have implemented a blue ocean strategy focusing on black spot areas in every state. The aim is to reduce the number of road death by half in 2020 [5]. Darma implemented an autoregressive integrated moving average model (ARIMA), transfer function-noise model and state-space model integrated into traffic fatality regression model by considering the correlation of the number of traffic fatalities, vehicle ownership, and road length with road safety campaigns in Malaysia [6]. Sapri et al. [7] demonstrated that accident caused by road geometry, vehicle type, age, and collision type are the most important factors that lead to non-fatal crash injuries in Kota Bharu. The research employed a decision tree with the application of Classification and Regression Trees (CART). Meanwhile, Hartika et al. [8] compared the predictability of road deaths between the conventional multilinear regression (MLR) model and Artificial Neural Networks (ANN) in a black spot area in Selangor. The study demonstrated that ANN outperformed the MLR model in predicting road fatalities at the black spot area, suggesting the efficacy of the machine learning model to provide a better accident prediction. A number of variables were used in the aforesaid study, namely hourly traffic volumes, 85th percentile speed, vehicles' gap and the number of the access point at the selected study area.

In this study, we are proposing a machine learning model known as the Support Vector Machines (SVM) or in regression studies, it is often known as Support Vector Regression. SVM has demonstrated to provide desirable prediction in different studies [9, 10], nonetheless, it is worth noting that the employment of machine learning, particularly SVM in road safety is scarce. Thus, the objective of this study is to develop an SVM model to forecast road deaths in Malaysia based on a number of features. The subsequent sections shall describe the dataset used, the development of the SVM model, as well as reporting the efficacy of its prediction.

## 2 Methodology

Road traffic accident data was extracted from reports by the Malaysian Public Works Department (JKR) [11] and Malaysia Road Safety Department (JKJR) [7], respectively. The number of road death based on Malaysian traffic accident scenario is predicted via the SVM model by considering a number of features that will be elaborated in the subsequent section.

## 2.1 Datasets

The road network length data, as well as population and number of registered vehicles from 1997 until 2017, were used in the road death (RD) model. Registered vehicles are expressed by the number of vehicles registered in the Road Transport Department Malaysia system, the population is the number of people estimated by the Department of Statistics Malaysia, and the road network length is in kilometre as reported by Public Works Department. It is worth noting that the road network length is further demarcated into the highway, federal road, federal territories road, institution road, industrial road as well as FELDA road. Therefore, a total number of eight (8) features or dependent variables are considered. The Support Vector Regression model was developed using MATLAB® 2016b.

## 2.2 SVM Model Development

SVM is a supervised machine learning model that is based on statistical learning theory that could either be used for classification or regression problems. For regression problems, the central notion, is essentially to minimize the loss function defined by the flatness of the  $\epsilon$ -tube, that in turn, minimizes the prediction error. The kernel function often influences the prediction outcome based on the nature of the data. In the present investigation, the linear kernel function is employed in developing the SVM model. The mathematical treatment of the different types of kernels is described in [8]. The generalized equation of the SVM model is described in Eq. (1). In which,  $\omega$  is the flatness that is required to be minimized,  $x$  is the input patterns and  $b$  is the bias. Moreover, the five-fold cross validation technique was employed in this study owing to the size of the data. Figure 2 illustrates the variables involved in developing the model.

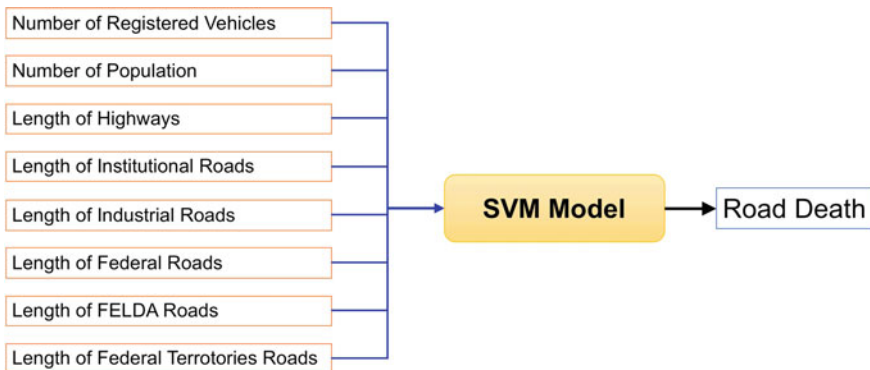


Fig. 2 Depiction of the overall model

$$f(x) = \langle \omega, x \rangle + b \tag{1}$$

### 3 Results and Discussion

Table 1 lists the performance evaluation of the proposed model. Linear based SVM model developed demonstrates its capability to predict road death with an accuracy of 85%. This is shown by the R-squared percentage. A very low mean average percentage error (MAPE) of 2% was also observed, further suggesting the efficacy of the developed model in predicting road fatalities.

The previous model developed by Radin Umar [2], which was further updated by Sarani et al. [3] predicted 8,760 road deaths in 2015. This is an overprediction of 30.6% (the actual number of road deaths in 2015 is 6,706). Our Linear based SVM model, on the other hand, predicted 6,961 road death in 2015, which brings down the overprediction to a mere 3.8%, suggesting that the model developed has a better prediction capability.

The prediction accuracy is further corroborated in the plot of the comparison between the actual and predicted road death as shown in Fig. 2. Also included in the plot is the prediction by Sarani et al. [3]. Both lines (actual and predicted) are very close to each other, with slight but acceptable discrepancies in some years. Nevertheless, our proposed model forecasted a similar trend of road deaths as compared to the actual data. On another note, it is observed that the number of road deaths in Malaysia shows an increasing trend, although gradually, despite the multitude of road safety campaign organised by the government agencies and non-government organisations (NGOs). Effective countermeasures are required to be planned immediately in order to impede this alarming trend (Fig. 3).

It is worth noting that other features ought to be considered, for instance, the number of vehicles equipped with safety features (anti-lock braking system and airbag), number of accidents at black spot areas, or road environment safety features amongst others in order to evaluate its influence towards the prediction of road fatalities Through such sensitivity or parametric analysis, appropriate suggestions could be made to policy makers as well as other relevant stakeholders in further reducing the fatality rate on Malaysian roads.

**Table 1** Performance evaluation of the developed SVM model

Evaluation metrics	SVM linear model
R-squared	0.85
RMSE	153
MAE	113.77
MAPE %	2%

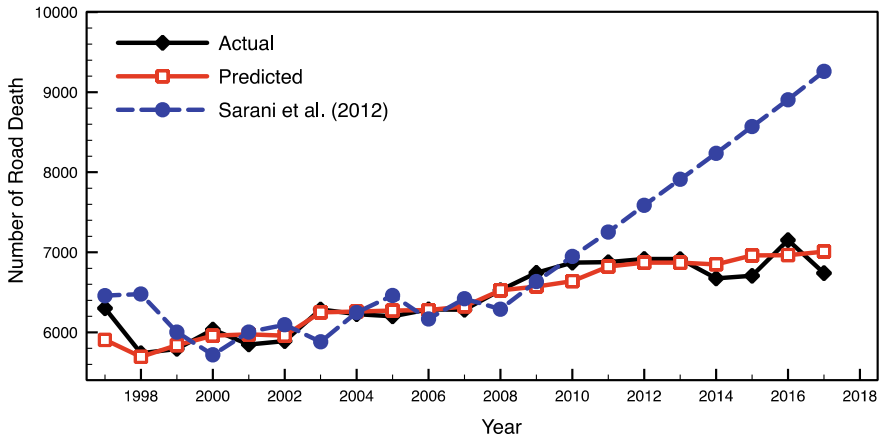


**Fig. 3** Actual and predicted number of road death in Malaysia from 1997 to 2017

## 4 Conclusion

Road deaths in Malaysia has been previously predicted using a time-series model known as ARIMA. Nonetheless, the model was found to overpredict the fatalities by more than 30%. On a serious note, the flawed prediction was used to set a target in the previous Road Safety Plan of Malaysia 2014–2020. This study introduces a new approach to forecasting road deaths, employing a machine learning model known as the Linear based Support Vector Machine. Eight features namely the number of population and registered vehicles, as well as the length of six different type of roads, were used in developing the proposed model. The model was used to predict 20 years of road deaths, from 1997 until 2017. The prediction accuracy was evaluated using the mean absolute percentage error and R-squared, among others. The proposed model demonstrates 85% prediction accuracy, with on 3% of MAPE. It also predicts the gradually increasing trend of road deaths in Malaysia well, in line with the actual road death data. Therefore, the developed model could be used by relevant stakeholders in charting pertinent policies that could eventually reduce the number of road fatalities in Malaysia.

**Acknowledgements** The authors would like to acknowledge ASEAN NCAP, FIA Foundation, Global NCAP, OEMs and the Society of Automotive Engineers Malaysia (SAE Malaysia) for funding this study under the ASEAN NCAP Holistic Collaborative Research (ANCHOR II) grant (UIC191504). Also, the authors are thankful to the Universiti Malaysia Pahang for providing the facilities to conduct the study.

## References

1. Department of Statistics Malaysia: Statistics on Causes of Death, Malaysia (2018)
2. Radin Umar RS (1998) Model kematian jalan raya di Malaysia: unjuran tahun 2000. *Pertanika J Sci Technol* 6(2)
3. Sarani R, Syed Mohamed Rahim SA, Mohd Marjan J, Wong SV (2012) Predicting Malaysian road fatalities for year 2020, MRR 06/2012. Malaysian Institute of Road Safety Research, Kuala Lumpur
4. Ministry of Transport Malaysia: Road Safety Plan of Malaysia 2014–2020 (2014)
5. World Highways (2017) Malaysia's road safety problem needs addressing. Route One Publishing Ltd., Kent, United Kingdom
6. Darma Y (2017) A time series analysis of road traffic fatalities in Malaysia. University of Malaya
7. Road Safety Department Malaysia (2018) Buku Statistik Keselamatan Jalan Raya. Kuala Lumpur, Malaysia
8. Hartika HA, Ramli MZ, Zaihafiz M, Abidin Z, Hafiz M (2017) Study of road accident prediction model at accident hotspot area: a case study at Selangor 3(5): 466–470
9. Taha Z, Razman MAM, Adnan FA, Abdul Ghani AS, Abdul Majeed APP, Musa RM, Sallehudin MF, Mukai Y (2018) The identification of hunger behaviour of *Lates calcarifer* through the integration of image processing technique and support vector machine. In: IOP conference series: materials science and engineering, vol 319, no 1
10. Taha Z, Musa RM, Majeed APPA, Abdullah MR, Abdullah MA, Hassan MHA, Khalil Z (2018) The employment of support vector machine to classify high and low performance archers based on bio-physiological variables. In: IOP conference series: materials science and engineering, vol 342, no 1
11. Public Works Department Malaysia (2016) Statistik Jalan Edisi 2016. Kuala Lumpur, Malaysia

# Investigation of Dimensionality Reduction on Numerical Attribute Features in a Finger Vein Identification System



Ei Wei Ting, M. Z. Ibrahim, D. J. Mulvaney, W. N. A. W. Samsudin and S. Khatun

**Abstract** With the large number of people travelling internationally, there is an increasing demand to be able to deal with security clearance rapidly and with a minimum of inconvenience. Using finger vein biometric traits fulfils these requirements. In previously-reported work, the data obtained from finger veins underwent dimensionality reduction using principal components analysis (PCA) followed by linear discriminant analysis (LDA) and this was shown to improve the identification rate compared to the more commonly applied Discrete Wavelet Transform (DWT). Although PCA was found to be effective at reducing the noise residing in the discarded dimension, this work demonstrates that the corresponding eigenvalue may in fact also contain useful local information that is important in identification and so should be retained. To overcome this problem, this paper proposes the use of feature extraction using DWT and local binary patterns (LBPs) to generate the feature vectors, before they undergo dimensionality reduction using PCA. Support Vector Machines (SVMs) are used for classification. The performance of the proposed method was compared with previous work, with the identification rate of the proposed method offering the best accuracy of 95.8%.

**Keywords** Finger vein · Dimensionally reduction · Discrete wavelet transform · Local binary patterns

## 1 Introduction

In this modern technological world, biometric technology has become an important focus of attention for the biometric-based research community. These technologies

---

E. W. Ting · M. Z. Ibrahim (✉) · W. N. A. W. Samsudin · S. Khatun  
Faculty of Electrical and Electronic Engineering, University Malaysia Pahang,  
26600 Pahang, Malaysia  
e-mail: [zamri@ump.edu.my](mailto:zamri@ump.edu.my)

D. J. Mulvaney  
School of Electronic, Electrical and Systems Engineering, Loughborough University,  
Loughborough L11 3TU, United Kingdom

© Springer Nature Singapore Pte Ltd. 2020  
A. N. Kasruddin Nasir et al. (eds.), *InECCE2019*, Lecture Notes in Electrical Engineering 632, [https://doi.org/10.1007/978-981-15-2317-5\\_23](https://doi.org/10.1007/978-981-15-2317-5_23)

are commonly used in identification, verification and security systems. The technologies that use the traditional biometrics traits (such as iris, fingerprint, and face) have limitations compared to the use of finger veins in their application [1]. The finger vein has advantages in term of its high immunity to counterfeit, vein aliveness and user friendliness. The finger vein location is covered by skin, making it very difficult for the finger vein pattern to be stolen or duplicated in some way [2]. The use of the finger vein is convenient, generally easy to access and uses a contactless method in the capture data.

## 2 Related Work

Previous research in finger vein recognition system has been able to demonstrate the potential of the approach. Wu and Ye [3] proposed a finger vein extraction using discrete wavelet transforms (DWTs) local binary patterns (LBPs) and to extract the local and global features from the finger vein structure. In [4], Miura et al. proposed repeated line tracking and a maximum curvature points technique to extract finger vein features for recognition. In 2015, Shrikhande [5] proposed performing finger vein recognition using discrete wavelet packet transform features when applied to the SDMULA HMT finger vein database. They used the average standard deviation and energy without the HH sub band as features and achieved a high recognition rate of 88.58% using a Euclidean classifier and 92.33% using Canberra as the classifier.

In 2011, Park [6] proposed the use of support vector machines (SVMs) for finger vein recognition and Wu and Liu [7] introduced PCA for feature extraction while retaining SVM as the finger vein identification system. Both researchers applied PCA at an early stage of feature extraction and it is proposed in the current work that such an application of PCA may potentially remove features that are unimportant for recognition. In 2017, finger vein verification using repeated line tracking with dimensionality reduction by PCA was shown to be able to improve the finger vein recognition rate in template matching from verification rate of 52.19–94.29% [8].

Most of the reported finger vein feature extraction methods use local vein structure, but it is known to be difficult to collect good quality images from such regions. To overcome this problem, a combination of features which are binary features (local features) and discrete wavelet transform (global features) are proposed in this paper. The local and global features are presented as numerical attributes whose feature vectors are long. Hence, dimensionality reduction using PCA on the feature vectors is proposed in order to allow the classification algorithms to concentrate on the most relevant features.



### 3 Propose Method

This paper proposes a finger vein identification system which improves on previous work by replacing the template matching method by a machine learning approach. The finger vein recognition system uses repeated line tracking with dimensionality reduction using PCA, following the approach in [8]. The method was applied to three samples from each of 20 subjects from the SDMULA-HMT finger vein database. The experiment was then repeated using 100 subjects with six samples from each subject. The feature extraction methods included the DWT and LBP, dimensionality reduction was carried out using PCA and the training and testing were carried out using SVMs.

#### 3.1 Finger Vein Database

Several finger vein databases are publicly available, but differ in a number of respects, such as the number of samples, number of fingers, format of images and so on. A number of the databases contain misaligned and skewed finger images which are not suitable for use in this research. The most widely used database is the SDMULA-HMT finger vein database, an open source database. Each of the database samples consists of images of six fingers, the index, ring and middle fingers of both the left and right hands. The total number of the images is 3816 with image resolution of  $320 \times 240$  pixels in 'bitmap' format. In the experimental work in this paper, the images of the index fingers available in the SDMULA-HMT database were used to compare finger vein recognition performance with that obtained from previously published work. Figure 1 shows examples of finger vein postures from the SDMULA-HMT database. Subsequent paragraphs, however, are indented.

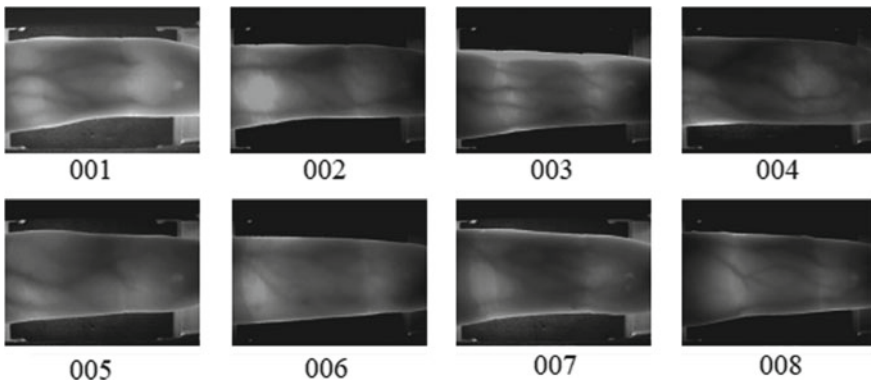
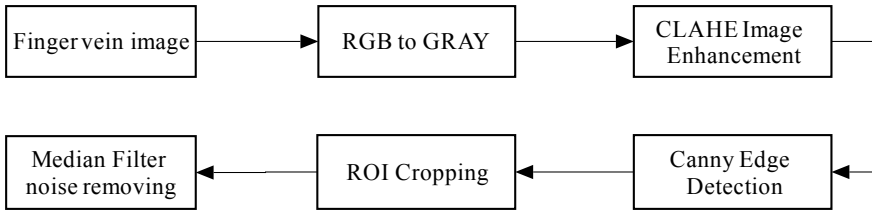
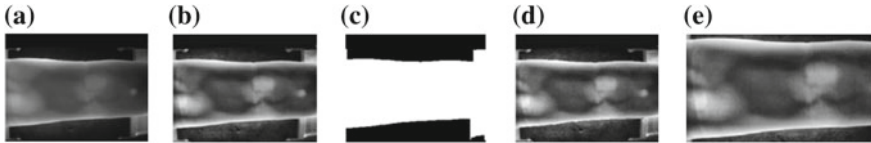


Fig. 1 Examples of finger vein postures in SDMULA-HMT



**Fig. 2** Image pre-processing stages



**Fig. 3** Image pre-processing: **a** original image; **b** CLAHE enhancement; **c** finger vein ROI extraction; **d** canny edge detection; **e** ROI of finger vein after median filtering

### 3.2 Image Processing

Image pre-processing plays an important role in ensuring that the original images are enhanced in such a way that the later classification has the best opportunity of being successful. In this work, both region of interest (ROI) extraction and image de-noising are carried out before performing feature extraction. The pre-processing steps are shown in Fig. 2.

Firstly, the finger vein image was converting from RGB to gray scale, followed by image enhancement using conventional contrast-limited adaptive histogram equalization (CLAHE), a method proposed by Zhu et al. to achieve contrast enhancement [9]. This approach involves computing several histograms, each corresponding to a distinct section of the gray scale finger vein image, while at the same time redistributing the brightness of the image. Following finger enhancement, the localization the finger vein region is used to generate a suitable ROI. Here, a  $3 \times 3$  median filter mask was used to reduce the noise generated by the image operation. Figure 3 shows the outputs of each stage in the image preprocessing of finger vein image.

### 3.3 Feature Extraction

In this paper, DWT and LBP were used to extract the finger vein features. Unlike the template matching vein pattern extraction applied in [8], the DWT and LBP approaches do not extract the x- and y-axis coordinates of each pixel in the image and the numerical attributes of the features are the mean and standard deviation.

### 3.3.1 Discrete Wavelet Transform (DWT)

The DWT can be used as a form of image compression and represents the signals in dynamic sub-band decomposition. It is an efficient and powerful tool for signal and image processing applications. The DWT was applied by passing the image signal through both low pass and high pass filters and its output was down sampled by a factor of two at each level. In this research, a 2D DWT was used for feature extraction as this provides a multi-resolution transforms yielding both time and frequency information. Figure 4 shows how each sub-band has been extracted using discrete wavelet decomposition. The process first decomposes the ROI of the finger vein using the 2D-DWT. The first level decomposition produces four subpart images known as the image approximation (cA), the horizontal details (cH), the vertical details (cV), and the diagonal details (cD). Then, each of the sub images was further decomposed (second level decomposition) into 16 sub-images, each of which is decomposed again (third level decomposition) to provide 64 sub-regions. Discrete wavelet decomposition has been previously used in feature extraction for other biometric identification purposes, such as finger print and palm vein classification [10]. Figure 5 shows the how the third-level discrete wavelet decomposition is carried out and also shows the output produced. Finally, the mean and standard deviation of each of the 64 blocks was taken as the features. From the 2D DWT, 128 features in total can be obtained from each finger vein image.

Previous published work on the classification of palm vein images decomposed the image approximation (cA) into additional levels to obtain high frequency information corresponding to noise content [11]. In this paper, as the finger vein images are less complex than the palm vein images, the decomposition of the images instead involved all of the four sub-parts of the image and ignored the high frequency details as these were less likely to cause the loss of important information relevant to the later classification.

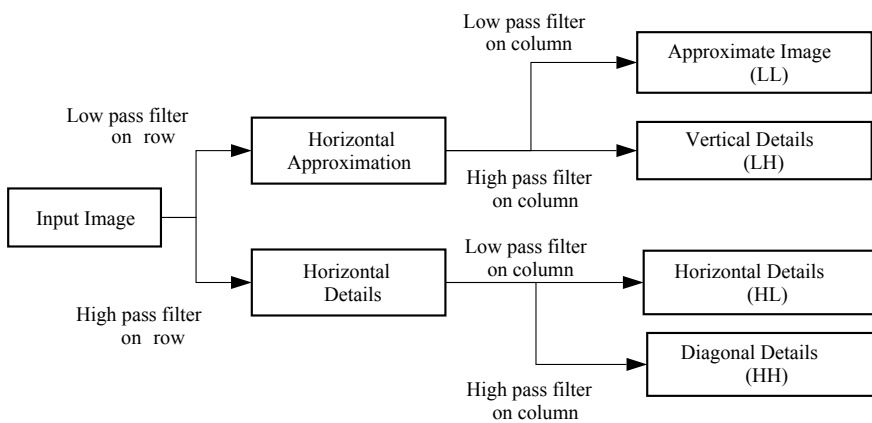


Fig. 4 DWT process flow

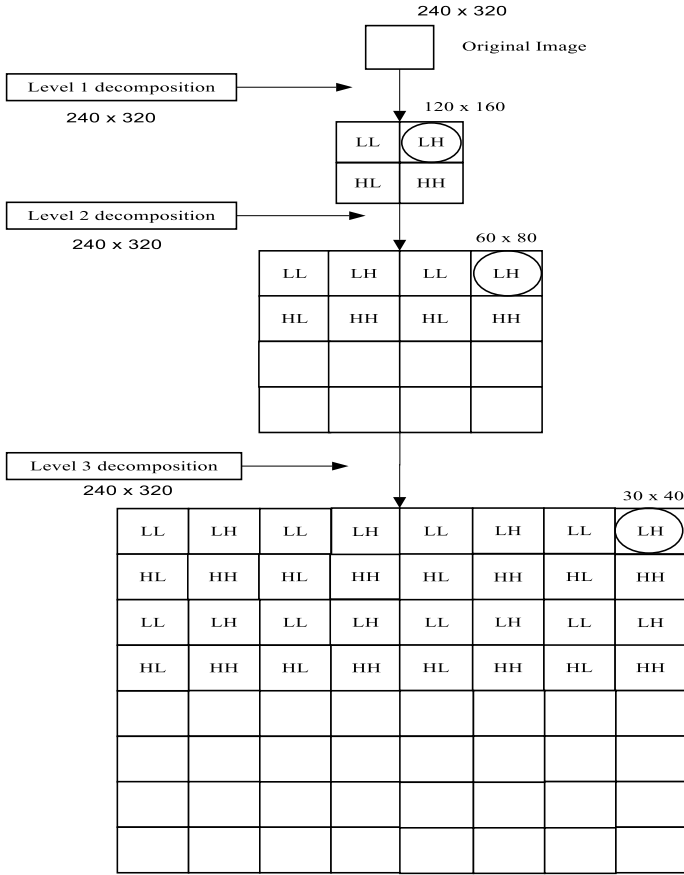


Fig. 5 Third level discrete wavelet decomposition

### 3.3.2 Local Binary Pattern (LBP)

The LBP is a method that is capable of extracting finger vein codes without requiring an accurate isolation of the finger vein region. In addition, this method is robust with respect to high degrees of saturation and irregular shading in finger vein images. The LBP is defined as an ordered set of binary neighborhood pixels surrounding the center pixels [6]. The LBP features are obtained using the following steps:

- Step 1: The finger vein image is divided into several cells as shown in Fig. 6.
- Step 2: In each cell, the neighbour pixels ( $N_p$ ) are compared with its centre pixel ( $N_c$ ), giving a 12 digit binary number that is converted to its decimal equivalent.
- Step 3: The histogram is computed over the cells.
- Step 4: Histogram normalization and concatenation of histograms of all divided cells are carried out to yield a feature vector.

**Fig. 6** Process flow of the LBP operator

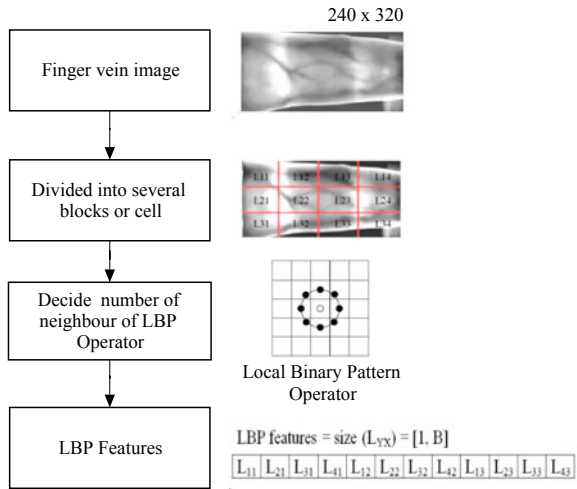


Figure 6 shows the process flow of the local binary pattern features extraction method. In this research, the neighbor parameter was set to 12 and the local binary pattern operator for 12 neighbors is shown in Fig. 6c.

The LBP operator also can be expressed in algorithmic form as can be seen in Eq. (1) which uses a gray-level comparison of its neighborhood of pixels. The original operator was a  $3 \times 3$  neighborhood of 8 pixels  $i_n$  around a center pixel  $i_c$ . The threshold  $s(x)$  for those neighborhood pixels is the value of the center pixel and the result can be represented as a binary number or as its decimal equivalent  $LBP(x_c, y_c)$ .

$$LBP(xC, yC) = \sum_{n=0}^7 s(in - ic)2^n \tag{1}$$

$$s(x) = \begin{cases} 1, & \text{if } x \geq 0 \\ 0, & \text{if } x \leq 0 \end{cases} \tag{2}$$

The feature vector of LBP can be defined as in Eq. (3), where the overall LBP feature length depends on the number of cells and the number of bins,  $B$  which in turn depends on the upright property and the number of neighbors,  $P$ .

$$LBP\ features = Size(Lxy) = [1, B] \tag{3}$$

The upright property represents the rotational invariance flag. The property is set as true if the features do not encode rotation information. In this paper, the upright property is set to false as the rotationally invariant features are required in the research.

### ***3.4 Principal Components Analysis (PCA) Dimensionality Reduction***

PCA is a popular, powerful, yet simple to apply dimensionality reduction technique that has been used in many data mining and pattern classification applications. It performs a linear mapping of higher dimensional data to a lower dimensional data in a manner such that the variance of the data in the lower dimensional representation is maximized. The approach permits a reduction in the quantity of data by removing those components least useful in the classification, but with minimal loss of information. In 2011, PCA and LDA were used in combination by Wu et al. and Liu et al. to extract finger vein patterns and both papers demonstrated a successful reduction in the dimensionality of an image while obtaining an improved identification rate of 98% with only seven PCA features and four LDA features [7].

Previous work that performed finger vein recognition using PCA was carried out by applying PCA directly to the two dimensional finger vein image. In this experiment, the PCA was applied to the  $500 \times 142$  numerical attributes obtained from DWT and LBP. In this paper, PCA is used for dimensionality reduction and Fig. 7 shows the overall process. The input data are the feature vectors of the finger veins obtained from 100 samples where each sample consists of five individual images. The feature vectors are transformed into a covariance matrix before undergoing dimensionality reduction. From the covariance matrix, the eigenvector and eigenvalues are determined, and, finally, a reduction in the number of feature vectors was obtained by setting a target number of dimensions for PCA and letting it choose the most significant features.

### ***3.5 Support Vector Machine (SVM)***

The linear SVM is a fast machine learning algorithm that provides multiclass classification implemented on an original proprietary version of cutting plane. It is efficient when dealing with large data sets and is able to make a simple linear separation between classes by finding the best hyper-plane that separates the feature points of one class from the other [11]. The largest margin between the two classes can be considered to be a the hyper-plane that provides the maximal width of the slab parallel to the hyper-plane that has no interior points as shown in Fig. 8.

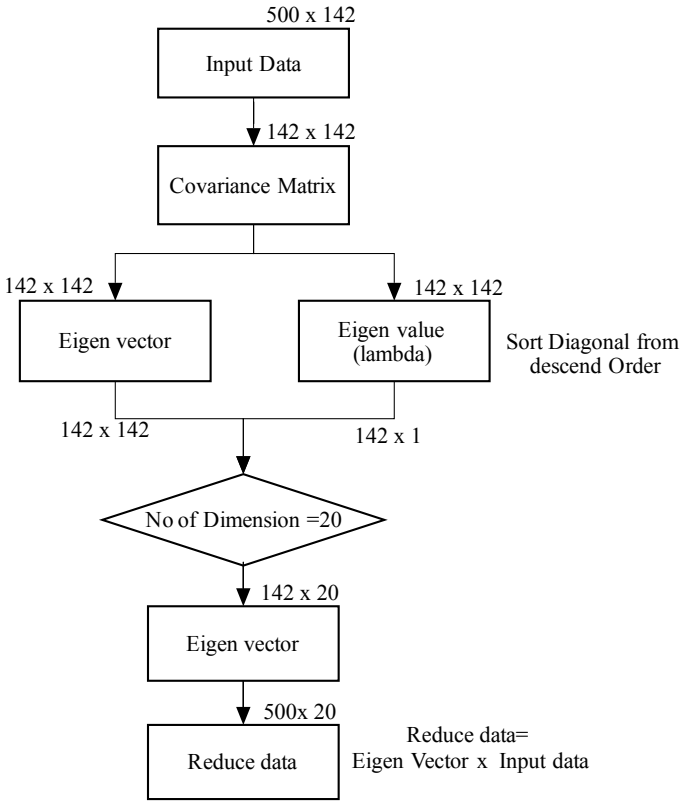
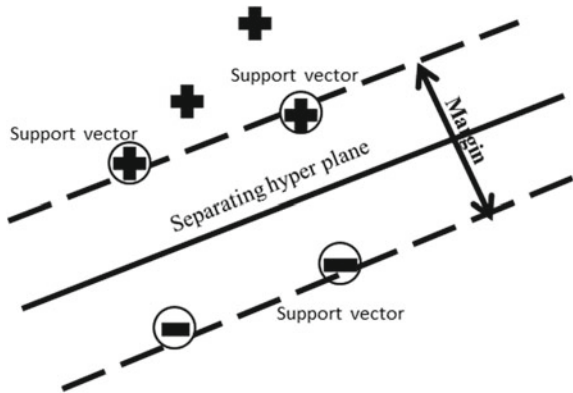


Fig. 7 Flowchart of PCA dimensionality reduction

Fig. 8 SVM implementation, where '+' indicates data points of type 1, and '-' indicates data points of type -1 [12]



## 4 Experimental Results and Discussion

In this experiment, finger vein images from 100 different subjects each providing six samples were extracted from the SDMULA-HMT finger vein database. Each of the samples was used to provide five images for training and the remaining one was used for testing. The ‘leave one out’ method was adopted in the training process and the linear SVM was used for classification purposes. The experimental procedure described in [8] was implemented in that numbers of subjects involved was gradually increased from 20 to 100. Figure 9 shows the performance of identification system using the different feature extraction methods.

From Fig. 9 it can be seen that the best identification accuracy was obtained by using maximum curvature as the feature extraction method and this achieved successful identification in 83.56% of cases; the next best being repeated line tracking with an accuracy of 80.8%. The accuracy of identification using DWT acting alone and LBP acting alone were both relatively low, but, when the features from DWT and LBP are combined, the accuracy increased to around 80%. The identification rates using the template-based feature extraction methods such as RLT and maximum curvature were found to be better than the numerical attributes feature extraction methods (DWT and LBP), probably because the template-based methods provided additional information. However, the numerical attributes methods’ features became increasingly powerful following dimensionality reduction using PCA. The experimental work was continued by analyzed the effect of PCA on the accuracy of the identification system using the different feature extraction methods. The three best-performing feature extraction methods found in the results shown in Fig. 9 were chosen for further investigation when using PCA dimensionality reduction and Fig. 10 compares the accuracy of the identification systems when implementing feature extraction both with PCA and without PCA.

From the observations recorded in Fig. 10, it can be seen that the performance of the identification obtained using maximum curvature was reduced by 0.28% when

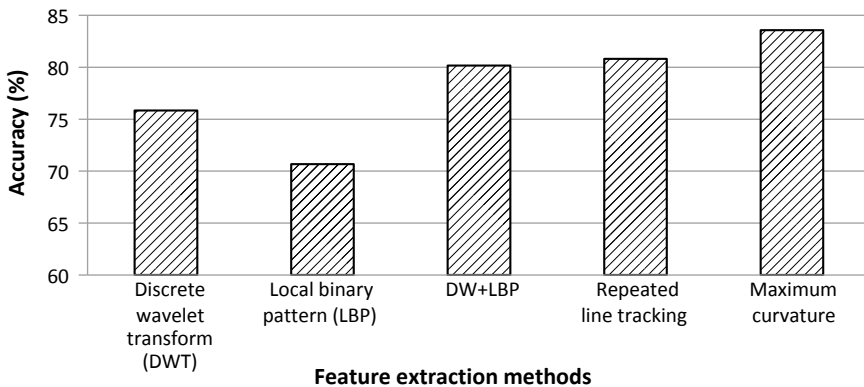
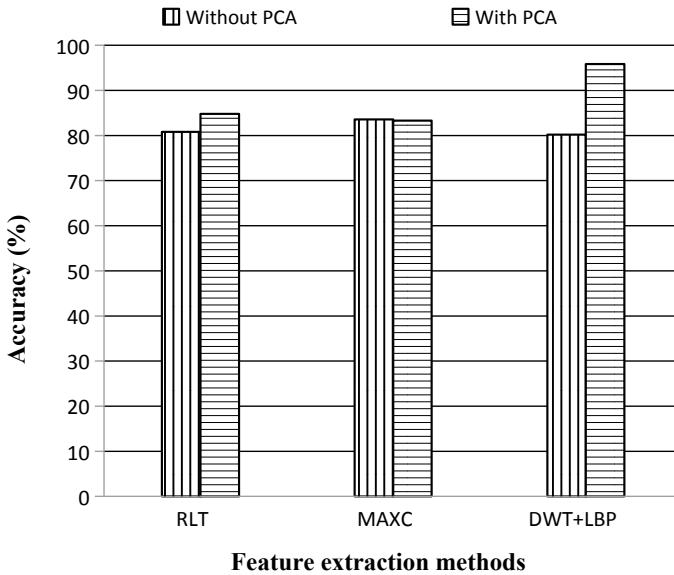


Fig. 9 Identification performance using different feature extraction method





**Fig. 10** The comparison of identification accuracy between different feature extraction methods with PCA and without PCA

PCA was employed, but the two remaining feature extraction methods exhibited an improvement in accuracy after applying dimensionality reduction using PCA. The identification accuracy using repeated line tracking was improved by 4%, and the combined DWT and LBP approach shows a significant improvement of 15.67%. This is an excellent demonstration that PCA enables improvements in the accuracy of identification systems where the features are represented in numerical attributes far better than when the x-axis and y-axis features are used.

The experiment was repeated several times to determine the number of dimensions that gives best accuracy following the application of PCA. Figure 11 shows the accuracy of the identification system following DWT and LBP pattern feature extraction for different numbers of dimensions.

The experiment was carried out with the number of dimension being 10, 20, 30, 50, and 80 and it can be seen that the accuracy of the identification system improved by 4% when the number of dimensions of the features increased from 10 to 20. This is because the first 10 principal components are not sufficiently unique to be able to distinguish between 100 subjects and the increased number of dimensions provides additional unique features for classification. No improvement in accuracy was apparent as the number of features was increased to 30 and then further to 50 and this might be caused by having an insufficient number of features to represent the data or due to the increase in noise content that will be obtained if superfluous features are present during classification. Hence, the best classification performance was obtained when PCA provided a number of features in the range 20–50. However, a

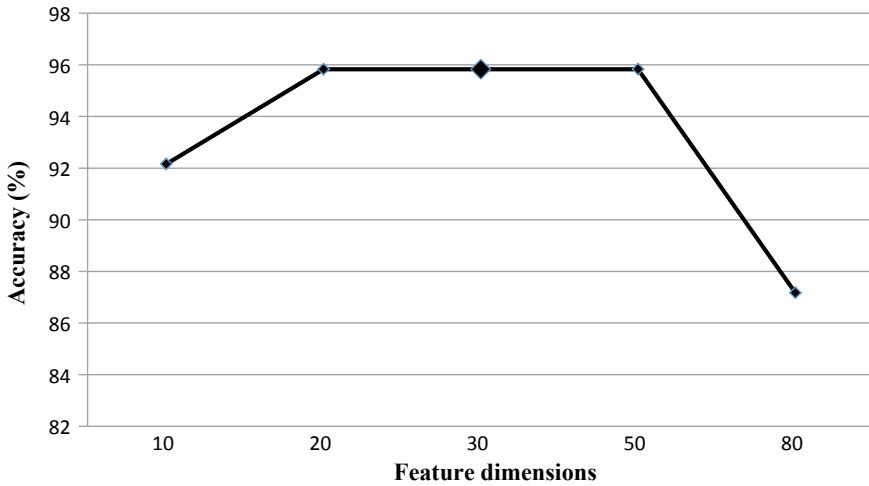


**Fig. 11** The accuracy of identification system with different number of dimension remained

20 dimension feature vector was selected rather than 30 or 50, as the fewer the number of dimensions then the shorter will be the processing time of the identification system.

Table 1 compares the identification rate of the proposed methods with other methods that have also used the SDMULA-HMT finger vein database. From the table, it can be seen that the proposed method was able to improve the accuracy of the identification system compared to other methods. Further, it is clear that that PCA is able to improve the identification rate by selected the most suitable features, while at the same time reducing the dimensionality of the features by reducing noise and removing non-unique features.

**Table 1** Comparison of the identification system performance of different methods

Method	Accuracy (%)
Wavelet transform	75.83
Local binary pattern	70.67
Wavelet + Local binary pattern	80.16
Max curvature	83.56
Repeated line tracking	80.80
Max curvature + PCA	83.28
Repeated line tracking + PCA	84.79
Wavelet + Local binary pattern + PCA (proposed method)	95.83

## 5 Conclusion

The paper has presented a finger vein identification system that uses a machine learning approach. The features were extracted by a combination of DWT and LBP, followed by dimensionality reduction using PCA to extract unique features for classification carried out using linear SVM. Compared to a range of methods in the literature that did not use PCA, the performance of the new approach when combined with PCA is substantially better. This is due to PCA being able to reduce the data to its most relevant components without significant loss of information. This releases the identification algorithm to concentrate on relevant targeted information that is best suited for classification and be unaffected by irrelevant data. Furthermore, the PCA-based methods for finger vein verification system had a shorter training vector leading to a reduced training time.

**Acknowledgements** This research is financially supported by the Fundamental Research Grant Scheme (FRGS/1/2016/ICT04/UMP/02/3) with the RDU number RDU160108 which is awarded by Ministry of Higher Education Malaysia (MOHE) and internal UMP grant RDU1703225 via Research and Innovation Department, Universiti Malaysia Pahang (UMP) Malaysia.

## References

1. Syazana-Itqan K, Syafeeza AR, Saad NM, Hamid NA, Saad WHBM (2016) A review of finger-vein biometrics identification approaches. *Indian J Sci Technol* 9(32)
2. Yang L, Yang G, Yin Y, Zhou L (2014) A survey of finger vein recognition. In: Chinese conference on biometric recognition, pp 234–243
3. Wu JD, Ye SH (2009) Driver identification using finger-vein patterns with radon transform and neural network. *Expert Syst Appl* 36(3 PART 2):5793–5799
4. Miura N, Nagasaka A, Miyatake T (2004) Feature extraction of finger-vein patterns based on repeated line tracking and its application to personal identification. *Mach Vis Appl* 15(4):194–203
5. Shrikhande SP (2015) Finger vein recognition using discrete wavelet packet transform based features, pp 1646–1651
6. Park KR (2011) Finger vein recognition by combining global and local features based on SVM. *Comput Informatics* 30(2):295–309
7. Wu J-D, Liu C-T (2011) Finger-vein pattern identification using SVM and neural network technique. *Expert Syst Appl* 38(11):14284–14289
8. Ting EW, Ibrahim MZ, Mulvaney DJ (2017) Investigation of dimensionality reduction in a finger vein verification system. *IT Convergence Secur* 2018:194–201
9. Zhu Y, Huang C (2012) An adaptive histogram equalization algorithm on the image gray level mapping. *Phys Procedia* 25:601–608

10. Elnasir S, Shamsuddin SM, Akbar S, Ahmad A, Hayat M (2014) Identification of fingerprint using discrete wavelet transform in conjunction with support vector machine. *Int J Adv Soft Comput Appl* 6(5):189–199
11. Awad M, Khanna R (2015) Support vector machines for classification. In: *Efficient learning machines: theories, concepts, and applications for engineers and system designers*. Apress, Berkeley, CA, pp 39–66
12. Ivanciuc O (2007) Applications of support vector machines in chemistry. *Rev Comput Chem* 23:291–400

# Intelligent Gender Recognition System for Classification of Gender in Malaysian Demographic



Yap Su Chi and Syafiq Fauzi Kamarulzaman

**Abstract** Identification of a person gender as a man or woman based on the past experiences through features of face such as eyes, mouth, cheek can be obtained through an intelligent gender recognition system. Detection of a person's gender can be difficult but important for security purposes, especially where safety issues concerning woman in public amenities. The objectives of this research are to identify the techniques for classifying features from man and woman facial images, through which embed as a system and validate using photos within Malaysian demographic. This research is focused on utilizing facial features for gender classification in real time, emphasizing on deep learning-based gender recognition and HAAR Cascade classifier using pre-trained caffe model in OpenCV library. Results show that under Malaysian demographic, probability of 86% accuracy of gender recognition were obtained.

**Keywords** Gender recognition · Gender classification · Deep learning

## 1 Introduction

Since year 2013, statistics highlighted over 50,000 sex crimes concerning domestic violence cases in Malaysia involving girls as young as six years old. On average, there were at least approximately eight cases reported daily within the country. Among the cases, a man was convicted for rape of a 19 years old girl in the woman lavatory of a shopping center within Kuala Lumpur. Another was a man convicted for hiding in the women's bathroom cubicle of a gasoline station, attempted rape on any unsuspecting victim. Such public amenities are commonly utilized by unsuspecting women where the probability of such crimes occurring exist remains a threat to public confidence in safety [1].

---

Y. S. Chi · S. F. Kamarulzaman (✉)  
Faculty of Computer Systems & Software Engineering,  
University of Malaysia Pahang, Kuantan, Malaysia  
e-mail: [syafiq29@ump.edu.my](mailto:syafiq29@ump.edu.my)

© Springer Nature Singapore Pte Ltd. 2020  
A. N. Kasruddin Nasir et al. (eds.), *InECCE2019*, Lecture Notes in Electrical Engineering 632, [https://doi.org/10.1007/978-981-15-2317-5\\_24](https://doi.org/10.1007/978-981-15-2317-5_24)

283

Digital video surveillance systems have been commonly implemented in multiple fields, such as shopping mall, train station, airport, and numerous others, due to the fast growth of internet, cloud computing, and multimedia technologies. Object identity can play a very significant role in government security in these digital video surveillance systems. Intelligent gender recognition is the capacity to identify an individual, whether man or woman, depending on the position and previous experience in detection of features of the face such as the mouth, nose or eyes [2].

In this research, artificial intelligence techniques used to classify gender were identified for gender classification under Malaysian demographic. The techniques was applied into a system that provides real-time recognition to be implemented in the public amenities. The application was validated through a series of images concerning individuals under the Malaysian demographic. Performance of the developed system were evaluated and the performance are discussed within this paper.

## 2 Related Works

There are different methods for gender classification. Nearly all works in gender classification involve pre-processing images, extracting characteristics from faces and classifying those characteristics using marked information. It can be classified on the basis of extraction and classification of features. Extraction of features can also be classified into techniques based on appearance and geometry. While this section will briefly discuss about previous work of classification method applied.

Eigenface algorithm is a Principal Component Analysis (PCA) application for analyzing human faces [3, 4]. Eigenfaces is an appearance-based approach to face recognition that looks to capture the variety in a collection of facial images and use the information to encode and compare the images of individual faces in a holistic way (rather than a component-based or feature-based approach). Eigenfaces are calculated by estimating the principal components of the facial images dataset. Frequently, this technique is used for facial recognition and detection of facial landmarks. Eigenfaces focus the significant facial data that could be directly identified with human facial instincts such as eyes, nose and lips. Capturing the statistical variation between face images is one of the approaches. In addition, Eigenfaces is used to decrease the complexity of computation and space, where each face image can be represented by a few parameters. The primary concept of Eigenface is to get the characteristics in mathematical sense instead of using mathematical transform for acceptance as a physical face element. Eigenfaces are sensitive to lighting conditions and head position, but recognition is time-consuming, while recognition results are highly affected by changes in size and easily affected by the recognized head orientation.

A holistic method is also used by the Fisherface algorithm. Fisherface varies from Eigenface, where Fisherface maximizes the mean range between class dispersion while minimizing the variance within class dispersion [5, 6]. With Eigenface improvement, Fisherface utilizes Linear Discriminant Analysis (LDA).Fisherface uses LDA to differentiate between two images of distinct classes where the variation

within a class can be minimized. LDA works better to classify various classes. The concept of Fisherface is quite easy, where the same classes should cluster together closely while in the reduced dimensional representation separate classes are as far separated from each other as feasible. Due to its invariant to light intensity, Fisherface can be used for age and gender classification. However, the scatter within the class could still be of comparatively big importance when the scatter between classes is big. Therefore, to perform facial recognition, it requires more processing rooms and time. A class of profound neural network is the Convolutionary Neural Network (CNN). Shift invariant is where CNN utilizes multilayer perceptron variation intended to require minimal pre-processing [7]. CNN is a series of layers in which each layer converts volume by differentiable function from one activation to another. Convolutionary Layer, Pooling Layer, and Fully Connected Layer are among the layers. The layers seen in periodic neural networks are the fully linked layer. Every CNN layer has its own features. Each subsequent output is the input of the next layer [8]. Each input image passes through convolutionary layers, pools, completely linked layers, and uses Softmax to classify an object. Pooling was conducted to decrease dimensional size. Due to these characteristics, even when modeling complex functions, extraction of features can be performed effectively. The only drawbacks is that it needs training, where effectiveness and precision are improved through training when more training iterations are performed.

Comparing the three above methods, we could summarize that the Convolutionary Neural Network (CNN) could provide greater effectiveness and precision than the Fisherface and Eigenface algorithm [5]. We therefore utilize CNN as a classification algorithm within this study to determine man and woman subjects from our data on the images.

### 3 Method

In this research, we proposed a system that can detect and classify gender using Convolutional Neural Network (CNN) technique. The system can be installed outside the public bathroom for facial recognition of people entering the bathroom. Through this system, it will detect the gender of the person real time and capture the face images. Later, CNN is utilized to recognize the gender. When the recognition result is man, the alert message is sent to the security department to alert the authorities, therefore improve the safety of the public bathroom users especially women [9].

Figure 1 shows the overall process of the system while Fig. 2 shows the context diagram, the relationship between the system and the external entities. The camera captures the real time face images The CNN technique is applied and results is shown. The alert message is sent to the security department if someone trespassing.

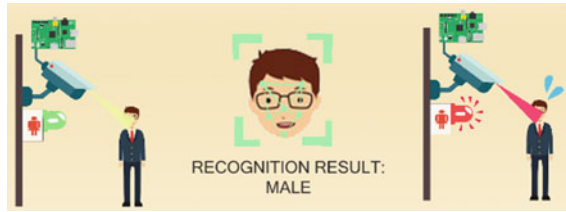


Fig. 1 The overall process of the system

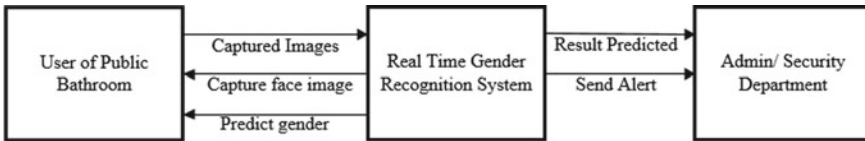


Fig. 2 The context diagram of the proposed system

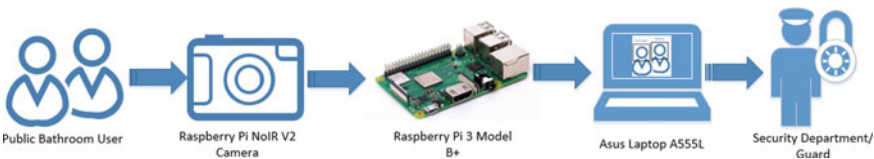


Fig. 3 The system architecture for implementation

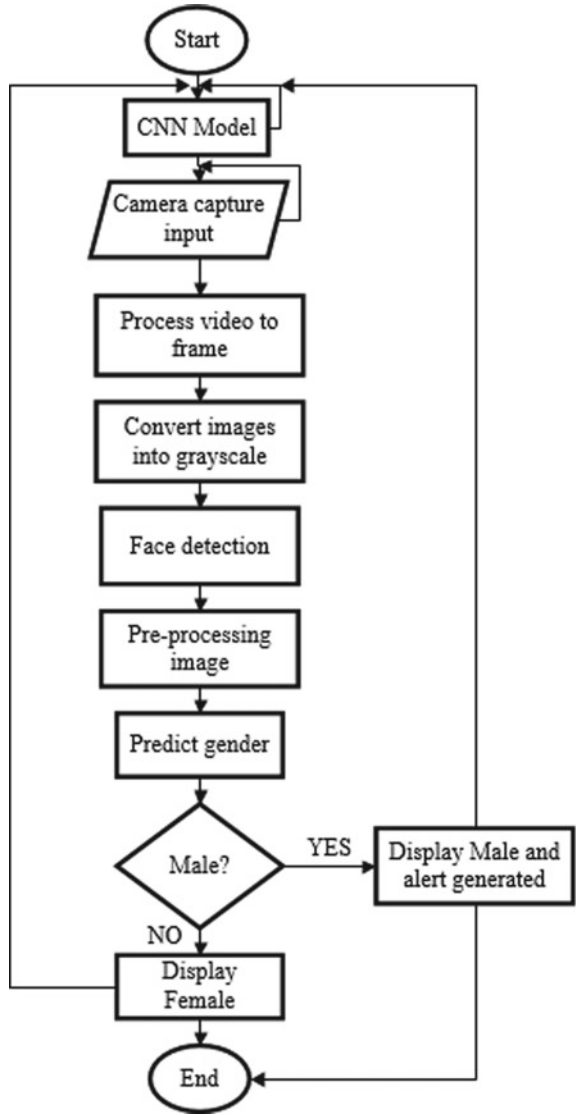
### 3.1 System Architecture

Figure 3 shows the system architecture for implementation of the system. Based on the figure, the faces of the user will be captured and transformed to images by the Raspberry Pi NoIR V2 camera. The images will be sent to the Raspberry Pi 3 Model B+. Then, by processing the cropped facial images, the forecast is carried out in Raspberry Pi. The outcome will be shown on the laptop’s camera windows. Only the safety guard can view the outcomes. If the identified gender is man, the alert will be sent via buzzer and email to the security department by creating the beep sound.

Figure 4 displays the system flowchart including the system features. First, the scheme begins with the camera being initialized for ongoing capture. The camera will keep capturing the picture constantly. The images were then transformed into frames. Continue with CNN algorithms to recognize the face. The images will then be transformed to pre-processed greyscale and gender prediction. The buzzer will behave as the alert and beep to notify customers in the event that the gender identified is man. An email will also be sent to customers to behave as a signal of warning.



Fig. 4 Flowchart of the proposed system



### 3.2 Convolutional Neural Network Technique

Convolutional Neural Network (CNN) is an architecture used for deep learning. It is used for object recognition by detecting features and perform segmentation. The CNN used for deep learning become more and more popular since it eliminates the requirement for manual feature extraction. The features are found instantly through CNN and can be train and retrain again for new recognition tasks which allow for

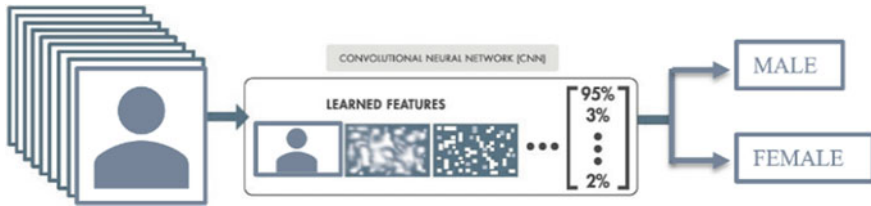


Fig. 5 Image passed through CNN and automatically learns the features and classifies the gender

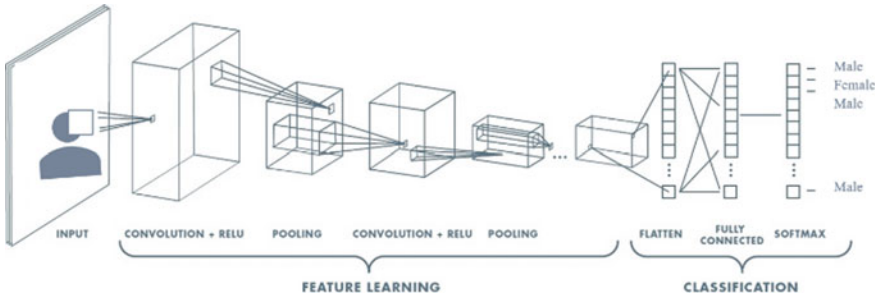


Fig. 6 CNN feature learning and classification of gender

improvement on previous existing networks [10]. Figure 5 shows that the image passed to CNN automatically learns the features and classifies the gender. The man and woman are the output of the image.

CNN can have many layers that determine distinct characteristics of an picture. Each layer filters the picture of the training at distinct resolution and the outputs/tensors are used as the input of the next filter. The filters can begin to more complicated characteristics as very simple features that can define the object in a unique way as the layers progress. The input picture will undergo a few changes and then pool the state to fully linked steps and lastly the output will be released. Figure 6 demonstrates how the CNN functions to extract functions as filters [10].

Caffe Model is a profound learning structure that takes into account expression, velocity and modularity. It is created by Berkeley AI Research (BAIR) and C++ community contributors and has bindings from Python and Matlab. This model is the pre-trained model used to recognize gender. The trained CNN models are used by the package of OpenCV. OpenCV provides Net class for the neural network to be populated in the package. The package can import structure for neural network models such as sex identification caffe model. The model of Caffe has two related documents, prototext file and model file of Caffe. In the prototext file, the CNN definition is entered here. Also defined here are the layers in the neural network, as well as the inputs, outputs and functionality of each layer, where the Caffe model file contains the trained model information [11].

CaffeNet uses the OUI-Adience Face collection to train the Caffe Model datasets. This dataset has a total of 26,580 gender and age label pictures. The complete amount



**Fig. 7** The cropped face images in OUI-Adience datasets

of topics is 2284. The data included were intended to be as close to the real environment where, without careful preparation, it attempts to capture the appearance where the images are taken. The information involves noise, pose, lighting and more information variants in addition to facial information sets. The source pictures in the dataset were from Flickr albums, compiled from iPhone 5 or later phones automatically uploaded and published to the general public by writers. Some of the cropped pictures used in this model's training are shown in Fig. 7. The prototext file demonstrates every layer, input and output features.

Haar Cascade is a machine learning object detection algorithm used to distinguish objects in an image or video where a lot of positive and negative image train the Cascade feature. Positive image imply the pictures are facial while adverse pictures are facial pictures. Haar Cascades is used in this system for face detection. In grayscale, this classifier processes pictures. This algorithm contains four phases [11].

**Stage 1: Haar Feature Selection.** To train the classifier and extract characteristics from it, positive images and negative images are used. Each characteristic is a single value acquired by subtracting the white rectangle pixel amount from the black rectangle pixel sum.

**Stage 2: Creating Integral Images.** Integral image is used to rapidly calculate the characteristics of the rectangle. Most of the characteristics calculated are meaningless. The chosen first edge characteristic appears to concentrate on the eye region. While the dark rectangle is on the side of the eyes and the white rectangle on the side of the cheek and nose, which is darker in the region of the eyes than in the region of the nose and cheek. The chosen second row characteristics are based on the fact that the eyes are darker than the nose bridge. But it is meaningless to apply the same windows to cheeks or other places.

**Stage 3: Adaboost Training.** This phase is used to pick the finest characteristics and to train the classifier. A set of weak classifiers were concatenated to produce a powerful classifier. Weak classification has restricted efficiency while powerful classification is useful for correct classification of the information. Adaboost builds a powerful classifier as a linear weak classifier mixture.

**Stage 4: Cascade Classifier** This phase comprises of stages compilation and each phase is a wear learner ensemble. To train each phase, the method of boosting is used. Boosting offers the capacity to train high-precision classifier by taking a weighted

average of weak learners' choices. If the picture goes through all the stages, the picture has a human face.

A facial recognition system that can classify gender can be created and implemented for safety reasons in government installations based on the features in the Convolutional Neural Network (CNN). The prototype was constructed and tested on the basis of these methods using a set of pictures representing Malaysian demographics.

## 4 Results and Discussion

### 4.1 Prototype Operation

The findings will be displayed in Figs. 8 and 9. Figures 8 and 9 displays the person's detection and gender data. The prototype will also display detection for all image frame faces as well as frame number per second (fps). If a man has been identified, he will beep the buzzer and send email.

While there is some delay in the frame per second, the process of gender recognition is running in real time. The customer will be able to see the produced output or outcome. The findings are the rectangle showing where the face is, the expected gender, the alert buzzer and the alert email notification if man is identified.

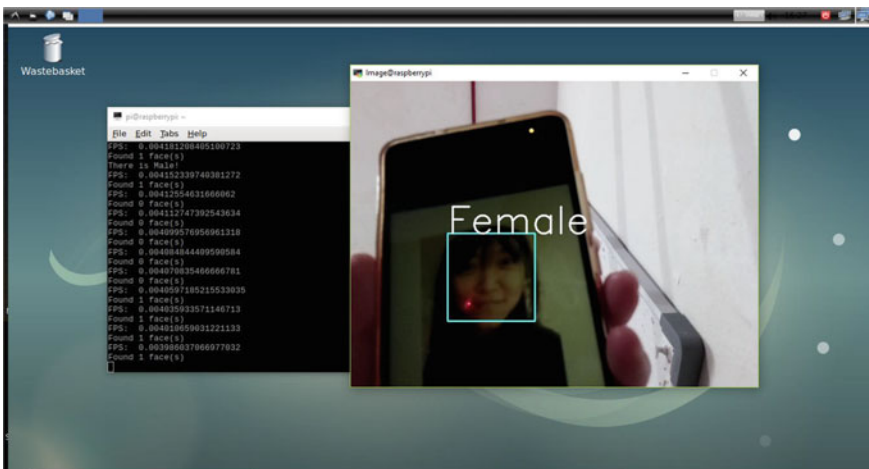


Fig. 8 Prototype detecting a woman photo

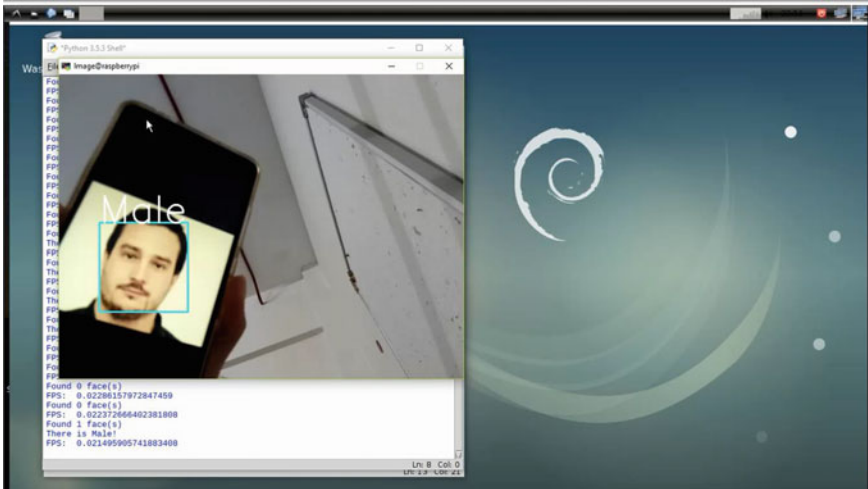


Fig. 9 Prototype detecting a man photo

### 4.2 Performance in Malaysian Demographic

Malaysian demographic consists of multiracial communities with different facial features and accessories applied. 50 selected images from Malaysian demographic based on different ethnic groups, gender and ages was selected to be tested on the system in real environment for verifying the accuracy of the system in predicting gender from images of persons in Malaysian demographic. The images used include 25 men with distinct races and 25 women. Figure 10 shows the image used to experiment. Each picture is screened 10 times to assess the system's precision that can predict the gender.

In the 1st image in Fig. 10, the test results showed 7 times woman and 3 times man detected. The probability that this picture will produce a man outcome is 0.3 and a woman outcome is 0.7, and the precision here is 70 percent. The test findings showed 8 times woman detected and 2 times man detected for the 2nd picture, and the outcome is in fact incorrect. We can conclude from here that the second picture probability is 0.2 for man and 0.8 for woman. So, the image's precision is just as small as 20%. The outcome overview using all the images in Fig. 10, is shown in Table 1.

Some limitations like the angle of the face captured in the image are important because it will impact the forecast of gender. It is also necessary to be concerned about the exposure of light because when the light exposure is low or very dark, the system could not detect the position of the faces as it could not acknowledge the position of the eyes, nose and mouth. If the light exposure is too large, the reverse will influence the precision of the gender forecast. Furthermore, camera pixel and resolution are as essential as images of low quality can impact the forecast of gender.

**Fig. 10** Images of individuals from Malaysian demographic



**Table 1** Result of detection from images of individuals from Malaysian demographic

Image	Actual	Man %	Woman %	Predicted	Accuracy
1st	Woman	30	70	Woman	Correct
2nd	Man	20	80	Woman	Wrong
3rd	Man	60	40	Man	Correct
4th	Woman	10	90	Woman	Correct
5th	Woman	40	60	Woman	Correct
6th	Man	100	0	Man	Correct
7th	Woman	80	20	Man	Wrong
8th	Man	60	40	Man	Correct
9th	Woman	10	90	Woman	Correct
10th	Woman	20	80	Woman	Correct
11th	Woman	10	90	Woman	Correct
12th	Woman	0	100	Woman	Correct
13th	Woman	30	70	Woman	Correct
14th	Woman	0	100	Woman	Correct
15th	Man	100	0	Man	Correct
16th	Man	100	0	Man	Correct
17th	Man	90	10	Man	Correct
18th	Man	100	0	Man	Correct
19th	Woman	30	70	Woman	Correct
20th	Woman	40	60	Woman	Correct
21st	Woman	80	20	Man	Wrong
22nd	Woman	0	100	Woman	Correct
23rd	Woman	60	40	Man	Wrong
24th	Man	100	0	Man	Correct
25th	Man	90	10	Man	Correct
26th	Man	100	0	Man	Correct
27th	Man	90	10	Man	Correct
28th	Man	100	0	Man	Correct
29th	Woman	0	100	Woman	Correct
30th	Woman	20	80	Woman	Correct
31st	Woman	0	100	Woman	Correct
32nd	Woman	0	100	Woman	Correct
33rd	Woman	100	0	Man	Wrong
34th	Woman	0	100	Woman	Correct
35th	Man	90	10	Man	Correct
26th	Man	80	20	Man	Correct
37th	Man	90	10	Man	Correct
38th	Man	100	0	Man	Correct

(continued)

**Table 1** (continued)

Image	Actual	Man %	Woman %	Predicted	Accuracy
39th	Man	100	0	Man	Correct
40th	Man	90	10	Man	Correct
41st	Woman	20	80	Woman	Correct
42nd	Woman	60	40	Man	Wrong
43rd	Woman	40	60	Woman	Correct
44th	Woman	30	70	Woman	Correct
45th	Man	100	0	Man	Correct
46th	Man	90	10	Man	Correct
47th	Man	20	80	Woman	Wrong
48th	Man	90	10	Man	Correct
49th	Man	90	10	Man	Correct
50th	Man	90	10	Man	Correct

Moreover, the system could not recognize the face place when the face is covered by mask. It is also hard to define the transgender problems because the characteristics are changing to the opposite gender where the system may be confused, and the gender detected may be incorrect as a consequence. Also essential is the model used for practice. The greater the number of qualified data sets, the greater the outcome precision. In this case, the pre-trained model is used because with big information, the training method takes time. If the trained datasets are not sufficient, the accuracy will be very low.

## 5 Conclusion

In this research, the artificial intelligence methods used to classify gender were recognized and a prototype of public bathroom gender recognition system was designed to enforce and check the efficacy of the defined technique. This project's case study focuses on gender recognition by using Artificial Intelligent in Malaysian demographics. This system was created by gender detection for safety reasons, preventing the opposite gender from entering another specified gender bathroom. Results show that 7 pictures are wrongly predicted out of the 50 pictures tested. Based on these 50 pictures, the general precision is properly estimated at 86%.

In the future, the present system characteristics will be improved to improve detection precision. Device or single board computer with greater processing power can enhance frame per second (fps) and decrease delay. Additionally, when the face is covered, motion detection can be introduced to the scheme to resolve the issue. Motion detection can also be used to begin the objective of classification, with the method



of gender forecast being taken when movements are detected. This decreases the system's workload and avoids overheating of the device.

The most significant aspect is the model that has been trained. We need to train our own datasets in the future by using Asian people's face pictures. Malaysia's four major races are Malay, Chinese, Indian and Indigenous. In order to increase prediction accuracy, we need to consider all the races in the face images in the datasets. In addition, the dataset should include more than 1000 faces of each race and gender to verify the learning process's efficiency through a convolutionary neural network.

**Acknowledgements** This research is supported by Universiti Malaysia Pahang internal grant RDU1803162.

## References

1. Bunyan J (2018) 50,000 sex crimes, domestic violence cases since 2013. malaymail, 23 July 2018
2. Juang LH, Lin SA, Wu MN (2017) Gender recognition based on computer vision system, 1
3. Turk M, Pentland A (1991) Eigenfaces for recognition. *J Cogn Neurosci* 3(1):71–86
4. Awang S, Yusof R (2011) Fusion of face and signature at the feature level by using correlation pattern recognition. *Eng Technol* 59:2291–2296 (World Academy of Science)
5. Jaiswal S (2011) Comparison between face recognition algorithm-eigenfaces, fisherfaces and elastic bunch graph matching. *J Global Res Comput Sci* 2(7):187–193
6. Osman MZ, Maarof MA, Rohani MF, Moorthy K, Awang S (2018) Multi-scale skin sample approach for dynamic skin color detection: an analysis. *Adv Sci Lett* 24(10):7662–7667
7. Levi G, Hassner T (2015) Age and gender classification using convolutional neural networks. In: *The IEEE conference on computer vision and pattern recognition (CVPR) workshops*, pp 34–42
8. Aytar OY, Ekenel HK (2016) How transferable are CNN-based features for age and gender classification? In: *2016 international conference of the biometrics special interest group (BIOSIG)*, Darmstadt, pp 1–6
9. Eidinge E, Enbar R, Hassner T (2014) Age and gender estimation of unfiltered faces. *IEEE Trans Inf Forensics Secur* 9(12):2170–2179
10. Raza M, Zonghai C, Rehman SU, Zhenhua G, Jikai W, Peng B (2017) Part-wise pedestrian gender recognition via deep convolutional neural networks. In: *2nd IET international conference on biomedical image and signal processing (ICBISP 2017)*
11. Singh V, Shokeen V, Singh B (2013) Face detection by Haar cascade classifier with simple and complex backgrounds images using OpenCV implementation 01(12):33–38

# A Novel Approach Towards Tamper Detection of Digital Holy Quran Generation



Md. Milon Islam, Muhammad Nomani Kabir, Muhammad Sheikh Sadi,  
Md. Istiak Morsalin, Ahsanul Haque and Jing Wang

**Abstract** Quran phrases are found in many Arabic websites. Lamentably, many mistakes and typos appear on most of the websites embedded with Quran texts. Therefore, it becomes very difficult to recognize the legal document of the religious book, whether the online document is tampered or not. Hence, verifying the Quran expression has become a crucial issue for most of the online users who read the digital copy. We propose a novel approach for the tamper detection of a digital document of the Holy Quran. We have implemented a desktop application, having modified UI that utilizes Jaro-Winkler distance and DiffliB function as String Edit distance algorithm to highlight the words in the Holy Quran for the verification purpose. A reliable and trustworthy Quran database was taken for testing. The results obtained from the application show higher performance. The system achieved the detection accuracy of 95.9% and 95% by Jaro-Winkler and DiffliB, respectively along with the precision of 93.29% and 96% in the case of diacritics. Additionally, F-score is 93.22% and 96.41% obtained by Jaro-Winkler and DiffliB, respectively in the case of no diacritics.

**Keywords** Quran expression · Quran verification · Quran words · String matching edit distance algorithm · Jaro-Winkler distance

## 1 Introduction

With the revolution of modern technology in very recent years, the number of internet users as well as the digital contents on the internet, has increased dramatically. This causes copyright violations which raise the problem of the genuineness of digital text, integrity and data vulnerability [1]. A very recent statistics from Pew Research Center [2], there are about 1.8 billion Muslims in the world which is approximately

---

Md. Milon Islam · M. S. Sadi · Md. I. Morsalin · A. Haque  
Department of Computer Science and Engineering, Khulna University of Engineering & Technology, Khulna 9203, Bangladesh

M. N. Kabir (✉) · J. Wang  
Faculty of Computing, Universiti Malaysia Pahang, Gambang, 26300 Kuantan, Pahang, Malaysia  
e-mail: [nomanikabir@ump.edu.my](mailto:nomanikabir@ump.edu.my)

© Springer Nature Singapore Pte Ltd. 2020

A. N. Kasruddin Nasir et al. (eds.), *InECCE2019*, Lecture Notes in Electrical Engineering 632, [https://doi.org/10.1007/978-981-15-2317-5\\_25](https://doi.org/10.1007/978-981-15-2317-5_25)

24% of the total population. The Holy Quran is a sacred book of Revelation for 1.8 billion Muslims in the world. Quran is the holy scripture of Islam which is the special book that constitutes the guidance for human life, suggestions for doing good deeds and refraining from evil deeds. According to Islamic history, it has been revealed to the Prophet Muhammad (peace be upon him) of Islam for a long time in the chunk of the twenty-three years. The Holy book was exposed about 1400 years ago and remains unchanged until now. This is the Holy Quran, the main source for Muslim Ummah to guide their life. Allah sent the Holy Quran, as the absolute revelation from Him to all human beings. More than a billion Muslims are bound to regard the Quran as the first criterion to guide and unite them in order to live in peace.

Nowadays the Quran is available in digital format on the internet. The overwhelming use of Internet everywhere has resulted in the fact that the traditional trend of learning from written books has diminished and a trend of using the internet for learning has become very prominent [3, 4]. The Holy Quran has no difference in this regard. The Quranic contents have many symbols and diacritics and the change of a single sign will change the meaning of the whole sentence which may mislead the many Muslims. The number of people trying to get access to the Holy Quran through the internet has grown tremendously over the years [5]. This includes Muslims and non-Muslims, and Arabic speaking and non-Arabic speakers. For the online-readers of the Quran, the authenticity of the Quranic text is thus very important.

There is a major problem in non-Muslim countries to find an authorized Quran teacher who can help to recite the Quran properly. To overcome the problem, the IT companies have developed some software, mobile application and web portal which can act as a Quran teacher for recitations, listening and memorization [6]. However, there are some web applications that check the authenticity of Quran verses and avoid any tampering and distortion [7]. Security is a main concern for the digital contents. But the present solutions to security issues for the digital Quran in desktop/mobile applications are ambiguous and of lack of strength.

Researches related to this field have become prominent due to the revolution of modern technology. Numerous works done in this area were reviewed in [8–10].

It is noteworthy that the original Quranic text did not include diacritics is used as the main principle. Obviously, deletion, alteration, and addition of fundamental Arabic characters are reported as errors, while deletion of a diacritic character at the correct location (for correct pronunciation) is not considered an error. In this research, we developed a novel approach for authentication and tamper detection of a digital document of Quran considering diacritics issues.

This following Section describes the related works that summarize the research in the field of digital Holy Quran. The research methodology of this research is explained in Sect. 3. Implementation phases including database are described in Sect. 4. Section 5 shows the exploratory results obtained from various approaches. The conclusion is drawn in Sect. 6.

## 2 Related Works

A lot of research has been done in the field of digital Holy Quran. As the online Quran is available in various formats like image, audio/video, and text format, etc., the researchers are working in different directions. They are also working on plain image, complex image, JPG image, PNG image and plain text, complex text, PDF file, word file, etc.

Kamsin et al. [11] developed a system that checks the authenticity of the digital Holy Quran. The goals of the system are to provide authentic and reliable Quran applications to the users as well as the authority of the various research center all over the world. But the system has not been fully implemented, and it was only an idea with a simple prototype. Adhoni et al. [12] developed an online cloud Quran portal in which all the authentic version of the Quran are available. The users can access the Quran through a personal computer, laptop, and mobile, etc. There is a user interface in a mobile application for quick access and translation option for the non-Arabic user. Sabbah and Selamat [13] proposed a system to identify Quranic verses which are available online. They worked only for diacritics text and calculate the diacritic ratio as well as the accuracy, precision, and recall which was 62%, 75%, and 78%, respectively. The system would not work for non-diacritical text and for more complex diacritical text the complexity became high which is the major drawback of the system. The researchers in [14] developed a software system which is worked in a web-browser tool to calculate the accuracy of digital Quran-verse. Digital certificates are used for verified Quranic-text. The system is user-friendly and provides higher authenticity for web-content.

An authentication system of Quranic verses is proposed by the authors of [15]. In this scenario, they used the two mostly wide methods named as digital signature and document control where the digital signature is used in terms of verification and document control is used to provide authorization before releasing the article online. They used different hashing techniques to check the integrity of the Arabic diacritics. The proposed method was appropriate only for single verse and collision can occur at any moment. A system for Quranic verse detection was introduced in [16]. The authors designed the system in such a way that the input of the system is Quranic verse and the output of the system is an authentic verse or not. Quranic quote filtering and verification are the principal components in this research where the quote filtering is used to eliminate the diacritics and special symbols and verification are used to verify the input verse comparing with the database. The accuracy of the system was 89%.

There are many digital Quran available in Portable Document Format (PDF). AlAhmad et al. [17] proposed a method for PDF format digital Quran. The watermark was completed by hashing the image features. The Discrete Cosine Transform (DCT) was used to extract the image features so less time was needed. The SLSB performed better than LSB in the case of color distortion. Tuncer et al. [18] introduced a technique for the color images which is the combination of LSB and XOR watermarking scheme because both LSB and XOR performed better in tamper detection.

It is almost impossible to extract the watermark with the absence of the original image while the XOR operation is performed. A digital watermarking technique for verifying the reliability of digital Quran which is available in PDF format is demonstrated in [19]. The authors used a Discrete Wavelet Transform (DWT) methods to gain the authenticity of the religious book. PSNR, MSE, and SSIM are used as evaluation criteria. The technique worked only for PDF format.

Khan et al. [20] described a reliable system for authentication and certification of digital Quran. The system worked only for the multimedia format. The system protects the digital Quran contents of all types of modification to get the customer's faith. Yassein et al. [21] proposed a technique in the view of network structure. An application layer protocol is introduced to provide the reliability of the holy book. The HQTP worked based on the Protocol Header and Protocol Payload. They compared two versions of the Quran. They only implemented HQTP but another protocol like RFC is not shown in the paper. The TF-IDF technique [22] is utilized in data retrieval and opinion mining. The developed system takes input from the multiple online and offline sources and provides the authentic verse of the religious book. The system shows higher performance both for the Quran and hadith and achieved 60% precision for Quran and 53% for hadith. The system worked only for the five authentic verse of the religious book.

According to a study conducted by Hamid et al. [23] for their project named Tanzil, a number of erroneous texts of Quran found on the internet was alarmingly high at the time of their study in 2007. In addition to this, the Quranic text is extremely malleable when it comes to tampering, meaning that a single addition, removal or alteration of a diacritic can have a devastating effect on the consequent meaning of the text. When reading the Quranic text online, the main concerns are the authenticity and the accuracy of the text [24, 25]. And on the web, to retain credibility the presented verses on any site must be accurately displayed from an authentic source. In addition to this, since a normal user cannot verify the Quranic text by them, a means to automatically authenticate the Quranic text by verifying against an existing authentic source is arduously important.

## 3 Methodology

### 3.1 System Design

We will build up a desktop application for verifying the Holy Quran whether it is tampered or not. The proposed framework has several fragments. The highlighted words of the Quran are found in the first stage. Then some preprocessing steps are applied to the highlighted words to crop the words, eliminate additional spaces and detect the existence of diacritical symbols. The diacritic search procedure has been utilized in the case of with diacritical symbols and the general search procedure has been utilized in the case of without diacritical symbols. The framework takes the input

and tries to find the exact match with the Quran database. At last, the output of both cases is defined in the prescribed language. When the diacritic search procedure is unable to find a similarity, the tokenization step which is the Arabic NLP procedure is carried out. In Natural Language Processing, tokenization of garbage words is done in the pre-processing stage.

The input text is accustomed by removing the latter word in the text when no similarity is found. In the case of no similarity, the latter word will be eliminated and the new text will be searched until finding a similarity. The flowchart of the proposed system is depicted in Fig. 1. As shown in the figure, the input data are retrieved from the Quran database and all the verses are found by parsing URL. The verses are split into words by invert index mapping. Then the similarity is measured. With no similarity, Jaro-Winkler distance method is applied, while normal string matching technique is used in case of similarity. Both of the results are combined and finally displayed.

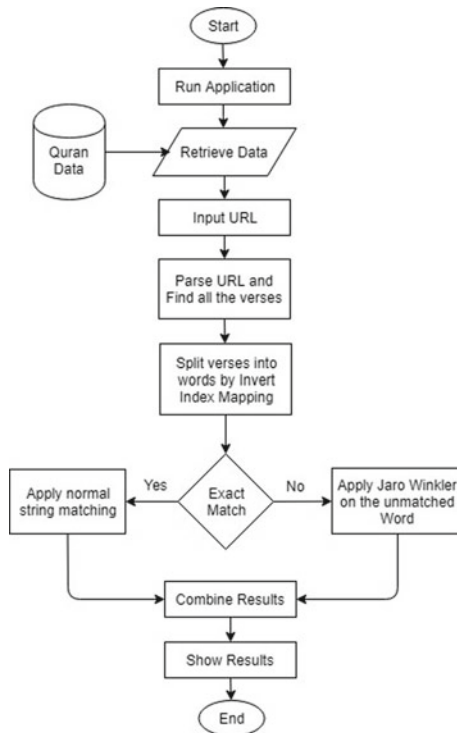


Fig. 1 Flowchart of the solution approach

### 3.2 Jaro-Winkler Similarity

The Jaro-Winkler distance is used to measure the similarity between two sequences. The higher value of Jaro-Winkler distance represents the more similarity between the sequences. The Jaro measure [26]  $d_j$  considers the quantity of character matches  $m$ , the length of first and second sequence  $s_1, s_2$  and the proportion of their transpositions  $t$ :

$$d_j = \begin{cases} 0 & \text{if } m = 0 \\ \frac{1}{3} \left( \frac{m}{|s_1|} + \frac{m}{|s_2|} + \frac{m-t}{m} \right) & \text{otherwise} \end{cases} \quad (1)$$

The equation returns a value from 0 to 1, where 0 represents no similarity and 1 represents exact similarity.

The Jaro distance is improved through the Jaro-Winkler measure [27]. This improvement was achieved through the observation of Winkler. The observation was that typing errors generally arise in the mid or at the end of a word, but very few errors occur in the beginning. Therefore, a boost threshold  $b_t$  is set as 0.7 to highlight on matching prefixes. The Jaro-Winkler distance  $d_w$  is defined as

$$d_w = \begin{cases} d_j & \text{if } d_j < b_t \\ d_j + (lp(1 - d_j)) & \text{otherwise} \end{cases} \quad (2)$$

where  $l$  means the length of the normal prefix,  $p$  is a weighting factor and  $d_j$  represents the Jaro distance. Winkler uses  $p = 0.1$  and  $l \leq 4$ . Note that  $lp$  must not be greater than 1.

### 3.3 Performance Measure Parameters

The performance of the proposed system is measured in terms of some performance parameters. A confusion matrix consisting of TP, TN, FP, and FN is formed to investigate the performance parameters. The significance of the terms is as follows.

*TP = True Positive (Correctly Identified)*

*TN = True Negative (Incorrectly Identified)*

*FP = False Positive (Correctly Rejected)*

*FN = False Negative (Incorrectly Rejected)*

There are a lot of parameters which describe some relation among the parameters of the confusion matrix that can help to measure the performance of a system. The performance of the proposed system is measured by the following formulas:

$$\text{Precision(Prec)} = |TP| / (|TP| + |FP|) \quad (3)$$

$$\text{Recall(Rec)} = (|TP|)/(|FN| + |TP|) \quad (4)$$

$$\text{Accuracy(Acc)} = (|TP| + |TN|)/(|TP| + |TN| + |FP| + |FN|) \quad (5)$$

$$\text{Specificity(Spec)} = (|TN|)/(|FP| + |TN|) \quad (6)$$

$$\text{Fscore} = (2 * |TP|)/((2 * |TP| + |FP| + |FN|)) \quad (7)$$

$$\text{Number of Letters} = \text{DR}/(\text{Number of Diacritics}) \quad (8)$$

The Diacritical Ratio (DR) of each word in the document will be calculated through the following equation. DR is characterized as the quantity of diacritics to the quantity of letters in the word.

## 4 Implementation Details

The digital documents of Quran are available in King Fahd Complex, Tanzil, Quran Database, and etc. But it is very difficult to find the authenticated version. The word documents are downloaded from the King Fahd Complex which has the font Hafs version 9. Then, some preprocessing steps are carried out to extract the suitable knowledge; and database is formed with the knowledge. A Not only SQL database is used to store the data and it has an ability to retrieve. The database is very simple and having control over availability.

We have used the pickle module for object serialization. The data format used in pickling a printable ASCII representation is very helpful for debugging purpose. PyQt API is used to develop the application which has a huge number of functions and classes. We have implemented the proposed scheme using PyQt which can easily verify the online texts in the Quran. We have used Quran phrases as an input in URL and compared them with our database. A case study is illustrated in Fig. 2 having a user interface with Sura, Ayat, and Match. Our scheme tries to get the exact match with the related verses by implementing its algorithm.

## 5 Experimental Results and Analysis

A subjective comparison with the existing methods reveals that the proposed approach can detect almost any kind of tampering, given the reference text being completely diacritical throughout, while many of the existing approaches fail to detect every tampering. The following outcomes were obtained from the proposed approach:



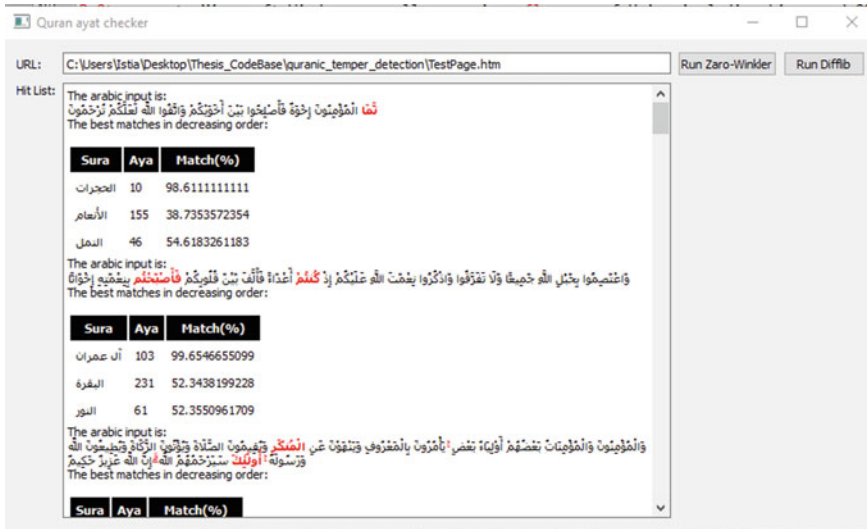


Fig. 2 Tamper detection of The Holy Quran

We have considered the first 293 ayat of Quran (Fatiha + Baqara) as a test case.

In Jaro-Winkler method, we have calculated the following parameter:

$$278 \text{ True Positive} = (278/293) * 100 = 94.88\%$$

$$20 \text{ False Positive} = (20/293) * 100 = 6.82\%$$

$$238 \text{ True Negative} = (238/293) * 100 = 81.23\%$$

$$2 \text{ False Negative} = (2/293) * 100 = 0.68\%$$

$$\text{Precision} = (278/(270 + 20)) * 100 = 93.29\%$$

$$\text{Recall} = (278/(2 + 278)) * 100 = 99.2\%$$

$$\text{Accuracy} = ((278 + 238)/(278 + 238 + 20 + 2)) * 100 = 95.9\%$$

$$\text{Specificity} = (238/(20 + 238)) * 100 = 92.25\%$$

$$\text{Fscore} = (2 * 278)/(2 * 278 + 20 + 2) * 100 = 96.19\%$$

In the similar way, we have calculated the value of TP, TN, FP, FN, Precision, Recall, Accuracy, Specificity and Fscore for DiffLib and Sabbah-Salamat [13] method as shown in Table 1.

From Python’s DiffLib module we used two classes extensively in our work, namely Sequence Matcher and Differ. The Differ class (its compare() method to be exact) is used to produce the deltas for the two sets of strings, the first set being the authentic verses read from the database, and the second set being those either directly input by the user, or scraped from the URL entered by the user. The graphical representation of Precision, Recall, Accuracy, Specificity, and F-score is depicted in Fig. 3. Figure 3 shows that Jaro-Winkler method works better than the other methods.

The Recall, Accuracy, and F-score for Jaro-Winkler method are comparatively high. The specificity for the Sabbah-Salamat [13] method is relatively low because of the highest value of FP (Correctly Rejected). Next, we have compared the Status

**Table 1** Status of identification/rejection with diacritics

Parameters	Methods		
	Jaro-Winkler (%)	Difflib (%)	Sabbah-Selamat [13] (%)
True positive	94.88	90.10	98.63
False positive	6.82	3.75	19.80
True negative	81.23	76.45	61.09
False negative	0.68	5.11	1.36
Precision	93.29	96	83
Recall	99.2	93.7	97.8
Accuracy	95.9	95	88.3
Specificity	92.25	95.32	75.52
Fscore	96.19	95.31	90.31

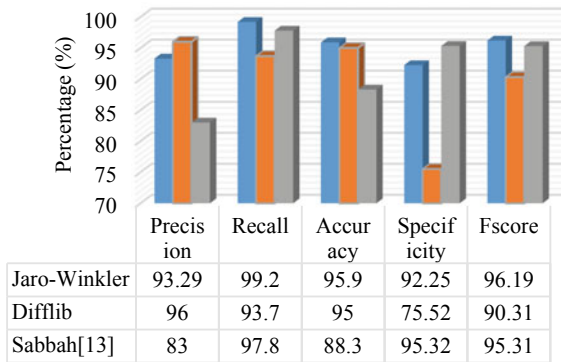


**Fig. 3** Performance measure parameters for Quranic tamper detection with diacritics

of Identification/Rejection without diacritics. In this case, we have got the following results shown in Table 2.

The graphical representation of Precision, Recall, Accuracy, Specificity, and F-score is illustrated in Fig. 4 for the case of without Diacritics. The figure shows the comparison of Jaro-Winkler and Difflib method performance. The figure illustrates that Difflib method works better because of the lowest value of FP (Correctly Rejected) and FN (Incorrectly Rejected).

Using Eq. (8) we have drawn the error rate graph which implies the error rate for different approaches in Fig. 5. The figure depicts that the Jaro-Winkler method has comparatively low error rate than the others. The Sabbah-Selamat [13] method has a high error rate. Hence, we can conclude that the Jaro-Winkler method performs better than other methods. The error rate increases with the large size of the data.

**Table 2** Status of identification/rejection without diacritics

Parameters	Methods	
	Jaro-Winkler (%)	Difflib (%)
True positive	91.79	92.02
False positive	7.13	5.67
True negative	71.36	70.21
False negative	6.23	1.19
Precision	92.79	94.16
Recall	93.64	98.72
Accuracy	92.43	95.94
Specificity	90.92	92.53
Fscore	93.22	96.41

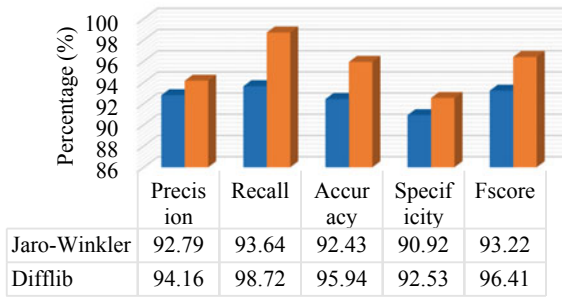


**Fig. 4** Performance measure parameters for Quranic tamper detection without diacritics

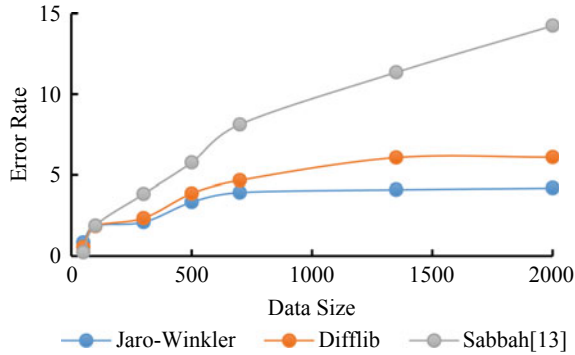


**Fig. 5** Error rates of different approaches in Quranic tamper detection

## 6 Conclusion

The novel approach towards tamper detection of digital Holy Quran is a web program service (e.g. Mozilla Firefox Internet Explorer and Google Chrome) that verifies the contents of Quran of online and offline versions. The scheme provides a verification of the highlighted texts for the cases of with and without diacritics by utilizing the search algorithms. It will be very helpful for protecting the religious book from any kind of tampering or distortion. The Jaro-Winkler method performs better than the other two methods. The detection accuracy obtained by the Jaro-Winkler is 95.9% and 92.43% for the case of with and without diacritics, respectively. The error rate for the Jaro-Winkler method is comparatively low although it is increased with the data size. Future work can be conducted on accelerating the search process in authentication [28, 29] by incorporating efficient search techniques.

**Acknowledgements** This work was supported by Universiti Malaysia Pahang (UMP) through University Research Grant (RDU170397).

## References

1. Internet World Stats, Usage and Population Statistics. <http://www.internetworldstats.com/emarketing.htm>. Last accessed 2019/3/20
2. Muslims and Islam: key findings in the U.S. and around the world. <http://www.pewresearch.org/fact-tank/2017/08/09/muslims-and-islam-key-findings-in-the-u-s-and-around-the-world>. Last accessed 2019/4/15
3. Kovacevic P, Spoljaric M, Vuk D (2014) The impact of internet use on education process. In: 56th international symposium ELMAR. IEEE, Zadar, Croatia, pp 1–4
4. Loan FA (2012) Impact of the internet surfing on reading practices and choices. *Webology* 9(1):1–10
5. Wan-Chik RZ (2014) A user study on the experience of information seeking for Islamic and Quranic information on the web. In: 5th international conference on information and communication technology for the Muslim world (ICT4M). IEEE, Kuching, Malaysia, pp 1–6
6. Adhoni ZA, Al Hamad H, Siddiqi AA, Parvez M, Adhoni ZA (2013) Cloud-based online portal and mobile friendly application for the Holy Quran. *Life Sci J* 10(12):524–538
7. Alginahi YM, Tayan O, Kabir MN (2013) A zero-watermarking verification approach for Quranic verses in online text documents. In: 2013 Taibah University international conference on advances in information technology for the Holy Quran and its sciences. IEEE, Madinah, Saudi Arabia, pp 42–46
8. Hakak S, Kamsin A, Tayan O, Idris MYI, Gani A, Zerdoumi S (2017) Preserving content integrity of digital Holy Quran: survey and open challenges. *IEEE Access* 5:7305–7325
9. Zakariah M, Khan MK, Tayan O, Salah K (2017) Digital Quran computing: review, classification, and trend analysis. *Arab J Sci Eng* 42(8):3077–3102
10. Hakak S, Kamsin A, Tayan O, Idris MYI, Gilkar GA (2019) Approaches for preserving content integrity of sensitive online Arabic content: a survey and research challenges. *InfProcess Manag* 56(2):367–380
11. Kamsin A, Gani A, Suliaman I, Jaafar S, Mahmud R, Sabri AQM, Razak Z, Idris MYI, Ismail MA, Noor NM, Ab Hamid SH (2014) Developing the novel Quran and Hadith authentication system. In: 5th international conference on information and communication technology for the Muslim world (ICT4M). IEEE, Kuching, Malaysia, pp 1–5

12. Adhoni ZA, Al Hamad H, Siddiqi AA, El Mortaji L (2013) Towards a comprehensive online portal and mobile friendly qur'an application. In: 2013 Taibah University international conference on advances in information technology for the Holy Quran and its sciences. IEEE, Madinah, Saudi Arabia, pp 138–143
13. Sabbah T, Selamat A (2013) A framework for Quranic verses authenticity detection in online forum. In: 2013 Taibah University international conference on advances in information technology for the Holy Quran and its sciences. IEEE, Madinah, Saudi Arabia, pp 6–11
14. Tayan O, Kabir MN, Alginahi YM (2014) Framework and process for digital-Quran integrity-verification using a browser plug-in. In: 2014 world symposium on computer applications and research (WSCAR). IEEE, Sousse, Tunisia, pp 1–2
15. Alsmadi I, Zarour M (2017) Online integrity and authentication checking for Quran electronic versions. *Appl Comput Inf* 13(1):38–46
16. Alshareef A, El Saddik A (2012) A Quranic quote verification algorithm for verses authentication. In: 2012 international conference on innovations in information technology (IIT). IEEE, Abu Dhabi, UAE, pp 339–343
17. AlAhmad MA, Alshaikhli I, Alduwaikh AE (2013) A new fragile digital watermarking technique for a PDF digital Holy Quran. In: 2013 international conference on advanced computer science applications and technologies. IEEE, Kuching, Malaysia, pp 250–253
18. Tuncer T, Ertam F, Avci E (2013) A watermarking application for authentication of Holy Quran. In: 2013 Taibah University international conference on advances in information technology for the Holy Quran and its sciences. IEEE, Madinah, Saudi Arabia, pp 37–41
19. Olanrewaju RF, Fajingbesi FE, Ishak NAB (2016) Watermarking in protecting and validating the integrity of digital information: a case study of the holy scripture. In: 6th international conference on information and communication technology for the Muslim World (ICT4M). IEEE, Jakarta, Indonesia, pp 222–227
20. Khan MK, Siddiqui Z, Tayan O (2017) A secure framework for digital Quran certification. In: International conference on consumer electronics (ICCE). IEEE, Las Vegas, USA, pp 59–60
21. Yassein MB, Wahsheh YA (2016) HQTP v. 2: Holy Quran transfer protocol version 2. In: 7th international conference on computer science and information technology (CSIT). IEEE, Amman, Jordan, pp 1–5
22. Darwiyanto E, Pratama GA, Widowati S (2016) Multi words quran and hadith searching based on news using TF-IDF. In: 2016 4th international conference on information and communication technology (ICoICT). IEEE, Bandung, Indonesia, pp 1–6
23. Tanzil Project. [http://tanzil.net/docs/Tanzil\\_Project](http://tanzil.net/docs/Tanzil_Project). Last accessed 2019/4/15
24. Azami MM (2003) The history of the Quranic text from revelation to compilation: a comparative study with the old and new testaments. UK Islamic Academy, UK, Leicester
25. Tayan O, Kabir MN, Alginahi YM (2014) A hybrid digital-signature and zero-watermarking approach for authentication and protection of sensitive electronic documents. *Sc World J Art ID* 514652:1–18
26. Dreßler K, Ngonga Ngomo AC (2017) On the efficient execution of bounded Jaro-Winkler distances. *Semant Web* 8(2):185–196
27. Winkler WE (1990) String comparator metrics and enhanced decision rules in the Fellegi-Sunter model of record linkage. Technical report, US Bureau of Census Statistics Research Division
28. Kabir MN, Hasan MM, Rahman MA, Tao H (2018) Development of a web-extension for authentication of online Hadith texts. *Int J Eng Technol* 7(2.5):19–22
29. Kabir MN, Tayan O, Alginahi Y, Hasan MM, Rahman MA (2019) On the development of a web extension for text authentication on Google Chrome. In: 2019 international conference on electrical, computer and communication engineering (ECCE). IEEE, Cox'sBazar, Bangladesh, pp 1–5

# A Comparative Study of AFM-Assisted Direct and Least-Square Attitude Determination Algorithm



Suqing Yan, Yue Wu, Yuanfa Ji, Kamarul Hawari Ghazali and Xiyan Sun

**Abstract** Based on GNSS (Global Navigation Satellite System) technology, the importance of vehicle attitude calculation has become more and more prominent in military and civilian fields. In this paper, an attitude determination algorithm assisted by ambiguity function method (AFM) is proposed. Due to the characteristics of the AFM algorithm is insensitive to cycle slip and independent of initial ambiguity, and considering the large amount of computation and the long computation time, it is used as an auxiliary means for initial attitude search and error correction in the search process, and C-LAMBDA algorithm is used to complete the ambiguity resolution. The attitude angle is calculated by direct and least square method, and the accuracy of the attitude angle based on the AFM-assisted method is compared. Through the static experiment of dual antenna direction finding and three antenna attitudes finding, the accuracy of direction and attitude angle is analyzed. It is concluded that the attitude calculation accuracy based on AFM-assisted least square method is usually higher.

**Keywords** AFM · The direct method · Least square method

---

S. Yan · Y. Wu · Y. Ji (✉) · X. Sun

Guangxi Key Laboratory of Precision Navigation Technology and Application,  
Guilin University of Electronic Technology, Guilin 541004, China  
e-mail: [jiyuanfa@163.com](mailto:jiyuanfa@163.com)

National & Local Joint Engineering Research Center of Satellite Navigation and Location Service, Guilin 541004, China

K. H. Ghazali  
University Malaysia Pahang, Pahang, Malaysia

© Springer Nature Singapore Pte Ltd. 2020

A. N. Kasruddin Nasir et al. (eds.), *InECCE2019*, Lecture Notes in Electrical Engineering 632, [https://doi.org/10.1007/978-981-15-2317-5\\_26](https://doi.org/10.1007/978-981-15-2317-5_26)

## 1 Introduction

Vehicle attitude information has become increasingly important in military and civil fields, and has become an important navigation information for aerospace, ground carrier operation, ocean navigation and other applications [1–3]. With the innovation and development of technology, the requirement for resolution accuracy of attitude angle is getting higher and higher. Successful integer ambiguity resolution has become an important factor in the success of attitude determination algorithm [4, 5]. Although the traditional LAMBDA (Least-Square Ambiguity Decorrelation Adjustment) [6, 7] algorithm improves the calculation accuracy of ambiguity and innovates the search method, due to the existence of nonlinear mapping from the real field to the integer domain, its computational complexity increases with the number of observations and the dimension of the double-difference ambiguity. For this, Teunissen proposed a new method called C-LAMBDA based on baseline constraints [8, 9], which further reduced the search range by using known baseline constraints to improve the accuracy of ambiguity resolution. In addition, since the ambiguity function method (AFM) is not susceptible to cycle slip and is independent of the initial ambiguity [10, 11], the attitude angle can be searched by combining the baseline length constraint, and finally the optimal initial solution of the attitude angle and the corresponding initial ambiguity solution can be obtained.

In this paper, a method of attitude calculation based on AFM is proposed [12]. The baseline vector is solved by C-LAMBDA algorithm based on baseline length constraint, and the attitude angle is calculated by direct and least square method [13–15]. If the solution is correct, the result is output directly. If the attitude angle deviation occurs, the optimal attitude angle and its corresponding integer ambiguity can be obtained by using the AFM algorithm to correct it (The correct attitude angle has been obtained from other platforms). Through the attitude measurement experiments of two antennas and three antennas, the error correction is completed and the accuracy of attitude angle calculation is improved [16]. The experiment proves that the least square algorithm assisted by AFM has the least error.

## 2 Ambiguity Resolution

### 2.1 Ambiguity Function Method (AFM)

For a short baseline with antennas 1, 2 as endpoints, the double-difference carrier phase equation is

$$\lambda(\varphi_{12}^{ik} + N_{12}^{ik}) = (I_1^i - I_1^k)^T \cdot b + v_{12}^{ik} \quad (1)$$

where  $\lambda$  is the carrier wavelength,  $\varphi_{12}^{ik}$  is the fractional part of the double-difference carrier phase observation of the satellite  $i$  to the reference satellite  $k$ , which  $I_1^i, I_1^k$  is the unit vector of the receiver to the satellite  $i, k$ , respectively, which  $b$  is the baseline vector to be sought, which  $N_{12}^{ik}$  is the double difference integer ambiguity to be estimated.  $v_{12}^{ik}$  is the observed noise. For the two-dimensional attitude angle, The NED (North-East-Down) three components in the local geographic coordinate system of  $(I_1^i - I_1^k)$ ,  $b$  can use heading angle and the pitch angle expressed as [10]

$$I_1^{ik} = I_1^i - I_1^k = \begin{bmatrix} I_N^{ik} \\ I_E^{ik} \\ I_D^{ik} \end{bmatrix} = |I_1^{ik}| \cdot \begin{bmatrix} c_{\beta^{ik}} c_{\alpha^{ik}} \\ c_{\beta^{ik}} s_{\alpha^{ik}} \\ s_{\beta^{ik}} \end{bmatrix} \tag{2}$$

$$b = \begin{bmatrix} b_N \\ b_E \\ b_D \end{bmatrix} = |b| \cdot \begin{bmatrix} c_p c_h \\ c_p s_h \\ s_p \end{bmatrix} \tag{3}$$

where  $\alpha^{ik}, \beta^{ik}$  are the heading angle and pitch angle of  $I_1^{ik}$ ,  $h, p$  are the heading angle and pitch angle of  $b$ , respectively, operators  $c$  and  $s$  represent  $\cos(\cdot)$  and  $\sin(\cdot)$ , and  $N, E, U$  are north, east, and down directions. By introducing formula 2 and formula 3 into formula 1, the following results can be obtained

$$\tilde{N}_{12}^{ik} = \lambda^{-1} \cdot (|b| \cdot |I_1^{ik}| \cdot \langle e_{ik}, e_b \rangle - \varphi_{12}^{ik}) \tag{4}$$

where  $\langle e_{ik}, e_b \rangle$  is the inner product of the unit vector.

$$\langle e_{ik}, e_b \rangle = \sin p \sin \beta^{ik} + \cos p \cos \beta^{ik} \cos(\alpha^{ik} - h) \tag{5}$$

For the correct value  $p$  and  $h$ ,  $\tilde{N}_{12}^{ik}$  should be an integer in theory, but due to the influence of the observation error, it can only be infinitely close to the integer. For the wrong, the deviation of  $\tilde{N}_{12}^{ik}$  is large far from the integer value, and for double difference ambiguity, the adapted function is defined as

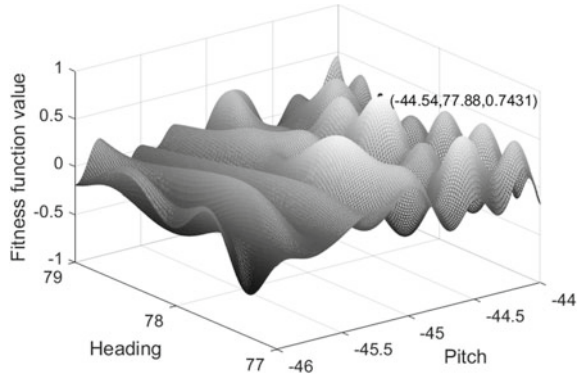
$$F(p, h) = \frac{1}{N} \sum_{i=1}^N \cos(2\pi N_{12}^{ik}) \tag{6}$$

According to the angular range of the angle  $p$  and  $h$ , and the selected step size, fitness function is calculated, and the maximum value corresponds to the coordinate  $(p, h)$  are the two-dimensional solution.

As shown in Fig. 1, the known baseline length is 0.575 m. The correct values of the pitch and heading angles obtained in advance are  $-45.013^\circ, 77.257^\circ$ , and the search step is set to  $0.01^\circ$ . The maximum fitness function is 0.67797. The calculated attitude angle coordinates are  $(-45.11^\circ, 77.52^\circ)$ . However, the smaller the step size, the higher the accuracy of the resulting attitude angle and the calculation amount is



**Fig. 1** AFM fitness function for single frequency single epoch



larger. Even if the step size is selected to be  $1^\circ$ , the search range for the pitch angle of  $180^\circ$  and the heading angle of  $360^\circ$  is very large. So, the AFM only can be an auxiliary algorithm.

### 2.2 New Method Based on AFM

It can be seen from Eq. (1) that the float solution of the ambiguity is

$$N_{12}^{ik} = \frac{1}{\lambda} (I_1^i - I_1^k)^T \cdot b - \varphi_{12}^{ik} \tag{7}$$

In the search process, the searched attitude angle is substituted into the Eq. (7) in order to improve the attitude angle resolution accuracy when using the AFM algorithm alone, after obtaining the ambiguity float solution, rounding off it to get the integer ambiguity. After knowing the integer ambiguity of all satellites, substituting it into the double-difference observation Eq. (1), using the least square method to calculate the high-precision baseline vector, and then high-precision attitude angle can be obtained. The linear form of Eq. (1) the design is

$$y = Bb + \varepsilon \tag{8}$$

where  $y = \lambda(\varphi_{12}^{ik} + N_{12}^{ik})$ ,  $b$  is baseline vector, the baseline vector and least square residual obtained by least square are

$$b_{LS} = (B^T C B)^{-1} B^T C y \tag{9}$$

$$R_y = \|y - B b_{LS}\|_{Q_y}^2 \tag{10}$$

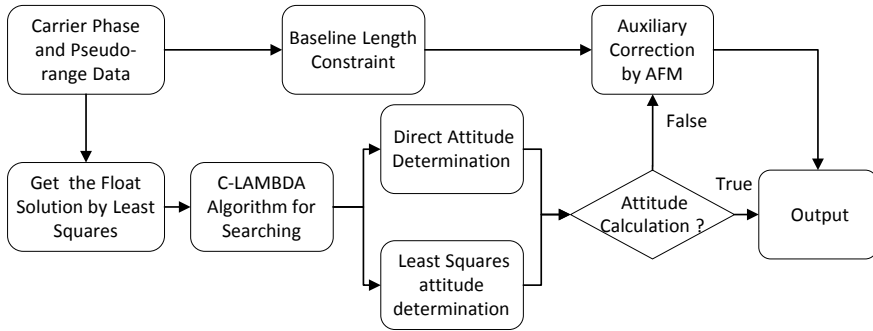


Fig. 2 A block diagram of a new algorithm based on AFM algorithm

The weighted residual obtained by the least square method can be used as a constraint. Thus, for the correct solution, the baseline vector based on residual should satisfy the following constraints:

- (1) The error between the baseline length and the true value is as small as possible;
- (2) The least square weighted residual is the smallest or nearly the smallest.

Therefore, the ambiguity candidate solutions can be filtered according to the constraint conditions, and the number of candidate solutions is gradually reduced. In this way, the C-LAMBDA algorithm is first used to solve the carrier attitude angle, and C-LAMBDA selects the correct integer ambiguity according to its fitness function and baseline length constraints.

When the accuracy of the floating solution is high, since the fixed solution is searched by C-LAMBDA, the time to find the correct solution will be short and efficient. Therefore, when the attitude solution is wrong, this paper uses AFM to improve the accuracy of floating solution, shortens the search time of C-LAMBDA and reduces the number of candidate solutions for C-LAMBDA termination condition, so that the float solution with poor quality is directly eliminated. One of the main problems with the original AFM algorithm is the large amount of computation and low search efficiency. Therefore, when the initial baseline and attitude angle conditions are utilized to narrow the AFM search range, the search efficiency is improved. The real-time performance of the entire algorithm can be guaranteed. The block diagram of the overall design is shown in Fig. 2.

### 3 Attitude Determination

#### 3.1 DAD Method (Direct Attitude Determination)

Definition of Different Coordinate Frames

**Fig. 3** Coordinate frame conversion

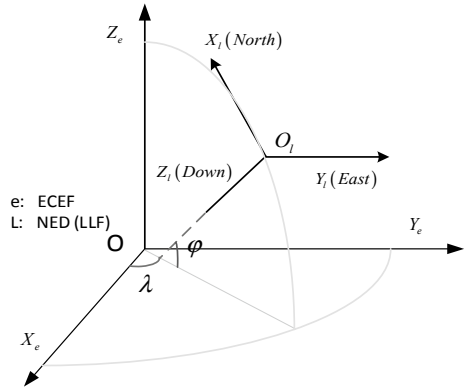
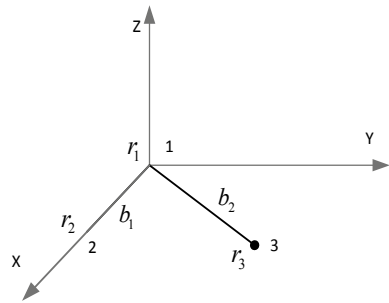


**Fig. 4** Antenna position in body frame (Reference antenna is 1, 2 and 3 are slave antenna) model of attitude determination



Two coordinate frames need to be first introduced: the local level coordinate frame (LLF) and the antenna body frame (ABF). The NED (North-East-Down) coordinate frame is used in this paper (one of LLF). The former one can be obtained by converting the coordinates of slave antennas given in the Earth Centered Earth Fixed (ECEF) coordinate frame with respect to the coordinate of the master antenna. The latter one is formed by the GPS antennas (Figs. 3 and 4).

Attitude can be determined using GNSS observation from more than two antennas. The measuring antenna is fixed on the rigid body, that is, the coordinates of the antenna are unchanged in the body frame, and the double baseline vector is formed in the geocentric coordinate frame

$$r_n - r_1 = R^T(h, p, r)b_n \tag{11}$$

where  $R^T(h, p, r)$  is rotation matrix from body frame to geocentric coordinate frame,  $n$  is the number of antennas,  $b_n$  is  $n$ -th baseline, based on the transformation relation of coordinate system, the baseline vector in body frame is expressed by attitude matrix.

$$\varphi_{1n}^{ik} = -\lambda^{-1}(I_1^i - I_1^k)^T \cdot R^T(h, p, r)b_n + N_{1n}^{ik} + \varepsilon_{\varphi,1n}^{ik} \tag{12}$$

where  $R$  is attitude matrix for geocentric coordinate frame to body frame. When the ambiguity of double difference is determined, there are only three unknown attitude angles. The baseline vector  $b_l$ , is obtained in the LLF (converting the geocentric coordinate), and the baseline vector,  $b_n$  denotes the positions of in the ABF, the baseline vectors in the two coordinate systems are related as follows:

$$b_n = R_r R_p R_h \cdot b_l$$

$$= \begin{bmatrix} c_r c_h - s_r s_p s_h & c_r s_h - s_r s_p c_h & -s_r c_p \\ -c_p s_h & c_p s_h & s_h \\ s_r c_h + s_r s_p s_h & s_r s_h - c_r s_p c_h & c_p c_h \end{bmatrix} \cdot b_l \tag{13}$$

where  $r, p, y$  represent the rotation matrix of roll, heading and pitch, respectively. Operators  $c$  and  $s$  represent  $\cos(\cdot)$  and  $\sin(\cdot)$ .  $R = R_r R_p R_h$  is a  $3 \times 3$  matrix containing the nine direction cosine element and three Euler angles (roll, heading and pitch).

Based on the definition of ABF, the coordinates of the antenna 2 in the ABF can be expressed as  $b_2 = [0 \ b_{12} \ 0]^T$ , respectively, where  $b_{12}$  is the baseline vector of antenna 1 and antenna 2. Substituting the ABF coordinate of antenna 2 into Eq. (13), and applying the orthogonality of the rotation matrix yield the LLF coordinate of antenna 2, the relation can be determined using

$$\begin{bmatrix} x_{2l} \\ y_{2l} \\ z_{2l} \end{bmatrix} = b_{12} \cdot \begin{bmatrix} -c_p s_h \\ c_p c_h \\ s_p \end{bmatrix} \tag{14}$$

Pitch and heading angle are acquirable only using the LLF coordinate of antenna 2 instead of using baseline length  $b_{12}$ , so  $b_{12}$  does not need to be measured in advance. Then the heading and pitch angle can be directly obtained using

$$h = -\arctan\left(\frac{x_{2l}}{y_{2l}}\right) \tag{15}$$

$$p = \arctan\left(\frac{z_{2l}}{\sqrt{x_{2l}^2 + y_{2l}^2}}\right) \tag{16}$$

If there are more than two antennas, then the coordinates of the antenna 3 in the LLF can be expressed as  $b_3 = [x_{3l} \ y_{3l} \ z_{3l}]^T$ , Applying the LLF coordinate of antenna 3, the roll value will be determined using

$$r = -\arctan\left(\frac{z'_{3l}}{x'_{3l}}\right) \tag{17}$$

where the  $z'_{3l}$  and  $x'_{3l}$  is determined by Rotating the LLF coordinate of antenna 3 by heading and pitch resulted from Eqs. (4) and (5) yields. The specific expression is as follows:

$$\begin{bmatrix} x'_{3l} \\ y'_{3l} \\ z'_{3l} \end{bmatrix} = \begin{bmatrix} 1 & 0 & 0 \\ 0 & c_p & s_p \\ 0 & -s_p & c_p \end{bmatrix} \begin{bmatrix} c_h & s_h & 0 \\ -s_h & c_h & 0 \\ 0 & 0 & 1 \end{bmatrix} \begin{bmatrix} x_{3l} \\ y_{3l} \\ z_{3l} \end{bmatrix} \tag{18}$$

### 3.2 LSAD Method (Least Square Attitude Determination)

From Eq. (13), three attitude angles  $r$ ,  $p$  and  $h$ , are included in the attitude matrix

$$R = R_r R_p R_h \tag{19}$$

The non-linear least square method is used to estimate the attitude angle, the three attitude angles are as follows

$$x = (r \ p \ h)^T \tag{20}$$

Linearization of non-linear equations, that is, the first order Taylor expansion of the equation in the matrix. Ignoring the higher order terms, then the nonlinear equation according to formula (12) can be approximated into the following linear equations expressed in matrix form

$$G \cdot \Delta x = \Delta y \tag{21}$$

The observation matrix can be expressed as [3]

$$G = \begin{bmatrix} \dots & \dots & \dots \\ \dots & -(I_1^s - I_1^k)^T \cdot \left( \frac{\partial R^T}{\partial x_l} \right) b_n & \dots \\ \dots & \dots & \dots \end{bmatrix} \tag{22}$$

where  $x_l (l = 1, 2, 3)$  are attitude angles,  $\partial R^T / \partial x_l$  is the partial derivative of attitude matrix for each attitude angle, its expression is as follow

$$\frac{\partial R^T}{\partial r} = \begin{pmatrix} -c_h s_r & 0 & c_h c_r - s_h s_p s_r \\ -s_h s_r + c_h s_p s_r & 0 & s_h c_r + c_h s_p s_r \\ -c_p c_r & 0 & -c_p s_r \end{pmatrix} \tag{23}$$

$$\frac{\partial R^T}{\partial p} = \begin{pmatrix} -s_h c_p s_r & s_h s_p & s_h c_p c_r \\ c_h c_p s_r & -c_h s_p & -c_h c_p c_r \\ s_p s_r & c_p & -s_p c_r \end{pmatrix} \quad (24)$$

$$\frac{\partial R^T}{\partial h} = \begin{pmatrix} -c_r s_h - c_h s_p s_r & -c_h c_p & -s_r s_h + c_h s_p c_r \\ c_h c_r - s_h s_p s_r & -s_h c_p & c_h s_r + s_h s_p c_r \\ 0 & 0 & 0 \end{pmatrix} \quad (25)$$

where  $\Delta y = \varphi_{1n}^{ik} - f(x_k)$ ,  $\Delta y$  is the deviation between the estimated result  $x_k$  of the state variable and the measured value  $\varphi_{1n}^{ik}$  in the  $k$ -th iteration, and its least square solution is

$$\Delta x = (H^T H)^{-1} H^T \Delta y \quad (26)$$

By establishing the above non-linear least square estimation equation, the estimation of unknown parameters can be completed under given initial attitude angle, and the attitude angle can be obtained by using carrier phase observation equation.

## 4 Verification and Analysis

### 4.1 Two Antenna Experiment

We have implemented our proposed method with MATLAB and applied it to the real measurements from two u-blox receivers. The experiment with 0.575 m baseline length is performed. The mask elevation was set to 10, 1020 common epochs and 8 satellites (PRN: 2, 5, 6, 9, 12, 17, 19, 25) were observed. On this basis, the parameters (heading, pitch, positions and the baseline error) were calculated and compared applying the direct, least square determination method (Figs. 5 and 6).

In Table 1: the mean value of the heading angle and the pitch angle obtained by the least square method and the direct method are not much different, but for the RMS value, the least square method obviously has a smaller error, only 0.525 and 0.341. That is, the accuracy of the least square method is higher than direct method.

### 4.2 Three Antenna Experiments

In order to compare the accuracy of the attitude measurement, a set of three-antenna GNSS static data is used for verification. The receiver type is u-blox, and the data sampling rate is 1 Hz. The antenna 1 is the main antenna, the antenna 2 and the antenna 3 are the auxiliary antennas, and the baseline length formed by the antenna 1 is 0.60 m and 0.92 m, respectively. The mask elevation was set to 10 degree, a total

of 8 satellites were observed within 1020 s of the experimental data acquisition time, and their PRNs were 2, 5, 6, 9, 12, 17, 19, 25 respectively.

We have implemented our proposed method with MATLAB and applied it to the real measurements from three u-blox receivers. The parameters (attitude angles, positions and the baseline error) were calculated and compared applying the direct method, least square determination method (Figs. 7 and 8).

In Table 2: the attitude angle stability obtained by the two methods, that is, the mean value is basically the same, but the RMS value of the heading angle and the roll angle obtained by the least square method is smaller than the direct method, that is to mean, the heading angle and the roll angle precision of the least square method is higher; and the values are  $0.590^\circ$  and  $1.695^\circ$ , respectively. For the pitch angle, the RMS error obtained by the least square method is slightly larger.

From the above analysis, it can be known that there are certain differences in the attitude angle accuracy of the two methods. In most cases, the accuracy of the least

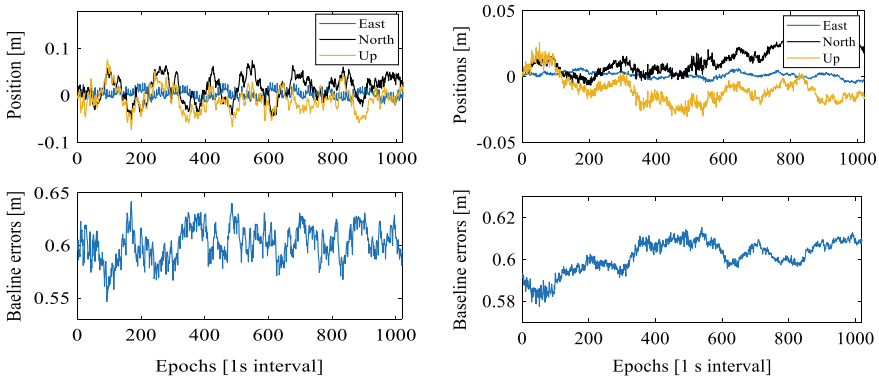


Fig. 5 Estimates of baseline components using direct and least-square method

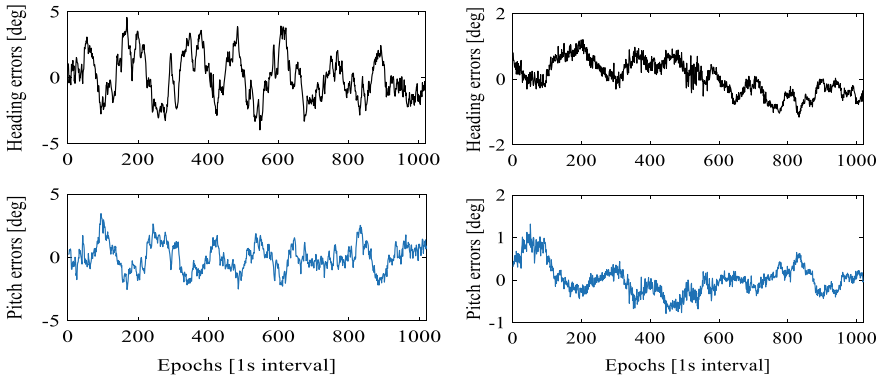
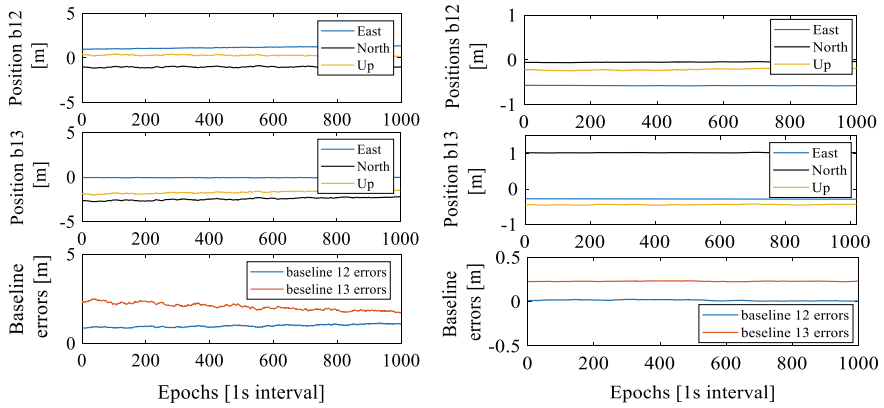


Fig. 6 Heading and pitch angles determination using direct and least-square method

**Table 1** Attitude mean value and RMS error

Number	Algorithm name	Attitude	Mean value/deg	RMS error/deg
1	Direct method	h	77.076	1.688
		p	-45.016	1.046
2	Least-square method	h	77.257	0.525
		p	-45.013	0.341



**Fig. 7** Estimates of baseline components errors using direct and least-square method

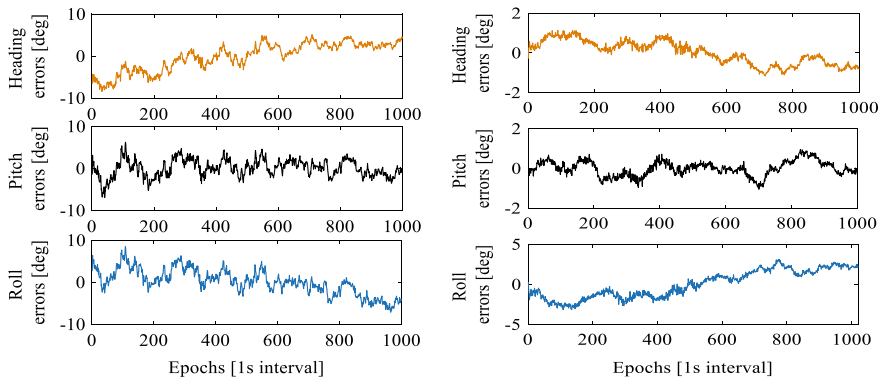


**Fig. 8** Attitude errors using direct and least-square method (the right shows the least square, and the left is the direct method)

square attitude method is better than the direct method. However, the stability of the two methods is basically the same, and there is only a difference in the estimation of the deviation of the pitch angle.



**Table 2** Attitude mean value and RMS error

Number	Algorithm name	Attitude	Mean value/deg	RMS error/deg
1	Direct method	h	-85.189	0.680
		p	-24.712	0.349
		r	-20.134	1.714
2	Least-square method	h	-85.868	0.590
		p	-24.793	0.373
		r	-19.800	1.695

## 5 Conclusions

This paper introduces a comparison of two attitude solving algorithms based on AFM-assisted solution of integer ambiguity. Given the high searching efficiency of LAMBDA algorithm with baseline constraints, and the AFM algorithm does not consider the initial conditions and will not be affected by the cycle slip. As an auxiliary means, when the integer ambiguity of the CLAMBDA algorithm is greatly deviated, the initial baseline length information is used to correct the search process using the AFM algorithm, and the candidate integer ambiguity of the CLAMBDA algorithm search is used. Further screening to improve the efficiency and accuracy of ambiguity resolution.

After obtaining the accurate integer ambiguity, the direct method and the least square method are used to obtain the attitude angle, and the baseline vector, baseline error and attitude angle error analysis are compared. The experimental results verify the feasibility of correcting the integer ambiguity based on AFM. When the error occurs in the CLAMBDA solution, the correct integer ambiguity can be corrected and the attitude angle can be solved.

**Acknowledgements** This work has been supported by the following units and projects. They are the National Key R&D Program of China (2018YFB0505103), the National Natural Science Foundation of China (61561016, 61861008), Department of Science and Technology of Guangxi Zhuang Autonomous Region (AC16380014, AA17202048, AA17202033), Sichuan Science and Technology Plan Project (17ZDYF1495), Guilin Science and Technology Bureau Project (20160202, 20170216), the basic ability promotion project of young and middle-aged teachers in Universities of Guangxi province (ky2016YB164), the 2019 School-level Graduate Innovation Program (2019YCXS024).

## References

1. Raskaliyev A, Patel S, Sobh T (2017) A dynamic model for GPS based attitude determination and testing using a serial robotic manipulator. *J Adv Res* 8
2. Chen W (2012) New method for single epoch, single frequency land vehicle attitude determination using low-end GPS receiver. *GPS Sol* 16(3):329–338

3. Wenshen Mao, Chuanwen Chang, Na Xia (2015) Vehicle attitude measurement based on navigation satellites. Nat Def Ind Press, Beijing
4. Wu H, Xiubin Z, Chunlei P et al (2018) A new multi-constrained GNSS single-frequency single-epoch attitude algorithm based on range. Acta Aeronautica Sinica 39(6)
5. Giorgi G, Teunissen PJG (2010) Carrier phase GNSS attitude determination with the multivariate constrained LAMBDA method. In: Aerospace conference, 2010 IEEE
6. Teunissen PJG (1995) The least-square ambiguity decorrelation adjustment: a method for fast GPS integer ambiguity estimation. J Geodesy 70(1–2):65–82
7. Teunissen PJG, Jonge PJD, Tiberius CCJM (1997) The least-square ambiguity decorrelation adjustment: its performance on short GPS baselines and short observation spans. J Geodesy 71(10):589–602
8. Gong A, Zhao X, Pang C et al (2015) GNSS single frequency, single epoch reliable attitude determination method with baseline vector constraint. Sensors 15(12):30093–30103
9. Park C, Teunissen PJG (2009) Integer least square with quadratic equality constraints and its application to GNSS attitude determination systems. Int J Control Autom Syst 7(4):566–576
10. Chen Wantong, Qin Honglei (2011) Research on fitness function of ambiguity function method in GPS attitude measurement. Shanghai Aerosp 28(5):50–54
11. Counselman CC, Gourevitch SA (1981) Miniature interferometer terminals for earth surveying: ambiguity and multipath with global positioning system. IEEE Trans Geosci Remote Sens GE 19(4):244–252
12. Cong L, Li E, Zhang L et al (2015) GPS/INS integrated navigation and positioning method based on INS-assisted CLAMBDA and AFM. Syst Eng Electr (4)
13. Zhang Fangzhao, Chai Yanju, Chai Hua et al (2016) Accuracy analysis of two multi-antenna GNSS attitude methods. Chin J Inert Technol 24(1):30–35
14. Li Q, Zhang L, Wu J et al (2017) A novel constrained ambiguity resolution approach for Beidou attitude determination. Adv Space Res
15. Habib TMA (2013) A comparative study of spacecraft attitude determination and estimation algorithms (a cost–benefit approach). Aerosp Sci Technol 26(1):211–215
16. Dai Z, Knedlik S, Loffeld O (2009) A MATLAB toolbox for attitude determination with GPS multi-antenna systems. Gps Sol 13(3):241–248; (4):333–341

# Design and Development of Wearable Human Activity Recognition for Healthcare Monitoring



Hamzah Ahmad, Nurul Syafiqah Mohd, Nur Aqilah Othman,  
Mohd Mawardi Saari and Mohd Syakirin Ramli

**Abstract** This research deals with development of a wearable sensing system for human activity recognition focusing on hand and leg assessments. The research attempts to sufficiently recognize the motion to provide physiotherapist about the patient condition in the remote area. The system is designed by applying Arduino as the main controller with the help of accelerometer to identify human movements and then classifying them into soft, medium and hard motions categories. From the research, data acquired from the assessment is then imported into Microsoft Excel by using Guino software to describe the human motions. The accelerometer sensors are placed as follows; the on the right hand for three positions which are on the wrist, on the elbow, and on the shoulder. Meanwhile on right leg for three position which is in thigh, calf and ankle. Experimental results show that the proposed system is capable to provide reliable information to both patient and physiotherapist about the motions. The recognition for the activity is based on physiotherapist consultation which provides early descriptions of human various activities using hands and legs. The proposed system can be applied for rehabilitation and monitoring system to realize a home-based smart monitoring and assessment system.

**Keywords** Activity recognition · Wearable system · Accelerometer · Hand and leg assessments

## 1 Introduction

Since the last decade, human activity recognition has become an important emerging field in research health monitoring systems. The main objective of activity recognition is to recognize the actions and goals of an agent or a group of agents based on the observations and assessment [1]. In a healthcare system especially, activity recognition is important in order to identify the behaviors and symptoms of a patient in real time, especially for rehabilitation. Rehabilitation is a process of recovering

---

H. Ahmad (✉) · N. S. Mohd · N. A. Othman · M. M. Saari · M. S. Ramli  
Faculty of Electrical and Electronics Engineering, Universiti Malaysia Pahang, 26600 Pekan,  
Pahang, Malaysia  
e-mail: [hamzah@ump.edu.my](mailto:hamzah@ump.edu.my)

© Springer Nature Singapore Pte Ltd. 2020  
A. N. Kasruddin Nasir et al. (eds.), *InECCE2019*, Lecture Notes in Electrical  
Engineering 632, [https://doi.org/10.1007/978-981-15-2317-5\\_27](https://doi.org/10.1007/978-981-15-2317-5_27)

323

human body to normal condition after an injury, illness or disease [2]. This rehabilitation process requires continuous monitoring from doctors or physicians to allow them to diagnosing the disease and then prescribe personalized treatment regimens. Patients who suffer from the fractures, for example, can be equipped and attached with small sensors and also enrolled in healthcare study for future references. Their conditions can be monitored continuously and data about their daily activities can be recorded. Sensors that are placed on the patients can monitor their daily activities and provides early warning and detections for doctors or physician of any abnormal conditions. By doing this, the patient can avoid congestion when commuting to the health institution for treatment and analysis.

There are a few different approaches that available to recognize human daily activity in order to improve human healthcare. Three approaches have been mainly employed for this purpose; video-based system through Automatic Activity Recognition [3–6], wearable sensor based [7–9] and environmental based [10–12]. A table comparing these techniques are presented in Table 1.

Along with the above three main approaches in recognizing human activities, artificial intelligence is mainly applied for analysis and verifications such as Fuzzy Logic [13, 14], Support vector machine [15, 16] and Neural Network [6, 9, 17]. Currently, most researcher applies a lot of sensors for the measurement process. However, the measurements are prone to failure due to sensitivity between sensors measurement

**Table 1** Comparison between available system on wearable devices

System	Video based system [3–6]	Wearable sensor based system [7–9]	Environmental sensor based [10–12]
Type of sensor used	Use camera to detect activity recognition	Worn a sensor on the body to detect activity recognition	Use ambient sensors to detect activity recognition
Advantages	<ul style="list-style-type: none"> <li>– Effective and works fine only in laboratory</li> </ul>	<ul style="list-style-type: none"> <li>– Suit to collect data on daily physical activity</li> <li>– The system is independent infrastructure</li> <li>– Low cost</li> <li>– Does not threat to people’s privacy</li> </ul>	<ul style="list-style-type: none"> <li>– Passively monitor their occupants all day, without requiring action from users</li> <li>– A large number of parameter can be monitor</li> </ul>
Disadvantages	<ul style="list-style-type: none"> <li>– Fails in achieving same accuracy under a real home setting</li> <li>– Higher cost</li> <li>– Inconvenience to setup multiple camera devices</li> <li>– Intrude user’s privacy</li> <li>– Needs to obtained adequate silhouette features</li> </ul>	<ul style="list-style-type: none"> <li>– Impractical for patient deployment</li> <li>– A change in position could lead to variation in received signal</li> <li>– Perform poorly if the device is only worn at the specific human body</li> </ul>	<ul style="list-style-type: none"> <li>– Fewer restriction in terms of size, weight, and power</li> <li>– The system is infrastructure dependent</li> <li>– Cannot monitor subject outside of home setting</li> </ul>

[17]. Hence, this research focusing only on one type of sensors i.e. accelerometers. The sensors are developed such that it still able to provide information on human motions with early detection of human motions. Besides, the research is not focusing on the characterization of motion i.e. soft, medium, hard motions and only referring to the available works of literatures for references.

In this research, the activity recognition needs to solve the two following issues. The first issue is to detect and analyses the hand motion movement for rehabilitation purpose. For this issue, sensors are needed to recognize and collect data from hand activities such as internal rotation, external rotation, shoulder flexion, shoulder extension, elbow flexion extension, forearm supination, and forearm pronation. The second issue is to identify the soft, medium and hard motion of hand movement from collective data. From the data collected, a conclusion can be made whether the movements can be categorized into soft, medium or hard motion movement which consistent with preceding works [2–4]. The work mainly focusing to identify the human activities in prescribed motions on different age to recognize the features which will then use for further analysis of motions.

This paper is organized in the following manner. Section 2 explains the system modeling and design of the proposed system which consists of controller and sensors with the application of Microsoft Excel. This is then followed by Sect. 3 which presents the results of several subjects' movements for hand and legs assessments. The contents mainly illustrates human capabilities in doing specific motions by looking on the aspect of the range of motions. Finally, Sect. 4 concludes the paper.

## 2 System Modelling and Design

The proposed system attempts to identify the human motions on both hands and leg by measuring each of seven different assessments as mentioned respectively. The system applies ARDUINO Mega 2560 to act as the controller to the system in identifying the signals and transmit the signal to be shown in graphical illustrations in Microsoft excel by software named GUINO. Nine inputs are recognized to be processed by the controller from the accelerometer ADXL335 expressing the data acquired from the human motions in x, y, z accelerations for each sensor. These sensors are positioned on hand and leg; elbow, shoulder and wrist, tight, knee and ankle. To perform the activities for assessment, the patient must be in the prescribed posture to avoid errors during measurements. Figure 1a shows the GUINO software which responsible to extract information from the sensor during assessment processes. Figure 1b describes one of the human motion in performing one of the assessment.

All the assessments are based on Table 2 Range of Motion (ROM) provided by the physiotherapist for hand and leg assessments.

Every subject is required to do all assessments to identify their capabilities in performing those activities. The subjects are healthy individuals did not involve and experience in any physical injuries due to accidents and did not receive any major medical treatments. By doing these exercises, then it is only possible to classify

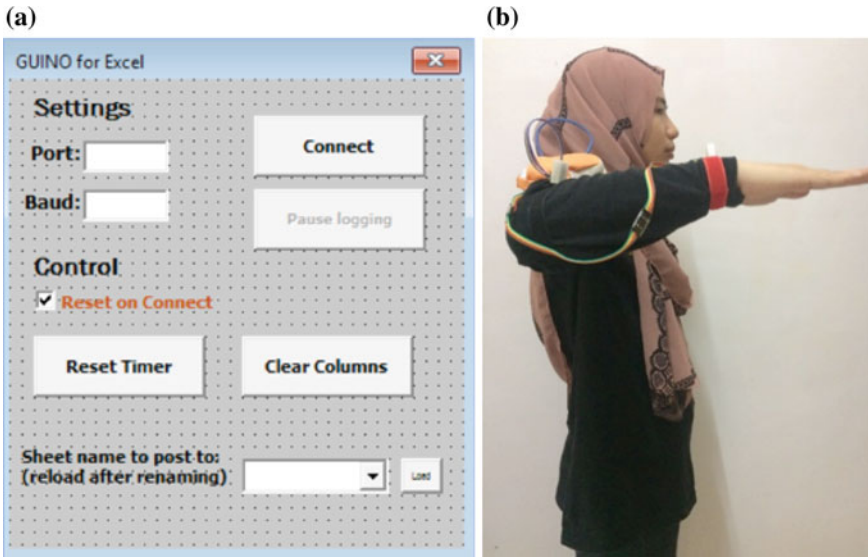


Fig. 1 a GUINO software in microsoft excel, b sample of assessment; internal pronation

Table 2 ROM for hand and leg assessments

Human body	ROM	Movement (°)
Hand	Forearm	Supination (0–90)
		Pronation (0–90)
	Shoulder	Flexion (0–180)
		Extension (0–50)
		Internal rotation (0–90)
		External rotation (0–90)
Elbow	Extension flexion	
Leg	Hip joint	External (0–30)
		Flexion (0–120)
		Abduction (0–40)
		Adduction (0–35)
	Knee joint	External-flexion (0–135)
	Ankle joint	Dorsiflex (0–15)
		Plantarflex (0–50)

the activities through soft, medium and hard motions which are identified based on previous works of literature e.g. [2–4]. This is presented in Table 3 associating all related assessments to the respected classifications.

**Table 3** Classification of activity based on hand assessment

No.	Activity	Type of activity	Activity classification
1	Internal rotation	Wearing pants	Soft level [2]
2	External rotation	Comb hair	Soft level
3	Shoulder flexion	Pick up the object from high place	Medium level
4	Shoulder extension	Tuck in shirt	Soft level
5	Forearm supination	Lifting the object	Medium level
6	Forearm pronation	Wiping the table	Medium level [2]
7	Elbow extension flexion	Eating/drinking	Soft level [2]
8	Hip joint extension	Running	Hard level
9	Hip joint flexion	Walking	Medium level
10	Abduction	Horse riding [14]	Medium level
11	Adduction	Balancing [14]	Soft level
12	Knee joint	Cycling [14]	Medium level
13	Dorsiflex	Climbing	Medium level
14	Plantarflex	Wearing shoes	Soft level

### 3 Results and Discussions

The hand and leg assessments are tested on 20 subjects whose been identified at different age ranges (under age 20 years old, under 40 years old and above age 50 years old). This is purposely done to identify any correlations, relations or any specific explanations that can be formulated based on the human age without significantly focus on gender. The test is conducted in room temperature. For every hand and leg assessment, the data is taken from the starting point which is from 0 to 7 s and the final point which is from 8 to 15 s. The initial timing is dedicated to ensuring that the test subject has prepared for the assessment to begin. The starting angle is recorded as this is very important to recognize the differences between the starting point of motions until the target positions. The results are then processed by the GUINO software to plot the motions on the specific human body parts each at hand and legs. The results focussed on the motion as the classification is generally referred to the preceding results [2–4].

The results and analysis of this research are explained below. There are a lot of figures presented to show the results on each hand and leg assessments. Due to this conditions, only 6 results are selected which demonstrates human daily routines, three each for the hand; internal rotation, external rotation, and shoulder flexion and legs; hip joint extension, hip joint flexion and plantarflex to explain and discuss our findings.

Remark that most of the movements are strongly related to the human sample flexibility in moving their hands and legs due to various reasons such as accidental injuries, effect of surgery or unidentified factors. However, in our experiments, all

human subjects have not experienced any shoulder or elbow injuries. This is to ensure that the measured data offers better reliability and consistency of the motions. In fact, these motions should still be able to provide general conditions on how the human hands and legs are moving and behaving based on the outlined activities.

Figures 2, 3 and 4 illustrates the measured ROM data for every single human subjects with respect to the internal rotations, external rotations and shoulder flexion on hands assessments respectively. There are 20 human subjects ranging from 20–70 years old performing the activity for internal, external rotations and shoulder flexion. Covering on soft and medium activities. The result has shown that the youngest subject has generally better flexibility in performing hand assessments compared to the older subjects. This is, in fact, consistent for all other human hand assessments.

On the other hand, looking into leg assessments, Figs. 5, 6 and 7 illustrates three activities namely the hip joint extension, hip joint flexion and plantar flex which describes the hard, medium and soft motions respectively. For the hip joint extension which is categorized as hard motions, younger human subjects have a higher range of motion compared to the elders. However, surprisingly both of the younger and elders human subjects do not have significant differences when medium and soft motions are performed. They are both have almost possessed the same capability for those two motions.

All of the above results can be further applied to identify the various human conditions in performing any actions such as walking, running, sitting and lifting part

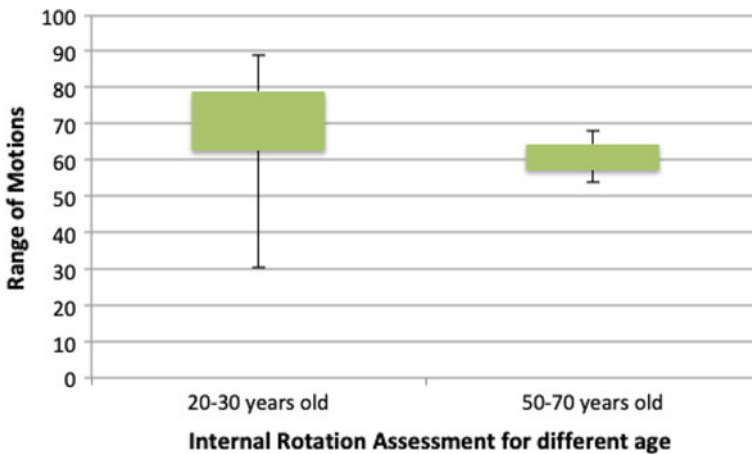


Fig. 2 Measured ROM data for internal rotation for different subject age respectively



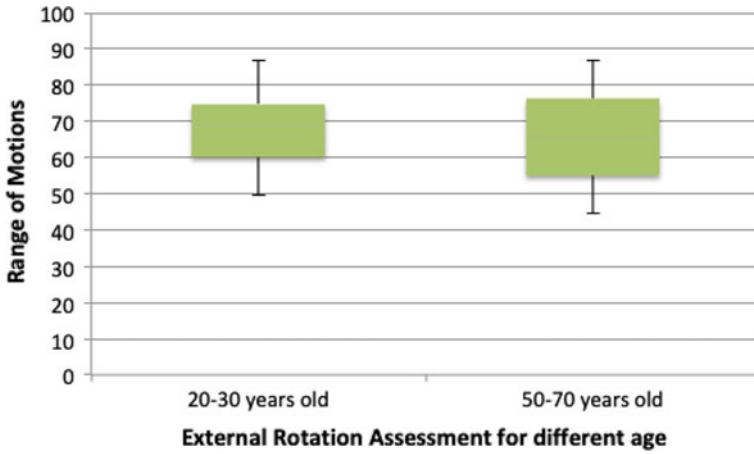


Fig. 3 Measured ROM data for external rotation for different subject age respectively

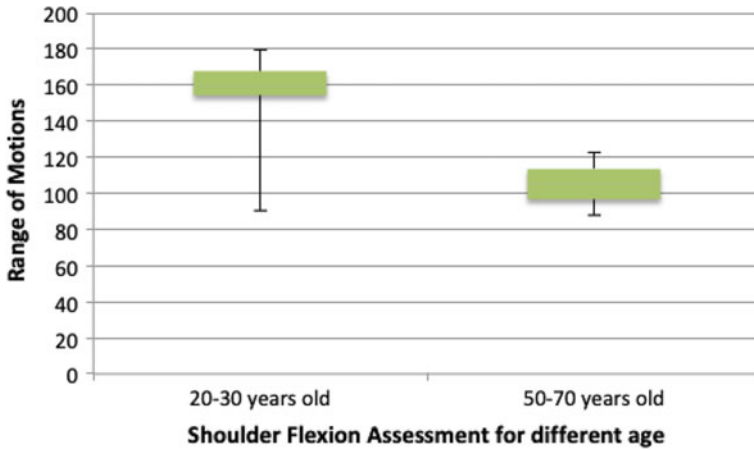


Fig. 4 Measured ROM data for shoulder flexion for different subject age respectively

as the organized assessments are conducted to simulate those actions on hands and legs. This has been mentioned in Table 3 which recognizes different human activities based on the assessment. Although there are no feature extractions technique been applied for verifications purposes on each motion, the results still produced an exemplary condition of human movements for various actions for different ages. Nevertheless, these results are also comparable with the existing techniques presented in [2–4]. The human errors are also avoidable and the proposed system has higher accuracy especially when comparing to the goniometer for measurement process. In fact, the measurements show a lower error than 7% compared to the goniometer if actual measurement is considered. Remark that these results have been verified by

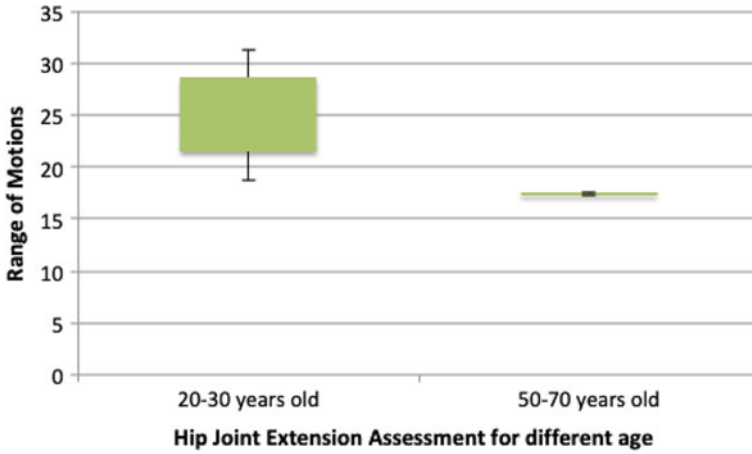


Fig. 5 Measured ROM data for hip joint extension for different subject age respectively

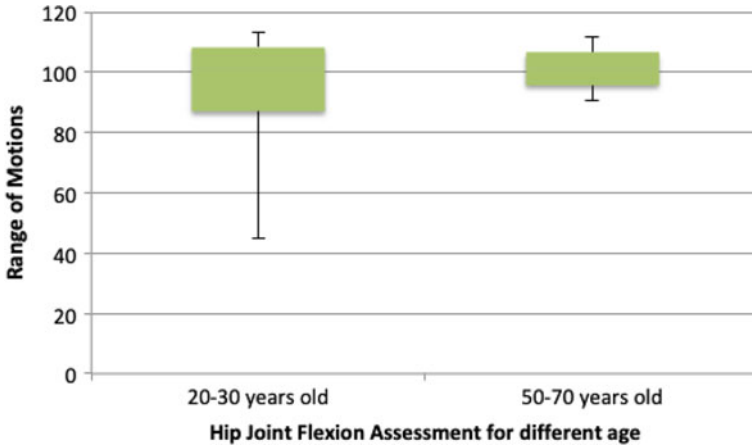


Fig. 6 Measured ROM data for hip joint flexion for different subject age respectively

the physiotherapist for each activity. Most importantly, the system is influential and reliable whenever remote monitoring is necessary between patient and physiotherapist. Moreover, based on the proposed results, there is also a significant correlation of measurement data and human age which in the end defines the human capabilities in performing any actions.

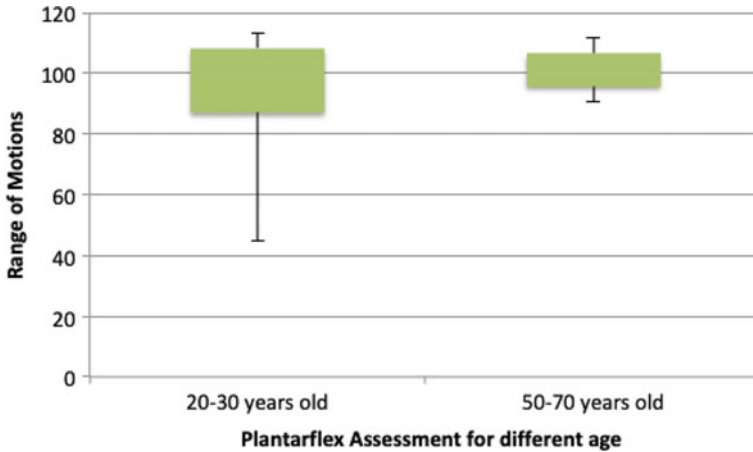


Fig. 7 Measured ROM data for plantarflex for different subject age respectively

## 4 Conclusion

This paper presents an analysis of human activity recognition using the accelerometer as a sensor based technique for various hands and legs motions. The results show that with only accelerometers, it is possible to predict the human motions with an acceptable range of motion. The motion can be further analyzed to categorize the human activities either running, walking, wearing shoes or lifting parts based on the results of assessments. Even without the existence of feature extraction of the human motion, the application of the accelerometers still produce consistent results on motions with different age. This technology can support the healthcare institutions which is more reliable than using the mechanical type sensor, i.e. goniometer. Furthermore, the results also described the different range of motions for human on different age which are important to be analyzed further by considering gender aspects as well.

## References

1. Suto J, Oniga S (2017) Recognition rate difference between real-time and offline human activity recognition. In: International conference on internet of things for the global community, pp 1–5
2. Usman M et al (2018) On the correlation of sensor location and human activity recognition in body area networks (BANs). *IEEE Syst J* 12(1):82–91
3. Wei Z, Bao T (2016) Research on a novel strategy for automatic activity recognition using wearable device. In: 8th IEEE international conference on communication software and networks (ICCSN), pp 488–492
4. Gaglio S, Re GL, Morana M (2014) Human activity recognition process using 3-D posture data. *IEEE Trans Hum Mach Syst* 45(5):586–597

5. Song B, Kamal AT, Soto C, Ding C, Farrell JA, Roy-Chowdhury AK (2010) Tracking and activity recognition through consensus in distributed camera networks. *IEEE Trans Image Process* 19(10):2564–2579
6. Noor S, Uddin V (2018) Using context from inside-out vision for improved activity recognition. *IET Comput Vision* 12(3):276–287
7. Fullerton E, Heller B, Munoz-Organero M (2017) Recognizing human activity in free-living using multiple body-worn accelerometers. *IEEE Sens J* 17(16):5290–5297
8. Hsu YL, Yang SC, Chang HC, Lai HC (2018) Human daily and sport activity recognition using a wearable inertial sensor network. *IEEE Access* 6:31715–31728
9. Lee SM, Yoon SM, Cho H (2017) Human activity recognition from accelerometer data using convolutional neural network. In: *IEEE international conference on big data and smart computing (BigComp)*, Jeju, pp 131–134
10. Mohamed R, Perumal T, Sulaiman MN, Mustapha N, Razali MN (2017) Conflict resolution using enhanced label combination method for complex activity recognition in smart home environment. In: *IEEE 6th global conference on consumer electronics (GCCE)*, Nagoya, pp 1–3
11. Perumal T, Chui YL, Ahmadon MAB, Yamaguchi S (2017) IoT based activity recognition among smart home residents. In: *IEEE 6th global conference on consumer electronics (GCCE)*, Nagoya, pp 1–2
12. Azkune G, Almeida A (2018) A scalable hybrid activity recognition approach for intelligent environments. *IEEE Access* 6:41745–41759
13. Chiang SY, Kan YC, Tu YC, Lin HC (2012) Activity recognition by fuzzy logic system in wireless sensor network for physical therapy. In: Watada J, Watanabe T, Phillips-Wren G, Howlett R, Jain L (eds) *Intelligent decision technologies. Smart innovation, systems and technologies*, vol 16. Springer, Berlin, Heidelberg, pp 191–200
14. Zhang H, Zhou W, Parker LE (2015) Fuzzy temporal segmentation and probabilistic recognition of continuous human daily activities. *IEEE Trans Hum Mach Syst* 45(5):598–611
15. Kolekar MH, Bharti N, Patil PN (2016) Detection of fence climbing using activity recognition by support vector machine classifier. In: *IEEE region 10 conference*, Singapore, pp 398–402
16. Nurhanim K, Elamvazuthi I, Izhar LI, Ganesan T (2017) Classification of human activity based on smartphone inertial sensor using support vector machine. In: *IEEE 3rd international symposium in robotics and manufacturing automation*, Kuala Lumpur, pp 1–5
17. Chen Y, Yu L, Ota K, Dong M (2018) Robust activity recognition for aging society. *IEEE J Biomed Health Informatics* 22(6):1754–1764

# Region of Interest Extraction of Finger-Vein Image Using Watershed Segmentation with Distance Transform



Lim Yuan Zhang and Bakhtiar Affendi Rosdi

**Abstract** Finger Vein Recognition System (FVRS) is a biometric technology that identifies or verifies an individual based on unique vein patterns. Region of interest (ROI) extraction is one of the essential steps in FVRS. Current ROI extraction methods cannot extract an accurate ROI for a finger vein image with non-uniform background illumination. In this paper, we propose a new ROI extraction method that is immune to non-uniform background illumination. To detect the edge of the finger for the ROI extraction, we utilise watershed segmentation with distance transform and Canny edge detector. Experimental results show that the proposed ROI extraction method can extract consistent ROI from a finger vein image with non-uniform background illumination.

**Keywords** ROI extraction · Finger vein recognition · Image processing

## 1 Introduction

The term biometrics refers to the measurement of human physical traits and behavioural traits. Several common physical traits used in biometric technologies are fingerprints, palm prints, face, iris while behavioural traits used are voice and gait [1]. Biometric technologies are widely used in various identity authentication and verification applications, namely customs, airports, banks and so on [2].

Among various biometrics developed, the fingerprint recognition system is the most established biometric technology where many applications can be seen utilising this system. Despite being the most common approach these days, a fingerprint recognition system still poses the risk of forgery due to the exposure of fingerprints easily. It also degrades the system's performance when it comes to obtaining unclear fingerprint images due to sweat or dry condition [3]. In response to the addressed drawbacks of current biometrics, researchers have put considerable attention to personal authentication using finger vein recognition system [4]. This is because finger

---

L. Y. Zhang · B. A. Rosdi (✉)

School of Electrical & Electronic Engineering, Engineering Campus, Universiti Sains Malaysia, 14300 Nibong Tebal, Penang, Malaysia  
e-mail: [ebakhtiar@usm.my](mailto:ebakhtiar@usm.my)

© Springer Nature Singapore Pte Ltd. 2020

A. N. Kasruddin Nasir et al. (eds.), *InECCE2019*, Lecture Notes in Electrical Engineering 632, [https://doi.org/10.1007/978-981-15-2317-5\\_28](https://doi.org/10.1007/978-981-15-2317-5_28)

333

veins are hidden under the skin and therefore it is almost impossible to be forged. It also provides extremely high security due to its distinctive patterns that no one finger, even twins or our fingers have the same vein pattern. Moreover, the finger vein pattern can only be obtained from a living person. Due to these characteristics of increased security and reliability; finger vein biometric outperforms other biometric identifiers.

Typically, a finger vein recognition system (FVRS) consists of three stages, namely, image acquisition, image pre-processing as well as feature extraction and matching. Of all stages, region of interest (ROI) extraction during image pre-processing is considered one of the most critical elements which have a direct impact on the accuracy of the system [5]. ROI of a finger vein image refers to the region of a finger which is filled with an abundant finger vein pattern network. ROI extraction aims to decide which part of the image is fit for finger vein feature extraction, thereby reserving the useful information in the ROI and removing the useless information in the background [6].

Many researchers had contributed to different ROI extraction methods. Yang and Shi [7] proposed an ROI extraction by using distal interphalangeal joint localisation. Distal interphalangeal joint is the joint near the fingertip and has a higher sum of grey value. They first calculate the sum of pixel values in each row of the image. Then, they estimate the position of the distal phalangeal joint by pinpointing the maximum row-sum. Finally, they extract ROI using a window where the phalangeal joint position is located at  $2/3$  the height of the window. This method is able to obtain localized ROI by estimating the position of the distal phalangeal joint. However, the calculation of row-sum value is easily affected by illumination. Moreover, it used a fixed window instead of edge detection in extracting ROI, thus it is more prone to extracting unwanted background noise.

Yang et al. [6] also extracted the ROI based on phalangeal joints but used a single sliding window as an improvement to the method [7]. First, they used the Sobel edge operator to detect finger edges. Based on the finger edges, they calculate the skew angle to correct finger orientation. For ROI extraction, Yang et al. [6] used a sliding window with 50 rows to estimate the position of the distal and proximal phalangeal joint, which are two joints of the finger. They slide the sliding window row by row from the top to the bottom of the key area to calculate the sum of grey value, where two highest sums are the two phalangeal joints. Lastly, they crop out ROI with two phalangeal joint positions as the height and internal tangent of the finger edge as the width. Sobel edge operator is sensitive to illumination. Hence this method is not accurate for FV images affected by uneven illumination.

Shahrimie et al. [8] proposed a different ROI extraction method which involves illumination correction and height and width definition. They corrected the orientation of the FV image based on the finger edge obtained by Canny edge operator and connected component labelling. For ROI extraction, they cropped the ROI with 300 pixels of height which was empirically set and with the width that was adaptively defined based on the bottom end of finger geometry. The method proposed by Shahrimie et al. [8] provides an accurate straight middle line as the fingertip point is taken. This ensures the rotation of skewed FV image to be more precise. However,

its finger edge detection was applied to FV images with a clear background and mild illumination. It is incapable of obtaining a clear finger edge if given a higher intensity of light interference.

Van et al. [9] proposed a method of ROI extraction that omits the orientation correction process. In the beginning, they detected finger edge with Canny edge detector. This separated finger image from the background. Then, they drew lines of finger edge with Hough transform. These lines served a means to estimate the direction of the finger. After that, Van et al. [9] synthesised a middle line based on finger edges. Finally, they cropped out the ROI by using a fixed rectangular window in the direction of the finger, with the synthesized middle line as reference and finger edges as boundaries. This method does not extract a good ROI as there is no localised benchmark or reference. ROI images extracted using this method are inconsistent as ROI image could be the higher or lower part of the finger depending on the placement of the finger. Moreover, the finger edge obtained could be inaccurate as the noise outside finger image was not masked out.

Most of the previously proposed ROI extraction techniques [6, 8, 9] utilise the edge-based method such as Canny and Sobel edge operators to detect the edge of the finger. Edge-based image segmentation method is not suitable to be applied on raw FV images captured under a severe non-uniform illumination. Apart from the edge-based image segmentation method, there is another category of segmentation method called region-based segmentation [10]. Region-based segmentation is based on continuity. It has not been used in FV image segmentation before because most FV images captured by different image acquisition device are not severely affected by background illumination. Some region-based segmentation methods are watershed segmentation, region growing, region splitting and region merging [11]. In this paper, we utilise watershed segmentation with a distance transform to detect the edge of the finger for ROI extraction. With the proposed method, a consistent ROI can be extracted from a finger vein image with non-uniform background illumination. This will increase the accuracy of an FVRS.

## 2 Proposed ROI Extraction Method

This research proposes an ROI extraction with three stages: Image segmentation and edge detection, image orientation correction and ROI extraction. For image segmentation and edge detection, instead of using an edge-based segmentation we propose a region-based segmentation, which is watershed segmentation with distance transform [12] and applied Canny edge detection. Edge-based segmentation detected finger edges along with many unwanted lines, which is not suitable for a finger vein image with a severe non-uniform background illumination. Details for each steps of the proposed ROI extraction method is explained in following sub-sections.

## 2.1 Finger Vein Image Segmentation and Edge Detection

First, we use a Laplacian filter with the  $3 \times 3$  s derivative kernel to enhance the finger edge region. Then, we sharpen the FV image by subtracting the Laplacian filtered image from the original FV image. After that, we apply Otsu binary thresholding to the sharpened image to obtain a binary image. Following that, we perform distance transform on the binary image to find foreground area as depicted in Fig. 1b. In FV image, the foreground area is the finger itself, while the background area is the background region or noise other than a finger.

Next, we apply a suitable threshold to obtain the marker for the foreground object. We label markers to mark the foreground region, and the background region. Figure 1c illustrates the marked regions. Next, we perform a watershed algorithm to obtain the shape of the foreground object and then invert it to become a mask image as shown in Fig. 1d. The FV image segmentation is completed as we applied the mask image onto the original image. Figure 1e shows the segmented FV image. Finally, we apply Gaussian blur and Canny operator to detect finger edges instead of Sobel operator as the Sobel operator is more sensitive to light interference. Figure 1f shows the Image of finger edges detected. Although there is little defect at the right side of the finger edge, it can be disregarded as it does not affect the process orientation correction and ROI extraction. Figure 2 shows the overall flow of FV image segmentation and edge detection.

## 2.2 Finger Vein Image Orientation Correction

For FV image orientation correction, we adapt Yang et al.'s method [6]. First, from the finger edge detected in the previous step, as shown in Fig. 3a, we cropped out part of the top and bottom of FV image with a predefined window of (48, 10, 136, 246), where noises could still reside due to the floating position. We calculate two midpoints based on the first two detected edge pixels in the top row and the first two detected edge pixels from the last row of cropped FV image. This is because there might be some severe light interference at the horizontal middle row of finger edge

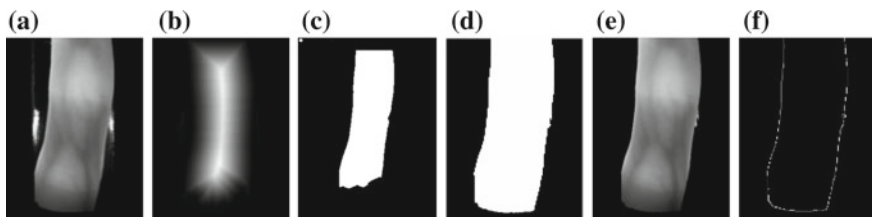


**Fig. 1** FV image segmentation and edge detection. **a** Raw image; **b** Distance transform; **c** Marker; **d** Mask; **e** Segmented FV image; **f** Finger edge



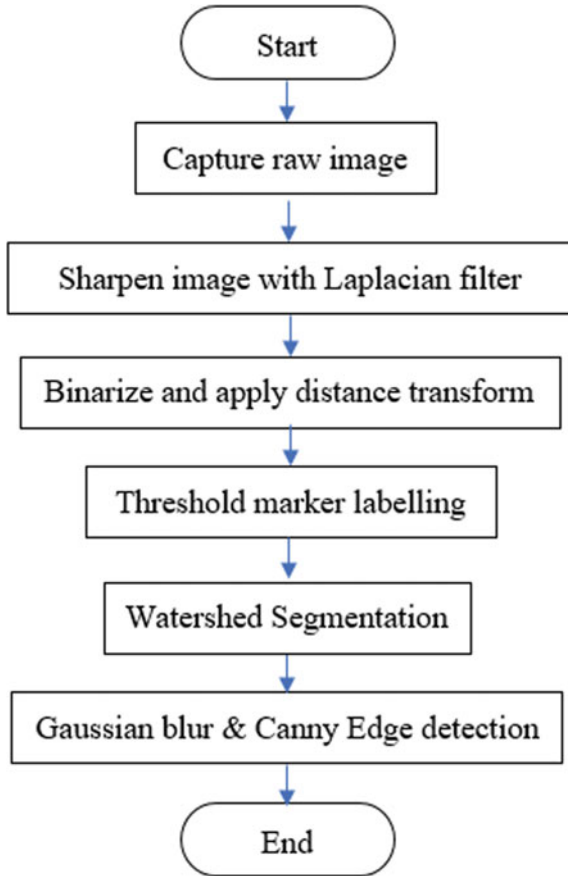


Fig. 2 Overall flow of the Finger Vein image segmentation and edge detection

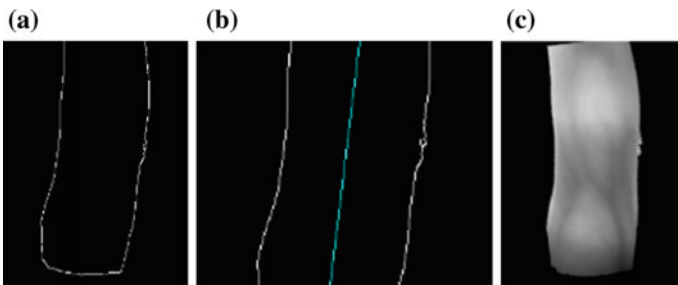


Fig. 3 FV image orientation correction

caused by different position. Figure 3b depicts the drawn middle line intersection two midpoints. Lastly, we compute the skew angle of the image based on the middle line using Eq. (1) and rotate the segmented FV image as shown in Fig. 3c.

$$\alpha = \arctan(a) \times 360/2\pi \quad (1)$$

where  $\alpha$  is the skew angle and  $a$  is the slope coefficient of the straight line obtained.

### 2.3 ROI Extraction

Finally, we adopt Yang et al.'s method [6] to extract ROI. First, we detect the inner contour of the FV image based on rotated finger edge as shown in Fig. 4a. Figure 4b shows the inner contour detected. Then we crop out the outside part of the contour as depicted in Fig. 4c. Following that, we enhance the remaining region with Contrast Limited Adaptive Histogram Equalization (CLAHE) using a clip limit of 6 as contrast limiting threshold and grid size for histogram equalisation of (6, 6). The use of CLAHE enhancement is to distinguish the grey values of the phalangeal joint further. Figure 4d illustrates the enhanced region.

For ROI localisation, although Qiu et al.'s [5] dual sliding window method is better in terms of insensitivity to light interference, we still chose to employ single sliding window method due to several reasons. First, it takes shorter computational time. Second, a raw image captured by FVRS developed in-house only have interference in the background but not in the finger vein itself. Furthermore, the region beyond the inner contour was already discarded to eliminate light interference. Figure 5 illustrates the sliding window process.

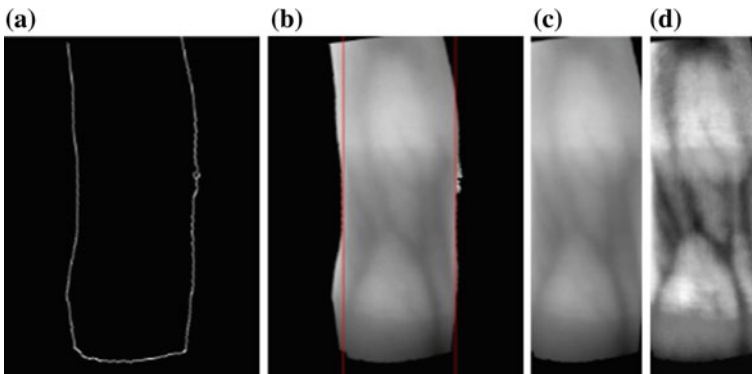


**Fig. 4** Inner contour detection. **a** Rotated finger edge; **b** Inner contour drawn in vertical red line; **c** Cropped key region; **d** Enhanced image

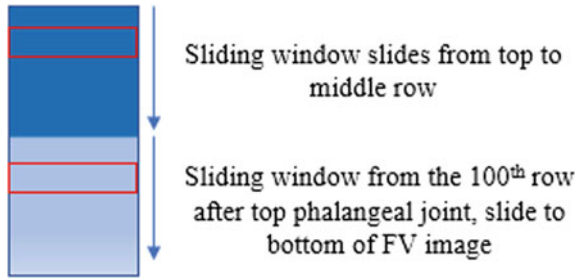


Fig. 5 Sliding windows' (red box) sliding process

In the first step of phalangeal joint detection, we divide FV image into two parts, top half and bottom half, as distal interphalangeal joint usually resides in the top half in FV image and proximal interphalangeal joint at the bottom half. We use a sliding window with 20 rows as shown in Fig. 6a to calculate the sum of grey value. Then, we slid the window from top to middle row of FV image and from the 100th row after top phalangeal joint to the bottom of FV image. This is because from Yang et al.'s [6] careful observation, distal phalangeal joint and proximal phalangeal joint are at least 100 rows apart. Next, we locate the phalangeal joints by obtaining the maximum sum of grey values in the top half and bottom half of FV image. Figure 6b depicts the estimated phalangeal joint position in the red line. Following that, we defined the height of ROI. For height, we select the rows at which top phalangeal

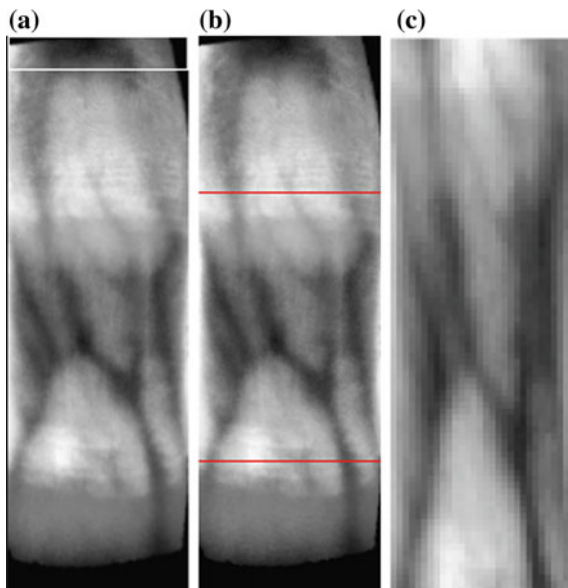


Fig. 6 ROI extraction. a Sliding window; b Estimated phalangeal joint in red line; d Resized ROI

joint and bottom phalangeal joint were detected. Lastly, we cropped out the ROI and resized it to  $30 \times 90$  based on the row and width defined. Figure 6c shows the final ROI extracted.

### 3 Results and Discussions

To demonstrate the effectiveness of the proposed region-based edge segmentation method two different types of experiments were conducted. First is the comparison between the proposed method with the existing edge-based segmentation methods [5, 11, 13] in the extracting of the finger edge. The second experiment is to evaluate the impact of the proposed method in the ROI extraction of FV image. In both of the experiments, we use 6 FV images with different finger positions to illustrate different scenarios where users may insert their fingers. The positions are as follows:

1. Straight (Not floating)
2. Slanted to the left (Not floating)
3. Slanted to the right (Not floating)
4. Straight (Floating)
5. Slanted to the left (Floating)
6. Slanted to the right (Floating)

All of the images used in the experiments are captured internally using our developed finger vein image acquisition device.

#### 3.1 Comparison of the Proposed and Previously Proposed Finger Edge Detection Methods

Here, we compare our proposed watershed segmentation with distance transform and Canny edge detector with previously proposed edge-based segmentation methods [6, 8, 9, 13]. Figure 7 shows finger edges detected using different edge detection methods. Based on observation, finger edges of positions 1–3 (non-floating) are successfully detected by methods [6, 9, 13]. However, there are unwanted lines on both sides of the finger edges caused by illumination. Clearer finger edges are found with our proposed method and method [8], where the unwanted lines are eliminated. Nevertheless, the method [8] is still affected by illumination, particularly where the finger and background light seem to ‘touch’ each other at positions 1 and 3. Failure of the method [8]’s connected component labelling at the affected areas could be the reason for the incomplete detection of finger edges. Our proposed method is almost unsusceptible to illumination for positions 1–3. There is little noise for position 1, but that can be ignored.

On the other hand, methods [6, 8, 9, 13] failed to determine finger edges of positions 4–6 (floating). Most edges detected are incomplete or too short. As shown

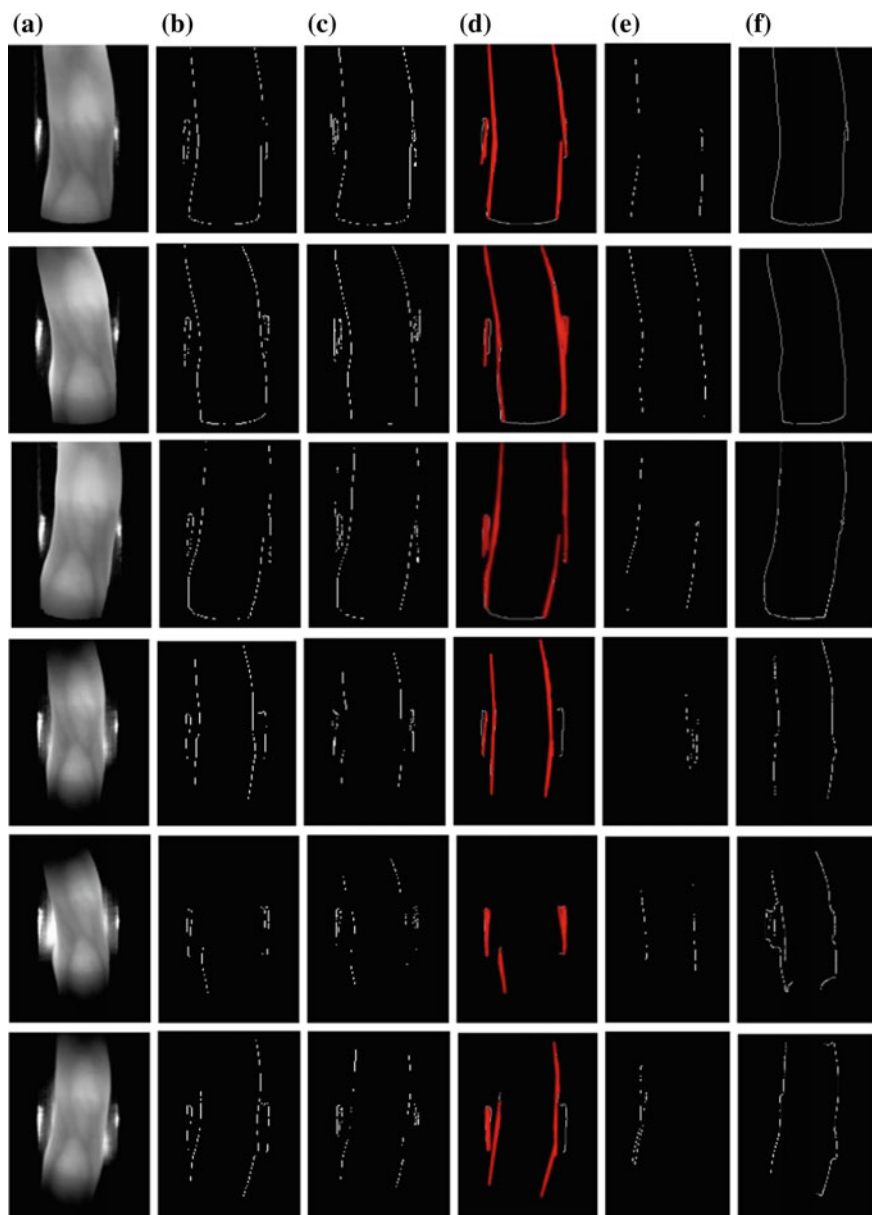


**Fig. 7** Edge detection comparison of left index finger with various positions. **a** Raw images with various positions; **b** Canny edge detector [13]; **c** Sobel edge detector [6]; **d** Canny edge detector and Hough transform [9]; **e** Canny edge detector and connected component labelling [8]; **f** Proposed method

in Fig. 7f our proposed method can detect the finger edge efficiently for a finger with floating positions. Although some unwanted lines remained especially for position 5, the orientation of FV image can still be continued as long as both edges are present and connected.

### 3.2 Comparison of Various ROI Extraction Methods

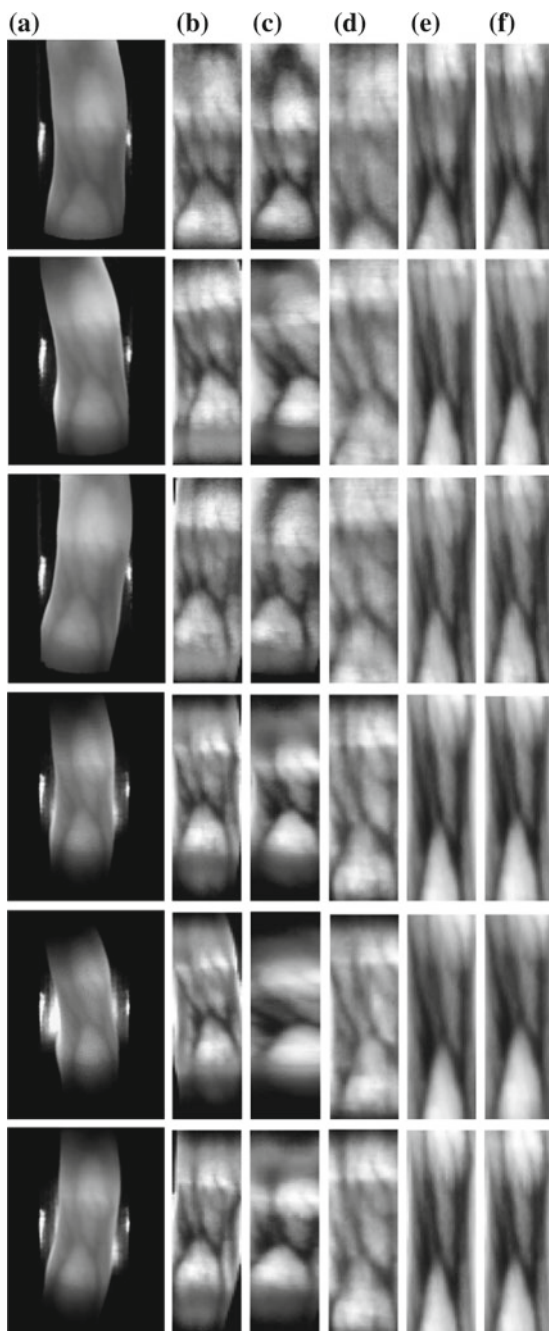
In our proposed method, we utilise the ROI extraction method in [6] to correct the orientation of the finger and also to extract the ROI. To justify the adoption of the method proposed in [6], five different ROI extraction methods are compared in this section. The compared methods are as follows:

- I. Fixed window method
- II. Inner contour based [13]
- III. Adapted finger direction based [9]
- IV. Adapted maximum row sum value based [7]
- V. Adapted single sliding window based [6].

Figure 8 shows the ROI extracted using different methods. Based on observation, it can be clearly seen that ROI extracted with methods I and II are not consistent. For both methods, FV patterns vary with different finger positions. Besides that, there are noises in the ROI. It can also be observed that large patches of non-informative black pixels are present at the top and bottom of the images, especially for floating finger positions 4–6. Furthermore, inner contour based ROI extraction of method II shows that it is highly susceptible to slanted finger positions.

For method III, FV patterns are more consistent than that of methods I and II. However, dark patches in ROI can still be seen in position 4–6. For methods IV and V, consistent ROIs were successfully extracted. There is little or no difference between these two methods because illumination affected area is eliminated before the process of localised benchmark estimation was carried out. Methods IV and V can be employed to extract ROI as it retains solely informative FV patterns and are consistent. In this case, method V was chosen. This is because there are still many variations that finger can be positioned. As illumination changes with the way finger is positioned shown in Fig. 7a position 5, FV images are still possible to be affected by illumination. Since it was proven by Yang et al. [6] that method V is more accurate in estimating phalangeal joints while method IV is more susceptible to illumination, method V was employed in ROI extraction.

**Fig. 8** ROI extraction comparison. **a** Raw images with various positions; **b** Fixed window method I; **c** Method II [13]; **d** Method III [9]; **e** Method IV [7]; **f** Method V [6]



## 4 Conclusion

In this paper, to detect the finger edge of a finger vein image with a non-uniform background illumination, we utilise watershed segmentation with distance transform and also Canny edge detector coupled with Gaussian blur. Following that, we correct the orientation of the image based on the edges obtained. Next, we push a single sliding window down the rows of FV image to calculate the sum of grey value to estimate the position of phalangeal joints. Finally, we extract the ROI based on the height of the phalangeal joint and width of inner contour of the finger edge. Experimental results prove that the proposed method can detect a consistent ROI from a finger vein image with various positions. This shows that the proposed region-based image segmentation plays an important role in ROI extraction of finger vein image.

**Acknowledgements** This work is supported by Universiti Sains Malaysia Bridging Fund No. 304.PELECT.6316321.

## References


1. Hsia CH, Guo JM, Wu CS (2017) Finger vein recognition based on parametric-oriented corrections. *Multimed Tools Appl*
2. Pham TD, Park YH, Nguyen DT, Kwon SY, Park KR (2015) Nonintrusive finger-vein recognition system using NIR image sensor and accuracy analyses according to various factors. *Sensors (Basel)* 15(7):16866–16894
3. Rosdi BA, Shing C, Suandi SA (2011) Finger vein recognition using generalized local line binary pattern. *Sensors* 11(12):11357–11371
4. Dong S, Yang J, Chen Y, Wang C, Zhang X, Park DS (2015) Finger vein recognition based on multi-orientation weighted symmetric local graph structure. *KSII Trans Internet Inf Syst* 9(10):4126–4142
5. Qiu S, Liu Y, Zhou Y, Huang J, Nie Y (2016) Finger-vein recognition based on dual-sliding window localization and pseudo-elliptical transformer. *Expert Syst Appl* 64:618–632
6. Yang L, Yang G, Yin Y, Xiao R (2013) Sliding window-based region of interest extraction for finger vein images. *Sensors (Basel)* 13(3):3799–3815
7. Yang J, Shi Y (2012) Finger-vein ROI localization and vein ridge enhancement. *Pattern Recogn Lett* 33(12):1569–1579
8. Shahrimie M, Asaari M, Suandi SA, Rosdi BA (2014) Expert systems with applications fusion of band limited phase only correlation and width centroid contour distance for finger based biometrics. *Expert Syst Appl* 41(7):3367–3382
9. Van HT, Thai TT, Le TH (2016) Robust finger vein identification base on discriminant orientation feature. In: *Proceedings—2015 IEEE international conference on knowledge and systems engineering, KSE 2015*, pp 348–353
10. Saini S, Arora K (2014) A study analysis on the different image segmentation. *Int J Inf Comput Technol* 4(14):1445–1452
11. Amoda N, Kulkarni RK (2013) Image segmentation and detection using watershed transform and region based image retrieval. *Int J Emerg Trends Technol Comput Sci* 2(2):89–94



12. Sinha A (2013) A new approach of watershed algorithm using distance transform applied to image. *Int J Innov Res Comput Commun Eng* 1(2):185–189
13. Choon Wei L (2016) Embedded finger vein recognition system using Raspberry pi. School of Electrical & Electronics Engineering, Universiti Sains Malaysia

# The Classification of Skateboarding Trick Manoeuvres Through the Integration of Image Processing Techniques and Machine Learning



Muhammad Nur Aiman Shapiee, Muhammad Ar Rahim Ibrahim, Mohd Azraai Mohd Razman, Muhammad Amirul Abdullah, Rabiū Muazu Musa, Mohd Hasnun Arif Hassan and Anwar P. P. Abdul Majeed 

**Abstract** More often than not, the evaluation of skateboarding tricks executions is assessed intuitively according to the judges' observation and hence are susceptible to biasness if not inaccurate judgement. Hence, it is crucial to underline the benchmark for analyzing the rate of successful execution of skateboarding trick for high level tournaments. The common tricks in skateboarding such as Kickflip, Ollie, Nollie, Pop Shove-it and Frontside 180 are investigated in this study via the synthetization of image processing and machine learning classifiers. The subject used for accomplishing the tricks is a male amateur skateboarder at the age of 23 years old with  $\pm 5.0$  years' experience using ORY skateboard. Each trick is collected upon five successful landings and the camera is placed 1.26 m from the subject on a flat cemented ground. The features extracted from each trick were engineered using Inception-V3 image embedder. Several classification models were evaluated, namely, Support Vector Machine (SVM), k-Nearest Neighbour (kNN), Logistic Regression (LR), Random Forest (RF) and Naïve Bayes (NB) on their ability in classifying the tricks based on the engineered features. It was observed from the preliminary investigation that the SVM model attained the highest classification accuracy with a value of 99.5% followed by LR, k-NN, RF, and NB with 98.6%, 95.8%, 82.4% and 78.7%, respectively. It could be inferred that the method proposed decisively provide the classification of skateboarding tricks efficiently and would certainly provide a more objective based judgment in awarding the score of the tricks.

**Keywords** Image processing · Machine learning · Skateboarding tricks · Classification

---

M. N. A. Shapiee · M. A. R. Ibrahim · M. A. Mohd Razman · M. A. Abdullah · R. M. Musa · M. H. A. Hassan · A. P. P. Abdul Majeed (✉)  
Innovative Manufacturing, Mechatronics and Sports Laboratory, Universiti Malaysia Pahang,  
26600 Pekan, Pahang Darul Makmur, Malaysia  
e-mail: [amajeed@ump.edu.my](mailto:amajeed@ump.edu.my)

## 1 Introduction

The net worth of the skateboarding industry is approximately \$USD 4.8 billion in 2010 [1]. It is worth noting that skateboarding will make its debut in the 2020 Tokyo Summer Olympics, suggesting the popularity and the traction that this game has made over the years. This growth somewhat demands new innovative approaches in evaluating the game in such significant competitions, especially with the judgment of the tricks executing which is conventionally carried out by judges through subjective means that is often liable to bias and imprecise assessment.

The implementation of machine learning on a computer vision system to classify skateboarding tricks are sparsely found in the literature. Auxiliary tools, for instance, the use of wearables technologies have been demonstrated to provide ample information of training and identifying athlete performances for instance in archery [2], golf [3] and badminton [4]. In skateboarding, a notable work was carried out by Groh et al. [5] to identifying tricks. The performance of classification rate between the models was compared using Support Vector Machine with a radial-basis kernel (RBF-SVM), Support Vector Machine with a linear kernel (LSVM) [6], k-Nearest Neighbor (kNN) [2], Random Forest (RF) [7] and Naïve Bayes (NB). The tricks were classified through data obtained from both motion capture system (Vicon MX) as well as IMU sensors. The datasets were collected from a total of eleven skateboarders within the range of  $23 \pm 4$  years of age, and  $179 \pm 5$  cm in height. In addition, the stances were segregated into two types of goofy and regular with five and six skaters, respectively. The findings suggest that RBF-SVM classifier provided the best classification with an accuracy of 89.1%.

Groh et al. [8], in an earlier study, classified six skateboarding tricks, namely Ollie, kickflip, nollie, pop shove-it with the addition of 360-flip and heelflip by utilizing four different machine learning models, viz. NB, SVM, radial basis kernel kNN and Partial Decision Tree (PART). The images were recorded by Panasonic Lumix DMC-FT5 digital camera and IMU sensors as well. The study mainly focuses on seven male athletes within the age range of  $25 \pm 4$  years old in which four of them possessing a goofy stance and the remaining three are regular. The classification evaluation was performed using Embedded Classification Software Toolbox (ECST) by Weka. The SVM and NB models both demonstrated reasonably accurate classification accuracy of 97.8%.

The classification of snowboarding tricks [9] was carried out by utilizing GoPro Hero3+ camera as well as IMU sensors, which has inherent similarities with skateboarding. Nine experienced male snowboarders (age:  $19 \pm 9$ ) were recruited for the study. The types of tricks evaluated were Ollie, standard jump, drop and step-up jump, respectively. It was shown from the study that the SVM model evaluated is able to provide a classification accuracy of 80.5%.

The paper aims to evaluate a number of classifiers, notably SVM, kNN, LR, RF and NB on their ability in classifying a number of skateboarding tricks, i.e. Nollie, Ollie, Shove-it, Kickflip and Frontside 180 based on features engineered via the Inception-V3 image embedder. The preliminary results from this investigation could provide an insightful quantitative based evaluation for the judges along with assisting the athletes themselves in improving their skills.

## **2 Methodology**

### **2.1 Experimental Setup**

The YI Action Camera with Full HD 1080p 60 frames per second was used to record the skateboarding tricks (Fig. 1). The specifications of the camera are tabulated in Table 1, whilst the experimental setup, with regards to the camera orientation, is depicted in Fig. 2.

### **2.2 Data Collection**

The test subject used in this study is a male skateboarder with seven years of experience recruited from the University Malaysia Pahang (UMP) skate park. The height and weight of the subject is 170 cm and 54 kg, respectively. As mentioned earlier, five distinctive tricks were performed, as shown in Table 2 and are repeated five times for each trick. The tricks were selected according to the skateboarder's capability and by performing a goofy stance as the rotational axis reference.

### **2.3 Image Processing**

The video of the tricks was recorded from the YI Action Cam. The extraction of the video was carried out using VLC media player 2.2.6. The video that is subsequently used for the image extraction process was taken for a period between 2 and 3 s (the execution of the trick only). It is worth noting that unrelated video scenes were ignored. The videos were then processed by using the video to jpg converter v. 5.0.101 to obtain the frame per frame images. The extraction of the images was set to 30 frames per video. A total of approximately 750 images were extracted from the 25 videos captured for the tested tricks.

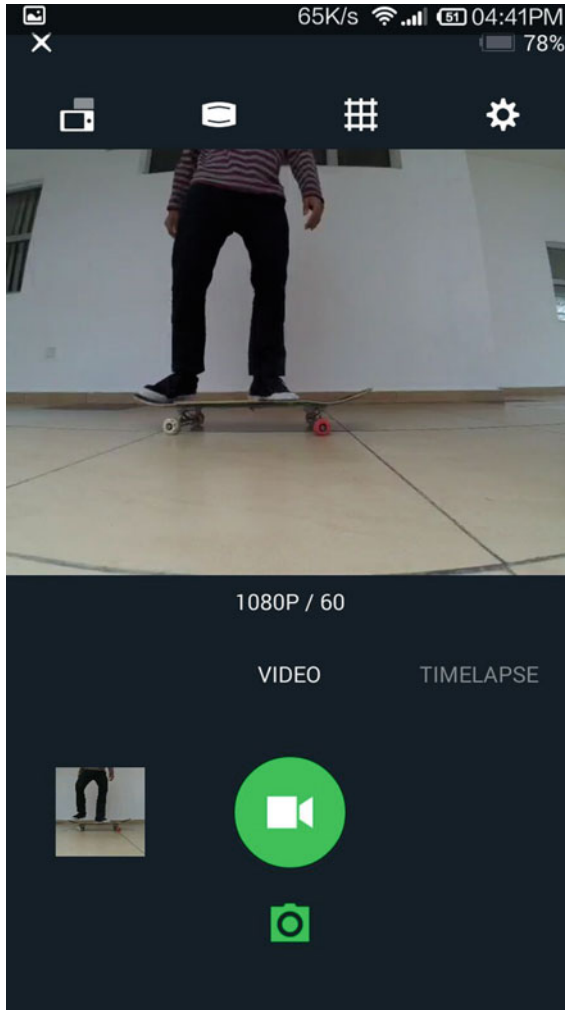


**Fig. 1** The interface of the YI Action Camera Official App

**Table 1** Specification of the YI Action Camera

Specifications	Description
Model	YI Action Camera
Lens	F2.8 aperture/155° wide-angle lens
Resolution	Full HD videos 1920 × 1080 (60 FPS)
Dimension	60 × 42 × 21 mm
Weight	72 g

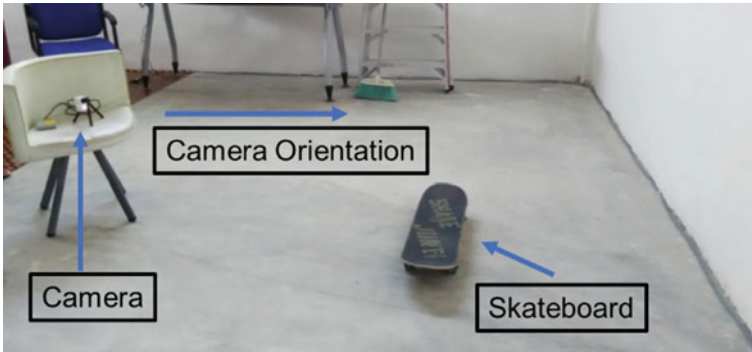


Fig. 2 Experimental setup

### 2.4 Machine Learning



**Image Embedding** Inception-v3 is used in the present investigation owing to its capability in providing a series of image descriptors or feature vectors [10]. It is a form of transfer learning that is based on the notion of convolution neural networks.

Table 2 Description of the tricks class

Tricks	Description	Figure
Ollie (O)	The skater “pops” (striking to the ground) the tail of the board down whilst jumping and slid the nose of the skateboard to achieve lift-off in order to make the board “pop” into the air	A photograph of a skater in a black t-shirt and dark pants performing an ollie. The skater is in mid-air, with their arms outstretched for balance. The skateboard is visible below their feet, appearing to be in motion. The background is a plain, light-colored wall.



(continued)

**Table 2** (continued)

Tricks	Description	Figure
Nollie (NFS)	The opposite of an Ollie, the skater “pops” the nose of the skateboard down while jumping and slid the tail of the board to achieve lift-off in order to make the board “pop” into the air	
Front-side 180 (FS180)	An Ollie where the skater and his board rotate 180 degrees (front-side) after lift-off from the ground with the skateboard sticking to the skateboarder’s feet	

(continued)

**Table 2** (continued)

Tricks	Description	Figure
Pop Shove-it (PS)	A similar trick as the Ollie with a snap of the tail spinning the board clockwise about the vertical axis at 180° or 360° underneath the skater and lock it in mid-air	
Kickflip (K)	The skater Ollie the board into the air and then flips it fully 360° along the axis. Then landing the board approximate as its original position	



**Feature Selection** The features generated from the image embedding was then evaluated using the Rank Widget that is available in Orange Data Mining software V3.11. Five best features are selected by comparing different scoring methods namely Information Gain (expected amount of information), Information Gain Ratio (reduces the bias in information gain) and Gini Decrease (inequality of a frequency distribution).

**Classifier** Several machine learning models were implemented to examine its performance in classifying the skateboarding tricks, i.e., SVM, kNN, LR, RF, and NB. The default settings of the Orange platform are used for the classifiers. The machine learning models were assessed accordingly through the classification accuracy, specificity, sensitivity, recall, precision and F1-score. The cross-validation technique applied in the present study is the leave-one-out method.

### 3 Results and Discussion

A total of 40 trick events were carried out by the skateboarder, and the success rate of the landings was recorded. From the 40 tricks, only 25 tricks were found to be successful and the data (herein the images, i.e., 46 for FS180, 48 for K, 39 for NFS, 37 for O and 46 for PS) obtained were then used to develop the machine learning models.

It can be ascertained from the Table 3, that the SVM and the LR model provided higher classification accuracies (CA) with 99.5 and 98.6% each, compared to the other classifier of kNN, RF and NB with a CA of 95.8%, 8.24%, and 7.87%, respectively. In addition, the confusion matrix of both the SVM and LR models illustrated in Figs. 3 and 4, respectively, revealed that the misclassification recorded by the SVM model came from the Pop Shove-it trick images that was recorded as Ollie, whereas LR model recorded the misclassification of Pop Shove-it (PS) images, again that was misclassified as Nollie Front Shove (NFS) and Ollie (O) images, respectively. The misclassification of PS on to O in Fig. 3 may due to the orientation of the skateboard where the vertical axis has difficulties in discriminating the counter-clockwise motion. In Fig. 4 the PS trick was misclassified as NFS as the skateboard tail (back of the board) has a small gap with the skater's foot during lift off [5]. The following conclusion can be drawn from the present preliminary investigation,

**Table 3** Performance evaluation of the classifiers

Method	AUC	CA	F1	Precision	Recall
SVM	1.000	0.995	0.995	0.995	0.995
Logistic regression	1.000	0.986	0.986	0.987	0.986
kNN	0.997	0.958	0.958	0.961	0.958
Random forest	0.962	0.824	0.822	0.824	0.824
Naïve Bayes	0.943	0.787	0.787	0.800	0.787

**Fig. 3** Confusion matrix of the SVM classifier

		Predicted					Σ
		FS180	K	NFS	O	PS	
Actual	FS180	46	0	0	0	0	46
	K	0	48	0	0	0	48
	NFS	0	0	39	0	0	39
	O	0	0	0	37	0	37
	PS	0	0	0	1	45	46
Σ		46	48	39	38	45	216

**Fig. 4** Confusion matrix of the logistic regression classifier

		Predicted					Σ
		FS180	K	NFS	O	PS	
Actual	FS180	46	0	0	0	0	46
	K	0	48	0	0	0	48
	NFS	0	0	39	0	0	39
	O	0	0	0	37	0	37
	PS	0	0	1	2	43	46
Σ		46	48	39	38	45	216

i.e., that the combination of the distinctive features obtained through the Inception V3 image embedder with various classifiers is capable of providing reasonably well classification accuracy in distinguishing the skateboarding tricks.

### 4 Conclusion

The following conclusions can be drawn from the present preliminary study, where a post-processing skateboarding tricks classification system was developed via image processing. It was demonstrated from the study that the features extracted by the Inception V3 image embedder are vital in contributing to a reasonable classification accuracy of the appraised skateboarding tricks. Furthermore, the findings suggest that both the SVM and LR model performed at a high CA of 99.5% and 98.6%, respectively. The present investigation will be further investigated by evaluating different image embedders, namely VGG-16 and VGG-19, amongst others apart from optimizing the hyperparameters of different machine learning models. Taken together, these preliminary results suggest that the appropriateness of the suggested system in producing a quantifiable based verdict on skateboarding tricks as opposed to the conventional subjective techniques that are currently being applied in this sport.

**Acknowledgements** The authors would like to gratefully acknowledge Universiti Malaysia Pahang for supporting this study via RDU190328.

## References

1. Corrêa NK, de Lima JCM, Russomano T, dos Santos MA (2017) Development of a skateboarding trick classifier using accelerometry and machine learning. *Res Biomed Eng* 33:362–369
2. Musa RM, Majeed APA, Taha Z, Chang SW, Nasir AFA, Abdullah MR (2019) A machine learning approach of predicting high potential archers by means of physical fitness indicators. *PLOS ONE* 14:e0209638
3. Taha Z, Razman MAM, Adnan FA, Majeed APA, Musa RM (2017) The development of the putt. it. in monitoring device and the establishment of its reliability: a solution for putting-in analysis in Golf. *Mov Health Exerc* 6
4. Taha Z, Wong MY, Yap HJ, Abdullah A, Yeo WK (2018) Evaluation of real time motion tracking accuracy of customised IMU sensor for application in a mobile badminton virtual reality training system. *MoHE* 7
5. Groh BH, Fleckenstein M, Kautz T, Eskofier BM (2017) Classification and visualization of skateboard tricks using wearable sensors. *Pervasive Mobile Comput* 40:42–55
6. Taha Z, Razman MAM, Adnan FA, Abdul Ghani AS, Abdul Majeed APP, Musa RM, Sallehudin MF, Mukai Y (2018) The identification of hunger behaviour of lates calcarifer through the integration of image processing technique and support vector machine. In: *IOP conference series: materials science and engineering*
7. Pavey TG, Gilson ND, Gomersall SR, Clark B, Trost SG (2017) Field evaluation of a random forest activity classifier for wrist-worn accelerometer data. *J Sci Med Sport* 20:75–80
8. Groh BH, Kautz T, Schuldhuis D (2015) IMU-based trick classification in Skateboarding. *KDD workshop on large-scale sports analytics*
9. Lee TJM (2015) Feature extraction and classification of skiing/snowboarding jumps with an integrated head-mounted sensor. Doctoral dissertation, Applied Sciences: School of Mechatronic Systems Engineering
10. Szegedy C, Vanhoucke V, Ioffe S, Shlens J, Wojna Z (2016) Rethinking the inception architecture for computer vision. In: *2016 IEEE conference on computer vision and pattern recognition (CVPR)*, pp 2818–2826

# Review and Analysis of Risk Factor of Maternal Health in Remote Area Using the Internet of Things (IoT)



Marzia Ahmed, Mohammad Abul Kashem, Mostafijur Rahman and Sabira Khatun

**Abstract** IoT is the greatest ingenious innovation in the modern era, which can exploit also in mission-critical like the healthcare industry. This paper demonstrates effective monitoring of pregnant women mostly in a rural area of a developing country, with the help of wearable sensing enabled technology, which also notifies the pregnant women and her family about the health conditions. There are many researchers have been researched to reduce the maternal and fetal mortality but the mortality rate is not reducing, where it should be in zero tolerance. This research intended to use machine learning algorithms for discovering the risk level on the basis of risk factors in pregnancy. In this research, an existing dataset (Pima-Indian-diabetes dataset) has been used for the analysis of risk factor and comparison of some machine learning algorithm shows that Logistic Model Tree (LMT) gives the highest accuracy in case of classification and prediction of the risk level. Regardless, few selected pregnant women's data has been collected (through IoT enabled devices) and the same process also applied for this dataset also by using LMT. Comparison results show that the prediction of risks is the same for the existing and real dataset.

**Keywords** Maternal risk factors · Internet of things · Wearable sensors

## 1 Introduction

Most of the pregnant women, die from the known and preventable complications of pregnancy and childbirth, live in low- and middle-income as such as developing countries who are ignorant about the risks factors that cause maternal mortality [1, 2]. Consistently, pregnancy should be monitored for making sure the healthy

---

M. Ahmed (✉) · M. A. Kashem

Department of Computer Science and Engineering, Dhaka University of Science and Technology, Gazipur, Dhaka, Bangladesh

M. Ahmed · M. Rahman

Department of Software Engineering, Daffodil International University, Dhaka, Bangladesh

S. Khatun

Faculty of Electrical and Electronics Engineering, University Malaysia Pahang, Gambang, Malaysia

© Springer Nature Singapore Pte Ltd. 2020

A. N. Kasruddin Nasir et al. (eds.), *InECCE2019*, Lecture Notes in Electrical Engineering 632, [https://doi.org/10.1007/978-981-15-2317-5\\_30](https://doi.org/10.1007/978-981-15-2317-5_30)

development of fetal and the safe delivery of the infant. Regardless, the greater portion of pregnancy-related devices is placed in health complex for being expensive and in consequence, passing through all the difficulties as proper transport, huge traffic jam, ruthless weather, environment pollution, extended queues to attain regular checkup in hospital [3]. Pregnancy-related complications will be possible to diminish by classifying risk factors, which is essential at the early stage of the symptoms [4]. The objective of this research is to provide efficacious care for pregnant women mostly living in a rural area by using smart technology based on IoT.

The IoT is the integration concept of all devices which are readable, addressable recognizable, locatable and manageable via the Internet through RFID (Radio-Frequency Identification), wireless local area network, wide area network, etc. Additionally, it provides real-time information and interacts with real-time users. The hardware layer is responsible for the interconnection between the physical devices through the sensors where miniaturization can be a challenge and in communication layer, lots of devices are connected in a network where bandwidth and electromagnetic spectrum may be a challenge that can be a barrier to transfer data effectively and efficiently. However, Internet of Things is an important medium for data transfer through the hardware layer with full communication between Person to Person and machine to machine, for improving the health monitoring system for patients [5].

This approach is an attempt to resolve a maternal healthcare problem presently the non-urban area of developing countries is facing. The foremost objective of this paper was to design a remote healthcare system to reduce the complications during pregnancy as well as the birth of an unborn child. It's encompassed three main parts. First one is finding patient's relevant medical data using IoT based medical sensors; second, processing the collected data for predicting maternal health status and the last part was transferring the collected data to medical experts for remote viewing that enables the medical team to monitor the mother and fetal health progress away from hospital premises.

Wearable sensing devices name as Radio Frequency Identification (RFID) tags in Body Area Network (BAN) will be connected by Bluetooth/ZigBee with Personal Area Network (PAN) and the database will be updated for getting monitored in anytime-anywhere, by the medical staffs.

## **2 Analysis of Risk Factor during Pregnancy**

### ***2.1 Literature Search and Selecting Risk Factors Intensity***

Analyzing medical profiles such as age, weight, blood pressure, existing health condition, heart rate, body temperature, physical activity, etc. these parameters and corresponding values and their intensity of risks for that specific patients can be predictable. It enhances knowledge about the risk level of women in pregnancy, e.g.

patterns of risk, relationships between medical factors related to pregnancy and precautions. Table 1 summarizes the level of risk parameters in pregnancy and their values, weights with references. Initially, analyzing these very basic medical factors in pregnancy to find out the risk level as well as the worst case of these factors.

**Table 1** Pregnancy-related medical parameters with corresponding values and their weights

Parameters	Low	Mid	High	References
Blood pressure	Systolic 120–139 mm Hg, diastolic 80–89 mm Hg	Systolic 140–159 mm Hg, diastolic 90–99 mm Hg	Systolic 160 mm Hg or greater, diastolic 100 mm Hg or greater	[6]
Heart rate	Heartbeat 75–80 bpm	Hear beat 90–140 bpm	Heartbeat >70 and <140 bpm	[7]
Body temperature	Averages about 98.6 F (37 °C)	<98.6 F (37 °C) and > 102 F (38.9 °C)	102 F (38.9 °C) or higher and (>35 °C or > 95 F) = Hypothermia	[8]
Fetal movement	10 movements such as kicks, flutters, or rolls. within 12 h; 6 k/2 h	10 movements flutters, or rolls. within 12 h; 6 k/2 h	>10 movements such as kicks, flutters, or rolls. within 12 h; >6 k/2 h	[8]
Age	20–29	30–35	35–45	[9]
BMI	(18.5–24.9 kg/m <sup>2</sup> )	(18.5–24.9 kg/m <sup>2</sup> )	Underweight (18.5 kg/m <sup>2</sup> ) overweight (25–29.9 kg/m <sup>2</sup> ), obese (30–34.9 kg/m <sup>2</sup> )	[9]
Blood glucose (2-h glucose)	<7.8 (<140) mmol/l (mg/dl)	<7.8 (<140) and ≥ 7.8 (≥ 140) mmol/l(mg/dl)	≥ 11.1 (≥200) mmol/l (mg/dl)	[10]
Blood glucose (Fasting glucose)	<6.1 (<110) mmol/l(mg/dl)	≥6.1 (≥ 110) and < 7.0(<126) mmol/l(mg/dl)	≥7.0 (≥ 126) mmol/l(mg/dl)	[10]
Blood glucose (HbA1c)	<42 mmol/mol	42–46 mmol/mol	≥48 mmol/mol	[10]

## 2.2 Analyzing the Common Risk Parameters from an Existing Diabetes Dataset for Women

In this research an existing dataset has been used [10]. Since the dataset was prepared for the diabetes patients and after analyzing it is found that some of the risk factors are common and after preprocessing and filtering this dataset, it is included into risk intensity level and categorized the risk according to the literature search and with the help of medical experts.

One of the data mining software named Waikato Environment for Knowledge Analysis (Weka), developed by ‘University of Waikato’ in New Zealand, which contains a large number of algorithms and imagining tools for data preprocessing and predicting the accuracy of the new model. It supports data mining tasks such as classification, regression, visualization, clustering, and feature selection. [10]

Two functionalities of ‘weka’ are focused, first one is for mining information from existing medical datasets; and another is to classify the risk level accurately with the help of machine learning algorithm for better prediction of the risk level. Fig 1 shows the comparisons of machine learning algorithms belongs to different types of groups to observe which part will provide better classification accuracy through the existing dataset.

LMT (logistic model tree) is one of the algorithms under the trees group of machine learning algorithm has the highest accuracy almost 98%. The classifier for constructing ‘logistic model trees’, which are classification trees with logistic regression functions at the leaves. One of the more convenient ways to deal with classification tasks is the combination of the logistic regression models and a tree structure in a single tree. Therefore, using logistic regression estimates class probability rather than just a classification. The algorithm can deal with binary and multi-class target variables, numeric and nominal attributes and missing values.

**Fig. 1** Comparisons between machine learning algorithms

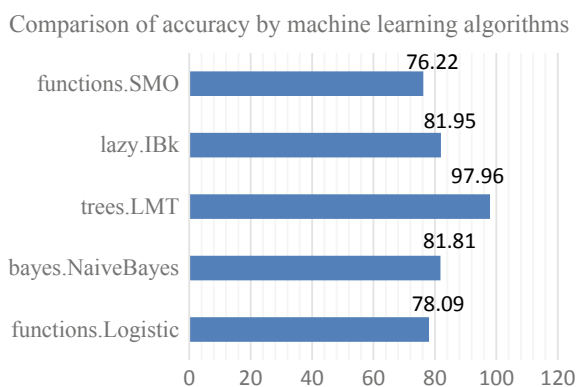
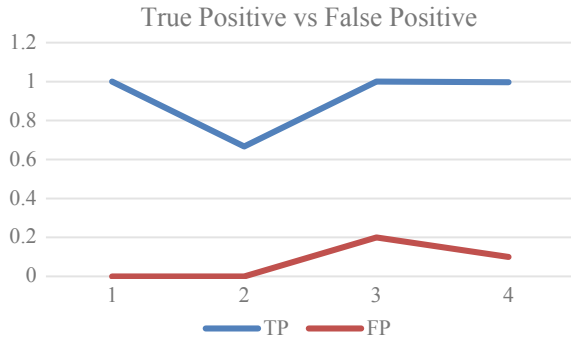


**Fig. 2** The detailed outcome of LMT for real dataset



### 2.3 Analyzing Sample Real Data to Explore the Status of Accuracy

Selected sample data are collected through IoT enabled devices and verified by a medical expert to provide the notification to the pregnant women and family about her risk level and health conditions.

The following algorithms are using for determining the classification of risk level accuracy. Few selected pregnant women’s data have been collected and with the help of medical experts, the risk level is determined that whether it is high, mid or low. Fig 2 shows the accuracy of correct identification of risk level in pregnancy for the given dataset of risk parameters. Among the entire machine learning algorithm, LMT provides the highest accuracy for correct classification in both training set data and cross folding validations.

At last, our proposed approach obtained 90% accuracy for the diagnosis of risks in pregnancy with faster training time and there is no misclassification in prediction because false positive (FP) and false negative (FN) is almost zero that shows in the below Fig. 2.

## 3 The Experimental Result Over Pima-Indians-Diabetes Data Set

### 3.1 Classification Accuracy

In Fig. 3 LMT is applied in the existing dataset and got almost 98% accuracy. LMT is the combination of logistic regression and tree induced machine learning algorithm. In the y-axis of this bar chart representing the risk intensity level of the existing dataset that is labeled as 3 instead of mid-level risk, 2 instead of low-level risk and 1 instead of a high-level risk for the better representation of the result.



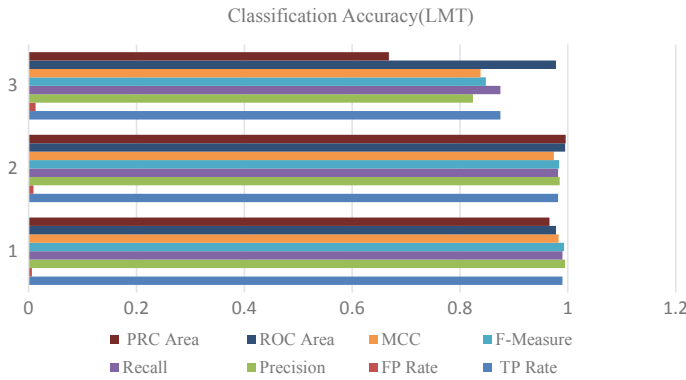


**Fig. 3** Classification accuracy summary for an existing dataset

Confusion matrix for this dataset representing the false positive and true positive rate clearly where the false positive rate is very low that maximizes the accuracy and performance of this algorithm.

Confusion matrix		High	Low	Mid
Predicted class	Low	<b>408</b>	0	4
	Mid	0	<b>271</b>	5
	High	2	4	<b>42</b>

### 3.2 Making Prediction

Prediction of risk level is determined by LMT without any errors which are shown in Fig. 4. The model has been trained by the existing dataset and five new patients' data has been supplied as test data. Evaluating the model on current test data using LMT predict the risk level accurately according to our standard categorization of risk level in Fig. 4.

**Fig. 4** Prediction of risk level using LMT

== Predictions on user test set ==				
inst#	actual	predicted	error	prediction
1	1:?	1:High		1
2	1:?	2:low		1
3	1:?	1:High		1
4	1:?	2:low		1
5	1:?	1:High		1

## 4 Proposed System Model

### 4.1 Integrated Model

Timely diagnosis and proper medication of pregnant women is the critical process during pregnancy. This proposed model attempts to provide better and real-time medical care with lower cost and easier. Fig 5 shows the proposed system model.

Reducing maternal mortality and taking care of pregnant women in rural areas is the primary goal of our proposed system model. Mostly, non-portable, sophisticated and expensive devices are used by the hospitals. Development of a compact assist system is the main goal of our proposed system model for accessing and assessing the vital signs such as blood pressure, physical activity, heart rate of rural pregnant women and the movement count, heart rate of the fetus with the help of RFID tags also named as wearable sensing devices. The continuous medical data will be stored in a database for analyzing. Finally, pregnant women and the respective doctor will get a notification for the patient’s current health status.

### 4.2 Model of IoT Device

The developed system in Fig. 6 represents the temperature, pulse and heart rate reading of patients properly.

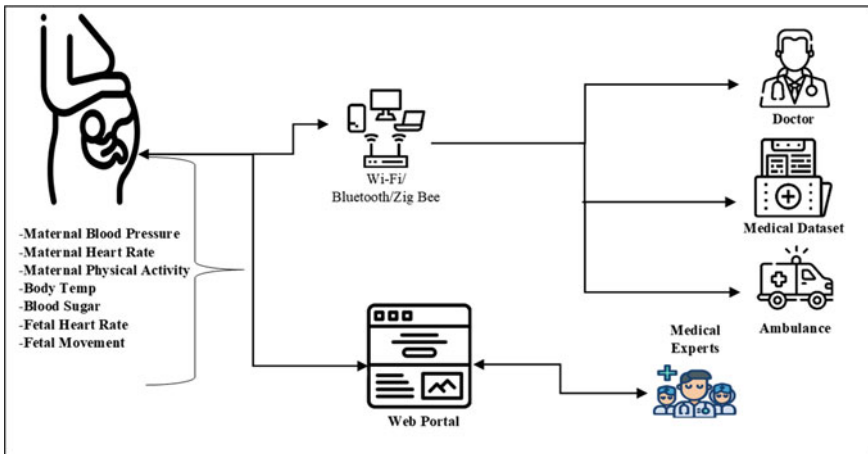
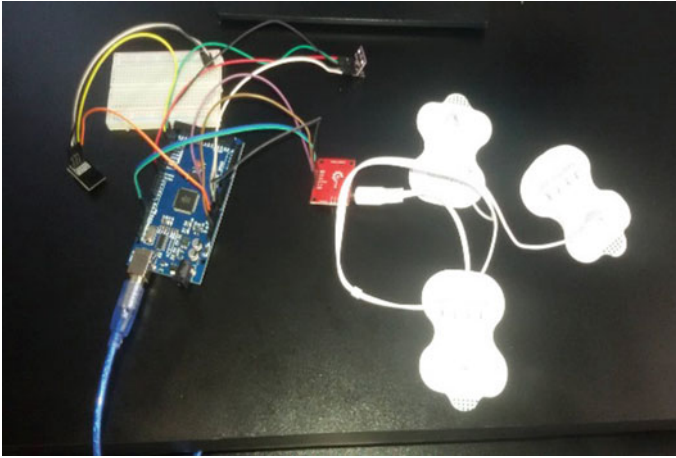


Fig. 5 Proposed system model



**Fig. 6** Reading heart rate, pulse data using Arduino mega 2560, ECG

## 5 Conclusion

In this research, different risks factors are identified and categorized with the help of medical experts. Machine learning algorithms have been used to classify and predict the risk level of an existing dataset. The result of the prediction has been coordinated with the selected sample data collected through the IoT enabled devices. The outcomes of this coordination have shown that prediction of risk level has been successful in both cases without any errors. Crowd sourcing approach can be adopted in this research for broadcasting risk factors to analyze and to provide better health monitoring for the patients and their family.

**Acknowledgements** Thanks to Dr. Shirin Shabnam for helping to prepare the categorization of risk parameter in a pregnancy-related medical dataset on the basis of intensity.

## References

1. Talpur MSH, Shaikh MH, Buriro RA, Talpur HS, Talpur F, Shafi H, Shaikh MA (2014) Internet of things as intimating for pregnant women's healthcare: an impending privacy issues. *Indonesian J Electr Eng Comput Sci* 12(6):4337–4344
2. Say L, Chou D, Gemmill A, Tunçalp Ö, Moller AB, Daniels J, Gülmezoglu AM, Temmerman M, Alkema L (2014) Global causes of maternal death: a WHO systematic analysis. *Lancet Glob Health* 2(6):e323–e333
3. Lyu P, Peng M, Lyu Y, Chen Y, Yang J (2013) A multi-communication-fusion based mobile monitoring system for maternal and fetal information. In: *IEEE 15th international conference on e-Health networking, applications and services (Healthcom)*. IEEE, pp 559–563

4. Bauserman M, Lokangaka A, Thorsten V, Tshetu A, Goudar SS, Esamai F, Garces A, Saleem S, Pasha O, Patel A, Manasyan A (2015) Risk factors for maternal death and trends in maternal mortality in low-and-middle-income countries: a prospective longitudinal cohort analysis. *Reprod Health* 12(2):S5
5. Megalingam RK, Pocklassery G, Thulasi AA, Jayakrishnan V, Mourya G, Nair MS (2015) Integrated embedded system for pre-natal health care. *Procedia Comput Sci* 57:313–322
6. Gomez J, O B, Zhuma E (2016) Patient monitoring system based on internet of things. *Procedia Comput Sci* 83:90–97
7. Kenny LC, Lavender T, McNamee R, O’Neill SM, Mills T, Khashan AS (2013) Advanced maternal age and adverse pregnancy outcome: evidence from a large contemporary cohort <https://doi.org/10.1371/journal.pone.0056583>
8. Ali S, Dornhorst A (2011) Diabetes in pregnancy: health risks and management. *Postgrad Med J* 87:417–427. <https://doi.org/10.1136/pgmj.2010.10915>
9. Pima Indians Diabetes Database, <https://raw.githubusercontent.com/jbrownlee/Datasets/master/pima-indians-diabetes.names>, 22 June 2019
10. Weka 3, <https://www.cs.waikato.ac.nz/ml/weka/> 23 June 2019

# Recent Trends and Open Challenges in EEG Based Brain-Computer Interface Systems



**Mamunur Rashid, Norizam Sulaiman, Mahfuzah Mustafa, Sabira Khatun,  
Bifta Sama Bari and Md Jahid Hasan**

**Abstract** Recent advances in computer hardware and signal processing have made possible the use of electroencephalogram (EEG) for communication between human brain and computers and this technology is known as brain-computer interface (BCI). Locked-in patients have now a way to communicate with the outside world using BCI technology. Nowadays, BCIs are getting popularity among the researchers to control devices using brainwaves especially in providing good assistance to disabled people. Impressive development and integration of both hardware and software in BCI have been carried out in the last two decades. However, some open challenges and limitations have also been exposed in the previous researches. In this paper, we have tried to mention some critical issues of EEG based BCI system including EEG modalities, EEG acquisition, signal processing algorithm and performance evaluation. These issues need to be solved to develop error-free BCI system. In addition, possible solutions and future directions have also been discussed.

**Keywords** Electroencephalogram (EEG) · Brain-Computer interface (BCI) · Brain-Machine interface (BMI) · Assistive technology

---

M. Rashid (✉) · N. Sulaiman · M. Mustafa · S. Khatun · B. S. Bari  
Faculty of Electrical and Electronics Engineering, Universiti Malaysia Pahang, 26600 Pekan,  
Pahang, Malaysia

N. Sulaiman  
e-mail: [norizam@ump.edu.my](mailto:norizam@ump.edu.my)

M. Mustafa  
e-mail: [mahfuzah@ump.edu.my](mailto:mahfuzah@ump.edu.my)

S. Khatun  
e-mail: [sabirakhatun@ump.edu.my](mailto:sabirakhatun@ump.edu.my)

M. J. Hasan  
Faculty of Mechanical and Manufacturing Engineering, Universiti Malaysia Pahang, 26600  
Pekan, Pahang, Malaysia

## 1 Introduction

Brain-computer interface (BCI) aims to provide a direct communication pathway between brain and external devices [1, 2]. In recent years, this new brain-computer interaction method has attracted people's attention for its potential applications in rehabilitation engineering, intelligent assistive robot and so on [3]. More specifically, it is very helpful to assist people with damaged motor functions, or completely paralyzed people. Currently, BCIs are employed in many non-medical fields such as gaming, virtual reality control, biometric identification etc. It is an interesting, vibrant and highly interdisciplinary research topic which involves medicine, psychology, neurology, signal processing and machine learning. Despite its expected success, BCI needs to overcome some technical difficulties as well as challenges. Abdulkader et al. [4] introduced usability and technical challenges of BCI system. In usability challenges, they discussed the issues related to the training process and information transfer rate. On the other hand, in technical challenges, they listed some issues including on Non-linearity, non-stationary and noise, small training sets and high dimensionality curse. Ramadan et al. [5] stated elaborately some of the BCI challenges including BCI standards, participants and stable classifications, non-linearity and non-stationarity in EEG, information transfer rate (ITR), data acquisition sensors, real-life applications, ethical issues, privacy and security, and agreement of the future directions. Another recent article in [6] discussed comprehensively potential problems with EEG-based BCI systems, and possible solutions are also proposed. In this paper, we have investigated the common challenges in both offline and online BCI system from a variety of perspectives. We have also recommended some possible solution to overcome these limitations. This paper is organized as follows: Sect. 2 introduces recent advancements in BCI system; Sect. 3 states the challenges in BCI system with possible solutions and finally, the paper concludes in Sect. 4.

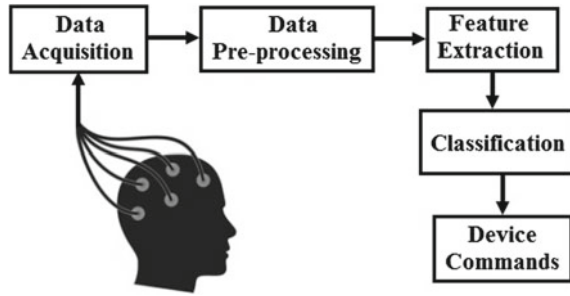
## 2 Recent Advancements in BCI System

BCI technology may enable the human being to communicate with external devices using brainwaves or EEG signals without involving physical contact with the devices [7]. A BCI model consists of five components which are signal acquisition, preprocessing, feature extraction, classification and control interface. Figure 1 illustrates a typical block diagram of EEG based BCI system.

### 2.1 Data Acquisition for BCI

A BCI system requires EEG signals directly from the human brain and the capturing of EEG can be done in 2 different ways; (i) invasive and (ii) non-invasive. The

**Fig. 1** Block diagram of BCI system



invasive of EEG capturing is described by placing EEG electrodes on the surface or deep inside the brain in order to obtain high quality of EEG signals, however, this method causes high inconvenience to human and might create risks to human health. Hence, due to the evolution in the EEG technology, researchers have come out with a more convenient and safe method to obtain EEG signal by inventing noninvasive technique to place the EEG sensors on the scalp of human's head [7, 8]. This technique still can capture high quality of EEG signals without causing risk to human's health. Therefore, non-invasive BCIs are more convenient and preferable by researchers to obtain EEG signals. Here, there are various non-invasive methods to measure the brain activity of human's cognitive state such as positron emission tomography (PET), functional magnetic resonance imaging (fMRI), functional near-infrared spectroscopy (fNIRS) and Magnetoencephalography (MEG) [8]. Among them, EEG is the most prevalent method of signal acquisition for BCI application due to the portability, low cost and user-friendly. Moreover, due to the vast temporal resolution of EEG recording, it is capable of capturing changes in neural activity that occur within a few milliseconds [9, 10].

## 2.2 EEG Modalities Used in BCI

Different EEG modalities are used in the BCI system. Among them, Steady-state Evoked Potentials (SSEP), P300 and motor imagery are the most preferable modalities by researchers. Steady state evoked potentials (SSEP) which are evoked by a modulated stimulus and stimulation frequency can cause an increase in neural activities. Here, the stimulation could be done either visually, auditory and somatosensory respectively. For example, the steady-state visually evoked potentials (SSVEP) occurred from the stimulation of the brain cognitive state using visual stimulus. In addition, an auditory evoked potentials (SSAEP) occurred by applying audio stimulus on the neural state. Meanwhile, the stimulation of a sensory pathway will produce a steady state somatosensory evoked potential (SSSEP) [11]. P300 is an event related potential (ERP) which evoked potentials are positive peaks in the EEG due to infrequent auditory, visual, or somatosensory stimuli. P300 occurred during the process

of decision making. The P300 responses are revealed about 300 ms after attending to an oddball stimulus among several frequent stimuli [12, 13]. Researchers have confirmed that the less probable of the stimulus, the larger the amplitude of the response peak [13]. In addition, the use of P300-based BCI does not require any training. However, the performance may be reduced because the user can get used to the infrequent stimulus and consequently, P300 amplitude might be decreased [13]. Here, the P300-based BCI provides an extremely low rate of information transmission because the classifier based on an average is too simple, and cause the poor accuracy of P300 potential detection [14]. Motor imagery is defined as the imagination of kinaesthetic movements of the left hand, right hand, foot and tongue. During the motor imagery, distinct mu/beta event-related (de)synchronization phenomena are generally shown around the motor cortex, which can be employed for the classification of an individual's intention [15].

### ***2.3 Data Pre-Processing***

Pre-processing of EEG signal is required in BCI to eliminate artifacts and noises because EEG signals are weak and can be contaminated easily with eye blinking, eye movement, heart activity, muscles and from the instrument itself such as EEG sensors or recording systems [5, 9, 10, 16]. Therefore, the clean EEG signals are required in order to secure the correct features which later will be classified by the classifier and increase the classifier performance. Here, the popular preprocessing techniques that are employed by researchers are Principle Component Analysis (PCA), Common Average Referencing (CAR), Surface Laplacian (SL), Adaptive Filtering (AF), and Independent Component Analysis (ICA) [9, 10, 16].

### ***2.4 Feature Extraction and Classification***

Here, feature extraction and classification methods definitely play a vital role in any EEG based BCI systems since for any incorrect selection of the EEG features and misclassification will cause wrong commands given to the devices. As a result, the BCI system might malfunction and cause harm to disabled people. In order to obtain excellent classification results, an effective method of feature extraction is required [5, 16]. There are various features used for different designs and applications of BCI systems. Among these, the prevalent features are principal component analysis (PCA), independent component analysis (ICA), band power spectrum (BP), power spectral density (PSD) values [17], energy spectral density (ESD) values, spectral centroid values, spectral entropy, cerebrospinal fluid (CSF), wavelet transformations (WT), wavelet packet decomposition (WPD), autoregressive (AR), adaptive autoregressive (ARR) parameters, fast Fourier transform (FFT) and short-time Fourier transform (STFT) [18]. Nowadays, applying a combination of EEG features is a



new trend for BCI applications. In addition, several experiments have shown that a combined set of features can produce a better classification performance rather than using feature independently [18]. After features have been selected and extracted using feature extraction techniques, the extracted vectors are fed and classified into various classifiers. Here, the most preferred classifiers by researchers in BCI application are Artificial Neural Network (ANN), k-Nearest Neighbor (k-NN) [19], Linear Discriminant Analysis (LDA) and Support vector machine (SVM) [20], Multi-Layer Perceptron (MLP) and Hidden Markov Models (HMM) [21].

## 2.5 EEG Based BCI Technologies

BCIs offer their users new communication and control channels without any intervention of peripheral nerves and muscles. Hence, BCI researchers are trying to build such BCI applications that could be helpful to physically disabled patients. BCI speller is one of the first BCI application to enable communication for people with severe disabilities. The speller systems are categorized according to major BCI paradigms: P300, steady-state visual evoked potential (SSVEP), and motor imagery (MI) [22]. However, P300 is widely using by the BCI researchers in BCI spelling. Recent developments and studies in BCI technologies have facilitated emotion detection and classification [23, 24]. The goal of the emotion classification is to recognize the emotional state of interest into a number of emotional feature inputs. User mental state recognition using EEG can be used to detect the driver's drowsiness level [25]. BCI researchers have attempted to developed brain control electric wheelchair in order to restore the mobility for disabled peoples and some remarkable improvements have been achieved in the last 10 years [26]. The Robotic arm is another non-invasive and cost-effective application for disabled people that can also be controlled by the neurophysiological signals with the help of BCI technology [27]. Other EEG based BCI applications are environment control [28], person authentication system [29], stress detection [30], age and gender classification [31], cursor control [32] and virtual reality and game [33] etc. Table 1 gives a summary of some EEG based BCI application.

## 3 Challenges in BCI System with Possible Solutions

Despite the significant advances in BCI technology, there are still many challenges to the real world BCI control, for example, absence of standard data acquisition protocol, low information transfer rate (ITR), BCI system cannot be operated autonomously by disabled people, dissimilar performance evaluation metric of BCI, etc.

**Table 1** Summary of EEG based BCI application

BCI application	Data acquisition	Methodology	Performance evaluation	Reference
BCI environment control	Modality: ERP No. of subject: 3	Classifier: BLDA	Average accuracy: 89.2%	[28]
BCI environment control	Modality: ERP No. of subject: 10	Classifier: LDA	Average accuracy: 93.7%	[34]
Wheelchair control	Modality: P300 No. of subject: 5	Feature: moving average technique classifier: SWLDA	No. of command: 18 Success rate: 100% Path length: 39.3 m Time: 659 s	[35]
Wheelchair control	Modality: SSVEP No. of subject: 9	Feature: PSD Classifier: decision tree	No. of command: 4 Success rate: $83 \pm 15\%$ ITR: $70.3 \pm 28.8$ bit/min	[36]
BCI speller	Modality: P300 No. of subject: 4	Tree matrix speller: classifier: SWLDA	Success rate: 95% ITR: 12 bit/min	[37]
BCI speller	Modality: P300 No. of subject: 4	Multi phase spellers; Classifier: SVM	Success rate: 96.04% ITR: 13 bit/min	[38]
Emotion recognition	Stimulation: movie clips No. of subject: 6	Feature: PSD Classifier: LDA	Emotion type: positive and negative Classification accuracy: 91.77%	[39]
Emotion recognition	Stimulation: Photos No. of subject: 11	Feature: PSD Classifier: SVM	Emotion type: Positive and negative. Classification accuracy: 85.41%	[40]
Cursor control	Modality: P300 + MI No. of subject: 11	Feature: CSP Classifier: SVM	No of command: 4 Success rate: 93.99% Trial duration: 18.19 s	[41]
Cursor control	Modality: MI No. of subject: 5	Feature: PSD Classifier: SVM	No of command: 4 Classification accuracy: 81.22%	[32]

(continued)

**Table 1** (continued)

BCI application	Data acquisition	Methodology	Performance evaluation	Reference
Person authentication system	No of subject: 40	Feature: average ERP Classifier: CNN, NN	Classification accuracy: 97.7%	[29]
Age and gender classification	No of subject: 40	Feature: PSD Classifier: SVM	Success rate: Age: 96.04% Gender: 97.1%	[31]
Virtual reality and game	No. of subject 2 Modality: P300	Feature: Shannon entropy; Classifier: LDA	Average accuracy: 82%	[33]
Virtual reality and game	No. of subject 10 Modality: MI	Feature: CSP; Classifier: LDA	Average accuracy > 70%	[42]
Robotic arm control	No. of subject 4 Modality: MI	Feature: FFT; Classifier: SVM	Classification accuracy: 85.45%	[27]

### ***3.1 Absence of Standard Data Acquisition Protocol***

Data acquisition for BCI consists of two phases namely EEG headset and participant or subject. There are some issues regarding EEG headset that needs to be solved. First of all, most of the EEG headsets require gel or liquid on electrodes which are very uncomfortable for the user. Dry electrodes may solve this problem. Already, some dry electrodes are available in the market but these headsets contain very few electrodes and the procedure is not standardized yet. There are thousands of devices already developed by different companies for BCI application. The number of electrodes (for example 1, 3, 4, 8, 14, 16, 20, 24, 32, 64, etc.) is varied from headset to headset and these headsets are not compatible with each other. Hence, the number of electrodes should be standardized for the specific signal. The high cost of EEG headset is another challenge to make the BCI technology affordable to the disabled people around the world [43]. Hence, the price of the EEG headset should be as low as possible. Although, the targeted user of BCI technology is physically disabled people, data from healthy users with excellent skills have been used in almost all the experiments. Moreover, the number of subjects is also very insufficient in some experiment. Hence, experimental studies must be conducted with disabled people who actually need the BCI technology and in the meantime the number of participants in the experiment must be increased. A threshold number of subject including healthy and disabled patients should be recommended by the BCI community to make the data as well as BCI system validation. From the previous experiments, it is clear that there is no standard way of evoking EEG stimulation. Different methods of evoking EEG stimulation have been used by the authors. Moreover, there is no clear recommendation regarding the environment of data acquisition surroundings. All these issues should be cleared and standardized. If all the specific BCI experiments maintain the same standard then it will be very easy to compare as well as to choose the best one.

### ***3.2 Low ITR of BCI System***

Higher ITR is the primary requirement of any effective BCI system. It is one of the most used performance evaluation metrics of BCI systems. ITR of the BCI system depends upon three factors namely target detection accuracy, the number of classes, and target detection time [5, 44]. The target detection accuracy can be improved through enhancing the signal-to-noise ratio (SNR) and separability of multiple classes. For reducing the SNR, several methods are used in the preprocessing phase which is described in Sect. 2.3. Secondly, with high ITR, the number of classes will be increased and more complex applications will be developed. Several stimulus coding methods including TDMA, FDMA and CDMA have been adapted for BCI systems [37, 45, 46]. TDMA, for instance, is used with P300 to code the target stimuli. FDMA and CDMA have been adopted in the VEP based BCI systems. Finally,

reducing the target detection time is one of the objectives of BCI systems to enhance the ITR. To do so, adaptive methods could be a solution to reduce the target detection time such as ‘dynamic stopping’ method. In addition, machine learning methods based on single-trial classifications. Moreover, optimized stimulus presentation by reducing the duration of the ISI between two flashes in stimulus presentation [47].

### ***3.3 Lack of Autonomous Operation of BCI System/Expert Dependency of BCI System***

BCI systems cannot be used autonomously by disabled people, because BCI systems require assistants to set up electrodes or signal-receiving devices. Most of the BCI applications are at the research stage and they are not ready to be introduced into people’s homes for continuous use in their daily life. Hence, BCI systems should be capable of operation by the disabled patients autonomously without any assistance of experts. Moreover, these applications should be portable, comfortable and user-friendly.

### ***3.4 Dissimilar Performance Evaluation Metric of BCI System***

Different types of performance evaluation metrics are used by BCI researchers. Among them, classification accuracy (CA), Kappa value, confusion matrix, sensitivity, specificity, ROC curve, ITR, etc. are highly used metrics. Many articles used task-specific metrics, such as task completion time and number of successful trials, number of collision etc. It is almost impossible to compare the same types of BCI systems which are evaluated by the dissimilar performance metrics. Hence, BCI research community should recommend certain performance metrics for specific BCI application. For example, number of control command, types of control command, distance covered, the time required, number of collision, classification accuracy, average success rate, etc. can be used in BCI wheelchair control. If the same types of performance metrics are used in same types of BCI application, then the comparison between different BCI experiments will be easier.

## **4 Conclusions**

This paper has uncovered some open challenges of current EEG based BCI technology. Moreover, a brief overview of EEG based BCI system and some recent related researches have also been surveyed. It has been noted that many breakthroughs were achieved in BCI research over the last 20 years. A wide variety of signal features

and classification algorithms have been tested in the BCI design. Many studies have demonstrated the valuable accuracy of BCIs and provided acceptable information bit rate. In spite of the recent important advances in the BCI field, some issues still need to be solved. These issues include the absence of standard data acquisition protocol, low ITR of BCI system, BCI system cannot be used autonomously by disabled people, dissimilar performance evaluation metric of BCI, etc. Hence, BCI research community should recommend complete standards of different phases of the BCI system. These standards help to compare the same category of BCI application as well as to choose the most efficient one. Nowadays, interest in the BCI field is getting attraction by the researchers around the world which will bring benefits to the daily lives of disabled people. Therefore, BCI systems may become a new mode of human-machine interaction with levels of everyday use in the near future.

**Acknowledgements** The author would like to acknowledge the great supports by the Faculty of Electrical and Electronics Engineering as well as Universiti Malaysia Pahang for providing financial support through research grant, PGRS 190326.

## References

1. Birbaumer N (2006) Breaking the silence: brain? Computer interfaces (BCI) for communication and motor control. *Psychophysiology* 43:517–532
2. Wang X-Y, Jin J, Zhang Y, Wang B (2014) Brain control: human-computer integration control based on brain-computer interface. *Acta Autom Sin* 39:208–221
3. Nicolas-Alonso LF, Gomez-Gil J Brain computer interfaces, a review
4. Abdulkader SN, Atia A, Mostafa MSM (2015) Brain computer interfacing: applications and challenges. *Egypt. Informatics J.* 16:213–230
5. Ramadan RA, Vasilakos AV (2017) Brain computer interface: control signals review. *Neurocomputing*
6. Abiri R, Borhani S, Sellers EW, Jiang Y, Zhao X (2018) A comprehensive review of EEG-based brain-computer interface paradigms. *J Neural Eng*
7. Stamatto Ferreira AL, Cunha de Miranda L, Cunha de Miranda EE, Gomes Sakamoto S A survey of interactive systems based on brain-computer interfaces
8. He B, Gao S, Yuan H, Wolpaw JR Brain-computer interfaces
9. Khorshidtalab A, Salami MJE (2011) EEG signal classification for real-time brain-computer interface applications: a review. In: 2011 4th international conference on mechatronics: integrated engineering for industrial and societal development, ICOM'11—conference proceedings
10. Zaizu Ilyas M, Saad P, Imran Ahmad M (2015) A survey of analysis and classification of EEG signals for brain-computer interfaces. In: 2nd international conference on biomedical engineering (ICoBE). Penang, Malaysia, pp 1–6
11. Muller-Putz GR, Scherer R, Neuper C, Pfurtscheller G (2006) Steady-state somatosensory evoked potentials: suitable brain signals for brain-computer interfaces? *IEEE Trans Neural Syst Rehabil Eng* 14:30–37
12. Polich J, Ellerson PC, Cohen J (1996) P300, stimulus intensity, modality, and probability. *Int J Psychophysiol* 23:55–62
13. Ravden D, Polich J (1999) On P300 measurement stability: habituation, intra-trial block variation, and ultradian rhythms. *Biol Psychol* 51:59–76
14. Rivet B, Souloumiac A, Attina V, Gibert G (2009) 2009\_B.Rivet\_xDAWN algorithm to enhance evoked potentials; application to brain-computer interface. *IEEE Trans Bio Eng* 56:2035–2043

15. Golub MD, Chase SM, Batista AP, Byron MY (2016) Brain–computer interfaces for dissecting cognitive processes underlying sensorimotor control. *Curr Opin Neurobiol* 37:53–58
16. Phothisonothai M, Nakagawa M (2008) EEG signal classification method based on fractal features and neural network. In: 2008 30th annual international conference of the IEEE engineering in medicine and biology society, pp 3880–3883
17. Rashid M, Sulaiman N, Mustafa M, Khatun S, Bari BS (2019) The classification of EEG signal using different machine learning techniques for BCI application. In: Jong-Hwan K, Kim Hyung Myung SML (eds) *Robot intelligence technology and applications*. RiTA 2018. Communications in computer and information science, vol 1015. Springer, Singapore, pp 207–221
18. Lakshmi MR, Prasad TV, Chandra Prakash V (2014) Survey on EEG signal processing methods
19. Ghosh T, Science P, Biswas T, Science P (2016) A feature extraction scheme to classify motor imagery movements based on bi-spectrum analysis of EEG. *IOSR J VLSI Sign Process* 6:28–35
20. Biswas T, Ahmad Fauzi MF, Abas FS, Nair HKR (2019) Superpixel classification with color and texture features for automated wound area segmentation. 2018 IEEE Student Conf Res Dev 1–6
21. Lotte F, Congedo M, Lécuyer A, Lamarche F, Arnaldi B (2007) A review of classification algorithms for EEG-based brain–computer interfaces. *J Neural Eng* 4:R1–R13
22. Rezeika A, Benda M, Stawicki P, Gemblar F, Saboor A, Volosyak I (2018) Brain-computer interface spellers: a review. *Brain Sci* 8:57
23. Al-Nafjan A, Hosny M, Al-Ohali Y, Al-Wabil A, Al-Nafjan A, Hosny M, Al-Ohali Y, Al-Wabil A (2017) Review and classification of emotion recognition based on eeg brain-computer interface system research: a systematic review. *Appl Sci* 7:1239
24. Ma X, Liu Z, Jiang T, Zhang X (2019) Study of the algorithm for the classification of brain waves. In: Zhang QLMJWF (ed) *Lecture notes in electrical engineering (LNEE, vol 463)*. Springer, Singapore, pp 2325–2331
25. Wali MK, Murugappan M, Badlishah Ahmad R Classification of driver drowsiness level using wireless EEG
26. Fernández-Rodríguez Á, Velasco-Álvarez F, Ron-Angevin R (2016) Review of real brain-controlled wheelchairs. *J Neural Eng* 13:061001
27. Bousseta R, El Ouakouak I, Gharbi M, Regragui F (2018) EEG based brain computer interface for controlling a robot arm movement through thought. *IRBM*. 39:129–135
28. Zhang R, Wang Q, Li K, He S, Qin S, Feng Z, Chen Y, Song P, Yang T, Zhang Y, Yu Z, Hu Y, Shao M, Li Y (2017) A BCI-based environmental control system for patients with severe spinal cord injuries. *IEEE Trans Biomed Eng* 64:1959–1971
29. Wu Q, Zeng Y, Zhang C, Tong L, Yan B (2018) An EEG-based person authentication system with open-set capability combining eye blinking signals. *Sensors*. 18:335
30. Singla R, Agrawal A, Kumar V, Verma OP (2018) Real-time mental workload detector for estimating human performance under workload. In: Karwal BSRTM (ed) *Lecture notes in electrical engineering (LNEE, vol 526)*. Springer, Singapore, pp 383–392
31. Nguyen P, Tran D, Huang X, Ma W (2013) Age and gender classification using EEG paralinguistic features. In: 2013 6th international IEEE/EMBS conference on neural engineering (NER). IEEE, pp 1295–1298
32. Bascil MS, Tesneli AY, Temurtas F (2016) Spectral feature extraction of EEG signals and pattern recognition during mental tasks of 2-D cursor movements for BCI using SVM and ANN. *Australas Phys Eng Sci Med* 39:665–676
33. Maby E, Perrin M, Bertrand O, Sanchez G, Mattout J (2012) BCI could make old two-player games even more fun: a proof of concept with “connect four. *Adv Human-Comput Interact*
34. Aydin EA, Bay OF, Guler I (2018) P300-based asynchronous brain computer interface for environmental control system. *IEEE J Biomed Heal Inform* 22:653–663
35. Iturrate I, Antelis JM, Kubler A, Minguez J (2009) A noninvasive brain-actuated wheelchair based on a P300 neurophysiological protocol and automated navigation. *IEEE Trans Robot* 25:614–627. <https://doi.org/10.1109/TRO.2009.2020347>

36. Mara S, Müller T, Freire T, Mário B, Filho S (2013) Proposal of a SSVEP-BCI to command a robotic wheelchair. *J Control Autom Electr Syst* 24:97–105
37. Farwell LA, Donchin E (1988) Talking off the top of your head: toward a mental prosthesis utilizing event-related brain potentials. *Electroencephalogr Clin Neurophysiol* 70:510–523
38. Ansari IA, Singla R (2016) BCI: an optimised speller using SSVEP. *Int J Biomed Eng Technol* 22:31
39. Wang X-W, Nie D, Lu B-L (2014) Emotional state classification from EEG data using machine learning approach. *Neurocomputing* 129:94–106
40. Jatupaiboon N, Pannngum S, Israsena P (2013) Emotion classification using minimal EEG channels and frequency bands. In: *The 2013 10th international joint conference on computer science and software engineering (JCSSE)*. IEEE (2013), pp 21–24
41. Long Jinyi, Li Yuanqing, Tianyou Yu, Zhenghui Gu (2012) Target Selection with hybrid feature for BCI-based 2-D cursor control. *IEEE Trans Biomed Eng* 59:132–140
42. Bonnet L, Lotte F, Lécuyer A (2013) Two brains, one game: design and evaluation of a multiuser BCI video game based on motor imagery. *IEEE Trans Comput Intell AI Games* 5:185–198
43. Abiyev RH, Akkaya N, Aytac E, Günsel I, Çağman A (2016) Brain-computer interface for control of wheelchair using fuzzy neural networks. *Biomed Res Int* 2016:1–9
44. Wolpaw JR, Birbaumer N, Mcfarland DJ, Pfurtscheller G, Vaughan TM (2002) Brain-computer interfaces for communication and control
45. Bin G, Gao X, Wang Y, Li Y, Hong B, Gao S (2011) A high-speed BCI based on code modulation. *VEP J Neural Eng* 8:025015
46. Jin J, Allison BZ, Sellers EW, Brunner C, Horki P, Wang X, Neuper C (2011) Optimized stimulus presentation patterns for an event-related potential EEG-based brain-computer interface. *Med Biol Eng Comput* 49:181–191
47. Schreuder M, Höhne J, Blankertz B, Haufe S, Dickhaus T, Tangermann M (2013) Optimizing event-related potential based brain-computer interfaces: a systematic evaluation of dynamic stopping methods. *J Neural Eng* 10:036025



# Early Rubeosis Iridis Detection Using Feature Extraction Process



Rohana Abdul Karim, Nur Amira Adila Abd Mobin,  
Nurul Wahidah Arshad, Nor Farizan Zakaria and M. Zabri Abu Bakar

**Abstract** Iris image analysis studies the relationship between human health and changes in the anatomy of the iris. One of the changes related to the anatomy of the iris is diabetes. This illness can be determined from the iris of human eyes because it affects the eyes. Latest advanced technologies are introduced in the image processing that helps automate the detection of diabetes based on the analysis of iris feature extractions. Various features are detected on iris such as texture, colour, histogram and shape. In this paper, the dataset of iris image from Warsaw Biobase are used to detect and recognise the rubeosis iridis by extracting their details using image processing methods. The results obtained from the experiment show that the normal and abnormal iris image can be classified using original and small size of iris image. Through this experiment, it was discovered that images for abnormal original are greater than 1,200,000 pixels while for small size are less than 35,000 pixels. On the contrary, normal original size are less than 1,200,000 pixels and for small are less than 25,000 pixel. By considering these results, the proposed method can be extended to the iris monitoring system.

**Keywords** Features extraction · Blood vessels · Diabetic

## 1 Introduction

An ordinary eye examination done by a specialist ophthalmologist is a manual path in diagnosing and measuring iris variations from the norm of every patient whether they have diabetes or not [1]. Essentially, this manual technique expands the expert's workload and they will be inclined to spend less time to diagnose each eye's image, hence higher propensity of blunder in the finding. Be that as it may, the clinical eye issue is not the same as the experimental situation.

In this paper, the image analysis is based on rubeosis iridis; defined as the presence of visible blood vessels on the surface of the iris detected during the slit-lamp

---

R. A. Karim (✉) · N. A. A. A. Mobin · N. W. Arshad · N. F. Zakaria · M. Z. A. Bakar  
Faculty of Electrical and Electronic Engineering, Universiti Malaysia Pahang, 26600 Pekan,  
Pahang, Malaysia  
e-mail: [rohanaak@ump.edu.my](mailto:rohanaak@ump.edu.my)

examination. The slit lamp microscope has a special mirrored gonioscopy lens used to examine the blood vessel growth in the front of the eye.

As the matter of fact, the limited number of ophthalmologists becomes a constraining factor to screen and audit the retinal images of the huge number of patients at the primary care clinics. This demonstrates how the profound cost of screening and lack of therapeutic experts hamper patients from taking the normal screening. In addition, patients are also required to queue for the examination in primary care clinics.

Nowadays, with the existing project that use the advancement of image processing technologies, the techniques can be applied to analyse iris images in the absence of expert ophthalmologists. Therefore, analysis techniques can help ophthalmologists in diabetes screening to detect the symptoms faster, easier and reducing their workload. This project explores the identification of iris feature extraction for early diabetic detection. Image processing techniques are introduced to detect and classify features of iris images into diabetic or normal. This is because the cases of diabetes are increasing and poses a great challenge to public health care. Diabetic prevalence rate in Malaysia has risen much faster than expected, almost doubling over the last decade [2].

For this project, image processing will be used to detect Rubeosis Iridis disease. Image processing is a method to get an enhanced image and to extract some useful information from it. It is a type of signal processing in which input is an image and output may be image or characteristics/features associated with that image.

## 2 Research Background

Previously, detecting diseases (diagnosis) using iridology principles were done manually. Nowadays, numerous technology provides additional tool to assist the ophthalmologist in diagnosing the patient. One of them is image processing, researcher use feature extraction in image processing to make an analysis of the iris image.

Some researchers used feature extraction such as mean, variance, standard deviation which is used in histogram feature. The region of interest can be identified according to the iridology chart [3].

Principal Component Analysis (PCA) is used for extracting the features of region of interest [4]. In general features, they used the application features such as colour, texture and shape. For example, images characterized by colour offers many advantages such as having texture, effectiveness, implementation simplicity, computational simplicity, low storage requirements. Besides, texture is an important part of image and powerful regional descriptor. It helps in the retrieval process which can be used to classify textured images from non-textured ones and then combined with another visual attribute like colour to make the retrieval system more effective. Texture is also one of the most important characteristic which has been used to classify something and have been used in finding similarities between various images in databases [5].

Sometimes, features such as blood vessels, exudates, micro-aneurysms and optic discs have been extracted for further analysis in medical treatment. The morphological operations such as opening, closing, erosion and dilation, as well as conversion into binary images are used in extraction process [6]. Feature analysis based on iridological visual inspection is an essential technique for extracting a feature in image. Besides that, other methods used for different image enhancement of feature extraction are spatial domain procedures such as grey scale manipulation, discrete formulation, images smoothing and histogram equalization.

However in this research, we directed more efforts on adaptive histogram equalization due to visual inspection based on iridology [7]. From the enhanced iris image, there are some distinctive features of the iris image such as furrows, ridges, and crypts being more visible than before as shown in Fig. 1. The iris pattern can be described if these features can be segmented out efficiently. In this research, to extract the iris features, an image segmentation method based on ICM neural network has been introduced [8]. The feature extraction is a key component of iris recognition system since it acquires the system's performance and the most valuable information in iris. The thresholding, template matching boundary detection and shape transform are the techniques for feature extraction. Therefore, the edge detection are conducted and focused to extract the iris information [9].

Iris consists of rich texture information and breaking of tissues of iris which is directly associated with these texture features. Wavelet transforms show its great potential in various fields such as in biomedical and telecommunication. Discrete Wavelet Transforms (DWT) are very suitable for non-stationary image analysis. A total of 63 statistical, texture, and DWT features were used to quantify the broken iris tissue information.

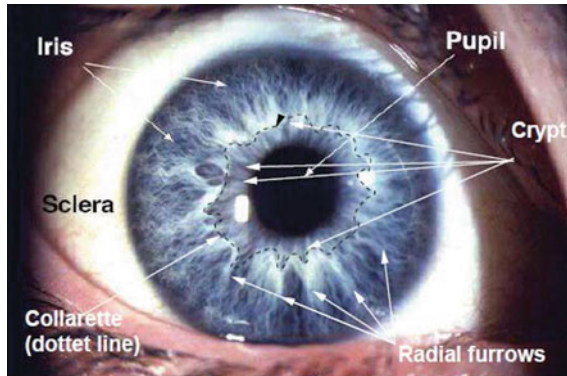


**Fig. 1** Visible features of the eye [10]

### 3 Methodology

In this manuscript, the Rubeosis Iridis detection was done using classification from datasets. From the eyes databases, the segmentation is done manually using photo editor software, LunaPIC to obtain only the iris image by removing all noises. LunaPIC extraction divides the image into two features which are colour and histogram. After that, the datasets of iris are tested, trained and categorised to detect Rubeosis Iridis (see Fig. 2). The datasets used for this project were obtained from Warsaw Biobase.

The method used for iris segmentation are manually cropped using photo editor software. First step, the image to be cropped and resized is uploaded to the photo editor software. The segmentation process is done up to 60 images for the test and training of feature extraction. After that, the outer layer is cropped to eliminate other parts of the eye, followed by cropping the pupil part of the iris to get exactly iris image only. Step 2 is cropping all noises and converting the deleted portion to black (see Fig. 3). Finally, it is saved in jpg format before being tested. They are divided



Fig. 2 Block diagram to detect Rubeosis Iridis

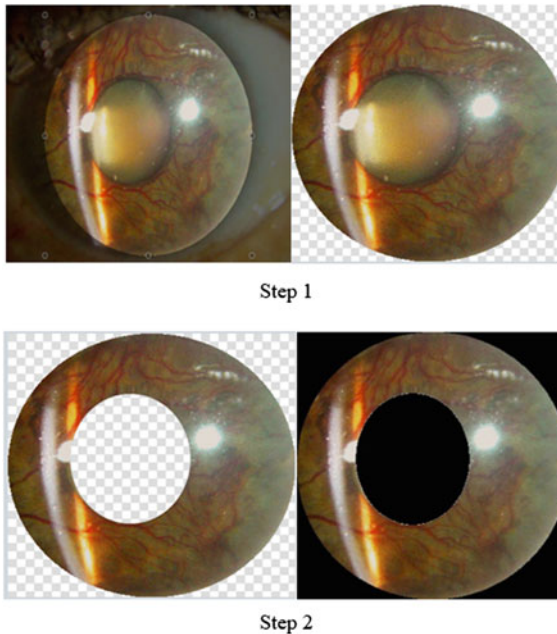
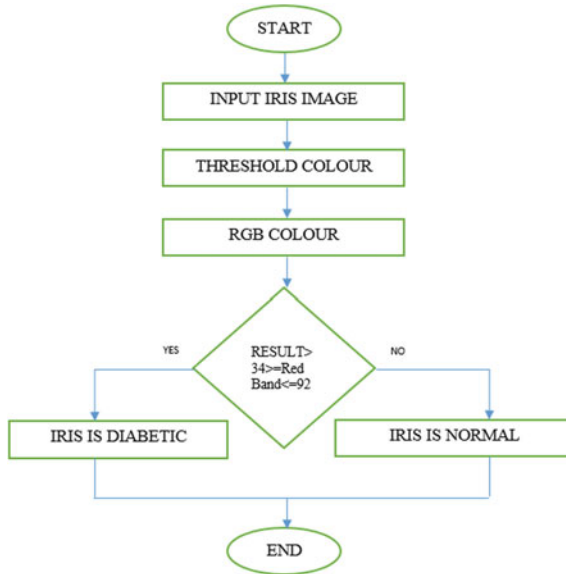


Fig. 3 Step for segmentation process



**Fig. 4** Flow chart for feature extraction of colour feature

into two categories, which are the original size image and resized small image. These method were applied to all images from Warsaw database obtained.

After completing the segmentation proses, the next step is feature extraction. Two methods of feature extraction are used in this project, colour feature and histogram. Matlab is used for coding the feature extraction to classify whether the iris are rubeosis or normal. In this project, no hardware is used because it only depends on software which is the important part of image processing.

By manipulating the iris image that are already segmented, feature extraction process for colour and histogram is carried out using the process flow shown in Figs. 4 and 5. Hierarchy threshold value are used to classify the conditions of iris, either normal or abnormal. Two parameter was observed, red band and red pixel count. The iris is classified as a diabetic if the range of red band between  $34 \geq \text{Red Band} \leq 92$  for RGB. Meanwhile, threshold for the red pixel count is  $\leq 1,200,000$  pixel. The sample for colour feature is 5 and histogram is 10.

The last step is classification using datasets from Warsaw Biobase Disease Iris v1.0 collection [11] and Warsaw Biobase Disease Iris v2.1 collection [12]. For this project, we collected just datasets of Rubeosis Iridis for test and training purpose. These collections have 603 Near Infrared (NIR) eye images and 222 corresponding colour eye images. Most of the images were acquired for eyes affected by different diseases. NIR images were captured by Iris Guard AD100, and colour images were captured by general-purpose Canon EOS 1000D as well as professional Topcon DC3 cameras. Each class of images for any unique iris is accompanied by an ophthalmological commentary as metadata.

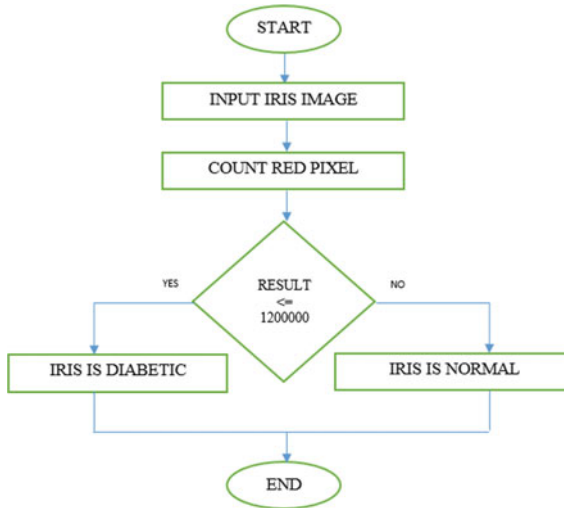


Fig. 5 Flow chart for feature extraction of histogram

## 4 Result and Discussion

This section presents the results and discussion of Rubeosis Iridis detection. From colour feature experiment, the pattern of RGB (Red, Green, Blue) from Warsaw databases were shown using colour threshold. Red serves as control while blue and green colours are kept as constant. Therefore, only the pattern of red colour histogram will change. In this experiment, red colour becomes the threshold to get the value of red part only on iris image. The value of red colour depends on control for normal and abnormal iris.

From experiment, the datasets were divided into two sizes which are original and small. It is done to differentiate between original and resized images and also to differentiate between normal and abnormal iris. Besides that, it enables comparison of the exact value of reddish part between two different sizes. From the original Warsaw for normal image, it is between 48 and 68 pixel and for normal resize Warsaw, are between 46 and 71 pixels. Then, for abnormal original Warsaw are between 34 and 130 and for resize abnormal Warsaw are between 41 and 126 pixel (see Figs. 6 and 7) for sample image that are already processed. Graph for Normal and Abnormal result from 5 datasets of colour feature original iris size image are shown in Fig. 8.

For histogram experiment, the value of red count pixel is analysed. By training abnormal and normal Warsaw, the histogram count pixel shown for original and resize image to differentiate the value, making the analysis smooth while classifying between two condition sizes. As a result, abnormal original are greater than 1,200,000 pixel. Besides, the experiment also get for normal original size which is less than 1,200,000 pixel (see Figs. 9 and 10).

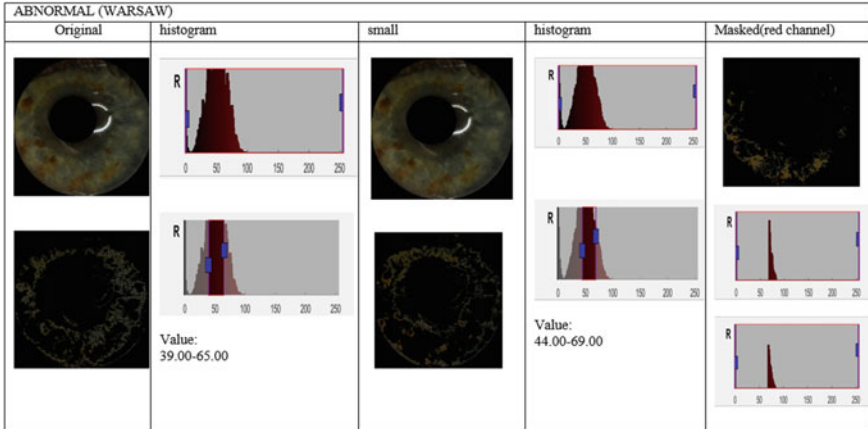


Fig. 6 Sample for abnormal from Warsaw datasets

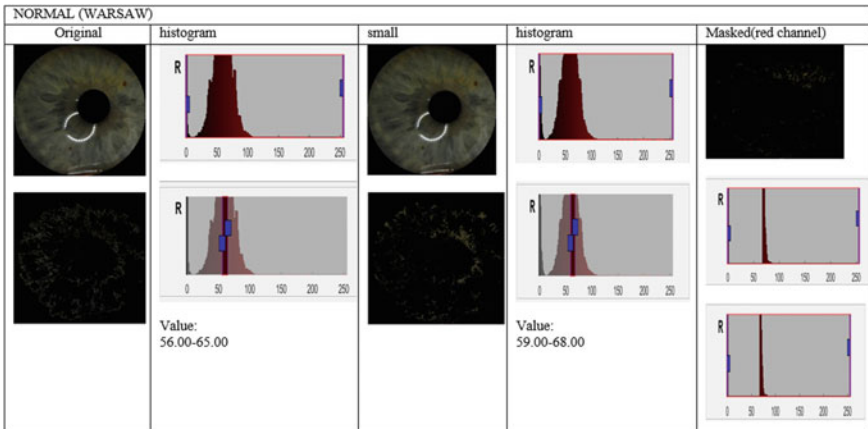
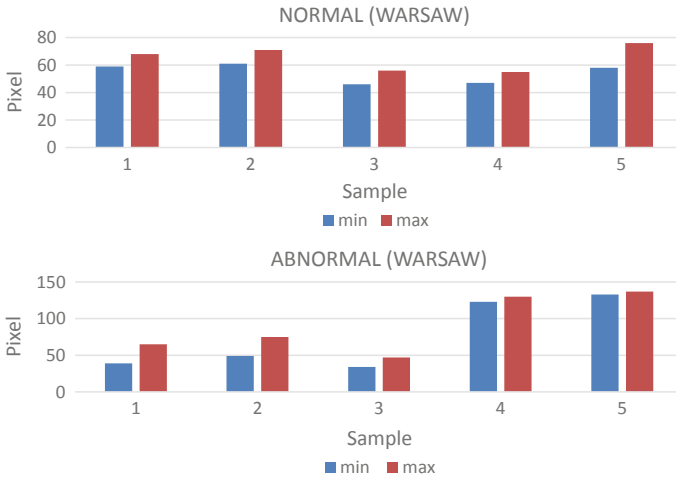


Fig. 7 Sample for normal from Warsaw datasets

### 5 Conclusion

This paper presents a Rubeosis Iridis detection method beginning from segmentation of iris image on Warsaw datasets, feature extraction and then classification. For clinical feature analysis, enhancement is essential for extraction of deep layer features. For feature extraction, the database of iris image enhancement method is applied on this project. The approach used is to prevent the user from contracting critical diabetes. This approach will be useful in the diagnosis field which is faster, user friendly



**Fig. 8** Graph for normal and abnormal result from 5 dataset of colour feature original iris size image

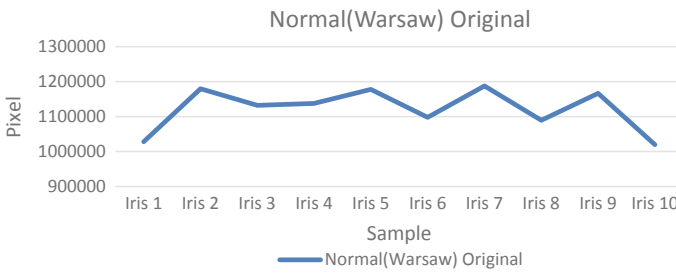


**Fig. 9** Graph for normal result of histogram original iris size image

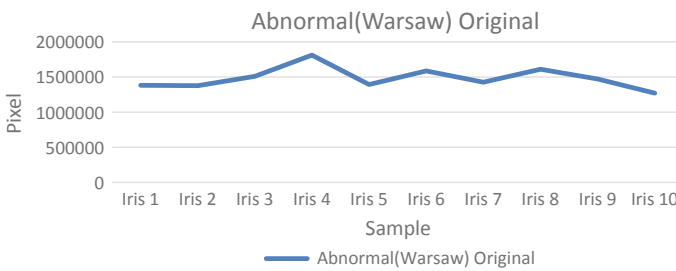


**Fig. 10** Graph for abnormal result of histogram original iris size image



and less time consuming. As a conclusion, this method is able to perform early diagnose for Rubeosis Iridis from the database that has already been captured. Further system or application to assist the ophthalmologist will be developed in real-time.

**Acknowledgements** This research work is supported by research grant funded by Universiti Malaysia Pahang (RDU1703233). The authors also would like to thank the Faculty of Electrical & Electronics Engineering, Universiti Malaysia Pahang for financial support.

## References

1. Wong TY et al (2018) Guidelines on diabetic eye care. *Ophthalmology* 125(10):1608–1622
2. Bhatia SK, Atole P, Kamble S, Telang P (2015) Methodology for detecting diabetic presence from iris image analysis. *Int J Adv Res Comput Eng & Technol (IJARCET)* 4(3)
3. Hussein SE, Hassan OA, Granat MH (2013) Assessment of the potential iridology for diagnosing kidney disease using wavelet analysis and neural networks. *Biomed Signal Process Control* 8:534–541
4. More SB, Pergad ND (2012) On a methodology for detecting diabetic presence from iris image analysis. In: *International Conference on Power, Signals, Controls and Computation 2012 Jan 3*, IEEE, pp 1–6
5. Walvekar M, Salunke G (2015) Detection of diabetic retinopathy with feature extraction using image processing. *Int J Emerg Technol Adv Eng* 5(1):133–137
6. Banzi JF, Xue Z (2015) An automated tool for non-contact, real time early detection of diabetes by computer vision. *Int J Mach Learn Comput* 5(3):225
7. Xu G, Zhang Z, Ma Y (2008) An image segmentation based method for iris feature extraction. *J China Univ Posts Telecommun* 15(1):96–117
8. Abidin ZZ, Manaf M, Shibghatullah AS, Anawar S, Ahmad R (2013) Feature extraction from epigenetic traits using edge detection in iris recognition system. In: *IEEE International Conference on Signal and Image Processing Applications*, pp 145–149
9. Samant P, Agarwal R (2017) Diagnosis of diabetes using computer methods: soft computing methods for diabetes detection using iris. *Threshold* 8:9
10. Lipton P, Chaturvedi M (2016) Improve the performance of iris recognition using genetic algorithm. *Int J Innovations Eng Technol (IJJET)* 7(1):296–304
11. BioBase-Disease-Iris v1.0 is publicly available for research and non-commercial use. See <https://zbum.ia.pw.edu.pl/EN/node/46>
12. BioBase-Disease-Iris v2.1 is publicly available for research and non-commercial use. See <https://zbum.ia.pw.edu.pl/EN/node/46>

# Multi-hop File Transfer in WiFi Direct Based Cognitive Radio Network for Cloud Back-Up



N. J. Shoumy, D. M. Rahaman, S. Khatun, W. N. Azhani, M. H. Ariff, M. N. Morshed, M. Islam, S. N. A. Manap and M. F. M. Jusof

**Abstract** In this chapter, an application for Android WiFi Direct multi-hop communications with log-file generation and cloud-based back-up have been proposed. WiFi Direct technology is used to peer-to-peer files transfer between neighboring devices without going through any access point. Distributed file systems for the cloud is a system that enables users to have access to the same data or file remotely (anytime any-where). The proposed custom WiFi Direct based Cognitive Radio (CR) application is able to create an ad-hoc network for multi-hop file transfer wirelessly using WiFi between two or more devices. Besides, to customize the channel according to the user demand, CR technique is used. An application (App) is developed and used in mobile devices (smart phones, note book, etc.) in a testbed to verify the system performances. This App detects and saves all the network activities information (in terms of log file) to keep track of the user activity and connection details in the network. The generated log files are stored in the cloud for further processing and security purpose. The performance of WiFi Direct based CR discovery service, channel detection, log file generation, multi-hop communication and WiFi Direct applications were successfully tested intensively with ~93% efficiency. Based on experimental data, an empirical model for multi-hop communication is proposed and validated. This shows, multi-hop file transfer and cloud back-up of log-files are possible through neighbor nodes with WiFi direct connection for at least one node in a network. This can be helpful for data safety, recovery and connection status monitoring/analysis for possible intrusion detection.

---

N. J. Shoumy · D. M. Rahaman  
School of Computing and Mathematics, Charles Sturt University, Wagga Wagga, Australia

S. Khatun (✉) · W. N. Azhani · M. H. Ariff · M. Islam · M. F. M. Jusof  
Faculty of Electrical and Electronics Engineering, Universiti Malaysia Pahang, Pekan, Malaysia  
e-mail: [sabirakhatun@ump.edu.my](mailto:sabirakhatun@ump.edu.my)

M. N. Morshed  
ICT Cell, Islamic University, Kushtia 7003, Bangladesh

S. N. A. Manap  
School of Computer and Communication Engineering, Universiti Malaysia Perlis, Kangar, Malaysia

**Keywords** WiFi direct · Cloud storage · Cognitive radio · Multi-hop file transfer · Cloud back-up

## 1 Introduction

Ad-hoc network based communication is getting popular day by day all over the world. WiFi directs is a very interesting feature for Android based Smartphones. Android is chosen as the platform because in the past few years it has become the market leader for smart phones. By the fourth quarter of year 2013, Android accounted for 77.83% and ahead of iOS with just 17.8% and Symbian with only 0.71% of global smart phones shipments [1].

Cognitive Radio Network (CRN) is developed to increase the spectrum efficiency, sharing the available channels with the needs of the devices at any moment in opportunistic manner. Cognitive Radio (CR) is a technology that allows an unlicensed user (secondary user) to use the spectrum that is already allocated to licensed users (primary user) [2]. Through this process the secondary users can use the spectrum while primary users are idle (not using it). It is used to solve the spectrum shortage problem due to the inflexible spectrum allocation. Spectrum sensing refers to as cognitive radio users. The focus of spectrum sensing is to detect unused spectrum that already been allocated to the primary users for the usage of secondary user without causing any interference to primary users. This is also to provide more spectrum access opportunities to cognitive users [3]. To customize the WiFi channel for secondary users as per user demand in this chapter CRN is considered to integrate with WiFi direct [4–23].

WiFi Direct, formerly known as WiFi Peer-to-Peer (P2P), is a standard that allows WiFi to connect easily with each other without the need for a wireless access point and communicate at the speed of a typical WiFi network. WiFi Direct device connections can happen anywhere, even when there is no access to a WiFi network. WiFi Direct devices are able to transmit a signal to other devices in a specific area. The process of connecting devices is much simpler than trying to use current tethering or Ad-hoc networking devices (laptops and smartphones). Basically WiFi direct technology uses channel numbers 1, 6 and 11 for its communication due to their independent and non-overlapping nature [4].

The implementation of Ad-hoc network features on Android device involves many issues that need to be investigated and settled. Multi-hop operation is usually required in situations where one or more intermediate nodes exist along the path (of a source–destination communication pair) that receive and forward packets via wireless links. Neighbor nodes can directly communicate with each other, while nodes that are not directly connected to Internet, use the intermediate neighbor nodes to forward the data to the destination. The appropriate routing protocol, Optimum Link State Routing (OLSR) was proposed by [10] for CR based Mobile Ad-hoc Networks data routing. It focused on direct routing in a testbed (with three devices), without considering

multi-hop peer-to-peer communication in a comprehensive environment. Hence, taking the advantage of CR detection [3, 4] and OLSR [10], focus of this chapter is to come out a comprehensive algorithm and to implement it in a full WiFi based CR network scenario (testbed) that can support peer-to-peer multi-hop file transfer without direct WiFi connection besides CR channel detection and communication. It can also support the dynamic topology change of Mobile Android devices, and cloud synchronization with data (log-file, etc.) back-up in cloud. Besides, extensive experiments were conducted to establish an empirical model.

## 2 The System Model

The whole development procedure is divided into four phases as follows. After routing protocol, the android application designed and created to cater the requirements for practical testing, which, mainly focuses on Cognitive Radio (CR), WiFi Direct discovery service, and cloud backup service.

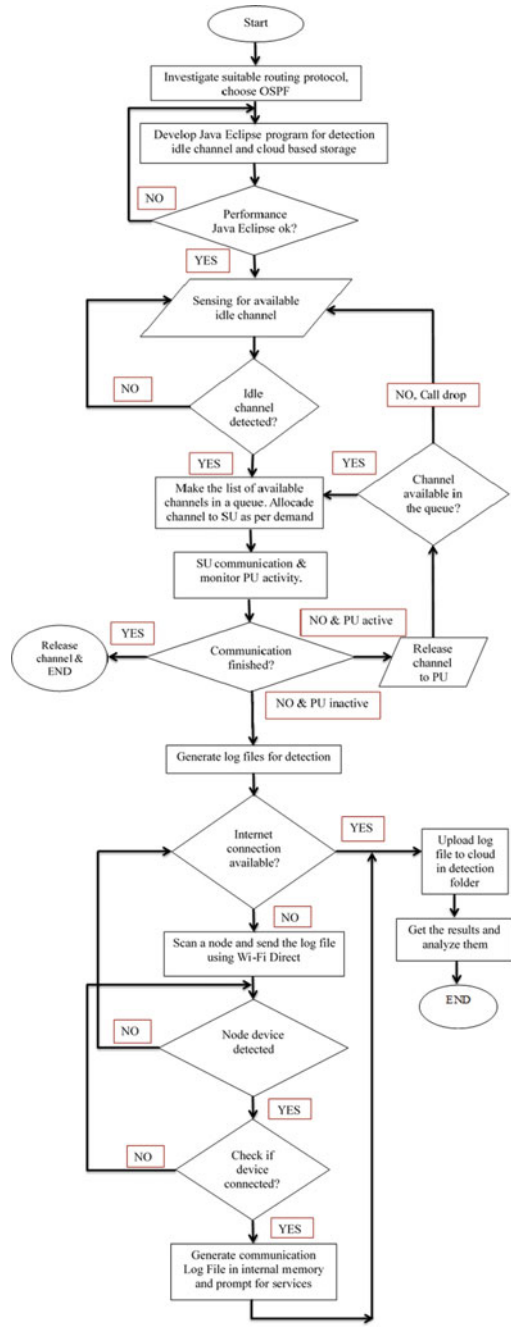
### 2.1 Routing Protocol Selection

The suitable routing protocol is needed to be identified that can be used with WiFi Direct. The pros and cons of some related routing protocols is shown in [10]. Similar to [10], to ensure optimum routing path and less energy consumption, OLSR is best suited for this research involving ad-hoc CR network with mobile devices. OLSR is also suitable to implement in most of the android based mobile devices for wireless communications.

### 2.2 Cognitive Radio Network (CRN) Activity Implementation

Java-eclipse programs with Graphical User Interface (GUI) are developed to support Cognitive Radio (CR) network activities. The program has two parts: (i) The first part is to sense the Primary User (PU) channel/spectrum using the cooperative method in a similar fashion as in [3, 4], so that the Secondary User (SU) can use it. (ii) The second part is for SUs to monitor PU's activity while using their channel/spectrum. This is to make sure, there is no interference to PUs caused by SUs. In case any PU becomes active and wants back the channel/spectrum for their use, SU has to release it instantly. Simultaneously, the SU can switch to another PU's channel/spectrum from the available pool of idle channels/spectrums incase of an ongoing communication. This process can be continued for the benefit of both secondary and primary users and to mitigate the channel/spectrum saturation problem (shown in Fig. 1).

**Fig. 1** The workflow of the CR-WiFi direct system



### ***2.3 WiFi Direct Based Multi-hop Data Transfer and Cloud Synchronization***

An android system application is developed for WiFi Direct based multi-hop-data transfer to cloud, along with cloud synchronization, and to interface with CR activities. This application is developed using Android version 4.0 to make it compatible with WiFi Direct technology. Figure 1 shows the proposed self-explanatory workflow of the proposed CR-WiFi Direct system.

### ***2.4 System Implementation***

We considered 5 stationary access points (APs) as PUs, who are fixed at specific location in a 200-m  $\times$  200-m area. The considered 10 SUs are free to move randomly within the area (or out of area) as per need. The PUs' have 13 specified 2.4 GHz dedicated channels for their use, which are non-overlapped to avoid inter-channel interference. The Android-based 8 smartphones and 2 tablets are considered as SUs. APs are located at various distances from the SUs with multiple hops.

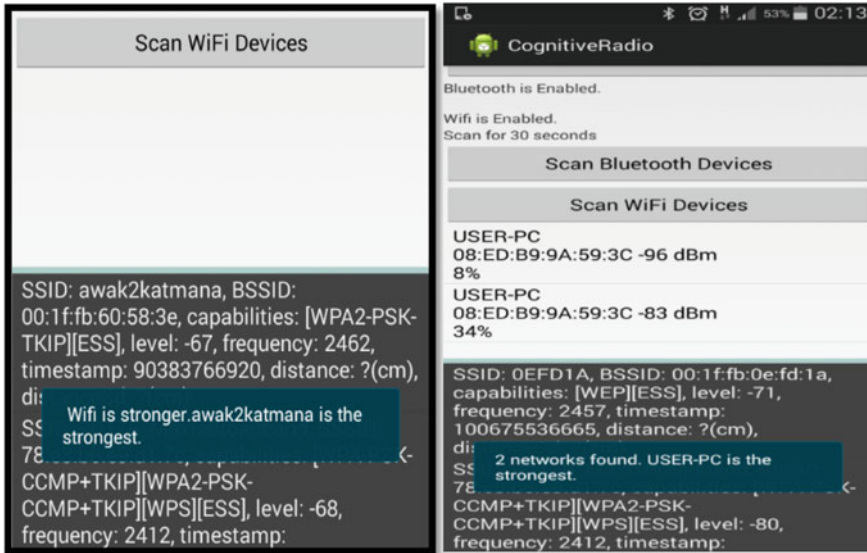
For experiments, we assumed noise floor between  $-45$  and  $-100$  dBm, which includes a variation from sunny weather to harsh weather (rain with thunderstorm), which is similar to works done in [3, 4, 10]. The overall system scenario for multi-hop file transfer was adopted from [10] along with its specifications. The practical experiments were conducted in an indoor (lab building) and outdoor (open playground) environment alternately. All the SU devices were equipped with developed application platform along with GUI and executed in a CR-WiFi Direct environment (similar to [3, 4]). Then the performances were investigated to validate the overall network/system functionality.

## **3 Performance Analysis**

The performance parameters were measured in the WiFi Direct and Bluetooth based CR network in terms of 10 'Trials' repeatedly for a particular application in an experimental set-up. The experiments were repeated 10 times at three different time instant (Clear/sunny morning, Cloudy noon, and Clear evening) on three different days, then saved the performance accuracy accordingly. The average performances were calculated and plotted to compare the results. The GUI of successfully uploaded Apps in SU devices for CR system implementation can be seen in Figs. 2, 3, 4, 5. Figure 2 shows the main GUI of WiFi Direct and Bluetooth based CR network. Here, the channels of WiFi Direct and Bluetooth are used as PU and SU channels for CR activities. Figure 4 shows CR network with successful channel detection for SU's use. The initiation of communication among devices, and generated log files



Fig. 2 Main GUI of CR-WiFi application



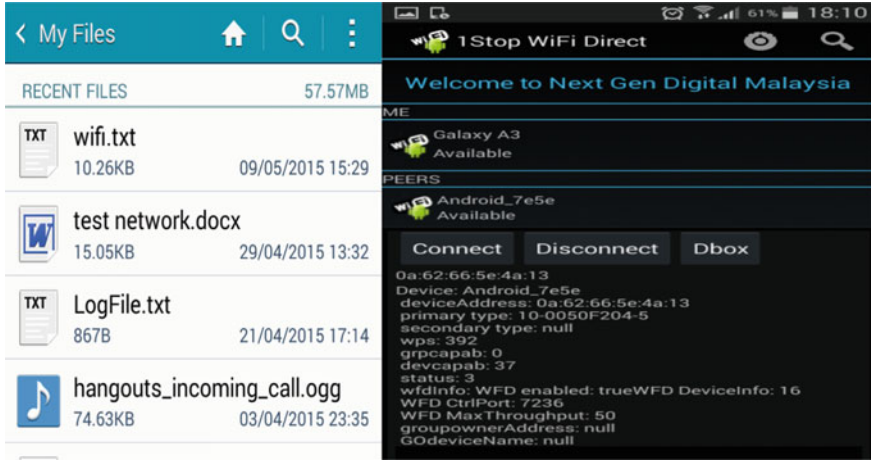
(a) WiFi detection.

(b) Bluetooth detection.

Fig. 3 Main GUI of CR-WiFi application

in SD cards of corresponding devices are shown in Fig. 4. “WiFi.txt” file contains all information about Bluetooth and WiFi scanned device as shown in Fig. 4a.

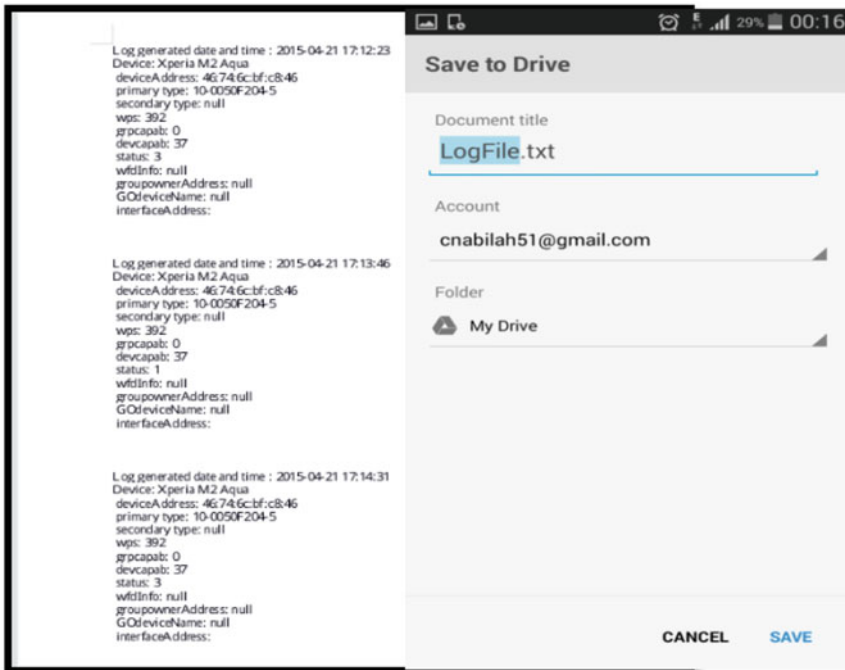
WiFi Direct discovery is linked with the CR function and based on WiFi Direct Service. CR function is used for detection of the available channel and data transmission for SUs through either WiFi Direct or Bluetooth channels. It scans all available



(a) Discovery summary with log file.

(b) WiFi neighbor discovered.

Fig. 4 CR-WiFi communication details



(a) LogFile contents.

(b) Log File saved in cloud.

Fig. 5 Layout for LogFile and upload to cloud



neighbor devices, find the channel with strongest signal strength, communicate with the required device, save the log file in device’s sd-card initially, and then transfer log files through neighbours (as multi-hop file transfer) to cloud. The discovered nearby/neighboring devices are shown in GUI in Fig. 4b. The reason for generating communication log file and save to in cloud is to keep track of the connection details and network activities among devices. This is also to retrieve information of the third-party device in case of security breaches occur and to keep the network secured. Dropbox and Gdrive are used for this application as cloud. Wifi.txt is the detection log file that contains available channel information and LogFile.txt is communication log file for WiFi Direct communication information to keep track of the connection detail of the connected/active devices as shown in Fig. 5.

Figure 6 shows the tested services detail (14 services/functions) for all 10 consecutive trials in three practical experimental CR-WIFI network set-up. The average success rate is determined by the number of successful tests over total number of tests conducted for a service. The performance is low for detection-log-file and discovery service due to harsh weather during that time.

Each service was tested in terms of 10 trials for a test set-up, with 10 times repetition results, a total number of 100 tests for a service type (with 10 trials and 10 times repetition). Finally, for 14 services, total 1400 tests were conducted to verify the system efficiency. The average performance is around 90%, bit low at the beginning due to initial synchronization and connection set-up.

Based on experimental data in Fig. 6 in terms of ‘correlation among trials’, ‘services’ and ‘success rate/efficiency’ an empirical model is formed as shown in Eq. (1).

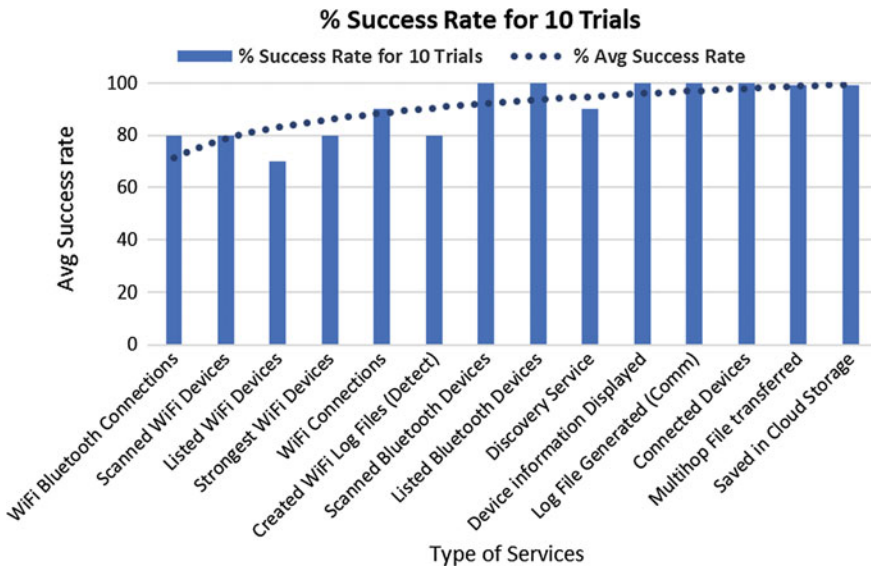


Fig. 6 The tested services and their average successes

$$y = 10.765 \ln(x) + 71.2 \tag{1}$$

Here,  $y$  is average success rate and  $x$  is the service-type, graphical representation is shown in terms of the dotted line in Fig. 6. For example,  $x = 1$  for WiFi Bluetooth connections,  $x = 2$  for connected WiFi devices, and so on. To verify the equation, if we consider,  $x = 3$  (means listed WiFi devices), Eq. (1) gives,  $y = 83.026\%$ , which is exactly the same average value as shown by the dotted curve in Fig. 6.

The average system efficiency per experiment [outdoor cloudy day experiment (1400 experiments)] and the average overall efficiency for all experiments ( $1400 \times 3 = 42,000$ ) are shown in Fig. 7. The average values per trial per experiment varies from 79.8 to 100%, whereas, the overall (average of all trials and applications) system efficiency is around 93% demonstrating the workability of the practical WiFi based CR network.

Figure 8 shows the efficiency percentage of multi-hop communications and cloud-backup service via active android smartphones in terms of multi-hop data transfer through the active neighboring devices in the service area. This is average performance for 10 number of trials with 10 repetitions done in 3 different days, i.e., total 300 tests conducted on android phone to check the efficiency of these systems. Most of the tests were successful, the average efficiency for multi-hop file transfer and cloud back-up are around 95% and 96% respectively. The efficiencies are lower at the beginning and at trial Number 8 due to initial set-up and hoarse weather conditions respectively. In comparison with [10], the cloud back-up efficiency is enhanced at least 4% due to our enhanced algorithm for the whole scenario.

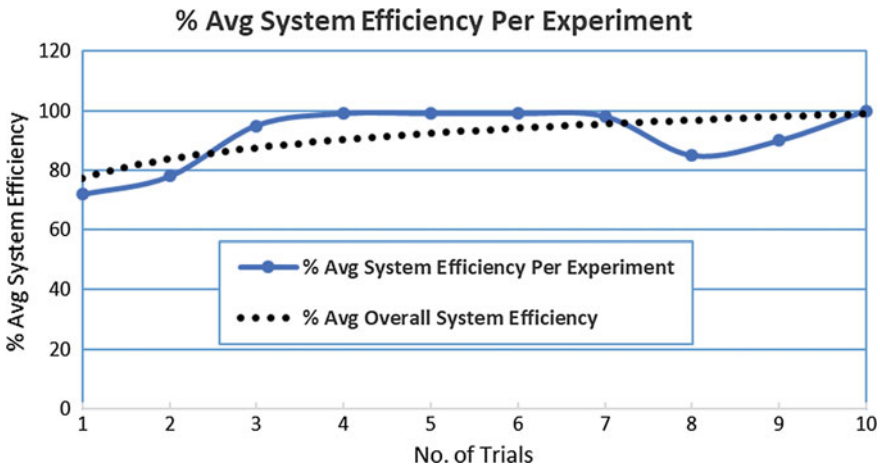


Fig. 7 Average percentage of successful detection and communication

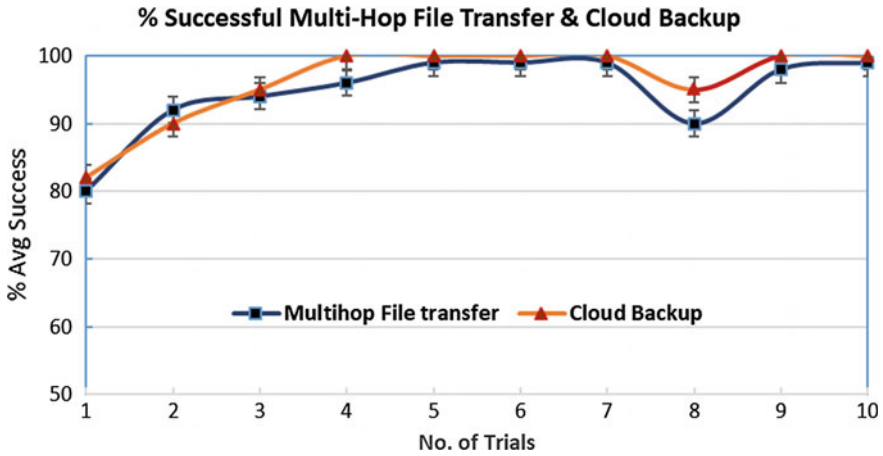


Fig. 8 Percentage of successful multi-hop file transfer and cloud backup

## 4 Conclusion and Future Works

An ad-hoc based enhanced CR network test-bed was developed with successful implementation of multi-hop-file transfer and cloud back-up using Android smartphones. A simple Android application platform with GUI was created to run on these devices in the network.

Log files that contain necessary networking information about connected devices were generated and saved SD card initially, then in cloud through multi-hop-file transfer and communication successfully. This could be useful for network monitoring and to identify the attacker (third-party/middle-man) in case of security breaches occur, where any third-party device tries to tap data while a communication/data-transfer in progress. This is convenient within an organization, such as, government/private offices and/or universities where all the users are usually connected to a common access point or router that connects the organization to outer world.

Future work is to upgrade the application detection of Bluetooth devices and WiFi devices automatically, then to save the log files in cloud autonomously through any connected (with Internet) device in a heterogeneous peer network. Also to test the test-bed network using 4G/5G on top of WiFi and Bluetooth.

**Acknowledgement** This research work is supported by research Grant No. RDU1703125 and RDU1703256 funded by Universiti Malaysia Pahang, <https://www.ump.edu.my/>. The authors would also like to thank the Faculty of Electrical & Electronics Engineering, Universiti Malaysia Pahang for financial support.

## References

1. Android, the world's most popular mobile platform, <https://developer.android.com/about/index.html>. Retrieved September (2014)
2. Morshed MN, Khatun S, Vijayararveswari V, Fakir MM, Ibrahim MZ, Hawari K, Ariff MH (2018) Cognitive radio based optimal channel sensing for resource allocation in communications. *J Telecommun Electron Comput Eng* 10(1-3):115-119
3. Won-Yeol L, Akyildiz IF (2008) Optimal spectrum sensing framework for cognitive radio networks. *IEEE Trans Wireless Commun* 7(10):3845-3857
4. Morshed MN, Khatun S, Kamarudin LM, AlJunid SA, Ahmad RB, Zakaria A, Fakir MM, Azmi N (2016) Performance measurement of 2.4 GHz WLAN channels for over-lapped and non-overlapped WiFi direct channel activity. *Int J Microwave Opt Technol* 11(4):268-273
5. Wei-Ho C (2004) Probabilistic analysis of routes on mobile ad-hoc networks. *IEEE Commun Lett* 8(8):506-508
6. Ping Y, Zhoulin D, Yi-Ping Z, Shiyong Z (2005) Resisting flooding attacks in ad-hoc networks, information technology. In: International conference on coding and computing, ITCC 2005
7. AODV Description, white paper (2014) Retrieved 20 Oct 2014, from <https://moment.cs.ucsb.edu/AODV/>
8. Optimized Link State Routing Protocol for Ad-hoc Network (2014) Retrieved 20 Oct 2014, from [www.olsr.org/docs/wos3-olsr.pdf](http://www.olsr.org/docs/wos3-olsr.pdf)
9. Perkins C, Belding-Royer E, Das S (2003) Ad-hoc on-demand distance vector (AODV) routing. RFC Editor
10. Morshed MN, Khatun S, Fakir MM, Ibrahim MZ, Razali S, Ramajayam Y (2018) Cloud-based routing resource allocation in cognitive radio networks. *J Telecommun Electron Comput Eng* 10(1-3):109-114
11. Fiawoo SY, Sowah RA (2012) Design and development of an Android application to process and display summarized corporate data. In: IEEE 4th international conference on adaptive science & technology (ICAST)
12. Morshed MN, Khatun S, Kamarudin LM, AlJunid SA, Ahmad RB, Zakaria A, Fakir MM (2016) Non-overlapping channel utilization and noise floor measurement of 2.4 GHz wireless LAN based cognitive radio network. *Int J Appl Eng Res* 11(12):7883-7887
13. Morshed MN, Khatun S, Kamarudin LM, Zakaria A, Azmi N (2014) Distributed cognitive radio detection using wasp mote sensor for windows based PC/laptop. In: 2nd international conference on electronic design (ICED)
14. Morshed MN, Khatun S, Kamarudin LM, AlJunid SA, Ahmad RB, Zakaria A, Fakir MM (2015) Adaptive threshold determination for efficient channel sensing in cognitive radio network using mobile sensors. In: 11th Asian conference on chemical sensor, Penang, Malaysia
15. Vijayararveswari V, Khatun S, Fakir MM, Morshed MN, Kamarudin LM, Jakaria A (2015) Cognitive radio based optimal channel sensing and resources allocation. In: 11th Asian conference on chemical sensors (ACCS)
16. Morshed MN, Khatun S, Kamarudin LM, AlJunid SA, Ahmad RB, Zakaria A, Fakir MM (2017) Adaptive threshold determination for efficient channel sensing in cognitive radio network using mobile sensors. In: AIP conference proceedings, vol 1808, no 1
17. Vijayararveswari V, Khatun S, Fakir MM, Morshed MN, Kamarudin LM, Jakaria A (2017) Cognitive radio based optimal channel sensing and resources allocation. In: American institute of physics conference series, vol 1808, no 2
18. Marzook AK, Ismail A, Ali BM, Sali A, Khalaf MH, Khatun S (2011) Analysis of joint channel estimation and joint data detection in TD-SCDMA systems. In: 17th IEEE Asia-Pacific conference on communications (APCC), pp 692-697
19. Sargolzaey H, Khatun S, Ali BM, Noordin NK (2010) Probabilistic route reliability with distance. In: 2010 IEEE international conference on computer and communication engineering (ICCCE), pp 1-5
20. Natsheh E, Khatun S, Jantan AB (2006) A model of routine lifetime optimization with linguistic knowledge in wireless ad-hoc networks. *Mathware & Soft Comput* 13(1)

21. Mokhtar RA, Khatun S, Ali BM, Ramli A (2009) Cooperative sensing in cognitive radio networks-avoid non-perfect reporting channel. *J Eng Appl Sci* 2:471–475
22. Mokhtar RA, Khatun S, Ali BM, Ramli AR (2008) Cooperative sensing under limited band control channel in cognitive radio networks. In: IEEE 6th national conference on telecommunication technologies and 2nd Malaysia conference on photonics NCTT-MCP, pp 377–380
23. Mokhtar RA, Khatun S, Ali BM, Ramli AR (2006) Cognitive radio technology for flexible spectrum sharing. In: IEEE 4th student conference on research and development, SCORED, pp 44–48

# The Multifocus Images Fusion Based on a Generative Gradient Map



Ismail and Kamarul Hawari Bin Ghazali

**Abstract** The limitation of camera lens is inability to make focus region for whole scene in one shot image. The camera creates one focus object for one image. It is needed several images to get many focus objects of the scene. It makes difficult to read many focus objects from several images. Multifocus image fusion is a process of combining many focus objects from several images into one image. This operation gives easier way to read focus information from many images clearer. It commonly needed in medical examination, robotics and bioinformatics fields. The clearness information enables machine, computer and human understand the image better and prevents any mistake. In an image, the clear object is only located in focus region. In order to generate all objects in focus region, the multi focus images will be fused into fused image. The methods generally use complicated mathematic equation and hard algorithm. In addition to handle the problem, we design a simple way and have accurate output. Our method is the multifocus image fusion based on generative gradient map. By generative gradient map, it quickly determines the initial prediction of focus region precisely. The Generative gradient map is the external information, generated from gradient of blurred random number image. This procedure substitutes complicated mathematical equations or hard algorithm sequence implementation. Finally, our algorithm able to produces a fused image with high quality. The assessment of our method is according to Mutual Information and Structure Similarity parameter.

**Keywords** Multifocus image fusion · Generative gradient map · Simple method

---

Ismail (✉) · K. H. B. Ghazali  
Universiti Malaysia Pahang, Gambang, Pahang, Malaysia

K. H. B. Ghazali  
e-mail: [kamarul@ump.edu.my](mailto:kamarul@ump.edu.my)

Ismail  
Politeknik Negeri Padang, Padang, Indonesia

# 1 Introduction

The application of camera as sensor device is ubiquitous nowadays, it is applied in many fields such as in robotics, medical equipment, remote sensing and so on. The need of clear and rich data of output image is a must. This clearness helps the machine or computer even human able to understand the data. Since, every parts of image give valuable information to the user, so the image should show very detail, clear and sharp of objects inside.

This condition is a bit problem for the general camera. The camera has inability to capture all objects of scene in focus in one shot or in an image. Furthermore, the collection of detail information of the scene needs many images with different focus of each image. These multifocus images are not efficient to read. The researchers have developed the methods to fuse multifocus images into one image that contain all objects in the scene showing in focus.

The fused image is a kind of process in image processing that collecting all most important information from multifocus images sequence and place them into one image [1]. The multifocus image fusion operation that has developed so far reached advancement with the various methods available nowadays. In general, these methods can be classified based on spatial domain and temporal domain fusion [2]. The spatial domain fusion is images fuse directly into fused image, such as the method segments image to compose an image fusion [3], the selection of distance pixel or variance is optimized with Genetic Algorithm to make a decision mode [4]. Other method is segmenting the images into several blocks, then each block from every input image is selected through iteratively comparing edge value of regions. The higher is selected to form a fused image [5]. The other method uses mean shift algorithm to determine the focus regions [6]. The other method, using saliency to determine the focus region [7]. Then, to achieve the better output, the fused image is generated from content based blurring region with adaptive threshold [8] and so forth. Secondly, the transform domain fusion method, it converts image data into transform coefficients. These coefficients combined together to generate fused image. This method applied with multi-scale wavelet technique [9]. Then, to increase the accuracy, the method selects the wavelet coefficient with consistency verification [10]. To maintain the consistency verification stronger, the other method uses Fuzzy Logic [11]. The other method solves the texture selection and block effect problems through generating hybrid spatial based model via Fast Discrete Curvelet Transform (FDCT) [12]. Finally, the use of wavelet to decompose focus images into high and low frequencies, then a deep CNN uses to make the model of mapping [13], and so on.

The above mentioned methods work perfectly through employ the complicated mathematical equations or hard algorithm procedures. They are used to process multifocus images data. These tough fashions deliver high cost to process.

Our proposed method is multifocus images fusion based on generative gradient map. The method not only uses important images information but also equipped with external information. The aim of our method is to practice the multifocus image

fusion procedure with a simple and accurate way. This procedure will avoid the use of complicated mathematical equations or hard algorithms.

The method provides the high ability to predict an accurate initial dense map. Furthermore, this method is robust to appearance clear of noise and unrelated objects. The accuracy dense map that has sharp and compact boundary shows the high accuracy of the previous procedures. The generating of precise dense map only needs a simple morphological filtering. The result presents that the fused image is very clear and fully strong with details.

We give assessment according to objective point of view. We measure the mutual information between input images and fused image. Then we also measure structure similarity also between input images and fused image. Our method is also robust to dynamic scene condition. The existence of generative gradient map makes our new algorithm look different with the previous methods. Our method structure is more ordinary than in segmentation based [3, 4] and less mathematically compare to previous method [12, 13].

## 2 Methodology

The multifocus image fusion is a kind of method in image processing to select the interesting information from multifocus images and place the required information in a fused image. The selecting information is read by many kinds of equipment such as machines, computers and human in order to understand what information inside the fused image. The accuracy of the fused image influences the understanding of the machines or computers. So, it is very important to keep the required information of input images during transfer into fused image. The algorithm should be able to maintain the required data of input images as the processing generates fused image.

Our algorithm takes the input images to build prediction of focus region. The prediction is helped by a generative gradient map. This completeness map assists algorithm to lessen frequency of using processing data of input images. The generative gradient map aids to predict initial dense map through gradient subtraction operation. Gradient subtraction operation involves gradient of input images and generative gradient map.

The generative gradient map has ability to absorb the poor gradient and leave the high gradient map. By this way, algorithm tries to keep the important information from the sources to the next stage of procedures. The high gradient map as an initial dense map used to generate dense map through morphological filter operation. Since the initial dense map is less of noise and unrelated object, the morphological filter operation is quite enough to build dense map.

The purposes of using morphological filtering are to create the connecting region among disconnected related object and to diminish the emerging of unrelated parts objects.

The dense map produced through morphological filter is then softened to adopt focus region image of camera lens. This goal achieved by using guided image filter.



The softened dense map optimizes the weight of dense map. The last section of the method is the procedure to compound the fused image from softened dense map and input images.

## 2.1 Multifocus Images Fusion

The multifocus images are a very important part in composing multifocus image fusion. The pair or sequence of focus images are obtained through the camera image. The focus image shows the object sets in focus appearance, the other region become blurry as shown in Fig. 1 (top left). The blurred image shows when the object set to blurred appearance and the background become focus as shown in Fig. 1 (top right). This sequence of focus images is as multifocus images in our experiments.

The focus image is the image part which is compounded by the almost converged the light from object as much as possible. Otherwise, blurred image is the image part that formed by non- converged light from the object. The camera lens does not produce focus image region to whole image parts. Some of the parts are in out of focus image [1].

Multifocus image fusion is an image with consist of many focus parts. To generate this image, the two or more images as inputs are extracted the focus parts and fuse them together to become one all focused image [see Fig. 1 (bottom)]. The format of the image can be in jpg, png and so on. I apply a pair of focus images in jpg format. The focus parts are on front part and at the rear part of the images.

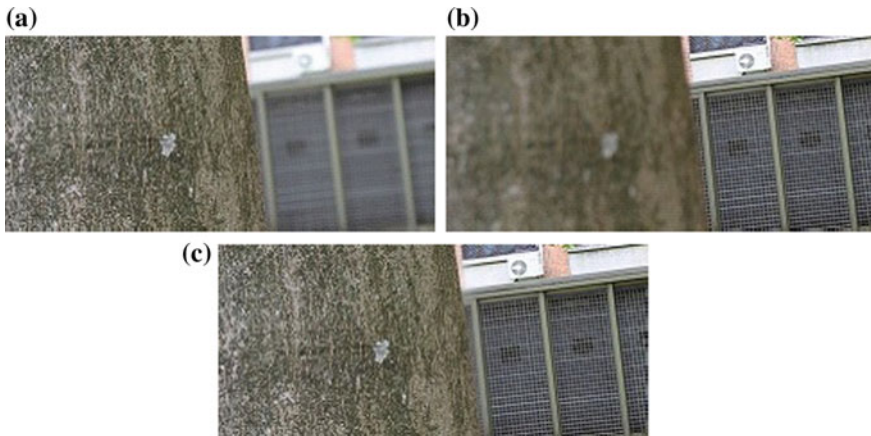


**Fig. 1** The method generates focus image (experiment 1): **a** the focus region is on the front part of image, **b** the focus region is on the rear part of image, **c** the all in focus image

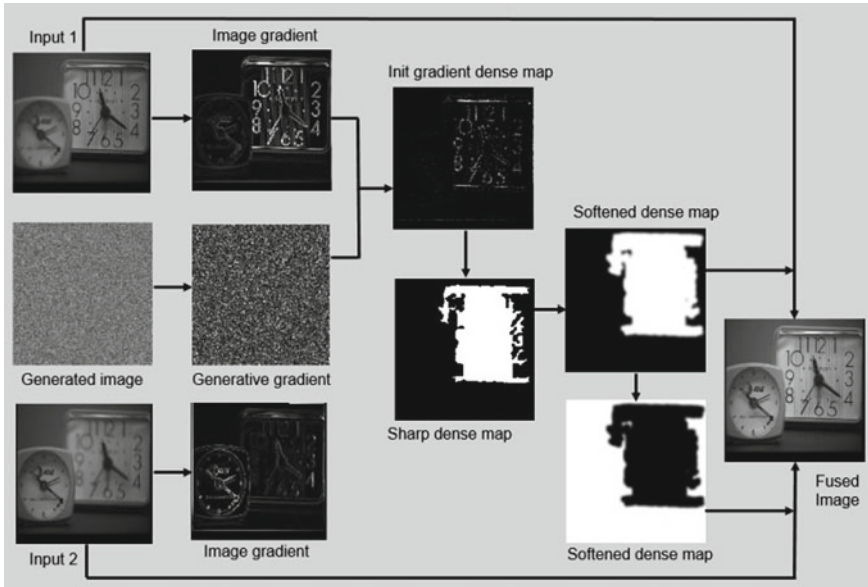


Fig. 2 Schematic diagram of proposed method

## 2.2 Multifocus Images Fusion with Generative Gradient Map

Multifocus image fusion is a process that combines every parts of required information of the image sequence into one focus information image (see Fig. 1 bottom).

The Multifocus images fusion based on generative gradient map is the fusion process helped by a generative gradient map. It started with the creation of random number matrix,  $M$  as big as images size. It is uniformly distributed random numbers. The range of random numbers is between 0 and 1 or randomness [14]. Then this matrix is transformed to image form,  $I^r$  (see Fig. 3a). The random number image,  $I^r$  then is smoothed by Gaussian filter (see Eq. 1) as in [15]. The process creates blurred random number image,  $J^{br}$ . The generative gradient map,  $G^{gg}$  is gradient of blurred random numbers image (see Eq. 2). Where,  $G_\sigma$  is Gaussian filter,  $\sigma$  is variance,  $W$  is kernel filter domain,  $s$  is central pixel of kernel,  $t$  is pixel at input image,  $I^r$ .

$$J_s^{br} = \sum_{s \in W} G_\sigma(\|s - t\|) I_t^r \quad (1)$$

$$G^{gg}(x, y) = \nabla J^{rb}(x, y) \quad (2)$$

$$G^{k,l}(x, y) = \nabla I^{k,l}(x, y) \quad (3)$$

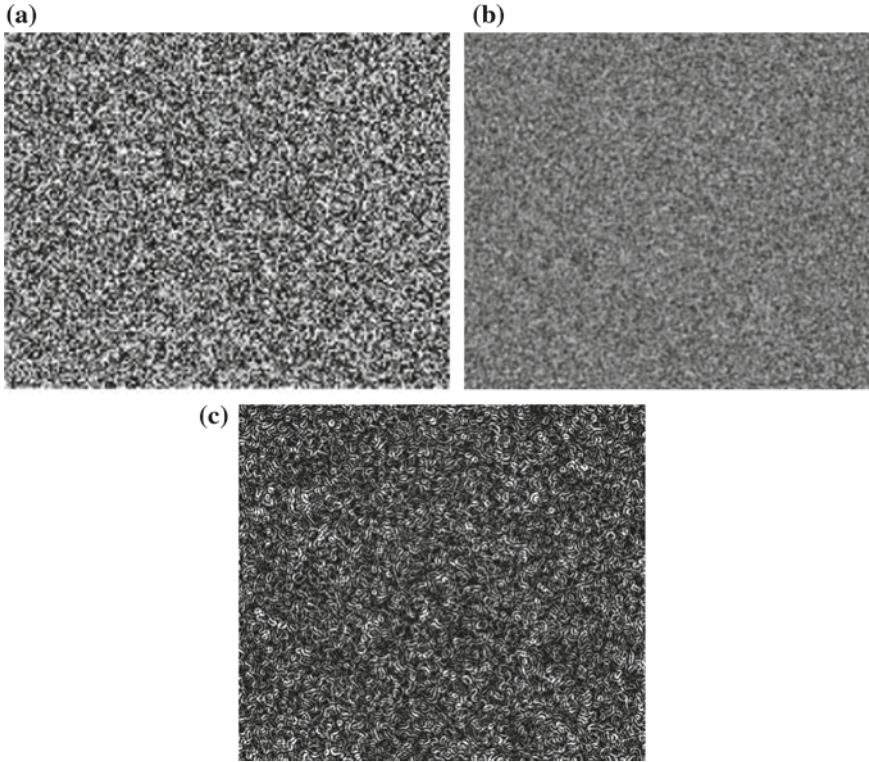


**Fig. 3** The generative gradient map: **a** random number image, **b** blurred random number image, **c** generative gradient map

On the other side, through the input images,  $I^k$  and  $I^l$ . We also build gradient image,  $G^k$  and  $G^l$  of the input images (see Eq. 3).

The initial dense map,  $G^{init}$  is generated by subtracting gradient operation. The operation subtracts gradient input images,  $G^{k,l}$  with the generative gradient,  $G^{gg}$ . The process is as following equation:

$$G^{initk,l} = G^{k,l} - G^{gg}, \tag{4}$$

To avoid negative pixels, we normalized as follow:

$$G^{initk,l} = \begin{cases} 0, & G^{initk,l} \leq 0 \\ 1 & \text{Otherwise} \end{cases} \tag{5}$$

The morphology filtering aim is to generate the dense map,  $G^{sh}$  from initial dense map. Morphological filtering consists of integrating the unconnected parts operation, **IUP** and small objects removing operation, **SOR**. They form a perfect dense region

shapes. It follows the equation below:

$$G^{shk,l} = \text{IUP}((G^{intk,l}), sw) \quad (6)$$

This operation enlarges the objects and unifies the neighbor parts. This operation is using of sliding window,  $sw$ . It compares large size of object region between  $G^{mitk}$  and  $G^{mitl}$ . Process selects the larger object region to be kept as a dense map. The larger object marked by less zero in the sliding window. Then the normalization performs to these maps to maintain the value in the range.

Secondly, the small object removing operation, SOR operation cleans the noise and useless objects. The operation as following formulation:

$$G^{shk,l} = \text{SOR}((G^{intk,l}), sw) \quad (7)$$

The result shows the initial dense maps is accurate to estimate the dense map. This dense map with sharp edge is a focus region image. In order to soften the boundaries as camera has, the guided image filter,  $GF$  with window radius,  $r_1$  and regularized parameter,  $\epsilon_1$  helps to solve the problem. It can build soften dense map image,  $G^{soft}$ . The process as the following equation:

$$G^{softk} = \text{GF}_{r_1, \epsilon_1}(G^{shk}, I^k) \quad (8)$$

Lastly, the multifocus image fusion,  $I^{fused}$  is synthesized through the following equation:

$$I^{fused} = I^k \cdot G^{softk} + I^l(1 - G^{softk}) \quad (9)$$

The schematic diagram of the processes is as (see in Fig. 2).

### 2.3 The Generative Gradient Map

The generative gradient map is a gradient map that generated from a blurred random numbers image with the size as same as the input images (see Fig. 3).

The purpose of this image is to perform the gradient subtraction. The gradient subtraction operation delivers a way to shorten technique to gain residual gradient. The residual gradient contains the initial approximation of focus region of the multifocus images.

## 2.4 Morphology Filtering

Mathematical Morphology is a kind of methodology based on object formation generally used for identifying object boundary accurately [16]. It can make a simplification operation based on formation in image data. It makes connection the related and removes the unrelated parts [16].

### Dilation

The dilation operator is concerning with the pixel formation modification. In the image processing, the pixel formation modification is implemented in the binary (0, 1) or gray scale (0–1) image. The operation of pixel formation is in the binary level image [16]. The dilation operation is a builds addition dimension of pixel forms. It works to merge two pixel formations using vector addition of each element.  $\mathbf{X}$  and  $\mathbf{Y}$  are pixel formation. The dilation of  $\mathbf{X}$  and  $\mathbf{Y}$  symbolized as  $\mathbf{X} \oplus \mathbf{Y}$  [19].  $\mathbf{x} \in \mathbf{X}$  is  $x$  subset  $\mathbf{X}$ . And formulated by

$$(\mathbf{X} \oplus \mathbf{Y})\mathbf{X} = \cup_{x \in \mathbf{X}} \mathbf{X}_y \quad (10)$$

$\mathbf{X}_y$  is a translation of  $\mathbf{X}$  by  $y$ . Since dilation is an operation of pixel formation modification, and it performs a lowest level image, this operation generally used to modify the shape structure image. It can be used to smooth, segment image and so on.

### Erosion

Erosion process works at pixel level image, in binary or gray image. It does as a decrement operation. If  $\mathbf{X}$  and  $\mathbf{Y}$  is the erosion operation  $\mathbf{X}$  by  $\mathbf{Y}$  symbolized as  $\mathbf{X} \ominus \mathbf{Y}$  [14].  $y \in \mathbf{Y}$  is  $y$  subset  $\mathbf{Y}$ .  $\mathbf{X}_{-y}$  is translation erosion  $\mathbf{X}$  by  $y$ . Mathematically, it formulated by following equation:

$$(\mathbf{X} \ominus \mathbf{Y}) = \cap_{y \in \mathbf{Y}} \mathbf{X}_{-y} \quad (11)$$

The erosion operation presents the discrepancy between two pixels form modification.

### Opening Operation

The opening operation is combination operation between erosion and dilation. This operation works starting with erosion and follow by dilation operation. Mathematically formulated as follow:

$$\mathbf{X} \circ \mathbf{Y} = (\mathbf{X} \ominus \mathbf{Y}) \oplus \mathbf{Y} \quad (12)$$

where  $\mathbf{X}$  is an image,  $\mathbf{Y}$  is structuring element. This equation gives smoothing, breaking uncorrelated and removing small objects. And, it also sharpens the binary image.

### Closing Operation

The closing operation of image or pixel form  $X$  by the structuring element  $Y$ , it symbolized as  $X \cdot Y$ . The closing operation presented as following equation:

$$(X \cdot Y) = (X \oplus Y) \ominus Y \quad (13)$$

The characteristic of closing operation, mainly are removing the small holes and filling the gaps among part pixel form.

## 2.5 Guided Image Filter

Guided image filter is a linear translation-variant filter that wraps together a guidance image  $R$ , filter input  $t$  and an output image  $S$ . The filtering process according to the following equation,

$$S_i = \sum_j K_{ij}(R) t_j \quad (14)$$

The filtering output at pixel is according to Eq. 14. There  $i$  and  $j$  are pixel indexes.  $K_{ij}$  is a window kernel as a function of guidance image and independent image. The characteristic of this filter is linear with respect to  $t$  [17].

## 3 Test and Results

For testing the method, we do some experiments. The experiment 1, the transformer, it gives the fused image as see in Fig. 1. We measure the mutual information,  $MI_f^{PQ}$  of fused image and input images [18]. The  $P$  and  $Q$  are input images, fused image is  $f$  and  $I(f, P)$  and  $I(f, Q)$  are mutual information between fused image,  $f$  and input images  $P$  and  $Q$ .  $H(f)$ ,  $H(P)$  and  $H(Q)$  are the entropy of the  $f$ ,  $P$ ,  $Q$  respectively.

The assessment as follow:

$$MI_f^{PQ} = \left[ \frac{I(f, P)}{H(f) + H(P)} + \frac{I(f, Q)}{H(f) + H(Q)} \right] \quad (15)$$

We get the values as show in column 3 of Table 1. To amplify the result, we also measure structure similarity,  $SSIM(P, Q)$  between reference image,  $P$  and fused image,  $Q$  [19]. The assessment equation:

$$SSIM(P, Q) = \frac{(2\mu_P\mu_Q + C_1)(2\sigma_{PQ} + C_2)}{(\mu_P^2 + \mu_Q^2 + C_1)(\sigma_P^2 + \sigma_Q^2 + C_2)} \quad (16)$$

**Table 1** The objective measurement values of experiments

No.	Experiment	Mutual information	SSIM
1	Experiment 1	0.7719	0.7723
2	Experiment 2	0.7724	0.9231
3	Experiment 3 (dynamic scene)	0.7546	0.7664
4	Experiment 4	0.8490	0.6567
5	Experiment 5	0.7218	0.8643

$C_1 = (K_1L)^2$ ,  $C_2 = (K_2L)^2$ , L is dynamic range (255).  $K_1 = 0.01$ ,  $K_2 = 0.03$ . The value 1 means two images are identical image. It showed in column 4 of Table 1. Here, we apply 5 datasets to complete testing our method. The result shows as see in the Table 1.

In the experiment 2, the input images are as in Fig. 4 (top left), the output is as see in Fig. 9a and Table 1. The SSIM value is high. The structural reference image and fused image are almost identical twins.

In the experiment 3, as shown in Fig. 4 (top right), we use image with dynamic scene condition, and the result as shown in Fig. 7b. We test our method with dynamic scene in order knowing the robustness of the method. The assessment quality is in Table 1.

The experiment 4, as shown in Fig. 4 (bottom). We also present the initial dense map (see Fig. 6a), sharp dense map (see Fig. 6b) and optimized dense map (see Fig. 6c). The boundaries among all maps provide similar shape. The fused image is as shown in Fig. 7c. They show that the generative gradient map is able to diminish noise and unrelated objects. The mutual information value is high. The miss information as processing is not significant. The experiment 5, the input images are shown in

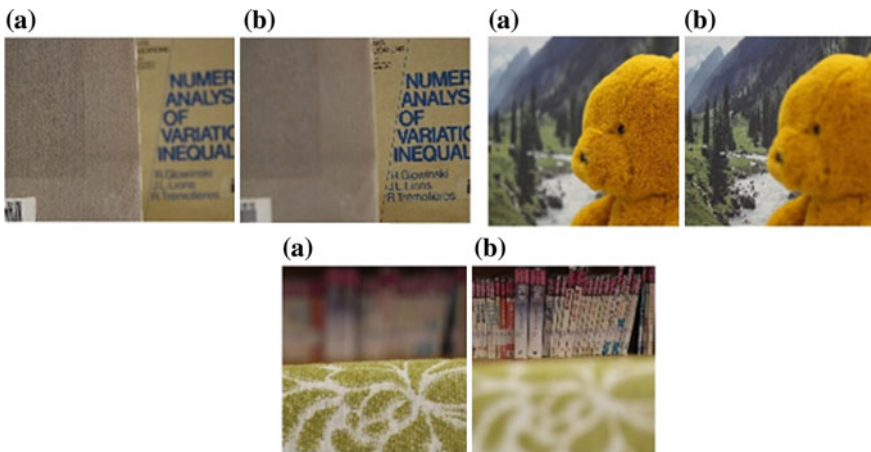


**Fig. 4** Input images: experiment 2 (top left); experiment 3 (top right); experiment 4 (bottom)

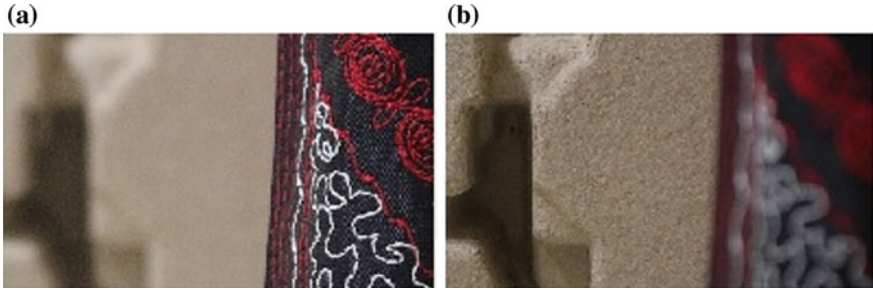


Fig. 5 Input images of experiment 5



Fig. 6 The dense map of experiment 4: a initial dense map, b dense map, c optimized dense map



Fig. 7 Fused images: a experiment 2, b experiment 3, d experiment 4, e experiment 5

Fig. 5, the result shows in Fig. 7d gives mutual information and SSIM are quite high. The process gives the acceptable result, fused image.

The most important is our new method success to substitute complicated mathematical equation and hard algorithm procedures in multifocus image fusion topics. The simple algorithm and acceptable result demonstrate the robustness of the method. Furthermore, we also demonstrate the ability of generative gradient map to handle dynamic scene situation and produces the acceptable result too. These contributes are evident that the new method is reliable.



## 4 Conclusions and Future Work

The settlement of the multifocus image fusion with a new method has already completed. The generative gradient map is able to substitute mathematical equation works. It gives acceptable quality. This method can be implemented in many fields.

The use of generative gradient map enhances resource methods to handle image fusion problem. The utilization of external information to support internal data gives a big impact to image processing fields.

The method obtains escalation of output quality. This is the power of our research actually and we can minimize the use of complicate mathematical equation and hard algorithm.

## References

1. Mishra D (2015) Image fusion techniques: a review. *Int J Comput Appl* 130(9):7–13
2. Masood S (2017) Image fusion methods: a survey. *J Eng Sci Technol Rev* 10(6):186–194
3. Li M (2006) A region based multi-sensor image fusion scheme using pulse coupled neural network. *Pattern Recogn Lett* 27:1948–1956
4. Abhyankar M, Khaparde A (2016) Spatial domain decision based image fusion using superimposition. In: Uehara K, Nakamura M (eds) 15th international conference on computer and information science (ICIS), IEEE/ACIS. IEEE, Okayama, pp 247–252
5. Shah P, Kumar A (2012) Multifocus image fusion algorithm using iterative segmentation based on edge information and adaptive threshold. In: Yang R, Chee Lai H (eds) 15th international conference on information fusion (FUSION). IEEE, Singapore, pp 1976–1981
6. Santiago T (2018) Region-based multifocus image fusion for the precise acquisition of pap smear images. *J Biomed Opt* 23(5):1–9
7. Bavirisetti DP (2018) Multi-focus image fusion using multi-scale image decomposition and saliency detection. *Ain Shams Eng J* 9:1103–1117
8. Farid MS (2019) Multi-focus image fusion using content adaptive blurring. *Inf Fusion* 45:96–112
9. Pajares G (2004) A wavelet-based image fusion tutorial. *Pattern Recogn* 37:1855–1872
10. Yang Y (2014) Multi-focus image fusion using an effective discrete wavelet transform based algorithm. *Measurment Sci Rev* 14(2):102–108
11. Jiang Q (2017) A novel multi-focus image fusion method based on stationary wavelet transform and local features of fuzzy sets. *IEEE Access* 5:20286–20302
12. Yang Y (2017) A hybrid method for multi-focus image fusion based on fast discrete curvelet transform. *IEEE Access* 5:14898–14913
13. Li J (2019) Multifocus image fusion using wavelet-domain-based deep CNN, research article. *Comput Intell Neurosci* 2019:1–23
14. Salhab O (2018) Survey paper: pseudo random number generators and security tests. *J Theor Appl Inf Technol* 96(7):1951–1970
15. Paris S (2009) A fast approximation of the bilateral filter using a signal processing approach. *Int J Comput Vision* 81(1):24–36
16. Rani S (2014) Detection of edges using mathematical morphological operators. *Open Trans Inf Process* 1(1):17–26
17. Kaiming H (2013) Guided image filtering. *IEEE Trans PAMI* 35(6):1397–1409

18. Hossny M (2008) Comments on 'information measure for performance of image fusion. *Electr Lett* 44(18):1066–1067
19. Wang Z (2004) Image quality assessment: from error visibility to structural similarity. *IEEE Trans Image Process* 13(4):600–612

# A Comparative Analysis of Four Classification Algorithms for University Students Performance Detection



**Dipta Das, Asif Khan Shakir, Md. Shah Golam Rabbani, Mostafijur Rahman, Syamimi Mardiah Shaharum, Sabira Khatun, Norasyikin Binti Fadilah, Khandker M. Qaiduzzaman, Md. Shariful Islam and Md. Shohel Arman**

**Abstract** The student's performance plays an important role in producing the best quality graduate who will responsible for the country's economic growth and social development. The labor market also concerns with student's performance because the fresh graduate students are considered as an employee depends on their academic performance. So, identification of the reason behind student's performance variation provides valuable information for planning education and policies. Many researchers try to find out the reason with different types of data mining approaches in different countries. However, none of them worked with Bangladeshi students. This paper proposed a model for identifying the key factors of variation Bangladeshi students' academic performance and predicts their results. This paper proposes a model which able to identify the students who need special attention. Different types of feature selection methods were used such as Co-relation, Chi-Square and Euclidean distance to select valuable features and feature selections result through decision tree, Naive Bayes, K-nearest neighbor and Artificial Neural Network classifiers algorithm were compared. The performance analysis is done by using student SGPA and review on given facilities from a university. From the performance analysis result it is found that, decreasing number of classes in dataset, the Artificial Neural Network (ANN) (93.70%) performs better than Decision Tree (DT) (92.18%), K-Nearest Neighbors (KNN) (77.74%) and Naive Bayes (NB) (68.33%). However, an increasing number of classes in dataset the DT perform better than ANN, KNN, NB.

**Keywords** Educational data mining (EDM) · Academic performance (AP) · Feature selection (FS) · Cumulative grade point average (CGPA) · Semester grade point average (SGPA)

---

D. Das · A. K. Shakir (✉) · Md. S. G. Rabbani · M. Rahman · K. M. Qaiduzzaman · Md. S. Arman

Department of Software Engineering, Daffodil International University, Dhaka, Bangladesh  
e-mail: [asif.swe@diu.edu.bd](mailto:asif.swe@diu.edu.bd)

S. M. Shaharum · S. Khatun · N. B. Fadilah

Faculty of Electrical and Electronics Engineering, University Malaysia Pahang, Gambang, Malaysia

Md. S. Islam

Institute of Information Technology, University of Dhaka, Dhaka, Bangladesh

© Springer Nature Singapore Pte Ltd. 2020

A. N. Kasruddin Nasir et al. (eds.), *InECCE2019*, Lecture Notes in Electrical Engineering 632, [https://doi.org/10.1007/978-981-15-2317-5\\_35](https://doi.org/10.1007/978-981-15-2317-5_35)

## 1 Introduction

Extracting knowledge from a large number of data has an impact on decision making and it has become an important component in many sectors. Educational data mining is such an emerging area through which student's learning process, learning characteristics and academic performance can be evaluated. Educational institutions like schools, colleges and universities can use their large amount of unique data to predict the performance of their students and explore the data to better understand the learning environment. In this research, concentration been given on feature selection techniques because it is an essential part of determining what influences the performance of a data mining model. The main goal of using feature selection for this research is to find the factors of a university which have much influence on student performance. Result of feature selection shows that university admission policy, admission procedure, sincerity and commitment, laboratories facilities, internet speed, gymnasium facilities etc. along with student result have more influence in student CGPA. After identifying all those attribute predict student performance using four different algorithms, KNN, NB, DT and ANN. The performance shows that the prediction accuracy increase as the number of prediction class decrease.

This paper is organized as follows. Section 1 provides an overview on the background of the study with problem statement and motivation. Followed by literature review and novelty of this research in Sect. 2, the experimental results in Sect. 3, the findings based on the experimental result in Sect. 4, and finally, the conclusion with future directions in Sect. 5.

## 2 Literature Review

In recent times, data mining gaining more and more popularity of the educational research field because of its potentials to educational institutes. Data mining can be used in the educational field to enhance our understanding of learning process to focus on identifying, extracting and evaluating variables related to the learning process of students as described by El-Halees [1]. Mining in the educational environment is called Educational Data Mining.

Pandey and Pal [2] conducted a study on the student performance by selecting 600 students data from different colleges of Dr. R.M.L. Awadh University, Faizabad, India. Employing Bayes Classification on category, language and background qualification, it was investigated whether newcomer students will performer or not.

Hijazi and Naqvi [3] conducted a study on the student performance by selecting a sample of 300 students (225 males, 75 females) from a group of colleges affiliated to Punjab university of Pakistan. The hypothesis that was stated as "Student's attitude towards attendance in class, hours spent in study on daily basis after college, student's family income, student's mother's age and mother's education are significantly related with student performance" was farmed. By means of simple linear regression

analysis, it was found that the factors like mother's education and student's family income were highly correlated with the student academic performance.

Baradwaj and Pal [4] collected data like attendance, class test, seminar and assignments marks from university student's previous database and predicted the performance at the end of the semester.

Al-Radaideh et al. [5] applied a decision tree model to predict the final grade of students who studied the C++ course. He used three different classification methods namely ID3, C4.5, and the Naive Bayes. After calculation, the results indicated that the Decision Tree model had better prediction than other models.

Ben-Zadok [6] used student's data to conduct a case study which analyzes students learning behavior to predict the results and to warn students at risk before final exams.

Bhardwaj and Pal [7] selected 300 students based on their academic performance from 5 different degree colleges who were undertaking the Bachelor of Computer Application course. By using the classification method, the result indicated that the factors like student's grade in the senior secondary exam, living location, the medium of teaching, mother's qualification, student's other habit, annual family income, and student's family status were highly correlated with students' academic performance.

Yassein et al. [8] proposed a pattern to predict students' performance. The research was conducted in two parts, firstly they investigated the factors that are related to course success rate, and the second one to determine predictors based on students performance. Both classification and clustering techniques were used to find the factors that affect students' performance.

Asif et al. [9] proposed a case study based on predicting student academic performance. By using different classifiers, data were extracted from 347 undergraduate students. Artificial neural networks, decision trees, k-nearest neighbor, naive Bayes, rule induction classification techniques were used in this study. The study showed the possibility of predicting fourth-year graduation performance with pre-university marks, along with university Year 1 and Year 2 marks. The accuracy on analyzing the datasets was satisfactory.

Nghe et al. [10] predicted academic performance considering the data from two different universities. First, they collected undergraduate students data from Can Tho University (CTU), Vietnam to predict GPA by using the student's record (faculty, English skill, age, gender, family, job, religion etc.) and 2nd year GPA. As the second step, they considered master's students' data from Asian Institute of Technology (AIT) by using students' admission information (like entry GPA, English proficiency marital status, academic institute, TOFEL score, income age, etc.). Then, they predicted the GPA of students at the end of first year of the masters' program. Decision tree and Bayesian networks were used in this study and their accuracies were compared. The accuracies were as follows: 73/71% for {fail, fair, good, very good}, 84/67% for {fail, good and very good} and 94/93% for {fail, pass} at the CTU/AIT respectively. The prediction of accuracy for 2 classes was much higher than that of 3 or 4 classes. They obtained higher accuracies using the decision tree classifier.

Díaz [11] collected data from 1178 secondary school children in Almeria City (Spain). An adaption of the TAMAI questionnaire and a measurement of school failure were used. The results of this survey showed that the variables such as parents'

academic level, gender, motivation, relationships between peers, and others have a direct influence on the school children performance.

Shahiri et al. [12] predicted students' performance using data mining. They focused on how the prediction algorithm can be used to identify the most important attributes in a student's data.

Asif et al. [13] predicted students' academic achievement at the end of a four-year study program and identified the low and high achieving students, which could result in timely warning to support a low achieving students.

Fok et al. [14] predicted model for students' future development by using deep learning and tensor flow artificial intelligence engine.

These works show that it is possible to predict student performance based on one background qualification, attendance, class test result, assignments mark, English skill, age, gender, family status, religion, marital status, attitude toward class, daily hours spent on study, family income, mother qualification, mother age, living location, living cost of student etc. The researcher also predicts one's performance using a certain subject one studied. Most of the case analyzer use classification and clustering technique where in few case they tried to find factors that are related to course. Nowadays more data are generated by the university while they take a review from the student. Where comes a question, is it possible to predict one performance using students review and other available data?

### 3 Methodology

This section of the paper describe how data been collected and analysis of the student academic performance is done. Firstly, Null data reduced from row data, after that label encoding applied on dataset, thereafter three feature selection algorithm Chi square, Euclidian distance, Correlation been implemented on dataset then result of all three-feature selection algorithm result been combined and after that four-classification algorithm implemented on combined result of feature selection. Different task that have been done throughout this research is described here.

#### 3.1 Data Collection

Precise data collection is fundamental to keeping up the trustworthiness of research, settling on educated business choices and guaranteeing quality affirmation. Data collection methods can be divided into two categories: secondary and primary methods of data collection. We used here both categories. Firstly, in secondary data collection methods, for the research purpose, the dataset gathered from web source named "Kaggle" (Student Survey, University level student survey for academic quality enhancement, 2017) [15]. We downloaded the dataset concentrated the survey analysis on the students' quality enhancement. We named the dataset as Student Survey (SS).

This dataset was collected by a survey conducted by Google forms for a Bangladeshi Universities in order to examine their current academic situation and their improvement. This Survey was part of the Institutional Quality Assurance Program, initiated by the University Grant Commission, Bangladesh and funded by the World Bank. After collecting data, we calculated the average CGPA for each student. Which are then used for data processing and further evaluation as shown in Fig. 1.

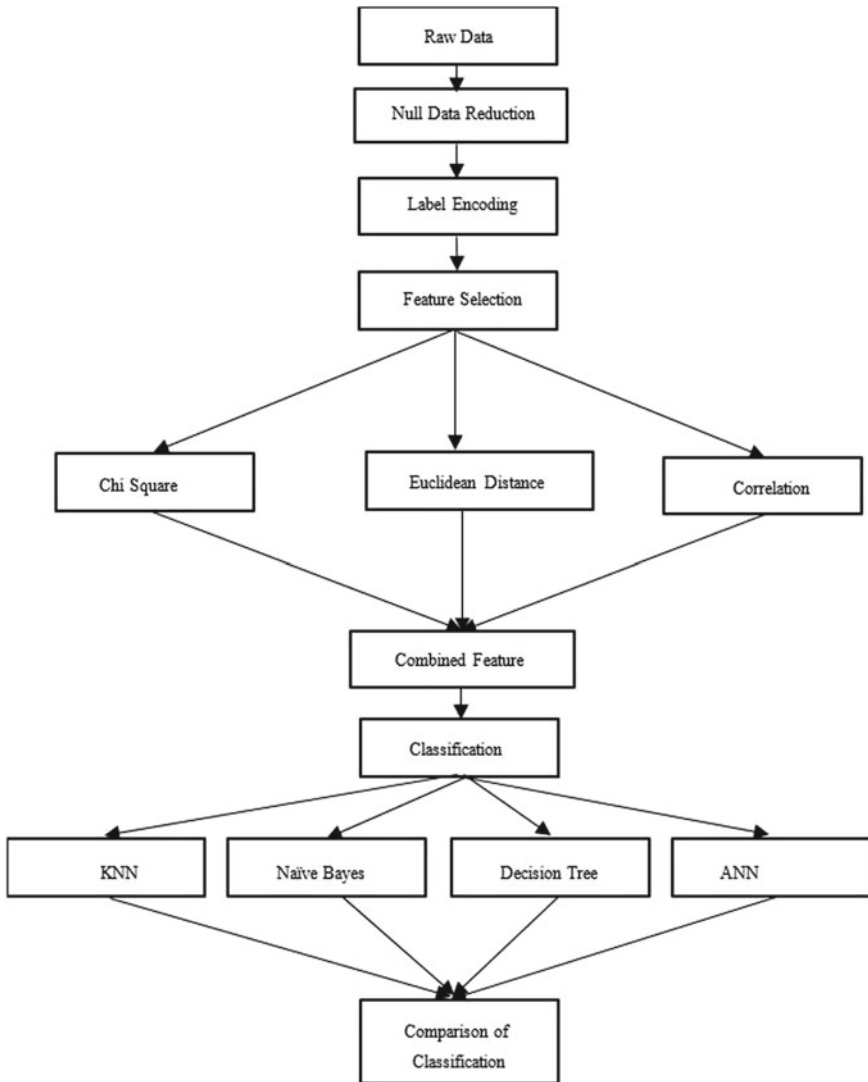


Fig. 1 Proposed data processing model

**Fig. 2** Algorithm for removing null data from dataset

```

1. Load Dataset ();
2. For each Column
3. {Calculate average of column;
4.  IF row of Column contains Null
5.    {Put average of column to Null field; }
6.  Else
7.    {Continue; }
    }
9. Save_Dataset ();

```

### 3.2 Null Data Reduction

In the SS database, there are some common properties such as incomplete, noisy and inconsistent data. There are various fields that have no recorded data for a number of rows, then the null values are removed through calculating the average of the column and putting the average value on null field. This method is not efficient when the percentage of missing values are increased. The algorithm for removing null data from dataset is shown in Fig. 2.

### 3.3 Label Encoding

In this research, the preparation data is named by words for mapping. To change over word names into numbers, a name encoder can be used. The name encoding refers to the manner toward changing the word names into the numerical frame. The coding label of categorical value, there is a function encloses in panda library to code the data and reverse the encoded values. The algorithm for label encoding is shown in Fig. 3.

```

1. Load_DataSet()
2. For each column of columns (Number of total columns/attribute) {
3. unique_values ← Finding unique values of the column
4. For I = 0 to M - 1 (M number of unique values) {
5. Encoding ← Encoded index of I unique_values
    }
  }
6. Save_DataSet()

```

**Fig. 3** Algorithm for label encoding



### 3.4 Feature Selection

**Chi Square.** The Chi-Square test of freedom is utilized to decide whether there is a significant connection between two categorical variables. The recurrence of every classification for one ostensible variable is determined over the classifications of the second ostensible variable. From the definition of chi-square, we can easily deduce the utility of chi-square approach in feature selection using Eq. (1) [16].

$$X^2 = \sum \frac{(O - E)^2}{E} \tag{1}$$

where O is our observed attribute like student SGPA, gender, *curriculumPressure*, *assessmentMeetsObjectives* etc. And E is the Expected value which is Student CGPA.

Chi Square with null hypothesis found out 39 important attributes along with different SGPA which are *studentType*, *curriculumPressure*, *coursesCurriculumArranged*, *modernDevicesUsed*, *admissionPolicy* etc. These attribute are very important features of the dataset.

**Euclidean Distance.** Euclidean distance is usually used to examine the core of the square difference within a pair of features/objects. For each feature, its Euclidean distance from all other features can be calculate using Eq. (2) [16].

$$(x, y) = \left\{ \sum i (X_i - Y_i)^2 \right\}^{\frac{1}{2}} \tag{2}$$

The output results show Euclidean distances of 39 important attributes (selected through Chi Square) for different SGPA from *internetSpeed*, *indoorAndOutdoor*, *medicalFacilities* have less distance. Hence, there are 39 attributes with the lowest distance selected for further evaluation.

**Correlation.** Correlation algorithm finds the correlation between input attributes and output attributes. On our dataset *libraryMaterials*, *resultAssessment*, *classroom-Facilities*, *internetSpeed*, *indoorandoutdoorMedicalMacilities* among with SGPA seem to be more correlated with student academic performance and then top 39 correlated attributes been selected using Eq. (3) for further evaluation [16].

$$r_x = \frac{k\bar{r}_{zi}}{\sqrt{k + k(k - 1)r_{ii}}} \tag{3}$$

**Combining Feature Selection Results.** From Chi-square, we found 39 feature as important. Then we choose the most relevant 39 from other feature selection algorithms. For feature combination, we selected the features that are within best 39 for each feature selection algorithm. From the best 39 features, 22 common feature are selected and named combined features: such as, *1stY1stSem*, *1stY2ndSem*, *1stY3rdSem*, *2ndY1stSem*, *2ndY2ndSem*, *2ndY3rdSem*, *3rdY1stSem*, *3rdY2ndSem*, *3rdY3rdSem*, *4thY1stSem*, *4tyY2ndSem*, *admissionPolicy*, *admissionProcedure*, *sincerityAndCommitment*, *laboratoriesFacilities*, *internetSpeed*, *gymnasiumFacilities*,

*adequateSafety, scholarshipsAvailable, opportunitiesOfcommunityServices, departmentDevelopmentPolicy and departmentServicePolicy.*

### 4 Results and Discussions

The prediction summary on dataset using DT, KNN, NB and ANN are shown in Figs. 4 and 5. These graph show details result for 3, 5 and 9 classes with different test and train data. Here, for class 3, the different classes are considered based on CGPA values as CGPA less than 2.00 as class 0, CGPA within 2.00–3.24 as class 1, and CGPA 3.25–4 as class 2. Class 5 is divided as CGPA less than 2.00 as class 0,

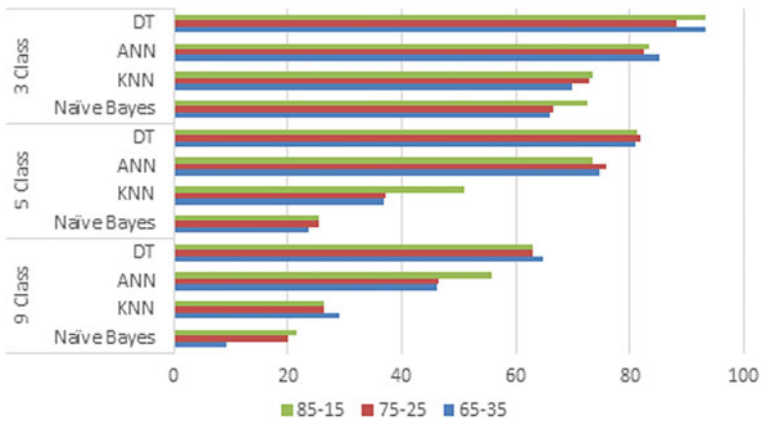


Fig. 4 Comparison of student performance prediction percentage before feature selection

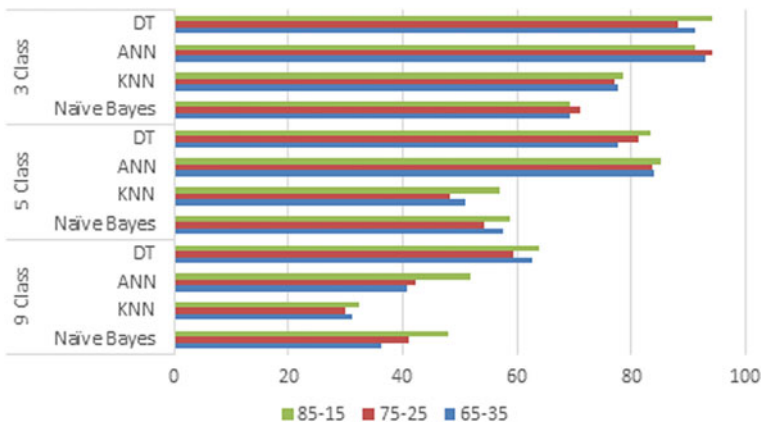


Fig. 5 Comparison of student performance prediction percentage after feature selection

2.00–2.49 as class 1, 2.50 to 2.99 as class 2, 3.00–3.49 as class 3 and 3.50 to 4.00 as class 4. Finally, Class 9 is classified as: CGPA less than 2.00 as 0, 2.00–2.24 as class 1, 2.25–2.49 as class 2, 2.50–2.74 as class 3, 2.75–2.99 as class 4, 3.00–3.24 as class 5, 3.25–3.49 as class 6, 3.50–3.74 as class 7, 3.75–4 as class 9. The result shows that as the number of class decreased accuracy improved in significant number. DT performs better with large number of classes but with feature selection; whereas for less class, ANN Gradually improves and beat DT. The accuracy of prediction after feature selection significantly improved.

Figure 4 shows that KNN Performance is lower than the other three algorithms. Naive Bayes (NB) performs slightly better than KNN with fewer train data but KNN shows better performance than NB with more train data. Here, for 9 class, the average accuracy of NB and KNN are 22.91% and 22.93% respectively. In comparison with KNN and NB, ANN shows better performance of 36.12% and 76.50% accuracy for 9 class and 3 class respectively. DT outperforms KNN, NB, and ANN with better accuracy for all classes. As the number of classes decreases such as for 3 class DT average accuracy is 90.91%.

Figure 5 shows the comparison of all feature selection results. It can be observed that with the increase of the number of class, the accuracy of KNN and NB algorithm decreases and vice-versa. DT also perform better with the higher classes. As the classifier decreases from 9 to 3, ANN shows better performance with an average accuracy of 93.70%, whereas it is 92.18% for DT. Therefore, a small number of class selection may tend to produce a more accurate result. Figure 5 also shows that the highest accuracies are achieved by using 3 class. Hence, the selection of features is a crucial fact to get better accuracy for predicting student academic performance.

## 5 Conclusions and Future Directions

In this research, data mining techniques such as feature selection and classification are applied to student survey dataset and predict university students' performance. Three feature selection algorithms namely Chi-square, Euclidean distance and correlation results are combined for predicting university students' performance. The KNN, NB, DT and ANN classification algorithms are used to predict student performance using 9, 5 and 3 classes. DT performs the best with an accuracy of 60.35% for 9 class. Even for 5 class DT perform better with 11.83% more accuracy than ANN. However, for 3 class ANN performance is 1% more accurate than DT. Therefore, it can be concluded that decreasing number of class may increase the accuracy. This research can be extended different ways, such as more feature selection algorithm and more classification algorithm can be used to evaluate the result more accurately. This research paper predicts student performance as CGPA using student SGPA and their review on university facilities. For future work, student SGPA can be predicted using this dataset.

**Acknowledgements** Publication of this research work is supported by internal research grant RDU170376 funded by University Malaysia Pahang, <https://www.ump.edu.my/>. The authors would also like to thank the Faculty of Electrical & Electronics Engineering, Universiti Malaysia Pahang for financial support.

## References

1. El-Halees AM (2009) Mining students data to analyze e-learning behavior: a case study 29
2. Pandey UK, Pal S (2011) Data Mining: a prediction of performer or underperformer using classification. *Int J Comput Sci Inf Technol (IJCSIT)* 2(2):686–690
3. Hijazi ST, Naqvi SMM (2006) Factors affecting student's performance: a case of private colleges. *Bangladesh E-J Sociol* 3(1)
4. Bharadwaj BK, Pal S (2011) Mining educational data to analyze students' performance. *Int J Adv Comput Sci Appl (IJACSA)* 2(6):63–69
5. Al-Radaideh QA, Al-Shawakfa EW, Al-Najjar MI (2006) Mining student data using decision trees. In: International Arab conference on information technology (ACIT'2006)
6. Ben-Zadok G, Hershkovitz A, Mintz E, Nachmias R (2007) Examining online learning processes based on log files analysis: a case study. In: Research, reflection and innovations in integrating ICT in education.
7. Bharadwaj BK, Pal S (2011) Data mining: a prediction for performance improvement using classification. *Int J Comput Sci Inf Secur (IJCSIS)* 9(4):136–140
8. Yassein NA, Helali RGM, Mohomad SB (2017) Predicting student academic performance in ksa using data mining techniques. *J Inform Tech Softw Eng* 7:213. <https://doi.org/10.4172/2165-7866.1000213>
9. Asif R, Merceron A, Pathan MK (2014) Predicting student academic performance at degree level: a case study. *Int J Intell Syst Appl* 7(1):49–61
10. Nghe NT, Janecek P, Haddawy P (2007) A comparative analysis of techniques for predicting academic performance. In: 2007 37th annual frontiers in education conference—global engineering: knowledge without borders, opportunities without passports, pp T2G-7–T2G-12. IEEE
11. Díaz AL (2003) Personal, family, and academic factors affecting low achievement in secondary school. *Electron J Res Educ Psychol Psychopedagogy* 1(1):43–66
12. Shahiri AM, Husain W, Rashid NA (2015) A review on predicting student's performance using data mining techniques. *Procedia Comput Sci* 72:414–422
13. Asif R, Merceron A, Ali SA, Haider NG (2017) Analyzing undergraduate students' performance using educational data mining. *Comput Educ* 113:177–194
14. Fok WWT, He YS, Yeung HHA, Law KY, Cheung K, Ai Y, Ho P (2018) Prediction model for students' future development by deep learning and tensorflow artificial intelligence engine. In: 2018 4th international conference on information management (ICIM), pp 103–106. IEEE
15. Mustafiz R (2018) Student survey. Retrieved May 1, 2018, <https://www.kaggle.com/razibmustafiz/student-survey>
16. Ladha L, Deepa T (2011) Feature selection methods and algorithms. *Int J Comput Sci Eng* 3(5):1787–1797

# Open-Set Face Recognition in Video Surveillance: A Survey



Wasseem N. Ibrahim Al-Obaydy and Shahrel Azmin Suandi

**Abstract** Face recognition has received a substantial attention by the vision community over the past few decades. Most of the proposed frameworks have adopted the closed-set form of face recognition. However, when a novel unregistered face is presented to the system, the result will be misclassification. A more general and challenging open-set face recognition scheme is highly desirable due to its ability in dealing with the unknown persons which are not enrolled before. We observed that there is a shortage in survey papers that explore the research endeavors in open-set face recognition. In this paper, we present a literature survey of the open-set face recognition approaches that have been introduced for real-world scenarios focusing on video surveillance applications. Moreover, we discuss the current difficulties and suggest the promising directions for future research. The paper also describes the evaluation metrics and available benchmarking face video surveillance databases.

**Keywords** Open-set face recognition · Video surveillance · Identity of Interest (IoI)

## 1 Introduction

Nowadays, the governments and private sectors aim to enhance screening and security by adopting automatic surveillance systems to monitor the crowd for identity of interest (IoI) recognition in many real-world scenarios for example, airports, transport stations, shopping malls, and others. The objective is to automatically recognize human faces regardless whether or not they are members in the reference database. In general, the automated facial recognition system performs as either a “closed-set” or an “open-set” [1]. The closed-set face recognition aims at identifying the identity of only previously registered subjects. The open-set face recognition recognizes the

---

W. N. I. Al-Obaydy (✉) · S. A. Suandi  
Intelligent Biometric Group, School of Electrical and Electronic Engineering, Universiti Sains  
Malaysia, Engineering Campus, 14300 Nibong Tebal, Pulau Pinang, Malaysia  
e-mail: [wasseem.alobaydy@student.usm.my](mailto:wasseem.alobaydy@student.usm.my)

W. N. I. Al-Obaydy  
Computer Engineering Department, University of Technology, Baghdad, Iraq

© Springer Nature Singapore Pte Ltd. 2020  
A. N. Kasruddin Nasir et al. (eds.), *InECCE2019*, Lecture Notes in Electrical  
Engineering 632, [https://doi.org/10.1007/978-981-15-2317-5\\_36](https://doi.org/10.1007/978-981-15-2317-5_36)

identity of registered subjects and detects the unregistered individuals. Section 2 describes these types in more detail. Thus, applying closed-set hypothesis in surveillance environments is not feasible and therefore should be turned to the open-set approach [2]. Open-set face recognition in video surveillance is utilized into two common applications, namely watch-list screening and face re-identification [3]. In the former, the systems recognize a small set of individuals who are on a watch-list and reject everyone outside the list. In the latter, we have a network of video surveillance cameras capturing different non-overlapping zones. The face recognition system is trained using faces acquired from video sequences in one zone, and seeks to re-identify them among other individuals as they move from one camera zone to another [4]. However, video surveillance scenarios are very challenging environments due to the uncontrolled complex conditions of image acquisition. Face images captured by video surveillance cameras suffer from large intra-subject variations such as changes in illumination, pose, facial expression, occlusion and orientation, and small inter-subject variations such as the facial similarity between individuals' appearances. Moreover, these images usually have low resolution, poor quality, small sizes, blurring and uncooperative subjects. Such challenges make the open-set face recognition in video surveillance a more complex task for researchers [5–7].

In this work, we present a survey of the approaches that recognize human face in an open-set style. Although several survey papers [8–11] have been introduced to categorize and summarize the existing face recognition approaches from different points of view, they have focused only on the closed-set recognition form. To the best of our knowledge, this paper represents the first state-of-the-art literature survey on open-set face recognition. The remaining part of this paper is organized as follows. Section 2 highlights the differences between the closed-set and open-set types of face recognition. Section 3 categorizes and describes the principles of existing open-set face recognition approaches. In Sect. 4, we discuss the problematic issues in the existing methods and suggest recommendations for future research. The evaluation metrics used for assessing the performance of open-set face recognition approaches are described in Sect. 5. Section 6 summarizes the available benchmarking face databases collected by video surveillance cameras. The conclusion of this paper is drawn in Sect. 7.

## 2 Closed-Set Versus Open-Set Face Recognition

In the closed-set face recognition, we ask the question: whose face is this? The answer is based on the fact that in the closed-set recognition, all identity classes that are examined during the identification phase were previously presented to the system at enrollment phase. This means that each probe face is known and should belong to an enrolled subject in the gallery. The recognition here is performed by matching the probe face image against all the subjects in the gallery and the best match is returned. However, the applicability of this kind of recognition may become questionable in real world situations, e.g. video surveillance, in which the face recognition systems

may confront unknown persons which are not registered in the database. In this case, if unregistered face is presented to the closed-set systems, it will be erroneously identified as one of the database faces. Since these systems have much smaller set of enrolled faces than what they observe, there will be a large number of misclassified faces and thus the face recognition problem in this case will be extended to the open-set problem [1, 12–14].

A recent study [15] has re-defined machine learning-based recognition as open-set recognition. The definition stated that open-set recognition represents the scenario when there is insufficient knowledge of the world at training time, and novel unknown objects can be submitted to the system during testing. That is to say, the open-set recognition may encounter new objects in testing that were not seen in training. In open-set face recognition, some identity classes that are presented during the identification stage were not previously registered in the enrollment stage. This means that each probe face may not have a counterpart in the gallery. Therefore, when a probe face is submitted to recognition, the question that should be asked here: do we know this face? In this case, prior to identity recognition, the system should be able first to decide whether the probe face is known or unknown. The case “known” means that the subject of the probe face was previously registered in the database and vice versa. If the probe face is declared as known, the system should provide the identity of the probe face. Otherwise, the system should either reject it (i.e., exclude it from identity recognition) or enroll it automatically as a new subject in the gallery [1, 13, 16, 17].

The open-set face recognition framework should provide multi-class classification and a rejection mechanism [15, 18, 19]. The multi-class classification task predicts the identity of the input face as one of the identities of training faces. The importance of rejection option is to decide whether the input face is unknown and does not belong to any of the training faces. Several methods were proposed in the literature to form the rejection functionality. Some approaches [7, 12, 20] proposed to project the probe face on a decision boundary so that the probe face is accepted as known if its projection is inside or on the boundary, otherwise the probe face is rejected as unknown if it is projected outside. Another rejection criterion may also be determined based on rejecting the classes that have the lowest posterior probabilities or likelihoods as proposed in [21]. Other approaches [16–18, 22–30] represented the rejection procedure as a decision threshold on which the probe face is decided as a familiar or unfamiliar face. As pointed out by Li and Wechsler [18] and Tjahyadi [31], estimating rejection thresholds automatically is very challenging due to their reliance on the quality and structure of training face images. The traditional approach of selecting a priori threshold is based on computing the distribution of intra-class and inter-class distances of the training set. The threshold value that equalizes the overlapping areas of the distributions is then selected.

### 3 Literature Review

In this section, a brief review is presented for the research efforts that tackle the problem of open-set face recognition particularly in video surveillance. Generally, methods addressing open-set face recognition can be divided depending on the type of basis classification into three major categories: one-class, two-class, and multi-class classification based approaches. Among these categories, multi-class classification based approaches are the predominant approaches recruited for open-set face recognition. We provide 18 research works in this category while 8 papers are reviewed for each of the one-class and two-class categories.

#### 3.1 *One-Class Classification Based Approaches*

The one-class (unary) classification models have been efficiently used to implement the multi-class classification with rejection option [32]. This paradigm is adopted by researchers to decompose the multi-class open-set face recognition problem into several one-class classification problems. The idea is, for each subject in the database, one or more one-class classification models are built using only training images of that subject. The probe face is then presented to each unary model to yield either a decision score, similarity score or reconstruction error to indicate how much the query face belongs to the corresponding subject. The resulted output scores are then employed to define a measure that is compared to a threshold to accept the probe face as a known face or reject it as unknown. Moeini et al. [33] introduced three open-set face recognition approaches to handle the look-alike faces based on 3D face reconstruction, sparse representation classification (SRC), collaborative representation classification (CRC) and combined SRC and CRC methods. Zhang and Patel [30] exploited the statistical extreme value theory (EVT) to extend the sparse representation-based classification (SRC) method to open-set recognition. Dhifi and Diallo [12] exploited support vector machine (SVM) to encompass all training images of each class in a minimum bounding hyper-sphere specified by a center and radius. Extending the sphere boundary may increase the chances of identifying the faces that belong to the corresponding class. Conversely, shrinking the sphere boundary may increase the chances of rejecting faces that do not belong to the associated class. Zhang and Hao [29] combined the kernel associative memory (KAM) with transductive confidence machine (TCM) for open-set face recognition. Kato et al. [34] developed an angle aware face recognition system based on a proposed angle feature extraction technique, independent component analysis (ICA), and multi-layer perceptron (MLP) classifiers. Chang et al. [35] applied one-class support vector data description (SVDD) on the local binary pattern (LBP) features of each training class to construct a super-sphere model specified with a core and radius for each database class. Stallkamp et al. [17] suggested a video-based face recognition approach based



on training one Gaussian mixture model (GMM) per person using the person's training discrete cosine transform (DCT)-based feature vectors. Kohir and Desai [21] trained one hidden Markov model (HMM) with 5 state ergodic for each registered subject using the discrete cosine transform (DCT)-based features extracted from the subject's training images.

### 3.2 Two-Class Classification Based Approaches

The multi-class classification problem has also been implemented using two-class (binary) classifiers [36]. A number of published works have invested this solution to address the open-set face recognition problem. One or more binary classifiers learn to distinguish between known and unknown classes by training using images of target subjects (positive classes) and images of other subjects inside and/or outside the dataset (negative classes). The process of identifying whether the query face is known or unknown is similar to that of the one-class classification based approaches. In this section, we review the approaches that employed two-class classification in open-set face recognition. Bashbaghi et al. [3] trained an ensemble of two-class support vector machines (SVMs) for each target person using multiple face representations extracted from a person's still image and many video images of other non-target unknown persons in the video surveillance scene. Vareto et al. [28] divided the registered subjects randomly into many two disjoint groups, namely positive and negative subsets. The authors trained a binary partial least squares (PLS) or fully connected networks (FCN) model for each group of both positive and negative sets. The work presented by dos Santos and Schwartz [16] suggested five approaches for open-set face recognition. One approach trains a binary partial least squares (PLS) regression model using the known gallery set and external background set. The remaining four approaches, namely support vector machine (SVM-All and SVM-Single), least squares (LS), and Chebyshev inequality (CI), depend on responses from the face identification. Qiu et al. [20] employed the morphing technique proposed in [7] to generate two image sets: borderline positive images (less morphed faces) and borderline negative samples (deeper morphed faces). The two sets were used to train two parallel SVM-based binary classifiers for each target individual. Pagano et al. [2] used an ensemble of two-class probabilistic fuzzy adaptive resonance theory map (PFAM) neural network classifiers (or ensemble of detectors, EoDs) per subject to propose a multi-classifier face recognition approach in video surveillance. Kamgar-Parsi et al. [7] proposed a face image morphing operator to generate two sets of synthetic images: borderline acceptable and borderline unacceptable face images. The two sets were then subsampled and used to train a neural network classifier for each person. Ekenel et al. [37] used support vector machines (SVMs) to construct multiple verifiers so that one SVM verifier is trained for each known subject in the gallery using the training images of the known subject and training images of unknown subjects outside the gallery. Hsu [38] reported to fuse hidden Markov model (HMM) and support vector machine (SVM) for each subject in the gallery.

The subject's HMM module measures the similarity likelihood between the testing face and each training subject face. The SVM modules then measure the distances of the candidates.

### 3.3 *Multi-class Classification Based Approaches*

In this section, we describe the approaches that use the conventional multi-class classification models to handle the problem of open-set face recognition. In this category, one or more multi-class classifiers are trained using the training data of all classes in the database. During testing, each classifier matches the query face with all trained faces and produces matching scores. The resulted scores are processed to yield a confidence score that is compared to a threshold to decide whether to accept or reject the query face. Xue and Zhu [39] combined visual geometry group (VGG) deep neural network and recursive label propagation based on statistical classification (ReLPBSC) algorithm to propose a low resolution and open-set face recognition framework. Al-Obaydy and Suandi [40] proposed an open-set single-sample face recognition in video surveillance using fuzzy adaptive resonance theory map (ARTMAP) neural network. The fuzzy ARTMAP either classifies the probe face as one of gallery faces or rejects it as unknown depending on a predefined vigilance parameter. Xie et al. [41] adopted deep transfer learning, multi-class support vector machines (SVMs) and extreme value statistical quantity (standard deviation) to solve the open-set face recognition problem. Toufiq and Islam [42] introduced a face recognition scheme with rejection option based on a proposed fusion technique and backpropagation neural network (BPNN) to classify principal component analysis (PCA)-based feature vectors. Zhang [43] proposed a face recognition with rejection option based on four ensembles of random subspace support vector machines (SVMs). A further face recognition with rejection approach was reported by Ravi et al. [24] based on dual-tree complex wavelet transform (DT-CWT) and local binary pattern (LBP). The work reported by Pankaj and Wilscy [44] proposed a fuzzy neural network classifier based on integrated adaptive fuzzy clustering (IAFC) algorithm to classify linear discriminant analysis (LDA)-based feature vectors. Theodorakopoulos et al. [27] proposed to use sparse coding procedure and nearest neighbor classifier for face recognition with rejection option. The sparse coding technique was employed for facial feature extraction based on two non-parametric dictionaries which are constructed using  $k$ -singular value decomposition (SVD) and generalized sparse coding neural gas (GSCNG) algorithms. Chen et al. [45] suggested a face recognition system with a rejection mechanism based on a margin-enhanced space. A further face recognition with rejection framework based on error correcting output codes (ECOC) and multi-layer perceptron (MLP) neural network was proposed by Hatami et al. [22] to classify principal component analysis (PCA)-based facial feature patterns. Nakamura and Takano [46] reported a rotation and size spreading associative neural network (RS-SAN net) to recognize registered and unregistered face images. Sing et al. [26] proposed a face recognition scheme with rejection criteria using

point symmetry distance-based radial basis function neural network (RBFNN). The research carried out by Sebastiao et al. [25] suggested to use view-morphing method and independent component analysis (ICA) with a rejection threshold to implement a face recognition system to control the access to restricted areas. Mu et al. [47] proposed a face recognition scheme with rejection mechanism using an associative memory neural network based on restricted Coulomb energy (RCE) network. Li and Wechsler [18] proposed an open-set face recognition approach based on transductive confidence machine (TCM) and  $k$ -nearest neighbors ( $k$  NN). Paliy et al. [23] presented a face recognition framework for access control applications using wavelet transform and ensemble of multilayer feedforward neural networks (EMNN) with a proposed decision rule based on using threshold and voting techniques. A face recognition approach based on ordinal correlation principle and automatic rejection threshold algorithm was proposed by Tjahyadi et al. [31] for the watch-list scenario. The last multi-class classification framework in this category is the face recognition system presented by Seow et al. [48] for real time surveillance based on composite principal component analysis (CPCA).

## 4 Current Problems and Future Research

We have concentrated in the previous section on the treatment of open-set face recognition problem from different perspectives. In this section, we discuss the shortcomings in the established techniques and propose the possible future research directions.

- The majority of approaches train several images per subject in order to address the intra-class variations (pose, illumination, facial expression and partial occlusion). However, in real-life face recognition applications, such as identity of interest recognition in video surveillance and ID card identification, the collection of many samples per person is hard to achieve due to the limited availability of face images and storage capacity. We anticipate that the open-set face recognition using single sample per person will receive more attention by the computer vision research community.
- Most of existing frameworks rely on a manually set criterion to decide whether to accept or reject the inquiry face. This criterion is determined empirically and it differs from one training set to another depending on the quality and structure of the training set. Therefore, estimating a decision criterion automatically is highly preferred, yet it is extremely challenging due to the intra-person and inter-person variations among training subjects.
- The two-class classification based approaches train non-target (negative) set as well as the target (positive) set to enable the system to detect the unknown faces. However, these negative classes are considered as insufficient data due to they do not describe the whole open universe of novel faces. The rejection performance

of these systems may decline when the ratio of unknown faces to known faces is large in the probe set during operation mode.

- The researches intended for surveillance applications have been evaluated using face datasets collected by high quality cameras under controlled conditions. However, such evaluation may not be reliable due to it does not reflect the real-world surveillance scenario. Alternatively, these approaches should be evaluated based on face databases captured by surveillance equipment under unconstrained conditions.

## 5 Performance Evaluation

The efficacy of open-set face recognition approaches is assessed based on evaluation paradigm that must include novel unseen subjects in the testing set [15]. A number of standard statistical performance measures are used to conduct the open-set evaluation. False acceptance rate (FAR) is the ratio of the number of unknown subjects that are falsely accepted as known persons to the total number of subjects in the testing set. False rejection rate (FRR) is the ratio of the number of known subjects that are falsely rejected as unknown persons to the total number of subjects in the testing set. FAR and FRR are normally illustrated using receiver operating characteristic (ROC) curve [49]. Equal error rate (EER) is the sum of FAR and FRR showing the total error of the system. The best performance of open-set face recognition approach is when EER is as minimum as possible. Correct classification rate (CCR) is the ratio of the number of known subjects that are correctly recognized (i.e. identified with the correct label) to the total number of known subjects in the testing set. Correct rejection rate (CRR) is the ratio of the number of unknown subjects that are correctly rejected as unknown to the total number of unknown subjects in the testing set. According to Scheirer et al. [15], the overall accuracy is measured as the proportion of the number of truly classified (known and unknown) subjects to the sum of the number of truly classified (known and unknown) subjects and the number of falsely classified (known and unknown) subjects. However, since in open-set recognition the number of known subjects is expected to be much smaller than the number of unknown subjects, this accuracy ratio is not precise. Alternatively, three new statistical measures, namely recall, precision and F-measure, are used to evaluate the classification performance in open-set recognition. Recall is the proportion of the number of known subjects that are correctly classified as known to the number of all known subjects in the testing set. Precision is the proportion of truly classified known subjects to the sum of truly classified known subjects and falsely classified unknown subjects. F-measure is defined based on recall and precision as in (1).

$$F\text{-measure} = 2 \times \frac{\text{Precision} \times \text{Recall}}{\text{Precision} + \text{Recall}} \quad (1)$$

Lastly, a measure called openness is defined by Scheirer et al. [15] to compute the degree of openness of open-set face recognition as in (2). This equation produces the openness as a percentage where 0 represents totally closed system and larger values more open system.

$$openness = 1 - \sqrt{\frac{2 \times |training\ classes|}{|testing\ classes| + |target\ classes|}} \quad (2)$$

## 6 Face Video Surveillance Databases

To prove that the open-set face recognition algorithms have a robust, feasible and reliable performance in video surveillance, they should be experimented on face databases collected by video surveillance cameras. Such datasets mimic the real-world uncontrolled conditions of surveillance applications in terms of illumination, pose, facial expression, partial occlusion, subject's cooperation and low image resolution. Three publicly available face video surveillance databases namely large variability surveillance camera face database [50], surveillance cameras face (SCface) [6], and ChokePoint [51] have been acquired for research purposes. The key characteristics of these databases are outlined in Table 1.

**Table 1** Key characteristics of existing face video surveillance databases

Database	Subjects	Images	Frame size	Cropped image size	Videos	Conditions	Modes
Large variability database [50]	100 36 males 64 females	20,000	704 × 576	N/A	200	Indoor Outdoor	v, n
SCface [6]	130 114 males 16 females	4160	680 × 556	100 × 75 144 × 108 224 × 168	N/A	Indoor	v, n
ChokePoint [51]	25 at portal 1 19 males 6 females 29 at portal 2 23 males 6 females	64,204	800 × 600	96 × 96	48	Indoor	v

The mode is denoted by (v) visible and (n) night vision

## 7 Conclusion

In this paper, we have presented a brief review of the existing open-set face recognition approaches and face databases in real-world scenarios emphasizing video surveillance. We have categorized the current approaches based on the type of basis classification model into one-class, two-class, and multi-class approaches. The multi-class classification based approaches generate decision boundaries that arise in complexity as the number of classes increases. They also may need to retrain when a new class is enrolled. One-class or two-class classification based approaches encapsulate training face images of each gallery subject in a separate classification model providing a better discrimination among enrolled faces. This separation also provides flexibility in adding or removing classes without the need to retrain the system. The one-class approaches have a key advantage over the two-class counterparts in that they do not need to train negative unknown faces. From this literature review, we conclude that the research attempts in open-set face recognition are still limited and have not reached a high maturity as in the closed-set face recognition research. Thus, open-set face recognition still represents an open research problem that needs to be investigated further.

## References

1. Jain AK, Li SZ (2011) Handbook of face recognition. Springer, Berlin
2. Pagano C, Granger E, Sabourin R, Gorodnichy DO (2012) Detector ensembles for face recognition in video surveillance. In: The 2012 international joint conference on neural networks (IJCNN), pp 1–8. IEEE
3. Bashbaghi S, Granger E, Sabourin R, Bilodeau GA (2017) Robust watch-list screening using dynamic ensembles of SVMs based on multiple face representations. *Mach Vis Appl* 28(1–2):219–241
4. De-la Torre M, Granger E, Sabourin R, Gorodnichy DO (2015) An adaptive ensemble-based system for face recognition in person re-identification. *Mach Vis Appl* 26(6):741–773
5. Gao H, Ekenel HK, Stiefelham R (2010) Robust open-set face recognition for small scale convenience applications. In: Joint pattern recognition symposium, pp 393–402. Springer, Berlin
6. Grgic M, Delac K, Grgic S (2011) SCface-surveillance cameras face database. *Multimedia Tools Appl* 51(3):863–879
7. Kamgar-Parsi B, Lawson W, Kamgar-Parsi B (2011) Toward development of a face recognition system for watchlist surveillance. *IEEE Trans Pattern Anal Mach Intell* 33(10):1925–1937
8. Abate AF, Nappi M, Riccio D, Sabatino G (2007) 2D and 3D face recognition: a survey. *Pattern Recogn Lett* 28(14):1885–1906
9. Chihaoui M, Elkefi A, Bellil W, Ben Amar C (2016) A survey of 2D face recognition techniques. *Computers* 5(4):21
10. Tan X, Chen S, Zhou ZH, Zhang F (2006) Face recognition from a single image per person: a survey. *Pattern Recogn* 39(9):1725–1745
11. Zhao W, Chellappa R, Phillips PJ, Rosenfeld A (2003) Face recognition: a literature survey. *ACM Comput Surv (CSUR)* 35(4):399–458
12. Dhifi W, Diallo AB (2016) Face recognition in the wild. *Procedia Comput Sci* 96:1571–1580

13. Sapkota A, Boulton TE (2013) Large scale unconstrained open set face database. In: 2013 IEEE sixth international conference on biometrics: theory, applications and systems (BTAS), pp 1–8. IEEE
14. Wechsler H (2009) Reliable face recognition methods: system design, implementation and evaluation, vol 7. Springer Science & Business Media, Berlin
15. Scheirer WJ, de Rezende Rocha A, Sapkota A, Boulton TE (2013) Toward open set recognition. *IEEE Trans Pattern Anal Mach Intell* 35(7):1757–1772
16. dos Santos CE Jr, Schwartz WR (2014) Extending face identification to open-set face recognition. In: 2014 27th SIBGRAPI conference on graphics, patterns and images (SIBGRAPI), pp 188–195. IEEE
17. Stallkamp J, Ekenel HK, Stiefelhagen R (2007) Video-based face recognition on real-world data. In: IEEE 11th international conference on computer vision, ICCV 2007, pp 1–8. IEEE
18. Li F, Wechsler H (2005) Open set face recognition using transduction. *IEEE Trans Pattern Anal Mach Intell* 27(11):1686–1697
19. Tax DM, Duin RP (2008) Growing a multi-class classifier with a reject option. *Pattern Recogn Lett* 29(10):1565–1570
20. Qiu J, Zhang Y, Sun J (2013) Face recognition in open world environment. In: Visual communications and image processing (VCIP), pp 1–6. IEEE
21. Kohir VV, Desai U (2000) Face recognition. In: The 2000 IEEE international symposium on circuits and systems, Proceedings, ISCAS 2000, Geneva, vol 5, pp 305–308. IEEE
22. Hatami N, Ebrahimipour R, Ghaderi R (2008) ECOC-based training of neural networks for face recognition. In: 2008 IEEE conference on cybernetics and intelligent systems, pp 450–454. IEEE
23. Paliy I, Sachenko A, Koval V, Kurylyak Y (2005) Approach to face recognition using neural networks. In: Intelligent data acquisition and advanced computing systems: technology and applications, IDAACS 2005, pp 112–115. IEEE
24. Ravi J, Tevaramani SS, Raja K (2012) Face recognition using DT-CWT and LBP features. In: 2012 international conference on computing, communication and applications (ICCCA), pp 1–6. IEEE
25. Sebastiao R, Silva JA, Padilha AJ (2006) Face recognition from spatially-morphed video sequences. In: International conference image analysis and recognition, pp 365–374. Springer, Berlin
26. Sing JK, Basu DK, Nasipuri M, Kundu M (2007) Face recognition using point symmetry distance-based RBF network. *Appl Soft Comput* 7(1):58–70
27. Theodorakopoulos I, Rigas I, Economou G, Fotopoulos S (2011) Face recognition via local sparse coding. In: 2011 IEEE international conference on computer vision (ICCV), pp 1647–1652. IEEE
28. Vareto RH, Silva S, de Oliveira Costa F, Schwartz WR (2017) Towards open-set face recognition using hashing functions. In: 2017 IEEE international joint conference on biometrics (IJCB), pp 634–641. IEEE
29. Zhang B, Hao H (2014) Open-set face recognition by transductive kernel associative memory. In: 2014 7th international congress on image and signal processing (CISP), pp 633–638. IEEE
30. Zhang H, Patel VM (2017) Sparse representation-based open set recognition. *IEEE Trans Pattern Anal Mach Intell* 39(8):1690–1696
31. Tjahyadi R, Liu W, An S, Venkatesh S (2005) Face recognition based on ordinal correlation approach. In: Proceedings of the 2005 international conference on intelligent sensors, sensor networks and information processing conference, pp 349–354. IEEE
32. Khan SS, Madden MG (2009) A survey of recent trends in one class classification. In: Irish conference on artificial intelligence and cognitive science, pp 188–197. Springer, Berlin
33. Moeini A, Faez K, Moeini H, Safai AM (2017) Open-set face recognition across look-alike faces in real-world scenarios. *Image Vis Comput* 57:1–14
34. Kato H, Chakraborty G, Ogata N, Chakraborty B (2011) A real-time angle aware face recognition system based on artificial neural network. In: 2011 3rd international conference on awareness science and technology (iCAST), pp 521–526. IEEE

35. Chen C, Zhan Y, Wen C (2009) Hierarchical face recognition based on SVDD and SVM. In: International conference on environmental science and information application technology, ESIAT 2009, vol 2, pp 692–695. IEEE
36. Tax DM, Duin RP (2002) Using two-class classifiers for multiclass classification. In: 16th international conference on pattern recognition. Proceedings, vol 2, pp 124–127. IEEE
37. Ekenel HK, Szasz-Toth L, Stiefelshagen R (2009) Open-set face recognition-based visitor interface system. In: International conference on computer vision systems, pp 43–52. Springer, Berlin
38. Hsu GSJ (2009) Fusion classifier for open-set face recognition with pose variations. *Int J Comput Electr Autom Control Inf Eng* 3(8):2099–2105
39. Xue S, Zhu H (2019) Low-resolution and open-set face recognition via recursive label propagation based on statistical classification. *Int J Wavelets Multiresolut Inf Process* 17(02):1940002
40. Al-Obaydy WNI, Suandi SA (2018) Open-set single-sample face recognition in video surveillance using fuzzy ARTMAP. *Neural Comput Appl*. <https://doi.org/10.1007/s00521-018-3649-0>
41. Xie H, Du Y, Yu H, Chang Y, Xu Z, Tang Y (2018) Open set face recognition with deep transfer learning and extreme value statistics. *Int J Wavelets Multiresolut Inf Process* 16(04):1850034
42. Toufiq R, Islam MR (2014) Face recognition system using PCA-ANN technique with feature fusion method. In: 2014 international conference on electrical engineering and information & communication technology (ICEEICT), pp 1–5. IEEE
43. Zhang B (2012) Reliable face recognition by random subspace support vector machine ensemble. In: 2012 International conference on machine learning and cybernetics (ICMLC), vol 1, pp 415–420. IEEE
44. Pankaj DS, Wilsy M (2011) Face recognition using fuzzy neural network classifier. In: *Advances in parallel distributed computing*, vol 203, pp 53–62. Springer, Berlin
45. Chen JC, Shi SY, Lien JJJ (2010) Face recognition and unseen subject rejection in margin-enhanced space. In: 2010 international conference on system science and engineering (ICSSE), pp 631–636. IEEE
46. Nakamura K, Takano H (2007) Unregistered face discrimination by the face orientation and size recognition. In: International joint conference on neural networks, IJCNN 2007, pp 1924–1928. IEEE
47. Mu X, Artiklar M, Watta P, Hassoun MH (2006) An RCE-based associative memory with application to human face recognition. *Neural Process Lett* 23(3):257–271
48. Seow MJ, Gottumukkal R, Valaparla D, Asari K (2004) A robust face recognition system for real time surveillance. In: International conference on information technology: coding and computing, Proceedings, ITCC 2004, vol 1, pp 631–635. IEEE
49. Fawcett T (2006) An introduction to ROC analysis. *Pattern Recogn Lett* 27(8):861–874
50. Salka TD, Hanafi M, Mashohor S, Ahamad SMS (2015) Large variability surveillance camera face database. In: 2015 seventh international conference on computational intelligence, modelling and simulation (CIMSIm), pp 108–112. IEEE
51. Wong Y, Chen S, Mau S, Sanderson C, Lovell BC (2011) Patch-based probabilistic image quality assessment for face selection and improved video-based face recognition. In: 2011 IEEE computer society conference on computer vision and pattern recognition workshops (CVPRW), pp 74–81. IEEE



# Hardware Development of Auto Focus Microscope



Dwi Pebrianti, Rosyati Hamid, Faradila Naim, Mohd Falfazli Mat Jusof, Nurul Wahidah Arshad and Luhur Bayuaji

**Abstract** The scientific instrument technology has growth faster than we all could imagine, there are many research team keeping their momentum in creating new innovation in scientific instrumentation technologies. The optical microscopes are still being used widely in the scientific research especially by researcher and medical practitioners. Manually deal with the microscope could make the user spend so much time to obtain the result of cleared image. It could cost hours to obtain the desire result. From this problem, this study proposes the development of hardware system for auto focused of an optical microscope. The proposed system consists of two stepper motors that will move the fine focus knob and the course focus knob on a microscope. The timing belts are being used as mounting between the stepper motor and the fine/course focus knob. The motor will move step by step in same degree given from the command of a program. The motor is able to be controlled and it moves slowly to perform an auto focus task. Additionally, it is able to move in a small angle to find the proper exposure of the images scan. The hardware implementation of auto focus on the optical microscope has been tested and it worked perfectly. The result presented in this study shows that the proposed system is able to do auto focus in precise step which is  $5^\circ$  step.

**Keywords** Motor control · Auto focus · Optical microscope

---

D. Pebrianti (✉) · R. Hamid · F. Naim · M. F. M. Jusof · N. W. Arshad  
Faculty of Electrical and Electronics Engineering, Universiti Malaysia Pahang, Pekan, Malaysia  
e-mail: [dwipebrianti@ump.edu.my](mailto:dwipebrianti@ump.edu.my)

L. Bayuaji  
Faculty of Computer Science and Software Engineering, Universiti Malaysia Pahang, Pekan, Malaysia

D. Pebrianti · L. Bayuaji  
Magister of Computer Science, Universitas Budi Luhur, Jakarta 12260, Indonesia

## 1 Introduction

The scientific instrument technology has growth faster than we all could imagine, there are many research team all over the world who keep their momentum in creating the new innovations in scientific instrumentation technology to help other researchers to obtain the precise result from the instrumentation used. Currently, optical microscopes are still being used widely in the scientific research especially in hospital and laboratories. This device helps a lot of researchers and medical practitioners to deal with the specimen under observed such as to find the cause of a disease.

The microscope is usually being used in laboratories, the user commonly used it for scanning the micro object which normal eye cannot see. The microscope helps human a lot in order to determine the problem. However, manually dealing with the microscope could spend much time and effort. Imagine if the objects that need to be scan are in a huge quantity, it could cost hours or even day. The new technology has proved that the innovations of an auto focus microscope can scan and obtain the cleared image for 42 objects just in minutes. By using this technology, the time spent on the analysis by using microscope to obtain the cleared images could be minimized.

The application of an auto focuses optical microscope is where the object, for example sputum is put on the stage of an optical microscope, and then scanned automatically to obtain clearer result image of the object. Here, the sputum is the mucus that forms through coughing, which it is not really the saliva and spit. The sputum is being used as the sample for the experiment. The characteristic of the sputum consists of the pus cell and the epithelial cell.

In auto focus optical microscope, stepper motors are used to move the stage of the microscope. The stepper motor will be mounted into the thick Perspex and connected to motor drivers. The motor drivers are a device with little current amplifier. It will take low current signal from a microcontroller and then turn it into a higher current signal to drive on the stepper motor. Here, the microcontroller plays the main role because it will process and transmit the input signal to motor driver in order to implement the auto focus for optical microscope.

The clearer image can be obtained by examining the images in sequential images formed by using the Hand-eye coordination of Z-axis of microscope. The different focus on the Z-axis of the microscope will generate the microscopic imaging with optimal focusing. Initially, the probability density function of image focusing by auto focus is obtained then the clearer imaging will be assigned as the reference images [1].

The high-speed autofocusing of multi-size micro-objects, proposed by Ohara et al. is for observing the multi-sized objects under a transmitted light microscope with high speed autofocus algorithm [2]. The object scanned is analyzed based on the intensity variation of the determined region of the objects in the frequency domain. It is claimed that the defocus function is highly recommended so then the clearer images scan can be obtained when the defocus function is close with the region around the focal plane.

Makapati [3] proposed the improved wavelet-based microscope autofocus for blood smears by using segmentation. By using a device that can produce the high quality of images, the video is recorded and the data is presented in term of plot of focus versus the frame number. The method proposed in the study is that the focus function is referred in a peak when the in focus frame is obtained. Previously, the varying degrees of performance by the specimen's observed can be identified by using the generic wavelet based schemes have been proposed. This method can be improved if the nature of the specimen being observed is identified. This scheme is being verified by videos taken from blood smears and the result shows that the segmentation step improves the wavelet-based measure.

In current applications, fast autofocus of microscopy images based on Depth-from-Defocus is widely being used in automated microscope system by Liguó et al. [4]. This is due to low efficiency of the application in micromanipulation system which needs fast autofocus for real time control. The Depth From Defocus (DFD) algorithm is being used to improve the performance of the auto focusing on the optical microscope.

Liu et al. [5] proposed the automated deep access ball bonder for MEMS packaging based on fast autofocus system with the flexible micro-vision system and the manual ball bonder. By analyzing the images of the continuous zoom by microscope, the clear imaging of different multiple images is obtained by using the zoom microscope auto focused method. Roughly the procedure is started with placing the large scale and recorded under low magnification. However, the high magnification is used for precise positioning by continuous variable characteristic to identify the wide range of valuable positioning. On the other hand, an integrated auto-focusing system for biomedical digital microscope is introduced. He et al. [6] proposed a method by combining an image definition calculation algorithm and the pre-reach/final-search auto-focus strategy. They developed and studied a set of integrated auto-focusing system that can automatically monitor the situation of cells or other microorganisms by following remote orders or local pre-set orders.

Considering the importance of auto focusing on optical microscope to support other area for example medical applications, this study proposes the development of auto focusing mechanism for optical microscope.

The outline of the paper will be as follow. Section 2 will discuss the detail methodology used in this study. Section 3 will be the result and discussion. Conclusion and future works will be explained in Sect. 4.

## 2 Methods

This project is divided into three parts. Those are the hardware configuration, circuit interfacing and software configuration. The hardware configuration is focusing on the development of the mechanical base design, mounting between the stepper motor, fine adjustment knob and course adjustment knob. The circuit interfacing will cover about the electronic circuit diagram and the detail of the Arduino as the interface

between software programming and the stepper motor. The software configurations are explaining about the programming and command written for the stepper motor angle movement.

## 2.1 Hardware Design

**Mechanical Base Design.** The microscope will be put on a base which is made from Perspex. The Perspex used is thick as it can resist the weight of the microscope. The thicknesses of the Perspex used is 10 mm. The microscope will be put in the middle right of the Perspex. The sewing machine belt has been used as the belt to move the adjustment of the fine and course from the stepper motor. The stepper motor is mounted to the Galvanized steel plate. The T-slotted aluminum is used as the poles that support the galvanised steel plate.

**Stepper Motors.** Two stepper motors are used in this project. The first stepper motor is connected to the course focus knob and the second stepper motor is connected to the fine focus knob. The stepper motors are used because it can be moved by a certain value of angle given through command coding.

The stepper motor used is 28BYJ-48 as shown in Fig. 1. The motor can be run by only using source of 5 V. Figure 2 shows the circuit of the motor drive. The circuit of the motor driver includes the switching system for ON/OFF of the system and also includes the voltage regulation and port hub for the power adapter.

**Fig. 1** Stepper motor model  
35BY48L



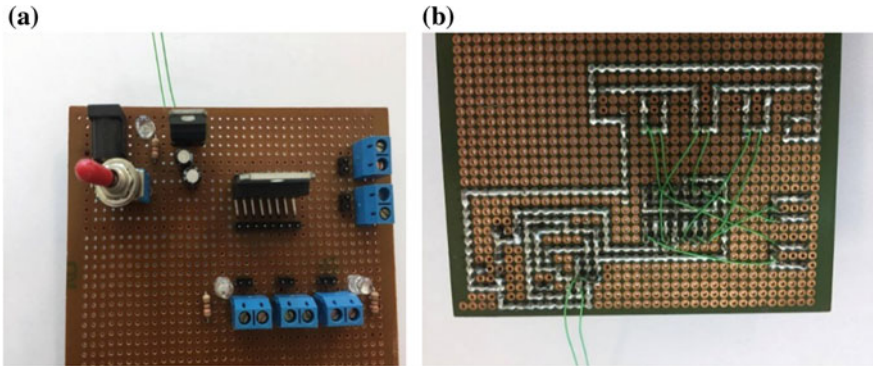


Fig. 2 Circuit of motor drive. **a** Front side and **b** back side

### 2.2 Circuit Interfacing

In this project, the electronic part consists of one Arduino Mega, two motor driver and circuit board for ON/OFF switch of the system.

Figure 3 shows the layout of full connection of the proposed system. The electronic circuit is connected to Arduino Mega, motor driver 1 and 2, power adapter, and stepper motor. The stepper motors are connected to motor driver 1 and 2. The timing belt is used for mounting between both stepper motors with the coarse and fine adjustment. The DinoEye Eyepiece device is connected to the computer to capture the image from the lens. The real hardware connection is shown in Fig. 4.

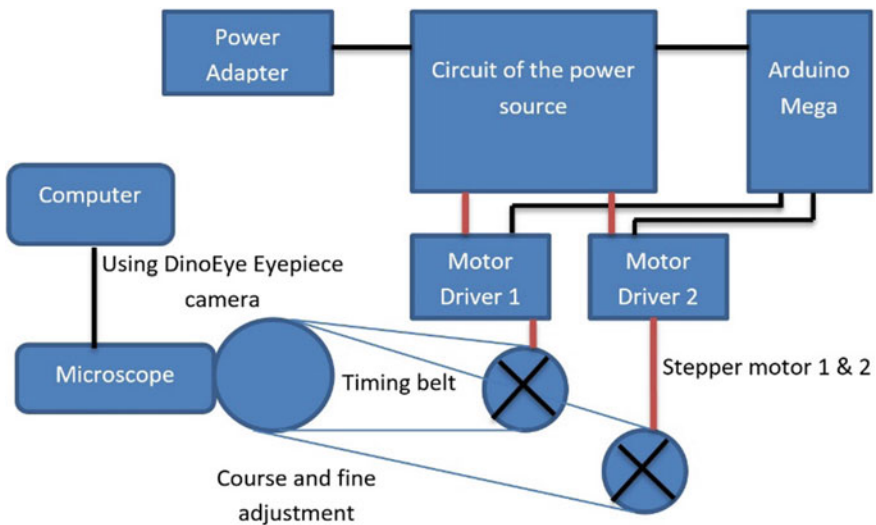
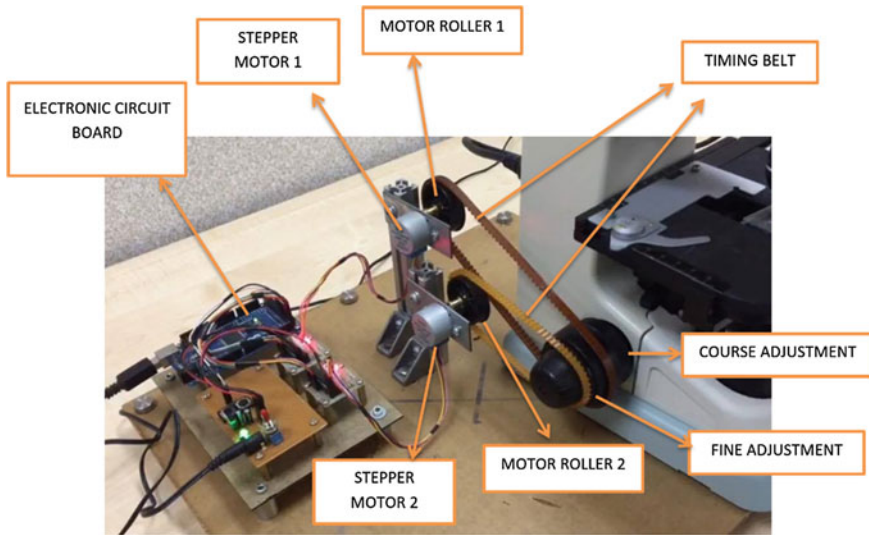


Fig. 3 Layout of full connection of the proposed system



**Fig. 4** Real hardware connection

### 2.3 System Workflow

The work flow of the proposed system is shown by flowchart in Fig. 5. The specimen which contains the sputum as the object is placed on the microscope. During this time, the stepper motor 1 for course adjustment is moved  $5^\circ$  and stepper motor 2 for fine adjustment is moved  $10^\circ$ .  $5^\circ$  is the smallest angle that stepper motor can handle. Combination of  $5^\circ$  and  $10^\circ$  is chosen from heuristic experimentation. Combination of  $5^\circ$  for both motors is not strong enough to move the knob. Meanwhile, combination of  $10^\circ$  for both motors is too strong for the adjustment.

After the both motors moved, then a process for examining whether the image obtained is overexposed or underexposed is conducted. Because this study is a preliminary study on the development of autofocus microscope, the examination process is conducted by human expert. If the image is overexposed then the motor will rotate clockwise, otherwise the motor will move anticlockwise. During the rotation for autofocus process, the image is captured for every step.

Figure 6 shows the result of the best image under the optimized exposure. An image is said to be well exposed by judgment based on bare eyes. If the image is sharp base on bare eyes observation, this image is said to be well exposed or under optimized exposure.

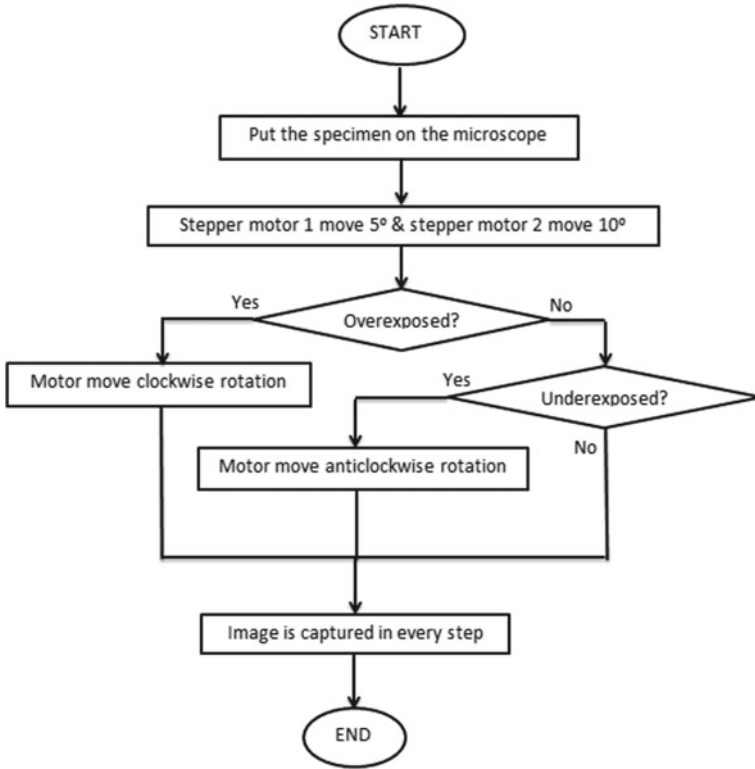


Fig. 5 Work-flow of the proposed system

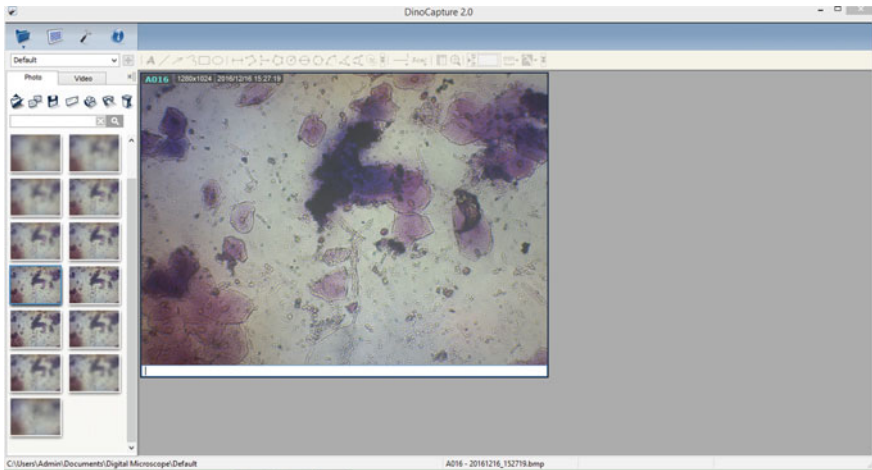


Fig. 6 Optimized exposure image of sputum

## 3 Results and Discussions

### 3.1 *Fine and Course Knob*

The fine and course focus knob are pulled by the stepper motors. The Arduino will process the command from the coding and transfer it to the motor driver to move the stepper motor step by step in same angle. Noted that the angle given to move the stepper motor must be in smaller range around  $2^{\circ}$ – $10^{\circ}$ . For the stepper motor 1, which is connected to the course adjustment, the motor only moves in  $5^{\circ}$  per step. The angle given is smaller because the course adjustment has the limitations, the course focus knob cannot be pushed downwards or upwards too much because it could bring damage to the microscope. For the stepper motor 2, which is connected to the fine focus knob, the angle given for the stepping motor move is  $10^{\circ}$  per step. The range is a little bit bigger because the fine adjustment does not have limitations like the course adjustment.

However, due to the size of the roller in the stepper motor is not same as the roller for controlling the fine and course focus knob, the angle given by the stepping motor will not be the same output in the both adjustment. For example if we give a command for the stepper motor 1 to move  $5^{\circ}$  per step, the course adjustment will not be exactly moved by  $5^{\circ}$ . The angle moved by the course adjustment could be bigger or smaller than the exact angle given by the stepping motor 1.

The course focus knob for the microscope type eclipse e100 Nikon is difficult to control the adjustment. Even to control by hand, it needs a high force to move the course adjustment.

There are 3 factors why the course adjustment cannot be pulled by a timing belt. The first one is due to the performance of the stepper motor, the torque and power of the stepper motor used is low which is considered as not in optimum performance. The second is due to the timing belt used. The timing belt used for pulling the course adjustment from the stepper motor is too thin and not really gripping the knob efficiently.

The third reason why it cannot rotate the course adjustment is because the positioning of the stepper motor and the course adjustment. The position of the stepper motor is too high while the position of the course adjustment is lower down parallel with the stepper motor 2. When the position of both stepper motor and the course adjustment are parallel, the stepping motor is able to pull the course adjustment. However, it only can move forward only and while step is reverse, the stepping motor does not perform well to pull the course adjustment. The proposed solution for the next is to change the position of the stepping motor 1 which the position of the stepping motor must be same as the course adjustment. However, this will produce another problem which is the position of the stepping motor 2 are too closed and it collides each other. The pole cannot be mounted to the base if the position of the stepper motor 1 and 2 are at same level. The factors of the length of the timing belt are additional reason why the stepper motor 1 and 2 cannot be at same level.



**Table 1** Stepper motor movement

Step	Condition for course adjustment	Exposure	Stepper motor 1 (°)	Condition for fine adjustment	Exposure	Stepper motor 2 (°)
1	UE	1	5	UE	1	10
2	UE	1	5	UE	1	10
3	UE	1	5	UE	1	10
4	OE	2	-5	UE	1	10
5	UE	1	5	OE	2	-10
6	OE	2	-5	UE	1	10
7	UE	1	5	OE	2	-10
8	UE	1	5	UE	1	10
9	PE	3	-5	PE	3	10

Notes *UE* Under-Exposure, *OE* Over-Exposure and *PE* Proper-Exposure

Therefore, the optimal position for the stepper motors and the course adjustment must be designed carefully.

To overcome this problem, we propose Eq. (1) that gives the exact value of angle that the fine adjustment and course adjustment will move to.

$$-\frac{R_1}{R_2} = -\frac{D_1}{D_2} \tag{1}$$

where  $R_1$  is angle of stepper motor 1 or stepper motor 2,  $R_2$  is angle of the fine adjustment or course adjustment,  $D_1$  is the diameter of roller in stepper motor 1 or stepper motor 2 and  $D_2$  is the diameter of roller in fine adjustment or course adjustment.

The stepper motor movement is shown in Table 1.

From Table 1, it can be seen that the stepping motor 1 and stepping motor 2 move step by step but in same angle. The concept is that the stepper motor 1 will move independently first then followed by stepper motor 2. The exposure is representing the value at the certain condition of scanned images. If the condition of the images is Under-Exposure (UE) the symbol is 1. For Over-Exposure (OE), the symbol is 2 and the Proper Exposure (PE), the symbol is 3. For the stepper motor movement, the experiment was conducted for the movement until it reaches step 9. Table 2 represents the real angle movement in roller for the stepper motor 1 and stepper motor 2.

To determine the exact degree of the fine focus knob and the course focus knob move, Eq. (1) is used. The real angle of stepper motor 1 and 2 will be used for  $R_1$ . The diameter for the roller in stepper motor 1 and 2 are same which is 39 mm. The diameter for the fine adjustment are 40 mm and the diameter for the course adjustment are 57 mm.

Table 3 represents overall result including the value of  $R_2$ , the real angle fine adjustment and course adjustment movement.

**Table 2** The angle of the roller for the stepping motor 1 and stepping motor 2

Step	Stepper motor 1 (°)	Real angle stepping motor 1 (°)	Stepper motor 2 (°)	Real angle stepping motor 2 (°)
1	5	5	10	10
2	5	10	10	20
3	5	15	10	30
4	-5	10	10	40
5	5	15	-10	30
6	-5	10	10	40
7	5	15	-10	30
8	5	20	10	40
9	-5	15	10	50

**Table 3** Overall result including the exact angle of fine and course adjustment

Step	Stepper motor 1 (°)	Real angle stepping motor 1 (°)	Course adjustment (°)	Stepper motor 2 (°)	Real angle stepping motor 2 (°)	Fine adjustment (°)
1	5	5	7.31	10	10	10.26
2	5	10	14.62	10	20	20.51
3	5	15	21.92	10	30	30.77
4	-5	10	14.62	10	40	41.03
5	5	15	21.92	-10	30	30.77
6	-5	10	14.62	10	40	41.03
7	5	15	21.92	-10	30	30.77
8	5	20	29.23	10	40	41.03
9	-5	15	21.92	10	50	51.28

From Table 3, it is observed that the behavior between stepper motor 1 and the course adjustment has a lot of differences. If the motor 1 move to 5°, the course adjustment knob will move to 7.31°. The reason is because by the differences of diameter between the roller motor 1 and the course adjustment knob. The roller diameter for the motor 1 and the course adjustment knob are 39 mm and the 57 mm, respectively. Those, the percentage of difference becomes 46.2%. The percentages of the differences are calculated as shown in Eq. (2).



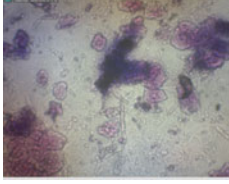
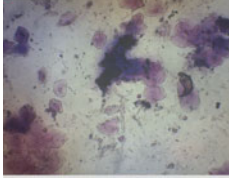
$$\text{Percentage of differences (\%)} = \frac{|\text{input value} - \text{output value}|}{\text{input value}} \times 100\% \quad (2)$$

### 3.2 Sputum Image Analysis

The sputum is the mucus that forms through coughing, which it is not really the saliva and spit. The sputum is used as the sample for the experiment in this study. The characteristic of the sputum consists of the pus cell and the epithelial cell.

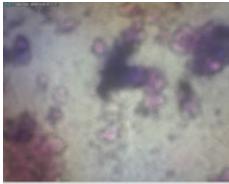

Table 4 shows the result for behavior of the stepper motor and the images captured on every step it moves. The initial position for the course adjustment is at the highest value of Y-axis. Then it is slowly moved down by adjusting the course focus knob to move 5° for every step. The image started from the Under-Exposure (UE), Proper-Exposure (PE) and Over-Exposure (OE).

**Table 4** The image of the sputum captured on several steps

Step	Angle of the motor rotation (°)	Condition of the object scanned	Image
1	5	UE	
2	15	UE	
3	35	PE	
4	-50	PE	

(continued)

**Table 4** (continued)

Step	Angle of the motor rotation (°)	Condition of the object scanned	Image
5	40	OE	
6	50	OE	

Notes *UE* Under-Exposure, *PE* Proper-Exposure and *OE* Over-Exposure

## 4 Conclusion and Future Works

In this research, the development of an auto focused microscope is presented. The project consists of three steps which are the hardware development, circuit interfacing and the software design. The result shows that the proposed design is able to move the stepper motor in a quite precise movement which is  $5^\circ$ . The result is also matched with the result of the image obtained from the optical microscope. It is observed that when the degree of stepper motor movement increasing, the result of the image will be more exposure.

Through the accomplishment of the project, there is still need a lot of improvement to be done. First is the electronic board. The system is running automatically when the user starts the switch, when the system declared that the images are at proper exposure the system will stop running. Eventually, the system can be added up by few mechanisms which are the button control for the manually handled. Therefore, addition of 5 push buttons more will improve the performance of the proposed system. The first button will be used to switch the system for manual control and automated control. The second and third buttons will be used to control the movement of the course adjustment. The fourth and fifth buttons will be for controlling the fine adjustments. When the computer system has failure which means the image processing method could not be run at some moment, the user still can control manually the microscope by using the buttons provided. The control button also can reduce the risk of microscope to be damage since the user will not be controlled by hand at the course focus knob and the fine focus knob.

**Acknowledgement** This work is supported by Universiti Malaysia Pahang (UMP), under Universiti Malaysia Pahang Research Grant RDU 1703142.

## References

1. Doğan H, Ekinci M (2014) Auto-focusing on microscopic imaging with image fusion method. In: 2014 22nd signal processing and communications applications conference (SIU), pp 1857–1860, Trabzon, Turkey
2. Nguyen CN, Ohara K, Takubo T, Mae Y, Arai T (2012) High-speed autofocusing of multisized microobjects. In: 2012 IEEE international conference on automation science and engineering (CASE), pp 34–39, Seoul, Korea
3. Makkapati VV (2009) Improved wavelet-based microscope autofocusing for blood smears by using segmentation. In: 2009 IEEE international conference on automation science and engineering, pp 208–211, Bangalore, India
4. Ligu C, Zhiliang Y, Lining S (2008) Fast autofocus of microscopy images based on depth-from-defocus. In: 2008 IEEE/RSJ international conference on intelligent robots and systems, pp 3115–3120, Nice, French
5. Liu Y, Wei X, Sun L, Chen L (2012) Automated deep access ball bonder for MEMS packaging based on fast autofocus system. In: 2012 IEEE international conference on mechatronics and automation, pp 1485–1489, Chengdu, Sichuan, China
6. He G, Li J, Huang X, Zou Y (2010) An integrated auto-focusing system for biomedical digital microscope. In: 2010 3rd International conference on biomedical engineering and informatics, pp 1420–1423, Yantai, China

# Overview on Fingerprinting Authentication Technology



N. Sulaiman and Q. A. Tajul Ariffin

**Abstract** This paper addresses the characteristics, technology, and possible future of fingerprints authentication method. Fingerprint physiology makes it an ideal for biometrics authentication, primarily the tiny details located on its surface called minutiae. Fingerprint scanning systems are designed to detect minutiae. Images of detected minutiae are processed through matching algorithms in order to verify a query fingerprint that is identical to a stored fingerprint. However, fingerprint authentication based on minutiae can be easily bypassed and the need for a more secure method is required. With respect to the issue, this work explores the possibility of detecting the thickness of the skin layer within a fingerprint as a method of biometrics authentication. Current thickness measuring methods that are non-invasive for that task are identified as Laser Scanning Microscopy (LSM), Optical Coherence Tomography (OCT) and Near Infrared Spectroscopy (NIR). Of the three listed, only OCT and NIR methodology seems viable for simple yet reliable use and can become as promising methods for authentication based on skin layer thickness.

**Keywords** Fingerprint · Biometrics · Skin thickness · Authentication · Security

## 1 Introduction

Fingerprints are the most established form of authentication. Historically, fingerprinting had been near exclusively used in forensics, but over the years, it has grown in popularity where it is now a common method used in various day-to-day services [1, 2]. As such, the need for a better technology to secure a person's fingerprint identity has also increased [3]. This paper aims to go over the characteristics of a fingerprint that allows for its use in authentication, the technology currently utilized in that endeavor and explore future methods that can be developed for this task.

---

N. Sulaiman (✉) · Q. A. Tajul Ariffin  
Faculty of Engineering, International Islamic University Malaysia, Kuala Lumpur, Malaysia  
e-mail: [nadzril@iium.edu.my](mailto:nadzril@iium.edu.my)

© Springer Nature Singapore Pte Ltd. 2020  
A. N. Kasruddin Nasir et al. (eds.), *InECCE2019*, Lecture Notes in Electrical Engineering 632, [https://doi.org/10.1007/978-981-15-2317-5\\_38](https://doi.org/10.1007/978-981-15-2317-5_38)

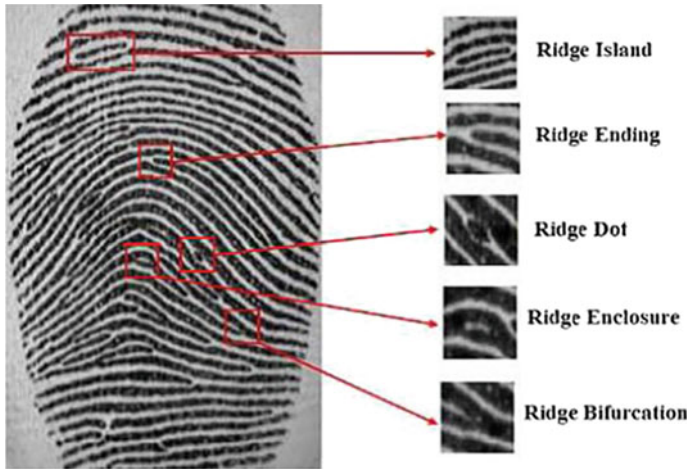


**Fig. 1** A fingerprint with multiple kinds of minutiae highlighted [4]

## 2 Fingerprint Characteristics

The human fingerprint has two characteristics that makes it ideal for biometric use. The fingerprint is able to generate unique details that enable it for use in identification. The structure of how a fingerprint forms allows for its pattern to remain permanent.

### 2.1 Identification

Fingerprints are unique due to the shapes and patterns that are formed by ridges. Called minutiae [1], the location of these patterns within the surface of the fingerprints are used to identify a person. It is unlikely for another person to have the exact same kind of minutiae in the exact same location, and this unlikeliness grows exponentially greater with each minutia added for comparison (Fig. 1).

In addition, the ridges of a fingerprint often follow a specific overall structure. As seen in Fig. 2, these structures, called types, are useful in categorizing fingerprints. An identification system is able to narrow down the number of images that they need to process in order to identify who the print belongs to.

### 2.2 Permanence

The human skin is made up of multiple layers but can be simplified to 3 main layers. The epidermis is the outermost layer and acts as a waterproof barrier. The dermis is

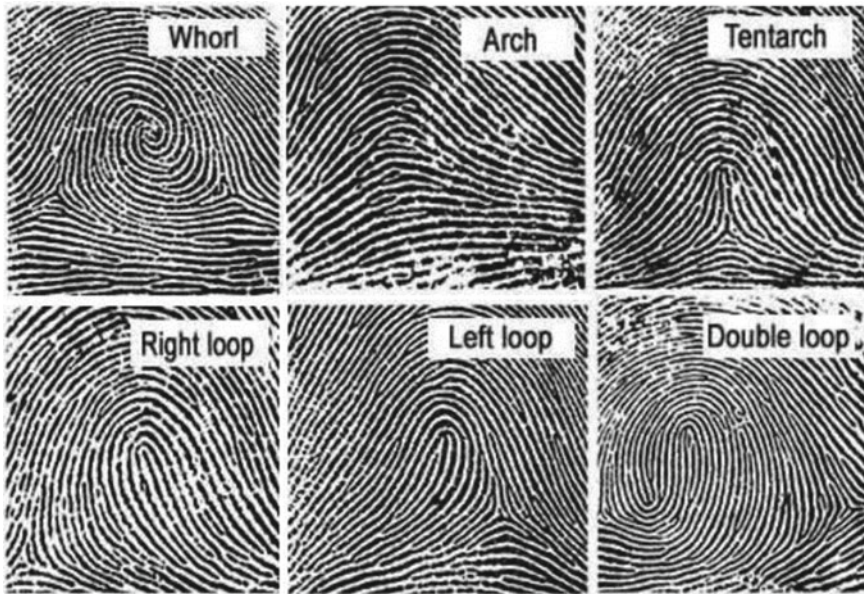


**Fig. 2** A showcase of the how various types of fingerprints may appear as [5]

the middle layer that is mainly composed of hair follicles, sweat glands, and tough connective tissue. The innermost layer is the hypodermis, which is composed of fat and connective tissue.

The fingerprint is formed in the dermis, specifically in the papillary layer that is right beneath the epidermis. This layer anchors to the epidermis using a “double row of peg like protuberances” [6] known as papillae, which forms the layout of the fingerprint. The ridges appear on the epidermis layer are determined by the position of the papillae in the epidermis layer.

This arrangement is what allows fingerprint to remain permanent throughout a person’s life. The papillae act as a “blueprint” that exists under the regenerative layer of the skin. Thus, whenever the epidermal layer restores itself, it will grow following the layout set by the papillae. As long as the papillae remain undamaged, a person’s fingerprint will repair itself to its original design.

### 3 Authentication System

Fingerprint authentication systems function on three fundamental stages: data acquisition, feature extraction, matching [7]. Data acquisition focuses on the method used by the system in order to extract fingerprint data. Feature extraction is the step where the system identifies unique features of the fingerprint data and stores it within the



database. Matching describes the step where a system is required to compare a read fingerprint to those within its database in order to authenticate a person's identity.

### 3.1 Data Acquisition

Currently, there are three main types of fingerprint authentication system, defined by their data acquisition methods, optical, capacitive, and ultrasonic fingerprinting. This section will go over their method of acquiring data.

**Optical Fingerprinting.** Is one of the oldest, cheapest and most common forms of biometric identification [8]. The scanner functions by creating a digital photo of the fingerprint (Fig. 3).

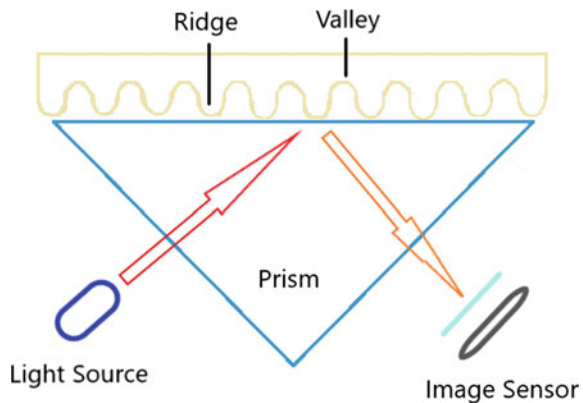
When a fingerprint is placed on the scanning surface, a light source is beamed towards print. An image is generated based on the difference in reflected light levels between ridges and valleys of a fingerprint. The reflected light travels to a light sensor that converts the image into a digital signal. The system performs a few checks to ensure that the generated image is at sufficient brightness before processing the image to be compared to a database of registered fingerprints.

Optical scanners are considered the easiest biometric systems to fool. Its method of simply detecting the changes in reflected light levels means that it can easily be spoofed by simply printing the fingerprint pattern onto a material, such as transparency paper and having the ink produce the ridges and valleys of the fingerprint [8].

**Capacitive Fingerprinting.** As its name suggest, uses capacitors to “read”s the electrical charges created by the ridges and air pockets of the fingerprint. It is currently the most popular form of fingerprint-based authentication in smartphones [1] (Fig. 4).

A capacitive scanner scanning surface is made up of an array of cells that are composed of conductive plates covered in a protective layer [9]. When the ridge of a fingerprint comes in contact with the surface, it acts as another conductive plate,

**Fig. 3** Model of how an optical scanner functions [8]



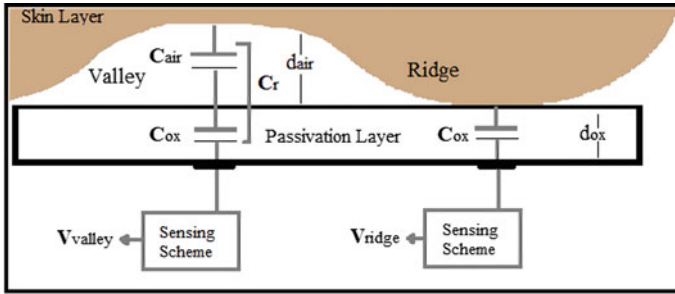


Fig. 4 Model of how a capacitive scanner functions [8]

which in turn charges that cell's conductor plate. The air pockets formed form the valleys however have minimal effect on the charge held by cell. An op-amp integrator is used to detect the changes and the output is recorded by an analog-to-digital converter.

Capacitive scanners, while more secure than optical scanners, have also fallen victim to being spoofed. Simple, 3d molds layered with conductive materials such as gold [10] has been used to successfully bypass most conventional capacitive sensors and complex molds, such as those casted in polydimethylsiloxane, are able to replicate fingerprints at the nanoscale [11].

**Ultrasonic Fingerprinting.** Is the newest entry in commercial fingerprint detection. They function by generating an ultrasonic pulse onto a finger that is in contact with the scanner. Depending on the details on the fingerprint, some of the pulses are absorbed while others are reflected back to a sensor that is able to detect mechanical stress. The varying intensity of the returned ultrasonic pulse throughout the sensor's surface creates a detailed 3D reproduction of the scanned fingerprint [9].

Ultrasonic scanners are currently considered of the most secure methods of fingerprint identification, but it has also been spoofed. A researcher was able to create a 3D printed, highly detailed model of a fingerprint to bypass a commercial ultrasonic sensor [12].

### 3.2 Feature Extraction

After acquiring data through one of the various methods mentioned, the system processes the image to help detect specific features on the fingerprint such as the overall pattern of the ridges or the various minutiae on its surface. The first layer of feature extraction revolves around whether the image remains gray-scale or goes through binarization (Fig. 5).

**Binarization** is a process where the gray-scale fingerprint scan is converted to 1's and 0's for their respective dark and light areas. This generates a much clearer image of the scan.

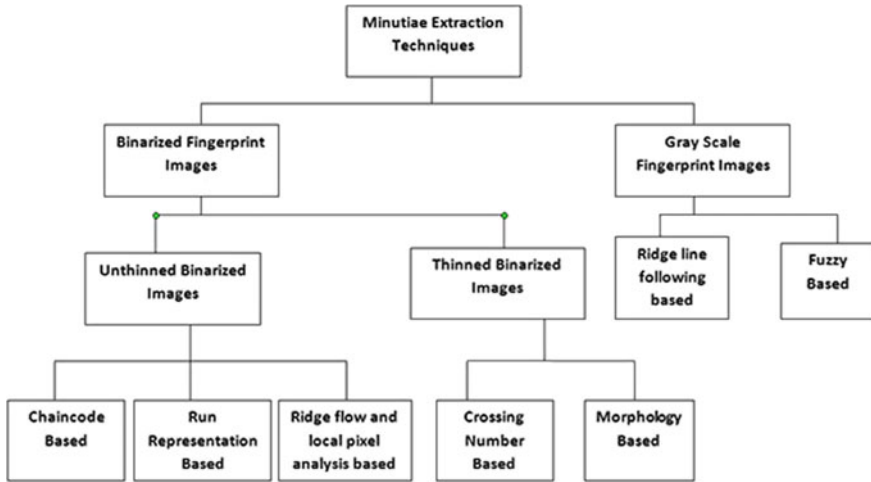


Fig. 5 Classification of minutiae extraction technique [4]

**Ridge Extraction** is a secondary process that can be applied to images that has gone through binarization. The binary image is filtered through a morphological filter that causes the ridges to be thinned [13] to one-pixel thickness. Techniques that utilizes binarization are as follows.

*Chaincode processing* is a method that traces a ridge along its boundary in a counter-clockwise direction. Ridge endings are detected when the trace makes a significant left turn, while bifurcations are detected when the trace makes a right turn.

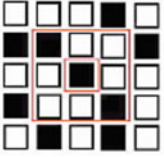
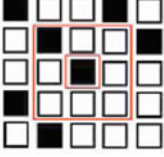
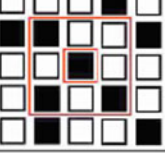
*Run representation based* is a method that performs a vertical and horizontal scan on to the image while applying run-length encoding to the pixels passed. Base on the adjacency of the runs, minutiae are able to be identified [14].

*Ridge flow and local pixel analysis* process the image through a  $3 \times 3$  mask that calculates the average of each pixel. Pixels that average less than 0.25 denotes a ridge ending while those greater than 0.75 denotes a bifurcation.

*Crossing-number based* processes the image through a  $3 \times 3$  window that detects the neighboring pixel. Each neighboring pixel adds to the “crossing number” which is a value used to determine the properties of the ridge at that pixel [14] (Fig. 6).

*Morphology based* processes the image through multiple filters that detect a specific shape. An output only appears if the scanned image is able to fully complete the desired shape.

**Gray-scale images** do have their own advantages over binarization. First of all, it’s able to function with low quality images. Second, binarization and ridge extraction is a time-consuming process, hence gray-scale based processing will often time perform much faster than their processed image counterpart [14]. Techniques based on gray-scale are as follows.

	<p>Crossing Number =2. Normal ridge pixel.</p>
	<p>Crossing Number =1. Termination point.</p>
	<p>Crossing Number =3. Bifurcation point.</p>

**Fig. 6** A breakdown of the crossing number method. Each “pattern” within the 3 × 3 window helps the system identify the minutiae [15]

*Ridge line following* based process functions by following the ridge flow lines set by the fingerprint type. By simply following the lines, the system can detect minutiae it passes through.

*Fuzzy based* technique uses fuzzy logic model to process the varying gray levels in order to detect minutiae.

### 3.3 Matching

In order to authenticate a user, the scanned image will be processed by a matching algorithm. This section will briefly describe some of the algorithms used in fingerprint authentication.

**Direct matching** is the most basic algorithm used for authentication. It functions simply by comparing the pixels of the input image against a template image stored within the database. This method however, requires the system to align the scanned image with the template. This uses a lot of computational power and requires samples to be very large to ensure that the image is aligned properly [16].

**Minutiae based matching** authentication is performed by detecting minutiae and classifying it based on its surrounding neighbors. The algorithm detects the location,

orientation, type and quality of the minutiae [17] and then compares it to ones detected in the print from the database.

**Euclidian distance authentication** involves identifying 2 minutiae and calculating the distance and angle they are from one another. This process may be repeated for multiple “minutiae pairs”. The system then compares the Euclidian distances of the print and those within its database to find a match [18].

### 4 System Security

Fingerprint authentication increased use in protecting private information has made the security of the system crucial. A compromised fingerprint has much bigger impact to a person than getting their password stolen since you can't just change the former as you could the latter.

Threats to the authentication system can be categorized into passive and active attacks. Passive attacks refer to methods that steal information from an authentication system, while active attacks are those that attempt to thwart the authentication service [19, 20]. An example of a passive attack would be a backdoor program that sends a copy of the scanned fingerprint to the attacker, while an example of an active attack would be using the scanned fingerprint to fool a biometric system (Fig. 7).

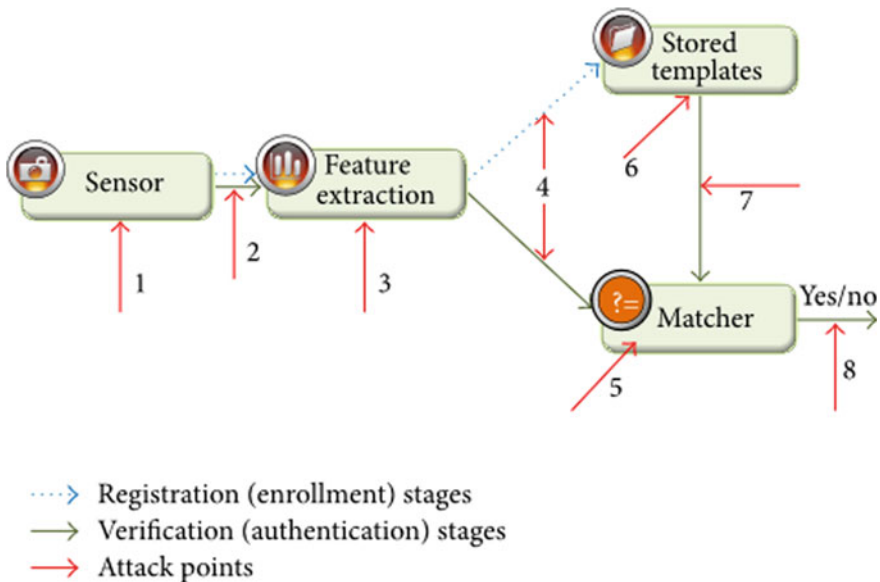


**Fig. 7** Flowchart of fingerprint authentication system for both enrollment and authentication function and the various points of attack that can occur [21]

## 5 Future Technology

New methods of fingerprint base authentication are necessary. Currently, there is a research on utilizing thickness of the skin within a fingerprint as a method of biometric identification. While there is no commercial method of thickness-based fingerprinting, there are currently multiple non-invasive methods to measure the thickness of the skin layer. This section aims to describe how these methods work and their potential application into fingerprinting authentication.

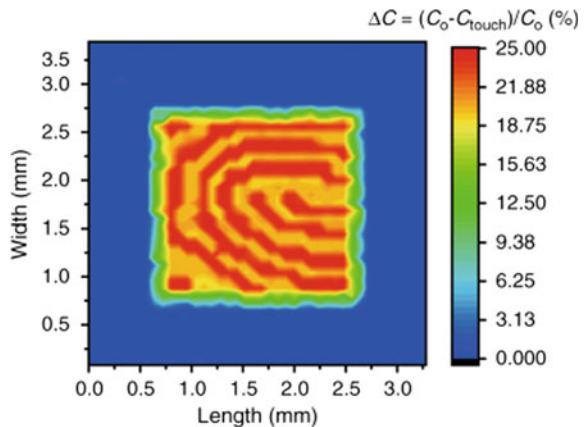
**Pyroelectric Sensor** are passive electronic component that is sensitive to infrared radiation. Changes in temperature causes a change in charge within the pyroelectric crystals within the component, which in turn will generate an electrical signal.

Similar to how a capacitive sensor works, a pyroelectric sensor is able to generate an image based on the location where the ridges of a fingerprint come in contact with the sensor’s surface. The heat generated by the ridges, will be higher than the air pockets within its valleys, which results in differences in the electrical signals generated at those location.

Pyroelectric sensor is potentially a viable method of fingerprinting authentication. The image it generates can easily be implemented into already established extraction and matching processes. A recent research [22] have managed to design a transparent thermal sensor, which increases the ability for its use in commercial smartphones. As seen in Fig. 8, the sensor is able to generate an accurate image of the fingerprint pattern.

**Laser Scanning Microscopy (LSM)** is an imaging technique that is able to capture multiple micrographs at different depths. It functions by transmitting a filtered, colored light through a pinhole onto the surface of the subject. The subject material is infused with fluorescent chemical that will react with the filtered light. The fluorescent chemical will emit its own filtered light, which will then pass through a dichroic to reach the camera. An image is generated by moving the subject along the x–y axis. The pinhole ensures that the filtered light only activates within a set depth,

**Fig. 8** Captured fingerprint pattern using pyroelectric sensor [22]



thus, only an image of that layer. By moving the subject along the z-axis, images for different depths can also be obtained [23, 24].

LSM is deemed a high-resolution technique with a resolution of less than 1  $\mu\text{m}$ , it does have a major drawback. In order for accurate detection to occur, a fluorescent agent must be properly injected into the subject. This results in an increased cost as the fluorescent agent must be resupplied for continuous use.

While it would be extremely difficult for someone to spoof the detection system, as they would have to make a multi-layered model that's able to replicate each layer exactly, the increased cost and requirement for proper fluorescent agent injection makes it not very viable for authentication use.

**Optical Coherence Tomography (OCT)** is another non-invasive imaging technique that functions similarly to echo-location. The OCT directs low-coherence light into a tissue. As the light travels throughout the tissue, some of it will scatter when it comes in contact with certain features and materials within the tissue. The OCT then detects the scattered light and utilizes interferometry to filter out photons that have scattered multiple times. This allows for the OCT to create a complete 3D image of the tissue (Fig. 9).

OCT is highly suggested for use in fingerprint authentication, with multiple research [25–27] have suggested methods of implementation. OCT's ability of producing an image of the dermis and epidermis layer of the fingerprint makes it extremely difficult to spoof. Furthermore, the ability for OCT to model individual layers of the skin [28] allows fingerprint thickness to be used as an additional metric for identification.

**Near Infrared Spectroscopy (NIRS)** is an imaging technique similar to OCT. It functions by beaming near infrared into a tissue sample. The NIRS light will be absorbed differently by different parts of the tissue. A detector is used to measure the change in the reflected light. Information on the thickness of the tissue can be determined by the change in transmittance of the infrared light [29–31].

Like OCT, NIRS is able to produce high information scans and is very easy to use. While not as popular as OCT methods of determining fingerprint biometrics, there have been successful research showing its viability to function in authentication [32,

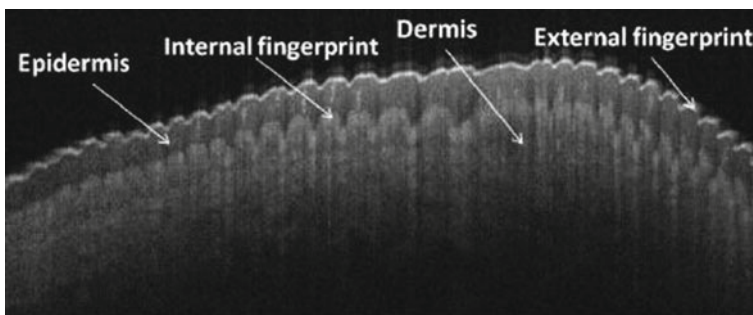


**Fig. 9** Cross-section of a fingerprint generated through OCT [23]

33]. However, in both methods, further testing into its consistency and reaction to various factors, such as skin color, before it can be proven truly viable for commercial use.

## 6 Conclusion

Fingerprints are essential in the use of biometric based authentication. Its physiology makes it a convenient and ideal tool for that purpose. The number of methodology and techniques used in fingerprint identification is vast, but not without weakness. Thus, alternative methods, such as fingerprint thickness and thermal based detection would be a welcome addition to further improving security.

Of the methods proposed in thickness-based fingerprinting, Optical Coherence Tomography and Near Infrared Spectroscopy are better candidates for further research for authentication application. Their ability to model high detail images of the layers under the epidermis greatly increases the difficulty of being spoofed.

**Acknowledgements** It is acknowledged that this work is supported by the Ministry of Education of Malaysia and the International Islamic University Malaysia under grant FRGS/1/2018/TK04/UIAM/02/24 (FRGS19-003-0611).

## References

1. Bhagavatula R, Ur B, Iancovino K, Kywe SM, Cranor LF (2015) Biometric authentication on iPhone and Android: usability, perceptions, and influences on adoption. In: USEC'15, San Diego, CA (2015)
2. Kumar Sharma A, Raghuwanshi A, Kumar Sharma V (2015) Biometric system—a review. *Int J Comput Sci Inf Technol* 6(5):4616–4619
3. InAuth (2017) Fingerprints: the most popular biometric. <https://www.inauth.com/blog/fingerprints-popular-biometric/>. Last accessed 28 March 2019
4. Thakkar D (2016) Minutiae based extraction in fingerprint recognition. *Bayometric*. <https://www.bayometric.com/minutiae-based-extraction-fingerprint-recognition/>. Last accessed 26 April 2019
5. Topaloglu N (2013) Revised: fingerprint classification based on gray-level fuzzy clustering co-occurrence matrix. *Energy Educ Sci Technol Part A: Energy Sci Res* 31(3):1307–1316
6. Hoover, J. E.: Finger. *Encyclopaedia Britannica* (2016), <https://www.britannica.com/topic/fingerprint>, last accessed 2019/3/28
7. Faridah Y, Nasir H, Kushairy AK, Safie SI, Khan S, Gunawan TS (2016) Fingerprint biometric systems. *Trends Bioinf* 9(2):52–58
8. Triggs R (2018) How fingerprint scanners work: optical, capacitive, and ultrasonic variants explained. *Android Authority*. <https://www.androidauthority.com/how-fingerprint-scanners-work-670934/>. Last accessed 29 March 2019
9. Tang K, Liu A, Wang W, Li P, Chen X (2018) A novel fingerprint sensing technology Based on electrostatic imaging. *Sensors* 19(9)
10. Arora SS, Jain AK, Paulter NG Jr (2017) Gold Fingers: 3D targets for evaluating capacitive readers. *IEEE Trans Inf Forensics Secur* 12(9):2067–2077



11. Schultz CW, Wong JXH, Yu H-Z (2018) Fabrication of 3D fingerprint phantoms via unconventional polycarbonate molding. *Sci Rep* 8(1)
12. Katz E, Halámek J (2016) Fingerprint spoofing and liveness detection. *Forensic science: a multidisciplinary approach*. Wiley
13. Abel R (2019) Researchers claim to trick Samsung Galaxy S10 fingerprint scanner using a 3D printed image. *SC Magazine*. <https://www.scmagazine.com/home/security-news/mobile-security/a-reddit-user-claims-to-have-fooled-the-ultrasonic-fingerprint-scanner-on-the-samsung-galaxy-s10-using-a-3d-printed-image/>. Last accessed 10 April 2019
14. KivutiNjeru S, Oboko DR (2016) Comparative analysis of minutiae based fingerprint matching algorithms. *Int J Comput Sci Inf Technol* 8(6):59–71
15. Guruprakash G, Vasanth AV (2014) Combined fingerprint minutiae template generation. *Int J Innov Res Comput Commun Eng* 2(1)
16. Mathur A, Gupta R (2016) Analysis of algorithms used in biometric. *Int Conf Adv Computing*, 398–403
17. Sahu D, Shrivastava R (2016) Minutiae based fingerprint matching for identification and verification. *Int J Sci Res* 5(3):2103–2106
18. Bhargava N, Kumawat A, Bhargava R (2015) Fingerprint matching of normalized image based on Euclidean distance. *Int J Comput Appl* 120(24):20–23
19. Joshi M, Mazumdar B, Dey S (2018) Security vulnerabilities against fingerprint biometric system
20. Hosseini S (2018) Fingerprint vulnerability: a survey. In: 4th international conference on web research (ICRW)
21. Jo Y-H, Jeon S-Y, Im J-H, Lee M-K (2016) Security Analysis and Improvement of Fingerprint Authentication for Smartphones. *Mobile Information Systems* 2016:1–11
22. An BW, Heo S, Ji S, Bien F, Park J-U (2018) Transparent and flexible fingerprint sensor array with multiplexed detection of tactile pressure and skin temperature. *Nat Commun* 9(1)
23. Bellinger R (2018) Principles of laser scanning confocal microscopes. *Tech Briefs*. <https://www.techbriefs.com/component/content/article/tb/supplements/pit/features/29736>. Last accessed 14 June 2019
24. Kamweru P, Diekmann S, Hoischen C (2015) Elucidation of the kinetochore structure using quantitative confocal laser Scanning microscopy based technique. In: *IONS/FOCUS Tunis 2015*, Carthage Tunis
25. Vyas S, Meyerle J, Burlina P (2015) Non-invasive estimation of skin thickness from hyperspectral imaging and validation using echography. *Comput Biol Med* 57:173–181
26. Wang H, Ma L, Chen P (2018) External and internal fingerprint extraction based on optical coherence tomography. In: Sixth International conference on optical and photonic engineering
27. Liu F, Liu G, Wang X (2019) High-accurate and robust fingerprint anti-spoofing system using optical coherence tomography. *Expert Syst Appl*
28. Li A, Cheng J, Yow AP, Wall C, Wong DWK, Tey HL, Liu J (2015) Epidermal segmentation in high-definition optical coherence tomography. In: 37th annual international conference of the IEEE engineering in medicine and biology society (EMBC)
29. Ozaki Y, Genkawa T, Futami Y (2017) Near-infrared spectroscopy. In: *Encyclopedia of spectroscopy and spectrometry*, 3rd edn, pp 40–49
30. *Near Infrared Spectroscopy*, L-A Write Now (2019). <https://lawrittenow.com/consulting/near-infrared-spectroscopy-nirs/>. Last accessed 18 June 2019
31. Miyamae Y, Kawabata M, Yamakawa Y, Tsuchiya J, Ozaki Y (2012) Non-invasive estimation of skin thickness by near infrared diffuse reflection spectroscopy—separate determination of epidermis and dermis thickness. *J Near Infrared Spectrosc* 20(6):617–622
32. Pena A, García M, Posada E, Ponce L, Reyes T (2014) Non-invasive optical method for epidermal thickness estimation. *OnLine J Biol Sci* 14:163–166
33. Souza-Barros L, Dhaidah G, Maunula M, Solomon V, Gabison S, Lilje L, Nussbaum EL (2017) Skin color and tissue thickness effects on transmittance, reflectance, and skin temperature when using 635 and 808 nm lasers in low intensity therapeutics. *Lasers Surg Med* 50(4):291–301

# Bandwidth and Gain Enhancement of a Modified Ultra-wideband (UWB) Micro-strip Patch Antenna Using a Reflecting Layer



**Bifta Sama Bari, Sabira Khatun, Kamarul Hawari Ghazali, Md. Moslemuddin Fakir, Mohd Hisyam Mohd Ariff, Mohd Faizal Jamlos, Mamunur Rashid, Minarul Islam, Mohd Zamri Ibrahim and Mohd Falfazli Mat Jusof**

**Abstract** A novel technique to enhance bandwidth and gain of an Ultra-Wideband (UWB) antenna using a reflecting layer is presented in this chapter. A Microstrip Patch Antenna (MPA) with T-shaped patch and partially grounded plane is used in this design where a T-slot is inserted into the patch. The proposed compact-size antenna is designed and simulated using Computer Simulation Technology (CST) Microwave Studio software by considering flame retardant 4 (FR-4) as substrate with a relative permittivity of 4.3 and a thickness 1.6 mm. The antenna efficiency includes, a wide impedance bandwidth of 9.31 GHz ranging from 3.19 to 12.5 GHz, for voltage standing wave ratio,  $VSWR < 2$ ; 5.74 dB gain; and 6.87 dBi directivity. In comparison with the MPA without the reflecting layer, the bandwidth, gain and directivity of the proposed antenna (with reflector) is increased by 123%, 3.64 dB, and 3.44 dBi respectively. Thus, the proposed antenna can cover a wider range than the UWB range (3.1–10.6 GHz) and can be suitable for the use of various bio-medical applications.

**Keywords** Microstrip patch antenna · Ultra-Wideband (UWB) · T-Slot

---

B. S. Bari · S. Khatun (✉) · K. H. Ghazali · M. H. M. Ariff · M. Rashid · M. Islam · M. Z. Ibrahim · M. F. M. Jusof

Faculty of Electrical and Electronics Engineering, Universiti Malaysia Pahang, Pekan, Malaysia  
e-mail: [sabirakhatun@ump.edu.my](mailto:sabirakhatun@ump.edu.my)

Md. M. Fakir  
CARIFF, Faculty of Chemical & Natural Resources Engineering, Universiti Malaysia Pahang, Pekan, Malaysia

M. F. Jamlos  
Faculty of Mechanical & Manufacturing Engineering, Universiti Malaysia Pahang, Pekan, Malaysia

## 1 Introduction

Ultra-wideband (UWB) is a wireless technology for transmitting information with high speed over a large bandwidth within a short distance. A bandwidth of 7.5 GHz ranging from 3.1 to 10.6 GHz is allotted to UWB applications by the Federal Communication Commission (FCC) [1]. It is beneficial with low power consumption, high data transmission, less complexity, low cost etc. It has wide applications in biomedical field including cardiology, breath pathways, obstetrics and arteries [2]. A significant usage of UWB systems is in microwave imaging for cancer identification in the human body [3, 4]. Microwave radar imaging is applied to the human body for biomedical use (especially for breast tumor/cancer detection) due to its health-friendly nature [5, 6]. The principle of this radar is transmitting a short duration pulses and then detecting the reflected pulse response [7]. Thus, an antenna plays an essential role in the UWB radar system for both transmitting and receiving the pulse wave [8].

Various designed antennas were reported over the past decades targeting for the application of radar-based UWB microwave breast imaging. For example, Fear et al. [9] developed a UWB microwave imaging system comprising of an array of 16 antennas. The stacked-patch [10] and wide-slot [11] antennas have been designed at the University of Bristol. None of the studies describes about the user friendly and handy system in a cost effective way. Although, there are different sorts of antenna; antennas with light weight, inexpensive, compact as well as capable of maintaining high performance over a wide range of frequencies are recommended. One of the antennas that may fulfill these criteria is the Microstrip Patch Antenna (MPA). It has some benefits including easy to fabricate, mechanically robust, simple structure etc. There are numerous substrates like FR-4, RT Duroid, Roger, etc. which can be used to design patch antennas with their respective dielectric constant as per targeted applications. The patch is usually made of conducting material like copper or gold with any possible shape (square, rectangular, circular, triangle etc.) [12]. The most widely utilized MPA is a rectangular patch antenna [13, 14]. However, there are some limitations such as low efficiency, low gain and narrow bandwidth (defined by  $-10$  dB return loss) [15]. Among these shortcomings, the narrow bandwidth is the main limitation. Moreover, an antenna with high gain makes its performance more effective. Thus, wider bandwidth and gain is in demand to obtain a high data rate. Many techniques are used to enhance the bandwidth, for example, introducing various slots into the patch of antenna, use of partial ground planes, optimization of feed line position on substrate [16–19]. Various shapes of patches and slots are reported such as rectangular, circular, dipole, triangular, disc shaped etc. in [10]. Nowadays, with the rapid improvement of microwave technology, there is a growing demand on the bandwidth [20–25]. Thus, this chapter introduces an approach to enrich the bandwidth and gain with UWB modified rectangular T-slot MPA using reflecting layer. A reflecting layer works as a reflector which is connected with the main antenna through spacers. The antenna is designed and simulated with  $50\text{-}\Omega$  microstrip feed line on the FR-4 substrate and used a reflector as a second layer. Initially, we have

designed a T-shaped patch antenna that is a modification of rectangular shape patch with inserting T-slot on it. Then, we have completed the desired antenna design by utilizing a reflecting layer in order to enhance gain and bandwidth of the antenna. After that, the parameters of the proposed antenna have been compared with the initial designed antenna (antenna without reflector). In our study, we have achieved good performance in antenna gain, directivity, bandwidth and return loss.

The chapter is configured as follows. Next section describes the methodology including proposed antenna design steps with necessary formulas. Followed by, results and discussions as well as parametric investigation of antenna in Sect. 3, and finally the conclusion.

## 2 Antenna Design

The basic layer design is based on microstrip rectangular shaped patch. Microstrip patch is chosen due to its thin shape and easy to configure. On the other hand, it has some negative aspects such as lower bandwidth. Our main objective of the chapter is to modify the physical structure by using a reflector to enhance the bandwidth as well as gain. We also analyze the parametric studies to obtain the optimum values of return loss, gain and bandwidth. The antenna is designed on FR-4 substrate with permittivity of 4.3, loss tangent of 0.025 and a thickness of 1.6 mm. The substrate is coated with annealed copper of 0.03 mm thickness at each side. The width and length of the antenna is 24 mm and 27.5 mm respectively. The dimension of the rectangular patch is 19 mm  $\times$  14 mm. Usually, rectangular patch antenna cannot afford wide frequency range due to its mismatch impedance behavior, especially at the bottom corner which leads to the power loss [26, 27]. In this work, we have made a T-shaped patch by modifying the lower bottom edges of a rectangular shape (as shown in Fig. 1a) to reduce the edge effect and then inserted a T-slot on the patch. The partially ground plane is used in this design as illustrated in Fig. 1b. In order to complete our full antenna design for increasing bandwidth, gain and directivity, we have connected a reflector as a second layer with main layer. The complete antenna layout is demonstrated in Fig. 2.

### 2.1 Calculation of the Associated Parameters

To develop the intended UWB antenna, first, a rectangular shaped patch antenna layout/dimensions have been calculated using the Eqs. (1) and (2) [15]. The optimized and considered antenna dimension can be seen in Table 1. Then, the rectangular shape patch has been modified as T-shape patch, additionally a T-slot is inserted on the patch as shown in Fig. 1.

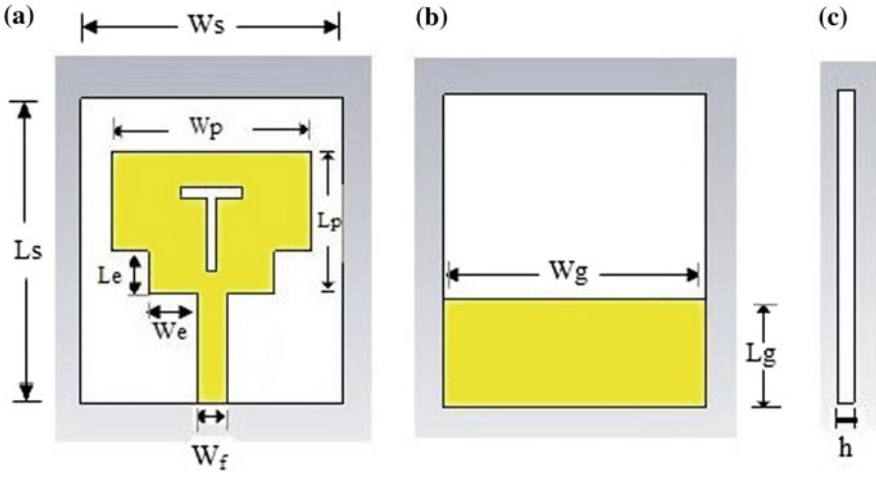


Fig. 1 Basic antenna layer (without reflector), a front view b back view c thickness

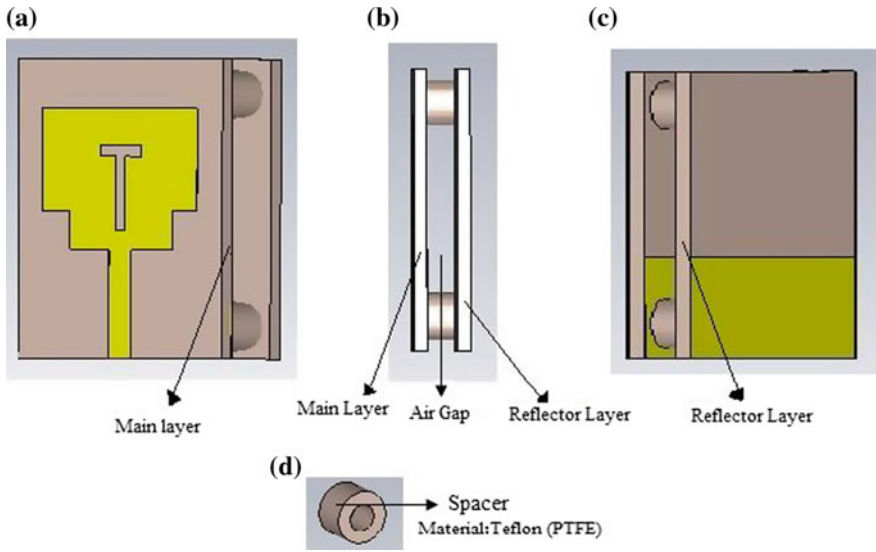


Fig. 2 The proposed antenna design

$$W_p = \frac{C}{2f_r \sqrt{\frac{\epsilon_r + 1}{2}}} \tag{1}$$

$$L_p = L_{eff} - 2\Delta L \tag{2}$$

**Table 1** Design specification of the proposed antenna

Design parameters	Value (mm)
Patch width, $W_p$	19
Patch length, $L_p$	14
Antenna width	24
Antenna length	27.5
Antenna thickness	8.26
Feedline gap, $G_{pf}$	1
Substrate thickness, $h$	1.6
Conductor thickness, $h_t$	0.03
Inner radius of spacer	1.4
Outer radius of spacer	2.8

$$L_{eff} = \frac{C}{2f_r \sqrt{\epsilon_{eff}}} \tag{3}$$

$$\Delta L = 0.412h \frac{(\epsilon_{eff} + 0.3) \left( \frac{W_p}{h} + 0.264 \right)}{(\epsilon_{eff} - 0.258) \left( \frac{W_p}{h} + 0.8 \right)} \tag{4}$$

where,

- $W_p$  The width of the Patch
- $L_p$  The length of the Patch
- $C$  Velocity of light,  $3 \times 10^8$  m/s
- $\epsilon_r$  Dielectric constant of the substrate
- $f_r$  Resonant frequency of antenna
- $L_{eff}$  Effective length which is defined by Eq. 3
- $\Delta L$  Extension length of the antenna which is defined by Eq. 4.

$$\epsilon_{eff} = \frac{\epsilon_r + 1}{2} + \frac{\epsilon_r - 1}{2} \left( \frac{1}{\sqrt{\left(1 + \frac{2h}{W_p}\right)}} \right) \tag{5}$$

$$W_g = 6h + W_p \tag{6}$$

$$L_g = 6h + L_p \tag{7}$$

$$W_f = \frac{7.48 * h}{e^{\left(\frac{\sqrt{\epsilon_r + 1.41}}{87}\right)}} - 1.25 h_t \tag{8}$$

where,

- $\epsilon_{\text{eff}}$  Effective Dielectric constant
- $W_g$  The width of ground plane
- $L_g$  The length ground plane
- $W_f$  Width of Feed line.

The gap between the Patch and the inset feed is usually 1 mm,  $G_{pf} = 1$  mm. To achieve a compact size design, the minimum size of the ground plane is preferred. In this study, we have designed a partially ground plane. The length and width of the step to modify rectangular patch to make it as T-shape patch are denoted by  $L_e$  and  $W_e$  respectively (Fig. 1a).

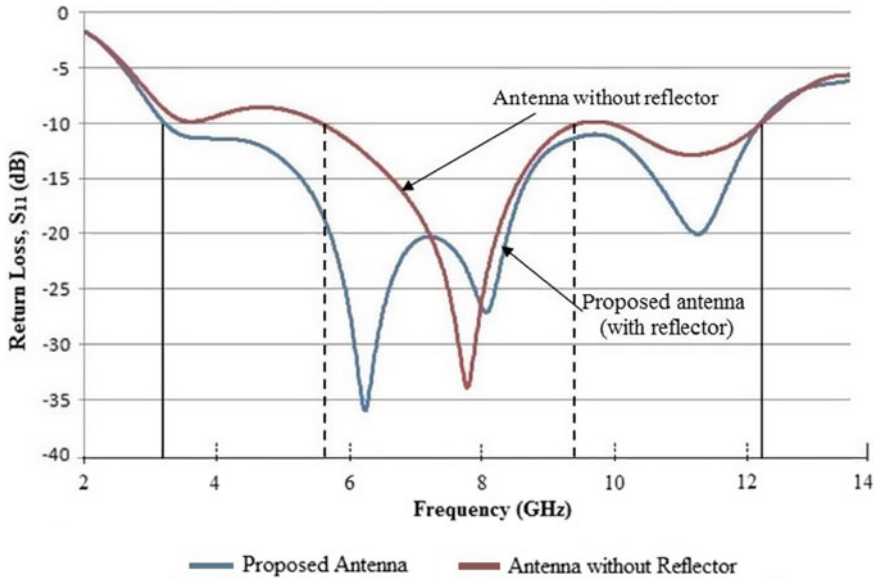
## 2.2 Reflecting Layer (A Second Layer of Antenna) Design

Figure 2 illustrates the complete design of the proposed antenna. Figure 2a, c presents the front and back view of the proposed antenna respectively, whereas Fig. 2b shows the side view. Figure 2d presents the spacer through which the reflector is connected with the basic layer. The overall antenna dimension is 24 mm  $\times$  27.5 mm  $\times$  8.26 mm. Four spacers are utilized that are made of a lossy material named “Teflon PTFE (polytetrafluoroethylene)” with relative permittivity of 2.1. A second FR-4 layer is positioned at a distance of  $0.04\lambda_0$  (spacing value) from the first FR-4 layer through spacers. The second layer acts as a reflector that makes the complete antenna design to acquire required bandwidth and gain. The values of inner and outer radius of the spacer, air gap/distance of reflector from main layer are considered according to the antenna performance. Table 1 shows the optimized parametric values of the proposed antenna.

## 3 Results and Discussions

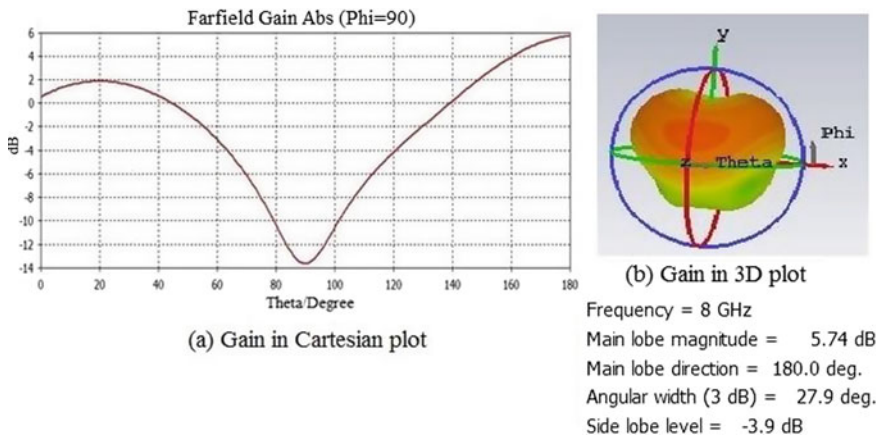
Initially, the basic antenna was designed by modifying a rectangular shaped (base) patch to a T-shaped patch without reflector. We have modified the rectangular shape and changed it as T-shape. Then, we have inserted T-slot on the patch. A reflector is used with the main antenna layer in order to get the desired performance.

Figure 3 shows the return loss is lower for our proposed antenna than the initial antenna without reflector as expected. It shows peak return losses of  $-36$  dB at 6.38 GHz and  $-34$  dB at 7.8 GHz for proposed and initial antennas respectively. The bandwidth of the proposed antenna is 9.31 GHz (3.19 to 12.5 GHz), whereas it is 4.17 GHz (5.6 to 9.77 GHz) for the initial antenna by demonstrating 123%  $\left[ \frac{(9.31 - 4.17)}{4.17} * 100\% \right]$  impedance bandwidth enhancement.



**Fig. 3** Comparison of the proposed reflector antenna with the initial antenna (antenna without reflector)

The gain and directivity of the proposed antenna is 5.74 dB and 6.87 dBi as shown in Figs. 4 and 5 respectively. The Voltage Standing Wave Ratio (VSWR) is 1.03 which is less than 2 (can be seen in Fig. 6). On the other hand, the initial antenna gain and directivity are 2.1 dB and 3.43 dBi respectively. This shows gain and directivity enhancement of 3.64 dB and 3.44 dBi respectively due to the addition



**Fig. 4** Antenna gain in Cartesian and 3D plot



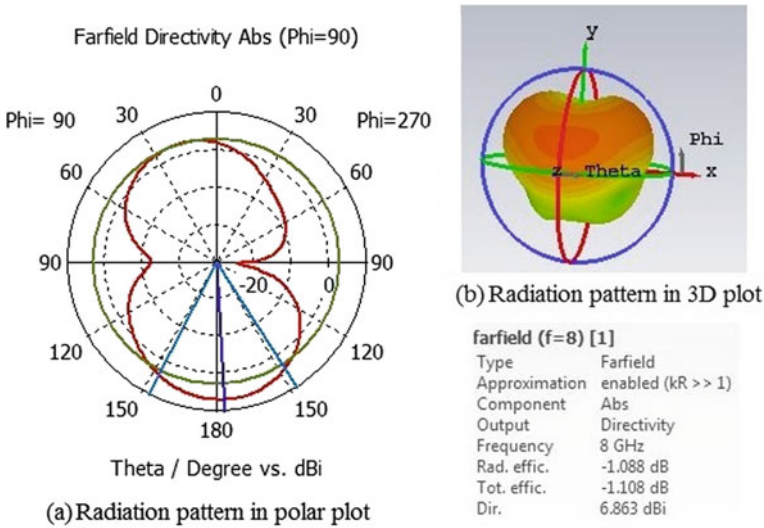


Fig. 5 Radiation pattern in polar and 3D plot

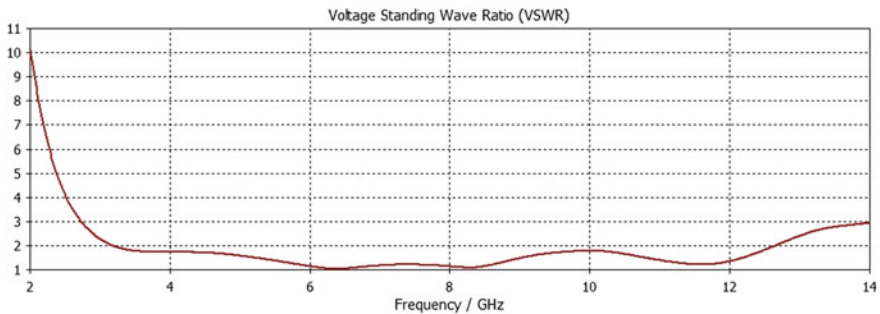


Fig. 6 Voltage standing wave ratio (VSWR)

of reflector. Thus, the proposed antenna (with reflector) shows better performance than the initial designed antenna (without reflector).

Table 2 illustrates the performance comparison of the proposed antenna (with reflector) with the initial antenna (without reflector) and one related existing antenna (with reflector and very similar to our proposed one). As bandwidth is the main concern and our target is to enhance it for bio-medical application uses. Hence, the bandwidth enhancement for the proposed antenna is about 5.14 GHz and 0.54 GHz, which are around 123% and 6.2% respectively compared to initial and Reza [27] antennas respectively, by showing its superiority.

This happened due to the optimized parameters of the proposed reflector antenna such as inner spacer radius, outer spacer radius, and air gap/distance, which are some of the key factors to enhance the antenna performance. These parameters should be

**Table 2** Comparison of the proposed antenna (with reflector) with initial designed antenna (without reflector) and an related existing antenna (with reflector)

Design	Gain (dB)	Directivity (dBi)	Bandwidth (GHz)	VSWR	Return loss, $S_{11}$
Proposed antenna (antenna reflector)	5.74	6.87	9.31	1.03	-36 dB (at 6.38 GHz)
Initial antenna (without reflector)	2.1	3.43	4.17	1.04	-34 dB (at 7.8 GHz)
Reza et al. [27]	6.09	8.15	8.77	-	-47 dB (at 6.8 GHz)

considered very carefully and precisely to achieve the desired bandwidth and gain of the antenna. During the study of bandwidth and gain enhancement of microstrip patch antenna, it is found that change in the shape of patch, introducing slots in patch and the reflector size and position aids in improving the bandwidth along with gain.

## 4 Conclusion

A low-cost and compact-size UWB antenna design to increase its bandwidth and gain have been proposed with simulation using CST software. The proposed antenna is designed by attaching a reflecting layer at the antenna back, connected through spacers with the main antenna layer to enhance bandwidth and gain. The patch of the main antenna layer is modified as T-shape rather than rectangular shape. As a result, the gain and bandwidth is improved with very low return loss to reach the desired goal. The proposed antenna shows excellent performance in terms of bandwidth with 9.41 GHz (3.19–12.6 GHz) which covers the whole UWB frequency, gain, directivity, and VSWR. It can be very suitable and usable for bio-medical research uses. Thus, the bandwidth as well as gain of any UWB microstrip patch antenna can be enhanced by changing the shape of patch, adding slots in patch and adding a reflecting layer at the antenna-back with proper reflector size and position.

**Acknowledgements** This work is supported by Universiti Malaysia Pahang (UMP), Internal Research Grant RDU1703125 and UMP Post-Graduate Research Scheme (PGRS190327). The authors would like to thank the Faculty of Electrical & Electronics Engineering (FKEE), UMP (<https://www.ump.edu.my>) for providing the facilities to conduct this work and for financial support throughout the process.

## References

1. FCC (2002) Ultra-wideband operation FCC report and order. In: Technical report US 47 CFR part15. [https://transition.fcc.gov/Bureaus/Engineering\\_Technology/Orders/2002/fce02048.pdf](https://transition.fcc.gov/Bureaus/Engineering_Technology/Orders/2002/fce02048.pdf). Last accessed 29 Apr 2019
2. McEwan TE (1996) Body monitoring and imaging apparatus and method. US patent No.5, 573,012A, Issued on November 12. <https://patents.google.com/patent/US5573012>. Last accessed 29 Apr 2019
3. Allen B, Dohler M, Okon EE, Malik WQ, Brown AK, Edwards DJ (2007) Ultra-wideband antennas and propagation for communications, radar and imaging. Wiley, Chichester, England
4. Bond EJ, Li X, Hagness SC (2003) Microwave imaging via space-time beamforming for early detection of breast cancer. *IEEE Trans Antennas Propag* 51:1690–1705
5. Allen B, Brown T, Schwieger K, Zimmermann E, Malik W, Edwards D, Ouvry L, Oppermann I (2005) Ultra wideband: applications, technology and future perspectives. In: Proceedings of the international workshop on convergent technologies (IWCT' 05). Oulu, Finland, 6–10 June 2005, pp 1–6
6. Fear EC, Sill JM (2003) Preliminary investigations of tissue sensing adaptive radar for breast tumor detection. In: Proceedings of the 25th annual international conference of the IEEE engineering in medicine and biology society, vol 4, Cancun, Mexico, 17–21 September 2003, pp 3787–3790
7. Chong CC, Watanabe F, Inamura H (2006) Potential of UWB technology for the next generation wireless communications. In: Proceedings of the 9th IEEE international symposium on spread spectrum techniques and applications (ISSSTA' 06). Manaus, Amazon, Brazil, 28–31 August 2006, pp 422–429
8. Guo YX, Khoo KW, Ong LC (2008) Wide band circularly polarized patch antenna using broadband Baluns. *IEEE Trans Antennas Propag* 56(2):319–326
9. Fear EC, Bourqui J, Curtis C, Mew D, Docktor B, Romano C (2013) Microwave breast imaging with a monostatic radar-based system: a study of application to patients. *IEEE Trans Microw Theory Techn* 61(5):2119–2128
10. Nilavalan R, Craddock IJ, Preece A, Leendertz J, Benjamin R (2007) Wideband microstrip patch antenna design for breast cancer tumour detection. *Microwaves Antennas Propag IET* 1(2):277–281
11. Gibbins DR, Klemm M, Craddock IJ, Hilton GS, Paul DL (2007) The design of a wide slot antenna for the transmission of UWB signals into the human body using FDTD simulation. In: Proceedings of the 2nd european conference on antennas and propagation (EuCAP' 07). IET, Edinburgh, UK, 11–16 November 2007, pp 1–5
12. Kashwan KR, Rajeshkumar V, Gunasekaran T, Shankar Kumar KR (2011) Design and characterization of pin fed microstrip patch antennae. In: Proceedings of the 8th International Conference on Fuzzy Systems and Knowledge Discovery (FSKD' 11). Shanghai, China, 26–28 July 2011, pp 2258–2262.
13. Alam AHMZ, Islam MR, Khan S (2007) Design and analysis of UWB rectangular patch antenna. In: Proceedings of the asia pacific conference on applied electromagnetic. IEEE, Melaka, Malaysia, 4–6 December 2007, pp 1–3
14. Werfelli H, Chaoui M, Ghariani H, Lahiani M (2013) Design of a pulse generator for UWB communications. In: Proceedings of the 10th international multi-conferences on systems signals & devices (SSD' 13). Hammamet, Tunisia, 18–21 March 2013, pp 1–6
15. Balanis CA (2005) Antenna theory, analysis and design, 3rd edn (Ch. 2), p. 34. Wiley
16. Baudha S, Vishwakarma DK (2016) Bandwidth enhancement of a planar monopole microstrip patch antenna. *Int J Microwave Wirel Technol* 8:1231–1235
17. Keskin U, Döken B, Kartal M (2017) Bandwidth improvement in microstrip patch antenna. In: 8th international conference on recent advances in space technologies (RAST' 17). Istanbul, Turkey, 19–22 June 2017, pp 215–219
18. Kumar A, Gupta N, Gautam PC (2016) Gain and bandwidth enhancement techniques in microwave patch antennas-a review. *Int J Comput Appl* 148:9–14

19. Jan JY, Su JW (2005) Bandwidth enhancement of a printed wide-slot antenna with a rotated slot. *IEEE Trans Antennas Propag* 53(6):2111–2114
20. Haykin S (2005) Cognitive radio: brain-empowered wireless communications. *IEEE J Sel Areas Commun* 23(2):201–220
21. Dey S, Mitra R (1996) Compact microstrip patch antenna. *Microwave Opt Technol Lett* 13(1):12–14
22. Xu J, Zhao M, Zhang R, Lei M, Gao X, Huang S, Bi K (2017) A wideband F-shaped microstrip antenna. *IEEE Antennas Wirel Propag Lett* 16:829–832
23. Xu J, Tao L, Zhang R, Hao Y, Huang S, Bi K (2017) Broadband complementary ring-resonator based terahertz antenna. *Opt Express* 25(15):17099–17104
24. Hao Y, Wang W, Gao X, Huang S, Bi K (2017) Frequency tunable slot-coupled dielectric resonators antenna. *J Alloy Compd* 702:664–668
25. Zhong S, Yan X, Liang X (2008) UWB planar antenna technology. *Front Electr Electron Eng China* 3(2):136–144
26. Akbar SA, Shah ASM, Faudzi AAM, Khatun S, Shaharum SM, Yusof NAT, Karim MSA (2019) Design of T-shaped UWB antenna with dual band rejection using inverted U- and C-shaped slots. In: *Proceedings of the 10th national technical seminar on underwater system technology 2018, Lecture Notes in Electrical Engineering*, vol 538. Springer Nature Singapore Pte Ltd
27. Reza KJ, Khatun S, Jamlos MF, Fakir MM, Morshed MN (2015) Performance enhancement of ultra-wideband breast cancer imaging system: proficient feature extraction and biomedical antenna approach. *J Med Imag Health Inf* 5:1246–1250

# Oil Palm Tree Detection and Counting in Aerial Images Based on Faster R-CNN



Xinni Liu, Kamarul Hawari Ghazali, Fengrong Han,  
Izzeldin Ibrahim Mohamed, Yue Zhao and Yuanfa Ji

**Abstract** Malaysian oil palm industry has been a great contributor to the country's creation of job opportunity, foreign exchange earnings and GDP. Information about the amount and the distribution of oil palm trees in a plantation are important for sustainable management. In this paper, we propose an oil palm tree detection and counting method based on the Faster Regions with Convolutional Neural Network algorithm (Faster R-CNN). Experiment on the oil palm tree images collected by a drone shows that the proposed method can effectively detect the oil palm trees and counting its number when the age of the trees in a plantation is different from 2 years old to 8 years old. The proposed approach can be used to predict the scale of the plantation and meets the requirements of real-time detection.

**Keywords** Object detection · Oil palm tree · Convolutional neural networks · Drone imagery

## 1 Introduction

Oil palm trees have been the key economic crops in Malaysia. In recent years, the Malaysian oil palm industry has been a great contributor to the creation of job opportunity, foreign exchange earnings and GDP [1]. Palm oil production is important for the economic development of Malaysia, where oil palm has become the most valuable oil crop in the world for it producing much more oil per hectare than soybean.

---

X. Liu (✉) · K. H. Ghazali · F. Han · I. I. Mohamed  
Faculty of Electrical and Electronics Engineering, Universiti Malaysia Pahang, 26600 Pekan,  
Malaysia  
e-mail: [PEG18006@stdmail.ump.edu.my](mailto:PEG18006@stdmail.ump.edu.my)

Y. Zhao  
College of Geography and Environment, Baoji University of Arts and Sciences, Gaoxin Road #1,  
Gaoxin District, Baoji 721013, China

Y. Ji  
Guangxi Key Laboratory of Precision Navigation Technology and Application, Guilin University  
of Electronic Technology, Guilin, China

In addition to palm oil, it also can be used to create several other products like furniture, paper, plywood. Typically, the information about the amount and distribution of oil palm trees in the plantation is important in the following aspects. Firstly, the number of trees is critical for predicting the yield of the crop and the further asset management of the plantation. Secondly, it helps identify the growing state of the trees, such as the survival rate or the age of the trees. Besides, it notifies the irrigation development, which combined to maximize the productivity of the plantation [2]. Therefore, monitoring the trees' growing situation, predicting the yield of the plantation as well as increasing their productivity are three important ways to improve the development of the oil palm industry.

In recent years, with the rise of remote sensing technology, large-scale observation implemented by means of aircraft, drones, and satellites make high-resolution remote sensing images are available [3]. Typically, a practical application like an estimate the yield of the plantation needs to collect the information of earth features, while most of the data collected through diversity sensing involve images [4]. Therefore, image analysis in remote sensing images is a key task due to the small object and high resolution of the collected images. Conducting discriminative image representation is at the significant stage of imaging analysis in remote sensing imagery. Generally, earlier oil palm tree classification and detection study employ the methods belonging to the computer vision field such as machine learning-based approaches K-Means, Fuzzy-C-Means, and PCA methods, etc. For instance, Meftah [5] utilized the color feature of the image, the oil palm fruit bunched are graded based on the RGB intense, which obtained by calculating the RGB histogram of the image. Besides, Siddesha [6] employed Fuzzy-C-Means and K-Means as unsupervised techniques as well as the other four supervised techniques MSRM, Random Walker, Grow Cut and Hill Climbing algorithm. The comparison result on 100 images showed that the MSRM algorithm is superior to other methods. In addition, Frisky [7] employed Gray Level Co-occurrence Matrix, Segmentation-based Fractal Texture Analysis, and Local Binary Pattern to extract the text feature of the image, later the K-Means clustering method was used to cluster palm trees in plantation areas into three categories. Fadilah [8] used an artificial neural network (ANN) to conduct the ripeness classification of oil palm fresh fruit bunch. However, the development of traditional image analysis methods is constrained due to the relatively poor accuracy, poor portability and the lack of generalization ability of the feature extracted by the artificial feature extraction approach.

With the development of computer vision, varieties of application based on deep learning (DL) have shown their superior at image classification and recognition tasks [9, 10]. As the popular network in DL, convolutional neural network (CNN) is capable of directly extracting discriminative features from a large amount of data. In addition, the network combines feature extraction and feature classification into an integrated model, which enhance the distinguishing power of features and make it significantly superior to traditional methods in object detection. CNNs have been successfully applied in object detection task and the CNN based approaches have achieved better performance compared to traditional methods [11, 12]. Recently, Ren et al. [13] proposed deep learning-based Faster Regions with Convolutional Neural Networks

(Faster R-CNN) algorithm [13], which integrates Fast R-CNN and Region Proposal Network (RPN) into one framework, and the feature sharing operation effectively increases the detection speed.

This paper proposes the Faster R-CNN based oil palm tree detection and counting approach. The approach includes using convolutional network to directly extract discriminative features from the raw dataset, utilizing the region proposal network to classify the generated bounding box and choose the proposal region, which later will be sent to the region of interest layer together and conduct the further classify and detection. The proposed method is validated on the data collected by drone.

The structure of this paper is organized as below: Sect. 2 presents the Faster R-CNN based oil palm tree detection and counting method, it explains the Faster R-CNN based approach and the process of the method, while the experiment results in oil palm trees collected by drone as well as the analysis of the results are shown in Sect. 3. Finally, the last section draws a conclusion of this paper and predict the work in future.

## 2 Methodology

The purpose of this study is to detect the position of the oil palm tree and then count the number of the target in the image. This paper employs a Faster R-CNN based deep learning algorithm to detect the oil palm tree in an aerial image. As shown in Fig. 1, the input of the Faster R-CNN framework is an aerial image of oil palm tree captured from a drone, the outputs are the classification and detection result (position of the bounding box). Firstly, the convolutional network is employed to extract the features maps of the input oil palm tree image, and then the region proposal network is used to generate the region proposal and the category, finally the following Region-of-Interest (RoI) layer combined the feature maps and the region proposal together to

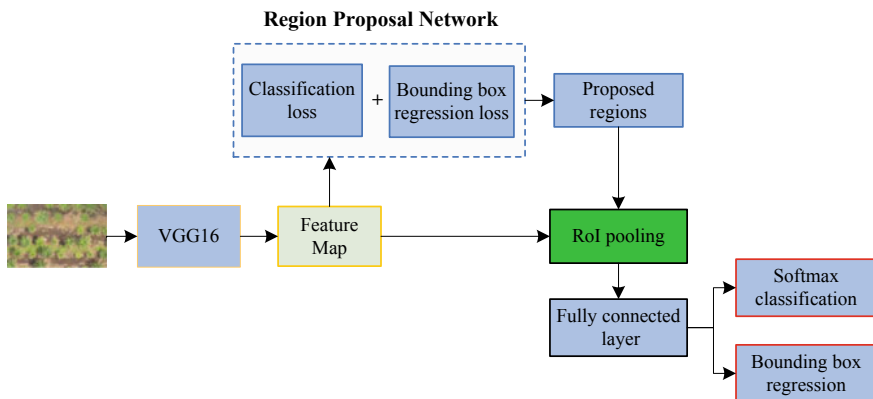


Fig. 1 Oil palm tree detection based on Faster R-CNN

collect proposal feature maps and send it to fully connected layer to conduct the final classification and detection. The process mainly includes the following four steps:

- (1) The convolutional layers. As a CNN based network object detection method, Faster RCNN utilized the basic convolution, ReLu, and pooling operation to extract the feature maps that contain high-level discriminative information in the image, which will be shared with the following RPN and fully connected layer.
- (2) Region Proposal Networks. The RPN network is used to generate the possible region which has the object. This layer determines the anchors contain oil palm tree or background through softmax firstly, later the bounding box regression is used to correct the generated proposed boxed to obtain precise proposals.
- (3) RoI Pooling. The layer gathers the feature maps generated by step 1 and region proposals by step 2 firstly, and then it integrates the information, extracts the proposal feature maps and sends them to the subsequent fully connected layer to perform the classification.
- (4) Classification and Detection. The proposal feature maps are used to classify the object in the image, the bounding box regression is used to choose the accurate position for the detected oil palm tree.

In this study, VGG16 model is selected as the backbone of the convolution network, which contains 13 convolutional layers with every layer followed by a ReLu layer and 4 pooling layers, the size of all the kernel in convolutional layers is 3, the value of the pad and stride is 1, the size of all the kernel in pooling layers is 2, the value for the pad is 0 and for the stride is 2. The advantage of Faster R-CNN is that it directly uses the RPN to generate the detection frame instead of utilizing the traditional sliding window and SS (Selective Search) approaches, which greatly improve the detection speed. Therefore, the RPN is the core partition of the whole network, the training objective is to set the loss function at minimum, the loss function of the network is as below:

$$L(\{p_i\}, \{t_i\}) = \frac{1}{N_{cls}} \sum_i L_{cls}(p_i, p_i^*) + \mu \frac{1}{N_{reg}} \sum_i p_i^* L_{reg}(t_i, t_i^*) \quad (1)$$

where  $i$  denotes the anchors (bounding box) index,  $p_i$  is the foreground softmax probability,  $p_i^*$  is the probability of ground truth predict (actual category). During the RPN training, Intersection over Union (IoU) value is selected to judge the anchors is foreground or background. when  $\text{IoU} > 0.7$  between the  $i_{th}$  anchor and ground truth, the anchor is considered as foreground,  $p_i^* = 1$ ; on the contrary, when  $\text{IoU} < 0.3$  the anchor is considered as background,  $p_i^* = 0$ ; for the rest, when  $0.3 < \text{IoU} < 0.7$ , these anchors will be discarded and not selected as training data;  $t_i$  denotes the predict bounding box,  $t_i^*$  is the corresponding ground truth box for foreground anchor. The whole loss contains two partitions: one is classification loss, that is the softmax loss calculated by RPN classification loss used for the network training of classifying the anchors is foreground or background, another is region loss used



for the network training of bounding box regression. In practical training, for the relatively big difference between  $N_{cls}$  and  $N_{reg}$ , the parameter  $\mu$  is used to balance the difference to make sure the two factors are considered.

### 3 Experiments

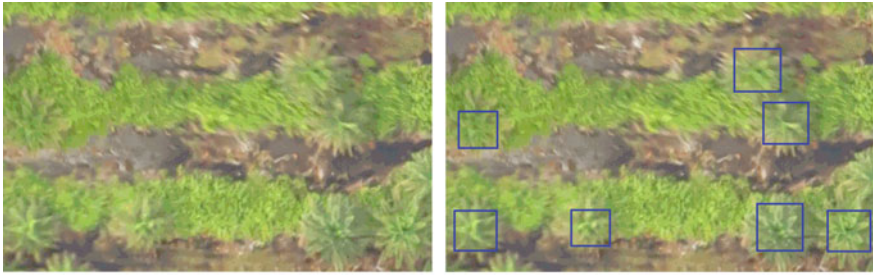
#### 3.1 Experimental Set-Up

The proposed method is tested on color oil palm tree image from aerial imagery collected by a drone over a commercial 20 ha oil palm plantation located in Malaysia Pahang state. The scale of the collected image is  $7837 \times 23,608$  with small target and high resolution. Therefore, we divided the image into small scales to improve performance. In this study, 400 training samples are selected as a training set, 50 training samples are choosing as a validated set, and 50 samples are choosing as a test set, the size of each sample is  $621 \times 391$  pixels. Later, the training and validated samples are manually labeled with a bounding box where oil palm tree center located in the area. For some samples, during the image divided from the original image, some target located on the bound will be divided into two parts, for this case, we labeled the target as the foreground if its center is visible, otherwise, it is considered as background. Based on the above label method, 450 images are labeled. A prototype code was written in Python used TensorFlow framework. Figure 2 shows several labeled samples.

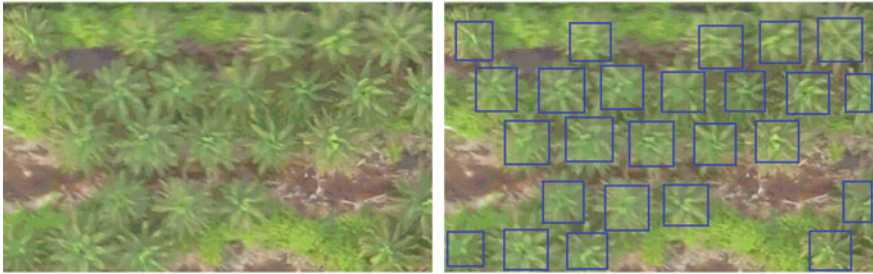
#### 3.2 Results and Discussion

Based on the Faster R-CNN method described in Sect. 2, the labeled image in 3.1 section is the training dataset of the network. Firstly, the RPN network is training to make the loss function Eq. (1) converged. After obtaining the trained Faster R-CNN model, 50 images are used to test the detection precision. In order to try to cover more situation, another two special situations are considered, for one situation some targets are too small for the young age of the oil palm tree, for another some targets in the image are crowded. For each testing image, we manually locate and count the mummer of oil palm trees in the image, and then the result will be compared with the Faster R-CNN automatic detected result. The whole time for training and test in this paper is no more than two hours, where the network training takes one and half hour with 300 iterations and the test on 50 images takes five minutes. Figure 3 shows the experiment result based on Faster R-CNN method.

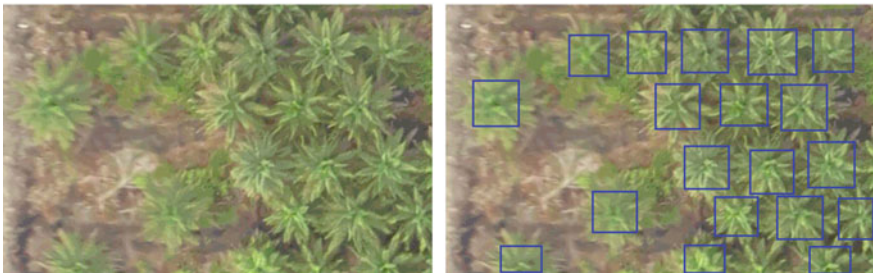
As shown in Fig. 3, take two test images as an example. After detection, for image (a) the number of the detected oil palm tree is 33 while the manually counted number is 34, there is only one target missing detection. However, for image (c) the number



(a) Image a and the labeled image



(b) Image b and the labeled image



(c) Image c and the labeled image

**Fig. 2** The original image and its labeled image. The left column is the original image, the right column is the corresponding labeled image

of the detected oil palm tree is 25 while the manually counted number is 20. The target in image (a) is clearer and large, so it is easy to classify from background, while the target in image (c) occupy small pixel and are blurred to be classified from the background, two backgrounds were detected as target and another three targets were detected as foreground that manually missed the three targets. Therefore, the younger oil palm trees with a blurred background are the most challenging scenario in automated detection. Table 1 shows the accuracy of the automatic detection result in 50 test images. As shown, manually detected palm trees is 1236, all detected objects using this method is 1204 and the correctly detected palm trees are 1188, the overall accuracy is 96.8%.

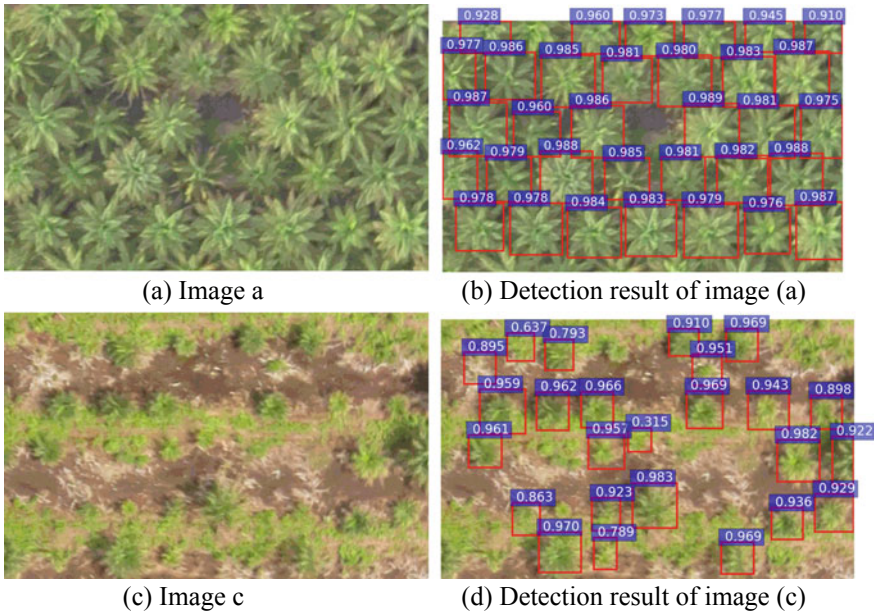


**Fig. 3** The detection result based on Faster R-CNN method

**Table 1** Detection results based on Faster R-CNN

Evaluation score	Value
All detected objects (B)	1204
Manually detected palm trees (C)	1236
Correctly detected palm trees (A)	1188
Precision: A/B (%)	97.4%
Recall: A/C (%)	96.1%
Overall accuracy (%)	96.8%

## 4 Conclusions

This study employed the Faster R-CNN algorithm to address the problem of oil palm trees detection and counting collected by drone. The Faster R-CNN approach used in this paper employed the VGG16 network to extract discriminative features of oil palm trees from the training dataset, which is followed by the RPN who was trained to get the proposal region for the object in the image, at last, the objects were detected and classified by integrating the information of the feature map and the proposal region. The proposed approach effectively discovered deep learning-based

CNN on oil palm tree detection with an average overall accuracy above 96%. The results illustrate that the speed and the accuracy in oil palm detection and counting meet the requirement for applied it in engineer application. The next step is to apply this method in practical of real detection and counting for oil palm plantation.

## References

1. Nambiappan B, Ismail A, Hashim N, Ismail N, Shahari DN, Idris NAN, Omar N, Salleh KM, Hassan NAM, Kushairi A (2018) Malaysia: 100 years of resilient palm oil economic performance. *J Oil Palm Res* 30(1):13–25
2. Surip SS, Jawaid M, Khalil HPSA, Mohamed AR, Ibrahim F (2012) A review of oil palm biocomposites for furniture design and applications: potential and challenges. *BioResources* 7(3):4400–4423
3. Ishimwe R, Abutaleb K, Ahmed F (2014) Applications of thermal imaging in agriculture—a review. *Adv Remote Sens* 3:128–140
4. Boonpook W, Tan YM, Ye YH, Torteeka P, Torsri K, Dong SX (2018) A deep learning approach on building detection from unmanned aerial vehicle-based images in riverbank monitoring. *Sensors* 18(11):3921–3933
5. Alfatni MSM, Shariff ARM, Shafri HZM, Saaed OMB, Eshanta OM (2008) Oil palm fruit bunch grading system using red, green and blue digital number. *J Appl Sci* 8(8):1444–1452
6. Siddesha S, Niranjant SK, Aradhya VNM (2017) Segmentation of oil palm crop bunch from tree images. In: *International conference on smart technologies for smart nation (SmartTechCon)*. IEEE, Bengaluru, pp 1621–1626
7. Frisky A, Harjoko A (2016) Palm oil plantation area clusterization for monitoring. In: *2nd International conference on science and technology-computer (ICST)*. IEEE, Yogyakarta
8. Fadilah N, Saleh JM, Ibrahim H, Halim ZA (2012) Oil palm fresh fruit bunch ripeness classification using artificial neural network. In: *4th International conference on intelligent and advanced systems (ICIAS2012)*. IEEE, Kuala Lumpur, pp 18–21
9. Deng L, Yu D (2014) Deep learning: methods and applications. *Found Trends® Sig Process* 7(3–4):197–387
10. Trujillano F, Flores A, Saito C, Balcazar M, Racoceanu D (2018) Corn classification using deep learning with UAV imagery. An operational proof of concept. In: *IEEE 1st Colombian conference on applications in computational intelligence (CoICACI)*. IEEE, Medellin, pp 1–4
11. Xu Y, Yu G, Wang Y, Wu X, Ma Y (2017) Car detection from low-altitude UAV imagery with the Faster R-CNN. *J Adv Transp* 2017:1–10
12. Long Y, Gong Y, Xiao Z, Liu Q (2017) Accurate object localization in remote sensing images based on convolutional neural networks. *IEEE Trans Geosci Remote Sens* 55(5):2486–2498
13. Ren S, He K, Girshick R, Sun J (2015) Faster R-CNN: towards real-time object detection with region proposal networks. *Advances in neural information processing systems*, pp 91–99

# EEG Pattern of Cognitive Activities for Non Dyslexia (Engineering Student) due to Different Gender



E. M. N. E. M. Nasir, N. A. Bahali, N. Fuad, M. E. Marwan, J. A. Bakar and Danial Md Nor

**Abstract** The purpose of this study is to identify the electroencephalogram (EEG) pattern of male and female engineering student during the cognitive activity. EEG is a method to monitoring electrical activity in the brain and has four main brain-wave signal Delta Wave, Theta Wave, Alpha Wave and Beta Wave. Delta wave is a slow wave generated in deepest meditation, Theta Wave usually occurs in sleep, Alpha Wave dominant in calming, relaxing condition and Beta Wave dominant in wakeful condition. The raw data collected analysis using SPSS and Microsoft Excel to analysis the accuracy and the brainwave pattern between male and female. The average, standard derivation, correlation and Q-Q Plot are used to identify the EEG pattern between male and female during cognitive activity. Cognitive is one of the bloom taxonomy formulate for education activities. The process involves in decision making, understanding of information, attitudes and solving. Subjects are given a set of question to answer. A total of 24 students, 12 males and 12 female involve recording their EEG signal while answering the cognitive question by wearing the Emotive Insight device. All subjects are from UTHM engineering students. Data collected are focused in Alpha Wave and Beta wave which exist in when someone is in awaken condition. The difference between male and female brainwave during the cognitive activity can be observed from the analysis and discussion of the result. For future recommendation for this research is the number of subject can be increased to get more accurate data.

**Keywords** Electroencephalogram (EEG) · Alpha wave · Beta wave · Cognitive · Male · Female

---

E. M. N. E. M. Nasir (✉) · N. A. Bahali · N. Fuad · J. A. Bakar · D. M. Nor  
Faculty of Electrical and Electronic Engineering, Universiti Tun Hussein Onn Malaysia, 86400 Parit Raja, Johore, Malaysia

E. M. N. E. M. Nasir · N. A. Bahali · N. Fuad · M. E. Marwan · J. A. Bakar  
Brainwave Research Group, Faculty of Electrical and Electronic Engineering, Universiti Tun Hussein Onn Malaysia, 86400 Parit Raja, Johore, Malaysia

M. E. Marwan  
Kolej Poly-Tech MARA Batu Pahat, Sri Gading, 83300 Batu Pahat, Johore, Malaysia

## 1 Introduction

The brain is one of the largest and most complex organs in the human body. It is made up of more than 100 billion nerves that communicate in trillions of connections called synapses [1]. It is an organ which is located in the skull of a head at the top of a body and brain constitutes only about two percent of the human body, yet it is responsible for all of the body's functions [2]. Brain receives information through our five senses sight, smell, touch, taste, and hearing which happens innumerable at one time. It assembles the messages in a way that has meaning for us, and can store that information in our memory [3]. The brain is composed of three parts, the brainstem which performs many automatic functions such as breathing, heart rate, body temperature, wake and sleep cycles, cerebellum function is to coordinate muscle movements, maintain posture, and balance, and cerebrum is the largest part of the brain and is composed of right and left hemispheres. It performs higher functions like interpreting touch, vision and hearing, as well as speech, reasoning, emotions, learning, and fine control of movement [4].

Electroencephalography (EEG) is a method for monitoring electrical activity in the brain. It uses electrodes placed on or below the scalp to record activity with coarse spatial but high temporal resolution. EEG can be used in cognitive research or to diagnose conditions such sleep disorders [5, 6]. Cells that formed in brain uses electricity to communicate with each other are call neurons. This can be detected using sensitive medical equipment such as EEG, measuring electricity levels over areas of the scalp. This activity is called brainwave pattern [5]. EEG measures voltage fluctuations resulting from ionic current within the neurons of the brain. It has several strong points as a tool for exploring brain activity. EEGs can detect changes over milliseconds, which is excellent considering an action potential takes approximately 0.5–130 ms to propagate across a single neuron, depending on the type of neuron [7]. Most of the cerebral signal observed in the scalp EEG falls in the range of 1–20 Hz. The EEG signal are separated and divided into four main types of brainwave consist of Beta Wave, Alpha Wave, Theta Wave and delta Wave [8, 9] as in Table 1.

Bloom's Taxonomy is used to promote higher forms of thinking in education, such as analyzing and evaluating concepts, processes rather than just remembering facts (rote learning) [11]. It is most often used when designing educational, training, and learning processes. The three domains of educational activities are Cognitive mental

**Table 1** Description type of wave [8, 10]

Type of wave	Range (Hz)	State	Description
Beta	12–40	High	High frequency low amplitude brain waves that are commonly observed while we are awake
Alpha	8–12	Moderate	It is the frequency range between beta and theta
Theta	4–8	Slow	Involved in daydreaming and sleep
Delta	0–4	Slowest	They are found most often in infants as well as young children

skills (knowledge), affective growth in feelings or emotional areas (attitude or self), psychomotor manual or physical skills (skills). Cognitive domain is when a student is learning using mental skill, there are gender differences in cognitive abilities [12–14]. Psychologists have gathered solid evidence that when it comes to how and how well to think, males and females differ in very few but in significant ways. Male and female brains show anatomical, functional and biochemical differences throughout life [6, 15, 16]. Many factors are involved in this differentiation physiological factors along with social norms, is another factor that brings changes [10, 17, 18].

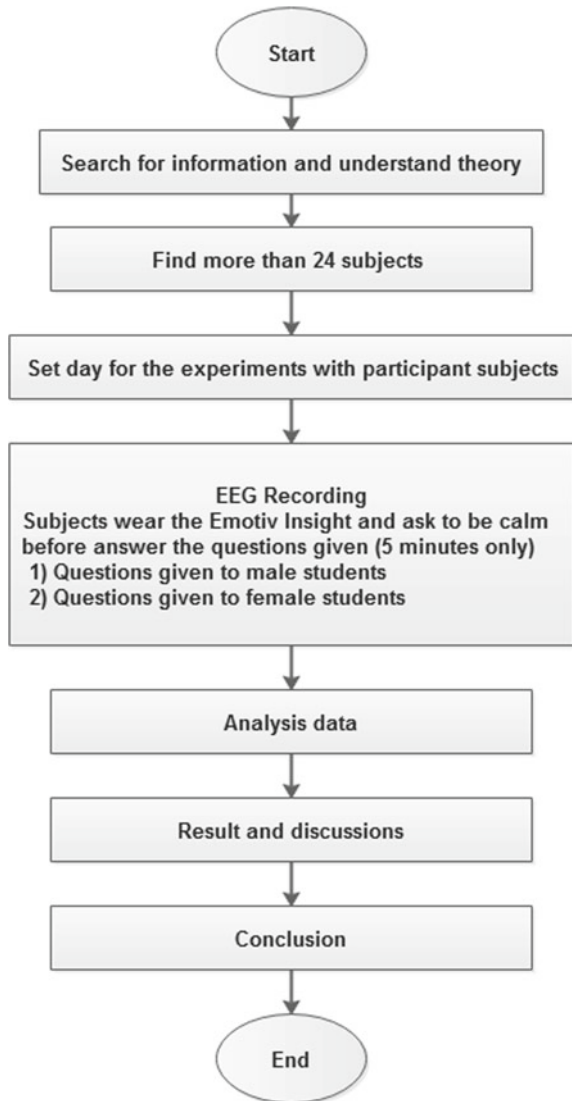
## 2 Methodology

There are four stages to be conduct so that this research can be completed. Figure 1 shows flow chart of the process and method that is implemented in this research. These four stages are related with each other to complete this research paper with success. The first stage is the literature review of the previous related researches. These stages are important to provide the relevant information and better understanding about the research. The second stage is finding more than 20 participants of subject, which consists of females and males. Each of the subjects needs to answer the cognitive question prepared for this research. Subject for the research is from the engineering student and they need to be in good condition as this is crucial to avoid the noise during raw data recording. Next stage is third stage is raw data collection using an Emotiv Insight device. Emotiv Insight is a user-friendly and wireless device used to Collect and record the raw of EEG signals. This device is relatively sensitive and must be handled with the correct way to get the good signal when the experiment is conducted. Last but not least, the fourth stage is the data analysis and this is the most important stage to achieve the objective of this research paper.

### 2.1 Subjects

There are 24 subjects of engineering student, which consist females and males. The subjects are divided into group of one male and one female subject per group. All subjects must answer the prepared question within the given time. The subjects involve in this experiment need to be in a healthy condition and are not on any medication to avoid noise on the brainwaves recorded during the experiment is conducted. The chosen subject will be among engineering student from Universiti Tun Hussein Onn's student within the group age of 19 until 30 years old.

**Fig. 1** Flow diagram of methodology



## 2.2 Data Collection

The subject is given a set of 15 cognitive questions which are divided in to 3 sections and needed to answer it within 5 min only. Firstly, the subject must be in relax condition and then will be asked to wear the Emotive Insight on their head. Once the quality contact is good the record button will be clicked. Question given have variety of mathematics, general knowledge, visualization and knowledge as well in





Fig. 2 The view of subject wearing all the equipment from sides, back and front view

English language. Figure 2 shows how the emotive must be wearing before taking the cognitive activity.

### 2.3 Analysis of Data

The raw data that has been collected using the Emotive Insight Equipment will be kept in cloud. The raw data will be retrieved by downloading from the cloud file. All the data related to this research will be processed by using Statistical Package for the Social Sciences (SPSS) software and Microsoft Excel software. This task is the most important part to generate the result and outcome from this research.

Descriptive statistics are specific methods used to calculate, describe, and summarize collected research data such as in a logical, meaningful, and efficient way [19]. Descriptive statistics are numbers that summarize the data with the purpose of describing what occurred in the sample [20]. This analysis can be chosen in SPSS system. Descriptive analysis helps user to calculate many data automatically and prevent from the error when the analysis is done manually.

## 3 Results and Discussions

### 3.1 Distribution Results

There are 24 subjects for this experiment. The result of distribution of 12 males and 12 females when answered the cognitive activity within five minutes are shown in line graph. The result is to observe the pattern of the EEG Wave and which subjects are dominant in cognitive. The dominant in cognitive will show the Beta Wave must higher than Alpha Wave. Table 2 shows Comparison for Alpha Wave and Beta Wave during cognitive activity of male and female.

**Table 2** Comparison for Alpha and Beta Wave during cognitive activity of male and female

Subject	Alpha Wave		Beta Wave	
	Male	Female	Male	Female
S1	Low	Low	High	High
S2	Low	Low	High	High
S3	High	Low	Low	High
S4	Low	Low	High	High
S5	Low	High	High	Low
S6	Low	Low	High	High
S7	Low	Low	High	High
S8	Low	Low	High	High
S9	Low	Low	High	High
S10	Low	Low	High	High
S11	Low	High	High	Low
S12	Low	Low	High	High

**Subject 1**

Figure 3a shows distribution graph of male subject 1 when conducted the cognitive activity. Beta Wave which remained consistent from the beginning can be compared to the Alpha Wave. The Alpha wave dropped in the beginning before increasing as the experiment continues. From the graph, Beta Wave remains as the highest. Figure 3b distribution of graph of female subject 1 which shows the Beta Wave is higher than Alpha Wave even though the Alpha Wave to go up steadily. The graphs shown for 2 subjects one male and one female that are dominant in cognitive domain.

**Subject 2**

Figure 4a shows distribution graph for male subject 2, from graph Beta Wave increased sharply from the start, whereas Alpha wave decreased significantly by showing the big difference between each other. From Fig. 4b, distribution graph for female subject 2 can be seen. It shows, the wave is almost similar between Alpha Wave and Beta Wave, but the Beta Wave increased slightly at the end of cycle. It

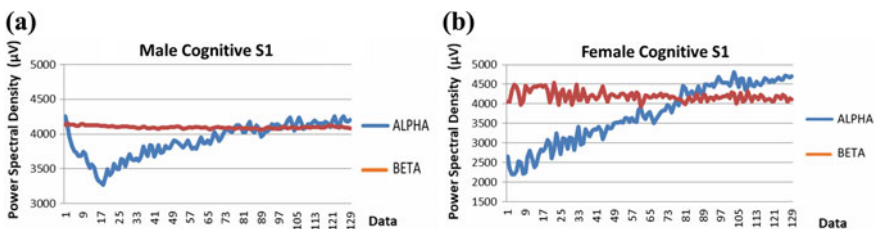


**Fig. 3** Distribution graph for cognitive activity **a** male subject 1, **b** female subject 1

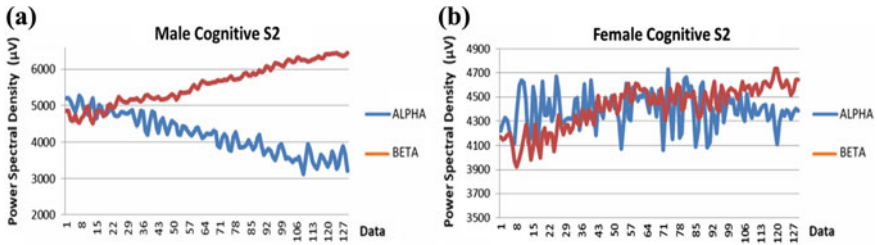


Fig. 4 Distribution graph for cognitive activity a male subject 2, b female subject 2

can be seen from the both graphs that Beta Wave is higher than Alpha, means, the subject 2 male and female are dominant in cognitive.

### 3.2 Results of Average

#### Male

Figure 5. shows the average Alpha Wave and Beta Wave of Male subjects during the cognitive activity. One cycle of EEG signal contains 0 until 128 from 129 total signal data. It shows that Beta Wave has higher average value compared to Alpha Wave. The smallest value is 3651.727 (S11) and highest value is 4207.152 (S2) of Alpha Wave from all 12 subjects. For Beta Wave, smallest average value is 4083.653 (S7) and highest value is 5582.385 (S2).

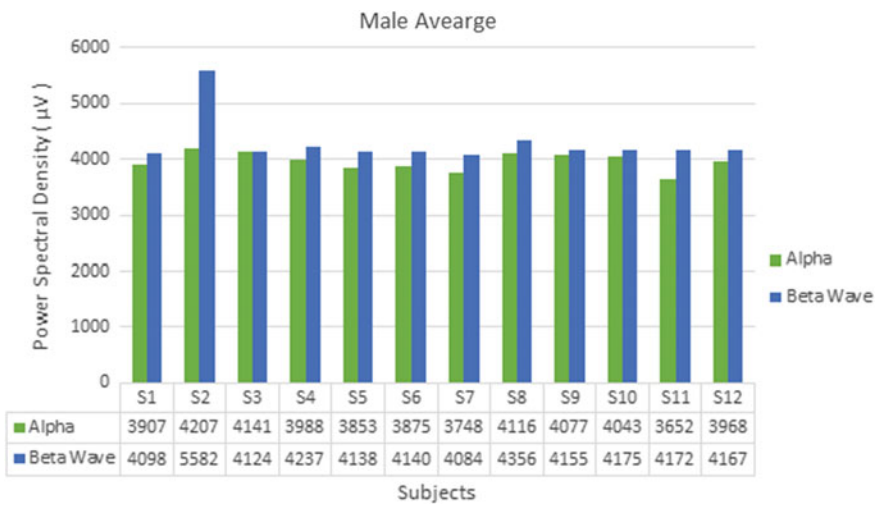


Fig. 5 Male average of Alpha Wave and Beta Wave

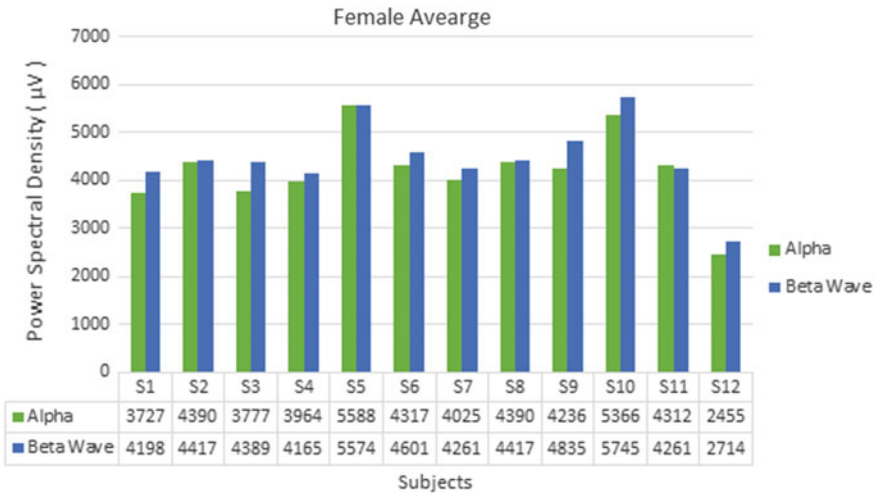


Fig. 6 Female average of Alpha Wave and Beta Wave

**Female**

Figure 6 shows the average Alpha Wave and Beta Wave of female subjects during the cognitive activity. It shows that Beta Wave has higher average compared to Alpha Wave. One cycle of EEG consists 0 until 128 out of 129 signal data. The smallest Alpha Wave from all 12 subjects is 2454.713 (S12) and highest is 5588.293(S5). Beta Wave smallest average is 2714.045 (S12) and the highest is 5744.854 (S10).

**Male and Female**

Table 3 shows the number of subject and percentage who has high Alpha Wave or high Beta Wave. The total subjects among male and female showing these results during the Cognitive activity are 12. Only Subject 3 of male has high Alpha Wave and the remains subjects have high Beta Wave. For female Subjects 5 and 11 have high Alpha Wave while the rest subjects have high Beta Wave. From the observation male Subject 3 has high Alpha Wave than Beta Wave. Subject 3 received almost perfect score and was in relax condition while answering the cognitive question. Female Subject 5 also shows the same condition as male Subject 3. For Subject 11, she showed the symptoms of drowsiness and tired when answer the cognitive question, as Alpha Wave lie in between wakeful and asleep.

Table 3 Total high Alpha Wave and Beta Wave male and female

Genders	Alpha Wave	Percentage (%)	Beta Wave	Percentage (%)
Male	1 org	8	11 org	92
Female	2 org	17	10 org	83

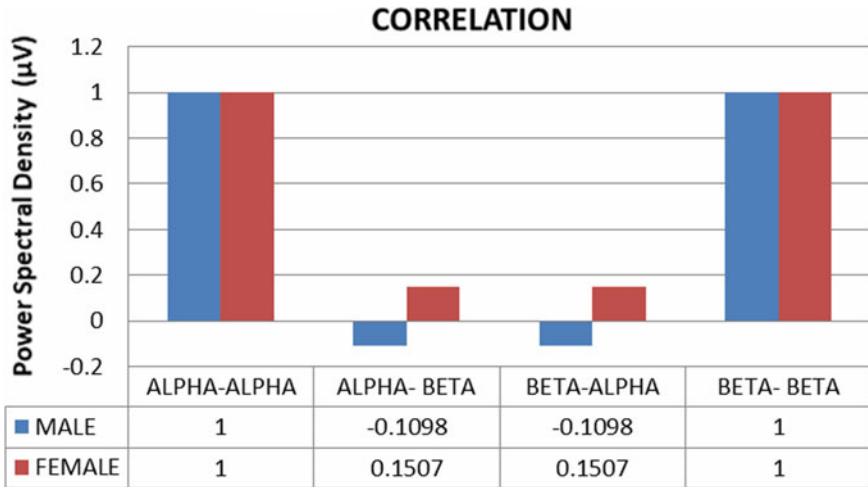


Fig. 7 Correlations Alpha Wave and Beta Wave of male and female

### 3.3 Correlation

Correlation is the method of statistical to measure the strength of relation between 2 variables. Here, 0 means no correlation, above 0.5 indicates strong correlations and below 0.5 shows weak correlations.

Figure 7 shows the correlation between the waves for male and female, both have the same correlation of Alpha-Alpha which shows the strong correlation towards each other ( $r = 1$ ). The similar case is showing for Beta–Beta which have strong correlation ( $r = 1$ ). Correlation Alpha–Beta Wave of male below 0.5 ( $-0.1098$ ) which indicates negative weak correlation between these 2 waves. Female correlation Alpha–Beta also shows the positive weak correlation ( $0.1507$ ).

## 4 Conclusion

There are total of 24 subjects consist 12 males and 12 females Engineering student of UTHM which are volunteer participants for this research. Two main waves are focused in this research it is Alpha Wave and Beta Wave. Theoretically Beta Wave is present when a person in alert, focus, awake and decision making condition. Alpha Wave appears in relaxing and meditative condition. The result shows Beta wave is higher than Alpha Wave for dominant in cognitive.

The research shows that the brainwave pattern between male and female are different. Male subject shows higher level of Beta Wave and female subject shows higher level of Alpha Wave while answering the cognitive question. It can be concluded that male subject shows more dominant in cognitive. This result is based on the analysis

of the data between male and female signal emitted by the subject's brain during the cognitive activity. In addition, from the observation male subjects shows higher concentration level and focus when answering the question. The outcome of this research can be concluded that the entire objective was successfully achieved.

**Acknowledgement** E. M. N. E. M. Nasir and team would like to thank the Research Management Centre (RMC), Universiti Tun Hussein Onn Malaysia (UTHM) for Tier grant code H268 and GPPS grant code H460 for this research. The gratification is also dedicated towards Faculty of Electrical and Electronic Engineering (FKEE) and members of Artificial Intelligent Laboratory, FKEE, UTHM for their cooperation and kindness. Appreciation also goes to Brainwave Research Group (BRG) for their support.

## References

1. Kolb B, Whishaw IQ (2008) *Fundamental of human neuropsychology*. Worth Publishers, New York, USA
2. Murat ZH, Taib MN, Lias S, Abdul Kadir RSS, Sulaiman N, Mustafa M (2010) The conformity between brainwave balancing index (BBI) using EEG and psychoanalysis test. *Int J Simul Syst Sci Technol* 11:85–91
3. Michael C (2014) Corballis: left brain, right brain: facts and fantasies. Published: January 21 <https://doi.org/10.1371/journal.pbio.1001767>
4. Huerta-Pacheco NS, Rebolledo-Mendez G, Hernandez-Gonzalez S (2016) Cognitive-affective modelling approach in tutoring system. In: 1st international workshop on emotional awareness in software engineering, pp 1–4
5. Gjlska B, M-Simoska S, Hinrikus H, Pop-Jordanova N, Pop-Jordanov J (2016) Brain topography of EMF-induced EEG—changes in restful wakefulness: tracing current effects, targeting, future prospects. *Contributions Sec Med Sci*, XXXVI 3:103–111
6. Steven RH, Galloway T, Borka C (2007) EEG related changes in cognitive workload, engagement and distraction as students acquire problem solving skills. Team Neorodynamic by Learning Chameleon Inc.
7. Teplan M (2002) Fundamentals of EEG measurement. *Measur Sci Rev* 2:1–11
8. Dahal N, Nandagopal N, Nafalski A, Nedic Z (2011) Modeling of cognition using EEG: a review and a new approach. In: *IEEE region conference*, pp 1045–1049
9. Fuad N, Jailani R, Omar WRW, Jahidin AH, Taib MN (2012) Three dimension 3D signal for electroencephalographic (EEG). In: *Proceedings—2012 IEEE control and system graduate research colloquium, ICSGRC 2012*, pp 262–266
10. Berka C, Levendowski DJ, Lumicao MN, Yau A, Davis G, Zivkovic VT, Olmstead RE, Tremoulet PD, Craven PL (2007) EEG correlates of task engagement and mental workload in vigilance, learning, and memory tasks. *Aviat Space Environ Med* 1–15
11. Anderson LW, Krathwohl DR (2002) *A taxonomy for learning, teaching and assessing: a revision of Bloom's taxonomy of educational objectives (Complete edition)*. Longman, New York, pp 1–35 (2001)
12. Plechawska-Wójcik M, Wawrzyk M, Wesołowska K, Kaczorowska M, Tokovarov M, Dmytruk R, Borys M (2011) EEG spectral analysis of human cognitive workload study. *Studia Informatica*
13. Bell MA, Cuevas K (2012) Using EEG to study cognitive development: issues and practices. In: *US national library of medicine national institutes of health. J Cogn Dev* 13(3):281–294
14. *Fundamentals of EEG Measurement (2002) M Teplan. Measur Sci Rev* 2:1–11

15. Nishizawa S, Benkelfat C, Young SN, Leyton M, Mzengeza SD, Montigny C, de Blier P, Diksic M (1997) Differences between males and females in rates of serotonin synthesis in human brain. In: US national library of medicine national institutes of health 94(10):5308–5313
16. Jahidin AH, Taib MN, Megat Ali MSA, Md Tahir N, Lias S, Haron MH, R MohdIsa, Omar WRW, Fuad N (2013) Evaluation of brainwave sub-band spectral centroid in human intelligence. In: IEEE 9th international colloquium on signal processing and its applications, 8–10 March 2013, Kuala Lumpur, Malaysia, pp 295–298
17. Nielsen JA, Zielinski BA, Ferguson MA, Lainhart JE, Anderson JS (2013) An evaluation of the left-brain versus right-brain hypothesis with resting state functional connectivity magnetic resonance imaging. Published: 14 August 2013, <https://doi.org/10.1371/journal.p1.0071275>
18. Fuad N, Taib MN, Jahidin AH, Mohd Isa R, Marwan ME (2013) Brainwave sub-band power spectral density characteristics for human brain balanced via three dimensional electroencephalographic model. In: The 15th international conference on biomedical engineering (ICBME2013), pp 543–545. National University of Singapore University Town, Singapore, December
19. Che-Him N, Nor ME, Md Kamaruddin NK, Asrah NM, Saharan S, Khalid K (2014) Engineering statistic. Universiti Tun Hussein Onn Malaysia
20. Cheryl Bagley Thompson Ph.D., RN (2009) Descriptive data analysis. Air Med J 28:2 March–April 2009. MS-52

# Intelligent Autism Screening Using Fuzzy Agent



Nurul Najihah Che Razali, Ngahzaifa Ab. Ghani and Syfak Izhar Hisham

**Abstract** In the diagnosis of diseases, either physical or psychological, there are situations causing reaching for second independent opinion very hard. This is especially true in the diagnosis of Autism due to the complex process of diagnosis. Apart from the complex process, the challenges include cost and the availability of experts. This, however, does not change the fact that having regular independent second opinions is crucial. Hence, this study proposes an intelligent autism screening model using fuzzy agent, to assist the expert and non-expert in making the diagnosis. In this study, the fuzzy inputs are assigned based on five categories, which are Communication, Gross Motor, Fine Motor, Problem Solving, and Personal Social, and is specifically for three-year-old children only. The proposed model will be able to produce output in the form of sequences based on lowest to highest mark of the scores for each category. This output will then relate to the suggestion of activities to autistic children by priority (based on the scores obtained).

**Keywords** Autism spectrum disorder (ASD) · Agent-Based · Fuzzy agent · Autistic children · Symptoms

## 1 Introduction

Autism or Autism Spectrum Disorder (ASD) is a common psychological disorder that affects 1 in 500 children [1]. It often remains undetected until after-toddlers age due to the difficulty in making the diagnosis, although in most cases, parents are aware that something is missing in the child development. The tool for diagnosis is not easily available, even if it is, it needs an expert's knowledge to interpret the result.

In most cases, the diagnosis of autism is not made until the two to three years because only then, the symptoms become obvious and the child starts to struggle to fit in the society. For children with ASD, being identified early has many advantages

---

N. N. C. Razali · N. Ab. Ghani (✉) · S. I. Hisham  
Faculty of Computer Systems & Software Engineering (FSKKP), Universiti Malaysia Pahang,  
Lebuh raya Tun Razak, 26300 Kuantan, Pahang Darul Makmur, Malaysia  
e-mail: [zaifa@ump.edu.my](mailto:zaifa@ump.edu.my)



and most likely will also improve the outcome as intervention and treatment can be done early [1]. Every ASD child is unique because each exhibits their impairments (or sometimes extraordinary skills) in unique combinations [2]. The impairments are usually both on physical and psychological developmental delays. Apart from that, ASD children are also usually troubled by sound, touches, or smells which seem normal to others [3].

At the beginning of autism disorder, early intervention allows early educational and developmental planning, prepares the family for supports, stress management, education arrangement, and also ensure delivery of appropriate medical care and treatment [1]. For the intervention (in the form of therapies) to happen, a child needs to be assessed or diagnosed firstly, and for that matter, an early diagnosis is very important, especially for those with learning disabilities [4–6]. However, as important as it is, the prediction of autism disorder is difficult than a prediction of disease because it relates to a variety of attributes [3], where the main challenges are imprecision, uncertainty, and vagueness [7–12].

## 2 Related Works

Diagnosis of autism have been done by using certain sets of questions that are answered by parents or guardians, and based on the score values, the child will be able to be identified as having autism disorder or not. The diagnosis involves assessment of behaviors and usually takes several hours to complete [13]. Many established diagnostic tool (questionnaires) have been published, among them are Modified Checklist for Autism in Toddlers (M-CHAT) and Childhood Autism Rating Scale (CARS). M-CHAT diagnosis results have been doubted by [14]. However, this is especially the case for children born very preterm. In their critical review, state that the instrument (CARS) may not be applicable for those with sensory and intellectual disabilities [15]. They also suggested that for this group of people, additional diagnosis instrument is needed.

Another established diagnostic screening tool is The Ages and Stages Questionnaires, 3rd edition (ASQ-3<sup>®</sup>) [16], which is developed for monitoring children in the age range of 2–60 months. This tool evaluates five elements such as communication, gross motor, fine motor, problem-solving, and personal-social, where each section consists of several questions to be completed by parents.

This method of diagnosis using established questionnaires, for the fact that it involves many questions and the results are not easily translatable by people of non-experts, make the diagnosis process lengthy and nearly impossible to be done without the presence of experts. There have been several studies done on proposing a diagnostic tool (system) to replace the lengthy questionnaires. However, most of them only diagnose the level. For example, Ahuja, R. and Kaur, D. developed a diagnosis method using neuro-fuzzy, but the diagnosis output is only either high (high level of autism) or low (low level of autism) [3]. To come out with this very simplified result, the extensive questionnaires still need to be answered to get the

score as input to their neuro-fuzzy system. This method is not, in any way helping in shortening or simplifying the process of diagnosis.

Two attempts to shorten the process of diagnosis have also been made [17, 18]. However, these two attempts have been criticized for not proving significant time reduction in the diagnosis process [19]. Al-diabat, M. then, suggested a fuzzy rule-based model consisting of 24 variables to diagnose children at the range of age between 4 to eleven years old [19].

Tariq, Q. proposed a solution to the lengthy and complicated process of diagnosis. He suggested the use of a 3-minute home video to assess the behaviors of an affected child where the video is shared in their established web portal and then rated by non-expert raters [13]. The non-expert raters will then assess the video by looking at certain characteristics such as eye contact, communication, etc. This method, although it can be considered as a very good alternative for diagnosis without the presence of experts, it is, however, again not in any way simpler because it needs an established platform and participation from the public. The result also very much relies on humans' opinion.

Being able to diagnose only the level of autism is useful but not quite enough. For the focused therapy to happen, the exact area (problem) must be determined. Knowing one is having severe autism is not enough, but knowing in which area the patient has a major problem with (communication, personal, social, behavior etc.) is very important. Based on the review on existing studies, apart from attempting to simplify the process of diagnosis, none of the works have attempted for detail diagnosis (diagnosing category) as well as the suggestion of therapy activities.

## 3 Methodology

### 3.1 Overview of Fuzzy Agents

This research applies fuzzy agent to classify human behavior of autistic children. Intelligent agents can perform flexible and independent autonomic actions to accomplish goals that have been set through computer systems. The agent will receive input and then it will act to change the environment.

According to [20], in most agent-based systems, the behavior of an agent that interacts with other agents of the system is composed of three phases, (1) receives information from another agent or perceives a change in its environment, (2) interprets the event and decides on actions to be performed by taking into account other agents, (3) sends a message or performs an action to modify the environment.

The agents, that implement ambiguous problems through fuzzy logic, are called fuzzy agents [21]. In their study, [22] provided fuzzy agents that can decide for more effective design when fuzzy design information is considered in a fuzzy interaction. As shown in Fig. 1, observe, decide, and act are the elements in the fuzzy agent. It can be applied for autism screening in this research, by providing input from

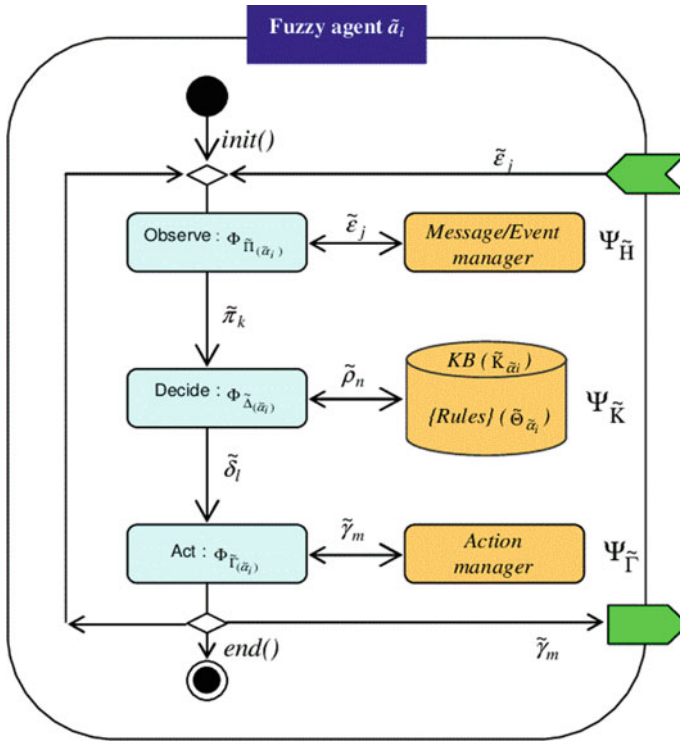


Fig. 1 Functional architecture of a fuzzy agent [20]

questionnaires (observe), then the autism challenges will be categorized in a specific category (decide). Finally, the fuzzy-agent-processed output known as activities (act) will be proposed as guidance or suggestion for autistic children specifically.

### 3.2 The Working Mechanism of Fuzzy Agent for Autism Screening

In the proposed model for this Intelligent Autism Screening, four processes are needed to produce data and get output using questionnaire data based on autistic parent responses, as demonstrated in Fig. 2.

Step 1. **Data Collection.** Autistic children data will be provided by parents through established questionnaires. This process will be assisted by Occupational Therapy (OT) from several Autism therapy centers in Malaysia. The data will then be pre-processed before being used as input for the next step.

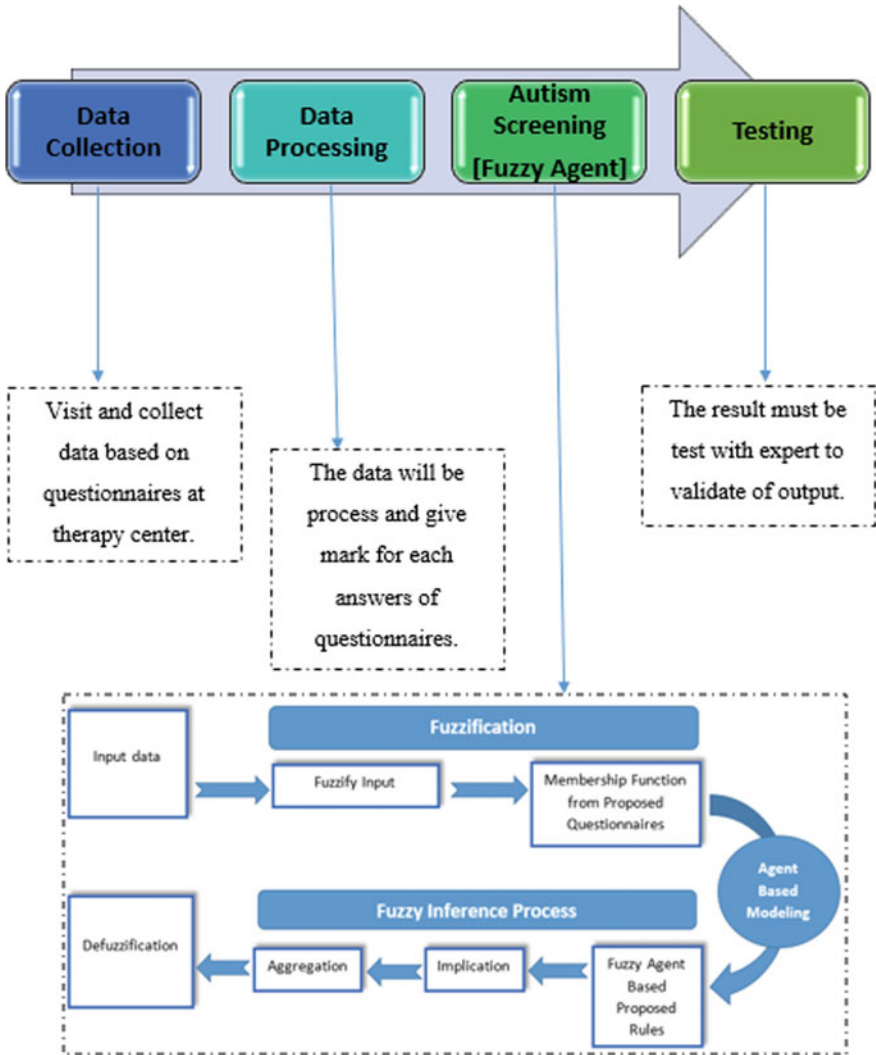


Fig. 2 The framework of intelligent autism screening diagram

- Step 2. **Data Processing.** All data from the questionnaire is processed before being fed into fuzzy rules. The output at this stage is mark/rating for each category involved and will use as input for the next process.
- Step 3. **Autism Screening using Fuzzy Agent.** After data is processed, the data will be fed into fuzzy-agent based model to obtain the final output, which is the suggestion of therapy activities.

Step 4. **Testing.** The results will be verified by experts (occupational therapies) to validate whether or not the developed model has provided a valid output, which is the suggestion of therapy activities based on ASD level of the child.

### 4 Results and Discussion

Figure 3 shows the agents involved, where the numbering of agents represents the rank of marks in order. Each agent will represent one category where in this case there are five categories: Communication, Gross Motor, Fine Motor, Problem Solving, and Personal-Social.

In Phase I, the rank marks are the output obtained from the questionnaires marks that have been fed through fuzzy rules. The output from this stage (rank of categories) will be fed through the next fuzzy agent-based model in Phase II. In Phase II, the fuzzy agent-based model will consider the three top categories (three highest marks from Phase I) as variables.

The example of fuzzy rules involved in Phase I is provided in Table 1 and the linguistic value and notation are provided in Table 2. The rules in Table 1 represent an only small part of the rules involved where one rule indicate one ASD child. For example, Rule 1 can be interpreted as follows:

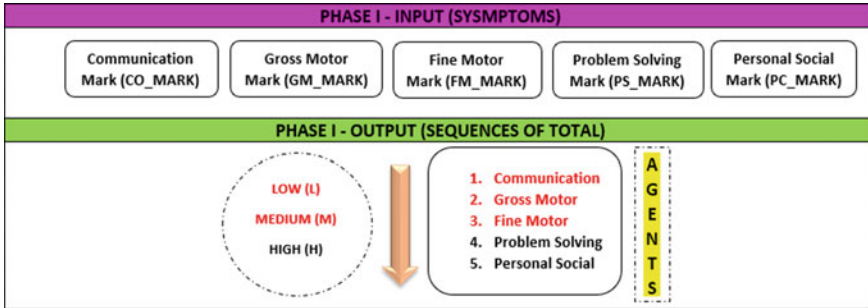


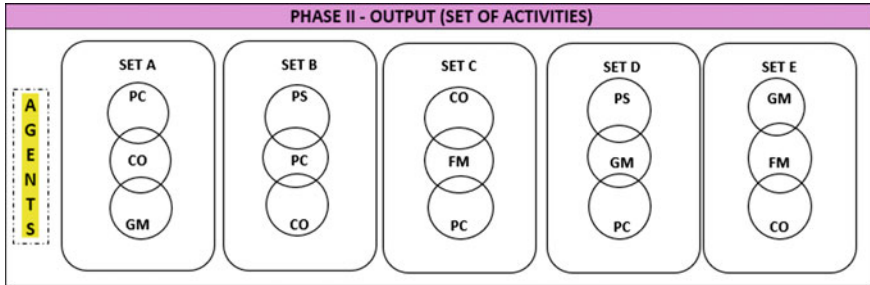
Fig. 3 Modeling of agent-based with input and output for phase I

Table 1 Rules of input and output from phase I

Rule	CO_MARK	GM_MARK	FM_MARK	PS_MARK	PC_MARK	Activity
1	MR(1)	RE(4)	MR(2)	NR(5)	MR(3)	C
2	RE(3)	RE(4)	NR(5)	MR(1)	MR(2)	B
3	NR(2)	NR(3)	NR(4)	NR(5)	MR(1)	A
4	NR(4)	RE(2)	NR(5)	MR(1)	RE(3)	D
5	RE(3)	MR(1)	MR(2)	NR(4)	NR(5)	E

**Table 2** Linguistic value and notation

Symptoms	Label	Status	Label
Low	L	Most required	MR
Medium	M	Required	RE
High	H	Not required	NR



**Fig. 4** Modeling of agent-based with input and output for phase II

If communication mark (CO\_MARK) is low,  
 AND gross motor mark (GM\_MARK) is medium  
 AND fine motor (FM\_MARK) is low and  
 problem-solving (PS\_MARK) is high  
 AND personal social (PC\_MARK) is low  
 THEN Activity is C.

According to the agents in Fig. 4, Activity C is the combination of ‘fine motor’ (FM) with ‘communication’ (CO) and also FM with ‘personal-social’ (PC). This result indicates that based on the scores of ASD child number 1 (Rule 1), the suggested activity is the activity involves with ‘fine motor’. The improvement in ‘fine motor’ will affect positively also on communication and personal-social.

Figure 4 shows five sets of agents that work in Phase II, in which each agent has one dominant variable. For example, agent Set A has CO as dominant variable meaning that if an ASD child is pointed to this agent (based on the scores from the questionnaire), the suggestion of therapy activity is focused mostly on communication associated with gross motor and personal-social. Agent Set B is focused on personal social activity that is associated with problem-solving and communication; agent Set C is focused on fine motor that is associated with communication and personal social; agent Set D is focused on gross motor that is associated with problem-solving and personal social; and agent set E is focused on fine motor that is associated with communication and gross motor.

## 5 Conclusions

Based on the proposed fuzzy agent-based model, an intelligent screening tool will be developed. One fully functional screening tool will be able to diagnose the level of severity and category, and also come out with the suggestion of suitable therapy activities. This tool will be a great help for parents and also trainee experts. However, the result must be verified and validated by the experts in the field.

## References

1. Filipek PA, Accardo PJ, Ashwal S, Baranek GT, Otr L, Cook EH, Volkmar FR (2000) Practice parameter: screening and diagnosis of autism report of the quality standards subcommittee of the american academy of neurology and the child neurology society 1–14
2. Tennyson MF, Kuester DA, Casteel J, Nikolopoulos C (2016) Accessible robots for improving social skills of individuals with autism as an intervention for individuals. *J Artif Intell Soft Comput Res* 6(4):267–277
3. Ahuja R, Kaur D (2014) Neuro-fuzzy methodology for diagnosis of autism 5(2):2171–2172
4. El Alami M, Tahiri N, De Arriaga F (2017) DIAUTIS: a fuzzy and affective multi-agent platform for the diagnosis of autism. *Br J Appl Sci Technol* 21(4):1–28
5. Hieu NV, Hien NLH (2018) Artificial neural network and fuzzy logic approach to diagnose autism spectrum disorder. *Int Res J Eng Technol* 5(6)
6. Puerto E, Aguilar J, Lopez C, Chavez D (2019) Using multilayer fuzzy cognitive maps to diagnose autism spectrum disorder. *Appl Soft Comput J* 75:58–71
7. Pratap A, Kanimozhi CS, Pramod KV, Vijayakumar R (2014) Functional fuzzy based autism assessment support system. *Int J Eng Technol* 6(5):2105–2114
8. Souza PVDC, Gumaraes AJ (2018) Using fuzzy neural networks for improving the prediction of children with autism through mobile devices. In: *IEEE Symposium on computers and communications (ISCC)*, pp 1086–1089
9. Sharma A, Khosla A, Khosla M, Rao Y (2018) Fast and accurate diagnosis of autism (FADA): a novel hierarchical fuzzy system based autism detection tool. *Australas Phys Eng Sci Med* 41:757–772
10. Thabtah F (2019) Machine learning in autistic spectrum disorder behavioral research: a reviews and ways forward. *Informatics for Health and Social Care* 44(3): 278–297
11. Bi XA, Liu YC, Jiang Q, Shu Q, Sun Q, Dai JH (2018) The diagnosis of autism spectrum disorder based on the random neural network cluster. *Front Hum Neurosci* (12):257
12. Thabtah F, Peebles D (2019) A new machine learning model based on induction of rules for autism detection. *Health Inform J*, p 1–23
13. Tariq Q, Daniels J, Schwartz JN, Washington P, Kalantarian H, Wall DP (2018) Mobile detection of autism through machine learning on home video: a development and prospective validation study. *PLoS Med* 15(11)
14. Gray PH (2017) M-CHAT autism screening may be inaccurate among toddlers born very preterm. *J Pediatr* 182:401–404
15. De Vaan G, Vervloed MPJ, Den Boom MH-D, Antonissen A, Knoors H, Verhoeven L (2016) A critical review of screening and diagnostic instruments for autism spectrum disorders in people with sensory impairments in addition to intellectual disabilities. *J Ment Health Res Intellect Disabil* 9(1–2):36–59
16. Robins D, Dumont-Mathieu T (2006) Early screening for autism spectrum disorders: update on the modified checklist for autism in toddlers and other measures. *J Dev Behav Pediatr JDBP* 27(2 Suppl):S111–S119

17. Wall D, Kosmicki J, DeLuca T, Harstad E, Fusaro V (2012a) Use of machine learning to shorten observation-based screening and diagnosis of autism, *Tradit Psychiatry* 2(4)
18. Wall D, Dally R, Luyster R, Jund J, Deluca T (2012b) Use of artificial intelligence to shorten behavioural diagnosis of autism. *Plos One* 7(8)
19. Al-diabat M (2018) Fuzzy data mining for autism classification of children. *Int J Adv Comput Sci Appl* 9(7):11–17
20. Fougères AJ (2013) A modelling approach based on fuzzy agents. <https://arxiv.org/abs/1302.6442>, pp 10
21. Jennings NR (2000) On agent-based software engineering 6, 117(September 1999):277–296
22. Ostrosi E, Fougères AJ (2011) Optimization of product configuration assisted by fuzzy agents. *Int J Interact Des Manuf* 5(1):29–44



# Ultra Wide Band (UWB) Based Early Breast Cancer Detection Using Artificial Intelligence



**Bifta Sama Bari, Sabira Khatun, Kamarul Hawari Ghazali, Md. Moslemuddin Fakir, Wan Nur Azhani W. Samsudin, Mohd Falfazli Mat Jusof, Mamunur Rashid, Minarul Islam and Mohd Zamri Ibrahim**

**Abstract** Breast cancer is a silent killer malady among women community all over the world. The death rate is increased as it has no syndrome at an early stage. There is no remedy; hence, detection at the early stage is crucial. Usually, women do not go to clinic/hospital for regular breast health checkup unless they are sick. This is due to the long queue and waiting time in the hospital, high cost, people's busy schedule, and so on. Recently, several research works have been done on early breast cancer detection using Ultra Wide Band (UWB) technology because of its non-invasive and health-friendly nature. Each proposed UWB system has its limitation including system complexity, expensive, expert operable in the clinic. To overcome these problems, a system is required which should be simple, cost-effective and user-friendly. This chapter presents the development of a user friendly and affordable UWB system for early breast cancer detection utilizing Artificial Neural Network (ANN). A feed-forward back propagation Neural Network (NN) with 'feedforwardnet' function is utilized to detect the cancer existence, size as well as the location in 3-dimension (3D). The hardware incorporates UWB transceiver and a pair of pyramidal shaped patch antenna to transmit and receive the UWB signals. The extracted features from the

---

B. S. Bari · S. Khatun (✉) · K. H. Ghazali · W. N. A. W. Samsudin · M. F. M. Jusof · M. Rashid · M. Islam · M. Z. Ibrahim  
Faculty of Electrical and Electronics Engineering, Universiti Malaysia Pahang, Pekan, Malaysia  
e-mail: [sabirakhatun@ump.edu.my](mailto:sabirakhatun@ump.edu.my)

K. H. Ghazali  
e-mail: [kamarul@ump.edu.my](mailto:kamarul@ump.edu.my)

W. N. A. W. Samsudin  
e-mail: [nurazhani@ump.edu.my](mailto:nurazhani@ump.edu.my)

M. F. M. Jusof  
e-mail: [malfazli@ump.edu.my](mailto:malfazli@ump.edu.my)

M. Z. Ibrahim  
e-mail: [zamri@ump.edu.my](mailto:zamri@ump.edu.my)

Md. M. Fakir  
CARIFF, Faculty of Chemical and Natural Resources Engineering, Universiti Malaysia Pahang,  
Pekan, Malaysia  
e-mail: [moslemuddin@ump.edu.my](mailto:moslemuddin@ump.edu.my)

received signals were fed into the NN module to train, validate, and test. The average system's performance efficiency in terms of tumor/cancer existence, size and location is approximately 100%, 92.43%, and 91.31% respectively. Here, in our system, use of 'feedforwardnet' function; detection-combination of tumor/cancer existence, size and location in 3D along with improved performance is a new addition compared to other related researches and/or existing systems. This may become a promising user-friendly system in the near future for early breast cancer detection in a domestic environment with low cost and to save precious human life.

**Keywords** Early breast cancer · Ultra wideband (UWB) · Neural network (NN) · Feed forward back propagation

## 1 Introduction

Breast cancer is the most often clinically diagnosed cancers among women community. It is the second cause of cancer death after lung cancer among women globally due to its high death rate [1]. According to the report of the Malaysian National Cancer Registry, breast cancer was accounted for 32.1% of all cancers among females in Malaysia from 2007 to 2011 [2]. The statistical view of American Cancer Society exposed that only in the United States in 2017, around 252,710 women and 2470 men were diagnosed with breast cancer [3]. The death rate due to breast cancer can be reduced by following proper screening and diagnosis technique at the initial stage before major physical symptoms appearing on the body. As there is no remedy, target is for long-run survival. In this case, early detection is essential. However, women are not conscious of their breast health. They have no eagerness of breast health checkup unless they are really sick. This happens because the breast health monitoring at the hospital is very expensive [4, 5]. According to Park et al. [6], if the breast tumor can be detected early enough, the five-year and ten-year overall survival rate are approximately 91.2% and 84.8% respectively. Thus, Regular breast health check-up (screening) and detection at an early stage are essential to reduce the mortality rate [5]. Hence, UWB is a notable wireless communication technology with large bandwidth and small power. This technology is appropriate to utilize in short range communication; for example, breast cancer detection as it is non-invasive, safe, cost-effective as well as harmless to users [7, 8].

There are different traditional methods to diagnose or detect breast cancer including mammograms, magnetic resonance imaging (MRI), biopsy, ultrasound and so on. In a mammogram, the breast of a patient is kept on a flat support plate and then compressed by a paddle which is very painful. Moreover, mammography is not suitable for dense breasts (especially who are under 30 years old) [9]. Some of them are expensive, cannot detect cancer at the primary stage and creates complexity in human health during or after the diagnose process [9, 10]. These limitations motivate the research to investigate and find alternate methods, such as UWB microwave

imaging technique which has added a new dimension for early breast cancer detection [5, 6]. UWB is considered as an advance alternative option to existing methods, because of its harmless property to human health. Different sorts of UWB system have been proposed by numerous researchers to identify breast cancer at an early stage. However, all the systems are operated by experts in the clinics/hospitals. A UWB experimental system was suggested by Alshehri et al. [11–15] for detecting the tumor existence, size and location; however, this system is expertly operable, expensive and not usable at home. Moreover, they detect tumor location in 3D, but they evaluate the location detection performance by varying x-axis only, where y-axis and z-axis are fixed. This may affect the overall performance. Reza et al. [16] detected the tumor size in two dimensions in order to increase the breast cancer detection performance with efficient feature extraction method. However, though their detection performance was good; they did not consider the location of the tumor. Vijayasarveswari et al. [17–20] worked on early breast cancer detection using UWB. In [17], they proposed a tumor detection system using UWB with location(x, y and z) detection efficiency is 78.17%, 70.66%, 92.46% respectively. Although their z-axis detection shows good performance, the x-axis and y-axis location's detection are not satisfactory. Many other researchers have worked on the detection of breast cancer including; Meaney et al. [21], Fear et al. [22], Abu Bakar et al. [23], Shahzad et al. [24], Salleh et al. [25]. However, they have their own shortcomings including only 2-dimensional detection system, high cost, lower efficiency, use of expensive Vector Network Analyzer (VNA) and so on. In this chapter, a non-invasive early breast cancer detection technique is presented in 3-dimension (x, y, and z-axis) using feed-forward back propagation Neural Network (NN) with 'feedforwardnet' function. It consists of UWB RCM Pulse-on device [26] as transceiver, two antennas/sensors for transmitting and receiving the signal, homogenous breast phantom constructed with accessible low-cost materials in lowest effort. Feed forward back propagation neural network is applied to identify tumor existence, size, and location. The proposed system shows detection efficiency on tumor existence, size, and location (x, y, z) are 100%, 92.43% and 91.31% (95.22%, 88.98%, 89.74%) respectively. Our proposed UWB based technique for early breast cancer detection could be efficient with this detection efficiency.

This chapter is organized as follows. The next section presents the methodology including the constructing method of the breast phantoms and tumor as well as experimental data collection. Followed by NN performance with training, testing, and validation; results with tumor existence, size and location, discussions and comparison with other existing systems; and finally the conclusion.

## 2 Methodology

The method of constructing the breast phantoms, tumors, experimental set-up, data collection as well as processing details are presented in this section.

## 2.1 The Experimental Set Up and Data Collection

**Breast Phantom and Tumor Preparation** A few researchers have proposed numerous sorts of breast phantom to investigate the breast cancer [11, 27, 28]. Alshehri et al. [11] proposed an easy way to form breast phantom and tumor in terms of low cost, easily accessible, and non-chemical materials. A homogeneous breast phantom has been developed in this research based on [11]. The Phantom is constructed using a glass of 1.6 (mm) thickness that is used as a skin and pure petroleum jelly is utilized as breast fatty tissue. A mixture of 10 g wheat flour along with 5.5 g water is utilized to construct the tumor with different sizes as per need. Then, and inserted into the phantom in a different location for each experimentation-trial. Table 1 shows the dielectric properties of considered materials of breast phantom and tumor [11]. The breast phantom has been placed in between the transmitter and receiver as shown in Fig. 1. The feeding cable is used here to connect the sensor with UWB transceiver. The UWB pulses are generated in transceiver; transmitted through transmitting sensor, whereas the receiver receives the pulses.

**Data Collection** The experimental system set-up for data collection of the proposed system is represented in Fig. 1. The UWB transceiver system P400 RCM from Time domain Co. has been utilized in this experiment [26]. This commercial UWB

**Table 1** Dielectric properties of the used material to construct breast phantom and tumor [11]

Breast phantom part	Material	Permittivity	Conductivity
Fatty tissue	Pure petroleum jelly	2.36	0.012
Skin	Glass	3.5–10	Negligible
Tumor	Mixture of water and wheat flour	23	2.57

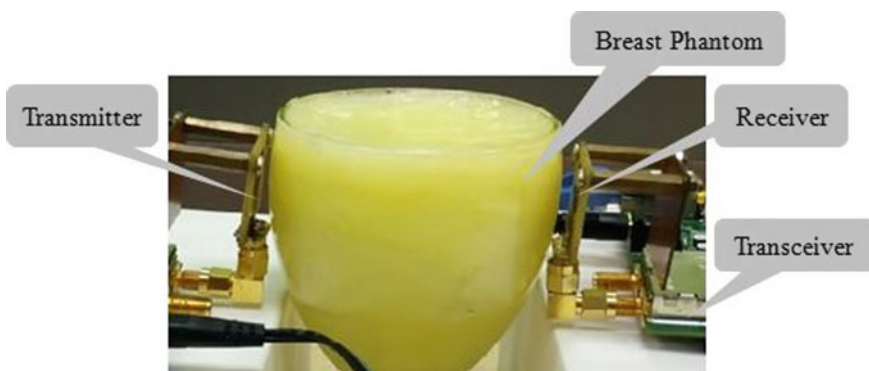


**Fig. 1** Experimental set-up for data collection

transceiver system is utilized to produce the UWB pulses as well as to receive the scattered waveform. Here, in the system, Discrete Cosine Transform (DCT) is used for analog to digital signal conversion process. Two pyramidal shaped UWB patch antennas/sensors (connected with UWB transceiver) [16] have been used to transmit and receive the UWB signals. The UWB transceiver was connected (through Ethernet hub) that was controlled by a PC. The sensor at the receiver side received the forward scattered signals transmitted by the transmit sensor and saved in PC for further processing. This procedure was repeated at various times for different tumor sizes and locations (x, y and z). The received signals were processed to attain related discrete 1632 data points for each sample. Total 448 data samples were collected and then used to train, validate and test this system. Among total data samples, 70% data is used for training, 15% is used for validation and 15% is used for testing. The received signals are preprocessed to obtain essential features (four features: max, min, mean, SD) before feeding to the neural network. The overall process of the system is shown in Fig. 2.

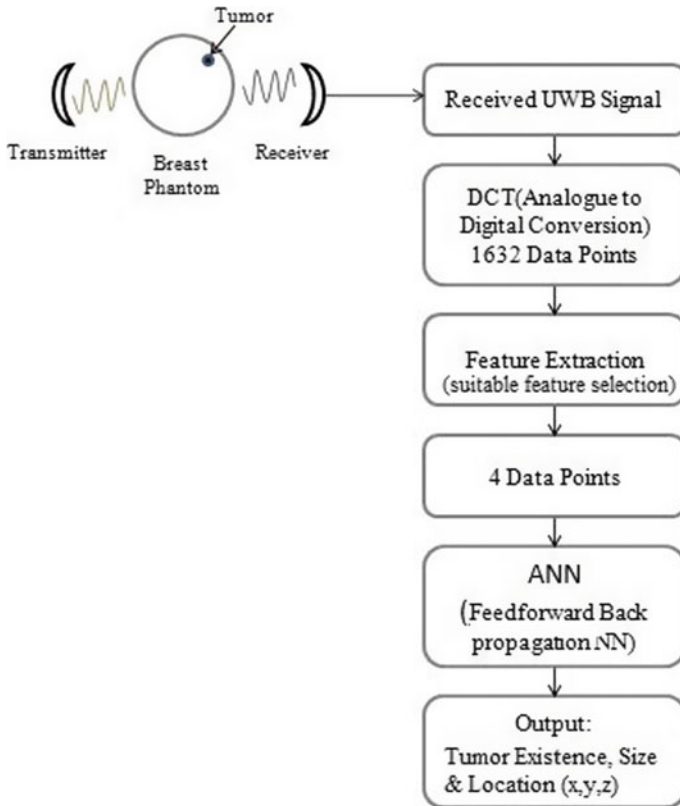


Fig. 2 The overall detection process

## 2.2 Feature Extraction

The training procedure may be interrupted by the huge numbers of input data. Therefore, researchers often attempt to train the ANN utilizing some characteristic values, that values are known as feature values. Before training, 1632 data points were minimized to 4 data features for each data sample through feature extraction by applying a similar process as in [16, 29]. Feature extraction is done to decrease computing time and complexity. Since the extracted four features are in the little group after feature extraction, the training can optimize and give a better result. For each data sample, the extracted 4 features were mean, standard deviation, maximum and minimum [16, 29]. The train was performed using feed forward back propagation NN with “feedforwardnet” function.

## 2.3 Artificial Neural Network (ANN)

An Artificial Neural Network (ANN) or simply a Neural Network (NN) is a computational model that resembles the biological neural network architecture and function. It comprises of nodes arranged in two or more layers. There are many NN types, in this study, a feed-forward back propagation NN is considered for tumor detection. It is a simple and powerful tool. It was developed by utilizing MATLAB software in which input turns to forward in one direction. Hence, input data goes through some hidden nodes with a various hidden layer (if exists) and lastly to the output node. The performance of the NN module can be expanded by changing the number of hidden neurons. However, the number of hidden neurons should not be very large since it may take longer a time to compute. After extracting the features from 1632 data points, the number of input nodes is 4. Then, the number of the hidden layer is 20 and the number of the output node is 1. The NN module performance was examined with collected data samples. Mean Square Error (MSE) of NN output can be calculated by subtracting output value from the target value. All trained networks are tested and their performance efficiency is analyzed based on the performance plots. “feedforwardnet” function is used here. To calculate the absolute error, the used formula is shown in Eq. 1 [13].

$$E = \frac{1}{N} \sum (t_n - y_n) \quad (1)$$

where  $t_n$  is the target or actual values and  $y_n$  is the predicted values by the NN.  $N$  is the number of samples. Hence, the used formula for relative performance rate is shown in Eq. 2 [14].

$$E = \frac{\max(y_i, t_i) - \min(y_i, t_i)}{\max(y_i, t_i)} \quad (2)$$

**Table 2** Performance efficiency for tumor location detection (x, y, z)

Location (x, y, z)	Target (mm)	NN output (mm)	Efficiency for each target (%)	Efficiency for each axis (%)	Overall efficiency (%)
x-axis	55	49.45	89.96	95.22	91.31
	42	36.11	86.05		
	48	49.10	97.75		
	50	48.71	97.40		
y-axis	17	14.40	84.57	88.98	
	19	20.07	94.63		
	22	24.11	91.24		
	24	20.10	83.68		
z-axis	17	18.79	90.45	89.74	
	19	18.88	98.69		
	21	18.90	89.80		
	25	33.10	75.51		

where  $y_i$  are the predicted and  $t_i$  are the target/actual values.

The predicted output for each data sample is evaluated and compared with the target value in order to get performance efficiency of the system using Eq. 3 [14].

$$Performance\ Efficiency(\%) = 100 - E(error\%) \quad (3)$$

Equation 3 is used to get performance efficiency for both tumor size (Table 3) and location (Table 2). In regard to tumor existence, any -ve output for an input signal sample, indicates no tumor presence (i.e., healthy breast), otherwise, tumor exists (for +ve output).

### 3 Result and Discussion

The training, testing and validation performance for the network is shown in Fig. 3. The best validation performance has occurred at epoch 4 (or iteration number 4). The testing and validation results are desirable as well as consistent that makes good network performance.

The developed system can detect tumor size and location (x, y, and z) in the homogeneous breast phantom. The cancer existence detection rate of approximately 100% is accomplished for our system. Different arbitrary locations (x, y, and z) and sizes of the tumor have been used to validate the efficiency of the system. Using Eq. 3, the overall performance efficiency of tumor size and location are determined

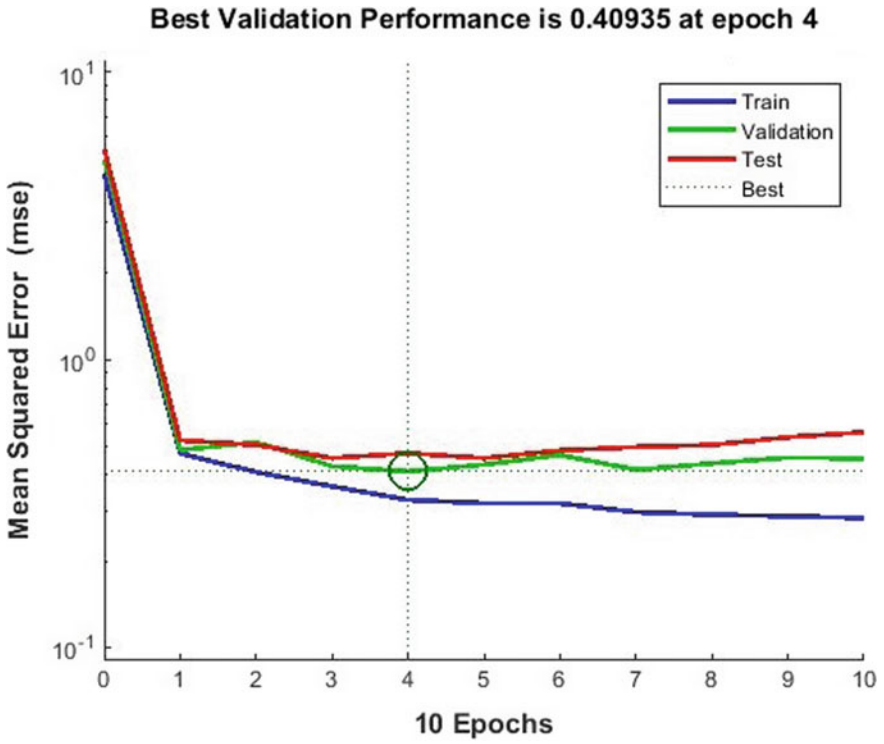


**Fig. 3** Neural network performance

which are approximately 92.43% and 91.31% respectively. Tables 2 and 3 show performance efficiency details of the system for tumor location and size respectively along with used actual data/target values and their respective estimated values.

Table 4 presents a comparison of the proposed system with other existing systems. It can be seen that, Conceicao et al. [30] used more data samples than others. However, they did not consider the detection of tumor location. Santorelli et al. [31] did not

**Table 3** Performance efficiency for tumor size

Target of size (mm)	NN output size (mm)	Efficiency for each target (%)	Overall efficiency (%)
4	3.16	79.19	92.43
5	5.16	96.82	
6	5.14	85.70	



**Table 4** Performance comparison with other methods

Detection system	Sample data	Method used	Existence (%)	Location (%)	Size (%)
Proposed system	448	FFBPNN (with 'feedforwardnet' function)	100	91.31	92.43
Conceicao et al. [30]	960	Linear classification	N/A	N/A	90.52
Santorelli et al. [31]	240	SVM	73.64	76.71	N/A
Vijayasarveswari et al. [17]	125	FFBPNN	100	89.06	85.86

detect tumor size and Vijayasarveswari et al. [17] used a small number of data sample than others. It is apparent that the proposed system performs better than other systems. Thus, our developed system can be able to detect early breast cancer more precisely than other systems.

## 4 Conclusion

An effective technique for early breast cancer detection is developed in terms of UWB hardware and Feed Forward Back Propagation Neural Network in 3-dimension using "feedforwardnet" function. The early tumor/cancer detection efficiency of the developed system is very satisfactory regarding the existence, size and location. This system is non-invasive, health-friendly as well as low cost. The system can be equally useable for both by doctors in the hospital for screening and the end users at home for breast health self-monitoring by adding a user friendly Graphical User Interface (GUI).

The breast cancer type (benign and/or malignant) detection is under progress in iCOE and AppECE Labs, FKKEE, UMP. The Graphical User Interface (GUI) is also been designed and will be integrated with the proposed system.

**Acknowledgements** This work is supported by Universiti Malaysia Pahang (UMP), Internal Research Grant RDU1703125 and UMP Post-Graduate Research Scheme (PGRS190327). The authors would like to thank the Faculty of Electrical & Electronics Engineering (FKKEE), UMP (<https://www.ump.edu.my>) for providing the facilities to conduct this work and for financial support throughout the process.

## References

1. Hadjiiski L, Sahiner B, Helvie MA, Chan HP, Roubidoux MA, Paramagul C, Blane C, Petrick N, Bailey J, Klein K, Foster M, Patterson SK, Adler D, Nees AV, Shen J (2006) Breast masses: computer-aided diagnosis with serial mammograms. *Radiol Cancer Center* 240(2):343–356
2. Azizah AM, Nor Saleha IT, Noor Hashimah A, Asmah ZA, Mastulu W (2015) Malaysian national cancer registry report 2007–2011, p 33. <https://www.crc.gov.my/wp-content/uploads/documents/report/MNCRRrepor2007-2011.pdf>. Last accessed 13 Apr 2019
3. American Cancer Society (2017) Cancer facts & figures 2017, Atlanta. <https://www.cancer.org/content/dam/cancer-org/research/cancer-facts-and-statistics/annual-cancer-facts-and-figures/2017/cancer-facts-and-figures-2017.pdf>. Last accessed 13 Apr 2019
4. Migowski A (2015) Early detection of breast cancer and interpretation of the results of survival studies. *Sci Collective Health* 20(4)
5. Seidman H, Stellman SD, Mushinski MH (1982) A different perspective on breast cancer risk factors: some implications of the non-attributable risk. *CA Cancer J Clin* 32:301–313
6. Park EH, Min SY, Kim Z, Yoon CS, Jung KW, Nam SJ, Oh SJ, Lee S, Park BW, Lim W, Hur MH (2017) Korean breast cancer society: basic facts of breast cancer in Korea in 2014: the 10-year overall survival progress. *J Breast Cancer* 20:1–11
7. Kwon S, Lee S (2016) Recent advances in microwave imaging for breast cancer detection. *Int J Biomed Imaging* 2016:1–26
8. Hang JA, Sim L, Zakar Z (2017) Non-invasive breast cancer assessment using magnetic induction spectroscopy technique. *Int J Integr Eng* 9(2):54–60
9. Griebisch I, Brown J, Boggis C, Dixon A, Dixon M, Easton D, Eeles R, Evans DG, Gilbert FJ, Hawnaur J, Kessar P, Lakhani SR, Moss SM, Nerurkar A, Padhani AR, Pointon LJ, Potterton J, Thompson D, Turnbull LW, Walker LG, Warren R, Leach MO (2006) Cost-effectiveness of screening with contrast enhanced magnetic resonance imaging vs x-ray mammography of women at a high familial risk of breast cancer. *Br J Cancer* 95:801–810
10. Force UPST (2009) Screening for breast cancer: U.S. preventive services task force recommendation statement. *Ann Intern Med* 151:716
11. Alshehri SA, Khatun S, Jantan AB, Raja Abdullah RSA, Mahmud R, Awang Z (2011) Experimental breast tumor detection using NN-based UWB imaging. *Prog Electromagnet Res* 111:447–465
12. Alshehri SA, Khatun S (2011) UWB imaging for breast cancer detection using neural network. *Prog Electromagnet Res C* 7:79–93
13. Alshehri SA, Khatun S, Jantan AB, Raja Abdullah RSA, Mahmud R, Awang Z (2011) 3D experimental detection and discrimination of malignant and benign breast tumor using NN-based UWB imaging system. *Progr Electromagnet Res* 116:221–237
14. Alshehri SA, Jantan A, Raja Abdullah RSA, Mahmud R, Khatun S, Awang Z (2011) A UWB imaging system to detect early breast cancer in heterogeneous breast phantom. In: Proceedings of the international conference on electrical, control and computer engineering (InECCE'11), 21–22 June 2011, Pahang, Malaysia, pp 238–242
15. Alshehri SA, Khatun S, Awang Z (2011) Homogeneous and heterogeneous breast phantoms for UWB imaging. In: Proceedings of the 4th international symposium on applied sciences in biomedical & communication technologies (ISABEL'11), 26–29 October 2011, Barcelona, Spain, pp 1–5
16. Reza KJ, Khatun S, Jamlos MF, Fakir MM, Morshed MN (2015) Performance enhancement of UWB breast cancer imaging system: proficient feature extraction and biomedical antenna approach. *J Med Imaging Health Inform* 5(6):1246–1250
17. Vijayasarveswari V, Khatun S, Fakir MM, Jusoh M, Ali S (2017) UWB based low-cost and non-invasive practical breast cancer early detection. In: Proceedings of the 11th asian conference on chemical sensors, AIP conference proceedings, 16–18 November 2015, Penang, Malaysia, vol 1808 (1), pp 1–5
18. Vijayasarveswari V, Khatun S, Jusoh M, Fakir MM (2016) Ultra-wideband (UWB) based classification of benign and malignant tumor. *Int J Appl Eng Res* 11(14):8345–8349

19. Vijayasarveswari V, Jusoh M, Khatun S (2017) Experimental UWB based efficient breast cancer early detection. *Indian J Sci Technol* 10(12):1–6
20. Vijayasarveswari V, Jusoh M, Sabapathy T, Aliana1 R, Khatun S, Ahmad ZA, Osman MN (2017) Performance verification on UWB antennas for breast cancer detection. In: *Proceedings of the international conference on emerging electronic solutions for IoT (ICEESI' 17), MATEC Web of Conferences*, 9–10 October 2017, vol 140 (01004), pp 1–4
21. Meaney PM, Paulsen KD, Hartov A, Crane RK (1995) An active microwave imaging system for reconstruction of 2-D electrical property distributions. *IEEE Trans Biomed Eng* 42(10):1017–1026
22. Fear EC, Sill JM (2003) Preliminary investigations of tissue sensing adaptive radar for breast tumor detection. In: *Proceedings of the 25th annual international conference of the IEEE engineering in medicine and biology society*, 17–21 September 2003, Cancun-Mexico, vol 4, pp 3787–3790
23. Abu Bakar A, Ireland D, Abbosh AM, Wang Y (2012) Experimental assessment of microwave diagnostic tool for ultra-wideband breast cancer detection. *Prog Electromagnet Res M* 23:109–121
24. Shahzad A, O'Halloran M, Jones E, Glavin M (2016) A multistage selective weighting method for improved microwave breast tomography. *Comput Med Imaging Graph* 54:6–15
25. Salleh SHM, Othman MA, Ali N, Sulaiman HA, Misran MH, Aziz A, Abidin MZA (2015) Microwave imaging technique using UWB signal for breast cancer detection. *ARPN J Eng App Sci* 10(2):723–727
26. RCM Pulse-On UWB Devices (2017) Time Domain Corporation, Comings Research Park, 330 Wynn Drive, Suite 300, Hantsville, Al 35805, USA
27. Lazebnik M, Madsen EL, Frank GR, Hagness SC (2005) Tissue-mimicking phantom materials for narrowband and ultrawideband microwave applications. *Phys Med Biol* 50:4245–4258
28. Porter E, Fakhoury J, Oprisor R, Coates M, Popović M (2010) Improved tissue phantoms for experimental validation of microwave breast cancer detection. In: *Proceedings of the 4th european conference on antennas and propagation*, 12–16 April 2010, Barcelona, Spain, pp 1–5
29. Khondker Jahid R, Sabira K, Faizal M, Ikram E, Ishwar Z, Khalib A (2013) Proficient feature extraction strategy for performance enhancement of NN based early breast tumor detection. *Int J Eng Technol* 5(6)
30. Conceicao RC, O'Halloran M, Jones E, Glavin M (2010) Investigation of classifiers for early-stage breast cancer based on radar target signatures. *Prog Electromagnet Res* 105:295–311
31. Santorelli A, Porter E, Kirshin E, Liu YJ, Popović M (2014) Investigation of classifiers for tumor detection with an experimental time-domain breast screening system. *Prog Electromagnet Res* 144:45–57

# Design and Analysis of Circular Shaped Patch Antenna with Slot for UHF RFID Reader



Mohd Hisyam Mohd Ariff, Muhammad Solihin Zakaria, Rahimah Jusoh, Sabira Khatun, Mohammad Fadhil Abas and Mohd Zamri Ibrahim

**Abstract** This paper presents an analysis of microstrip circular shaped antenna with slot for ultra-high frequency (UHF) portable radio frequency identification (RFID) reader applications. The fabricated antenna is designed to work with UHF RFID system in Malaysia with frequency allocated from 919 to 923 MHz. The antenna design was made with circular patch and rectangular slot that has the dimension of 122 mm × 122 mm. Moreover, the FR-4 material used in this project has thickness of 1.6 mm with dielectric constant of 4.7 and loss tangent of 0.019. Thus, it is easily connected to the portable RFID reader module together with the antenna characteristics of easy fabrication, low profile and simple structure. From the results, the antenna has the reflection coefficient ( $S_{11}$ ) less than  $-10$  dB along the bandwidth of 3.6% (903–936 MHz) for operating frequency at 921 MHz.

**Keywords** Microstrip antenna · Radio frequency identification · Ultra high frequency · Return loss

## 1 Introduction

Radio Frequency Identification (RFID) is a new value tool toward electronic identification and inventory information system. The RFID comprise a reader which can read tag containing the electronic product code (EPC) data that includes the many details on the inventory item. Furthermore, the RFID technology has growing perceptibility in various applications such as animal identification, warehouse, health care industry, transportation and logistics [1–3].

---

M. H. M. Ariff (✉) · M. S. Zakaria · S. Khatun · M. F. Abas · M. Z. Ibrahim  
Faculty of Electrical & Electronics Engineering, Universiti Malaysia Pahang, 26600 Pekan,  
Pahang, Malaysia  
e-mail: [hisyam@ump.edu.my](mailto:hisyam@ump.edu.my)

R. Jusoh  
Faculty of Industrial Sciences & Technology, Universiti Malaysia Pahang, 26300 Gambang  
Pahang, Malaysia

The fundamental of RFID is a mobile technology that uses radio frequency wave to transmit information data for identification purposes. In contrast with the barcode technology, the RFID reader does not require a direct path to read multiple tags simultaneously [4].

The RFID system consists of readers, tags and hosts, which normally have a microchip with a small antenna inserted to it. There are four categories of RFID frequency systems such as 30 to 300 kHz for low frequency (LF), 3 to 300 MHz for high frequency (HF), 300 MHz to 3 GHz for ultra-high frequency (UHF) and 2.4 to 2.48 GHz for super high frequency (SHF) [5, 6], but usually readers send electromagnetic waves with a tag signal designed to react. In the passive tag, there has no source of power and appeal power from the field made from the reader and utilize it to channel the microchip circuitry. The chips then modulate the wave that tags transmit back to the reader that transforms the new signal into digital information data. In the active tags, it have their own power source and broadcast their signals to the reader. The host can process the data and then save it to the database for further processing into a specific identification [7].

Over the past years, many researchers were design the antenna that suitable for portable RFID reader such as quadrifilar type antenna [8], helical type antenna [9], loop type antenna [10] and PIFA type antenna [11]. By choosing the similar printed analogy as disclose above, the designed antenna design hold an advantages on FR-4 substrate substance.

The microstrip patch antenna (MPA) consists of emitting patch on upper side and ground on the lower side. The MPA are widely used in electronic wireless communication system because it has advantages such as conformal design, less weight, low profile, low cost, easy to integrate and fabricate. The main demerits of choosing these types of antenna are lower impedance bandwidth, lower gain, poor efficiency due to conductor and dielectric losses that affect the performance of the design antenna. Nowadays, there are many techniques found by the researchers to cater the MPA drawbacks by using different method of patch geometry such as using U shaped patch [12], T shaped patch [13] and C shaped patch [14]. In practical usage, other research approached to scale down these disadvantages involves the use of different thickness [15], use different substrate of dielectric substance [16], antenna array [17], slashing various slots [18] and creating notches [19] in the patch outline for increasing the performance which make this antennas have been widely spotted in wireless implementations such as RFID system, GPS, military track and trace purpose and satellite communication.

This paper is arranged as follows. In Sect. 2 details the antenna design procedures profiles which leads to practical design of circular microstrip antennas together with rectangular slot. The experimental result and discussion of antenna analysis component in this paper with other algorithms are also described in Sect. 3. Finally, our work of this paper is conducted in the last section.

## 2 Antenna Geometry and Design

Figure 1 shows the geometry of the initial proposed modified circular patch antenna with rectangular slot for single band operation. The proposed antenna is designed on FR-4 substrate with dielectric constant ( $\epsilon_r$ ) of 4.7, loss tangent of 0.019 and the thickness of 1.6 mm. Copper material was used for ground and patch of the designed antenna with the thickness of 0.035 mm.

The calculation for patch radius ( $a$ ), dielectric constant ( $\epsilon_r$ ), resonant frequency ( $f_r$ ) and thickness of substrates has been determined using the following equations [20]:

$$a = \frac{F}{\left\{ 1 + \frac{2h}{\pi \epsilon_r F} \left[ \ln\left(\frac{\pi F}{2h}\right) + 1.7726 \right] \right\}^{1/2}} \tag{1}$$

where

$$F = \frac{8.791 \times 10^9}{f_r \sqrt{\epsilon_r}} \tag{2}$$

The above mode has not been taken into account over the fringing impact. Due to the enlargement of the patch electrically by fringing, hence, the effective radius ( $a_e$ ) of the patch is implemented and can be formulated as:

$$a_e = a \left\{ 1 + \frac{2h}{\pi a \epsilon_r} \left[ \ln\left(\frac{\pi a}{2h}\right) + 1.7726 \right] \right\}^{1/2} \tag{3}$$

The relationship between the velocity of light ( $v_o$ ) and resonant frequency ( $f_r$ ) is given as;

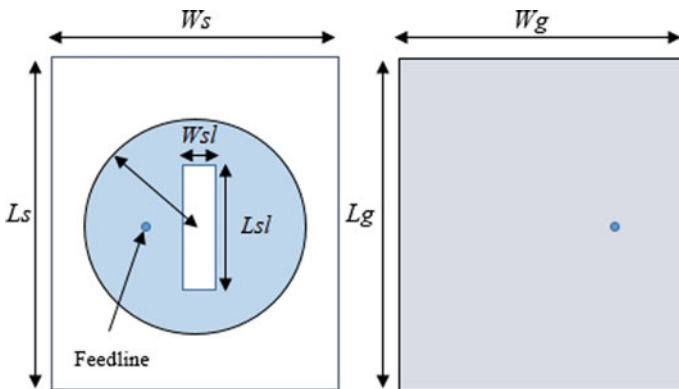


Fig. 1 The geometry of the proposed antenna

**Table 1** The optimal dimensions of the antenna

Parameter	Symbol	Segment	Dimension (mm)
Patch	$a$	Radius	41
Slot width	$W_{sl}$	Width	6
Slot length	$L_{sl}$	Length	20
Substrate	$W_s$	Width	122
	$L_s$	Length	122
	$h$	Thickness	1.6
	$\epsilon_r$	Dielectric constant	4.7
Ground	$W_g$	Width	122
	$L_g$	Length	122

$$(f_r)_{110} = \frac{1.8412v_0}{2\pi a_e \sqrt{\epsilon_r}} \tag{4}$$

The circular shaped microstrip antenna comprises of slot etched into metallised dielectric substrate. The ground stage controls one area of the dielectric, which does not fall straightly beneath the monopoles. The antenna is probe fed through the microstrip ground engaged with the circular patch. The optimal dimension value of the proposed antenna are listed in Table 1 and Fig. 2 shows the fabricated microstrip antenna.

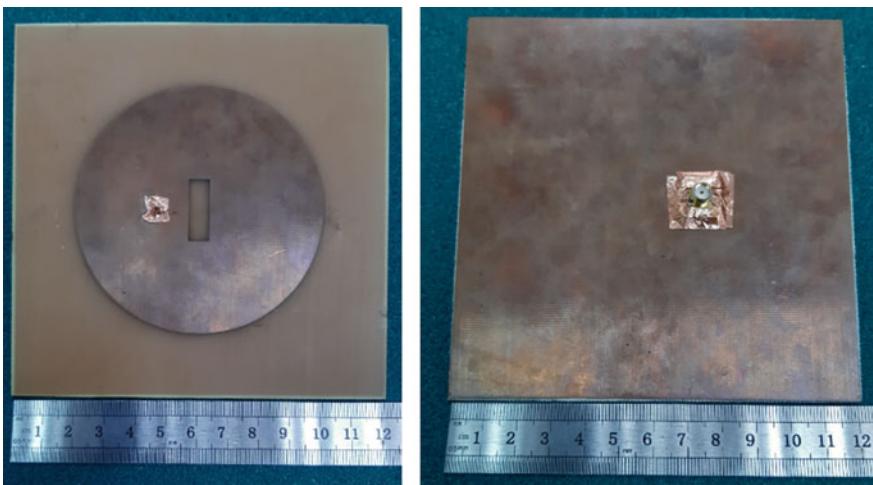


**Fig. 2** The fabricated antenna

### 3 Results and Discussions

#### 3.1 Result of Simulation of the Proposed Antenna

The better performance of an antenna can be realized when the value of return loss should be less than  $-10$  dB. All the simulation results in this work obtained by using CST Microwave 2014 and Vector Network Analyzer (VNA) is used to measure the return loss for fabricated antenna.

The proposed antenna for simulated  $S_{11}$  and measured return loss was illustrated in Fig. 3. In this study, the single bands analysis classified into Malaysia RFID frequency bands range from 921 to 923 MHz.

The simulation result for operating frequencies shows in 921 MHz region has produced the bandwidth of 15 MHz (913–928) MHz. Furthermore, for the measured values, the frequency band range from shifted to 903–936 MHz with bandwidth of 33 MHz. The difference measured and simulated bandwidth values shows increasing of bandwidth by 18 MHz. The value of  $S_{11}$  for simulation and measured are  $-34$  dB and  $-23$  dB, respectively.

Figure 4 shows the voltage standing wave ratio (VSWR) of the antenna. The VSWR is an indication of total amount of mismatch between feed line and with an antenna connecting to it. The VSWR value is less than 2 is consider suitable for most RFID antenna applications.

The antenna radiation pattern is a graphical image of the radiation plots of the antenna by a sphere and assess the magnetic fields (far field radiation fields) at a length equal to the sphere radius. The value of directivity as in Fig. 5 for an antenna is 5.963 dBi and this 3D radiation pattern shows the directional radiation pattern. In

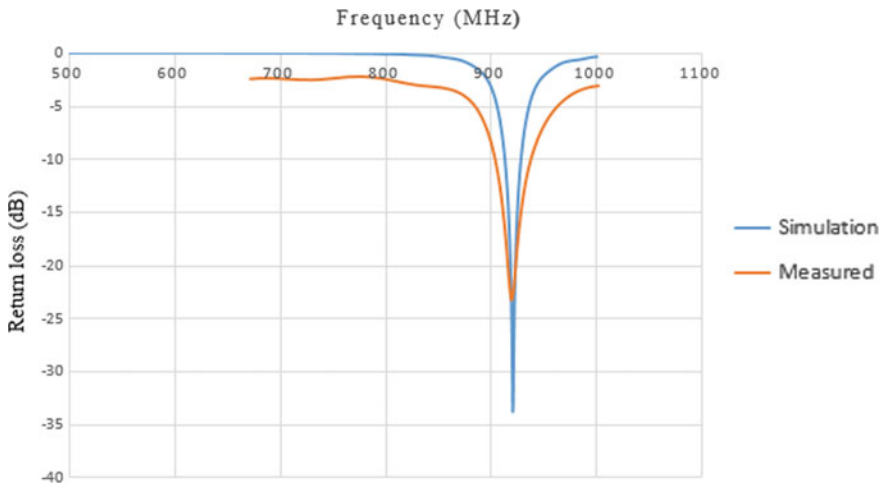


Fig. 3 The simulated and measured  $S_{11}$  versus frequency



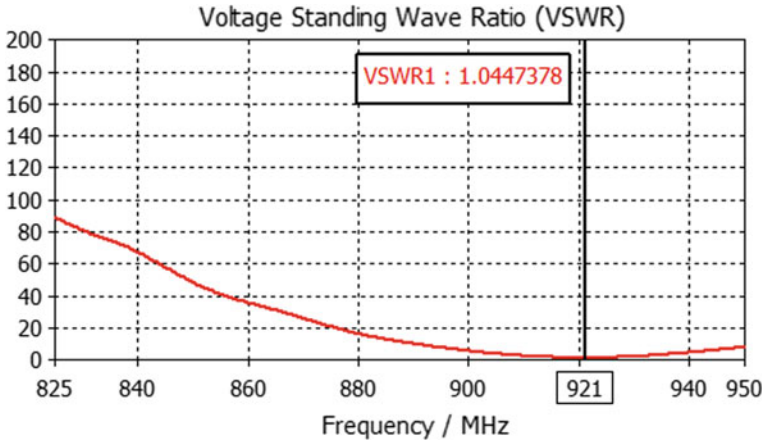


Fig. 4 The voltage standing wave ratio

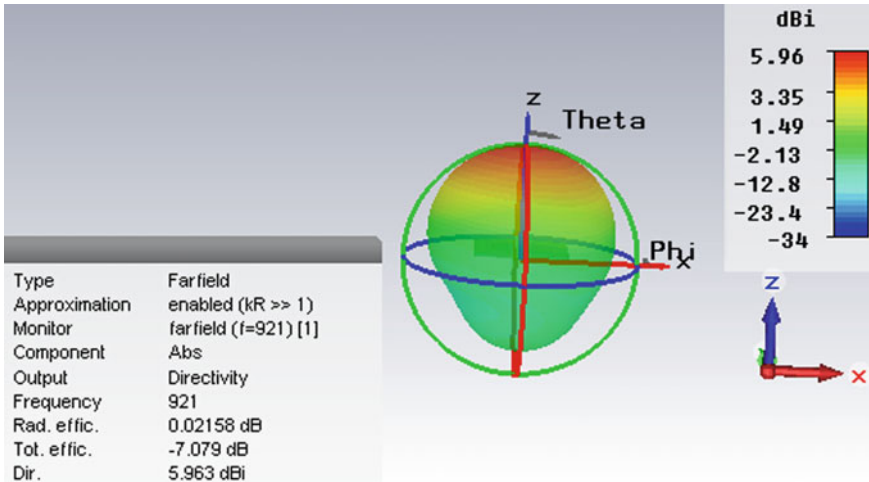


Fig. 5 The simulated far-field view 3D radiation pattern for 921 MHz

RFID, directional radiation tend to produce longer read ranges due to concentration of the beamwidth.

Another important impact in the radiation pattern analysis of an antenna also recognized as beamwidth where it shows area receives signal by antenna. The main lobe in the radiation pattern of an antenna is the main beam of the antenna where constant and maximum energy radiated by the antenna outflow. The main lobe magnitude is 5.96 dBi and the beamwidth is 96.3° as in Fig. 6. Both if this results shows the antenna has an adequate radiation specification compatible with UHF RFID reader.

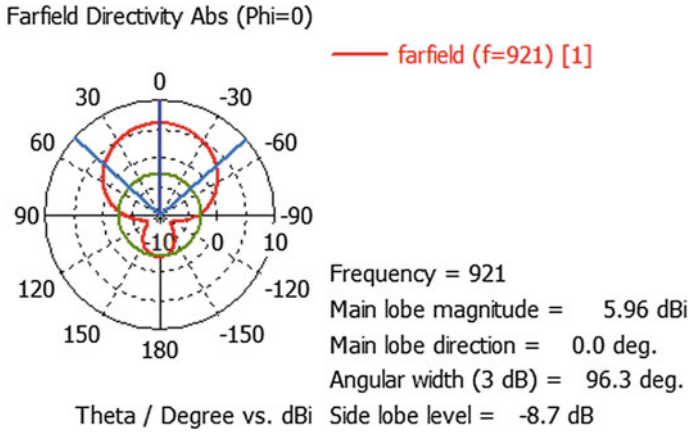


Fig. 6 The simulated radiation pattern view in polar plot

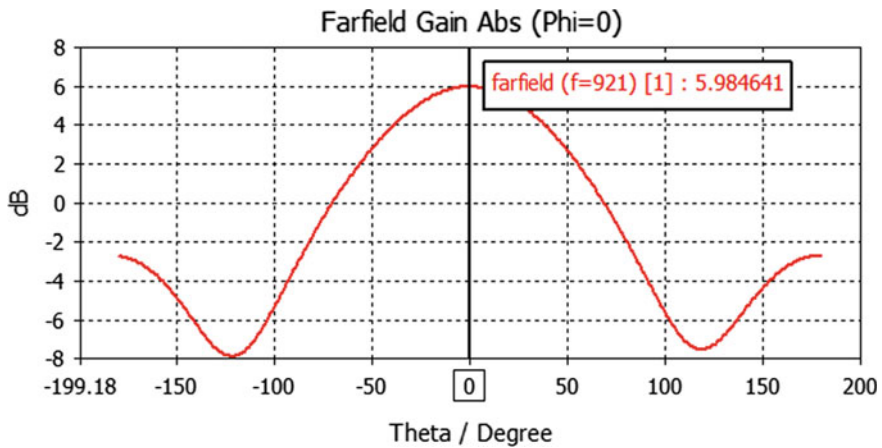
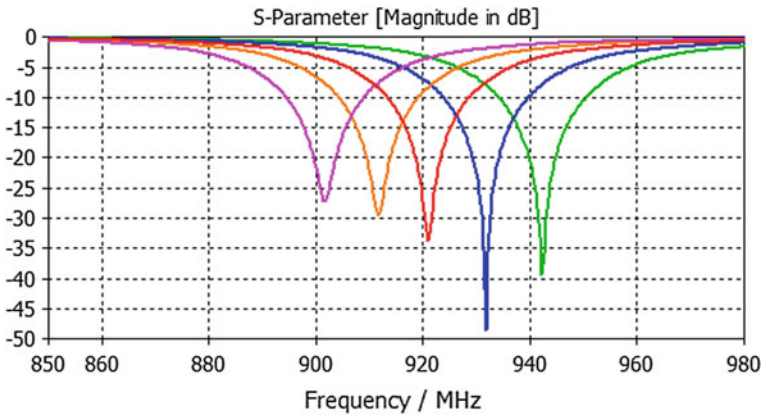


Fig. 7 Simulated gain in Cartesian plot

It is also become aware that simulated gain in Fig. 7 also show antenna power gain is 5.98 dB which combines electrical efficiency and antenna’s directivity. In transmitting antenna, the gain acts how good the antenna change input power into radio waves moved in a specified directions.

### 3.2 Parametric Studies

The proposed antenna consists of rectangular slot that share the same basic circular patch. In experimental views, the results of return loss, bandwidth and the resonance



**Fig. 8** The effect of varying patch diameter

frequency can be varied by changing the dimensions of the antenna. Three selected parameter has choose such as modification of radius of patch, length and width for slot.

#### **Effects of the Diameter Patch**

Figure 8 shows that the result of simulated diameter of patch with values of 80 mm (purple), 81 mm (orange), 82 mm (red), 83 mm (blue) and 84 mm (green). The patch diameter with values 83 mm give a higher return loss of  $-47$  dB for 931 MHz operating frequency. Thus, in order to increase the return loss, the best range of patch diameter optimization are from 80 to 83 mm.

#### **Effects of the Rectangular Slot Width**

Figure 9 illustrates the result of return loss  $S_{11}$  and operating frequency antenna for different values of simulated rectangular slot width. The width has been set as 4 mm (green), 5 mm (blue), 6 mm (red), 7 mm (orange) and 8 mm (purple). Apparently, the most prominent result has been obtained with 6 mm width where the result shows the return loss of  $-34.2$  dB and frequency of 921 MHz. The results of the other width display a similar trend of return loss but with slightly different values of frequencies. The result of return loss and frequency for 7 mm (orange) is nearly overlap with 8 mm (purple) width.

#### **Effects of the Rectangular Slot Length**

The effects of different size of rectangular slot length to the return loss and antenna frequency are shown in Fig. 10. The simulation has been done with slot length of 18 mm (green), 19 mm (blue), 20 mm (red), 21 mm (orange) and 22 mm (purple). Figure 10 obviously shows that the best result has been generated with 20 mm slot length. A good result of return loss should be less than  $-10$  dB. However, the other length sizes do not achieved this value.

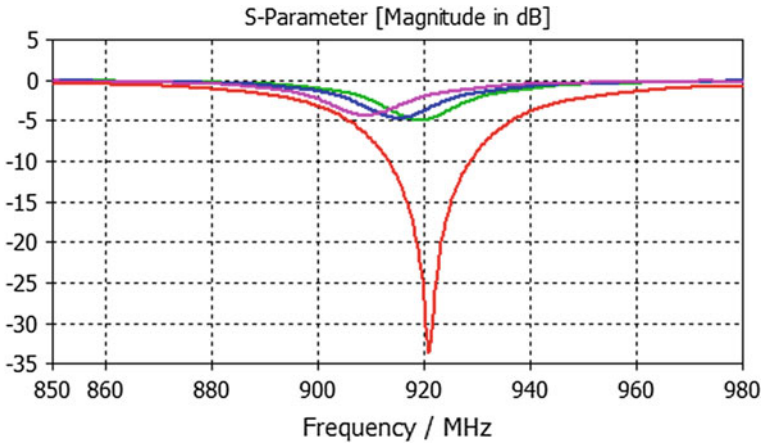


Fig. 9 The effect of varying slot width

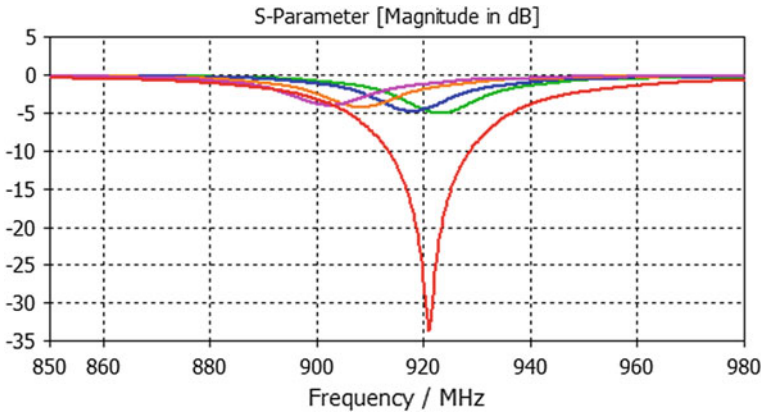


Fig. 10 The effect of varying slot length

### 4 Conclusion

A simple microstrip patch with slot derived from an ordinary circular shaped antenna was proposed. The circular patch radiated the single frequencies antenna that working for radio frequency identification reader with the antenna became more compact with the dimensions of only 122 mm × 122 mm × 1.6 mm is the longest wavelength in the operating bandwidth. These acted in two ways: one is the size reduction of the diameter of patch, and the other is a slot used for bandwidth enhancement, as a part of the antenna. This design used a 50 Ω SMA connector with pin fed connected to the feeding point. The antenna was shown to have the impedance bandwidth up to 3.6% for the operating frequency at 921 MHz. On the other hands, with VSWR

less than 2 contributes the good efficiencies of the antenna design. For the return loss below than  $-10$  dB for this design shows that the design antenna worked in desired frequency ranging from 919 to 923 MHz which covering the UHF RFID in Malaysia. The presented structure was fabricated, and measured, shown a good compliance with simulated results.

**Acknowledgements** This work is supported by Universiti Malaysia Pahang under internal grant RDU170381. The authors would also like to thank the Faculty of Electrical & Electronics Engineering, Universiti Malaysia Pahang and Faculty of Industrial Sciences & Technology, Universiti Malaysia Pahang for providing the facilities to conduct this technical and research support throughout the process.

## References

1. Ravi S, David A, Imaduddin M (2018) Controlling & calibrating vehicle-related issues using RFID technology. *Int J Mech Prod Eng Res Dev* 8:1125–1132
2. Ariff MH, Ismarani I, Shamsuddin N (2015) Livestock information system using android based architecture. *J Sci Technol Trop* 11:73–83
3. Ariff MH, Ismarani I (2018) RFID application development for a livestock monitoring system. Apple Academic Press, USA
4. Pedraza C, Vega F, Manana G (2018) PCIV, an RFID-based platform for intelligent vehicle monitoring. *IEEE Intell Transp Syst Mag* 10:28–35
5. Gope P, Amin R, Islam SH, Kumar N, Bhalla VK (2018) Lightweight and privacy-preserving RFID authentication scheme for distributed IoT infrastructure with secure localization services for smart city environment. *Future Gener Comput Syst* 83:629–637
6. Ariff MH, Hisyam MY, Ibrahim MZ, Ismarani I, Shamsuddin N (2018) Circular microstrip patch antenna for UHF RFID reader. *J Telecommun Electron Comput Eng* 10:61–65
7. Awakhare M, Parmal N, Dhawale S, Dongre P, Jamgade S, Tambe A, Deulkar S, Meshram B (2018) RFID based e-attendance system & child security system. *Int J Eng Sci* 16162
8. Chiu CW, Wang WH, Wang HC (2018) Quarter-wavelength printed quadrifilar helical antenna design for UHF RFID handheld reader applications. *Microw Opt Technol Lett* 60:742–748
9. Naqvi AH, Park JH, Baek C-W, Lim S (2018) V-band planar helical antenna using TGSV technology. In: 2018 International symposium on antennas and propagation (ISAP), IEEE
10. Yang X, Feng Q, Zheng Z (2018) First-order minkowski fractal circularly polarized slot loop antenna with simple feeding network for UHF RFID reader. *Prog Electromagn Res Lett* 77:89–96
11. Sun L, Li Y, Zhang Z, Iskander MF (2019) Low-cost compact circularly polarized dual-layer PIFA for Active RFID reader. *IEEE Trans Antennas Propag* 67:681–686. <https://doi.org/10.1109/TAP.2018.2880093>
12. Jeong MG, Lee WS (2019) A smart blood bag management system using a load-integrated U-shaped near-field RFID antenna array. *IEEE Trans Antennas Propag* 67:1837–1843
13. Sethi WT, AlShareef MR, Ashraf M, Behairy HM, Alshebeili S (2017) Compact dual polarized aperture coupled microstrip patch antenna for UWB RFID applications. *Microw Opt Technol Lett* 59:1317–1321
14. Ariff MH, Ismarani I, Shamsuddin N (2017) Analysis based on C shaped patch antenna for ultra-high frequency radio frequency identification readers. *Adv Sci Lett* 23:5439–5442
15. Chrysler AM, Furse CM, Hall KL, Chung Y (2017) Effect of material properties on a subdermal UHF RFID antenna. *IEEE J Radio Freq Ident* 1:260–266

16. Liu X, Liu Y, Tentzeris MM (2015) A novel circularly polarized antenna with coin-shaped patches and a ring-shaped strip for worldwide UHF RFID applications. *IEEE Antennas Wirel Propag Lett* 14:707–710
17. Norzeli SM, Ismail I, Din NM, Ali MT, Saravani S, Almisreb AA (2018) Design of high gain microstrip patch reader array antenna with parasitic elements for UHF RFID application. *Int J Eng Technol* 7:463–467
18. Chaouki G, Omrane N, Said G, Ali G (2017) An electrical model to U-slot patch antenna with circular polarization. *Int J Adv Comput Sci Appl* 8:62–66. <https://doi.org/10.14569/ijacsa.2017.080310>.
19. Yeh CH, Chen BS, Chen CC, Sim CYD (2015) L-shaped probe feed patch antenna with circular polarization radiation for UHF RFID applications. In: 2015 IEEE MTT-S international microwave workshop series on RF and wireless technologies for biomedical and healthcare applications, IMWS-BIO 2015—proceedings, pp 214–215
20. Constantine B (2016) *Antenna theory: analysis and design*. Wiley, Hoboken

# Analysis of EEG Features for Brain Computer Interface Application



**Mamunur Rashid, Norizam Sulaiman, Mahfuzah Mustafa, Mohd Shawal Jadin, Muhd Sharfi Najib, Bifta Sama Bari and Sabira Khatun**

**Abstract** Electroencephalography (EEG) based assistive devices are the great support to the paralyzed patients to be in contact with their surroundings. These devices use Brain-Computer Interface (BCI) technology which is presently getting more attention by the related research community. In this paper, EEG features from multiple cognitive states have been explored for BCI applications. Here, Power Spectral Density (PSD), log Energy Entropy (logEE) and Spectral Centroid (SC) have been investigated as EEG feature. The EEG data have been captured from three different cognitive exercises; (i) solving math problem, (ii) playing game and (iii) do nothing (relax). The average PSD, average logEE and average SC of EEG Alpha and Beta band for three mental exercises are calculated in order to determine the best features that can be used for BCI application. The results of the research show that the EEG features when considering PSD, logEE and SC can be used to indicate the change in cognitive states after exposing the human to several cognitive exercises.

**Keywords** Brain-computer interface (BCI) · Power spectral density (PSD) · Electroencephalography (EEG) · EEG feature

## 1 Introduction

Brain-Computer Interface (BCI) can be familiarized as a direct communication pathway that makes the interaction between the human brain and digital computer to control the external devices. The whole process is carried out only by brain waves without any command or touch from the muscular body part. Due to the easy operation of this technology, disabled patients especially who have lost their control on the muscular body can handle BCI systems. Besides medical applications, currently, the BCI field has been extended to some non-medical applications including virtual reality and games [1, 2], spelling system [3], mouse and keyboard control [4], human emotional state monitoring [5], controlling prosthetic limb [6], handling

---

M. Rashid · N. Sulaiman · M. Mustafa · M. S. Jadin · M. S. Najib · B. S. Bari · S. Khatun (✉)  
Faculty of Electrical & Electronics Engineering, Universiti Malaysia Pahang, 26600 Pekan,  
Pahang, Malaysia  
e-mail: [sabirakhatun@ump.edu.my](mailto:sabirakhatun@ump.edu.my)

wheelchair [7], biometrics, environment control [8] or controlling Smartphone [9] to help disabled persons. Nowadays, BCI is an interesting, vibrant and highly interdisciplinary research topic which involves psychology, neurology, signal processing, and machine learning. Generally, BCI can be segmented into five different phases or segments. The first phase involves the acquisition of EEG signals from the human's head, the second phase is pre-processing of EEG signals to remove artifacts, third phase is to extract the most effective features, fourth phase is to classify the EEG signals according to the selected EEG features and the final phase is to control devices by translating the classified features into machine code [10–12]. Among all these phases, feature extraction acts as the most vital role in any EEG based BCI system because of incorrect selection of the EEG features will cause misclassification that may create wrong commands given to the devices. As a result, the BCI system might malfunction that may cause harm to disabled people. A huge number of EEG features have been explored by the BCI researchers in the last two decades. The amplitude frequency analysis (AFA), the density matrix (DM) and the recurrence quantification analysis have been merged to generate the phase space feature (PSF) vector [13]. This feature is efficient to classify the left hand and right-hand movement. The combination of EMD and BP from the EEG signals for feature extraction has been proposed in [14]. Here, EMD is applied to select only the IMFs corresponding to sensor motor rhythms (mu and beta) using Welch-based Power Spectral Density (PSD) to extract the reliable information of EEG signals. Analytic intrinsic mode functions (AIMFs) have been proposed in [15] as features for automatic classification of EEG signals based on MI tasks. Empirical mode decomposition and Hilbert transform are applied on raw data to form AIMFs. Spectral moment of power spectral density, raw moment of the first derivative of instantaneous frequency, the peak value of PSD and area are the features obtained from AIMFs. During wavelet packet analysis (WPA), a slow cortical potential (SCP) has been studied instead of using traditional time or frequency domain methods. Applying WPA with the combination of log energy entropy enables to find cortical negativity as well as cortical positivity in self-regulation of SCPs, as discussed in the article [16]. In article [17], the features have been computed from beta and gamma bands and the features were the combinations of Wavelet decomposition, standard deviation, mean and PSD. In this paper, EEG features with regards to average PSD, average logEE and average SC of alpha and beta frequency band have been investigated to find the best possible feature that may increase the classifier accuracy. The remainder of this paper is arranged in the following sections i.e. Sects. 2 and 3 discusses issues related to methodology and results with discussion respectively; finally, Sect. 4 deals with the conclusion.

## 2 Methodology

There are some fundamental steps that must be done to make a BCI system and these steps are data capturing, pre-processing, feature extraction, classification and device command. Among these basic steps, feature extraction from EEG performs a



crucial role to form a BCI application because the best-suited feature increases the classification accuracy as well as the performance of BCI devices. Various EEG features and feature extraction techniques have been come out by the BCI researchers that to be used in the BCI applications. The most usable EEG features by the BCI researcher are Principal Component Analysis (PCA), Independent Component Analysis (ICA), Band Power Spectrum (BP), Power Spectral Density (PSD), Energy Spectral Density (ESD), Spectral Centroid, Spectral Entropy, Cerebrospinal Fluid (CSF), Wavelet Transformations (WT), Wavelet Packet Decomposition (WPD), AutoRegressive (AR), Adaptive Autoregressive (ARR) parameters, Fast Fourier Transform (FFT) and Short-time Fourier Transform (STFT), Common Spatial Pattern (CSP), cross-correlation, variant, co-variant and Shannon's entropy [18, 19]. Among these feature power spectral density, log energy entropy and spectral centroid have been investigated, the complete methodology of this study is shown in Fig. 1.

## ***2.1 EEG Measurement and Protocol***

There are a lot of EEG headsets in the market to capture EEG raw data. In this work, Neurosky Mindwave EEG headset was selected to capture EEG raw data due to its low cost and dry electrode. This EEG capturing device is made up of single electrode which is positioned on the FP1 area of the brain following the 10/20 system and the reference electrode is attached with the ear lobe. The raw EEG data is recorded at a sampling rate of 512 Hz with this EEG amplifier. An android application named as EEGID was used to capture EEG data in CSV format. During data acquisition, the mobile phone and the Neurosky Mindwave were paired through the Bluetooth which is presented in Fig. 2 [20].

For this research, two male and one female subject were selected and their age range is from 20 to 27 years old where subject-1 is male and age of 23, subject-2 is female and age of 25, subject-3 is male and age of 25. There are three modes of mental exercises are set-up to capture EEG data which are do nothing (relax), solving math quickly and playing game. In case of relaxed state EEG capturing, subjects were suggested to be seated on the chair in a relaxed manner. Moreover, subjects were also suggested to avoid the eye blinking and movement of the entire body. Alternatively, subjects were instructed to answer the math challenges randomly from the website [21] during the cognitive state of quick math solving. During data collection of playing game, subjects were playing a racing game by android phone. The duration of every data collection was 30 s.

## ***2.2 Preprocessing and Feature Extraction***

After data collection, the first step is to pre-process the EEG data. EEG data affected by the eye blinking has been considered as artifacts and during the pre-processing

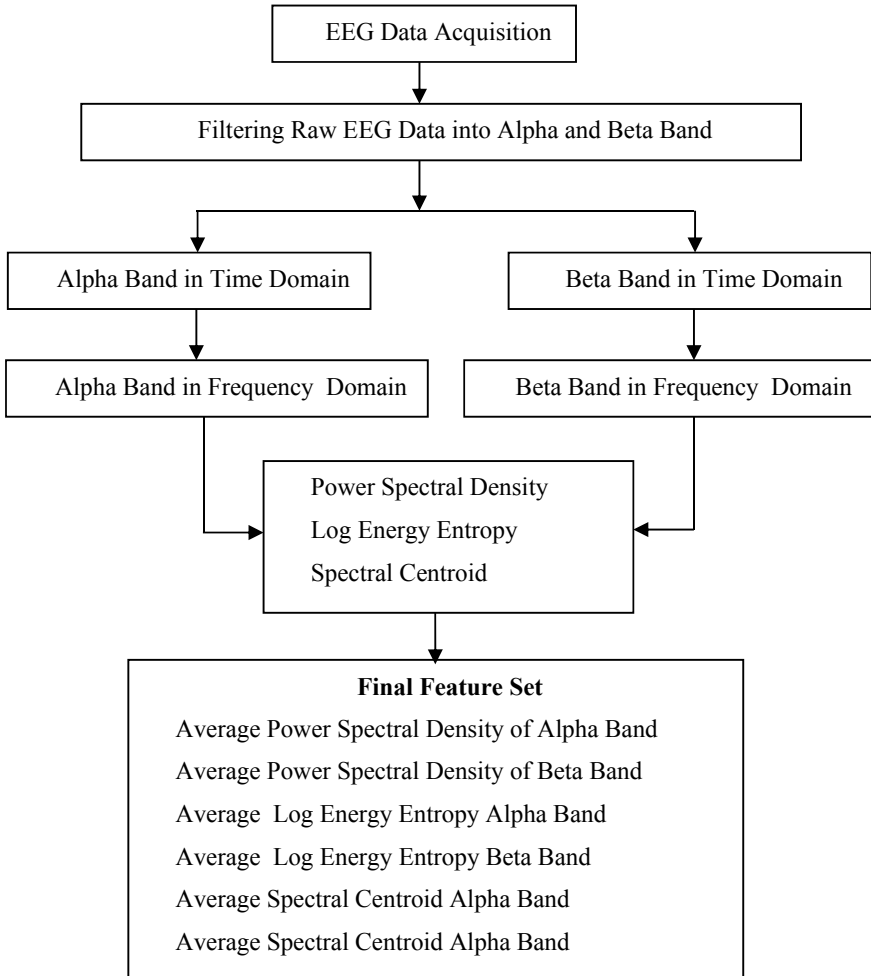


**Fig. 1** Methodology of the experiment

step, the data containing eye blinking effects have been omitted. Then a 5th order bandpass Butterworth filter has been applied to separate alpha, beta and gamma signals. In order to extract features, average PSD, average logEE and average SC of Alpha and Beta frequency band were studied in this research. The PSD of EEG raw data was computed By making use of Fast Fourier Transformation (FFT). The FFT [22] can be presented by Eq. (1), whereas, Eq. (2) was used to calculate the PSD as follow.

$$X(k) = \sum_{k=1}^{N-1} X(n)W_N^{kn}; K = 0 \dots N - 1 \tag{1}$$

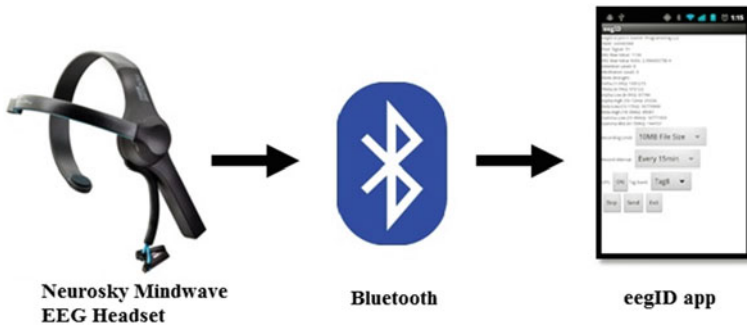


Fig. 2 EEG data acquisition procedure

$$W_N = e^{-j\frac{2\pi}{N}}$$

$$PSD = |X(k)|^2 = \left| \sum_{n=0}^{N-1} x(nTs)e^{-j2\pi nk/N} \right|^2 \tag{2}$$

where,  $k = 0, 1 \dots N - 1$  and one particular value of  $k$  contains  $N$  complex multiplications. Since the value of  $n$  belongs to  $0$  to  $N - 1$ , the multiplication of  $w^{kn}$  and  $x(n)$  was performed for  $N$  times. The Eq. (3) was employed to figure out SC of EEG data.

$$C = \frac{\int xg(x)dx}{g(x)dx} \tag{3}$$

Through the help of SC, the centre of every single EEG frequency bands can be computed [18].

Generally, entropy helps to figure out exactly how much data is transmitted by a signal. This means that entropy is able to study with exactly how much randomness is going to be in the signal. However, the entropy of discrete random variable of a finite length,  $X = [x(0) x(1) \dots x(N - 1)]$  with probability distribution function can be symbolized as  $p(x)$  which is defined by

$$H(x) = - \sum_{i=0}^{N-1} P_i(x) \log_2(P_i(x)) \tag{4}$$

In Eq. (4),  $i$  denotes single discrete states and the entropy is significantly larger with the similar probability of occurrence of single discrete state. The LogEE of  $x$  is expressed by Eq. (5) [23],

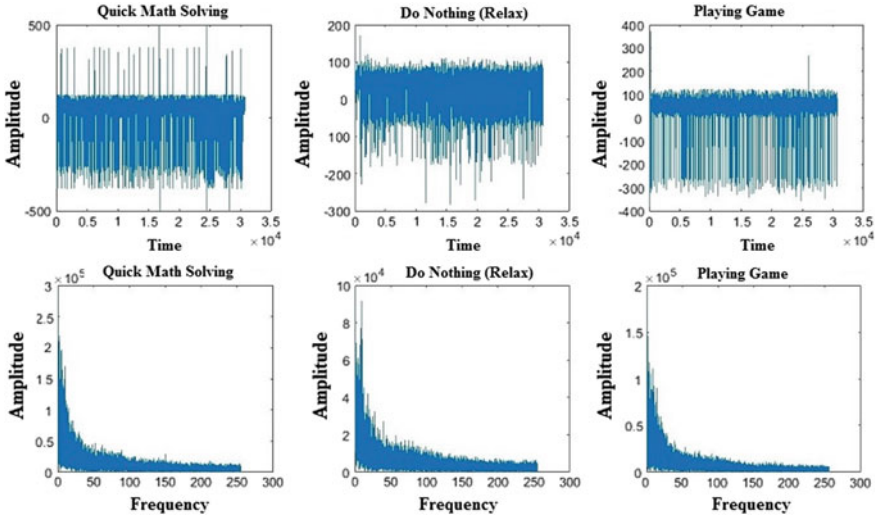


Fig. 3 Raw EEG data in time and frequency domain

$$H_{\log En} = - \sum_{i=0}^{N-1} (\log_2(P_i(x)))^2 \tag{5}$$

### 3 Result and Discussion

#### 3.1 EEG Raw Data

In Fig. 3, the raw EEG data for three modes of mental exercise have been plotted. The first row of this figure represent raw EEG data in the time domain and the second row represents raw EEG data in the frequency domain. This figure is plotted with the data from subject-1. Similar figures can be plotted with the data from subject-2 and subject-3.

#### 3.2 Filtered EEG Data

After preprocessing, the EEG data have been filtered into two frequency band known as Alpha and Beta frequency band. Bandpass Butterworth filter has been applied to separate alpha and beta signals and the order of the filter was 5th. The frequency range of Alpha and Beta band are (8–13 Hz) and (14–30 Hz) respectively. Figure 4

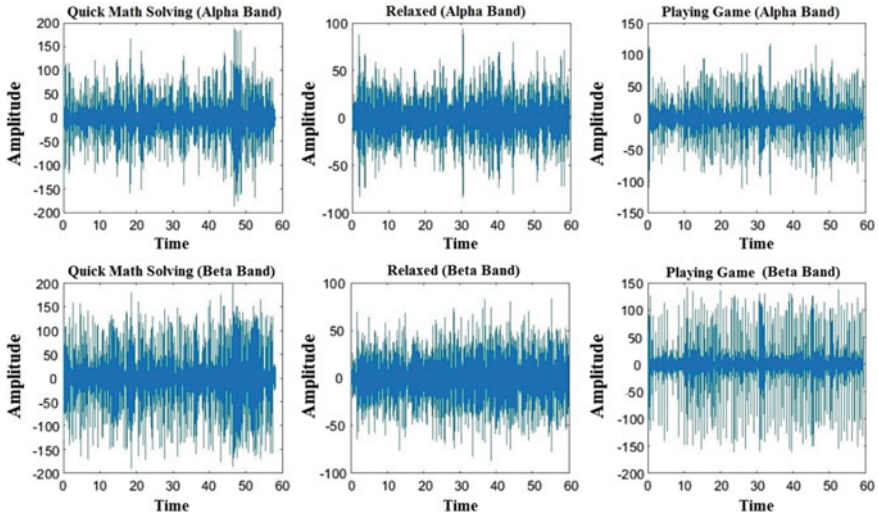


Fig. 4 EEG alpha and beta band in time domain

shows the plotting of Alpha and Beta band in the time domain for subject-1 with three mental exercises. Similarly, Fig. 5 shows the plotting of Alpha and Beta band in the frequency domain for subject-1 with three mental exercises.

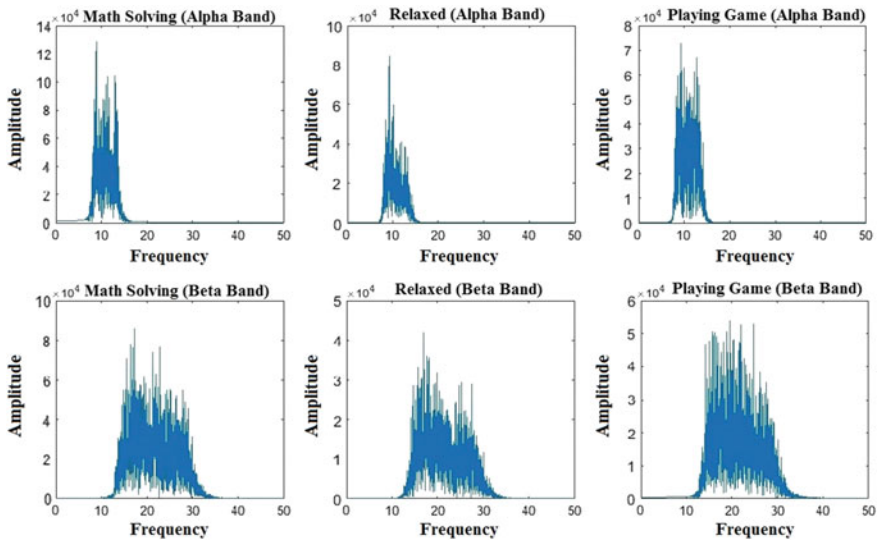
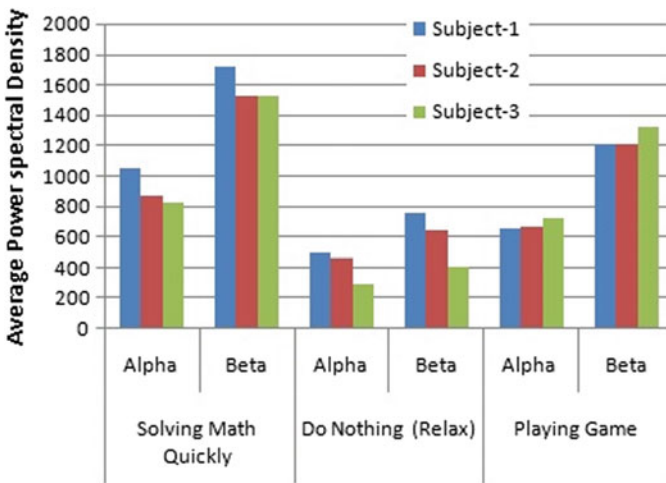


Fig. 5 EEG alpha and beta band in frequency domain

**Table 1** Average power spectral density

Subjects	Frequency band	Three mode of mental exercise		
		Math solve	Relaxed	Playing game
Subject-1	Alpha	1048.9	497.4	659.7
	Beta	1719.2	753.5	1211.3
Subject-2	Alpha	873.2	465.8	671.5
	Beta	1528.6	640.8	1213.9
Subject-3	Alpha	829.6	293.3	721.7
	Beta	1521	403.7	1326.4



**Fig. 6** Average power spectral density of alpha and beta band

### 3.3 Average Power Spectral Density

The average power spectrum of EEG alpha and beta band for all subjects with three modes of mental exercise have been calculated and listed in Table 1. These values have also been plotted in Fig. 6. From Fig. 6, it is clear that the average power spectrum of the beta band is higher than the alpha band for all subjects in three modes of mental exercise.

### 3.4 Average Spectral Centroid

The spectral centroid is another effective feature for BCI classification. Like the average power spectrum, spectral centroids of EEG alpha and beta band for three

**Table 2** Average spectral centroid

Subjects	Frequency band	Three modes of mental exercise		
		Math solve	Relaxed	Playing game
Subject-1	Alpha	37.57	38.7	44.72
	Beta	135.7	113.4	82.5
Subject-2	Alpha	38.2	41.6	38.8
	Beta	148.7	135.2	145.9
Subject-3	Alpha	47.9	40.4	37.5
	Beta	159.2	103.8	93.1

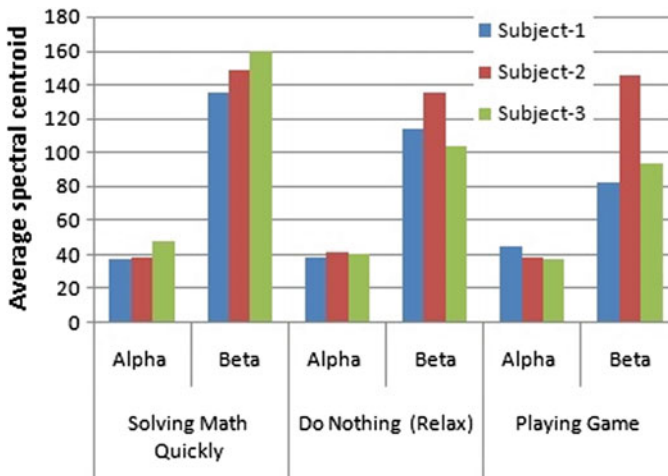


**Fig. 7** Average spectral centroid of alpha and beta band

subjects were computed in Table 2 and also plotted in Fig. 7. Here, the average spectral centroid of the beta band is also higher than the alpha band.

### 3.5 Average Log Energy Entropy

Average log energy entropy of alpha and beta band for all data have been listed in Table 3 and also plotted these values in Fig. 8. In this case, the average log energy entropy of alpha band is higher than the beta band for all subjects when they were in a relaxed condition. When the subjects were doing math quickly and playing game then the average log energy entropy of beta band is higher than the alpha band.

From the previous research findings as shown in Table 4, it is obvious that the EEG feature in term of power spectral density is efficient and preferred by researchers to

**Table 3** Average log energy entropy

Subjects	Frequency band	Three mode of mental exercise		
		Math solve	Relaxed	Playing game
Subject-1	Alpha	6694.2	3576	4429.4
	Beta	7075.5	3181	4886.1
Subject-2	Alpha	5900.2	3365.7	4689.2
	Beta	6305.3	2647.6	5044.2
Subject-3	Alpha	5763.1	2097.6	4760.1
	Beta	6324.8	1682.7	5437.9

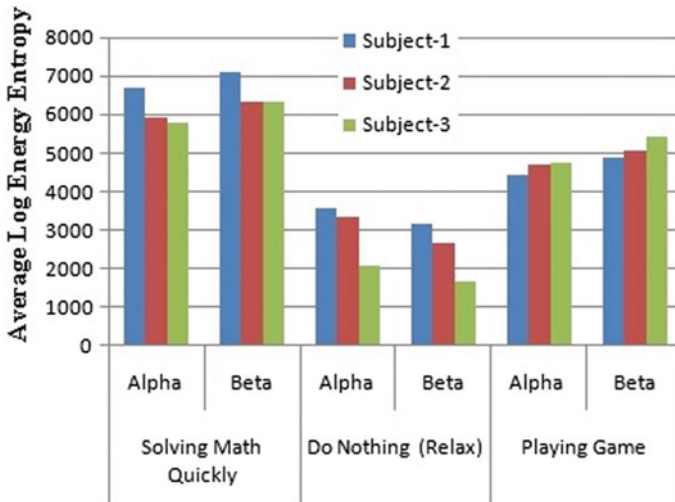


**Fig. 8** Average log energy entropy of alpha and beta band

**Table 4** Comparison with previous researches

References	BCI application	Feature	Classifier	Accuracy(%)
[24]	Emotion classification	Fractal dimension	RBF SVM	60
[25]	BCI speller	Common spatial patterns	LDA	92.93
[26]	Emotion classification	DWT	MLPNN	77.44
[27]	Movement intention detection	Power spectral density	LDA	97.2
[28]	Control of wheelchair	Power spectral density	SVM	100



indicate the changes in neural activities [24–28]. Hence, this feature can be employed by the classifier to provide the suitable machine code parameters to be used for BCI applications.

## 4 Conclusion

This research is conducted to determine the suitable EEG features that can be used to implement various BCI applications as illustrated in Table 4. From the initial results, it can be shown that the average power spectral density, log energy entropy and the spectral centroid of EEG alpha and beta band may be capable to identify the change in the human cognitive state. To make the final decision whether these features are efficient or not, different classification algorithms need to apply to these features. If the classification accuracy is satisfactory level, then the classifier results will be translated into device commands to run the BCI applications such as BCI wheelchair. Moreover, the number of subjects who contribute to supply EEG data will be increased.

**Acknowledgements** This research has been conducted with great supports by the Faculty of Electrical and Electronics Engineering. The author would also like to thank Universiti Malaysia Pahang for financial support through a research grant, RDU1703125.

## References

1. Bos DP, Poel M, Nijholt A (2013) Experiencing BCI control in a popular computer game. *IEEE Trans Comput Intell AI Games* 5(2):176–184
2. Jiang D (2009) Research of auxiliary game platform based on BCI technology. In: 2009 Asia-Pacific conference on information processing, vol 1, pp 424–428
3. Vo K, Nguyen DN, Kha HH, Dutkiewicz E (2017) Real-time analysis on ensemble SVM scores to reduce P300-speller intensification time. In: Proceedings of the annual international conference of the IEEE engineering in medicine and biology society. Seogwipo, pp 4383–4386
4. Aydemir O, Kayikcioglu T (2014) Decision tree structure based classification of EEG signals recorded during two dimensional cursor movement imagery. *J Neurosci Methods* 229:68–75
5. Zhang B, Jiang H, Dong L (2017) Classification of EEG signal by WT-CNN model in emotion recognition system. In: IEEE 16th international conference on cognitive informatics & cognitive computing, pp 109–114
6. Yasir M, Laiba L, Tehmina N, Aasim H, Sanay R, Umar M, Muhammad S, Majdi A, Syed A, Anwar M Brain computer interface based robotic arm control
7. Singla R, Khosla A, Jha R (2014) Influence of stimuli colour in SSVEP-based BCI wheelchair control using support vector machines. *J Med Eng Technol* 38(3):125–134
8. Anindya SF, Rachmat HH, Sutjiredjeki E (2017) A prototype of SSVEP-based BCI for home appliances control. In: 1st international conference on biomedical engineering: empowering biomedical technology for better future, pp 1–6
9. Kumar P, Saini R, Sahu PK, Roy PP, Dogra DP, Balasubramanian R (2017) Neuro-phone: an assistive framework to operate smartphone using EEG signals. In: IEEE international symposium on technologies for smart cities. Cochin, pp 1–5

10. Sanei S (2013) *Jonathon chambers: EEG signal processing*. Wiley
11. Millin, JR (1920) On the need for on-line learning in brain-computer interfaces, pp 2877–2882
12. Nicolas-Alonso LF, Gomez-Gil J (2012) Brain computer interfaces, a review. *Sensors*
13. Al-suify M, Al-atabany W, Eldosoky MAA (2018) Classification of right and left hand movement using phase space and recurrence quantification analysis. In: 35th national radio science conference, pp 457–464
14. Trad D, Al-Ani T, Jemni M (2016) A feature extraction technique of EEG based on EMD-BP for motor imagery classification in BCI. In: 5th international conference on information and communication technology and accessibility. Marrakech, pp 1–6
15. Taran S, Bajaj V, Sharma D, Siuly S, Sengur A (2018) Features based on analytic IMF for classifying motor imagery EEG signals in BCI applications. *Measurement* 116:68–76
16. Göksu H (2018) Oriented EEG analysis using log energy entropy of wavelet packets. *Biomed Signal Process Control* 44:101–109
17. Khurana V, Kumar P, Saini R, Roy PP (2018) EEG based word familiarity using features and frequency bands combination. *Action editor : Ning Zhong. Cogn Syst Res* 49:33–48
18. Sulaiman N, Taib MN, Lias S, Murat ZH, Aris SAM, Hamid NHA (2011) Novel methods for stress features identification using EEG signals. *Int J Simul Syst Sci Technol* 12:27–33
19. Shen K, Ong C, Li X, Hui Z, Wilder-smith EPV (2007) A Featur Sel Method Multilevel Ment Fatigue EEG Classif 54:1231–1237
20. Rashid M, Sulaiman N, Mustafa M, Khatun S, Bari BS (2019) The classification of EEG signal using different machine learning techniques for BCI application. In: Kim J-H, Myung H, Lee S-M (eds) *Robot intelligence technology and applications. RiTA 2018. Communications in computer and information science*, vol 1015. Springer, pp 207–221
21. Arithmetic Game. <https://arithmetic.zetamac.com/>. Accessed 19 July 2019
22. Otsuka T, Watanabe K, Hirano Y, Kubo K, Miyake S, Sato S, Sasaguri K (2009) Effects of mandibular deviation on brain activation during clenching: an fMRI preliminary study. *Cranio J Craniomandib Pract* 27:88–93
23. AydIn S, Saraoğlu HM, Kara S (2009) Log energy entropy-Based EEG classification with multilayer neural networks in seizure. *Ann Biomed Eng* 37:2626–2630
24. Kaur B, Singh D, Roy PP (2018) EEG based emotion classification mechanism in BCI. *Proc Comput Sci* 132:752–758
25. Yu Y, Jiang J, Zhou Z, Yin E, Liu Y, Wang J, Zhang N, Hu D (2016) A self-paced brain-computer interface speller by combining motor imagery and P300 potential. In: 8th international conference on intelligent human-machine systems and cybernetics. Hangzhou, pp 160–163
26. Özerdem MS, Polat H (2017) Emotion recognition based on EEG features in movie clips with channel selection. *Brain Inform* 4(4):241–252
27. Kamavuako EN, Jochumsen M, Niazi IK, Dremstrup K (2015) Comparison of features for movement prediction from single-trial movement-related cortical potentials in healthy subjects and stroke patients. *Comput Intell Neurosci*, Article ID 858015, 8 pp
28. Abiyev RH, Akkaya N, Aytac E, Günsel I, Ça A (2015) Brain based control of wheelchair. In: *International conference artificial intelligence*, pp 542–547

# Hybrid Sampling and Random Forest Based Machine Learning Approach for Software Defect Prediction



Md Anwar Hossen, Md. Shariful Islam, Nurhafizah Abu Talip Yusof, Md. Sakib Rahman, Fatema Siddika, Mostafijur Rahman, Sabira Khatun, Mohamad Shaiful Abdul Karim and S. M. Hasan Mahmud

**Abstract** The software has turn into an imperious part of human's life. In the recent computing era, many large-scale complex network systems and millions of modern technological devices produce a huge amount of data every second. Among these data, the amount of imbalanced data is relatively excessive. The machine learning model is miss leaded by these imbalanced data. Software Defect Prediction (SDP) is a standout amongst the most helping exercises during the testing phase. The estimated cost of finding and fixing defects is approximately billions of pounds per year. To reduce this problem, software defect prediction has come forth but need fine tuning to have expected efficiency. In this chapter, we have proposed a new model based on machine learning approach to predict software defect and identify the key factors that may help the software engineer to identify the most defect-prone part of the system. The proposed model works as follows. First, need to remove highly correlated features and turn all the feature in the same scale using the scaling feature approach. Second, we have used Synthetic Minority Over-Sampling Technique (SMOTE), Adaptive Synthetic (ADASYN) and Hybrid sampling method to balance highly imbalanced datasets. Third, Random Forest Importance and Chi-square algorithms are chosen to find out the factors which have high effect on software defect. Cross validation is used to remove overriding problem. Scikit-learn library is used for machine learning algorithms. Pandas library is used for data processing. Matplotlib, and PyPlot are used for graph and data visualization respectively. The hybrid sampling method and Random Forest (RF) algorithms achieved the highest prediction accuracy about 93.26% by showing its superiority.

**Keywords** Software defect prediction · Machine learning · Imbalanced dataset · Chi square · Random forest importance

---

M. A. Hossen (✉) · Md. S. Islam · Md. S. Rahman · M. Rahman · S. M. H. Mahmud  
Department of Software Engineering, Daffodil International University, Dhaka, Bangladesh  
e-mail: [anwar.swe@diu.edu.bd](mailto:anwar.swe@diu.edu.bd)

N. A. T. Yusof · S. Khatun · M. S. A. Karim  
Faculty of Electrical and Electronics Engineering, Universiti Malaysia Pahang, Pekan, Malaysia

F. Siddika  
Department of Computer Science and Engineering, Jagannath University, Dhaka, Bangladesh

© Springer Nature Singapore Pte Ltd. 2020

A. N. Kasruddin Nasir et al. (eds.), *InECCE2019*, Lecture Notes in Electrical Engineering 632, [https://doi.org/10.1007/978-981-15-2317-5\\_46](https://doi.org/10.1007/978-981-15-2317-5_46)

## 1 Introduction

Software defect prediction models are usually used to detect defected modules in the software based on software metrics. Syntax error, spelling error, requirement, wrong program statement, and design or specification errors are considered as software defect [1]. Software defect prediction approaches are utilized when a product organization needs to convey a completed item while it has restricted the time and spending plan for testing it [2]. However, the prediction accuracy of machine learning models significantly affected if the real world data is highly imbalanced and redundant module features. The aim of this chapter is to generate well performed model to predict software defects. The performance of the proposed model has been compared to other existing approaches. We also compared the classification result between all the features and reduced features. There are three main types of feature selection: filters, wrappers, and embedded. In the context of Software engineering, the significant and expensive task of a software development life-cycle is testing. The main goal of software defect prediction is to find the accurate data. Different developers have different coding styles, commit frequencies, and experience levels, causing different defect patterns. When the defects of different developers are combined, such differences are obscured, and hurting prediction performance. Making effective prediction of defect-prone components of software is an essential part of modern software engineering. Software quality depends on the efficiency, reliability, and security. The main task of software defect prediction is to predict defect-prone modules in a software code system. Based on the prediction results, the developer assigns efficient prioritization on that modules and allocate an uncommon test case to test the system [3, 4]. Machine learning approach is a suitable candidate for defect prediction, increase the quality and reduce the cost of software testing process, which is taken into account to propose an enhanced model for overcoming software defect prediction problems.

## 2 Related Works

There are various defect prediction methods which have been tested with arguable accuracy. Feature selection is an important data preprocessing activity and has been broadly studied in the data mining and machine learning sector. The main goal of feature selection is to select a subset of features that minimizes the prediction errors of classifiers. Khoshgoftaar et al. [5] examined seven filter-based features ranking techniques for comparison using 16 software dataset in their approach. Vashisht et al. [6] analyzed a software dataset which consists of 50 real life project, among them 40 projects were used a training set and other 10 projects used as test dataset. They used Neural Network (NN) algorithms to predict the defect with maximum accuracy around 92%. Wrapper-based feature ranking techniques applied to imbalanced software quality using a sub-set of attributes, and the random under sampling technique

**Table 1** Highly correlated features [10]

Features	Correlated with	r
cyclomatic_complexity	branchCount	1.0
time_estimator	Effort	1.0
IOCode	Halstead_b	1.0
total_opnd	total_Op	1.0
total_operators&operands	Volume	1.0
total_operators&operands	total_Opnd	1.0

[5] dataset. Hall and Holmes [7] viewed six attribute selection techniques that produce highest lists of attributes and applied them to fifteen software datasets from the UCI dataset repository. In a modern study [8], we observed various feature selection techniques inclusive filter-based and wrapper-based methods in the software quality engineering realm.

In this chapter, we have investigated the performance tradeoff of the classification models when more than 75% of the features were eliminated from the original dataset.

### 3 Data Pre-processing

In this study, we used the PROMISE repository (JM1) [9] publicly available dataset. This dataset contains 22 attributes and 10,887 observations.

#### 3.1 Removing Highly Correlated Features

Correlation is widely used in machine learning and statistics for relevance analysis. Here, we applied Pearson Correlation Coefficient (PCC) [10] and found 6 highly correlated feature as shown in Table 1, where correlation coefficient value of  $r$  is 1.

#### 3.2 Feature Scaling

Most of the machine learning algorithms use the Euclidean distance between two data points in their computations [11]. This will create problem when the features are highly varying in magnitudes, units, and range. We need to bring all the features to the same level of magnitudes which can be Rescaling (Min–Max Normalization) [12] into all the features.

### 3.3 Feature Selection

**Random Forest Importance:** A naïve variable importance measure to use in tree-based ensemble methods is to merely count the number of times each variable is selected by all individual trees in the ensemble [13]. It provides two straight forward methods for feature selection: mean decrease impurity and mean decrease accuracy [14]. The features are shown in Table 2.

**Chi-Square:** Chi square calculation is essentially used to decide the most noteworthy esteemed highlights from the test set [15]. If the target variable is independent of the feature variable, we can discard that feature variable. If they are dependent, the feature variable is very important. The Chi-square weight parameters along with their weight is show in Table 3. The mathematical equation has given below:

$$X = \sum_{s=1}^2 \sum_{t=1}^n \frac{U_{st} - V_{st}}{V_{st}} \tag{1}$$

Here, n = classes, Ust = patterns in sth epoch Vst = expected frequency of Ust.

**Table 2** Random forest importance [13]

Features	Importance
mc_line_count	0.149059
Intelligence	0.084143
time_estimator	0.082824
total_operators&operands	0.078428
cyclomatic_complexity	0.077434
Difficulty	0.075016
IOCode	0.067324
uniq_Opnd	0.065663
design_complexity	0.063474
IOBlank	0.060374
uniq_Op	0.053941
essential_complexity	0.047919
IOComment	0.038688
program length	0.035956
IOCodeAndComment	0.019757

**Table 3** Chi-square weight results [15]

Variable	Chi square weight
time_estimator	1794.03
program_length	1594.89
IOCodeAndComment	989.62
IOComment	938.15
essential_complexity	889.63
Intelligence	768.90
total_operators&operands	701.86
Difficulty	642.80
cyclomatic_complexity	618.46
design_complexity	562.50
IOBlank	523.17
IOCode	521.80
uniq_opnd	450.55
mc_line_count	441.62
uniq_op	239.30

### 3.4 Algorithms for Random Forest Importance and Chi-Square

The algorithms work procedures for Random Forest Importance and Chi Square Weights are shown in Figs. 1 and 2.

---

**Algorithm 1:** Algorithm for Random Forest Importance

---

**I. Input:** Features and Label

**Output:** Random Forest Importance for Features

**Function** RandomForestImportance (Features, Label):

```

rf ← RandomForestClassifier()
rf.fit(Features, Label)
fe_imp ← rf.feature_importances_
df ← DataFrame(fe_imp, index = Features. name)
return df.sort_by_descending()
    
```

**End Function**

---

**Fig. 1** Random forest importance algorithm

**Algorithm 2:** Algorithm for Chi Square Weights

**2. Input:** Features

**Output:** Chi-Square weights for Features

**Function** CalculateChiSquareWeight(Features) :

```
chi2 ← stats.chisquare(Features)
df ← DataFrame(chi2; index = Features:name)
return df.sort_by_descending()
```

**End Function**

Fig. 2 Chi square weights algorithm

### 4 Proposed Methodology

The proposed system model consists of several components as shown in Fig. 3. First, we pre-processed the dataset, then applied classification algorithms with all the features and did not apply any sampling techniques on the pre-processed dataset. The second, third and fourth experiments were conducted by applying SMOTE, ADASYN, and Hybrid sampling respectively on the pre-processed dataset. For fifth experiment, we performed feature selection using Random Forest Feature Importance and Chi-Square Test. Based on Random Forest Importance and Chi-Square Test results, we selected 5 features with higher weight as: mc\_line\_count, intelligence, time\_estimator, program\_length, IOCodeAndComment.

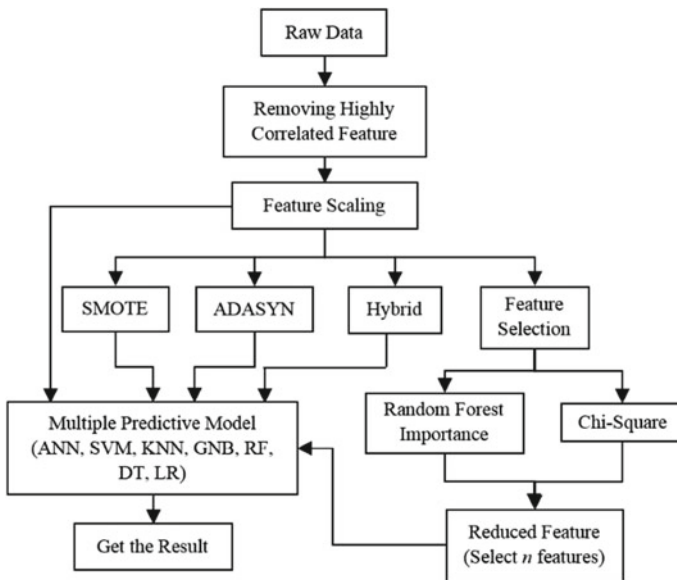


Fig. 3 Proposed prediction model



## 4.1 Imbalanced Dataset

A dataset is imbalanced when one class has majority number of data than other classes. However, Machine learning predictive model is not appropriate when the data is imbalanced [16]. To overcome the above problem and correctly evaluate our model we per-considered three different sampling methods: SMOTE, ADASYN, and Hybrid.

**SMOTE** is an over-sampling method that creates synthetic (not duplicate) samples of the minority class. Hence making the minority class equal to the majority class. SMOTE does this by selecting similar records and altering that record one column at a time by a random amount within the difference to the neighboring records.

**ADASYN** is an improved version of SMOTE. The key idea of ADASYN algorithm is to use a density distribution  $r^i$  as a criterion to automatically decide the number of synthetic samples that need to be generated for each minority data example [17].

**Hybrid** is combining over and under sampling techniques and our goal is to achieve superior classification performance compared to the SMOTE and ADASYN learning approach [18]. Oversampling and undersampling method can't perform well individually. So, we combined those two techniques and applied a hybrid sampling technique named SMOTEENN which is the combination of SMOTE and Edited Nearest Neighbor (ENN). SMOTE used as oversampling technique and ENN used as undersampling method. As SMOTE generated multiple instance of some of the minority classes and ENN reduced the instance of multiple copy of the majority classes. So the number of instance for minority and majority classes are well balanced than the unsampled data.

## 5 Experiment Results

In this chapter, Accuracy, Recall, Precision and F1-score considered as evaluation matrix. Results are displayed in table and graphs. Using Bar-Chart, line graph are used to analyze the results. It may not be conceivable to develop a classifier that could impeccably arrange every objects from the approval set [19].

### 5.1 Evaluation Matrices

Evaluation Matrix is helpful to consider the appropriate and feasible data collection method for each of the arguments identified in the evaluation plan. Some of the considered evaluation matrix are as follows:

TP (True Positive), TN (True Negative), FP (False Positive). FN (False Negative).

**Accuracy:** It is a measure that computes the classifier's general exactness. It is defined as:

$$Accuracy = \frac{TN + TP}{FN + TP + FP + TN} \quad (2)$$

**Recall:** It is the extent of those cases which are accurately named ‘True Positive’ and ascertained as:

$$Recall = \frac{TP}{FN + TP} \quad (3)$$

**Precision:** It is division of the anticipated positive examples that described as accurately stirred. Formally it can be communicated as:

$$Precision = \frac{TP}{TP + FP} \quad (4)$$

**F-Measure:** F-score is not the only measure used in the research covering the software defect prediction models. Here, it is used to evaluate the prediction accuracy of a defective prediction model. The accuracy can be defined as:

$$F-Measure = \frac{Recall * Precision}{Recall + Precision} \quad (5)$$

## 5.2 Results and Analysis

Various machine learning classification algorithms are applied on sampled data sets. We have applied 5 different approaches with 7 different classification algorithms to find the classification. So, we have tried 35 different approaches with the combination of these processes. Major 5 approaches are:

- i. Classification algorithms with all the features, without any sampling
- ii. SMOTE sampling technique and then apply classification algorithms
- iii. ADASYN sampling technique and then apply classification algorithm
- iv. Hybrid sampling technique and then apply classification algorithms
- v. Chi-square and Random forest importance features selection algorithms to extract the key feature and then apply classification algorithms.

In this chapter, we have extracted key factors for defect prediction. We also applied 7 different classification algorithms on the selected features. Table 5, shows the accuracy obtained for all features and reduced features. It can be noticed that without using any sampling and with all features ANN achieved 81.54% accuracy, which is 0.15% improved compared to reduced features (RF) 81.39%.

We have calculated Accuracy, Precision, Recall and F1-score for all the 5 different approaches and shown in the Table 4. The Accuracy comparison of reduced and all features are shown in Table 5.

**Table 4** Classification score for all the experiments

Models	Evaluation metrics	Unsampled dataset	SMOTE	ADASYN	Hybrid	Reduced feature
ANN	Accuracy	0.8154	0.6712	0.6516	0.7747	0.8085
	Precision	0.97	0.67	0.65	0.78	0.97
	Recall	0.82	0.67	0.65	0.77	0.81
	F1-Score	0.88	0.67	0.65	0.78	0.88
SVM	Accuracy	0.8007	0.6513	0.6280	0.7499	0.8021
	Precision	1.00	0.72	0.64	0.75	1.00
	Recall	0.80	0.65	0.63	0.75	0.80
	F1-Score	0.89	0.66	0.63	0.75	0.89
KNN	Accuracy	0.8007	0.8155	0.8238	0.8907	0.8058
	Precision	0.86	0.82	0.83	0.89	0.95
	Recall	0.80	0.82	0.82	0.89	0.81
	F1-Score	0.83	0.82	0.82	0.89	0.86
GNB	Accuracy	0.8039	0.5983	0.5643	0.6184	0.8090
	Precision	0.88	0.84	0.83	0.81	0.93
	Recall	0.80	0.60	0.56	0.62	0.81
	F1-Score	0.83	0.65	0.63	0.64	0.86
RF	Accuracy	0.8067	0.8935	0.8960	0.9326	0.8131
	Precision	0.89	0.89	0.90	0.93	0.97
	Recall	0.81	0.89	0.90	0.93	0.81
	F1-Score	0.84	0.89	0.90	0.93	0.87
DT	Accuracy	0.7599	0.8218	0.8319	0.9020	0.8039
	Precision	0.75	0.82	0.83	0.90	0.99
	Recall	0.76	0.82	0.83	0.90	0.80
	F1-Score	0.76	0.82	0.83	0.90	0.88
LR	Accuracy	0.8081	0.6547	0.6382	0.7549	0.8085
	Precision	0.98	0.66	0.64	0.76	0.97
	Recall	0.81	0.65	0.64	0.75	0.81
	F1-Score	0.88	0.66	0.64	0.76	0.88

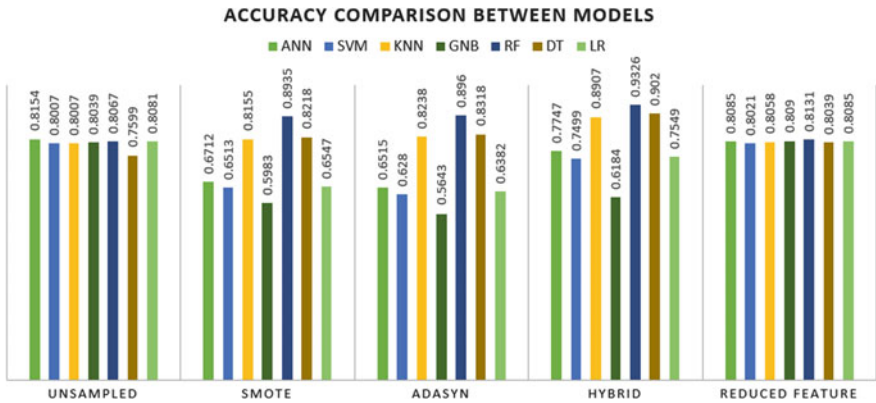
Figure 4 shows that hybrid sampling method with Random Forest classification shows highest accuracy 93.26% compared to all other approaches. Hybrid sampling method with Decision Tree classification performed second best classifier with 83.19% accuracy.

Figure 5 shows that reduced features with decision classifier achieved 99.00% precision, which is top-most among all approaches. Logistic Regression classification with unsampled data performed second best classifier with 98.00% precision.

Figure 6, depicts that hybrid sampling method with Random Forest classifier out-

**Table 5** Accuracy comparison of reduced and all feature

Models	Accuracy (all feature) (%)	Accuracy (reduced feature) (%)
ANN	81.54	80.85
SVM	80.07	80.21
KNN	80.07	80.58
GNB	80.40	80.90
RF	80.67	81.31
DT	75.99	80.39
LR	80.81	80.85



**Fig. 4** Accuracy comparison with different sampling method and reduced features

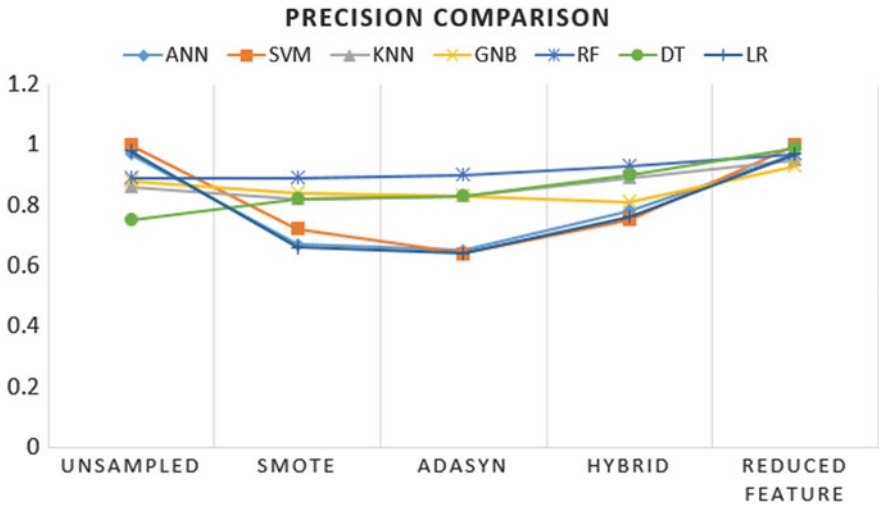


**Fig. 5** Precision comparison with different sampling method and reduced features

perform all the approach with 93.00% recall achievement. Hybrid sampling method with Random Forest classifier performed as second best classifier with 90.00% recall.

The hybrid sampling method with Random Forest classifier shows 93.00% F-1 score compared to all the approach as shown in Fig. 7. Hybrid sampling method with Random Forest classifier performed as second best classifier with 90.00% F-1 score.

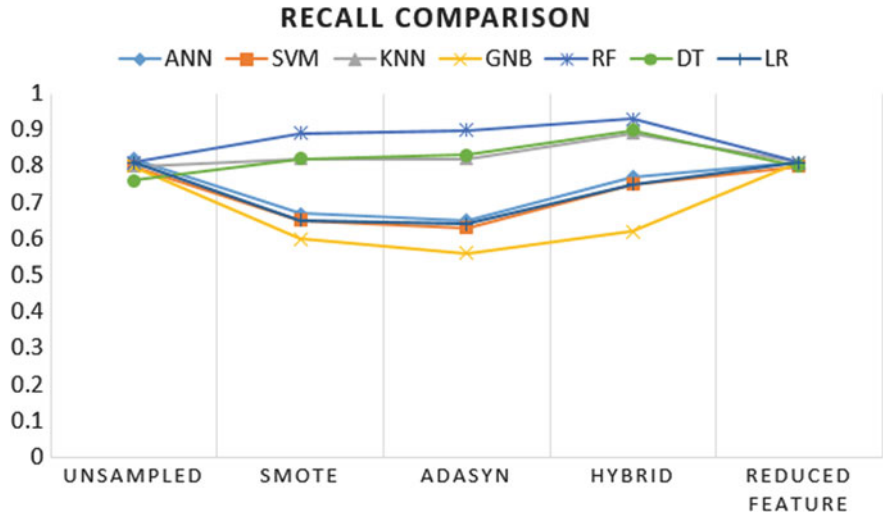


Fig. 6 Recall comparison with different sampling method and reduced features

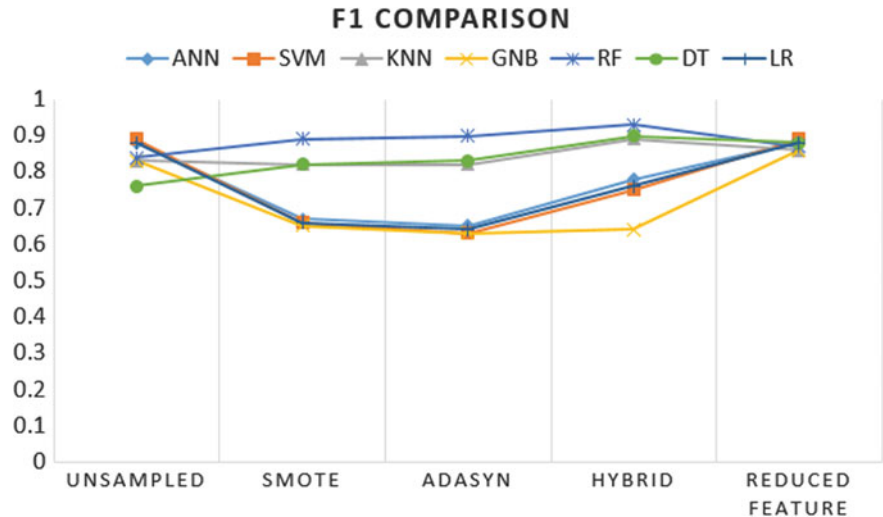


Fig. 7 F1-score comparison with different sampling method and reduced features

### 5.3 Results Discussion

Experiment results shows that hybrid sampling with Random Forest classifier outperforms all the 35 different combination by establishing its superiority. For unsampled data, ANN showed the highest accuracy value, which is approximately 81.54% compared to other 6 different classifiers. For SMOTE sampling method based model, Random Forest shows good accuracy, around 89.35% among all considered classifiers. For ADASYN sampling method based model, Random Forest shows ~89.60% accuracy compared to other classifiers. For Hybrid sampling method based model, Random Forest achieved ~93.26% accuracy among all considered classifiers. For reduced feature based model, Random Forest shows ~81.31% accuracy among all classifiers. From the results, we can finally conclude that random forest classifier is the best classifier among the 7 considered classifiers, whereas, hybrid sampling method is the best sampling method among the considered three methods. Hence, the combination of hybrid sampling method with Random Forest classifier outperform all possible 35 different approach by showing its superiority to be used for software defect prediction in near future.

## 6 Conclusion

This chapter presents different feature selection and sampling techniques to deal with high dimensional imbalanced datasets. By reducing the number of features, it reduces the model complexity and increases the model predictive force. Hybrid sampling played a vital role to deal with the imbalanced dataset. Random Forest with Hybrid sampling gives the highest accuracy across all the models. SMOTE, ADASYN sampling method with ANN, SVM, KNN, GNB, DT, and LR algorithms were considered with feature reduction from 15 to 5 to reduce the complexity of the experimental models. The combination of hybrid sampling method with Random Forest classifier turns out to be the best method for software defect prediction in near future. Implement ensemble methods to achieve even better performance can be investigated in future, which is under consideration by our research team.

**Acknowledgements** This research work is supported by research grant RDU1703236 funded by Universiti Malaysia Pahang, <https://www.ump.edu.my/>. The authors would also like to thank the Faculty of Electrical & Electronics Engineering, Universiti Malaysia Pahang for financial support.

## References

1. Menzies T, Greenwald J, Frank A (2007) Data mining static code attributes to learn defect predictors. *IEEE Trans Softw Eng* 33:2–13
2. Lin J-C, Wu K-C (2007) Digging high risk defects out in software engineering. In: International conference on intelligent information processing. Springer US, pp 20–23
3. Gray D, Bowes D (2011) The misuse of the NASA metrics data program data sets for automated software defect prediction. In: IET conference proceedings. The Institution of Engineering & Technology, pp 96–103 (2011)
4. Lessmann S, Baesens B (2008) Benchmarking classification models for software defect prediction: a proposed framework and novel findings. *IEEE Trans Software Eng* 34(4):485–496
5. Khoshgoftaar TM, Gao K, Napolitano A (2012) An empirical study of feature ranking techniques for software quality prediction. *Int J Softw Eng Knowl Eng* 22:161–183
6. Vashisht V, Lal M, Sureshchandar GS (2016) Defect prediction framework using neural networks for software enhancement projects. *Br J Math Comput Sci (BJMCS)* 16(5)
7. Hall MA, Holmes G (2003) Benchmarking attribute selection techniques for discrete class data mining. *IEEE Trans Knowl Data Eng* 15(6):1437–1447
8. Wang H, Khoshgoftaar TM, Gao K, Seliya N (2009) Mining data from multiple software development projects. In: Proceedings of the 3rd IEEE international workshop mining multiple information sources, pp 551–557, Miami, FL
9. Promise Dataset, <https://promise.site.uottawa.ca/SERepository/datasets/jml1.arff>. Last accessed 4 April 2019
10. Benesty J, Chen J, Huang Y, Cohen I (2009) Pearson correlation coefficient. In: Noise reduction in speech processing. Springer, Berlin, Heidelberg, pp 1–4
11. Danielsson P-E (1980) Euclidean distance mapping. *Comput Graph Image Process* 14(3):227–248
12. MinMaxScaler, <https://scikit-learn.org/stable/modules/generated/sklearn.preprocessing.MinMaxScaler.html>. Last accessed 4 April 2019
13. Strobl C, Boulesteix A-L, Zeileis A, Hothorn T (2007) Bias in random forest variable importance measures: illustrations, sources and a solution. *BMC Bioinform* 8(25):25
14. Random forest feature importance, <https://blog.datadive.net/selecting-goodfeatures-part-iii-random-forests/>. Last accessed 1 Oct 2018
15. Sklearn.feature-selection.chi2, <https://scikitlearn.org>. Last accessed April 2019
16. Chawla NV, Bowyer KW, Hall LO, Kegelmeyer WP (2002) SMOTE: synthetic minority over-sampling technique. *J Artif Intell Res* 16:321–357 (2002)
17. He H, Bai Y, Garcia EA, Li S (2008) ADASYN: adaptive synthetic sampling approach for imbalanced learning. In: International joint conference on neural networks, IJCNN 2008, pp 1322–1328
18. Seiffert C, Khoshgoftaar TM, Van Hulse J (2009) Hybrid sampling for imbalanced data. *Integr Comput Aided Eng* 16(3):193–210
19. Burez J, Van den Poel D (2009) Handling class imbalance in customer churn prediction. *Expert Syst Appl* 36(3):4626–4636

# kNN and SVM Classification for EEG: A Review



M. N. A. H. Sha'abani, N. Fuad, Norezmi Jamal and M. F. Ismail

**Abstract** This paper review the classification method of EEG signal based on k-nearest neighbor (kNN) and support vector machine (SVM) algorithm. For instance, a classifier learns an input features from a dataset using specific approach and tuning parameters, develop a classification model, and use the model to predict the corresponding class of new input in an unseen dataset. EEG signals contaminated with various noises and artefacts, non-stationary and poor in signal-to-noise ratio (SNR). Moreover, most EEG applications involve high dimensional feature vector. kNN and SVM were used in EEG classification and has been proven successfully in discriminating features in EEG dataset. However, different results were observed between different EEG applications. Hence, this paper reviews the used of kNN and SVM classifier on various EEG applications, identifying their advantages and disadvantages, and also their overall performances.

**Keywords** Electroencephalogram (EEG) · Classification · kNN · SVM

## 1 Introduction

Electroencephalogram (EEG) signal is an electrophysiological signal which represents the oscillatory brain activity in microvolt range signal. The first recorded EEG signal was pioneered by Hans Berger in 1924 [1]. Conventionally, EEG signal was visually analyzed by trained clinician and neurologist expert based on the graph chart

---

M. N. A. H. Sha'abani (✉) · M. F. Ismail  
Centre for Diploma Studies, Universiti Tun Hussein Onn Malaysia, 86400 Parit Raja, Johor,  
Malaysia  
e-mail: [nhafiz@uthm.edu.my](mailto:nhafiz@uthm.edu.my)

N. Fuad · N. Jamal  
Faculty of Electrical and Electronic Engineering, Universiti Tun Hussein Onn Malaysia, 86400  
Parit Raja, Johor, Malaysia

N. Fuad  
Computational, Signal, Imaging and Intelligent Focus Group (CSII), Universiti Tun Hussein Onn  
Malaysia, 86400 Parit Raja, Johor, Malaysia



for diagnosis of several brain neurological and physiological abnormalities [2]. However, the drawback of this traditional assessment is sometimes tedious, subjective and time-consuming [3]. Due to that, the automated analysis of the EEG signal has been recently invented using fully computerized systems based on machine learning algorithms and advanced signal processing techniques to interpret EEG signal pattern. It has been proven to give promising results as observed in the literature.

Since EEG offers a cheap, safe and non-invasive measurement, a wide number of research field showing interest in utilizing EEG modalities. According to iMotion [4], a biometric research platform provider, EEG signal based approach has been widely used in several applications such as Brain-Computer Interface (BCI) [5, 6], clinical and psychiatric studies [7, 8], neurosciences and physiology studies [9, 10], social interaction [11, 12] and neuromarketing [13, 14]. The mutual objective of these researches is to achieve a better and deeper insight of brainwave behaviour by accurately classifying the EEG pattern respective to a specific application. Classification is one of the most important stages in EEG signal processing. The accuracy of the classification indicates how reliable the developed system. However, processing the EEG signals is a challenging task due to the contamination of EEG signal by various noises and artefacts, non-stationary and poor in signal-to-noise ratio (SNR) [15]. On the other hand, to do the automated analysis, factors such as data variability and high dimensionality of feature vector may scarce the classification performance [16]. To date, there are numerous classifiers that have been used in analyzing the EEG signals including k-nearest neighbor (kNN), support vector machine (SVM), neural network (NN), discriminant analysis, Bayesian, fuzzy-based and few other approaches and enhanced version of classifiers. Several classifiers predict class using the concept of similarity distance, and others based on features itself such as colours, edges, etc. This paper intends to review kNN and SVM classifiers. This is due to both classifier are capable to solve the non-linear problem in EEG application. However, there are strength and drawback of both classifiers in term of computational complexity and their suitability in a certain application which will be discussed later.

A general search has been done to find the number of publications in EEG signal analysis using kNN and SVM classifiers between 2010 and 2019. The search has been done in the Scopus database with the keyword "EEG AND kNN" and "EEG AND SVM". The result of the searching is shown in Fig. 1. Generally, the number of publications using SVM classifier increase significantly than kNN classifier in the last decade. The publications using kNN remain steady between 2010 and 2014 and slightly increase in recent years. Be noted, the search results does not mean all the works found are using kNN or SVM. In fact, some works used these classifiers for comparison purpose [17, 18]. It is obviously shown that the SVM based classification is more popular than kNN classification in EEG analysis. Therefore, this paper will review the used of kNN and SVM on various applications of EEG signals, identifying their pros and cons to the EEG signal dataset, and also their overall performances.

This paper is organized as follows: Sect. 2 brief the characteristics of the EEG signal and its general processing stages. Then, Sect. 3 provides a review on previous work in EEG signal that using kNN and SVM classifier and also comparison studies between the classifiers in different EEG applications. Finally, Sect. 5 concludes the

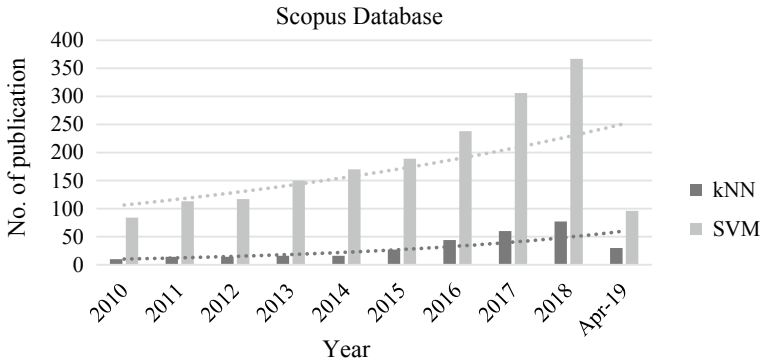


**Fig. 1** The number of publications in Scopus database for kNN and SVM classification in EEG research between 2010 and April 2019 (accessed on 13 April 2019)

verdict of the review. To be mentioned here, the performance of kNN and SVM classifiers cannot be directly compared due to the diversity of parameters setting, dataset, and feature extraction. In addition, the review does not provide any standard validation assessment which leads to non-uniform evaluation.

## 2 EEG Signal Processing Architecture

EEG signal is recorded using a standard 10–20 system of electrode placement. In the 10–20 system, electrodes are distributed evenly to provide adequate coverage of all head region. Currently, EEG has been found to comprise of several frequency bands, where each band related to specific brain activity. For instance, delta rhythm (0.5–4 Hz) detectable in babies and in deep sleep, theta rhythm (4–8 Hz) found in ‘idling’ state, unconscious and deep meditation, alpha rhythm (8–13 Hz) observed in relaxed state and in concentration, motor activities suppression in beta rhythm (13–30 Hz) and gamma (30–100 Hz) for short term memory tasks [19]. Although there are other frequency band found such as mu band (8–12 Hz), it is actually composed of the alpha band.

Classification of EEG signal consists of two phases; training and testing, as shown in Fig. 2. The only difference between these two phases is the learning process. In the training phase, the classifier learns the input features, while in the testing phase, the classifier predicting the class of the input features belongs to. Initially, the raw EEG signal is typically undergo filtering process and artefact removal before features are extracted. Feature extraction is a process of taking out any possible information contained in the EEG signal either in the time domain, frequency domain or time–frequency domain [19]. In order to make the classifier performing at its best possible manner, the extracted features are being selected, so that only the most correlated features to the target output are chosen for training. The final output of the trained

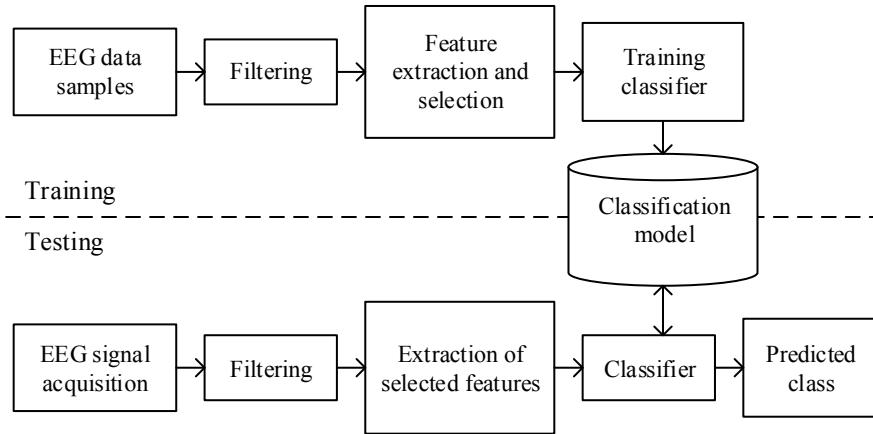


**Fig. 2** Processes involved in typical EEG signal classification

classifier is the development of a classification model. The model then is used as a reference to the classifier in predicting the class of new inputs during the testing phase. The performance of the classification is often measured by its accuracy or F1-score, which both obtained from the confusion matrix [20].

### 3 Previous Studies

#### 3.1 *k*-Nearest Neighbour

kNN is a well-known multiclass classifier, constructed based on distance approach which offers a simple and flexible decision boundaries [21]. The term ' $k$ ' is the number of nearest neighbors that taken into account in assigning a class of a new instance. Generally, a small value of  $k$  makes the kNN classification will have a higher influence from noise. While the too large value of  $k$  makes it computationally expensive. If  $k = 1$ , then a new instance is simply classified to the closest neighbor. However, when the number of  $k$  is larger, and two or more neighbors influence the classification, a simple majority voting can be used [22]. It is also recommended that the number of ' $k$ ' is an odd sequence to avoid a tied problem [23]. A brief explanation of kNN classifier can be found here [22].

In EEG application, several researchers carried out their research on classification using kNN for different applications such as BCI [24–27], physiological [9, 11, 28–31] and clinical [7, 32, 33] application with different features. For BCI application, in a study conducted by Yazdani et al. [24], it was shown that Dempster-Shafer kNN classifier achieved a higher correct classification rate compared to other classical voting kNN classifier and the distance-weighted kNN classifier at 90.08%. Next,

**Table 1** Previous studies in EEG signal processing using kNN classifier

Application	Author	Features	Classifier	Performance (%)
Brain-computer interface	Mousa et. al. [27]	Wavelet coefficient	kNN	63.80
Clinical and psychiatric studies	Rezaee et al. [7]	Wavelet coefficient	Adaptive kNN	98.00
Neurosciences and physiology studies	Fuad et. al. [9]	Power spectral density (PSD)	kNN	88.46
Social interaction	Murugappan et. al. [11]	Wavelet coefficient	kNN	83.26
Neuromarketing	Murugappan et. al. [13]	PSD Spectral Centroid Spectral Energy	kNN	93.64

Bhattacharyya et al.’s comparative study found that kNN classifier outperformed to other classifier techniques, which its accuracy is 84.29% with average band power estimate vector features [25]. Similarly, Mousa et al. assert that kNN classifier produced better accuracy of 67.7% compared to SVM and NN classifier based on wavelet features [27].

In physiological application, most researches contributed to emotion classification [11, 28–31] and only a few researchers studied on brain balance index based on EEG signal [9]. Murugappan et al. reported that kNN classifier’s accuracy is 83.26%, which worked well with Absolute Logarithmic Recoursing Energy Efficiency (ALREE) features in human emotion classification [11]. Other researchers, however, who have looked at the classification of depression patients and normal subjects, as mentioned in [29] found that logistic regression classifier performed better than LDA and kNN classifier. Next, Fuad et al. used kNN classifier to predict the brain balancing with 88.46% accuracy based on maximum power spectral density features [9]. Otherwise, Rezaee et. al., in their study on seizure detection, reported that 98% true seizures detection based on general tensor discriminant analysis [7] and Zainuddin et al. optimized kNN classifier in classification of dyslexic and normal children based on power band features from discrete wavelet transform of EEG signal for clinical application [33]. Table 1 shows several previous studies in EEG applications and their performance accuracy.

### 3.2 Support Vector Machine

SVM utilize a discriminant hyperplane to identify classes. It selects the optimal hyperplane and map data into a high dimensional space. SVM can be found both

in linear and non-linear. In the case of the linearly separable dataset, linear SVM is essentially to be used. Otherwise, non-separable dataset requires non-linear SVM. Non-linear SVM creates decision boundary by using kernel function [34] such as Radial Basis Function (RBF) and polynomial, which is also called as 'kernel trick'.

In order to get a good performance of SVM, two parameters have to be chosen carefully [35]. The first parameter is regularization parameter C. It is defined from the optimal equation:

$$\min \frac{1}{2} \|w^2\| + C \sum_i \xi_i \quad (1)$$

Parameter C determine the trade-off between the misclassification number and width of the hyperplane margin. A too-small value of C will lead to a larger margin size and consequences to misclassification. Conversely, a large value of C parameter will lead to a smaller-margin hyperplane, resulting in good classification performance. The second parameter is the kernel parameter (i.e.  $d$  or  $\sigma$ ) of non-linear SVM. Kernel parameter defines the nonlinear mapping from input space to a high-dimensional feature space. For instance, a high value of  $\sigma$  will effectively ignore data that are farther away. In comparison, a small value of  $\sigma$  will consider to include distant data. A practical guide in using SVM can be found here [36].

In EEG application, SVM has been used to quantify mental stress level amongst twelve healthy subjects on arithmetic tasks [10]. The study decomposed raw EEG signals into four sub-band frequency using wavelet transform and extracted the mean absolute values of the wavelet coefficient, the average power, and energy as features. SVM then was used to classify the three-level of mental stress. The result shows SVM is able to identify mental stress level with the accuracy of 94%, 85% and 80% at each level. Al-Qazzaz et al. [8] used a non-linear SVM classifier with RBF kernel functions and kNN classifier to discriminate the EEG signals activity during working memory tasks between 15 stroke-related patients, 5 vascular dementia patient and 15 control healthy subject. To test the irregularity and complexity, permutation entropy and fractal dimension features are extracted. In this study, SVM achieved 91.48% accuracy in differentiating those subjects, which is higher than using kNN classifier with 89.63% accuracy.

It is also reported that a multiple kernel SVM (MKL-SVM) performs better than the single kernel of multiple class problem. Li et al. [37] has proposed a multiple kernel SVM (i.e. a combination kernel of RBF and polynomials) and compared it with the single kernel of RBF and polynomial on mental task and cognitive task problem. This method gives flexibility on optimizing kernel function that fits the data structure. As a result, multiple kernel SVM gives higher overall accuracy than SVM based on a single kernel. Table 2 shows several previous works in various EEG application that used SVM based classification.

**Table 2** Previous studies in EEG signal processing using SVM based classifier

Application	Author	Features	Classifier	Performance (%)
Brain computer interface	Li et. al. [37] <sup>a</sup>	Granger causality	MKL-SVM	89.24
			RBF-SVM	81.61
			Polynomial SVM	77.14
Clinical and psychiatric studies	Al-Qazzaz et al. [8]	Permutation entropy and fractal dimension	RBF-SVM	91.48
Neurosciences and physiology studies	Al-Shargie et. al. [10]	Mean absolute values, the average power and energy	SVM	86.33
Social interaction	Kraljević et. al. [12]	Wavelet coefficient	RBF-SVM	62.45
Neuromarketing	Wei et. al. [14]	13 emotion-related features	Linear SVM	77.28

<sup>a</sup>Results of cognitive task

### 3.3 Comparison Studies

The performance of kNN and SVM are also being compared between different EEG dataset in recent studies. Mousa et. al. [27] compare the results of kNN, SVM and neural networks in classifying motor imagery tasks in BCI Competition IV dataset using wavelet coefficient as features. The authors claimed that kNN outperforms SVM and neural network. Nguyen et. al. [38] introduced an interval type-2 fuzzy logic system with wavelet transform to classify motor imagery in BCI Competition II dataset. The evaluation results also show kNN give better performance than SVM. In the clinical field, Li et. al. [39], proposed a method based on dual-tree complex wavelet transform (DT-CWT) by extracting Hurst exponent, Fractal Dimension and Permutation Entropy for automated epileptic detection. The experiment results, however, show that the combination of SVM with the proposed method has higher overall accuracy than kNN, decision tree, and random forest. Acharya et. al. [40], used SVM, kNN and other five classifiers as one of the comparison criteria also found that SVM gives better accuracy than kNN. The proposed method extracting features based on entropy. Table 3 summarize several previous studies that used kNN and SVM classifier either for comparison purpose or method evaluation.

**Table 3** Summary of studies that compares the classification results of kNN and SVM

Application	Author	Features	Problem	Classifier	Performance (%)
Brain-computer interface	Mousa et al. [27]	Wavelet coefficient	Multiclass	kNN	63.80
				SVM	51.40
Brain-computer interface	Nguyen et. al. [38]	Wavelet coefficient	Binary	Dataset Ia	
				kNN	86.01
				SVM	78.50
				Dataset Ib	
				SVM	53.33
Motor imagery	Bashar et al. [41]	Time and frequency domain	Binary	kNN	90.36
				SVM	87.50
Epileptic diagnosis	Acharya et al. [40]	Entropy	Multiclass	kNN	93.00
				SVM	95.90
Epileptic detection	Li et al. [39]	Hurst exponent, fractal dimension and permutation entropy	Binary	kNN	97.80
				SVM	98.87
Emotion classification	Mehmood and Lee [31]	Hjorth parameters	Multiclass	kNN	47.76
				SVM	36.66

## 4 Discussion

The main challenge in the classification of EEG signals is the quality of the acquired signal. Moreover, the non-linear signal of EEG contains many brain activities occur at the same time. Hence, raw EEG signals need to be cleaned properly using an advance filter technique, while the extracted features need to be selected based on the most correlate to their desired output [19]. Based on the reviewed classification works, kNN and SVM have been widely used in EEG applications. Most of the recent EEG classification is based on supervised learning. kNN and SVM are two of several classifiers that are based on supervised learning and capable to solve a linear and non-linear problem in EEG signal.

kNN amongst the simplest classification algorithm that assumes a new input belongs to the majority of nearest neighbor's class. Despite its simplicity, kNN can approximate any function if the number of  $k$  is sufficiently high [42]. kNN is very useful for non-linear data and performs better in low dimensional EEG dataset. However, in a high dimensional dataset, kNN becoming significantly slow and not

practically chosen for an application that needs rapid prediction such as online BCI. Fortunately, this problem can be improved by feature selection or feature weighting [22]. Nevertheless, reviews in kNN classification show that the extended version of kNN such as adaptive kNN can give higher accuracy than the standard kNN.

Linear SVM can be used to classify separable data and kernelized SVM for non-separable data. SVM has regularization characteristics, which let it avoid misclassification and prevent it from overfitting [42]. Unlike kNN, SVM can handle high dimensional classification problem even if the data size is small. If the dataset used is large, the training time will get higher. Thus, SVM looks more computationally intensive. However, since SVM is capable to handle high dimensional data, it is more popular to use in classifying EEG signals than kNN, as shown in the previous general search results in Fig. 1.

## 5 Conclusion

The objective of the paper is to review the implementation of kNN and SVM classifier in various EEG applications. The results obtained from the previous studies have shown that both classifiers are feasible to be used in analyzing the EEG dataset. Nevertheless, the classification of EEG signals is a challenging task due to non-stationary in nature, as well as noises and artefact contaminated in the signals. The right chose of the classifier, the correct tuned parameter and the appropriately selected features of the respective EEG dataset are the criteria to achieve a good result of classification. In order to compare the performance of kNN and SVM properly, a standardized EEG database, the same device specifications, and standard evaluation procedures are needed to be carried out in the future.

**Acknowledgements** The authors would like to thank the Research Management Center of Universiti Tun Hussein Onn Malaysia (UTHM) by funding this study under the Tier 1 research grant code H268 and U923. Appreciation also goes to the Faculty of Electrical Engineering, Centre of Diploma Studies, members of Artificial Intelligent Laboratory and Brainwave Research Group (BRG) for their support.

## References

1. Haas L (2003) Hans Berger (1873–1941), Richard Caton (1842–1926), and electroencephalography. *J Neurol Neurosurg Psychiatry* 74:9
2. Sanei S, Chambers JA (2013) EEG signal processing. Wiley
3. Vaid S, Singh P, Kaur C (2015) EEG signal analysis for BCI interface: a review. In: 2015 fifth international conference on advanced computing & communication technologies, pp 143–147
4. iMotion, Top 6 most common applications for human EEG research, 2015
5. He L, Hu D, Wan M, Wen Y, Deneen KMV, Zhou M (2016) Common Bayesian network for classification of EEG-based multiclass motor imagery BCI. *IEEE Transa Syst Man Cybern Syst* 46:843–854



6. An X, Kuang D, Guo X, Zhao Y, He L (2014) A deep learning method for classification of EEG data based on motor imagery. *Cham*, pp 203–210
7. Rezaee K, Azizi E, Haddadnia J (2016) Optimized seizure detection algorithm: a fast approach for onset of epileptic in EEG signals using GT discriminant analysis and K-NN classifier. *J Biomed Phys Eng* 6:81–94
8. Al-Qazzaz NK, Ali SHBM, Ahmad SA, Islam MS, Escudero J (2018) Discrimination of stroke-related mild cognitive impairment and vascular dementia using EEG signal analysis. *Med Biol Eng Comput* 56:137–157
9. Fuad N, Taib M, Jailani R, Marwan M (2014) Brainwave classification for brain balancing index (BBI) via 3D EEG model using k-NN technique. *Int J Comput Electr Autom Control Inf Eng* 8
10. Al-Shargie F, Tang TB, Badruddin N, Kiguchi M (2015) Mental stress quantification using EEG signals. In: *International conference for innovation in biomedical engineering and life sciences*, pp 15–19
11. Murugappan M, Ramachandran N, Sazali Y (2010) Classification of human emotion from EEG using discrete wavelet transform. *J Biomed Sci Eng* 3:390
12. Kraljević L, Russo M, Sikora M (2017) Emotion classification using linear predictive features on wavelet-decomposed EEG data. In: *2017 26th IEEE international symposium on robot and human interactive communication (RO-MAN)*, pp 653–657
13. Murugappan M, Murugappan S, Gerard C (2014) Wireless EEG signals based neuromarketing system using Fast Fourier Transform (FFT). In: *2014 IEEE 10th international colloquium on signal processing and its applications*, pp 25–30
14. Wei Z, Wu C, Wang X, Supratak A, Wang P, Guo Y (2018) Using support vector machine on EEG for advertisement impact assessment. *Front Neurosci* 12
15. Teplan M (2002) Fundamentals of EEG measurement. *Measur Sci Rev* 2:1–11
16. Lotte F, Bougrain L, Cichocki A, Clerc M, Congedo M, Rakotomamonjy A et al (2018) A review of classification algorithms for EEG-based brain–computer interfaces: a 10 year update. *J Neural Eng* 15:031005
17. Zheng WL, Zhu JY, Peng Y, Lu BL (2014) EEG-based emotion classification using deep belief networks. In: *Proceedings—IEEE international conference on multimedia and expo*
18. An X, Kuang D, Guo X, Zhao Y, He L (2014) A deep learning method for classification of eeg data based on motor imagery. In *Lecture notes in computer science (including subseries Lecture notes in artificial intelligence and lecture notes in bioinformatics)*, vol 8590 LNBI, pp 203–210
19. Subha DP, Joseph PK, Acharya R, Lim CM (2010) EEG signal analysis: a survey. *J Med Syst* 34:195–212
20. Sokolova M, Lalpalme G (2009) A systematic analysis of performance measures for classification tasks. *Inf Process Manage* 45:427–437
21. Cover TM, Hart PE (1967) Nearest neighbor pattern classification. *IEEE Trans Inf Theory* 13:21–27
22. Cunningham P, Delany SJ (2007) k-Nearest neighbour classifiers
23. Hassanat AB, Abbadi MA, Altarawneh GA, Alhasanat AA (2014) Solving the problem of the K parameter in the KNN classifier using an ensemble learning approach. *arXiv preprint arXiv:1409.0919*
24. Yazdani A, Ebrahimi T, Hoffmann U (2009) Classification of EEG signals using Dempster Shafer theory and a k-nearest neighbor classifier. In: *2009 4th international IEEE/EMBS conference on neural engineering*, pp 327–330
25. Bhattacharyya S, Khasnobish A, Chatterjee S, Konar A, Tibarewala D (2010) Performance analysis of LDA, QDA and KNN algorithms in left-right limb movement classification from EEG data. In: *2010 International conference on systems in medicine and biology*, pp 126–131
26. Ahangi A, Karamnejad M, Mohammadi N, Ebrahimpour R, Bagheri N (2013) Multiple classifier system for EEG signal classification with application to brain–computer interfaces. *Neural Comput Appl* 23:1319–1327

27. Mousa FA, El-Khoribi RA, Shoman ME (2015) EEG Classification based on machine learning techniques. *Int J Comput Appl* 975:8887
28. Aditya S, Tibarewala D (2012) Comparing ANN, LDA, QDA, KNN and SVM algorithms in classifying relaxed and stressful mental state from two-channel prefrontal EEG data. *Int J Artif Intell Soft Comput* 3:143–164
29. Hosseinifard B, Moradi MH, Rostami R (2013) Classifying depression patients and normal subjects using machine learning techniques and nonlinear features from EEG signal. *Comput Methods Programs Biomed* 109:339–345
30. Soroush MZ, Maghooli K, Setarehdan SK, Nasrabadi AM (2019) Emotion classification through nonlinear EEG analysis using machine learning methods. *Int Clin Neurosci J* 5:135–149
31. Mehmood RM, Lee HJ (2015) Emotion classification of EEG brain signal using SVM and KNN. In: 2015 IEEE international conference on multimedia & expo workshops (ICMEW), pp 1–5
32. Guo L, Rivero D, Dorado J, Munteanu CR, Pazos A (2011) Automatic feature extraction using genetic programming: an application to epileptic EEG classification. *Expert Syst Appl* 38:10425–10436
33. Zainuddin A, Lee KY, Mansor W, Mahmoodin Z (2016) Optimized KNN classify rule for EEG based differentiation between capable dyslexic and normal children. In: 2016 IEEE EMBS conference on biomedical engineering and sciences (IECBES), pp 685–688
34. Alonso LFN, Gil JG (2012) Brain computer interfaces, a review. *Sensors* 12:1211
35. Duan K, Keerthi SS, Poo AN (2003) Evaluation of simple performance measures for tuning SVM hyperparameters. *Neurocomputing* 51:41–59
36. Hsu C-W, Chang C-C, Lin C-J (2003) A practical guide to support vector classification
37. Li X, Chen X, Yan Y, Wei W, Wang Z (2014) Classification of EEG signals using a multiple kernel learning support vector machine. *Sensors* 14:12784–12802
38. Nguyen T, Khosravi A, Creighton D, Nahavandi S (2015) EEG signal classification for BCI applications by wavelets and interval type-2 fuzzy logic systems. *Expert Syst Appl* 42:4370–4380
39. Li M, Chen W, Zhang T (2017) Automatic epileptic EEG detection using DT-CWT-based non-linear features. *Biomed Signal Process Control* 34:114–125
40. Acharya UR, Molinari F, Sree SV, Chattopadhyay S, Ng K-N, Suri JS (2012) Automated diagnosis of epileptic EEG using entropies. *Biomed Signal Process Control* 7:401–408
41. Bashar SK, Das AB, Bhuiyan MIH (2015) Motor imagery movements detection of EEG signals using statistical features in the Dual Tree Complex Wavelet Transform domain. In: 2015 International conference on electrical engineering and information communication technology (ICEEICT), pp 1–6
42. Lotte F, Congedo M, Lécuyer A, Lamarche F, Arnaldi B (2007) A review of classification algorithms for EEG-based brain–computer interfaces. *J Neural Eng* 4:R1

# Flexible Graphene-Silver Nanowires Polydimethylsiloxane (PDMS) Directional Coupler



Nor Nadiah Aliff, Noorlindawaty Md Jizat, Nazihah Ahmad and Mukter Uz-Zaman

**Abstract** In this research paper, graphene-silver nanowires are demonstrated as the transmission line of directional coupler fabricated on an elastomeric substrate Polydimethylsiloxane, PDMS at 2.4 GHz for wireless wearable application. In the experimental process, highly conductive of 0.6 mg/ml silver nanowires (AgNWs) is embedded in the graphene dispersion and spin coated onto flexible PDMS elastomer. The proposed directional coupler provides excellent return loss lower than  $-10$  dB, good mutual coupling of  $-3 \pm 1$  dB and comparable phase difference between output ports between  $S_{21}$  and  $S_{31}$  with value of  $90^\circ \pm 1^\circ$ . Comparison of return loss and phase difference between output port performances was performed in three different angles of bending,  $0^\circ$ ,  $90^\circ$  and  $180^\circ$ . The simulation and measurement outcomes show promising results, indicate that graphene-silver nanowires on PDMS elastomer as a good material for flexible devices and able to withstand mechanical strains without degrading the performance of the directional coupler. The compact sizes and unique properties of the coupler can be realized for wireless wearable electronics applications.

**Keywords** Flexible · Graphene-silver nanowires · Polydimethylsiloxane (PDMS) · Directional coupler · Wireless wearable application

## 1 Introduction

Graphene has emerged as a unique atomic configuration to substitute indium tin oxide (ITO) owing to extraordinary properties including a very large surface area, transport mobility, high-level transparent conductor [1–3], high percentage of electrical/thermal conductivity, tunable band gap, high Young's modulus, own mechanical strength [4–6] and have high elasticity [7]. Various applications of graphene based materials modified by doping effectively used for radio frequency application and applications in biomedical [8, 9].

---

N. N. Aliff · N. M. Jizat (✉) · N. Ahmad · M. Uz-Zaman  
Faculty of Engineering, Multimedia University, Cyberjaya, Selangor, Malaysia  
e-mail: [noorlindawaty.jizat@mmu.edu.my](mailto:noorlindawaty.jizat@mmu.edu.my)

© Springer Nature Singapore Pte Ltd. 2020  
A. N. Kasruddin Nasir et al. (eds.), *InECCE2019*, Lecture Notes in Electrical Engineering 632, [https://doi.org/10.1007/978-981-15-2317-5\\_48](https://doi.org/10.1007/978-981-15-2317-5_48)

To realize the potential commercial of such flexible properties, the devices must be able to withstand the mechanical/thermal strains of bending processes and enduring repeated loading of different environmental conditions. Among all the materials used for flexible electronic technology, silver nanowires (AgNWs) have advantages of high conductivity, a range of biological photovoltaic sensors, the ability to stabilize other polymers in low temperature and ease of application on any substrate [10–13]. Various applications of graphene for wearable communication system using PDMS substrate, making electronic devices less obtrusive [14, 15], light weight, high flexibility, easy to integrate and maximize comfort for the wearer.

Due to these advantages, graphene-silver nanowires were chosen as the directional coupler's transmission line. The proposed design was fabricated on flexible PDMS substrates with metalized copper sheet as the ground. Before fabrication, an initial simulation was obtained by the design modelled in Computer Simulation Technology, CST. In the purpose of shielding the directional coupler, the thin film of PDMS was coated to the upper and lower part of the design by using spin coating technique. As for the experimental verification,  $25.8 \Omega/\text{cm}$  resistivity obtained shows good compatibility between the conductive layer and the PDMS substrate. The measurement results for the proposed design showed good agreement with the simulation validated the design approach presented in this work and can be potentially used as the signal combiner/divider in wearable antenna.

## 2 Experimental Method

Silver nanowires, Ag diameter  $\times$  L  $60 \text{ nm} \times 10 \mu\text{m}$ , 0.5% (isopropyl alcohol suspension), (Sigma-Aldrich, Malaysia) and Conductive Graphene Dispersion, (Graphene Laboratories, Supermarket, UK), were used for AgNW synthesis without further purification. The directional coupler was fabricated from conductive thin film graphene-silver nanowires. The transmission line mesh was spin coated using 0.6 mg/ml graphene-silver nanowires dispersion on 1 mm substrate thickness of Polydimethylsiloxane (PDMS) with dielectric constant of  $\epsilon_{R1} = 2.7$ . Before fabrication, mould was made using plastic film with thickness of 1.5 micrometers. Final coating was made with thin film PDMS using spin coating technique with 500 rpm for 10 s and 1000 rpm for the next 30 s before the substrate cured for 5 min at  $100^\circ\text{C}$ .

### 2.1 Graphene–Silver Nanowires Dispersion

Soluble graphene-silver nanowires dispersions were prepared according to the technique of uniform deposition for graphene surface [16]. A low-boiling solvent such as acetone is used for freeze-drying because of the high-vapour pressures. Subsequently, sonication was carried out in a sonic bath for four hours and 30 min to maintain sonication efficiency and prevent overheating. The flask was kept in an

ice-water bath and the samples were left to stand overnight. The dispersions were then centrifuged at 2000 rpm for 30 min.

## 2.2 PDMS Substrate

In order to prepare for the PDMS substrate, base polymer and base curing were mixed with a ratio of 10:0.5 to maintain the hydrophilic surface. The mixture was vigorously stirred for 5 to 10 min in a beaker container to enable uniform cross-linking. Consecutively, the surface of the PDMS fluid was flattened by pouring the mixture into the mold. Immersion method was used where the silicon substrate is soaked into a beaker that filled with a specified level of acetone for 15 min.

## 2.3 Directional Coupler Design

A directional coupler is commonly used for power division or power combination. If the power fed at Port 1, power incident will couple to port 2 (the through port) and port 3 (the coupled port), but not to isolated port 4. The fraction of power coupled from port 1 to port 3 is given by the coupling,  $C$  with the coupling factor  $|S_{13}|^2 = \beta^2$  to indicate the fraction of the input power that is coupled to the output. The leakage of power from port 1 to port 4 is given by the isolation,  $I$ . Another quantity that characterized the coupler is directivity,  $D = 1 - C$  (dB), which indicates the coupler's ability to isolate forward and backward waves as in the isolated port.

The ideal coupler is characterized solely by the coupling factor, and impedance matching at all ports. Following are three quantities used to characterize a directional coupler as given in Eq. (1–3) [17]:

$$\text{Coupling} = C = 10 \log \frac{P_1}{P_3} = -20 \log \beta \text{ dB} \quad (1)$$

$$\text{Directivity} = D = 10 \log \frac{P_3}{P_4} = 20 \log \frac{\beta}{|S_{14}|} \text{ dB} \quad (2)$$

$$\text{Isolation} = I = 10 \log \frac{P_1}{P_4} = -20 \log |S_{14}| \text{ dB} \quad (3)$$

In the directional coupler design, two transmission lines with  $\lambda_0/4$  electrical length and impedance of  $Z_0$  shunt branch were connected with  $\lambda_0/4$  electrical length and impedance of  $Z_0/\sqrt{2}$  series branch. In Fig. 1, shunt branch with length of 13.66 mm and width of 2.06 mm was connected with a series branch of 13.66 mm length and 1.06 mm width transmission line. A  $0.125 \lambda_0$  coupler was designed at the centre frequency, 2.4 GHz with the matched impedance. A PDMS substrate ( $\epsilon_r = 2.7$ , loss

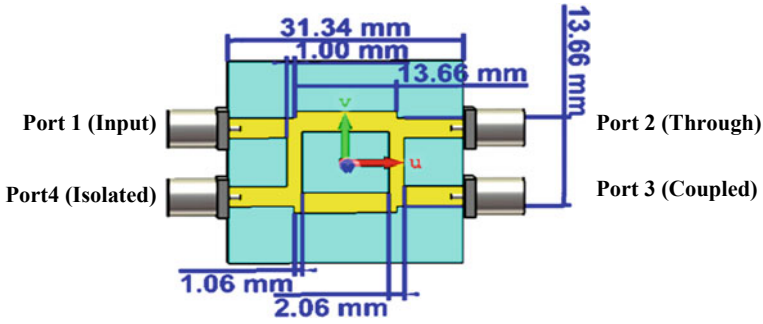


**Fig. 1** Geometry of the proposed coupler

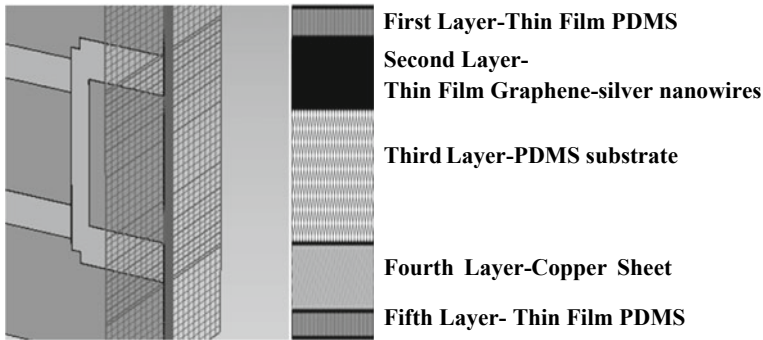


**Fig. 2** Cross section view of directional coupler material by layer

tangent = 0.04) with the thickness of 1 mm is used while the copper sheet is kept metalized at the back of the coupler for ground.

The power applied at port 1 is evenly split between ports 2 and 3, with a 90° phase shift with the port closer to input port leading in phase. Line impedance is matched to maximize the power transfer and minimize reflection from the load [18–21]. Port 4 is the isolated port, and therefore no power is coupled to this port. The cross section of the five layers proposed design is illustrated in Fig. 2.

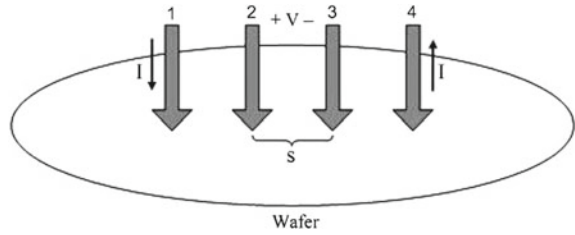
### 2.4 Four-Point Probe Technique

Four-point probe measurement was performed to measure the resistivity value of this proposed directional coupler. The following Table 1 provides information obtained from the measurement and the resistivity value was calculated from Eq. 4. The resulting surface resistivity of graphene-silver nanowires from Eq. 4 [22] provides the value of 25.8 Ω cm.

**Table 1** Resistivity using four-point probe measurement

Parameter	Description	Value
V	Voltage between inner probe	2.79 V
I	Current through outer probes	0.49 A
S	Needle spacing	0.1 cm
t	Substrate thickness	1 mm

**Fig. 3** Four point probes technical diagram



$$\rho_s = \frac{V}{I} \frac{\pi t}{\ln \left| \frac{\sinh \frac{t}{s}}{\sinh \frac{t}{2s}} \right|} [\Omega \text{ cm}] \tag{4}$$

In order to perform four-point probes measurement, power supply, digital multi-meter, and four probes were arranged as shown in Fig. 3, where two outer probes were used to supply current and inner probes were used to measure the voltages.

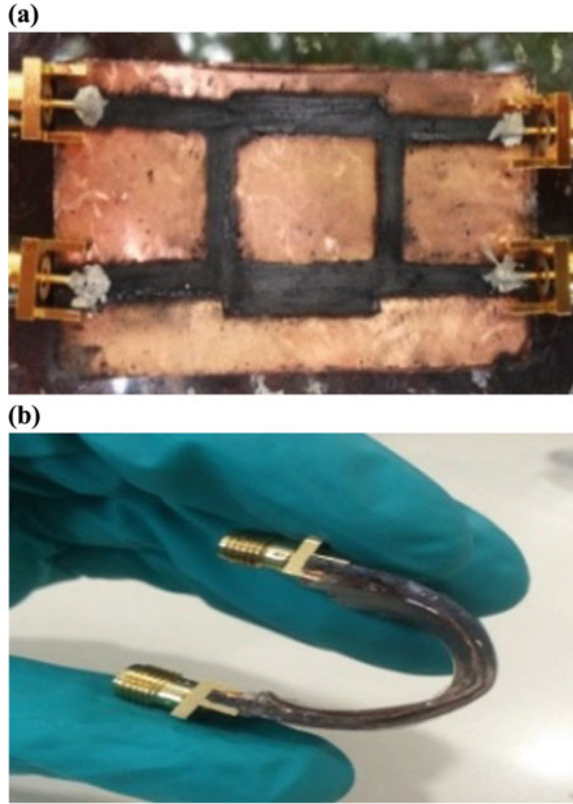
### 3 Results and Discussion

The proposed graphene-silver nanowires coupler has been fabricated and measured. The prototype of the proposed design has been illustrated in Fig. 4a and flexibility is tested in Fig. 4b.

As shown in Fig. 5a, the simulated return loss,  $S_{11}$ , and isolation,  $S_{41}$  are  $-20.03$  dB and  $-19.17$  dB while measured results of the return loss and isolation for flexible coupler are  $-16.42$  dB and  $-22.48$  dB, respectively. The return loss value indicated that high percentage of signal was transmitted between input and output ports of the directional coupler. The simulated result for coupling,  $S_{31}$  and insertion loss,  $S_{21}$  are  $-3.28$  dB and  $-3.06$  dB while for the measured coupling and insertion loss, the values are found to be  $-4.03$  dB and  $-3.88$  dB, respectively. The comparable value of simulation and measurement results proves that 50% of the power is coupled to the coupled port of the coupler and the rest of the power is routed to the output port of the coupler.

The proposed flexible coupler is operated at 2.4 GHz with 10-dB impedance bandwidth of 570 MHz (2.15–2.72 GHz). Figure 5b shows promising phase difference with minimal error in the range of  $90^\circ \pm 5^\circ$ . Comparable value of transmission and

**Fig. 4** Photograph of the directional coupler **a** prototype, **b** flexible bending



tight coupling at the value of less than  $-10$  dB and  $-3$  dB  $\pm 1$ , respectively proved maximum transmitted signals are achieved. A detailed comparison of the coupler performance is tabulated in Table 2. Voltage Standing Wave Ratio, VSWR shows the comparable value of 1.22 that matched the impedance of the transmission line.

The flexible directional coupler was tested under various bending angle as illustrated in Fig. 6. Based on the results tabulated in Table 3, the measured return loss,  $S_{11}$ , directivity,  $S_{21}$ , coupling,  $S_{31}$  and isolation value,  $S_{41}$  were tabulated. Due to changes in capacitance and inductance, the operating frequency of the coupler changed once the bending angle is increased. The propagation of mechanical stress is governed by the inherent physical properties of the material and characteristics of the stress wave. Due to this, the phase difference can be seen to be varied once bending was performed where the phase difference between the output ports have an acceptable range of  $\pm 10^\circ$ . Attributable to these advantages, the proposed design becomes suitable to be used for bending in any range of conformal surface without deteriorating the performance.

From Table 4, it can be seen that the performance of the proposed directional coupler using graphene-silver nanowires fabricated on PDMS substrates is comparable



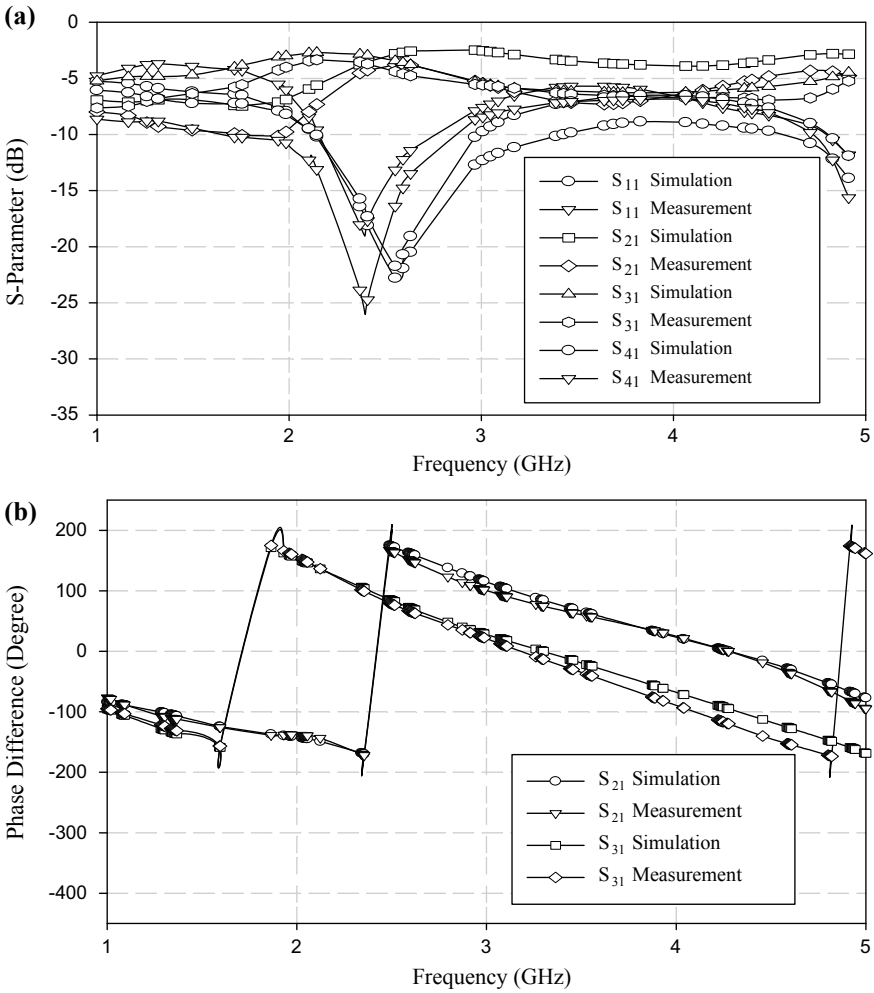


**Fig. 5** Simulated and measured results of **a** S-parameter, **b** phase difference

**Table 2** Simulated and measurement results of the proposed coupler

S-Parameter	Simulation (dB)	Measurement (dB)
$S_{11}$ (dB)	-20.03	-16.42
$S_{21}$ (dB)	-3.28	-4.03
$S_{31}$ (dB)	-3.06	-3.88
$S_{41}$ (dB)	-19.17	-22.48
Phase difference ( $^{\circ}$ )	$(179.42 - 90.81)^{\circ} = 88.61^{\circ}$	$(173.32 - 85.13)^{\circ} = 88.19^{\circ}$

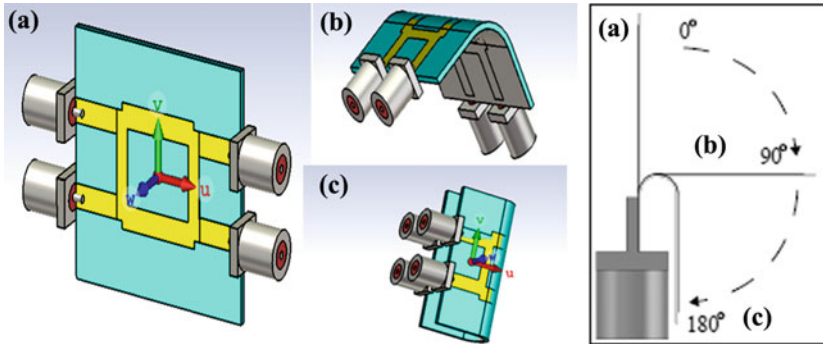


**Fig.6** The directional coupler and its 3D bending configuration at **a** 0°, **b** 90°, **c** 180°

**Table 3** Measurement results for proposed coupler bend at 0°, 90° and 180°

S-parameter	Measurement Bend at 0°		Measurement Bend at 90°	Measurement Bend at 180°
$S_{11}$ (dB)	-16.42	-15.26		-10.29
$S_{21}$ (dB)	-4.03	-4.82		-6.68
$S_{31}$ (dB)	-3.88	-3.59		-3.38
$S_{41}$ (dB)	-22.48	-18.75		-13.98
Phase difference (°)	88.19°	89.09°		82.74°

with the result obtained in those reported previous work of literature [23–26]. The good compatibility of conductive coating on the PDMS elastomer substrate made it possible to maintain coupler's performance for flexible application.

## 4 Conclusion

Graphene-silver nanowires have been utilized as the conductive layer of the directional coupler with flexible PDMS elastomer as the substrate. The proposed design has been fabricated, measured, and compared with the simulation result. As a result, the proposed design has a compact size, low insertion loss, ability to be processed in low temperature and flexible. Within the frequency range of operation, the proposed coupler produces a good performance in both return loss,  $S_{11}$  and the isolation,  $S_{41}$  which are below the theoretical value of  $-10$  dB. Promising results of coupling value,  $S_{21}$  and insertion loss,  $S_{31}$  of  $-3 \pm 1$  dB indicate the ability of the coupler to equally split signal at the output ports for signal divider/combiner function. Also, a good surface resistivity value of  $25.8 \Omega \text{ cm}$  that is measured using four-point probe technique

**Table 4** Comparison results of previous flexible directional coupler literatures

Refs.	Material coating	Substrate	Freq (GHz)	S <sub>11</sub> (dB)	S <sub>21</sub> (dB)	S <sub>31</sub> (dB)	S <sub>41</sub> (dB)	Phase (°)	Size
[23]	Silver	Polyimide film	5.8	< -10	9.3	8.5	< -10	127	(30 × 74)mm <sup>2</sup>
[24]	Silver paint	Polyjet	12.165 and 11.805	-17.8	-2.12	-2.62	-23.9	90	(388 × 202×38) mm <sup>3</sup>
[25]	Metal finishing	Arlon 25	2.5	-31.5	-3 ± 0.78	-3 ± 1.7	< -40	180 ± 0.2°	18.3 mm × 19.65 mm
[26]	Thick metal claddings	(RT/Duroid 5880)	2.4	< -37	-3.5	< -3	< -10	90	-
This work	Graphene-silver nanowires	Polydimethylsiloxane, PDMS	2.4	-16.4	-4.03	-3.88	-22.48	88.19°	13.66 × 13.66 mm

shows the sustainability of the coupler's conductivity. Based on the presented method, graphene-silver nanowires fabrication enables excellent mechanical flexibility on PDMS and suitable for directional coupler design for wireless wearable applications.

**Acknowledgements** The authors wish to thank in particular, support from Research Management Centre MMU, SAP ID MMUI/160072 and Faculty of Engineering, Multimedia University.

## References

1. Hsu CL (2009) Dual-band branch line coupler with large power division ratios. In: Proceedings of Asia-Pacific microwave conference, pp 1–4
2. Jaafar E, Kashif M, Sahari SK, Ngaini Z (2018) Study of morphological, optical and electrical properties of graphene oxide thin film relative to the reaction time of synthesis. *J Telecommun Electron Comput Eng* 10(1):25–28
3. Hsu CL (2010) Design of quadrature hybrid with closely separated dual-passband using three-branch line coupler. In: Microwave proceedings (AMC), pp 1232–1235
4. Zhong YL, Tian ZM, Simon GP, Li D (2015) Scalable production of graphene via wet chemistry: progress and challenges. *Mater Today* 18(73)
5. Atif R, Shyha I, Inam F (2016) Mechanical, thermal, and electrical properties of graphene-epoxy nanocomposites—a review. *Polymers* 8(281)
6. Cao J, Chen C, Chen K, Lu Q, Wang Q, Zhou P, Liu D, Song L, Niu Z, Chen J (2017) High-strength graphene composite films by molecular level couplings for flexible supercapacitors with high volumetric capacitance. *J Mater Chem A* 5(29):15008–15016
7. Abdullah N et al (2016) Investigation on graphene based multilayer thin film patch antenna. In: 10th European conference on antennas and propagation (EuCAP), pp 1–5
8. Shen H, Zhang L, Liu M, Zhang Z (2012) Biomedical applications of graphene. *Theranostics* 2(3):283–294
9. Sierroset KA et al (2009) Stress-corrosion cracking of indium tin oxidecoated polyethylene terephthalate for flexible optoelectronic devices. *Thin Solid Films* 517:2590–2595
10. Akter T, Kim WS (2012) Reversibly stretchable transparent conductive coatings of spray-deposited silver nanowires. *ACS Appl Mater Interfaces* 4(4):1855–1859
11. Agar J, Durden J, Staiculescu D, Zhang R, Gebara E, Wong CP (2011) Electrically conductive silicone nano-composites for stretchable RF devices. In: Proceedings of Microwave Symposium, pp 1–4
12. Komoda N et al (2012) Printed silver nanowire antennas with low signal loss at high-frequency radio. *Nanoscale* 4(10):3148–3153
13. Johnson D (2016) Silver nanowires and graphene join forces for touch screen displays. *IEEE Spectrum Magazine*, September 2016
14. Sakhirul MS, Jusoh M, Sahadah A, Nor CM, Hasliza AR (2014) Embroidered wearable textile antenna on bending and wet performances for UWB reception. *Microwave Opt Technol Lett* 56:2158–2163
15. Salomen P, Hurme H (2003) A novel fabric WLAN antenna for wearable applications. In: Proceedings of IEEE APS international symposium, Columbus, OH, vol 2, pp 700–703
16. Abbott S (2002) Wet web coatings on transparent plastic foils. In: Klages CP, Gläser HJ, Aegerter MA (eds) Proceedings of the 4th international conference on coating on glass (4th ICCG), Braunschweig/Germany, p 395
17. Pozar DM (1998) *Microwave engineering*, 2nd edn. Wiley, New York, p 566
18. Sun Z (2013) Ag-stabilized few layer graphene dispersions in low boiling point solvents for versatile nonlinear optical application. *Carbon* 62:182–192

19. Jizat NM et al (2015) 3-dB branch-line coupler using coupled line radial stub with no restriction on coupling power. In: 2015 IEEE 12th Malaysia international conference on communications, MICC, pp 258–263
20. Jizat NM et al (2013) Beamforming network using dual band-dual beam reduced size butler matrices. *Radioengineering* 22(3):769–775
21. Lin CP, Chang CH, Cheng YT, Jou CF (2011) Development of a flexible SU-8/PDMS-based antenna. *IEEE Antennas Wireless Propagation Letter* 10:1108–1111
22. Schroder D, Hoboken NJ (2006) Semiconductor material and device characterization. IEEE Press; Wiley, Piscataway NJ
23. Kim S, Aubert H, Tentzeris M (2014) An inkjet-printed flexible broadband coupler in substrate integrated waveguide (SIW) technology for sensing RFID and communication applications. In: IEEE 2014 IEEE MTT-S International Microwave Symposium (IMS2014), June 1–6
24. Laplanche E et al (2017) A Ku-band diplexer based on 3 dB directional couplers made by plastic additive manufacturing. In: 2017 47th European microwave conference (EuMC), Nuremberg, 2017, pp 428–431
25. Slomian I, Wincza K, Staszek K, Gruszczynski S (2017) Folded single-layer 8 x 8 Butler matrix. *J Electromagnet Waves Appl* 31(14):1386–1398
26. Kilani MB, Nedil M, Kandil N, Nendini TA, Chang D (2012) Design of conformal microstrip Butler matrix at 2.4 GHz. In: 2012 IEEE international symposium on antennas and propagation proceedings, Chicago, USA, pp1–2

# Investigating the Possibility of Brain Actuated Mobile Robot Through Single-Channel EEG Headset



Mamunur Rashid, Norizam Sulaiman, Mahfuzah Mustafa, Sabira Khatun, Bifta Sama Bari, Md Jahid Hasan and Nawfan M. M. A. Al-Fakih

**Abstract** Brain-computer interface (BCI) is a fast-growing technology involving hardware and software communication systems that allow controlling external assistive devices through Electroencephalogram (EEG). The primary goal of BCI technology is to ensure a potential communication pathway for patients with severe neurologic disabilities. A variety of BCI applications have been presented in the last few decades which indicate that the interest in this field has dramatically increased. In this paper, the possibility of a brain-actuated mobile robot using single-channel EEG headset has been investigated. EEG data has been collected from Neurosky Mindwave EEG headset which consists of a single electrode. EEG feature in terms of power spectral density (PSD) has been extracted and classified this feature using the support vector machine (SVM). Then the classified signal has been translated into three devices command to control the mobile robot. This mobile robot can be driven in three directions namely forward, right and left direction. Data collection from EEG headset and sending commands to a mobile robot, the entire process has been done wirelessly.

**Keywords** Electroencephalogram (EEG) · Brain-computer interface (BCI) · Neurosky · Mobile robot

## 1 Introduction

Generally, healthy users can operate the robots with a conventional input device such as a keyboard, a mouse, or a joystick. These devices are, however, difficult to use for elderly or disabled individuals. For this reason, some special interfaces like sip-and-puff systems, single switches, and eye-tracking systems have been proposed [1]. However, these special interfaces do not work for some severely disabled

---

M. Rashid (✉) · N. Sulaiman · M. Mustafa · S. Khatun · B. S. Bari · N. M. M. A. Al-Fakih  
Faculty of Electrical & Electronics Engineering, Universiti Malaysia Pahang, 26600 Pekan,  
Pahang, Malaysia

M. J. Hasan  
Faculty of Mechanical & Manufacturing Engineering, Universiti Malaysia Pahang, 26600 Pekan,  
Pahang, Malaysia

© Springer Nature Singapore Pte Ltd. 2020

A. N. Kasruddin Nasir et al. (eds.), *InECCE2019*, Lecture Notes in Electrical Engineering 632, [https://doi.org/10.1007/978-981-15-2317-5\\_49](https://doi.org/10.1007/978-981-15-2317-5_49)

579

people with illnesses such as amyotrophic lateral sclerosis (ALS). These severely disabled individuals cannot convey their intentions or operations to robots with these interfaces. Therefore, although autonomous systems exist, it is still necessary to develop alternative interfaces that can be used by the severely disabled population for communication with autonomous systems. BCIs have been developed to address this challenge. The basic idea of BCI is to translate user-produced patterns of brain activity into corresponding commands for external devices. When a mobile robot is operated by the user's brain signal then the system is termed as BCI mobile robot.

A large number of articles have been published relating to the BCI mobile robot in the last few decades but very few articles have been found relating to the controlling mobile robot using single-channel EEG headset. Stephygraph and Arunkumar [2] proposed an EEG-based wireless BCI mobile robot which can be controlled by human eye blink strength and attention level. The motor is started and moved forward by three consecutive blinks and turn to the left and right directions by the left blink and right blink respectively. The most important issue of this methods is to generate left blink and right blink separately. Ruşanu et al. [3] presented the development of controlling a BCI mobile robot by the eye-blinks strength. Basically, their system was based on the integration between the NI myRIO system using LabVIEW programming environment and a NeuroSky headset with a wireless connection to a computer. Subject may able to drive a mobile robot to forward, backward, left and right direction. The author in [4] proposed a method to control a prosthetic moving robotic gripper with the use of brain waves. They have taken into consideration the blink strength and attention level to control this system such that long blink—forward, quick blink—backward, stress blink—stop, two blink—move left, two stress blink—move right, normal attention—pick and strength attention—place. In reference to [5], a preliminary assessment of the NeuroSky's sensor in detecting drowsiness has been presented. The experiment was conducted with 14 participants and the primary result demonstrates that the brainwaves used in the analysis fail to detect drowsiness. An attention level indicator system was proposed by Kan et al. [6] to monitor one's attention level especially for Attention Deficient Disorder (ADD) patient. Here, NeuroSky Mindwave mobile headset, MATLAB, and Arduino UNO were integrated to implement the project. Finally, they figure out higher attention on visual-based activity than audio or hands-on activities from their experiment. Bright et al. [7] developed EEG-based BCI prosthetic arm with the help of Neurosky Mindwave headset to yield the two main movements of fingers in the arm: Flexion and Extension. The prosthetic arm module consists of Arduino coupled with servo motors to perform the command. The flexion and extension of fingers can be successfully controlled with an accuracy of 80%.

In this paper, controlling a mobile robot using EEG signal collected from low-cost single-channel EEG headset has been investigated. Power spectral density (PSD) and support vector machine (SVM) have employed for feature extraction and classification. Finally, a prototype has also been designed to test the overall performance. This paper has been organized in the following sections i.e. Sects. 2 and 3 discusses issues related to methodology, results and discussion respectively; finally, Sect. 4 deals with the conclusion.

## 2 Methodology

A BCI system comes with five elements including signal acquisition, signal preprocessing, feature extraction, classification as well as device command [8]. Figure 1 shows the complete flow chart of the conducted experiment where the first step was the subject selection for EEG data collection.

Then, suitable EEG capturing device has been selected according to the literature review. According to the literature review, the most user-friendly and cheapest single-channel EEG headset is Neurosky Mindwave. No need to use any conductive gel and the data can be captured wirelessly with this device. A measurement protocol has been designed to capture EEG data in the right manner. After data collection, the first step is to pre-process the EEG data. EEG data affected by the eye blinking has been considered as artifacts and during the pre-processing step, the data containing eye blinking effects have been omitted. Then, the most suitable EEG feature in term of PSD has been extracted according to the literature review. Nowadays machine learning is used to solve different types of complex problem such as image and signal classification, natural language processing, image segmentation, etc. [9]. Hence, the selected features have been classified using different machine learning algorithms. After EEG signal classification, a translational algorithm has been developed to convert the classifier output into device commands. Finally, a prototype has been designed and tested.

### 2.1 Data Acquisition Protocol

The first step of this experiment was the subject selection for data acquisition. Although the targeted user's of this technology are physically disabled patients, initially EEG data from healthy individuals have been collected for this experiment. If the error-free complete BCI system is achieved by the healthy subject, then the experiment will be conducted with the data from disabled patients. Total six healthy subjects have contributed to captured EEG data and Table 1 shows their description.

During the selection of EEG capturing equipment, some factor like price, electrode number, type of electrode and the complexity level have been considered. Finally, Neurosky Mindwave EEG headset has been selected due to its low price (around \$100), single dry electrode and easy use. This EEG headset contains one electrode that is placed on the FP1 area of the human brain. The FP1 area of the brain is shown in Fig. 2. There is a reference electrode which is connected with the ear lobe. This EEG amplifier captures the raw EEG data at 512 Hz sampling rate.

After subject and equipment selection, a measurement protocol has been developed shown in Fig. 3. Here, an android mobile app called eegID in the mobile phone and the Neurosky Mindwave is paired through the Bluetooth. Three classes of mental exercise have been considered in this research namely relax (do nothing), quick



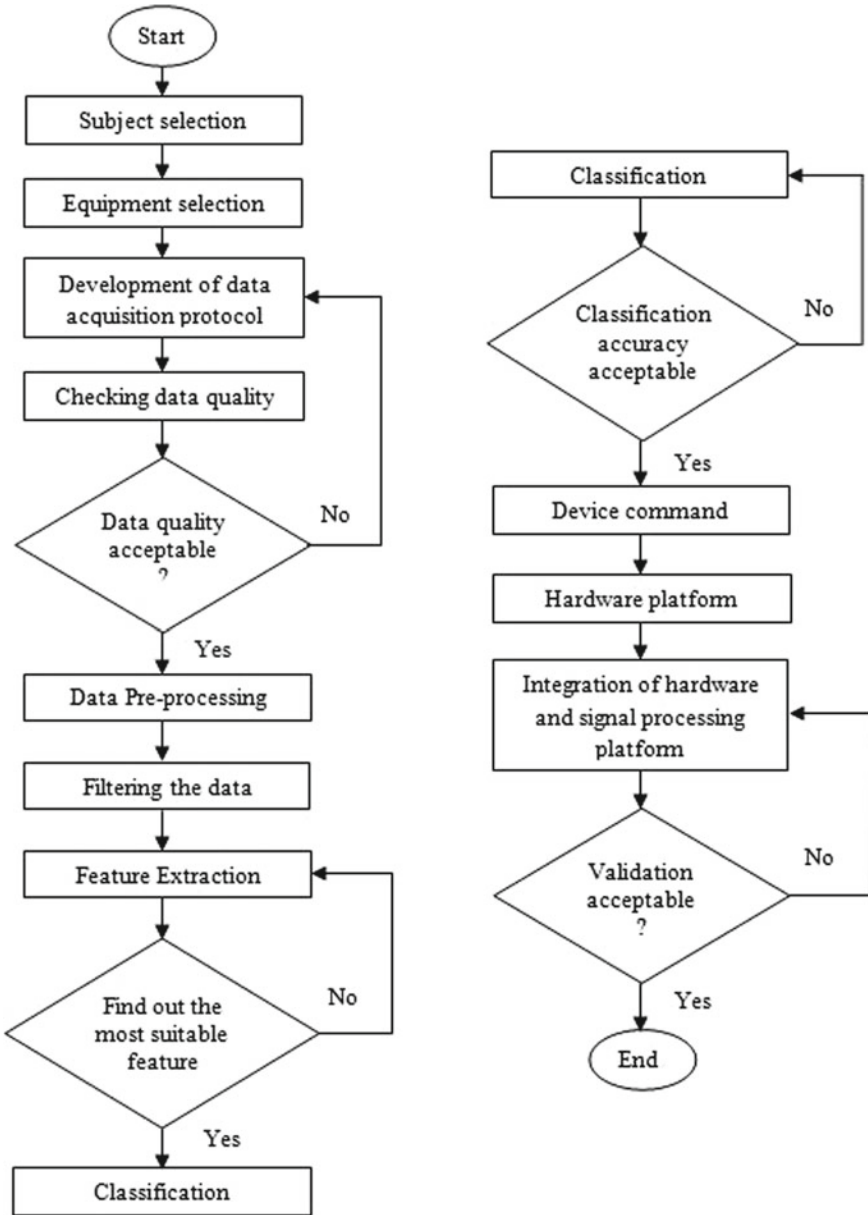
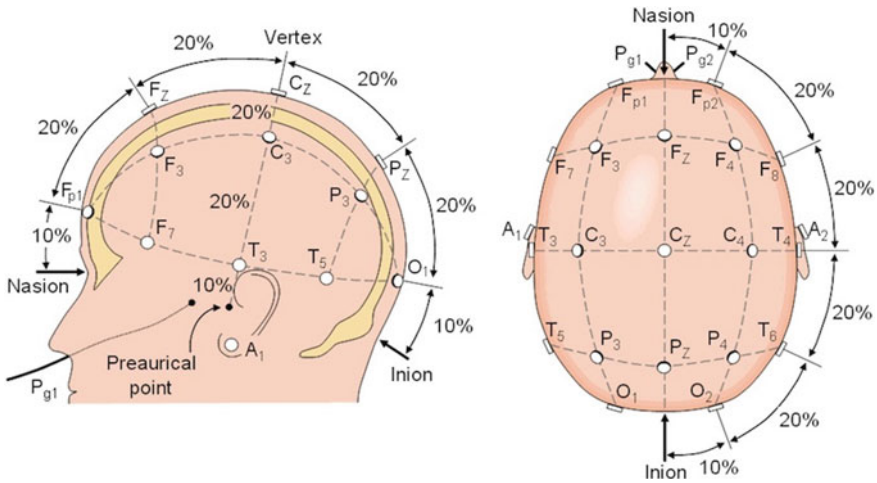


Fig. 1 Complete flow chart of the conducted algorithm

**Table 1** Subjects for EEG data collection

Subject	Sex	Age	Subject	Sex	Age
Subject-1	Male	25	Subject-4	Male	19
Subject-2	Female	23	Subject-5	Male	22
Subject-3	Male	21	Subject-6	Female	20



**Fig. 2** Electrode positioning system

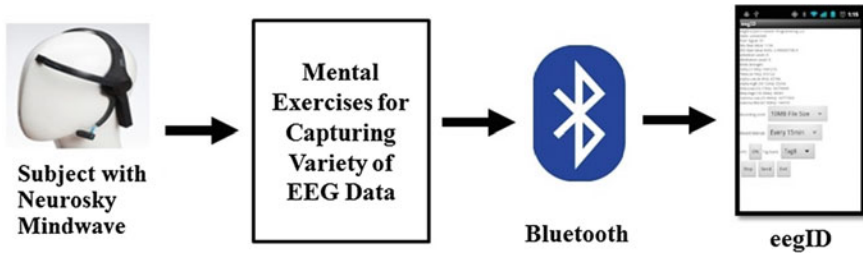


**Fig. 3** EEG data acquisition protocol

math solving and playing a game. During the data collection of relaxing state, subjects were said to sit on the chair very comfortable and avoid the movement of the whole body. In case of quick math solving, subjects were said to solve the math problems randomly as quick as possible from the website [10]. On the other hand, during playing game, subjects were said to play an android racing game on a smartphone. Duration of all the data was 30 s.

## 2.2 Feature Extraction and Classification

After collecting EEG, the raw data have been plotted to see the effect of an eye blink. The amplitude of EEG and the number of missing samples in raw data have also been monitored. EEG data affected by the eye blinking has been considered as artifacts and during the pre-processing step, the data containing eye blinking effects have been omitted. Generally, there are five frequency bands for each EEG channel, which are delta (0.5–4 Hz), theta (4–8 Hz), alpha (8–13 Hz), beta (14–30 Hz) and gamma (30–45 Hz) [11]. Bandpass Butterworth filter has been applied to separate alpha, beta and gamma signals and the order of the filter was 5th. In this research, the EEG data was filtered into alpha, beta and gamma band. The frequency range and activity of EEG bands have been shown in Table 2.

In this experiment, power spectral density has been used to extract the feature. With the help of fast Fourier transformation (FFT), the power spectrum of the EEG alpha, beta, and gamma-band has been calculated. The Eq. (1) for FFT [12] and Eq. (2) for power spectral density are shown as follow.

$$X(k) = \sum_{n=1}^{N-1} X(n)W_N^{kn}; K = 0 \dots N - 1 \quad (1)$$

$$W_N = e^{-j\frac{2\pi}{N}}$$

$$PSD = |X(k)|^2 = \left| \sum_{n=0}^{N-1} x(nTs)e^{-j2\pi nk/N} \right|^2 \quad (2)$$

After calculating the average PSD of alpha, beta, and gamma band, we have made a feature vector to apply the machine learning algorithm. To classify the signal accurately we have applied support vector machine( SVM), K-nearest neighbor (K-NN) and linear discriminant analysis (LDA). The best accuracy has appeared with SVM.

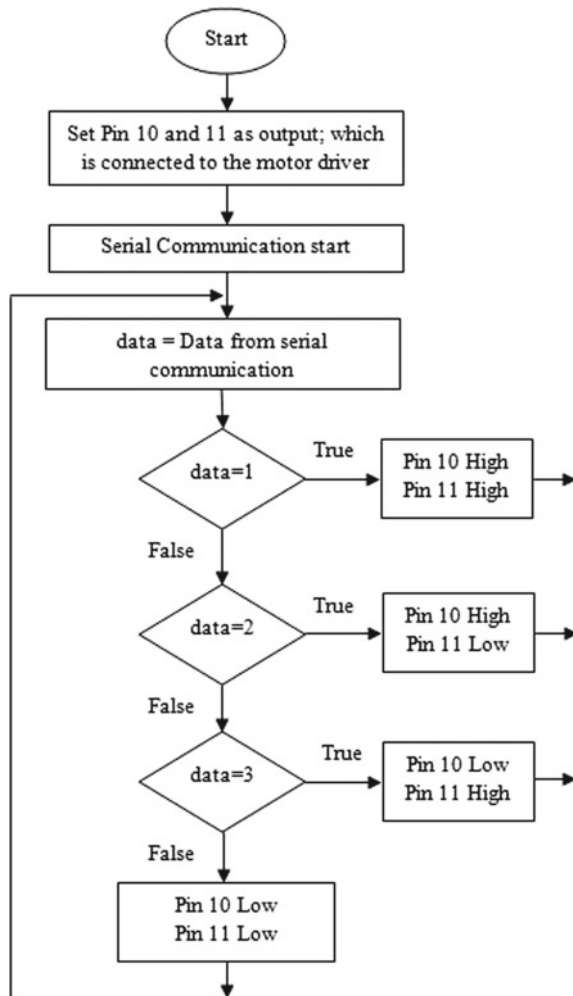
**Table 2** EEG bands with their activity [8]

Band	Frequency ( Hz)	Activity
Delta	0.5–4	Deep sleep
Theta	4–7	Drowsiness, light sleep
Alpha	8–13	Relaxed
Beta	14–29	Active thinking, alert
Gamma	30–50	Hyperactivity

### 2.3 Translational Algorithm and Device Command

After the classification of EEG data, the classified results need to convert into device commands. This can be achieved with the help of a translational algorithm. The flow chart of the translational algorithm is shown in Fig. 4. EEG data of three types of mental exercise have been captured for this experiment namely relax, quick math solving and playing a game and these exercises have been denoted as 1, 2 and 3 respectively during training the classifier. According to the translational algorithm, the classifier outputs 1, 2 and 3 represent the motor direction as go forward, right and left respectively. If the mental exercise is in relax state then the classifier output will be “1”. In this case, the output pin 10 and 11 of Arduino UNO will be “High”,

Fig. 4 Flow chart of the translational algorithm



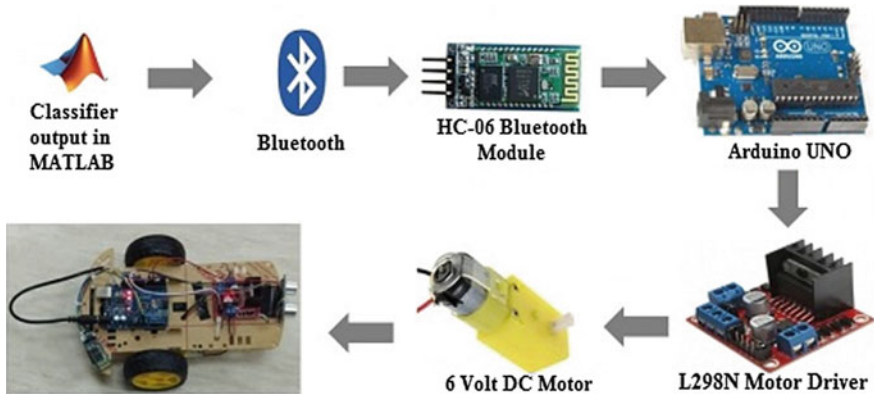


Fig. 5 Components of the mobile robot

resulting in the dc motor will be directed to go forward. If the subjects solve math quickly, the classifier output will be “2”. In such a case, the output pin 10 and 11 will be “High” and “Low” respectively. This phenomenon enables the dc motor to go in the right direction. Finally, If the mental state in “playing game” state, the classifier output will be “3”. In such a case, the output pin 10 and 11 will be “Low” and “High” respectively. This phenomenon enables the dc motor to go in the left direction.

## 2.4 Hardware Setup

In order to make the hardware platform, the components which have been used are shown in Fig. 5. This part consists of HC-06 Bluetooth module, Arduino UNO, L298N motor driver, 6 Volt DC motor, chassis, wheel, battery, switch, connecting wires.

In this part, the classifier output from MATLAB is transferred to the Arduino UNO by Bluetooth Module. The Arduino UNO converts the classifier output into device command using the pre-loaded translational algorithm in the Arduino UNO. The motor driver controls the dc motors using these device commands. Figure 6 shows the complete connection diagram of hardware set up.

## 3 Result and Discussion

The overall performance of the mobile robot greatly depends on classification accuracy and the classification accuracy depends on the selection of the most suitable feature. In our previous experiment, we have analyzed power spectral density, spectral centroid, and log energy entropy. According to our analyzed result and the latest

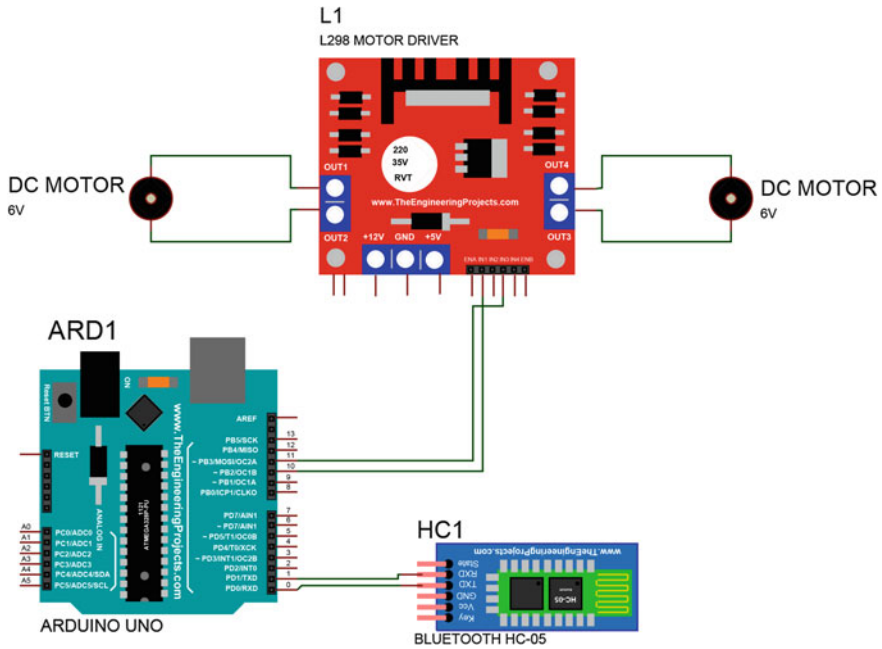


Fig. 6 Connection diagram of the mobile robot

related research (see Table 3), PSD gives better accuracy among those features. To classify the signal accurately we have applied support vector machine( SVM), K-nearest neighbor (K-NN) and linear discriminant analysis (LDA). The best accuracy has been achieved with SVM. The highest classification accuracy was 92% using quadratic SVM. The classification accuracy has also been evaluated by confusion matrix shown in Figs. 7 and 8. The confusion matrix in Fig. 7 shows the number of observations where each class has a total of eighteen observations. Among eighteen observations, class 1, 2 and 3 can identify accurately 16, 17 and 17 observations respectively.

Figure 8 shows the true positive rate (TPR) and false-positive rate (FPR) where TPR for class 1, 2 and 3 are 89%, 94%, and 94% respectively. Similarly, the FPR for class 1, 2 and 3 are 11%, 6%, and 6% respectively. Table 3 shows the summary

Fig. 7 Number of observations

		Model 1.2		
		1	2	3
True class	1	16		2
	2		17	1
	3		1	17
		1	2	3
		Predicted class		

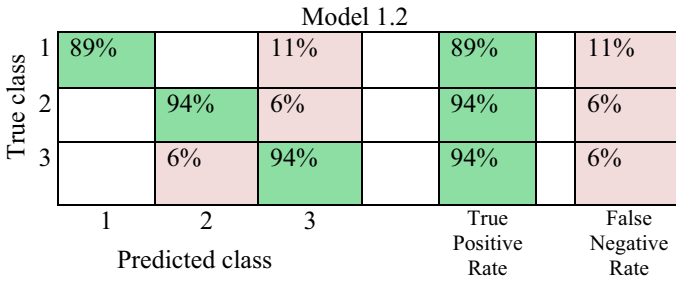


**Fig. 8** True positive rate and false negative rate

**Table 3** Comparison table of related methods

Reference	No. of class	Feature	Classifier	Accuracy (%)
[13]	2	PSD	SVM	92.26
[14]	2	PSD	KNN	70
[15]	NA	Wavelet analysis (RBF)	ANN	84.5
[16]	2	CSP	SVM	74.17
[17]	5	AR and FFT	SVM	88.51
[18]	2	PSD	SVM	85.4
[19]	5	Entropy	KNN	82.87
[20]	5	Entropy	KNN	83
[21]	3	PSD	SVM	63
Proposed method	3	PSD	SVM	92

of some related researches. From this table, it is clear that PSD with SVM provides better classification accuracy.

After integration of the signal processing and hardware platform, the prototype of a mobile robot has been prepared for the testing. This robot has been tested in an off-line manner. The mobile robot can follow three directions successfully. There are some issues that need to solve in order to make a complete EEG based BCI mobile robot. First of all, this mobile robot can follow only three commands which are go forward, right and left but an effective mobile robot should have at least eight commands which are the start, stop, go forward, go backward, go right, go left, speed up and speed down. To create more device commands, EEG data from various types of mental exercises should be captured. But Neurosky Mindwave is unable to capture various types of mental exercises due to having a single channel only. Hence, EEG headset of more electrodes should be used which is capable of capturing P300, steady-state visual evoked potential (SSVEP), and motor imagery signal. Secondly, the controlling of this mobile robot is not real-time. Hence, it should be controlled in real-time to make the system more valid. Although the targeted users of this technology are physically disabled patients, here EEG data from healthy

subjects have been used. Moreover, the EEG data have been captured in a controlled environment by highly trained subjects. Hence, the performance will be unstable when the data will be collected from the subjects without training.

## 4 Conclusion

In this paper, signal processing and hardware platform of EEG based mobile robot have been presented. In the signal processing platform, PSD and SVM have been used as feature and classifier respectively. The classification accuracy was 92%. The complete mobile robot prototype has been successfully tested. This mobile robot can follow three directions namely forward, right and left. To make it capable of following more commands including start, stop, forward, backward, right, left, speed up and speed down, multi-channel EEG capturing device should be used.

**Acknowledgements** The author would like to acknowledge the great supports by the Faculty of Electrical & Electronics Engineering as well as Universiti Malaysia Pahang for providing financial support through research grant PGRS 190326.

## References

1. Bi L, Fan X-A, Liu Y (2013) EEG-based brain-controlled mobile robots: a survey. *IEEE Trans. Human-Machine Syst.* 43:161–176
2. Stephygraph LR, Arunkumar N (2016) Brain-actuated wireless mobile robot control through an adaptive human-machine interface. In: Suresh L, Panigrahi B (eds), *Proceedings of the international conference on soft computing systems (Advances in intelligent systems and computing)*, vol 397. Springer, New Delhi
3. Ruşanu OA, Cristea L, Luculescu MC, Cotfas PA (2018) A brain-computer interface based on the integration of NI myRIO development device and NeuroSky mindwave headset. *IOP Conf Ser Mater Sci Eng* 444
4. Prathibha R, Swetha L, Shobha KR (2017) Brain computer interface: design and development of a smart robotic gripper for a prosthesis environment. In: *2017 International conference on networks & advances in computational technologies (NetACT)*, pp 278–283
5. Patel K, Shah H, Dcosta M, Shastri D (2017) Evaluating NeuroSky's single-channel EEG sensor for drowsiness detection. Presented at the (2017)
6. Kan DPX, Lim VWW, Lee PF (2015) Signal conversion from attention signals to light emitting diodes as an attention level indicator. In: Su FC, Wang SH, Yeh ML (eds) *IFMBE proceedings of the 1st global conference on biomedical engineering & 9th Asian-Pacific conference on medical and biological engineering*, vol 47. Springer, Cham
7. Bright D, Nair A, Salvekar D, Bhisikar S (2016) EEG-based brain controlled prosthetic arm. In: *Conference on advances in signal processing, CASP 2016*, pp 479–483 (2016)
8. Rashid M, Sulaiman N, Mustafa M, Khatun S, Bari BS (2019) The classification of EEG signal using different machine learning techniques for BCI application. In: Kim J-H, Myung H, Lee S-M (eds) *Robot intelligence technology and applications. RiTA 2018. communications in computer and information science*, vol 1015. Springer, Singapore, pp 207–221



9. Biswas T, Ahmad Fauzi MF, Abas FS, Nair HKR (2018) Superpixel classification with color and texture features for automated wound area segmentation. 2018 IEEE Student Conference on Research and Development (SCORED), pp 1–6
10. No Title, <https://arithmetic.zetamac.com/>
11. Atkinson J, Campos D, John Atkinson DC (2016) Improving BCI-based emotion recognition by combining EEG feature selection and kernel classifiers. *Expert Syst. Appl.* 47:35–41
12. Otsuka T, Watanabe K, Hirano Y, Kubo K, Miyake S, Sato S, Sasaguri K (2009) Effects of mandibular deviation on brain activation during clenching: an fMRI preliminary study. *Cranio J. Craniomandib. Pract.* 27:88–93
13. Liu Y, Yu M, Zhao G, Song J, Ge Y, Shi Y (2017) Real-time movie-induced discrete emotion recognition from EEG signals. *IEEE Trans Affect Comput*, 1
14. Bastos-Filho TF, Ferreira A, Atencio AC, Arjunan S, Kumar D (2012) Evaluation of feature extraction techniques in emotional state recognition. In: 4th International conference on intelligent human computer interaction (IHCI 2012)
15. Srinivas V, Rama V, Rao CBR (2016) Wavelet based emotion recognition using RBF algorithm. *Int J Innov Res Electr Electron Instrum Control Eng* 4:29–34
16. Pan J, Li Y, Wang J (2016) An EEG-based brain-computer interface for emotion recognition. In: Proceedings of the international joint conference on neural networks
17. Lokannavar S, Lahane P, Gangurde A, Chidre P (2015) Emotion recognition using EEG signals. *Int J Adv Res Comput Commun Eng* 4:118–127
18. Jatupaiboon N, Pan-Ngum S, Israsena P (2013) Emotion classification using minimal EEG channels and frequency bands. In: Proceedings of 2013 10th international joint conference on computer science and software engineering (JCSSE 2013), pp 21–24
19. Murugappan M (2011) Human emotion classification using wavelet transform and KNN. In: 2011 international Conference on pattern analysis and intelligence robotics. IEEE, pp 148–153
20. Murugappan M, Nagarajan R, Yaacob S (2011) Combining spatial filtering and wavelet transform for classifying human emotions using EEG signals. *J Med Biol Eng* 31:45–51
21. Chanel G, Kierkels JJM, Soleymani M, Pun T (2009) Short-term emotion assessment in a recall paradigm. *Int J Hum Comput Stud* 67:607–627

# Campus Hybrid Intrusion Detection System Using SNORT and C4.5 Algorithm



Slamet, Izzeldin I. Mohamed and Fahmi Samsuri

**Abstract** The rapid development of the internet greatly helps human work. However, the number of information system security incidents has risen sharply, so that in fact the sides of human life are threatened. Detection techniques against attacks on computer networks must be continuously developed so that integrity, availability, and confidentiality on a computer network become more secure. In general, intrusion detection systems currently use two detection methods, namely anomaly detection, and misuse detection, which both have their own deficiencies. In this paper, the authors built a Hybrid Intrusion Detecting System combines anomaly detection system with the misuse detection system. Snort is used as the basis of misused detection module and Algorithm C4.5 detector is used to construct an anomaly detection module. This system works by creating alerts built from an engine that reads the parameters in the attacker's IP address. Webmin is used to simplify rule management. Whereas for analyzing logs (attack history), an ACID (Analysis Console for Intrusion Databases) is used. Attack and detection testing are carried out in the campus network of Institut Bisnis dan Informatika Stikom Surabaya. The system implementation uses a PC Router with the Ubuntu 18.04 Linux as the operating system. As a result of implementing this system: the signature of attacks as misuses detection module uses to detection the known attacks; unknown attacks can be detected by the anomaly detection module; signature of attacks that are detected by Anomaly Detection System module extracted by signature generation module, and maps the signatures into snort rules.

**Keywords** Intrusion detection · Attack · Snort · C4.5

---

Slamet (✉)

Faculty of Technology and Information, Department of Information Systems, Institut Bisnis dan Informatika Stikom Surabaya, Surabaya, Indonesia  
e-mail: [slamet@stikom.edu](mailto:slamet@stikom.edu)

I. I. Mohamed · F. Samsuri

Faculty of Electrical and Electronic Engineering, University Malaysia Pahang, Kuantan, Malaysia

© Springer Nature Singapore Pte Ltd. 2020

A. N. Kasruddin Nasir et al. (eds.), *InECCE2019*, Lecture Notes in Electrical Engineering 632, [https://doi.org/10.1007/978-981-15-2317-5\\_50](https://doi.org/10.1007/978-981-15-2317-5_50)

591

## 1 Introduction

Speed of internet development invites new problems in network security. It becomes an important subject to be researched and improved, so it does not become a serious problem for humans due to the possibility of attacking in the network [1].

In-depth insight into network attacks from campus network users, including detecting a number of incomplete and unclear network data, vague data from campus network users can help provide comprehensive evidence for school administrators in making decisions. It allows preventive actions against unwanted network attacks. In a broader perspective, this condition can create a learning environment that is beneficial for students and will have a major influence on the environment of higher education [2].

Intrusion detection systems (IDS) are usually used to prevent network attacks. Based on how to detect, there are two ways of intrusion detection, namely anomaly-based detection and misuses-based detection [3].

In misuses-based detection [4], there is a database that contains many known signatures of attacks. The content of the database in IDS is compared with many known signatures data collected by the IDS. A notification will be generated if a match is found. However, if there is an event that does not match one of the attack models, the event will be considered as part of legitimate activity. The advantage of misuses-based systems produces very few positive errors. But the disadvantage is cannot detect attacks that have never been known before, and cannot even detect new variations of known attacks.

In addition, another detection model is anomaly-based detection [4]. This detection model is behavior-based. The behavior-based means that all activities are assumed to be dangerous activities and all attacks are part of abnormal activities. After that, this model builds a normal model of system behavior, it looks for anomalous activities that are not in accordance with the specified model.

However, because it is not possible to describe all user activities in the system that lead to activities with a relatively high false-positive rate, and most IDSs currently use one of two detection methods [4], we combine the method of misuse-based detection with anomaly detection to improve the performance of IDS into the latest research on hybrid IDS.

## 2 Related Works

In [5], Peng et al. propose two stages in hybrid intrusion detection and visualization system that utilizes the ability of signature and anomaly-based detection methods. This hybrid system can identify known and unknown attacks on system calls. However, the results of evaluating the system disappeared in the paper. This work is more like an introduction to how to implement several stages of intrusion detection to improve IDS detection capabilities. Based on the idea of integrating the excess

false positives of low IDS-based signatures and the advantages of anomaly intrusion detection systems to detect new attacks or unknown attacks, Hwang et al. proposed a new hybrid intrusion detection system (HIDS) in [6].

Evaluation of the three IDSs used by Wang et al. concluded that the low computing resources used by Snort and the rules succeeded in accurately classifying legitimate and malicious network traffic. Researchers have evaluated the performance of three IDSs in a simulated environment consisting of physical and virtual computers. Snort has a negative impact on network traffic using more than two other IDSs tested in the experimental results [7].

Snort IDS was used to conduct experiments by Bulajoul et al. [8] in designing real networks. The results show Snort IDS weaknesses in processing packets at high speed and it easily dropping packets without analyzing them accurately. The conclusion of this study is that Snort IDS failed to process network traffic at high speeds and higher packet reduction rates. As a solution to reduce the decline rate of the packet, the researchers introduced parallel IDS. A dynamic traffic awareness histogram is used to improve the performance of IDS Snort. The most effective way has been discussed in this study is using the order of attack signature rules and sequence of rules. The approach is to use a histogram in predicting the next signature rule and the order in the field. The simulation shows that the proposed approach can significantly improve the performance of Snort [9].

Regardless of the amount of research conducted to date, there are still fewer works that investigate the performance of network IDS in campus networks. To this extent, this paper has made further use of Snort IDS as a system capable of detecting known attacks and C45 data mining techniques are used to detect unknown attacks. Thus, the performance of the monitoring and assessment process throughout the campus network can be improved in the direction of developing learning mechanisms for detecting unknown attacks.

### **3 Hybrid Intrusion Detection System**

There are two functions in Hybrid IDS, the anomaly detection technique detects unknown attacks, and the signature detection technique detects known attacks.

#### ***3.1 Component of Hybrid Intrusion Detection System***

The Hybrid Intrusion Detection System must be able to detect a known and unknown attack on the campus network. The components that must exist in the Hybrid Intrusion Detection System include Snort, rule module, alert module, and C4.5 Algorithm Detector.

### **3.2 *Intrusion Detection System (IDS)***

Judging from the way of working in analyzing whether the data packet is considered as infiltration or not, IDS is divided into 2 based: knowledge-based or misuses detection and behavior-based or anomaly detection [10].

Knowledge-based IDS can recognize data flow on a computer network by tapping a data packet, then comparing it with the rules in the IDS database that contain signs of an attack packet. If the captured data packet has the same pattern or at least one pattern in the IDS database rules, then this packet will be considered as an attack. However, if the data packet captured does not have the same pattern as in the pattern of the IDS rule database, then this data packet is not considered as an attack in the network [10].

Behavior-based or anomalies based can detect data flow by observing irregular relationships in a network system, or observe any deviations from normal conditions. For example, there is a sharp increase in memory usage of Server, or there is an IP Address with multiple connections using a huge capacity of bandwidth at the same time and same place. This condition is considered a deviation which is then based on the type of IDS anomaly considered as an attack.

While seen from the ability to detect intrusions on the network, IDS is divided into two based, namely: host-based and network-based. Host-based is able to detect only the host where IDS is implemented, while network-based IDS is able to detect all hosts that are in a network with hosted IDS implementation. This paper specifically uses network-based IDS and knowledge-based [11].

## **4 Research Methods**

The steps used in completing this study are as shown in Fig. 1.

The research method that used is the Security Policy Development Life Cycle (SPDLC) method [12]. With SPDLC, the network system development life cycle is defined in a number of phases, including analysis, design, implementation, enforcement, and enhancement.

### **4.1 *Stage of Analysis***

The SPDLC model begins its network system development cycle at the analysis stage. At this stage, the system specifications will be analyzed, the tools needed such as software and hardware needed for the IDS system.

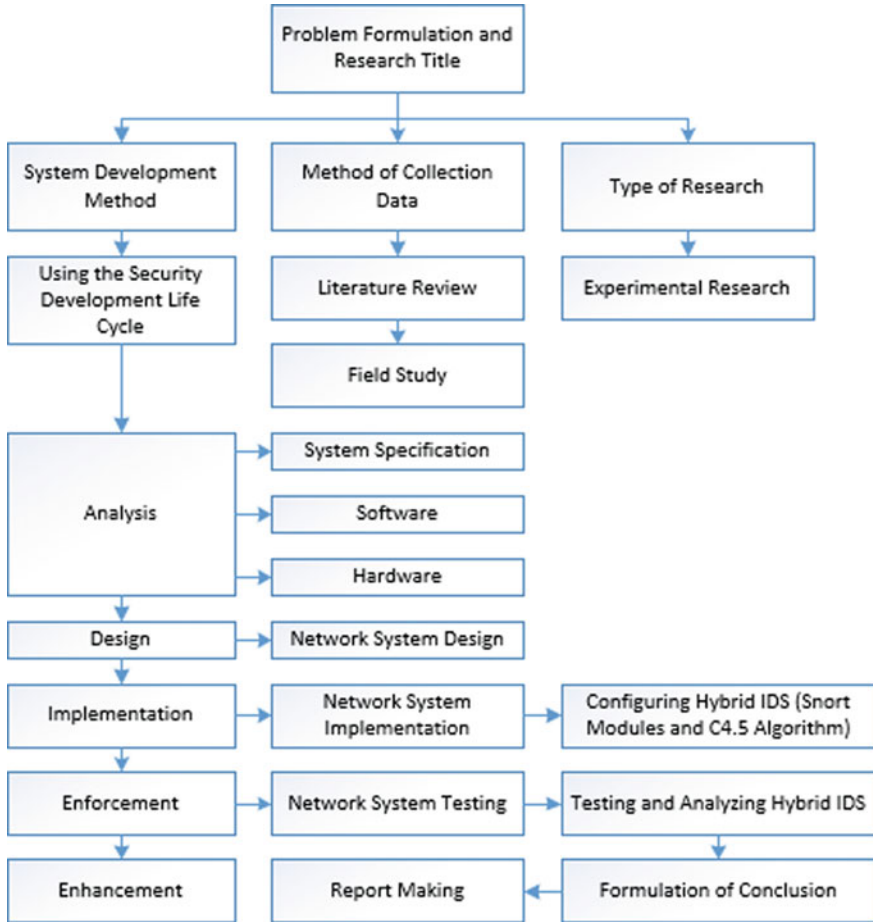


Fig. 1 Research flow chart

### 4.2 Stage of Design

This design is based on concepts and descriptions that explain the actual device. Intrusion detection system developed by the Network Intrusion Detection System (NIDS) type. This is because this type of IDS is placed in a strategic place/point or a point in a network to supervise the traffic that leads to and originates from all devices (devices) in the network. All scanning from the outside and inside the network is carried out by the scanning process ideally. The following (Fig. 2) is the design of topology when applied to Hybrid IDS.

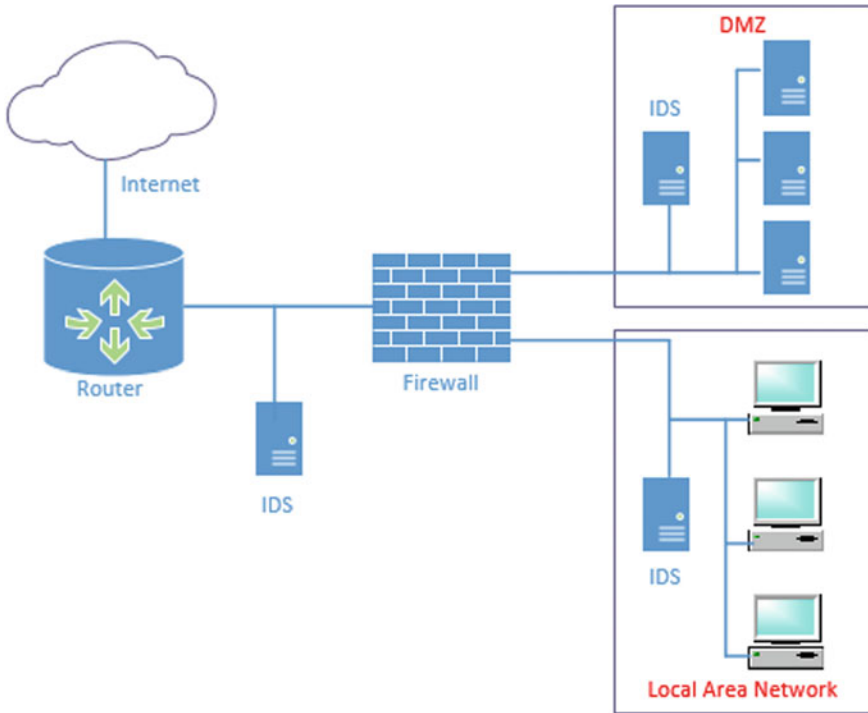


Fig. 2 Network topology design

### 4.3 Stage of Implementation

The next phase is the implementation of a detailed topology design and system design. Design details are used as instructions or guidelines for the implementation stage so that the system built becomes relevant to the system that has been designed.

**Implementation of Hybrid Intrusion Detection System.** The main modules and supporting modules are needed to build the functional requirements of the Hybrid Intrusion Detection System. The main modules are: snort engine, snort rule, C4., and alert module. While supporting modules are: ACID (event management) and Webmin (rule management).

The target of implementing Hybrid Intrusion Detection System on Ubuntu Linux systems is 18.04. The block diagram of the Hybrid Intrusion Detection System designed as follows.

Intrusion detection system model is designed in this paper, combined with the advantages of misuses detection and anomaly detection technology, instead of the single detection technology. As shown in Fig. 3, it includes misuse detection module based on snort, anomaly detection module based on the Decision Tree C4.5, and alarm log. Packet data (known attack) is used by the Snort to detect known malicious

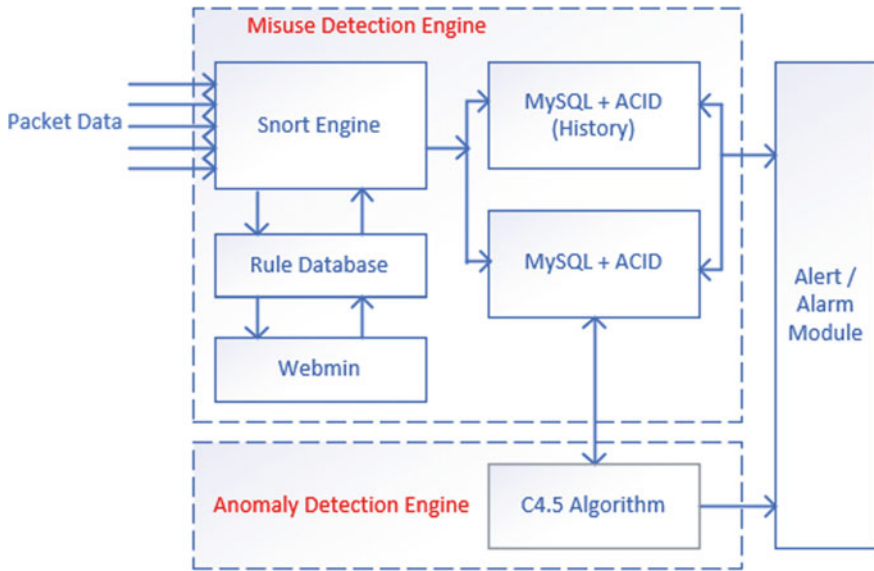


Fig. 3 Hybrid intrusion detection system infrastructure

attacks, and traffic classification and detection of unknown attack used for Decision Tree C4.5 [13]. The detailed testing process as depicted in Fig. 4.

When detecting, matching the characteristic of network traffic with the rule database, once matched, we considered it is an intrusion behavior, in this way, the

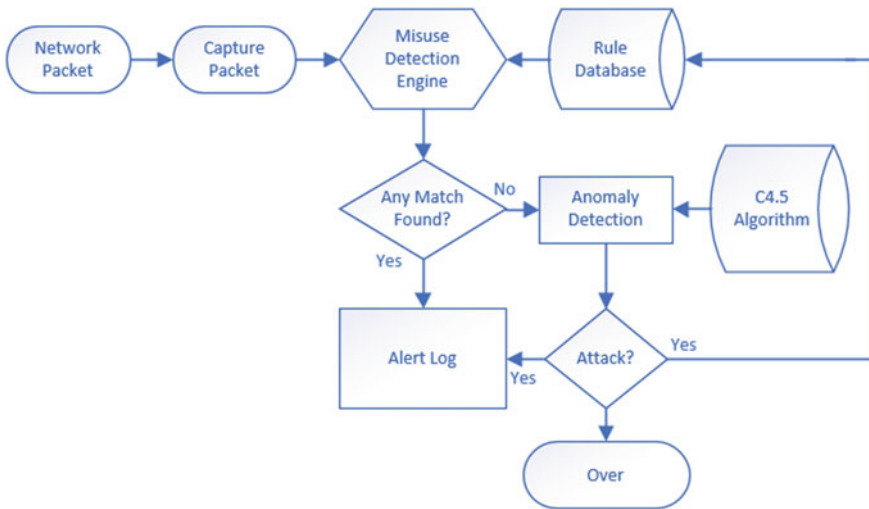


Fig. 4 The flow of the testing process



known malicious attacks can be detected rapidly and accurately. Once found malicious behaviors, will immediately alert, when don't match, the data packets will send to the anomaly detection module, if discovery it is unusual, and alarm, at the same time to save the network events into the feature database; if not, then add data to the training set in the database, to ensure the real-time update of the database. It is able to accurately detect known attacks, but also can discover the new, unknown attacks, and achieve the goal of all-round protect the network security.

**Rule Database.** This module provides rules in the form of pattern type attacks. This rule is a text file that is compiled with certain rules [14, 15].

**Snort Engine.** This module serves to read data packages and compare them with rule databases, if the data package is punished as an intrusion/attack, then the Snort engine will write it to an alert (in the form of a log file) and to the database (which is used in this experiment is a MySQL database) [14, 15].

**Alert.** This section is a record of attacks on a log file.

**Webmin.** Webmin (<http://www.webmin.com/>) which has been added to the snort rule module is used to manage the rule. Which Rule will be enabled and disabled can be set via Webmin, it can even be used to add rules manually with a web-based editor.

**ACID (Analysis Console for Intrusion Databases).** ACID (<http://www.cert.org/kb/acid>) is used to manage security event data, the advantages of using ACID include: log-logs that were hard to read become easy to read, data can be searched and filtered accordingly with certain criteria, Managing Large Alert Databases (Deleting and Archiving), and for certain cases can refer alerts on database security sites such as Securityfocus, CVE, arachNIDS.

**C4.5 Algorithm.** Intrusion detection algorithm based on C4.5 is divided into three steps [13]:

Step 1: Make a decision tree, Algorithm: C4.5 Trees produce decision trees from the provided training data. Input: T training sample set, candidate attribute collection, attribute-list. Output: A Decision tree.

- (a) Create N root node.
- (b) If T belongs to the same category C, then return N as a leaf node then mark it as class C.
- (c) If the remaining sample T is less than the given value or the list of attributes is empty, return N as the leaf node, then mark it as the most frequently occurring category.
- (d) Calculate the information acquisition ratio for each attribute in the attribute-list.

- (e) If test attributes are attributes that have the highest information acquisition ratio in the attribute list, noting that the test attribute is the N test attribute.
- (f) Find the division threshold if the test attribute is continuous.
- (g) For each new leaf node grown by node N, calculate the classification error rate of each node, and then prune the tree.

Step 2: Extract rules of classification.

In the decision tree, each branch will represent the test output, and each leaf node will represent the category or distribution category. Follow each path from the root node to the leaf node. Conjunctions of each attribute value are antecedents of rules, while leaf nodes are a consequence of rules. Thus, decision trees can be easily converted to IF-THEN rules.

Step 3: Determine patterns of network behavior.

New behavior patterns in the network are determined by patterns that are classified as intruders or not based on classification rules.

### 4.4 Stage of Enforcement

The SPDLC computer network system development model categorizes enforcement at the testing stage. The testing process is needed to ensure the system built is in compliance with the design specifications and meets the needs of the problems at the Institut Bisnis dan Informatika Stikom Surabaya.

**Modeling the Attack.** An attack on the network requires a target server that is running FTP, HTTP, and SSH services as shown in the network topology (Fig. 2). This experiment produces seven types of malicious traffic and legitimate traffic as shown in Table 1. This traffic is intentionally injected into the IDS to be attacked, and each IDS will check all existing traffic, whether legitimate or malicious traffic. When input traffic matches the rules set, it will trigger an alarm to carry out its function. Snort accuracy in classifying network traffic will be determined by the number of alarms (true positive, false positive, and false-negative). This malicious traffic with various exploits and payloads is generated using the Metasploit framework.

**Table 1** Number of rule set

No	Type of malicious traffic and rules	Rule set number
1	ARP	25
2	Dos/Ddos	70
3	ICMP	130
4	Scan	35
5	SSH	10
6	FTP	80
7	HTTP	120

In running an exploit requires information about the target attack system such as information about the operating system and what services are being run. This information can be searched and collected using a port scanning application or other exploitation tools. This Metasploit is modular and can be mixed or matched with different exploits to achieve the required results. The following is an example of the Snort IDS rule using the same syntax in this case. A general Snort rule is: alert ICMP any any; any any (msg:“ICMP Packet”; sid:476; rev:4;). This rule indicates that there is “ping traffic” or an ICMP packet.

**Experiment Scenario 1: Ping Attack (ICMP Attack).** Hybrid IDS is implemented on a network router that connects intranet and DMZ networks. In this test, large ICMP packages were sent so that they were categorized by IDS as a DOS attack (denial of service).

The following tests are carried out through the client on the internal network.

```
Ping 172.25.83.30 -l 5000 -t
Pinging 172.25.83.30 with 5000 bytes of data
Reply from 172.25.83.30: bytes = 5000 time = 10 ms TTL = 63
Reply from 172.25.83.30: bytes = 5000 time = 10 ms TTL = 63
Reply from 172.25.83.30: bytes = 5000 time = 10 ms TTL = 63
Reply from 172.25.83.30: bytes = 5000 time = 10 ms TTL = 63
Ping statistics for 172.25.83.30
Packets: Sent = 4, Received = 4, Lost = 0 (0 Approx round trip times in m-seconds
Minimum = 0 ms, Maximum = 10 ms , Average = 3 ms.
```

This DOS attack will be detected immediately by the snort engine, then the snort engine will send alerts to alert logs, MySQL ACID and MySQL ACID history. The IDS engine reads alerts on the MySQL ACID and then instructs the firewall to update the rule by adding a rule to block access from detected IP attackers. Observation of this experiment was carried out in 2 places: in the client where the attack was carried out and on the IDS system.

**Experiment Scenario 2: Nmap Port Scanning Attack.** In this case, the author will simulate and analyze the types of port scanning activities using Nmap, which are carried out from both the attack machine, internal (Client) and external attackers.

The first step is to make rules/signatures to define this type of activity. Based on the results of traffic analysis, the author defines Nmap ping as follows:

```
alert icmp any any-> any any (msg: “ICMP PING NMAP attack”; dsize: 0; itype5:
rev: 1; sid: 1003;).
```

The above signatures or rules will generate Snort alerts if they detect access to the ICMP protocol originating from external or internal network segments, through any port to any port 172.25.83.254 (machine server): statement rules: “ICMP PING NMAP attack”; 0 byte packet size; use ICMP type 5; First revision rules: ID number rules 1003.

The second step is to apply these new rules/signatures by placing them in the rules directory Snort (/etc./snort/rules). In this study, the author keeps this signature with the name localrules. After that, the Snort process must be restarted, so Snort can detect, read, and apply the new rules to the core code.

**Experiment Scenario 3.** This technique was analyzed using a KDD Cup99 Network Intrusion Dataset [16] carried out by the Lincoln Laboratory at MIT. This data is a standard dataset has been reviewed and includes training and testing sets. The training set is about 7 GB of binary TCP chunk data that has been compressed from 7 weeks of network traffic with around 3 million connections. The test set was taken from three weeks of network traffic with around 3 million connections [17] (Table 2).

In this experiment, we use 295,078 records from the KDD data set (corrected.zip). The number of samples is shown in Table 3. From this data, 10% of the data was extracted by sampling, 34% was dedicated to the test set and 66% of this new set belonged to the training set. After the training set process, 23 types of attacks were found in 37 types of attacks available in the KDD Cup dataset. Therefore, this test set can be used to predict the ability to detect unknown attacks or new attacks.

The following metrics can be used to measure attack detection [18]: 1. False-positive (FP) or a false alarm, when normal behavior that is incorrectly classified as intrusive by the IDS; 2. False-negative (FN), when an attack that is missed by the IDS, and classified as normal; 3. True positive (TP), when an attack that is

**Table 2** The experiment of attack categories

Category of attack	Method of attacking
DoS (Denial of Services)	Udpstorm, teardrop, smurf, processtable, neptune, mailbomb, apache2, backland
Probing	Nmap, satan, mscan, Ipsweep, portsweep, saint
R2L	Worm, sendmail, named, ftp-write, imap, guess password, warezmaster, multihop, snmpgetattack, spy, warezclient, xsnoop, snmpguess
U2R	Xterm, rootkit, perl, Buffer_overflow, oadmodule, ps, sqlattack, httpptunnel
Normal	Normal

**Table 3** Number of samples in the dataset

Category of attack	Number of samples
DoS (Denial of Services)	215,000
Probing	4500
R2L	15,500
U2R	178
Normal	59,900
Total	295,078

**Table 4** Result of C4.5 algorithm for 200 and 30% records

Parameter	200 record	30% record
Accuracy (%)	95.5	95.15
False alarm rate (%)	9.35	9.56
Detection rate (%)	99	99

successfully detected by the IDS; and 4. True negative (TN), when normal behavior that is successfully labeled as normal by the IDS.

Detection rates and false alarm levels measure the accuracy of the intrusion detection system.

The two terms used to calculate the efficiency of the IDS system are: (1) Detection Rate: is the percentage of attacks detected between all attack data, with the following formula:  $\text{Detection rate} = \frac{TP}{TP + TN} \times 100$ ; (2) False alarm level: is the percentage of normal data that is incorrectly recognized as an attack, with the following formula:  $\text{False alarm level} = \frac{FP}{FP + TN} \times 100$ . We get the results with the appropriate values for C4.5 Algorithms for 200 and 30% records are shown below in Table 4.

#### 4.5 Stage of Enhancement

In this phase, the activities include improvements to the system that has been built. Enhancement phase through a series of improvement processes carried out for a number of purposes: (a) Correcting a number of errors found in the previous system implementation (existing system). (b) Add functionality to specific components or the latest additional features to complement the shortcomings in the previous system. (c) Adapting a system that has been built on new platforms and technologies in overcoming a number of developments in new problems that arise. (d) Thus, the repair phase can effectively guarantee the reliability of the performance of the IDS.

## 5 Conclusions and Recommendations

The Hybrid Intrusion Detection System has functions: detection of known attacks and unknown attacks. A hybrid of the C4.5 Detection and Snort algorithms can increase detection rates 99% of 200 records, and also reduce false alarm levels 9.35% of 200 records from the Intrusion Detection System.

Parameters such as Accuracy, Detection Level, and False Alarm Level is done as comparison tools. In the next study, building an effective intrusion detection model with good accuracy and real-time performance is very important. For this

reason, other techniques are needed from the initial processing and other data mining approaches that can be tested for better detection rates in future research in Hybrid IDS System.

**Acknowledgements** The research is funded by University Malaysia Pahang, UMP Lab2Market Research Fund (UIC170901). This acknowledgment also goes to the Faculty of Electrical and Electronic Engineering for providing us with facilities to conduct this research.

## References

1. Öğütçü G, Testik ÖM, Chouseinoglou O (2016) Analysis of personal information security behavior and awareness. *Comput Secur* 56:83–93
2. Huang L, Wang X (2016) On the construction of university campus culture under the network environment. In: 3rd international conference on education, management and computing technology (ICEMCT 2016)
3. Chun G, Ping Y, Liu N, Luo S-S (2016) A two-level hybrid approach for intrusion detection. *Neuro Comput* 214:391–400
4. Gisung K, Seungmin L, Sehun K (2014) A novel hybrid intrusion detection method integrating anomaly detection with misuse detection. *Expert Syst Appl* 41(4 Part 2):1690–1700
5. Peng J et al (2006) A hybrid intrusion detection and visualization system. In: Proceedings of the 13th annual IEEE international symposium and workshop on engineering of computer based systems, p 2
6. Peddabachigari S et al (2007) Modeling intrusion detection system using hybrid intelligent systems. *J Netw Comput Appl* 30(1):114–132
7. Wang X, Kordas A, Hu L, Gaedke M, Smith D (2013) Administrative evaluation of intrusion detection system. In: Proceedings of the 2nd annual conference on research in information technology, RIIT' 13. ACM, NY, USA, pp 47–52
8. Bulajoul W, James A, Pannu M (2013) Network intrusion detection systems in high-speed traffic in computer networks. In: 2013 IEEE 10th international conference on e-Business engineering (ICEBE), pp 168–175
9. Trabelsi Z, Zeidan S (2014) IDS performance enhancement technique based on dynamic traffic awareness histograms. In: IEEE international conference on communications (ICC), pp 975–980
10. Vishnu Balan E, Priyan MK, Gokulnath C, Usha Devi G (2015) Hybrid architecture with misuse and anomaly detection techniques for wireless networks. In: International conference on communications and signal processing (ICCSP)
11. Snapp SR, Brentano J, Dias G, Goan TL, Heberlein LT (2017) DIDS (distributed intrusion detection system)—motivation, architecture, and an early prototype. [dl.lib.mrt.ac.lk](http://dl.lib.mrt.ac.lk)
12. Tuyikeze T, Pottas D (2010) An information security policy development life cycle. In: Proceedings of the South African information security multi-conference (SAISMC)
13. Kosamkar V, Chaudhari SS (2014) Improved intrusion detection system using C4.5 decision tree and support vector machine. *Int J Comput Sci Info Technol* 5(2):1463–1467
14. SnortTM Users Manual (2019) <http://www.snort.org/>. The Snort Project
15. Snort FAQ (2019) <http://www.snort.org/>. The Snort Project
16. <http://kdd.ics.uci.edu/databases/kddcup99> (2019)
17. Wu S-Y, Yen E (2009) Data mining-based intrusion detectors. *Expert Syst Appl* 36(3):5605–5612
18. Caulkins BD, Lee J, Wang M (2005) A dynamic data mining technique for intrusion detection systems. In: Proceedings of the 43rd annual southeast regional conference, vol 2, ACM, pp 148–153

# Image Segmentation of Women's Salivary Ferning Patterns Using Harmony Frangi Filter



Heri Pratikno and Mohd Zamri Ibrahim

**Abstract** Medical research proves that entering the fertile period, especially during ovulation, all-female body fluids contain ferning patterns in the form of crystallization of salt shaped like a fern tree. Until now, not many research topics have been carried out related to the segmentation process in the salivary ferning pattern, this is due to several problems including first, the unavailability of a database of image salivary ferning pattern online. Second, the salivary ferning pattern has several hidden layers and uneven intensity. The purpose of this study was to detect and determine the line shape of the salivary ferning crystal pattern using the Harmony Frangi Filter method based on the Hessian matrix operation. The results of the segmentation process from this study are a crucial basis in determining the level of accuracy and precision at the next stage of research, namely: the prediction process of a woman's ovulation in each menstrual cycle. The measurement of segmentation results has an average value of MSE 2.25, PSNR 44.86 dB, FSIM 0.954, accuracy 99.88%, sensitivity 99.98% and specificity 99.88%.

**Keywords** Salivary ferning · Frangi filter · Ovutest scope

## 1 Introduction

WHO-ICMAR infertility is a disease or problem in the reproductive system that is defined by the failure to achieve a clinical pregnancy after 12 months or more of sexual intercourse without using contraception. Infertility can occur from both women and men caused by many factors, including factors from within abnormalities of reproductive organs, diseases, hormonal disorders or irregular menstrual cycles. While the causes of external factors, namely: trauma, stress, free radicals, pollution or the use of contraceptive pills that have been long. Infertile couples, the chance

---

H. Pratikno (✉)

Faculty of Technology and Information, Department of Computer Engineering, Universitas Dinamika, Surabaya, Indonesia  
e-mail: [heri@dinamika.ac.id](mailto:heri@dinamika.ac.id)

H. Pratikno · M. Z. Ibrahim

Faculty of Electrical and Electronic Engineering, Universiti Malaysia Pahang, Kuantan, Malaysia

© Springer Nature Singapore Pte Ltd. 2020

A. N. Kasruddin Nasir et al. (eds.), *InECCE2019*, Lecture Notes in Electrical Engineering 632, [https://doi.org/10.1007/978-981-15-2317-5\\_51](https://doi.org/10.1007/978-981-15-2317-5_51)

605

to get pregnant in the first year of marriage is 85%, in the second year the number increases by 92% and the rest experience infertility. In general, the first two months of marriage in the first year had a 30% chance of getting pregnant.

Infertility in men can be analyzed using a variety of clinical interventions as well as laboratory evaluations of semen. The method often used by women to detect fertility is: use a test-pack to detect hormones through urine, BTT Thermometer to detect increases in body temperature, menstrual cycle calendar system and the use of Ovutest Scope [1]. The main disadvantage of using a test-pack is that it is only a single-use device and that during the fertile period strip line indicators have been seen so that it is difficult to determine when ovulation occurs because the peak of the hormone progesterone and estrogen occurs after ovulation as shown in Fig. 1.

Another traditional method used to detect ovulation is by measuring the body temperature of women every day, where the flow of hormones at ovulation is predicted to occur between the end of the second week and the beginning of the third week of the start of the menstrual cycle which is usually marked by a rise in body temperature between 0.3 and 0.6 °C above normal body temperature within 12–24 h is shown in Fig. 1, ovulation is also difficult to determine because body temperature will increase when stressed, tired and the body will get sick. Whereas the determination of ovulation through observing saliva using Ovutest Scope manually is also difficult to decide because sampling as a dataset must be done regularly and the process of reading the data is still subjective.

Eissa et al. [3] created software and designed hardware to detect microcontroller-based ovulation times using infra-red Thermometer sensors which can produce three parameters, namely: temperature factor, the time factor, and decision making (processing and training mode). The end result of this tool is still a prototype and is difficult to make for laymen because they have to understand hardware and software.

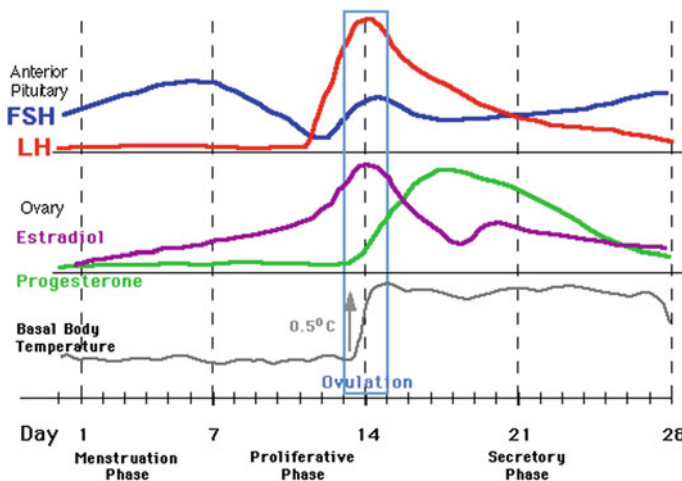
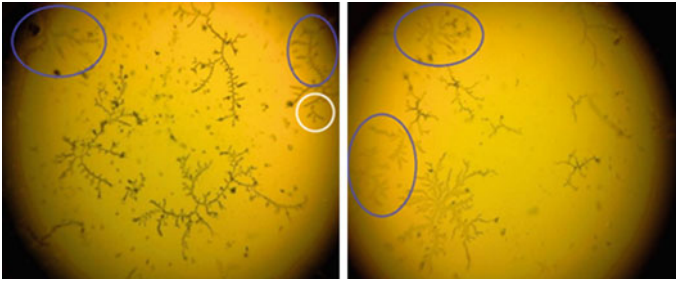


Fig. 1 Women's body temperature change cycle [2]





**Fig. 2** The main problem in the salivary ferning image layer pattern

Determination of ovulation through salivary ferning besides being able to be applied to a woman turned out to also be applicable to animals, the study was carried out on buffaloes (*Bubalus bubalis*) female [4] and female Bornean orangutans (*Pongo pygmaeus*) [5].

The results of the latest research which were linearly based on this study were conducted by Hui-Ching Wu in 2015 with a classification result of 84% of 100 examples of saliva [6]. The application of the Harmony Frangi Filtering method is believed by the authors to contribute to an increase in accuracy and precision of more than 84%, besides that the application of the Frangi Filter Harmony method is a method that has never been applied to salivary ferning objects so that this makes the renewal factor because so far Frangi Filter widely applied to brain nerve tissue, human eye nerves and detection of branching of plant roots.

The main problem of segmentation of salivary ferning crystal pattern is the presence of overlapping, intermittent fern line patterns, several layers of hidden or transparent fern line patterns and not evenly distributed intensity on salivary ferning surfaces such as Fig. 2. The main objective of this study is to improve accuracy, sensitivity, and specificity in the segmentation of the introduction of salivary ferning patterns. Next is a feature vector calculation to measure the similarity value of the results of segmentation and evaluate the consistency of its accuracy for three consecutive months of each volunteer menstrual cycle.

## 2 Research Method

One important step in image processing is segmentation, image segmentation is the process of separating images into several homogeneous parts if the parts are extracted will become observable objects in the region of interest. Segmentation of the ferning pattern of saliva, its region of interest can be in the form of contours and fern-like based on intensity values, namely discontinuity and similarity. The discontinuity approach of images is divided based on sudden changes in intensity such as edge detection. While the image similarity approach is separated into similar regions based on a criterion, for example, thresholding, region growing and region splitting [7].

Segmentation using the Hessian matrix is mostly done in the medical field such as detection of blood vessels [8], detection of the respiratory tract and other organs in the body that form the channel. In the field of plant, biology used the Hessian matrix to detect branching from the main stem of the plant, then Mohammed Amean et al. [9] combined the Hessian and Hough Transform matrices for plant stem segmentation. By analyzing the eigenvalues of the Hessian matrix, channel, flat plane and bubble structures can be detected in both 2D and 3D images.

Based on the paper [10–12] that detecting and predicting ovulation women can help when the time is right for married couples to have children immediately or avoid pregnancy for certain reasons. The application of segmentation method in this study uses Harmony Frangi Filter in the hope that it can increase the value of accuracy, sensitivity, and specificity in segmenting the shape of the image line pattern from salivary ferning. The results of the segmentation process will be continued with the analysis process of calculating the feature vector value to determine how much the similarity value between the segmented images and the ground truth images.

## ***2.1 Hessian Matrix as Edge Detection Method***

Matrix is an arrangement of numbers arranged based on rows and columns where entries in a matrix are called elements. Hessian Matrix is a matrix where each element is formed from the second partial derivative of a function. Suppose that a function  $f(x)$  with  $n$  fruit variables has a second partial derivative and a continuous derivative, then the Hessian matrix of  $f(x)$  is the matrix  $H$  [13].

The Hessian matrix is used to test the derivative of both functions more than one variable by identifying the local optimum. The function of two variables is used because the intensity of the pixel image  $I(x, y)$  has two variables namely  $x$ , and  $y$ . The optimum value can be searched using the eigenvalue of the Hessian matrix as follows, if  $A$  matrix has the order  $(n \times n)$  and  $\lambda$  a scalar that satisfies the  $Ax$  equation  $= \lambda x$  for a nonzero column vector in  $n$  dimension space, then:

1.  $\lambda$  is called eigenvalue or characteristic roots of matrix  $A$ .
2.  $x$  is called the eigenvector or characteristic vector of the matrix  $A$ .
3. The eigenvectors  $x$  form the eigenvector space of  $A$  which is linearly free called base for eigenvalue corresponding to the eigenvalue  $\lambda$ .

**Table 1** Relationship of eigenvalues in the Hessian matrix and image structure

2D		3D			Structure orientation	Keterangan
$\lambda_1$	$\lambda_2$	$\lambda_1$	$\lambda_2$	$\lambda_3$		
<b>L</b>	<b>L</b>	<b>L</b>	<b>L</b>	<b>L</b>	<i>No structure</i>	<b>L</b> = low
<b>L</b>	<b>L</b>	<b>L</b>	<b>L</b>	<b>H-</b>	<i>Sheet-like (bright)</i>	<b>H+</b> = high positive
<b>L</b>	<b>L</b>	<b>L</b>	<b>L</b>	<b>H+</b>	<i>Sheet-like (dark)</i>	<b>H-</b> = high negative
<b>L</b>	<b>H-</b>	<b>L</b>	<b>H-</b>	<b>H-</b>	<i>Tubular (bright)</i>	$\pm$ = eigen value sign
<b>L</b>	<b>H+</b>	<b>L</b>	<b>H+</b>	<b>H+</b>	<i>Tubular (dark)</i>	
<b>H-</b>	<b>H-</b>	<b>H-</b>	<b>H-</b>	<b>H-</b>	<i>Blob-like (bright)</i>	
<b>H+</b>	<b>H+</b>	<b>H+</b>	<b>H+</b>	<b>H+</b>	<i>Blob-like (dark)</i>	

$$H(f) = \begin{bmatrix} \frac{\partial^2 f}{\partial x_1^2} & \frac{\partial^2 f}{\partial x_1 \partial x_2} & \cdots & \frac{\partial^2 f}{\partial x_1 \partial x_n} \\ \frac{\partial^2 f}{\partial x_2 \partial x_1} & \frac{\partial^2 f}{\partial x_2^2} & \cdots & \frac{\partial^2 f}{\partial x_2 \partial x_n} \\ \vdots & \vdots & \ddots & \vdots \\ \frac{\partial^2 f}{\partial x_n \partial x_1} & \frac{\partial^2 f}{\partial x_n \partial x_2} & \cdots & \frac{\partial^2 f}{\partial x_n^2} \end{bmatrix} \tag{1}$$

The Hessian matrix gives the second derivative of the variation in the local intensity of the image to the pixels around it. The eigenvalues and eigenvectors of the Hessian matrix are used to analyze the image structure. Frangi, defines the relationship between eigenvalues  $\lambda_1, \lambda_2, \lambda_3$  with  $|\lambda_1| \leq |\lambda_2| \leq |\lambda_3|$  in Table 1.

To get the Hessian matrix in 2D images, the second partial derivative of an image is calculated:  $D_{xx}, D_{yy}$ , and  $D_{xy}$  [14].

$$H(x, y) = \begin{bmatrix} D_{xx} & D_{xy} \\ D_{xy} & D_{yy} \end{bmatrix} \tag{2}$$

The Frangi filter combines the image enhancement smoothing process using Gaussian convolution with the second derivative to detect “vesselness” in the image. For example in the case of 1D, the response image of the filter is given in Eq. (3) [15].  $I(x)$  is an input image and  $*$  is a convolution operator.

$$D(x, \sigma) = \left\{ -\frac{d^2 G(x, \sigma)}{dx^2} \right\} * I(x) \tag{3}$$

Calculation of image response  $D(x, \sigma)$  is a Gaussian scale space, Lindeberg [16] explains the theory of scale-space as a series of 1D images blended with index blur  $\sigma$  or standard deviation of a Gaussian function. The  $\sigma$  blur index is defined as “scales”, namely: the size of a Gaussian kernel that affects the results of image blur. For

a simple Gaussian smoothing function shown in Eq. (4), while to get the Hessian matrix element in the form of the second partial derivative of the image, the image is convoluted with the second derivative Gaussian function, namely:  $D_{xx} = I(x) * G_{xx}$ ,  $D_{xy} = I(x) * G_{xy}$ ,  $D_{yy} = I(x) * G_{yy}$ . The Gaussian scale-space functions are  $G_{xx}$ ,  $G_{xy}$ , and  $G_{yy}$  and are shown in Eqs. (5), (6) and (7).

$$D(x, y, s) = \frac{1}{2\pi s^2} e^{-\frac{x^2+y^2}{2s^2}} \quad (4)$$

$$G_{xx} = \frac{\partial^2 G(x, y, s)}{\partial^2 x} = \frac{1}{2\pi s^4} \left( \frac{x^2}{s^2} - 1 \right) e^{-\frac{x^2+y^2}{2s^2}} \quad (5)$$

$$G_{yy} = \frac{\partial^2 G(x, y, s)}{\partial^2 y} = \frac{1}{2\pi s^4} \left( \frac{y^2}{s^2} - 1 \right) e^{-\frac{x^2+y^2}{2s^2}} \quad (6)$$

$$G_{xy} = \frac{\partial^2 G(x, y, s)}{\partial^2 xy} = \frac{xy}{2\pi s^6} e^{-\frac{x^2+y^2}{2s^2}} \quad (7)$$

with  $x, y \in [-3s: 3s]$  so that the second derived Gaussian kernel filter is generated. The eigenvalue is searched using Eqs. (8) and (9), with  $\alpha = ((D_{xx} + D_{yy})^2 + 4D_{xy}^2)^2$  then the eigenvalue is sorted so that  $\lambda_2 > \lambda_1$ .

$$\lambda_2 = \frac{D_{xx} + D_{yy} + \alpha}{2} \quad (8)$$

$$\lambda_1 = \frac{D_{xx} + D_{yy} - \alpha}{2} \quad (9)$$

The eigenvalues are used to detect the structure of all pixels, based on Table 1, pixels which are part of the vessel region are marked with  $\lambda_1 \approx 0$  and  $\lambda_2 \gg \lambda_1$ . The requirement is formulated by the blobness measure feature, namely  $Rb = (\lambda_1/\lambda_2)^2$ , while  $S = \|\mathcal{H}\|F = (\lambda_2 + \lambda_1)^2$  is a "second-order structureness". The S value will be low if the background has no structure. In parts with high contrast, the norm value will be greater because one of the eigenvalues will increase. The features of Rb and S are mapped by vesselness measure Eq. (10) [17].

$$vo(s) = \begin{cases} 0, & \lambda_2 > 0 \\ \exp\left(-\frac{Rb^2}{2\beta^2}\right) \left(1 - \exp\left(-\frac{S^2}{2c^2}\right)\right) & \end{cases} \quad (10)$$

In Eq. 10,  $\beta$  and  $c$  are threshold values that control the sensitivity of the Hessian matrix line filter. The filter response of the line will be maximum on the scale that matches the original ferning. Thresholding results are analyzed on a different scale  $s$  as in Eq. (11).

$$Vo = \max_{S_{\min} \leq s \leq S_{\max}} Vo(s) \quad (11)$$

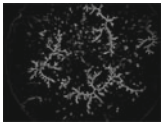
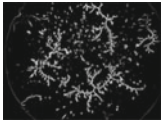
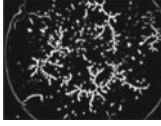
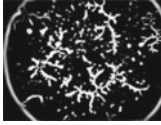
## 2.2 Harmony Frangi Filter

In this study propose a method called Harmony Frangi Filter which is the development of the Frangi Filter method introduced by Marc Schrijver in 2001, improved by D. Kroon from the University of Twente in 2009, then further developed by T. Germany from the University of Ljubljana in 2014.

In this research, harmonization began from the pre-processing stage, Frangi Filtering to the post-processing stage. The Frangi Filtering method has been compared with the twelve other Filtering methods, including Canny, Robinson, Kirsch, Gradient, Coye, Extracted Largest Blob, Convolve, Hill Shade, Differentials Laplacian, Frangi and German Frangi Team. Furthermore, the Frangi Filter method is harmonized with three thresholding methods, namely: imadjust, histeg, and adapthisteg to get the best foreground display results.

The next step is to configure several parameters from the Frangi Filter method to get the most realistic and natural foreground close to the shape of the display as in the original image. The parameters that can be configured on Frangi Filter include scale range (sigma), scale ratio, frangi beta 1, frangi beta 2 and so on. The results of the Frangi Filter parameter configuration can be seen in Table 2.

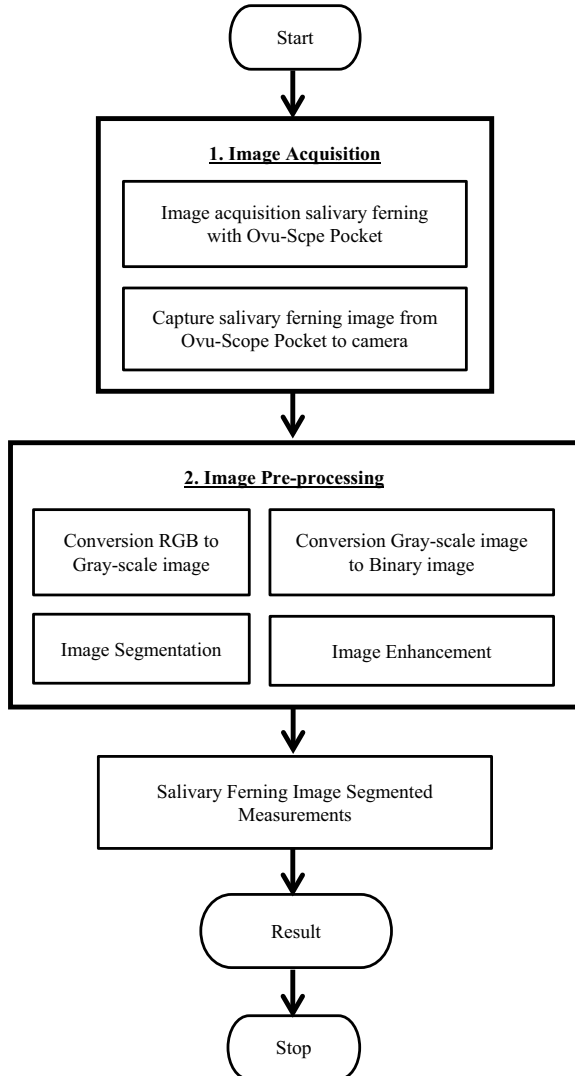
**Table 2** Results of a configuration comparison of several Frangi filter parameters

No.	Salivary ferning	Frangi filter configuration
1		Scale range (sigma) = 1 Scale ratio = 1 Frangi beta 1 = 1 Frangi beta 2 = 6.5
2		Scale range (sigma) = 2 Scale ratio = 1 Frangi beta 1 = 1 Frangi beta 2 = 6.5
3		Scale range (sigma) = 4 Scale ratio = 1 Frangi beta 1 = 1 Frangi beta 2 = 6.5
4		Scale range (sigma) = 8 Scale ratio = 1 Frangi beta 1 = 1 Frangi beta 2 = 6.5

### 2.3 Block Diagram

Image processing in this study uses Matlab with methods, and algorithms incomplete block diagram is shown in Fig. 3, which has four main stages, namely: image acquisition, image pre-processing, image segmented measurement, result. While the stages of the detailed salivary ferning segmentation process carried out in this study are shown in Fig. 4.

**Fig. 3** Block salivary ferning system diagram



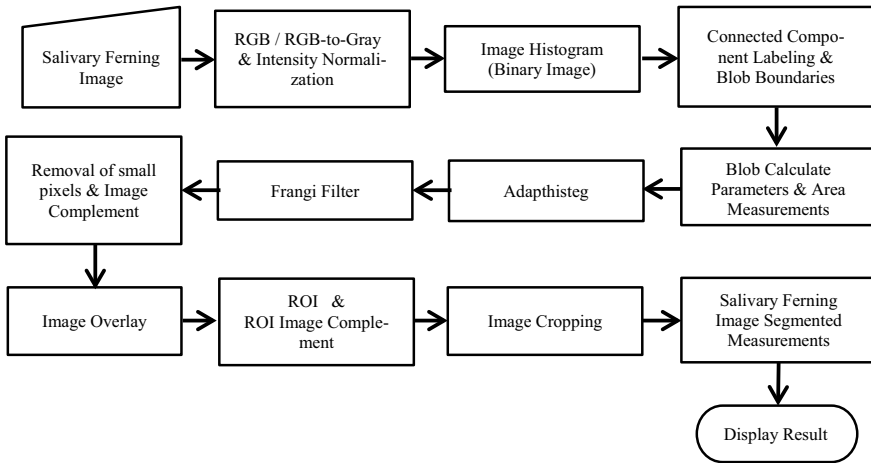


Fig. 4 Block segmentation process diagram

### 3 Results and Analysis

Up to this stage, the results of research that have been achieved are two, namely: a dataset has been obtained from three female volunteers for three consecutive months and the results of the comparison of the Frangi Filtering Harmonization method to the twelve other segmentation methods. In the early stages, image salivary imaging was taken as an initial contribution to building a database of three women of productive age (20–40 years) with conditions in good health, not using contraceptive pills, not smoking and not consuming alcoholic drinks for 3 consecutive months. with their average menstrual cycle for 24 days, so that a dataset of  $24 \times 3 \times 3 = 216$  images of salivary ferning was collected. One example of data that has been taken during the 1-month menstrual cycle from one of the volunteers is shown in Fig. 5.

#### 3.1 Stages of the Image Segmentation Process

Segmentation can be done using the region merging and splitting approach, in the edge detection of image segmentation through identification of object boundaries. Limits are locations where there is a change in intensity in the approach based on the region, then identification is carried out through the area contained in the object. Segmentation attempts to separate an image into groups of homogeneous pixels into a set according to each of the criteria, where each group is called a segment.

This image segmentation is the first step and a crucial step for the computing process at the next image processing stage. Image segmentation is a method for clustering in an image, where images will be grouped in regions that have several

**SALIVARY FERNING - 3rd MONTH**  
( Elizabeth - 23 Days )

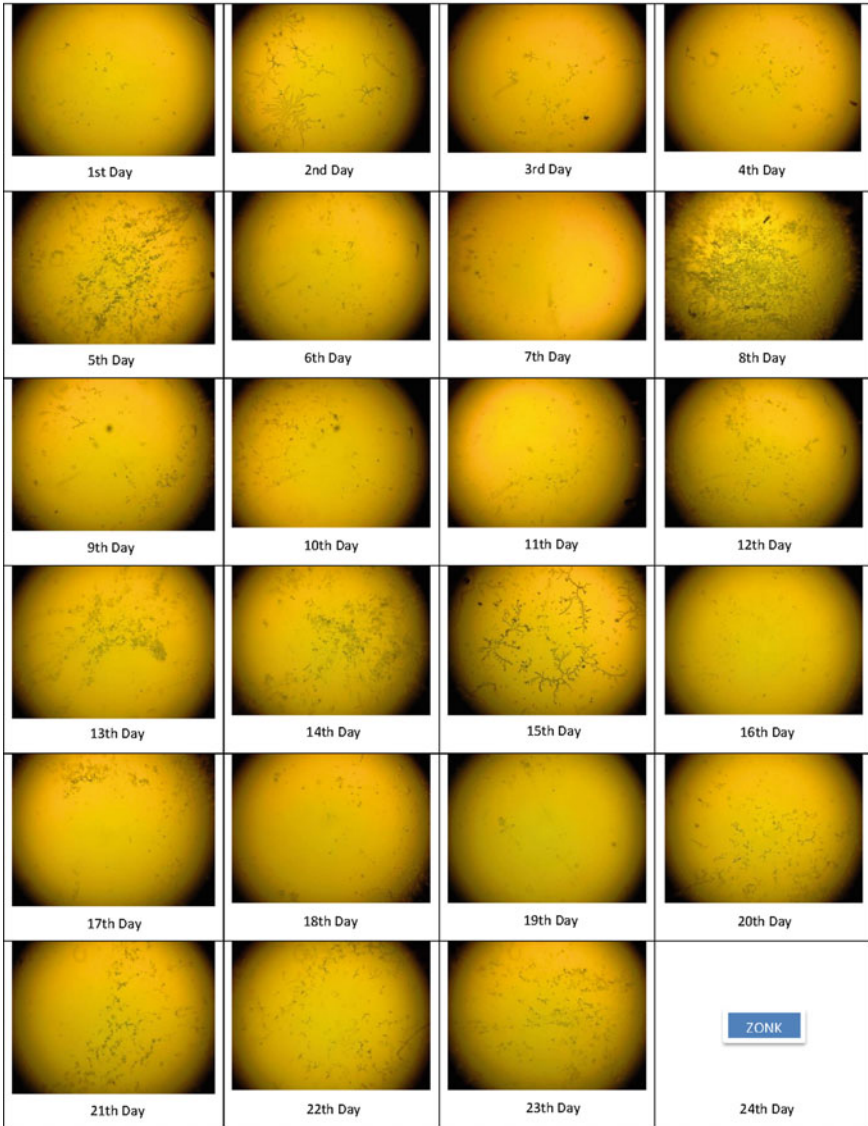


**Fig. 5** Example of salivary ferning data



**Fig. 6** One example of a salivary ferning image



features in common, including grayscale, texture, color, and motion. in Fig. 6 displays an example of an original image of salivary ferning.

**Convert RGB Color Space to Gray.** In the pre-processing process, the process of converting salivary ferning images from RGB to Gray color space can be done through two methods, namely the first method, using the percentage of color channel compositions from the RGB color space in this study to produce the best salivary ferning segmentation. RGB color to Gray is 29.89% color channels Red, 58.7% color channels Green and 7.22% color channels Blue.

The percentage of RGB to Grayscale color conversion with the results of 29.89% Red color channels ( $0.2989 * R$ ), 58.7% color channels Green ( $0.587 * G$ ) and 7.22% color channels Blue ( $0.0722 * B$ ) are the results of empirical experiments carried out during research based on the formula [18], In the article stated that in image recognition, it is often assumed that the method used to convert color images to grayscale has only a small impact on recognition performance. They compared thirteen different grayscale algorithms with four types of image descriptors and showed that this assumption was wrong: not all color-to-grayscale algorithms work well, even when using powerful descriptors for illumination changes.

Average method ( $RGB/3 = 33\%$  Red, 33% Green, and 33% Blue), but the reality is not the case. The solution for this has been given by the method of luminosity (weighted). The weighted method has a solution to that problem. Because red has more wavelengths than all three colors, and green is a color that not only has less wavelength than red but also green is a color that gives a more calming effect on the eyes. This means that we have to reduce the contribution of red and increase the contribution of green, and put the blue contribution between the two.

The luminance algorithm is designed to match the perception of brightness of the human eye using a RGB-weighted channel combination with the formula: *new grayscale image* =  $((0.2989 * R) + (0.587 * G) + (0.0722 * B))$ . According to this equation, Red has a contribution of 29.89%, Green contributes 58.7% greater in all three colors and Blue contributes 7.22%, so the image is brighter.

The second method uses the `rgb2gray` function from Matlab which is then followed by the process of normalizing the intensity of pixel values in the range [0 1] to reduce

the difference in illumination of images that lack contrast or glare. Normalization of intensity is also called contrast stretching or histogram stretching, normalizing transformation values of the intensity of n-dimensional grayscale images in the range (Min, Max),  $I: X \subseteq R^n \rightarrow \{Min, \dots, Max\}$  becomes  $I_N$ 's new image:  $X \subseteq R^n \rightarrow \{newMin, \dots, newMax\}$  with range intensity values (newMin, newMax). The linear normalization formula of a digital image is:

$$I_N = (I - Min) \frac{newMax - newMin}{Max - Min} + newMin \tag{12}$$

An example of calculating the results of measuring the number of pixels in the salivary ferning image area in Fig. 7 is shown in Table 3.

**Image Texture.** The texture is an intrinsic characteristic of an image associated with the level of roughness, granularity and regularity structural arrangement of pixels. The texture is the key to visualizing one's perceptions or perspectives and rules that are very important in the work of computer vision. Texture analysis is commonly used as an intermediate process for performing image classification and interpretation. An image classification process based on texture analysis generally requires feature extraction, which can be divided into four types of methods, namely: statistical, geometry, model-based, and signal processing.

**Fig. 7** RGB to Gray conversion

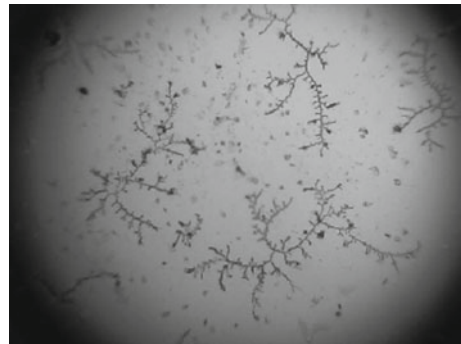


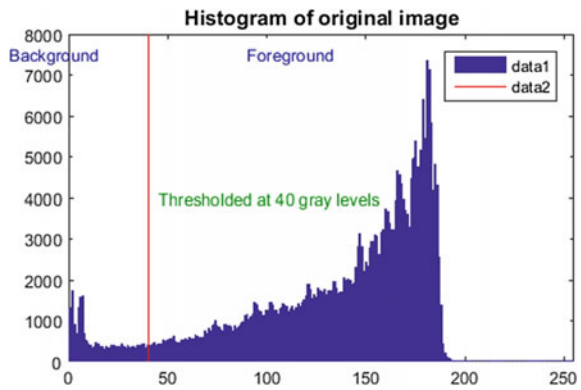
**Table 3** Results of area measurements from saliva images

Blob#	Mean intensity	Area	Perimeter	Centroid		Diameter
				X-axis	Y-axis	
# 1	140.8	279,984	2096.3	334.9	236.6	597.1
# 2	41	1	0	16	152	1.1
# 3	41	1	0	48	65	1.1
# 4	41.6	7	7.7	63.9	416.1	3
# 5	42	8	8.3	79.6	21	3.2

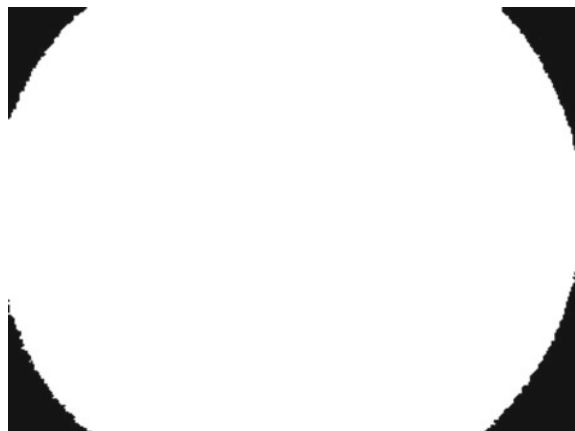
**Thresholding.** Based on the shape and size of all salivary ferning database images, logical operations to obtain a binary image (0 and 1) in this study are set to 40. The result of this threshold can be separated between the foreground and background in the image. as shown in Fig. 8, to get a bright object (close to a value of 1, white), the selected area is an object that has a value greater than the threshold value ( $>$ threshold), as shown in Fig. 9 as well as the reverse process, if desired to get a darker object area (black color, close to 0) then a smaller value is needed than the threshold value ( $<$ threshold).

**Blob Boundaries.** Based on the display form of the salivary ferning image in Fig. 7, to determine the region of interest that will be segmented, it is necessary to label each circle form in the image. The largest circle shape that will be selected as in Fig. 10a. Next blob boundaries will give the outer edge of the circle shape as shown in Fig. 10b while the results of the blob boundaries capture process are shown in Fig. 10c.

**Fig. 8** Salivary ferning image histogram



**Fig. 9** Binary image of thresholding



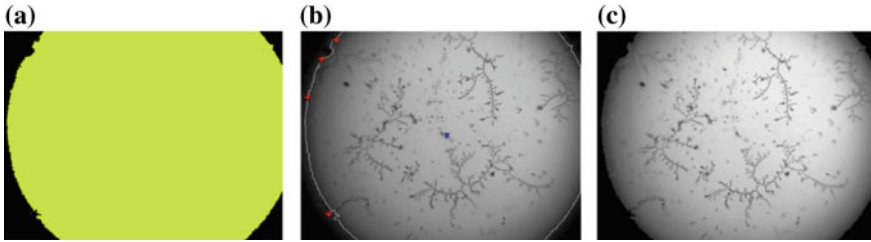


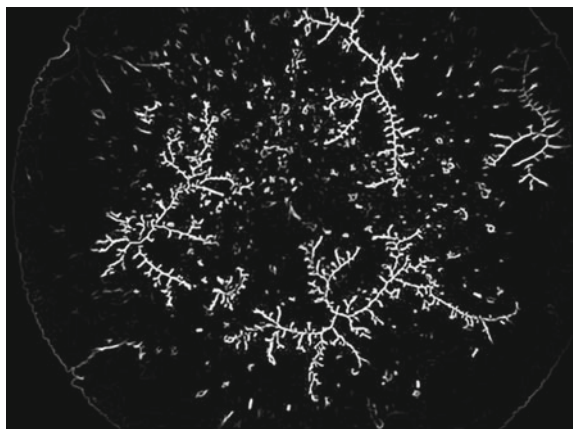
**Fig. 10** Blob boundaries

**Harmony Frangi Filter.** Computational results using the Harmony Frangi filter with configuration scale parameters ( $\sigma$ ) = 1, ratio scale = 1, frangi beta 1 = 1 and frangi beta 2 = 6.5, will produce image segmentation of saliva ferns as shown in Fig. 11. To obtain values from Scale range ( $\sigma$ ) parameters, Scale ratio, Frangi beta 1 and Frangi Beta 2 are done manually by the user, where the magnitude of the values is the best threshold value from the experimental process that has been empirically done on all salivary ferning images in the study this.

Value parameters from Scale range ( $\sigma$ ), Scale ratio, Frangi beta 1 and Frangi Beta 2 function to control the level of sensitivity of the filtering process to vessels measures in recognizing the shape of the ferning line pattern in saliva. The high and low values of the four parameters will affect a lot or the least number of edges during the edge detection extraction process. Then delete the pixel group below the number of 45 pixels, followed by the ROI image inversion process that results from segmentation as shown in Fig. 12.

To see and ensure the accuracy of the ROI of the segmented image from the Harmony Frangi Filter, it is necessary to overlay it to the original image of the salivary ferning in the RGB color space shown in Fig. 13.

**Fig. 11** Computational results of the Harmony Frangi filter method



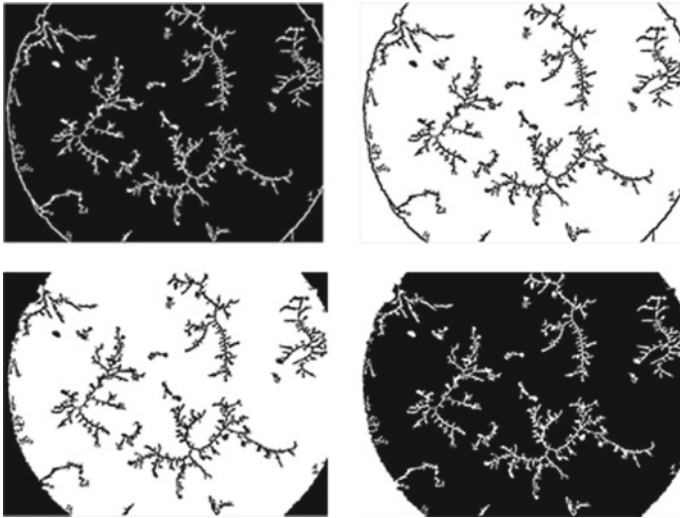


**Fig. 12** Determination of pixel group deletion and ROI image inversion

**Fig. 13** Overlaying ROI image segmentation to original RGB images



### 3.2 Measurement of Segmentation

After collecting voluntary salivary ferning datasets, the segmentation process was then carried out using the Harmony Frangi Filter method, then the next step of the research was to process the performance results of the segmentation. The test parameters or measurement methods are carried out using: PSNR (*Peak Signal to Noise Ratio*), MSE (*Mean Square Error*), RMSE (*Root Mean Squared Error*), FSIM (*Feature SIMilarity*), DSC (*Dice Similarity Coefficient*) and ROC (*Receiver Operating Characteristic*).

The performance measurement results from the salivary ferning image segmentation process using the measurement method: PSNR, MSE, RMSE, FSIM can be seen in Table 4, through a comparative process of pixel uniformity between segmented image and original image with similarity results having similarities above 90%.

## 4 Conclusion

In this study, the aim is to process the salivary ferning crystal pattern in women, namely: separating between the background and the foreground in the form of a line pattern like a fern tree. Segmentation in the form of a line pattern on salivary ferning has a fairly high degree of difficulty because there are several layers that appear to be transparent, hidden and of varying color intensity. The application of the Frangi Filter method in this study was the first to be carried out in research with salivary ferning objects.

The output of the segmentation pattern of the salivary ferning crystal line is more efficient, effective, higher accuracy and more natural compared to the thirteen other filtering methods, this is caused by several factors, including the first factor, Frangi Filter supports the multiscale concept so that the ferning pattern has different thicknesses on each branch can be extracted during the segmentation process. The second factor, the Frangi Filter segmentation process based on the calculation of the Hessian Matrix produces an eigenvalue that is useful for analyzing the structure of the salivary ferning and eigenvector used to analyze the characteristics of the salivary ferning structure. The comparison of the two eigenvalues ( $\lambda_1$ ,  $\lambda_2$ ) can detect whether the salivary ferning line pattern is in the form of sheet-like, blob-like or tubular?, the results of the measurement of segmentation performance have an average value of MSE 2.25, PSNR 44.86 dB, FSIM 0.954, accuracy of 99.88%, sensitivity of 99.98% and specificity of 99.88%.

The results of segmentation in this study can be developed for further research, namely: to predict the time of ovulation of a woman at the time of full ferning. Based on other medical studies to detect or predict ovulation, a woman or female animal can be carried out through salivary ferning through tears and cervical mucus. By knowing that ovulation can be used by a married couple to immediately have children or to avoid pregnancy because of joining a family planning program or for certain reasons.

**Table 4** Results of measuring salivary ferning image segmentation

Image name	MSE	PSNR (dB)	FSIM	Dice Coef	TP	FP	TN	FN	Sensitivity (%)	Specificity (%)	Accuracy (%)
Ferning 1	2.20	44.7492285	0.9511	1	301,811	667	308,295	4	99.9987	99.7841	99.8901
Ferning 2	1.97	45.2109440	0.9586	1	872,313	1491	887,397	3	99.9997	99.8323	99.9152
Ferning 3	1.41	46.6689528	0.9681	1	916,920	984	923,478	15	99.9984	99.8936	99.9457
Ferning 4	3.43	42.8096357	0.9390	1	910,704	3627	918,450	711	99.9220	99.6066	99.7634
Average	2.25	44.8596903	0.9542	1	750,437	1692	759,405	243	99.9797	99.7792	99.8786

## References

1. Patel DK, Prajapati DG (2018) Study the accuracy of salivary ferning test as a predictor of ovulation. *Int J Reprod Contracept Obstet Gynecol* 7(7):2699–2705
2. Dorling Kindersley™ Limited (2009) Temperature and mucus changes during the menstrual cycle
3. Eissa HM, Ahmed AM, Elsehely EA (2014) Implementatin of smart ovulation detection device. *Recent Adv Biomed Chem Eng Mater Sci*. ISBN: 978–1-61804-223-1
4. Ravinder R, Kaipa O, Baddela VS (2016) Saliva ferning, an unorthodox estrus detection method in water buffaloes (*Bubalus bubalis*). *Theriogenology* 86:1147–1155
5. Kubatova A, Fedorova T (2016) Saliva crystallization occurs in female bornean orangutans (*Pongopygmaeus*): could it be a new option for monitoring of menstrual cycle in captive great apes? *PLoS ONE* <https://doi.org/10.1371/journal.pone.0159960>
6. Wu H-C, Lin C-Y, Huang S-H, Tseng M-H (2015) An intelligent saliva recognition system for women's ovulation detection, Part I, LNAI 9011. Springer, Switzerland, pp 614–623
7. Gonzalez RC, Woods RE, Eddins SL (2009) *Digital image processing using MATLAB*, vol 2. Gatesmark, Knoxville
8. Oloumi F, Dhara AK, Rangayyan RM, Mukhopadhyay S (2014) Detection of blood vessels in retinal fundus images. *Comput Sci J Moldova* 22(2):65
9. Mohammed Amean Z, Low T, McCarthy C, Hancock N (2013) Automatic plant branch segmentation and classification using vesselness measure. In: *Proceedings of australasian conference on robotics and automation*, University of New South Wales, Sydney Australia, 2–4 Dec 2013
10. Stanford JB, White GL, Hatasaka H (2002) Timing intercourse to achieve pregnancy: current evidence. *Obstet Gynecol* 100(6):1333–1341
11. Melnick H, Goudas VT (2014) The detection of a salivary ferning pattern using the Knowhen ovulation monitoring system as an indication of ovulation. *J Women Health Care* 4(3):1000235
12. Su H-W, Yi Y-C, Wei T-Y, Chang T-C (2017) Detection of ovulation, a review of currently available methods. *Bioeng Trans Med AICHe* 2:238–246
13. Leon SJ (2010) *Linear algebra with application*, 8th edn. Macmillan, New York (US)
14. Kroon D (2009) Numerical optimization of kernel based image derivatives. Short Paper University Twente
15. Sato Y, Nakajima S, Shiraga N, Atsumi H, Yoshida S, Koller T (1998) Three-dimensional multi-scale line filter for segmentation and visualization of curvilinear structures in medical images. *Med Image Anal* 2(2):143–168
16. Lindeberg T (1996) Edge detection and ridge detection with automatic scale selection. *Conf on Comp Vis and Pat Recog* 30(2):465–470
17. Frangi AF, Niessen WJ, Vincken KL, Viergever MA (1998) Multiscale vessel enhancement filtering. In: Wells WM, Colchester A, Delp SL (eds) *Medical Image computing and computer-assisted intervention—MICCAI'98*, Oct 11–13, Cambridge, MA. Springer, Berlin, pp 130–137
18. Kanan C, Cottrell GW (2012) Color-to-grayscale: does the method matter in image recognition? *PLoS ONE* 7:e29740



# Autonomous Self-exam Monitoring for Early Diabetes Detection



Rohana Abdul Karim, Nur Alia Fatiha Azhar, Nurul Wahidah Arshad,  
Nor Farizan Zakaria and M. Zabri Abu Bakar

**Abstract** Diabetes can be prevented by early detection. In Malaysia, new case of diabetes is increasing year by year. Insufficient number of physicians tasked to treat a large number of patients will increase their burdens and also make them more stressed. An autonomous self-exam monitoring is developed in order to assist the physicians in identifying diabetes at the early stage. Iris image is used to recognise the early detection of diabetes. Based on iridology theory, the image is evaluated by detecting the presence of broken tissues and change in colour pattern. It can be integrated with computer vision for an accurate identification of abnormality in iris image. This paper focuses on developing an iris imaging system that extracts the presence of orange pigmentation which is the sign of diabetes. This project comprises of three stages which are pre-processing, processing and post processing stage. The designed tool convert an iris image into new picture using image processing algorithms and analyses some changes in colour pattern and lastly diagnose whether it is diabetic or non-diabetic iris. The experimented images in this project are the iris image that was taken from public database UBIRIS.v1. At the end of this project, we discovered whether this system can detect the presence of broken tissues and change in colour pattern of iris or not. The final result shows the accuracy of 80% for detecting the orange pigmentation as the sign for early diabetes detection.

**Keywords** Iris diabetes · Image processing · Classification

## 1 Introduction

According to Bernama, the Ministry of Health (MOH) Disease Control Division has stated in 2017 that diabetes is the main fatal disease of Malaysians besides the heart problem [1]. Back in 2011, MOH has estimated that Malaysians consume 26 teaspoons of sugar every day, thus, proving that diabetes is not a new health issue in this country [2]. Reportedly in 2010, the number of doctors in Malaysia is 30,000 and

---

R. A. Karim (✉) · N. A. F. Azhar · N. W. Arshad · N. F. Zakaria · M. Z. A. Bakar  
Faculty of Electrical and Electronic Engineering, Universiti Malaysia Pahang, 26600 Pekan,  
Pahang, Malaysia  
e-mail: [rohanaak@ump.edu.my](mailto:rohanaak@ump.edu.my)

this need to increase into 90,000 by 2020. Unfortunately, the numbers of physicians are less than the number of population in Malaysian. This fact shows that Malaysians do not have enough physicians to treat every patient.

This paper describes an algorithm that can aid the detection of early diabetes. Diabetes occurred due to damages in the pancreatic islets of Langerhans which produces insulin to control blood glucose level. Among the resulting complications of diabetes is the destruction of retinal blood vessels which is the most common blindness cause in Malaysia. An autonomous self-exam to mass-screen the iris for early diabetes detection is needed to assist specialized ophthalmologists. Therefore, the aid of a Computer Vision System (CVS) is required in order to extract features deep inside the iris using image processing techniques, to interpret and analyse the iris image.

The images of iris from online database are used to assist the ophthalmologists. Current approach, doctors manually examined iris colour for diagnosis. From there, extraction of iris features can be used to determine whether the eyes are from normal or diabetic patient. Integrating with computer vision system, iridodiagnosis becomes a reference for an accurate identification of abnormalities in pigmentation of the iris.

Iris damage from diabetes occurred when a lot orange pigmentation formed within the black area (in the case of patients having a black iris). Black area has been stained by orange pigmentation which most commonly points to blood sugar issues, thus showing the person's iris is diabetic iris. There are new vessels appearing on the iris, and this condition is called rubeosis iridis.

In the year 2015, Malaysia has recorded 3.3 million cases of diabetes, which was associated to the most common cause of blindness among working age individuals. An early detection and treatment are essential as it may deter vision loss and blindness [3].

## 2 Research Background

The investigation of iridology to detect abnormality of human organs by examining the iris was much improved after the invention of computer technology which expanded the exactness of determination. They proposed an iridology model that comprises of the iris image pre-processing, texture feature analysis and disease classification. Their test result demonstrates that the proposed iridology analysis model is quite effective and promising for medical diagnosis and health surveillance for both hospital and public use [4].

The conventional method for diagnosing diabetes is not real time and seems to cause inconvenience and discomfort to many people. It involves fasting and puncturing of the body tissue (skin) to collect blood sample. This may cause problems like swelling or hardness under the skin, severe pain and sometimes fever or other possible complications [5]. The proposed method for diabetes determination involves no-contact, are real time, portable and more convenient as it tends to be utilised both in the hospital and at home for self-diagnosis.

Besides that, other researchers proposed the detection of diabetes through the corresponding region of pancreas in the iris of the eye based on color coding system and visual inspection. In the future, this detection method should be converted into metric form so that the diabetes status of the patient can be categorised as mild, moderate and severe [6].

The contribution of CVS linked with iridology has been exposed in the medical field in recent years. Image processing in CVS gives major benefits to the medical field on vital part of the early detection, diagnosis and providing treatments to a large number of patients in the world. Moreover, image processing methods such as extracting, quantifying, classifying and interpreting information are effective in providing better understanding and insight into the structure and function of the organs being imaged [7].

CVS are the systems that intelligently assist physicians in interpreting digital medical images and making proper diagnosis. It gives plenty of useful information towards planning of treatment. Throughout this project, CVS and iridology practice are integrated for the early diabetes detection [8].

In 2009, Weill Medical Cornell did a research on evaluating patients health and diagnose diseases especially cancer via analysis of three-dimensional images using the technology of computer system. The high resolution medical image analysis has been installed in New York Hospital with advance three-dimensional segmentation and three-dimensional visualisation.

Iridology, also known as iridodiagnosis is an alternative medical practice in which patterns, colours and other characteristics of the iris are examined for information regarding patient's health. On the other hand, iridology is the science of analysing the fibres' colours and signs in the eye and gathers the information regarding imbalances in the body, where they are and how severe they are. Other than that, iridodiagnosis will identify systematic diseases through observation of changes in the form and colour of iris. Plus, in health diagnosis, iris plays an important role by following the iridology [1] and gives the best result regarding disease [9].

An American iridologist specified that iridology analyses are more reliable and give much more information regarding the body condition and the examination of Western medicine [10]. However, Russell S. Worrall, O. D., an assistant clinical professor of optometry at School of Optometry, University of California, Berkeley noted that iridology theory might have some disadvantages due to new challenging and critical disease appearing in the future. Fortunately, due to some cases, iridology theory is acceptable.

Different journal have different method for classification of diabetes and non-diabetes. Most of the researcher use Support Vector Machine (SVM) technique for features extraction and classification. SVM is a method that uses separating hyper-plane in order to differentiate the classified form. Other than that, Neural Network is also used by researcher for classification [11]. For patterning, neural network are good enough at recognising patterns such as to classify a tumor as benign or malignant, based on the uniformity of cell size, meiosis and mitosis.

Image Processing Technique (computer vision) is also popular on classification such as on pattern recognition, statistical pattern, mathematical concept and spatial

filtering. Image will be converted into digital form for image processing techniques. Last but not least is the Fuzzy C-Means Clustering. This technique ensures each of the data point belongs to a cluster up to some degree that is quantified by membership grade. Jim Bezdek introduced this classification method in 1981 [12] to show how to group data points that populate some multidimensional space into specific number of different clusters.

The methodology of autonomous self-exam monitoring for early diabetes detection will be described in Sect. 3. Section 4 provides the experimental results and discussion. The conclusion and some recommendations for future direction are stated in Sect. 5.

### 3 Methodology

In this section, the proposed method is explained in several sub-chapters. First, the data collection will be described in detail, followed by segmentation, threshold in MATLAB, feature extraction process and finally, classification (see Fig. 1).

#### 3.1 Data Collection

In this project, a number of 59 samples of iris image are tested. The images were downloaded from UBIRIS.v1. This online database provides diabetic and non-diabetic iris images. By using this database and the result between diabetic and normal iris can be obtained and compared.

The database consists of 30 normal iris images and 29 diabetic iris images. The images were captured under 2 sessions. For the first session of iris image, all the noise factors have been minimised, especially with those related to reflections, luminosity and contrast.

The second session was setting the place with natural factor by enhancing the propitiation of appearance of iris image with respect to reflections, contrast, luminosity and focus problems. During this stage, image collected was taken by a vision system with or without insignificant active participation from the subjects adding several noise problems. Compared to the first stage, the second session image provided will be more recognised.



**Fig. 1** Block diagram for this project

### 3.2 Segmentation

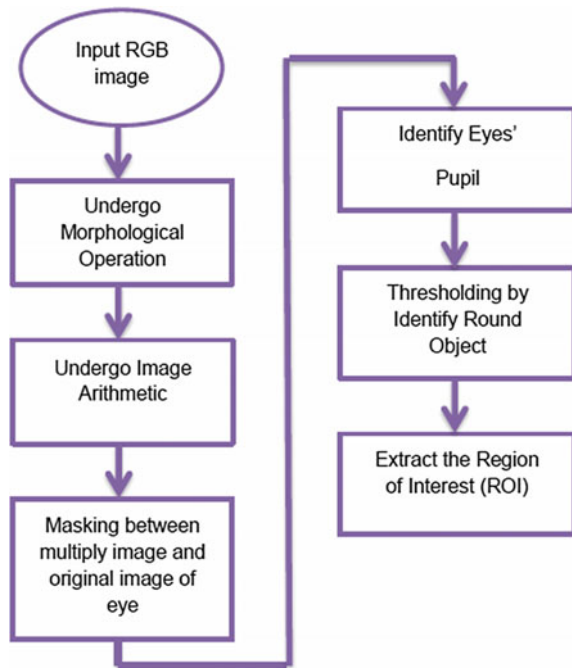
This process consists of morphological operation and image arithmetic operations to identify eye’s pupil and obtain the region of interest (ROI). The flow chart of this process is shown Fig. 2.

During morphological operations, the RGB (red, green, blue) image which is coloured image must be converted into black and white (BW) image format. The function is called erode operation which deletes the structure of element object. Erode function is when the binary erosion of A by B, denoted  $A \ominus B$ , is defined as the set operation  $A \ominus B = \{z|BZ \subseteq A\}$ . In other words, it is the set of pixel locations z, where the structuring element translated to location z overlays only with the foreground pixels in A. Mostly, grayscale erosion is completed with a flat structuring element ( $B(x, y) = 0$ ). To make an equivalent of local minimum operator, grayscale erosion is used for those structuring elements (see Fig. 3).

To obtain the ROI in image of the eye, arithmetic operations such as multiply and sum are used. Multiply function is an operation where it multiplies every single element in morphological operation’s result through matching the element in original image that has been changed from RGB to grayscale format. Hence, it returns the product in the matching element of the final output image.

Next task is locating the pupil to acquire the value of perimeter, centroid and area. First step is setting the threshold of the image by changing its colour into black

Fig. 2 Flow chart of the ROI



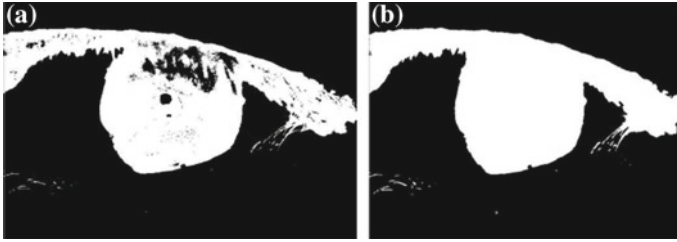


**Fig. 3** **a** Image before morphological operation, **b** Output image after morphological operation

and white format. This is done to prepare for the boundary tracing using boundaries (bwboundaries) function. Once again, erode and dilate function are used to delete and fill the holes in order to give a better and exact round shape.

Second, in order to find round object, it requires obtaining boundaries which concentrate merely on exterior boundaries. According to coding, `[B, L] = bwboundaries(bw'noholes')`; the option of 'noholes' will smooth the processing by preventing boundaries (bwboundaries) function from searching for inner contours.

After the required boundaries, round object are determined by estimating each object's area and perimeter using formula,  $metric = 4 * \pi * area / perimeter^2$  which only equals to one circle. The resulting value would be less than one for any other shape. Moreover, 'regionprops' are used to gain the value of estimation for all area of the object.

Throughout thresholding method, the centroid, perimeter, area and matrices of round object are obtained. The values of area and centroid, has fulfilled the requirement for finding the ROI of pupil. Right before cropping the ROI, masking function is applied between multiplied image and original image of eye. Therefore, the only thing required is the formation of orange pigmentation at nerve rings area to analyse whether it is diabetic or normal eyes (see Fig. 4).

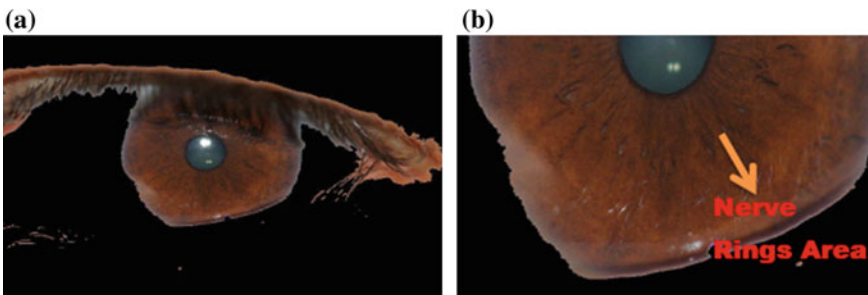


**Fig. 4** **a** Multiplied image are masked with original image of eye, **b** Region of Interest (ROI)

### **3.3 Threshold**

The image thresholding in MATLAB software are simple, however it is effective in the way of partitioning an image into a foreground and background. Image analysis technique is a type of image segmentation that separates the object by converting grayscale image into binary image. Binary image is a digital image that has only two possible values for each pixel. Normally, black and white are used for a binary image, yet any two of them can be used. Foreground colour is the colour used for the object in the image while the rest of the image is background colour.

### **3.4 Feature Extraction**

This section is done with two extractions and analysis, first to the black colour and second to the orange pigmentation.

To determine the range for black colour in histogram, 29 samples of diabetic and 30 samples of normal iris are tested. For diabetic iris, value at x-axis must be in a pixel range between 0 and 125, while y-axis must be in a pixel range between 4000 and 8000. Vice versa for normal iris, the range for x-axis and y-axis must be out of the range stated. Both value range of x-axis and y-axis are showing the intensity of the colour black that exists in 59 samples of iris image.

In order to find the intensity of orange pigmentation, colour threshold application is used. All 59 samples of iris image are tested by colour threshold application, provided by MATLAB software that gives the exact value of orange pigmentation threshold on iris image. Colour threshold application loads image from workspace, thus the intensity of orange pigmentation is more accurate. There are several colour space provided in colour threshold application which is RGB, HSV, YCbCr and  $L^*a^*b^*$  that provide the best colour separation for segmentation. For calculating orange pigmentation intensity, RGB colour space are chosen.

### **3.5 Classification**

This method is included in the algorithm in order to test the 59 samples of iris image and to analyse whether it is diabetic or normal iris. After the testing, result shows that the orange pigmentation intensity is higher than black colour intensity, thus indicating that it is an early diabetes iris according to iridology. There are major challenges in segment between orange pigmentation and other colours in iris image. First, some of the database images are in low contrast eventhough filtering and enhancement has been done. Second, the presence of numerous unusual crypts in several database images has caused difficulties on segmentation operation. Colour map editor is used to ensure the values of interpolating colour space are correct.

## 4 Result and Discussion

In this paper, several techniques are developed including morphological operations, image arithmetic operations, masking and colour threshold. In this chapter, all methods and algorithms are combined in the form of graphical user interface using MATLAB Graphical User Interface Development Environment (GUIDE) to form a complete an autonomous self-exam monitoring for a system that can be employed for diabetes detection at an early stage. For this project, there are three steps for result analyses which are black colour detection, orange and red pigmentation detection and orange pigmentation detection.

The database sample consists of 29 diabetes iris images. After being tested by histogram method, 9 of the images are passed by histogram method. This gives the information that, for 9 images that are passed, the value obtained for black colour exist at nerve rings area are smaller. The other 20 images did not pass the test. For normal iris consisting of 30 images, only one of them passed the histogram method. This means that only one image is confirmed to be normal iris using histogram method. The value obtained for black colour existing at nerve rings area are higher. While for the other 29 images that did not pass meant that the value obtained for black colour that exists at nerve rings are smaller, thus need to be tested again using colour threshold method.

There are several stages outlined to detect diabetes using this system. The initial stage uses histogram method, and if the result is false, it proceeds to the second stage which is the detection of orange/red pigmentation. If the result is false too, it will move to the third stage which is the detection of orange pigmentation only. All these three stages are used in order to recognise whether the iris image is diabetic or normal. The outcome of the second stage result increased by 18 for diabetes iris image and 30 over 30 for normal iris image.

For the testing by orange pigmentation detection method, it can be simplified that all diabetes and normal iris images passed the second stage. This means that all images are confirmed by orange/red pigmentation detection method. The summary of the deciding method are as shown as graph in Fig. 5.

The result of finding three method are formed in confusion matrix, which consists of TP, TN, FP, and FN as shown in Table 1 and the equation for accuracy is using Eq. 1. The system achieves 80% of accuracy, however some of the algorithm is not perfectly robust. Moreover, the pixels of image database also affect the creation of the algorithm. The challenge in creating algorithm is to further enhance the features in nerve rings area which needs more advance tools, software and robust algorithm.

$$\text{Accuracy} = (TP + TN)/(TP + FP + FN + TN) \quad (1)$$



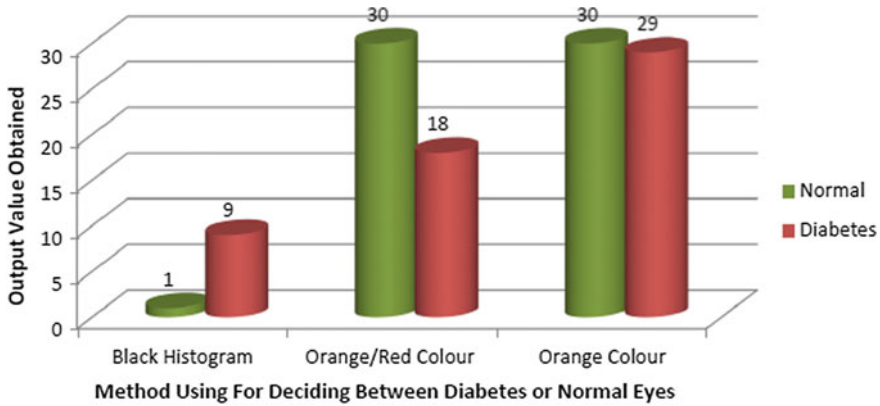


Fig. 5 Graph of using three method for deciding between diabetes or normal eyes

Table 1 Outcome for both normal and diabetes iris image

Condition	Score
True Positive (TP) (diabetes iris that is correctly identified as diabetes)	18
False Positive (FP) (normal iris that is incorrectly identified as diabetes)	0
True Negative (TN) (normal iris correctly identified as normal)	30
False Negative (FN) (diabetes iris incorrectly identified as normal)	11

## 5 Conclusion

An autonomous self-exam monitoring is developed using image processing techniques in MATLAB software for the purpose of detecting diabetes at early stage. The purpose in developing the system is to extract robust iris key features for diabetes. This is used to evaluate and validate the proposed algorithm which can classify normal or abnormal iris. To build this system, the iris key features are extracted by performing morphological operations, image arithmetic operation, masking the features and finding the colour threshold with guidance of iridology theory. According to the process that has been done, the result shows a successful classification of 59 samples of data into 30 normal iris images and 29 diabetes iris images. This has achieved the objective with 80% accuracy of the system, concluding that an autonomous self-exam system can detect for diabetes and non-diabetics.

**Acknowledgements** This research work is supported by research grant funded by Universiti Malaysia Pahang (RDU1703233). The authors also would like to thank the Faculty of Electrical & Electronics Engineering, Universiti Malaysia Pahang for financial support.

## References

1. NST Homepage <https://www.nst.com.my/news/2017/04/228008/73-msians-die-hypertension-diabetes-heart-disease-moh>, last accessed 15 Apr 2019
2. Kesan Penyakit <https://vitamin-cerdik.com/kesan-penyakit-kencing-manis-atau-diabetes-ke-atas-penghidap/>, last accessed 15 Apr 2019
3. Vashist P, Singh S, Gupta N, Saxena R (2011) Role of early screening for diabetic retinopathy in patients with diabetes mellitus: an overview. *Indian J Community Med* 36(4):247–252
4. Ma L, Li N (2008) Texture feature extraction and conference on medical biometrics. In: *Proceeding of ICMB, LNCS 4901, Hong Kong*, pp 168–175
5. World Health Organization (2011) Use of glycated haemoglobin (HBA1C) in the diagnosis of diabetes mellitus. WHO publication 20 Avenue Appia, 1211 Geneva 27, Switzerland
6. Jamal Firmat Banzi (2015) An automated tool for non-contact, real time early detection of diabetes by computer vision. *Int J Mach Learn Comput* 5(3):225–229
7. Othman Z (2012) Anton Satria Prabuwo: preliminary study on iris recognition system: tissues of body organs in Iridology, Center for Artificial Intelligence Technology (CAIT), Faculty of Information Science and Technology, Universiti Kebangsaan Malaysia, 43600 UKM Bangi, Selangor, Malaysia
8. Banzi JF, Member, SCIEI and Xue Z (2015) An automated tool for non-contact, real time early detection of diabetes by computer vision. *Int J Mach Learn Comput* 5(3)
9. Ms. Tathe PB, Mrs. Dr. Patil M (2015) Analysis of health condition based on iris image. Novateur Publication's International Journal of Innovation in Engineering, Research and Technology (IJERT), ICITDCEME' 15 Conference Proceedings
10. <https://www.quackwatch.org/01QuackeryRelatedTopics/iridology.html>. Last accessed 18 Apr 2019
11. Haykin S (2009) *Neural networks and learning machines*. Pearson Education Inc.
12. Bezdec JC (1981) *Pattern recognition with fuzzy objective function algorithms*. Plenum Press, New York

# Quantitative Assessment of Remote Code Execution Vulnerability in Web Apps



Md Maruf Hassan, Umam Mustain, Sabira Khatun,  
Mohamad Shaiful Abdul Karim, Nazia Nishat and Mostafijur Rahman

**Abstract** With the exponentially increasing use of online tools, applications that are being made for day to day purpose by small and large industries, the threat of exploitation is also increasing. Remote Code Execution (RCE) is one of the topmost critical and serious web applications vulnerability of this era and one of the major concerns among cyber threats, which can exploit web servers through their functionalities and using their scripts/files. RCE is an application layer vulnerability caused by careless coding practice which leads to a huge security breach that may bring unwanted resource loss or damages. An attacker may execute malicious code and take complete control of the targeted system with the privileges of an authentic user with this vulnerability. Attackers can attempt to advance their privileges after gaining access to the system. Remote Code Execution can lead to a full compromise of the vulnerable web application as well as the web server. This chapter highlights the concern and risk needed to put under consideration caused by RCE vulnerability of a system. Moreover, this study and its findings will help application developers and its stakeholders to understand the risk of data compromise and unauthorized access to the system. An exploitation algorithm is proposed to identify RCE vulnerability in web application. Then based on it, around 1011 web applications were taken under consideration and experiments were conducted by following manual double blinded penetration testing strategy. The experiments show that more than 12% of web application were found vulnerable to RCE. This study also explicitly listed the critical factors of Remote Code Execution vulnerability and improper input handling. The experimental results are promising to motivate developers to focus on security enhancement through proper and safe input handling.

**Keywords** Web application vulnerabilities · Remote code execution (RCE) · Input validation · Data breach

---

M. M. Hassan · U. Mustain · N. Nishat · M. Rahman (✉)  
Department of Software Engineering, Daffodil International University, Dhaka, Bangladesh  
e-mail: [mostafijur.cse@gmail.com](mailto:mostafijur.cse@gmail.com)

S. Khatun · M. S. A. Karim  
Faculty of Electrical and Electronics Engineering, Universiti Malaysia Pahang, Gambang,  
Malaysia

## 1 Introduction

Web applications have a great impact on every part of this modern life. It has become the key instrument for business and communication nowadays. Everyday millions of users are accessing web applications for several purposes that allow these web applications to store, process or manipulate sensitive user data. A large volume of sensitive data and the ability to manipulate particular systems are turning web applications into an attractive target for security attacks. Till date, there has been many attacks and threats encountered by web applications. Security breaches are becoming more and more advanced and structured day by day as attackers are changing the exploitation techniques with the update of technology. Among the web application attacks, Remote Code Execution (RCE) is one of the more damaging threats [1]. Authenticity and integrity of an application or system can be affected by RCE. The attacker can input and execute server-side scripts and even take total control of the system with this cross-site-scripting attack. As per the studies conducted by SANS and OWASP Remote Code Execution (RCE) is one of the most common web vulnerabilities [2–4] along with SQLi [5], Cross-Site-Scripting (XSS) [6], Buffer Overflow [7], Local File Intrusion (LFI) [8] and Broken Authentication [9]. Due to the potential of damage to a system of an organization, multiple research work has taken place. RCE is one of the most critical web app vulnerability that brings huge security risk that can lead to a full compromise of the application and server. The security threat of this vulnerability opens the door of discussion and research to prevent and mitigate the risk caused by it. User authentication and access control problem has been mentioned in many researches. They also include prevention techniques for vulnerability.

This paper presents an assessment and structured analysis on Remote Code Execution (RCE) vulnerability and several types of exploitation techniques, reason and risk factors along with a short discussion on defense mechanism. This investigation is organized as follows. Section 2 provides a literature review. Section 3 describes the exploitation process, Sect. 4 describes the methodology Sect. 5 displays experimental results and analysis, followed by discussion and conclusion with the significance of the result and future works.

## 2 Literature Review

In recent years due to IT security breach companies and their clients, and even governments are facing losses. These attacks cause issues such as identity theft, information theft, data loss, system failure and also financial losses. Though a number of investigations have been conducted on cyber-attack and web vulnerability. But the attackers are changing and updating their techniques. To be protected, we need to be thought in our approaches towards the attacks and reducing the damage caused by these threats, malware and cybercriminals. A study focused on SQLi, BAC and

cross-site-scripting (XSS) web application vulnerability reveals application layer weaknesses by performing code level problem analysis and recommended a guideline for the developers to develop a secure web application [10]. Another research conducted on XSS detection, mainly focused on GET and POST method of the applications which prevents stored, reflected and DOM-based XSS [11]. In research [12], an algorithm was proposed for automatically detecting RCE vulnerability in PHP based platform by considering context sensitive and procedural analysis [13]. In paper [14], the author mentioned the existence of RCE vulnerability on Basilic (1.5.14) software that had the security loopholes and the problem was in line 39 of a php file named Diff.php inside of 'config' folder. However, escapeshellarg() method has been found useful to prevent RCE vulnerability through filtering special characters. In Bangladesh, 86% of websites were found vulnerable to SQL injection [15]. A study was conducted by experimenting on 359 different educational websites. Another study was conducted on XSS vulnerabilities which shows 75% web applications are found to be vulnerable to CSRF and 45% web applications are found to be vulnerable to XSS among 500 data set samples [15]. Research identifying the importance of influence factor behind success rate of remote arbitrary code execution attacks on server and client sides was done that shows that the success rates of the attacks on the server were between 15 and 67% and client-side was between 43 and 67% respectively [16]. A survey has been done upon web app vulnerability detection tools like Nessus, ZAP and Acunetics for comparing the accuracy along with manual penetration testing method [17]. Some other study shows explanations and approached types of access control policies of web applications. In [18], a logic-based policy management scheme has been introduced focusing on XACML policies and can be considered as specifying and enforcing access control policies for various applications and services in the web. Given the discussion above, it is found that insignificant research work has been conducted on Remote Code Execution and XSS vulnerabilities. More RCE vulnerability focused research needs to run to handle the security threat caused by it. This paper presents detailed RCE exploitation techniques and the recent web applications condition against this vulnerability.

### 3 RCE Exploitation Process

At the beginning of the exploitation, the process (shown in Fig. 1) checks the \$\_GET and \$\_POST based possible URLs. Meanwhile, the task gets divided into two portions on the ground of their type. As per \$\_GET URLs, the model extracts inputable parameters from the URLs and inject malicious codes in them using the previously developed criteria we detect RCE vulnerability. Afterward, a method titled as 'shel\_exec()' gets executed forcefully which provides return values for the action.

On the other hand, \$\_POST URLs get examined to find fields, which is the destination for injecting the malicious code using the cookie manager by taking the malicious data from POST Tab. Subsequently, a custom query gets executed forcefully, which also provides some responses in return. After the evaluation of the responses in return

---

**Algorithm 1** Exploitation Process of RCE
 

---

```

1: Start
2: if check_URL($_GET())||$_POST() then
3:   for $_GET() do
4:     Check Inmutable Parameters ∈ URL Parameters
5:     Inject Malicious Code → URL
6:     Force Execute → shell_exec()
7:     if response == true then
8:       return ← RCE vulnerability
9:     else
10:      return ← Zero vulnerability
11:    end if
12:  end for
13:  for $_POST() do
14:    Check Injectable Fields ∈ POST Data
15:    Inject Malicious Code → Cookie Manager
16:    Input Malicious Data → POST Tab
17:    Force Execute → query()
18:    if response == true then
19:      return ← RCE vulnerability
20:    else
21:      return ← Zero vulnerability
22:    end if
23:  end for
24: end if

```

---

**Fig. 1** Algorithm for RCE exploitation process

based on data collected on RCE, it can be determined whether the web application is vulnerable to RCE or not.

## 4 Methodology

The methodology is divided into two phases with detail description as follows.

### 4.1 Data Collection

To collect the sample, we examined 1011 selected websites using dork. Dork contains the combination of search string and search operators to find desired information for a user.

Some of the inputs used for this examinations includes “inurl admin/upload.php”, “inurl admin/config.php”, “inurl admin/dashboard.php”, “inurl admin/login.php”, “inurl site/backup.zip”, “inurl site/database.sql”. Change in syntax during dork production may vary depending on the given requirement as well as different search engines’ (such as Bing, Qwant, and Yahoo) basic criteria. As soon as the primary sites are observed, it is ready to forward to the pre-processing phase to ensure the get ability of RCE vulnerability in the selected site.

## 4.2 Pre-Processing Phase

Pre-processing is an important phase to create a valid data set from raw data which is usually incomplete, inconsistent and tempered.

After receiving the list of selected sites from the output of the dork, it was examined through three exploitation techniques such as Get Based RCE, Post Based RCE, OS Based RCE to verify the existence of RCE in those sites.

In this study regarding Remote Code Execution, small sample size procedure is used as the sampling method as shown in Eq. (1) [19]:

$$s = X^2 + (1 - P) \div d^2(N - 1) + X^2 P(1 - P) \quad (1)$$

In this equation ‘*s*’ represents the required sample size, where ‘ $X^2$ ’ is the table value of chi-square for one degree of freedom at the desired confidence level, i.e. 3.841, ‘*d*’ is the degree of precision expressed as a proportion. ‘*N*’ and ‘*P*’ is the population size and population proportion respectively. G8Power 3.1.9.2, a statistical tool, was used to identify the sample size of this experiment by using the Eq. (1). Untwisted several regression tests have been shown under F tests family where the number of prognosticators is selected as four in this investigation since the maximum prognosticator of the used testing model is the type of exploitation. 0.05 was set as the value of  $\alpha$  err prob and 0.95 was set as the value of Power ( $1 - \beta$  err prob) in the tool.

## 5 Results

By using Eq. (1), the tool, G8Power 3.1.9.2 provides the result where it required a minimum of 129 valid samples to execute the study. The total number of 1011 samples were used in this investigation, among those 12.76% websites were found affected with Remote Code Execution (RCE), whereas the rest of 87.24% web applications were not affected by RCE vulnerabilities.

In this study, unauthorized access to redirection settings and access to cookies, misconfiguring sensitive data recovery was effectively caused by the RCE vulnerable collection sample. For this experiment, Double Blinded Manual Penetration Testing

**Table 1** Frequency analysis for the existence of RCE vulnerability among five sectors

Sector	Frequency	Percentage (%)
Education institute	54	41.86
E-commerce	29	22.48
Medical sector	25	19.38
Online portal	7	5.43
Government counterpart	14	10.85
Total	129	100

Strategy [20, 21] was regarded to assemble material. Primarily this dataset has been studied with the demographics i.e. sectors. For investigating associations among the factors of RCE that also includes reason of RCE attack, platform, and exploitation technique.

Binary Logistic Regression, Pearson's  $\chi^2$ -value, odd ratios and  $p$ -value tests were conducted. The analysis which has been made is discussed below. Table 1 represents the frequency analysis for the existence of RCE vulnerability in several sectors (education, e-commerce, government counterpart, health, and private company) of our sample.

As shown in Table 1, it can easily be observed that the educational web applications are affected the most by the REC vulnerability, which is 41.86% due to compromise their access privileges. The Online Portal have decent percentages (5.43%) of REC vulnerability, which is the least affected sector for the given exploitation type. Others like E-commerce sites, the counterpart of the government and Health institution sites were vulnerable with RCE percentage of 22.48%, 19.38%, and 10.85% respectively. The analysis table was organized by considering  $p$ -value frequency distribution, odds ratio with a prognosticator confidence interval, and factor-coalition. Table 2 shows the frequency distribution of RCE web apps vulnerability with their noteworthy variation among risk factors. The table helps to understand the fact 'Sector', 'Programming language', and 'Platform' ( $p < 0.000$ ) are remarkably interconnected with mentioned RCE vulnerability. Here to observe, 'Reason of RCE' is very closely connected ( $p < 0.001$ ) and 'Exploitation Techniques' ( $p < 0.013$ ) are also connected with RCE vulnerability. The prognosticator's noticed effect on RCE vulnerability in web apps has been discussed in Table 3. In Table 3, Odds ratio (OR) has been used to compare different groups with 95% confidence interval (CI).

The primary parameters of RCE exploitation techniques include Reason of RCE, Exploitation Techniques, Sector, programming language, and platform have risk factor 0.636, 0.749, 0.778, 0.665, 0.373 times greater respectively. Other factors, such as the reason for Directory Readability, exploitation of Unauthorized Cookie Access, and web applications developed with PHP platform, are 36,812, 26,912, and 147,769 times higher than those that have no interrelationship with the above-mentioned factors.  $P$ -value Pearson's  $\chi^2$  test with among the important factors is shown in Table 4.  $P$ -value of less than 0.01 (<1%) among coalition factors is highly noteworthy, while  $p$ -value of less than 0.05 (<5%) is highly significant. It can be



**Table 2** Frequency Distribution with a *p*-value of risk factors between reason of RCE, exploitation techniques, sectors, platforms, and OSs versus the presence of RCE vulnerability in the web application

Factors		RCE vulnerability status		<i>P</i> -value
		Found	Not found	
Reason of RCE	Use of executable function	41	278	0.001*
	Input sanitization	75	433	
	Privilege escalation	13	171	
Exploitation techniques	Get based RCE	64	357	0.013*
	Post based RCE	40	295	
	OS based RCE	25	230	
Sectors	Education institute	54	260	0.000*
	E-commerce	29	201	
	Medical sector	25	190	
	Online portal	7	101	
	Government counterpart	14	130	
Programming language	PHP	82	375	0.000*
	Java	32	302	
	.Net	15	205	
Platform	UNIX	106	349	0.000*
	WINDOWS	23	354	
	MAC	0	179	

\* indicates the highly associated with RCE vulnerability

**Table 3** Odds ratio (OR) with confidence interval (C.I.) of predictors

Predictors	Sig	OR	95% C.I for OR	
			Lower	Upper
Reason of RCE	0.001	0.636	0.491	0.824
Exploitation techniques	0.013	0.749	0.596	0.941
Sectors	0.000	0.778	0.683	0.885
Programming language	0.000	0.665	0.520	0.825
Operating system	0.000	0.373	0.225	0.618

observed from the above table that all factors are remarkably interrelated, i.e. highly notable relationship between RCE Existence.

**Table 4** Associations among the factors of RCE vulnerability

	Reason of RCE	RCE exploitation techniques	Platform	Sectors	Programming language
$\chi^2$	41.806	6.310	25.494	21.343	13.714
<i>P</i> -Value	0.000	0.043	0.000	0.000	0.001
$\chi^2$		6.314	8.624	66.739	9.536
<i>P</i> -Value		0.000	0.000	0.000	0.000
$\chi^2$			1211.500	1100.917	102.994
<i>P</i> -Value			0.000	0.000	0.000
$\chi^2$				58.293	843.762
<i>P</i> -Value				0.000	0.000
$\chi^2$					54.393
<i>P</i> -Value					0.000

## 6 Discussions

This study has been conducted over 1011 web applications that include 129 RCE vulnerable and 882 nonvulnerable web applications. The participant sectors of web application involved with Education, E-commerce, Govt. Counterpart, Health, and Private Company that were developed with PHP, Java, and .Net platform. The operating platform UNIX, Windows and Cent-OS are used respectively in the hosting server of sample applications. To get exploited through RCE vulnerabilities, this study has been revealed that the leading factors of the applications are “RCE Exploitation Techniques”, ‘Sector’, ‘Programming language’, and ‘Platform’. It has been observed from the sample data, 63.57%. RCE vulnerability is found in “PHP” developed application. Whereas the application that is built on “JAVA” and “.Net” platform is get affected by RCE with 24.81% and 11.62% respectively. At the same time, the applications hosted in “UNIX” are more prone to RCE with “82.17%” whereas “Windows” has the probability of 17.83%. “IOS” hosted application is unlikely to be vulnerable from RCE. After analyzing the results, it cannot be claimed that the “Platforms” are directly responsible for creating REC vulnerability in a web application. However, it can be stated that PHP developers are less careful about RCE. In this investigation, it is notable that the web applications that have “Session Misconfiguration”, “Improper Input Validation”, and “Sensitive Data Disclosure” are more prone to be affected by RCE vulnerability. This vulnerability is leading to providing privileged access to an unauthorized user. The sites that have improper input validation problem are more intense with the risk compare to the applications that are adequately validated the input. Three factors are found significantly in both the  $\chi^2$  test and binary logistic regression analysis mentioned in the above.

## 7 Conclusion

Remote Code Execution is a web application vulnerability that should not be taken lightly. Due to the sharp incline of web application uses in recent years, the threat of such attacks is increasing through sending or inserting malicious code into vulnerable applications that harms both applications and users. Although there is enough RCE patching, we can never assure the concerned security. Attackers always find new ways to break the security of the targeted applications. So, we have to increase the analysis of RCE vulnerable patterns and then use prevention technique efficiently. In this chapter, an algorithm for RCE exploitation process is proposed to overcome the mentioned problems. Based on the algorithm, we have presented investigation performances on System based, Web based and Server based RCE vulnerability. Through experimental tests on 1011 real-world web applications, a total 129 RCE vulnerabilities were successfully identify during the examination time by showing the usability of the proposed algorithm.

**Acknowledgements** The authors want to acknowledge and credit the Cyber Security Centre of Daffodil International University for help in conducting this study. Also, want to show gratitude to the authorities of the organizations who have given permission to examine their web applications.

This research work is supported by Fundamental Research Grant Scheme (FRGS), RDU190140 funded by Ministry of Higher Education (MOHE). The authors would also like to thank the Faculty of Electrical & Electronics Engineering, Universiti Malaysia Pahang (<https://www.ump.edu.my/>) for financial support.

## References

1. Top 10-2017 Top 10. In: OWASP. [https://www.owasp.org/index.php/Top\\_10\\_2017-Top\\_10](https://www.owasp.org/index.php/Top_10_2017-Top_10). Accessed 15 June 2020
2. Mahmoud QH, Kauling D, Zanin S (2017) Hidden android permissions: remote code execution and shell access using a live wallpaper. 2017 14th IEEE annual Consumer Communications & Networking Conference (CCNC). <https://doi.org/10.1109/ccnc.2017.7983184>
3. Mohammad S, Pourdavar S (2010) Penetration test: A case study on remote command execution security hole. 2010 Fifth International Conference on Digital Information Management (ICDIM). <https://doi.org/10.1109/icdim.2010.5664671>
4. Zhang L, Zhang H, Zhang X, Chen L (2007) A new mechanism for trusted code remote execution. 2007 International Conference on Computational Intelligence and Security Workshops (CISW 2007). <https://doi.org/10.1109/cisw.2007.4425561>
5. Farah T, Alam D, Kabir MA, Bhuiyan T (2015) SQLi penetration testing of financial Web applications: investigation of Bangladesh region. 2015 World Congress on Internet Security (WorldCIS). <https://doi.org/10.1109/worldcis.2015.7359432>
6. Shrivastava A, Choudhary S, Kumar A (2016) XSS vulnerability assessment and prevention in web application. 2016 2nd International Conference on Next Generation Computing Technologies (NGCT). <https://doi.org/10.1109/ngct.2016.7877529>
7. Buffer overflow attacks (2005). <https://doi.org/10.1016/b978-1-932266-67-2.x5031-2>
8. Hassan MM, Bhuyian T, Sohel MK, Sharif MH, Biswas S (2018) SAISAN: an automated local file inclusion vulnerability detection model. *Int J Eng Technol* 7:4

9. Huluka D, Popov O (2012) Root cause analysis of session management and broken authentication vulnerabilities. World congress on internet security (WorldCIS-2012), Guelph, ON, pp 82–86
10. Al-Khurafi OB, Al-Ahmad MA (2015) Survey of web application vulnerability attacks. 2015 4th International Conference on Advanced Computer Science Applications and Technologies (ACSAT). <https://doi.org/10.1109/acsat.2015.46>
11. Gupta K, Singh RR, Dixit M (2017) Cross site scripting (XSS) attack detection using intrusion detection system. 2017 International Conference on Intelligent Computing and Control Systems (ICICCS). <https://doi.org/10.1109/iccons.2017.8250709>
12. Zheng Y, Zhang X (2013) Path sensitive static analysis of web applications for remote code execution vulnerability detection. 2013 35th International Conference on Software Engineering (ICSE). <https://doi.org/10.1109/icse.2013.6606611>
13. Gupta BB, Arachchilage NAG, Psannis KE (2017) Defending against phishing attacks: taxonomy of methods, current issues and future directions. *Telecommun Syst* 67:247–267
14. Sommestad T, Holm H, Ekstedt M (2012) Estimates of success rates of remote arbitrary code execution attacks. *Inf Manage Comput Secur* 20:107–122
15. Alam D, Bhuiyan T, Kabir MA, Farah T (2015) SQLi vulnerability in education sector websites of Bangladesh. 2015 second International Conference on information security and cyber forensics (InfoSec). <https://doi.org/10.1109/infosec.2015.7435521>
16. Hassan MM, Nipa SS, Akter M, Haque R, Deepa FN, Rahman MM, Siddiqui M, Sharif MH (2018) Broken authentication and session management vulnerability: a case study of web application. *Int J Simul: Syst Sci Technol*. <https://doi.org/10.5013/ijssst.a.19.02.06>
17. Wu J, Arrott A, Osorio FCC (2014) Protection against remote code execution exploits of popular applications in Windows. 2014 9th International Conference on Malicious and Unwanted Software: the Americas (MALWARE). <https://doi.org/10.1109/malware.2014.6999416>
18. Ahn G-J, Hu H, Lee J, Meng Y (2010) Representing and Reasoning about Web Access Control Policies. 2010 IEEE 34th Annual Computer Software and Applications Conference. <https://doi.org/10.1109/compsac.2010.20>
19. Krejcie RV, Morgan DW (1970) Determining sample size for research activities. *Educa Psychol Meas* 30:607–610
20. Stefinko Y, Piskozub A, Banakh R (2016) Manual and automated penetration testing. Benefits and drawbacks. Modern tendency. 2016 13th International Conference on Modern Problems of Radio Engineering, Telecommunications and Computer Science (TCSET). <https://doi.org/10.1109/tcset.2016.7452095>
21. Liu H, Li Z (2008) Methodology of Network Intrusion Detection System Penetration Testing. 2008 The Ninth International Conference on Web-Age Information Management. <https://doi.org/10.1109/waim.2008.69>

# **Sustainable Energy and Power Engineering**

# A Salp Swarm Algorithm to Improve Power Production of Wind Plant



Ahmad Zairi Mohd-Zain and Mohd Ashraf Ahmad

**Abstract** Currently, the main problem of wind plant power production is definitely the control system of a wind generator that is not able to cope with the impact of turbulence and thus weakens complete power output. In this paper a Salp Swarm Algorithm (SSA) is proposed as a data-driven method to improve the controller variable and thus optimize the complete power production of the wind plant. The SSA is among of the meta-heuristic technique and imitates the salps chain's swarm movement depending on the food placement. The model used in this study originates from Denmark's actual Horns Rev wind plant. The analysis result demonstrates the SSA generates significantly better total wind power production as opposed to the Spiral Dynamic Algorithm (SDA) and the Particle Swarm Optimization (PSO) technique.

**Keywords** Salp swarm algorithm (SSA) · Data-driven · Wind plant optimization · Power production

## 1 Introduction

There has been an enormous development in wind energy through the entire world recently. It is noteworthy that wind energy is among the most economical and vital sources of renewable energy. One of the wind plant study's main problems at the moment is that an individual turbine's optimal controller variables do not promise a wind plant's optimum power production. There are many control variables that require to maximizing the power production of the wind plant, such as generator torque and yaw and blade angle. Contrary to the condition of finding one turbine's control variables that normally resolve by utilizing the model-based technique, the state of improving the controller variables of an array of wind plant turbines is undoubtedly more challenging. The efficient operation of the wind plant needs complete recognition of turbulence connections together with the behavior of the turbine.

---

A. Z. Mohd-Zain (✉) · M. A. Ahmad  
Faculty of Electrical & Electronics Engineering, Universiti Malaysia Pahang, Kuantan, Pahang, Malaysia

There are many approaches proposed so far to get the optimum controller variables for an array of wind plant turbines. As a result, a data-driven technique has been verified as a feasible option for producing the wind plant's optimum power production. Cooperative static control [1] and Safe Experimentation Dynamics (SED) [2, 3] are included in these studies. These alternatives are in the group of a game theoretical technique which identifies each turbine's controller variable for a player to achieve the provided objective of optimum power production. In [4, 5], the researcher introduces the suggested Optimum Energy Point Tracking (MPPT) technique that incorporates a time-changing assessment of wind plant power production and therefore provides far quicker convergence over the technique through [3]. Likewise, Multi-resolution Simultaneous Perturbation Stochastic Approximation (MR-SPSA) [6] operates similarly as in [5] and can generate even greater total power. Fundamental of Random Search in [7] demonstrated that technique can give greater power production than the SED method. On the other hand, the Spiral Dynamics Algorithm (SDA) [8] provides considerably better power production compared to SED and Particle Swarm Optimization (PSO) techniques through the use of similar problem and population-centered optimization. It seems that Moth Flame Optimization MFO [9] substantially improves power production instead of SDA technique in [8], whereas Modified Sine Cosine [10] provides a slightly higher total amount of power production as compared to the PSO technique.

Similarly, the Salp Swarm Algorithm (SSA) [11] technique, presented as one of the meta-heuristic techniques by Seyedali Mirjalili in 2017, is definitely a decent program to optimize the production of wind plants. The reason for this is that the SSA technique offers successfully resolved numerous types of actual world drawbacks including seismic exit structural system [12], distributed generator allocation [13], PEM fuel cells [14], short-term load forecasting [15], fish image segmentation [16], power loss reduction [17], power system stabilizer [18], chemical compound activity [19], soil water retention [20] and a lot more. Furthermore, it will be really beneficial researching the capabilities of the SSA-based technique to optimize the total power production of the current wind plant.

This study examines the effectiveness of the Salp Swarm Algorithm (SSA) as a data-driven technique for assessing the efficiency and optimizing wind plant power production by having ten single line wind turbines. Analyses on the maximum iteration and number of agents are also evaluated as this pairing might affect the wind plant's performance. The evaluation of best, worst, mean, and also standard deviation of the production of wind plant power is shown after that. In addition, SSA results will be assessed alongside SDA [8] and PSO [10].

## 2 Problem Framework

Reflect on  $P_j(\beta_1, \beta_2, \dots, \beta_M)$  ( $j = 1, 2, \dots, M$ ) as the power production of the turbine and  $M$  is the maximum number of wind turbines possibly in the random or complete configuration. The control mechanism is displayed as  $\beta_j$  ( $j = 1, 2, \dots, M$ ) for

each turbine  $j$ . The controller  $\beta_1, \beta_2, \dots, \beta_{j-1}, \beta_{j+1}, \dots, \beta_M$  that are not attached turbine  $j$  may also influence turbine  $P_j$  power production due to the aerodynamic connection through turbines. In addition, any  $\beta_j$  controller adjustments basically change the power production yet also even the power production of additional turbines  $P_1, P_2, \dots, P_{j-1}, P_{j+1}, \dots, P_M$ . At last, the association among  $P_j$  power production and  $\beta_1, \beta_2, \dots, \beta_M$  controllers presumes to stay unidentified given the fact that turbulence pattern through the turbine is rather complex and complicated to attain an accurate dynamic wind plant or mathematical model.

On the other hand, the wind plant’s maximum total power production is usually shown as:

$$\bar{P}(\beta_1, \beta_2, \dots, \beta_M) = \sum_{j=1}^M P_j(\beta_1, \beta_2, \dots, \beta_M). \tag{1}$$

Subsequently, the problem of data-driven control of the wind plant could be expressed as:

**Problem 2.1** The  $P_j(j = 1, 2, \dots, M)$  functions are unidentified with respect to its control mechanism  $\beta_j(k = 1, 2, \dots, M)$  based on the full total power production specified in (1). After that, find each turbine’s controller variable  $\beta_j(j = 1, 2, \dots, M)$  in a manner that maximizes power production.

### 2.1 Salp Swarm Algorithm (SSA) Mathematical Model

In this area, the suggested SSA is an important approach to solving Problem 2.1. First of all, the SSA presented by [11] is explained. In the beginning, reflect on the objective function and is a variable of design in which  $N$  is an agent number. The maximization problem is therefore suggested as:

$$\max_{\varphi_1, \varphi_2, \dots, \varphi_N} f_k(\varphi_j). \tag{2}$$

Using a revised equation, the Salp Swarm Algorithm enhanced  $\varphi_k(k = 1, 2, \dots, N)$  as:

$$\varphi_k^1 = \begin{cases} S_k + c_1((ub_k - lb_k)c_2 + lb_k) & c_3 \geq 0, \\ S_k - c_1((ub_k - lb_k)c_2 + lb_k) & c_3 < 0, \end{cases} \tag{3}$$

in which  $(k = 1, 2, \dots, N)$ . Equation (3) displays the leader  $\varphi_k^1$  basically shifts his position as regards the food source  $S_i$  in the  $i$ th dimension.  $ub_k$  proposed the maximized  $k$ th dimension limit,  $lb_k$  implies the minimized  $k$ th dimension limit subsequently  $c_1, c_2$  and  $c_3$  are random numbers [11]. The  $c_1$  coefficient is very important



variable through SSA for exploration as well as exploitation balances and can be explained as follows:

$$c_1 = 2e^{-\left(\frac{4r}{R}\right)^2} \quad (4)$$

The current iteration is  $r$  and  $R$  is the iterations maximum number. The placement of the salp follower can be revised through Newton's law of motion relation as:

$$\varphi_k^i = \frac{1}{2}at^2 + v_0t \quad (5)$$

where  $i \geq 2$  in  $j$ th dimension and the salp follower is  $\varphi_k^i$  placement in  $i$ th dimension.  $v_0$  is the initial velocity, time is  $t$ ,  $v = \frac{x-x_0}{t}$  and  $a = \frac{v_{final}}{v_0}$ . Taking into account the  $v_0$  is equal to 0 and different iteration is equal to 1, therefore the following Eq. (5) shall be;

$$\varphi_k^i = \frac{1}{2}(\varphi_k^i + \varphi_k^{i-1}). \quad (6)$$

## 2.2 SSA Approach to Increase Wind Plant Power Production

The procedure for applying the SSA technique to increase wind plant power production is shown through this section. The process can be provided by using the SSA mathematical model in the last section as:

- Step 1 Verify the maximum number of iterations,  $R$  and number of agents  $N$ .
- Step 2 Determine the initial variable of control, in the search area, randomly. Use the equation in (4) to estimate the  $c_1$  coefficient.
- Step 3 Perform SSA mathematical model in (2) by configuring and  $\beta_j (j = 1, 2, \dots, M) =$  for every agent  $n$ .
- Step 4 Improving the procedure by updating the equation in (6). Proceed with Step 2 unless the  $R$  necessity is met. With the ideal solution  $\beta_j^* (j = 1, 2, \dots, M)$ , the algorithm stops and the total production of power are registered.

Figure 1 highlights the approach of the data-driven SSA-based wind plant.

## 3 Results and Discussion

Initially, a wind plant model generally stands for an actual wind plant is assumed to assess the data-driven approach. The wind plant model is utilized from [21], will be discussed. A row wind plant model is used for the upcoming SSA approach.

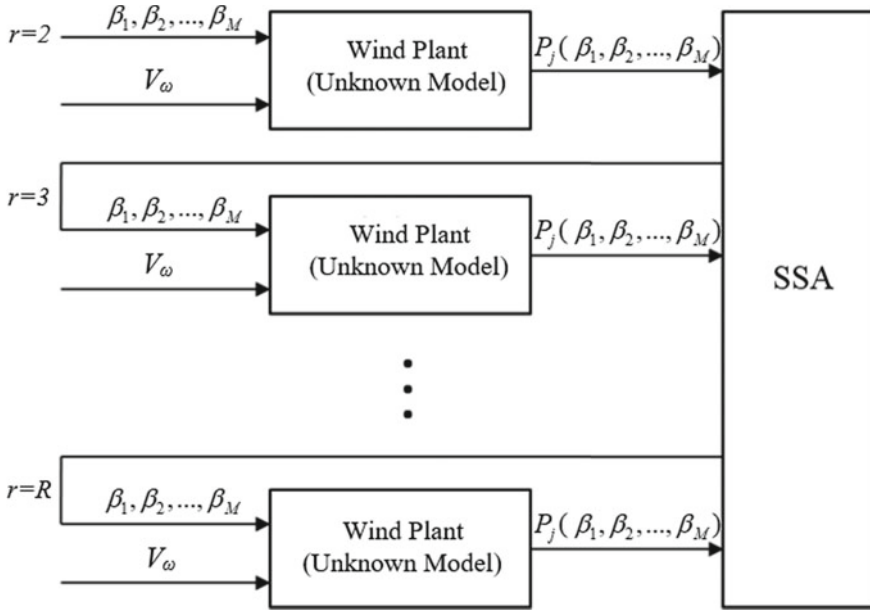


Fig. 1. SSA data-driven wind plant structure [10]

### 3.1 Wind Plant Dynamic Model

Assume that every turbine  $j$  power production is regarded as:

$$P_j = 2\rho A_j \beta_j (1 - \beta_j)^2 V_j^3, \tag{7}$$

where  $V_j$  is the wind velocity build-up produced by the leading wind turbines, the turbine  $j$  rotor swept region is  $A_j$  and the air density is  $\rho$ .

In the wind plant, assume that  $m$  wind turbines are presented as  $x = 1, 2, \dots, m$ ,  $D_j$  is turbine rotor’s diameter and  $V_\omega$  as the velocity of incoming wind. The variables concerning roughness explain as the sign  $\phi$  indicates an incline of turbulence propagation and the region around turbine  $k$  swept and turbine  $j$  overlapping turbulence is recognized as  $V_{j \rightarrow k}^{ov}$ . The wind turbine turbulence midpoint within the array of turbine rotor circle plane is defined as  $(z, r_\omega)$  meanwhile  $r_\omega$  being the array between turbine rotor axis and the center. The  $V_j$  expression is therefore provided by:

$$V_j = V_\omega \left( 1 - 2 \sqrt{\sum_{l \in x: z_k < z_j} \left( \beta_j \left( \frac{D_j}{D_j + 2\phi(z_{jk})} \right)^2 \frac{A_{j \rightarrow k}^{ov}}{A_j} \right)^2} \right), \tag{8}$$

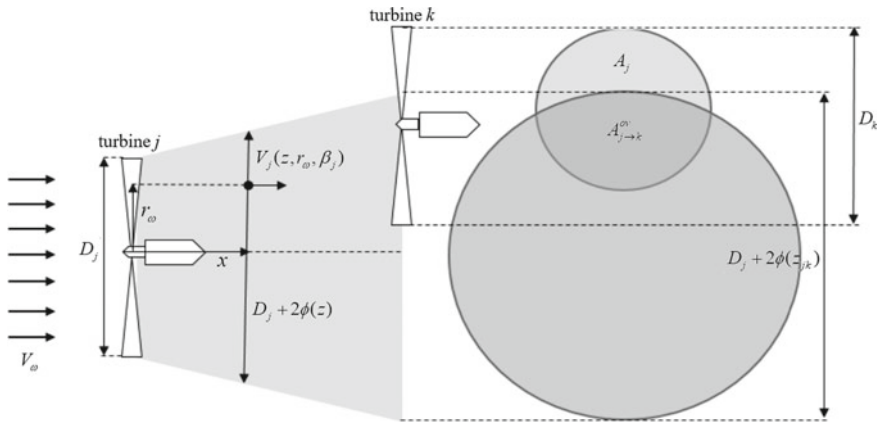


Fig. 2. Two turbines turbulence correlation [9]

in which  $Z_{jk}$  can be the range from front turbine  $j$  to turbine  $k$ . The turbulence correlation among two turbines is demonstrates in Fig. 2.

**Remarks** The proposed SSA only requires information on complete wind plant production in this research without knowing the comprehensive model by (7) as well as in (8). To signify this wind plant’s dynamic model, the algorithm will obviously review the total power collection data once the incoming wind has traveled most of the turbine out of the first row to the very last. Due to this cause, this proposed approach offers an exceptional opportunity to get applied inside actual wind plant system, pondering it only required total power production data while not even requiring the advance aerodynamic correlation through the turbine.

### 3.2 Example of a Singular Row Wind Plant Consisting of 10 Turbines

The SSA’s potency is viewed through this section. As shown in Fig. 3, SSA’s functionality could be confirmed together with a 10 turbine row wind plant. Every rotor of the wind turbine has a diameter of 80 m. Ten wind turbine can be positioned in a line between each turbine with a precise length of 560 m. Other variables like the density of the air and the coefficient of roughness are and are corresponding. To be able to achieve substantial turbulence effect, the wind speed is and considered to be consistent at 90-degree direction.

This study considers a reasonable assessment in terms of optimum power production through the proposed SSA, SDA and PSO. Optimum function evaluation numbers are assigned as 10,000. The input for SDA in [9] are described as  $r = 0.97$ ,  $\alpha = \pi/4$ ,  $c_0 = 0.9$  meanwhile PSO variables [10] are described by  $R = 500$ ,  $N = 20$ ,

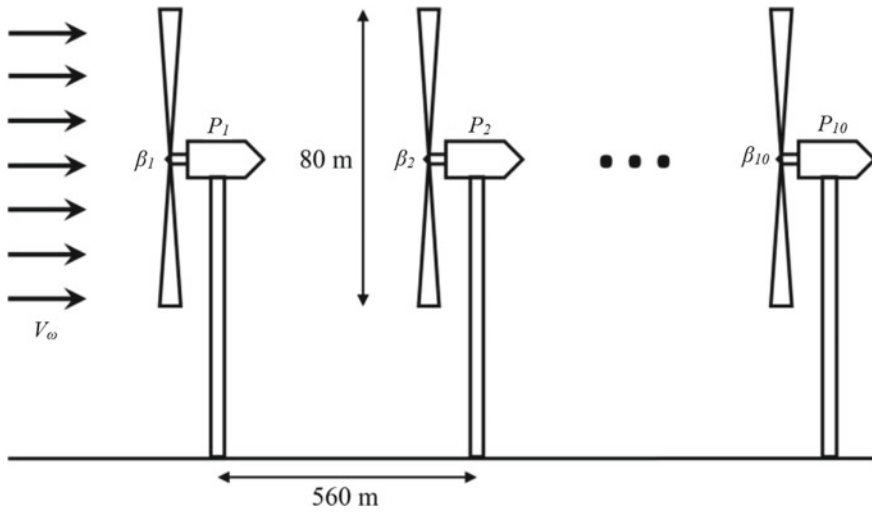


Fig. 3. The placement of 10 turbines in single row wind plant [10]

$c_1 = 0.1$  and  $c_2 = 0$ . The configuration of agent numbers,  $N$  and an optimum iteration numbers,  $R$  is ascertained in such a manner that better total power output is achieved. Throughout consider the irrelevant behavior together with proposed techniques, 100 trials most certainly conclude being conducted in arrays 0 to 1/3 together with the main control variables of every turbine for SSA, SDA, as well as PSO.

Table 1 structured the overall power production information output for SSA by evaluation numbers of 10,000. The best, worst, mean and standard deviations are utilized as a method of determining the complete wind plant power production’s total output.  $R = 500$  and  $N = 20$  are the ideal value of agent numbers and a maximum number of iterations to generate the exact analysis with smaller standard deviation value. Figures 4 demonstrate the convergence curve by using MATLAB as an outcome of the simulation for SSA’s total power production responses to the wind plant.

Table 1 Maximum power production (MW) effectiveness comparison for varied maximum numbers of iteration,  $R$  and numbers of an agent,  $N$

Max. numbers of iteration, $R$	Numbers of agent, $N$	Best (MW)	Worst (MW)	Mean (MW)	Standard deviation
100	100	4.7648415724	4.7648415724	4.7648415724	0.00028640
125	80	4.7648415724	4.7648415724	4.7648415724	$1.308 \times 10^{-6}$
200	50	4.7648415724	4.7648415724	4.7648415724	$6.073 \times 10^{-8}$
250	40	4.7648415724	4.7648415724	4.7648415724	$5.065 \times 10^{-8}$
<b>500</b>	<b>20</b>	<b>4.7648415724</b>	<b>4.7648415724</b>	<b>4.7648415724</b>	<b><math>3.469 \times 10^{-8}</math></b>
1000	10	4.7648415724	4.7648415724	4.7648415724	$3.945 \times 10^{-8}$

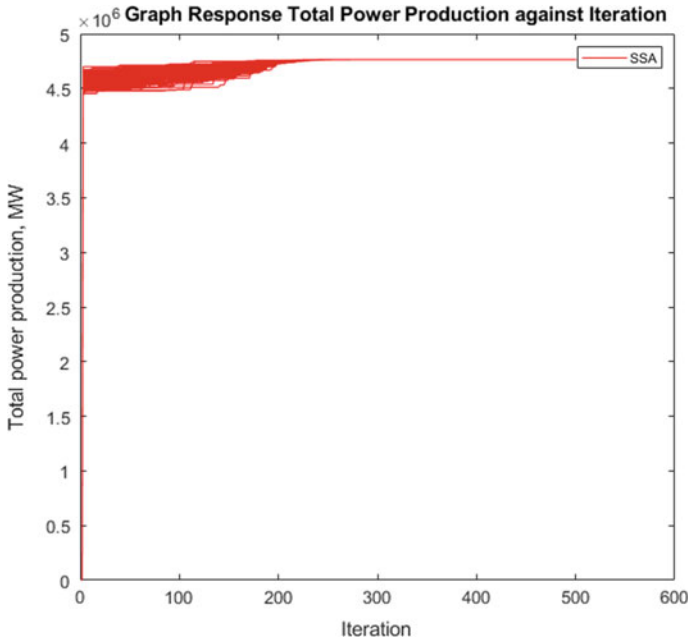


**Fig. 4.** The convergence curve of SSA’s total power production

**Table 2.** Maximum power production (MW) effectiveness comparison among SSA, SDA, and PSO

Statistical results	SSA	SDA [9]	PSO [10]
Best (MW)	<b>4.7648415724</b>	4.7648415723	4.7648415723
Worst (MW)	<b>4.7648415724</b>	4.7648415723	4.7648414855
Mean (MW)	<b>4.7648415724</b>	4.7648415723	4.7648415625
Standard deviation	<b>6.073 × 10<sup>-8</sup></b>	1.1039824 × 10 <sup>-7</sup>	0.0141665007

It can be noted that the SSA generates the highest complete energy output with a value of 4.7648415724 MW in Table 2, followed by SDA (4.7648415723 MW) as well as PSO (4.7648415723 MW). The same pattern can also be seen with respect to the best, worst and mean value of maximum power production. The result shows that for the wind plant, SSA can persistently generate total power production.

### 4 Conclusions

A data-driven approach determined by the Salp Swarm Algorithm (SSA) was studied in this research. This research study aims to propose SSA for wind plant power

production and to compare the outcomes with SDA and PSO method. Based on the model of the Horn Rew wind plant in Denmark; the analysis result demonstrates that in terms of maximum power production, SSA produces a significantly better result than PSO and SDA. This demonstrates SSA's capacity as a data-driven wind plant approach.

**Acknowledgements** Our study for this project was assisted by UMP and Ministry of Education (MOE) under Fundamental Research Grant Scheme with reference no. FRGS/1/2017/ICT02/UMP/02/2 or RDU170104.

## References

1. Park J, Law KH (2016) A data-driven, cooperative wind plant control to maximize the total power production. *Appl Energy* 165:151–165
2. Marden JR, Ruben SD, Pao LY (2012) Surveying game theoretic approaches for wind plant optimization. In: *Proceedings of the AIAA aerospace sciences meeting*, Nashville, Tennessee, pp 1–10
3. Marden JR, Ruben SD, Pao LY (2013) A model-free approach to wind plant control using game theoretic methods. *IEEE Trans Control Syst Technol* 21(4):1207–1214
4. Gebraad PM, van Dam FC, van Wingerden JW (2013) A model-free distributed approach for wind plant control. In: *Proceedings american control conference*, Washington DC, USA, pp 628–633
5. Gebraad PM, van Wingerden JW (2015) Optimum power-point tracking control for wind plants. *Wind Energy* 18(3):429–447
6. Ahmad MA, Azuma SI, Sugie T (2014) A model-free approach for maximizing power production of wind plant using multi-resolution simultaneous perturbation stochastic approximation. *Energies* 7(9):5624–5646
7. Ahmad MA, Hao MR, Raja Ismail RMT, Nasir ANK (2016) Model-free wind plant control based on random search. In: *Proceedings of IEEE international conference on automatic control and intelligent systems*, Shah Alam, Malaysia, pp 131–134
8. Hao MR, Raja Ismail RMT, Ahmad MA (2017) Using spiral dynamic algorithm for maximizing power production of wind plant. In: *Proceedings of IEEE International conference on applied system innovation*, Sapporo, Japan, pp 1706–1709
9. Md Idris MA, Hao MR, Ahmad MA (2019) A data driven approach to wind plant control using moth-flame optimization (MFO) algorithm. *Int J Adv Sci Eng Inf Technol* 18–23
10. Suid MH, Mohd Tumari MZ, Ahmad MA (2019) A modified sine cosine algorithm for improving wind plant energy production. *Int J Electr Eng Comput Sci* 16(1):101–106
11. Mirjalili S, Gandomi AH, Mirjalili SZ et al (2017) Salp Swarm algorithm: a bio-inspired optimizer for engineering design problems. *Adv Eng Softw* 114:163–191
12. Hadad Baygi SM, Karsaz A, Elahi A (2018) A hybrid optimal PID-Fuzzy control design for seismic exited structural system against earthquake: a salp swarm algorithm. In: *6th Iranian joint congress on fuzzy and intelligent system*, Kerman, Iran, pp 220–225
13. Tolba M, Rezk H, Zaki Diab AA et al (2018) A novel robust methodology based Salp Swarm algorithm for allocation and capacity of renewable distributed generators on distribution grids 11(10):1–34
14. El-Fergany A (2018) Extracting optimal variables of PEM fuel cells using Salp Swarm optimizer. *Renew Energy* 119:641–648
15. Wang J, Gao Y, Chen X (2018) A novel hybrid interval prediction approach based on modified lower upper bound estimation in combination with multi-objective Salp Swarm algorithm for short-term load forecasting. *Energies* 11:1–30

16. Ibrahim A, Ahmed A, Hussein S et. al (2018) Fish image segmentation using salp swarm algorithm. In: The international conference on advanced machine learning technologies and applications, pp 42–51
17. Yodphet D, Onlam A, Siritaratiwat A et al (2019) Electrical distribution system reconfiguration for power loss reduction by the Salp Swarm algorithm. *Int J Smart Grid Clean Energy* 8: 156–163
18. Ekinci S, Hekimoglu B (2018) Variable optimization of power system stabilizer via Salp Swarm Algorithm. In: 5th international conference on electrical and electronic engineering, Istanbul, Turki, pp 143–147
19. Hussein AG, Hassanien AE, Houssein EH (2017) Swarming behaviour of salp algorithm for predicting chemical compound activities. In: Eighth international conference on intelligent computing and information systems, Cairo, Egypt, pp 315–320
20. Zhang J, Wang Z, Luo X (2018) Variable estimation of the soil water retention curve using the Salp Swarm algorithm. *Water* 10:815
21. Scholbrock AK (2011) Optimizing wind plant control strategies to minimize wake loss effects. Univ. Colo, Boulder

# Improvement of Performance and Response Time of Cascaded Five-Level VSC STATCOM Using ANN Controller and SVPWM During Period of Voltage Sag



Mohamad M. Almelian, Izzeldin I. Mohd, Abu Zaharin Ahmad, Mohamed A. Omran, Muhamad Z. Sujod, N. M. Elasager and Mohamed Salem

**Abstract** Power system is an extremely nonlinear system with a number of interconnected loads. When the system is subjected to the faults, the stability of the system will be disturbed. The major problem dealt here is voltage sag. A static synchronous compensator (STATCOM) is one of the FACTS devices which can inject proper reactive current at the point of common coupling (PCC) to compensate voltage sag. A non-linear controller like artificial neural network (ANN) is used with the FACTS devices for better performance. This paper introduces the design of a cascaded 5-level voltage source converter (VSC) STATCOM based on the ANN controller and space vector PWM (SVPWM) technique to nullify the impacts of voltage sag. ANN and SVPWM were employed to enhance the performance and response time (RT) of STATCOM with regard to correction of voltage magnitude and power factor (PF) amplitude during voltage sag period. The performance of STATCOM was analyzed using MATLAB in IEEE 3-bus system with two different types of faults, which are single line to ground (SLG) fault and line to line (LL) fault (both creates voltage sag). The simulation result showed that the ANN-based STATCOM control circuit performed efficiently compared to the PI controller. The ANN controller was able to recover voltage magnitude very quickly (during 0.02 s) with unity.

**Keywords** Cascaded H-bridge five-level VSC STATCOM · Artificial neural network · SVPWM · Voltage sag

---

M. M. Almelian · I. I. Mohd (✉) · A. Z. Ahmad · M. A. Omran · M. Z. Sujod  
Faculty of Electrical and Electronics Engineering, Universiti Malaysia Pahang (UMP), 26600  
Pekan, Pahang, Malaysia  
e-mail: [izzeldin@ump.edu.my](mailto:izzeldin@ump.edu.my)

N. M. Elasager  
College of Technical Sciences, Bani-Walid, Libya

M. Salem  
School of Electrical and Electronic Engineering, Engineering Campus, Universiti Sains Malaysia (USM), 14300 Nibong Tebal, Pulau Pinang, Malaysia



## 1 Introduction

Power quality (PQ) problem is one of the great sources of concern for consumers in the power utility sector. This problem is very difficult to be detected in the power distribution system [1, 2]. It is the wish of power consumers that rated voltage and frequency should be maintained, however, there are always deviations in the received voltage from normal. Several short-time PQ problems exist, such as voltage sag, which causes significant changes in the voltage magnitude and PF amplitude over a short period, leading to the tripping of motors and malfunctioning of the motor controller and production failures in bulk industries [3]. It is a common knowledge that more equipment will be damaged if voltage sag is not mitigated at the consumer point [4]. Custom power devices such as STATCOM were introduced to mitigate voltage sag issues in power distribution systems.

The performance of STATCOM mainly relies on how accurately and quickly error signals are compensated. Various traditional control approaches, such as the PI controller, are still in use with STATCOM. A STATCOM model based on sinusoidal PWM (SPWM) technique and the PI controller has been proposed by Biabani et al. [5] where the authors presented the enhancement of voltage sag and total harmonic distortion (THD). Furthermore, the mathematical modeling of STATCOM in d-q method with a PI controller to maintain the dc voltage at a constant value and to also control the flow in the reactive power system has been discussed in the literature [6]. PI controller design procedure has been proposed for 2-level VSC STATCOM for voltage stability [7]. However, the PI controller has two tuning parameters ( $K_p$  and  $K_i$ ) which interact with one another. This interaction can make it challenging to arrive at the best tuning values. In recent years, artificial intelligence techniques are having a significant impact on power electronics. While maintaining the stability of the converter system over a wide operating range, the ANN-based controller provides a fast dynamic response [8].

In fact, several kinds of literature have proposed voltage stability using STATCOM based on the ANN controller [8–10]. These works used SPWM method for generating a pulse signal of VSC switches. For SPWM, the dc bus utilized for the operation is restricted to 0.5 Vdc while SVPWM shows a better utilization at 1.73 Vdc, which is around 15% more when compared to SPWM. Thus, SVPWM techniques offer higher amplitude modulation indexes and reduced switching losses and THD compared to the SPWM technique [11]. Furthermore, there are no studies on the performance of STATCOM and its response time with regard to correction of voltage magnitude and PF amplitude during voltage sag period.

In this paper, the ANN controller with a simple circuit of SVPWM technique has been designed to operate a cascaded 5-level VSC STATCOM under voltage sag; this combination (STATCOM) gives a fast voltage and PF regulation.

## 2 Proposed STATCOM

A STATCOM is comprised of a cascaded 5-level VSC, a coupling inductance ( $L_f$ ) represented L filter, SVPWM technique, and a control circuit as depicted in Fig. 1. This sort of configuration gives the capacity to absorb or generate controllable active and reactive power. Mainly, STATCOM is used for voltage regulation and PF correction. It is deployed for the provision of continuous voltage regulation using a directly controlled converter [12].

As shown in Fig. 1, voltage sag is corrected by the shunt injected current  $I_{ST}$  through the adjustment of the voltage drop across the systems' impedance  $Z_{TH}$ . The value of  $I_{SH}$  is regulated by adjusting the output voltage of the cascaded 5-level VSC. The shunt injected current  $I_{ST}$  can be written as,

$$I_{ST} = I_{LOAD} - I_S = I_{LOAD} - ((V_{TH} - V_{PCC}) / Z_{TH}). \tag{1}$$

The complex power injection of the STATCOM can be expressed as,

$$S_{ST} = V_{PCC} I_{SH}^*. \tag{2}$$

Notably, the effectiveness of STATCOM in voltage sag correction depends on the value of  $Z_{TH}$  or the fault level at the PCC bus. When  $I_{ST}$  is in quadrature with  $V_{pcc}$ ,

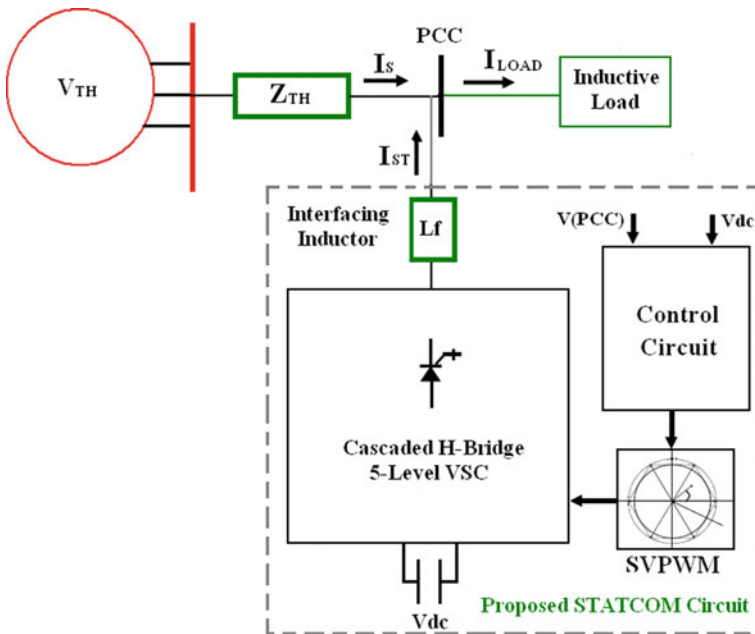


Fig. 1 Schematic representation of proposed STATCOM

it is possible to achieve the desired voltage correction without the need for injecting any active power into the system. Contrarily, a reduction in the value of  $I_{ST}$  will require a minimum apparent power injection into the system to achieve the same voltage correction.

### 2.1 Cascaded 5-Level VSC

The cascaded multilevel VSC is comprised of several H-bridge inverter units, each unit having a separate dc source. The cascaded 5-level VSC topology is depicted in Fig. 2, where two H-bridges (H1 and H2) are serially connected, with each H-bridge being able to produce 3 different voltage levels ( $+V_{dc}$ , 0, and  $-V_{dc}$ ) through the connection of the dc source to the ac output side via different combinations of the 4 switches. For each H-bridge, the ac output is serially connected such that the generated output voltage waveform will reflect the sum of all of the individual H-bridge outputs [13].

$$L_f = V_{PCC} / (2\sqrt{6} * I_n * f_{sw}), \tag{3}$$

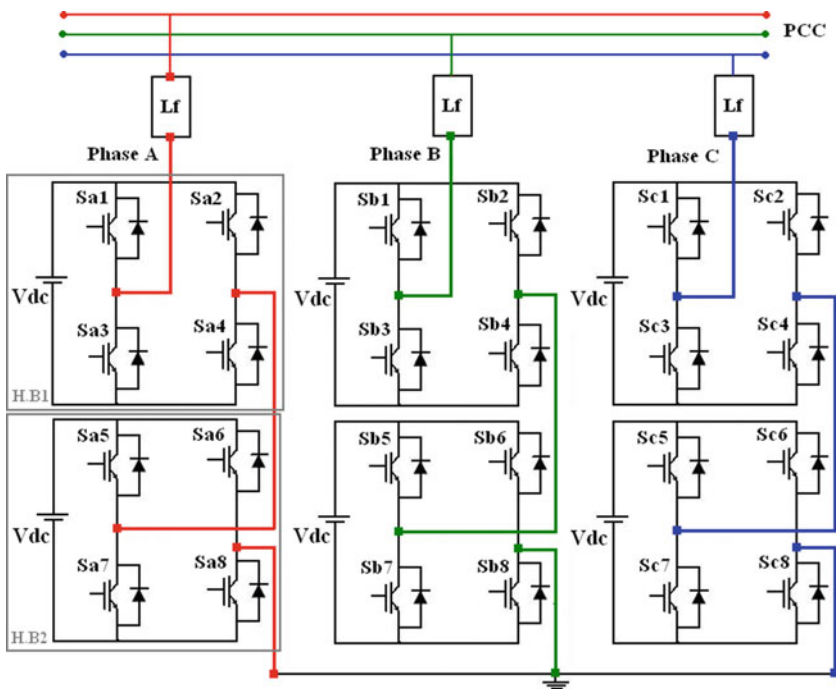


Fig. 2 Cascaded H-bridge five-level VSC

where  $f_{sw}$  is the switching frequency,  $I_n$  equals 15% of peak value fundamental harmonic current.

### 2.2 SVPWM Circuit Scheme

The SVPWM technique has been increasingly used in the last decade to generate an output voltage of VSC because it allows the reduction of commutation losses and voltage output harmonic. It is also used to achieve higher amplitude modulation indexes compared to the traditional SPWM technique [11].

In general, the traditional SVPWM implementation requires the following steps: Sector identification of the position of the instantaneous reference space vector, mapping of this sector through coordinate transformations to an appropriate sector in the inner hexagon, determination of the switching times of the inverter vector, and using of switching sequence tables to select the appropriate individual vectors [14]. Therefore, this section presents a simple and low-cost implementation of SVPWM technique in which the PWM switching times for the inverter legs are derived directly from the sampled amplitudes of the reference phase voltages. The SVPWM technique scheme is displayed in Fig. 3, where in each phase, the proper pulses for each H-bridge in each inverter legs are generated by comparing the output of the space vector circuit with the PWM signal (carrier signal). All the carrier signals have the same frequency and the peak-peak amplitude with a phase shift between any two PWM generator for one phase is  $120^\circ$  [14]. The new SVPWM technique used is completely based on the instantaneous value of the reference phase voltage of all the phases. To obtain the output signal of the space vector circuit, a reference phase voltage  $V_{ref}$  is added to the common mode voltage  $V_{set}$ .

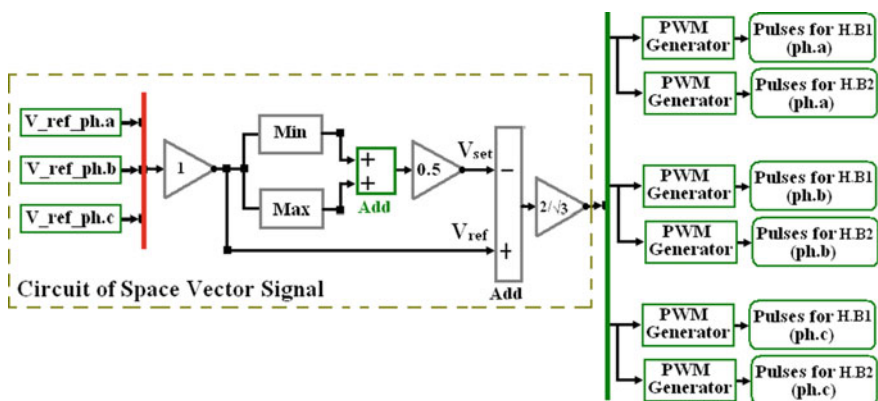


Fig. 3 Block diagram of SVPWM technique

### 2.3 Control Circuit of STATCOM

The main objective for STATCOM control circuit is to correct voltage magnitude and PF amplitude under voltage sag by injecting reactive power to the power system. The control approaches used for the proposed STATCOM is direct control. Here, the reactive output current can be controlled directly by changing the switching angles of 5-level switches (i.e. varying the modulation index) while maintaining the dc voltage at a constant level [13]. The power system circuit (IEEE 3-bus system) and the control circuit of the proposed cascaded 5-level VSC STATCOM are represented in Fig. 4.

From Fig. 4, the reference voltage of bus-3 is compared with the actual voltage of bus-3, and then, the difference is processed through a PI/ANN controller (control unit I) which produces a value of modulation index (MI). Besides that, a small amount of active power (P) flow is made possible by phase shifting (lagging) the STATCOM voltage with respect to the bus-3 voltage by a small angle ( $\varphi$ ) in order to keep the dc capacitor voltages constant ( $\varphi$  is computed by another PI/ANN controller (control unit II) according to the difference between  $V_{dc\_ref}$  and the  $V_{dc}$ ). Lastly,  $\varphi$  and the output of Phase lock loop (PLL) ( $\delta$ ) are supplied to the phase shifter block to produce the sinusoidal control signals. These control signals are fed to the product block together with MI to create reference signals which passed to the SVPWM block to generate the firing pulses for switches of H-bridge 1 and H-bridge 2 in each phase. PLL has been used to maintain the synchronization to the bus-3 line voltage.

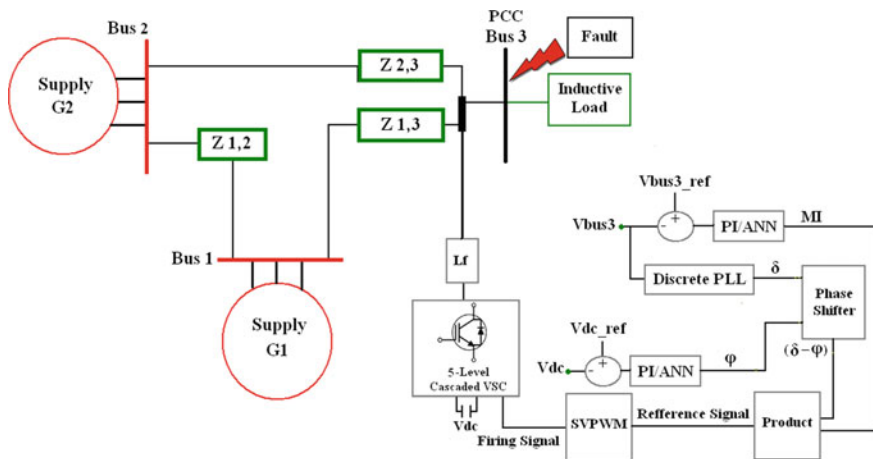


Fig. 4 IEEE 3-bus system with proposed STATCOM control circuit

### 2.4 ANN Controller

The ANN was developed as an established technology that provides an alternative approach to solving complex problems because it does not require any detailed system information. ANN learns the input–output variables relationship by studying the pre-recorded data. ANNs can be trained and used for the approximation of an arbitrary input–output mapping of a system. Several ANN architectures exist and one of such is the feed-forward neural network. The standard structure of the ANN controller is depicted in Fig. 5 [9]. Scaled data enter into ANN network via the input layer neurons and are forwarded to the output neuron via the intermediate layers. Each connection is directly associated with a weight which modifies the signal strength. Training a neural network usually demands iterative techniques. The back-propagation method is the common technique trained by using the gradient descent method owing to its stability, robustness, simplicity, and ease of implementation [10].

In this paper, the input and output data are stored in an array taken from the PI controller. The ANN controller structure has 3 layers, which are the input layer, the hidden layer (consists of 10 neurons), and the output layer. The number of epochs required to train the ANN controller for control unit I was 1000 and the best validation performance was 0.000000148 at epoch 6. Meanwhile, the number of epochs for control unit II was 1000, and the best validation performance was 0.00241 at epoch 5.

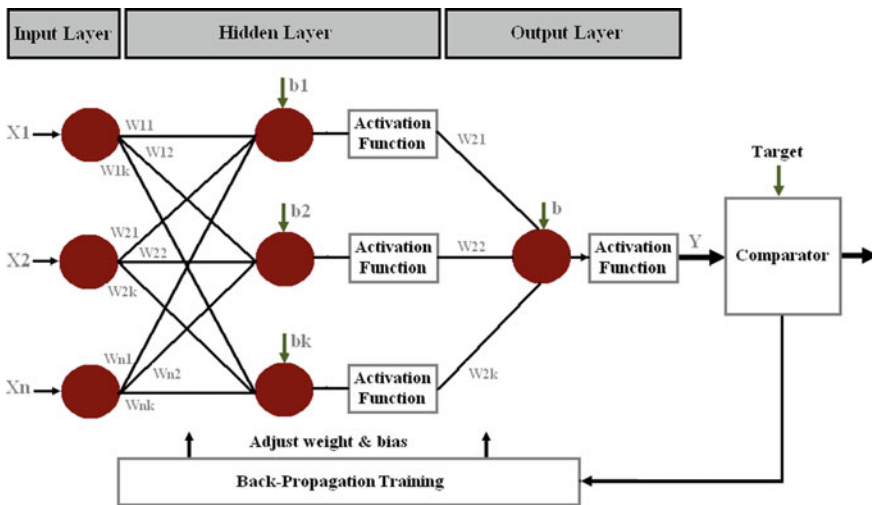


Fig. 5 Structure of ANN controller

### 3 Simulation Results

The cascaded 5-level VSC STATCOM was simulated in Simulink/Matlab, where the parameters of the power circuit have been presented in Table 1.

To verify the working of the STATCOM under PI/ANN controller so as to estimate its performance during voltage sag period, an SLG/LL fault was switched on between 0.8 and 1.3 s.

#### 3.1 Case A: Voltage Sag Engendered by SLG Fault

##### A. Voltage magnitude during SLG fault

During the SLG fault period without using STATCOM, the voltage of PCC was 0.824 pu, which is 14.2% with respect to the reference voltage (0.966 pu) as shown in Fig. 6, where the reference voltage was less than 1 pu because of an inductive load connected to the system.

The sag amplitude, as displayed in Fig. 7a, was mitigated to 0.949 pu (improvement 12.5%) in 0.078 s by the PI controller, while Fig. 7b showed that the ANN minimized the deviation between the measured voltage and reference voltage within 0.02 s to reach a PCC voltage of 0.982 pu (improvement 15.8%). Here, the STATCOM injected the reactive power into the system to decrease the voltage sag.

##### B. PF amplitude during SLG fault

As the load is receiving large active power from the source during the period of SLG fault, the PF of PCC increased to unity as seen in Fig. 8. However, the interference of STATCOM with PI control algorithm stabilized the PF at 0.998 within 0.095 s; within 0.02 s, the ANN controller maintained the value of PF at an ideal maximum value as given in Fig. 9a and b.

**Table 1** Value of parameters used in the simulation

Parameter	Value
Rated voltage	6.6 kV (L-L)
Frequency	50 Hz
Impedance	$0.89 + j5.18 \Omega$
$Z_{1,2}$	$0.05 + j0.2 \Omega$
$Z_{1,3}$	$0.02 + j0.1 \Omega$
$Z_{2,3}$	$0.036 + j0.12 \Omega$
Inductive load	1 MW + 1 MVAR
Dc voltage	6 kV
Inductor of filter	10.7 mH
Switching frequency	2 kHz

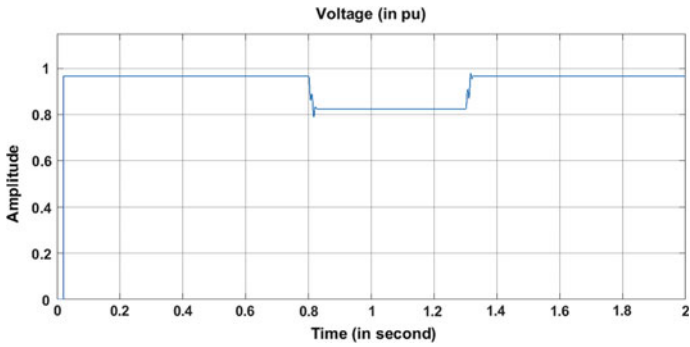


Fig. 6 Voltage magnitude during SLG fault period without STATCOM

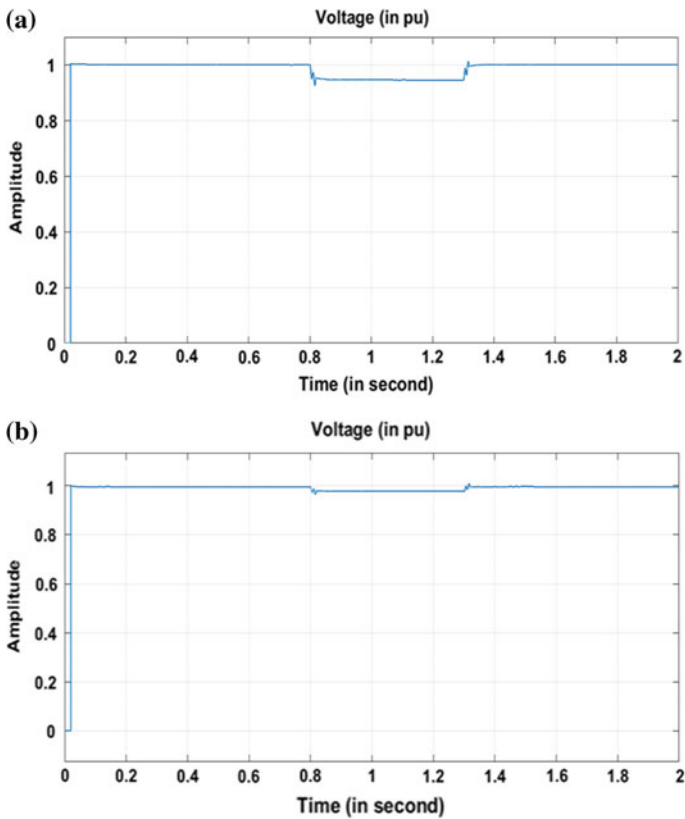


Fig. 7 Voltage magnitude during SLG fault period with STATCOM based on; a PI, b ANN



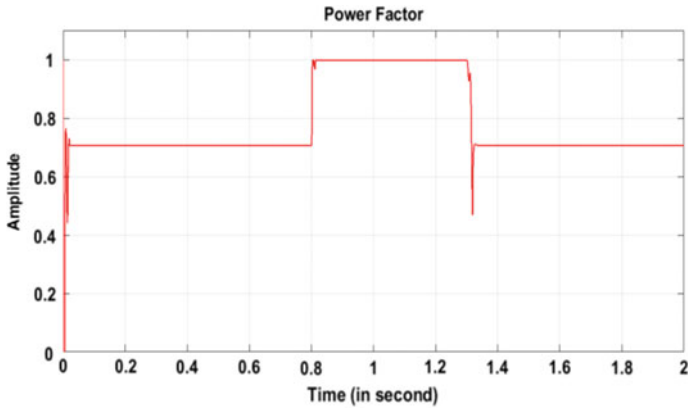


Fig.8 PF of PCC during SLG fault period without STATCOM

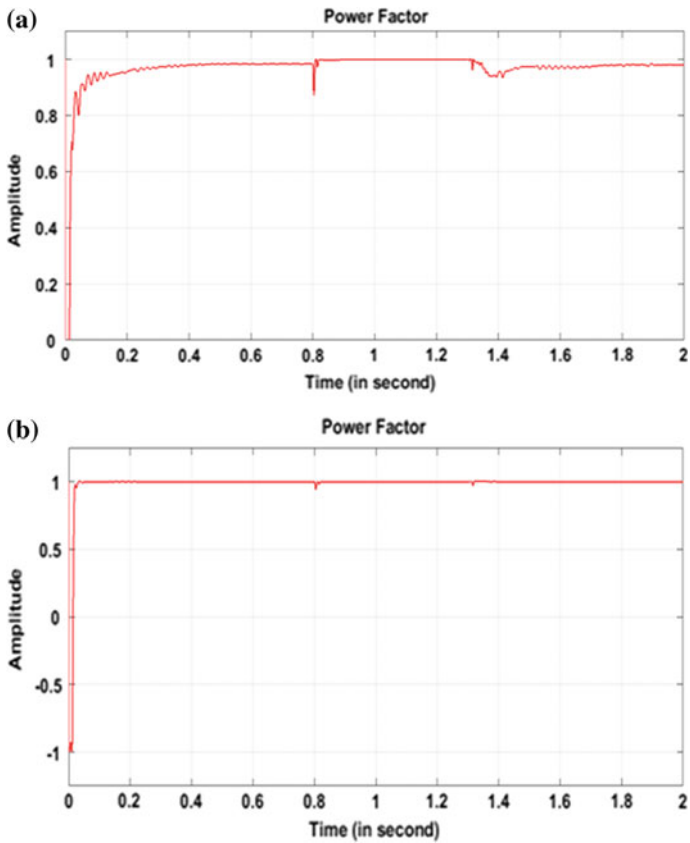
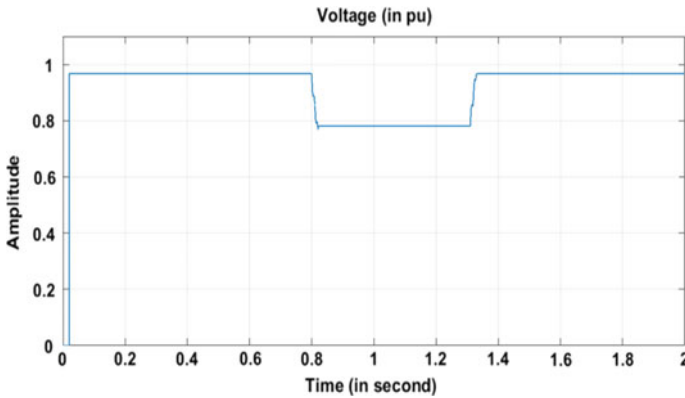


Fig. 9 PF of PCC during SLG fault period with STATCOM based on: a PI, b ANN



**Fig. 10** Voltage magnitude during LL fault period without STATCOM

### 3.2 Case B: Voltage Sag Engendered by LL Fault

#### A. Voltage magnitude during LL fault

The LL fault was applied at PCC, where the voltage sag was 0.78 pu without using STATCOM as depicted in Fig. 10. When the STATCOM based on PI controller was connected, the voltage magnitude increased to 0.942 pu within 0.07 s. However, the STATCOM based on the ANN controller took 0.02 s to improve the voltage to 0.974 pu as shown in Fig. 11a and b, respectively.

#### B. PF amplitude during LL fault

In this case, the PF was 0.79 without applying STATCOM due to the inductive load, as displayed in Fig. 12. With the compensation of the reactive power by the STATCOM, the PF came back to 0.979 within 0.396 s by employing a PI controller. Meanwhile, the ANN aided STATCOM to achieve unity PF within 0.02 s as demonstrated in Fig. 13a and b.

## 4 Conclusion

In this paper, an ANN controller and a simple circuit of SVPWM technique were presented for increasing the performance of cascaded 5-level VSC STATCOM in correcting voltage magnitude and power factor amplitude during periods of SLG. The performance of the ANN-controlled algorithm was successfully proven, where the voltage magnitude reached 0.98 while PF tends to unity within 0.02 s under a voltage sag case. This means that the intelligent control method gives a fast dynamic response and good efficiency to the system under all operating conditions compared to a conventional controller.

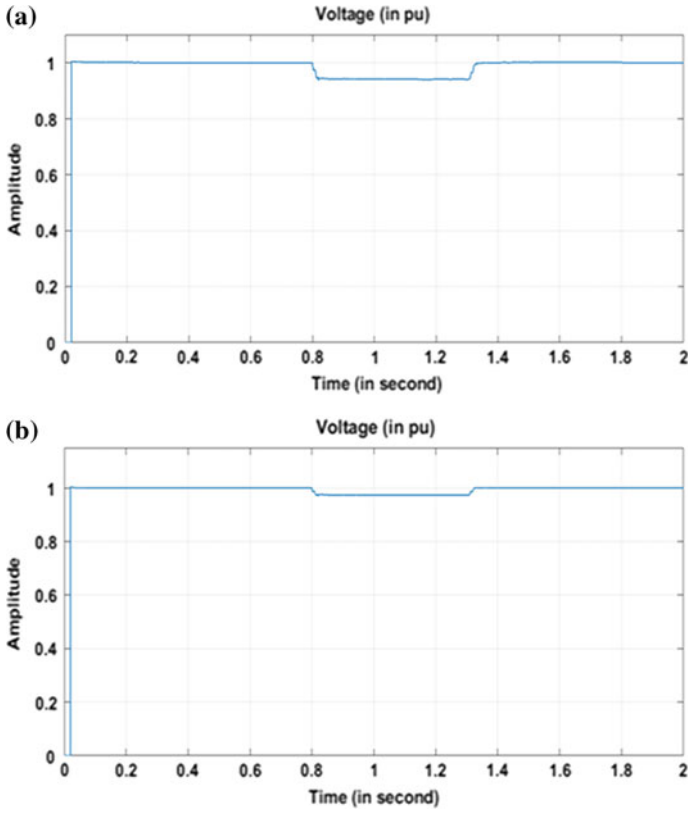


Fig. 11 Voltage magnitude during LL fault period with STATCOM based on; a PI, b ANN

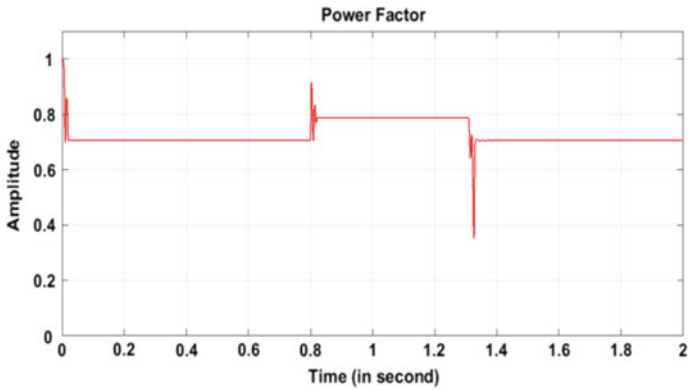
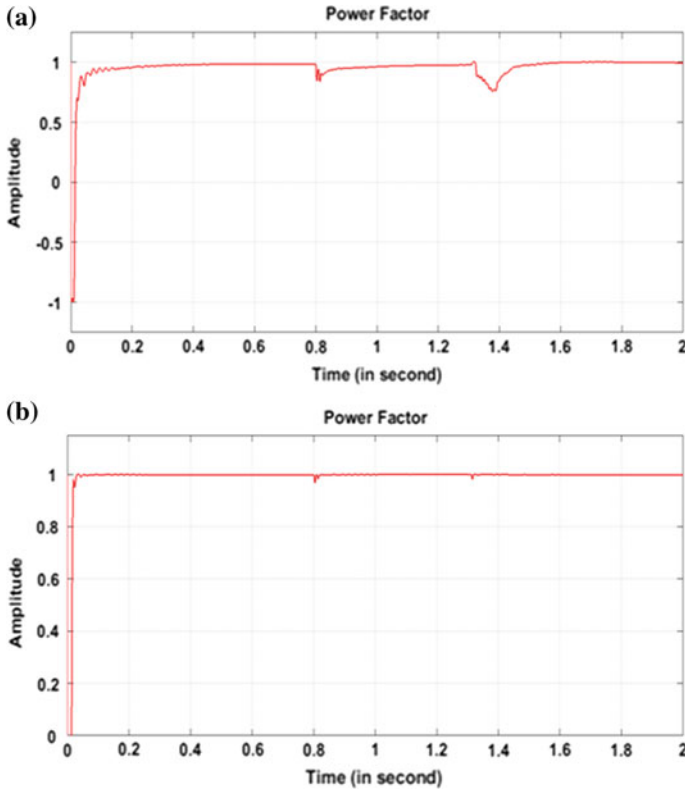


Fig.12 PF of PCC during LL fault period without STATCOM



**Fig.13** PF of PCC during LL fault period with STATCOM based on; **a** PI, **b** ANN

**Acknowledgements** This research is funded by Universiti Malaysia Pahang (UMP) Research Grant Scheme (RDU 1803165). This acknowledgment also goes to the Faculty of Electrical and Electronics Engineering for providing us with facilities to conduct this research.

**References**

1. Ghosh A, Ledwich G (2012) Power quality enhancement using custom power devices. Springer Science & Business Media
2. Almelian MM et al (2018) Performance of unified power quality conditioner (UPQC) based on fuzzy controller for attenuating of voltage and current harmonics. In: IOP conference series: materials science and engineering, vol 342, no 1. IOP Publishing
3. Ibe OG, Onyema AI (2016) Concepts of reactive power control and voltage stability methods in power system network. IOSR J Comput Eng 11(2):15–25. In: Conference 2016, LNCS, vol 9999. Springer, Heidelberg, pp 1–13
4. Soomro DM, Almelian M (2015) Optimal design of a single tuned passive filter to mitigate harmonics in power frequency. ARPN J Eng Appl Sci 10(19):9009–9014

5. Biabani MAK, Ali SM, Jawed A (2016) Enhancement of power quality in distribution system using D-Statcom. In: 2016 international conference on signal processing, communication, power and embedded system (SCOPE), IEEE
6. Hashempour MM, Lee T-L (2017) Integrated power factor correction and voltage fluctuation mitigation of microgrid using STATCOM. In: 2017 IEEE 3rd international future energy electronics conference and ECCE Asia (IFEEEC 2017-ECCE Asia), IEEE
7. Kasari PR et al (2017) Analysis of D-STATCOM for power quality enhancement in distribution network. In: TENCON 2017–2017 IEEE region 10 conference, IEEE
8. Kumar TA, Rao LS (2017) Improvement of power quality of distribution system using ANN-LMBNN based D-STATCOM. In: 2017 innovations in power and advanced computing technologies (i-PACT), IEEE
9. Jayachandran J, Sachithanandam RM (2015) Neural network-based control algorithm for DSTATCOM under nonideal source voltage and varying load conditions. *Can J Electr Comput Eng* 38(4):307–317
10. Ahmad MT, Kumar N, Singh B (2017) Generalised neural network-based control algorithm for DSTATCOM in distribution systems. *IET Power Electron* 10(12):1529–1538
11. Tiwa S (2017) Space vector pulse width modulation based two level inverter. *Res J Eng Sci* 6(8):8–12
12. Dixon J et al (2005) Reactive power compensation technologies: state-of-the-art review. In: *Proceedings of the IEEE* 93(12):2144–2164
13. Majed A, Salam Z (2015) Multilevel D-STATCOM for sag and swell mitigation using modulation index control. In: 2015 IEEE conference on energy conversion (CENCON), IEEE
14. Gaballah M et al (2011) Implementation of space vector-PWM for driving two level voltage source inverters. *J Eng Sci Assiut Univ* 39(4):871–884

# Development of Maximum Power Point Tracking for Doubly-Fed Induction Generators in Wind Energy Conversion Systems



Duy C. Huynh, Khai H. Nguyen and Matthew W. Dunnigan

**Abstract** Maximum power point tracking (MPPT) control is one of the essential requirements in harnessing wind power of wind energy conversion systems (WECS). The more precise the maximum power point (MPP) is determined, the more optimal the WECS is operated. Amongst MPPT algorithms, a hill-climb search (HCS) algorithm is preferred because of its simplicity however it also has few drawbacks such as the difficulty of selecting an appropriate step size, the premature convergence phenomenon and the speed-efficiency trade-off. A cuckoo search (CS) algorithm is proposed in this paper for finding out a MPP of a WECS driven by a doubly-fed induction generator (DFIG) under various wind speeds which mostly overcomes the above disadvantages. Then, the DFIG-WECS is controlled to track the MPP. This ensures that the DFIG-WECS is always operated at MPPs regardless of various wind speeds. It is realized that the proposed CS algorithm is also a population-based algorithm inspired from the breeding behavior of cuckoos but it is quite simple, powerful and especially requires less parameters to define optimal solutions than a genetic algorithm (GA) and a particle swarm optimization (PSO) algorithm. Though numerical results, the CS algorithm shows its effectiveness in finding out MPPs in the DFIG-WECS. Furthermore, the obtained results using the CS algorithm are also compared with those using the HCS and PSO algorithms. The comparison demonstrates that the convergence value and speed of the CS algorithm are always better than those of the HCS and PSO algorithms in the MPPT application in the DFIG-WECS.

**Keywords** Maximum power point tracking · Doubly-Fed induction generators · Wind energy conversion systems

---

D. C. Huynh (✉) · K. H. Nguyen  
Ho Chi Minh City University of Technology, Ho Chi Minh City, Vietnam  
e-mail: [duy.c.huynh@ieee.org](mailto:duy.c.huynh@ieee.org)

M. W. Dunnigan  
Heriot-Watt University, Edinburgh, UK

## 1 Introduction

In the world's sustainable energy development strategy, the wind energy has been attracting wide attention in research, utilization and development. It has low environmental impact and is considered as one of the solutions for the significantly growing energy demand. The WECS consists of the fixed and variable speed systems. It is realized that the capture efficiency of the wind energy is improved, 20–30% in the variable speed operation mode compared with that of the fixed speed operation mode. Furthermore, in the variable speed systems, the DFIG is one of the wind generators widely used because of its emerging technology.

With the aim of improving the extraction efficiency of the wind power, the MPPT techniques almost have to be applied in the WECS. It is obvious that the optimal generation power of the WECS mainly depends on the accuracy of defined MPPs. There are several MPPT control approaches applied for the WECS such as tip speed ratio (TSR), power signal feedback (PSF) and hill-climb search (HCS) approaches [1].

The TSR approach is to obtain an optimal TSR where power generated is maximum through controlling the rotor speed of the wind generator. The technique requires the values of the wind and turbine speeds which can affect the controlling results if the measured speed signals are not precise.

The PSF approach is to maintain an optimized mechanical power of the wind generator based on an optimal reference mechanical power of the wind turbine. The simulations or off-line experiments are required to achieve a maximum power curve for each wind turbine under various wind speeds where the optimal reference mechanical powers are on. These result in a cost required.

The HCS approach is to search MPPs of the WECS showing its disadvantages in detecting MPPs such as the difficulty of selecting an appropriate step size and the premature convergence phenomenon when the wind speed is changed continuously; and the speed-efficiency trade-off. Then, a HCS algorithm with an adaptive step size was introduced to overcome one of the drawbacks but the convergence speed of the adaptive HCS algorithm was obviously increased in the WECS [2].

On the other hand, there have been others such as a fuzzy logic controller (FLC) [3, 4], an adaptive neural-network based fuzzy inference system (NN-FIS) [5]. Apart from the FLC and NN-FIS, it is obvious that the overall cost and complexity were increased in the WECS.

Bio-inspired algorithms have been recently developed and used as one of the efficient techniques to solve optimization problems. These algorithms are based on a population and simulate behaviors of each individual; however, they sometimes have several disadvantages and difficulties relating to the convergence speed, requirement of many algorithm parameters and implementation in real time which make them inflexible and complicated.

Cuckoo search algorithm is a stochastic global search algorithm based on the interesting breeding behaviors of cuckoos [6, 7]. It has been applied for several problems in finding out the global optimal solutions [8, 9]; however, it seems that it

has not been applied yet for searching MPPs of the WECS. Additionally, it is obvious that it is quite simple, powerful and requires less parameters to define the optimal solutions than a GA and a PSO algorithm [8].

The CS algorithm is proposed for searching MPPs in the DFIG-WECS regardless of various wind speeds. The MPP, corresponding to the optimal rotor speed and the optimal output mechanical power in the DFIG-WECS is firstly defined by the proposed CS algorithm at the certain wind speed. Then, the current rotor speed of the wind turbine, which is also the current rotor speed of the DFIG, is controlled to track the optimal rotor speed at the achieved MPP. This ensures that the DFIG-WECS is always operated at MPPs under various wind speeds.

## 2 MPPT in DFIG-WECS

The output mechanical power of a wind turbine is given by [1]:

$$P_m = \frac{1}{2} \times C_p \times \rho \times A \times v_w^3 \tag{1}$$

where

- $P_m$  The output mechanical power of a wind turbine (W);
- $C_p$  The turbine power coefficient;
- $\rho$  The air density ( $\text{kg/m}^3$ );
- $A$  The area swept by a turbine blade ( $\text{m}^2$ );
- $v_w$  The wind speed (m/s).

The turbine power coefficient is related to the blade tip speed ratio,  $\lambda$  and blade pitch angle,  $\beta$  as follows [1]:

$$C_p(\lambda, \beta) = c_1 \left( c_2 \times \frac{1}{\lambda_w} - c_3 \beta - c_4 \right) e^{-\frac{c_5}{\lambda_w}} + c_6 \lambda \tag{2}$$

$$\frac{1}{\lambda_w} = \frac{1}{\lambda + 0.08\beta} - \frac{0.035}{1 + \beta^3} \tag{3}$$

where

$c_1, \dots, c_6$ : the turbine coefficients, ( $c_1 = 0.5176, c_2 = 116, c_3 = 0.4, c_4 = 5, c_5 = 21$  and  $c_6 = 0.0068$ ).

The blade tip speed ratio of a wind turbine is as follows:

$$\lambda = \frac{R\omega_m}{v_w} \tag{4}$$



where

$$\omega_m = n_r \times \frac{2\pi}{60} \tag{5}$$

- $R$  The rotor radius (m);
- $\omega_m$  The rotor speed (rad/s);
- $n_r$  The rotor speed (rpm).

The air density and configuration parameters of the wind turbine are assumed constant. Thus, the power extracted by the wind turbine depends on the turbine power coefficient at a specific wind speed in (1). Consequently, the output mechanical power is optimal as the turbine power coefficient is optimal. Furthermore, the turbine power coefficient is optimal as the rotor speed is optimal from (2)–(4) for a constant blade pitch angle. This means that the rotor speed must be controlled to an optimal value defined by (6), so that the DFIG-WECS is always operated at MPPs under various wind speeds.

From (1)–(2) and (4)–(5), the optimal output mechanical power of a wind turbine is:

$$P_m^{opt} = \frac{1}{2} \times \left[ c_1 \left( c_2 \times \frac{1}{\lambda_w} - c_3\beta - c_4 \right) e^{-\frac{c_5}{\lambda_w}} + c_6 \left( \frac{Rn_r^{opt}}{v_w} \times \frac{2\pi}{60} \right) \right] \times \rho \times A \times v_w^3 \tag{6}$$

The CS algorithm is proposed to define MPPs in the DFIG-WECS presented in the next section.

### 3 CS Algorithm Based MPPT in DFIG-WECS

The CS algorithm is presented as a stochastic global search algorithm which is based on the interesting breeding behaviors of cuckoos through the following principles [6, 7].

Each cuckoo only lays one egg at a time and dumps its egg in the randomly chosen nest, each egg is a solution.

The best nests with high quality of eggs will carry over to the next generation.

The availability of host nests is fixed and a probability,  $p_a \in [0, 1]$  represents the possibility of an alien egg to be discovered by host bird.

In the CS algorithm based MPPT application in the DFIG-WECS, the cuckoo selects randomly the nest position to lay an egg which is a new rotor speed,  $n_{ri}^{t+1}$  through the Lévy flight behavior [6–9].

$$n_{ri}^{t+1} = n_{ri}^t + \alpha \oplus Levy(\gamma) \tag{7}$$

where

- $\alpha > 0$  The step size;
- $i$  The  $i$ th host nest,  $i = [1, \dots, k]$ ;
- $j$  The  $j$ th random nest,  $j = [1, \dots, k]$ ;
- $k$  The number of the host nest;
- $t$  The  $t$ th iteration;
- $G$  The number of maximum iteration;
- $\oplus$  The entry wise multiplications.

The Lévy flight behavior (7) is essentially the stochastic description for a random walk which is a Markov chain. Its next location depends on the current location,  $n_{ri}^t$  and the transition probability,  $\alpha \oplus Levy(\gamma)$ .

The Lévy distribution is given by [6]:

$$Lévy(\gamma) = t^{-\gamma}, g \in (1, 3] \quad (8)$$

The flowchart of the CS algorithm based MPPT application in the DFIG-WECS is described as in Fig. 1.

## 4 Numerical Result

The DFIG-WECS with the CS algorithm based MPPT controller is represented as in Fig. 2.

The CS algorithm is proposed to define the MPP in the DFIG-WECS corresponding to the optimal rotor speed and optimal output mechanical power. In the rotor side controller, the reference rotor speed is the optimal rotor speed obtained by the proposed CS algorithm. Then, the rotor speed of the DFIG is controlled to track the optimal rotor speed and the output mechanical power always certainly tracks the optimal mechanical power regardless of various wind speeds.

Table 1 is the simulation parameters of the CS algorithm.

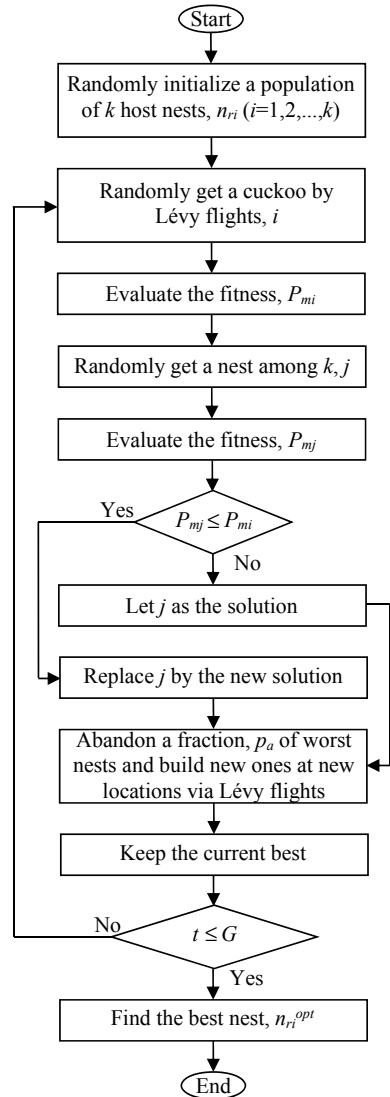
Figure 3 is the characteristics of the output mechanical power and rotor speed at various wind speeds in the theoretical conditions. It is realized that there is always the MPP corresponding to the optimal output mechanical power and optimal rotor speed as in Fig. 3. The  $MPP_1$ ,  $MPP_2$ ,  $MPP_3$ ,  $MPP_4$ ,  $MPP_5$  and  $MPP_6$  are the MPPs summarized as in Table 2.

Figure 4 is the wind speed assumed from 5 (m/s) to 9 (m/s).

Figures 5 and 6 are the numerical results of the optimal output mechanical power and optimal rotor speed in the DFIG-WECS by applying the CS algorithm based MPPT controller. It is shown that the output mechanical power has tracked the MPPs regardless of the variations of the wind speed as in Fig. 5.

Table 3 is a comparison between the obtained numerical results by applying the HCS, PSO and CS algorithms. The comparisons show that the optimal output

**Fig. 1** Flowchart of the CS algorithm based MPPT application in the DFIG-WECS



mechanical powers always track well the theoretical optimal output mechanical powers under various wind speeds and the error percentages are always less than 3% by using the CS algorithm based MPPT controller. Additionally, the achieved results of applying the CS algorithm are always better than those of applying the HCS and PSO algorithms as well.

Figures 7 and 8 are the convergence characteristics of the optimal output mechanical power in the DFIG-WECS by applying the CS and PSO algorithms respectively at the wind speed,  $v_w = 5$  (m/s). The convergence speed and value are 15th and 1730

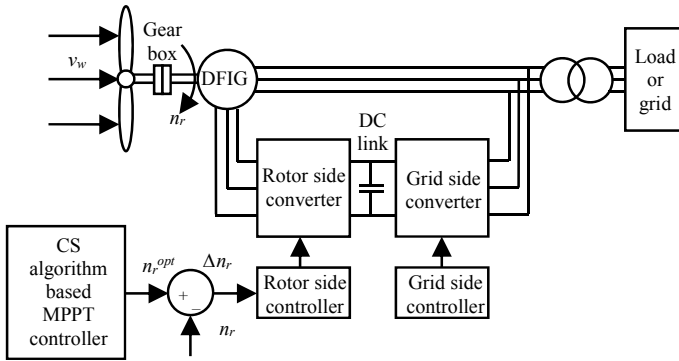


**Fig. 2** DFIG-WECS with the CS algorithm based MPPT controller

**Table 1** Parameters of the CS algorithm

Parameter	Value
Number of host nest, $N$	10
Number of maximum iteration, $G$	100
Step size of Lévy flight, $\alpha$	0.5
Possibility of alien egg, $p_a$	0.6

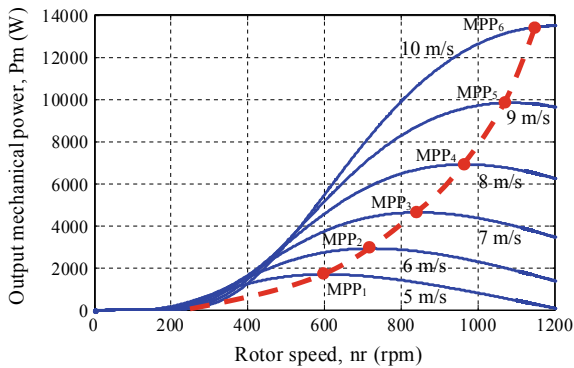


**Fig. 3** Characteristics of the output mechanical power,  $P_m$  (W) and the rotor speed,  $n_r$  (rpm) in the DFIG-WECS at various wind speeds

(W) respectively by using the CS algorithm as in Fig. 7 whereas these values are 31st and 1597 (w) respectively by using the PSO algorithm as in Fig. 8. The PSO algorithm has been obviously converged premature. This also mean that the result has been stuck the local optimal solution.

**Table 2** MPPs at various wind speeds

Wind speed, $v_w$ (m/s)	MPP	Optimal rotor speed, $n_r^{opt}$ (rpm)	Optimal output mechanical power, $P_m^{opt}$ (W)
5	MPP <sub>1</sub>	600	1686
6	MPP <sub>2</sub>	730	2914
7	MPP <sub>3</sub>	845	4628
8	MPP <sub>4</sub>	965	6908
9	MPP <sub>5</sub>	1090	9835
10	MPP <sub>6</sub>	1185	13,480

**Fig. 4** Wind speed

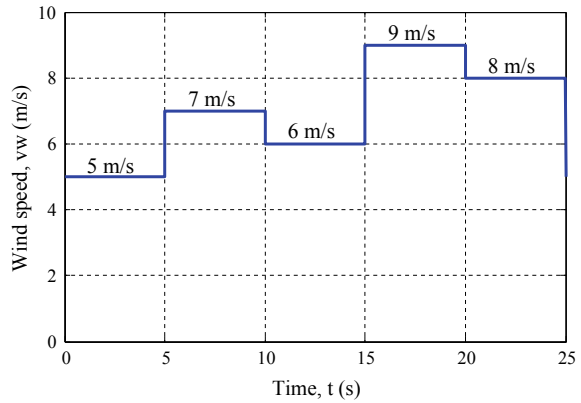
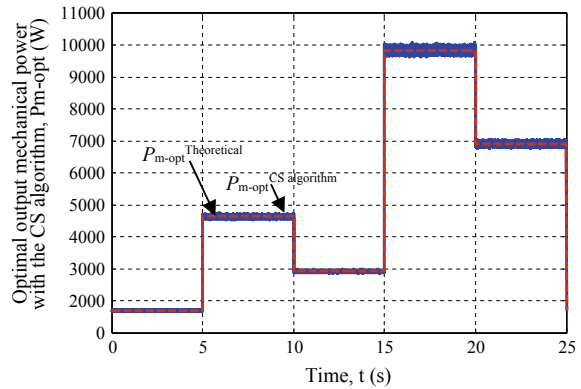


**Fig. 5** Optimal output mechanical power applying the CS algorithm



These numerical results confirm that the CS algorithm is better than the PSO algorithm in both of the convergence speed and value in the MPPT application in the DFIG-WECS.

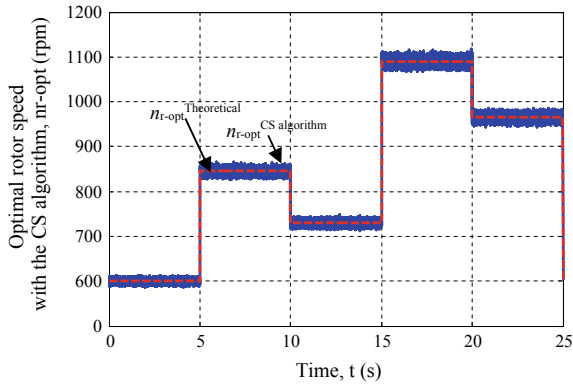


**Fig. 6** Optimal rotor speed applying the CS algorithm

**Table 3** Optimal output mechanical power in the DFIG-WECS applying HCS, PSO and CS algorithms

Time, $t$ (s)	Wind speed, $v_w$ (m/s)	Theoretical	HCS algorithm		PSO algorithm		CS algorithm	
		$P_m$ (W)	$P_m$ (W)	$\Delta P_m$ (%)	$P_m$ (W)	$\Delta P_m$ (%)	$P_m$ (W)	$\Delta P_m$ (%)
0–5	5	1686	1587	5.87	1597	5.28	1730	2.61
5–10	7	4628	4333	6.37	4352	5.96	4754	2.72
10–15	6	2914	2720	6.66	2736	6.11	2997	2.85
15–20	9	9835	9232	6.13	9280	5.64	10,097	2.66
20–25	8	6908	6434	6.86	6475	6.27	7114	2.98

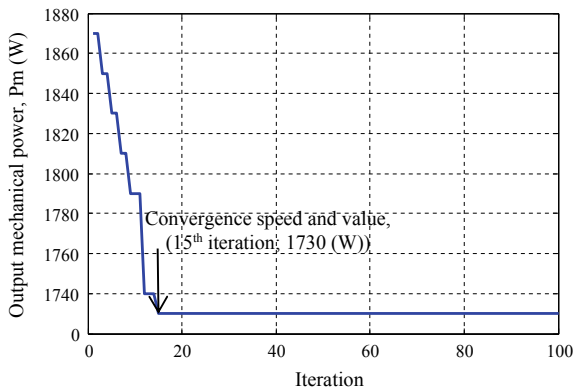


**Fig. 7** Convergence characteristic of the optimal output mechanical power for the CS algorithm based MPPT controller in the DFIG-WECS at the wind speed,  $v_w = 5$  (m/s)

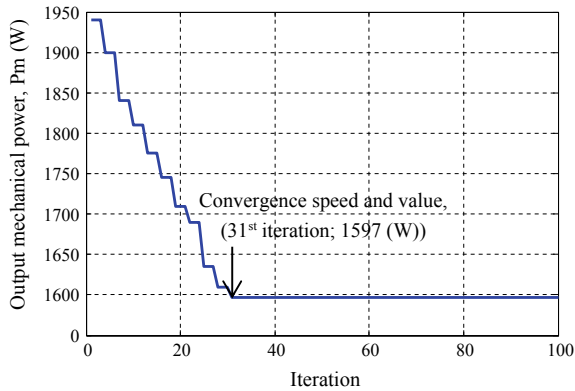


**Fig. 8** Convergence characteristic of the optimal output mechanical power for the PSO algorithm based MPPT controller in the DFIG-WECS at the wind speed,  $v_w = 5$  (m/s)

## 5 Conclusion

A novel CS algorithm based MPPT application has been proposed to define the MPPs in the DFIG-WECS. The DFIG is controlled through the achieved MPPs by using the CS algorithm to ensure that the DFIG-WECS is always operated at MPPs under various wind speeds. The obtained results of using the CS algorithm validated the proposal. Moreover, the solution with the CS algorithm is always better than the solutions with the HCS and PSO algorithms in the MPPT control strategy in the DFIG-WECS.

## References

1. Munteanu I, Bratcu AI, Cutululis N, Ceanga E (2008) Optimal control of wind energy systems: Towards a global approach. Springer-Verlag, London
2. Ifte KA, Uddin MN (2017) MPPT based efficiently controlled DFIG for wind energy conversion system. In: IEEE international electric machines and drives conference, USA, pp 1–6
3. Bouchaib R, Mustapha E, Elhassane A (2019) Fuzzy logic control for wind energy conversion system based on DFIG. In: International conference on wireless technologies, embedded and intelligent systems, Morocco, pp 1–6
4. Guolian H, Zhou, J., Yu, Y., Jianhua, Z.: Variable universe fuzzy controller used in MPPT based on DFIG wind energy conversion system. In: Chinese control and decision conference, China, pp 5871–5875
5. Dilip B, Subhendu SS, Tripathi PM, Kalyan C (2018) Maximum power point tracking for wind energy system by adaptive neural-network based fuzzy inference system. In: International conference on recent advances in information technology, India, pp 1–6
6. Yang X, Deb S (2009) Cuckoo search via Lévy flights. In: World congestion on nature and biologically inspired computing, India, pp 210–214
7. Yang XS (2008) Nature-inspired meta-heuristic algorithm. Luniver Press, UK

8. Huynh DC, Nair N (2015) Economic dispatch integrating wind power generation farms using cuckoo search algorithm. In: IEEE conference on innovative smart grid technologies, Thailand, pp 1–6
9. Huynh DC, Nair N (2015) Chaos PSO algorithm based economic dispatch of hybrid power systems including solar and wind energy sources. In: IEEE conference on innovative smart grid technologies, Thailand, pp 7–12



# Development of PV Module Power Degradation Analyzer



Mohd Shawal Jadin, Muhammad Aiman Ibrahim and Norizam Sulaiman

**Abstract** The aim of this paper is to design and develop a system that can analyze the performance degradation of a PV module based on real operating condition (ROC). In this research, the system will capture voltage and current under the real operating condition in order to get the Standard Test Condition (STC) parameters. Then this system will calculate the power degradation of the tested PV module. The experiment showed that the proposed system can estimate the PV module performance degradation by up to 90% accuracy. The system has been designed so that it can be a portable device which can be easily taken everywhere at any time.

**Keywords** Solar module · Standard test condition · Power degradation

## 1 Introduction

Solar energy comes from the direct conversion of sunlight into electricity [1–4]. It is important to understand the characteristics of particular PV modules under different light conditions in order to determine the performance of a panel or an array of panels [5, 6]. The problem that most people encounter in order to measure solar energy is that the photovoltaic (PV) analyzer cost that is too expensive. In order to measure the performance parameters of the solar panel, many monitoring systems have been designed [7]. This project is developed in order to measure solar energy of a PV module. The design of this project involves a low-cost component so that it can be exposed as most people cannot afford a PV analyzer that is too expensive. Another problem that most people encounter is to get the accurate reading of solar energy of a PV module. This project tends to minimize the measurement error as minimum as possible so that the accuracy will be high.

Usually, when people need to know the STC parameters of a PV module, they need to do manual calculations. There is no device that can extract directly the STC parameters of a PV module. First, they need to get the ROC parameters of their PV

---

M. S. Jadin (✉) · M. A. Ibrahim · N. Sulaiman  
Faculty of Electrical and Electronic Engineering, Universiti Malaysia Pahang (UMP), 26600  
Pekan, Pahang, Malaysia  
e-mail: [mohdshawal@ump.edu.my](mailto:mohdshawal@ump.edu.my)

module. Then they need to calculate manually the STC parameters. Apart from that, there is no device that can determine the degradation of a PV module. This research basically focused on the method to extract PV module parameters such as voltage and current under the real operating condition and reverse calculation to get the Standard Test Condition (STC) parameters. When the STC parameters are collected, then this system will generate the power degradation of the PV module from time to time.

## 2 Literature Review

### 2.1 PV Module's Parameters

There are two types of PV module's parameters. The first one is ROC parameters and the second one is STC parameters. The ROC parameters are obtained when tested the PV module on a normal cell temperature, normal solar irradiance and normal solar spectrum (air mass). Irradiance is the rate of solar radiation falling on a given area at a moment in time. It can be daily, monthly and annually. The STC parameters of a PV module are set at 25 °C of the cell temperature, 1000 Wm<sup>-2</sup> of the solar irradiance and 1.5 of the air mass. Normally in a datasheet of a PV module, the manufacturer will give the STC parameters of that PV module as well as the Nominal Operating Cell Temperature (NOCT).

The PV module's parameters or specification that is normally given by the manufacturer are maximum power, maximum voltage, maximum current, short-circuit current and open circuit voltage. Apart from that, the manufacturer will also give the value of the PV module's temperature coefficient. The temperature coefficient usually consists of open-circuit voltage temperature coefficient, short-circuit current temperature coefficient and maximum power temperature coefficient. However, there are few manufacturers that did not give the temperature coefficient information on the datasheet. The temperature coefficient is very important in order to do a reverse calculation to find STC parameters. If the manufacturer did not give the value of the temperature coefficient, then the default temperature coefficients must be used in order to calculate the STC parameters of our PV module. Default temperature coefficients depend on the type of our PV module which are  $-0.45\%/^{\circ}\text{C}$  for a monocrystalline while  $-0.5\%/^{\circ}\text{C}$  for the polycrystalline module.

After several years, the PV module's output or performances will not be the same as in the first year it was produced. For example, a 10 years old PV module, we will not get the maximum power as provided in the datasheet although it was tested at STC. This is because it has degraded. There are several factors that cause the degradation of a PV module. The obvious one is ageing. The older the PV module, the more it will degrade. It also depends on the type of material of that PV module, solar radiation intensity, cell temperature, cloud and shading effect, dust, PV module orientation, weather and geographical location. These factors are important to be considered if deal with a PV module or solar system.

## 2.2 Recent Studies

Several recent studies [1–9] have suggested that the important parameters of a PV module that need to be focused on are the open-circuit voltage, short-circuit current, temperature, power, irradiance and light intensity. These parameters are very important in the solar system because by obtaining this, the STC parameters of the PV module obtained and the power degradation of the PV module can be determined. Study in [10] has claimed that solar irradiance is very important in the solar system. That is why they design reliable and inexpensive solar irradiance measurement system. There are many commercialize devices in order to determine solar irradiance. One of the devices is solarimeter. For them, in order to determine the solar irradiance, they have some methods. In order to determine the irradiance, PV cells are series coupled and directly connected with a shunt resistor useful for sampling the voltage generated by the sunlight. The time-dependent analogue signal is directly dependent on the intensity of sunlight and is the input of the following digital sensor interface. This paper presented an innovative low-cost sensor and algorithm for the monitoring and measuring the solar irradiance. However, the result is slightly different compared to commercial pyranometer.

Authors in [11] have conducted a study of actual optical and thermal performance of PV-Modules. The actual efficiency of PV generators is often lower than predicted. It is caused by an underestimation of reflection losses and solar cell temperature. They have conducted an investigation by simulation and some verifying experiments. The parameters they have obtained are electrical and thermal. The results that they obtained are the model and the simulation program developed to allow them to predict optical and thermal performance under realistic operating conditions and they are promising tools for evaluating PV power plants with the aim of increasing efficiency. In [12], the paper has suggested that it is very important to determine the PV performances after a long period of time. The method they used is the power output ratio between  $P_{\max}$  and minimum  $P_{\max}$  at STC and compared with the present output power which is the  $P_{\max}$  corrected value at STC. They measured the power output of selected samples from different lots of modules to get the average of the results. The results they obtained are the crystalline modules degraded sharply violating the warrantee boundaries, however, a-Si modules showed excellent performance over the period of operation. From the I–V curve, it showed a very high percentage of degradation in  $P_{\max}$  (58%, 37%) and field factor, FF (42%, 24%).

Study in [13] has conducted an experimental investigation of optimum wind speed for material dependent temperature loss compensation in PV modules. The method they used is the experimental setup consisting of 2 PV modules of the same power and size. To control the artificial irradiance, halogen lamps are connected through the regulated switch. The fan is connected to behind the module to create artificial wind. The output module is connected to the measuring unit. From this experiment, they concluded that wind cooling decreases the module temperature which improves the electrical efficiency of the PV module but after a certain wind speed, the efficiency becomes constant. Wind speed is directly proportional to electrical efficiency [14].

Study in [15] has conducted a study on power degradation and performance evaluation of PV modules after 31 years of work. The method that they used are outdoor measurements were carried outside on a clear sunny day. There are various temperatures and various irradiance densities they obtained. They used I–V tracer and power measurements instrument marked as PVP1000C. Apart from that, Phox sensor is attached at top of the model. By this experiment, they obtained current, voltage and maximum power. The results that they obtained is the lifetime for crystalline PV modules can be extended to forty years or more. There is a degrade of 2 PV modules that were recorded about 13.86% degrade.

### 3 Methodology

#### 3.1 Overview

Generally, this system is developed to extract the current at STC parameter of a PV module. This is because the STC parameters of a PV module tend to slightly degrade from time to time. The parameters include open circuit voltage,  $V_{oc}$ , short circuit current,  $I_{sc}$  and cell temperature. First and foremost, the system will capture the parameters like  $V_{oc}$  and  $I_{sc}$  under real operating condition (ROC). Next, by using the formula of STC parameters, the system will calculate the STC parameters of a PV module with the help of user's input which is the temperature coefficient. This is because the STC parameters of a PV module cannot be calculated without knowing the temperature coefficient. After calculating the current STC parameters of a PV module, the system will generate the percentage of degradation of a PV module by comparing the current STC parameters with the STC parameters that are provided by the manufacturer.

#### 3.2 System Design

The voltage will be measured using a voltage divider circuit. In this case, the value of  $R_1$  and  $R_2$  are 10 k $\Omega$  and 1 k $\Omega$ , respectively. For example, if the value of the voltage source is 40.0 V, then by using the voltage divider formula and taking these values of  $R_1$  and  $R_2$  then the output voltage will be 3.64 V. 3.64 V is still in the voltage range that Arduino ADC pin can receive. The current will be measured using the ACS712 current sensor. ACS712 can measure current up to 30 A. The ambient temperature will be measured using LM35 current sensor. Initially, the user needs to insert the value of the temperature coefficient in order to calculate the PV module current STC parameters and power degradation. Current, temperature and voltage as the ADC input of the Arduino Board and the output will be displayed at the LCD screen. Figure 1 shows the block diagram of this system.

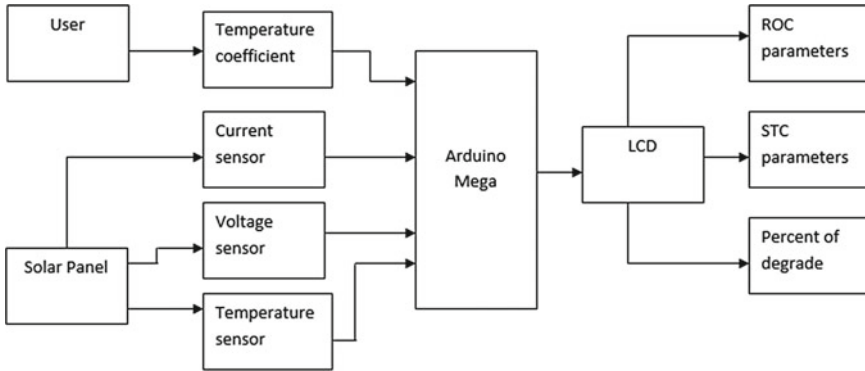


Fig. 1 Block diagram of this project

Figure 2 shows the flowchart of the proposed system. For the ambient temperature, the LM35 temperature sensor was chosen. LM35 is a precise integrated circuit temperature device with an output voltage directly proportional to the Centigrade temperature. The LM53 device has the benefit over linear temperature sensors calibrated in Kelvin, as the user is not required to minus a big constant voltage from the output to obtain convenient Centigrade scaling. This device does not need any external calibration or trimming to provide typical accuracy of plus-minus 0.25 °C at room temperature and plus-minus 0.75 °C over a full -55 to 150 °C range of temperature.

In order to get the real value of the  $P_{max\_roc}$ , it needs to be multiplied by the ratio between the standard solar irradiant and the measured irradiance. Therefore, the actual output power at STC of the PV module can be formulated as:

$$P_{max\_roc\_real} = G_{ratio} \times P_{max\_roc} \tag{1}$$

where the  $G_{ratio}$  is the ratio between solar irradiance at STC and the irradiance at ROC. Meanwhile, the approximate measured  $P_{mp\_stc\_meas}$  can be derived as follows:

$$P_{mp\_stc\_meas} = \frac{P_{max\_roc\_real}}{[1 + \{\gamma_{Pmp} \times (T_{STC} - 25)\}]} \tag{2}$$

Finally, the percentage of PV module power degradation can be calculated as

$$\text{Percentage of power degradation (\%)} = \frac{P_{mp\_stc} - P_{mp\_stc\_meas}}{P_{mp\_stc}} \times 100\% \tag{3}$$

where  $P_{mp\_stc}$  is the original power at STC as stated in the datasheet.

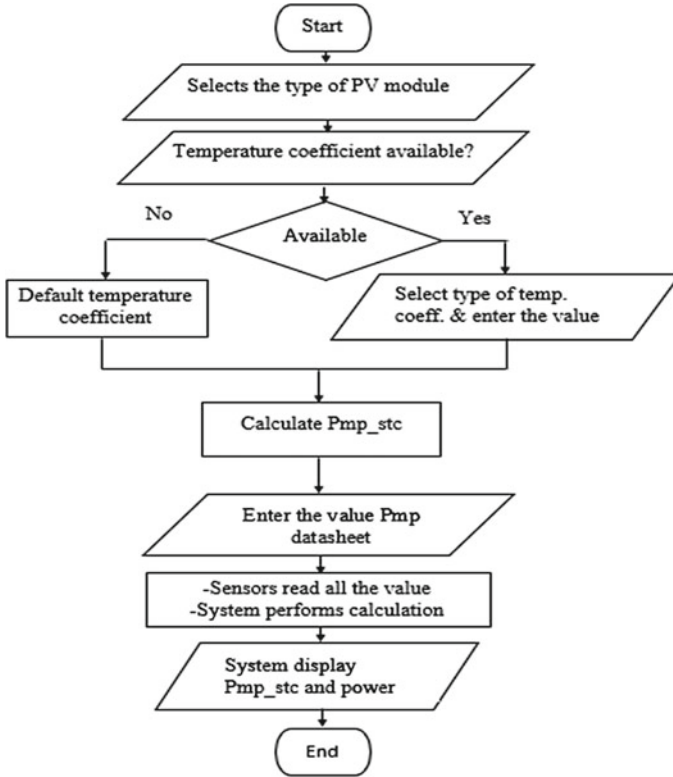


Fig. 2 Flowchart of this system

## 4 Result and Discussion

### 4.1 Comparison with I–V Tracer

The overall result such as open-circuit voltage, short-circuit current and maximum power of this system were compared to the commercialize I–V tracer. As can be seen in Fig. 3, there is a slight difference between results obtained by using I–V tracer and by using this system because of the accuracy factor of the sensors used in this system. There are some losses at the voltage sensor and the current sensor. Figures 3 and 4 show the comparison between this system’s output and commercialize I–V tracer’s output in term of voltage and current respectively.

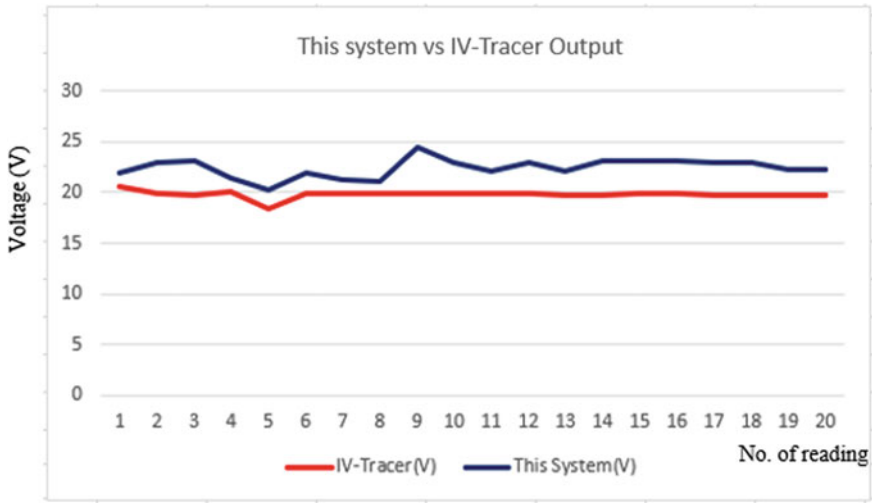


Fig. 3 Comparison of voltage reading obtained by this system and I–V tracer

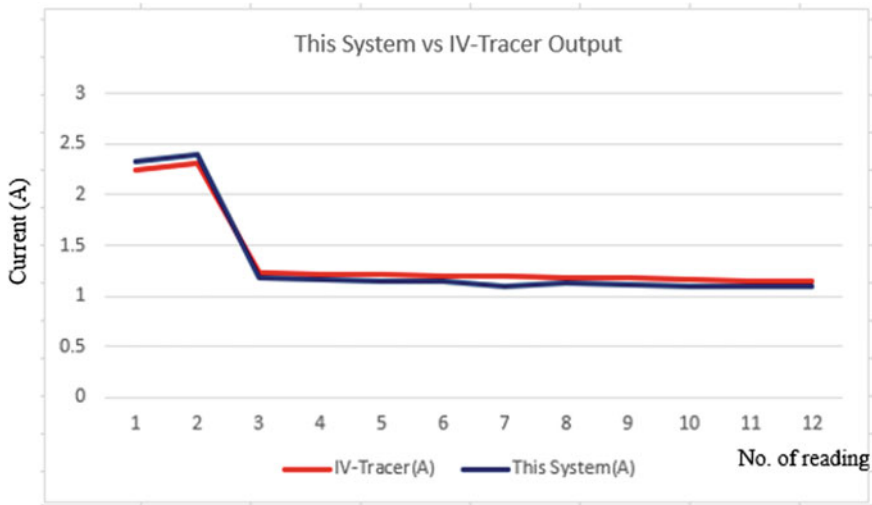


Fig. 4 Comparison of current reading obtained by this system and I–V tracer

### 4.2 Degradation Calculation

For the percentage of the PV module power degradation, one random PV module was selected. In this case, an 80 W PV module was tested. This PV module is a one-year-old PV module. The STC parameter that can be obtained from this PV module datasheet is the maximum power which is 80 W. However, the value of the

**Table 1** Parameters of the tested PV module

Solar irradiance	335 Wm <sup>-2</sup>
V <sub>max_roc</sub>	16.01 V
I <sub>max_roc</sub>	1.32 A
P <sub>max_roc</sub>	21.32 W
Cell temperature	60 °C

**Table 2** Datasheet of the tested PV module at STC

P <sub>max</sub>	100 W
V <sub>mp</sub>	18.59 V
I <sub>mp</sub>	5.38 A
V <sub>oc</sub>	22.42 V
I <sub>sc</sub>	5.76 A
Tolerance	±3%

temperature coefficient was not given. But it is not a problem because the default temperature coefficient will be used. Since this PV module is monocrystalline type, so the value of the temperature coefficient will be  $-0.45\%/^{\circ}\text{C}$ .

Since the solar irradiance at that time was only 335 Wm<sup>-2</sup>, so some ratio calculation needs to be done because in order to know the real value of the STC parameters which is at 1000 Wm<sup>-2</sup> value of the solar irradiance. Table 1 shows the parameters of the tested PV Module. These parameters are used in the calculation of the P<sub>mp\_stc</sub>. Meanwhile, the STC parameters of the PV modules presented in Table 2.

Based on the experiment, the obtained parameters as provided in Table 1, the calculated solar irradiance data for this particular example gives approximately 3. Therefore, it is found that the tested PV module yielded the ROC power about 64 W of the power output. Using Eq. (2), the power output at STC of the PV module is about 75.96 W. Since the original power output at STC of the module is 80 W, therefore, the performance degradation can be calculated a using Eq. (3) to give about 5.04%. Figure 5 shows the prototype of the developed system.

## 5 Conclusion

In conclusion, the using of PV module or solar energy is very interesting and will give us a lot of benefits. However, it is very important for us to know and understand the parameters of our PV modules. This is because by knowing these parameters, the factors that affect the PV module performances can be examined. The ROC parameters of our PV module can be obtained instantaneously. ROC and STC parameters must be obtained in order to determine the percentage of our PV module's power



**Fig. 5** The final prototype of the proposed system



degradation. Apart from that, it is also very important to study the factors that affect the PV module's performance such as solar irradiance, cell temperature, shading effect etc.

**Acknowledgements** The authors gratefully acknowledge Universiti Malaysia Pahang (UMP) under UMP Research Grant (RDU1703128) for their financial support and facilities.

## References

1. Jumaat SA, Othman MH (2018) Solar energy measurement using arduino. In: MATEC web of conferences, vol 150, p 01007
2. Anand R, Pachauri RK, Gupta A, Chauhan YK (2016) Design and analysis of a low-cost PV analyzer using arduino UNO. In: 2016 IEEE 1st international conference on power electronics, intelligent control and energy systems (ICPEICES), pp 1–4
3. Gusa RF, Sunanda W, Dinata I, Handayani TP (2018) Monitoring system for solar panel using smartphone based on microcontroller. In: 2018 2nd international conference on green energy and applications (ICGEA), pp 79–82
4. Haider-e-Karar I, Khuwaja AA, Sattar A (2015) Solar power remote monitoring and controlling using arduino, LabVIEW and web browser. In: 2015 power generation system and renewable energy technologies (PGSRET), pp 1–4
5. Dhole SV, Kumar S, Grover A, Kaduskar VP, Kumar J (2017) Review of solar energy measurement system. *Int J Recent Innov Trends Comput Commun (IJRITCC)*, 5(1)
6. Rasheed S, Karthik SS (2016) Solar panel parameters monitoring using Arduino. *Imp Int J Eco-friendly Technol (IJJET)* 1(1):129–134
7. kumar A, Dwivedi Ak (2013) Solar power parameter calculator. *Int J Eng Sci Invent* 2(5):44–50. [www.ijesi.org](http://www.ijesi.org)
8. Ranhotitogamange C, Mukhopadhyay SC, Garratt SN, Campbell WM (2011) Measurement and monitoring of performance parameters of distributed solar panels using wireless sensors network. In: 2011 IEEE international instrumentation and measurement technology conference, pp 1–6
9. Patil S, Vijayalashmi M, Tapaskar R (2017) Solar energy monitoring system using IoT. *Indian J Sci Res* 15(2):149–155

10. Orsetti C, Muttillio M, Parente FR, Pantoli L, Stornelli V, Ferri G (2016) Reliable and inexpensive solar irradiance measurement system design. *Proc Eng* 168:1767–1770. <https://doi.org/10.4067/S0718-58392014000100012>
11. Krauter S, Hanitsch R (1994) Actual optical and thermal performance of PV-modules. In: *Proceedings of 1994 IEEE 1st world conference on photovoltaic energy conversion—WCPEC (A joint conference of PVSC, PVSEC and PSEC)*, vol 1, pp 734–737
12. Aziz T, Ketjoy N, Sirisamphanwong C (2014) Determination of PV module power output degradation after long term operation. In: *2014 international conference and utility exhibition on green energy for sustainable development (ICUE)*, pp 1–6
13. Chandra S, Yadav A, Agrawal S, Chauhan DS (2017) Experimental investigation of optimum wind speed for material dependent temperature loss compensation in PV modules. In: *2017 3rd international conference on condition assessment techniques in electrical systems (CATCON)*, pp 31–35
14. Kechiche OBHB, Hamza M, Sammouda H (2016) Performance comparison of silicon PV module between standard test and real test conditions. In: *2016 7th international renewable energy congress (IREC)*, pp 1–6
15. Alshushan MAS, Saleh IM (2013) Power degradation and performance evaluation of PV modules after 31 years of work. In: *2013 IEEE 39th photovoltaic specialists conference (PVSC)*, pp 2977–2982

# Direct Power Control Method of Maximum Power Point Tracking (MPPT) Algorithm for Pico-Hydrokinetic River Energy Conversion System



W. I. Ibrahim , M. R. Mohamed  and R. M. T. R. Ismail 

**Abstract** In this paper, a design of maximum power point tracking (MPPT) algorithm for the pico-hydrokinetic system in river application has been proposed. The design topology consists of the permanent magnet synchronous generator (PMSG), a three-phase bridge rectifier and a DC boost converter. The proposed MPPT algorithm is a combination of modified hill-climbing search algorithm (MHCS) with the current PI-controller. The MPPT concept is based on measuring the rectifier output voltage and current respectively to produce the reference current ( $I_{MPP}$ ). The PI-controller has been used to tune the error signal between  $I_{MPP}$  and actual inductance current ( $I_{dc}$ ) to provide the duty-cycle of the boost converter. A comparison is performed between the fixed step HCS and the proposed MPPT to investigate the performance of the algorithm. The results show the proposed algorithm able to harness the maximum power with 96.32% efficiency.

**Keywords** MPPT · Hill climbing search algorithm · Hydrokinetic

## 1 Introduction

The use of renewable energy as a clean and sustainable energy resource is rapidly increasing every year and expected to keep growing worldwide. This is due to the exhaustion of fossil fuels and the environmental concern such as the emission of CO<sub>2</sub> and greenhouse effect [1]. Instead of solar PV, wind energy, biomass and geothermal, the pico-hydrokinetics also has been explored for future energy resources.

The pico-hydrokinetic system has many advantages such as the system generate the electricity without requires any dam or other structures and give minimal impacted

---

W. I. Ibrahim (✉) · M. R. Mohamed

Sustainable Energy & Power Electronics Research Group, Faculty of Electrical & Electronics Engineering, Universiti Malaysia Pahang, 26600 Pekan, Pahang, Malaysia  
e-mail: [wismail@ump.edu.my](mailto:wismail@ump.edu.my)

R. M. T. R. Ismail

Instrumentation & Control Engineering (ICE), Faculty of Electrical & Electronics Engineering, Universiti Malaysia Pahang, 26600 Pekan, Pahang, Malaysia

© Springer Nature Singapore Pte Ltd. 2020

A. N. Kasruddin Nasir et al. (eds.), *InECCE2019*, Lecture Notes in Electrical Engineering 632, [https://doi.org/10.1007/978-981-15-2317-5\\_58](https://doi.org/10.1007/978-981-15-2317-5_58)

691

to the environment [2]. This type of energy harnessing can be applied at the rivers, man-made waterway and other flowing facilities with an optimal water velocity [3].

The maximum power point tracking (MPPT) algorithm can be implemented to the pico-hydrokinetic system to extract more power by keeping the optimum steady voltage across the load. In addition, the fluctuation of water velocity in a river is a challenging issue especially to design the control system that able to harness the maximum output power with high efficiency.

The MPPT algorithm from the wind energy conversion system (WECS) and solar PV has been adopted in this study to be implemented in the pico-hydrokinetic system. This is due to the concepts of operation, electrical hardware and variable speed generator are similar to WECS [4]. Therefore, the MPPT algorithm from WECS is the primary reference for details research in this field.

The MPPT algorithm can be categorised into three groups in general, an indirect power control (IPC), a direct power control (DPC) and soft-computing method (SCM) as shown in Fig. 1. The IPC MPPT is based on maximising the mechanical power ( $P_m$ ) while DPC MPPT algorithm directly maximised the output power ( $P_o$ ) [5].

The IPC based MPPT algorithm such as the tip speed ratio (TSR) and optimal torque (OT) are commonly used for large wind turbine system. The system algorithm requires the sensor to measure the wind speed and both rotational speed of turbine and generator. In [6] the quantum neural network (QNN) has been used as a controller to enhance the efficiency of TSR and OT MPPT method in the WECS.

The DPC MPPT algorithm is suitable for small scale wind turbine system. This algorithm is also a sensorless method and not required turbine parameters knowledge in designing the control algorithm. Hence, this type of algorithm is more reliable and less complex with a lower cost [7]. The perturb and observe (P&O) and also known as hill-climbing search (HCS) are broadly used because of the flexible and

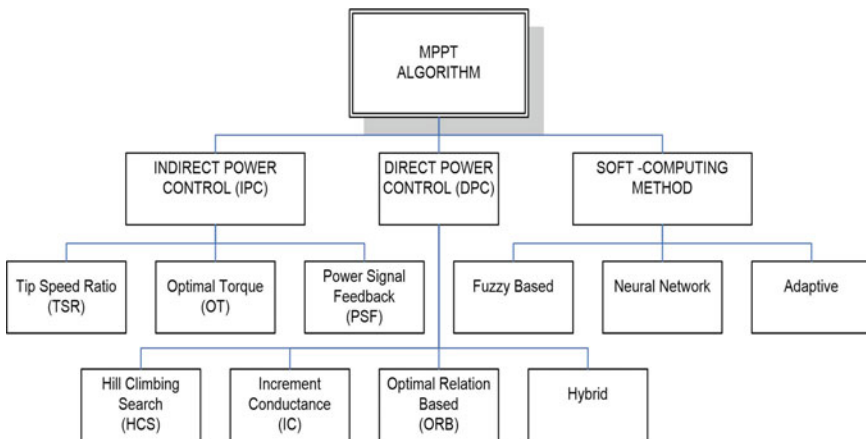


**Fig. 1** The MPPT algorithm classification

straightforward algorithm [8]. In [9], the variable-step HCS has been proposed to solve the wrong direction tracking of conventional HCS algorithm.

Several MPPT algorithms using soft computing method have been proposed in [10–13]. The methods are promising with higher efficiency and excellent performance under varying wind speed conditions. However, the algorithm is very sophisticated and the convergences speed is low due to the quantity of iteration and training knowledge in the programming. In reference [14] the online step and offline step are required to train the different set of neural network parameters for the optimal neural network controller. Hence, the trained neural network can quickly map the relationship between input and output data.

In this paper, direct power control based MPPT algorithm for the pico-hydrokinetic system has been designed to harness the maximum power in the variation of water. The design topology consists of PMSG, uncontrolled rectifier and DC boost converter as a control circuit. The modified hill-climbing search algorithm with the current PI controller has been proposed to enhance the capturing of maximum output power and efficiency of the system.

## 2 Pico-Hydrokinetic System Configuration

Figure 2 shows the circuit topology of the pico-hydrokinetic system used in this studied. The water turbine is directly coupled to the permanent magnet synchronous generator (PMSG). A three-phase uncontrolled rectifier is used to rectify the generator output voltage. The DC Boost converter is used to perform the MPPT operation by controlling the IGBT switching. By using this circuit topology, the system required only one active power switch. This method will reduce the cost and simplified the control of the hydrokinetic system. Also, the resistance ( $R$ ) is directly connected to the output of the boost converter as a load to consume the energy of the system. However, this topology can be substituted by the power inverter for a grid-connected and stand-alone operation.

### 2.1 Turbine Model

Water velocity is an input of the pico-hydrokinetic while the output is the mechanical power ( $P_m$ ) and torque developed ( $T_m$ ) to drive the generator shaft. The amount of power that could be harnessing in the river is given by

$$P_m = \frac{1}{2} \rho A V^3 C_p \quad (1)$$

where,  $\rho$  is water density (1000 kg/m<sup>3</sup>),  $A$  is the cross-sectional area of the turbine (m<sup>2</sup>),  $V$  is the water current velocity (m/s) and  $C_p$  is the power coefficient of the

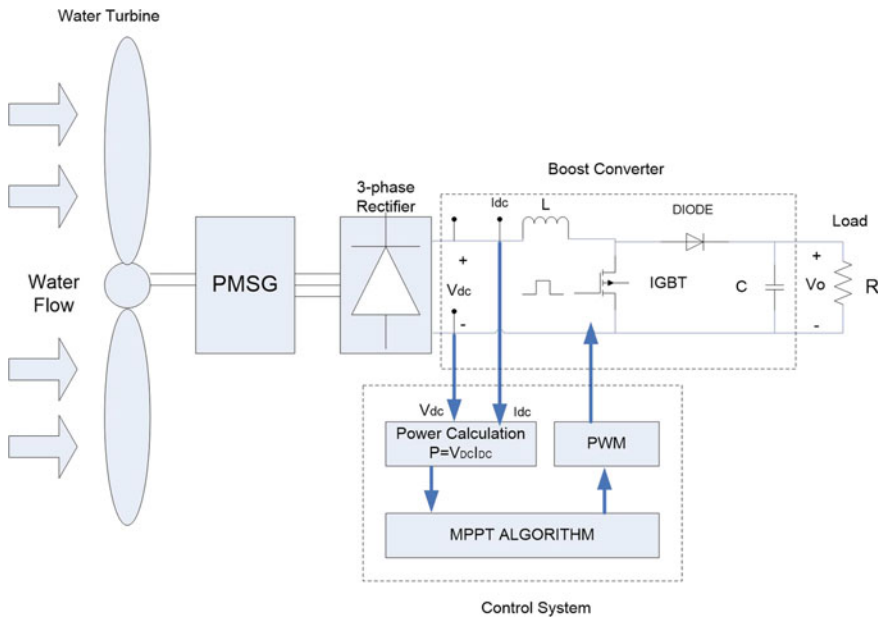


Fig. 2 Circuit topology understudied

turbine. The pitch angle ( $\beta$ ) is fixed for the water turbine. Hence, the  $C_p$  is merely a function of the tip speed ratio ( $\lambda$ ) which is the ratio of the linear speed of the blade to the water current velocity.

$$TSR(\lambda) = \frac{\omega R}{V} \tag{2}$$

where, the  $\omega$  is the rotational speed of the turbine and  $R$  is the turbine radius. The turbine characteristic indicates that there is one specific  $TSR$  value which turbines are working at the most efficient operating point. Thus, the  $TSR$  value should be kept at an optimal operating point for all water current velocity to achieve the maximum energy harnessing.

The turbines power coefficient ( $C_p$ ) is determined by the  $TSR$ , shape and radius of the turbines [15]. The relationship between  $C_p$  and  $TSR$  used in this paper is expressed as;

$$C_p(\lambda) = -0.022\lambda^6 + 0.04\lambda^5 - 0.26\lambda^4 + 0.72\lambda^3 - 0.77\lambda^2 + 0.27\lambda - 0.011 \tag{3}$$

The turbine mechanical torque ( $T_m$ ) can be given by;

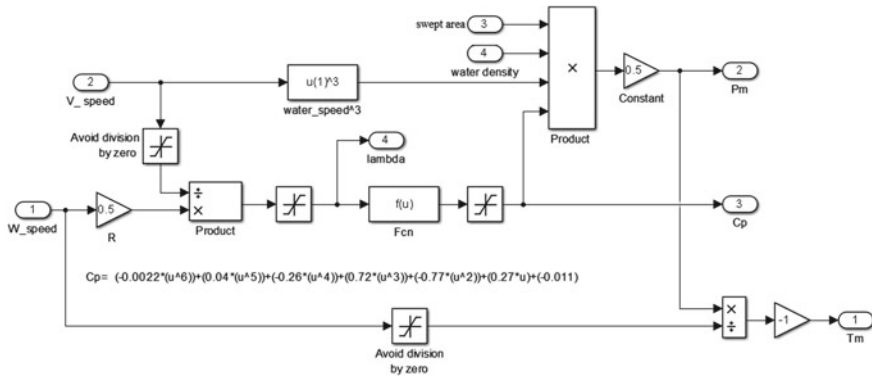


Fig. 3 Pico-hydrokinetic turbine model

$$T_m = \frac{P_m}{\omega_m} \tag{4}$$

where  $P_m$  is the mechanical power and  $\omega_m$  is the turbine rotational speed. Figure 3 shows the modelling of the hydrokinetic turbine based on the derivation of Eqs. (1)–(4). It is observed that the power produced by the turbine depends on the value of the water density ( $\rho$ ), the swept area ( $A$ ), power coefficient ( $C_p$ ) and input water velocity ( $V$ ).

### 2.2 Analysis of PMSG and Rectifier

The PMSG has been used to convert the turbine rotational speed into electrical power. The back electromotive force ( $E$ ) of the PMSG with constant flux is given by,

$$E = k\omega_m \tag{5}$$

where  $K$  is a constant coefficient and  $\omega_m$  is the generator rotor speed (rad/s). The terminal phase voltage in a balanced steady state is given by

$$V_s = E - I_s(R_s + j\omega_e L_s) \tag{6}$$

where  $I_s$ ,  $R_s$  and  $L_s$  is the stator current, stator resistance, and stator inductance respectively. Whereas,  $\omega_e$  is the electrical frequency. The relationship between the electrical frequency ( $\omega_e$ ) and the mechanical frequency ( $\omega_m$ ) is given by;

$$\omega_e = p\omega_m \tag{7}$$

where  $p$  is the number of PMSG poles. The function of the bridge rectifier to convert the generated AC voltage from PMSG to a DC voltage. The relationship between the DC Voltage ( $V_{DC}$ ) and a phase AC voltage of PMSG ( $V_s$ ) can be expressed as;

$$V_{DC} = \frac{3\sqrt{6}}{\pi} V_s \quad (8)$$

The approximate relationship between  $V_{DC}$  and  $\omega_m$  can be expressed from (5)–(8) [16]

$$V_{DC} \approx \omega_m \quad (9)$$

The considering the output power conversion from PMSG into DC power through the rectification process is at unity power factor with no losses, the output power ( $P_g$ ) can be expressed as [17];

$$P_g = 3V_s I_s = V_{DC} I_{DC} \quad (10)$$

### 2.3 Design of DC Boost Converter

The DC Boost converter is commonly used because of the high efficiency in power transfer. However, the energy can be transfer when the output stage voltage is higher than the input voltage [18]. The output voltage of the boost converter can be controlled by varying the duty cycle. Figure 4 shows the equivalent circuit of the DC boost converter with insulated gate bipolar switch (IGBT) used as a power switch (S). By varying the duty cycle ( $D$ ), the load seen by the generator will be changing. Thus, the output voltage and rotational rotor speed will be adjusted accordingly [19].

The ratio between the output voltage ( $V_{out}$ ) to the input voltage  $V_{DC}$  is given by;

$$\frac{V_{out}}{V_{DC}} = \frac{1}{1 - D} \quad (11)$$

where,  $D$  is the duty cycle and  $V_{DC}$  is the output voltage from rectifier or input voltage to boost converter.

In continuous conduction mode (CCM) operation, the value of inductor and capacitor can be given;

$$L = \frac{V_{DC} D}{2\Delta I_L f_s} \quad (12)$$

where  $\Delta I_L$  is the desired inductor current peak ripple and  $f_s$  is the boost converter switching frequency. The value of the capacitor (C) can be determined by:



**Fig. 4** DC boost converter equivalent circuit

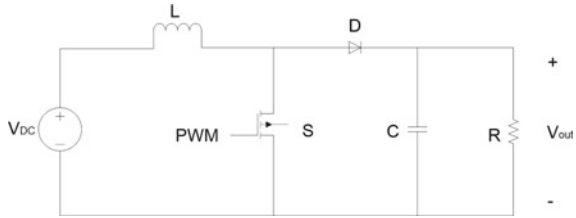


**Table 1** The parameter of the boost converter

Parameter	Values
Input capacitor, $C_{in}$ ( $\mu F$ )	100
Output capacitor, $C_{out}$ ( $\mu F$ )	245
Inductance, $L$ (mH)	1.85
Load resistance $R_{Load}$ ( $\Omega$ )	10.0
Switching frequency, $f_s$ (kHz)	20

$$C = \frac{V_{out}D}{2\Delta_{vo}Rf_s} \tag{13}$$

where  $\Delta_{vo}$  is the output voltage peak ripple and  $R$  is the resistance load. Table 1 shows the parameter design of boost converter used in this studied.

### 3 MPPT Control Algorithm

#### 3.1 Hill-Climbing Search Algorithm

Hill-climbing search (HCS) algorithm will locate the local maximum point by climbing the curve by adding the fixed step size ( $\Delta S$ ). The HCS algorithm is based on perturb and observe (P&O) concept that used to climb the power curve of the turbine. The algorithm will monitor any changes in the output power and rotational rotor speed with respect to water velocity. The maximum power  $P_{MPP}$  can be generated from the PMSG when the variation of power over the variation of rotor speed equal to zero as shown in Fig. 5.

The flow-chart of HCS MPPT algorithm was shown in Fig. 6. In this approach, if the operating point is at the left region of the peak point ( $P_{MPP}$ ), the controller must move it to the right by climbing the curve to the nearest peak point. The step size ( $\Delta S$ ) must be added and the generator must increase the speed to achieve the  $P_{MPP}$ . In another side, if the operating point is in the right region of the peak point ( $P_{MPP}$ ), the controller must move to the left by reducing the step size ( $\Delta S$ ). Therefore, the generator must reduce the speed to achieve the  $P_{MPP}$ .

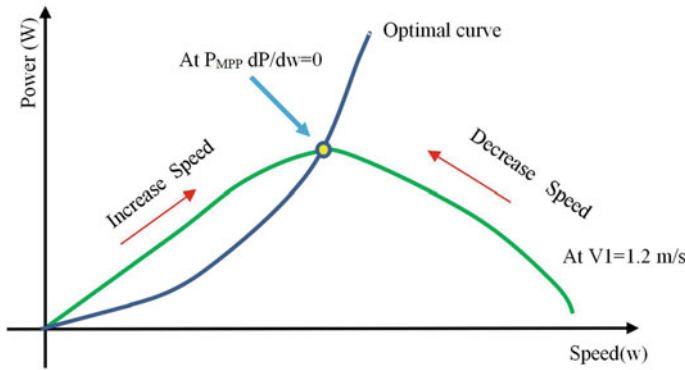


Fig. 5 HCS Concept based on the regulation of the duty cycle

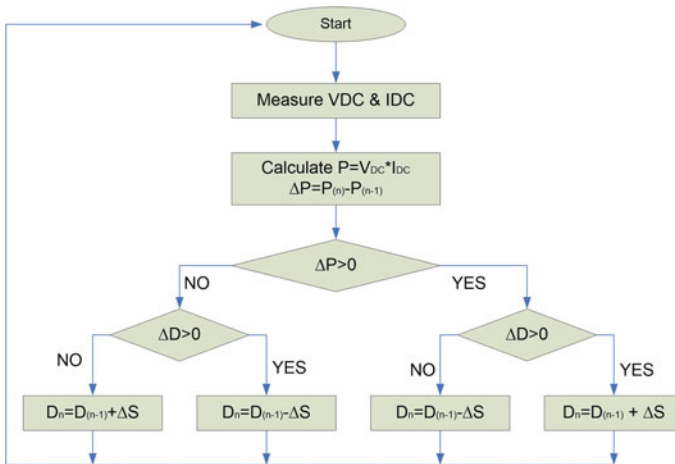


Fig. 6 HCS MPPT algorithm

### 3.2 Proposes Modify Hill-Climbing Search with PI Current Controller

The modified HCS algorithm will improve the fixed step HCS algorithm by reducing the oscillation at the steady-state condition. The simpler way to modify the algorithm is by changing the step-size ( $\Delta I$ ) as shown in Fig. 7. The  $\Delta I$  is multiple by a constant value in order to provide the very responsive algorithm with maximum energy harnessing.

The following step describes the modified HCS algorithm with PI controller

Step 1: Measure the  $V_{DC}$  and  $I_{DC}$

Step 2: Calculate the power and change in electrical power  $\Delta P$

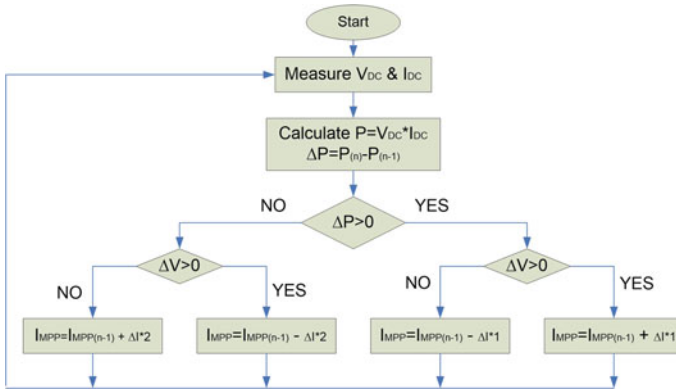


Fig. 7 Modified hill climbing search algorithm

Step 3: Calculate the change in electrical voltage  $\Delta V$

Step 4: Determine the direction of the perturbation and observe the optimal operating condition

Step 5: Increment or decrement the  $I_{MPP}$  and step size ( $\Delta I$ ) according to the formula as given;

$$I_{MPP} = I_{MPP(n-1)} \pm \Delta I \tag{14}$$

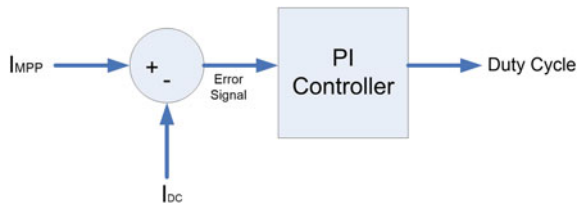
If the operating point at the left of  $P_{MPP}$ , increase the ( $\Delta I$ ) by multiple by 1. Otherwise, reduce the step size by multiple by 2.

Step 6: Updated the next actual value of  $P$ ,  $V$  and  $I_{MPP}$  for the next sample time.

Step 7: Calculate the error between  $I_{MPP}$  and  $I_{dc}$  and fed into PI-Controller.

The comparison between the actual current ( $I_{DC}$ ) and reference current ( $I_{MPP}$ ) to produce an error signal as shown in Fig. 8. Then, the error signal is fed into the PI- controller for the tuning process. The output signal is compared to the repetitive triangular frequency waveform to generate the PWM for switching the DC Boost converter.

Fig. 8 PI-controller block diagram



### 4 Results and Discussion

The Matlab/Simulink environment is used to perform the simulation study of the pico-hydrokinetic system in the river. Two performance indicators for the MPPT algorithm has been investigated in this study. First is the tracking ability of the algorithm and the second is the ability to capture the maximum output power at the fluctuation of water. Figure 9 shows the complete system of the pico-hydrokinetic system with MHCS-PI controller.

The input water velocity is varied from 0.5 to 2.0 ms<sup>-1</sup> as shown in Fig. 10 to investigate the tracking ability of the MPPT techniques.

Figure 11 shows the tracking ability of both algorithms. As can be seen both algorithm able to track the variation of the input water velocity for optimal energy harnessing. Also, the Modified HCS-PI algorithm able to harness more output power than the HCS algorithm even at the fluctuation of water.

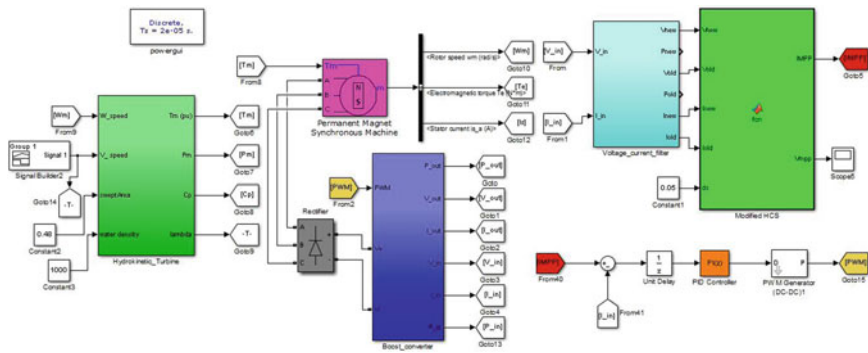


Fig. 9 The pico-hydrokinetic system with MPPT algorithm

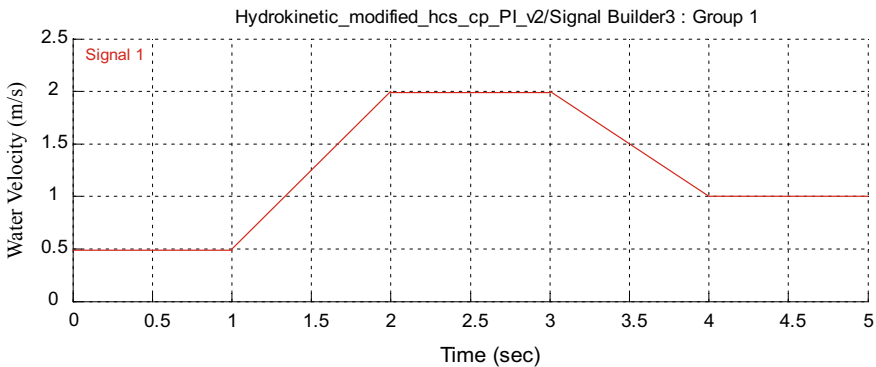
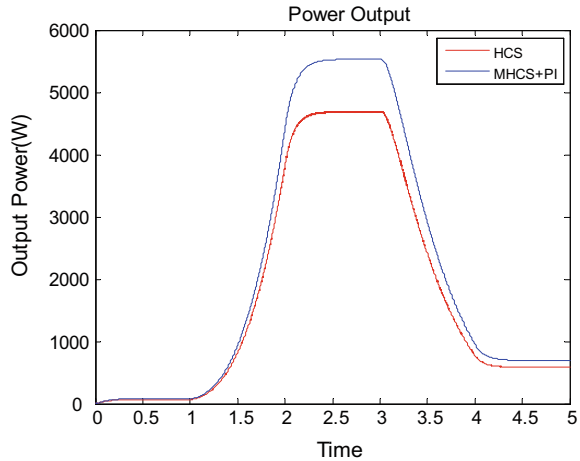


Fig. 10 The input water velocity

**Fig. 11.** The output powers



**Table 2** The comparison output power and efficiency of the MPPT algorithm

Water velocity (m/s)	Theoretical (W)	Output power (W)		Efficiency (%)	
		HCS	MHCS + PI	HCS	MHCS + PI
0.4	46.08	37.3	43.7	81.0	94.8
0.8	368.64	299.2	353.4	81.1	95.8
1.2	1244.16	1016.0	1201.0	81.6	96.5
1.6	2949.12	2421.0	2862.0	82.0	97.0
2.0	5760.00	4756.0	5617.0	82.6	97.5

Table 2 shows the performance comparison of HCS and MHCS-PI algorithm base MPPT controller. Both algorithms have been tested at fixed water velocity starting from 0.4 ms<sup>-1</sup> up to 2.0 ms<sup>-1</sup> to investigate total power generated and the efficiency of the algorithm. As can be seen, the MHCS-PI algorithm shows outstanding performance compared to the HCS algorithm. The MHCS-PI algorithm can harness the maximum power between 43.7 and 5617 W with average efficiency at 96.32%. However, the HCS algorithm only gains 81.66% efficiency with output power between 37.34 and 4756 W.

## 5 Conclusion

In this paper, the design topology for the pico-hydrokinetic system is presented. The proposed design consists of PMSG, uncontrolled rectifier, and DC boost converter. The HCS and MHCS-PI algorithm has been simulated to track the maximum power in different water velocity. The advantages of the proposed system have not required any

sensors to measure the water velocity and operation of variable speed PMSG. Besides, the knowledge of turbines parameters and characteristics also not essentials in the proposed design. The results show that the pico-hydrokinetic system can harness between 43.7 and 5617 W with 96.32% efficiency by MHCS-PI algorithm.

**Acknowledgements** The authors would like to thank to Universiti Malaysia Pahang for funding support under UMP Postgraduate Research Scheme (PGRS190318).

## References

1. Yazici İ, Yaylaci EK (2017) Maximum power point tracking for the permanent magnet synchronous generator-based WECS by using the discrete-time integral sliding mode controller with a chattering-free reaching law. *IET Power Electron* 1751–1758
2. Alvarez Alvarez E, Rico-Secades M, Corominas EL, Huerta-Medina N, Soler Guitart J (2018) Design and control strategies for a modular hydroKinetic smart grid. *Int J Electr Power Energy Syst* 95:137–145
3. Yuce MI, Muratoglu A (2015) Hydrokinetic energy conversion systems: a technology status review. *Renew Sustain Energy Rev* 43:72–82
4. Koko SP, Kusakana K, Vermaak HJ (2017) Optimal energy management of a grid-connected micro-hydrokinetic with pumped hydro storage system. *J Energy Storage* 14:8–15
5. Kumar D, Chatterjee K (2016) A review of conventional and advanced MPPT algorithms for wind energy systems. *Renew Sustain Energy Rev* 55:957–970
6. Ganjefar S, Ghassemi AA, Ahmadi MM (2014) Improving efficiency of two-type maximum power point tracking methods of tip-speed ratio and optimum torque in wind turbine system using a quantum neural network. *Energy* 67:444–453
7. Dalala ZM, Zahid ZU, Yu W, Cho Y, Lai JS (2013) Design and analysis of an MPPT technique for small-scale wind energy conversion systems. *IEEE Trans Energy Convers* 28(3):756–767
8. Raza Kazmi SM, Goto H, Guo HJ, Ichinokura O (2011) A novel algorithm for fast and efficient speed-sensorless maximum power point tracking in wind energy conversion systems. *Ind Electron IEEE Trans* 58(1):29–36
9. Mousa HHH, Youssef A, Mohamed EEM (2019) Electrical power and energy systems variable step size P & O MPPT algorithm for optimal power extraction of multi-phase PMSG based wind generation system. *Electr Power Energy Syst* 108(2018):218–231
10. Hong CM, Chen CH, Tu CS (2013) Maximum power point tracking-based control algorithm for PMSG wind generation system without mechanical sensors. *Energy Convers Manag* 69:58–67
11. Abdullah MA, Al-Hadhrami T, Tan CW, Yatim AHM (2018) Towards green energy for smart cities: particle swarm optimization based MPPT approach. *IEEE Access* 6:1–1
12. Kumar K, Babu RN, Prabhu KR (2017) Design and analysis of RBFN-based single MPPT controller for hybrid solar and wind energy system. *IEEE Access* 5:15308–15317
13. Li S, Wang H, Tian Y, Aitouche A (2015) A RBF neural network based MPPT method for variable speed wind turbine system. *IFAC-PapersOnLine* 28(21):244–250
14. Messalti S, Harrag A, Loukriz A (2017) A new variable step size neural networks MPPT controller: review, simulation and hardware implementation. *Renew Sustain Energy Rev* 68(2015):221–233
15. Tiwari R, Babu NR (2016) Fuzzy logic based MPPT for permanent magnet synchronous generator in wind energy conversion system. *Int Fed Autom Control* 49(1):462–467
16. Xia Y, Ahmed KH, Williams BW (2011) A new maximum power point tracking technique for permanent magnet synchronous generator based wind energy conversion system. *IEEE Trans Power Electron* 26(12):3609–3620

17. Hussain J (2016) Adaptive maximum power point tracking control algorithm for wind energy conversion systems. *IEEE Trans Energy Convers* 31(2):697–705
18. Licari J, Zammit D, Staines CS, Micallef A, Maurice A (2017) Incremental current based MPPT for a PMSG micro wind turbine in a grid-connected DC microgrid. *Energy Procedia* 142:2284–2294
19. Abdullah MA, Yatim AHM, Tan CW, Saidur R (2012) A review of maximum power point tracking algorithms for wind energy systems. *Renew Sustain Energy Rev* 16(5):3220–3227

# Load Estimation of Single-Phase Diode Bridge Rectifier Using Kalman Filter



Nor Syuhaida Othman and Hamzah Ahmad

**Abstract** These days most electronic loads are nonlinear. Electronic equipment such as audio devices, personal computers and electronic ballasts for discharge lamps are the example of nonlinear loads. These electronic loads are works in DC voltage. As the energy distribution system is performed in AC voltage, the AC voltage need to change into DC voltage. The single-phase rectifier performed the conversion of AC voltage to DC voltage in low power applications. The main drawback of these rectifiers is that they generate significant harmonic distortion. Components aging, power system efficiency lessen and excessive heat of equipments are the effects of harmonics in power system. Thus, the self-resonance, non-dielectric and hysteresis existed in the power system affected system designer to choose the passive components for the simulation. This paper portrays the study and development of an estimation method for the values of the electrical parts in the majority of the electronic equipment accessible in the market. It is conceivable to identify the values of equivalent capacitance, resistance and inductance that associated with the rectifier through this method. Simulation results validate the better accuracy of the proposed method when contrasted to the measurement-based method. The proposed method using Kalman filter to this rectifier topology enabled the expansion for future works to think about their harmonic effect on the power quality (PQ) of power distribution systems.

**Keywords** Kalman filter · Parameter estimation · Single-phase rectifier

## 1 Introduction

Electronic devices parts such as (resistance, inductors, capacitors, etc.) [1], and devices dealing with them like motors [2], work with wide-signals described by high harmonic content. Therefore, the self-resonance, non-dielectric and hysteresis

---

N. S. Othman (✉) · H. Ahmad  
Fakulti Kejuruteraan Elektrik & Elektronik, Universiti Malaysia Pahang (UMP), 26600 Pekan,  
Pahang, Malaysia

H. Ahmad  
e-mail: [hamzah@ump.edu.my](mailto:hamzah@ump.edu.my)

© Springer Nature Singapore Pte Ltd. 2020

A. N. Kasruddin Nasir et al. (eds.), *InECCE2019*, Lecture Notes in Electrical Engineering 632, [https://doi.org/10.1007/978-981-15-2317-5\\_59](https://doi.org/10.1007/978-981-15-2317-5_59)



existed in the power system and effected system designer to choose the passive components for the simulation. Electrical models and equivalent systems typically used by the designers. This reality prompted the requirement for building up a particular research towards the modeling of these loads. The behavior of resistive, inductive and capacitive passive component represented by models made up by time-invariant components respectively. There are a few papers managing the point estimation of R, L and C parameters [3–7]. Souza and Ribeiro in their work exhibited [3] an answer in time-domain for parameters estimation in single-stage electronic non-straight loads. Hence, a complementary proposal of modeling was created to expand the analysis to loads with different nonlinearities.

The study performed in [4] introduces a measurement-based method to estimate R, L and C in the equivalent circuit. The authors recommended that the R, L and C parameters could be gotten once a current waveform under different voltage is measured. Then, the equivalent circuit was used to perform the harmonic simulation studies under other voltage conditions. In [5], the authors was analyzed a parameter estimation of the rectifier and introduces a non-linear least-square procedure. The rectifier model relies upon the standardized parameters called invariants. Additionally, in [6], the frequency-domain model developed by [8] analyzed the capacitive characteristics of single-phase diode bridge converter based loads. This is because, the effect of circuit parameters and supply voltage on the load fundamental characteristic not examined in detail yet.

Gautam and Majumdar, in their work [7], presents parameter estimation of a single-phase rectifier using extended Kalman filter (EKF). EKF is used for estimation reason in different applications [9, 10]. Linearized model of the nonlinear system was used to implement Kalman filtering. Besides, EKF was designed to estimate the states of a nonlinear system as it is one of the most popular modifications of the KF. In a linear system, Kalman filter was established in order to estimate parameter [11]. Since this paper deals with linear systems, the Kalman filter-based parameter estimation is proposed. Then, the simulation results verify the better accuracy of the proposed method as compared to the measurement-based method [4]. Still, the proposed method using Kalman filter to this rectifier topology allowed the extension for future works to deal with their harmonic that affected power quality (PQ) of power distribution systems. This paper is arranged as follows. Section 2 introduces Kalman filter method based on RLC estimation. The theoretical analysis was developed in Sect. 3. Section 4 introduces simulation results and analysis. Finally, Sect. 5 presents conclusions.

## 2 Kalman Filter Method-Based on RC Estimation

The full-wave rectifier equivalent circuit model is presented in Fig. 1. An inductor, L in this equivalent circuit is contracted to lessen the electromagnetic interference (EMI). Besides, the capacitor, C is incorporated to smooth the dc voltage while equivalent resistance, R representing the supplied load. The values of R, L, and C

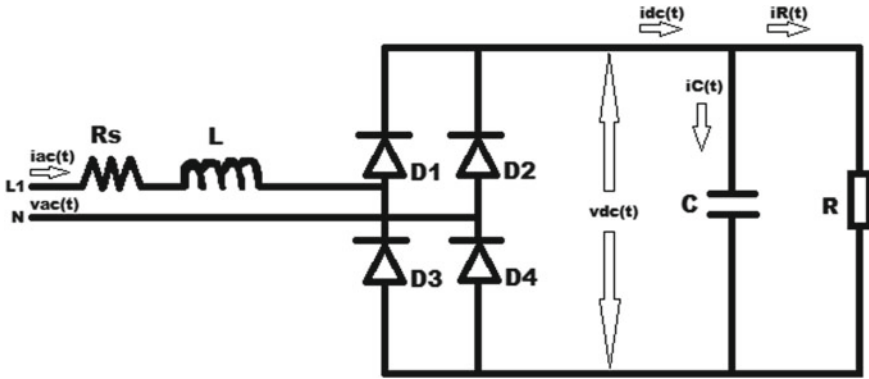


Fig. 1 Single-phase diode-bridge rectifier equivalent circuit

need to be known for simulating, modeling, or analyzing the circuit behaviors on different equipment. This is because they are dependent on the type of load. Figure 2 shows the dc and ac voltage and ac current waveforms for a measured single-phase diode-bridge rectifier-based load (in this case, the load is a PC). Figure 2 presents common waveforms for this nonlinear load as an illustration.

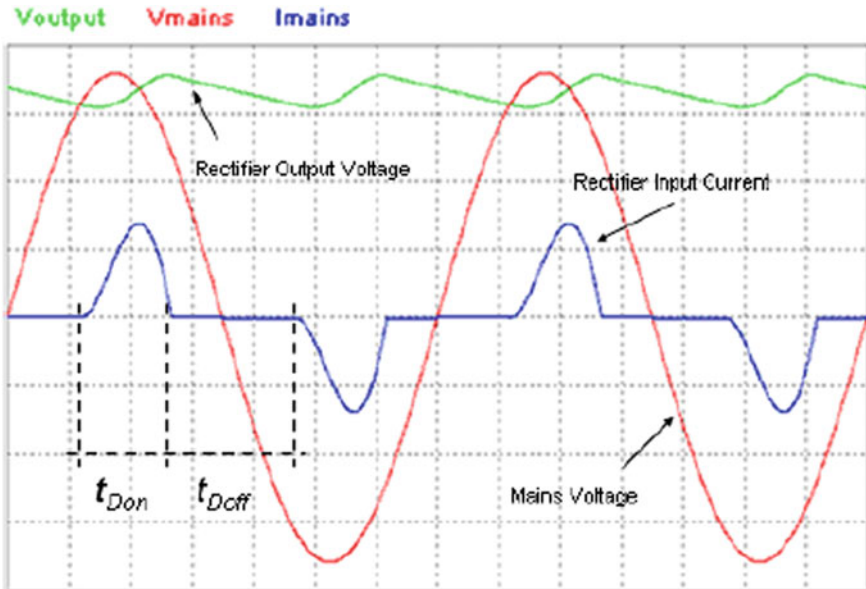


Fig. 2 Input voltage, input current and output voltage waveforms for a single-phase diode bridge rectifier-based [3]

## 2.1 Kalman Filter

In 1960, Rudolf E. Kálmán invented a state estimation technique [12]. The Kalman filter is the efficient iterative filter that involves two major steps which is prediction and updation. The process model of Kalman filter for a linear system is presented as,

$$X_k = AX_{k-1} + BU_k + W_k \quad (1)$$

$$Z_k = HX_k + V_k \quad (2)$$

where  $X_k$  is the estimation value of  $X$ ,  $X_{k-1}$  is the estimate value on the previous state,  $U_k$  is the control input,  $W_k$  and  $V_k$  is noise covariance matrix,  $A$ ,  $B$  and  $C$  will be numerical constant. *Prediction* (time update) is the stage to estimate priori estimation of state and its error covariance matrix, where  $P_k$  is the prior error covariance. Hence, the measurement update equations used that prior value. While *Correction* (measurement update) is the second stage of Kalman filter algorithm to provide correction based on the measurement  $Z_k$  in order to yield the posteriori state estimate and its error covariance, where  $K_k$  is the Kalman gain. The stages of Kalman filter algorithm are listed as follows:

- *Prediction* (time update):

$$X_k = AX_{k-1} + BU_k \quad (3)$$

$$P_k = AP_{k-1}A^T + Q \quad (4)$$

- *Correction* (measurement update):

$$K_k = P_k H^T (H P_k H^T + R)^{-1} \quad (5)$$

$$X_k = X_k + K_k(Z_k - HX_k) \quad (6)$$

$$P_k = (1 - K_k H) P_k \quad (7)$$

Figure 3 shows the general model of Kalman filter. The initial setup to the modeling of Kalman filter is to design the general model above. Hence, the process model and Kalman filter model included by using Eq. (1) until Eq. (7) accordingly.

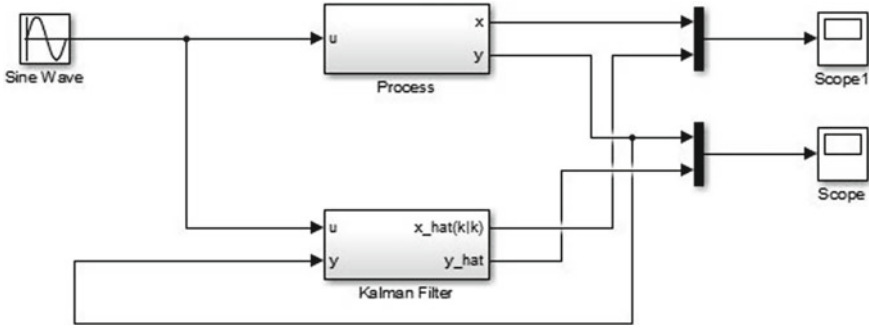


Fig. 3 General model of Kalman filter

### 3 Theoretical Analysis

Single phase rectifier has been used in many applications such as variable speed motor drive [13, 14], split capacitor full bridge rectifier [15], and single phase full-bridge resonant circuit [16]. The frequently applied topology is the full-bridge rectifier that used a bulky capacitor as output filter. Figure 1 shows the structure composed the input stage of switching mode power supplies. The analysis of these rectification topologies presented a study that to identify the values of the components on Fig. 1: the equivalent capacitor C and the equivalent resistor R. Figure 1 shows single-phase full wave rectifier circuit. The input voltage is  $V_{ac}$ . The circuit consists of inductor L and resistor  $R_s$ . The capacitor C is used at the output, which is in parallel with the load resistance R.  $I_{ac}$  and  $V_{dc}$  are the input current and output voltage respectively. Remark that the diode used is ideal diode, thus, there is no voltage drop at the component. The circuit equations of rectifier have been obtained using Kirchhoff's voltage and current laws. They are:

$$I_{ac(t)} = C \frac{d}{dt} V_{dc(t)} + \frac{V_{dc(t)}}{R} \tag{8}$$

$$V_{ac(t)} = R_s I_{ac(t)} + L \frac{d}{dt} I_{ac(t)} + V_{dc(t)} \tag{9}$$

Representing (8) and (9) in terms of state equations,  $\frac{d}{dt} X = AX + BU$  where,

$$X = \begin{bmatrix} I_{ac(t)} \\ V_{dc(t)} \end{bmatrix} \tag{10}$$

$$A = \begin{bmatrix} -\frac{R_s}{L} & -\frac{1}{L} \\ \frac{1}{C} & -\frac{1}{CR} \end{bmatrix} \tag{11}$$

$$B = \begin{bmatrix} \frac{1}{L} \\ 0 \end{bmatrix} \tag{12}$$

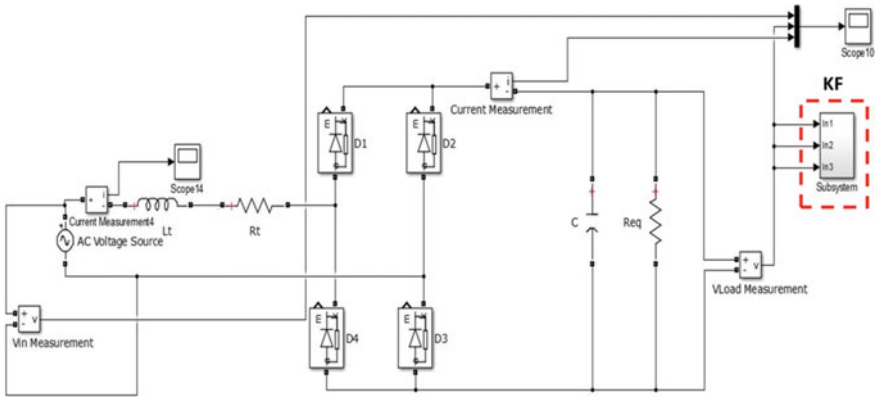


Fig. 4 Kalman filter model for output voltage single-phase diode bridge rectifier

$$U = [V_{ac}(t)] \tag{13}$$

The state space model is given as:

$$\frac{d}{dt} \begin{bmatrix} I_{ac}(t) \\ V_{dc}(t) \end{bmatrix} = \begin{bmatrix} \frac{-R_s}{L} & \frac{-1}{L} \\ \frac{1}{C} & \frac{-1}{CR} \end{bmatrix} \begin{bmatrix} I_{ac}(t) \\ V_{dc}(t) \end{bmatrix} + \begin{bmatrix} \frac{1}{L} \\ 0 \end{bmatrix} [V_{ac}(t)] \tag{14}$$

The measurement model is given as,  $Z = HX$  where,

$$Z = \begin{bmatrix} 0 & 0 \\ 0 & 1 \end{bmatrix} \begin{bmatrix} I_{ac}(t) \\ V_{dc}(t) \end{bmatrix} \tag{15}$$

In general, the Eqs. (14) and (15) were simulated in Kalman filter for estimation. The estimated value obtained from the estimation is  $I_{ac}$  and  $V_{dc}$ . But, in this paper, the research focused to the load side. Hence, the value of  $I_{dc}$  was estimated too.

Figures 4 and 5 shows that the Kalman filter model for output voltage,  $V_{dc}$  and output current,  $I_{dc}$  of single-phase diode bridge rectifier. The analysis observes the  $V_{dc}$  and  $I_{dc}$  value based on different process noise condition. When the  $V_{dc}$  and  $I_{dc}$  value is known, the R and C parameter can be estimated.

### 4 Simulation Results and Analysis

The estimation process on RC parameters of the equivalent model for a nonlinear load need to be illustrates. The behavior of a typical desktop was simulated by using MATLAB in order to get the estimation values. The behavior of a 100 W single-phase non-linear load supplied by 120V<sub>RMS</sub> was simulated shown in Fig. 6. Figure 7

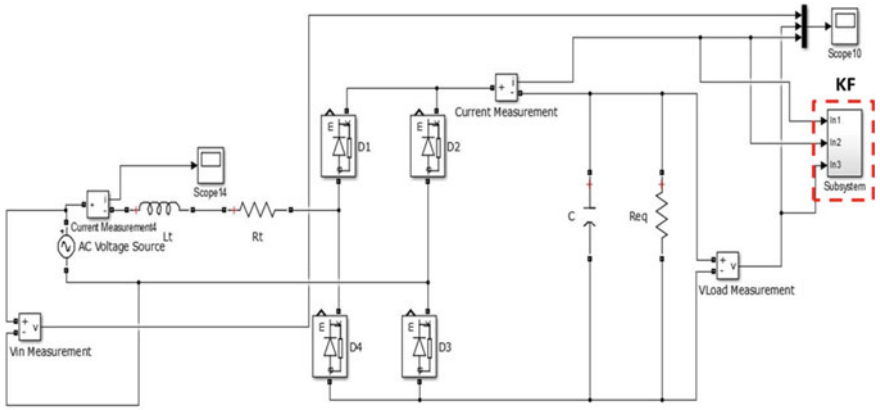


Fig. 5 Kalman filter model for output current single-phase diode bridge rectifier

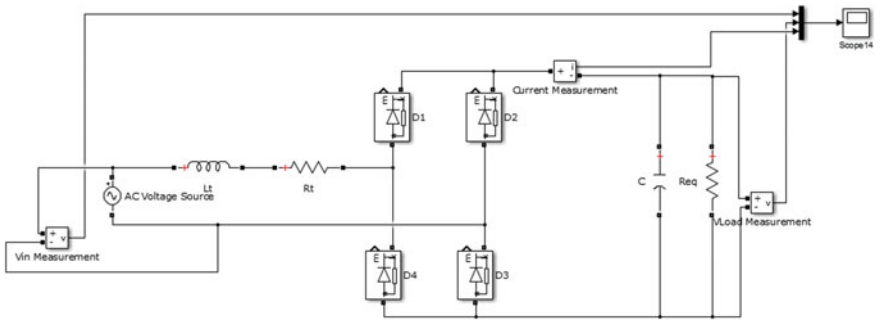


Fig. 6 Single-phase diode bridge rectifier model by Simulink

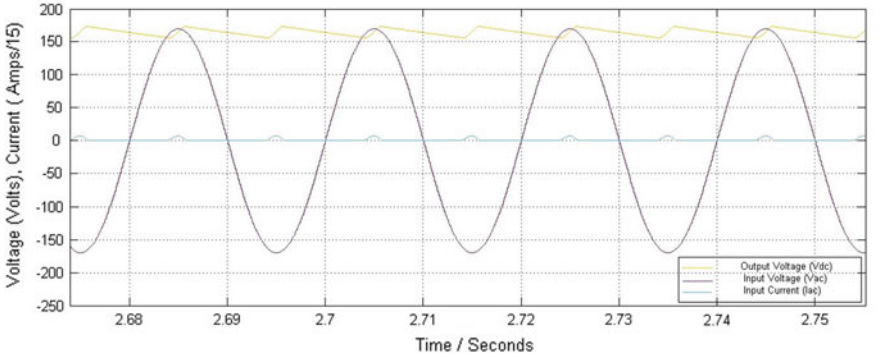


Fig. 7 AC voltage and current waveforms for the single-phase diode bridge rectifier

**Table 1** Voltage and current waveforms simulated by using MATLAB Simulink

	Real value (average)
$V_{dc}$ (V)	173.202
$V_{ac}$ ( $V_{peak}$ )	169.700
$I_{ac}$ (A)	6.850

represents the voltage and current waveforms. This representation of voltage and current waveforms clearly illustrates the concept of linearity of the non-linear load [9]. The results simulated in Fig. 7 are common for a single phase rectifier with capacitive filter (in this case, the load is a Desktop PC). The components that applied in the simulation are 1 mH input inductor  $L$ , 370  $\mu$ F capacitor  $C$ , 216  $\Omega$  load resistor  $R$  and 0.4  $\Omega$  of  $R_s$ . The value of voltage and current waveforms simulated by using MATLAB were listed in Table 1.

The estimation of  $V_{dc}$  and  $I_{dc}$  has been investigated in previous section. Thus, this subsection explores the consequences to the estimation RC parameter of single-phase diode bridge rectifier with diverse noise conditions. Simulation of unknown parameters in this paper considers process noise of real and 0.05. Next, the Kalman filter simulated those values and result obtained was used in order to estimate R and C parameter. Tuning process occur in the simulation of the equivalent circuit of single-phase diode bridge rectifier. The intention of this process is to achieve a good estimation results. Figures 8 and 9 show the real and estimated values of  $V_{dc}$  and  $I_{dc}$  over a period of time.

Figure 8 shows the real output voltage and the average of estimated voltage which are 173.202 V and 173.203 V respectively with process noise of real. Next, Fig. 9 shows the real and estimated values of  $I_{dc}$ . The process noise of real is takes into account in this simulation. The real value of output current,  $I_{dc}$  is 0.8019 A and the average value of estimated are 0.802 A. Hence, the real and estimated values are having small differences between them. The value of  $V_{dc}$  and  $I_{dc}$  involved shows the higher consistency. It could be due to the approximate results between real and estimated values.

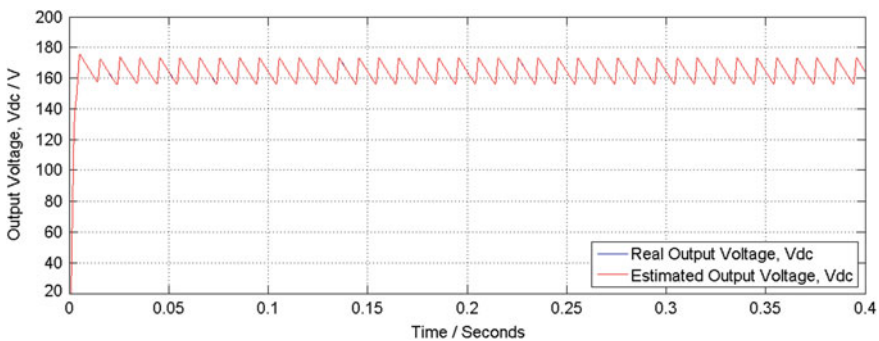


**Fig. 8** Graph of real and estimated value of output voltage,  $V_{dc}$

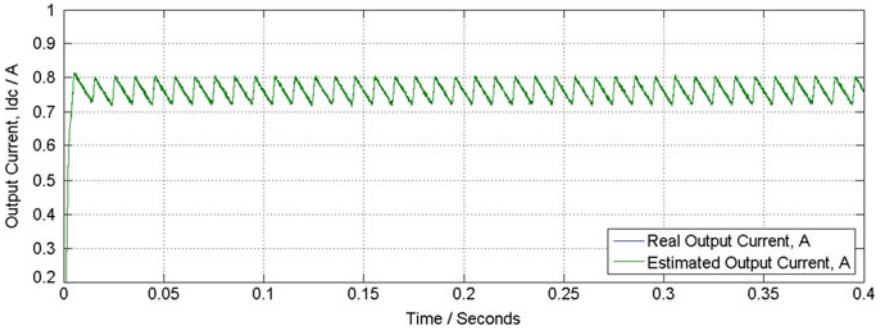


Fig. 9 Graph of real and estimated value of output current,  $I_{dc}$

Besides, the Figs. 10 and 11 shows the results with higher process noise which is 0.05. The value of real output voltage is 177.92 V while the average value of the estimated are 178.356 V shows in Fig. 10. Next, Fig. 11 shows the value of real output

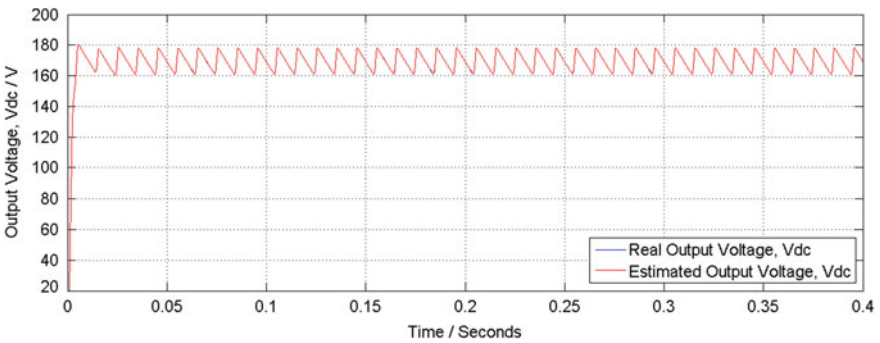


Fig. 10 Graph of real and estimated value of output voltage,  $V_{dc}$

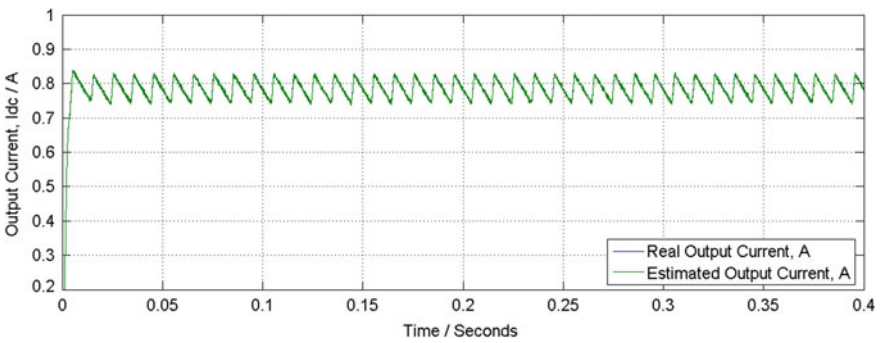


Fig. 11 Graph of real and estimated value of output current,  $I_{dc}$



**Table 2** Output voltage and output current noise

Parameter	Real value (average)	Calculated value (average)	Estimation value (average)	Accuracy (%)
<i>Process Noise = Real</i>				
V <sub>dc</sub>	173.202	173.2104	173.203	99.99
I <sub>dc</sub>	0.8019	0.8019	0.802	99.99
<i>Process Noise = 0.05</i>				
V <sub>dc</sub>	177.92	178.20	178.356	99.75
I <sub>dc</sub>	0.825	0.8237	0.8273	99.72

current with 0.825 A and the average value of estimated are 0.8273 A respectively. The greater noise in the single-phase diode bridge rectifier gives the huge difference to the real and estimated V<sub>dc</sub> and I<sub>dc</sub>.

Table 2 shows the output voltage and output current value with noise. The process noise of real and 0.05 was considered to the system parameters in MATLAB Simulink model. The process noise of real shows the higher accuracy to the output voltage and output current in the system with 99.99% and 99.99% respectively. Therefore, smaller value of noise gives higher estimation accuracy to the system. The table shows the accuracy of output voltage and output current in the system with process noise of 0.05 which is 99.75% and 99.72% respectively. Hence, the increasing noise in the system make the accuracy in the system decrease is proven.

According to the values of V<sub>dc</sub> and I<sub>dc</sub> in the table above, the value of noise affected the accuracy of the estimation in the single-phase diode bridge rectifier. The performance degrades when the value of process noise increased. Comparison accuracy of V<sub>dc</sub> between Measurement-based method and Kalman filter also has been done. The Measurement-based method is the approach that verified by measurement. In [4], the author recommended that parameter of R, L and C can be obtained once a current under different of voltage is measured. The results presented in Table 2 shows that the Kalman filter give a higher accuracy compared to the Measurement-based method. Kalman filter is a better method for an estimation process compared to the other mentioned method. The real and calculated value of R and C parameters presented in Table 3. The value of R was directly get from Eq. (16). For capacitance, the value of X<sub>c</sub> must be calculated first by using Eq. (17). Then, the value C obtained from the Eq. (18). The value of calculated C is far away from the actual value. This could be due to difference between components were employed in the simulation since this load are made by various manufacturers. Remark that the value used in

**Table 3** Comparison output voltage value for different method

	Measurement-based method	Accuracy (%)	Kalman filter-based method	Accuracy (%)
V <sub>dc</sub> (V)	160.600	92.72	173.203	99.99

**Table 4** Parameters value

	Real value	Calculated value
R ( $\Omega$ )	216	215.98
C (F)	0.00037	0.00011

this paper is the average value. Thus, the Table 4 shows that calculated value are vary from the actual value.

For resistance,

$$V = IR \quad (16)$$

While for capacitance,

$$V_c = X_c I_c \quad (17)$$

$$X_c = \frac{1}{2\pi f C} \quad (18)$$

## 5 Conclusion

It was shown that the estimation of parameter R and C still can be done by using only output voltage,  $V_{dc}$  and output current,  $I_{dc}$ . The diverse of accuracy between Kalman filter method and Measurement-based method has been investigated in this research. As it is one of the optimal methods nowadays, thus, Kalman filter can be used for estimation for real- time line parameter estimator.

**Acknowledgements** The authors would like to thank MOE to support this research under grant RDU160145, FRGS/1/2016/TK04/UMP/02/17. Thanks to UMP for the assistance and support on this research.

## References

1. Czarnecki LS, Staroszczyk Z (1996) On-line measurement of equivalent parameters for harmonic frequencies of a power distribution system and load. IEEE Trans Instrum Meas 45(2):467–472
2. Marino P, Mungiguerra V, Russo F, Vasca F (1996) Parameter and state estimation for induction motors via interlaced least squares algorithm and Kalman filter. In: PESC record. 27th annual IEEE power electronics specialists conference, vol 2, pp 1235–1241
3. Souza RRN, Coutinho DF, Dos Reis FS, Ribeiro FS (2008) Estimation of parameterized non-linear loads: a time-domain approach. In: 2008 IEEE power electronics specialists conference, pp 4617–4623

4. Yong J, Chen L, Chen S (2010) Modeling of home appliances for power distribution system harmonic analysis. *IEEE Trans Power Deliv* 25(4):3147–3155
5. Mesas JJ, Sainz L, Molina J (2011) Parameter estimation procedure for models of single-phase uncontrolled rectifiers. *IEEE Trans Power Deliv* 26(3):1911–1919
6. Wang Z, Yong J (2013) Investigation on the capacitive characteristics of single-phase diode-bridge converter based loads. In: 2013 IEEE PES Asia-Pacific power and energy engineering conference (APPEEC), pp 1–4
7. Gautam AK, Majumdar S (2018) Parameter estimation of diode circuit using extended Kalman filter. *Int J Electr Comput Energ Electron Commun Eng* 12:604–610
8. Yong J, Chen L, Nassif AB, Xu W (2010) A frequency-domain harmonic model for compact fluorescent lamps. *IEEE Trans Power Deliv* 25(2):1182–1189
9. Gautam AK, Majumdar S (2018) Parameter estimation of RC circuits using Extended Kalman Filter. *Int J Adv Manag Technol Eng Sci* 8(1):83–91
10. Bansal R, Majumdar S (2017) Implementation of extended Kalman filter on stochastic model of LPF. *Int J Adv Manag Technol Eng Sci* 7(12):120–130
11. Yim S, Seok J, Lee J (2012) State estimation of the nonlinear suspension system based on nonlinear Kalman filter. In: 2012 12th international conference on control, automation and systems, pp 720–725
12. Kalman RE (1960) A new approach to linear Filtering and prediction problems. *J Basic Eng* 82(1):35–45
13. Son Y, Ha J (2017) Discontinuous grid current control of motor drive system with single-phase diode rectifier and small DC-link capacitor. *IEEE Trans Power Electron* 32(2):1324–1334
14. Son Y, Ha J (2015) Direct power control of a three-phase inverter for grid input current shaping of a single-phase diode rectifier with a small DC-link capacitor. *IEEE Trans Power Electron* 30(7):3794–3803
15. Gupta S, Nimesh V, John V (2016) Diode bridge rectifier with improved power quality using capacitive network. In: 2016 IEEE international conference on power electronics, drives and energy systems (PEDES), pp 1–6
16. Wang P, Liu C, Guo L (2013) Modeling and simulation of full-bridge series resonant converter based on generalized state space averaging BT. In: Proceedings of the 2nd international conference on computer science and electronics engineering

# A Study on Residual Current Device Nuisance Tripping Due to Grounding Resistance Value



Izzatul Liyana, Farhan Bin Hanaffi and Mohd Hendra Bin Hairi

**Abstract** Protection against leakage current is vital in an electrical system to protect humans and equipment from electric shocks and fire risk. Residual Current Device (RCD) is a protective device used for protection against small leakage current. This device is designed to disconnect the circuit whenever a fault is occurred, by measuring the different value of current between phase and neutral. However, inappropriate tripping also known as nuisance tripping is influenced by the improper grounding system, high frequency from power supplied and presence of harmonics. The aim of this paper is to investigate the residual operating current and operating time of RCD behavior towards the poor grounding resistance value. Besides that, the effect of different type of load were considered in the experiments. The sensitivity of RCD sample used in this research is 30 mA type-AC. RCD operating current and voltage are evaluated and compared with the requirement by international standard. The results show grounding system with high resistance value affects the operating time of RCD, thus lead to nuisance tripping.

**Keywords** Leakage current · Residual current · Grounding resistance

## 1 Introduction

RCDs are designed to disconnect the circuit when the residual current beyond a preset limit due to a circuit failure for safety purposes. However, these devices are usually prone to nuisance tripping that occur due to non-fault conditions such as extraneous earth leakage path, switching transients and supply voltage spikes. Standards IEC 61008 [1] and MS 60755 [2] state that RCDs shall operate if the residual current equal to or greater than  $I_{\Delta n}$ , where  $I_{\Delta n}$  is the rated residual operating current. Additionally, these standards state that maximum values of break time for type-AC of RCD in the event of alternating earth fault current equal to  $I_{\Delta n}$  is 300 ms. Meanwhile, in Suruhanjaya Tenaga: Guidelines for Electrical Wiring in Residential Building [3], the operating time should be less than 200 ms. In the previous research, there are

---

I. Liyana · F. Bin Hanaffi (✉) · M. H. Bin Hairi  
Universiti Teknikal Malaysia Melaka, Hang Tuah Jaya, 76100 Durian Tunggal, Melaka, Malaysia  
e-mail: [farhan@utem.edu.my](mailto:farhan@utem.edu.my)

© Springer Nature Singapore Pte Ltd. 2020  
A. N. Kasruddin Nasir et al. (eds.), *InECCE2019*, Lecture Notes in Electrical Engineering 632, [https://doi.org/10.1007/978-981-15-2317-5\\_60](https://doi.org/10.1007/978-981-15-2317-5_60)

1717

numerous analysis regarding to the nuisance tripping that occurs due to many factors. The nuisance tripping mostly caused by these three factors which are poor grounding resistance value, high frequency current and harmonics participation.

Different experiments have been conducted in order to study the behavior of RCD towards poor grounding system, high frequency and harmonics present which high-order harmonics, low-order harmonics and non-sinusoidal waveform, also the effect of loads. From researches [4–8] nuisance tripping is occurred caused by the high frequency generated from the power supply. The high frequency affects the sensitivity of RCD, where it was found that the higher the frequency, the higher the level of RCD sensitivity, which also means the RCD becomes insensitive towards high frequency. Besides that, findings in [4–9] state that the presence of harmonics affect the sensitivity of RCD. The RCD becomes less sensitive if there is a presence of high amplitude of high order harmonics, while more sensitive with low amplitude of high order harmonic. The presence of low order harmonic such as 3rd order with angle also increase the RCD sensitivity. Moreover, nuisance tripping of RCD has been traced to high level of residual currents through electronic loads present in the power supply system [10]. The connections and disconnections of loads produced high frequency voltage transients in RCD tripping that will make RCD insensitive [8, 11]. Thus, the loads influence the RCD operation which caused the nuisance tripping. In addition, poor grounding which has high grounding resistance values influence the operation of RCD, especially operating time. The higher the grounding resistance value, the longer the time for RCD to operate [12, 13]. Hence, leads to nuisance tripping. Overall, these factors mentioned above will trigger the RCD to nuisance tripping. However, there is not much stress on nuisance tripping regarding the improper grounding system effect. Albeit, this effect gives the same disastrous damage towards equipment as well to person touched the live part when earth fault occurred. Therefore, in this paper different grounding resistance value and type of load are considered to investigate its effect operating current and operating time of RCD.

## 2 Experiment Arrangement

Figure 1 shows the block diagram of the equipment setup for this research from applying the standard voltage AC source to the system being earthed. The main equipment involved in this study are type-AC of RCD with sensitivity of 30 mA, RCD Tester (KYORITSU Model 5402D), current probe (Tektronix A622), oscilloscope, synchronous motor, induction motor, and power resistor to the ground.

Power resistors of 10 W with different values of resistance are chosen in order to investigate the behavior of RCD. These power resistors represent as the actual grounding resistance value. The values of resistance used in this research are from 1 to 3.5 k $\Omega$  with different value of 100  $\Omega$ . Besides, the residual operating current and operating time are measured without the presence of the power resistor as the reference value of this research. Then, the unbalanced current is applied for 2000 ms

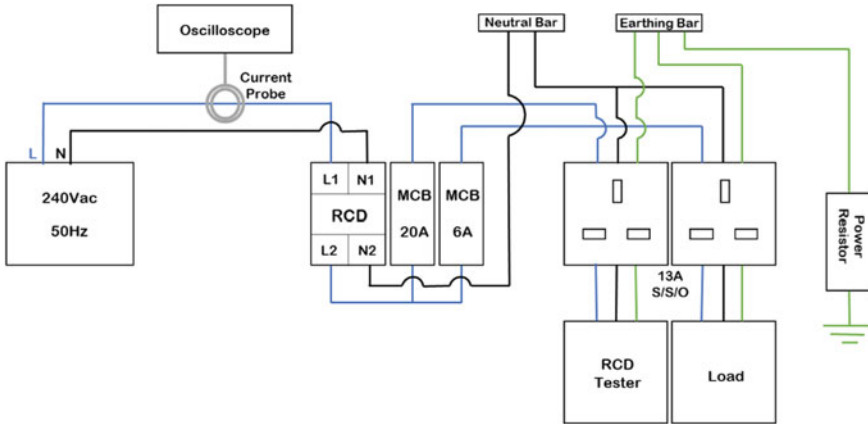


Fig. 1 Experiment set up

maximum by using the RCD Tester trip test. The sample of RCD’s residual operating current shall equal to the rated residual operating current,  $I_{\Delta n}$  which is 30 mA, while the operating time shall not more than 200 ms.

### 3 RCD Performance Due to Grounding Resistance Value

#### 3.1 Effect of Grounding Resistance

Figure 2 shows residual operating current with different values of grounding resistance. The reference value of the residual operating current of the RCD sample measured is approximately equal to 30 mA which is 29 mA with the grounding resistance measured of  $0.07 \Omega$ , which is nearly  $0 \Omega$ . Next, for the presence of power resistor, the sample of RCD’s residual operating current measured for  $1 \text{ k}\Omega$  till  $3.4 \text{ k}\Omega$  of grounding resistances are also about 30 mA. However, for grounding resistance value of  $3.5 \text{ k}\Omega$  and above, the RCD sample does not trip for maximum of 2000 ms applied unbalanced current. The highest value measured for operating current is 30 mA at grounding resistance value from  $2.7 \text{ k}\Omega$  to  $3 \text{ k}\Omega$ ,  $3.3 \text{ k}\Omega$  and  $3.4 \text{ k}\Omega$ , while the lowest operating current measured is 28.2 mA which grounding resistance value of  $1.9 \text{ k}\Omega$ . The data recorded above prove that grounding resistance below than  $3.4 \text{ k}\Omega$  does not affect the operating current of the RCD sample as the value measured is almost the same which is approximately equal to 30 mA.

RCDs shall not operate if the r.m.s value of the earth fault (residual) current is equal to or less than  $0.5I_{\Delta n}$  and shall operate if the residual current is equal to or larger than  $I_{\Delta n}$ , where  $I_{\Delta n}$  is the rated residual operating current. For this research,  $I_{\Delta n}$  of the sample of RCD type-AC used is 30 mA. The residual operating current of

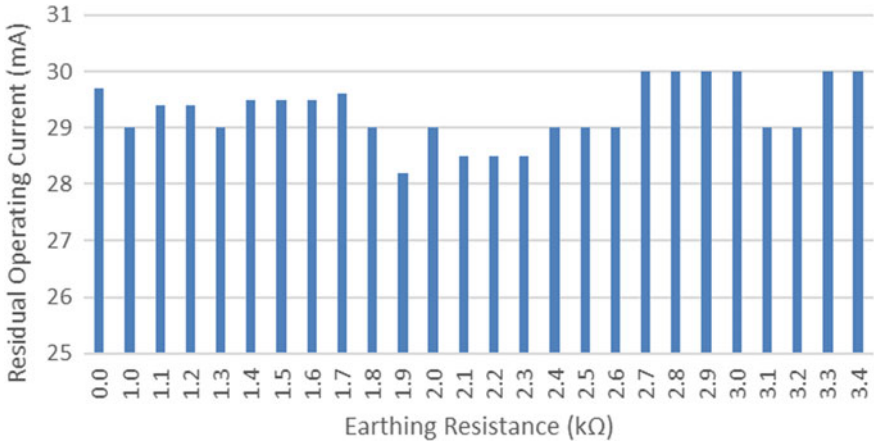


Fig. 2 Residual operating current (mA) of RCD type-AC with different values of grounding resistance (kΩ)

RCD sample is considered passed for grounding resistance below than 3.4 kΩ since the results obtained is higher than  $0.5I_{\Delta n}$ . However, the grounding resistance above 3.5 kΩ is failed the requirement because RCD sample does not operate for applied earth fault current of 30 mA.

Figure 3 shows the different grounding resistance value against the operating time of RCD sample. The reference value for  $0.07 \Omega$  of grounding resistance gave the operating time of RCD sample measured approximately 30 ms for  $0^\circ$  (negative

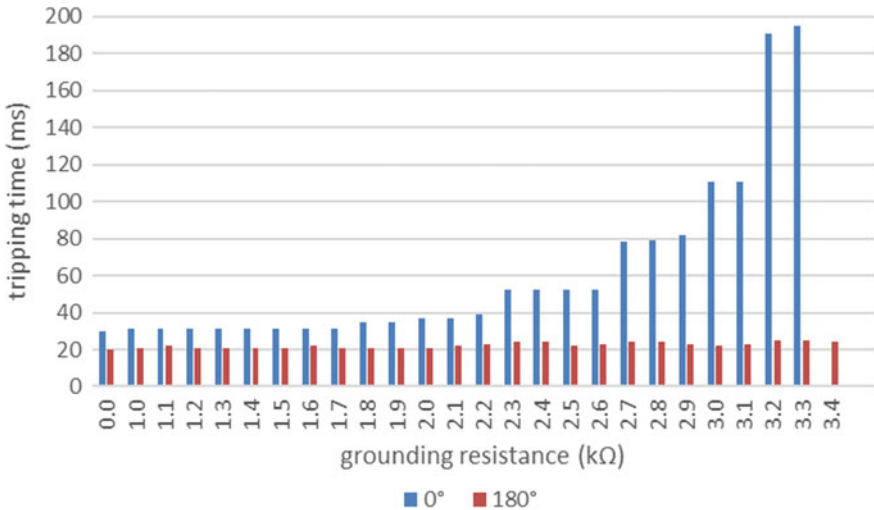


Fig. 3 Operating time (ms) of RCD type-AC with different grounding resistance value (kΩ)

waveform) and 20 ms for 180° (positive waveform). At phase angle of 0°, the value of operating time is increased as the value of grounding resistance increases. The fastest operating time of RCD sample is 30 ms which at the reference value and the slowest operating time is 195 ms which at the value of grounding resistance of 3.3 kΩ. The sample of RCD does not trip for maximum of 2000 ms applied unbalanced current with grounding resistance value of 3.4 kΩ and above at 0° phase angle. Meanwhile, the operating time of the RCD sample measured for grounding resistance values from 1 to 3.4 kΩ at 180° phase angle are almost the same as the reference value which is 20 ms. Then again, at the value of grounding resistance of 3.5 kΩ and above, the sample of RCD does not trip for 2000 ms of maximum applied unbalanced current at phase angle of 180°.

### 3.2 Effect of Load and Grounding Resistance Value

In this section, three different loads which are resistive load bank, induction motor and synchronous motor are used to investigate effect of loads towards the operating time of RCD. The grounding resistance for this system is varied from 1 to 3.5 kΩ. The reference value which is pure grounding resistance, without the presence of the power resistor is measured first as the unbalanced current is applied for 2000 ms maximum by using the RCD Tester trip test to the system. Figure 4 shows the results obtained for operating time of RCD sample for different loads as the grounding resistance value increased. The reference value for all the loads and without load show nearly same operating time measured which is within 30 and 31 ms. As the resistance of

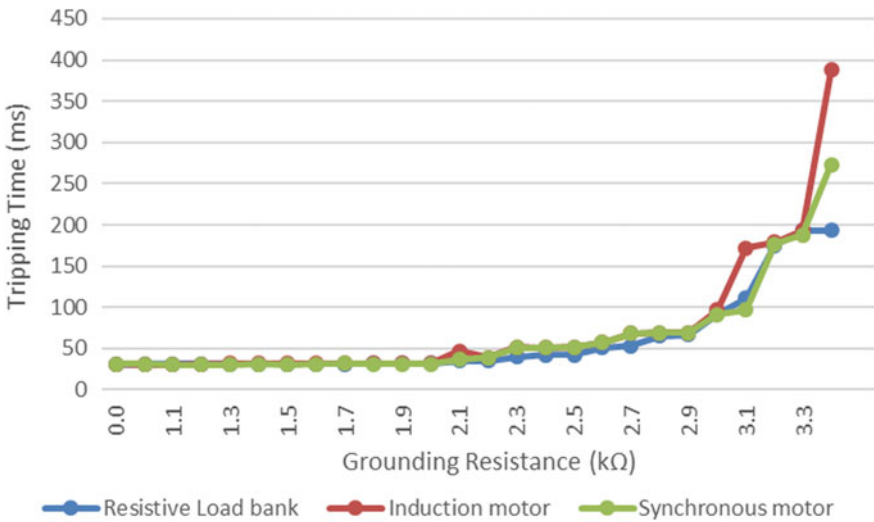


Fig. 4 Operating time (ms) of RCD type-AC for different load at 0° phase angle



grounding increased, the operating time of RCD sample for all loads and without load are increase. Besides, the pattern shows that the induction motor load increases the RCD sample operating time higher than other loads, which at 388 ms for grounding resistance value of 3.4 k $\Omega$ . This value is already exceeding the time requirement to operates an RCD as stated in Suruhanjaya Tenaga: Guidelines for Electrical Wiring in Residential Building [3] and BS EN 61008-1:2012 [1] which are 200 ms and 300 ms respectively. The results show equipment that contain resistive and inductive loads took longest time for RCD to trigger the coil to break the circuit when earth fault occurs than equipment that only comprise with resistive load. The type of load depends on how the wave for the voltage and the wave for current line-up.

## 4 Conclusion

In electrical system, value of grounding resistance is one of the vital element needs to be considered to ensure the proper grounding system installation. In this paper, different value of grounding resistance from 1 to 3.5 k $\Omega$  have been tested to analysis the characteristic of RCD in terms of residual operating current and operating time. From the results obtained, the grounding resistance does not affect the residual operating current of the RCD sample as the residual operating current measured for all value of grounding resistance tested show approximately equal to 30 mA. The RCD is required to operate when residual current is higher than 50% of rated residual current. As the grounding resistance is increased, the RCD sample is still operated as per required. So, the RCD sample is considered passed in terms of its residual operating current. In the meantime, the RCD supposedly operates below than 200 ms when residual current flow through it. The results show that the operation of RCD sample delayed as the value of grounding resistance increased. Besides, it does not operate for value of grounding resistance above than 3.4 k $\Omega$  when residual current is applied at maximum of 2000 ms. Thus, this conclude that if the grounding resistance value is increase, the RCD take some time to energize the trip coil after receiving the signal and it will not trip for the grounding resistance value above than 3.4 k $\Omega$ . In addition, RCD sample took the longer time to operate for inductive loads than resistive loads. The operating time of RCD sample measured for inductive loads such induction motor and synchronous motor reached the unacceptable value as it is operated more than 200 ms when the grounding resistance value passed 3.3 k $\Omega$ . Also, the results obtained show the RCD sample does not trip for grounding resistance value above than 3.5 k $\Omega$  for applied residual current maximum of 2000 ms. Hence, the high-power consumption loads take more time for RCD to trigger the coil when residual current is presented and the value of grounding resistance above than 3.5 k $\Omega$  caused the RCD to not function. Therefore, it important to maintain the grounding connection and grounding resistance value to make safety environment for electrical system.

## References

1. Residual current operated circuit-breakers without integral over-current protection for household and similar users (RCCBs) Part 1: General rules (IEC 61008-1:2010, modified), in BS EN 61008-1:2012+A11:2015. BSI Standards Limited, 2016
2. General requirements for residual current operated protective devices, in MS 60755:2011. Department of Standards Malaysia, 2011
3. Guidelines for electrical wiring in residential buildings, 2008th edn. Suruhanjaya Tenaga, 2008
4. Freschi F (2012) High-frequency behavior of residual current devices. *IEEE Trans Power Deliv* 27(3):1629–1635
5. Lee TM, Chan TW (1995) The effects of harmonics on the operational characteristics of residual-current circuit breakers. In: *Proceedings 1995 international conference energy management power delivery, EMPD '95*, vol 2(95)
6. Czapp S (2009) The effect of earth fault current harmonics on tripping of residual current devices. *Elektron ir Elektrotehnika* 3:85–88
7. Luo X, Du Y, Wang XH, Chen ML (2011) Tripping characteristics of residual current devices under nonsinusoidal currents. *IEEE Trans Ind Appl* 47(3):1515–1521
8. Porta CR, Escriva-Escriva G, Carcel-Carrasco F-J (2014) Nuisance tripping of residual current circuit breakers: a practical case. *Electr Power Syst Res* 106:180–187
9. Xiang Y, Cuk V, Cobben JFG (2011) Impact of residual harmonic current on operation of residual current devices. In: *2011 10th international conference environment electrical engineering IEEEIC.EU 2011*
10. Liew AC (1990) Nuisance trippings of residual current circuit breakers or ground fault protectors of power sources connected to computer and electronic loads. *Electr Power Syst Res* 20(1):23–30
11. Escriva-Escriva G, Porta CR, de Jong ECW (2016) Nuisance tripping of residual current circuit breakers in circuits supplying electronic loads. *Electr Power Syst Res* 131:139–146
12. Abdullah MZ, Ariffin R (2013) Power quality analysis of residual current device [RCD] nuisance tripping at commercial buildings. *ISIEA 2013—2013 IEEE symposium industrial electronics and applications*, pp 122–125
13. Suhailee MH (2017) Effect of grounding resistance and harmonics on residual current device (RCD). Bachelor thesis, Universiti Teknikal Malaysia Melaka

# DC-Link Protection for Grid-Connected Photovoltaic System: A Review



Wan Nur Huda Aqilah Alias, Muhamad Zahim Sujod  
and Nor Azwan Mohamed Kamari

**Abstract** As the economic growth and population increase, the demand for energy supply has also increased. The disadvantages that power generation based on non-renewable energy sources bring to the environment has stimulate the idea of generating clean and sustainable power in a huge amount from renewable energy sources like solar and wind energies. In recent years, photovoltaic (PV) systems are mostly used due to its light and easy-installable characteristics. It has two approaches which are stand-alone PV system and grid-connected PV system (GCPV). Although it is said to be the most promising renewable energy, it could not avoid disturbance. In GCPV, faults could occur on the grid side, leading to overshoot voltage in DC-link and overshoot grid current. These situations could stress electrical components and decrease power quality of the system. Therefore, many protection schemes have been introduced to overcome this matter. A brief discussion on the growth of GCPV technology together with the impacts of grid faults on it were presented in this paper. Then, several conventional protection schemes implemented in GCPV were also reviewed. In the end, a new protection scheme namely zero state protection scheme that has the same function to limit the overshoot DC-link voltage was proposed.

**Keywords** Dc-link protection · GCPV system · Overshoot DC-link voltage

## 1 Introduction

Energy crisis in 1970s where the world's major industrial countries like the U.S suffered from fossil fuel shortage has become a kick-start to develop a renewable energy technology like PV power system. Since that, the amount of installed PV system has increased rapidly [1]. For instance, the amount of installed PV plants from the year 2000 has increased from 1.3 GW to about 509.3 GW in 2018 [2]. It is forecasted that the installed PV system will increase up to 580 GW in 2023 [3,

---

W. N. H. A. Alias · M. Z. Sujod (✉)  
Fakulti Kejuruteraan Elektrik & Elektronik, Universiti Malaysia Pahang, Pekan, Malaysia  
e-mail: [zahim@ump.edu.my](mailto:zahim@ump.edu.my)

N. A. M. Kamari  
Jabatan Kejuruteraan Elektrik & Elektronik, Universiti Kebangsaan Malaysia, Bangi, Malaysia

© Springer Nature Singapore Pte Ltd. 2020

A. N. Kasruddin Nasir et al. (eds.), *InECCE2019*, Lecture Notes in Electrical Engineering 632, [https://doi.org/10.1007/978-981-15-2317-5\\_61](https://doi.org/10.1007/978-981-15-2317-5_61)

4]. Stability and reliability become important issues for the large-scale PV system, especially when linked to the utility grid.

Similar to any other electric power generation systems, GCPV is vulnerable to fault too. Fault could happen in the grid-side of GCPV thus causing voltage sags which will affect the whole system. To address this issue, various techniques have been proposed worldwide. GCPV system needs to be maintained, monitored and improved from time to time to ensure an optimal system performance and for more reliability.

In this paper, the development of GCPV technology will be expressed and the effects of grid faults on GCPV were discussed. Also, several conventional protection schemes implemented in GCPV will be reviewed. It will focus on the protection schemes in DC-link of converter system. Then, it proposed a new protection scheme which reduce overshoot DC-link voltage by controlling zero state switching of neutral point clamp (NPC) converter.

## 2 Photovoltaic (PV) System

PV system is categorized into two; stand-alone and GCPV. Though, this study only focusses on GCPV. There are two topologies that have been frequently used in this system which are single-stage and two-stage GCPV. In single-stage topology, it composes of only DC-AC converter while for two-stage, it has DC-DC and DC-AC converters. Recently, most of the installed grid-connected systems are single-stage structured. This is because it has a relatively high efficiency and reliability. Also, it requires low cost and small in size compared to two-stage grid-connected PV system [5]. However, two-stage GCPV produced less total harmonic distortion and has a better DC voltage stability [6].

## 3 Impacts of Grid Faults on Grid-Connected PV System

Generally, grid fault is categorized into two different types which are symmetrical fault and asymmetrical fault. Symmetrical fault or commonly known as three-phase balanced fault is a fault where all of three conductors on the grid are short-circuited. Although it is the least occurrence type of fault, the impact it brings to the grid is the most severe compared to other faults [7]. On the other hand, asymmetrical fault consists of, double line-to-ground fault, single line-to-ground fault and line-to-line fault.

In the event of fault, voltage sags will occur. Voltage sags or dip is a situation where the rms voltage drops for a duration from half cycle to one minute [8]. The voltage sags owing to grid fault is classified into seven types. One type is from symmetrical fault while the other six are from asymmetrical fault. It will cause excessive DC-link voltage and excessive grid current to occur. In [9, 10], authors

have discussed about the effects of grid voltage sags on two-stage grid-connected PV system. During symmetrical voltage sags, output power of boost converter will exceed inverter instantaneous output power, then lead to power imbalance and the excessive power will be deposited in DC-link capacitor. Accordingly, the voltage in DC-link rises. Then, the instantaneous decrease in PCC voltage leads to the overshoot in grid-side current. Moreover, asymmetrical grid voltage sags also cause the aforementioned issues. As an example, the impacts of two different types of grid fault on grid-connected PV system with 50% voltage drop are presented in Fig. 1.

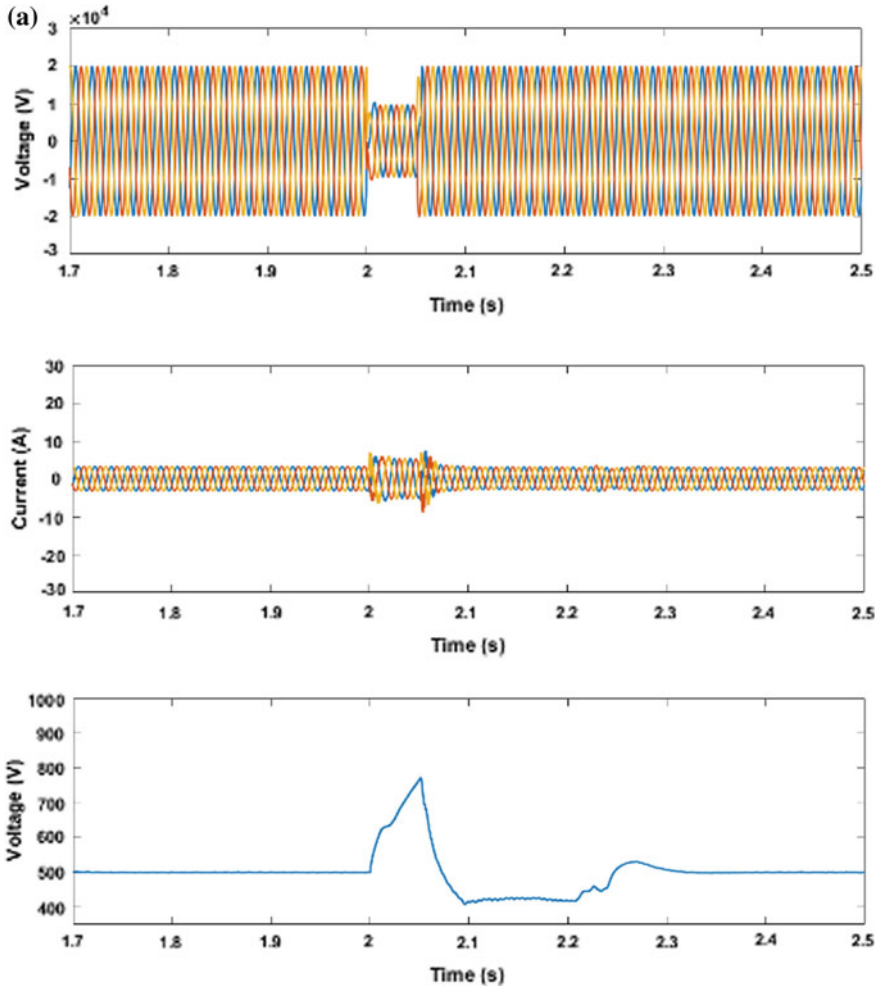


**Fig. 1** Electrical behavior of grid voltage, grid current and DC-link voltage during **a** Symmetrical fault **b** Asymmetrical fault (SLG) (at 50% voltage drop)

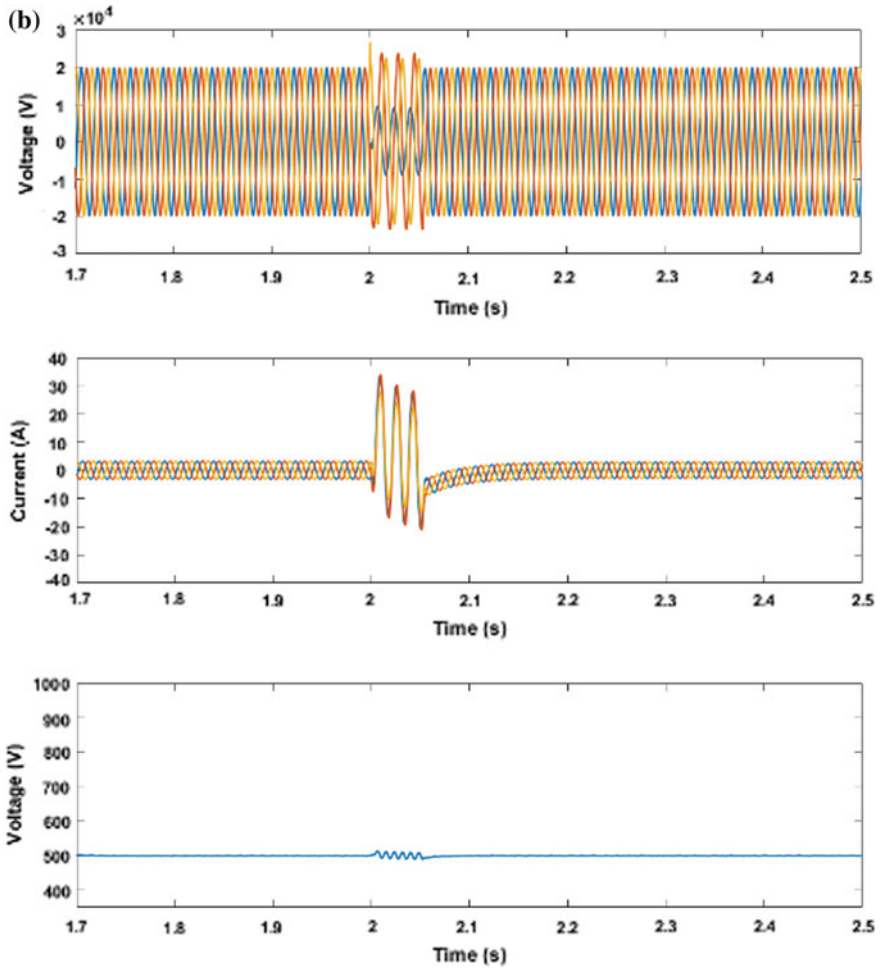


Fig. 1 (continued)

### 4 Conventional Protection Schemes of Grid-Connected PV System

There are numerous of attempts have been proposed in technical literature to lessen overshoot DC-link voltage and uprush of grid-side current matters for both GCPV topologies. During voltage sags, the inverter switch current increases dramatically and cause overcurrent on grid side. Therefore, for two-stage grid-connected PV system, the use of a superconductive fault current limiter which is linked in series with circuit breaker has been proposed in [8]. Unfortunately, it is unable to help the system to recover its output power speedily after the voltage sags. Hence, the author in [11] has overcome this matter by adding an over-current control logic to the

inverter control as shown in Fig. 2. Next, a vector current controller with feed forward (VCCF) (Fig. 3) of negative-sequence components of PCC voltage is used in [12] to alleviate the risk of overcurrent by eliminating negative-sequence components of grid current.

As mentioned earlier, grid faults will also cause overvoltage on DC-link due to power imbalance. Badran et al. [13] and Dehghani Tafti et al. [14] stated that it could cause semiconductor devices to overheat and damage. Owing to this matter, Badran et al. [13] has used MPPT controlling technique to avoid power imbalance by using PSCAD software. In this method, a new operation mode namely fault mode

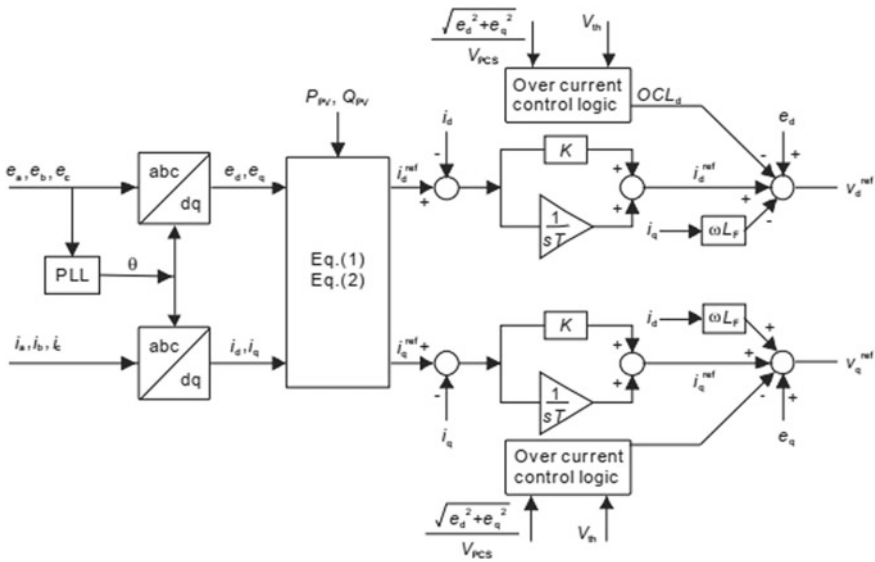


Fig. 2 Block diagram of modified inverter control [11]

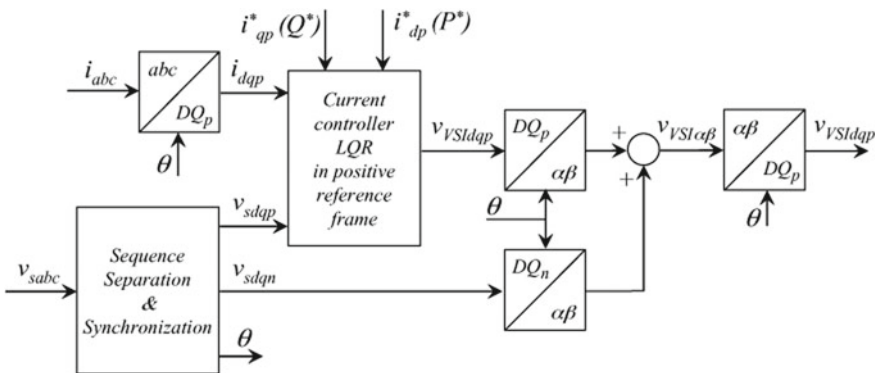


Fig. 3 Control block diagram of VCCF [12]

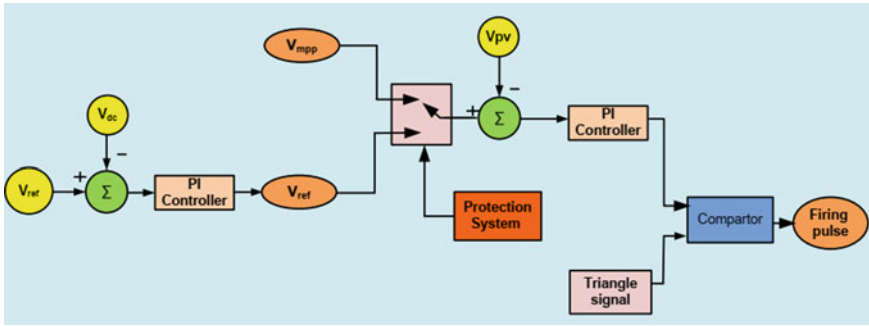


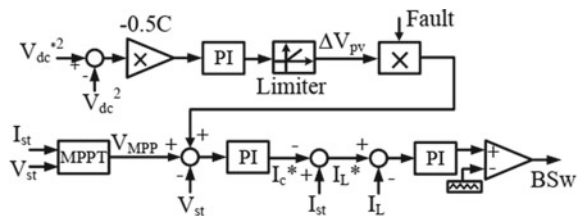
Fig. 4 Block diagram of MPPT controlling technique [13]

was applied to DC-link control system as presented in Fig. 4. When fault occur, the protection system will switch the control system from normal to fault mode, making the PV system to generate active power equivalence to active power that is injected to the grid by using PI controller. Hence, the power between DC-link is kept balanced and DC-link voltage does not increase. The parameters of PI controller on fault mode were defined by using “try and error” method. Though, the problem of latch-up and wind-up will arise during the changing of control system from normal mode to fault mode.

Next, another solution has been proposed in [14] by implementing DC-link control strategy into DC-DC boost converter (Fig. 5). It reduces the overshoot of DC-link voltage by decreasing the amount of extracted PV power to inverter’s output. During grid fault, the reference voltage of PV string is changed from maximum power point voltage to a new value of voltage point with reduced power by mathematical means. All the simulations of this proposed method were done using Simulink and MATLAB software.

Moreover, several methods which can overcome both overvoltage and overcurrent problems have been presented in technical review. For instance, in [15, 16] a super capacitor is installed at the DC-link bus of single-stage and two-stage GCPV respectively to suppress the surge in DC-link voltage and overshoot of grid current. Super capacitor is able to absorb the excessive or recoup the output power deficiency in the event of fault. However, the system cost will increase (Fig. 6).

Fig. 5 DC/DC boost converter control structure during grid faults [14]





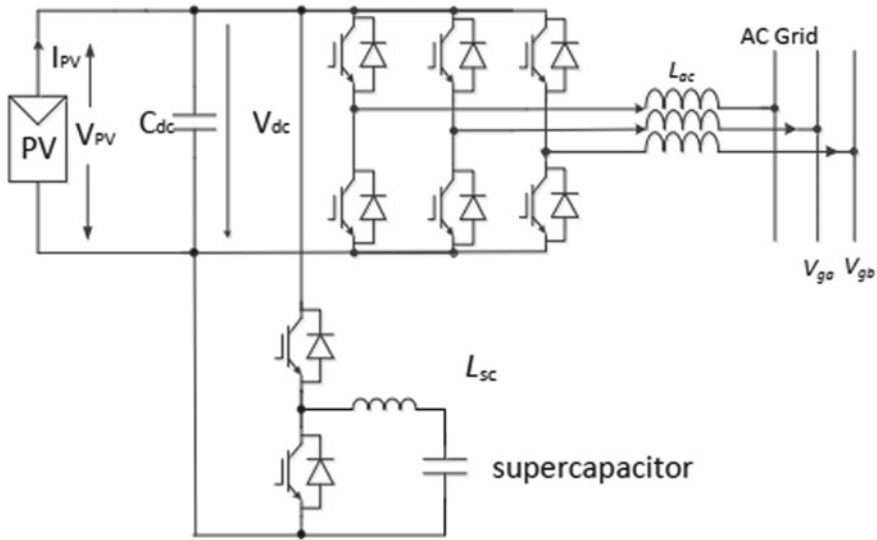


**Fig. 6** Topology of single-stage GCPV with super capacitor [15]

In an attempt to overcome the aforementioned matter, Xu et al. [9] introduced a new control strategy with similar function without the needs of any additional component. Figure 7 represents the block diagram of this proposed method which is implemented in two-stage T-type three-level photovoltaic inverter. A full feed forward of point common coupling (PCC) voltage is used to limit the increase of grid current eliminate its negative-sequence components under an unbalanced voltage sags by using MATLAB and Simulink software. Then, for overvoltage protection, a modified PV voltage reference generation method is adopted. It makes the PV panels to work at a point where power balance can be automatically achieved.

According to Saeedul et al. [17], under voltage could also happened in DC-link of PV system and cause the whole system to trip. Therefore, a new protection scheme which can overcome both over and under voltage issues is presented in this paper. This method utilized the control of DC-DC boost converter to address over voltage issue. It minimizes the rise in DC-link voltage based on the command signal of duty ratio that is modified depending on the value of grid voltage. If the value of grid voltage is below a threshold value, the reference duty ratio will become zero or reduces it suitably according to fault severity.

In contrast, every integral controllers of voltage source inverter will be reset at time where DC-link voltage is lower than a threshold value. Hence, the voltage is improved. Figure 8 depicts the block diagram of this method. This method is only applicable in two-stage grid-connected PV system as it needs to be implemented in DC-DC boost converter. In addition, Saeedul et al. [17] has also discussed the effectiveness of DC-chopper (Fig. 9) in preventing the voltage at DC-link from continually rising beyond a certain level. Up to now, DC chopper has been implemented broadly

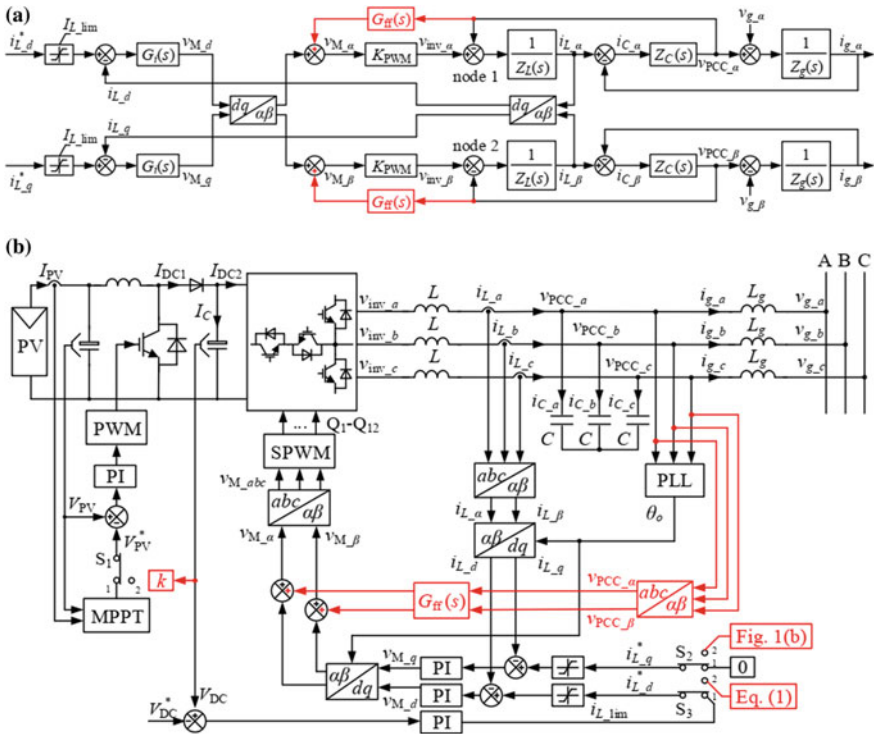


Fig. 7 Control schematic diagram of a) Complementation of PCC voltage full feed forward in hybrid frame for overcurrent protection b) DC-link voltage control strategy [9]

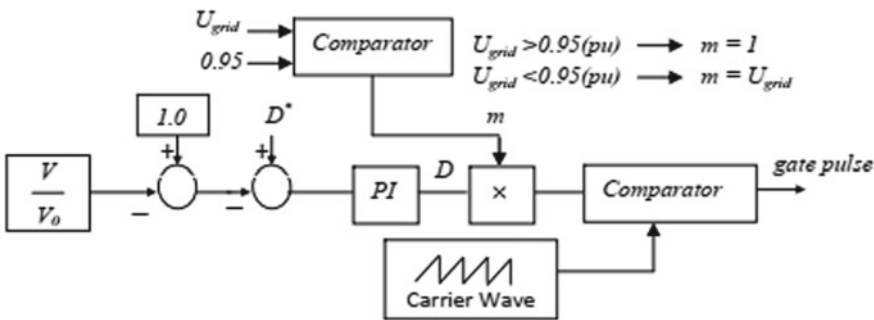


Fig. 8 Block diagram of DC-link protection by means of MPPT control [17]

in wind turbine application and HVDC grid [18, 19]. A chopper circuit which consists of braking resistor connected in series with IGBT is added to DC-link parallel with DC-link capacitor. The function of braking resistor is to absorb the surplus energy produced due to the imbalance power between grid and PV side that happened during

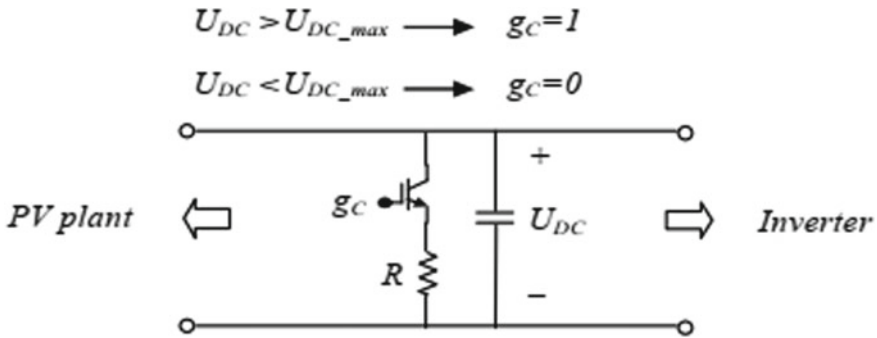


Fig. 9 Chopper circuit [17–19]

grid fault. When DC-link voltage is beyond the threshold value, the gate pulse of IGBT will be prompted and it will then activate the chopper circuit. For that reason, the chopper circuit limits the DC-link voltage from continually rising. Though, the system cost will increase as additional component is required too.

### 5 Proposed New Protection Scheme (Zero State Protection Scheme)

The effectiveness of this scheme in limiting DC-link voltage in wind turbine application has been proved in [20] where it is implemented to make the switching state of machine side converter (MSC) to be in zero state during grid fault. It also discussed about the use of DC chopper circuit in wind turbine application. Figure 11 shows the DC-link voltage in wind turbine application using zero protection scheme and DC chopper. Nowadays, DC chopper circuit were broadly installed in GCPV to overcome the risk of overshoot DC-link voltage. As mentioned before, the cost to implement this circuit is quite high as it requires extra component to limit the voltage. For that reason, a new protection scheme namely zero state protection scheme which has similar function as DC chopper is proposed in this paper as an alternative to DC chopper. The operation is simpler and does not account for any additional component. It limits the increase in DC-link voltage by forcing the phase current to flow through neutral link of NPC inverter during grid fault. As a result, DC capacitors will not be charged and DC-link voltage will not increase as no power imbalance occur. In order to make the current flows through neutral link, this inverter needs to be in zero switching state so that only inner IGBTs are turn on whilst the other are turn off as stated in Table 1. However, this scheme can only be applied in a multi-level converter with neutral point clamp. This is because, two-level converter does not has zero switching state. Also, according to the authors in [20], the current rating of the inner switching devices must be two times higher. Figure 10 shows the block diagram of zero protection scheme.

**Table 1** Switching state of 3-level NPC converter [16]

Switching states	Switching devices				Output phase voltage
	T <sub>x1</sub>	T <sub>x2</sub>	T <sub>x3</sub>	T <sub>x4</sub>	
Positive state (+)	1	1	0	0	$V_{dc}/2$
Zero state (0)	0	1	1	0	0
Negative state (-)	0	0	1	1	$-V_{dc}/2$

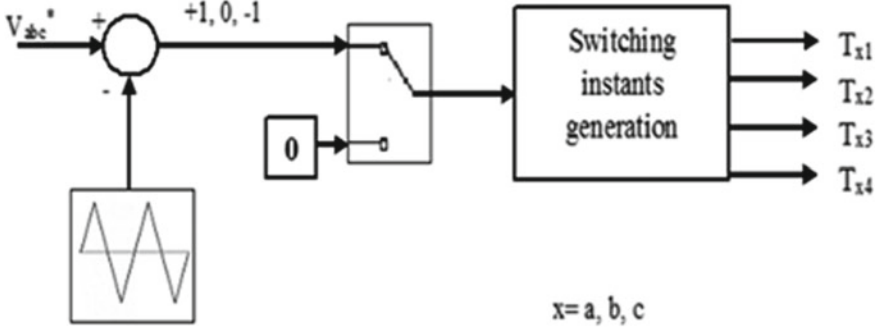


**Fig. 10** Block diagram of proposed scheme [20]

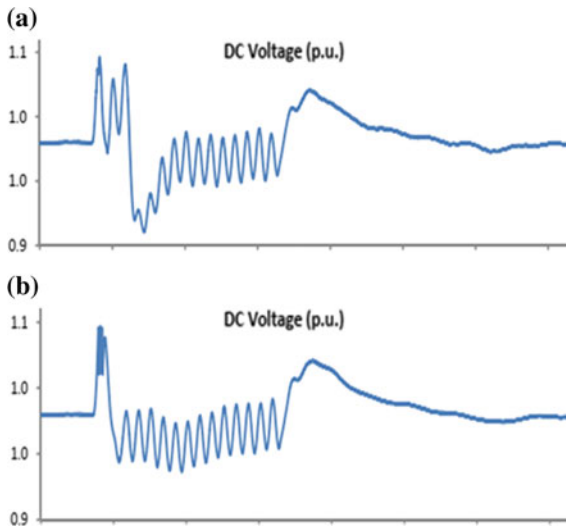


**Fig. 11** DC-link voltage in wind turbine application using **a** Zero protection scheme **b** DC chopper [20]

## 6 Conclusion

Protection scheme plays such a big role to maintain the effectiveness and stability of GCPV. Faults must be cleared as quickly as possible to prevent the system from major breakdown and affect its consumer. In this paper, several protection schemes in DC-link of GCPV have been reviewed. Each protection scheme has its own objective, constraint, advantages and disadvantages. A new protection scheme using zero state switching of NPC converter which has been implemented in wind turbine system was also reviewed. The new protection scheme which is low in cost with a simpler operation is proposed for GCPV and will be further studied and presented in the next paper.

**Acknowledgements** The research is funded by Universiti Malaysia Pahang (UMP) Research Grant Scheme (RDU 1803165). This acknowledgement also goes to Faculty of Electrical and Electronics Engineering for providing us with facilities to conduct this research.

## References

1. H. co. Editors (2018) Energy crisis (1970s). A&E Television Networks. [Online]. Available <https://www.history.com/topics/1970s/energy-crisis>. Accessed 26 June 2019
2. Wang T (2019) Cumulative installed solar PV capacity worldwide from 2000 to 2018 (in megawatts) [Online]. Available <https://www.statista.com/statistics/280220/global-cumulative-installed-solar-pv-capacity/>. Accessed 26 June 2019
3. Pesala B (2019) Solar photovoltaics: semiconductors, pp 1–10
4. Mohammadi P, Eskandari A, Milimonfared J, Moghani JS (2018) LVRT capability enhancement of single-phase grid connected PV array with coupled supercapacitor. In: 9th Annual international power electronics drives systems technologies conference PEDSTC 2018, vol 2018-January, pp 193–198
5. Sezen S, Aktas A, Ucar M, Ozdemir E (2014) A three-phase three-level NPC inverter based grid-connected photovoltaic system with active power filtering. In: 16th International power electronics motion control conference exposition, PEMC 2014, February 2014, pp 1331–1335
6. Zhu YL, Yao JG, Wu D (2011) Comparative study of two stages and single stage topologies for grid-tie photovoltaic generation by PSCAD/EMTDC. In: APAP 2011—proceedings 2011 international conference advance power system automation protection, vol 2, pp 1304–1309
7. Willy L, Badi A (2014) Unbalanced faults analysis in grid—connected PV system, pp 360–365
8. Taghizadeh M, Sadeh J, Kamyab E (2011) Protection of grid connected photovoltaic system during voltage sag. In: APAP 2011—proceedings 2011 international conference advance power systems automation protection, vol 3, pp 2030–2035
9. Xu C, Xuehua W, Xinbo R, Huanyu W, A low-voltage ride-through control strategy for two-stage T-Type three-level photovoltaic inverters limiting DC-link overvoltage and grid-side overcurrent keywords, pp 1–10
10. Hossain MK, Ali MH (2017) Fuzzy logic controlled power balancing for low voltage ride-through capability enhancement of large-scale grid-connected PV plants. In: 2017 IEEE Texas power energy conference TPEC 2017, pp 1–6
11. Iioka D, Saitoh H (2016) Enhancement of fault ride through capability using constant current control of photovoltaic inverters. In: IEEE PES innovative smart grid technologies conference European, pp 1083–1088

12. Alepuz S et al (2009) Control strategies based on symmetrical components for grid-connected converters under voltage dips, vol 56, no 6, pp 2162–2173
13. Badran EA, Abo-Al-Ez KM, Muelou H (2016) A proposed control strategy to improve the low voltage ride through capability of PV system with keeping the dc link voltage constant. *J Electr Eng* 16(2):144–155
14. Dehghani Tafti H, Maswood AI, Lim Z, Ooi GHP, Raj PH (2015) NPC photovoltaic grid-connected inverter with ride-through capability under grid faults. In: *Proceeding international conference power electronics drive systems*, vol 2015-Augus, no 1090, pp 518–523
15. Tian H, Gao F, Ma C (2012) Novel low voltage ride through strategy of single stage grid-tied photovoltaic inverter with supercapacitor coupled, pp 1188–1192
16. Worku MY, Abido MA (2015) Grid-connected PV array with supercapacitor energy storage system for fault ride through BT. In: *2015 IEEE international conference on industrial technology, ICIT 2015*, March 17, 2015–March 19, 2015, vol 2015-June, no June, pp 2901–2906
17. Saeedul Islam GM, Al-Durra A, Muyeen SM, Tamura J (2011) Low voltage ride through capability enhancement of grid connected large scale photovoltaic system. In: *IECON proceeding (Industrial electronics conference)*, pp 884–889
18. Debre P, Juneja R, Tutakane DR, Ramteke MR (2015) Overvoltage protection scheme for back to back converter of grid connected DFIG. *IECON 2015—41st annual conference IEEE industrial electronics society*, pp 3159–3162
19. Nentwig C, Haubrock J, Renner RH, Van Hertem D (2016) Application of DC choppers in HVDC grids. In: *2016 IEEE international energy conference ENERGYCON 2016*
20. Sujod MZ, Erlich I (2013) A new protection scheme for three-level NPC converter based DFIG using zero state control. In: *2013 4th IEEE/PES innovative smart grid technologies Europe ISGT Europe 2013*, pp 1–5

# An Improved Efficiency of Solar Photovoltaic System Applications by Using DC-DC Zeta Converter



A. S. Veerendra, M. R. Mohamed, M. H. Sulaiman and K. Peddakapu

**Abstract** This study investigates on how a DC-DC Zeta converter act as intermediate among SPV and VSI, in which it drags the maximum power from the solar photovoltaic (SPV) system and to drive a BLDC motor connected to a water pumping system application. Here INC-MPPT (Incremental Conductance Maximum Power Point Tracking) method is utilized smartly to control the zeta converter in order to drive brushless DC (BLDC) motor smoothly. Soft starting current prevents the influence of peak starting current on the BLDC motor windings. The fundamental frequency of Electronic computational from the BLDC motor is used to avoid the voltage source inverter losses. The proposed converter is also suitable to increase the voltage of DC link connected to the VSI. The major benefit of this configuration is designed and modelled in such a way that even under dynamic conditions, the performance of a solar photovoltaic application is not affected. The suggested system is developed by using MATLAB/Simulink software.

**Keywords** Electronic commutation · BLDC motor · INC-MPPT · Solar PV array · VSI and zeta converter

## 1 Introduction

With continuous effort for environmental protection, gradual diminishing of crude oils and everlasting energy from the sun have inspired researchers to apply an array generate electric power to solar photovoltaic (SPV) for different applications [1]. Among all applications, based on solar, the Water pumping system is now receiving considerable attention. To improve the efficiency of the solar based applications, regardless of operating conditions; the Maximum response is required for the solar [2–4]. Using different DC-DC converters does this MPPT action. However, SPV applications with zeta converter [5–8] is yet unexplored. To trigger the IGBT switch in zeta converter, an incremental conductance MPPT (INC-MPPT) algorithm method

---

A. S. Veerendra (✉) · M. R. Mohamed · M. H. Sulaiman · K. Peddakapu  
Sustainable Energy & Power Electronics Research (SuPER) Cluster, Universiti Malaysia Pahang,  
26600 Kuantan, Pahang, Malaysia

[2] is utilized to provide pulsating signals. The different arrangement of zeta converters have been studied, which these topologies are not appropriate for water pumping applications because of the high cost incurred by the power electronic devices and the number of components.

Solar Photo Voltaic fed applications have different configurations in which the accepted structure consists of two priorities, such as MPPT from the solar array and produce low Total Harmonic Distortion (THD) ac current. Due to these advantages, solar-based applications is effectively operated. BLDC motors have more advantages in  $N - \tau$  characteristics, increased efficiency, maximum operational life, and low maintenance than DC motors and induction motors. In the accepted structure, an inverter is used to energize stator windings of BLDC motor and also a ripple-free voltage to the inverter through the high DC link is connected. It is observed that the expense of the BLDC motor drive is about 5–15 percent in the total system cost. Using the DC link capacitor of the inverter reduces the torque ripples at the motor.

Due to its merits [7–9], the BLDC motor is selected for use in the improvement of an appropriate water pumping system. To avoid the voltage source inverter (VSI) losses caused by high switching frequency an electronic commutation from the BLDC is used in order to operate voltage source inverter with fundamental [10–13]. The simulation responses display that the proposed system can be worked for different operating and environmental conditions. In conventional SPV fed BLDC motor presented in Fig. 1, in which the voltage and current references sensed from solar by the MPPT to offer the gating pulses for the DC-DC converter. BLDC motor control uses two-phase currents with a Hall signal feedback is used resulting in higher costs. The complexity to control the BLDC motor speed and also the additional control scheme increases the cost. In addition, the VSI switching losses are more due to the high-frequency PWM pulses leads to decrease in efficiency.

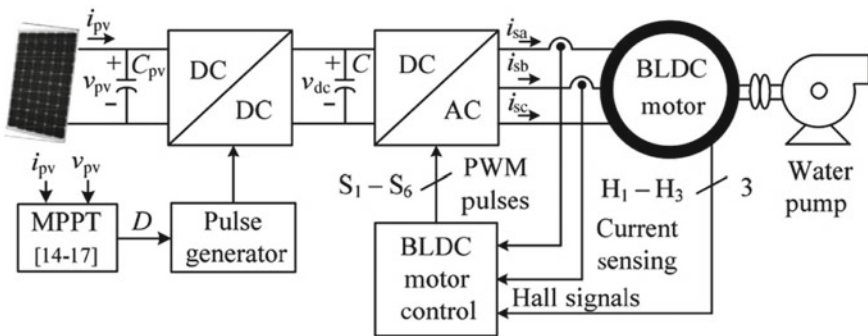


Fig. 1 Structure of conventional solar photo voltaic based DC-DC converter



## 2 Detailed Arrangement of Projected System

The projected configuration is shown in Fig. 2. It comprises of Solar Photo Voltaic array, a DC-DC zeta converter, a DC-AC VSI, a BLDC motor with an embedded encoder with an application as a water pumping system. In Sect. 2, a cleared operation of the intended system is explained.

### 2.1 SPV Based Zeta Converter Control

The Solar Photo Voltaic array produces the electrical power required for the motor pump from DC-DC converter via voltage source inverter (VSI). The proposed configuration is presented in Fig. 2. From the figure, the Zeta converter is benefited to transfer the required voltage gain for the VSI from the SPV array. In practice, the required voltage gain for VSI is not sufficient due to losses [14]. The reference voltage and current values from the SPV array utilized to generate duty cycle and comparing with high-frequency carrier wave to produce required gating pulses for a Zeta Converter which increases the efficiency of solar Photo voltaic array.

The required voltage for the motor to operate is dragged from the zeta converter via voltage source inverter (VSI). The VSI is operated via an electronic commutation through BLDC motor supported by in-built encoder so as to eliminate the losses.

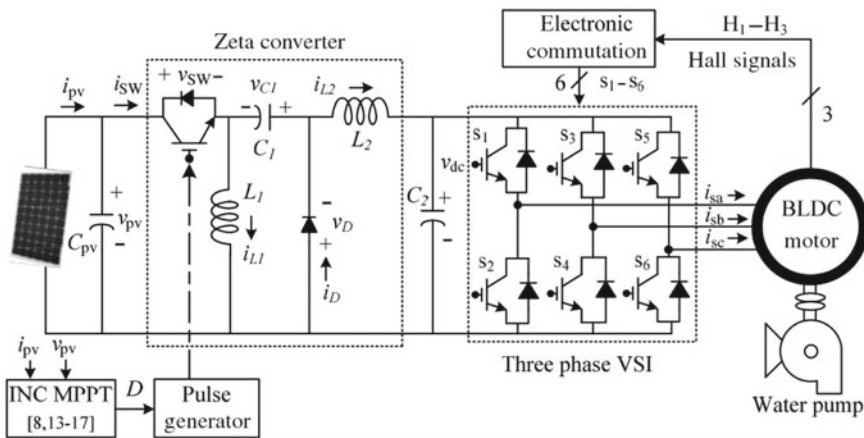


Fig. 2 Structure of suggested SPV with INC-MPPT basing zeta converter

## 2.2 Scheme of Projected System

The suggested configuration is designed in such a way that it can operate under uncertain conditions shown in Fig. 2. A 2.89-kW BLDC motor and 3.4 kW Peak Power Capacity Solar PV array is considered for a testing scenario or Standard Test Conditions (STC). The following segments explain about several steps like Solar PV array, DC-DC zeta converter, DC-AC converter and water pumping system.

### 2.2.1 Scheme of Solar PV Array

In practical converters, due to the different components, there exist various power losses. Moreover, in this BLDC fed water pumping system structure is also affected with mechanical and electrical losses. In order to avoid the losses, a high peak power capacity, SPV array is selected for suitable operation irrespective of power losses. The chosen Practical Solar PV array under Standard conditions is STC: 1000 W/m<sup>2</sup>, 25 °C, AM 1.5 is therefore marginally in excess, that required for selected motor pump and its specifications are made appropriately. In practical case, for testing solar array [15] Table 1 lists, the electrical specifications of this module and the number of modules needed to connect in series/parallel are basing on voltage of the SPV array.

The  $I_{mpp}$  of array at MPP is predictable as

$$I_{mpp} = \frac{P_{mpp}}{V_{mpp}} = 3400/187.2 = 18.16 \text{ A} \tag{1}$$

The total series modules used are as follows:

$$N_S = \frac{V_{mpp}}{V_m} = \frac{187.2}{31.2} = 6 \tag{2}$$

The total parallel modules used are as follows:

$$N_P = \frac{I_{mpp}}{I_m} = 18.16/9.07 = 2 \tag{3}$$

**Table 1** Specification of practical solar PV module [15]

Parameters	Rating
Peak power, $P_m$ (W)	280
Open circuit voltage, $V_o$ (V)	39.5
Voltage at MPP, $V_m$ (V)	31.2
Short circuit current, $I_s$ (A)	9.71
Current at MPP, $I_m$ (A)	9.07
Number of cells connected in series, $N_{ss}$	60

The SPV array with the corresponding size is proposed, and it is having six series modules and two parallel strings.

### 2.2.2 Scheme of Zeta Converter

The proposed Zeta Converter is comprised of different parameters like inductor  $L_1$  at the input side, inductor  $L_2$  at the output side and capacitor  $C_1$  is in between them. This structure is operated in Continuous Current Mode leads to decrease the stress on components and power electronic devices. The duty cycle estimated to zeta converter is as follows [6].

$$D = \frac{V_{dc}}{V_{dc} + V_{mpp}} = \frac{200}{200 + 187.2} = 0.52 \tag{4}$$

where  $V_{dc}$  = dc link voltage at the VSI

The  $I_{dc}$  at VSI is estimated as

$$I_{dc} = \frac{P_{mpp}}{V_{dc}} = \frac{3400}{200} = 17 \text{ A} \tag{5}$$

Let  $L_1$ ,  $L_2$ , and  $C_1$  are predictable as

$$L_1 = \frac{DV_{mpp}}{F_{sw}\Delta I_{L1}} = \frac{0.52 \times 187.2}{20,000 \times 18.16 \times 0.06} = 4.5 \times 10^{-3} \approx 5 \text{ mH} \tag{6}$$

$$L_2 = \frac{(1 - D)V_{dc}}{F_{sw}\Delta I_{L2}} = \frac{(1 - 0.52) \times 200}{20,000 \times 17 \times 0.06} = 4.7 \times 10^{-3} \approx 5 \text{ mH} \tag{7}$$

$$C_1 = \frac{DI_{dc}}{F_{sw}\Delta V_{C1}} = \frac{0.52 \times 17}{20,000 \times 200 \times 0.1} = 22 \mu\text{F} \tag{8}$$

where

$F_{sw}$  IGBT switching frequency

$I_{L1}$   $I_{mpp}$  current through inductor  $L_1$

$I_{L2}$   $I_{dc}$  current through inductor  $L_2$

$V_{C1}$  Permitted ripple in voltage across  $C_1$ , same as  $V_{C1} = V_{dc}$ .

### 2.2.3 Assessment of DC-Link Capacitor of VSI

In the three-phase supply system, the sixth harmonic component of the supply (ac) voltage is reproduced as a dominant harmonic on the dc side [16]. The minimum speed for pump the water by the BLDC motor is estimated from the VSI output voltage frequencies to the rated speed. Hence two frequencies are utilized to estimate

their corresponding capacitor Ratings. Between the two assessed capacitors, a larger one is chosen for suitable operation in suggested topology even though the solar irradiance level is low.

Let  $\omega_{rated}$  approximated as,

$$\omega_{rated} = 2\pi f_{rated} = 2\pi \frac{N_{rated}P}{120} = 2\pi \times \frac{3000 \times 6}{120} = 942 \text{ rad/s} \quad (9)$$

The minimum speed required to pump the water by BLDC motor is estimated as ( $N = 1100 \text{ r/min}$ )

$$\omega_{min} = 2\pi f_{min} = 2\pi \frac{NP}{120} = 2\pi \times \frac{1100 \times 6}{120} = 345.57 \text{ rad/s} \quad (10)$$

where

$f_{rated}$  Rated frequency

$f_{min}$  Minimum frequency for motor

$N_{rated}$  Rated BLDC motor speed

$P$  Number of poles

The  $C_2$  value of VSI at  $\omega_{rated}$  is as follows

$$C_{2,rated} = \frac{I_{dc}}{6 \times \omega_{rated} \times \Delta V_{dc}} = \frac{17}{6 \times 942 \times 200 \times 0.1} = 150.4 \mu\text{F} \quad (11)$$

Correspondingly, a value of  $C_2$  of VSI at  $\omega_{min}$  is as follows:

$$C_{2,min} = \frac{I_{dc}}{6 \times \omega_{min} \times \Delta V_{dc}} = \frac{17}{6 \times 345.57 \times 200 \times 0.1} = 410 \mu\text{F} \quad (12)$$

where  $\Delta V_{dc}$  = permitted ripple in voltage of  $C_2$

### 2.2.4 Scheme of Water Pump

For the chosen water pumping system, its power-speed characteristics [17] are utilized to approximate the proportionality constant.

$$k = \frac{P}{\omega_r^3} = \frac{2.89 \times 10^3}{\left(2\pi \times \frac{3000}{60}\right)^3} = 9.32 \times 10^{-5} \quad (13)$$

where;

Rated power developed by the BLDC engine ( $P$ ) = 2.89 kW

Rated rotor mechanical speed ( $\omega$ ) = 3000 r/min

Hence the water pumping system is chosen basing on above data.

### 3 Control of Projected System

It can be monitored in two methods as follows, namely MPPT and Electronic commutation.

#### 3.1 INC-MPPT Algorithm

This method [9] is used for the smooth run of BLDC motor by dragging the maximum power from the Solar PV array. However, it permits to interrupt the voltage of the solar PV array or the gating pulses of the zeta converter. In the conventional method, the proportional integral controller (PI) is utilized to generate the pulsating signals [9], which increase the complexity of the converter. Hence a direct pulsating control is revised to this work. The disturbance direction of INC-MPPT algorithm is based on the  $P_{pv} - V_{pv}$  characteristics as presented in Fig. 3.

By considering Fig. 3, the slope MPP at the peak is zero, at left and at the right of MPP, i.e., negative.

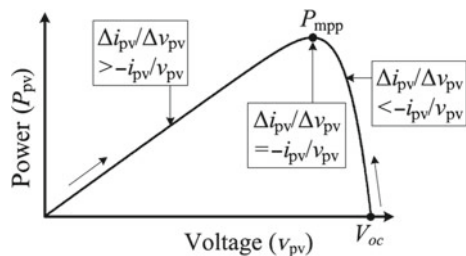
$$\left. \begin{aligned} \frac{dP_{pv}}{dV_{pv}} &= 0; \text{ at mpp} \\ \frac{dP_{pv}}{dV_{pv}} &> 0; \text{ left of mpp} \\ \frac{dP_{pv}}{dV_{pv}} &> 0; \text{ right of mpp} \end{aligned} \right\} \quad (14)$$

Since

$$\frac{dP_{pv}}{dV_{pv}} = \frac{d(V_{pv} * i_{pv})}{dV_{pv}} = i_{pv} + V_{pv} * \frac{di_{pv}}{dV_{pv}} \cong i_{pv} + V_{pv} * \frac{\Delta i_{pv}}{\Delta V_{pv}} \quad (15)$$

Therefore, (14) is reproduce as

**Fig. 3** Graphical representation of solar PV characteristics



$$\left. \begin{aligned} \frac{\Delta i_{pv}}{\Delta V_{pv}} &= -\frac{i_{pv}}{V_{pv}}; \text{ at } mpp \\ \frac{\Delta i_{pv}}{\Delta V_{pv}} &> -\frac{i_{pv}}{V_{pv}}; \text{ left of } mpp \\ \frac{\Delta i_{pv}}{\Delta V_{pv}} &< -\frac{i_{pv}}{V_{pv}}; \text{ right of } mpp \end{aligned} \right\} \quad (16)$$

Consequently, the controller chooses the way of perturbation and variation of pulsating signals depends on the characteristics shown in Fig. 3. In practical the operating point oscillates at MPP Preferably, when the operating point reaches the MPP, the disturbance will stop. As the size of the disturbance decreases, the controller takes longer to track the SPV array's MPP. To justify the MPPT and BLDC soft start, an intelligent method has to take care between tracking time and size of interruption. The operating of soft start and reduces the oscillation around MPP, the initial value is assumed as zero and size of the optimum perturbation as almost  $\Delta D = 0.001$ .

### 3.2 BLDC Motor Under Electronic Commutation

An Electronic Commutation switch operates the VSI in order to control BLDC motor. The Electronic commutation operates from BLDC motor exciting current to sense the three Hall signals in such a way that it generates six gating signals to the VSI converter. Here based on the rotor position, an embedded encoder generates these Hall signals.

The specific rotor position range, for each  $60^\circ$  of the interval, a specific combination of Hall-effect signals is generated [6]. Table 2 tabulates the generation of six gating pulses with rotor position approximation, and only two switches is on at a time, ensuing in VSI operating mode of  $120^\circ$  conduction, consequently the decreased conductive losses. The VSI losses are due to high frequency is eliminated by providing the basic VSI frequency switching. The corresponding steady state and dynamic performance of the proposed system simulation diagrams are shown in Figs. 4 and 6 and its responses in Figs. 5 and 7 respectively.

## 4 BLDC Speed Controller Method

A Hall sensor or a shaft encoder senses the rotor position of BLDC. The drive control system is having speed control at external and current control at internal loops. Here only one sensor is used for sensing the current instead of three separate current sensors, which it is placed on DC connection.

**Table 2** Electronic commutation switching's basing on rotor position of BLDC motor

Rotor position ( $\theta^0$ )	Hall signals			Switching states					
	H3	H2	H1	S1	S2	S3	S4	S5	S6
NA	0	0	0	0	0	0	0	0	0
0-60	1	0	1	1	0	0	1	0	0
60-120	0	0	1	1	0	0	0	0	1
120-180	0	1	1	0	0	1	0	0	1
180-240	0	1	0	0	1	1	0	0	0
240-300	1	1	0	0	1	0	0	1	0
300-360	1	0	0	0	0	0	1	1	0
NA	1	1	1	0	0	0	0	0	0

### 4.1 Control Speed of BLDC Motor

Here speed control blocks a proportional integral (PI) controller is utilized to compare measured process variable and desired value in order to process corrective action by avoiding the error. The calculation of the PI controller involves the proportional mode to determine the current error response and the integral mode for recent error based on the action in two separate modes. The two modes sum is the control element corrective action. Because of its ease of model and simple configuration, the PI controller is widely utilized in the industry. It is possible to implement the PI controller algorithm as

$$output(t) = k_p e(t) + k_i \int_0^t e(\tau) d\tau \tag{17}$$

In the speed controller the input as speed error. The controller’s response is counted as reference torque. A boundary is located on the output of the speed controller, subjected to the maximum winding currents allowed. Figure 8 shows the simulation of closed loop speed control of BLDC motor and the corresponding speed-Torque, EMF responses are displayed in Figs. 9, 10, and 11.

## 5 MATLAB/Simulation Results

See Figs. 4, 5, 6, 7, 8, 9, 10 and 11.

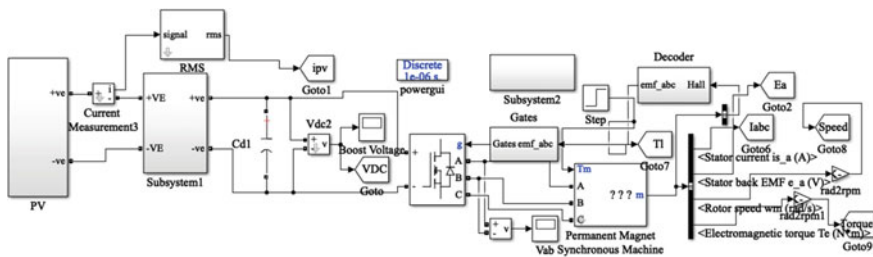
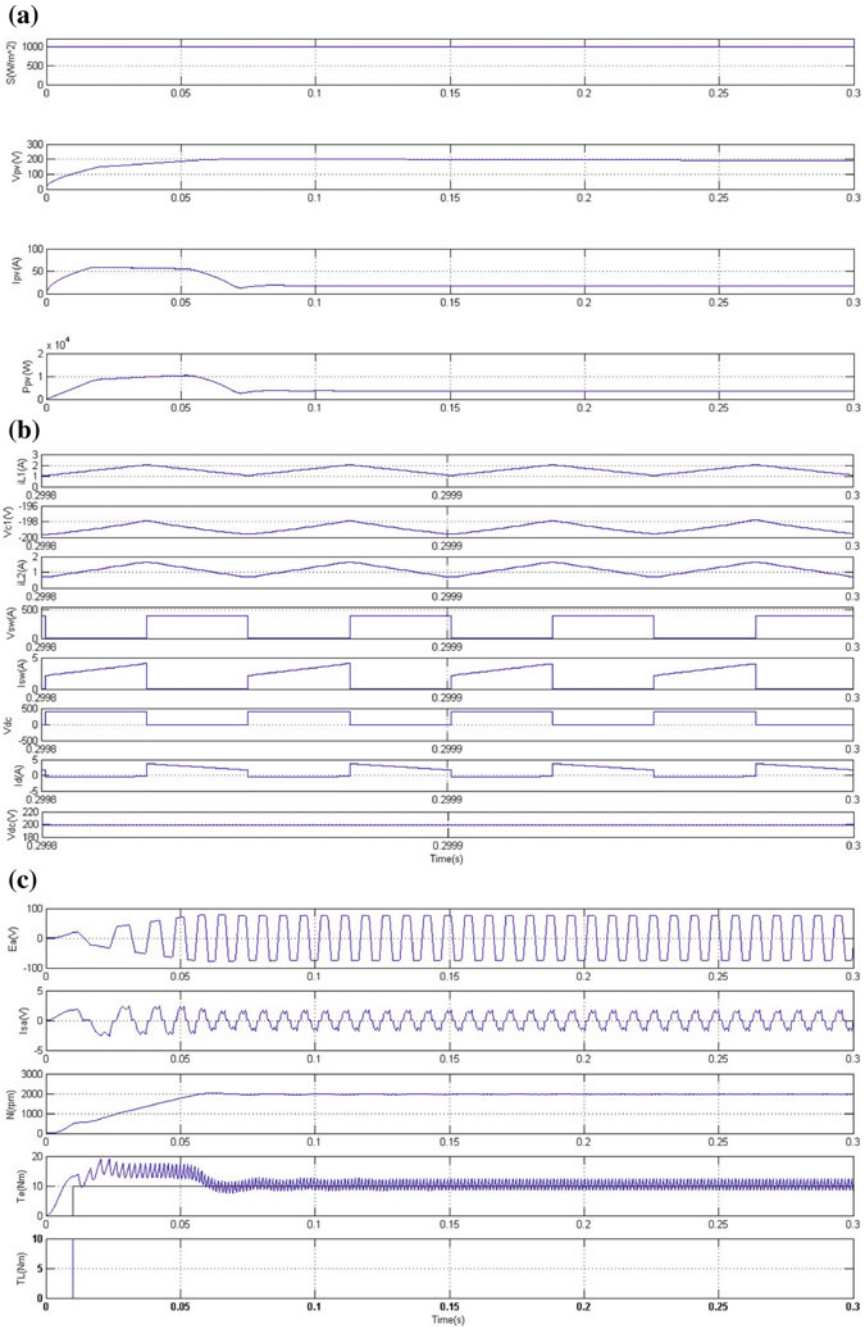


Fig. 4 Matlab/Simulink circuit under steady state





**Fig. 5** Under steady state **a** Array variables for SPV. **b** Variables for the zeta converter. **c** Variables of the BLDC motor pump

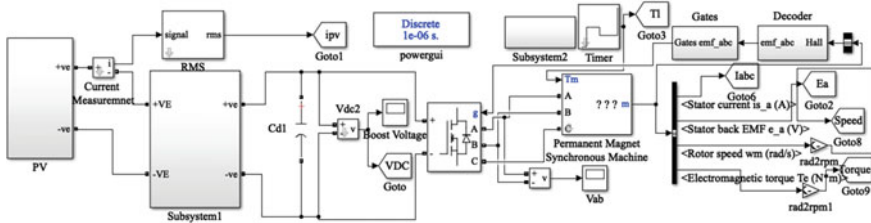


Fig. 6 Matlab/Simulink circuit under dynamic state

## 6 Conclusion

A DC-DC Zeta converter based BLDC motor has been proposed in a solar PV application. The entire configuration is evaluated by simulink software. Simulated results have shown that the proposed configuration is suitable for SPV based applications under uncertain conditions. To avoid the effects caused by variations in atmospheric conditions and inclusive losses, attention has to be done on the size of the solar PV array in such a way that the proposed zeta converter is used for MPPT. In the configuration, if the zeta converter was operated in continuous current mode leads to diminish component stress. The fundamental frequency advantage by the electronic commutation is utilized to eliminate the losses in VSI. Other important features of the proposed system are stable operation for the water-pumping system and safe start for the BLDC motor.

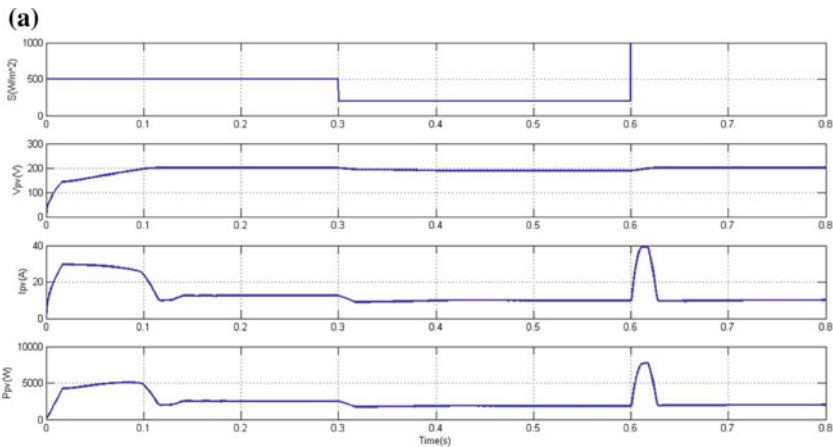


Fig. 7 Under dynamic state a Variables of the solar photo voltaic array. b Variables for the zeta converter. c Variables of the BLDC motor pump

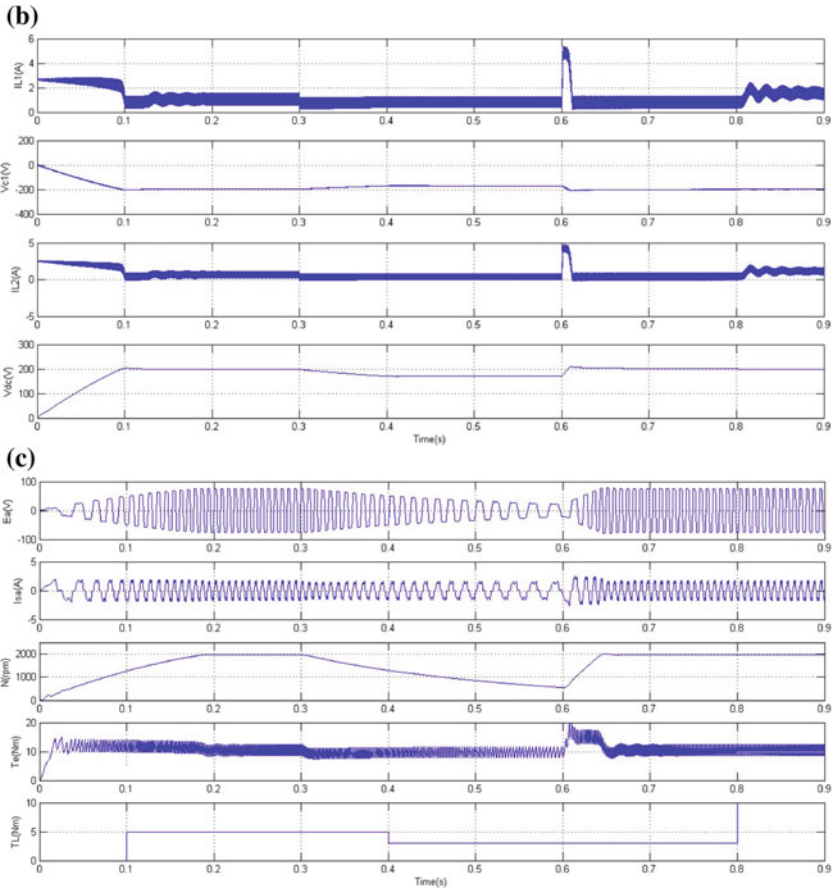


Fig. 7 (continued)

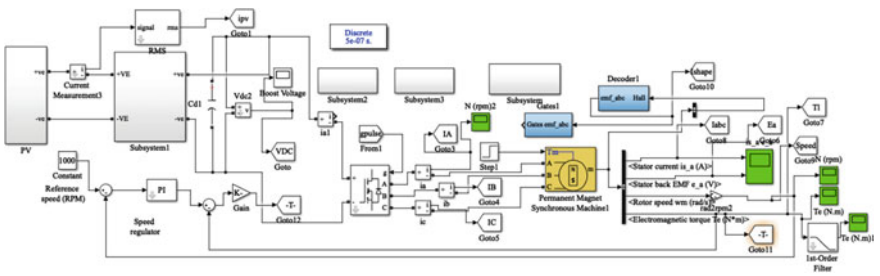


Fig. 8 Closed loop speed control of proposed system Simulink circuit

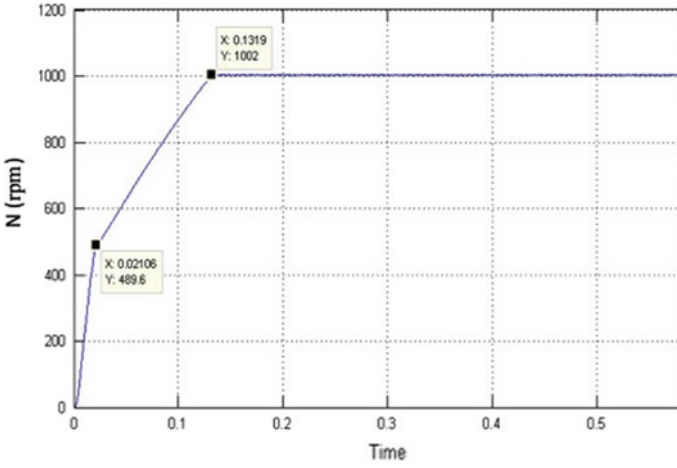


Fig. 9 Speed

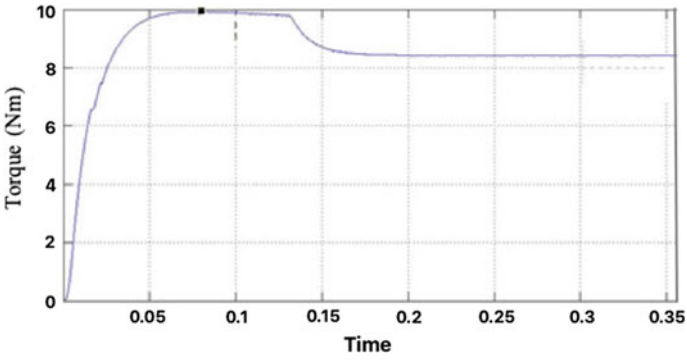


Fig. 10 Torque

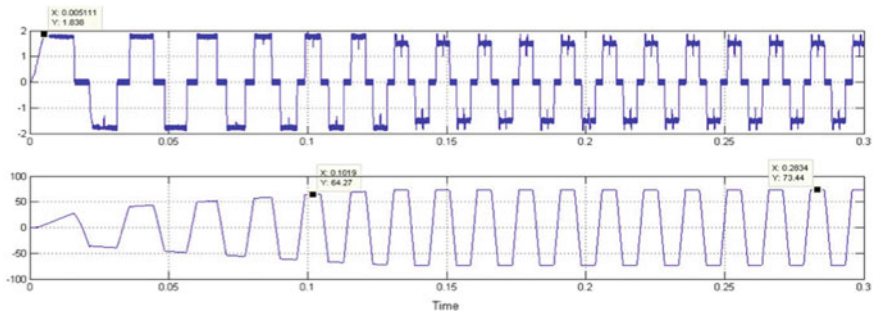


Fig. 11 Stator current and electro motive force

**Acknowledgement** This research was supported by University Malaysia Pahang (UMP) for the internal grant no: RDU151316.

## References

1. Uno M, Kukita A (2015) Single-switch voltage equalizer using multistacked buck–boost converters for partially shaded photovoltaic modules. *IEEE Trans Power Electron* 30(6):3091–3105
2. Arulmurugan R, Suthanthiravanitha N (2015) Model and design of a fuzzy-based Hopfield NN tracking controller for standalone PV applications. *Electr Power Syst Res* 120:184–193
3. Satapathy S, Dash KM, Babu BC (2013) Variable step size MPPT algorithm for photo voltaic array using zeta converter-A comparative analysis. In: 2013 Students conference on engineering and systems (SCES), IEEE, pp 1–6
4. Kumar R, Singh B (2016) BLDC motor-driven solar PV array-fed water pumping system employing zeta converter. *IEEE Trans Ind Appl* 52(3):2315–2322
5. Singh B, Bist V, Chandra A, Al-Haddad K (2015) Power factor correction in bridgeless-Luo converter-fed BLDC motor drive. *IEEE Trans Ind Appl* 51(2):1179–1188
6. Singh B, Bist V (2014) Measurement, and Technology, “Power quality improvements in a zeta converter for brushless DC motor drives”. *IET Sci, Meas Technol* 9(3):351–361
7. Coelho RF, Dos Santos WM, Martins DC (2012) Influence of power converters on PV maximum power point tracking efficiency. In: 2012 10th IEEE/IAS international conference on industry applications, IEEE, pp 1–8
8. Sitbon M, Schacham S, Kuperman A (2015) Disturbance observer-based voltage regulation of current-mode-boost-converter-interfaced photovoltaic generator. *IEEE Trans Ind Appl* 62(9):5776–5785
9. Elgendy MA, Zahawi B, Atkinson DJ (2013) Assessment of the incremental conductance maximum power point tracking algorithm. *IEEE Trans Sustain Energy* 4(1):108–117
10. Lu DD, Nguyen QNJ (2012) A photovoltaic panel emulator using a buck-boost DC/DC converter and a low cost micro-controller. *Sol Energy* 86(5):1477–1484
11. Xuesong Z, Daichun S, Youjie M, Deshu C (2010) The simulation and design for MPPT of PV system based on incremental conductance method. In: 2010 WASE international conference on information engineering, vol 2. IEEE, pp 314–317
12. Reisi AR, Moradi MH, Jamasb SJR (2013) Classification and comparison of maximum power point tracking techniques for photovoltaic system: a review. *Renew Sustain Energy Rev* 19:433–443
13. Bendib B, Belmili H, Krim FJR (2015) A survey of the most used MPPT methods: conventional and advanced algorithms applied for photovoltaic systems. *Renew Sustain Energy Rev* 45:637–648
14. Shahin A, Payman A, Martin JP, Pierfederici S, Meibody-Tabar F (2010) Approximate novel loss formulae estimation for optimization of power controller of DC/DC Converter. In: IECON 2010: 36th annual conference of the IEEE industrial electronics society, IEEE
15. Sun module® Plus SW 280 Mono (2013) Performance under standard test conditions [Online]. Available: [http://www.sfe-solar.com/wpcontent/uploads/2013/07/SunFields-SolarWorld\\_SW265-270-275-280\\_Mono\\_EN.pdf](http://www.sfe-solar.com/wpcontent/uploads/2013/07/SunFields-SolarWorld_SW265-270-275-280_Mono_EN.pdf)
16. Babu AV, Kumar GK (2014) Electromagnetic compatibility and better harmonic performance with seven level CHB converter based PV-battery hybrid system. *Int J Sci Res* 3(11):1259–1263
17. Singh B, Kumar R (2016) Solar photovoltaic array fed water pump driven by brushless DC motor using Landsman converter. *IET Renew Power Gener* 10(4):474–484
18. El Khateb AH, Rahim NA, Selvaraj J, Williams BWJ (2015) DC-to-DC converter with low input current ripple for maximum photovoltaic power extraction. *IEEE Trans Industr Electron* 62(4):2246–2256

# Hydrophobic Sol-Gel Based Self-cleaning Coating for Photovoltaic Panels



Siti Nur Nashya Azlika Hamidon, Amirjan Nawabjan,  
Ahmad Sharmi Abdullah and Siti Maherah Hussin

**Abstract** Maintaining photovoltaic performance from soiling issues using manual cleaning is costly and tedious which has been a major concern in deploying this technology. Therefore, a soiling mitigation technique with self-cleaning properties such as hydrophobic coating is effective to minimize performance degradation of photovoltaic panels using sol-gel as a low-cost and scalable fabrication method. This study proposes the development and application of hydrophobic sol-gel based coating in the photovoltaic system. The aims include synthesizing a hydrophobic sol-gel based self-cleaning coating for solar panel and characterizing the hydrophobic sol-gel based self-cleaning coating. A solution is prepared using sol-gel process comprises of three different materials including vinyltriethoxysilane (VTES), tetraethoxysilane (TEOS) and tetrabutoxytitanate (TTBU) called VTT (VTES-TEOS-TTBU) sol as the organic-inorganic hybrid sol. Then, this sol is applied onto glass substrates using spin-coating method for laboratory-scale working samples. Coated samples have undergone characterizations including water contact angle measurement to obtain hydrophobic properties and surface morphology observation using microscope. The resultant VTT sol samples proven to exhibit self-cleaning ability with contact angle of 99.58° when undergo 150 °C post-bake process. The switchability of sol (hydrophilic-hydrophobic) was achieved and better transparency was observed with transmittance of 90.73% when the samples undergoing different thermal treatment during pre-bake and post-bake processes.

**Keywords** Photovoltaic panels · Soiling mitigation techniques · Sol-gel · Self-cleaning coating · Hydrophobic

---

S. N. N. A. Hamidon · A. Nawabjan (✉) · S. M. Hussin  
Centre of Electrical Energy Systems, Institute of Future Energy, Universiti Teknologi Malaysia,  
81310 UTM Johor Bahru, Johor, Malaysia  
e-mail: [amirjan@utm.my](mailto:amirjan@utm.my)

S. N. N. A. Hamidon  
e-mail: [snnazlika2@live.utm.my](mailto:snnazlika2@live.utm.my)

A. S. Abdullah  
School of Electrical Engineering, Universiti Teknologi Malaysia, 81310 UTM Johor Bahru, Johor,  
Malaysia

## 1 Introduction

The rising demand for PV energy comes with the increasing drawbacks mostly related to maintaining the technology efficiency such as the soiling issues. Sand dust particles deposition and pollution particles deposition are the main causes of dirtiness in the panels' surface. These effects are translated into a decrease of about 40% in solar power conversion for each 4 g of dust per square meter [1]. The solar panels can lose incident light through reflection by the cover glass and mainly through scattering or absorption by particulates on the solar panels decreasing its power conversion efficiency. The reduction in PV power output can be anywhere between 2 and 50% depending on a range of factors, including local climate, dust composition and concentration, as well as whether a mitigation strategy is employed [2]. There is a need for regular maintenance to maintain the efficiency and the overall performance of the PV solar panels. Cleaning of solar panels from contaminants to maintain the optimum solar harvesting capabilities is time-consuming and expensive. Since the last decade, self-cleaning coatings such as hydrophobic coating have attracted attention in the scientific community and industrial exploitation. These coatings have been made artificially by mimicking biological surfaces, such as lotus leaf, gecko and water striders [3]. Some of the self-cleaning coatings applications are the textile industry, automobile industry, and optical industry. In this study, a self-cleaning coating is focused on PV application mainly to reduce dust accumulation on PV panels. Hydrophobic coatings provide a variety of conveniences including a reduction in maintenance cost, the extermination of dreary manual work as well as minimizing time spent on cleaning. The application of hydrophobic coatings on PV solar cells can be a cost-effective and alternative solution to reduce the efficiency losses from dust accumulation [4–6].

## 2 Experimental Details

### 2.1 Materials

Ethanol (98–99%), hydrochloric acid (3.7%), aluminium acetyl acetone (AIAA), triethoxyvinylsilane (VTES, 97%), titanium butoxide (TTBu, 97%) and tetraethyl orthosilicate (TEOS, 98%) were purchased from IChem Solution Sdn. Bhd., Malaysia. All materials were used as received without any further purification.

## 2.2 Fabrication of VTT Sol-Gel Based Coating

Hydrophobic coating (VTT) in this study was prepared using sol-gel method, which comprised of stages including sol preparation, sol deposition and drying (thermal treatment).

**Sol preparation.** Sol is a mixture where solid particles are dispersed in liquid dispersion medium. This liquid dispersion medium is known as solvent. Water and alcohol are among the typical solvents used in sol-gel synthesis. Conversely, gel is a mixture in which liquid is dispersed in solid dispersion medium. In other word, a colloidal system is recognized as gel when the liquid and solid phases of colloidal dimension are continuous [7].

A sol-gel coating is commonly composed by inorganic silicon alkoxides precursors which are commercially available and widely used; tetraethoxysilane, TEOS ( $\text{Si}(\text{OC}_2\text{H}_5)_4$ ) and tetramethoxysilane, TMOS ( $\text{Si}(\text{OCH}_3)_4$ ). TEOS is more commonly used in the sol-gel process because it readily reacts as a precursor, promotes the formation of cross-linking and has networker characteristics [8, 9]. Besides the inorganic precursor discussed above, there is also organically modified silicon alkoxide used in this study which is the vinyltriethoxysilane (VTES). It is also a crosslinking agent that reacts towards water and moisture to form silicon-oxygen-silicon bonds as well as adhesion promoters for glass treatments. The organic groups in VTES which are vinyl is polymerizable and later mixed with polymerization catalyst used in this study, the aluminium acetylacetonate (AlAA). Titanium butoxide (TTBu) is another precursor used in preparing the sol for this study. While it is soluble in most organic solvents, TTBu also often used as a liquid source of titanium dioxide which further used in this study to be deposited as coating [10]. Due to its favourable physical and chemical properties,  $\text{TiO}_2$  is the most preferable material for a self-cleaning surface.

In this study, the solvent and catalyst used were ethanol (EtOH) and hydrochloric acid (HCl) respectively because they were widely used in sol-gel method and have better properties in controlling sols from being unstable. They were needed to accelerate the reaction time of hydrolysis, prevent liquid-liquid phase separation during the initial stages of the hydrolysis reaction and ensure the sol was evenly dispersed without aggregation [11]. For this study, the sol was prepared as in Fig. 1. Before preparing samples of sols, all apparatus used need to be cleaned using ultrasonic vibration and dried with EtOH. The amount of each solution used was weighed according to specific ratio to achieve the best composition to produce VTT sol. The solution was mixed using magnetic stirrer to ensure particles were evenly dispersed. Stirring speed and temperature were fixed at 1250 rpm and ambient respectively, while stirring time was fixed according to its composition. Following the sol-preparation, sample substrates were prepared for sol-deposition.

**Sol deposition.** Technique used to deposit sol onto substrate in this study was spin-coating method. This method was chosen due to its fast and facile application as well as having advantage of equal distribution of sol [12]. Transparent glass substrates were used as working samples for this study. Before deposition of sol onto glass substrates, they undergo pre-treatment using ultrasonic bath to minimize the presence



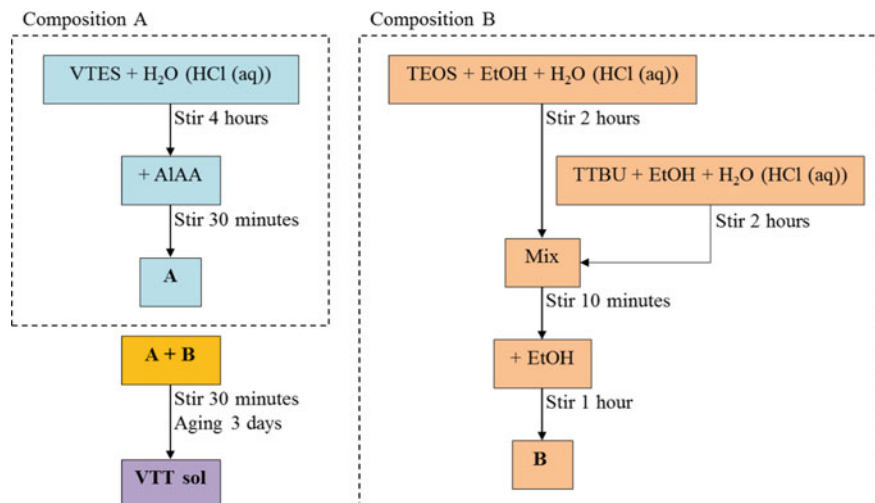


**Fig. 1** Preparation of VTT sol

of impurities. Substrates were soaked into de-ionized water which was poured in a beaker beforehand. The beaker was then put into an ultrasonic bath which then filled with water. The timer was set to 10 min for the substrate to be properly cleaned. When the timer stop, the beaker was taken out of the bath and the de-ionized water in it was poured out of the beaker into the sink. The substrates were taken out using tweezers and then cleaned using high-absorbent tissue paper in order to remove excess water. The substrate then rinsed with ethanol solvent and dried using air blower. Upon completion of substrate cleaning, spin coater was prepared to deposit the VTT sol onto the glass substrate. Spin coater was set up by specifying speed and time for the desired thickness. The glass substrate was placed in the spin coater and 10  $\mu\text{L}$  of VTT sol was dropped onto it using pipette.

**Drying (Thermal treatment).** Following the coating application as described in previous section, the coated glass samples were pre-baked using hot plate with temperature of 80 °C for 10 min. This step was essential to ensure moisture present in the coating could be minimized. The pre-baked samples were then kept in a dry box to prolong the elimination process of moisture before it could be post-baked using oven the next day, with temperature varied from 75 to 150 °C.

### 2.3 Characterization

Characterizations technique used to study the coating produced were the measurement of static water contact angle and observation of the surface structure using optical microscope.

**Contact angle measurements.** The wettability of the coated dried glass samples were determined using the Sessile drop method. In each sample, a drop of pure water was generated with a syringe and deposited in approximately the center of substrate. The sample was placed in ambient temperature. The images of drops were obtained through a video camera mounted on a microscope and they were examined by running the drop shape analysis (AmScope) software.

The Sessile drop method used in this work was to determine the static contact angle based on the hydrophobic concept. Basically, the wettability of the surface can be characterized by the contact angle (CA). Contact angle can be defined as the angle which the droplet or edge of the liquid (water) makes with the solid plane [13, 14]. This method is only applicable to measure static contact angle when the droplet is standing on the surface in which the three-phase boundary (solid plane) is not moving.

**Optical microscope observation.** Another characterization done besides contact angle measurement is the evaluation of surface morphology visuals through optical microscope. The microscope is adjusted to achieve the best focus, magnification, resolution, contrast and working distance. Surface of the coated glasses was observed in order to determine presence of cracking that could be formed during the thermal treatment. Scanning Electron Microscope (SEM) analysis was carried out to further study the surface morphology and compare between samples with and without post-bake treatment. The samples were coated with platinum (Pt) before the analysis done to make the coating conductive. Meanwhile, the surface chemical composition of sample with highest hydrophobicity was characterized using Energy-Dispersive X-Ray Spectroscopy (EDX) to identify the chemical element present in the material along with its respective weight percentage.

**Transmittance measurement.** Based on the observation of samples through optical microscope, sample with the best characteristics were taken for transmittance measurement to determine the amount of light transmitted through the coated glass. This measurement was done using UV-Vis Spectrophotometer (Perkin Elmer Lambda 1050) with an ultraviolet-visible spectral region set between 250 and 800 nm. Based on this measurement, plots obtained were Absorbance (A) versus wavelength ( $\lambda$ ). While this study requires percentage of transmission, %T versus  $\lambda$ , the following calculations were made [15]:

$$A = -\log T \quad (1)$$

$$A = 2 - \log(\%T) \quad (2)$$

Transmittance can be defined as the amount of light that is able to pass through a material without the material reflecting or absorbing the incident light. When a material has a 100% transmission, it means that the material is transparent. Therefore, a higher percentage of transmission is said to have a better transparency.

### 3 Results and Discussions

#### 3.1 Experimental Preparation of VTT Sol

VTT sol was prepared as described earlier in Fig. 1 while Table 1 shown the results of the prepared solution. The recipe is based on M. H. Ibrahim et al. and modified to simplify the fabrication process in the room temperature without the need for controlled condition using chamber [16]. The preparation involved three stages for

**Table 1** Results for preparation of VTT sol

Preparation	Sample	Variables				Data records		Remarks	
		Ratio	Stir time	Stir speed (rpm)	Stir temp.	Colour	State		
B	SiO <sub>2</sub> sol (TEOS + EtOH + HCl)	1	3:4:12	1 h	1250	30 °C	Clear	Solid	Mixed without cap
		2	3:4:12	1 h	1250	20 °C	Clear	Solid	Mixed without cap
		3	3:4:12	2 h	1250	Ambient	Clear	Liquid	–
	TiO <sub>2</sub> sol (TTBu + EtOH + HCl)	1	3:4:12	10 min	1250	Ambient	Cloudy	Liquid (precipitation)	–
		2	0.5:8:12	1 h	1250	Ambient	Clear	Liquid	EtOH ratio increased
	SiO <sub>2</sub> – TiO <sub>2</sub> hybrid sol	1	1:1	1 h	1250	Ambient	Light yellow	Liquid	–
A	Organic sol (VTES + HCl)	1	2:1	10 min	1250	30 °C	Cloudy	Solid	Mixed without cap
		2	2:2	1 h	1250	Ambient	Clear	Gel-like liquid	–
		3	3:2	4 h	1250	Ambient	Clear	Liquid (concentrated)	–
	Organic polymer sol (VTES + HCl + AIAA)	1	2:100	30 min	1250	Ambient	Clear	Liquid (concentrated)	–
		2	2:100	4 h	1250	Ambient	Light yellow	Liquid	Mixed altogether with organic sol, covered with latex
	3	2:100	2 h	1250	Ambient	Clear	Liquid	Covered with plastic	
VTT sol (A + B)	1	1:1	30 min	1250	Ambient	Dark yellow	Liquid	Yellow colour from sol A	
	2	1:1	30 min	1250	Ambient	Light yellow	Liquid	–	

Composition B which is for  $\text{SiO}_2$  sol,  $\text{TiO}_2$  sol and  $\text{SiO}_2$ - $\text{TiO}_2$  hybrid sol while Composition A comprised with two stages; organic sol and organic polymer sol. VTT sol was prepared by combining the resulting two compositions.

As seen in Table 1, each stages of preparation consist of a number of samples as samples production were continued until expected result of solution was achieved. Marked samples in the table showed the best solution characteristics hence achieving hydrophobic properties of VTT sol.

It was observed that throughout the samples preparation, few steps need to be considered to ensure the solution of each sample can be mixed successfully. For example, during stirring, the beaker used must be enclosed with a cap to prevent any particles to be evaporated into air and causing the mixture to turn into solid. Precipitation occurred due to insufficient amount of solvent (EtOH) for the TEOS/TTBu to be completely dissolved, therefore, the amount of solvent must be increased to observe better dispersion and composition of  $\text{TiO}_2$  sol. Cap of the beaker used (latex) caused material being prepared to be contaminated due to unnecessary reaction that leads to dark yellowish liquid. Consequently, the cap used was replaced with plastic cap that improved the colour of resulting VTT sol (light yellowish liquid).

### 3.2 Heat Treatment of the Coating

As seen in Table 2 and Fig. 2a–d, the increasing temperature during post-bake results to higher contact angle due to the elimination of moisture or water, leaving only air filled between molecules thus roughening the structure of low surface energy material (inorganic  $\text{TiO}_2$ ). The air trapped in the voids will repel water thus enhancing its hydrophobicity [17].

Water contact angle results show that different heat treatment produce different self-cleaning properties confirming the flexibility of material fabricated using sol-gel method [18]. Highest contact angle ( $99.58^\circ$ ) achieved meet the requirement of hydrophobic properties. The preparation of  $\text{TiO}_2$  sol using hydrolysis and condensation process decrease the contact angle which may be due to reaction of titanium with water.

### 3.3 Transmittance and Transparency

As seen in Fig. 3a, b, the images shown are the samples of glass slide coated with  $\text{SiO}_2$ - $\text{TiO}_2$  hybrid sol and VTT sol. Based on observation,  $\text{SiO}_2$ - $\text{TiO}_2$  hybrid sol showed cracking on coating which is due to the absence of VTES as adhesive promoter. While VTT sol showed clear coating without cracking. Two samples were placed side-by-side to compare the transparency of both samples with respect to post-bake treatment. The left sample is coated glass that did not undergo post-bake treatment and it was foggier than the ones that undergo post-bake treatment. This is

**Table 2** Results for VTT sol varied heat treatment to self-cleaning properties

Preparation	Sample	Variables							Characterization	
		Coating speed (rpm)	Coating layer	Pre-bake (°C)	Post-bake (°C)	Aging time (day)	Contact angle (°)	Remarks		
VTT sol	1—Fig. 2a	1250	1	75	75	1	63.43	Hydrophilic		
	2—Fig. 2b	1250	1	–	100	1	80.36	Hydrophilic		
	3—Fig. 2c	1250	1	75	125	1	90.62	Hydrophobic		
	4—Fig. 2d	1250	1	–	150	1	99.58	Hydrophobic		

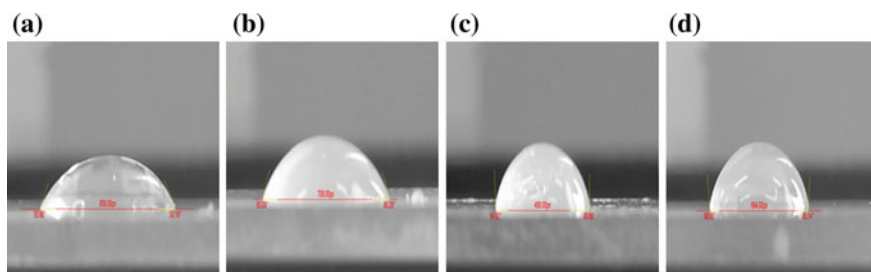


**Fig. 2** a CA = 63.43°; b CA = 80.36°; c CA = 90.62°; d CA = 99.58°

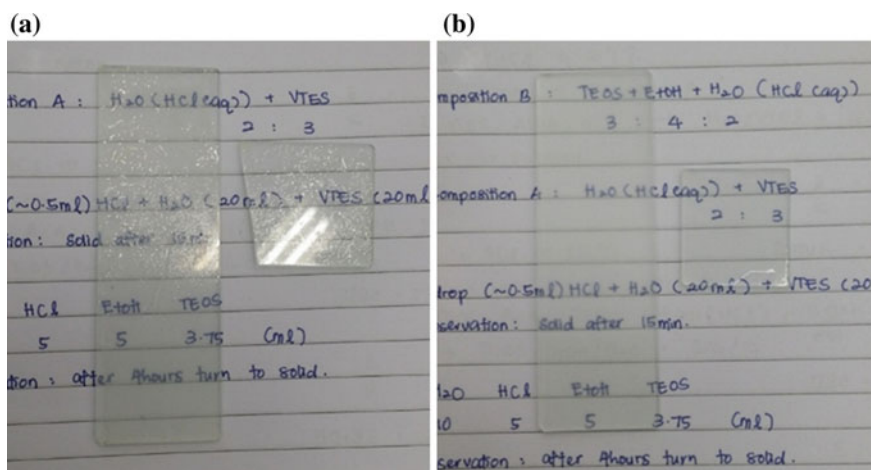


**Fig. 3** a Two glasses coated with SiO<sub>2</sub>-TiO<sub>2</sub> hybrid sol: left is without post-bake, right is with post-bake; b Two glasses coated with VTT sol: left is without post-bake, right is with post-bake

due to the presence of moisture in the coating material that should be eliminated or minimized during post-bake treatment that results to lower transparency.

As shown in Fig. 4a, b, two samples from Fig. 3b were tested for SEM analysis. The images showed that rougher structure was observed in VTT sol with post-bake treatment due to the moisture that has been minimized during the heat treatment, as mentioned in the previous section. Both samples showed almost similar images with small difference in aggregation formed. This is expected as both samples were prepared with identical chemical composition, but only with different stages of post-bake treatment. Despite the observation of a few cracks, a homogenous coating was generally observed. EDX analysis for VTT sol with post-bake treatment was provided in Fig. 5. Without a doubt, the data indicated the presence of Si and Ti as the main element in the coating composition, which played a big role to determine the hydrophobic properties. The presence of C along with O accounted for the functionalizing chemicals used.

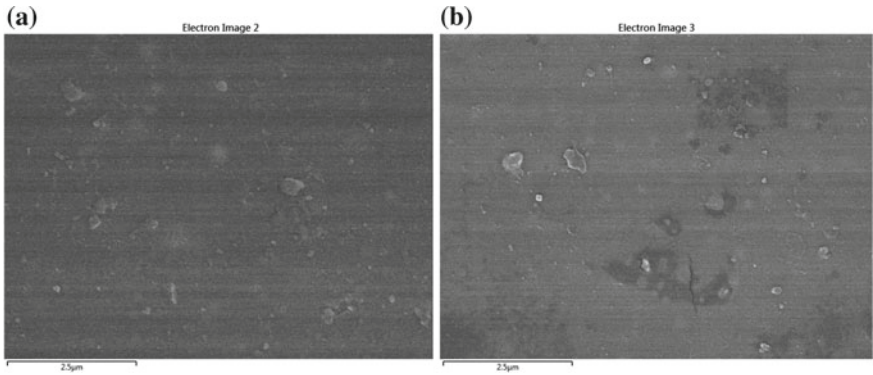


**Fig. 4** a SEM image for VTT sol without post-bake; b SEM image for VTT sol with post-bake

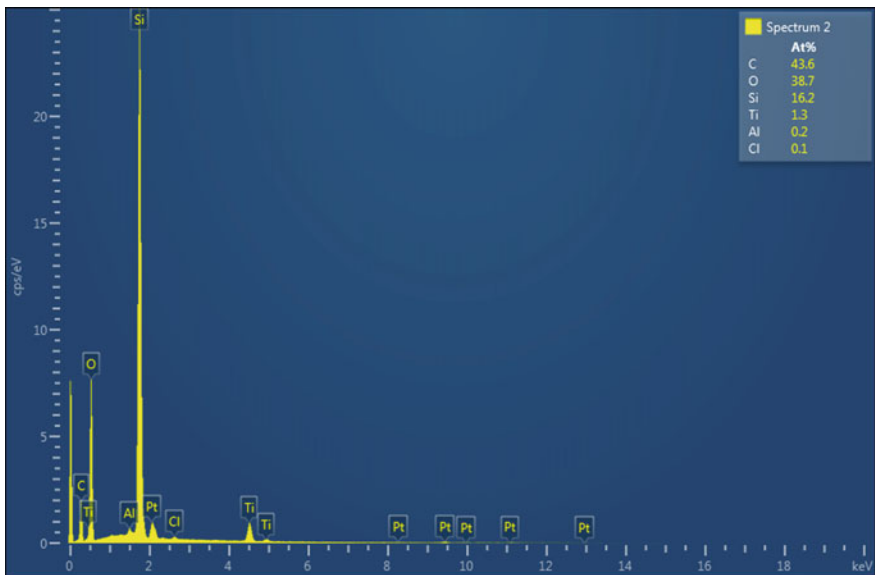


**Fig. 5** EDX spectrum analysis of VTT sol with post-bake treatment

Based on the given transparency results, sample with post-baked VTT sol from Fig. 3b undergone the UV-Vis spectrophotometer to determine its %T. Results as shown in Fig. 6 shows %T with average of 90.73% along the wavelength interval. At  $\lambda$  interval between 300 and 400 nm, occurrence of noise can be observed due to instrumentation error. Similar to the recipe prepared by M. H. Ibrahim et al., a recent study by X. Zhang et al. also have developed sol-gel based coating using organically modified silica (VTES/TEOS) with percentage of transmission of ~99% under

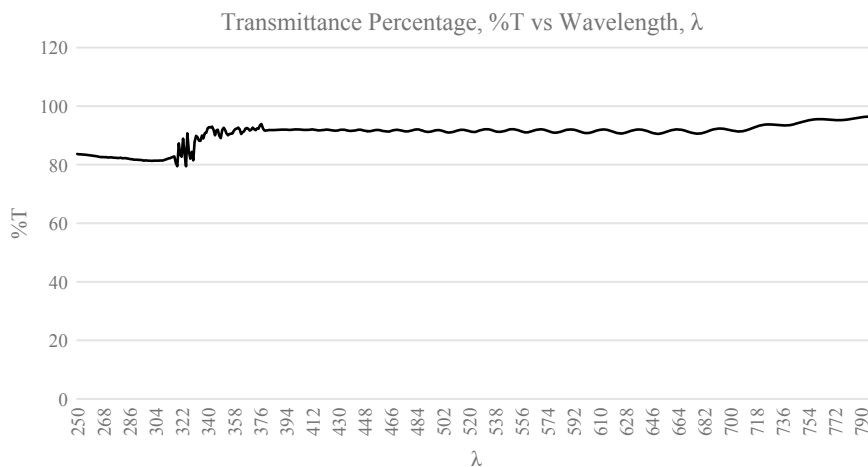


**Fig. 6** Optical transmission spectra for glass sample coated with VTT sol with post-bake treatment

controlled condition [16, 19]. Comparing these studies, although there are difference in %T, the VTES/TEOS sol-gel based coating was prepared in a chamber with controlled environment (temperature and humidity) while this study is advantageous by preparing hydrophobic VTT sol-gel based coating in ambient environment. This allows for flexibility and simplification in fabricating the coating in bulk for industrial application with varied condition for different coating preparation.

## 4 Conclusions

Dust accumulation and soiling issues on the PV panel are, without a doubt, one of the main problems in maintaining PV performance. This has garnered research interest across the world to study the use of self-cleaning coating for solar panels in order to reduce the soiling issues. Various materials have been tested to achieve good self-cleaning properties; mainly focusing on hydrophobic coating. According to literature, application of  $\text{SiO}_2$  or  $\text{TiO}_2$  in self-cleaning coatings prepared via the sol-gel route have been proven to enhance hydrophobicity [20, 21]. Some of the advantages of preparing coating using sol-gel are: improvement in low refractive index, thermal and chemical stability which results to a better performance of PV panels in soiling mitigation [22, 23].

In this study, the developed unique VTT sol samples proven to exhibit self-cleaning ability based on hydrophobic properties shown ( $\text{WCA} > 90^\circ$ ). Besides, it also shown flexibility of the sol to be switched between hydrophobic and hydrophilic properties when undergo different temperature of thermal treatment, in accordance to a literature [18]. The coating also exhibited good transparency and transmittance of 90.73% that helped this self-cleaning coating to be applied on solar panels while



maintaining a good optical characteristic. This coating was prepared in ambient condition, reducing the need for controlled condition to suit the varied temperature and humidity for different coating preparation. This coating could be extensively used for further improvement by utilizing more variables such as coating layer, thickness or different materials in order to achieve superhydrophobicity ( $WCA > 150^\circ$ ) that promises better self-cleaning properties.

**Acknowledgement** The authors wish to thank the Ministry of Higher Education (MOHE) Malaysia and Universiti Teknologi Malaysia (UTM) for the award of the grant that enabled the research, leading to this article under the Research University Grant (VOT No.: Q.J130000.2523.19H40).

## References

1. He G, Zhou C, Li Z (2011) Review of self-cleaning method for solar cell array. *Procedia Eng* 16:640–645
2. Maghami MR, Hizam H, Gomes C, Radzi MA, Rezadad MI, Hajighorbani S (2016) Power loss due to soiling on solar panel: a review. *Renew Sustain Energy Rev* 59:1307–1316
3. Mozumder MS, Mourad AHI, Pervez H, Surkatti R (2019) Recent developments in multifunctional coatings for solar panel applications: a review. *Sol Energy Mater Sol Cells* 189:75–102
4. Jamil WJ, Abdul Rahman H, Shaari S, Salam S (2017) Performance degradation of photovoltaic power system: review on mitigation methods. *Renew Sustain Energy Rev* 67:876–891
5. Hirohata T, Ota Y, Nishioka K (2013) Effect of anti-soiling coating on performance of Fresnel lens for concentrator photovoltaic module
6. Rahmanian A, Rahmani A (2018) Effects and properties of double-layer anti-reflective coating  $\text{In}_2\text{O}_3/\text{Conic Al}_2\text{O}_3$  and three-layer anti-reflective coatings of  $\text{TiO}_2/\text{In}_2\text{O}_3/\text{Conic Al}_2\text{O}_3$  on silicon substrate. *Optik* 155:163–170
7. Liu H, Gao S, Cai J, He C, Mao J, Zhu T, Chen T, Huang J, Meng K, Zhang K, Al-Salem S, Lai Y (2016) Recent progress in fabrication and applications of superhydrophobic coating on cellulose-based substrates
8. Yan H, Yuanhao W, Hongxing Y (2017) TEOS/silane coupling agent composed double layers structure: a novel super-hydrophilic coating with controllable water contact angle value. *Appl Energy* 185:2209–2216
9. Lin J, Chen H, Fei T, Zhang J (2013) Highly transparent superhydrophobic organic–inorganic nanocoating from the aggregation of silica nanoparticles. *Colloids Surf, A Physicochem Eng Aspects* 421:51–62
10. Salim MR, Abdullah A, Nawabjan A, Ibrahim M, Kassim NM (2011) Simulation of optical wavelength filter using multimode interference (MMI) based on sol-gel derived organic–inorganic hybrid materials
11. Liu S, Liu X, Latthe S, Gao L, An S, Yoon S, Xing R (2015) Self-cleaning transparent superhydrophobic coatings through simple sol-gel processing of fluoroalkylsilane. *Appl Surf Sci* 351:897–903
12. Šiffalovič P, Jergel M, Benkovičová M, Vojtko A, Nádaždy V, Ivančo J, Majková E (2014) Towards new multifunctional coatings for organic photovoltaics. *Sol Energy Mater Sol Cells* 125:127–132
13. Ennaceri H, El Alami H, Brik H, Mokssit O, Khaldoun A (2014) Lotus effect and superhydrophobic coatings for concentrated solar power systems (CSP). In: International conference on composite materials & renewable energy applications (ICCMREA)

14. Baquedano E, Torné L, Caño P, Postigo P (2017) Increased efficiency of solar cells protected by hydrophobic and hydrophilic anti-reflecting nanostructured glasses. *Nanomaterials* 7(12):437
15. Swinehart DF (1962) The Beer-Lambert law. *J Chem Educ* 39(7):333
16. Ibrahim MH, Abdullah AS, Nawabjan A, Kassim NM, Mohammad AB, Supa'at ASM (2013) A thermo-optic multimode interference switch structure based on vinyltriethoxysilane (VTES) hybrid organic-inorganic sol-gel. *Optik* 124(13):1532–1535
17. Li C, Sun Y, Cheng M, Sun S, Hu S (2018) Fabrication and characterization of a TiO<sub>2</sub>/polysiloxane resin composite coating with full-thickness super-hydrophobicity. *Chem Eng J* 333:361–369
18. Ganesh V, Kumar H, Nair S, Ramakrishna S (2012) A review on self-cleaning coatings. *J Mater Chem* 21
19. Zhang X, Lin W, Zheng J, Sun Y, Xia B, Yan L, Jiang B (2017) Insight into the organic-inorganic hybrid and microstructure tailor mechanism of Sol-gel ORMOSIL antireflective coatings
20. Ye L, Zhang Y, Zhang X, Hu T, Ji R, Ding B, Jiang B (2013) Sol-gel preparation of SiO<sub>2</sub>/TiO<sub>2</sub>/SiO<sub>2</sub>-TiO<sub>2</sub> broadband antireflective coating for solar cell cover glass
21. Ye L, Zhang Y, Song C, Li Y, Jiang B (2017) A simple Sol-gel method to prepare superhydrophilic silica coatings. *Mater Lett* 188:316–318
22. Agustín-Sáenz C, Sánchez-García JÁ, Machado M, Brizuela M, Zubillaga O, Tercjak A (2018) Broadband antireflective coating stack based on mesoporous silica by acid-catalyzed Sol-gel method for concentrated photovoltaic application. *Sol Energy Mater Sol Cell* 186:154–164
23. Zhi J, Zhang L-Z (2018) Durable superhydrophobic surface with highly antireflective and self-cleaning properties for the glass covers of solar cells. *Appl Surf Sci* 454:239–248

# Effect of Graphene Oxide Nanoparticles on Thermal Properties of Paraffin Wax



Nurul Humaira Muhd Zaimi, Amirjan Nawabjan,  
Shaharin Fadzli Abdul Rahman and Siti Maherah Hussin

**Abstract** Whereas previous studies analyzed thermal properties of pure paraffin, this paper analyzed thermal properties of paraffin added with Graphene Oxide (GO) nanoparticles experimentally. The tested samples are paraffin wax and GO added at various percentages of weight, 1 wt%, 3 wt%, 5 wt% which typically used for photovoltaic panel cooling. The objective is to explore the effect of various weight percentages of GO nanoparticles addition on the thermal properties of the paraffin. All the thermal properties were measured by using thermographic camera, and Differential Scanning Calorimetry (DSC). DSC showed that melting and solidification temperature for paraffin/5 wt% GO has highest reduction which is at 45.91 °C and 41.85 °C, followed by paraffin/3 wt% GO with 46.15 °C and 42.02 °C, and then paraffin/1 wt% GO with 46.25 °C and 42.02 °C, when compared to 63 °C and 59.5 °C for pure paraffin. Thermographic camera recorded the melting temperature history of all samples for 600 s. From the measurement, it is revealed that paraffin/5 wt% GO has largest heat transfer rate. This is shown by the bigger average temperature gradient of paraffin/5 wt% GO which is at 2.93 followed by paraffin/3 wt% GO at 2.69, paraffin/1 wt% GO at 2.52 and paraffin at 2.03. DSC also revealed that paraffin/5 wt% GO has highest improvement in latent heat which is 163.99 kJ/kg, followed by paraffin/1 wt% GO, paraffin/3 wt% GO and pure paraffin each at 155.85 kJ/kg, 155.0813 kJ/kg and 102 kJ/kg. Paraffin/5 wt% GO also can be seen to have the largest amount of heat stored with 0.62 kJ, followed by paraffin/3 wt% GO, paraffin/1 wt% GO and lastly pure paraffin with 0.44, 0.4 and 0.33 kJ respectively. The results indicate that the rise of GO nanoparticles percentages weight added results in better thermal properties

---

N. H. Muhd Zaimi · A. Nawabjan (✉) · S. M. Hussin  
Faculty of Engineering, School of Electrical Engineering, Centre of Electrical Energy Systems,  
Institute of Future Energy, Universiti Teknologi Malaysia, Johor Bahru, Malaysia  
e-mail: [amirjan@utm.my](mailto:amirjan@utm.my)

N. H. Muhd Zaimi  
e-mail: [nhumaira3@live.utm.my](mailto:nhumaira3@live.utm.my)

S. F. A. Rahman  
Faculty of Engineering, School of Electrical Engineering, Universiti Teknologi Malaysia,  
Johor Bahru, Malaysia

of paraffin. With better charging and discharging rate, highest latent heat, largest amount of heat can be stored, paraffin/5 wt% GO is the most favorable to be used as a photovoltaic panel coolant.

**Keywords** Phase change material · Paraffin · Graphene oxide · Photovoltaic · Temperature regulation

## 1 Introduction

During the last two decades, rising prices of fossil fuel and increasing worries about global warming have reenergized the idea to rapidly move towards renewable energy resources. Over the years, photovoltaic (PV) has been gaining interest. PV offers the most abundant, reliable and pollution-free power source in the world [1, 2]. PV is a technique of converting sunlight into electricity by using semiconductor materials through photovoltaic effect.

By the end of 2018, global cumulative installation of PV already exceeded astonishing number of 515GW with an average commercial efficiency of 17% [3]. However, efficiency of PV panel declines with an increase in temperature, especially in hot climate countries including Malaysia. In many instances, a solar cell can get as hot as 65 °C, causing the panel to become less efficient and therefore produce less power. For instance, every increment of 1 °C of PV panel operating temperature will decrease as much as 0.4% of electricity production [4].

Thus, many techniques have been done to cool the PV panel including water sprinkler at the front of panel, using heat sinks, and connecting air channel at the back of PV panel. One of the passive methods is by integrating phase change materials (PCM) into the back of PV panel in order to reduce the temperature of the PV itself [5–12]. It has shown major advantages in improving PV output performance by maintaining the temperature of PV panel close to the ambient. PV/PCM systems can control the rapid increase of PV cell temperatures during the daytime and keep PV panel temperatures lower during the peak solar hours of the day, thus improving PV efficiency and electrical energy output.

Although many studies have used PCM in cooling PV, PCM has low thermal conductivity which results in low heat transfer. In order to improve the thermal conductivity of the PCM, few previous studies were conducted by using nanoparticles [9, 13]. So, through the combination of PCM and nanoparticles, the thermal properties can be adjusted including enhancing its thermal conductivity and thus resulting in a better heat transfer [14]. As a result, PCM will be better at reducing the temperature of the PV panel during hot climate leading to more efficient output power.

Nevertheless, further studies need to be done on the heat transfer process and thermal properties of PCM material when added by nanoparticles. PCM material can be found in various practical applications including PV panel. In PV panel application, paraffin wax is the most used by researchers. Few studies on paraffin wax application can also be found in the literature [9–12, 15–20]. In this study, the thermal

properties of PCMs and effect of nanoparticles are investigated experimentally. The tested PCMs and nanoparticles are paraffin wax and various percentages of weight of GO nanoparticles added to paraffin. The objective of this study is to explore the thermal properties of PCMs when GO nanoparticles at various percentages of weight are added. The results are expected to provide the necessary information on development of PV performance that is suitable for Malaysian climate.

## 2 Methods

### 2.1 Fabrication of Nano-enhanced PCM

Paraffin is weighed to obtain a mass of 10 g followed by GO nanoparticles. The paraffin is melted at temperature of 80 °C until it is ensured fully melted. GO nanoparticles and 0.2 g Sodium Dodecylbenzenesulfonate (SDBS) are then added to the molten paraffin. SDBS are added to ensure the dispersion of mixture and avoiding agglomeration of samples. The temperature was maintained at 80 °C throughout the experiment. The mixing is prepared by using magnetic stirrer for 15 min. The mixture is then poured into a petri dish and is allowed to crystallize at room temperature. The experiments are carried out for three different percentages of GO nanoparticle's weight, which are at 1 wt%, 3 wt% and 5 wt%. The experimental procedure to fabricate PCM nanocomposites are shown as in Fig. 1.

### 2.2 Analysis Methods

#### 2.2.1 Melting and Solidification Process

The melting and solidification process of the PCM nanocomposites was recorded using thermal camera and the time taken for the process was measured. For melting process, each sample was put on the hot plate with temperature of 80 °C until it is fully melted, and the time taken for the sample to fully melt was recorded. Then, it was allowed to solidify at room temperature and the time taken for the sample to fully solidify was recorded. The experiment was repeated for pure paraffin, paraffin/1 wt% GO, paraffin/3 wt% GO and paraffin/5 wt% GO. Next, experiment was conducted to study the increasing of PCM nanocomposites temperature during melting process. The experimental setup was as in Fig. 2. The hot plate is ensured to have uniform temperature so that it will provide uniform heat transfer to the sample. A picture of initial temperature of hot plate was provided in Fig. 4. There were 9 points taken from sample for measurement to obtain most accurate average temperature and temperature gradient of sample. During the melting process, the hot plate was set constant

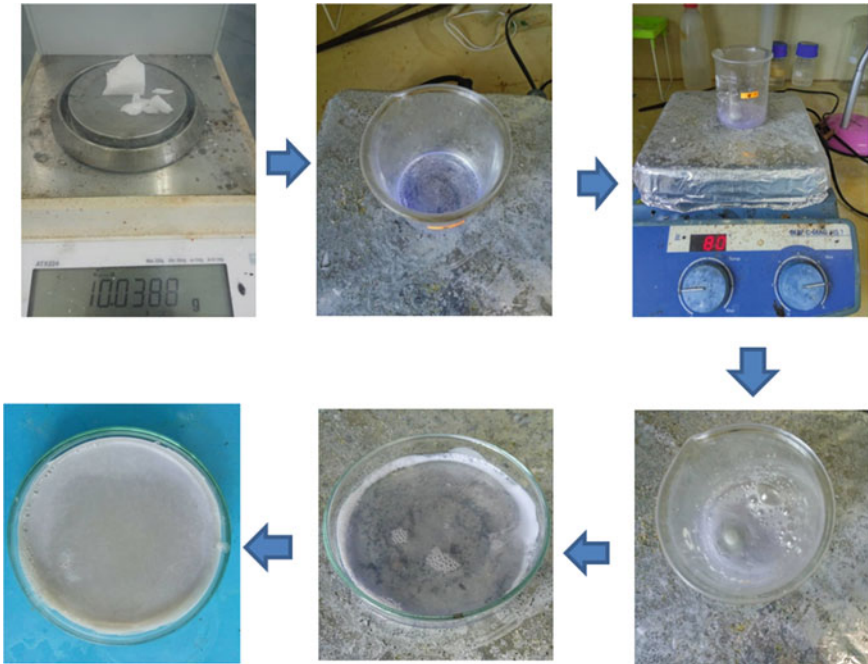


**Fig. 1** Fabrication of paraffin/GO nanocomposites

at 100 °C and the PCM nanocomposites' temperature was measured by using thermographic camera for each 60 s interval until it was fully melted. Every experiment was carried out for 600 s and repeated for pure paraffin, 1 wt% GO, 3 wt% GO and 5 wt% GO. All the 9 points of melting temperature measurement were collected and a graph was generated to analyse the gradient from the obtained temperature history graph. Heat transfer can be compared for all the samples by comparing gradient of the graph [21].

### 2.2.2 Differential Scanning Calorimeter

Characterization of the phase change materials, including melting/solidification temperatures, latent heat and specific heat capacity of the paraffin/GO nanocomposites samples was performed by using Differential Scanning Calorimeter (DSC). A complete run of the DSC test consists of two heating and cooling cycles that were run from 30 to 100 °C, in order to embrace the melting point of paraffin wax. The first melting cycle was carried out to remove the effect of uneven heating of samples, and hence the data from the second cycle were recorded. Paraffin/GO nanocomposites sample of 5 mg of each material was heated from 30 to 100 °C at a heating rate of 5 °C min<sup>-1</sup> and cooled at the same rate.

**Fig. 2** Experimental setup for melting and solidifying process using thermographic camera



### 2.3 Theoretical

Performance of the samples prepared must be evaluated and before the analysis could be carried out, several parameters need to be specified and investigated. One of the parameters is the latent heat storage (LHS). This parameter is depending on the heat absorption when the material changing phases from solid into liquid, or vice versa. The amount of heat required for the material to change from one phase to another is defined as follows:

$$Q_L = m \times a_m \times \Delta h_m \quad (1)$$

where,

- $Q_L$  Total latent heat (Joule).
- $m$  Mass (kg).
- $a_m$  PCM's melting fraction.
- $\Delta h_m$  Latent heat specific (Joule/kg).

The amount of heat stored during the absence of phase-changing (the material is either in solid or liquid phase) can be formulated as follows:

$$Q_S = m \times c_p \times \Delta T \quad (2)$$

where,

- $Q_S$  Total heat stored (Joule).
- $m$  Mass (kg).
- $c_p$  Heat capacity (kJ/kgK).
- $\Delta T$  Temperature difference (m<sup>2</sup>).

Combining these two formulas, the performance analysis of PCM can be determined while taking into account all the parameters involved.

### 3 Results and Discussion

The experiments on all four samples, pure paraffin, paraffin/1 wt% GO, paraffin/3 wt% GO and paraffin/5 wt% GO were carried out. The results were analyzed based on the time taken for all samples to fully melt and solidify, temperature history during melting processes, heat transfer rate, melting and solidification point, latent heat and total heat stored by samples.

#### 3.1 Melting and Solidifying Time

Figure 3 shows the melting process of PCM nanocomposites. The time taken for melting and solidifying is recorded by using stopwatch.

Temperature and time for Melting and solidification process are the two main parameters which influence the performance of PCM. Melting and solidification time can be measured by using stopwatch. In order to investigate the charging and discharging characteristics of PCM, melting and solidification time also needs to be



Fig. 3 Melting process of nanocomposites



**Table 1** Melting and solidification time of PCM nanocomposites

Sample	Solidifying time (s)	Melting time (s)
Pure paraffin	730	1260
Paraffin with 1 wt% GO	340 (53.42%)	435 (65.48%)
Paraffin with 3 wt% GO	242 (66.85%)	367 (70.87%)
Paraffin with 5 wt% GO	200 (72.60%)	349 (72.30%)

considered. The melting time of the PCM decreases with the insertion of nanoparticles. Table 1 shows the variation of paraffin and paraffin/GO nanocomposites melting time with respect to temperature. The percentage time savings for paraffin/1 wt% GO for complete melting was found to be 65.48% as compared to pure paraffin. While the percentage time savings for paraffin/3 wt% GO and paraffin/5 wt% GO for complete melting were found to be 70.87% and 72.30% as compared to pure paraffin. The time taken for complete melting of paraffin, paraffin/1 wt% GO, paraffin/3 wt% GO, and paraffin/5 wt% GO was found to be 1260 s, 435 s, 367 s and 349 s respectively. It can be observed that the time taken for complete solidification of paraffin was highest compared to all paraffin/GO nanocomposites samples. The percentage time savings in solidification time of paraffin/1 wt% GO, paraffin/3 wt% GO and lastly paraffin/5 wt% GO were found to be 53.42%, 66.85% and 72.60% respectively as compared to pure paraffin. The time taken for complete solidification for paraffin was 730 s, paraffin/1 wt% GO 340 s, paraffin/3 wt% GO 242 s, and paraffin/5 wt% GO was found to be 200 s. The image of complete melting process of paraffin/GO nanocomposites is depicted in Fig. 3. Thus the addition of higher percentage of GO nanoparticles weight also improves the charging and discharging period of the PCM.

### 3.2 Temperature of Melting Process

As mentioned before, there was 9 points taken for temperature reading and the initial temperature of hot plate is measured to ensure uniform heating. The initial temperature of hot plate is as in Fig. 4. Figure 5 shows the temperature history during melting process for all paraffin/GO nanocomposites samples when the heat source at 100 °C. The temperature for paraffin, paraffin/1 wt% GO, paraffin/3 wt% GO and paraffin/5 wt% GO are shown by Fig. 5a–d.

According to theory, during the heating process of solid PCM material, its temperature will undergo increment as time increases until it reach its melting point. During the melting process, its temperature will remain constant after all of the PCM material have become liquid. After all the melting process has finished, the temperature will continue to increase with time. This experiment shows an agreement with theoretical one pattern. This is because, in Fig. 5a, during the first 60 s, temperature

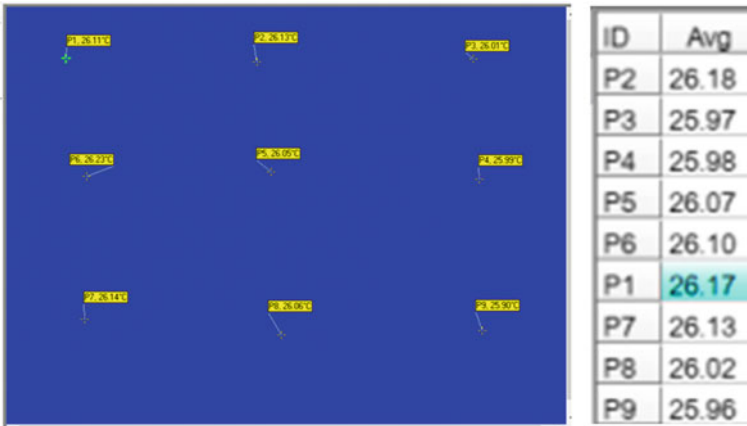


**Fig. 4** Initial temperature of hot plate

of paraffin wax increases as time increases. It starts from initial temperature which is at 27 °C. After reaching its melting point, the temperature remain constant. This means the PCM nanocomposites is currently undergoing melting process. After the melting has finished, the temperature continue to increase. This means that the experiments follow the theoretical one. All the other 9 points of temperature shows the same consistency of graph. The same trend also shown by other samples as shown in Fig. 5b–d.

After 360 s, for pure paraffin, it can be seen that in the graph, some of the temperature point is increasing rapidly and higher compared to other points. This is due to the uneven heating of the sample which causes at some of the point, the paraffin start to melt first, only then followed by other part of samples. The same trend can be seen by all the other samples, paraffin/1 wt% GO, paraffin/3 wt% GO and paraffin/5 wt% GO.

Temperature measurements of melting processes have been done. The results are analyzed. Table 2 shows final average temperature of all paraffin/GO nanocomposites and it can be seen that the paraffin/5 wt% GO has the highest final melting temperature that is 63.99 °C. It is then followed by paraffin/3 wt% GO, 61.20 °C, paraffin/1 wt% GO, 59.56 °C, and lastly pure paraffin, 56.04 °C. Next, Table 3 shows the average gradient of all paraffin/GO nanocomposites. The comparison between Fig. 5a–d shows that heat transfer rate of paraffin/5 wt% GO is largest than all the other samples. This is also shown by the bigger average temperature gradient value in Table 3. It can be seen paraffin/5 wt% GO in comparison with others which is 2.93 followed by paraffin/3 wt% GO at 2.69, paraffin/1 wt% GO at 2.52 and paraffin at 2.03. All the samples, paraffin/5 wt% GO, paraffin/3 wt% GO and paraffin/1 wt% GO follow the trend that states the addition of nanoparticles will increase the rate of heat transfer.

It also can be concluded that paraffin/5 wt% GO has the highest thermal conductivity compared to other samples, this is because of the high heat transfer rate by paraffin/5 wt% GO, since thermal conductivity can be defined as the rate of heat

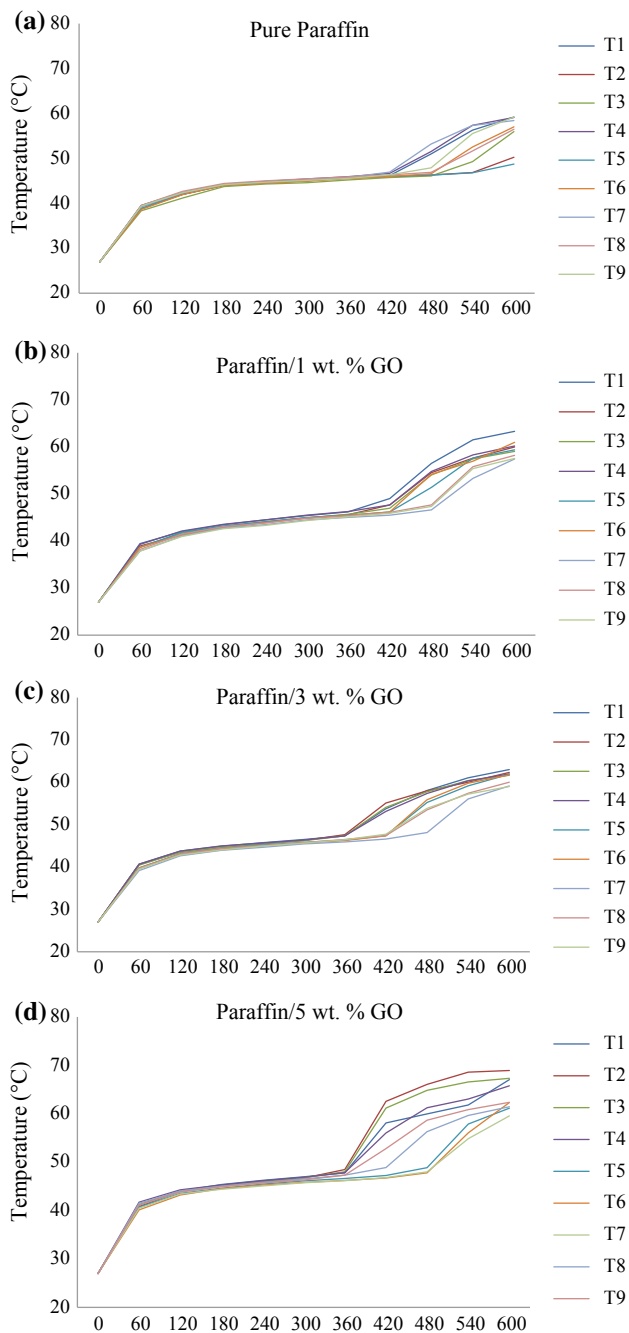


**Fig. 5** **a** Melting temperature history of paraffin, **b** melting temperature history of paraffin/1 wt% GO, **c** melting temperature history of paraffin/3 wt% GO, **d** melting temperature history of paraffin/5 wt% GO

**Table 2** Average final temperature of paraffin/GO nanocomposites

Final temp	Paraffin (°C)	Paraffin/1 wt% GO (°C)	Paraffin/3 wt% GO (°C)	Paraffin/5 wt% GO (°C)
1	59.2	63.31	63.02	67.04
2	50.26	59.98	62.34	68.94
3	55.94	59.04	61.65	67.31
4	59.11	60.19	61.98	65.78
5	48.74	59.36	61.89	61.15
6	57.03	60.96	61.75	62.31
7	58.43	57.42	59.13	59.56
8	56.48	58.2	60.01	61.44
9	59.2	57.55	59.01	62.35
Average	56.04	59.56	61.20	63.99

**Table 3** Average gradient of paraffin/GO nanocomposites

Gradient	Paraffin	Paraffin/1 wt% GO	Paraffin/3 wt% GO	Paraffin/5 wt% GO
1	2.38	2.97	2.94	3.25
2	1.51	2.64	2.92	3.86
3	1.89	2.56	2.88	3.64
4	2.41	2.64	2.84	3.21
5	1.43	2.49	2.68	2.38
6	2.04	2.63	2.73	2.36
7	2.44	2.16	2.28	2.18
8	1.94	2.30	2.50	2.64
9	2.25	2.28	2.48	2.89
Average	2.03	2.52	2.69	2.93

transfer through unit thickness of the material per unit area per unit temperature difference [22]. A high value for thermal conductivity indicates that the sample is a good conductor heat, which is one of the important characteristic in order to become a PV coolant. Hasan states that PCM should have a high thermal conductivity [15].

### 3.3 Differential Scanning Calorimetry Curve

Figures 6, 7, 8 and Table 4 shows each melting and solidification characteristic of paraffin, paraffin/1 wt% GO, paraffin/3 wt% GO and paraffin/5 wt% GO. A reduction can be observed in both melting and solidification temperature for all paraffin/GO nanocomposites when compared to pure paraffin. Initially, the melting temperature

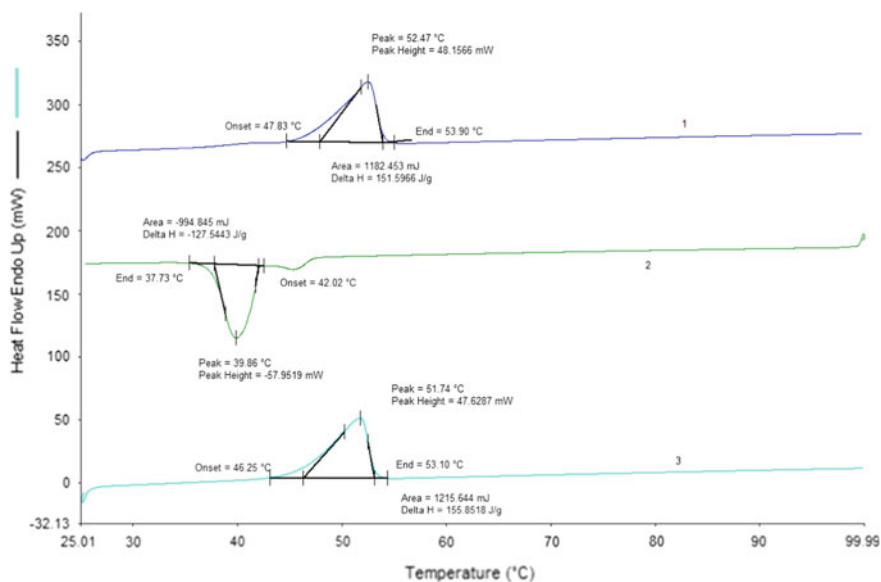


Fig. 6 DSC curves of paraffin/1 wt% GO

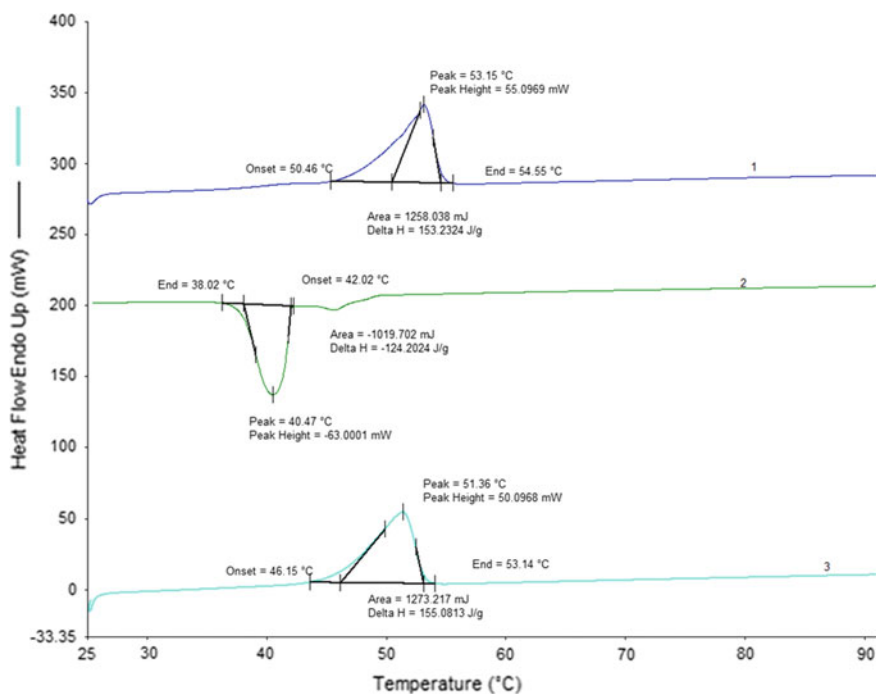
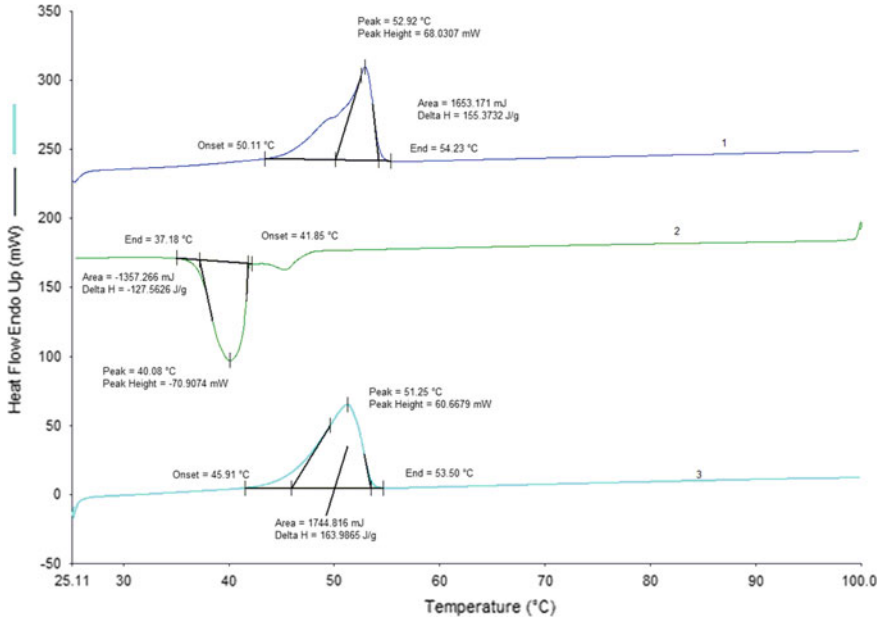


Fig. 7 DSC curves of paraffin/3 wt% GO



**Fig. 8** DSC curves of paraffin/5 wt% GO

**Table 4** Latent heat, melting and solidification point of samples

Sample	Melting point (°C)	Solidification point (°C)	Latent heat (kJ/kg)
Pure paraffin	63	59.5	102
Paraffin with 1 wt% GO with SDBS	46.25	42.02	155.85
Paraffin with 3 wt% GO with SDBS	46.15	42.02	155.08
Paraffin with 5wt% GO with SDBS	45.91	41.85	163.99

of pure paraffin was 63 °C, however, when 1 wt% GO nanoparticles was impregnated in Paraffin, the melting point reduced to 46.25 °C. While, when 3 wt% GO nanoparticles was added, the melting point reduced to 46.15 °C, and lastly when 5 wt% GO nanoparticles added, the melting point reduced to 45.91 °C. Solidification temperature for the entire PCM nanocomposites also shows the same behavior. The solidification temperature of pure paraffin was found to be 59 °C and when 1 wt% GO nanoparticles was impregnated in paraffin, the solidification point decreased to 42.02 °C. While, when 3 wt% GO nanoparticles was added, the solidification point decreased to 42.02 °C, and lastly when 5 wt% GO nanoparticles added, the melting point reduced to 41.85 °C. To summarize, the higher percentage of GO nanoparticles have tendency to reduce more melting and solidification temperature. This can be

seen from paraffin/5 wt% GO has lowest melting and solidification point, followed by paraffin/3 wt% GO, next is paraffin/1 wt% GO and lastly pure paraffin.

DSC analysis was used to measure the latent heat of paraffin and paraffin/GO nanocomposites. All the data have been recorded in Table 4. The latent heat of paraffin measured was 102 kJ/kg and when GO nanoparticles was added, an interesting characteristic can be seen, which was higher percentage of GO nanoparticles shows higher increment in latent heat than that pure paraffin. The latent heat of paraffin/5 wt% GO was highest at 163.99 kJ/kg followed by paraffin/1 wt% GO with 155.08 kJ/kg and paraffin/3 wt% GO at 155.85 kJ/kg. Both paraffin/5 wt% GO, and paraffin/1 wt% GO follows the rules that states higher addition of nanoparticles improve better latent heat of PCM. However, for the paraffin/3 wt% GO, it differ with the rules as it has lower latent heat than paraffin/1 wt% GO. This may be due to the carbon and oxygen bond arrangement in structural lattice, hydrophilic material, aggregation property, and dispersing property with organic solvents [23]. Still, the latent heat of paraffin/3 wt% GO is higher than pure paraffin. Hence, higher improvement in latent heat and latent heat energy storage capacity of pure paraffin can be observed when larger GO nanoparticles weight was added in paraffin.

### 3.4 Total Heat Stored

The performance of the paraffin/GO nanocomposites will be analysed by using total heat stored, defined by Eq. (2). Calculations were carried out by using all the data recorded throughout experiments. Table 5 shows the calculation result for total heat stored. Data of the table shows that the higher percentage of GO nanoparticles impregnated into paraffin, the higher final melting temperature captured through thermographic camera. It can be seen that paraffin/5 wt% GO can store the heat better than all the other samples as it has highest temperature difference, highest heat capacity compared to all the other samples, resulting in highest heat stored. Study shows that amount of heat transfer is directly proportional to the temperature change [22]. As thermal energy storage, paraffin/5 wt% GO is better than all the other samples. This is because paraffin/5 wt% GO can store more energy compared to others.

**Table 5** Calculation result for total heat stored

Materials	Heat source	Mass (kg)	$C_p$ (kJ/kgK)	$T_f$ (°C)	$T_i$ (°C)	$Q_s$ (KJ)
Paraffin wax	100	0.01	1.14	56.04	27	0.33
Paraffin/1 wt% GO	100	0.01	1.22	59.56	27	0.4
Paraffin/3 wt% GO	100	0.01	1.27	61.2	27	0.43
Paraffin/5 wt% GO	100	0.01	1.64	63.99	27	0.62

## 4 Conclusion

A new PCM composite was prepared by adding various percentages of Graphene oxide nanoparticles weight to paraffin wax that can be used to cool PV panel. Thermal properties such as melting and solidification point, phase change temperature, latent heat and total heat stored of the new phase change material were investigated experimentally to study the effect of various percentages of GO nanoparticles weight added to paraffin. Melting temperature history and latent heat were measured by using thermographic camera and DSC, while heat stored was calculated from the data obtained. Based on the results, the following conclusions can be made.

Higher percentages of GO nanoparticles result in higher improvement of paraffin thermal properties. This can be observed as for the melting and solidification temperature for paraffin/5 wt% GO has largest reduction, at 45.91 °C and 41.85 °C, followed by paraffin/3 wt% GO with 46.15 °C and 42.02 °C, and lastly paraffin/1 wt% GO with melting and solidification temperature 46.25 °C and 42.02 °C respectively compared to 63 °C and 59.5 °C for pure paraffin. Paraffin/5 wt% GO also showed better charging and discharging rates decreased by 72.30% and 72.60%, followed by paraffin/3 wt% GO with 70.87% and 66.85% reduction and lastly paraffin/1 wt% GO with 65.48% and 53.42% reduction respectively compared to pure paraffin. Next, heat transfer rate of paraffin/5 wt% GO is largest than all the other samples. This is shown by the bigger average temperature gradient of paraffin/5 wt% GO compared to others which is at 2.93 followed by paraffin/3 wt% GO at 2.69, paraffin/1 wt% GO at 2.52 and paraffin at 2.03. Besides, paraffin/5 wt% GO also showed highest improvement in latent heat compared to others which is 163.99 kJ/kg, followed by paraffin/1 wt% GO, paraffin/3 wt% GO and pure paraffin at 155.85 kJ/kg, 155.0813 kJ/kg and 102 kJ/kg. Both paraffin/5 wt% GO and paraffin/1 wt% GO follows the trend that states higher percentages of nanoparticles, resulting in better thermal properties except for paraffin/3 wt% GO. This is due to the existence of aggregation in the samples. The same thing can be observed for the heat stored by paraffin/5 wt% GO. It has the largest amount of heat stored with 0.62 kJ, followed by paraffin/3 wt% GO, paraffin/1 wt% GO and lastly pure paraffin with 0.44, 0.4 and 0.33 kJ respectively.

Thus, it can be concluded that higher percentage of GO weight nanoparticles, improve better thermal properties of paraffin. As a PV panel coolant, paraffin/5 wt% GO is favorable to be used as a PV panel coolant, as it has better charging and discharging rate, highest latent heat, better heat transfer and can store most amount of heat compared to all the other samples.

## References

1. Shukla A et al (2017) Cooling methodologies of photovoltaic module for enhancing electrical efficiency: a review. *Sol Energy Mater Sol Cells* 160:275–286
2. Sargunanathan S, Elango A, Mohideen ST (2016) Performance enhancement of solar photovoltaic cells using effective cooling methods: a review. *Renew Sustain Energy Rev* 64:382–393



3. *Global Market Outlook 2018–2022*. 2018; Available from <https://www.solarpowereurope.org/global-market-outlook-2018-2022/>
4. *The effect of temperature on solar panel performance*. [cited 2018 10/10/18]; Available from <https://solarcalculator.com.au/solar-panel-temperature/>
5. Smith CJ, Forster PM, Crook R (2014) Global analysis of photovoltaic energy output enhanced by phase change material cooling. *Appl Energy* 126:21–28
6. Jun Huang M (2011) The effect of using two PCMs on the thermal regulation performance of BIPV systems. *Sol Energy Mater Sol Cells* 95(3):957–963
7. Ma T et al (2015) Using phase change materials in photovoltaic systems for thermal regulation and electrical efficiency improvement: a review and outlook. *Renew Sustain Energy Rev* 43:1273–1284
8. Nada SA, El-Nagar DH (2018) Possibility of using PCMs in temperature control and performance enhancements of free stand and building integrated PV modules. *Renew Energy* 127:630–641
9. Nada SA, El-Nagar DH, Hussein HMS (2018) Improving the thermal regulation and efficiency enhancement of PCM-Integrated PV modules using nano particles. *Energy Convers Manage* 166:735–743
10. Sharma S et al (2017) Nano-enhanced phase change material for thermal management of BICPV. *Appl Energy* 208:719–733
11. Sharma S et al (2016) Performance enhancement of a building-integrated concentrating photovoltaic system using phase change material. *Sol Energy Mater Sol Cells* 149:29–39
12. Stropnik R, Stritih U (2016) Increasing the efficiency of PV panel with the use of PCM. *Renew Energy* 97:671–679
13. Alshaer WG et al (2015) Numerical investigations of using carbon foam/PCM/Nano carbon tubes composites in thermal management of electronic equipment. *Energy Convers Manage* 89:873–884
14. Moghadassi A, Hosseini M, Henneke D (2010) Effect of CuO nanoparticles in enhancing the thermal conductivities of monoethylene glycol and paraffin fluids, vol 49
15. Hasan A et al (2017) Yearly energy performance of a photovoltaic-phase change material (PV-PCM) system in hot climate. *Sol Energy* 146:417–429
16. Khanna S, Reddy KS, Mallick TK (2018) Climatic behaviour of solar photovoltaic integrated with phase change material. *Energy Convers Manage* 166:590–601
17. Khanna S, Reddy KS, Mallick TK (2018) Optimization of finned solar photovoltaic phase change material (finned pv pcm) system. *Int J Therm Sci* 130:313–322
18. Khanna S, Reddy KS, Mallick TK (2018) Optimization of solar photovoltaic system integrated with phase change material. *Sol Energy* 163:591–599
19. Hasan A, Alnoman H, Rashid Y (2016) Impact of integrated photovoltaic-phase change material system on building energy efficiency in hot climate. *Energy Build* 130:495–505
20. Wu Y (2009) Thermal management of concentrator photovoltaics. University of Warwick
21. Ambarita H et al (2017) Experimental study on melting and solidification of phase change material thermal storage, vol 180, p 012030
22. Bahrami M, Steady conduction heat transfer. Available from <https://www.sfu.ca/~mbahrami/ENSC%20388/Notes/Steady%20Conduction%20Heat%20Transfer.pdf>
23. Dsilva Winfred Rufuss D et al (2017) Low mass fraction impregnation with graphene oxide (GO) enhances thermo-physical properties of paraffin for heat storage applications. *Thermochim Acta* 655:226–233

# Reliability Performance of Low Voltage (LV) Network Configuration



Mohd Ikhwan Muhammad Ridzuan , Muhammad Adib Zufar Rusli   
and Norhafidzah Mohd Saad 

**Abstract** Networks are typically modelled in single phase diagram especially for medium voltage (MV) and high voltage (HV) networks. For low voltage (LV) networks, it is not suitable to model it in a single phase diagram. The reliability performance of LV network may be overestimated or underestimated if the network is modelled in a single phase diagram. Analytical technique is used to quantify the performance of LV network in single and three phase network diagrams. Three phase LV network diagram illustrates the true reliability performance compared to single phase LV network diagram in term of the best, median and worst location of customers. Accurate network configuration may benefit in minimizing energy core losses and reducing paying penalty to the customer by distribution network operators (DNOs).

**Keywords** Reliability · Distribution network · Single phase diagram · Three phase diagram

## 1 Introduction

Typically, the importance of reliability in distribution system has received less attention compared to generation and transmission systems. The main reason of these two systems are significant due to these two systems carries high current that affects a vast number of customer (indirectly) and considers as a backbone of electrical supply (especially transmission network). However, the importance of distribution network should not be neglected as it directly connected to the end customer.

Since distribution network supplying the most customer, it ties up by the target or minimum customer satisfaction level imposed by Energy Regular, which in Malaysia is Energy Commission (EC). These targets mostly involved the frequency and duration of interruption. To attain that target, distribution network operators (DNOs) must correctly assess their reliability performance. Therefore, it is critical to have accurate

---

M. I. Muhammad Ridzuan (✉) · M. A. Z. Rusli · N. Mohd Saad  
Faculty of Electrical & Electronics Engineering, Universiti Malaysia Pahang, 26600 Pekan,  
Pahang, Malaysia  
e-mail: [ikhwanr@ump.edu.my](mailto:ikhwanr@ump.edu.my)

distribution network configurations and parameters. However, due to the size of distribution network, low voltage (LV) network often represented by aggregate model [1–6].

Typically, the aggregate model of LV network is represented by active and reactive power downstream from the point of aggregation. For certain steady-state analysis, the LV representation of active and reactive powers are enough, but in term of reliability perspective, additional information is required especially in fault rates and mean time to repair (MTTR) input. The detail reliability input from LV representation may decide the performance level of distribution network.

Furthermore, in the EC report [7], a vast number of customer interruption is originated from LV network, compared to medium voltage (MV) and high voltage (HV) networks as in Fig. 1. Customer Average Interruption Duration Index (CAIDI) is defined as average interruption time per customer affected by the interruption. In the same report, CAIDI from LV network is higher than MV and HV networks as in Fig. 2. From these statements, the distribution network should include reliability input of LV network for analyses of MV or HV/MV networks. Therefore, by properly illustrating the configuration of LV networks in MV or HV/MV networks, no components will be neglected in regards to the load aggregation from lower to higher voltage.

Another concern related with LV network is modelling of network diagram. Typically, most of the network is modelled as a single line diagram, where all customer of each phases (red, yellow and blue phases) are connected to single conductor. In another word, if the blue phase is faulty/interrupted, other phases (red and blue) also interrupted. The modelling of LV network in single line diagram is incorrect as the protection devices in LV network operate in individual phase. For MV and HV networks, the modelling of network as single line diagram is correct as the protection

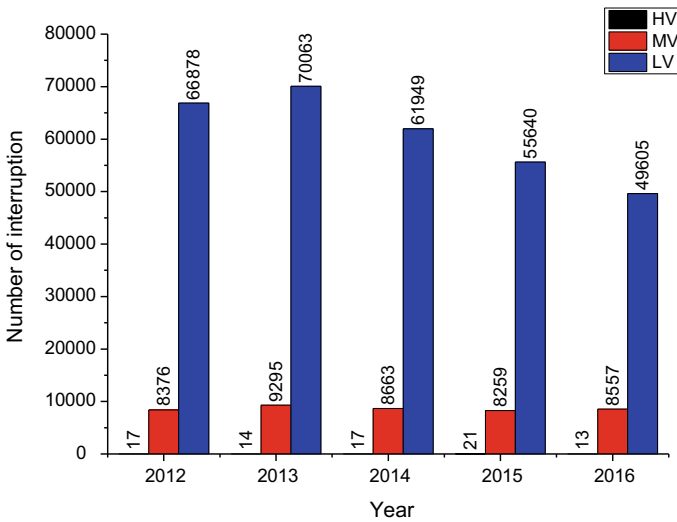
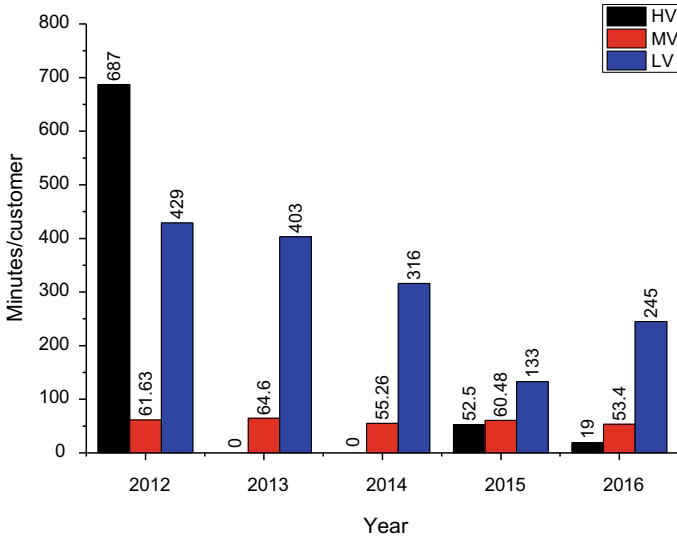


Fig. 1 Number of interruption by voltage variation



**Fig. 2** Duration of interruption by voltage variation

devices are operating in three phases system [8–13]. Hence, ignoring the design of LV network in three phases diagram will underestimate the reliability performance of network.

Therefore, accurate reliability performance can be obtained with detail and correct design of LV network for analyses of MV or HV/MV networks. Concerning this matter, the paper aims to present the methodology of formulating accurate LV distribution network model based on reliability inputs of network component, component parameters and network configuration.

## 2 Reliability Input

The reliability assessment of distribution system required distribution network complete with its configurations and parameters and reliability input in term of fault rates and mean times to repair (MTTR) of network components.

### 2.1 LV Distribution Network

The considered network for these analyses is rural LV distribution network. The network consists of a single transformer with a rating of 500 kVA, and the line feeder is

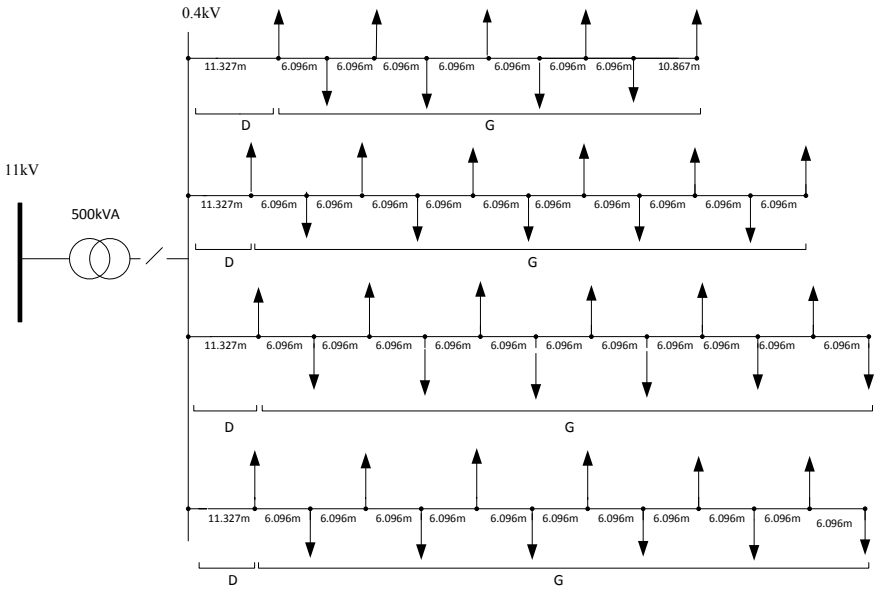


Fig. 3 Rural LV distribution network (single phase diagram)

mostly overhead lines carrying 230 V for each phases supplying a total of 44 domestic customers. Star connection is used allowing the employment of two different voltages; 230 and 400 V. The network configuration is radial without normally open network reconfiguration or back-up supply. Figures 3 and 4 present rural LV network in single and three phases diagram respectively. Tables 1 and 2 provide more details for the network components.

### 2.2 Mean Fault Rates and Repair Times

Past recording and statistic data are significant for predicting and assessing future and present reliability performance of distribution network. These data are required for simulation technique to characterise the performance of distribution network under analysis. Two of three (i.e. mean fault rates, MTTR and unavailability) general reliability input are required to perform the simulation. The mean fault rates represent the total number of times in a year the component has to be removed from service for repair due to the failure that occurs while MTTR represents the average times required to repair the components that affected by the failure. Table 3 presents the statistic of mean fault rates and MTTR of network components.

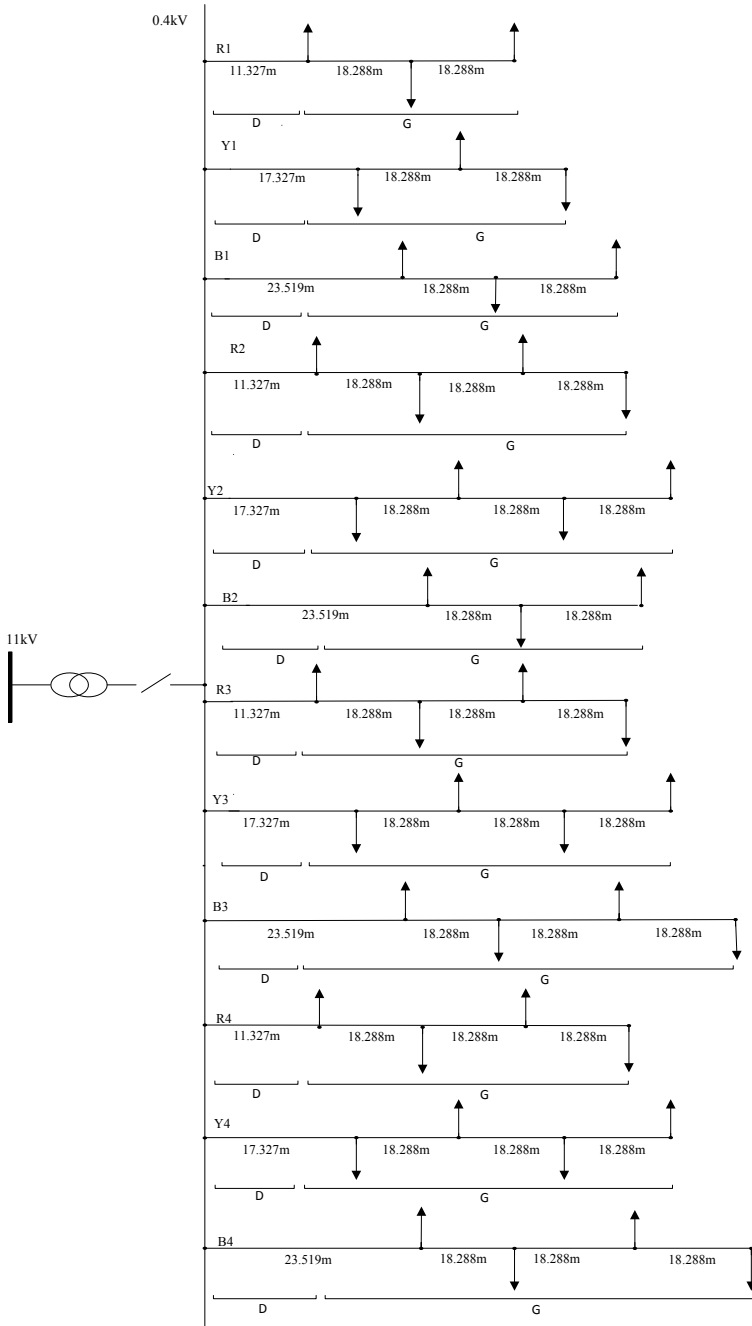


Fig. 4 Rural LV distribution network (three phase diagram)

**Table 1** Feeder parameters

LV feeder	Id.	Cross section (mm <sup>2</sup> )	Maximum sustained current (A)	R <sub>ph</sub>	X <sub>ph</sub>
Underground cable Ethylene propylene rubber	A	25	110	0.87	0.085
	B	70	190	0.443	0.076
	C	120	250	0.253	0.071
	D	185	320	0.164	0.074
	E	300	400	0.1	0.073
Overhead lines Aerial bundle conductor (ABC)	F	1 × 16 + 25	80	2.33	0.139
	G	3 × 16 + 25	80	2.33	0.13
	H	3 × 95 + 70	190	0.39	0.108
	I	3 × 185 + 120	300	0.2	0.103

**Table 2** Transformer parameters

Rating	Connection	Tapping range	Load losses at 75 °C (W)	No-load losses (W)	Impedance (%)	Model parameters (p.u. on 100 MVA)	
						RLV	XLV
500	Dyn11	±5% in 2.5% taps	5100	680	4.75	2.04	9.28
315			3420	580	4.75	3.4444	14.6794
200			2900	540	4.75	7.5	22.5

### 3 Reliability Assessment

The Analytical technique is used to assess the performance of LV networks. Typical indices are used to assess the performance of distribution networks.

#### 3.1 Reliability Method

The technique that used to determine power system reliability is a classical method which is an analytical method [23]. In this paper, the analytical method is used to measure reliability performance. The reliability indices that have been evaluated using classical concept are the three primary ones of average failure rate  $\lambda_s$ , average outage duration  $r_s$ , and average annual unavailability or average annual outage time  $u_s$ . These indices are expected average values of total customers of the LV distribution system [23, 24]. This term of reliability indices is used to determine the number and duration of interruption.

**Table 3** Mean fault rates and MTTR

Power component	Voltage level (kV)	Mean fault rate $\lambda_{\text{mean}}$ (faults/year)		MTTR $\mu_{\text{mean}}$ (hours/fault)	
		[14]	[15–22]	[14]	[15–22]
		Overhead lines	<11	0.168	0.21
	11	0.091	0.1	9.5	–
	33	0.034	0.1	20.5	55
Cables	<11	0.159	0.19	6.9	85
	11	0.051	0.05	56.2	48
	33	0.034	0.05	201.6	128
Transformers	11/0.4	0.002	0.014	75	120
	33/0.4	0.01	0.014	205.5	120
	33/11	0.01	0.009	205.5	125
Buses	0.4	–	0.005	–	24
	11	–	0.005	–	120
	>11	–	0.08	–	140
Circuit breakers	0.4	–	0.005	–	36
	11	0.0033	0.005	120.9	48
	33	0.0041	–	140	52
Fuses	<11	0.0004	–	35.3	–

Average failure rate;

$$\lambda_s = \sum_i \lambda_i \tag{1}$$

Average outage time;

$$U_s = \sum_i \lambda_i r_i \tag{2}$$

Average annual outage time;

$$r_s = \frac{U_s}{\lambda_s} = \frac{\sum_i \lambda_i r_i}{\sum_i \lambda_i} \tag{3}$$

Analytical method has numerous attractive features which a precise method and computationally well-organised and possibly most important, it offers the developer with understanding of the relationship between input variables and final results. Also, analytical model and techniques have been necessary to provide planners and designers with the results necessary to conclude reliability performance. Analytical



techniques denote the system by mathematical model and evaluation of the reliability indices from this model using direct numerical. Besides, they provided expectation indices in relatively short computing time.

### 3.2 Reliability Indices

The reliability performance of rural LV distribution networks are assessed through the calculation of a set of reliability indices. The System Average Interruption Frequency Index (SAIFI), and System Average Interruption Duration Index (SAIDI) are typical set of indices used by most countries [24]. These set of indices also used by Tenaga Nasional Berhad (TNB) for reporting the performance of distribution network in most area in Malaysia to EC.

System average interruption frequency index, SAIFI. It indicates how frequent an average customer is subjected to sustained interruption over a predefined time interval.

$$SAIFI = \frac{\text{Total number of customer interruptions}}{\text{Total number of customers served}} = \frac{\sum \lambda_i N_i}{N_i} \quad (4)$$

System average interruption duration index, SAIDI. The interruption index of power supply is indicated in minutes per customers.

$$SAIDI = \frac{\text{Sum of customer interruption durations}}{\text{Total number of customers}} = \frac{\sum U_i N_i}{\lambda_i N_i} \quad (5)$$

## 4 Result

The network area located at the rural residential with about 44 customers. The type of house that related to this study are terrace house with load demand 1.5 kW per houses, with a total load of this region is 69.47 kVA. Based on Fig. 3 (single phase) feeder 1, 2, 3 and 4 consist of 9, 11, 12, 12 loads respectively. For three phase network (Fig. 4), it has the same number of load in single phase network, but the connection of the load to the supply is three phase network. For feeder 1, it received supply only from red wire, while feeder 2 received supply from yellow wire and feeder 3 received supply from blue wire.

**Table 4** Reliability indices (average of all customer)

Network	SAIFI	SAIDI
Single phase	0.99363	6.58907
Three phases	0.67881	4.49607

## 5 Discussion

Table 4 present the average value of indices for all customer. It clearly shows that by the value of SAIFI and SAIDI for LV network of single phase diagram are higher than three phase diagram. It indicates that neglecting the real configuration of LV distribution network should overestimate the reliability performance. Single phase diagram has a higher value compared to three phase diagram due to the fault rates of the main feeder. In single phase diagram, all phases (red, yellow and blue) of main feeders are connected together, although in reality, it doesn't operate in such way. For example, if red phase of the main feeder is faulted, yellow and blue phases also faulted, resulting in more interruption and duration of interruption experience by customers.

Table 5 illustrate the type of customer based on reliability performance; best customer for low-value indices, median customer for average value indices, and worst customer for a high value of indices. The best customer typically located near the source and short in electrical supply path, which directly related to Eq. (1). Worst customer is opposite factors of the best customer; located further from source and long in electrical supply path. Hence, a better organisation of emergency staff/source plan during fault can be employed to decrease the frequency and duration of interruption.

By knowing the correct reliability performance of each customer, type of network component in the planning phase can be utilized to minimise energy losses. For instance, low core energy losses of conductor or underground cable may be employed for a long feeder supplying a high number of customer. Another suggestion of earlier distribution planning is configuring various network configuration by getting the best reliability performance and lowest energy losses. Reliability performance of every customer is important nowadays due to penalty enforcement by EC (for Malaysia). Each customer has its maximum experience frequency and duration of interruption.

**Table 5** Reliability indices (focus on the type of customer)

Network	Type of customer	SAIFI (location)	SAIDI (location)
Single phase	Best	0.0157 (1)	0.86309 (1)
	Median	1.0147 (15, 26, 38)	6.67844 (15, 26, 38)
	Worst	2.0227 (44)	12.49379 (44)
Three phases	Best	0.33770 (33)	1.86841 (21)
	Median	0.67370 (19, 23, 26, 30, 35)	4.71299 (19, 26, 30, 35)
	Worst	1.01470 (44)	6.74819 (17)

If the customer experience interruption/duration exceed the maximum value by EC, DNOs must pay the penalty to the customer. Therefore, distribution network planning is crucial for DNOs to minimise paying the penalty.

## 6 Conclusion

Modelling the correct configuration of the distribution network is important as it affects the overall performance of distribution network; aggregation of all downstream network (LV networks) to the upstream network (MV and HV networks). The modelling of network configuration depending on the operation and protection system of network. For MV and HV networks, the protection system employed in three phases operation, which single, double or three phases fault should lockout (isolate from healthy part) all phase. It differs for LV network, where the protection system employed in single phase operation. If one phase fault, only that phase is lockout, another two phases continue in supply. Another reasons for correct configuration are to minimize losses and penalty. DNOs may utilise low energy losses component for critical feeder and configure optimal network configuration during distribution network planning phase.

**Acknowledgements** Universiti Malaysia Pahang Internal Grant RDU1703260 supports this research. The authors would also like to thank the Faculty of Electrical & Electronics Engineering Universiti Malaysia Pahang for providing facilities to conduct this research and financial support throughout the process.

## References

1. Kazemi S (2011) Reliability evaluation of smart distribution grids. Ph.D. thesis, Aalto University, Espoo, Finland
2. Siirto O, Loukkalahti M, Hyvarinen M, Heine P, Lehtonen M (2012) Neutral point treatment and earth fault suppression. In: Electric power quality and supply reliability conference (PQ), pp 1–6
3. Katsanevakis M, Stewart RA, Junwei L (2019) A novel voltage stability and quality index demonstrated on a low voltage distribution network with multifunctional energy storage systems. *Electr Power Syst Res* 171:264–282
4. Jeong M-G et al (2017) Optimal voltage control using an equivalent model of a low-voltage network accommodating inverter-interfaced distributed generators. *Energies* 10(8):1180
5. Afandi I, Ciuffo P, Agalgaonkar A, Perera S (2018) A holistic approach for integrated volt/var control in MV and LV networks. *Electr Power Syst Res* 165:9–17
6. Di Fazio A, Russo M, De Santis M, Di Fazio AR, Russo M, De Santis M (2019) Zoning evaluation for voltage optimization in distribution networks with distributed energy resources. *Energies* 12(3):390
7. Energy Commission Malaysia (2016) Performance and statistical information in Malaysia 2016. Suruhanjaya Tenaga, p 103

8. Papadopoulos P, Cipcigan LM, Jenkins N, Grau I (2009) Distribution networks with electric vehicles. In: 2009 Proceedings of the 44th international universities power engineering conference (UPEC), pp 1–5
9. Costa P, Matos M (2009) Assessing the contribution of microgrids to the reliability of distribution networks. *Electr Power Syst Res* 79(2):382–389
10. Mohammadi Chabanloo R, Ghotbi Maleki R, Mousavi Agah SM, Mokhtarpour Habashi E (2018) Comprehensive coordination of radial distribution network protection in the presence of synchronous distributed generation using fault current limiter. *Int J Electr Power Energy Syst* 99:214–224
11. Amohadi M, Fotuhi-Firuzabad M (2019) Optimal placement of switching and protection devices in radial distribution networks to enhance system reliability using the AHP-PSO method. *Turkish J. Electr Eng Comput Sci* 27(1):181–196
12. Jia Q, Dong X, Mirsaedi S (2019) A traveling-wave-based line protection strategy against single-line-to-ground faults in active distribution networks. *Int J Electr Power Energy Syst* 107:403–411
13. Ates Y et al (2016) Adaptive protection scheme for a distribution system considering grid-connected and islanded modes of operation. *Energies* 9(5):378
14. National system and equipment performance report (2010) Energy Networks Association (ENA)
15. Allan R, De Oliveira M (1980) Evaluating the reliability of electrical auxiliary systems in multi-unit generating stations. In: IEE proceedings C—generation, transmission and distribution, vol 127, no 2, pp 65–71
16. Stanek E, Venkata S (1988) Mine power system reliability. *IEEE Trans Ind Appl* 24(5)
17. Farag A, Wang C, Cheng T (1998) Failure analysis of composite dielectric of power capacitors in distribution systems. *IEEE Trans Dielectr Electr Insul* 5(4)
18. The performance of networks using alternative splitting configurations. Final report on technical steering group workstream
19. Roos F, Lindah S (2004) Distribution system component failure rates and repair times—an overview. Nordic distribution and asset management conference
20. Anders G, Maciejewski H (2006) A comprehensive study of outage rates of air blast breakers. *IEEE Trans Power Syst* 21(1):202–210
21. Office of Gas and Electricity Markets, Review of electricity transmission output measures. Final report
22. He Y (2010) Study and analysis of distribution equipment reliability data. Elforsk, AB
23. Billinton R, Allan R (1996) Reliability evaluation of power systems, 2nd edn. New York
24. IEEE guide for electric power distribution reliability indices. *IEEE Std 1366*, p 43, 2012

# Detailed Non-Linear Constrained Multi-Objective Optimal Operation of Power Systems Including Renewable Energy Sources



Duy C. Huynh, Hong V. Nguyen and Matthew W. Dunnigan

**Abstract** A modified cuckoo search (MCS) algorithm is proposed in this paper for an optimal operation problem of power systems with renewable energy sources including solar and wind energy sources. A non-linear constrained multi-objective optimal operation problem is formulated and detailed for an integrated power system in order to make it more realistic. Furthermore, the cuckoo search (CS) algorithm is modified to increase the convergence rate that is called the MCS algorithm. This variant mentions the step size of the Lévy flight. The modified IEEE 10-generator power system with integrated solar and wind power sources is considered in this paper. The numerical results on the above power system confirm the effectiveness of the proposal for the optimal operation of the integrated power system. A comparison with the CS algorithm and variants of the particle swarm optimization (PSO) algorithm indicates the superiority of the MCS algorithm for resolving complicated optimal operation problems of integrated power systems.

**Keywords** Optimal operation · Integrated power systems

## 1 Introduction

Normally, the main purpose of resolving the optimal operation problem is to find out a fuel cost minimized for the power system [1–4]. Due to emissions produced by thermal power plants, the classical optimal operation problem can no longer be only considered to minimize the fuel cost recently. In addition, the emission optimization problem is proposed to minimize the emissions of  $\text{SO}_x$  and  $\text{NO}_x$  caused by thermal power plants [5–7, 11].

Additionally, the demand of electricity utilization has significantly increased in many countries, especially in Industry 4.0 which led to an energy crisis. In order to resolve this issue, there are a lot of research moving towards renewable energy

---

D. C. Huynh (✉) · H. V. Nguyen  
Ho Chi Minh City University of Technology, Ho Chi Minh City, Vietnam  
e-mail: [duy.c.huynh@ieee.org](mailto:duy.c.huynh@ieee.org)

M. W. Dunnigan  
Heriot-Watt University, Edinburgh, UK

© Springer Nature Singapore Pte Ltd. 2020  
A. N. Kasruddin Nasir et al. (eds.), *InECCE2019*, Lecture Notes in Electrical Engineering 632, [https://doi.org/10.1007/978-981-15-2317-5\\_66](https://doi.org/10.1007/978-981-15-2317-5_66)



$P_{PV, STC}$	The rated PV power at the MPP considered in the standard testing condition (STC) (W);
$G_T$	The irradiation level ( $W/m^2$ );
$\gamma$	The power temperature coefficient at the MPP ( $\%/^{\circ}C$ );
$T$	The cell temperature ( $^{\circ}C$ );
$N_{PVs}$ and $N_{PVp}$	The number of PV modules in series and parallel composing the PV generator, respectively.

The obtained power of a solar thermal plant is [8]:

$$P_{Ther} = \eta \times A_c \times G_T \quad (2)$$

where

$P_{Ther}$	The obtained power of a solar thermal plant (W);
$\eta$	The collector efficiency;
$A_c$	The collector area ( $m^2$ ).

## 2.2 Wind Power

The obtained power of a wind turbine is [8]:

$$P_{wind} = \frac{1}{2} \times C_e \times \rho \times A_s \times V_{wind}^3 \quad (3)$$

where

$P_{wind}$	The obtained power of a wind turbine (W);
$C_e$	The efficiency factor;
$\rho$	The air density, $\rho = 1.225 \text{ kg/m}^3$ ;
$A_s$	The surface area traversed by the wind ( $m^2$ );
$V_{wind}$	The wind speed (m/s).

## 3 Optimal Operation of Integrated Power Systems

The optimal operation problem is to minimize the objective functions of the fuel cost and emission with the equality and inequality constraints established as follows.

### 3.1 Objective Function

#### \* Fuel cost

The objective function of the fuel cost,  $C(P_G)$  is the quadratic function based on the fuel cost curves of thermal generators. The valve loading effects is considered through a sine component. Then, the objective function of the fuel cost is [9]:

$$f_1 = C(P_G) = \sum_{i=1}^{N_g} a_i + b_i P_{Gi} + c_i P_{Gi}^2 + \left| d_i \sin \left[ e_i \left( P_{Gi} - P_{Gi}^{\min} \right) \right] \right| \quad (4)$$

where

$C(P_G)$	The fuel cost (\$/h);
$a_i, b_i$ and $c_i$	The cost coefficients of the $i$ th generator;
$d_i$ and $e_i$	The cost coefficients of the $i$ th generator reflecting valve-point effects;
$P_{Gi}$	The output active power of the $i$ th generator, $i = 1, \dots, N_g$ ;
$P_{Gj}$	The output active power of the $j$ th generator, $j \neq i$ and $j = 1, \dots, N_g$ ;
$P_{Gi}^{\min}$	The lower limit of the output active power of the $i$ th generator;
$P_{Gi}^{\max}$	The upper limit of the output active power of the $i$ th generator;
$P_G$	The vector of the output active powers of $N_g$ generators defined as follow:
$P_G$	$[P_{G1}, P_{G2}, \dots, P_{GN_g}]^T$ ;
$N_g$	The total number of thermal generators in a power system;
$T$	The time of one day.

#### \* Emission

The objective function of the emission,  $E(P_G)$  is [9]:

$$f_2 = E(P_G) = \sum_{i=1}^{N_g} \alpha_i + \beta_i P_{Gi} + \gamma_i P_{Gi}^2 + \xi_i \exp(\omega_i P_{Gi}) \quad (5)$$

where

$E(P_G)$	The emission (ton/h);
$\alpha_i, \beta_i, \gamma_i, \xi_i$ and $\omega_i$	The emission coefficients of the $i$ th generator.

#### \* Objective function of fuel cost and emission

It is obvious that the optimal operation problem of the fuel cost and emission is to minimize  $f_1 = C(P_G)$  and  $f_2 = E(P_G)$  where the objective functions of the fuel cost and emission can be weighted according to their relative importance described as follows:



$$f = \begin{cases} wC(P_G) \\ (1-w)E(P_G) \end{cases} \quad (6)$$

where

$w$  The weighting coefficient,  $w \in [0, 1]$ ;

If  $w = 0$  then  $f$  is the objective function of the emission and if  $w = 1$  then  $f$  is the objective function of the fuel cost.

A trade-off can be obtained as the weighting coefficient,  $w$  is varied from zero to one in order to ensure the optimization in operating.

Additionally, the uncertainty of solar and wind powers makes the optimal operation problem of the integrated power system more complicated. Therefore, these powers are treated as negative loads in order to make it more simple.

Then, the actual load power is:

$$P_{Actual\_load} = P_{Total\_load} - (P_{solar} + P_{wind}) \quad (7)$$

where

$P_{Actual\_load}$  and  $P_{Total\_load}$  The actual and total load powers, respectively (W);  
 $P_{solar}$  and  $P_{wind}$  The solar and wind powers, respectively (W).

### 3.2 Constraint Condition

The active power balance, power generation limits and ramp rate limits are the constraints considered in this paper.

#### \* Active power balance

The total generation power must cover the actual load power,  $P_{Actual\_load}$  and the active power loss in transmission lines,  $P_{loss}$ . Then, the constraint of the active power balance is:

$$\sum_{i=1}^{N_g} P_{Gi} = P_{Actual\_load} + P_{loss} \quad (8)$$

where

$P_{loss}$  The active power loss in transmission lines (W).

$$P_{loss} = \sum_{i=1}^{N_g} \sum_{j=1}^{N_g} P_{Gi} B_{ij} P_{Gj} + \sum_{i=1}^{N_g} B_{i0} P_{Gi} + B_{00} \quad (9)$$

where

$B_{ij}$ ,  $B_{i0}$  and  $B_{00}$  The  $B$ -coefficients of the power loss of the power system depending on the impedance parameters of transmission lines.

**\* Power generation limits**

The generation powers should be within the limits as follows:

$$P_{Gi}^{\min} \leq P_{Gi} \leq P_{Gi}^{\max}, \quad i = 1, \dots, N_g \tag{10}$$

$$0 \leq P_{solar} \leq P_{solar}^{\max} \tag{11}$$

$$0 \leq P_{wind} \leq P_{wind}^{\max} \tag{12}$$

where

$P_{solar}^{\max}$  The upper limit of the solar power (W);

$P_{wind}^{\max}$  The upper limit of the wind power (W).

**\*Ramp rate limits**

The ramp rate limits for thermal power plants are described as follows:

$$P_{G_i(t)} - P_{G_i(t-1)} \leq P_{G_i,up} \tag{13}$$

$$P_{G_i(t-1)} - P_{G_i(t)} \leq P_{G_i,down} \tag{14}$$

where

$P_{Giup}$  and  $P_{Gidown}$  The up and down ramp rate of the power of the  $i$ th generator, respectively (W).

## 4 Optimal Operation of an Integrated Power System Using a MCS Algorithm

The CS algorithm is reviewed in Sect. 4.1 followed by a description of the MCS algorithm. The MCS algorithm is proposed to define the optimal operation solutions for an integrated power system.

## 4.1 CS Algorithm

The CS algorithm is a stochastic global search algorithm based on the interesting breeding behaviors of cuckoos through the following principles [10].

Each cuckoo only lays one egg at a time and dumps its egg in the randomly chosen nest, each egg is a solution. The best nests with high quality of eggs will carry over to the next generation. The availability of host nests is fixed and a probability,  $p_a \in [0, 1]$  represents the possibility of an alien egg to be discovered by host bird.

In this application, the cuckoo selects randomly the nest position to lay an egg which is a new generation power,  $P_{Gi,k}^{iter+1}$  through the Lévy flight behavior.

$$P_{Gi,k}^{iter+1} = P_{Gi,k}^{iter} + \varepsilon \oplus Levy(\sigma) \quad (15)$$

where

- $\varepsilon > 0$     The step size;
- $k$          The  $k$ th host nest,  $k = [1, \dots, m]$ ;
- $l$          The  $l$ th random nest,  $l = [1, \dots, m]$ ;
- $m$          The number of the host nest;
- $iter$       The  $iter$ th iteration;
- $Iter^{\max}$    The number of maximum iteration;
- $\oplus$          The entry wise multiplications.

The Lévy flight behavior (15) is essentially the stochastic description for a random walk which is a Markov chain. Its next location depends on the current location,  $P_{Gi,k}^{iter}$  and the transition probability,  $\varepsilon \oplus Levy(\sigma)$ .

The Lévy distribution is [10]:

$$Levy(\sigma) = t^{-\sigma}, \sigma \in (1, 3]. \quad (16)$$

## 4.2 MCS Algorithm

With the aim of improving the searching ability as the solutions get closer to the optimal result, the MCS algorithm is proposed and applied for the optimal operation problem of the integrated power system.

It is realized that one of the CS algorithm parameters, affecting the searching ability of the CS algorithm, is the Lévy flight step size,  $\varepsilon$ . Normally, this step size is assumed constant in this CS algorithm whereas it is proposed to decrease as the number of generations increases for improving the searching efficiency in the MCS algorithm.

Therefore, the Lévy flight step size at each generation is:

$$\varepsilon_i = \frac{\varepsilon_0}{\sqrt{iter}} \quad (17)$$

where

$\varepsilon_0$  The initial value of the Lévy flight step size.

The flowchart of the MCS algorithm, applied for the optimal operation problem is shown as in Fig. 1.

## 5 Numerical Results

The numerical results of the non-linear constrained multi-objective optimal operation problem are achieved by the MCS algorithm on the modified IEEE 10-generator power system with the fuel cost coefficients and active generation limits; the emission coefficients; and the values of the  $B$ -coefficients matrix [11].

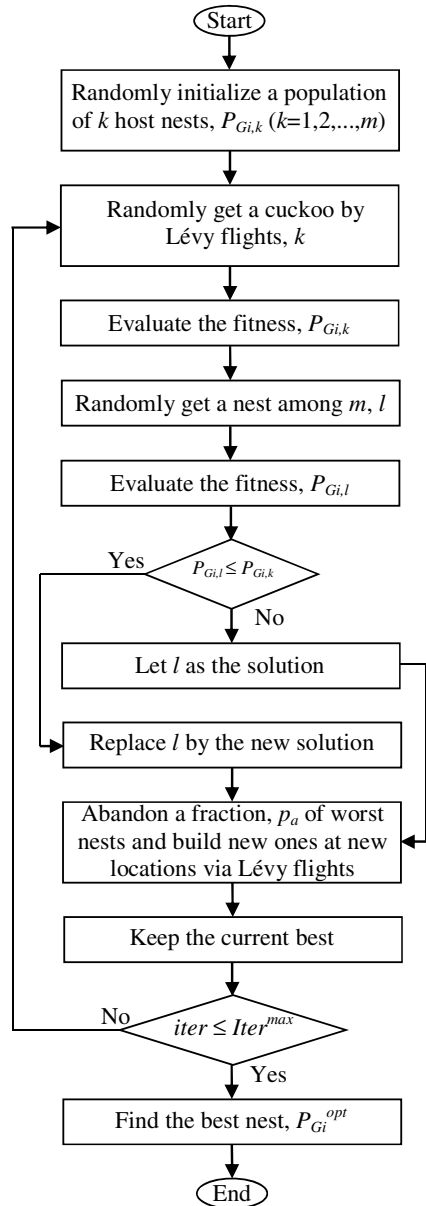
Table 1 is the total load demand; the solar power,  $P_{solar}$  including the PVs' power,  $P_{pv}$  and the power of solar thermal plants,  $P_{Ther}$ ; as well as the wind power,  $P_{wind}$  in 24 h.

Figure 1 obviously shows that the total power of traditional thermal generators has been cut down by the solar and wind powers. The average reduction is 22.64%. In the period of 8–12 h, the total solar and wind powers generated is highest, 170 MW including the solar power,  $P_{solar} = 90$  MW and the wind power,  $P_{wind} = 80$  MW. The percentage of the total power of traditional thermal generators cut down is largest in the period of 5–8 h, 26.79%. These positively impact on the factors concerning on the fuel cost and emission minimization of the power system. This also confirms a tendency towards power systems with renewable energy sources in the future.

Table 2 is the parameters of the CS and MCS algorithms. The difference between these two algorithms is the chosen value of the Lévy flight step size,  $\varepsilon$ . It is constant,  $\varepsilon = 0.5$  in the CS algorithm and is a generation-varying variable in the MCS algorithm. This is to increase the convergence ability including the convergence speed and value of the CS algorithm.

Tables 3 and 4 are the best solution of the fuel cost and emission of the IEEE 10-generator power system with the objective function of the fuel cost,  $w = 1$  and the objective function of the emission,  $w = 0$ , respectively. The optimal operation problem is considered with and without the valve point effect using the time varying acceleration based PSO (PSO-TVAC), Chaos PSO, CS and MCS algorithms. The fuel cost and emission are always improved using the MCS algorithm compared with other algorithms in Tables 3 and 4. Without considering the valve point effect, the fuel cost is  $1.0803 \times 10^5$  \$/h and the emission is 4533.6 ton/h by using the MCS algorithm which are less than  $1.1105 \times 10^5$  \$/h and 4541.2 ton/h by using the PSO-TVAC algorithm;  $1.1103 \times 10^5$  \$/h and 4540.8 ton/h by using the Chaos PSO algorithm; and  $1.1002 \times 10^5$  \$/h and 4539.1 ton/h by using the CS algorithm. Similarly, with considering the valve point effect, the fuel cost and emission by using

**Fig. 1** Flowchart of the MCS algorithm applied for the optimal operation problem



the MCS algorithm are less than those by using the PSO-TVAC, Chaos PSO and CS algorithm.

Furthermore, Tables 5 and 6 are the best solution of the fuel cost and emission of the IEEE 10-generator power system with the objective function of the fuel cost,  $w = 1$  and the objective function of the emission,  $w = 0$ , respectively. In Table 5,

**Table 1** Total and actual load demands in day and night of 24 h

Time (h)	$P_{Total\_load}$ (MW)	$P_{solar}$ (MW)	$P_{wind}$ (MW)	$P_{solar} + P_{wind}$ (MW)	$P_{Actual\_load}$ (MW)	$\Delta \sum P_{Gi}$ (%)
0–5	168	2.25	38	40.25	127.75	23.96
5–8	308	22.50	60	82.50	225.50	26.79
8–12	712	90.00	80	170.00	542.00	23.88
12–18	476	45.00	70	115.00	361.00	24.16
18–24	336	5.00	40	45.00	291.00	13.39
Total	2000	164.75	288	452.75	1547.25	22.64

**Table 2** Parameters of the CS and MCS algorithms

Parameter	Value	
	CS	MCS
Number of host nest, $m$	10	10
Number of maximum iteration, $Iter^{max}$	200	200
Step size of Lévy flight, $\epsilon$	0.5	Equation (17)
Possibility of alien egg, $p_a$	0.6	0.6

**Table 3** Comparison of the best solution for the fuel cost minimization with and without the valve point effect

Algorithm	Without valve point effect		With valve point effect	
	C (\$/h) $\times 10^5$	E (ton/h)	C (\$/h) $\times 10^5$	E (ton/h)
PSO-TVAC	1.1105	4541.2	1.1108	4541.7
Chaos PSO	1.1103	4540.8	1.1106	4541.1
CS	1.1002	4539.1	1.1005	4539.3
MCS	1.0803	4533.6	1.0903	4534.2

**Table 4** Comparison of the best solution for the emission minimization with and without the valve point effect

Algorithm	Without valve point effect		With valve point effect	
	C (\$/h) $\times 10^5$	E (ton/h)	C (\$/h) $\times 10^5$	E (ton/h)
PSO-TVAC	1.1609	3910.5	1.1613	3911.6
Chaos PSO	1.1607	3910.3	1.1610	3911.4
CS	1.1603	3910.2	1.1606	3911.1
MCS	1.1590	3907.6	1.1597	3910.2

the MCS algorithm is proposed to solve the optimal operation problem of the power system with and without the solar and wind power sources based on the fuel cost minimization. The obtained results by using the MCS algorithm are compared with

**Table 5** Comparison of the best solution for the fuel cost minimization with and without the solar and wind powers considering the valve point effect

Algorithm	Without the solar and wind powers (I)		With the solar and wind powers (II)		Comparison between (I) and (II)	
	C (\$/h) × 10 <sup>5</sup>	E (ton/h)	C (\$/h) × 10 <sup>5</sup>	E (ton/h)	ΔC (%)	ΔE (%)
PSO-TVAC	1.1108	4541.7	0.8906	3588.85	19.82	20.98
Chaos PSO	1.1106	4541.1	0.8899	3587.01	19.87	21.01
CS	1.1005	4539.1	0.8800	3583.17	20.04	21.06
MCS	1.0903	4533.6	0.8611	3529.41	21.02	22.15

**Table 6** Comparison of the best solution for the emission minimization with and without the solar and wind powers considering the valve point effect

Algorithm	Without the solar and wind powers (I)		With the solar and wind powers (II)		Comparison between (I) and (II)	
	C (\$/h) × 10 <sup>5</sup>	E (ton/h)	C (\$/h) × 10 <sup>5</sup>	E (ton/h)	ΔC (%)	ΔE (%)
PSO-TVAC	1.1613	3911.6	0.9171	3207.5	21.03	18.12
Chaos PSO	1.1610	3911.4	0.9384	3109.6	19.17	20.43
CS	1.1606	3911.1	0.9011	3062.4	22.36	21.27
MCS	1.1597	3910.2	0.8917	3077.3	23.11	21.34

those by using the PSO-TVAC, Chaos PSO and CS algorithms. Obviously, the fuel cost and emission are also improved using the MCS algorithm compared with other algorithms in Tables 5 and 6. Especially, the improvement percentages of the fuel cost and emission, 21.02 and 22.15% by using the MCS algorithm are always higher than 19.82 and 20.98% by using the PSO-TVAC algorithm; 19.87 and 21.01% by using the Chaos PSO algorithm; and 20.04 and 21.06% by using the CS algorithm. Obviously, the reduction percentages are always higher than 19% by integrating the power system with the solar and wind power sources. Additionally, the modifications of the CS algorithm have improved more the reduction. Then, the reduction percentages are highest by using the MCS algorithm. Similarly, in Table 6, the optimal operation problem is based on the emission minimization. The PSO-TVAC, Chaos PSO, CS and MCS algorithms are alternately applied for this problem. The improvement percentages of the fuel cost and emission, 23.11 and 21.34% by using the MCS algorithm are always higher than 21.03 and 18.12% by using the PSO-TVAC algorithm; 19.17 and 20.43% by using the Chaos PSO algorithm; and 22.36 and 21.27% by using the CS algorithm. Obviously, the reduction percentages are always higher than 18% by integrating the power system with the solar and wind power sources and the reduction percentages are highest by using the MCS algorithm.

Figures 2, 3, 4 and 5 are the convergence characteristics of the fuel cost and emission for the fuel cost and emission minimization without and with the solar and wind power sources considering the valve point effect using the MCS algorithm. It is obvious that the convergence speed and value of the MCS algorithm are good.

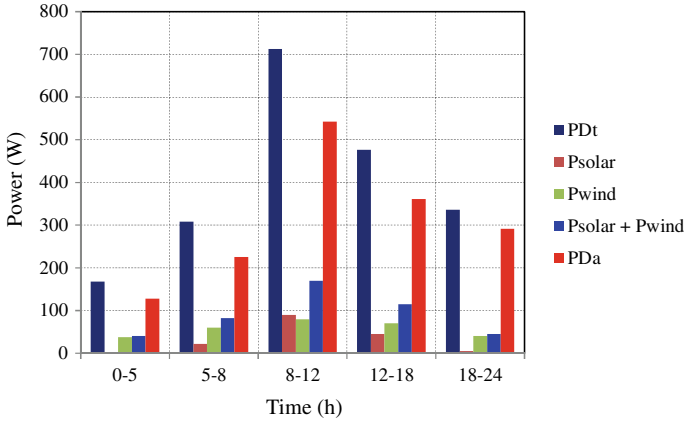


**Fig. 2** Total and actual load powers; and the solar and wind powers obtained in day and night

**Fig. 3** Convergence characteristic of the fuel cost for the fuel cost minimization without the solar and wind powers considering the valve point effect using the MCS algorithm

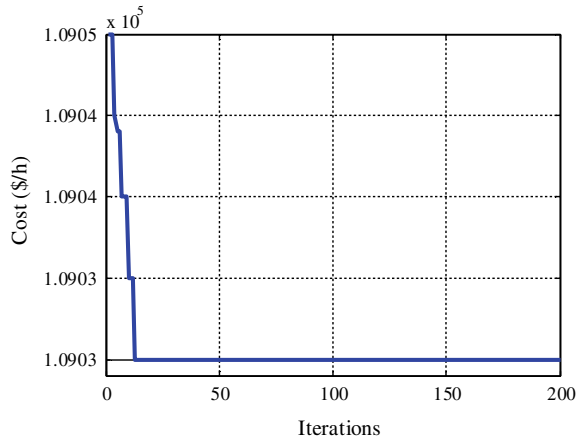


**Fig. 4** Convergence characteristic of the emission for the fuel cost minimization without the solar and wind powers considering the valve point effect using the MCS algorithm

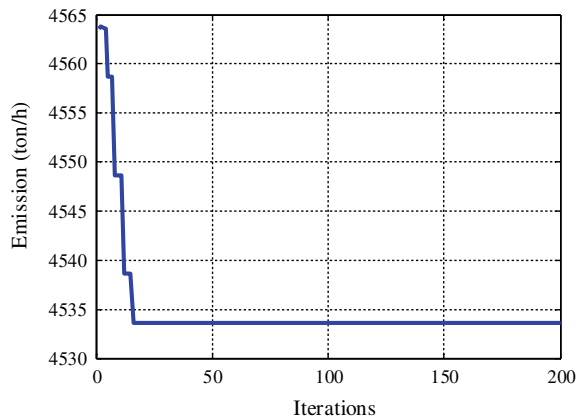




**Fig. 5** Convergence characteristic of the fuel cost for the fuel cost minimization with the solar and wind powers considering the valve point effect using the MCS algorithm

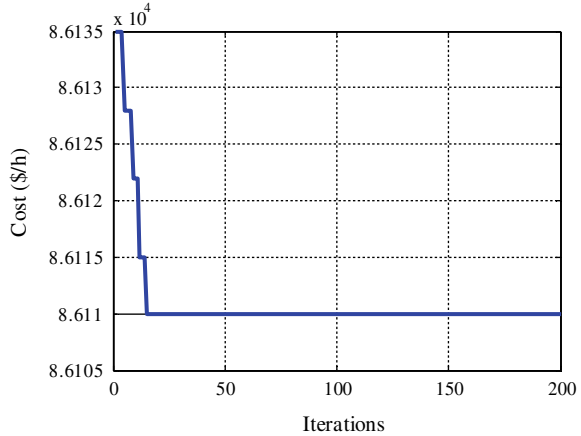
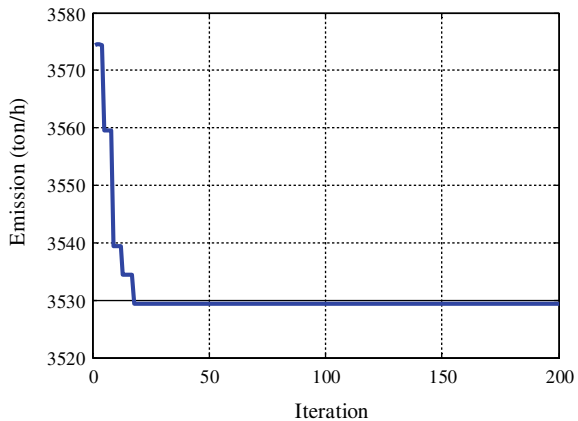


**Fig. 6** Convergence characteristic of the emission for the fuel cost minimization with the solar and wind powers considering the valve point effect using the MCS algorithm



The MCS algorithm always converges at the iteration steps which are less than 20. Furthermore, the convergence value of the MCS algorithm is also better than this of the PSO-TVAC, Chaos PSO and CS algorithms (Fig. 6).

## 6 Conclusion

The solar and wind powers have been integrated more popular into the existing power system for resolving the issues of the energy crisis and environmental pollution. This made the optimal operation problem more complicated. The MCS algorithm has been proposed to find out the optimal operation strategy based on the minimization of the fuel cost and emission for the integrated power system. The MCS algorithm is the variant of the CS algorithm with the generation varying Lévy flight step size proposed

to improve the ability of searching as the solutions get closer to the optimal result. The achieved results by using the MCS algorithm are always better than those by using the PSO-TVAC, Chaos PSO and CS algorithms.

## References

1. Tang C, Xu J, Tan Y, Sun Y, Zhang B (2019) Lagrangian relaxation with incremental proximal method for economic dispatch with large numbers of wind power scenarios. *IEEE Trans Power Syst* 34(4):1–10
2. Li X, Fang L (2016) Research on economic dispatch of large power grid based on granular computing. In: *IEEE PES Asia-Pacific power and energy engineering conference, China*, pp 1130–1133
3. Huynh DC, Nair N (2015) Chaos PSO algorithm based economic dispatch of hybrid power systems including solar and wind energy sources. In: *IEEE conference on innovative smart grid technologies, Thailand*, pp 1–6
4. Huynh DC, Nair N (2015) Economic dispatch integrating wind power generation farms using cuckoo search algorithm. In: *IEEE conference on innovative smart grid technologies, Thailand*, pp 7–12
5. Kumar RG, Rohith A, Priyanka G, Vamsipriya G (2017) Multi-objective optimal economic emission power dispatch using Bat algorithm. In: *Innovations in power and advanced computing technologies, India*, pp 1–5
6. Manojkumar T, Singh NA (2018) Solution of environmental/economic (EED) power dispatch problem using particle swarm optimization technique. In: *International conference on control, power, communication and computing technologies, India*, pp 347–351
7. Suppakarn C, Karn S, Phakphoom B (2018) Modified DE/Sin for economic dispatch and environmental dispatch. In: *International conference on business and industrial research, Thailand*, pp 297–302
8. Pazheri FR, Othman MF, Malik NH, Safoora OK (2012) Economic and environmental dispatch at highly potential renewable area with renewable storage. *Int J Env Sci Dev* 3(2):177–182
9. Khodja F, Younes M, Laouer M, Kherfane RL, Kherfane N (2014) A new approach ACO for solving the compromise economic and emission with the wind energy. In: *International conference on technologies and materials for renewable energy, environment and sustainability, India*, pp 893–906
10. Yang X, Deb S (2009) Cuckoo search via Lévy flights. In: *world congress on nature and biologically inspired computing, India*, pp 210–214
11. Hadji B, Mahdad B, Srairi K, Mancner N (2015) Multi-objective PSO-TVAC for environmental/economic dispatch problem. In: *Conference on technologies and materials for renewable energy, environment and sustainability, Malaysia*, pp 102–111

# Voltage Sag Immunity Testing for AC Contactors in Industrial Environment



Hazri Dahalan Razip and Abu Zaharin Ahmad

**Abstract** The voltage sag is one of the prominent power quality issues faced by industrial consumers in Malaysia. Frequent voltage sag incidences have caused sensitive equipment to trip causing significant production losses. One of the identified weak links is the AC contactor. In addition, there are many ageing contactors which are still in service in the industry due to their robust design and long lifetime. This paper aims to study the immunity of voltage sag of AC contactors which are installed in a petrochemical plant. New and ageing contactors have been chosen to undergo practical testing. Well-defined test procedures are carried out based on the IEC 61000-4-11 standard. The AC contactors were exposed to rectangular voltage sag with variations in magnitude, duration and point on wave. The results are compared to IEC 61000-4-37 voltage tolerance curve. New contactor's voltage tolerance curve exhibits nearly consistent response and a slight deviation between different points on wave. It also recorded minimum sensitivity at voltage sag magnitude of 25%. On the other hand, ageing contactor exhibits mixed conformity to the IEC curve, with minimum sensitivity at 55% of voltage sag magnitude. To summarise, the ageing contactor is more sensitive to voltage sag magnitude and point on wave has little influence to the voltage tolerance curve of the new contactors.

**Keywords** Voltage sag · Voltage tolerance curve · AC contactor

## 1 Introduction

### 1.1 Voltage Sag

The voltage sag has continued to place significant effect to industrial consumers in Malaysia. It is one of the most common problems within the subject of power quality. Frequent incidences of voltage sag lead to high financial consequences, such as loss of revenue, opportunity loss, downtime, product or equipment damage and inevitable

---

H. D. Razip (✉) · A. Z. Ahmad  
Universiti Malaysia Pahang, Pekan, Malaysia  
e-mail: [mee17002@ump.edu.my](mailto:mee17002@ump.edu.my)

© Springer Nature Singapore Pte Ltd. 2020  
A. N. Kasruddin Nasir et al. (eds.), *InECCE2019*, Lecture Notes in Electrical Engineering 632, [https://doi.org/10.1007/978-981-15-2317-5\\_67](https://doi.org/10.1007/978-981-15-2317-5_67)

restarts [1]. The IEEE Std 1668-2017 defines voltage sag as a reduction in any or all phases of supply to between 0.1 and 0.9 pu in rms voltage or current at the power frequency for durations of 0.5 cycle (20 ms) to 1 min. The amplitude of voltage sag is the value of the remaining voltage during the sag [2]. Figure 1a and b illustrate the actual sinusoidal and rms waveforms of voltage sag experienced by an integrated petrochemical plant in Kuantan, Malaysia.

To most industrial plant which relies on process automation, voltage sag poses a serious problem. It will cause interruption to programmable logic controllers (PLC), variable frequency drives (VFD) and motor contactors. AC contactors which are normally used in motor control circuits are sensitive to voltage sag and identified as the weak link in the electrical process. Many contactors are left ageing in the industrial environment due to their robust design and long lifetime. The study of their response to voltage sag has not been done. As a result, many industrial plants and processes are exposed to voltage sag occurrences. This paper will discuss on the practical testing of AC contactors in a petrochemical plant to study their immunity in the event of voltage sag.

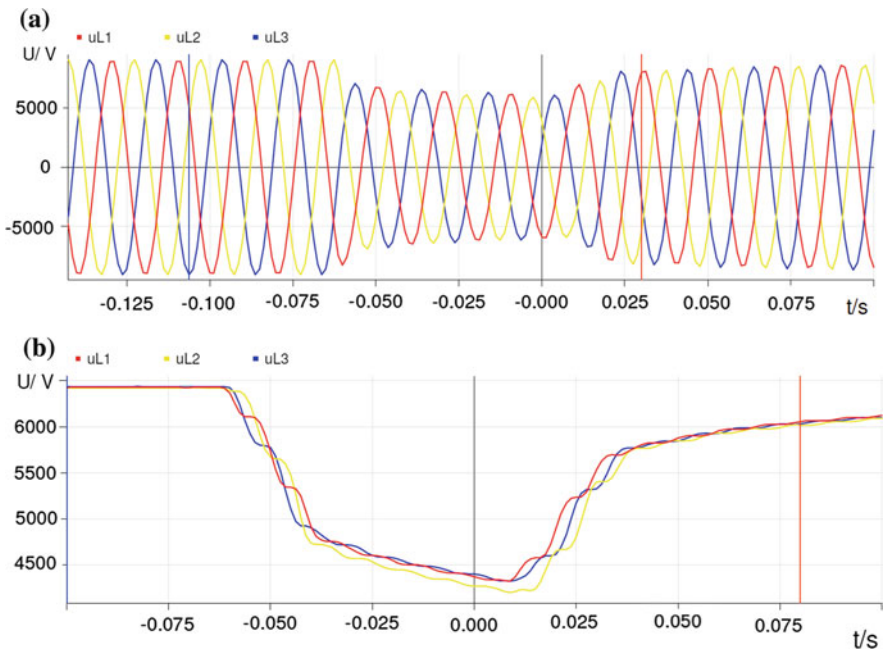


Fig. 1 a Sinusoidal waveform of voltage sag and b RMS waveform of voltage sag

### 1.2 AC Contactors

Switching elements such as relays, contactors and miniature circuit breakers are widely used in the electrical system for power distribution and control. Alternating current (AC) contactors offers an economic and simple solution for motor control applications, and can be integrated to perform many tasks. Figure 2 illustrates a typical motor-contactor control circuit for industrial application [3].

AC contactor is an electromechanical device, which acts as a switch to the electrical/power circuit as shown in Fig. 3. The switching capability is provided by the coil and electromagnet. When the coil is energised with power supply typically 230 V AC, the armature will be drawn to the electromagnet overcoming the force of spring. The movable contact which is attached to the armature will be in a close position allowing current to flow in the power circuit. Once the power supply to the control circuit is switched off, the electromagnetic force diminishes and the armature will retract to its original position aided by the spring force. The movable contact will be in an open position preventing the current flow in the power circuit [4].

During voltage sag, disturbance of the AC power supply affected the contactor coil and in most cases, the contactor will disengage causing the circuit and load to be interrupted. Thus, contactors have been known as the weak link in electrical processes when subjected to voltage sag. It is important to ascertain the response of this equipment in order to predict its behaviour [5].

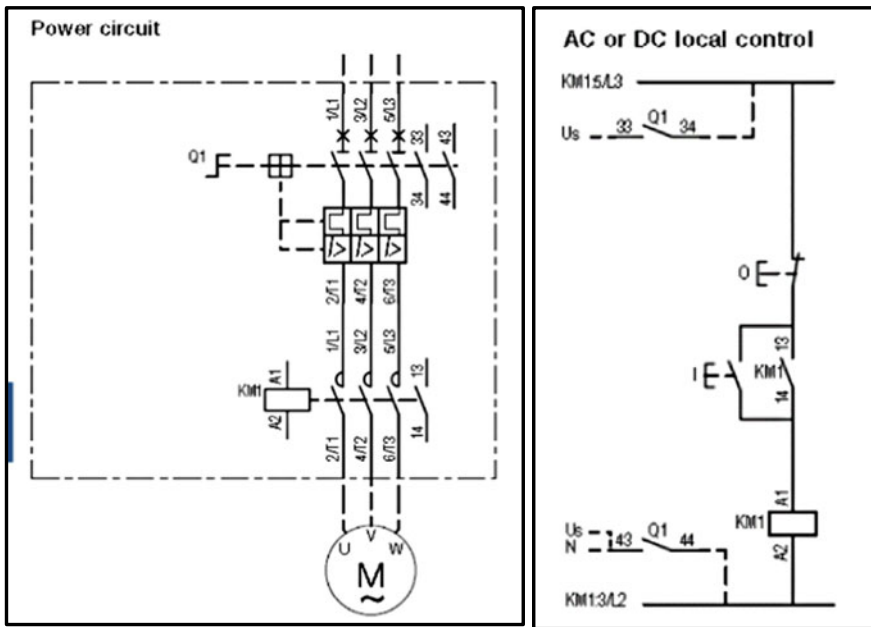


Fig. 2 Typical motor contactor and its control circuit

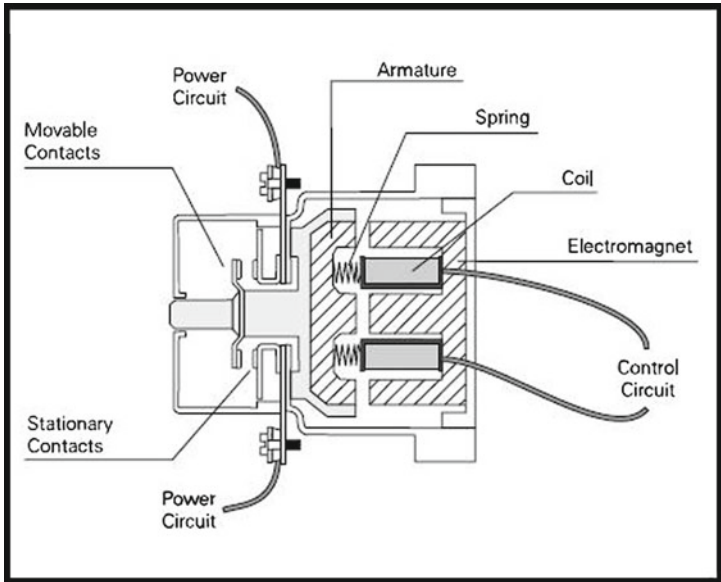


Fig. 3 Structure of an AC contactor

## 2 Previous Research

### 2.1 Laboratory Testing

Extensive tests had been conducted in the laboratory using new contactors, thus their ageing effect has not been studied [6]. The test setup utilised a voltage sag generator and a data acquisition system. The output of the voltage sag generator was voltage sag with different sag magnitudes, durations, point on waves and phase shifts. The waveforms were captured by the data acquisition system. This test had considered only unloaded AC contactor. The nominal voltage of 230 V was used to energise the contactor's coil. Several units of contactors from different manufacturers and different nominal voltages were selected for testing.

In addition, the AC contactors were subjected to several tests conditions such as rectangular, non-rectangular and actual sags recorded in a real power system. For the rectangular voltage sags, supply from perfect and non-perfect voltage source was considered. For non-rectangular voltage source, the voltage sag is modelled with multiple stages caused by motor starting.

The sensitivity curves have distinct shapes for  $0^\circ$  and  $90^\circ$  of the point on wave as shown in Fig. 4. In addition, the point on wave of voltage sag initiation has been shown to have a significant influence on the behaviour of the AC coil contactor.

The subsequent research focused on rectangular voltage sag and its effect on the immunity of the AC contactors. Data was acquired to establish the minimum voltage

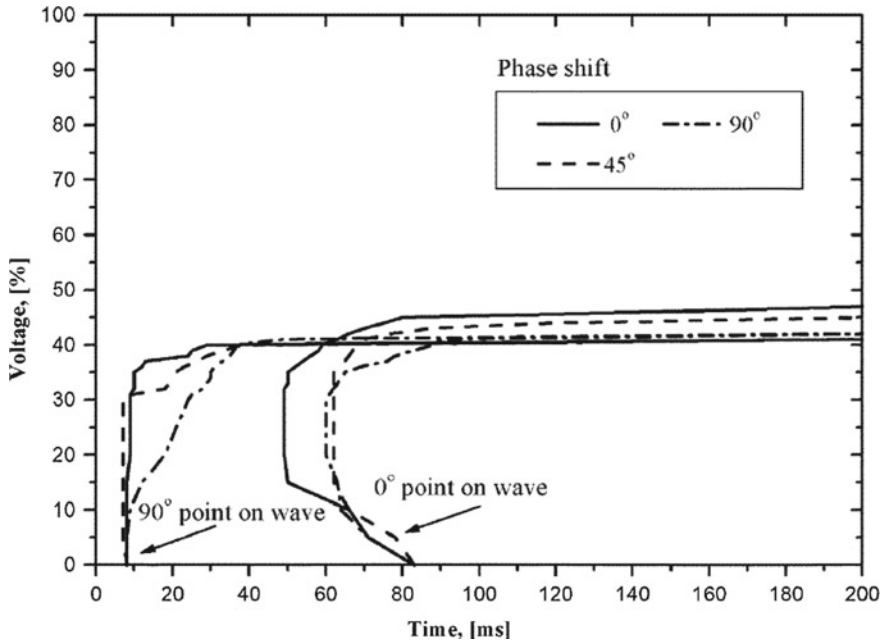


Fig. 4 Voltage tolerance curve for AC contactor with 240 V rated coil

and maximum duration needed to disengage the power contacts under the influence of point on wave of sag initiation [7]. Three different AC contactors rated 16–32 A with different rated coils, construction, operating mechanism, shading ring design and nominal voltages were tested. The contactors were exposed to rectangular voltage sag with no connected load. They are positioned according to the manufacturer's recommendation in order to make the effect of gravitational forces consistent. The point on wave has also been found to affect the behaviour of AC contactors significantly.

Small contactors with current rating 20–25 A and 240 V rated coils had been tested in another laboratory experiment [8]. In this research, voltage sag magnitude was varied in the range of 70–10% in steps of 10% decrements using a voltage sag generator. The sag duration was adjusted from 5 to 600 ms and the point on wave of voltage sag initiation was set from 0° to 90° in 15° steps. The test was repeated three times to avoid errors in contactor performance. It was observed that there was no effect for sag of less than 60% and above for all durations.

Thus far, the approach for test procedure was developed independently. However, test methodology based on IEC 61000-4-11 standard had also been adopted [9]. Four units of AC contactors with current rating 18–50 A were chosen, with two of them were in a used state. A 2 kW load was connected to simulate a condition under operation. Industrial power corruptor, data acquisition system and signal processing system was used in the experiment setup. The contactors' responses to rectangular

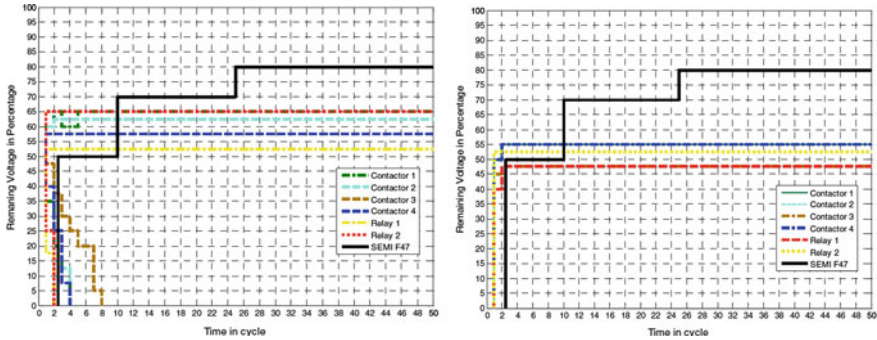


Fig. 5 Voltage tolerance curve 0° and voltage tolerance curve 90°

voltage sag were compared to SEMI F47-0200 voltage tolerance curve as shown in Fig. 5.

The tests of contactors using three-phase load banks had also been performed in the laboratory [10]. The contactor was energised from one phase and three phase was connected through the AC contactor’s power contact. Voltage sag was generated using equipment MX 45, a voltage sag generator. The contactor’s response was also compared to SEMI F47-0606 standard curve. The impact of load change was found negligible on the performance of contactor.

### 3 Methodology

#### 3.1 Selection of AC Contactors

The available contactor ratings which are typically installed in the petrochemical plant is as shown in Table 1. The sizes were divided based on their range of power (kW) ratings. Contactors were sampled randomly to represent small, medium and large sizes. Another important characteristic is the age of the contactors and is determined by the number of years it has been in service. In this paper, the category of ageing contactor is defined by a minimum of 15 years of service life. On the other hand, a new contactor is defined by a service life of 3 years and less.

Table 1 Range of AC contactor ratings and categories

Range of rating	Size category
<30 kW	Small
Between 30 and 90 kW	Medium
>90 kW	Large



**Table 2** Details of AC contactor under test

Tag number	Size	Rating, kW	Rating, A	Years of Service	Category
PM 2301	Medium	55	125	18 years	Ageing
RA 01	Medium	45	116	3 years	New

Two medium size AC contactors were sampled for new and ageing categories for the practical test. The details are presented in Table 2.

### 3.2 Practical Test Setup

The test setup was built according to the recommendation made in the IEC 61000-4-11 standard [11]. The setup included a utility power source, voltage sag generator, a power quality recorder and AC contactors as equipment under test. An Industrial Power Corruptor was utilised to generate bad quality power. The compact and portable equipment is manufactured by Power Standards Lab and it is capable to test single or three phase equipment up to 480 V rms nominal voltage [9]. Relevant voltage sag standards such as IEC 61000-4-37, SEMI F47 and ITIC specifications are also available as a built-in feature. Furthermore, the initiation angle of voltage sag (point on wave) could also be adjusted manually.

All contactors were tested without any load connected to their power circuit. Furthermore, they were exposed to rectangular voltage sag with variable magnitude, duration and point on wave in this test.

### 3.3 Test Procedure

The procedure of testing the AC contactor was derived from combination of steps outlined from previous research [7, 9]

1. The AC coil was energised with nominal voltage 230 V AC from the voltage sag generator. As a result, the movable contact would have engaged with the fixed contact (refer Fig. 1). As a result, the contactor would be in a closed position.
2. The contactor was left for 5 min for the coil to warm up.
3. Started from the nominal voltage which was 230 V, generated voltage sag with different magnitudes was applied in steps of 5% towards 0 V. The initial duration and point of wave were set to 1 cycle and  $0^\circ$  respectively.
4. The status of the main contactor whether remain closed or opened was observed and recorded. Each test was conducted three times to ensure consistency in the test result.
5. The voltage sag duration was increased gradually up to 1 s and the measurement defined in step 3 and 4 is repeated. The point on wave was maintained at  $0^\circ$ .

**Table 3** Variables selected for the practical testing

Steps of Vsag magnitude	Steps of duration	Steps of point on wave	Power quality standard	Test repetition
5%	1–50 cycles	15°	IEC 61000-4-37	3 times

- As the final step, the point on wave angle was gradually increased up to 90° in steps of 15° and measurement defined in steps 3, 4 and 5 was repeated.

### 3.4 Selection of Variables

Most of the previous research studied the effect on AC contactor when exposed to rectangular voltage sag characterised by specific magnitude and duration. The point of voltage sag initiation or “point on wave” was later proven to be an important variable which significantly affects the behaviour of AC contactors. As this paper aims to study the response of AC contactors which are installed in the industrial environment, the variables were selected based on the feasibility of carrying out the testing activity within the limited time during the shutdown of the industrial plants (Table 3).

## 4 Result and Analysis

The voltage tolerance curve for new and ageing power contactors which were subjected to test are presented. The curves are corresponding to a different point on waves from 0° to 90° in steps of 15°. They are compared to IEC 61000-4-34 voltage immunity limit curve (gray line). The area at the top of the curve denotes the acceptable operation region, whereas the bottom part is the unacceptable operation condition.

### 4.1 New and Ageing Contactor

The new contactor shows better response compares to the IEC 61000 voltage tolerance curve in Fig. 6. It only disengaged at a voltage magnitude of 25% and duration of 20 ms. The same observation is also recorded when it was subjected to 15° point on wave as shown in Fig. 7. For the ageing contactor when subjected to 0° point on wave, it is observed that it does not conform to IEC 61000 from 20 to 40 ms and remaining voltage of 45%. From 50 to 200 ms, it records unwanted disengagement

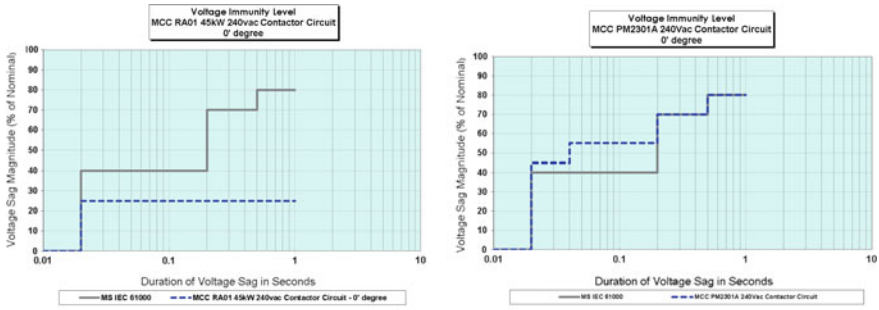


Fig. 6 Voltage tolerance curve for new and ageing contactor—point on wave 0°

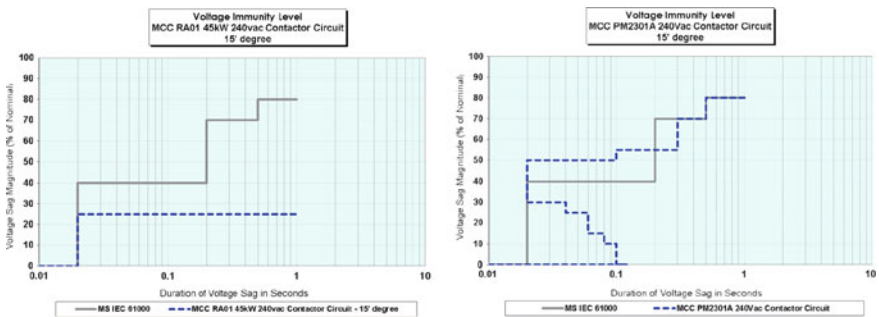


Fig. 7 Voltage tolerance curve for new and ageing contactor—point on wave 15°

at 55% remaining voltage. After 200 ms, the contactor’s response conforms to the IEC tolerance curve.

As observed in Fig. 7 for the ageing contactor subjected to 15° point on wave, from the voltage sag duration 10–100 ms, the contactor exhibits better response compares to IEC 61000 tolerance curve. The contactor is able to sustain very low remaining voltage up to 0% with duration up to 100 ms. The general shape is also very distinct from the 0° point on wave. However, at voltage magnitude of 50%, the contactor records disengagement from duration 20–200 ms. This area of operation is not conforming to the IEC 61000 curve. Nonetheless, from 200 ms to 1 s the contactor response shows conformity to the IEC curve.

From Fig. 8, when subjected to 30° point on wave, the new contactor exhibits the same response as 0° and 15° curves. For ageing contactor, although that the waveform is almost identical to case 15° point on wave, there is a difference in the response from duration 20–200 ms. The disengagement occurred at 55% of the remaining voltage, which is at a higher threshold. At the same time, the contactor is also able to withstand a voltage of 0% up to 120 ms and is better than the IEC curve.

As the ageing contactor was subjected to 45° point on wave, the voltage tolerance curve has shifted to the left as shown in Fig. 9. The maximum duration which it withstands 0% remaining voltage has been reduced to 80 ms from previously 120 ms.

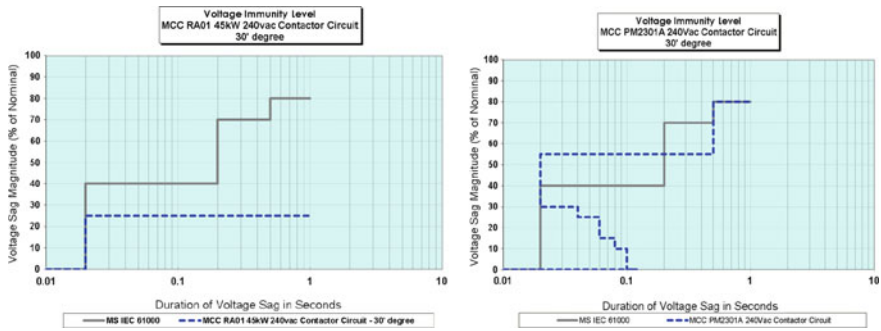


Fig. 8 Voltage tolerance curve for new and ageing contactor—point on wave 30°

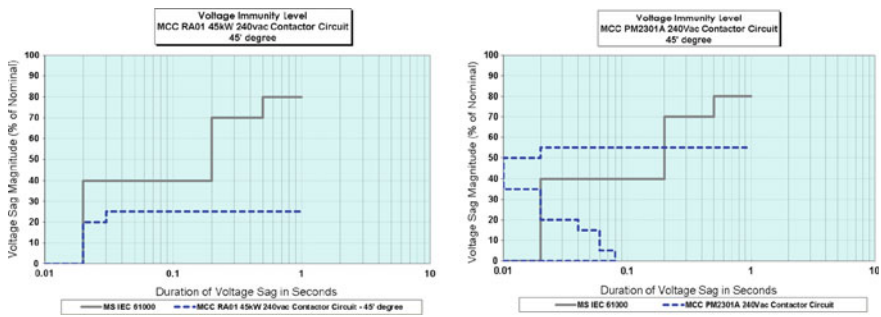


Fig. 9 Voltage tolerance curve for new and ageing contactor—point on wave 45°

The upper voltage threshold for contact disengagement is also between 50 and 55% with the duration band has also widened from 10 to 200 ms. This does not conform to IEC tolerance curve. For an extremely short time at 10 ms, the remaining voltage threshold (vertical limit) is between 35 and 50%.

For 60° point on wave test it is observed that there is a different response for the new contactor as shown in Fig. 10. For the remaining voltage from 10 to 20%, the withstand duration increased up to 40 ms, which exceeded the requirement of IEC curve. As for the ageing contactor, the upper threshold (horizontal) remained at 55% of remaining voltage. Nevertheless, for an extremely short time less than 10 ms, the remaining voltage threshold (vertical limit) is between 20 and 50% band.

From Fig. 11, it is observed that the new contactor, when subjected to 75° point on wave is able to withstand the 0% remaining voltage up to 40 ms compared to IEC curve at 20 ms. On the contrary, for the ageing contactor it could only withstand 50% voltage sag at 10 ms. The tolerance for 50% continues up to 120 ms then becomes more sensitive at 55% voltage up to 300 ms.

As shown in Fig. 12 the new contactor exhibited similar voltage tolerance characteristics as 0°, 15° and 30° point on wave. Comparably, the ageing contactor has also shown the exact response as of the 75° point on wave.

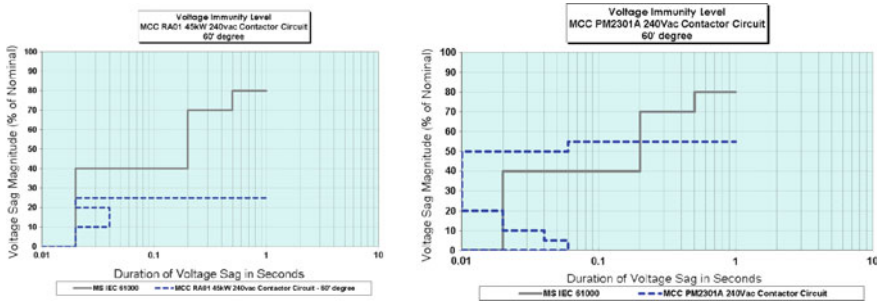


Fig. 10 Voltage tolerance curve for new and ageing contactor—point on wave 60°

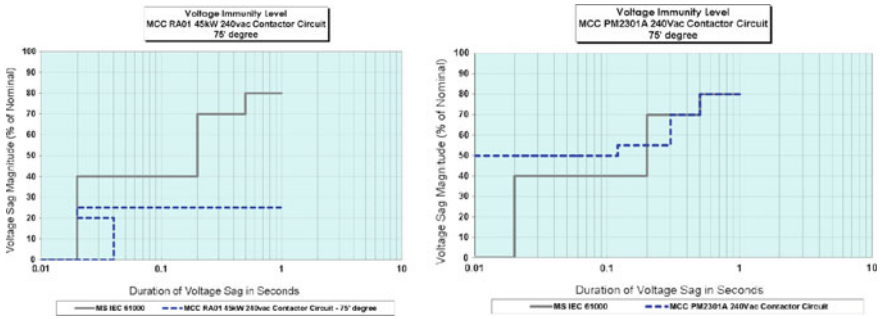


Fig. 11 Voltage tolerance curve for new and ageing contactor—point on wave 75°

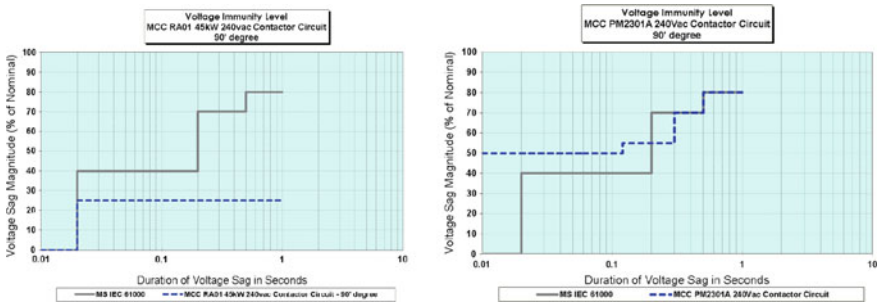


Fig. 12 Voltage tolerance curve for new and ageing contactor—point on wave 90°

### 5 Conclusion

The new contactor have shown better response to the IEC 61000 voltage tolerance curve compare to the ageing contactor. It also conformed consistently to the requirement of the standard when subjected to point on wave from 0° to 90°. On the other hand, ageing contactor exhibit mixed conformity to the IEC 61000 curve and found

to be more sensitive. For deep voltage sag, the ageing contactor had shown partial conformity to the standard. The voltage tolerance curve of new contactor is not significantly influenced by the point on wave. In contrast, the response of ageing contactor is significantly influenced by the point on wave.

## References

1. Milanovic JV, Zhang Y (2010) Global minimization of financial losses due to voltage sags with facts based devices. *IEEE Trans Power Deliv* 25:298–306
2. IEEE Std 1668-2017 (2017) IEEE recommended practice for voltage sag and short interruption ride-through testing for end-use electrical equipment rated less than 1000 V. *IEEE Ind Appl Soc*
3. ABB (2017) Motor protection and control manual motor starters, contactors and overload relays
4. Contactors and motor starters. <https://plc-scada-dcs.blogspot.com/2012/01/contactors-and-motor-starters.html>. Last accessed 22 June 2019
5. McGranaghan M, Mueller D (1991) Voltage sag in industrial system. In: Conference record. Industrial and commercial power systems technical conference 1991, IEEE, Memphis, TN, pp 18–24
6. Djokić SŽ, Milanović JV, Kirschen DS (2004) Sensitivity of AC coil contactors to voltage sags, short interruptions, and undervoltage transients. *IEEE Trans Power Deliv* 19:1299–1307
7. Kushare BE, Ghatol AA (2007) Investigation of cost effective method to improve voltage sag ride through capability of AC coil contactors. In: IET-UK international conference on information and communication technology in electrical science, pp 452–457
8. Hardi S, Daut I, Irwanto M (2010) Testing of contactors under voltage sag and non-sinusoidal voltage conditions. In: 2010 IEEE international conference on power energy, pp 683–688
9. Shareef H, Marzuki N, Mohamed A, Mohamed K (2010) Experimental investigation of AC contactor ride through capability during voltage sag. In: 2010 9th conference on environment electrical and engineering, EEEIC 2010, pp 325–328
10. Weldemariam LE, Gärtner HJ, Cuk V, Cobben JFG (2017) Mitigation strategies to improve the performance of AC contactor against voltage dips. In: Proceedings—2016 51st international universities power engineering conference, UPEC 2016, pp 1–6
11. IEC 61000-4-11 Electromagnetic compatibility (EMC)—Part 4-11 (2004) Testing and measurement techniques—voltage dips, short interruptions and voltage variations immunity tests. *Int Electrotech Comm*, p 29

# Vertical Axis Wind Turbines: An Overview



A. Yusof and M. R. Mohamed

**Abstract** In recent decades, wind energy becoming one of the most important types of renewable energy in electrical power production. It has been recognized as an encouraging renewable choice and one of the cleanest way to generate electricity. This paper provides brief ideas of a few types of vertical axis wind turbine (VAWT) utilized in the electrical power generation system. The growth and implementations of wind energy harnessing, wind turbine behaviors, related findings and the future trends of VAWTs were analyzed. The existence of some energy issues such as global warming and the diminishing of fossil fuels throughout the world nowadays need to be concerned and it was perceived that VAWT plays an important role in handling these current energy issues. VAWT seems to be more advantageous compared to HAWT in term of cost basis and simple design, but lags in performance efficiency. However, VAWT demonstrates better execution in complex wind condition with small wind access, which discussed throughout this paper. Currently, a lot of researches about the enhancement and augmentation of VAWT to increase the power production efficiency are ongoing. From the literature, the maximum VAWT's efficiency reached only about 40–50% which is still below the theoretical efficiency of the wind turbine. This shows the potential for further improvement in VAWTs to enhance the performance of wind turbine efficiencies. In summary, it can be concluded that further studies are critically needed to establish a greater acceptance of VAWTs as a feasible, reliable and reasonable power generation system especially for the low wind speed countries like Malaysia.

**Keywords** Wind energy · Vertical axis wind turbine · Low wind speed

## 1 Introduction

Renewable energy harvesting nowadays is becoming one of the most considerable alternative energy sources all around the world. Many nations are aware of the reality that fossil fuels are not sustainable and depleting drastically day by day. In addition,

---

A. Yusof (✉) · M. R. Mohamed

Sustainable Energy and Power Electronics Research (SuPER) Group, Faculty of Electrical and Electronics Engineering, Universiti Malaysia Pahang, 26600 Pekan, Pahang, Malaysia

© Springer Nature Singapore Pte Ltd. 2020

A. N. Kasruddin Nasir et al. (eds.), *InECCE2019*, Lecture Notes in Electrical Engineering 632, [https://doi.org/10.1007/978-981-15-2317-5\\_68](https://doi.org/10.1007/978-981-15-2317-5_68)

821

this conventional energy source causes some of the bad environmental problems such as global warming, carbon emissions, and acidic rain which can affect the state of human health. Hence, the current trends of the energy generation system need to be improved and replaced with cleaner sources. Renewable energy is a clean energy source that gives a lower environmental impact than conservative energy technology [1]. It is identified as an energy obtained from the sources of nature such as sunlight, wind, wave, water and so on.

The goal to reach full-scale renewable energy implementation in the future has been bringing interest to many countries in the world. According to the global renewable status report 2018, global wind market implementation had increased by around 11% for onshore and 30% for offshore in two years of time. The cumulative total installed capacity marked around 539 GW globally, with the addition of 52 GW wind power in the current year [2]. It was proved that the wind energy has been accepted as an encouraging renewable energy option worldwide.

## 2 Wind Energy

Wind is naturally caused by the expansion and convection of air that is absorbed by the Earth as a solar radiation. These thermal effects combined with dynamic effects from the Earth's rotation to produce wind [3]. Energy in wind is basically the energy of air flows from one place to another over the Earth's surface. Wind produces energy by using a wind turbine that usually consists of propellers or blades. Wind turbine system works when the rotor receives kinetic energy from air, which is then converted to mechanical and electrical energy, depending on the end use. These forms of energy extracted from the wind significantly depend on the rotor efficiency and turbine blade design connected to the wind power generation system.

### 2.1 Wind Power

Wind power is a process of creating electricity using the kinetic energy of wind that is produced due to its motion and mass. Kinetic energy per unit time is known as kinetic power ( $P$ ), can be expressed by:

$$P = \frac{1}{2} \dot{m} V^2, \quad (1)$$

where,  $\dot{m}$  is the air mass flow rate and  $V$  is the air velocity.

Most of the wind turbines today are used for generating electricity. As for that, wind turbines are associated with electrical networks. These networks include energy storage circuits, residential scale power systems, remote or island networks, and large scale utility grids [4]. Large scale utility grids usually used large wind turbines in



generating electrical energy. The wind power plants mainly stated in the countries which have strong wind speed all around the year, first mostly in United States and European countries and more recently in China and India. The largest onshore wind farm to date is Gansu Wind Farm, situated in China with the capacity nearly 7900 MW [5–7].

In this 21st century era, with the abundance of wind energy resources throughout the world, people are now moving forward with the vigorous initiatives to put a spurt on the development of wind energy technologies to enhance environmental quality and indirectly provide new jobs opportunities. Wind power is a promising alternative power source not only for large scale, but also for small scale and distributed power generation applications. Offshore wind is stronger and stable than onshore, but the construction and maintenance cost is much higher [8]. The onshore wind highlights a more economical source for electricity generation, competitive with the coal and gas plants.

## ***2.2 Global Expansion of Wind Energy Generation***

Wind energy is the next significant renewable energy resources after solar energy. There was a rapid extension of wind power growth globally. From December 2001 till December 2016 (15 years), global wind power capacity installed has increased drastically from 23,900 to 486,749 MW, with an annual growth rate at 22.25% [9]. It continues to grow as the wind power capacity reached 600 GW worldwide, with 53.9 GW added in 2018 [10].

Wind energy is emerging in the various locations, with the new market developing rapidly in Latin America, Asia, and also Africa [11]. Asia, which is led by China marked as the most growing countries for wind energy application in recent years. Since global wind energy installation is expanding significantly year by year, a lot of researches related to the wind energy harvesting technology has been conducted recently. The studies emerged not only for the technological state of wind turbine but also with the other alternatives of wind energy harvesting, for example by using drones with turbine blades and kites to harness wind energy.

## ***2.3 Implementation of Wind Energy Generation in Malaysia***

In Malaysia, renewable energy was first introduced into the energy mix under the Eight Malaysia Plan (2001–2005) via Fifth Fuel Policy. It is aimed to minimize the dependency of fossil fuels and becoming a major role in addressing global energy concern [12]. Ninth Malaysia Plan (2006–2010) next brought some thorough initiatives to the execution of renewable energy. Unfortunately, the target set was unachievable under this period of time [13]. Several new initiatives are then further reinforced in

the Tenth Malaysia Plan (2011–2015) to achieve the new target of total renewable electricity generation in Malaysia.

Despite all the initiatives effort and overall demand for renewable energy, the scale of wind power development in Malaysia is quite slow due to a few reasons. Malaysia has a relatively low wind speed throughout the year with an average velocity of 2–3 m/s. It is far lower than the velocity acquired in European countries. Therefore, the development of new power generation system that can work well in low wind speed is critically demanded in the country like Malaysia.

### **3 Wind Turbine Classification**

Wind turbine can be classified by two categories which are horizontal axis wind turbine (HAWT) and vertical axis wind turbine (VAWT). The HAWTs seem to be more advanced in their applications over the last decade and marked as the dominant technology in the modern wind energy industry. The higher efficiency of HAWTs has led to its wide application [14]. However, this higher energy efficiency only works in high wind speed with a fixed direction. In contrast, for low wind speed areas where the wind direction changes regularly, VAWTs are favored.

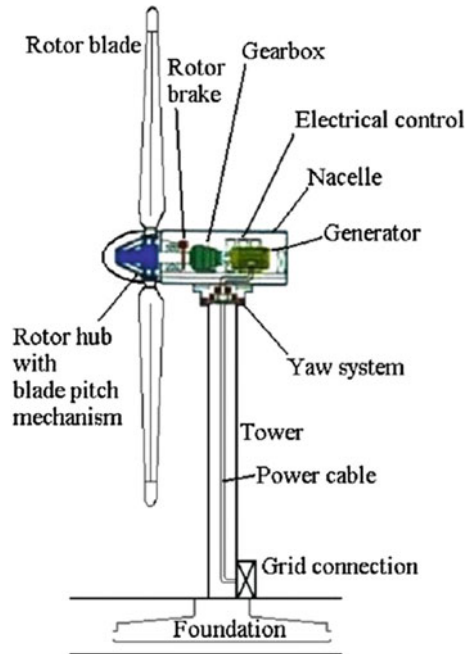
#### ***3.1 Horizontal Axis Wind Turbine (HAWT)***

Horizontal axis wind turbine is a turbine which the axis of rotation is parallel to the ground. HAWTs are generally connected to the grid-system due to their higher efficiency. The rotor is optimally designed with two or three blades to catch energy from the wind. The main advantages of HAWTs are better power production, high efficiency, and flexibility of the control system. Nevertheless, some drawbacks also have been noted such as high tower requirement to ensure a large amount of wind energy captured, high noise pollution, and bird's mortality. Apart from that, HAWTs need higher maintenance because of some external disturbances such as radio interference, TV transmission and radar [15]. Furthermore, for multi-directional and low wind speed areas, HAWT seem unfavorable [16]. Figure 1 shows a typical configuration of HAWT.

#### ***3.2 Vertical Axis Wind Turbine (VAWT)***

Vertical axis wind turbine is a turbine which the axis of rotation is perpendicular to the ground. VAWTs had overcome HAWTs in several conditions especially when dealing with the complex and low-speed wind pattern. Additionally, it provides better space installation due to the smaller and simple design. Another merits are less noise

**Fig. 1** Typical configuration of HAWT system [17]



pollution, can receive wind from any direction and produce lower forces on the support structure, due to the location near to the ground. VAWTs require less wind to generate power, making them suitable for low wind speed areas such as cities and urban areas. This low wind level requirement making them fit to be installed in the low wind speed areas which are closer to the ground. As they are being nearer to the ground, controlled and maintenance processes can be easily done [18].

VAWT is advantageous when comparing to the HAWT due to the needlessly of yaw control system, as it can harness wind from any directions. The benefit of omni-directional behavior of VAWT had overcome many other limitations, such as: fluctuation of the power output, the need of guy wires and the inability of Darrieus VAWTs to self-start. In addition, VAWTs are also quieter when compared to the HAWTs, with an experimental noise reading of about 95 dB, which resembles the sound of cars passing by a highway. When measured at the same location and condition of VAWT, noise reading is only 38 dB, which resembles the sound of whispered conversation [19]. This happened due to some factors, one of them is due to the low tip speed ratio of VAWTs.

Despite all the merits of VAWTs, there are also few drawbacks identified. Some of the significant ones were discussed. Sometimes, VAWTs cannot function well under gusty winds condition. The blades of VAWT are risky to the types of fatigue due to the large variation of applied forces in every rotation. The blades of conventional vertical turbines became bent with the rotor rotation, thus caused them to crack. By

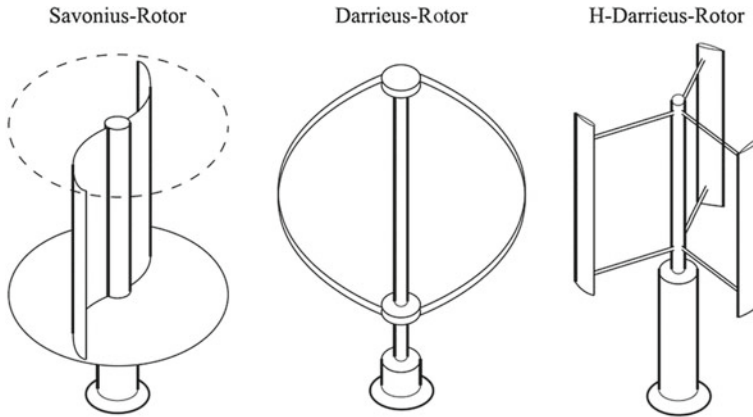


**Fig. 2** Standard types of vertical-axis wind turbines [21]

the time, the blades had broken and eventually tend to the turbine failure. These factors, unfortunately, led to the low reliability of VAWTs.

VAWTs can be divided into two main types that are Savonius-type (drag-driven) and the Darrieus-type (lift-driven). The Savonius uses drag forces and functions similarly to a water wheel. On the other hand, the Darrieus uses lift forces and employs blades similar to the one used on HAWTs. In VAWT, the shaft of the rotor is positioned vertically. The generator can be connected to the bottom of that axis shaft. With the fact that it can harness wind from any direction, this type of turbine does not need any yaw mechanism. In term of efficiency, lift type turbines are better than the drag type turbines. Thus, a lot of researches today are focusing on the lift type turbines. The first design of this turbine type was patented in U.S (1931) by G. J. M. Darrieus [20]. Figure 2 shows the conventional types of VAWTs.

The efficiency of turbine in converting the wind to electrical energy is known as a power coefficient,  $C_p$ . It is generally described as the ratio of electrical power produced by the wind turbine to the wind power that entered the turbine. According to the Betz Limit theory, the wind turbine can only reach maximum efficiency of around 59% [22]. A wind turbine will achieve its maximum efficiency at optimum tip speed ratio (TSR). TSR was defined as a ratio of the wind speed to the tips speed of wind turbine blades. The relationship between the rotor efficiency and the TSR is shown in Fig. 3. It can be seen that, for different turbine designs, the maximum efficiency occurred at different TSR value.

### 3.3 Savonius Type

The Savonius drag-based turbine was originated in 1922 by a Finnish engineer, S. J. Savonius. Their blade resembles a scoop or “S” shape and this is the simplest

**Fig. 3** Power coefficient of various VAWTs [23]

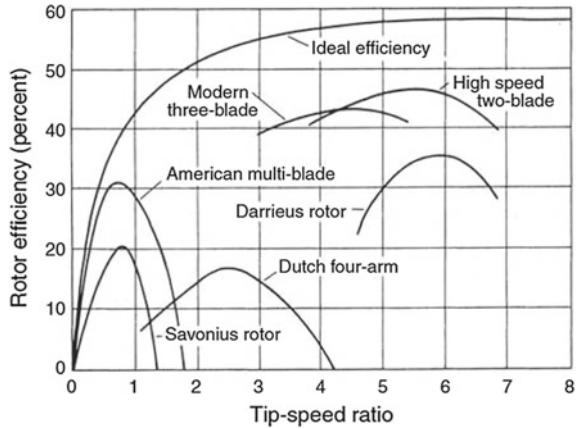
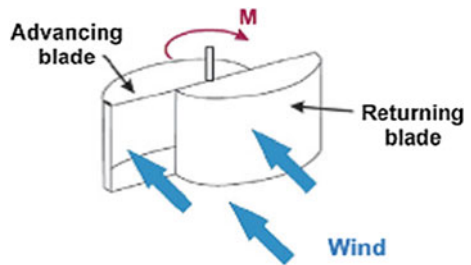


**Fig. 4** Drag-type VAWT Savonius rotor [25]



design among all VAWTs. This type of turbine tends to produce high starting torque hence lower the cut-in speed. Thus, it requires a low wind speed for the turbine to start rotating. Savonius turbines practically have low efficiency compared to other turbines but they still drew the attention of many researchers due to the merits explained [24]. Conventional Savonius turbines are not suitable for electricity generation due to its inability to rotate faster than the wind speed. However, previous researches verified that the generator rotation can be increased with the used of gearbox. As Savonius VAWT has lower power coefficient, many researches have been focusing on the enhancement of the turbine efficiency. This is due to the fact that Savonius turbines have better self-starting ability over the other VAWTs. Figure 4 shows the Savonius rotor of VAWT.

### 3.4 Darrieus Type

The lift force Darrieus wind turbine originated in 1927 by a French engineer, G. J. M. Darrieus. These turbines generally can be found in curved or straight bladed design. The lower bending of curve-bladed Darrieus turbines has better performance than

a straight bladed design. Nevertheless, straight blades Darrieus are favored because of its design simplicity [26, 27]. When compared to the Savonius turbine, Darrieus produces low starting torque, requiring them to have an external power source to start spinning, but when they spin, they are much faster than Savonius type. In term of efficiency, Darrieus type is notable with the higher power coefficient than Savonius type at high wind speed. Therefore, Darrieus turbines are much favorable to generate electricity rather than to pump water or similar activities [28]. Figure 5 shows the Darrieus type VAWT.

The arrangement effectiveness in vertical type turbines is independent of the wind direction [29]. Cut-in speed for Darrieus turbine is measured at 4–5 m/s, while the Savonius turbine has a lower cut-in speed of about 1 m/s. The Darrieus type needs external support to start, contrast with Savonius which have the self-starting ability. In order to overcome this shortcoming of Darrieus, some configurations improvement were executed to transform these machine to be versatile in all situations. One of the remarkable designs is H-blade turbine, which is a Darrieus turbine with a straight blade configuration. This type of turbines has a better performance than the conventional design with a simpler design and manufacturing process. The design was further improved in the recent decades into the fixed-pitch type and can be found in several variations which are articulating, titled, and helical rotor blade. Figure 6 shows the development timeline of Darrieus VAWT.

In literature, a comparison between phi-type, H-type, and helical-type rotor blade has been analyzed [31]. The result shows that the most fluctuating torque occurred in phi-rotor blade with the  $C_p$  varied about 0.3, followed by H-rotor with the  $C_p$  varied about 0.2 and the least fluctuation produced in helical-rotor blade with only 0.03  $C_p$  variation. The modeled rotor performance is shown in Fig. 7. Despite all the drawbacks and benefits gained, the acceptance of Darrieus design was strongly depending on their cost-effectiveness, reliability and self-starting ability.

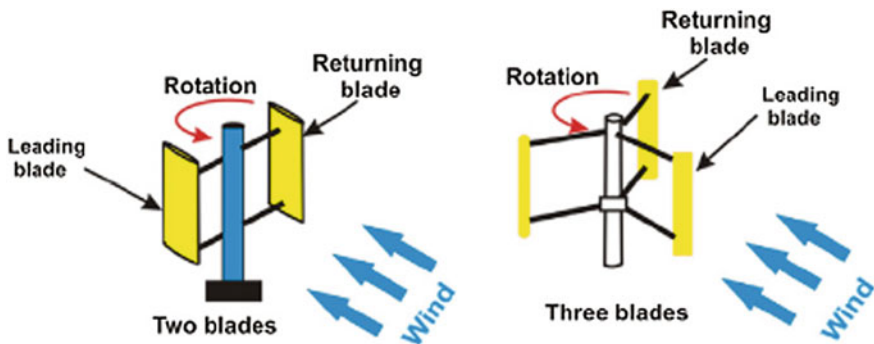


Fig. 5 Lift-type VAWT Darrieus rotor [25]

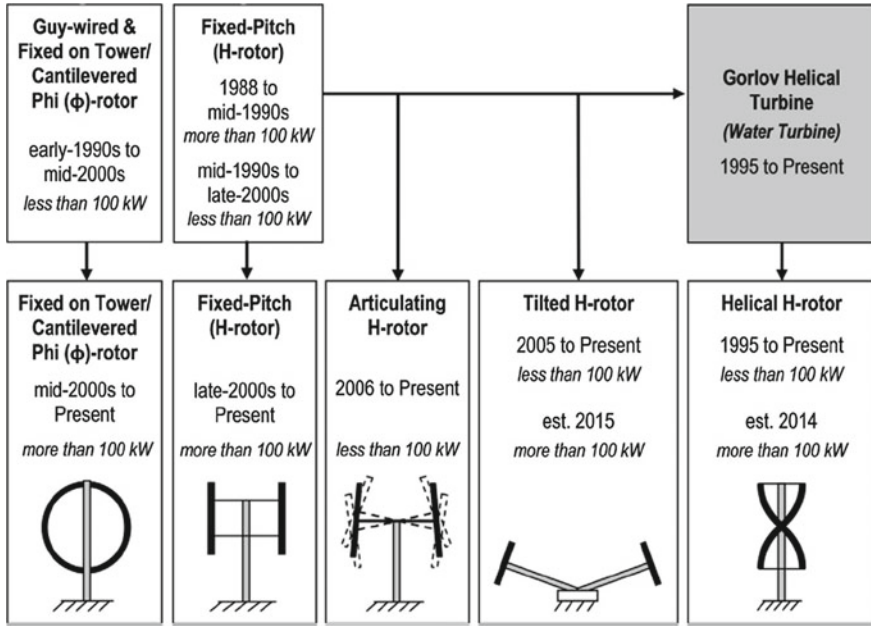


Fig. 6 Darrieus VAWT timeline development [30]

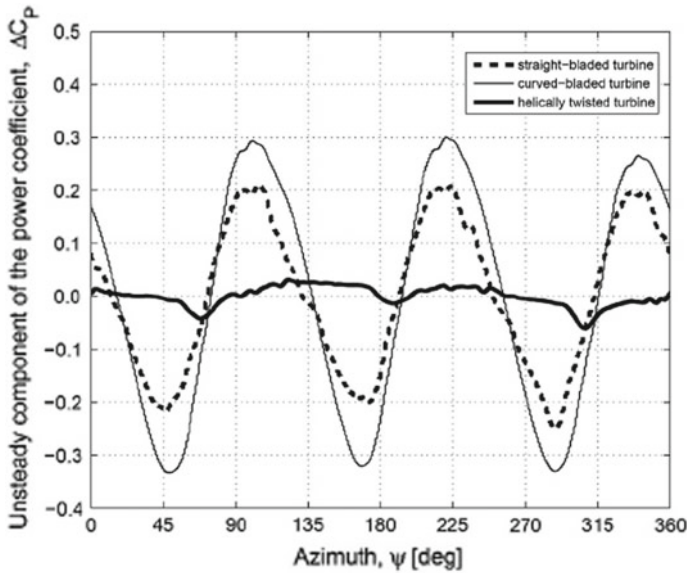


Fig. 7 Power coefficient variation of typical phi-rotor, H-rotor and helical-rotor blade [31]

**Fig. 8** Hybrid Savonius–Darrieus VAWT [33]



### 3.5 Hybrid Savonius–Darrieus VAWT

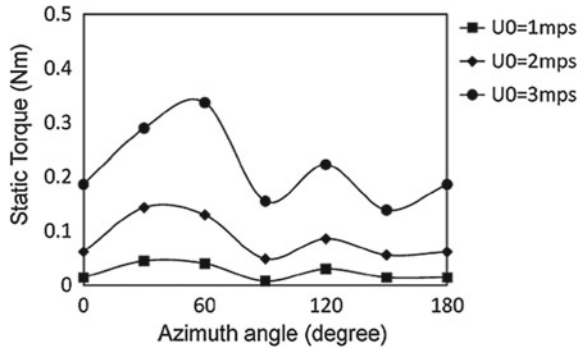
Another type of VAWT which have been used over the years is Hybrid VAWTs. This type of turbine proposed to overcome the limitations of each type of VAWTs. It's combined both the Savonius and Darrieus type turbine, and was developed on the basis of the previous designs. Figure 8 shows an example of a hybrid VAWT. In the current commercial developments of small wind turbines, this hybrid design has gathered much popularities. It is due to some beneficial characteristics including self-starting ability, low wind speed requirements and multi-directional wind access [32].

A lot of researchers have been involved with these turbine designs to overcome the demerits of previous VAWTs explained. There is a good strategy proposed by Korprasertsak and Leephakpreeda [34] to study the starting performances and efficiency of Darrieus–Savonius type through the effect of attachment angle and radius ratio of the blades. This hybrid turbine consists of a two-bladed Savonius rotor within a two-bladed Darrieus rotor. The combination of individual torque from those two design has shown an increased in the operational ability of the turbine, with the best coefficient performance,  $C_p$  of 0.363 at tips speed ratio (TSR) of 2.8. At this best  $C_p$ , the hybrid turbine started to rotate at wind speed as low as 2 m/s, as shown in Fig. 9. However, higher power efficiency Darrieus rotor is expected in further study to improve the efficiency.

A new design of the hybrid turbine was presented in another research with the objective of better wind energy extraction. The hybrid turbine was made by attaching a three-bladed Darrieus at the upper and a two-bladed Savonius at the bottom part



**Fig. 9** Start-up performance of combined Darrieus–Savonius rotor [34]



in the same shaft. It was reported that the turbine can generate a maximum power of 100 W at an optimal rotational speed of 245 rpm [35]. This speed was achieved with the variation of the solidity and the blades aspect ratio. From the power curve shown in Fig. 10, it can be seen that the power produced by the hybrid turbine is the summation of power achieved by the individual Darrieus and Savonius rotor.

In another research, an innovative hybrid VAWT was designed for a more sustainable and robust system with better self-starting characteristic [36]. The hybrid turbine is structured with two tiers; each tier has four two-bladed Savonius rotors and a three-bladed Darrieus turbine, with the position of Savonius is within the Darrieus turbine. By optimizing the configuration, a maximum  $C_p$  of 0.414 at 2.5 TSR was produced. Figure 11 shows the coefficient curve for single Darrieus and hybrid VAWT. Although the Darrieus demonstrated higher  $C_p$  compared to hybrid type, it cannot start-up independently due to the low initial torque. This arrangement showed enhancement in term of efficiency and their operational range when compared to the

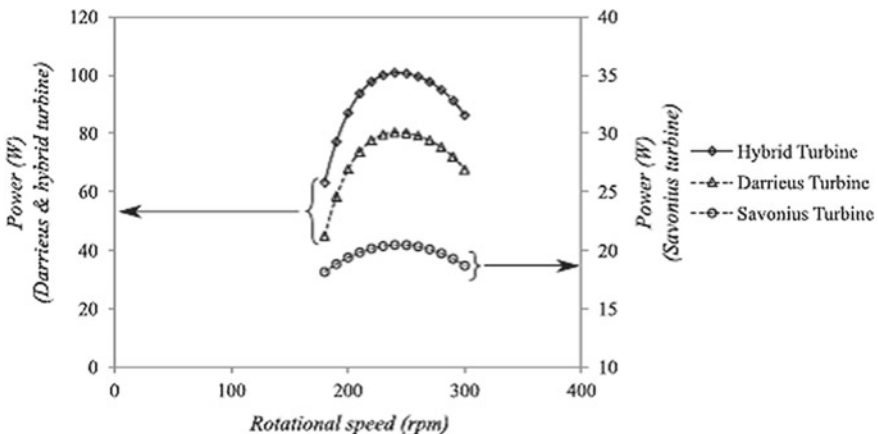
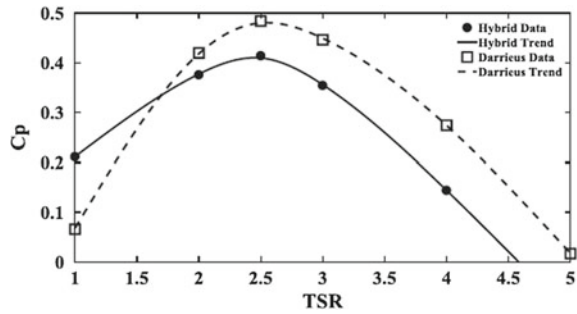


**Fig. 10** The power curve for individual and hybrid turbine [35]

**Fig. 11** The power coefficient comparison between Darrieus and hybrid turbine [36]



previous literature of hybrid VAWT. However, the aerodynamic performance can still be improved in future studies by implementing a control analysis technique.

#### 4 Proposed Design Methodology for Hybrid VAWT

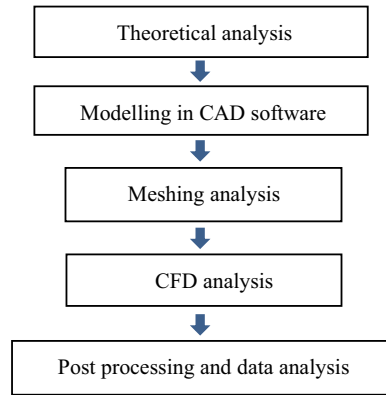
From literature, it is discovered that the performance of the Savonius turbine did not change much with the change in turbine design. In contrast, even a small change in the design affected the Darrieus turbine. Due to this characteristic, a hybrid VAWT design will be proposed by following these design and analysis steps:

1. Design and studies of individual Savonius turbine
2. Design and studies of individual Darrieus turbine
3. Design and studies of hybrid Savonius–Darrieus turbine.

For each step, CAD modeling will be done in Solidworks, before the geometry design imported to ANSYS software for meshing analysis. Analysis of Computational Fluid Dynamics (CFD) will then be done using ANSYS Fluent. Finally, the data will be interpreted into MATLAB for power coefficient calculation. The flow chart of turbine analysis is shown in Fig. 12.

The proposed hybrid turbine will have two tiers; each tier has a two-bladed Savonius turbine within an H-Darrieus turbine. The Darrieus blade number will be studied as one of the design parameters. The proposed design will use contra-rotating concept where two rotors in each tier will spin in the opposite direction to each other. This concept and configuration were achieved based on the review of previous optimization literature on the individual and hybrid design of VAWTs.

**Fig. 12** The flow to analyze turbine performance



## 5 Future Development of VAWTs for Energy Generation

Based on the presently available data from previous researches, the future of where VAWTs technology goes can be predicted. From literature, it can be said that the major problem encountered in VAWTs is low air capture that resulting in low-performance efficiency. An augmentation system such as deflector and guide vane can solve this problem by enhancing the wind flow towards turbine rotors. Many researchers are doing this at present. Previous literature also shows that a lot of researchers have designed and modeled basic wind turbine with some modifications to discover the significant performance which directly dependent on the turbine changing parameters. The example of studies covered the blade solidity impact, lift and drag forces, angle of attack, and also the blade material used. The modern VAWTs commonly employed NACA 4-digit series due to the well documented of airfoils aerodynamic characteristics [37].

A hybrid Savonius–Darrieus type has gained much popularities in order to overcome the low self-starting capability in the Darrieus turbine. This is generally used for small power applications, especially in cities and urban areas. In term of design, the helical arrangement has been verified in increasing the power coefficient by 9% compared to the straight type under the same operational condition [38].

## 6 Conclusion

In the near future, many nations all over the world will face a lot of problems due to the diminishing of fossil fuels and non-renewable energy sources. Thus, it is a crucial action to take into account the renewable energy option such as wind, solar, tidal current and so on as an alternative source of the power generation system.

Enhancement of VAWTs performance will give a huge advantage to so many countries worldwide. With this improvement, VAWTs are possible to be implemented

in many places for electricity generation. As the impact, the dependency on fossil fuel and conventional energy sources will be decreased, hence contributes to the reduction of carbon emission and global warming issues.

This paper intended to provide an initial useful knowledge for future studies of VAWT. Further study of the novel turbine configuration will be conducted to address some limitations of the current studies. The new design is expected to have higher efficiency and more robust system. Consequently, by the analysis associated with the VAWTs, it can be concluded that this technology undoubtedly will be with us in the near future, as has happened to other renewable energy range such as HAWT and PV.

## References

1. Koroneos CJ, Koroneos Y (2007) Renewable energy systems: the environmental impact approach. *Int J Global Energy Issues* 27(4):425
2. REN21 (2017) REN21 highlights. Highlights REN21 renewables 2017 GSR perspective, p 45
3. Ptasiński KJ (2015) Renewable energy resources, vol 89
4. Wu B, Lang Y, Zargari N, Kouro S (2011) Power conversion and control of wind energy systems
5. Sawe BE (2018) The world's 10 largest wind farms [Online]. Available <https://www.worldatlas.com/articles/the-10-largest-wind-farms.html>. Accessed 10 Apr 2019
6. Vyas K (2018) The 11 biggest wind farms and wind power constructions that reduce carbon footprint. *Interesting engineering* [Online]. Available <https://interestingengineering.com/the-11-biggest-wind-farms-and-wind-power-constructions-that-reduce-carbon-footprint>. Accessed 10 Apr 2019
7. Kanter D (2019) The world's biggest wind farms. *Bloomberg news* [Online]. Available <https://www.forbes.com/pictures/mef45ehmdh/gansu-wind-farm/#7a6dc67145d3>. Accessed 10 Apr 2019
8. Hevia-Koch P, Klinge Jacobsen H (2019) Comparing offshore and onshore wind development considering acceptance costs. *Energy Policy* 125:9–19
9. Power and renewable energy market review (2018)
10. Statistics (2019) World wind energy association [Online]. Available <https://wwindea.org/information-2/information/>. Accessed 18 Apr 2019
11. Global Wind Energy Council (2015) Global wind report annual market update 2014. *Wind Energy Technol*, 75
12. Hashim H, Ho WS (2015) Renewable energy policies and initiatives for a sustainable energy future in Malaysia. *Renew Sustain Energy Rev* 15(9):4780–4787
13. Petinrin JO, Shaaban M (2015) Renewable energy for continuous energy sustainability in Malaysia. *Renew Sustain Energy Rev* 50:967–981
14. Kumar R, Raahemifar K, Fung AS (2018) A critical review of vertical axis wind turbines for urban applications. *Renew Sustain Energy Rev* 89:281–291
15. Chaudhari SS, Chaudhary AO, Gole PP, Patil KT (2017) Design and construction of combined axis wind mill turbine for maximise efficiency. *IJARIII* 3(3):1914–1921
16. Saad MMM, Asmuin N (2014) Comparison of horizontal axis wind turbines and vertical axis wind turbines. *IOSR J Eng* 4(8):27–30
17. Ciang CC, Lee JR, Bang HJ (2008) Structural health monitoring for a wind turbine system: a review of damage detection methods. *Meas Sci Technol* 19(12)
18. Hettiarachchi N (2014) Design fabrication and testing of a vawt with wind deflectors 2017
19. AZoCleantech (2014) An introduction to vertical wind turbines [Online]. Available <https://www.azocleantech.com/article.aspx?ArticleID=457>. Accessed 01 Apr 2019

20. Beri H, Yao Y (2011) Numerical simulation of unsteady flow to show self-starting of vertical axis wind turbine using fluent. *J Appl Sci* 11(6):962–970
21. Schaffarczyk AP (1983) Introduction to wind turbine engineering
22. Thongam JS, Ouhrouche M, Ragheb M, Ragheb AM (2011) Wind turbines theory—the betz equation and optimal rotor tip speed ratio. In: *Fundamental and advanced topics in wind power*, vol 1, no 1, pp 339–360
23. Edition S (2013) *Wind and solar power systems: design, analysis, and operation*. *Choice Rev Online* 43(06):43–3410
24. Patel N, Uddin MN (2012) Design and performance analysis of a magnetically levitated vertical axis wind turbine based axial flux PM generator. In: *2012 7th international conference electrical and computer engineering, ICECE 2012*, pp 741–745
25. Mohamed MH (2013) Impacts of solidity and hybrid system in small wind turbines performance. *Energy* 57:495–504
26. Li Y (2019) Straight-bladed vertical axis wind turbines: history, performance, and applications. *IntechOpen*, p 13
27. Li C, Xiao Y, Xu Y, Peng Y, Hu G, Zhu S (2018) Optimization of blade pitch in H-rotor vertical axis wind turbines through computational fluid dynamics simulations. *Appl Energy* 212:1107–1125
28. REUK.co.uk, Darrieus wind turbines. The renewable energy website [Online]. Available <https://www.reuk.co.uk/wordpress/wind/darrieus-wind-turbines/>. Accessed 02 Apr 2019
29. Ragheb M (2011) Vertical axis wind turbines, pp 1–39
30. Tjiu W, Marnoto T, Mat S, Ruslan MH, Sopian K (2015) Darrieus vertical axis wind turbine for power generation I: assessment of Darrieus VAWT configurations. *Renew Energy* 75:50–67
31. Scheurich F, Fletcher T, Brown R (2013) The influence of blade curvature and helical blade twist on the performance of a vertical-axis wind turbine, pp 1–16
32. Korprasertsak N, Leephakpreeda T (2016) Analysis and optimal design of wind boosters for vertical axis wind turbines at low wind speed. *J Wind Eng Ind Aerodyn* 159:9–18
33. Vertical axis wind turbines Darrieus type wind turbine [Online]. Available <https://www.seao2.com/vawt/>. Accessed 30 Apr 2019
34. Liang X, Fu S, Ou B, Wu C, Chao CYH, Pi K (2017) A computational study of the effects of the radius ratio and attachment angle on the performance of a Darrieus–Savonius combined wind turbine. *Renew Energy* 113:329–334
35. Jacob J, Chatterjee D (2019) Design methodology of hybrid turbine towards better extraction of wind energy. *Renew Energy* 131:625–643
36. Hosseini A, Goudarzi N (2019) Design and CFD study of a hybrid vertical-axis wind turbine by employing a combined Bach-type and H-Darrieus rotor systems. *Energy Convers Manag* 189:49–59
37. Yi M, Jianjun Q, Yan L (2018) Airfoil design for vertical axis wind turbine operating at variable tip speed ratios. *Open Mech Eng J* 9(1):1007–1016
38. Damota J, Lamas I, Couce A, Rodríguez J (2017) Vertical axis wind turbines: current technologies and future trends. *Renew Energy Power Qual J*, 530–535

# Hyperheuristics Trajectory Based Optimization for Energy Management Strategy (EMS) of Split Plug-In Hybrid Electric Vehicle



Muhammad Ikram Mohd Rashid, Ahmad Amir Solihin Mohd Apandi, Hamdan Daniyal and Mohd Ashraf Ahmad

**Abstract** To date, with the advancement in energy-related technology, the regulations prior to the environment and energy emission are also strictly increasing due to the impact of global warming. Hence, many electric vehicles are affected since one of their principles is closely related to the issue of short-range storage capacity and long charging time which are not in favor to most of the automotive customers. Thus, it embarks many kinds of research to establish development of an efficient energy management storage (EMS) to fulfill the objectives at the same time keeping the vehicle performance at its convincing standard. This work presents the Hyperheuristics Trajectory Based Optimization for Energy Management Storage (EMS) of The Split Plug-in Hybrid Electric Vehicle. The Split Plug-in Hybrid Electric Vehicle is discussed in different and recent perspective by zooming into other aspects of EMS point of view. A comprehensive discussion is elaborated by comparing various strength and weaknesses of this research concept. The performance results from this improved approach are compared with the conventional HEVs. The analytical modeling methods such as physics-based Resistive Companion Form technique and Bond Graph method are presented with some powertrain component and system modeling application examples.

**Keywords** Hyperheuristic · Energy management strategy (EMS) · Split plug-in hybrid electric vehicle (PHEV)

## 1 Introduction

The introduction of Hybrid electric vehicles (HEV) assists the user to scale back their fuel consumption when using the vehicle through the help of an electrical system. This is as a result of HEV which uses a combination of 2 supplies that are Internal Combustion Engine (ICE) and an electrical generator for the backup supply of power. ICE uses oil usually diesel or petrol to get the energy to maneuver the car whereas the

---

M. I. Mohd Rashid (✉) · A. A. S. M. Apandi · H. Daniyal · M. A. Ahmad  
Faculty of Electrical and Electronic Engineering, Universiti Malaysia Pahang, 26600 Pekan,  
Pahang, Malaysia  
e-mail: [mikram@ump.edu.my](mailto:mikram@ump.edu.my)

© Springer Nature Singapore Pte Ltd. 2020  
A. N. Kasruddin Nasir et al. (eds.), *InECCE2019*, Lecture Notes in Electrical Engineering 632, [https://doi.org/10.1007/978-981-15-2317-5\\_69](https://doi.org/10.1007/978-981-15-2317-5_69)

837

function of the generator is to produce electricity to works the electrical motor. HEV provides a minimum fuel uses because the electric motor accustomed to move the vehicle from the remainder and ICE support the vehicle once it begins to move faster. The price of fuel gives a bonus to HEV type vehicle than ICE. Energy Management Strategy (EMS) could be a methodology in improving the divided consumed by electrical motor and oil so as in presenting the most effective improvement of petrol usage. The EMS is most perform in power management. Automotive and communication management make a cooperative analysis that specializes in fuel usage improvement [1]. Several approaches have projected to control the petrol usage that remains to think about numerous features in the model supported the methodology as the best management control.

Several things that could be improved in the model. The aspect that can be optimized is the power usage in four components in HEV model which are ICE, generator, electric motor and battery. Most HEV analysis is specializing in optimization using advanced control algorithms which result in a decrease of the energy flow loss [2]. The energy consumption has been optimized through decreasing the losses of power from that 4 components to get an improvement of the performance of the model.

The methodology that will use to improve model performance is simultaneous perturbation stochastic approximation (SPSA). SPSA is amongst stochastic approximation cluster methodology. This type of stochastic approximation has possible applications in an exceeding range of scope to statistic model and control [3]. Therefore, SPSA is the best suited for this project.

Lastly, we required EMS to assist any event of HEV for the upcoming day for an improved presentation in competing for other kinds of motorcars.

## 2 HEV Free Model

To make the process of optimization easy, a simple HEV model has been chosen from MATLAB library archive. This model is used in the simulation process. HEV model from MATLAB library contains operational circuit that able it to yield output like car movement in term of velocity, fuel usage in term of power losses, and so on. The model contains electric and physical part. HEVs contain a couple of energy bases which are, (1) Internal Combustion Engine (ICE) and (2) battery. Figure 1 is the block diagram of the simple HEV model.

There are the engine, electric generator, electric motor, and battery which are four constraints that being adjusted in order to adjust the results which are power loss and petrol usage. One gain will be put inside the four constraints. The starting output is taken before the tuning process is done. The power graph has been recorded to compare the final result.

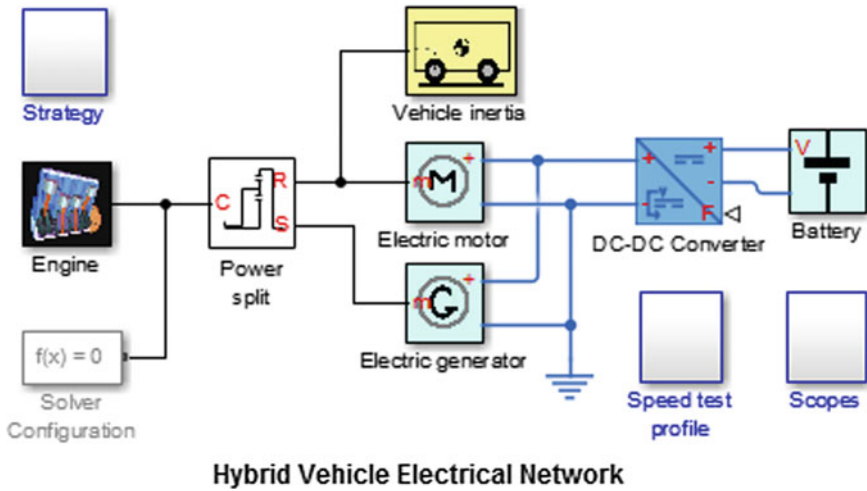


Fig. 1 HEV models MATLAB Simulink

L, H, Y, and U gain has been used. This four gain is located in the four constraints in the model and the initial gain value is set to 1. First, a simulation will be run with this initial value. The result of the first simulation will be recorded. After that, the initial value is replaced with new gain value by using the simulated Annealing Algorithm and getting the new result.

### 3 Methodology

The way to implement the design into the HEV system is explained in this section. The implementation process needs to use the combination of Simulink and M-File in MATLAB software. The Simulink is needed for HEV model and M-File is needed to control the gains in the Simulink based on Hyperheuristic methodology. A Hyperheuristics is one of the heuristics search techniques purposely that seeks intelligently based on Artificial Intelligence to automate the incorporation of (1) the process of selecting, (2) combining, (3) generating or adapting a few of simpler heuristics to efficiently achieve optimal computational search problem solutions. One of the vital motivations of thorough hyperheuristics investigation is to develop systems that can offer an alternative way of handling clusters of problems rather solve an only dedicated and specific problem [4-6].



A multiple heuristics may have their own unique strength and weaknesses depending on the problems to be solved. However, manual selection of an optimal heuristics has become no more practical to solve clusters of problem. Hence, the Hyperheuristics is the idea to automatically devise algorithms by combining the unique strength and rectification of the weaknesses of identified heuristics [7]. In a common hyper-heuristic solving framework, there are two major elements that constructively contribute to either constructive or perturbative heuristics, which are a high-level methodology incorporated with a set of low-level heuristics. Given a problem example, the high-level method take which low-level heuristic should be applied at any given time, depending upon the existing problem state, or in search stage [5]. Below is the hyper-heuristic algorithm:

The general optimization problem is given

$$\Psi = e^{-\delta * T / q}, \tag{1}$$

where  $\delta$  is the difference in fitness value between current solution (Si) and the previous solution (So) example  $\delta = f(Si) - f(So)$ , T is the iteration counter, q is a control parameter for consecutive non-improving iterations.

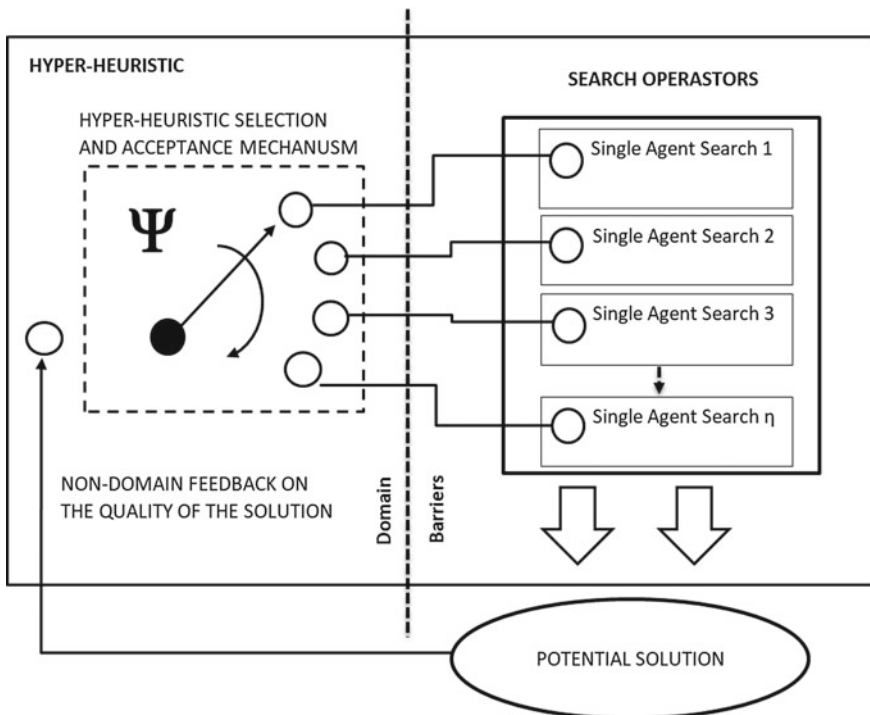


Fig. 2 Hyperheuristic configuration

**Table 1** Parameters and gain name in Simulink block

Gain name	Parameter
L	Electric motor
Y	Internal combustion engine
U	Battery
H	generator

By referring Fig. 2 of Hyperheuristic algorithm, the simulation for this project is as below:

1. Get the maximum iterations. Then, recognize four gain with a starting value of 1.
2. Justify the objective function value in every iteration by performing the selection of Monte-Carlo Hyperheuristic algorithm given before.
3. If already get the maximum iteration number, select the lowermost value of power losses to compare with the pure model in the final valuation.

Hyperheuristic procedure was implemented inside the M-file to create the new number in the constraints for every iteration. Then the value generated will be sent to the parameter in the Simulink block diagram. The HEV in Simulink is called using M-file to run repeatedly. The running process will stop at the maximum number of iterations. Then, the output of the constraint will differ continuously and get different result of power losses. Table 1 shows the constraints and name of the gain added:

Figures 3, 4, 5 and 6 show the place of each gain that has been added.



**Fig. 3** Gain in battery

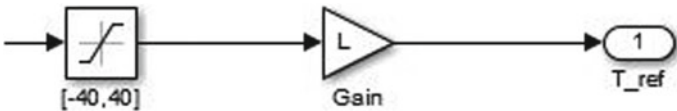


**Fig. 4** Gain in motor



**Fig. 5** Gain in generator



Fig. 6 Gain in engine

### 4 Result

Figures 6 and 7 show how the control parameter behaving due to the driving cycle time. Each of the control parameters works independently along with time. These are the reason why the control parameter affects the objective function. Thus to obtain the best objective function, the control parameter needs to have the best gains values which will be searched by the MATLAB simulations. The simulation period is set to 40 s. This includes the acceleration and deceleration of the vehicle in order to mimic the real movement of a vehicle. Figure 6 shows how the control parameters (generator, engine, battery, and motor) behaving during the simulation. Each of the parameters works together to produce the outputs which are the fuel loss and electrical loss. The most suitable value of the parameter for the model will be discussed in this section. In the simulation that already done, variety values have been used. Every value that yield is produced by the hyperheuristic algorithm that was used in the m-file Matlab. Every parameter yields a different result for every iteration to lower the energy losses. The analysis takes place to decide the suitable gain values after getting the lowermost value of losses. The hyperheuristic-based method can be prolonged to another difficult condition while the objective function might be calculated [8]. The distinguishing of the pure and the adjusted model. Figures 7 and 8 show gain value (L, Y, H and U) and also the energy losses ( $P_{loss}$ ) convergence graphs show in Figs. 9 and 10 for trial 1 and 2.

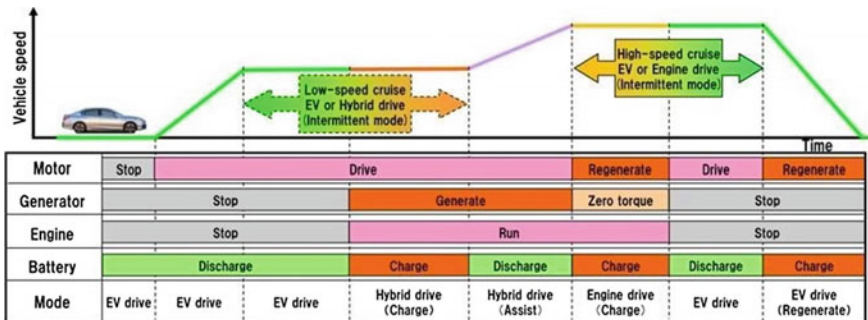


Fig. 7 Driving cycle configuration for HEV

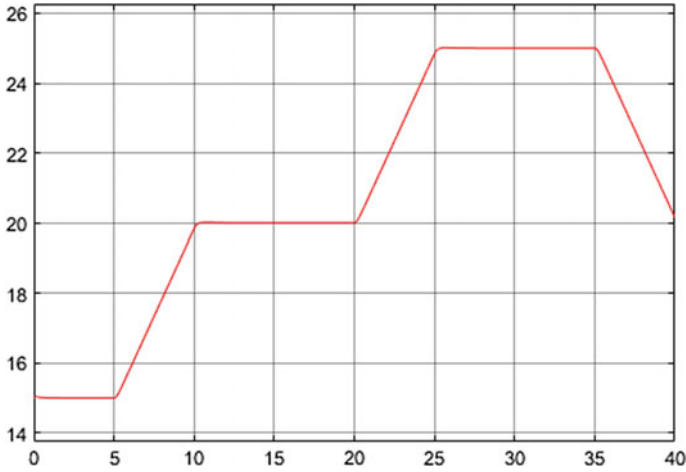


Fig. 8 Driving cycle from MATLAB Simulink

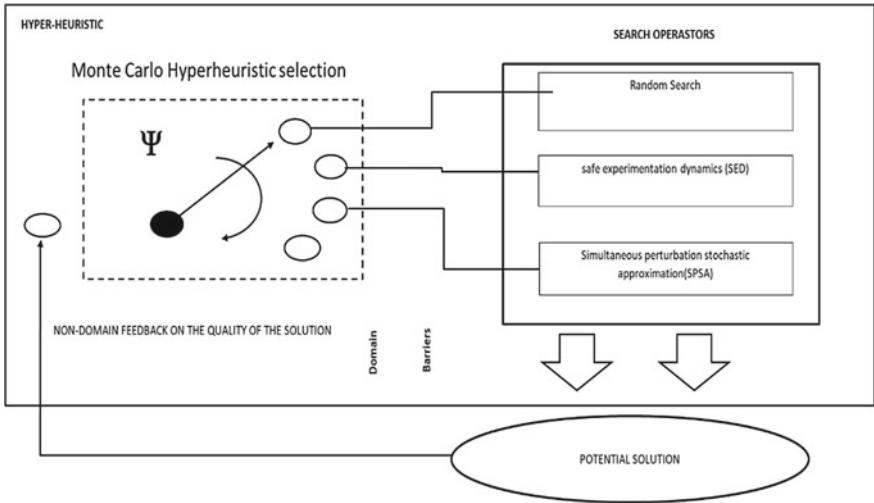


Fig. 9 Propose hyperheuristic configuration

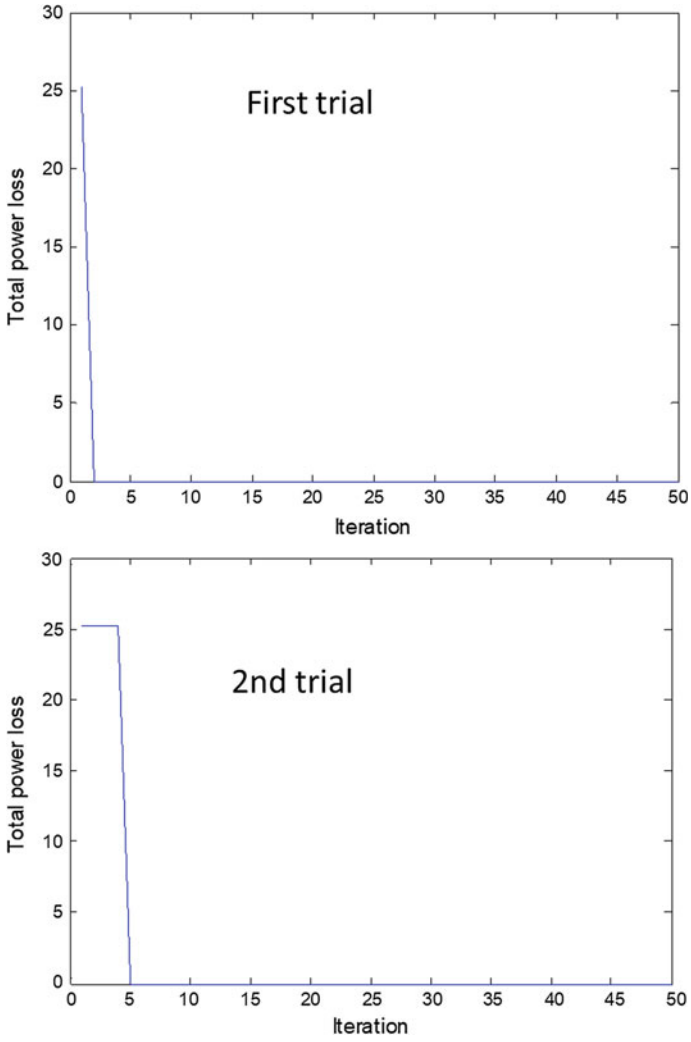


Fig. 10 Convergent graph from simulation

**Table 2** Recommend gain value for parameter

Parameter	Gain value
Internal combustion engine	1.5232
Electrical motor	0.1594
Electrical generator	1.0878
Battery	0.8821

The result showed that the Elapsed time taken was 66,595.654213 s. The average percentage of successful of SPSA is 13.5593, and the average percentage of successful of RS is 38.1356 while the average percentage of successful of SED is 48.3051. The average optimal objective function is  $5.5682e-20$ . At last, a pitted comparison between the original scheme and the problem of power losses problem is explained.

## 5 Discussion

The final result that we get from this project will be discussed in this section. We can see from the result before, the lowermost losses that we got is at 8th iteration with 0.1407 whereas the most is 0.2282 at 3rd iteration. From the behavior of this trend, it can be comparatively seen that the present model which is 852.7655 value of losses and it is obviously different between both iterations. The lowermost losses have been determined and the compatible gain for the parameter is obtained. Table 2 shows all the four parameters with their gain values.

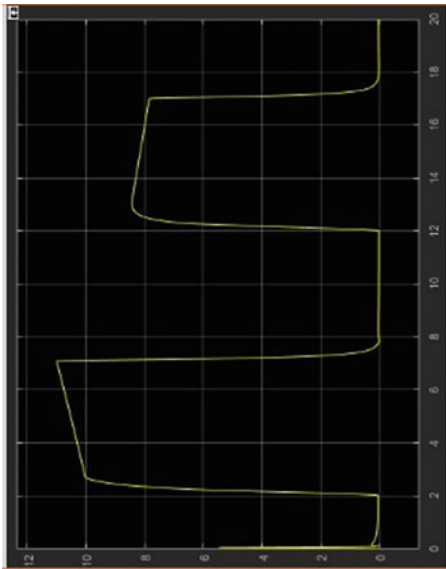

For additional information, Table 3 shows the comparison between the optimized model and the original model.

Since the shaft speed is maintained as the same, it is mean that both models moving at the same speed and reducing the power consumption and power loss by the HEV model.

## 6 Conclusion

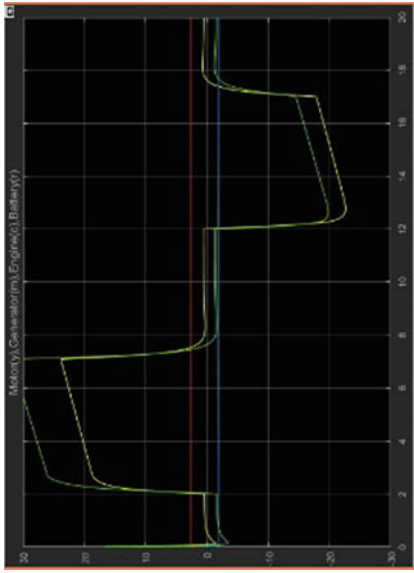
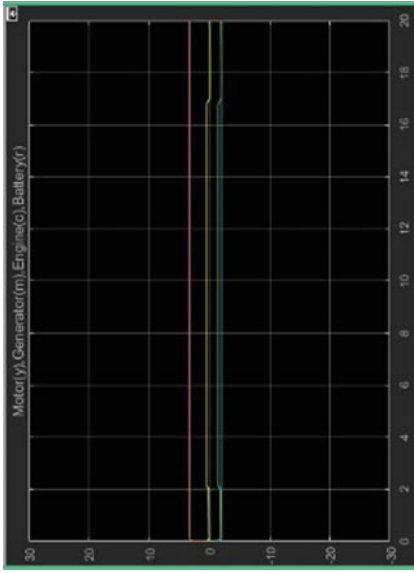
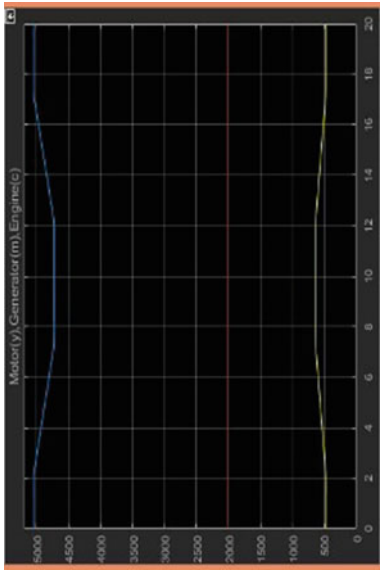
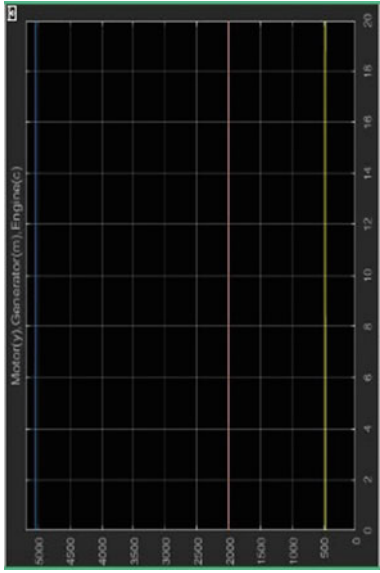
In this paper, a framework of a Hyperheuristics Trajectory Based Optimization in EMS for HEV system has been applied. The minimal losses of energy value posses a potential improvement to increase the efficiency of electrical condition as compared to the efficiency established based on the initial value. It can be seen that the performance can be efficiently improvised by contemplating and applying this approach to systematically tune the gain value for HEV system with the consideration based on the gain value normal system as a comparative judgment. These single-agent selector methods were bench-marked with other existing technique to cross-validate its performance through stand-alone single-agent technique. The technologies of HEV can be creatively enhanced in the future to compete in the automotive industry. As the

Table 3 Power graph

Model graph	Original model	Optimize model
Power loss		

(continued)

Table 3 (continued)

Model graph	Original model	Optimize model
<p>Power</p> 		
<p>Shaft speed</p> 		



results have proven its positive and high potential approach, this project can be considerably remarked as a successful and innovative application platform to the HEV suitability. Due to the free model characteristic HEV, there is a room of improvement that can be optimized and explored further in future work.

**Acknowledgements** This research study is supported by the Ministry of Higher Education Malaysia (MoHE) and Universiti Malaysia Pahang under the Fundamental Research Grant Scheme FRGS/1/2017/TK04/UMP/03/1 or RDU170129.

## References

1. Ahmad MA, Azuma S, Baba I, Sugie T (2014) Switching controller design for hybrid electric vehicles. *SICE J* 7(5):273–282
2. Wang Q, Frank AA (2014) Plug-in HEV with CVT: configuration, control, and its concurrent multi-objective optimization by evolutionary algorithm. *Int J Automot Technol* 15(1):103–115
3. Spall JC (1992) Multivariate stochastic approximation using a simultaneous perturbation gradient approximation. *IEEE Trans Autom Control* 37(3)
4. Burke EK, Hart E, Kendall G, Newall J, Ross P, Schulenburg S (2003) Hyper-heuristics: an emerging direction in modern search technology. In: Glover F, Kochenberger G (eds) *Handbook of metaheuristics*. Kluwer, The Netherlands, pp 457–474
5. Ross P (2005) In: Burke EK, Kendall G (eds) *Hyper-heuristics, search methodologies: introductory tutorials in optimization and decision support techniques*. Springer, Berlin, pp 529–556
6. Ozcan E, Bilgin B, Korkmaz EE (2008) A comprehensive analysis of hyper-heuristics. *Intell Data Anal* 12(1):3–23
7. Ozcan E, Bilgin B, Korkmaz EE (2006) Hill climbers and mutational heuristics in hyperheuristics. *Lecture notes in computer science*. In: *The 9th international conference on parallel problem solving from nature*. Springer, Berlin, pp 202–211
8. Ahmad MA, Baba I, Azuma S, Sugie T (2013) Model free tuning of variable state of charge target of hybrid electric vehicles. *The International Federation of Automatic Control*

# Utilization of Filter Harmonic Current Based on Shunt HPF Within the Acceptable IEEE-519 Standard



Mohamed A. Omran, Izzeldin I. Mohd, Abu Zaharin Ahmad, Mohamad M. Almelian, Fahmi Samsuri, Muhamad Z. Sujod, Walid K. A. Hasan and Mohamed Salem

**Abstract** Harmonic-related problems such as communication noise, malfunctioning of the solid-state control circuit, etc., are often encountered in industrial plants that have a significant amount of rectification. Different techniques to eliminate harmonics current from power systems to the ground have been proposed and one of them is shunt HPF which is an effective and widely-used method for power quality improvement. This paper presents the idea of reusing the HPF harmonic current created based on STF–SRF theory to feed AC load within the limits of IEEE-519 (Less 5%). The circuit has been simulated in the MATLAB-Simulink and tested under distorted source voltage with varying loads. The outcomes of the simulations showed the THD at PCC to be less than 5% even when the HPF current was connected to the system (increasing the source current).

**Keywords** Total harmonic distortion (THD) · Passive power filter · Hybrid power filter · Self-tuning filter · LMBP controller

## 1 Introduction

The generation of harmonic current from the widespread use of nonlinear loads has greatly impacted the quality of grid currents. The effects of harmonic currents on the grid include overall system efficiency degradation via worsening the systems' power factor (PF) performance [1–4], as well as other related problems like overheating of equipment, sensitive device failures, and blowing of capacitors. Thus, there is a need to ensure a reduced level of harmonic currents in a power system. The minimization

---

M. A. Omran · I. I. Mohd (✉) · A. Z. Ahmad · M. M. Almelian · F. Samsuri · M. Z. Sujod  
Faculty of Electrical and Electronics Engineering, Universiti Malaysia Pahang (UMP), 26600  
Pekan, Pahang, Malaysia  
e-mail: [izzeldin@ump.edu.my](mailto:izzeldin@ump.edu.my)

W. K. A. Hasan  
Faculty of Engineering/Jadu, University of Aljabal Algharbi, Ghiryan, Libya

M. Salem  
School of Electrical and Electronic Engineering, Universiti Sains Malaysia (USM), Engineering  
Campus, 14300 Nibong Tebal, Pulau Pinang, Malaysia

© Springer Nature Singapore Pte Ltd. 2020

A. N. Kasruddin Nasir et al. (eds.), *InECCE2019*, Lecture Notes in Electrical  
Engineering 632, [https://doi.org/10.1007/978-981-15-2317-5\\_70](https://doi.org/10.1007/978-981-15-2317-5_70)

of harmonic currents demands various mitigation efforts and, in this regard, several solutions such as the use of passive/active power filters and hybrid power filters [5–7]. However, the most efficient way of reducing harmonic current-related issues is the shunt-typed hybrid power filter (SHPF) which has been proven to improve PF performances via the reduction of reactive power burden on a power system while ensuring a low level of harmonic currents generation. The SHPF generally works by introducing opposition current back into the system with harmonic current, thereby allowing the reclaiming of the sinusoidal characteristics (with fundamental frequency) of the polluted source current [8].

The efficiency of SHPF depends predominantly on the accuracy and rate of its reference current generation method and its controller performs in generating the required reference current even during the alternative conditions of source and load. The previous studies have applied several methods such as instantaneous power ( $p-q$ ) method, Instantaneous Active and Reactive Current Method ( $I_d-I_q$ ), synchronous detection method (SDM), Constant Active Power method (CPM), fast Fourier transform (FFT), Constant power factor method (CPFM), Wavelet-Based Reference-Generation method, synchronous reference frame (SRF), Self-tuning filter (STF) and Soft Computing Algorithms [artificial neural network ANN, fuzzy logic and genetic algorithm (GA)] [9]. Considering the available reference methods of current generation, the STF has often been applied to improve the capability of phase-locked loops (PLLs),  $p-q$  and SRF methods in working under non-sinusoidal source voltages.

Presently, in order to ameliorate the harmonic isolator performances under non-conditions of source voltage (unbalanced/distorted), the STF is a better alternative than optimization algorithms because the optimization algorithms involve complex iterative approaches and require careful tuning of the damping ratio and adaptability gain to work perfectly. The STF is also better than the conventional methods which use to estimate the reference current [10].

Several types of research have focused on the removal of harmonic currents and voltage instead of harvesting it and using it as an exploitable power. Al-bayaty et al. [11–14] tried to exploit harmonic currents for feeding different electrical loads using PPF and APF methods. However, in spite of the success of their method in the utilization of harmonic current, the THD of the current accede the specified limitation of IEEE standard as their achieved THD value was 3% which is higher than that of the required target value of IEEE standard (5%). Thus, this study presents the possibility of achieving a THD value lower than that of the above-mentioned specified value by using shunt HPF with BPNN controller based on STF-SRF theory under distorted source voltage.

## 2 System Description

The SHPF has been designed by using STF-SRF theory to test all systems under non-ideal source voltages and variation of the load as shown in Fig. 1. More details of the mathematical modelling are found in [15].

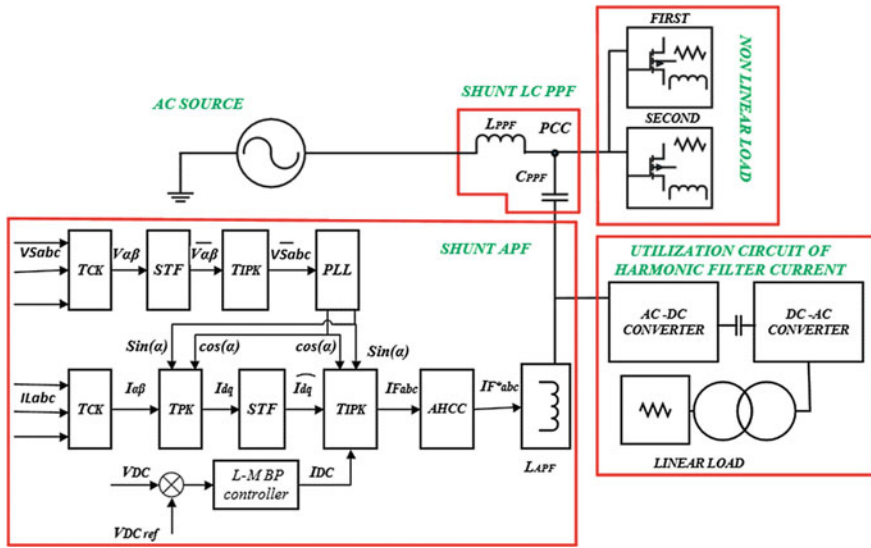


Fig. 1 System configuration with practical realization of shunt HPF

To compensate for the converter active losses, a dc link capacitor voltage was processed in the second part by a BPNN controller to ensure active losses in the converter under different load conditions. The generation of accurate converter reference currents was ensured by adding an additional fundamental component ( $I_{dc}$ ) which was derived from the controllers' outputs. In the next part, the load current contains the fundamental, reactive and harmonic parts; a sinusoidal source current waveform can be generated if the active power filter can compensate the total reactive and harmonic parts [16]. Hence, an accurate compensation can be guaranteed by comparing the 3-phase SHPF reference current with the three phase PCC current. Now, 3 reference currents are applied to the hysteresis current controller (HCC) to produce the required gating pulses that will switch the IGBT-VSI devices since it only deals with dc quantities, and the computation is instantaneous.

Finally, the utilization circuit of filter harmonic current was connected between the inductance of APF and capacitor of PPF as shown in Fig. 1. This circuit consists of an AC-DC converter which converts the filter harmonic current to DC current with a capacitor to reduce the ripple of its outputs (DC current contains no harmonics) and then reconvert it to pure sinusoidal AC current. The magnitude of DC-AC output current might be so small; thus, will use the set-up transformer to feed the current to R load.

### 2.1 Simulation Results and Discussion

Figure 2 depicts the block diagram of the simulation model; the output was observed for the following cases: without shunt HPF, with shunt HPF, and with the utilization of circuit. The main parameters used in the simulation are shown in Table 1.

For the first case, the system was simulated using MATLAB/SIMULINK under distorted source voltage 480 V. 33% of 5th, 11th, 13th, and 19th harmonics were

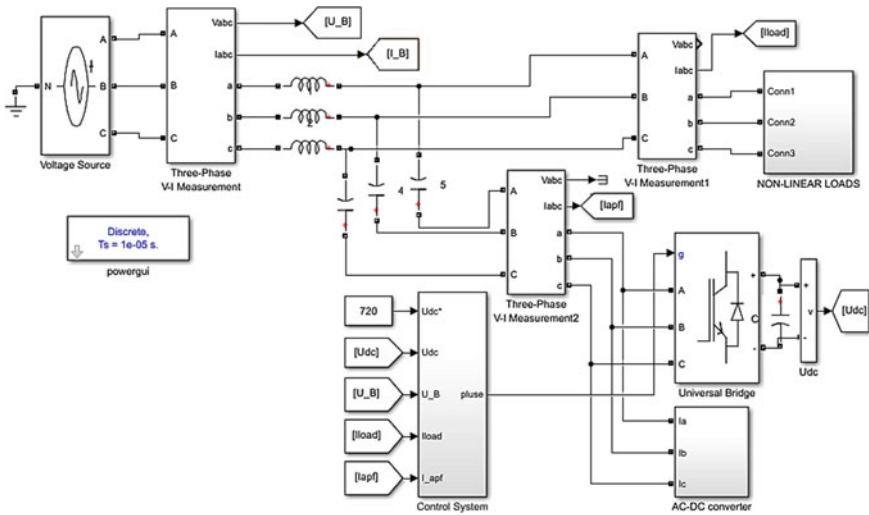
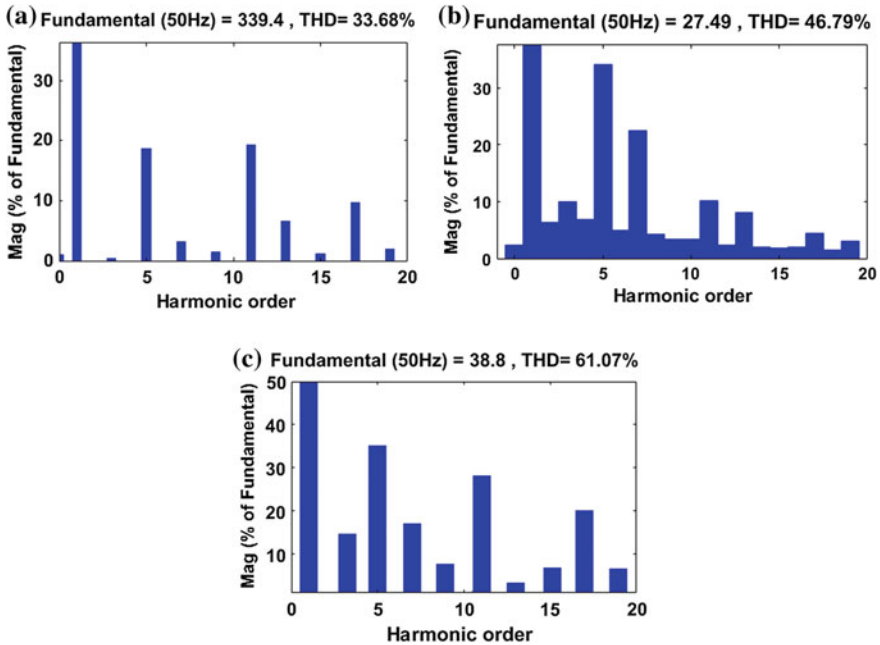


Fig. 2 Simulink model of the shunt HPF with the utilization circuit scheme

Table 1 Main parameters used in the simulation

System parameters	Values
Source voltage (peak)	480 V
Source resistance	$1e-3 \Omega$
Source inductance	$1e-8$ H
First load (R + L)	$30 \Omega, 0.05$ H
Second load (R + L)	$20 \Omega, 0.1$ H
PPF inductor	$5.2e-3$ H
PPF capacitor	$6.2e-3$ F
Reference for capacitor voltage	720 V
Dc-side capacitor of APF	$4800e-6$ F
APF inductor	$2.35e-3$ H
Utilization load resistance	1 $\Omega$
Capacitor of AC-DC converter	$20e-6$ F
Resistance of AC-DC converter	55 $\Omega$



**Fig. 3** Performance of test system without shunt HPF, **a** harmonic spectra of source voltage, **b** harmonic spectra of current before (0.3 s), **c** harmonic spectra of current after (0.3 s)

injected into the source (calculated as 18.50%, 19.2%, 7.8%, and 9.14%, respectively) for phase Bas shown in Fig. 3a. Using FFT, from Fig. 3b, c, the magnitudes of 3th, 5th, 7th, 9th, 11th, 13th, 15th, 17th, and 19th harmonic orders for first load were 11.7%, 34.8%, 23.2%, 4.0%, 9.8%, 6.92%, 2.5%, 4.15%, and 3.02%, respectively whilst for the second load, the magnitudes were 14.2%, 35.01%, 18.3%, 0.8%, 29.0%, 3.4%, 5.8%, 20.7% and 7.38%, respectively.

The transient performance of the SHPF was presented in Fig. 4 which showed the three phases of source voltage, load currents, the source current with filter and DC voltage in top-to-bottom order. Nonlinearity can be seen in the load current whereas the source current was sinusoidal due to the injected filter current generated by STF–SRF method with BPNN controller as exhibited in Fig. 5. Moreover, when the filter was switched ON by providing the gate pulses to IGBT’s of the VSI, DC capacitor activates to reach the reference value of 720 V. Even during the alteration of the loads, the BPNN controller was able to maintain the VDC value close to the reference value (Fig. 4d).

However, Fig. 6 shows the THD of current at PCC which was less than 5% (THD = 1.87% and 3.09 for both loads) in compliance with the IEEE-519 harmonic standards.

Now, the utilization circuit of filter harmonic current was connected to the system. Figure 5 displays the injected harmonic filter current which will serve as the input

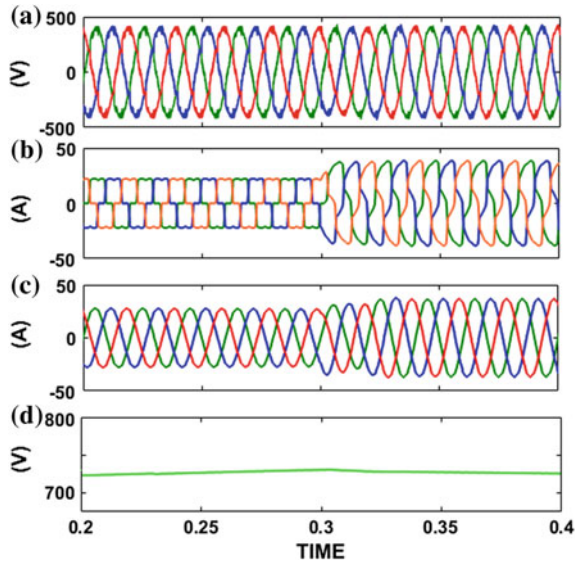


Fig. 4 Transient performance of the shunt HPF

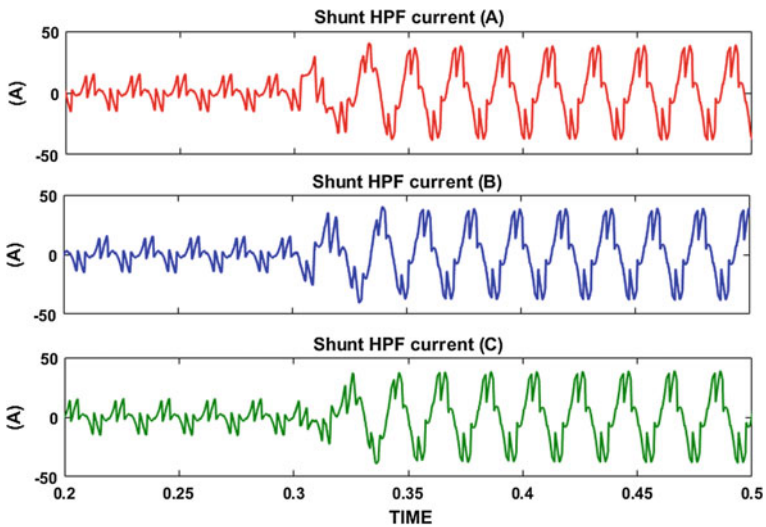


Fig. 5 Injected filter currents for all phases

to the DC-AC converter. The filter current contains all harmonics (THD = 91.27%) with a high quantity of 3th, 5th, 7th, 9th, 11th, 13th, 15th, and 19th harmonic orders in phase B being 17.47%, 32.93%, 29.55%, 18.84%, 23.61%, 15.51%, 16.30%, 16.97%, respectively as shown in Fig. 7.

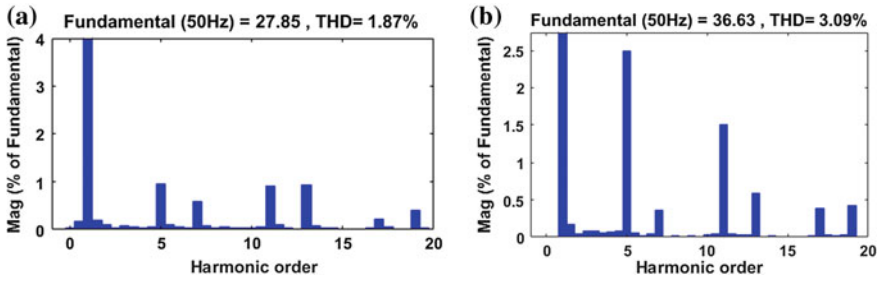


Fig. 6 Harmonic spectra of current at PCC for a first load b second load

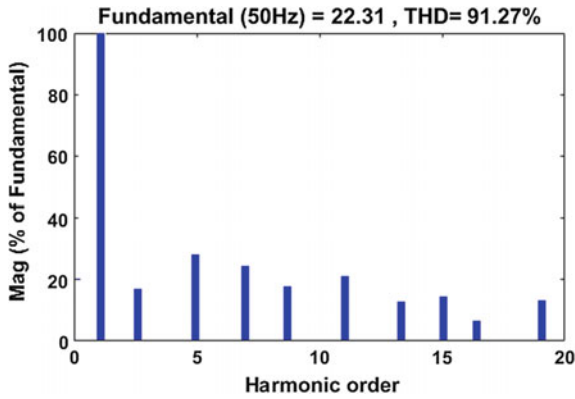


Fig. 7 Harmonic spectra of filter current

However, the results of using the utilization filter harmonics circuit showed the DC current of 2.5 A from the inverter to serve as the input for re-conversion to AC, as shown in Fig. 8. Thus, Fig. 9 shows the output of the DC-AC converter of three

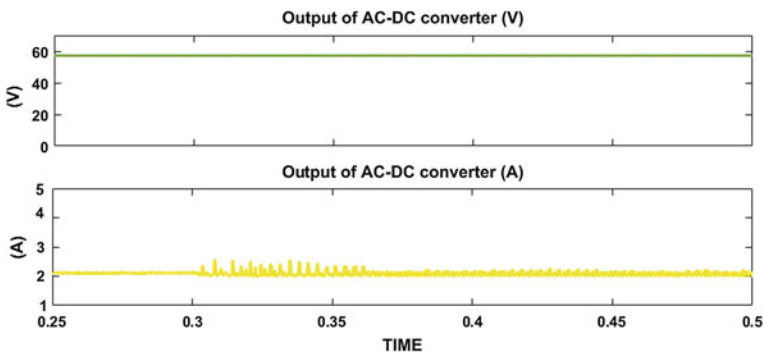


Fig. 8 Outputs of AC-DC converter



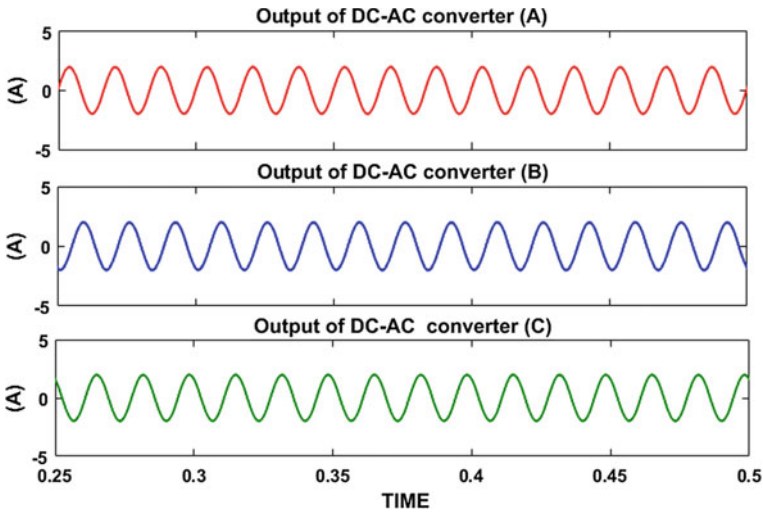


Fig. 9 Outputs of the DC-AC converter

phases where the waveforms of all the phase current were sinusoidal (around 2.2 A rms). Due to its small values, the transformer was used to step up the current to feed the R Loads. The waveforms of the utilized current in R load are presented in Fig. 10. From all the figures and Table 2, it can be easily concluded that even when the source voltage is distorted, the SHPF was more suitable for the reduction of harmonics currents at PCC even though the utilization circuits of filter current is connected to the system (that increases the source current). The THD of the source current in a, b, c phases was still less than the IEEE recommended (3.%, 3.98%, and 2.81%, respectively).

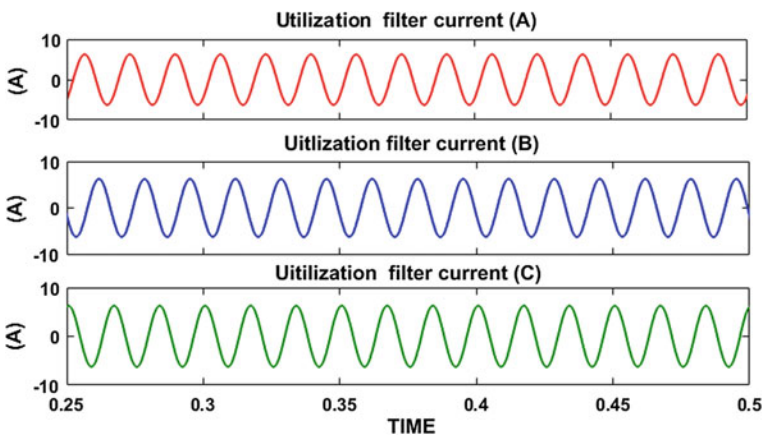


Fig. 10 Output current of R load

**Table 2** Values of THD at PCC under different cases

Harmonic N	Without shunt HPF		With shunt HPF		
	First load	Second load	First load	Second load	Filter current
3th	11.7	14.2	0.04	0.09	17.47
5th	34.8	35.01	0.93	2.49	32.93
7th	23.2	18.03	0.63	0.35	29.55
9th	4.0	4.8	0.02	0.02	18.84
11th	9.81	29.0	0.92	1.51	23.61
13th	6.92	13.4	0.93	0.59	15.15
15th	2.5	5.8	0.03	0.01	16.30
17th	4.1	20.7	0.20	0.39	2.74
19th	3.02	7.39	0.43	0.42	16.97
THD %	<b>46.79</b>	<b>61.07</b>	<b>1.87</b>	<b>3.04</b>	<b>91.27</b>

### 3 Conclusion

This paper presents a shunt HPF scheme which uses independent STF-SRF method with BPNN controller to estimate the fundamental voltage and current components in order to utilize HFP harmonics current which passes through a utilization circuit that consists of an AC-DC converter and a DC-AC re-converter; to use the AC current, the 3-phase step-up transformer was used to raise the voltage before feeding the AC loads to the R load. The results of the simulation showed that the value of the THD of the current decreased to an acceptable level of IEEE standard at PCC in both loads with the utilization circuit of HPF current. Despite the excellent reduction of harmonic, the source current was increasing due to the components of the utilization circuit.

**Acknowledgements** This research is funded by University Malaysia Pahang, UMP Lab2Market Research Fund (UIC170901). This acknowledgment also goes to the Faculty of Electrical and Electronics Engineering for providing us with facilities to conduct this research.

### References

1. Tang Y et al (2012) Generalized design of high performance shunt active power filter with output LCL filter. *IEEE Trans Ind Electron* 59(3):1443–1452
2. Subjak JS, Mcquilkin JS (1990) Harmonics-causes, effects, measurements, and analysis: an update. *IEEE Trans Ind Appl* 26(6):1034–1042
3. Omran MA et al (2018) Shunt hybrid active power filter based on two compensation strategies with PI and fuzzy logic controllers. *J Telecommun Electron Comput Eng (JTEC)* 10(1–3):75–79
4. Almelian MM et al (2018) Performance of unified power quality conditioner (UPQC) based on fuzzy controller for attenuating of voltage and current harmonics. In: *IOP conference series: materials science and engineering*, vol 342, no 1. IOP Publishing, UK

5. Mohamed MA (2015) Design of a shunt active power filter to mitigate the harmonics caused by nonlinear loads. Doctoral dissertation, Universiti Tun Hussein Onn Malaysia
6. Zobia AF (2014) Optimal multiobjective design of hybrid active power filters considering a distorted environment. *IEEE Trans Ind Electron* 61(1):107–114
7. Soomro DM, Almelian M (2015) Optimal design of a single tuned passive filter to mitigate harmonics in power frequency. *ARN J Eng Appl Sci* 10(19):9009–9014
8. Hoon Y et al (2017) Control algorithms of shunt active power filter for harmonics mitigation: a review. *Energies* 10(12):2038
9. Martinek R et al (2019) Least mean squares and recursive least squares algorithms for total harmonic distortion reduction using shunt active power filter control. *Energies* 12(8):1545
10. Hoon Y et al (2017) A refined self-tuning filter-based instantaneous power theory algorithm for indirect current controlled three-level inverter-based shunt active power filters under non-sinusoidal source voltage conditions. *Energies* 10(3):277
11. Al-bayaty H, Ambroze M, Ahmed MZ (2014) Taking advantage of the harmonics at the load side using passive filters. In: The 2014 2nd international conference on systems and informatics (ICSAI 2014). IEEE
12. Al-bayaty H, Ambroze M, Ahmed MZ (2016) Feeding loads via harmonics utilization in ac circuit systems. In: 2016 international conference for students on applied engineering (ICSAE). IEEE
13. Al-bayaty H, Ambroze M, Ahmed MZ (2015) The benefit of harmonics current using a new topology of hybrid active power filter. In: 2015 IEEE 5th international conference on power engineering, energy and electrical drives (POWERENG). IEEE
14. Al-bayaty H, Ambroze M, Ahmed MZ (2016) Utilization of harmonics current in single phase system. In: 2016 17th international conference on harmonics and quality of power (ICHQP). IEEE
15. Omran MA et al (2018) Investigating the ability of shunt hybrid power filter based on SRF method under non-ideal supply voltage. In: IOP conference series: materials science and engineering, vol 342, no 1. IOP Publishing, UK
16. Montero MIM, Cadaval ER, González FB (2007) Comparison of control strategies for shunt active power filters in three-phase four-wire systems. *IEEE Trans Power Electron* 22(1):229

# Vehicle-to-Grid as Frequency Regulator in a Micro Grid System



Mohd Redzuan Ahmad and Laylatun Qadrina Amrizal

**Abstract** This paper evaluated the capability of the Vehicle-to-Grid (V2G) to provide frequency regulation in a micro grid system. To begin with, the impact of sudden increase of residential peak load due to the Electric Vehicle charging load is investigated. Then the Plug-in Hybrid Electric Vehicle Charging Load Profile (PHEVCLP) is generated based on real the data taken from National Household Travel Survey 2017. In this project, the model of V2G in a micro grid system is developed and analyzed using MATLAB software. The results show that the integration of PHEV on a micro grid has an impact on peak load and system frequency. Moreover, the rise of the total number of PHEVs penetration has a significant impact on system frequency. The percentage of improvement in system frequency as V2G system implemented increased as the charger power level increased. It can be concluded that V2G on a micro grid improved and regulated system frequency.

**Keywords** PHEV · V2G · Frequency regulations · Micro grid

## 1 Introduction

Due to growing global interest towards alternative energy resources and environmental concerns, PHEV has proved to be the best alternative and are fast developing in the recent 21st century. Based on the forecasts, the total number of PHEVs that will be available on the road worldwide will reach up to more than 100 million by 2030 [1]. In recent decades, the advances of technology related to batteries and smart grid system have facilitated the vehicle industry to change their focus to introduce, plan and produce electric vehicles [2]. An increase in PHEV integration with a power system network raises concerns about the health of the electrical power grid due to the increase of total load. Excessive of PHEV charging load during a peak load period could cause severe damage to the power system network if it is not properly

---

M. R. Ahmad (✉) · L. Q. Amrizal  
Faculty of Electrical and Electronics Engineering, Universiti Malaysia Pahang, 26600 Pekan,  
Pahang, Malaysia  
e-mail: [mredzuan@ump.edu.my](mailto:mredzuan@ump.edu.my)

planned in advance. Impact on electric grids caused by many electric vehicles in distribution networks including phase imbalances, voltage sags, harmonics, excessive energy demand and power system load and stability [3–7].

Therefore, V2G systems have been introduced to control peak load demand and provide frequency regulation in the power system network [8–12]. From the previous study, it is found that the majority of vehicles stays at the parking lot most of the time in a day [9]. This increases the possibility of the vehicle being available for V2G. Since Kempton proposed the concept of V2G in 1997, V2G has shown great applications such as load peak shifting, voltage regulation, and frequency regulation [8]. Furthermore, various research institutes and researchers focus on V2G technologies, implementations and its impacts in recent years [10–24]. The objectives of this work are to investigate the impact of PHEV penetration in the power system network with a different type of charging level and to analyze the system frequency before and after the implementation of V2G.

## **2 Plug-in Hybrid Electric Vehicle Charging Load Profile (PHEVCLP)**

V2G is a technology that offers the electrical power to flow from vehicles back to the grid system instead of drawing power from the grid as a normal power system load. PHEV has the potential to play the V2G role as the vehicle becomes an asset in a smart grid with bi-directional chargers. By using the V2G network, public utilities can provide a more stable and better service to meet the sudden load demand. The V2G system can also provide financial benefits to the owner, thereby reducing the overall cost of purchasing electric vehicles. V2G allows vehicle owners to generate income from frequency regulation service market [8].

PHEV aggregator is an essential component to integrate the PHEV fleet into the power system electricity market. The PHEV is connected to an aggregator in order to charge or discharge its electrical power to the grid. Depending on the system price, the PHEV battery can have three modes which are waiting mode, charge mode and discharging mode. Moreover, the waiting mode can be set to inhibit high price hours, and request for discharges can be changed to peak times. In the grid to vehicle (G2V), batteries are charged by purchasing electricity from the grid.

The discharging mode or known as the V2G can restore the energy back to the grid. PHEV aggregators interact with system operators (SO) to decide PHEV mode in order to minimize system losses, reduce costs, increase voltage profiles and provide ancillary services such as regulatory and operational reserves by monitoring system and market conditions in real time [14, 15]. PHEV is considered to be a burden impaired or delivering capable resources within the power system. Hence, PHEV could be one of the energy storage applications.

The investigation of PHEVCLP has been carried out based on three different types of charging level which are charging level 1, charging level 2, and DC fast charging.

**Table 1** Electric vehicle charging levels

Charging level	Power supply	Charger power	Miles/hour of charge	Charging time from empty to full
				PHEV
Level 1	120 VAC single phase	1.4 kW, 12 A	~3–4 mile	~7 h
Level 2	240 VAC single phase	3.3 kW	~8–10 mile	~3 h
		6.6 kW	~17–20 mile	~1.4 h
DC fast charge	200–450 VDC up to 90 (200 A)	45 kW	~50–60 mile	~10 Min

Furthermore, four levels of PHEV penetrations has been considered. The required data to obtain the PHEVCLP can be summarized as; number and types of PHEVs, battery capacity, driving activity, distance driven, charging time and charging level. Based on these data, the total energy required to fully charge the battery State of Charge (SOC) and the charging duration could be calculated, hence the PHEVCLP is developed.

The National Household Travel Survey website consists the transportation data regarding the travel and transportation are used to explore topics about travel behavior, traffic safety, congestion, and etc. in the United States. This survey was sponsored by the US Department of Transportation [24]. From the previous paper, it is also found that the U.S. residential utility customer consumed an average of 10,399 kilowatt-hours (kWh) per year, 867 kWh per month, 29 kWh per day and 1.2 kWh per hour in average [25]. In this study, residential demand curve has a peak value of 10 MW. Therefore, the average number of residential is 8333. Each of the residential is assumed to own one vehicle per house. From 8333 vehicles, around 20–30% of the vehicles are assumed to be PHEV. The PHEVCLP is developed considering four levels of PHEV penetrations which are 1500, 2000, 2500 and 3000 of PHEVs. The PHEVCLP also have been developed according to different charging level which are charging level 1, level 2, and DC fast charging as shown in Table 1 [25]. In order to develop the PHEVCLP, there are two important data that need to be obtained from the NHTS which are Vehicle Daily Mileage and Vehicle Arrival Time.

### 2.1 Vehicle Daily Mileage Analysis

Vehicle Daily Mileage that consists of the daily mileage travel by each vehicle is one of the important factors to build the PHEVCLP. Based on VEHPUB.csv file, the attribute of ANNMILES for 1500, 2000, 2500 and 3000 are tabulated in Minitab Software to process the data. The data has been analyzed using Minitab, Excel and Matlab in order to build the bar graph of Vehicle Daily Mileage for each of the total vehicle. The result of travel distance for 1500, 2000, 2500 and 3000 total of vehicles

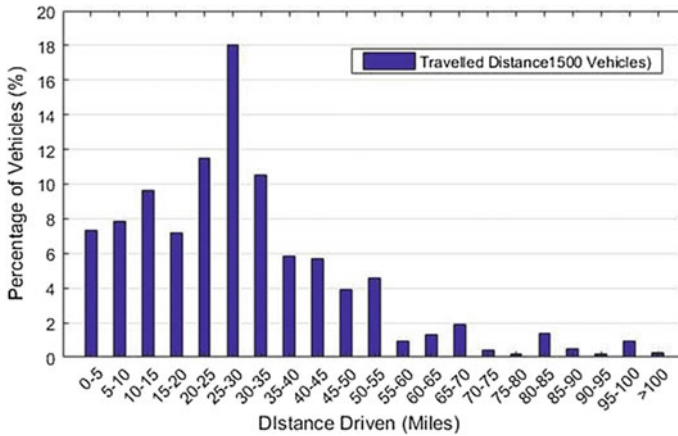


**Fig. 1** Percentage of 1500 vehicles versus their daily distance driven (miles)

has been analyzed. Since the pattern of travel distance is similar for all four cases, only the case of 1500 vehicles is shown in Fig. 1.

Figure 1 illustrate the bar graph of the percentage of 1500 vehicles versus their daily distance driven in miles. Most of the vehicle travelled between 25 and 30 miles throughout the day with percentages are 16–18% of the total vehicles. More than 70% of the vehicle travelled for a distance of less than 35 miles or 56 km per day. The PHEV’s State of Charge (SOC) and the energy necessary for charging the battery depend on the miles driven by vehicle. Longer of distance driven means more energy is required to fulfil the PHEV’s battery back to 100% SOC.

## 2.2 Vehicle Arrival Time Analysis

Besides Vehicle Daily Mileage, the second important factor to configure the PHEV-CLP is charging start time. The time of the vehicle start to charge is unable to be accurately determined, but the vehicle’s last travel time gives some information. People can depend on the ENDTIME attribute according to the assumption that the owner will plug in their vehicle when they arrived at their destination. The bar graph of Vehicle Arrival Time has been plotted using Matlab for four different number of vehicle penetration levels. Since the pattern of vehicle arrival time is similar for all four cases, only the case of 1500 vehicles is shown in Fig. 2.

Figure 2 illustrates the bar graph of 1500 vehicles versus their arrival time. The percentage of vehicles arrived is low at early morning and further increases toward evening and again low during late night. The peak arrival time of the vehicles is between hours 17:00 and 17:30 with a percentage of 3–3.4%. From these results, an assumption can be made where the peak arrival time of the vehicles is between hours

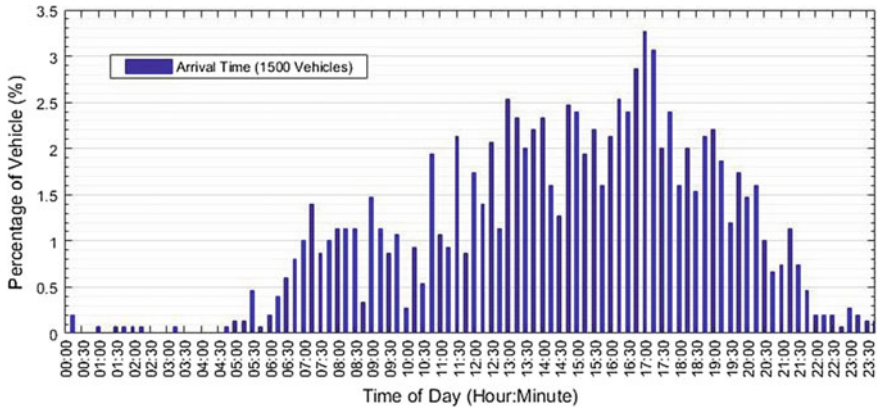


Fig. 2 Percentage of 1500 vehicles versus their final arriving time

17:00 and 17:30, this is also the peak time for the vehicle owners start to charge their vehicle. Hence, at this hour, there will be a significant increase of load due to the high penetration of PHEV charging their vehicles.

### 2.3 PHEV Load Charging Profile

This section describes the method used to develop the PHEVCLP for four different number of PHEV penetration levels which are 1500, 2000, 2500 and 3000. The number of PHEV used for this analysis is assumed to be the total number of Electric Vehicle that will be used in the micro grid area. The PHEVCLP also has been developed according to three different charging levels which are charging rate level 1, level 2, and DC fast charging as shown in Table 1. Figure 3 shows the stages used to build the PHEVCLP. These steps are the summarize of how to develop the programming in MATLAB [4].

There are steps used to develop PHEVCLP:

- (1) In the initialization, required data has been collected; number of PHEV ( $N$ ), Types of PHEV ( $T$ ), rate of charge ( $r$ ), distance ( $D$ ), energy capacity ( $E_{max}$ ) and time of arrival ( $t_s$ ), energy-per-mile (EPM).
- (2) Energy consumed by each PHEV's,  $Ec_i$ :

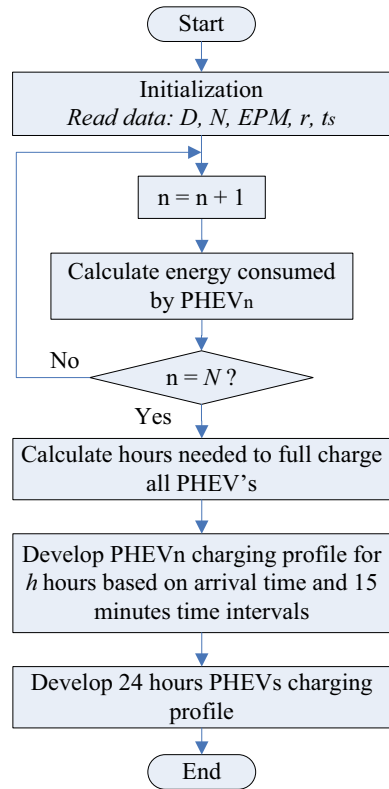
$$Ec_i = D_i \times EPM_i; \quad 0 \leq Ec_i \leq E_{max} \tag{1}$$

- (3) Duration to fully charge the battery SOC to 100%,  $E_{max}$ .

$$h_i = \frac{Ec_i}{r}; \quad 0 \leq Ec_i \leq E_{max} \tag{2}$$



**Fig. 3** Flow chart of PLCP development process



(4) PHEVCLP based on the 15-minutes time frame:

$$E_{C_i} = E_{C_{i,1}} + E_{C_{i,2}} + \dots + E_{C_{i,m}} \tag{3}$$

$$E_{C_i} = \sum_{t=1}^m E_{C_{i,t}}; \quad 1 \leq t \leq m \tag{4}$$

i.e.  $m$  is the number of 15-minutes time frames. So,  $m = 4 \times h$ .

(5) Total 24 h PHEVCLP based on individual PHEV's charging at each step  $t$  is then calculated by:

$$E_{TC_t} = E_{C_{1,t}} + E_{C_{2,t}} + \dots + E_{C_{i,t}} \tag{5}$$

$$E_{TC_t} = \sum_{i=1}^m E_{C_{i,t}} \quad 1 \leq t \leq m \tag{6}$$

After the PHEVCLP for each charging level with different penetration of PHEVs was obtained, the charging load was then added to the original residential loads of case study in MATLAB Simulink to analyze its impact towards the power system network.

### 2.4 Model of Vehicle-to-Grid (V2G) System

The analysis of a V2G system in a Micro Grid model is done in MATLAB Simulink software. This model is based on 24 h simulation of a V2G [26]. In this model, several events are conducted during the day and the system frequency is regulated using the V2G. Figure 4 shows the Simulink model of a Vehicle-to-Grid (V2G) System that has been used to study a full one-day period or 24 h. As illustrated, the main components used in this model consist of 15 MW diesel generator, 4.5 MW wind farm, 8 MW PV farm, loads (10 MW residential load and 0.16 MW asynchronous machine and V2G system).

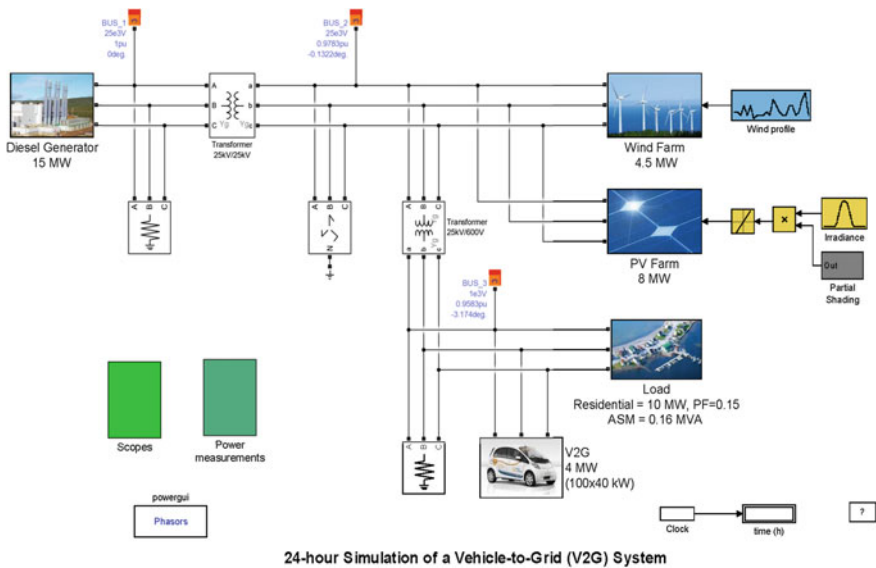


Fig. 4 Vehicle-to-grid (V2G) system model

### 3 Results and Discussion

The developed PHEVCLP has been added to the original residential load in micro grid model to investigate the impact of PHEV integration in the power system network with different charging level and to analyze the system frequency before and after the implementation of V2G.

#### 3.1 Increases of Residential Load Due to the PHEV Charging

Figure 5 shows the results of PHEVCLP for four different number of PHEVs penetrations with Charging rate level 1. It can clearly be seen that there has been a huge increase of charging load starting from 6 a.m. and rise to a peak at 5 p.m. From the curve, it is found that most of the PHEVs owner charged their vehicle during the evening. Moreover, a higher number of PHEVs penetration caused a higher charging load. The peaks of the charging load for 1500, 2000, 2500 and 3000 PHEVs penetration are 0.87, 1.17, 1.45, and 1.75 MW, respectively.

Figure 6 illustrates the results for a similar experiment but with a charging rate level 2. The charging load curve is not as smooth as the charging load with a charging rate level 1. This is because the time taken for the PHEV with the charging rate level 2 to fulfil its SOC to 100% is shorter than the charging rate level 1. In contrast, the peak charging load is greater than the charging rate level 1 for all numbers of PHEV penetration levels. Based on the charging load curve, the peak charging load is at 5.30–6 p.m. The peaks of the charging load for 1500, 2000, 2500 and 3000 PHEVs penetration are 1.53, 2.05, 2.53, and 3.08 MW, respectively.

Figure 7 demonstrates the results of PHEVCLP considering a DC fast charging. It is shown that the charging load curve is not as smooth as the previous case study. This is because the time taken for the PHEV to fully charge its SOC is shorter

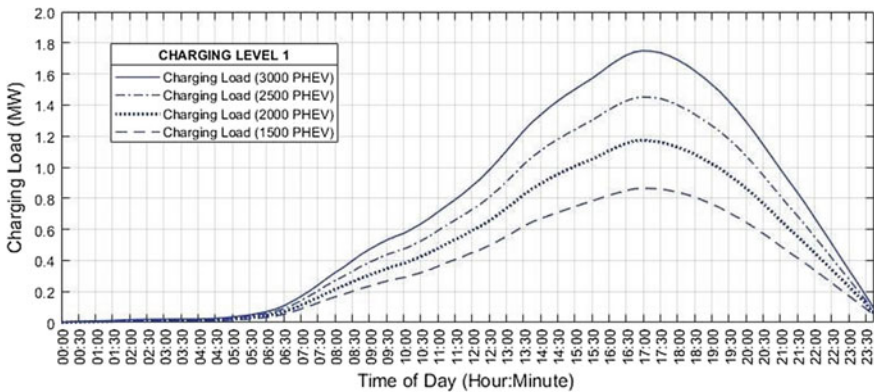


Fig. 5 The PHEVCLP for charging rate Level 1

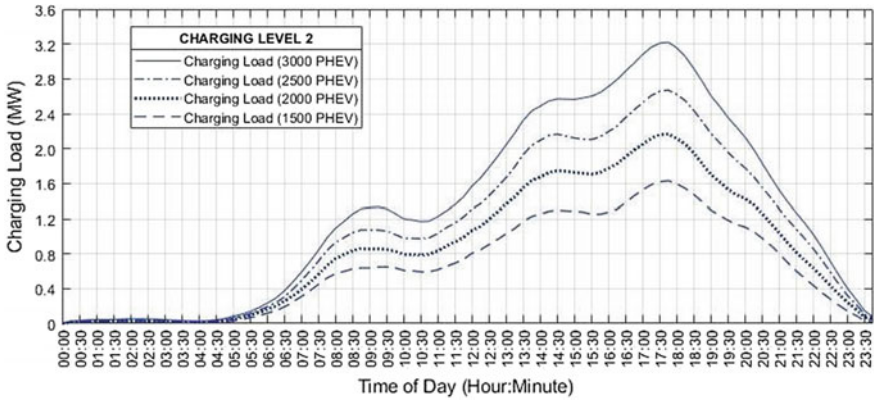


Fig. 6 The PHEVCLP for charging rate Level 2

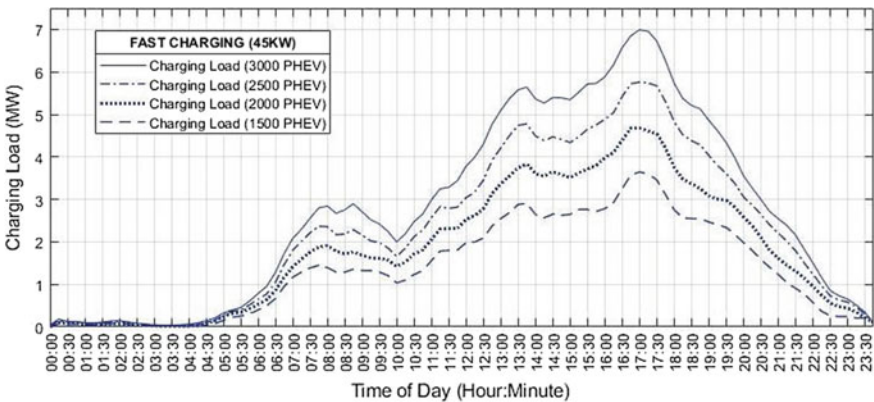


Fig. 7 The PHEVCLP for DC fast charging

than the charging rate level 1 and level 2. In contrast, the peak charging load for DC fast charging is greater than the previous case studies for all number of PHEV penetrations. Based on the charging load curve, the peaks of the charging load for 1500, 2000, 2500 and 3000 PHEVs penetrations are 3.60, 4.61, 5.74, and 6.96 MW, respectively.

### 3.2 Different Charging Level and Its Impact on System Frequency

The PHEVCLP for a different number of PHEV penetrations has been added to the original 24 h residential load of the micro grid. The sudden load increase will

cause the diesel generator to generate more power to meet the required demand. The rotor speed of the synchronous machine has also reacted instantly and leads to the frequency deviation since the speed of the rotor is proportional to the frequency.

Figure 8 shows the curve of total residential loads with the charging level 1 after the 24 h PHEVCLP is added to the original 24 h residential load. It is found that the peak of the residential load caused by four different numbers of PHEVs penetration i.e. 1500, 2000, 2500 and 3000 PHEVs penetration, increased by 7.76, 10.82, 11.45, and 16.56% respectively. On the other hand, since the frequency for all penetrations are normal, there is no V2G implementation needed. Hence, the PHEV charger of type level 1 is suitable in a micro grid system for 20–30% penetration of PHEVs with 10 MW residential load.

Figure 9 demonstrates the curve of the total residential load with the charging rate level 2 after the 24 h PHEVCLP is added to the original 24 h residential load. The peaks of the residential load caused by four different PHEVs penetrations i.e. 1500, 2000, 2500 and 3000 PHEVs, are increased by 14.31, 19.60, 24.35, and 29.81% respectively. It also found that system frequency does not have a significant impact and there is no V2G implementation is needed.

Figure 10 illustrates the curve of the total residential load with the DC fast charging after the 24 h PHEVCLP is added to the original 24 h residential load. The peaks of the load for 1500, 2000, 2500 and 3000 PHEVs penetrations are increased significantly by 33.94, 44.62, 55.56, and 66.74% respectively.

Table 2 tabulates the percentages of residential peak loads for four different numbers of PHEV penetrations and three different charging levels. The percentage increment of the total residential load increases as the number of PHEV increases, as well as when the charging rate level rises. From the results, it is shown that for all number of PHEVs penetrations with the charging level 1, there is no frequency deviation occurred. Not only that, for the case 1500 and 2000 PHEVs penetrations with the charging level 2, the system frequency is still in the normal condition. The percentage

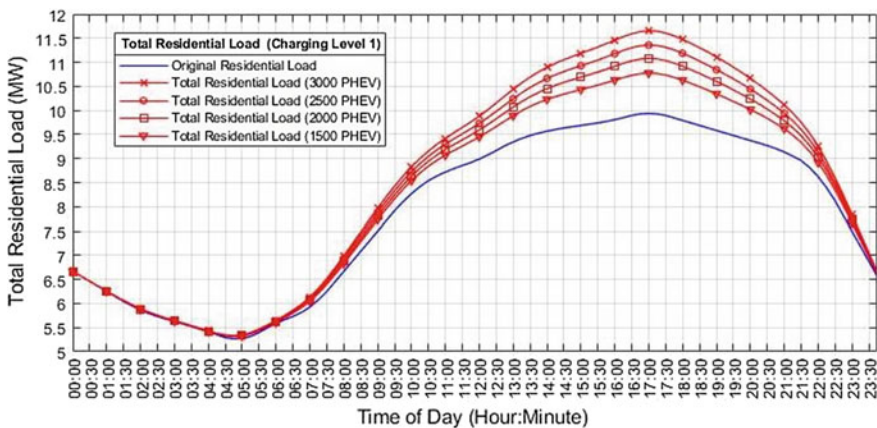


Fig. 8 Total residential load for charging rate Level 1

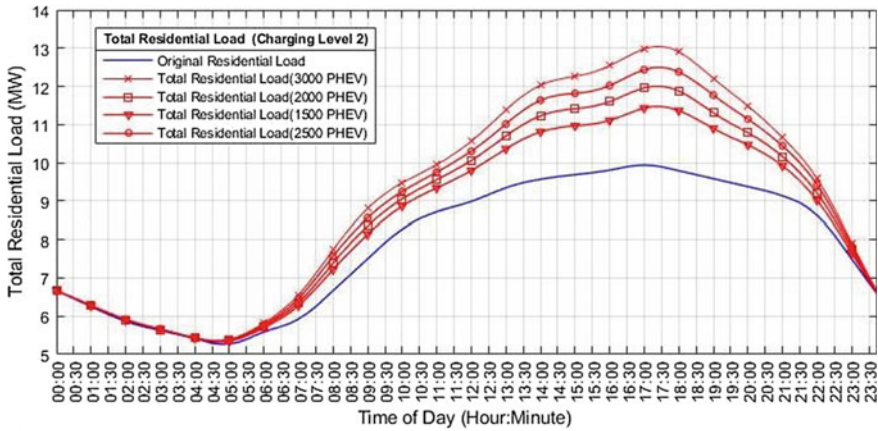


Fig. 9 Total residential load for charging rate Level 2

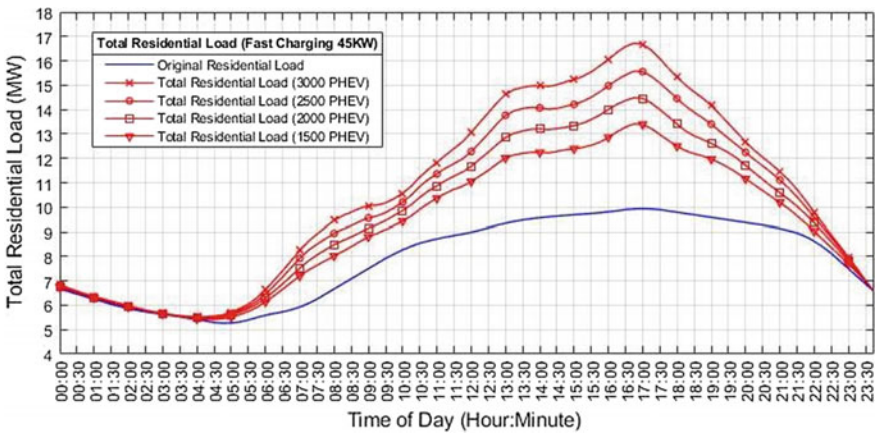


Fig. 10 Total residential load for DC fast charging

Table 2 Percentages increment of total residential load at peak hour 5 p.m. for four different numbers of PHEV penetrations and with three different charging levels

Percentages of peak load increased				
Charging rate level	Number of PHEV penetration			
	1500 (%)	2000 (%)	2500 (%)	3000 (%)
Charging level 1 (1.4 kW)	7.76	10.82	13.60	16.55
Charging level 2 (6.6 kW)	14.3	19.60	24.35	29.81
DC fast charging (45 kw)	33.94	44.62	55.56	66.74

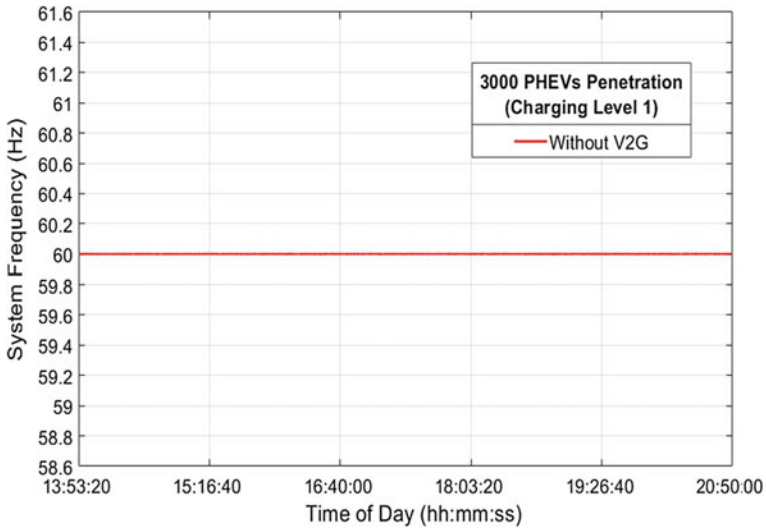


Fig. 11 System frequency of 3000 PHEVs penetration with charging level 1

of peak load increment for these cases was below than 20%. Hence, for the increment of residential load that below than 20%, the system frequency is still normal and do not require any V2G implementation. On the other hand, if the residential load exceeds 20% from its original load, the system frequency needs to be regulated by the V2G system.

Figure 11 shows the simulation results of micro grid system frequency of 3000 PHEVs penetration for the charging level 1. As can be seen, the system frequency for PHEVs penetration at the charging rate level 1 is normal. There is no frequency deviation for low power at the charging level 1.

Figure 12 shows the system frequency of the micro grid system of 3000 PHEVs penetration with the charging level 2. As can be seen, the red color line shows the system frequency starts to deviate between 59.4 and 60.6 Hz from the nominal value 60 Hz when there is no V2G system on the micro grid system. This occurs between hours 15:30 and 19:00 i.e. while many PHEV owners recharge their vehicle. The duration of system frequency deviation occurred is depended on the PHEV charging load. The time at which the total residential load exceeds 20% from the normal load, is the time of system frequency starts to deviate. When the V2G system is available, the system frequency of the micro grid has less deviation and improves significantly as shown by the blue line.

Figure 13. shows the system frequency of micro grid system of 3000 PHEVs penetration with the DC fast charging. As can be seen, the red color line shows the system frequency starts to deviate between 59.0 and 60.8 Hz from the nominal value 60 Hz when there is no V2G system on the micro grid system. This occurs between hours 12:00 and 20:30 i.e. while many PHEV owners recharge their vehicle. The duration of system frequency deviation occurred is depended on the PHEV charging

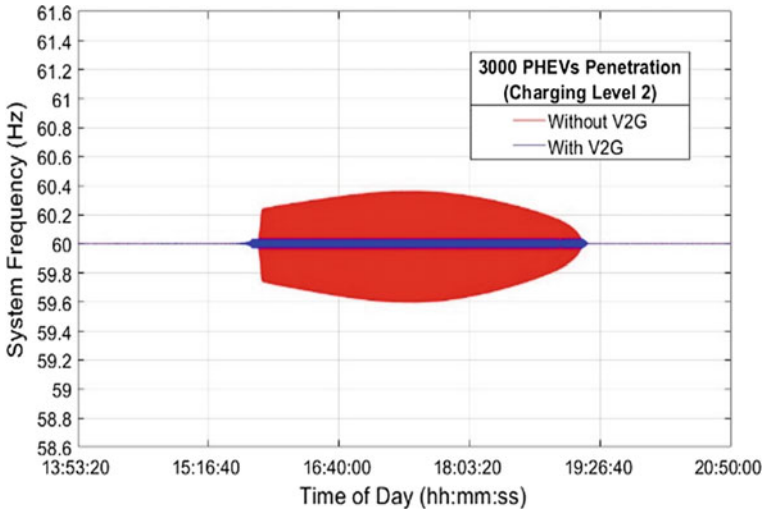


Fig. 12 System frequency of 3000 PHEVs penetration with charging level 2

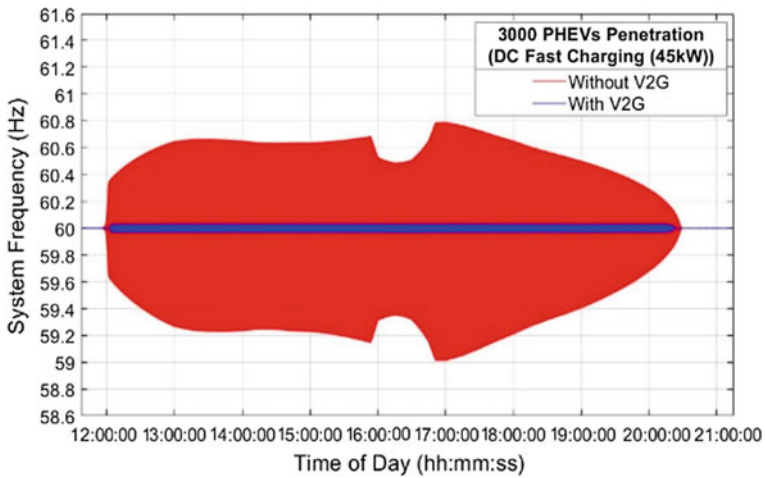


Fig. 13 System frequency of 3000 PHEVs penetration with DC Fast charging

load. The time at which the total residential load exceeds 20% from the normal load, is the time of system frequency started to deviate. When the V2G system is available, the system frequency of the micro grid has less deviation and improves significantly as shown by the blue line. It shows that the micro grid system frequency could be improved by V2G system in place.



## 4 Conclusion

The impact of PHEV integration in the power system network with different charging levels and the system frequency before and after the implementation of V2G system has been analyzed. From the study, the DC fast charging has more significant impacts to a micro grid system as compared to the lower power charging levels i.e. charging level 1 and level 2. Furthermore, it shows that the system frequency of a micro grid starts to deviate when PHEV charging load is more than 20% of micro grid peak load. In conclusion, the implementation of V2G system has significantly improved the system frequency of the micro grid system.

**Acknowledgements** The authors would like to acknowledge the Research Management Center of Universiti Malaysia Pahang and Ministry of Higher Education Malaysia (MOHE) for the financial support of this research under grant number of RDU1703219.

## References

1. Kempton W, Tomi J (2005) Vehicle-to-grid power implementation: from stabilizing the grid to supporting large-scale renewable energy. *J Power Sour* 144(1):280–294
2. Tahir M (2017) Electric vehicles and vehicle-to-grid technology: How utilities can play a role. UIT—The Arctic University of Norway
3. Jiang C, Torquato R, Salles D, Xu W (2014) Method to assess the power quality impact of plug-in electric vehicles. In: *Proceedings of international conference on harmonics and quality of power, ICHQP*, pp 177–180
4. Rahmat A, Ahmad MR, Othman MM, Musirin I (2014) Impact of charging PHEV at different penetration levels on power system network. In: *3rd IET international conference on clean energy and technology, CEAT*
5. Darabi Z, Ferdowsi M (2012) Impact of plug-in hybrid electric vehicles on electricity demand profile. *Power Syst* 53:319–349
6. Yong JY, Ramachandaramurthy VK, Tan KM, Mithulanathan N (2015) A review on the state-of-the-art technologies of electric vehicle, its impacts and prospects. *Renew Sustain Energy Rev* 49:365–385
7. Bass R, Harley R, Lambert F, Rajasekaran V, Pierce J (2001) Residential harmonic loads and EV charging. In: *Proceedings IEEE power engineering society transm distrib conference 2 no. Winter meeting*, pp 803–808
8. Kempton W, Letendre SE (1997) Electric vehicles as a new power source for electric utilities. *Transp Res Part D Transp Environ* 2(3):157–175
9. Tu Y, Li C, Cheng L, Le L (2011) Research on vehicle-to-grid technology. In: *Proceedings international conference on computer distributed control and intelligent environmental monitoring, CDCIEM 2011*, pp 1013–1016
10. Janfeshan K, Masoum MA, Deilami S (2015) V2G application to frequency regulation in a microgrid using decentralized fuzzy controller. In: *Proceedings of 2014 international conference on modelling, identification and control, ICMIC 2015*, pp 361–364
11. Capuder T, Kuzle I (2015) Value of flexible electric vehicles in providing spinning reserve services. *Appl Energy* 157:60–74
12. Yilmaz, Krein PT (2012) Review of benefits and challenges of vehicle-to-grid technology. In: *2012 IEEE energy conversion congress and exposition, ECCE 2012*, pp 3082–3089

13. Luo Z, Hu Z, Song Y, Xu Z, Lu H (2013) Optimal coordination of plug-in electric vehicles in power grids with cost-benefit analysis—part I: enabling techniques. *IEEE Trans Power Syst* 28(4):3546–3555
14. Fan H, Jiang L, Zhang C-K, Mao C (2016) Frequency regulation of multi-area power systems with plug-in electric vehicles considering communication delays. *IET Gener Transm Distrib* 10(14):3481–3491
15. Grunditz EA, Thiringer T (2016) Performance analysis of current BEVs based on a comprehensive review of specifications. *IEEE Trans Transp Electr* 2(3):270–289
16. Yilmaz M, Krein PT (2013) Review of battery charger topologies, charging power levels, and infrastructure for plug-in electric and hybrid vehicles. *IEEE Trans Power Electron* 28(5):2151–2169
17. Pani P, Athreya AR, Panday A, Bansal HO, Agrawal HP (2015) Integration of the vehicle-to-grid technology. In: International conference on energy economics and environment—1st IEEE Uttar Pradesh section conference, UPCON-ICEEE 2015
18. Chehaly MEI, Saadeh O, Martinez C, Joos G (2009) Advantages and applications of vehicle to grid mode of operation in plug-in hybrid electric vehicles. In: 2009 IEEE electrical power and energy conference, EPEC 2009
19. Sortomme E (2012) Combined bidding of regulation and spinning reserves for unidirectional vehicle-to-grid. In: 2012 IEEE PES innovative smart grid technologies, ISGT 2012
20. Sortomme E, El-Sharkawi MA (2012) Optimal combined bidding of vehicle-to-grid ancillary services. *IEEE Trans Smart Grid* 3(1):70–79
21. Cundeva S, Dimovski A (2017) Vehicle-to-grid system used to regulate the frequency of a microgrid. In: 17th IEEE international conference on smart technologies, EUROCON 2017—conference proceedings
22. Pillai JR, Bak-Jensen B (2010) Vehicle-to-grid systems for frequency regulation in an islanded Danish distribution network. In: 2010 IEEE vehicle power and propulsion conference, VPPC 2010
23. Tian W, He J, Niu L, Zhang W, Wang X, Bo Z (2012) Simulation of vehicle-to-grid (V2G) on power system frequency control. In: 2012 IEEE innovative smart grid technologies—Asia, ISGT Asia 2012
24. NTA, National Household Travel Survey 2017. <https://nhts.ornl.gov/>. Last accessed 2019/1/5
25. U.S Energy Information Administration Annu Energy Rev. <https://www.eia.gov/>. Last Accessed 1 May 2019
26. MathWorks, 24 hour Simulation of a Vehicle-to-Grid (V2G) System

# Development of PV Module Hotspot Detector



Mohd Shawal Jadin, Kamil Ashman Bin Zamridin  
and Ahmad Syahiman Mohd Shah

**Abstract** The aim of this paper is to develop an analyzer for detecting and evaluating hotspot in problem in a photovoltaic (PV) module. There are many causes that can lead to the hotspot in PV modules such as shading effect, impurities present on the module surface and many more. The proposed system will capture the thermal images of the PV module and analyze each region in the image. The system will detect the hotspot regions and evaluate the severity level of the hotspots. Though the experiment, the proposed system could produce a reliable result compared to the conventional approach.

**Keywords** Photovoltaic module · Solar hotspot · Infrared thermal camera

## 1 Introduction

There has been an increasing global awareness of solar photovoltaic energy use. The reasons behind this are not only to address climate change, but also to create new financial opportunities and, most importantly, to give access to energy for countless people still deprived of modern energy facilities. Solar energy can be said as the greenest energy due to its non-pollutant process to the environment [1]. However, there is a common problem that can cause the performance of PV modules degraded that is the solar hotspot [2]. Hotspot phenomenon is a degrading performance occasion for the photovoltaic module. It is caused due to shading effect cell degradation or any impurities present on the surface of the solar module that prevents any light from entering the cell. When there is one cell is blocked from getting light, it will operate in a reverse-biased while others will do the other hand. Thus, damaged cells will dissipate power and consequently resulting in an abnormal rise in temperature [3]. Therefore, overcoming solar hotspot problem is important to keep the sustainability of an installed photovoltaic system by reducing any source of the fault, structural defect or malfunction during either manufacturing or operating stage [4].

---

M. S. Jadin (✉) · K. A. B. Zamridin · A. S. M. Shah  
Faculty of Electrical and Electronic Engineering, Universiti Malaysia Pahang (UMP), 26600  
Pekan, Pahang, Malaysia  
e-mail: [mohdshawal@ump.edu.my](mailto:mohdshawal@ump.edu.my)

This research focuses on identifying that particular solar hotspot phenomenon that commonly happens on the surface of a PV module. Thermal images of the overall cell temperature are taken using a thermal camera. The system is based on a non-invasive technique that can detect and localized hot areas and quantify the area by finding the potential cause of PV cells degradation in PV systems. This is done by using an infrared thermography technique which is a well-accepted non-destructive evaluation technique that allows contactless and real-time inspection. The images will be quantized according to its region and the temperature difference between the region with ambient temperature is calculated. The system developed allows the user to visually determine solar hotspot using infrared thermography. This method is proved to be invasive towards the PV module as it does not have physical contact with the target objects [5].

This hotspot analyzer of the PV module can detect hotspot with a minimal procedure. It can save time and give the user an easier way to instantaneously know which solar cell on the PV module has a hotspot. The previous method has numerous steps need to be conducted such as data collection, calculation of temperature, measuring output power and image processing. The hotspot occasion is sometimes misjudged by analyzing using the visual method because the high temperature in the solar cell cannot prove that the particular solar cell has a hotspot. Therefore, the main objective is to develop a system that can allow the user to instantly detect hotspot in a PV module. The development starts with the design an automatic hotspot detection of a solar module using thermal image analysis. The next step is to determine the severity level of the hotspot.

## 2 Literature Review

Amongst existing condition monitoring techniques and non-destructive testing methods today, infrared thermography is considered as a promising tool for fast and reliable fault detection. It a method which detects infrared energy from the solar module, convert it into temperature and displays image of temperature distribution. It is a reliable method to observe the performance of solar cell whether it is operating in a normal condition or not. Infrared thermography uses mid-wave (MWIR, from ~3 to 5  $\mu\text{m}$ ) or long-wave (LWIR, from ~7 to 14  $\mu\text{m}$ ) infrared sensors to obtain thermal images or thermogram of objects under inspection according. Based on Planck's black body radiation law, all objects emit infrared radiation proportional to their temperatures [6].

A solar hotspot is a major problem for this alternative energy as it can give a significant effect on the solar module performance. The cells exposed to the shading condition adversely affects the performance of the PV module due to the increase in the power loss according to Samantaray [7]. Until now, there is no complete and effective method to prevent this significant problem toward solar energy. Hence, this problem should be monitored and replaced quickly in order to prevent the module

performance from getting even worse. Thus, methods to effectively detect solar hotspot is important to keep the solar module performance at its best.

Numerous studies had been attempted to explain about how to detect or cluster solar hotspot problem on the solar module through infrared thermography. K-means colour quantization is a useful method to quantize a certain area of the solar module. It is easy to identify the part of a solar module if the module is classified into a region based on their temperature. One of the methods used k-means colour quantization and CIE L\*a\*b\* colour space to quantize local heating spot. Through infrared thermography and k-means clustering, local heating areas were isolated [8]. In other research, the k-means clustering was used to produce the quantized image represented by the contours while DBSCAN resulted in the segmented image isolating the hotspot area as one of its clusters. Ultimately, the area of the hotspot can be determined and, with more data sets, may be correlated to the drop in the efficiency of the solar PV module [9]. Another visual method to determine solar hotspot is through in-line thermography has been conducted by Stefan Schenk, using an uncool bolometric camera and take a continuous series of image, first image as a reference. According to this research, this method is fast because it analyses the solar module in the interval of 70 ms. The images during that interval are observed and the parameter coefficient of the module is analyzed for references [10].

Visual inspection method also can be done to observe the overall performance of the solar module such as checking physical defects on the surface of the solar module. Projects by E. Lorenzo had done three different methods altogether, visual inspection, infrared inspection and electrical inspection. The research used to checks the physical defects and followed by the infrared thermography by comparing temperature difference. Then, an electrical inspection is done by connecting 'T' connectors at the output wires. Voltage losses are compared due to the hotspot. It is proposed to reject any module exhibiting hotspots whose corresponding voltage losses (in relation to a non-defective module being part of the same string), within the PV system in normal operation, exceeds the allowable peak power losses fixed at standard warranties. This is also applicable to PV modules with defective by-pass diodes, regardless of the derived hotspot temperature [11].

Solar cell will usually operate at a certain range of temperature, which can be seen through numerous data collection of cells operating under certain condition or surrounding. Different ambient temperature will result in different efficiency on how the solar panel can deliver power as it receives different solar irradiance and operates at different temperature. Home solar panels are tested at 25 °C and thus solar panel temperature will generally range between 15 and 35 °C during which solar cells will produce at maximum efficiency. However, solar panels can get as hot as 65 °C at which point solar cell efficiency will be hindered [4]. Thus, in this project, the normal operating temperature of the solar cell based on normal ambient temperature is between 20 and 65 °C.

All of the methods are related to how to detect hotspot through visual images and analyzing parameters such as voltages. However, there is still no method exist in order to prevent or distinguish solar hotspot permanently but only a way to minimize the effect. Hence, this research is performed for getting to identify solar hotspot

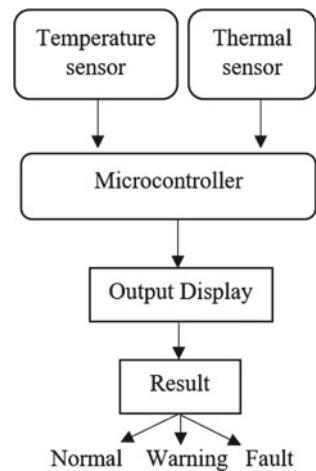
automatically. Thus, the user can easily know where the hotspot occurs on solar panel and finding a solution to overcome that particular cell from being affected by the problem.

### 3 Methodology

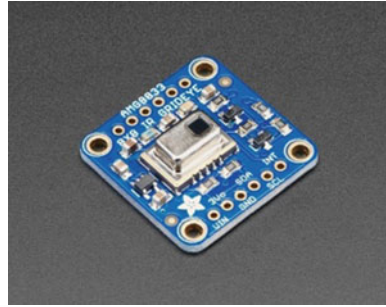
Figure 1 shows the block diagram of the proposed system. The thermal images of the solar panel will be captured by using the Adafruit AMG8833 IR Thermal Camera Breakout. Then, infrared images will be displayed on the SPFD5408 2.4-inch TFT LCD display. Thermal Camera Breakout will be connected through the microcontroller which is the Arduino Mega 2560 to undergo an algorithm that detects hotspot automatically based on temperature difference based on the environment. An extra sensor which is the LM35 Temperature Sensor will also be connected alongside the thermal camera breakout to display the ambient temperature of the surrounding area.

Figure 2 shows the system design that consists of the thermal camera breakout and temperature sensor as the main input. The type of sensor used for visual imaging is an Adafruit AMG8833 IR Thermal Camera Breakout which displays an  $8 \times 8$  array of infrared thermal sensors. When connected to the microcontroller, it will return an array of 64 individual infrared temperature readings over I<sup>2</sup>C. It's like those other thermal cameras, but compact and simple enough for easy integration. User can interface with the system design by capturing thermal images of solar panel in order to perform the hotspot detector algorithm. Then, the thermal images are sent to the microcontroller to be analyzed and k-means colour quantization is performed on the images. This process will quantize the captured image into a discrete number

**Fig. 1** Block diagram of the overall process of the system design



**Fig. 2** Adafruit AMG8833 IR thermal camera breakout that is used as thermal visualize



of colours. Hence, local heating area on the solar module can be localized because of the dominant colour from the thermal images.

Other major parts that are important in this system design is the temperature sensor. This sensor is responsible to measure the temperature of the surrounding area. The LM35 is a type of commonly used temperature sensor, that can be used to measure temperature with an electrical output comparative to the temperature in °C. LM35 is used in industries and commercial buildings where high accuracy of temperature measuring is needed.

The Arduino Mega 2560 is a microcontroller board based on the ATmega2560 microcontroller. This microcontroller board come along with 54 digital input or output pins. 14 of them can be used as PWM outputs. 16 of them can be used as analogue inputs. 4 of them are UARTs (hardware serial ports). It also comes with a 16 MHz crystal oscillator, a power jack, USB connection, reset button and an ICSP header. To support the microcontroller, it contains everything. It can be simply connected with a USB cable or it can be powered with an AC-to-DC adapter or battery to make it alive. This microcontroller or microcontroller board is compatible with many shields that are designed for Arduino. The operating voltage of this microcontroller board is 5 V. The input voltage that is recommended is 7–12 V. The input voltage limit is 6–20 V. The DC current per I/O pins is 40 mA. The DC current for the 3.3 V pin is 50 mA. The flash memory is about 256 kB of which 8 kB used by the bootloader. The clock speed of this microcontroller is 16 MHz which is quite high for this affordable board. This can be counted as the brain of this system design as it is important for the solar hotspot automatic detector. All of the data collected will be received by this microcontroller to be analyzed and calculated.

The system design flow starting with capturing thermal images of the solar panel to be analyzed. Firstly, K-means colour quantization will be held to the clustered a certain region that is abnormal due to its colour (red indicating high temperature). It is easy to identify which cell is affected when the area of the solar module is clustered into a certain region. Then, the value of the temperature of each array from the thermal camera is taken into account. Each array temperature is compared with the ambient temperature in order to get the temperature difference of the solar cell. Solar panels are tested at 25 °C and thus solar panel temperature will generally range between 15 and 35 °C during which solar cells will produce at maximum efficiency.

However, solar panels can get as hot as 65 °C at which point solar cell efficiency will be hindered. Install factors like how close the panels are installed to the roof can impact the typical heat of your solar system. This algorithm will analyze temperature using two different conditions which are comparing it with an average temperature of solar cell and comparing with the range of normal operating range of temperature during normal condition.

$$\Delta T_{HS1} = T_{cell(max)} - T_{average} \quad (1)$$

$$\Delta T_{HS2} = T_{cell(max)} - T_{ambient(max)} \quad (2)$$

$$T_{ambient(max)} = T_{ambient} + 30^{\circ}\text{C} \quad (3)$$

where  $T_{cell(max)}$  is the highest temperature of solar cell captured by the thermal array sensor and  $T_{average}$  is the average temperature of the solar cell. Temperature difference,  $\Delta T_{HS1}$  that is more than 20 °C can be counted as a solar hotspot and will display 'FAULT' as the condition. If the  $\Delta T_{HS1}$  is within the range of 5 and 20 °C, the display will set the condition as 'WARNING'. If the  $\Delta T_{HS1}$  exceed 20 °C, 'FAULT' will be displayed as the condition on the LCD display. However, the algorithm will set as 'FAULT' when the second condition is a positive value. This is because the highest temperature exceeds the normal range of solar operating temperature. The highest temperature will be compared with the highest range from the ambient temperature. This algorithm will calculate and identify which region can be classified as a hotspot. The flowchart of this system design is shown in Fig. 3. Next, the identified region will be displayed on the LCD along with the thermal images. User can view the thermal images of a solar panel including with label that said it is the region of the hotspot.

## 4 Results and Discussion

This work is conduct to roughly the overview on how this project might flow in order to detect solar hotspot in a solar panel. Thermal images of solar several solar modules are taken under direct sunlight as shown in Fig. 4 and the temperature is displayed through the infrared camera. Moreover, the short circuit current and open circuit voltage are also measured using a multimeter in order to analyse the PV module performance under normal operating conditions. As shown in Fig. 4, it is found that the maximum cell temperature is 41.3 °C, therefore, using Eq. (2), the temperature against the ambient ( $\Delta T_{HS2}$ ) is 16.3 °C.

It can be assumed that there no hotspot phenomenon on that solar module as its temperature difference does not exceed 30 °C. As illustrated in Fig. 5, it can be seen that there is no significant difference in the solar cell temperature. The temperature difference between the hotspot and the ambient is 14.3 °C.

Figure 6 shows the final system development of the hardware with the proposed



**Fig. 3** Flowchart of the process to detect solar hotspot algorithm

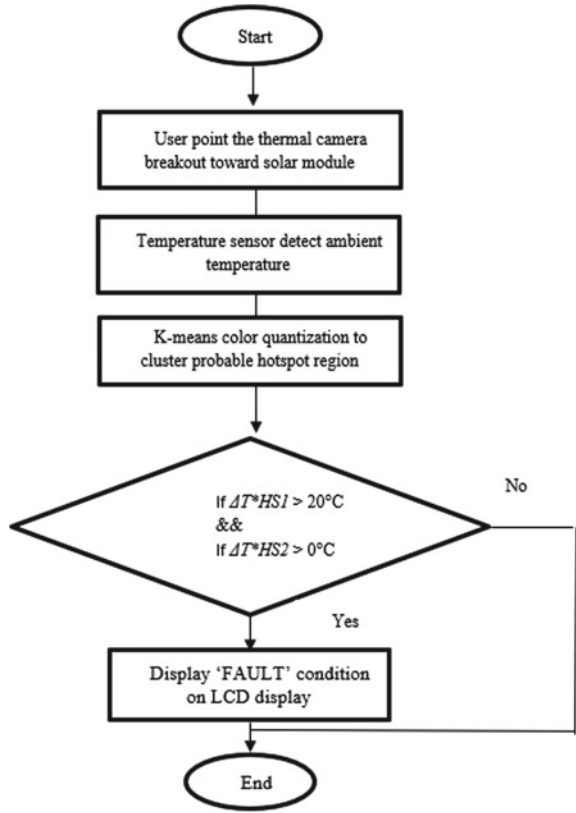
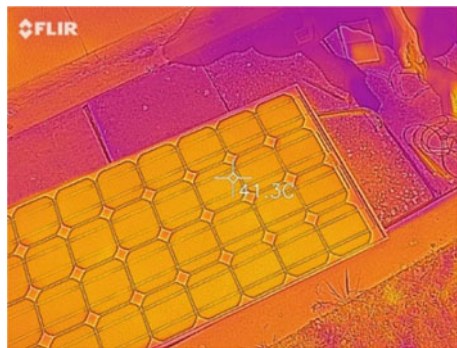


**Fig. 4** The temperature of the solar cell of module 1 captured with a FLIR infrared camera



algorithm embedded within the microprocessor in order to detect and evaluate the hotspot. The overall display on the LCD shows the parameters used in the algorithm such as ambient temperature, maximum temperature, average temperature and type of condition of the highest cell temperature (maximum temperature). As illustrated, the

**Fig. 5** The temperature of the solar cell of module 2

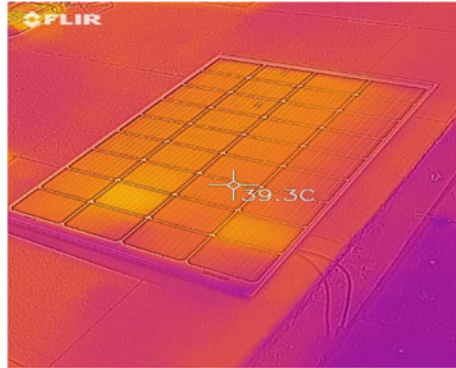


**Fig. 6** Display of the hardware in normal room temperature



normal temperature shown indicates that there is no hotspot present as the temperature difference did not meet the requirement set in the algorithm.

Figure 7a shows an example of the normal condition where there is no significant rise in the temperature captured by the thermal camera breakout. In this case, it can be seen that the maximum temperature is compared with the average temperature. The difference is not greater than 5 °C, which is set to be 'NORMAL' for the condition of the highest temperature. As can be seen in the calculation above, the value for the difference in temperature for both maximum and average is 1.44 °C which is not more than 5 °C, the first condition set for normal condition.

Meanwhile, Fig. 7b shows the 'WARNING' condition of the temperature when there is a rise in one of the solar cells from the solar module, captured by the thermal camera. In this case, the maximum temperature is also compared with the average

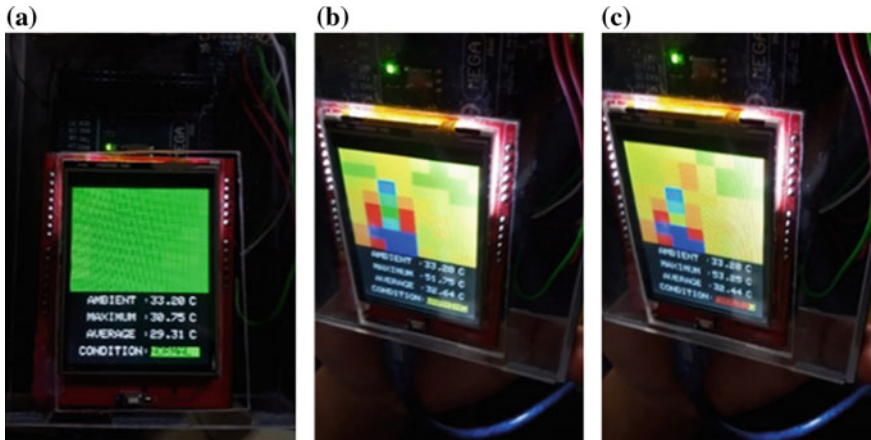


**Fig. 7** Example of the first condition that can be displayed a ‘NORMAL’ condition, b ‘WARNING’ condition, c ‘NORMAL’ condition

temperature as the ambient temperature is still showing the normal surrounding temperature that is sensed by the DS18B20 Temperature Sensor. From the calculation above, the value for the difference in temperature for both maximum and average is 19.11 °C which is within the range of 5 and 20 °C, the condition is set to be ‘WARNING’ as there is a slight rise of temperature on some of the solar cell.

Figure 7c shows the last condition of the temperature when there is a significant difference between the maximum temperature and the average temperature. The value obtained from the calculation (which is 20.81 °C) clearly shown that the difference between the maximum and average temperature exceeds 20 °C, which is in this project is set to be the limit for the hotspot condition. Thus, the condition is set to be ‘FAULT’ to indicate that there is a hotspot phenomenon on the solar module that the camera captured.

The results of captured temperature from thermal camera breakout used in this project show look convincing as it can be captured and displays an 8 × 8 array of temperature in the form of the heat map. Distance between the thermal camera and the surface of the solar panel is set to exact 1 m, as it can capture an image of the covered area of 3.6 m as the wide-angle view of the thermal camera lens is 60°. The value of temperatures captured by the sensor is shown in the form of the heat map, and only the highest temperature from the 64 arrays of data is shown in the parameter of the display alongside with ambient, average and condition of solar panel whether it has a hotspot or not. However, the values obtained will be not accurate if the thermal camera is moved further away from the surface of the solar panel. It can be said that the accuracy of the thermal camera used in this project decrease over distance. Thus, the camera needs to be close to the solar panel, which is at the maximum 1 m so that it can give the coverage field of view up to 3.6 m<sup>2</sup>.

## 5 Conclusion

This paper proposed a method for detecting and analyzing the hotspot in the PV module. The developed algorithm is proved to be effective and can perform its job without any interruption. However, there are certain things that can be added or improvise in this research in order to make it more functional and accurate. One of the improvements is to use the higher resolution of the thermal sensors. In addition, the system should be designed to consider different emissivity of the target object. For a better result, advanced image processing method could be implemented into the system to locate the hotspot accurately.

**Acknowledgements** The authors gratefully acknowledge Universiti Malaysia Pahang (UMP) under UMP Research Grant (RDU1703128) for their financial support and facilities.

## References

1. Khambalkar V, Nage S (2010) Renewable energy: an assessment of public awareness
2. Dhimish M, Holmes V, Mather P, Sibley M (2018) Novel hot spot mitigation technique to enhance photovoltaic solar panels output power performance. *Sol Energy Mater Sol Cells* 179:72–79
3. Dhimish M, Holmes V, Mehrdadi B, Dales M, Mather P (2018) PV output power enhancement using two mitigation techniques for hot spots and partially shaded solar cells. *Electr Power Syst Res* 158:15–25
4. Islam M, Hasan G, Ahmed I, Amin M, Dewan S, Rahman MM (2019) Infrared thermography based performance analysis of photovoltaic modules. In: 2019 international conference on energy and power engineering (ICEPE), Dhaka, Bangladesh, pp 1–5
5. Kaplanis S, Kaplani E (2011) Energy performance and degradation over 20 years performance of bp c-Si PV modules. *Simul Model Pract Theory* 19(4):1201–1211
6. Ibarra-Castaneda C, Bendada A, Maldague X (2011) Infrared vision applications for the nondestructive testing of materials. In: 5th pan American conference for NDT, Cancun
7. Samantaray P, Sasmita S (2016) Performance of solar photovoltaic module under partial shading conditions. In: 2016 10th International conference on intelligent systems and control (ISCO), pp 1–4
8. Salazar AM, Macabebe EQB (2016) Hotspots detection in photovoltaic modules using infrared thermography. In: MATEC web of conferences, vol 70, p 10015
9. Ngo GC, Macabebe EQB (2016) Image segmentation using K-means color quantization and density-based spatial clustering of applications with noise (DBSCAN) for hotspot detection in photovoltaic modules. In: 2016 IEEE region 10 conference (TENCON), pp 1614–1618
10. Ramspeck K, Schenk S, Duphorn D, Metz A, Meixner M (2014) In-line thermography for reliable hot spot detection and process control. *Energy Proc* 55:133–140
11. Moretón R, Lorenzo E, Narvarte L (2015) Experimental observations on hot-spots and derived acceptance/rejection criteria. *Sol Energy* 118:28–40

# Comparative Analysis for LED Driver with Analog and Digital Controllers



Shaheer Shaida Durrani, Abu Zaharin, Bakri Hassan  
and Ruhaizad Bin Ishak

**Abstract** The trend of utilizing light emitting diodes (LEDs) in some applications has attracted the attention of many researchers, to study its applications. This article investigates the performance analysis of the dc–dc converter systems based on analog and digital controllers for a low voltage dc–dc buck converter, to drive strings of LEDs at different conditions, to judge system’s robust performances. This converter comprises of a single controller, working with a voltage control feedback system, in a continuous conduction mode. The analog and digital type-3 controllers are designed for the said system while using standard frequency response techniques. Simulations are shown to validate the design and the response of these controllers under various dynamic load conditions.

**Keywords** Buck converter · Controller · DC–DC converter

## 1 Introduction

The LEDs driver can be easily divided into two main classes, i.e. constant current controller and a constant voltage controller. For constant current LEDs driver; their current–voltage (I–V) characteristics are very much similar to conventional p–n junction diodes. The buck converter design in this paper regarding LED driver is implemented as a constant current source. Analog, as well as digital controllers relating to LED, are designed and compared.

According to the report of [1], conventional voltage regulation of the DC–DC converter is made with the help of analog control techniques. Analog control systems give high bandwidths, though it is theoretically infinite [2]. The analog controller reacts almost immediately to perturbation because of the continuous sampling of the analog signal and the increased slew rate of the operational amplifiers. Duty cycle is developed with the process of comparing the values of error voltage to a sawtooth

---

S. S. Durrani (✉) · A. Zaharin · B. Hassan · R. B. Ishak  
Sustainable Energy & Power Electronics Research (SuPER), Faculty of Electrical & Electronics Engineering, University Malaysia Pahang, Pekan, Pahang, Malaysia  
e-mail: [shaheerdurrani@homail.com](mailto:shaheerdurrani@homail.com)

signal. However, an analog system is physically developed from some discrete hardware that includes controller gains or algorithms, along with an excessive number of components. With the advancements in the designing of the controller processor such as DSP (Digital Signal Processor) and microcontrollers, the application of digital control is now become a powerful candidate in the coming variants of switch mode power supplies.

With reference to an article [3], a significant technological breakthrough has been witnessed in power electronics because of the development of enabling technologies that improves the performance of power systems with its relevance to higher efficiency and reduced cost. Furthermore, it has been discussed in the article [4, 5], that with an adaptation of digital control approach a significant energy efficient system can be achieved. According to articles [6, 7], it has also been found that since LEDs system based on digital control system are energy efficient systems, are recommended for dimming applications.

Most of the digital processors are mostly immune to the aging and environmental or parameter variations phenomena. The complexity issue related to the control system can be implemented easily with a software algorithm [8]. Furthermore, a microcontroller which is used as a digital controller for voltage regulation through the feedback system has the ability to do multi-tasks, as discussed in [9, 10]. It has been noted during the design process, the very first component which influences the overall performance of the digital controller is the analog to digital converter (ADC). The digital controller produces a delay in the output, which is required to sample the feedback and compute the error. Various methods of digital controller design have been discussed. According to the article [11], a discrete pole placement approach has been used, whereas frequency domain design is employed [12], and controller design with the help of suitable allocation of poles and zeros is reported in [13]. It is reported that most of the DC–DC converters use type-3 controllers, as discussed in [14]. The implementation of 3P3Z (3-pole 3-zero) of the digital controller using DSC (Digital Signal Controller) that needs only one input channel with analog to digital conversion capabilities if voltage mode control is used.

Concerning an article [14], two PWM outputs are required, which are operated by MOSFET control. Various low-cost digital devices provide such operational requirements; the objective is to design the control system with the aims to get an acceptable processing time, for the desired system. Thus it is important to discuss that information losses do occur during the operation of quantization, output resolution, acquisition times and processing times can be accentuated by the limitations in an inexpensive digital implementation. Buck converter either digital or analog is not an ideal device, it suffers from current and voltage ripples due to the switching operation of the semiconductor device, and this problem tends to be larger at high switching frequencies. Some applications use a digital or analog converter, depending upon the favorable controller for their designated application. To do analyzes regarding the selection of the best kind of controller either analog or digital for the application comprises of LEDs, a comparative analysis has been required between the digital and analog controllers and in this regard a comprehensive analysis has been done in this paper.

## 2 Modelling of the Controller

In these proposed controllers, analog and digital controllers are designed to regulate the control of the LEDs. The fastest and simplest method of designing and implementing a digital control is to make it in the analog domain and transpose it in its digital equivalent. During designing the desired controller, a basic mathematical model is essentially required. The converter model of the particular system has been taken from the work done in [11], according to which, the system is designed for the optimum performance of the backlight system. This said system consists of two strings of LEDs, along with sensing resistances in each string (each string consists of three LEDs), a synchronous buck converter and current controllers in each string, with a feedback mechanism. The model of the multi-string LEDs with its current controllers, and sensing resistors is discussed in the article [15]. This approximation does not influence the dynamic response of the converter.

The same circuit model of article [15], is represented by the small signal equivalent model, comprising of the nonlinear components, by using Vorperian averaged-switch model as discussed in the articles [10] and [15].

Hence concerning articles [16–20], the control-to-output transfer function has been calculated with the help of the following equation, which is based on the work with reference to the articles [10] and [15].

$$\frac{v_o}{d} = \left[ \frac{1 + sR_c C}{1 + s \left( R_c C + (R_{LOAD}/R_L)C + \frac{L}{R_{LOAD} + R_L} \right) + s^2 LC \left( \frac{R_{LOAD} + R_c}{R_{LOAD} + R_L} \right)} \right] \quad (1)$$

## 3 Parameter Calculations

With reference to articles [16–18], the buck converter output filter storage elements are selected to satisfy the allowed ripple magnitudes of the inductor current and capacitor voltage. The numeric value of the inductor can be found using the following Eq. (2) as discussed in article [14].

$$L = \frac{DV_{IN}(1 - D)}{f_s \Delta I} = 150 \mu\text{H} \quad (2)$$

Meanwhile, the value of the capacitor is dependent on the allowed output ripple voltage, since the capacitor of the output filter in a buck converter is connected in parallel with the load. Concerning an article [15], the capacitor in the output can be found by using the following equation.

$$C = \frac{DV_{IN}(1 - D)}{8f_s^2 L \Delta I v_c} = 100 \mu\text{F} \quad (3)$$

**Table 1** Key parameter list of the DC–DC power stage

Parameter	Value
Input Voltage (VIN)	24 volts
Output Voltage (VO)	13 volts
Output Current (IO)	400 mA
Frequency	200 kHz
Parasitic	Rc = 150 m Ω Rl = 370 m Ω
Ripple Inductor Current	0.2 A
Ripple Output Voltage	1.2 m Volts

Each string of LEDs is rated at 200 mA, and thus, buck converter needs to deliver a total output current of 400 mA. The key components and parameters for the design of buck driver are shown in Table 1.

A type III compensation that uses a PID controller consist of two zeros and three poles is implemented in this compensator [16, 17]. The transfer function of this type of compensation network is presented in Eq. (4),

$$G_C(s) = \frac{R_1 + R_2 \left( s + \frac{1}{R_3 C_3} \right) \left( s + \frac{1}{(R_1 + R_2) c_1} \right)}{R_1 R_2 C_2 s \left( s + \frac{c_3 + c_3}{R_3 C_2 C_3} \right) \left( s + \frac{1}{R_2 c_1} \right)} \quad (4)$$

The design of the voltage mode feedback controller for the buck converter is based on Eq. (1) and the parameters presented in Table 1. The load of the buck converter is assumed to be resistive (RLOAD), such that;

$$V_{out} = I_{out} \times R_{out} \quad (5)$$

In this paper, RLOAD is considered equal to the parallel combination of two LED strings. Therefore, the effective resistance of each string, RSINGLE\_STRING, is the series combination of equivalent DC resistance of the LED that can be derived such as;

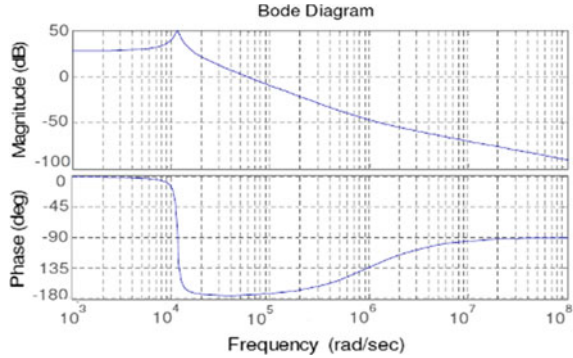
$$R_{EQU} = \frac{V_{FWD}}{I_{LED-String}} \quad (6)$$

By taking into account, the on-resistance related to the MOSFETs (RMOSFET) and the sensing resistor (RSENSE) [15], the following RLOAD can be estimated. Since there are three LEDs per string and the typical forward voltage of the chosen LED is 3.5 V. Thus the equivalent DC resistance of the LED strings [8] is calculated as;

$$R_{EQU} = 3 \times \frac{3.5}{0.2} = 52.5 \Omega \quad (7)$$



**Fig. 1** Open-loop bode plot of the buck driver



Therefore, the resistance of each string;

$$R1_{single} = R_{EQU} + R_{FET} + R_S = 52.5 + 1.8 + 0.68 = 54.98 \Omega \tag{8}$$

$$\text{Hence, Total load} = R1_{SINGLE} // R3_{SINGLE} = 27.49 \Omega \tag{9}$$

Substituting the values of total load and the parameter values from Table 1, the transfer function for the buck driver is simplified as,

$$G_p(s) = \frac{2.4 \times 10^{-5}s + 24}{7.495 \times 10^{-9}s^2 + 6.343 \times 10^{-5}s + 1} \tag{10}$$

Then, the open loop Bode plot of the above transfer function is obtained (refer to Fig. 1). The transfer function has two conjugate poles at  $-(4.23 \pm j10.75) \times 10^{-3}$  radian/s, and a left half plane zero at  $-1 * 10^6$  rad/s. Based on these results, a suitable type III compensation (PID) network is designed to meet the requirement for gain, crossover frequency, and phase margins (recommend two zeros and three poles). The two zeros are required to boost up the phase's value with 180°, to undo the influence of the double output pole. Above stated transfer function for the stated above type III compensator has been shown in the following Eq. (11). i.e.

$$H_C(s) = \frac{\omega_{po} \left[ \frac{s}{\omega_{z1}} + 1 \right] \times \frac{s}{\omega_{z2}} + 1}{s \left[ \frac{s}{\omega_{p2}} + 1 \right] \times \left[ \frac{s}{\omega_{p3}} + 1 \right]} \tag{11}$$

where, the  $\omega_p$  and  $\omega_z$  coefficients show the values of angular frequencies of the poles and zeros of the compensator. For the sake of simplicity, the angular frequencies have been replaced by frequencies in Table 1. The frequencies (angular) of the said poles and zeros, as well as the numeric values of the passive components of the compensator, are presented in the following Eqs. (12)–(16) i.e.

$$\omega_{z1} = \frac{1}{C_1 \times R_2} \tag{12}$$

$$\omega_{z2} = \frac{1}{R_1 * C_1 \times R_3} \tag{13}$$

$$\omega_{p0} = \frac{1}{(C_1 + C_3) \times R_2} \tag{14}$$

$$\omega_{p2} = \frac{(C_1 + C_3)}{R_1 \times C_1 \times C_3} \tag{15}$$

$$\omega_{p3} = \frac{1}{R_3 \times C_2} \tag{16}$$

By carefully selecting the particular frequencies for the poles and zeros of the stable system, which has the potential for the quicker response of the converter at load changes. The positions of the poles and zeros are selected on the base of the parameters of the buck converter, with the help of simple approximate method, as discussed in Eqs. (17) and (18).

$$F_{LC} = \frac{1}{2.\pi . \sqrt{C_{out} \times L_{out}}} \tag{17}$$

$$F_{ESR} = \frac{1}{2.\pi . ESR . C_{out}} \tag{18}$$

where,  $V_{ramp}$  is the magnitude of the sawtooth signal, where  $f_x$  is designated as crossover frequency, and  $f_{sw}$  is designated for the switching frequency of the converter. Whereas, the  $F_{LC}$  and  $F_{ESR}$  are considered in Eqs. 14 and 15. Thus, by various calculations, different parameters of the buck converter are shown in Table 2, whereas the values of the poles and zeros frequencies for the compensator (type III) are shown in Table 2.

From Eqs. 9–13, the  $R_1$  is chosen up to 20 kΩ. The numeric values of different passive components for the analog type III compensator has been calculated and is shown in the following Table 3.

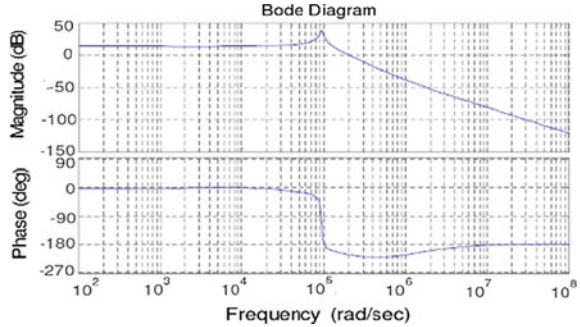
**Table 2.** Poles and zeros based on the parameters of the converter

$F_{p0}$	$F_{p2}$	$F_{p3}$	$F_{z1}$	$F_{z2}$
$\frac{V_{ramp} \cdot f_x}{V_{in}}$	$F_{ESR}$	$\frac{f_{sw}}{2}$	$\frac{F_{LC}}{2}$	$F_{LC}$
2.30 kHz	10.61 kHz	100 kHz	0.79 kHz	1.5 kHz

**Table 3.** Type III compensator passive components

$R_1$	$R_2$	$R_3$	$C_1$	$C_2$	$C_3$
20 kΩ	1.5 kΩ	47 kΩ	6800 pF	0.22 nF	0.022 μF

**Fig. 2** Closed-loop bode plot of the buck driver



Then, by using Matlab/Simulink environment, the PID controller has been designed with the position of poles at the origin as well as at  $(9.79 \pm j11.74) * 10^4$  and positions of zeros at  $-968$  radians/s, as well as at  $-6.83 * 10^3$  rad/s, respectively, as shown in Fig. 1. The Bode plot of the closed loop of the driver concerning Fig. 2, shows that the system bandwidth is almost 32 kHz, and the phase margin is about  $35^\circ$ . The calculated transfer function of the designed PID controller is based on Eq. (4), which is,

$$G_C(s) = (3.26 \times 10^6) \times \frac{s^2 + 7.80 \times 10^5 + 6.62 \times 10^8}{s^3 + 1.96 \times 10^5 s^2 + 9.58 \times 10^9 s} \tag{17}$$

The analog controller transfer function is needed to be transformed into its digital equivalent, for comparative analysis, by using matched pole-zero methods with the help of a sampling frequency of  $20 \mu\text{s}$ . Thus, the z-transform of the transfer function is as follows;

$$\text{Digital compensator} = \frac{8.976z^5 - 7.654z^2 - 8.954z + 7.676}{z^3 - 1.021z^2 + 0.02093z + 0.0005105} \tag{18}$$

### 4 Simulation

The performances of the proposed controllers for the LED driver have been verified through Matlab/Simulink. The LEDs are modeled in Simulink by the mathematical accord between the applied voltage to the current (load current) flowing through the LEDs. The forward voltage drop across the LEDs are deduced from Eq. (19).

$$V = iR_s + nV_T \ln\left(\frac{i}{r_s}\right) \tag{19}$$

where,  $n$  is considered as constant,  $i$  is considered as the forward current in the LEDs,  $V_T$  is the numeric value of thermal voltage, and  $I_s$  is the value of saturation current. The controllers are designed to have 24 V as input voltage, 13 V as output voltage and output current of 0.4 A. Since the designated load is LED, its resistive nature depends on the junction temperature. The increasing in junction temperature, its resistive values vary from high to low. Different step sizes of period 0.02 s are used to reduce the resistive values of the LED's load, from range a of 20 to 90%. Three different cases are carried out for analysis.

**Case 1:** In the first case, the load is reduced by 10%. From the simulation, it has been observed that the analog controller is comparatively unable to maintain the tracking outputs both in output voltage and current, as compared to the digital controller (refer to Figs. 3 and 4 for analog/digital controller performance respectively). Whereas, the output voltage is slightly lesser than 13 volts, which in turn, slightly increases the load current.

**Case 2:** In the second case, the load variations are increased up to 40%. It is observed that the output responses of both controllers are more or less comparable. However, it is observed that there are more ripples present in the output response of the digital controller than the output response of the analog controller as presented in Fig. 5 (analog controller) as well as in Fig. 6 (digital controller) respectively.

**Case 3:** The last scenario is about to have a load variation of up to 90% as shown in Figs. 7 and 8 respectively. It is observed that at the first instant the performance of the

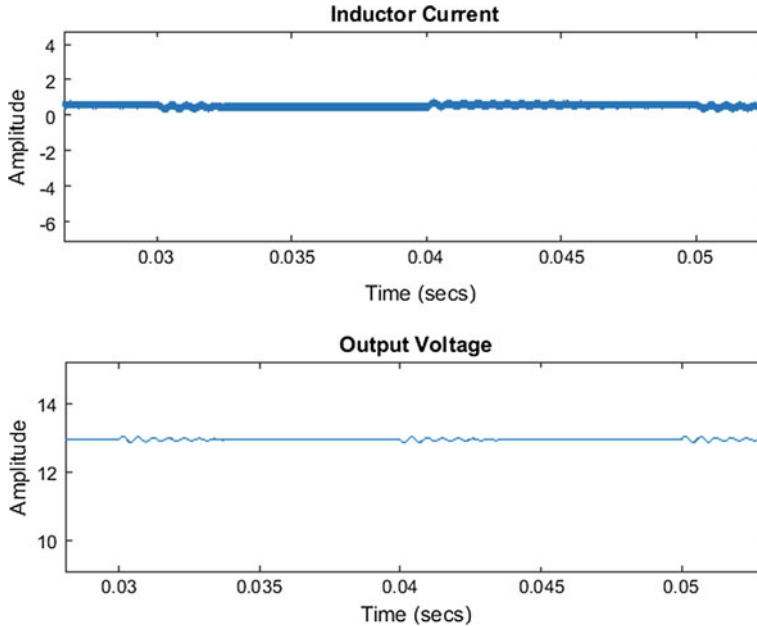


**Fig. 3** 10% reduces load variation of the analog controller

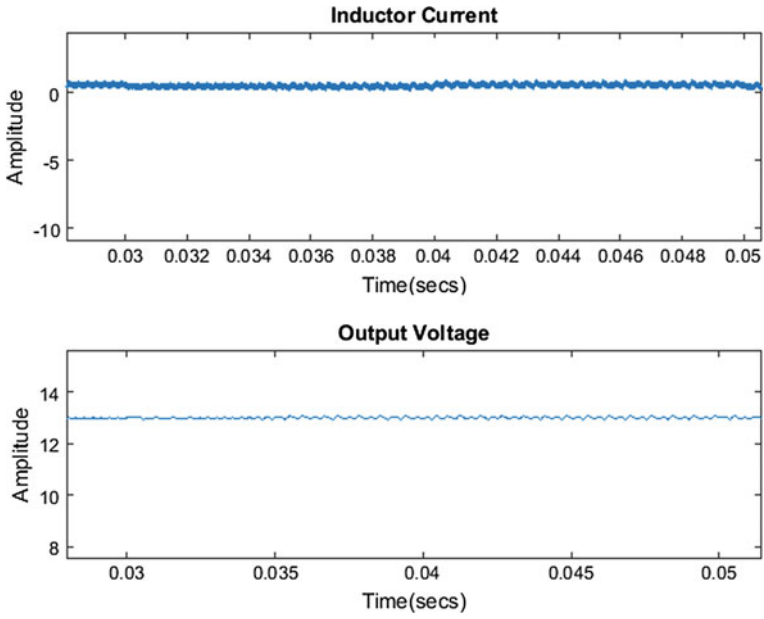


Fig. 4 10% reduces load variation of digital controller

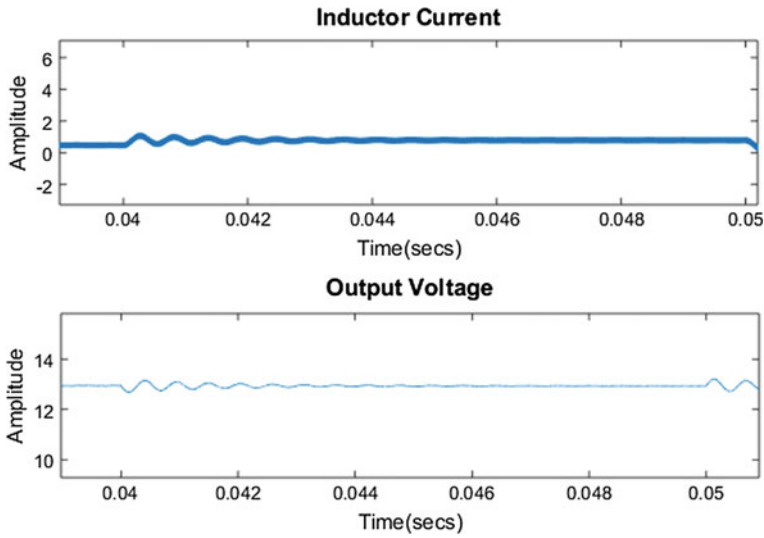


Fig. 5 40% increase load variation of the analog controller

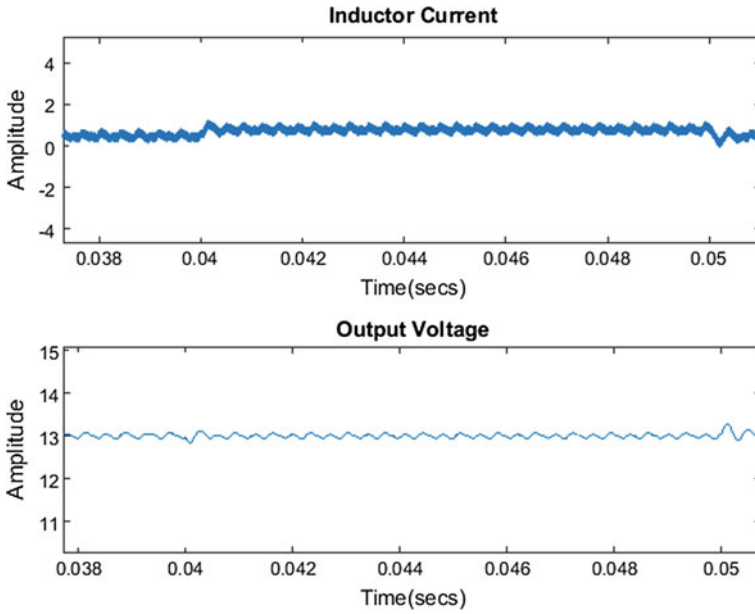


Fig. 6 40% increase in load variation of the digital controller

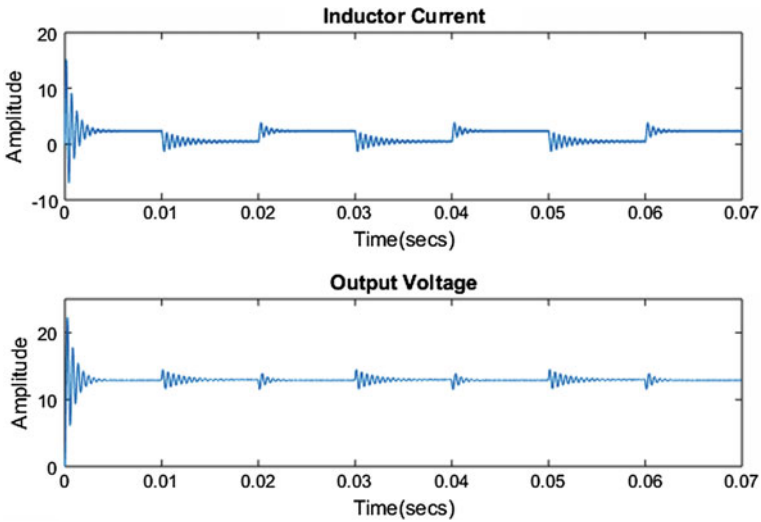
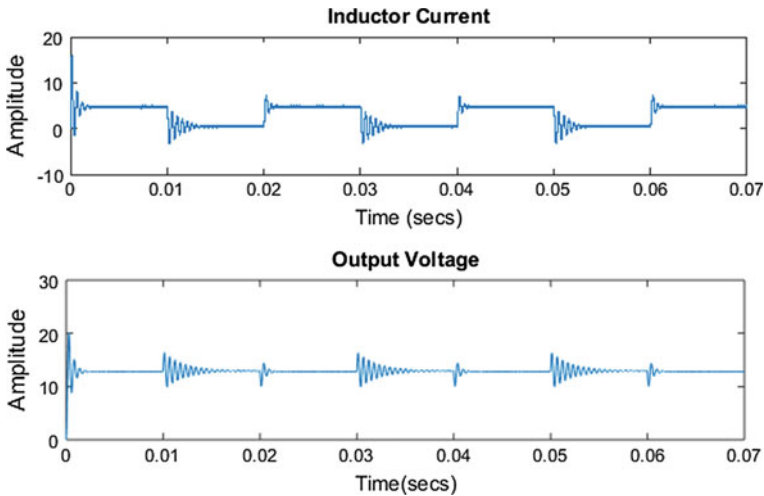


Fig. 7 The output of the analog controller with 90% increase variations



**Fig. 8** The output of the digital controller with 90% increase variations

analog and digital controller is look alike. But if the results are observed precisely, it is shown that the response of the digital controller has larger spikes in magnitude than an analog controller for sudden change variation in its tracking outputs.

## 5 Conclusions

The above results suggest that, for taking care of LED load variations, both the controllers (analog and digital) have different performances under various junction temperature conditions. Analog controller suits to the conditions where abrupt changes in load variation that possible for junction temperature, whereas digital controllers, should be used where there is a likelihood of small changes of variations. From the simulation analysis, both controllers do not show optimum performances under different conditions of junction temperature. The only possibility is to give optimum performances to all variations in LEDs load is through the use of a controller that can hold the characteristics of both analog and digital controllers. The analog compensator, as well as digital controller, have been designed, to make an analytical comparison and to highlight the advantages as well as disadvantages of each controller, designed for a particular LED load. It has been observed that the analog controller requires a number of calculations to calculate the different parameters of the analog components, which are used for the compensator and it has been noted that if the parameters of the converter are needed to be changed the mathematical calculations must be done again to get the new values of the compensator components. Whereas, the main advantage of the digital controller is its adaptability. Systems which are based on digital control have been seen to replace the analog control to obtain more

reliable, efficient, and versatile power converters. Simulations in Simulink environment validate the methods used for implementing digital controllers, and it has also been observed that digital controller can be used for synchronous buck converters without any further recalculating different parameters of the converter as long as the small variations remain in LED load.

**Acknowledgements** The author would like to acknowledge Universiti Malaysia Pahang and Fundamental Research Grant RDU170128 for financially supporting the project.

## References

1. Soman S, Sangeetha TS, Bindu S (2015) Development of digital controller for synchronous buck converter. In: 2015 International conference on signal processing, computing and control (ISPCC), pp 30–35, 24 Sep 2015
2. Etz R, Daraban SR, Petreus DM, Rusu AR (2010) A Comparison between digital and analog control for a buck converter. In: 33rd International spring seminar on electronics technology, pp 314–319, 12 May 2010
3. Navaro D, Lucía O, Barragán LA, Urriza I, Jiménez O (2013) High-level synthesis for accelerating the FPGA implementation of computationally demanding control algorithms for power converters. *IEEE Trans Ind Informat* 9(3):1371–1379
4. Swathi CA, Kumar SH, Annappa AR (2014) Smart street lighting system based on sensors using PLC and SCADA. In: Proceedings of the 2nd international conference on current trends in engineering and management ICCTEM 2014, Mysore, Karnataka, India, July 2014
5. Hwang JHPIC (2017) A current mode digital controlled buck-boost DC–DC Converter for LED driver. *IEEC J Integ Circu Sys* 3(1)
6. Brown S (2015) Digital control in LED drivers delivers better dimming in lamps. *LEDs MAGZINE*
7. Nguyen Van Ha (2014) Design of a digital controller for an LED driver with a digital dimming. *IEICE Electron Expr* 11(4):1–6
8. Emadi A, Khaligh A (2009) Integrated power electronic converters and digital control. CRC Press/Florida, US. ISBN: 13–978–1439800690
9. Martin TW, Ang SS (1995) Digital control for switching converters. In: Proceedings of the IEEE international symposium on industrial electronics, pp 480–484, 10 July 1995
10. Buso S, Mattavelli P (2006) Digital control in power electronics. Morgan and Claypool, San Rafael, CA
11. Cho JH, Seong HW, Jung SM, Park JS, Moon GW, Young MJ (2010) Implementation of digitally controlled phase shift full bridge converter for server power supply. In: Proceedings in IEEE energy conversion congress and exposition, pp 802–809, 12 Sep 2010
12. Kocybik PF, Bateson KN (1995) Digital control of a ZVS full-bridge DC–DC converter. In: Proceedings in 10th annual applied power electronics conference and exposition, pp 687–693
13. Lim JG, Lim SH, Chung SK (2007) Digital control of phase- shifted full-bridge PWM converter. In: Proceedings of 7th international conference power electronics, pp 772–777, 22 Oct 2007
14. Basso C (2014) Switch-mode power supplies. McGraw-Hill Education, New York, US. ISBN: 0071823468, 9780071823463 2014
15. Hasan J (2012) topics on light-emitting-diode driver research. <http://www.scholarworks.uark.edu>
16. Vorperian V (1990) Simplified analysis of PWM converters using the model of PWM switch. Part I: continuous conduction mode. *IEEE Trans Aerosp Electron Syst* 26(3):490–496



17. Guo L, Hung JY, Nelms RM (2009) Evaluation of DSP-based PID and fuzzy controllers for DC–DC converters. *IEEE Trans Ind Electron* 56(6):2237–2248
18. Guo L (2007) Implementation of digital PID controllers for DC–DC converters using digital signal processors. *IEEE Int Electro/Information Technology*, pp 306–311
19. Zamierczuk MK, Cravens II RC, Reatti A (1994) Closed-loop impedance of PWM buck derived DC–DC converters. *IEEE Int Symp on Circuits and Systems*, pp 61–64
20. Narendra P (2007) Disturbance accommodation control of a buck converter using a fixed point digital signal processor. MS thesis, Dept Elect Eng, Univ Arkansas, Fayetteville

# Characterization of Positive Porous Electrode Felt for Organic Redox Flow Battery Application



A. C. Khor, K. F. Chong and M. R. Mohamed

**Abstract** The newly emerging organic redox flow battery (RFB) as one of the most promising technology for energy storage system due to their flexible molecule modification. Nevertheless, the study on treated electrode in electrocatalytic activity for organic chemistry is limited. Most of the conventional studies reported a single treatment for carbon porous electrode and mostly focus on vanadium electrochemistry. To investigate the effect of sulphonation and oxidation of carbon felt in organic active material, two-stage surface treatment involving acid with thermal treatment was introduced in this study. The electrochemical investigation of acid treated felt and pristine felt were performed using cyclic voltammetry (CV) for selected positive electrolyte benze-1,4-diol in supporting acid—sulfuric acid. The results disclosed the potential of acid treated felt with good reversibility in cyclic voltammetry analysis with increase anodic peak potential.

**Keywords** Carbon felt · Surface modification · Benze-1,4-diol

## 1 Introduction

Electrochemical energy storage system has been recognized as a potential technology in term of enhancing the output from unsteady renewable resource and maintaining the grid stability associated with distributed generation. It has outranged electrical and mechanical due to their robust characteristics, shorter response time and faster compared to others. Electrochemical Energy Storage (ESS) offers a lower environmental impact for user especially compare to mechanical storage systems (pumped water, compressed water, flywheel etc.), as it can be sited nearer to the consumer area. Among electrochemical systems, redox flow battery (RFB) represents one of

---

A. C. Khor · M. R. Mohamed (✉)  
Faculty of Electrical and Electronics Engineering, Universiti Malaysia Pahang,  
26600 Pahang, Malaysia  
e-mail: [rusllim@ump.edu.my](mailto:rusllim@ump.edu.my)

K. F. Chong  
Faculty of Industrial Science and Technology, Universiti Malaysia Pahang,  
26300 Pahang, Malaysia

© Springer Nature Singapore Pte Ltd. 2020

A. N. Kasruddin Nasir et al. (eds.), *InECCE2019*, Lecture Notes in Electrical Engineering 632, [https://doi.org/10.1007/978-981-15-2317-5\\_74](https://doi.org/10.1007/978-981-15-2317-5_74)

the promising large-scale energy storage solutions for stationary energy storage. RFB offers environmentally friendly for stationary-large energy storage and might soon dominate mobility application [1]. The most established vanadium system is initialized and pioneered by Skyllas-Kazakos research group [2], with to the advantageous of electrolyte crossover elimination and reasonable energy densities ( $20\text{--}35\text{ Wh L}^{-1}$ ). Driven by restriction of inorganic characteristics such as vanadium material reserves and their narrow temperature range, organic couples mainly quinone, received much attention recently on their chemistry and biochemistry by means of advantageous of having infinite chemical space and broader design space via molecular modification. Felt is one of the favorable electrode candidates for organic redox flow battery (ORFB) due to its resistance toward strong acid and broader operating potential. Nevertheless, carbon felt suffers from severe drawbacks such as inferior hydrophilic, low surface area as well as poor kinetic reversibility and electrochemical activity, which might result in poor battery performances of RFB. Morphology and surface chemistry of electrode are strongly affected both kinetic and concentration polarization. Therefore, carbon felt is subjected to pre-treatment before taking role in charge-discharge of RFB to enhance the kinetic reversibility by reducing charge transfer resistance, electrochemical active area, and wettability properties. Several modification methods have been widely investigated in order to increase the active surface area and kinetic reversibility of carbon felt electrode. Single stage surface modification such as thermal, chemical, and plasma treatment [3–8] were proposed to achieve more electroactive surface area of carbon felt by introducing more oxygen functional group onto the surface. A large investigation [9–11] involving single stage surface modification were conducted with most of the research, however, only focusing on the electrochemical reaction of modified felt with vanadium ions. Only limited number of studies reported the investigation of treated felt in quinone based electroactive material. Therefore, the study on potential porous electrode surface characterization must be well understood for electrochemical kinetics of electrode along with selected quinone electroactive material such as benzene-1,4-diol. Worth to mention that the main objective of this paper is to investigate the effect of acid treated felt with comparison of untreated felt in benze-1,4-diol.

## 2 Methodology

### 2.1 Material Preparation

For felt investigation, electrolytes with active species were prepared by dissolving 0.1 M benzene-1,4-diol (also known as 1,4-benzenediol) in 1 M  $\text{H}_2\text{SO}_4$ .

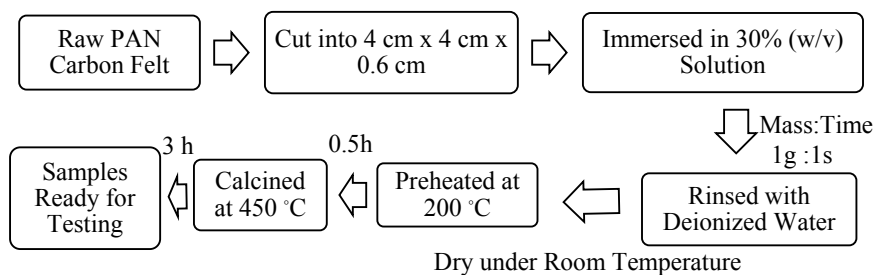


Fig. 1 Flow for the fabrication of treated felt samples

## 2.2 Felt Preparation

Polyacrylonitrile (PAN) based carbon felt (4 cm × 4 cm × 0.6 cm) was used as pristine electrode material for comparison and further modifications. The similar PAN type felt was used to undergo two-stage surface treatment. The undertaken stage for surface treatment illustrated in Fig. 1. For acid treated, the carbon felt sample was treated by immersing in acid treated carbon felt sample was treated by immersing in 30% (w/v) of sulfuric acid solution with mass against time ratio of 1 to 1. After that, the treated felt samples were rinsed by using deionized water to remove the excessive solution. The samples were left for drying under room temperature. Following these, treated felt samples were preheated at 200 °C for 0.5 h, and subsequently calcined at 450 °C for 3 h under N<sub>2</sub> atmosphere in a horizontal furnace. The representation of sulfuric acid treated with thermal was known as CF<sub>H<sub>2</sub>SO<sub>4</sub></sub> was used.

## 2.3 Electrochemical Investigation

For the felt investigation, an autolab potentialstat, M101 with a higher current rate was hired. The CV studies also employed a three-electrode system configuration, where the carbon felt sample replaced the glassy carbon electrode. A piece of 0.25 cm × 0.25 cm was cut from 4 cm × 4 cm × 0.6 cm sample using cutter tool with a platinum wire was used to hook up the felt. This setup was repeated with different types of treated felt. Platinum wire and silver-silver chloride (Ag|AgCl) were used as counter and reference electrodes, respectively. For CV measurements, the electrode potential was swept initially from 0 to 1.0 V versus Ag|AgCl, and back to 0 V versus Ag|AgCl in the reversed scan from 10 to 20 mV s<sup>-1</sup>.

### 3 Result and Discussion

The cyclic voltammograms of untreated felt in benzene-1, 4-diol solution is measured using glassy carbon electrode with scanning rates ranging  $2\text{--}10\text{ mV s}^{-1}$ . CVs illustrated in Fig. 2 have shown two proton-electron peaks as one at the positive and another one lies at a negative potential. These peaks correspond to the electrochemical formation of benzene-1,4-diol. As the potential was scanned cathodically, peak cathodic current ( $I_{pc}$ ) is observed which the current is distributed by the delivery of BQ ion via diffusion from the bulk solution. As time passed the diffusion layer becomes thicken and this slows down the diffusion of BQ ion to the surface of electrode, as this caused the decrease in cathodic current as the scan continued.

Cyclic voltammetry was performed from 2 to  $10\text{ mV s}^{-1}$  displayed an increase of anodic current ( $I_{pa}$ ) from 0.078 to 0.200 A. As observed in Table 1, peak cathodic current ( $I_{pc}$ ) for pristine felt is decreasing from  $-0.052\text{ A}$  to  $-0.171\text{ A}$  with the increasing of scan rates.

The reversibility of treated felt is considered poor when  $\Delta E_a$  is approximately 0.605 V, while  $|I_{pa}/I_{pc}|$  is larger than 1. Overall, the cyclic voltammetry projected in

**Fig. 2** Cyclic voltammetry of pristine felt in 0.1 M benzene-1,4-diol in 1 M of  $\text{H}_2\text{SO}_4$  with range of scan rate from 2 to  $10\text{ mV s}^{-1}$

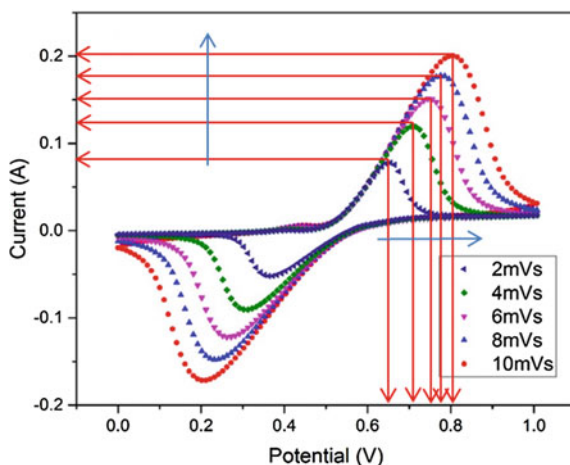


**Table 1** Measured data for untreated felt in 0.1 M benzene-1,4-diol in 1.0 M of  $\text{H}_2\text{SO}_4$  in term of anodic current ( $I_{pa}$ ), cathodic current ( $I_{pc}$ ) and potential ( $E_p$ )

Scan rate, mV/s	$I_{pa}$ , A	$I_{pc}$ , A	$E_{pa}$	$E_{pc}$	$\Delta E_a$	$I_{pa}/I_{pc}$
2	0.078	-0.052	0.655	0.363	0.292	-1.50
4	0.119	-0.090	0.705	0.312	0.393	-1.32
6	0.151	-0.121	0.745	0.262	0.483	-1.24
8	0.178	-0.147	0.775	0.232	0.543	-1.27
10	0.200	-0.171	0.806	0.201	0.605	-1.17

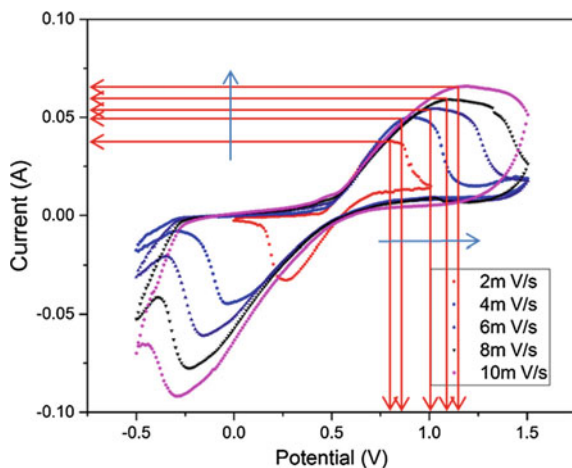


**Fig. 3** Cyclic voltammety curves of acid with thermal treated felt, CF<sub>H<sub>2</sub>SO<sub>4</sub></sub> in 0.1 M benzene-1,4-diol in 1 M H<sub>2</sub>SO<sub>4</sub> ranging from 2 to 10 mV s<sup>-1</sup>

**Table 2** Measured data for acid with thermal treated felt in 0.1 M benzene-1,4-diol in 1.0 M of H<sub>2</sub>SO<sub>4</sub> in term of anodic current (I<sub>pa</sub>), cathodic current (I<sub>pc</sub>) and potential (E<sub>p</sub>)

Scan rate, mV/s	I <sub>pa</sub> , A	I <sub>pc</sub> , A	E <sub>pa</sub>	E <sub>pc</sub>	ΔE <sub>a</sub>	I <sub>pa</sub> /I <sub>pc</sub>
2	0.0265	0.033	0.790	0.266	0.524	-0.80
4	0.0419	-0.044	0.905	-0.040	0.945	-0.95
6	0.0464	-0.060	1.031	-0.158	1.189	-0.77
8	0.052	-0.075	1.100	-0.223	1.323	-0.72
10	0.0581	-0.085	1.117	-0.278	1.395	-0.68

Fig. 3 presented C<sub>r</sub>E<sub>r</sub> mechanism that indicated the reversibility in a homogeneous chemical reaction. The definition of C is homogeneous chemical reaction, E indicated electron transfer step and subscript r represent reversibility.

Note that the difference between anodic and cathodic peak potential is presented in Tables 1 and 2, where anodic peak potential for CF<sub>H<sub>2</sub>SO<sub>4</sub></sub> is higher than pristine carbon felt. Noticed that the value of |I<sub>pa</sub>/I<sub>pc</sub>| is nearer to 1 with the peak separation (ΔE<sub>a</sub>) is near to 0.059 V when the scan rate is 2 mV s<sup>-1</sup>, indicated good reversibility of BQ ion. The results suggested that treated CF<sub>H<sub>2</sub>SO<sub>4</sub></sub> improves the electrode electrochemical activity which leads to a lower anodic peak value and higher cathodic peak value. From observation, the anodic current for CF<sub>H<sub>2</sub>SO<sub>4</sub></sub> decreases compared to untreated felt ranged from 0.0265 to 0.0582 A for all scan rate.

## 4 Conclusion

The investigation to compare the effect acid treated with untreated carbon felt. As the medium energy storage in RFB, the electrolyte and electrode determined the capacity. The redox reaction of electrolyte in active area affected by the electrode reaction kinetics and the resistance of the battery. It is necessary to investigate the pros and cons of treated carbon felt at which can provide a reference to extend the organic-based RFB application. In this study, two-stage treatment involving acid and thermal was investigated for carbon felt modification for the organic-based positive electrolyte. The activity and reversibility of modified carbon felt with benze-1-diol has been reported. The sulphonation with oxidation in carbon felt has increased the value of anodic electrode potential 0.135–0.311 V of the selected positive electrolyte from 2 to 10 mV s<sup>-1</sup>.

**Acknowledgements** This study was part of the Ph.D. Programme of Khor Ai Chia and funded through Research Acculturation Collaborative EVort (RACE) RDU151316, Ministry of Education Malaysia and Postgraduate Research Grant Scheme (PGRS) PGRS160376, Universiti Malaysia Pahang.

## References

1. Zhang C, Zhang L, Ding Y, Peng S, Guo X, Zhao Y, He G, Yu G (2018) Progress and prospects of next-generation redox flow batteries. *Energy Storage Material* (15):324–350
2. Skyllas-Kazacos M, Rychick M, Robins R (1998) All-vanadium redox battery. Google Patents (US4786567A)
3. Moreno-Castilla C, Ferro-Garcia M, Joly J, Bautista-Toledo I, Carrasco-Marin F, Rivera-Utrilla J (1995) Activated carbon surface modifications by nitric acid, hydrogen peroxide, and ammonium peroxydisulfate treatments. *Langmuir* (11):4386–4392
4. Sun B, Skyllas-Kazacos M (1992) Chemical modification of graphite electrode materials for vanadium redox flow battery application—part II. Acid treatments. *Electrochimica Acta* 37(13):2459–2465
5. Sun B, Skyllas-Kazacos M (1992) Modification of graphite electrode materials for vanadium redox flow battery application—I. Thermal treatment. *Electrochimica Acta* 37(7):1253–1260
6. Wu X, Xu H, Xu P, Shen Y, Lu L, Shi J, Fu J, Zhao H (2014) Microwave-treated graphite felt as the positive electrode for all-vanadium redox flow battery. *Journal of Power Sources* 263:104–109
7. Jiang H, Shyy W, Ren Y, Zhang R, Zhao T (2019) A room-temperature activated graphite felt as the cost-effective, highly active and stable electrode for vanadium redox flow batteries. *Applied Energy* 233:544–553
8. Jiang H, Shyy W, Wu M, Zhang R, Zhao T (2019) A bi-porous graphite felt electrode with enhanced surface area and catalytic activity for vanadium redox flow batteries. *Applied Energy* 233:105–113

9. Hawthorne KL (2014) Iron-ligand electrokinetics towards an all-iron hybrid redox flow battery (Doctoral dissertation). Retrieved from Open Access Theses and Dissertations Database (Accession No.:1405002859)
10. Zhou H, Zhang H, Zhao P, Yi B (2006) A comparative study of carbon felt and activated carbon based electrodes for sodium polysulfide/bromine redox flow battery. *Electrochimica Acta* 51(28):6304–6312
11. Kok MD, Khalifa A, Gostick JT (2016) Multiphysics simulation of the flow battery cathode: cell architecture and electrode optimization. *Journal of Electrochemical Society* 163(7):A1408–A1419